C55.612/2: 970-71

A UNITED STATES
DEPARTMENT OF
COMMERCE
PUBLICATION

COLLECTED REPRINTS: 1970-1971
WAVE PROPAGATION LABORATORY

U.S. DEPARTMENT OF COMMERCE
NATIONAL OCEANIC AND ATMOSPHERIC ADMINISTRATION
Environmental Research Laboratories

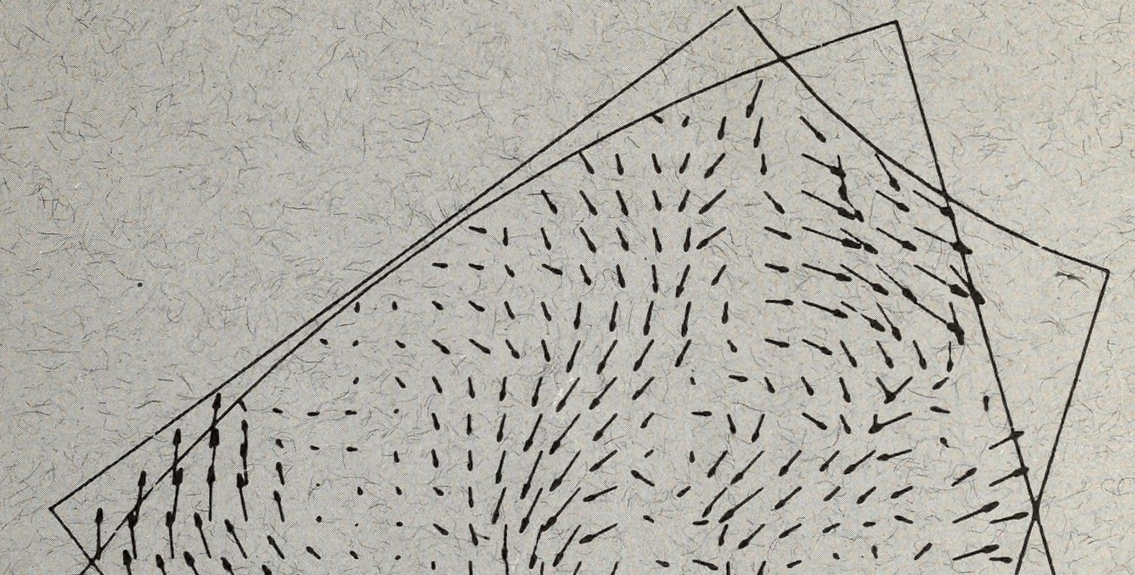

PENNSYLVANIA STATE UNIVERSITY
NOV 20 1972
DOCUMENTS COLLECTION

BOULDER,
COLORADO
August 1972

U.S. DEPARTMENT OF COMMERCE
Peter G. Peterson, Secretary

NATIONAL OCEANIC AND ATMOSPHERIC ADMINISTRATION
Robert M. White, Administrator

ENVIRONMENTAL RESEARCH LABORATORIES
Wilmot N. Hess, Director

Collected Reprints: 1970-1971
Wave Propagation Laboratory

BOULDER, COLO.
August 1972

U. S. Depository Copy

Digitized by the Internet Archive
in 2012 with funding from
LYRASIS Members and Sloan Foundation

http://archive.org/details/collectedreprin197071wave

FOREWORD

Advances in geophysical research frequently occur through new or improved measurement techniques. Since its creation in 1967, the Wave Propagation Laboratory has focused its resources on developing new methods for remote sensing of atmospheric parameters. The philosophy of this approach is that remote probing is not merely an extension of standard in situ measurements but typically produces orders-of-magnitude more information on the medium than previously available. As a result, totally new insights on the internal structure and processes of the atmosphere are obtained.

This second volume of Collected Reprints of the Wave Propagation Laboratory comprises work published from January 1, 1970 through December 31, 1971. The papers contained in this volume have been selected to minimize inclusion of duplicate or extraneous material. Readers should note that only the abstracts of WPL NOAA Technical Reports and Memorandum Reports (obtainable through the National Technical Information Service, Operations Division, Springfield, Virginia 22151) are included in this volume.

It is hoped that this and subsequent volumes will provide a summary of the results of this laboratory that will be useful and stimulating to both researchers and interested laymen. The insights already provided by these new techniques of remote sensing clearly demonstrate the potential of this field.

C. Gordon Little

C. Gordon Little

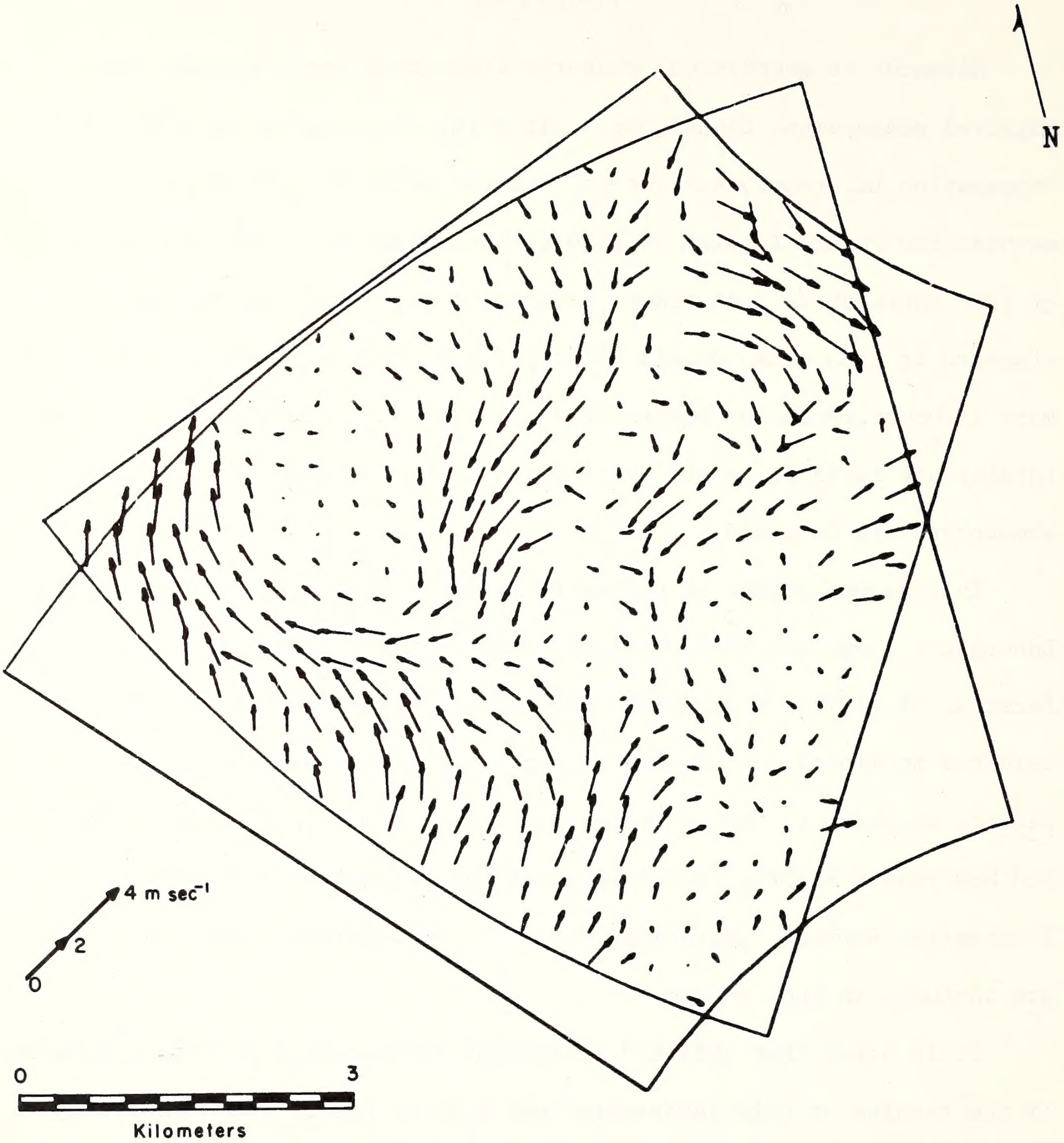

Cover:

Two-dimensional vector eddy flow field obtained from the radial velocity fields measured by two Doppler radars operated in the COPLAN scanning mode. Data was obtained east of the Rocky Mountain foothills on January 3, 1962, during light, steady snowfall.

CONTENTS

SECTION I

Basic Wave Propagation Studies

Theoretical, experimental and equipmental studies of the propagation of waves through a medium.

Page

A. Acoustic and Acoustic Gravity Waves

1. Clifford, S. F., and E. H. Brown, Propagation of Sound in a Turbulent Atmosphere, *Journal of Acoustical Society of America* 48, No. 5, 1123-1127, 1970. 1

2. Cook, R. K., Penetration of a Sonic Boom into Water, *Journal of Acoustical Society of America* 47, No. 3, 1430-1436, 1970. 6

3. Strand, O. N., Numerical Study of the Gain Pattern of a Shielded Acoustic Antenna, *Journal of Acoustical Society of America* 49, No. 6, 1698-1703, 1971. 13

4. Bedard, A. J., Seismic Response of Infrasonic Microphones, *Journal of Research of the NBS - C. Engineering and Instrumentation* 75, No. 1, 41-45, 1971. 19

See also papers 22-31, 51-52, 57, 60-61, 67.

B. Radio Waves

5. Taylor, W. L., and K. Sao, ELF Attenuation Rates and Phase Velocities Observed from Slow-Tail Components, *Radio Science* 5, No. 12, 1453-1460, 1970. 24

6. Dougherty, H. T., The Application of Stationary Phase to Radio Propagation for Finite Limits of Integration, *Radio Science* 5, No. 1, 1-6, 1970. 32

7. Dougherty, H. T., Diffraction by Irregular Apertures, *Radio Science* 5, No. 1, 55-60, 1970. 38

8. McGavin, R. E., H. T. Dougherty, and C. B. Emmanuel, Microwave Space and Frequency Diversity Performance Under Adverse Conditions, *Transactions of the IEEE, Communications Technology,* COM-18, No. 3, 261-263, 1970. 44

9. Thayer, G. D., Reflections from Elevated Layers in Transhorizon Radio Propagation, *Proceedings of the AGARD/EWPP XVIth Symposium,* No. 70, pp. 16-1 through 16-13, 1970. 47

10. Thayer, G. D., Radio Reflectivity of Tropospheric Layers, *Radio Science* 5, No. 11, 1293-1299, 1970. 60

11. Dougherty, H. T., R. E. McGavin, and R. W. Krinks, An Experimental Study of the Atmospheric Conditions Conducive to High Radio Fields, Telecommunications Research Report, OT/ITSRR 4, 1970. 67

See also papers 32-45, 51-52.

C. Optical Waves

12. Clifford, S. F., and J. W. Strohbehn, The Theory of Microwave Line-of-Sight Propagation Through Turbulent Atmosphere, *Transactions of the IEEE, Antennas and Propagation,* AP-18, No. 2, 264-274, 1970. 68

13. Lawrence, R. S., G. R. Ochs, and S. F. Clifford, Measurements of Atmospheric Turbulence Relevant to Optical Propagation, *Journal of Optical Society of America* 60, No. 6, 826-830, 1970. 79

14. Lawrence, R. S., and J. W. Strohbehn, A Survey of Clear-Air Propagation Effects Relevant to Optical Communications, *Proceedings of the IEEE* 58, No. 10, 1523-1545, 1970. 84

15. Bouricius, G. M. B., and S. F. Clifford, Experimental Study of Atmospherically-Induced Phase Fluctuations in an Optical Signal, *Journal of Optical Society of America* 60, No. 11, 1484-1489, 1970. 107

16. Bouricius, G. M. B., and S. F. Clifford, An Optical Interferometer Using Polarization Coding to Obtain Quadrature Phase Components, *The Review of Scientific Instruments* 41, No. 12, 1800-1803, 1970. 113

17. Kleen, R. H., and G. R. Ochs, Measurements of the Wavelength Dependence of Scintillation in Strong Turbulence, Letter to the Editor, *Journal of Optical Society of America* 60, No. 12, 1695-1697, 1970. 117

18. Clifford, S. F., Temporal Frequency Spectra for a Spherical Wave Propagating Through Atmospheric Turbulence, *Journal of Optical Society of America* 61, No. 10, 1285-1292, 1971. 120

19. Clifford, S. F., G. M. B. Bouricius, G. R. Ochs, and M. H. Ackley, Phase Variations in Atmospheric Optical Propagation, *Journal of Optical Society of America* 61, No. 10, 1279-1284, 1971. 128

20. McNice, G. T., and V. E. Derr, Relative Power Losses at the Two Mirrors of an Asymmetric, Confocal Laser Interferometer, *Journal of Optical Society of America* 60, No. 8, 1035-1037, 1970. 134

21. Calfee, R. F., A Note on Terminologies Used in Gaseous Absorption Processes, NOAA Technical Report, ERL 211-WPL 15, 1971. 137

See also papers 46-52.

SECTION II

Remote Sensing Concepts

Theoretical and experimental studies of remote sensing concepts.

A. Acoustic and Acoustic Gravity Waves

22. Little, C. G., Acoustic Sounding of the Lower Atmosphere, *Meteorological Monographs* 11, No. 33, 397-404, 1970. 138

23. Beran, D. W., Acoustic Radar Detection Techniques, *Proceedings of FAA Turbulence Symposium,* March 22, 1971. 146

24. Beran, D. W., Acoustics: A New Approach for Monitoring the Environment near Airports, *American Institute of Aeronautics and Astronautics, Journal of Aircraft* 8, No. 11, 934-936, 1971. 165

25. Hall, F. F., Acoustic Remote Sensing of Temperature and Velocity Structure in the Atmosphere, *Proceedings of NATO Advanced Study Institute, Statistical Methods and Instrumentation in Radio-Meteorology,* April 15-22, 1971, 167-180, 1971. 168

26. Beran, D. W., and B. C. Willmarth, Doppler Winds from a Bistatic Acoustic Sounder, *Proceedings of the 7th International Symposium on Remote Sensing of Environment* 1, No. 10259-1-X, May 17-21, 1971, 1699-1714, 1971. 182

27. Hall, F. F., J. W. Wescott, and W. Simmons, Acoustic Echo Sounding of Atmospheric Thermal Wind Structure,,*Proceedings of the 7th International Symposium on Remote Sensing of Environment* 1, No. 10259-1-X, May 17-21, 1971, 1715-1732, 1971. 199

28. Beran, D. W., F. F. Hall, J. W. Wescott, and W. D. Neff, Application of an Acoustic Sounder to Air Pollution Monitoring, *Proceedings of Air Pollution, Turbulence and Diffusion Symposium,* New Mexico State University, December 7-10, 1971, 66-72, 1971. 218

29. Beran, D. W., C. G. Little, and B. C. Willmarth, Acoustic Doppler Measurements of Vertical Velocities, *Nature* 230, 160-162, 1971. 225

30. Wescott, J. W., W. R. Simmons, and C. G. Little, Acoustic Echo-Sounding Measurement of Temperature and Wind Fluctuations, ESSA Technical Memorandum, ERL TM-WPL 5, 1970. 228

31. Simmons, W. R., F. F. Hall, and J. W. Wescott, Acoustic Echo Sounding as Related to Air Pollution in Urban Environments, NOAA Technical Report, ERL 216-WPL 17, 1971. 229

See also papers 1-4, 51-52, 57, 60-62, 67.

B. Radio Waves

1. Active

32. Bean, B. R., and R. E. McGavin, Electromagnetic Phase Variability As A Measure of Water Vapor and Temperature Variations over Extended Paths, *AGARD Conference Proceedings No. 33,* Library of Congress Cat. No. 69-19961, 729-744, 1970. 230

33. Ottersten, H., Radar Observations of the Turbulent Structure in Shear Zones in the Clear Atmosphere, *Proceedings of the 14th Radar Meteorology Conference,* November 17-20, 1970, 111-116, 1971. 246

34. Bean, B. R., H. T. Dougherty, and R. E. McGavin, Remote Probes for the Study of Atmospheric Sources of Fading on Optical and Microwave Line-of-Sight Paths, *Proceedings of the 1971 International Symposium on Antennas and Propagation, Japan,* Vol. 2-IV B2, 237-238, 1971. 252

35. Bean, B. R., R. E, McGavin, R. Chadwick, and B. D. Warner, Preliminary Results of Utilizing the High Resolution FM Radar as a Boundary Layer Probe, *Boundary Layer Meteorology* 1, No. 4, 466-473, 1971. 254

36. Lhermitte, R. M., Measurement of Wind and Wind Field by Microwave Doppler Radar Techniques, *Proceedings of Symposium on Advances in Instrumentation for Air Pollution Control, Atmospheric Environment,* Vol. 5, 691-702, 1970. 262

37. Lhermitte, R. M., Dual Doppler Radar Observation of Convective Storm Circulation, *Proceedings of the 14th Radar Meteorology Conference,* November 17-20, 1970, 139-144, 1971. 275

38. Wilson, D. A., Doppler Radar Studies of Boundary Layer Wind Profile and Turbulence in Snow Conditions, *Proceedings of the 14th Radar Meteorology Conference,* November 17-20, 1970, 191-196, 1971. 281

39. Lhermitte, R. M., Probing of Atmospheric Motion by Airborne Pulse Doppler Radar Techniques, *Journal of Applied Meteorology* 10, No. 2, 234-246, 1971. 287

40. Lhermitte, R. M., and L. J. Miller, Doppler Radar Methodology for the Observation of Convective Storms, *Proceedings of the 14th Radar Meteorology Conference,* November 17-20, 1970, 133-138, 1971. 300

2. Passive

41. Decker, M. T., and E. J. Dutton, Radiometric Observations of Liquid Water in Thunderstorm Cells, *Journal of Atmospheric Sciences* 27, No. 5, 785-790, 1970. 306

42. Westwater, E. R., Microwave Determination of Low Altitude Temperature Profiles, *Proceedings of the 7th International Symposium on Remote Sensing of Environment* 1, No. 10259-1-X, May 17-21, 1971, 585-594, 1971. 312

43. Snider, J. B., Recent Results in Ground-Based Sensing of Atmospheric Temperature Profiles, *Proceedings of Symposium on Air Pollution, Turbulence and Diffusion,* December 7, 1971, New Mexico State University, 56-65, 1971. 323

44. Strand, O. N., Optimization of Frequencies Used in Indirect Sensing by Inversion, NOAA Technical Report, ERL 202-WPL 14, 1971. 333

45. Taylor, W..L., Review of Electromagnetic Radiation Data from Severe Storms in Oklahoma during April 1970, NOAA Technical Memorandum, ERL WPL-6, 1971. 334

See also papers 5-11, 50-51, 55-56.

C. Optical Waves

46. Schwiesow, R. L., and V. E. Derr, A Raman-Scattering Method for Precise Measurement of Atmospheric Oxygen Balance, Letter, *Journal of Geophysical Research* 75, No. 9, 1629-1632, 1970. 335

47. Derr, V. E., Research Problems in the Use of Lidar in Anti-Pollution Studies, *Proceedings of Workshops on Research Problems in Air and Water Pollution,* University of Colorado, August 3-15, 1970, 309-321, 1971. 339

48. Cohen, A., The Size Spectrum Determination of Spherical Aerosols by Light Scattering Method, *Proceedings of Air Pollution, Turbulence and Diffusion Symposium,* December 7-9, 1971, New Mexico State University, 93-99, 1971. 351

49. Strauch, R. G., V. E. Derr, and R. Cupp, Atmospheric Temperature Measurement Using Raman Backscattering, *Applied Optics* 10, No. 12, 2665-2669, 1971. 358

See also papers 12-21.

D. Combination and Comparison

50. Derr, V. E., and C. G. Little, A Comparison of Remote Sensing of the Clear Atmospheric by Optical, Radio, and Acoustic Radar Techniques, *Applied Optics* 9, No. 9, 1976-1992, 1970. 363

51. Little, C. G., V. E. Derr, R. H. Kleen, R. S. Lawrence, R. M. Lhermitte, and G. D. Thayer, Remote Sensing of Wind Profiles in the Boundary Layer, ESSA Technical Report, ERL 168-WPL 12, 1970. 380

SECTION III

Geophysical Environmental Studies

Theoretical and experimental studies of the physical nature of the environment.

52. Lerfald, G. M., and C. G. Little, D-Region Electron Temperature at the Northern Auroral Zone, *Radio Science* 5, No. 7, 1017-1028, 1970. 381

53. Stephenson, D. A., and R. G. Strauch, Water Vapor Spectrum Near 600 GHz, Letter to the Editor, *Journal of Molecular Spectroscopy* 35, No. 3, 494-495, 1970. 393

54. Bean, B. R., Turbulence and Irregularities of the Atmosphere, *Proceedings of the NATO Advanced Study Institute*, August 29 - September 6, 1969, 139-155, 1970. 395

55. Thayer, G. D., B. R. Bean, and B. A. Hart, World-Wide Characteristics of Refractive Index and Climatological Effects, *Proceedings of the AGARD/EWPP XVIth Symposium*, 3-1 through 3-13, 1970. 412

56. Hooke, W. H., The Ionospheric Response to Internal Gravity Waves: 1. The F_2 Region Response, *Journal of Geophysical Research, Space Physics* 75, No. 28, 5535-5544, 1970. 425

57. Georges, T. M., Amplification of Ionospheric Heating and Triggering of 'Spread F' by Natural Irregularities, *Journal of Geophysical Research, Space Physics* 75, No. 31, 6436-6438, 1970. 435

58. Georges, T. M., and W. H. Hooke, Wave-Induced Fluctuations in Ionospheric Electron Content: A Model for Indicating Some Observational Biases, *Journal of Geophysical Research, Space Physics* 75, No. 31, 6295-6308, 1970. 438

59. Hooke, W. H., The Ionospheric Response to Internal Gravity Waves: 2. Lower F Region Response, *Journal of Geophysical Research, Space Physics* 75, No. 34, 7229-7238, 1970. 452

60. Hooke, W. H., Ionospheric Response to Internal Gravity Waves: 3. Changes in the Densities of the Different Ion Species, *Journal of Geophysical Research, Space Physics* 75, No. 34, 7239-7243, 1970. 462

61. Hooke, W. H., Quasi-Stagnation Levels in the Ion Motion Induced by Internal Atmospheric Gravity Waves at Ionospheric Heights, *Journal of Geophysical Research* 76, No. 1, 248-250, 1971. 467

62. Hooke, W. H., Ionospheric Response to an Isotropic Spectrum of Internal Gravity Waves, *Journal of Planetary and Space Science* 18, 1793-1797, 1970. 470

63. Whitehead, J. D., and W. H. Hooke, Divergence of Ion Velocity in the E-Region Due to Vertical Winds, *Journal of Geophysical Research* 76, No. 10, 2523-2525, 1971. 477

64. Sterling, D. L., W. H. Hooke, and R. Cohen, Traveling Ionospheric Disturbances Observed at the Magnetic Equator, *Journal of Geophysical Research* 76, No. 16, 3777-3782, 1971. 480

65. Hooke, W. H., On the Role of Vertical Neutral-Gas Motions in Producing Ion Convergence at E-Region Heights, ESSA Technical Report, ERL 175-ITS 112, 1970. 486

66. Georges, T. M., A Program for Calculating Three-Dimensional Acoustic-Gravity Ray Paths in the Atmosphere, NOAA Technical Report, ERL 212-WPL 16, 1971. 487

67. Wilson, D. A., The Kinematic Behavior of Spherical Particles in an Accelerating Environment, NOAA Technical Report, ERL 187-WPL 13, 1970. 488

68. McFadden, J. D., C. W. Travis, R. O. Gilmer, and R. E. McGavin, Water Vapor Flux Measurements from ESSA Aircraft, *Proceedings of the Symposium on Tropical Meteorology,* June 2-11, 1970, B-III-1 through B-III-6, 1970. 489

69. Hart, B. A., G. D. Thayer, and H. T. Dougherty, Local and Diurnal Variations in Ground-Based Radio Refractivity Gradients at Tropical Locations, Telecommunications Research and Engineering Report OT/TRER 23, 1971. 495

Author Index 497

Further Reading Reference 505

Reprinted from Journal of Acoustical Society of America 48,
No. 5, 1123-1127, 1970.

Propagation of Sound in a Turbulent Atmosphere

S. F. Clifford and E. H. Brown

ESSA Research Laboratories, Boulder, Colorado 80302

Applying a perturbation technique to the correct form of the equation for the acoustic pressure field in a viscous turbulent atmosphere yields the power spectra for the amplitude and phase fluctuations of a propagating plane wave. The development includes the effects of absorption and removes the restrictions on wavenumber that previously prevented solution of the problem for other than ultrasonic frequencies. For a wide range of propagation parameters, the amplitude and phase spectra found by Tatarski for optical propagation are shown to be good approximations for acoustic waves. Complete expressions, without limitation on the assumed refractive-index spectra, determine the range of validity of this result and also provide an exact first-order solution.

INTRODUCTION

The first edition of the monograph by Tatarski[1] presents most of the early work on the propagation and scattering of waves in a turbulent fluid. For sound, the theory of Tatarski and earlier work of Mintzer[2–4] begins with an incorrect form of the equation for the pressure; and the condition that the wavelength λ and inner scale of turbulence l_0 satisfy the inequality $\lambda \ll l_0$ restricts the development to ultrasonic frequencies. Little[5] has emphasized the many advantages of acoustic probes in studies of the lower atmosphere—for typical acoustic radar research $l_0 < \lambda < L_0$, where L_0 is the outer scale of turbulence. The following analysis, based on the correct pressure equation, uses a technique suggested by Clifford[6] to obtain the first-order perturbation of sound waves without restriction on λ.

I. PRESSURE EQUATION

In 1953 Kraichnan[7] derived the correct form of the equation for the acoustic pressure field in a turbulent fluid, assuming that the Stokes relation holds and that the local velocity of sound c is a constant c_0—thus attributing all scattering to the turbulent velocity fluctuations. For the case of a plane unperturbed wave, Monin[8] developed a similar equation (neglecting the viscous terms) which expressed the randomness of the velocity of sound explicitly in terms of the temperature fluctuation ratio $\tau = T'/T_0$ by means of the perfect-gas approximation $c^2 = c_0^2(1+\tau)$. In his revised monograph Tatarski[9] generalized Monin's form of the equation to arbitrary unperturbed waves. Truesdell[10] made a careful analysis of the Stokes relation $\lambda_v/\mu_v = -\frac{2}{3}$, where λ_v is the volume viscosity and μ_v the shear viscosity, concluding on both theoretical and experimental grounds that the relation was completely invalid (experimentally, for atmospheric gases, $\lambda_v/\mu_v > 0$, with typical values ranging from a few hundred to 1000 for CO_2; in the atmosphere the ratio varies with water vapor). Since a subsequent paper will study backscatter from semi-infinite atmospheres, retention of viscous terms becomes essential; the backscatter solution is the first step in finding the gated reception of an acoustic radar pulse. A brief sketch of the derivation of the equation for the acoustic pressure field retaining both viscosities follows.

In a Newtonian fluid,[10] the stress t_{ij} depends linearly on the rate of deformation $e_{ij} = \frac{1}{2}(\partial_i v_j + \partial_j v_i)$:

$$t_{ij} = -p\delta_{ij} + \lambda_v e \delta_{ij} + 2\mu_v e_{ij}, \tag{1}$$

where p is the thermodynamic pressure, $e = e_{ii} = \partial_i v_i$, and λ_v, μ_v are constants of the mean fluid state. The continuity and momentum equations are

$$d_t \rho + \rho e = 0 \tag{2}$$

and

$$d_t(\rho v_i) + \rho v_i e = \partial_j t_{ij}, \tag{3}$$

where $\partial_i = \partial/\partial x^i$, $d_t = d/dt$, $\partial_t = \partial/\partial t$, and the particle time derivative d_t is related to the point time derivative ∂_t by $d_t = \partial_t + v_i \partial_i$. Writing $\nu = \mu_v/\rho_0$, $\eta = 2\nu + \lambda_v/\rho_0$ (for constant kinematic viscosity, the definition $\nu = \mu_v/\rho$ would destroy the linearity of Eq. 1) and substituting Eqs. 1 and 2 in Eq. 3 gives the *exact* Navier–Stokes equation,

$$\partial_t v_i+v_j\partial_j v_i=-\frac{1}{\rho}\partial_i p+\frac{\rho_0}{\rho}\nu\Delta v_i+\frac{\rho_0}{\rho}(\eta-\nu)\partial_i e. \qquad (4)$$

Since in general $\langle v_i\rangle=v_i^0\neq 0$, the left-hand-side terms in Eq. 4 involve *one* small fluctuating factor. With the notation $\rho_0/\rho=1+\xi$, the terms $-\xi/\rho_0\partial_i p$, $\xi\nu\Delta v_i$, and $\xi(\eta-\nu)\partial_i e$ include the product of *two* small fluctuations. Neglecting such terms gives

$$\partial_t v_i+v_j\partial_j v_i=-(1/\rho_0)\partial_i p+\nu\Delta v_i+(\eta-\nu)\partial_i e, \qquad (5)$$

which reduces to the customary form of the Navier–Stokes equation (see e.g., Batchelor[11]) on introduction of the Stokes relation.

Splitting the velocity into "longitudinal" and "transverse" parts (Kraichnan[7]) gives $v_i=u_i+w_i$, where w_i satisfies the set of equations

$$\partial_t w_i+w_j\partial_j w_i=\nu\Delta w_i-(1/4\pi r)*\partial_i\partial_j\partial_k(w_j w_k) \qquad (6a)$$

and

$$\partial_i w_i=0,\ \langle w_i\rangle=v_i^0 \qquad (6b)$$

($*$ indicates convolution), and subtracting Eq. 6a from Eq. 5 provides the equation relating the fluid velocity u_i due to sound waves and the acoustic pressure p_a to the turbulent velocity field w_i:

$$\begin{aligned}\partial_t u_i&+(1/\rho_0)\partial_i p_a\\ &=\nu\Delta u_i+(\eta-\nu)\partial_i e-w_j\partial_j u_i-u_j\partial_j w_i, \qquad (7)\end{aligned}$$

neglecting the second-order term $u_j\partial_j u_i$. Writing as in Monin[8] $p_a=\gamma p_0\pi$, $c^2=c_0^2(1+\tau)$, and noting that the acoustic pressure p_a varies adiabatically, gives Eqs. 2 and 7 as

$$e=--\partial_t\pi-w_i\partial_i\pi \qquad (8)$$

and

$$\begin{aligned}\partial_t u_i+c_0^2\partial_i\pi=-c_0^2\tau\partial_i\pi+\nu\Delta u_i&+(\eta-\nu)\partial_i e\\ &-w_j\partial_j u_i-u_j\partial_j w_i, \qquad (9)\end{aligned}$$

the second-order term in Eq. 8 again being neglected.

For slowly varying turbulence, $\pi(x_i,t)=e^{-i\omega t}\Pi(x_i,t)$, and the time derivative of Π can be neglected compared to that of $e^{-i\omega t}$. Taking the divergence of Eq. 9, introducing the new variable Π, substituting Eq. 8 in Eq. 9, and linearizing separately in the acoustic variables u_i, Π and the turbulence parameters w_i, τ leads to the equation

$$\begin{aligned}\left(1-i\frac{k}{c_0}\eta\right)\Delta\Pi+k^2\Pi&=-\partial_i(\tau\partial_i\Pi)\\ &+\frac{2i}{c_0k}\partial_i\partial_j(w_i\partial_j\Pi)-\frac{\eta}{c_0^2}\Delta(w_i\partial_i\Pi), \qquad (10)\end{aligned}$$

where $k=\omega/c_0$, which reduces to that of Tatarski[9] when $\eta=0$. When the last two right-hand-side terms are expanded and terms are compared in the result (real with real and imaginary with imaginary) in both cases, all terms containing η are negligible if η satisfies $\eta\ll c_0l_0$, which certainly holds in the atmosphere. Writing

$$d=k^2\eta/2c_0,\quad h^2=\frac{k^2}{1-2i(d/k)}\approx k^2+2ikd,\quad h\approx k+id,$$

gives the equation for the acoustic pressure field in the final form

$$\Delta\Pi+h^2\Pi=-\frac{h^2}{k^2}\partial_i(\tau\partial_i\Pi)+2i\frac{h^2}{c_0k^3}\partial_i\partial_j(w_i\partial_j\Pi). \qquad (11)$$

II. PERTURBATION SOLUTION

Let $\Pi=\Pi_0+\Pi_1$, Π_0 being an initial, damped, but unscattered plane wave traveling in the x direction; $\Pi_0=A_0e^{ihx}$:

$$\Delta\Pi_0+h^2\Pi_0=0. \qquad (12)$$

Then Π_1 satisfies the equation

$$\Delta\Pi_1+h^2\Pi_1=2i(h^2/k)\partial_x(n'\Pi_0), \qquad (13)$$

where the fluctuation in effective index

$$n'=-[(\tau/2)+(w_x/c_0)]$$

results from combination of the two right-hand-side terms in Eq. 11 using the acoustic refractive index $n=c_0/c=1-\tau/2$.

Assuming local homogeneity, n' and Π_1 possess the two-dimensional Fourier–Stieltjes representations

$$\Pi_1(x,y_\alpha)=\Pi_1(x,0)+\int d\rho(x,\kappa_\alpha)(1-e^{iy_\alpha\kappa_\alpha})$$

and (14)

$$n'(x,y_\alpha)=n'(x,0)+\int d\nu(x,\kappa_\alpha)(1-e^{iy_\alpha\kappa_\alpha}),$$

where $y_\alpha=(y,z)$, $\kappa_\alpha=(\kappa_y,\kappa_z)$, and $\kappa^2=\kappa_\alpha\kappa_\alpha$. Substitution of Eq. 14 reduces Eq. 13 to the two equations

$$\begin{aligned}\partial_x^2\Pi_1(x,0)&+h^2\Pi_1(x,0)\\ &=2i\frac{h^2}{k}\partial_x[n'(x,0)\Pi_0(x)]-\int\kappa^2d\rho(x,\kappa_\alpha), \qquad (15)\end{aligned}$$

and (using Eq. 15)

$$\begin{aligned}\partial_x^2d\rho(x,\kappa_\alpha)&+(h^2-\kappa^2)d\rho(x,\kappa_\alpha)\\ &=2i\frac{h^2}{k}\partial_x[d\nu(x,\kappa_\alpha)\Pi_0(x)]. \qquad (16)\end{aligned}$$

With $q(\kappa)=(h^2-\kappa^2)^{\frac{1}{2}}$, $q_0=h$, the elementary equation corresponding to both Eqs. 15 and 16 is

$$\partial^2{}_x f(x)+q^2 f(x)=\delta(x), \tag{17}$$

and then the identity $\partial(f*g)=\partial f*g=f*\partial g$ gives the solution of Eq. 16 as

$$d\rho(x,\kappa_\alpha)=2i(h^2/k)\partial_x f(x)*[d\nu(x,\kappa_\alpha)\Pi_0(x)], \tag{18}$$

and the solution of Eq. 15 as

$$\Pi_1(x,0)=2i(h^2/k)\partial_x f_0(x)*[n'(x,0)\Pi_0(x)]-2i\frac{h^2}{k}f_0(x)*$$
$$\times\int\kappa^2\partial_x f(x)*[d\nu(x,\kappa_\alpha)\Pi_0(x)], \tag{19}$$

where f_0 is the function f when $q=q_0$. Let $q=q_a+q_b$, where $q_a=Y(k-\kappa)(a+ib)$, $q_b=Y(\kappa-k)(b+ia)$, Y is the Heaviside step function,

$$\begin{aligned}Y(x)&=0,\ x<0,\\&=1,\ x\geq 0,\end{aligned}$$

and

$$\begin{aligned}a(\kappa)&=\tfrac{1}{2}(|q|^2+2kd)^{\frac{1}{2}}+\tfrac{1}{2}(|q|^2-2kd)^{\frac{1}{2}},\\ b(\kappa)&=\tfrac{1}{2}(|q|^2+2kd)^{\frac{1}{2}}-\tfrac{1}{2}(|q|^2-2kd)^{\frac{1}{2}}.\end{aligned} \tag{20}$$

Then, $a\geq b\geq 0$ and the only elementary solution of Eq. 17 satisfying the conditions

$$\lim_{|x|\to\infty}f(x)=0,\quad \int_{-\infty}^{\infty}f(x)dx=\frac{1}{q^2}$$

is $f(x)=-(i/2q)e^{iq|x|}$, for which

$$\partial_x f(x)=\tfrac{1}{2}[Y(x)-Y(-x)]e^{iq|x|}. \tag{21}$$

By using the condition $d\nu(-|x|,\ \kappa_\alpha)=0$ for a semi-infinite field of turbulence, the solution of Eq. 16 becomes explicitly

$$d\rho(x,\kappa_\alpha)=i\frac{h^2}{k}e^{iqx}\int_0^x dx'd\nu(x',\kappa_\alpha)e^{i(h-q)x'}$$
$$-i\frac{h^2}{k}e^{-iqx}\int_x^\infty dx'd\nu(x',\kappa_\alpha)e^{i(h+q)x'}, \tag{22}$$

where the first integral represents forwardscatter, and the second, backscatter.

III. AMPLITUDE AND PHASE SPECTRA

Since $|\Pi_1|\ll|\Pi_0|$, $\ln(\Pi/\Pi_0)\approx\Pi_1/\Pi_0$, and $\ln(\Pi/\Pi_0)=\ln(A/A_0)+i(S-S_0)\approx(A_1/A_0)+iS_1$, then the quantity $d\varphi(x,\kappa_\alpha)=d\rho(x,\kappa_\alpha)/\Pi_0(x)$ provides the Fourier–Stieltjes measures of amplitude ratio and phase of the scattered wave:

$$d\alpha(x,\kappa_\alpha)=\tfrac{1}{2}[d\varphi(x,\kappa_\alpha)+d\varphi^*(x,\ -\kappa_\alpha)]$$

and (23)

$$d\sigma(x,\kappa_\alpha)=(1/2i)[d\varphi(x,\kappa_\alpha)-d\varphi^*(x,\ -\kappa_\alpha)].$$

Writing $\epsilon=\arctan(2d/k)\approx 2d/k$, $|h^2|/k=k\sec\epsilon\approx k$, $Y_-=Y(k-\kappa)$, $Y_+=Y(\kappa-k)$, and using the fact that $n'(x)$ real implies $d\nu^*(x,\ -\kappa_\alpha)=d\nu(x,\kappa_\alpha)$,

$$d\alpha(x,\kappa_\alpha)=k\int_0^x dx'd\nu(x',\kappa_\alpha)\{Y_-e^{-(b-d)(x-x')}\sin[(k-a)(x-x')-\epsilon]+Y_+e^{-(a-d)(x-x')}\sin[(k-b)(x-x')-\epsilon]\}$$
$$+k\int_x^\infty dx'd\nu(x',\kappa_\alpha)\{Y_-e^{-(b+d)(x'-x)}\sin[(k+a)(x'-x)+\epsilon]+Y_+e^{-(a+d)(x'-x)}\sin[(k+b)(x'-x)+\epsilon]\}, \tag{24}$$

and

$$d\sigma(x,\kappa_\alpha)=k\int_0^x dx'd\nu(x',\kappa_\alpha)\{Y_-e^{-(b-d)(x-x')}\cos[(k-a)(x-x')-\epsilon]+Y_+e^{-(a-d)(x-x')}\cos[(k-b)(x-x')-\epsilon]\}$$
$$-k\int_x^\infty dx'd\nu(x',\kappa_\alpha)\{Y_-e^{-(b+d)(x'-x)}\cos[(k+a)(x'-x)+\epsilon]+Y_+e^{-(a+d)(x'-x)}\cos[(k+b)(x'-x)+\epsilon]\}. \tag{25}$$

Both $d\alpha$ and $d\sigma$ retain two integrals—the first representing forwardscatter and the second, backscatter.

For homogeneous turbulence, the two-dimensional refractive-index spectrum F_n satisfies

$$\langle d\nu(x',\kappa_\alpha)d\nu^*(x'',\kappa_\alpha')\rangle$$
$$=\delta(\kappa_\alpha-\kappa_\alpha')F_n(x'-x'',\ \kappa_\alpha)d^2\kappa_\alpha d^2\kappa_\alpha'. \tag{26}$$

Amplitude and phase, however, are homogeneous only in y_α planes; thus, F_A and F_S are functions of two values of x or, equivalently, of an "initial" point x and a separation $x'-x$. Using an obvious notation for the case $x'=x$,

$$\langle d\alpha(x,\kappa_\alpha)d\alpha^*(x,\kappa_\alpha')\rangle=\delta(\kappa_\alpha-\kappa_\alpha')F_A(x;\,0,\kappa_\alpha)d^2\kappa_\alpha d^2\kappa_\alpha', \tag{27}$$

and

$$\langle d\sigma(x,\kappa_\alpha)d\sigma^*(x,\kappa_\alpha')\rangle=\delta(\kappa_\alpha-\kappa_\alpha')F_S(x;\,0,\kappa_\alpha)d^2\kappa_\alpha d^2\kappa_\alpha'. \tag{28}$$

Substitution of Eqs. 26 and 24 in Eq. 27 yields

$F_A(x;0,\kappa_\alpha)$; similarly, Eqs. 26 and 25 in Eq. 28 give $F_S(x;0,\kappa_\alpha)$. Two facts facilitate the calculations; first, $Y_-Y_+=0$ for all κ; second, the "interference terms" represented by averages of products of forwardscatter and backscatter waves not only are small, but also are experimentally unobservable with other than physically unrealizable isotropic point receivers.

IV. THE FORWARDSCATTER SOLUTIONS

For forwardscatter with the source at the plane $x=0$, the value of x at the observation point equals the path length L. By neglecting the small phase shift ϵ and making the transformation $\xi=x'-x''$, $\zeta=x''$, F_A and F_S become

$$\begin{Bmatrix} F_A \\ F_S \end{Bmatrix} = k^2 \int_0^L d\xi F_n(\xi,\kappa_\alpha) \int_0^{L-\xi} d\zeta \times \{ Y_- e^{-(a-d)(2\zeta+\xi)} [\cos(k-a)\xi \mp \cos(k-a)(2\zeta+\xi)] + Y_+ e^{-(a-d)(2\zeta+\xi)} [\cos(k-b)\xi \mp \cos(k-b)(2\zeta+\xi)] \}. \tag{29}$$

Several valid approximations simplify the integrations. First, $b \ll k$ and $d \ll a$ for all κ imply $k-b \approx k$ and $a-d \approx a$. Second, after the ζ integration, the integrand will contain the factors

$$F_n(\xi,\kappa_\alpha) e^{-(b-d)(2L-\xi)}, \quad F_n(\xi,\kappa_\alpha) e^{-(b-d)\xi},$$

and

$$F_n(\xi,\kappa_\alpha) e^{-a(2L-\xi)}, \quad F_n(\xi,\kappa_\alpha) e^{-a\xi};$$

then, the inequalities $F_n(\xi,\kappa_\alpha) \approx 0$ for $\xi \geq L_0$ and $L \gg L_0$ imply that the factors are very nearly equal to

$$F_n(\xi,\kappa_\alpha) e^{-2(b-d)L}, \quad F_n(\xi,\kappa_\alpha),$$

and

$$F_n(\xi,\kappa_\alpha) e^{-2aL}, \quad F_n(\xi,\kappa_\alpha).$$

Third, since $F_n(\xi,\kappa_\alpha)$ is even and decreases rapidly with ξ, the odd part of the integrand contributes little to the ξ integral and can be neglected. Fourth, the definitions of $a(\kappa)$, $b(\kappa)$ imply

$$(b-d)/[(b-d)^2+(k-a)^2] \approx 0,$$
$$(k-a)/[(b-d)^2+(k-a)^2] \approx 1/(k-a),$$

for all $\kappa \leq k$; similarly,

$$a/[a^2+(k-a)^2] \approx 0, \quad k/[a^2+(k-a)^2] \approx 0,$$

for all $\kappa \geq k$. Then, Eq. 29 becomes

$$\begin{Bmatrix} F_A \\ F_S \end{Bmatrix} = k^2 \int_0^L d\xi F_n(\xi,\kappa_\alpha) \left\{ Y_- L e^{-(b-d)L} \left[\frac{\sinh(b-d)L}{(b-d)L} \mp e^{-(b-d)L} \frac{\sin 2(k-a)L}{2(k-a)L} \right] \cos(k-a)\xi + Y_+ \frac{e^{-aL}}{a} \sinh aL \cos k\xi \right\}. \tag{30}$$

Since $F_n(\xi,\kappa_\alpha)$ decreases rapidly with ξ and the periodic functions are bounded, the upper limit of integration can be extended to ∞ with little error. Substituting the three-dimensional refractive-index spectrum $\Phi_n(\kappa_0)$, where $\kappa_0^2=\kappa_x^2+\kappa^2$, defined by

$$\pi\Phi_n(\kappa_0) = \int_0^\infty F_n(\xi,\kappa_\alpha) \cos\kappa_x\xi d\xi,$$

gives the final form of the amplitude and phase spectra for forward scatter:

$$\begin{Bmatrix} F_A \\ F_S \end{Bmatrix} = \pi k^2 L Y_- e^{-(b-d)L} \left[\frac{\sinh(b-d)L}{(b-d)L} \mp e^{-(b-d)L} \frac{\sin 2(k-a)L}{2(k-a)L} \right] \Phi_n\{[(k-a)^2+\kappa^2]^{\frac{1}{2}}\} + \pi k^2 L Y_+ e^{-aL} \frac{\sinh aL}{aL} \Phi_n[(k^2+\kappa^2)^{\frac{1}{2}}]. \tag{31}$$

For $\kappa \ll k$, $a \approx k$, $2(k-a)L \approx \kappa^2 L/k$, $b-d \approx 0$, and the spectra coincide with those found by Tatarski[1]:

$$\begin{Bmatrix} F_A \\ F_S \end{Bmatrix} = \pi k^2 L \left(1 \mp \frac{k}{\kappa^2 L} \sin\frac{\kappa^2 L}{k}\right) \Phi_n(\kappa), \quad \kappa \ll k. \tag{32}$$

In a small interval about $\kappa=k$, $a \ll k$, $b \approx a \gg d$ and, by using $Y_-+Y_+=1$ and $kL \gg 1$, the spectra become

$$\begin{Bmatrix} F_A \\ F_S \end{Bmatrix} = \pi k^2 e^{-L(kd)^{\frac{1}{2}}} \frac{\sinh L(kd)^{\frac{1}{2}}}{(kd)^{\frac{1}{2}}} \Phi_n[(k^2+\kappa^2)^{\frac{1}{2}}],$$

$$k-\delta < \kappa < k+\delta. \tag{33}$$

For $\kappa \gg k$, $a \approx \kappa$. Thus,

$$\begin{Bmatrix} F_A \\ F_S \end{Bmatrix} = \frac{\pi k^2}{2\kappa} \Phi_n(\kappa), \quad \kappa \gg k. \tag{34}$$

Several comments on the various ranges are appropriate. Since $b-d \approx 0$, for $\kappa \ll k$, damping will be negligible at low wavenumbers; however, the damping will increase as $\kappa \rightarrow k$. Since $kL_0 > 1$, $\Phi_n(\kappa_0)$ decreases near $\kappa=k$ and, thus, F_A and F_S are smoothly decreasing in an open neighborhood of $\kappa=k$. Since $\Phi_n(\kappa)$ is decreasing, F_A and F_S continue to decrease even more rapidly for $\kappa \gg k$, and the solutions are independent of d. Finally, F_A and F_S differ from each other only for $\kappa < k$, where

$$\lim_{\kappa \to 0} F_A = 0$$

and

$$\lim_{\kappa \to 0} F_S = 2\pi k^2 L \Phi_n(0).$$

With the refractive index a passive additive, $\Phi_n(\kappa_0)$ varies in the same way as the velocity spectrum $\Phi_w(\kappa_0)$.

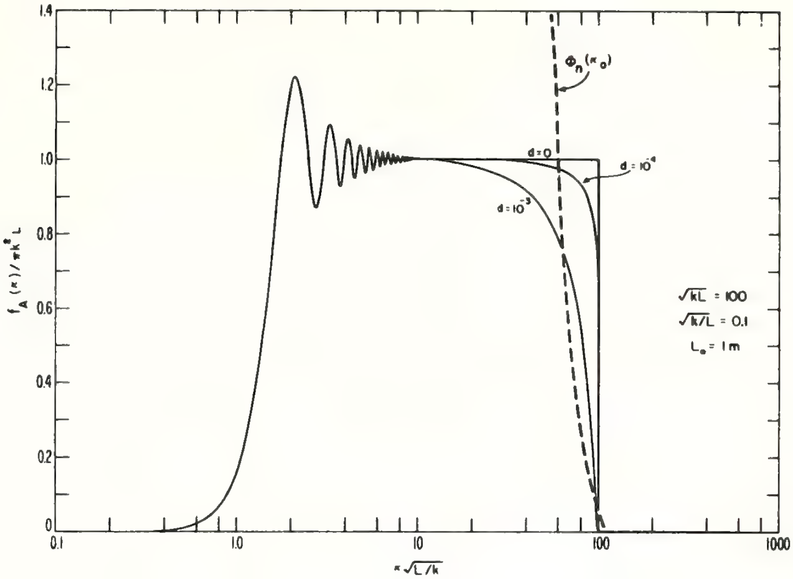

FIG. 1. Behavior of the amplitude filter functions $f_A(\kappa) = F_A(\kappa)/\Phi_n(\kappa_0)$ with normalized wavenumber $\kappa/(k/L)^{\frac{1}{2}}$ for the values $k = 10$ m^{-1} and $L = 10^3$ m. See text.

A study by Saffman[12] based on a hypothesis for *vorticity* moments found $\Phi_w(0)$ nonzero and finite; an earlier paper by Batchelor and Proudman[13] using a stronger assumption for *velocity* moments found a κ_0^2 dependence near $\kappa_0 = 0$, implying $\Phi_w(0) = 0$. The above results lend additional conformation to Saffman's conclusions, since $F_S(0) \neq 0$ can be expected on physical grounds (unlike amplitude, no dominant eddy scale is associated with phase, which implies a nonzero integral of the phase covariance over a y_α plane).

V. CONCLUSIONS

Figure 1 illustrates the behavior of the amplitude filter functions $f_A(\kappa) = F_A(\kappa)/\Phi_n(\kappa_0)$ with normalized wavenumber $\kappa/(k/L)^{\frac{1}{2}}$ for the values $k = 10$ m^{-1} and $L = 10^3$ m. The dashed line represents the inertial subrange spectrum ($\kappa_0^{-11/3}$) of refractive index for an outer scale $L_0 = 1$ m. The curves for three values of the absorption parameter $d = k^2\,\eta/2C_0$ clearly indicate that —for atmospheric propagation—only large values of attenuation produce noticeable effects in the observed amplitude and phase spectra. Given a reasonable value of the outer scale ($L_0 \geq 1$ m), the spectrum of turbulence causes a more rapid decay than absorption and, thus, emphasizes the region $\kappa \ll k$. The same conclusion follows for phase.

As a consequence, the amplitude and phase spectra found by Tatarski for the case of optical propagation also apply to acoustic propagation for most of the range of wavenumbers, path lengths, and attenuation coefficients found in typical experiments. Insertion of particular experimental parameters in Eq. 31 directly determines the relative size of the various terms. The exact expression (Eq. 29) gives the detailed behavior without restriction on wavelength, absorption, or path length. Since the development has placed no conditions on the form of $\Phi_n(\kappa_0)$, the relative sizes of the contributions from Eqs. 32–34 depend on the exact behavior of the assumed refractive-index spectrum.

---

[1] V. I. Tatarski, *Wave Propagation in a Turbulent Medium* (McGraw-Hill, New York, 1961).
[2] D. Mintzer, J. Acoust. Soc. Amer. **25**, 922 (1953).
[3] D. Mintzer, J. Acoust. Soc. Amer. **25**, 1107 (1953).
[4] D. Mintzer, J. Acoust. Soc. Amer. **26**, 186 (1954).
[5] C. G. Little, Proc. IEEE **57**, 571 (1969).
[6] S. F. Clifford, PhD thesis, Dartmouth College (1969).
[7] R. H. Kraichnan, J. Acoust. Soc. Amer. **25**, 1096 (1953).
[8] A. S. Monin, Sov. Phys. Acoust. **7**, 370 (1962).
[9] V. I. Tatarski, *Propagation of Waves in a Turbulent Atmosphere* (Nauka, Moscow, 1967) (in Russian).
[10] C. Truesdell, J. Rat. Mech. Anal. **1**, 125 (1952).
[11] G. K. Batchelor, *Fluid Mechanics* (Cambridge U. P., Cambridge, England, 1967).
[12] P. G. Saffman, Phys. Fluids **10**, S301 (1967).
[13] G. K. Batchelor and I. Proudman, Proc. Roy. Soc. (London) **A248**, 369 (1956).

2

Reprinted from Journal of Acoustical Society of America *__47__, No. 3, 1430-1436, 1970.*

Penetration of a Sonic Boom into Water

Richard K. Cook

Geoacoustics Group, Environmental Science Services Administration, Rockville, Maryland 20852

An aircraft in level flight at a supersonic speed over water produces a sonic-boom pressure on the water surface. Usually the N wave of the incident sound pressure moves across the surface at a subsonic speed, relative to the speed of sound in water. Therefore, the boom energy is totally reflected, and the sound pressure in the water falls off with depth below the surface. The penetration depth, comprising well over half of the underwater energy, is about the same as the N-waveform length on the surface. The analysis shows further that the wave reflected into the atmosphere has (a) two infinitely large pressure spikes at the leading and trailing edges of the N wave, and (b) a weak precursor and a weak tail. The same is true of the underwater wave just at the surface. The spikes, precursor, and tail have positive sound pressures and are even functions of distance from the center of the N wave.

INTRODUCTION

An aircraft in level flight through the atmosphere, in a straight line at a constant supersonic velocity, gives rise to a shock wave. This waveform might have a complicated pressure structure near the aircraft, but as it moves away with the speed of sound in a homogeneous atmosphere, it arranges itself into a stable sound waveform commonly called an N wave. Viewed in the large, the N wave forms the Mach cone accompanying the supersonic flight, with the axis of the cone being the straight line of the flight path. The wave including its audible effect is called the sonic boom.

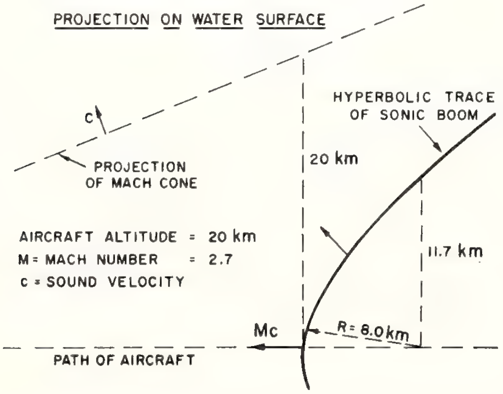

Fig. 1. Hyperbolic intersection of a Mach cone with the water surface.

For an aircraft in flight over a plane surface, such as a smooth body of water, the intersection of the Mach cone with the interface is a hyperbola, whose vertex advances over the surface with the supersonic velocity of the aircraft, and therefore has the same Mach number. Figure 1 shows the hyperbolic trace for a possible supersonic flight. The radius of curvature (8000 m) indicated for the axis of the hyperbola is substantially greater than a typical N-wave thickness, which is of the order of 100 m. This suggests that the principal features of the penetration of a sonic boom into water can be deduced from a plane N wave. Therefore, we base the analysis in what follows on plane incident waves that are tangent to the Mach cone at the vertex of its hyperbolic intersection with the water surface.

The present analysis has two main purposes. The first is to find the sound-pressure distribution underwater caused by the incidence of the sonic boom onto the water surface. The second is to find the waveform of the wave reflected into the atmosphere from the water surface.

The N wave in its ideal form is characterized by a discontinuous jump increase of sound pressure at the front of the wave, followed by a linear (in time and space) decrease, and terminated by a discontinuous jump increase, returning the pressure to its ambient atmospheric value. Atmospheric irregularities, such as the incompressible-flow turbulent eddies of the wind near the ground, can substantially change the structure of an N wave passing through. But various theoretical investigations (see e.g., DuMond *et al.*[1]) show that the waveform is a stable form for a sound wave traveling through a homogeneous atmosphere. Hubbard[2] and his associates frequently find it in almost perfect N-wave form, when measurements are made near the surface of the earth.

The air speeds of present and planned supersonic aircraft are less than 1000 m/sec and therefore are substantially less than the speed of sound in water (about 1500 m/sec). At speeds less than 1000 m/sec, the N wave originating from an aircraft in level flight has its angle of incidence (on the water surface) greater than 19°. This minimum angle of incidence is greater than the critical angle for the passage of a sound wave from air into water, which is about 14°. Each sinusoidal component of the N wave is therefore totally reflected from the surface and is accompanied by a plane wave in the water having a subsonic phase velocity, whose sound-pressure amplitude evanesces exponentially with depth below the surface. These subsonic waves are referred to as "inhomogeneous" by Brekhovskikh,[3] who gives a brief treatment of them.

The total reflection of plane-wave pulses of arbitrary waveform at an interface has some interesting features. Fischer[4] gives the analysis for the total reflection of a δ-function pulse going from air into hydrogen. Friedlander[5] has studied the total reflection of transverse (shear) wave pulses in an elastic solid. He considered a rectangular pulse, a unit displacement for a finite time. Towne's[6] analysis arrives at a plane-wave solution for total reflection at a fluid–fluid interface, as a limiting case for spherical waves originating at a distant point source. The general conclusions of these and other investigations[3] are that the reflected and refracted waveforms (a) differ substantially from the incident waveform, (b) have infinitely long precursors and tails, and (c) are accompanied by infinite spikes at finite discontinuities in the incident pulse. We shall see how these results apply to the sonic-boom problem.

I. ANALYSIS OF REFLECTION AND REFRACTION OF AN N WAVE

The general procedure is use of the Fourier integral method to solve the Cauchy problem posed by the sonic-boom penetration into water. The first step is to find the reflected and refracted waves for an incident sinusoidal wave. The second step is to find the Fourier transform of the incident N wave, and so finally to arrive at the total reflected and refracted waves (caused by the N wave) by linear superposition of the effects of the incident sinusoidal components.

A. Incident Sinusoidal Wave

The well-known analysis for sinusoidal waves incident on a plane boundary at an angle greater than the critical angle has been set forth in various places (see, for example, Rayleigh.[7]) We present here only the basic assumptions and the results, all in a convenient notation.

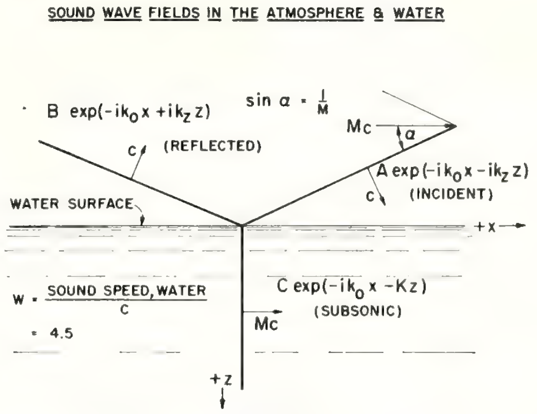

FIG. 2. Geometry of sinusoidal incident, reflected, and inhomogeneous (subsonic) refracted waves.

Figure 2 shows the geometry for the reflected atmospheric plane wave and the refracted underwater subsonic wave, both caused by an incident sinusoidal plane wave having a time variation of $\exp(i\omega t)$. The surfaces of constant phase are all planes parallel to the y axis (which is perpendicular to the plane of the paper). The sound pressure p in the atmosphere is the sum of the incident and reflected waves, the sum satisfying the sound-wave equation. For the sound field underwater, the sound pressure p_w satisfies the underwater-wave equation and represents a wave having a subsonic phase velocity.

Atmosphere:

$$p=A\ \exp i(\omega t-k_0x-k_zz)+B\ \exp i(\omega t-k_0x+k_zz)\qquad z\leqq 0$$

Water: (1)

$$p_w=C\ \exp i(\omega t-k_0x)\ \exp(-Kz)\qquad z\geqq 0$$

The (x,y,z) components of the wavenumber vector for the incident wave are $(k_0,0,k_z)$. The magnitude of the vector is $k=(k_0^2+k_z^2)^{1/2}=\omega/c$, where c is the velocity of sound in the atmosphere. The underwater wave has $(k_0, 0, -iK)$ for the components of its wavenumber vector, and $(k_0^2-K^2)^{1/2}=\omega/Wc$, where Wc is the velocity of sound in water. $W\approx 4.5$ is the ratio of the speed of sound in water to that in the atmosphere.

The wavenumber k_0 applies in particular to the sound-pressure wave at the interface between the atmosphere and water. The phase velocity of this wave must be chosen to be Mc, where M is the Mach number of the supersonic source. The complete table of wavenumbers (all in terms of the incident wavenumber $k=\omega/c$) is as follows:

$$k_0=k/M=k\ \sin\alpha;$$
$$k_z=(1-1/M^2)^{1/2}k=k\ \cos\alpha;$$
$$K=(1/M^2-1/W^2)^{1/2}k.$$

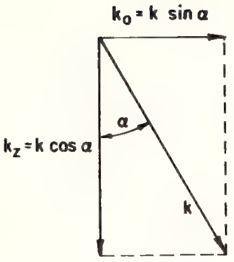

FIG. 3. Wavenumber vector k for the incident sinusoidal wave of Fig. 2.

The geometrical relationships involving the various wavenumbers are shown in Fig. 3.

The reflected-wave factor B and refracted factor C are obtained from the following boundary conditions at the air–water boundary $z=0$: the sound pressure is continuous across the surface, and the perpendicular (z) component of particle velocity is continuous. The final result is

$$B=(1+i\delta)/(1-i\delta)\times A,$$
$$C=2/(1-i\delta)\times A, \tag{2}$$

and

$$\delta=(\rho/\rho_w)(1-M^2/W^2)^{\frac{1}{2}}/(M^2-1)^{\frac{1}{2}},$$

where ρ and ρ_w are the densities of air and water, respectively. We note that when $W>M>1$, then $|B| = |A|$. Since $\rho/\rho_w \approx 0.001$, then $|C| \approx 2|A|$. The amplitude B of the reflected wave is the same as that of the incident wave, and there is a small and significant difference in phase, whose amount is approximately equal to 2δ rad.

Consider the special case $M=2.7$, which is about the greatest Mach number to be expected for supersonic aircraft in level flight. An incident sound ray has an angle of incidence greater than the critical angle. When $c=340$ m/sec, $W=4.5$, and the sinusoidal frequency is $10/\pi$ Hz ($\omega=20$), then $K=0.0174$/m. The "penetration depth" into water for this frequency, at which the sound pressure is less than that at the surface by a factor of $1/e$, is $1/K=57.5$ m.

An interesting special case is that in which the phase velocity of the sinusoidal wave traveling over the water–air interface is exactly the same as the speed of sound in water, $M=W=4.5$. Then $B=A$, and $C=2A$. Also $K=0$; the sound field consists of equal-intensity incident and reflected waves in the atmosphere, "balanced" by an infinite plane wave in the water, traveling in the direction parallel to the surface, and lying in the plane of the incident and reflected rays. The incident ray is at the critical angle of incidence. All three waves have exactly the same phase.

For the general case in which $M>W=4.5$, there is a sound field corresponding to incidence at less than the critical angle. An example is the shock waves generated by satellites traveling with $M \approx 23$ at altitudes of about 110 km; these have been observed at ground level. In this familiar analytical situation, there is a refracted wave into the water, and the relation between the angles of incidence and refraction is given by Snell's law. The reflected wave has less intensity than the incident wave but has exactly the same waveform. The intensity difference is the same as the intensity of the refracted wave. This latter wave satisfies the Sommerfeld radiation condition and carries sound power underwater off to infinity in a direction away from the surface.

B. Fourier Transform of the N Function

The transform most convenient for our purpose is that one for the spatial distribution of incident sound pressure in the interface plane $z=0$. To arrive at this, we consider first a linear transformation from the original (x,y,z) coordinate system to a new one (x',y',z'), moving in the $+x$-axis direction with a speed Mc; the new coordinates of any point are $x'=x-Mct$, $y'=y$, $z'=z$. After transformation, the time factor $\exp(i\omega t)$ will not appear explicitly in Eq. 1. Otherwise stated, the whole wavefield will be stationary in time in the (x',y',z') coordinates. This is because the incident, reflected, and refracted wavefields were all moving in the $+x$-axis direction with a phase velocity Mc.

We consider in particular the sound-pressure distribution of the incident wave in the plane $z'=0$ (see Fig. 4). The N wave has a length L and peak pressure p_0.

A simplified N waveform, convenient for the ensuing analysis, is the N function, whose definition is $N(x)=0$, for $x>1$ and $x<-1$; $N(-1)=-\frac{1}{2}$; $N(x)=x$, $-1<x<+1$; $N(+1)=\frac{1}{2}$. Then the incident N-wave pressure in the plane $z'=0$ can be written as $p_0N(2x'/L)$, and anywhere in the atmosphere ($z'\leq 0$) the incident pressure is

$$p=p_0N[2(x'\sin\alpha+z'\cos\alpha)/L\sin\alpha].$$

The N-wave thickness is $L\sin\alpha$.

The Fourier transform (spectrum) of $N(x)$ is

$$\begin{aligned} f(\kappa) &= \int_{-\infty}^{\infty} N(u)\exp(i\kappa u)du \\ &= \int_{-1}^{1} u\exp(i\kappa u)du \\ &= (2i/\kappa)(\sin\kappa/\kappa-\cos\kappa) \\ &= -2i(d/d\kappa)(\sin\kappa/\kappa). \end{aligned} \tag{3}$$

By the Fourier integral theorem, we know that

$$\begin{aligned} N(x) &= \frac{1}{2\pi}\int_{-\infty}^{\infty} f(\kappa)\exp(-i\kappa x)d\kappa \\ &= \frac{-i}{\pi}\int_{0}^{\infty} f(\kappa)\sin\kappa x d\kappa \end{aligned} \tag{4}$$

since $f(\kappa)$ is an odd function of κ. $N(x)$ is an odd function of x, and so by a well-known lemma, $f(\kappa)\sim\kappa$ for small κ; Eq. 3 is consistent with this. For large κ, the zeros of $f(\kappa)$ are very near those of $\cos\kappa$, and the envelope of $|f(\kappa)|\sim 1/\kappa$. Detailed descriptions of the N-function spectrum have appeared in numerous places (see, for example, Howes[8]).

Each sinusoidal component of the N-wave intersection with the plane $z=0$ has associated with it unique incident, reflected, and refracted sinusoidal spatial waves. We therefore arrive at the total spatial distribution corresponding to an incident acoustical N wave by superposing the sinusoidal waves weighted with the spectrum $f(\kappa)$.

C. Underwater Sound Pressure Field, $M<W$

We combine Eqs. 1 and 2, choosing $A=1$, and recall that $x'=x-Mct$. Then the incident sinusoidal pressure at the surface, $p=\sin k_0x'$, causes an underwater sound pressure,

$$p_w=2\cos\Delta\,\sin(k_0x'-\Delta)\,\exp(-k_0\mu z'), \tag{5}$$

where $\mu=(1-M^2/W^2)^{\frac{1}{2}}$, and

$$\Delta=\tan^{-1}\delta\approx\delta. \tag{6}$$

The phase angle $\Delta\ll 1$ radian and is a constant independent of k_0. See Eq. 2 for the definition of δ.

To find the total sound pressure, we multiply Eq. 5 by the N-function spectrum, Eq. 3, and integrate over all $\kappa(0$ to $\infty)$ (see Eq. 4):

$$p_w(x',z')=-\frac{4\cos\Delta}{\pi}\int_0^\infty \exp(-\kappa\mu z')\times\sin(\kappa x'-\Delta)\frac{d}{d\kappa}\left(\frac{\sin\kappa}{\kappa}\right)d\kappa. \tag{7}$$

This is the sound pressure underwater when the incident pressure (in the plane $z'=0$) is $N(x')$. Expanding $\sin(\kappa x'-\Delta)$ and writing $\mu z'=h$ leads to

$$p_w(x',h)=2\cos\Delta(I_1\cos\Delta+I_2\sin\Delta),$$

$$\pi I_1=-2\int_0^\infty \exp(-h\kappa)\,\sin\kappa x'\frac{d}{d\kappa}\left(\frac{\sin\kappa}{\kappa}\right)d\kappa, \tag{8}$$

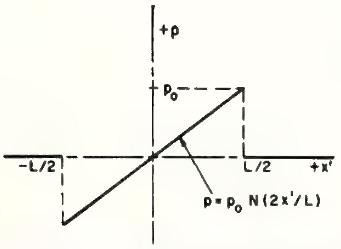

FIG. 4. Sound pressure of the incident N wave in the plane $z'=0$ of the moving coordinate system.

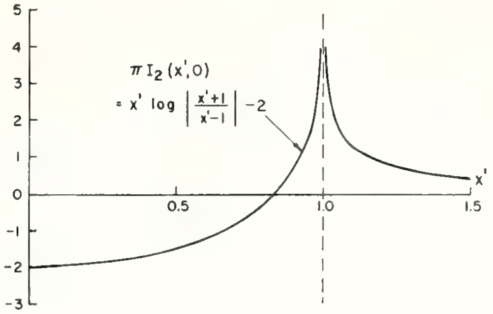

FIG. 5. The spike-function part of the reflected and refracted waves at the water surface. $I_2(x',0)=I_2(-x',0)$.

and

$$\pi I_2=2\int_0^\infty \exp(-h\kappa)\,\cos\kappa x'\frac{d}{d\kappa}\left(\frac{\sin\kappa}{\kappa}\right)d\kappa.$$

From Eq. 2, $\Delta=4\times10^{-4}$, when $M=2.7$. Therefore, $\cos\Delta\approx 1-\Delta^2/2=1.0000$, and $\sin\Delta\approx\Delta=4\times10^{-4}$. $I_1\cos\Delta$ makes up the principal part of the sound pressure. It is almost everywhere substantially larger than $I_2\sin\Delta$.

The two infinite integrals I_1 and I_2 are uniformly convergent throughout any region of the (x',h) half-plane $h\geq 0$, from which the points $(+1,0)$ and $(-1,0)$ are excluded by small semicircles. The integrals have the format of Laplace transforms. They can be expressed in terms of elementary functions with the help of tables of such transforms (see, for example, Roberts and Kaufman.[9]) The final expressions are

$$\pi I_1(x',h)=-\frac{h}{2}\log\left[\frac{h^2+(x'+1)^2}{h^2+(x'-1)^2}\right]+x'\tan^{-1}\left[\frac{2h}{h^2-1+(x')^2}\right],$$

and

$$\pi I_2(x',h)=\frac{x'}{2}\log\left[\frac{h^2+(x'+1)^2}{h^2+(x'-1)^2}\right]+h\tan^{-1}\left[\frac{2h}{h^2-1+(x')^2}\right]-2. \tag{9}$$

The term $Q=\tan^{-1}[2h/(h^2-1+x'^2)]$ is a multiple-valued function. For $h\neq 0$, $0<Q<\pi$ is the correct branch for $-\infty<x'<\infty$. For $h=0$, $Q=0$ for $-\infty<x'<-1$ and $+1<x'<\infty$; $Q=\pi$ for $-1<x'<+1$, and $Q=\pi/2$ at $x'=\pm1$. Therefore, $I_1(x',0)=N(x')$; the principal part of the underwater sound pressure has an N waveform just at the surface $(h=0)$. The function $I_1(x',h)$ has jump discontinuities at the points $(+1,0)$ and $(-1,0)$.

The function $I_2(x',h)$, which is an even function of x', increases without limit on approach to the same points and becomes logarithmically infinite at them. This is seen from $\pi I_2(x',0)=x'(\log|1+x'|-\log|1-x'|)-2$.

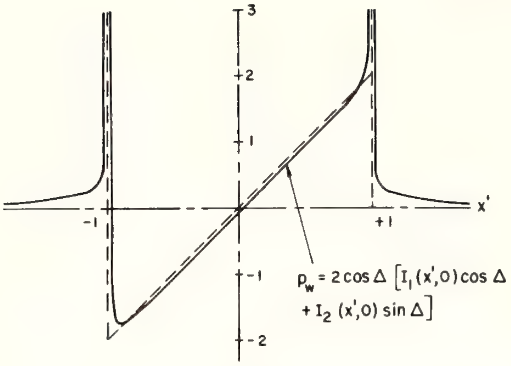

FIG. 6. Total sound pressure just at the water surface. The infinitely high spikes, not drawn to scale, are much narrower and sharper than illustrated.

Figure 5 illustrates this function. The sound pressure just at the water surface, which is the same in the atmosphere as in the water, is illustrated in Fig. 6.

Equations 8 combined with Eqs. 9 furnish the complete exact solution for the underwater sound-pressure field caused by an N wave incident on the surface. To arrive at the pressure field in the original (stationary) x–z coordinate system, replace x' by $x-Mct$ and h by μz.

D. The Reflected Wave

The sound wave reflected from the water surface into the atmosphere can be found by a continuation of the foregoing analysis. As was mentioned above, the reflected wave is stationary in time in the moving (x',y',z') coordinate system. Combination of Eqs. 1 and 2, and again we choose $A=1$, leads to the reflected wave p_r caused by an incident sinusoidal wave:

$$\begin{aligned} p_r &= \sin(k_{0x}x'-k_zz'-2\Delta)\\ &= \sin k_0(x'-z'\cot\alpha)\cos 2\Delta \\ &\qquad -\cos k_0(x'-z'\cot\alpha)\sin 2\Delta, \end{aligned} \tag{10}$$

where α = angle of reflection (= angle of incidence), and Δ is defined by Eq. 6.

The total reflected sound wavefield is obtained by multiplication of Eq. 10 by the N-function spectrum, Eq. 3, and integration over all κ (0 to ∞). The final expression for the reflected sound pressure is

$$\begin{aligned} p_r &= N(x'-z'\cot\alpha)\cos 2\Delta+\frac{\sin 2\Delta}{\pi}\\ &\times\left[(x'-z'\cot\alpha)\log\left|\frac{1+(x'-z'\cot\alpha)}{1-(x'-z'\cot\alpha)}\right|-2\right]. \end{aligned} \tag{11}$$

II. PRINCIPAL FEATURES OF THE SOUND FIELD

A. Underwater

The main part of the sound pressure is given by $I_1(x',h)$ (see Eqs. 8 and 9). The function spreads out underwater so as to have infinitely long precursor and tail waves. This comes about because the sound field was initiated at $t=-\infty$ (so to speak), and so the underwater sound runs ahead of the atmospheric sonic boom to form a precursor. At the surface, the function $I_1(x',0)$ has the N waveform, which we referred to earlier, and therefore $I_1(x',h)$ is the solution for the sound pressure due to a traveling pressure N waveform applied to the surface. Sawyers[10] has also worked out the solution for this; his Eq. 13 agrees with $I_1(x',h)$.

But the function $I_2(x',h)$ is also a part of the complete underwater sound field. I_2 has logarithmically infinite spikes at the points $x'=\pm1$, $h=0$, and it has infinitely long precursor and tail waves. But it makes a negligible contribution, less than $10^{-3}\,p_0$, to the total sound pressure, whenever $h^2+(x'\pm1)^2>10^{-4}$. For example, the sound pressure attributable to $I_2(x',h)$ is at least 60 dB less than the incident peak pressure p_0, at all points underwater more than 10 cm away from the leading and trailing edges of an N wave 100 m long.

Plots of the total underwater sound pressure as a function of x', at various depths $z'(=h/\mu)$ below the surface, are shown in Fig. 7. The total pressure is not quite an odd function of x'. But practically speaking, the curves of Fig. 7 can be used both for the forward half of the wavefield ($x'>0$, $p_w>0$) and for the trailing half ($x'<0$, $p_w<0$).

The total underwater elastic energy V_w per unit width, parallel to the y axis, of the sound field is (apart from a proportionality constant)

$$\begin{aligned} V_w &= \int_0^\infty\int_{-\infty}^\infty p_w^2(x',h)\,dx'dh\\ &= (1+\cos 2\Delta)^2\int_0^\infty\int_0^\pi I_1^2(r,\theta)\,r\,d\theta dr \\ &\qquad +\sin^2 2\Delta\int_0^\infty\int_0^\pi I_2^2(r,\theta)\,r\,d\theta dr. \end{aligned} \tag{12}$$

The latter integrals are over the polar coordinates, $r=[(x')^2+h^2]^{\frac{1}{2}}$ and $\theta=\tan^{-1}(h/x')$. The cross-product term I_1 (odd function of x')$\times I_2$ (even function of x') vanishes during the integration. The infinite integrals are finite, as can be seen from the asymptotic forms of I_1 and I_2 as r becomes large. These forms are

$$I_1\sim 2\sin 2\theta/3\pi r^2,$$

and (13)

$$I_2\sim -2\cos 2\theta/\pi r^2.$$

Therefore, the infinite integral

$$\int_R^\infty I_1^2(r,\theta)\,r\,dr$$

is of the order of $1/R^2$. The same is true of the integral for $I_2(r,\theta)$.

We conclude that the elastic energy V_w per unit width of the underwater sound field is finite. The field can therefore be established almost completely in a finite time. For example, suppose a sonic-boom wave travels over land, across a beach, and is then suddenly incident upon a water surface. The underwater sound field will be fully established, for all practical measurement purposes, in a few seconds of time.

B. At The Surface

The sound pressure p_s in the atmosphere at the water surface is the same as the underwater pressure there (see Fig. 6):

$$\begin{aligned} p_s &= (1+\cos 2\Delta)I_1(x',0)+\sin 2\Delta\, I_2(x',0) \\ &= (1+\cos 2\Delta)N(x')+(\sin 2\Delta/\pi) \qquad (14) \\ &\qquad \times[x'\log|(x'+1)/(x'-1)|-2]. \end{aligned}$$

We proceed to examine the relative amounts of elastic energy in the N-function part of the sound pressure and in the spike function $I_2(x',0)$.

Consider the total elastic energy in a cylinder parallel to the x' axis, and of unit cross-sectional area. This energy V_0 is found by proceeding as earlier for calculation of the total underwater energy V_w. We omit a constant of proportionality, square the right-hand side of Eq. 14, and integrate over x' from $(-\infty)$ to $(+\infty)$. During the integration the cross-product term $I_1(x',0)I_2(x',0)$ vanishes as before. The result is

$$V_0=(1+\cos 2\Delta)^2\int_{-1}^{1} N^2(u)du+\frac{8\sin^2 2\Delta}{\pi^2} \times\int_0^{\infty}\left[\frac{x'}{2}\log\left|\frac{x'+1}{x'-1}\right|-1\right]^2 dx \qquad (15)$$

The first integral $=\frac{2}{3}$. The second (infinite) integral can be evaluated in terms of elemenatry functions and the dilogarithm function[11]; its value is $\pi^2/12$. This can be obtained also by an application of the Hurwitz–Lyapunov theorem to the totally reflected wave (see Sec. II-C).

The first term in Eq. 15 is the N-function elastic energy at the surface, including both the incident and reflected waves. The second term is the spike-function energy, which is much less than the first. The ratio of the latter (spike) energy to the former is $\sin^2 2\Delta/(1+\cos 2\Delta)^2 \approx 1.6\times 10^{-7}$, for the same Mach number $M=2.7$ as assumed earlier. The spike energy at the water surface is 68 dB less than the N-function energy.

C. In the Atmosphere

The wave reflected into the atmosphere has a sound-pressure p_r distribution given by Eq. 11. The reflected wave has (a) infinitely long, but very weak, precursor and tail waves and (b) infinitely (logarithmically) high spikes of sound pressure at the leading and trailing edges of its N wave. The waveform of p_r is, of course, the same as the surface pressure p_s, after subtraction from the latter of the incident N wave, $N(x')$; compare Eqs. 11 and 14 at $z'=0$.

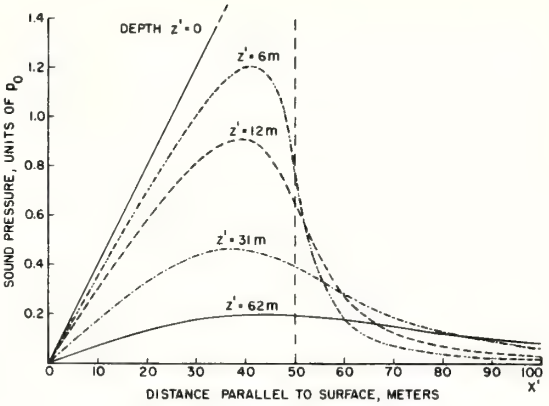

FIG. 7. Underwater sound pressure at various depths $z'=h/\mu$ below the surface, for an N wave of length $L=100$ m; $\mu=(1-M^2/W^2)^{\frac{1}{2}}=0.80$.

The calculation of the elastic energy therefore parallels the above analysis for the energy at the surface. Consider the energy V_r in an (infinite) cylinder of unit area perpendicular to the plane wavefront of the reflected wave. V_r is given by the integral of p_r^2 along an (infinite) straight line perpendicular to the wavefront. We again omit constants of proportionality,

$$V_r=\int_{-\infty}^{\infty} p_r^2 du=\frac{1}{\pi}\int_0^{\infty} |f_r(\kappa)|^2 d\kappa \qquad (16)$$

by the Hurwitz–Lyapunov theorem (completeness relation); $f_r(\kappa)$ is the spectrum of p_r. Similarly, for the incident N wave, p_i:

$$V_i=\int_{-\infty}^{\infty} p_i^2 du=\frac{1}{\pi}\int_0^{\infty} |f_i(\kappa)|^2 d\kappa. \qquad (17)$$

But each sinusoidal component of p_r has the same amplitude as in p_i, there being only a phase shift 2Δ (see Eq. 10). Therefore,

$$|f_i(\kappa)|=|f_r(\kappa)|,$$

and so

$$V_r=V_i;$$

$$\begin{aligned} &\tfrac{2}{3}\cos^2 2\Delta+(\text{SPIKE-FUNCTION ENERGY})=\tfrac{2}{3}; \\ &\therefore \text{SPIKE-FUNCTION ENERGY}=\tfrac{2}{3}\sin^2 2\Delta. \end{aligned} \qquad (18)$$

The ratio of the spike energy to the N-wave elastic energy of the reflected wave is $\tan^2 2\Delta \approx 0.64\times 10^{-6}$ for Mach number $M=2.7$. The spike energy of the reflected wave is 62 dB less than the N-wave energy.

III. SUMMARY AND DISCUSSION

The final expression for the underwater sound pressure p_w is given by Eqs. 8 and 9, for the atmosphere reflected pressure p_r by Eq. 11, and for the surface pressure p_s by Eq. 14. Figures 5–7 are graphical illustrations of the formulas. In all of these expressions, the unit of pressure is p_0, which is the peak pressure in the incident wave, and the unit of length $L/2$ is one-half the N-wave length on the water surface. Also, the sound pressures are stationary in time in an (x',y',z') coordinate system moving with speed Mc.

Measurements must be made, however, with microphones in the fixed (x,y,z) coordinate system, with sound pressures varying in time. These are obtained by applying the transformation $x'=x-Mct$, $y'=y$, $z'=z$ to the various sound-pressure expressions. For example, replacement of x' by $-Mct$ and z' by z in Fig. 7 will give the variation in time of the underwater sound pressure p_w in the plane $x=0$ of the stationary coordinate system.

Detection and measurement of the positive pressure spikes in the reflected and underwater waves will be difficult to achieve. The spikes contain only a very small fraction, about 0.64×10^{-6}, of the reflected N-wave elastic energy for Mach number $M=2.7$. The fraction increases as M decreases (see Eqs. 2, 6, and 18). For $M=1.12$, the spike-energy fraction is 23×10^{-6}, 46 dB less than the incident elastic energy.

Passage of an N wave through a nonuniform atmosphere can also produce spikes at the leading and trailing pressure jumps.[2,12] Atmospheric inhomogeneities influence the incident N wave, whereas effects at a reflecting surface influence only the reflected wave. Therefore, the two effects can be separated by observations of sound pressure at points above the surface, where the pressure jumps of the incident and reflected waves are separated in time.

ACKNOWLEDGMENTS

The author is indebted to M. W. Bottomley and to Miss S. Nicholson for assistance in the computations.

[1] W. M. DuMond, E. R. Cohen, W. K. H. Panofsky, and E. Deeds, "A Determination of the Wave Forms and Laws of Propagation and Dissipation of Ballistic Shock Waves," J. Acoust. Soc. Amer. **18**, 97–118 (1946).

[2] H. H. Hubbard *et al.*, "Proceedings of the Sonic Boom Symposium," J. Acoust. Soc. Amer. **39**, No. 5, Pt. 2, S1–S42 (1966).

[3] L. M. Brekhovskikh, *Waves in Layered Media* (Academic, New York, 1960), p. 4 on inhomogeneous plane waves. See p. 122 and following for a summary on the reflection of pulses by a plane boundary.

[4] F. A. Fischer, "Uber die Totalreflexion von ebenen Impulswellen," Ann. Physik. **2**, 211–224 (1948).

[5] F. G. Friedlander, "On The Total Reflection of Plane Waves," Quart. J. Mech. Appl. Math. **1**, 376–384 (1948).

[6] D. H. Towne, "Pulse Shape of Totally Reflected Plane Waves as a Limiting Case of the Cagniard Solution for Spherical Waves," J. Acoust. Soc. Amer. **44**, 77–83 (1968).

[7] Lord Rayleigh, *The Theory of Sound* (MacMillan, London, 1940), Vol. 2, p. 84.

[8] W. L. Howes, "Farfield Spectrum of the Sonic Boom," J. Acoust. Soc. Amer. **41**, 716–717 (1967).

[9] G. E. Roberts and H. Kaufman, *Table of Laplace Transforms* (Saunders, Philadelphia, 1966), pp. 27–32.

[10] K. N. Sawyers, "Underwater Sound Pressure from Sonic Booms," J. Acoust. Soc. Amer. **44**, 523–524 (1968).

[11] *Handbook of Mathematical Functions* (Nat. Bur. Std., Washington, D. C., 1964), pp. 1004–1005.

[12] A. D. Pierce, "Spikes on Sonic-Boom Pressure Waveforms," J. Acoust. Soc. Amer. **44**, 1052–1061 (1968).

Reprinted from THE JOURNAL OF THE ACOUSTICAL SOCIETY OF AMERICA, Vol. 49, No. 6 (Part 1), 1698–1703, June 1971
Copyright, 1971, by the Acoustical Society of America.

Numerical Study of the Gain Pattern of a Shielded Acoustic Antenna

OTTO NEALL STRAND

Wave Propagation Laboratory, Environmental Research Laboratories, National Oceanic and Atmospheric Administration, Boulder, Colorado 80302

The farfield gain pattern of a shielded acoustic antenna is studied numerically by the use of Kirchhoff's integral. Circular symmetry and perfectly absorbing walls are assumed. Results are reported for a frequency of 2 kHz.

INTRODUCTION

In the acoustic radar work at the Wave Propagation Laboratory, it has been found necessary to suppress the side lobes of the horn-reflector acoustic antenna in use. An experiment by Simmons and Wescott[1] was conducted in which an antenna was surrounded by absorbing material and the sound signal at 80° and 90° from the axis of the antenna was compared with that which would be received in the absence of any shielding. A theoretical numerical model for this experiment is derived in this article, and numerical results arising from this model are presented.

The geometrical configuration being considered is shown in Fig. 1. A planar antenna with circular symmetry is assumed. The dimensions studied for the configuration of Fig. 1 are as follows (all dimensions are in feet): $2\leq h\leq 12$, $r_{(\max)}=2$, $r_{s(\max)}=4$ and 6, and wavelength $\lambda=0.5$, corresponding to a frequency of approximately 2 kHz.

The procedure used to calculate the farfield gain pattern may be summarized as follows (see Fig. 1): Kirchhoff's integral, which may be used for acoustic waves as well as electromagnetic waves, is calculated to derive an "equivalent illumination" across the horizontal aperture at height h above the shielded antenna. This equivalent illumination is then truncated at $r_s=r_{s(\max)}$. A two-dimensional Fourier transform (derived from Kirchhoff's integral) is then used to obtain the farfield resulting from the equivalent illumination. Finally, the absolute value of the farfield signal is

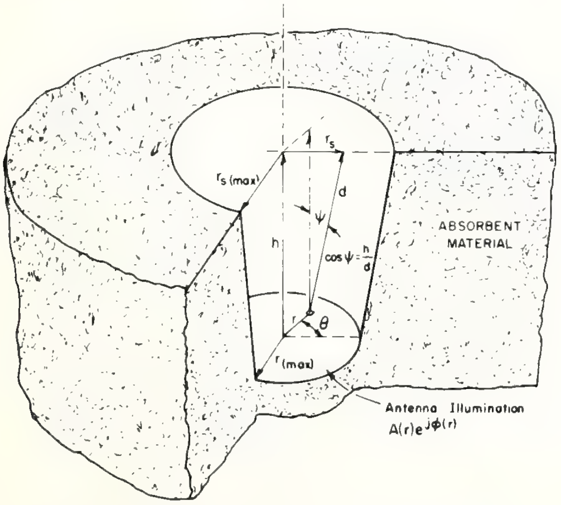

FIG. 1. Assumed geometry of shielded antenna.

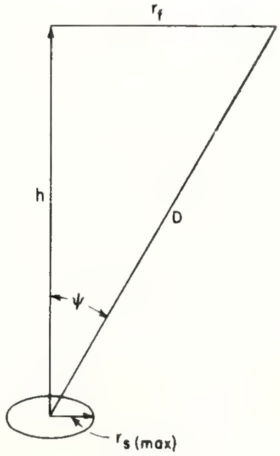

FIG. 2. Farfield approximation, $h\gg r_{s(\max)}$.

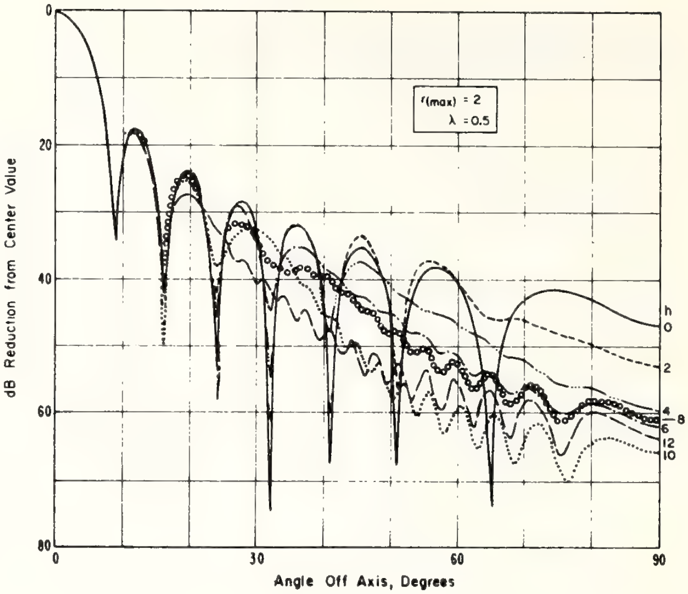

FIG. 3. Relative gain patterns for various values of h; uniform illumination, $r_{s(max)}=6$.

converted to decibels below the center value to obtain the gain pattern.

I. THEORY

It is easily derived from Kirchhoff's integral for diffraction[2] that the illumination, $I_h(r_s)$, at height h above the antenna is given approximately (except for a constant multiplier) by

$$I_h(r_s)=\int_0^{2\pi}\int_0^{r(\max)} A(r)\exp[j\phi(r)]$$
$$\times\exp\left(\frac{j2\pi}{\lambda}(d-h)\right)\gamma(d)rdrd\theta, \quad (1)$$

where

$$d=[(r\sin\theta-r_s)^2+r^2\cos^2\theta+h^2]^{\frac{1}{2}};$$

$A(r)\exp[j\phi(r)]$ is the illumination of the shielded antenna, as indicated in Fig. 1; $\gamma(d)$ is a factor describing the decay of the amplitude of the acoustic signal with distance, d; $rdrd\theta$ is the area element at the position (r,θ) on the shielded antenna; and r_s is the radius at which the illumination, $I_h(r_s)$, is to be obtained. The factor $\exp[(j2\pi/\lambda)(d-h)]$ describes the change of phase of the acoustic signal over distance d.

For the conditions described here, the choice of $\gamma(d)$ given by

$$\gamma(d)=\frac{1}{d}\left(\frac{1+\cos\psi}{2}\right)=\frac{1}{2d}\left[1+\frac{h}{d}\right] \quad (2)$$

is appropriate (for some conditions, such as $h\rightarrow 0$, this assumption would be untenable).

The farfield approximation for use with the equivalent illumination to obtain the farfield gain pattern is derived as follows (see Fig. 2). Let r_s play the role of r in the Kirchhoff integral and assume that $h\gg r_{s(\max)}$. Then $h/D\simeq\cos\psi$ where D is constant for all points on the outer aperture. In considerations of phase, we use the binomial series to obtain the first-order approximation

$$d=(r_s^2+h^2-2r_fr_s\sin\theta+r_f^2)^{\frac{1}{2}}=D\left(1-\frac{2r_fr_s\sin\theta-r_s^2}{D^2}\right)^{\frac{1}{2}}$$
$$\cong D\left[1-\left(\frac{2r_fr_s\sin\theta}{D^2}\right)\right]^{\frac{1}{2}}\cong D\left[1-\left(\frac{r_fr_s\sin\theta}{D^2}\right)\right]$$

or

$$d\cong D-\sin\psi(r_s\sin\theta). \quad (3)$$

Incorporating these approximations into Eq. 1 gives the farfield, $I(\psi)$, (except for a complex constant multiplier) as

$$I(\psi)=\frac{1+\cos\psi}{2}\int_0^{2\pi}\int_0^{r_{s(\max)}} A(r_s)\exp[j\phi(r_s)]$$
$$\times\exp\left[\frac{-j2\pi}{\lambda}\sin\psi(r_s\sin\theta)\right]r_sdr_sd\theta, \quad (4)$$

TABLE I. Location of zeros of gain pattern for $h=0$.

Zero of $J_1(u)$	$\sin\psi$	ψ(deg)
3.8317	0.1525	8.8
7.0156	0.2791	16.2
10.1735	0.4048	23.9
13.3237	0.5301	32.0

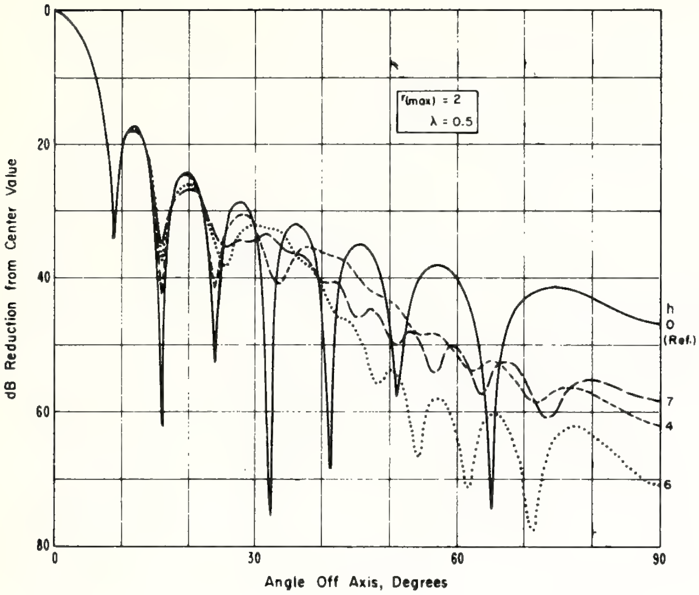

FIG. 4. Relative gain patterns for various values of h; uniform illumination, $r_{s(max)}=4$.

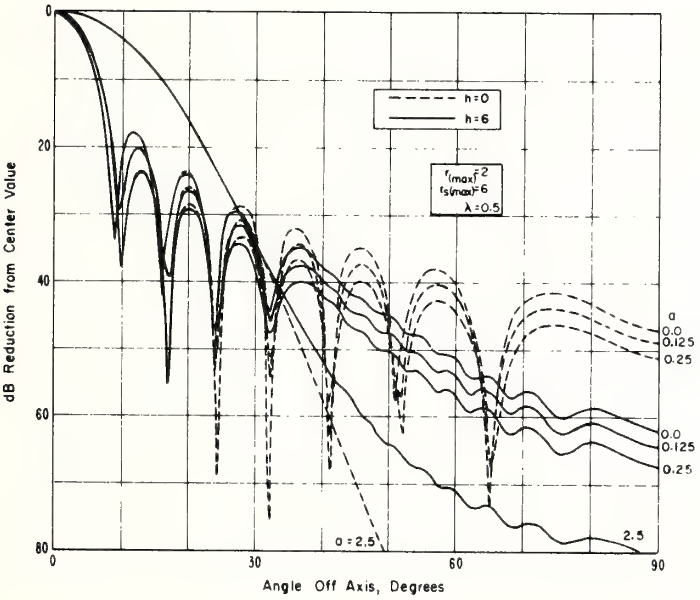

FIG. 5. Effect of taper on gain pattern for $h=0$ and $h=6$.

where $A(r_s)\exp[j\phi(r_s)]$ is the equivalent illumination of the outer aperture. The integral of Eq. 4 can be transformed into the more usual form,[3,4] i.e., one with a kernel of the form $\exp[(+j2\pi/\lambda)\sin\psi(r_s\sin\theta)]$, by replacing θ by $-\theta'$ in the outer integration to get

$$I(\psi)=\frac{1+\cos\psi}{2}\int_0^{2\pi}\int_0^{r_{s(max)}} A(r_s)\exp[j\phi(r_s)] \times\exp\left[\frac{+j2\pi}{\lambda}\sin\psi(r_s\sin\theta')\right]r_s dr_s d\theta'. \quad (5)$$

This is a special case of the Fourier-transform farfield as is usually given in the literature[2]; the factor $(1+\cos\psi)/2$ in Eq. 5 gives improved accuracy for the larger values of ψ. Performing the integration first with respect to θ' gives the formula

$$I(\psi)=2\pi\frac{(1+\cos\psi)}{2}\int_0^{r_{s(max)}} A(r_s) \times\exp[j\phi(r_s)]J_0\left(\frac{2\pi r_s\sin\psi}{\lambda}\right)r_s dr_s. \quad (6)$$

Formula 6 was used for the computation of farfield results. To obtain the farfield gain pattern, we compute

$$\text{Relative gain (in decibels)} = 20\log_{10}\left|\frac{I(\psi)}{I(0)}\right|. \quad (7)$$

II. NUMERICAL METHODS

The Fortran computer program contained two major subroutines. The first was a two-dimensional numerical integration which summed over segments of concentric circles to evaluate Eq. 1. The second performed a one-dimensional numerical integration in accordance with Eq. 6. A linear interpolation of the results of Eq. 1 was used to provide input for this second subroutine.

Various comparisons indicated that the numerical results were valid to at least three significant figures. These comparisons consisted of computing known cases and varying the increment sizes both for the integration of Eq. 1 and the interpolation of the equivalent outer-aperture illumination. The integration of Eq. 6 was performed and the results compared using Gaussian integration formulas involving 20, 40, and 43 abscissas/cycle of J_0. The fine details of the computer program are not presented here. The program is presently available and could be used for further calculations if necessary.

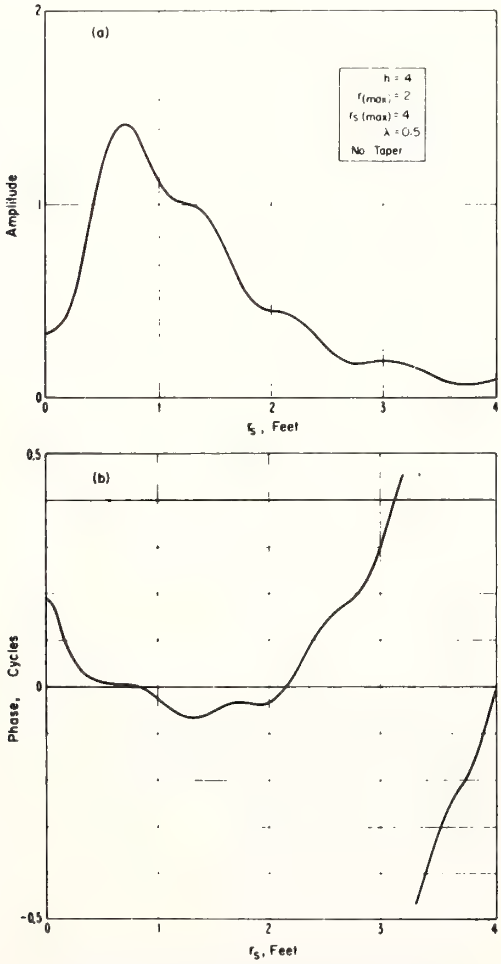

FIG. 6. Equivalent outer-aperture illumination.

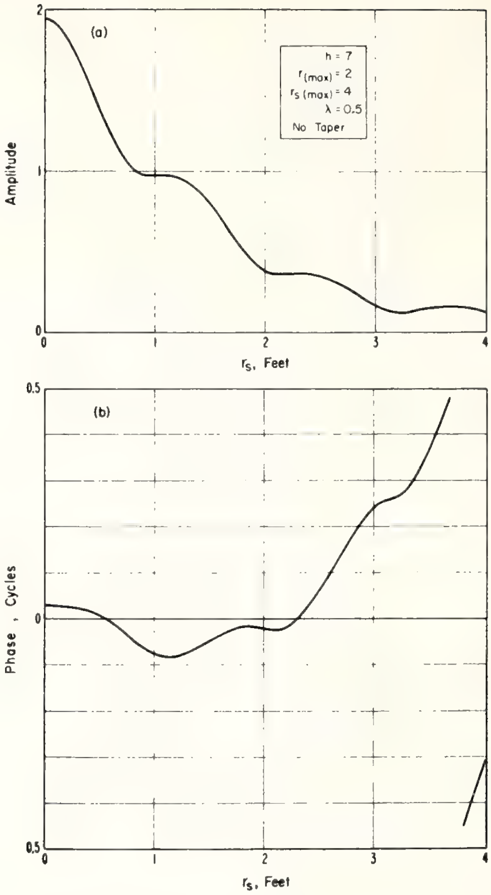

FIG. 7. Equivalent outer-aperture illumination.

III. RESULTS

All results are given in graphical form; although the numerical results are valuable for check out, the graphs give a much clearer indication of the behavior of the farfield as certain parameters are varied. The graphs were originally drawn by the Cathode Ray Plotter with the CDC 3800 computer, but have been redrafted, as required, for comparison. The main question to be answered is: What is the effect of shielding the antenna on the farfield gain pattern? Figure 3 presents the gain patterns for $r_{s(\max)} = 6$ ft, $r_{(\max)} = 2$ ft, and a zero-phase constant-amplitude illumination of the shielded an-

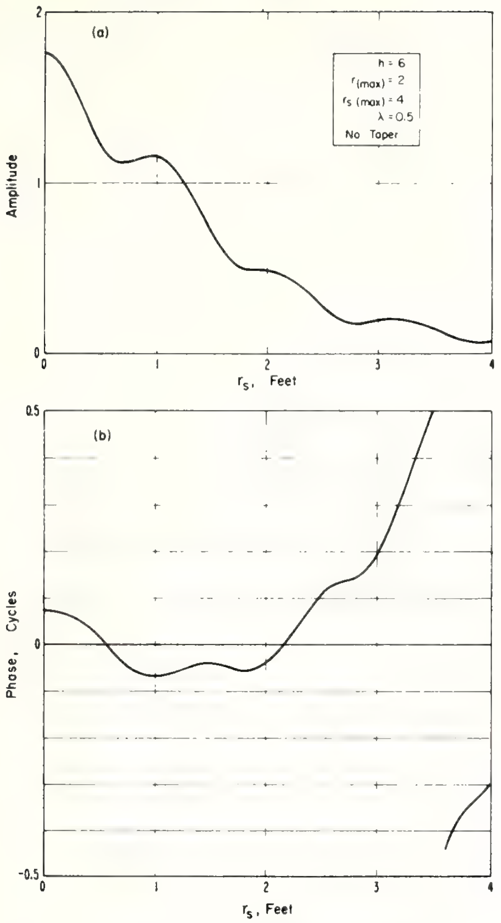

FIG. 8. Equivalent outer-aperture illumination.

tenna. The curve for $h=0$ depicts the pattern which would be observed if the antenna were not shielded, and it serves as a reference. It can be shown[4] that for $h=0$, the farfield is given (up to a constant multiplier) by

$$I(\psi)=J_1(u)/u, \tag{8}$$

where

$$u=\frac{2\pi r_{(\max)}\sin\psi}{\lambda}=8\pi\sin\psi$$

under the given conditions. A few successive zeros of J_1 (Ref. 5) are given in Table I, together with corresponding angles ψ.

Thus, in the reference curve $h=0$ of Fig. 3, we observe drops in the relative gain at these angles. (The reference curve was obtained by numerical integration and not by Eq. 8.) The attenuation corresponding to zeros of J_1 is not complete in the plot, as the values for plotting were obtained only at increments of one degree. The curves for $h=2$, 4, 6, 8, 10, and 12 show the effect of varying h. The non-monotone character of the relative gain at $\psi=90°$ may be attributed to the undulatory nature of the equivalent illumination (illustrated in Figs. 6–9). The amount of attenuation depends to a certain extent on the location of the truncation value $r_{s(\max)}$ with respect to high and low points of the equivalent illumination. Figure 4 gives results for several values of h with $r_{s(\max)}=4$ and uniform illumination.

The effects of tapering the illumination of the shielded antenna were studied for $h=6$ and $r_{s(\max)}=6$ by using the illumination

$$A(r)\exp[j\phi(r)]=\exp(-ar^2),\quad r\leq r_{(\max)}=2,$$

where the following values of a were used: $a=0.125$ (tapered to $e^{-\frac{1}{2}}$), $a=0.25$, (tapered to e^{-1}), and $a=2.5$ (tapered to e^{-10}). Note that uniform phase is used for

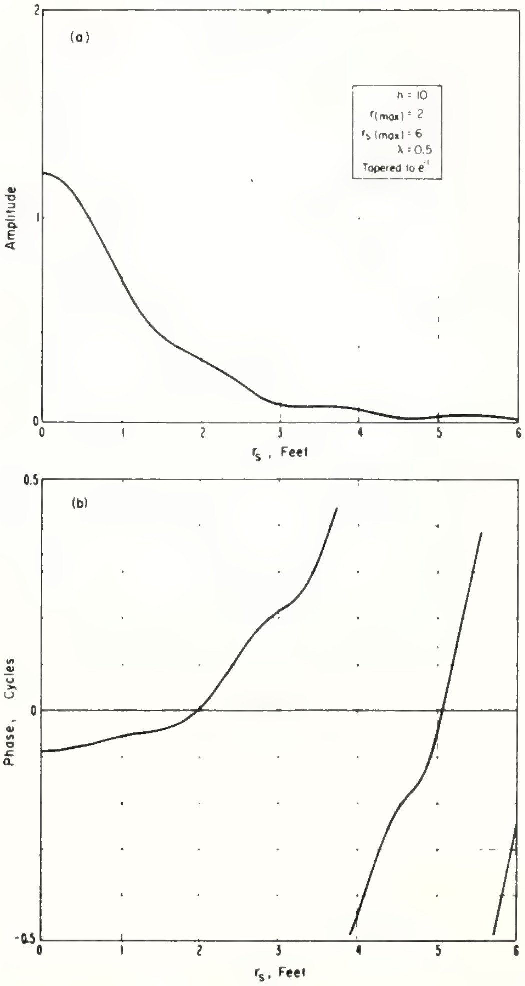

FIG. 9. Equivalent outer-aperture illumination.

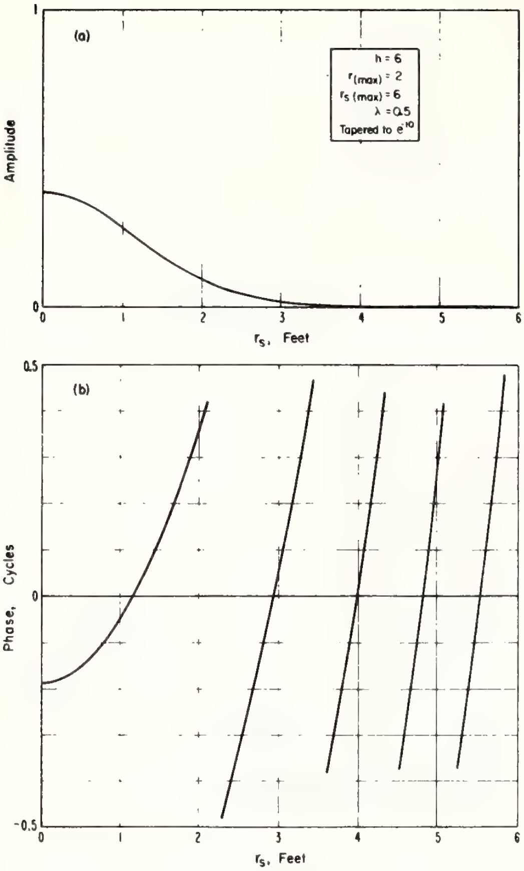

FIG. 10. Equivalent outer-aperture illumination.

all tapers. Such tapering has an effect on both the reference relative gain pattern ($h=0$) and the pattern for $h=6$. These results for $a=0$ (untapered), $a=0.125$, $a=0.25$, and $a=2.5$ are shown in Fig. 5. Note also that the reference curve, $h=0$, gives a lower relative gain for a taper to e^{-10} than the curve for $h=6$.

Finally, Figs. 6–10 give amplitude and phase curves for the equivalent illumination across the aperture at height h above the antenna for five different conditions, as noted. One may observe the undulatory character of the amplitudes in Figs. 6–9 and the substantial phase variation in all five figures.

ACKNOWLEDGMENTS

The author acknowledges valuable discussions with Mr. Robert S. Lawrence, Dr. Steven F. Clifford, and Dr. C. Gordon Little. In addition, Mr. Lawrence supplied a computer program used in checking out the present program, and Dr. Little suggested the general method used in this paper.

---

[1] W. R. Simmons and J. W. Wescott, "Acoustic Echo Sounding as Related to Air Pollution in Urban Environments," NOAA Tech. Rep. (to be published).

[2] J. D. Jackson, *Classical Electrodynamics* (Wiley, New York, 1962), p. 282.

[3] E. G. Bowen, Ed., *A Textbook of Radar* (Cambridge U. P., Cambridge, England, 1954), pp. 254 ff.

[4] H. Jasik, Ed., *Antenna Handbook* (McGraw-Hill, New York, 1961), pp. 2-28, 2-29.

[5] M. Abramowitz and I. A. Stegun, Eds., *Handbook of Mathematical Functions* (Nat. Bur. Stand., U. S. Gov. Printing Office, Washington, D. C., 1964), p. 414.

Reprinted from Journal of Research of the NBS - C. Engineering and Instrumentation 75, No. 1, 41-45, 1971.

Seismic Response of Infrasonic Microphones[*]

Alfred J. Bedard, Jr.[**]

(November 19, 1970)

Factors affecting the (unwanted) seismic response of infrasonic microphones are indicated. Past measurements of ground motion deduced from the radiated atmospheric sound measured with infrasonic microphones are reviewed, and such measurements are compared with seismometer measurements of ground motion. Seismic motions caused by the Japanese earthquake of May 1968 are used in this example. The seismic response of the infrasonic microphone used for this measurement was experimentally determined and the results are presented. A simple method of compensating for interfering seismic effects on microphones is described.

Key words: Compensation; ground motion; infrasonic microphones; seismic response.

1. Introduction

If seismic motions caused by a distant earthquake are strong enough, an earthquake-associated air-pressure wave may be observed. These air-pressure changes are observed coincident with vertical motions of the earth in the immediate vicinity of the microphone, and are caused by radiation of sound into the atmosphere by the ground motions. Observations on such acoustical radiation have been reported previously [Cook and Young, 1962; Donn and Posmentier, 1965]. The amplitudes of vertical ground motion deduced from the air pressure measurements have been compared with ground motions measured with seismometers operated in the vicinity of the infrasonic microphones [Cook, 1965; Donn and Posmentier, 1965; Golitsyn and Klyatskin, 1967]. In general quite good agreement has been obtained using the two methods.

In addition to the infrasound caused by local ground motions, air pressure waves have been observed originating from both the vicinity of the epicenter of an earthquake [Benioff and Gutenberg, 1939; Mikumo, 1968] and from intermediate regions along the seismic wave propagation path [Benioff et al., 1951; Donn and Posmentier, 1965; Press and Ewing, 1951]. The Alaskan earthquake of 1964 provided examples of both these classes of earthquake-associated atmospheric sound waves [Donn and Posmentier, 1965].

An example of an atmospheric pressure disturbance generated by the local passage of seismic waves from distant seismic activity is the record shown in figure 1. The acoustic data from microphones in the vicinity of Washington, D.C., appear in the upper portion of this figure. The microphone array at a typical station is designed for measuring four principal characteristics of infrasonic waves: (1) the amplitude and waveform of the incident sound pressure, (2) the azimuth of arrival of the wave, (3) the horizontal phase velocity, and (4) the dominant period of the wave. An infrasonic station normally has four or more microphones equipped with noise-reducing devices located at ground level, approximately in the same plane and spaced about 7 to 10 km apart. Figure 2 shows the microphone layout for the Washington, D.C., station.

Each line-microphone produces frequency-modulated voltages proportional to the sound pressure in the atmosphere. The tones are usually transmitted by telephone wires to a recording location. At this central recording location these tones are demodulated, amplified, filtered, and recorded in analog form both as ink-on-translucent-paper traces, and on magnetic tape. The system pass-band is designated N7 and is shown in figure 3.

The disturbance shown in figure 1 is related to an earthquake on May 16, 1968, with the epicenter under the sea floor 100 miles east of Hachinohe, Honshu, Japan (U.S. Coast and Geodetic Survey, Preliminary Determination of Epicenter: $0 = 00^h\ 48^m\ 55.4^s$ UT, 40.84° N, 143.22° E, $h = 7$ km, $M_s = 7.9$). This disturbance was much smaller at Washington, D.C., than the disturbance following the 1964 Alaskan earthquake. It was thought that the smaller ground motions would make intercomparison with seismic data more feasible. Note that this disturbance was distinguished from local pressure changes caused by turbulent motions of the wind, because of its presence at all of the microphones of a multipartite array.

The analog acoustic record shown in figure 1 is a superposition of the recordings from the various microphone sites. The waveform coherence between the various sites is quite good. Note that the time marks are almost coincident at the chart speed of ¾ in/min, indicating a high horizontal phase velocity. The disturbance was distinguished from acoustic waves propagating in the atmosphere parallel to the earth's surface, by its higher horizontal phase velocity. Rayleigh waves on the earth's surface have a horizontal phase velocity of about 3 km/s, compared with 330 m/s for acoustic waves in the atmosphere.

The disturbance started at 0135 UT and was lost in noise at about 0214 UT. The observed periods ranged from 17 s to 40 s. The maximum amplitude occurred at

---

[*] An invited paper.

[**] Present address: National Oceanic and Atmospheric Administration, Wave Propagation Laboratory, Geoacoustics Group, Rockville, Md. 20852.

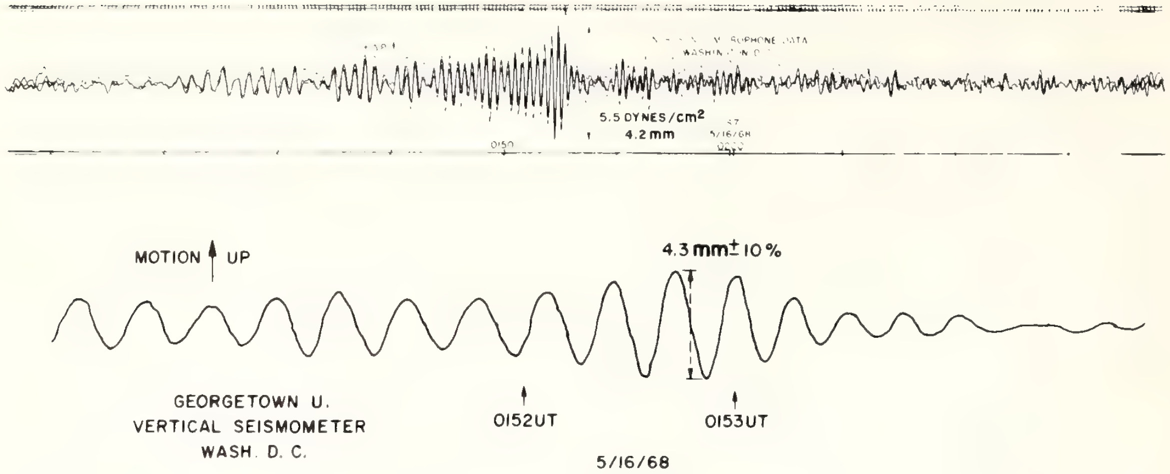

FIGURE 1. *Seismic disturbance of May 16, 1968.*

0153 UT and was 5.5 μbars at a period of 19 s. The ground displacement computed from these pressure data was 4.2 mm. The ground motion determined from seismometers located in Washington, D.C., was 4.3 mm. The Georgetown University Seismometer Laboratory made the recordings of ground motion shown in figure 1 available. The short-period worldwide standard seismograph was used in making the recording. The seismic data were corrected for system amplitude response before being compared with the infrasonic microphone records. Both measurements may be considered accurate to within ± 10 percent.

R. K. Cook [1965] has shown that the air pressures for such a disturbance are due to an integrated effect of the sound radiated by Rayleigh waves over a large area, as opposed to a seismometer which measures motion at a point; hence, it seems reasonable to consider infrasonic microphone data in order to obtain a more representative picture of ground motion over an area of the earth's surface. Infrasonic data will be useful for measurement of very large amplitude ground motions because the sound pressure levels will probably be larger than the pressure variations due to local winds. It is possible that for very large ground motions the dynamic range of sensitive seismometers will be exceeded, and then acoustical measurements can provide the desired measurements of the motions. But the microphones must perforce be

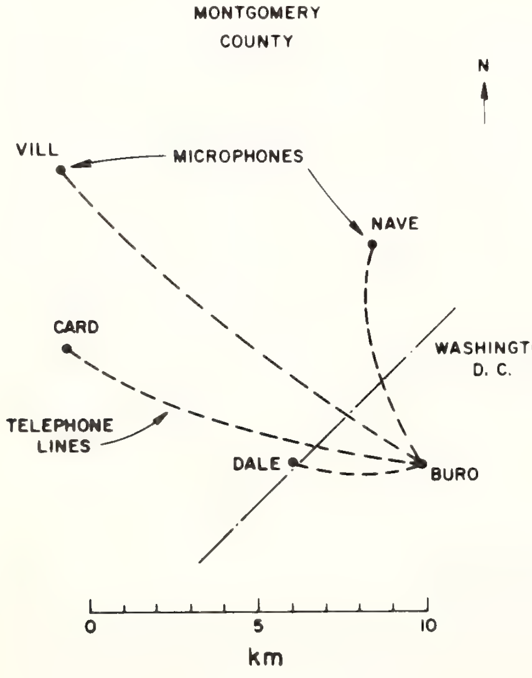

FIGURE 2. *Microphone site layout.*

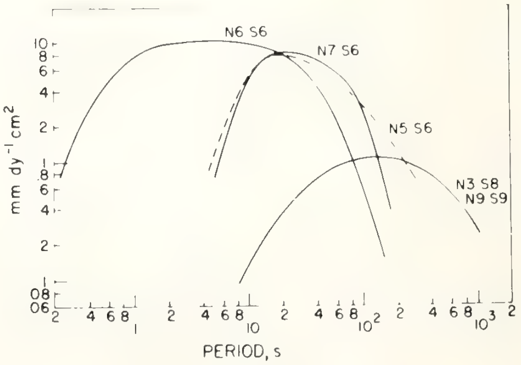

FIGURE 3. *Microphone system response.*

located on the surface of the earth, and they are therefore subjected to the latter's seismic motions. It is therefore necessary to determine the effects of the microphone's seismic motions on its electrical output. The effects might be small or negligible, but they must be known quantitatively.

2. Seismic Response Considerations

In attempting to test and evaluate the seismic response of infrasonic microphones several factors must be considered. Rayleigh waves occurring at the location of the pressure transducer generate peak pressure changes in the atmosphere calculated according to the relation

$$\Delta P = \rho c \omega X$$

where

$\omega = 2\pi f$
$f =$ frequency of the wave
$X =$ double amplitude of ground motion
$\Delta P =$ peak-to-peak pressure change in the atmosphere
$\rho =$ density of air
$c =$ velocity of sound in air.

This pressure change would be measured by the microphone together with any other instrumental seismic response effects that might be present. A frequently used form of infrasonic microphone is one that uses the motion of a diaphragm to detect pressure changes. This is the type of detector that will be considered here.

In addition to the pressure $\Delta P = \rho c \omega X$, such a transducer will respond to accelerations independently of any pressure changes occurring in the atmosphere. A transducer such as that shown in figure 4 will show seismic response due to both the diaphragm inertia and the inertia of air columns in the unit. Also, when the transducer is moved vertically through the atmosphere, a pressure change will be introduced whose magnitude will be equal to $\rho g X$. Pressure changes due to air motion past the microphone's openings to the atmosphere could also occur. The various factors contributing in theory to the seismic response are summarized as follows:

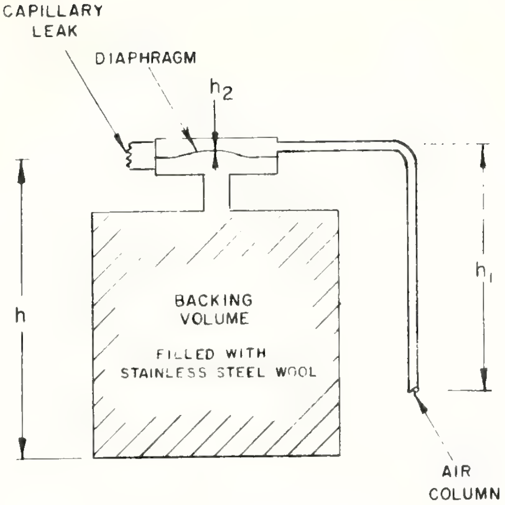

FIGURE 4. *Schematic view of microphone.*

$$\begin{array}{ccccc}
\text{Total Pressure Change} & & \text{Hydrostatic Equation*} & & \text{Bernoulli Pressures*} \\
\Delta P_{\text{Total}} & = & \rho g X & + & 1/2\,\rho V^2 + \dots
\end{array}$$

$$\begin{array}{ccccccc}
\text{Open Tube Air Column Effects*} & & \text{Diaphragm Inertia} & & \text{Local Radiation} & & \text{Closed Tube Air Column Effects} \\
\dots\ \rho\omega^2 h_1 X & + & \omega^2 \rho_{\text{brass}} h_2 X & + & \rho\omega c X & & \dots + 1/2\,\rho\omega^2 h X
\end{array}$$

where:

$g =$ local gravitational acceleration
$X =$ displacement double amplitude
$h_1 =$ vertical height of microphone's external air column
$h_2 =$ thickness of diaphragm
$h =$ length of microphone's internal air column
$V =$ maximum velocity of motion
$\omega = 2\pi f$
$\rho =$ density of air
$\rho_{\text{brass}} =$ density of the diaphragm
$c =$ velocity of sound in air.

In experimentally testing seismic response on a vibration shaker, the effect of translating the transducer vertically through the atmosphere will have to be taken into account. Effects of local sound radiation by the shaker will be negligible. Note that the relation listed for air column effects is valid for an open-ended tube at low frequencies. The closed tube relation is half of this value. Microphone response to vertical displacements was tested at the National Bureau of Standards at Gaithersburg, Maryland, where Mr. James R. Houghton made available a shaker capable of producing approximately sinusoidal, vertical motions. The tests were performed at an ambient temperature of 22° C, a relative humidity of 20 percent, and an ambient pressure of 757 mm of Hg. The frequency of vertical motion was adjustable over the range 1 Hz to 0.01 Hz. The double amplitude was set to 4 in.

The microbarograph system consisted of a pressure transducer [Cordero et al., 1957] equipped with a 7.5 s high-pass acoustical filter. The system pass-band including Discriminator N4 and Filter Amplifier N10 had 3 dB points at 1 and 20 s. Figure 4 shows a schematic view of the system microphone mechanical configuration. The microbarographic system was calibrated with a pistonphone, and a portable fixed-frequency pressure calibrator was operated before and after the seismic response tests. The pistonphone was a stainless steel wool-filled 50-gal volume equipped with a brass bellows variable-volume element to produce dynamic pressure changes. Theoretical considerations made it desirable to vary the key parameters while subjecting the infrasonic microphone to vertical displacements on a shaker at a number of frequencies. Since the experiment was performed in the presence of local atmospheric pressure variations, a time of low atmospheric pressure noise was chosen. Further, it was necessary to choose vibration amplitudes large enough for the expected pressure variations to be larger than the local noise level.

---

* There are no contributions due to the hydrostatic equation or Bernoulli pressures during seismic wave transit. These two effects are important during an experimental evaluation of the microphone with a vibration shaker. The relation shown for open tube air column effects is valid only during vibration shaker type experiments at low frequencies.

3. Experimental Results

The system response on a vibration shaker table was found, within experimental error, to be independent of the orientation of the microphone inlet to the atmosphere. Hence, it is inferred that inlet air blast and Bernoulli effects did not contribute to the electrical output of the microphone.

At longer periods than 5 s per cycle, the observed change in pressure closely approached the value to be expected from the hydrostatic term in the pressure equation. There is no direct frequency dependence involved in this term. Figure 5 shows the pressure measured as a function of frequency.

If the value for ΔP determined from the hydrostatic equation is subtracted from the observed pressure changes and the resulting data plotted as a function of frequency squared, the result is approximately a straight line in agreement with the predicted f^2 dependence. See figure 6 for a log-log plot of ΔP versus frequency squared.

The vertical external tubing length was varied in 5-in increments and the output of the system measured with the frequency of vibration kept constant at 1 Hz. The variation of pressure as a function of length of tubing below this valve is linear and changes as expected ($\Delta P \approx 1.2\ h_1$ at 1 Hz, where h_1 is in inches; fig. 7). This is approximately the slope of the line in figure 7.

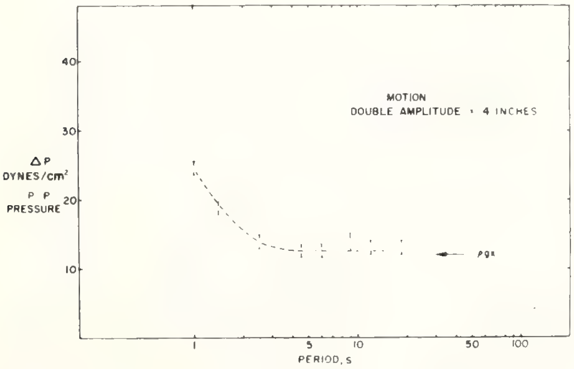

Figure 5. *Experimental response of microphone as a function of frequency of vertical motion.*

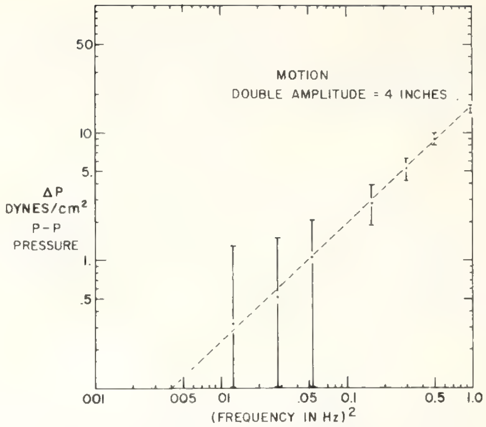

Figure 6. *Response of microphone as a function of frequency squared.*

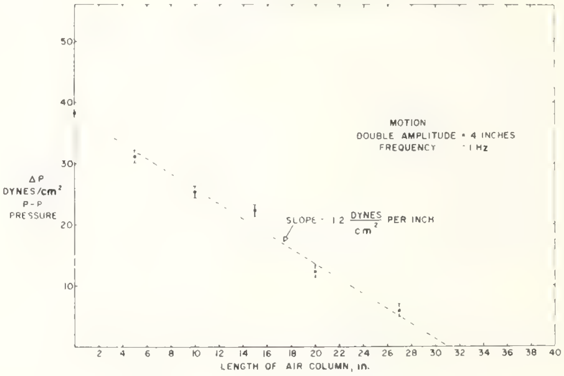

Figure 7. *Effect of air column length.*

Table 1 presents the contributions of the various seismic response mechanisms to the total pressure change observed. The outputs have been computed at frequencies of 1 Hz and 0.1 Hz and for displacement amplitudes of 0.001 in, 0.01 in, 0.1 in, and 1 in. Typical values are included in this table to show the relative importance of the various effective elements. The hydrostatic relation is also included for comparison purposes, although normally it would not be a factor in determining Rayleigh wave seismic response. The diaphragm compliance and effect of any backing volume sensitivity will reduce the system response, but these effects are not included in this worst-case consideration.

Because local background seismic noise amplitudes can be over 20 μm, the displacement amplitude of 0.001 in is a reasonable reference to use. Table 1 shows that the "loudspeaker action" effect from seismic waves will domi-

TABLE 1. *Seismic response contributions*

Generation mechanism		Displacement X, inches			
		$X = 0.001$	$X = 0.01$	$X = 0.1$	$X = 1$
1 Hz	$\rho g X$	0.003 μbar	0.03 μbar	0.3 μbar	3 μbar
	$\omega c \rho_{air} X$	.638 μbar	6.38 μbar	63.8 μbar	638 μbar
	$\omega^2 \rho_{brass} h_2 X$	.002 μbar	.02 μbar	.2 μbar	2 μbar
	$\omega^2 \rho_{air} h_1 X$	.003 μbar	.03 μbar	.3 μbar	3 μbar
0.1 Hz	$\rho g X$	0.003 μbar	0.03 μbar	0.3 μbar	3 μbar
	$\omega c \rho_{air} X$	.0638 μbar	.638 μbar	6.38 μbar	63.8 μbar
	$\omega^2 \rho_{brass} h_2 X$	$.2 \times 10^{-4}$ μbar	2×10^{-4} μbar	.002 μbar	.02 μbar
	$\omega^2 \rho_{air} h_1 X$	$.3 \times 10^{-4}$ μbar	3×10^{-4} μbar	.003 μbar	.03 μbar

$h_1 = 10$ in
$h_2 = 0.001$ in
$\rho_{brass} = 8.7$ g/cm^3
$g = 980.1$ cm/s^2

nate. The effects due to transducer seismic response are typically less than 1 percent of the "loudspeaker effect" at the pertinent frequencies. Thus, for this infrasonic microphone configuration, it is quite reasonable to deduce ground motions from observed pressure changes without correcting for instrument seismic response. Also, with the proper length of air column termination, one can null out the seismic response of the microphone at infrasonic frequencies. In the NOAA infrasonic microphone, the return hose from the microphone to the noise-reducing array accomplishes this. The open tube relation used here for computing this form of seismic compensation is valid only for shaker-type experiments with negligible local radiation. A seismically compensated microbarograph has been described [Ewing and Press, 1953] for use at periods longer than 20 s. A different method of seismic compensation is used.

Consideration of air column effects would suggest that caution should be exercised, for example, in installing an infrasonic microphone in a deep well and routing a tube to the surface. Since the air column seismic response is directly proportional to the length of the air column, a person might, in fact, be constructing a system sensitive to vibration. For 0.001-in tube displacements at 1 Hz, the seismically induced pressure amplitudes for an air column 10 ft long would be 0.03 μbar. This is over three times the internal noise level of the microphone now used by NOAA. Noise due to local vibrations would be increased.

I am grateful to Mr. Frank Baldwin, who did the art work on the illustrations, and to Rev. McConnell of Georgetown University, who provided the seismic records.

4. References

Benioff, H., Ewing, E. M., and Press, F., (1951), Sound waves in the atmosphere generated by a small earthquake, Proc. Natl. Acad. Sci. **37,** 600–603.

Benioff, H., and Gutenberg, B., (1939), Waves and currents recorded by electromagnetic barographs, Bull. Am. Meteorol. Soc. **20,** 421.

Bolt, B. A., (1964), Seismic air waves from the great 1964 Alaskan earthquake, Nature **202,** 1095–1096.

Cook, R. K., (1965), Radiation of sound by earthquakes, Fifth Congress International D'Acoustique, Liege.

Cook, R. K., and Young, J. M., (1962), Strange sounds in the atmosphere, Sound **1,** No. 3, 25–33.

Cordero, F., Matheson, H., and Johnson, D. P., (1957), A non linear instrument diaphragm, J. Res. Nat. Bur. Stand. (U.S.), **58,** No. 6, 333–337.

Donn, W. L., and Posmentier, E. S., (1965), Ground-coupled air waves from the great Alaskan earthquake, J. Geophys. Res. **69,** No. 24, 5357–5361.

Ewing, M., and Press, F., (1953), Further study of atmospheric pressure fluctuations recorded on seismographs, Trans. Am. Geophys. Union **34,** No. 1, 95–100.

Golitsyn, G. S., and Klyatskin, V. I., (1967), Atmospheric oscillations caused by movements of the earth's surface, Izv, Atmospheric and Oceanic Physics **3,** No. 10, 1044–1052.

Mikumo, T., (1968), Atmospheric pressure waves and tectonic deformation associated with the Alaskan earthquake of March 28, 1964, J. Geophys. Res. **73,** No. 6, 2009–2025.

Press, F., and Ewing, M., (1951), Ground roll coupling to atmospheric compressional waves, Geophysics **16,** 416–430.

(Paper 75C1–313)

Reprinted from Radio Science 5, No. 12, 1453-1460, 1970.

ELF attenuation rates and phase velocities observed from slow-tail components of atmospherics

W. L. Taylor

Department of Commerce, National Oceanic and Atmospheric Administration
ERL, Wave Propagation Laboratory, Boulder, Colorado 80302

K. Sao

Research Institute of Atmospherics, Nagoya University, Toyokawa, Aichi, Japan

(Received May 8, 1970; revised August 3, 1970.)

Slow-tail portions of atmospherics were recorded simultaneously in Japan and the United States from sources located in the Pacific Ocean area. The amplitude and phase spectra of forty pairs of selected atmospherics were computed, and propagation parameters for the zero-order wave-guide mode were calculated for nighttime conditions only. Attenuation rates for W–E propagation extended from about 0.5 db/Mm at 20 Hz to 2.0 db/Mm at 300 Hz and for E–W propagation from 0.8 db/Mm at 20 Hz to about 2.8 db/Mm at 300 Hz. The phase velocities extended from about 0.7 and 0.8 the velocity of light for W–E and E–W propagation, respectively, at 20 Hz to about 0.93 the velocity of light for either direction at 300 Hz.

INTRODUCTION

ELF slow-tail components of atmospherics were observed simultaneously in the United States and Japan beginning in 1966. After several preliminary observations in the spring of 1967, observational techniques were established and recording equipment sensitivities were adjusted at Tottori, Japan, and Lafayette, Colorado, to give, from lightning sources in the Pacific Ocean area, slow-tail wave forms that could be analyzed.

This report is based on observations made between 1200 and 1300 UT on September 13, 15, 18, and 20, 1967. Nighttime conditions existed over the entire Pacific Ocean area from which sources of atmospheric slow tails were likely to be recorded at both Tottori and Lafayette. ELF attenuation rates and phase velocities computed from data obtained for approximate easterly and westerly propagation during nighttime conditions over the Pacific Ocean area are presented.

Actual data recording was limited to a 30-second period every 10 minutes starting on the hour for a total of 6 periods each day. The Tottori data were recorded with a multi-channel paper chart oscillograph, and the Lafayette data were recorded with a 35-mm strip film camera photographing two multibeam oscilloscopes. Tottori data included the ELF response of a 15-meter vertical monopole antenna and an indication of signal arrival direction from VLF crossed loop antennas. Lafayette data included the ELF response of a 2-meter vertical monopole antenna and the direction of arrival with sense from VLF equipment. Time marks synchronized with either JJY (standard-time transmissions in Japan) or WWV (standard-time transmissions in the United States) were recorded with the data at each location.

DATA REDUCTION

Selecting data was a very difficult task. First, chart paper and photographic film were processed at both locations. Then, the time of arrival, amplitude, and direction of arrival of all slow-tail wave forms that were suspected to have been also observed at the other location were tabulated. These tabulations were then exchanged between laboratories. After independent comparison of the tabulation entries, ELF wave forms were exchanged for those entries most likely to have resulted from the same lightning stroke. Finally, forty ELF slow-tail wave-form pairs of sufficient quality for spectrum analysis were selected. It was required that the VLF component of the atmospheric be recognizable at both observation sites

Copyright © 1970 by the American Geophysical Union.

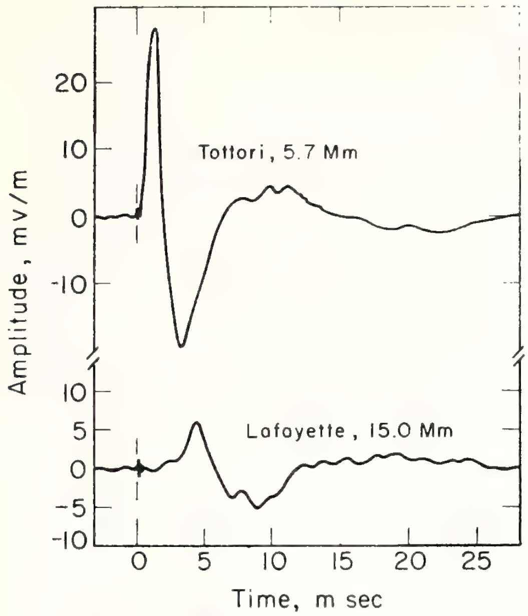

Fig. 1. Example of slow-tail wave forms.

for time delay measurements and that the VLF atmospheric be of sufficient amplitude at the Lafayette site to produce an accurate direction-of-arrival display. An example of a slow-tail wave-form pair recorded at both Tottori and Lafayette from a lightning stroke near Java, Indonesia (at point A in Figure 6), is shown in Figure 1. The calculation of the propagation distances indicated by each wave form will be covered later. Increased dispersion with distance is very evident upon comparing the general wave-form shapes of these examples. The amplitude ratio between these pulses is about 6:1, and there is an obvious time delay with increased distance. Zero on the time scale was established as the time of arrival of the VLF component.

The time between the initial part of the VLF component and the peak amplitude of the first half-cycle of the ELF component is called the separation time δ. This is the sum of the delay t between the beginnings of the VLF and ELF components and the quarter period $\tau/4$ which is one-fourth the cycle time of a sine wave that best fits the first half-cycle of the ELF component. *Hepburn and Pierce* [1953] established the following relationships for all nighttime conditions:

$$t = 0.13d - 0.14 \qquad (1)$$

$$\tau/4 = 0.50 + 0.08d \qquad (2)$$

therefore,

$$\delta = 0.36 + 0.21d \qquad (3)$$

where d is the distance in megameters and t, τ, and δ are in milliseconds. Values for separation times of 1.4 and 3.7 msec, measured for the examples, compare favorably with 1.5 and 3.5 msec obtained from (3) using 5.7 and 15.0 Mm, respectively.

Each selected wave-form record was enlarged so that a time base of about 3 msec/cm was realized. Wave forms were traced on graph paper, and the amplitude of the wave-form trace was tabulated each millimeter or (for wave forms with rapid rise times characteristic of relatively near sources) each half millimeter. This was done over the time period of each wave form, which usually involved 20 to 40 msec. Time base and amplitude values were established for each wave form from various calibration procedures. All required data and instructions were delivered to an electronic computer programmed to calculate the Fourier spectrum. Amplitude and phase were calculated each 2 Hz from 10 to 40 Hz, each 5 Hz from 45 to 100 Hz, each 20 Hz from 120 to 400 Hz, and each 50 Hz from 400 to 1000 Hz.

The amplitude spectra of the example wave forms are shown in Figure 2. These spectra are not smooth because there was background noise associated with each wave form. Perturbations at frequencies less

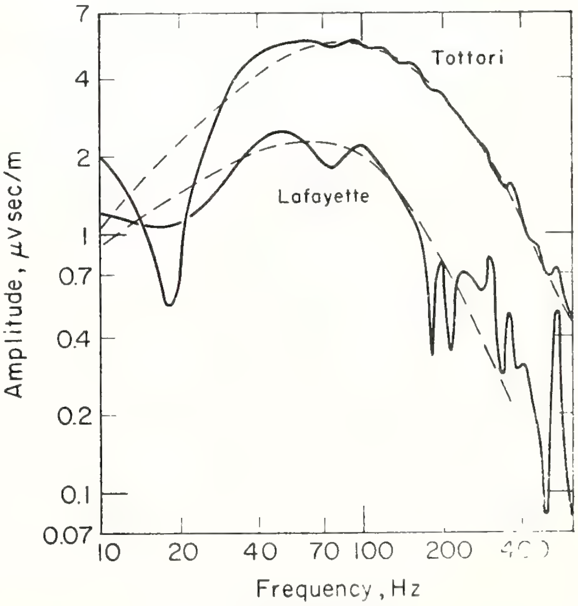

Fig. 2. Amplitude spectra.

than 30 or 40 Hz (particularly large for the Tottori spectrum) are the result of an improper baseline level for each wave form. Rapid fluctuations in amplitude versus frequency at the upper end of the spectra (very large for the Lafayette spectrum) were caused by noise and harmonic interference from commercial power lines. The dashed lines in the figure were an attempt to smooth the spectra and minimize the effects of background interference. Their validity rests on the assumption that the results produced by causes of perturbations would tend to be random and that an individual spectrum would tend to be relatively smooth and free of source induced or propagation induced perturbations.

Figure 3 shows the phase spectra of the example wave forms. Positive degrees of phase correspond to a lag or a delay. For all frequency components, the Lafayette wave form was more delayed in arrival time (relative to the velocity of the VLF component, which is assumed to travel at the velocity of light) than was the Tottori wave form. Perturbations are evident in the phase curves, but they are not as noticeable as the corresponding perturbations on the amplitude curves. Again, the dashed lines were an attempt to smooth out the background-noise induced perturbations.

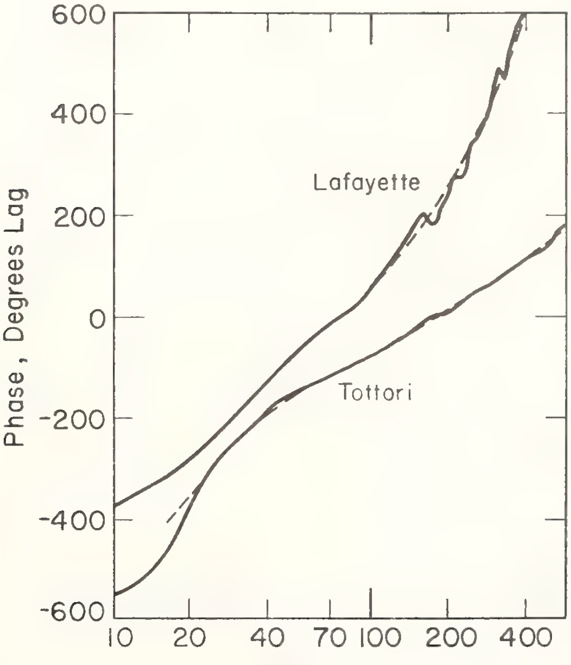

Fig. 3. Phase spectra.

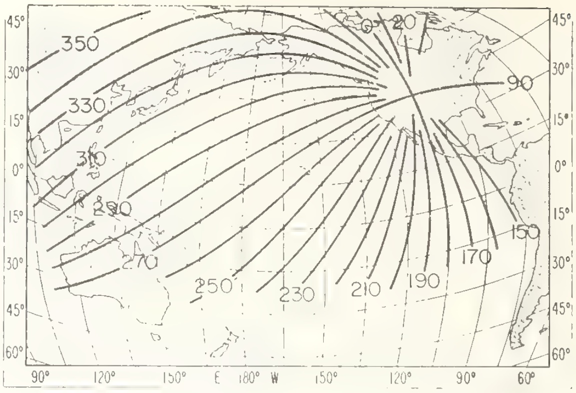

Fig. 4. Direction of arrival at Lafayette.

To attain attenuation rates and phase velocities, a location for each lightning stroke producing a selected pair of ELF slow tails must be determined. We originally desired to show direction of arrival at each observation site, but it was not possible to develop this facility at the Tottori site. The Lafayette site could show VLF direction of arrival, and both locations could record the arrival time of the atmospherics relative to time marks synchronized to either WWV or JJY, so a method was devised whereby the direction of arrival at Lafayette and the time difference of arrival between Lafayette and Tottori could be used to determine a lightning-source location.

The direction of arrival at Lafayette for each 10° of azimuth covering the Pacific Ocean area is shown in Figure 4. Time differences (the time of arrival at Lafayette minus the time of arrival at Tottori given in milliseconds) are shown in Figure 5 for the Pacific Ocean area. The directional grid runs generally E–W for Lafayette directions, whereas the time difference grid runs essentially N–S over the primary areas of interest.

Direction of arrival could be measured to an accuracy of ±2° for an ideal transient source from the wide-band df display at the Lafayette site. An accuracy of only about ±5° was generally believed realized because of relatively high noise level associated with small VLF atmospherics from very distant sources, but in some cases an accuracy of only ±10° could be ascribed to a particular atmospheric.

Timing measurements at each site could be made to an accuracy of ±1 msec. Variation in reception of standard time signals and timing drift of the local

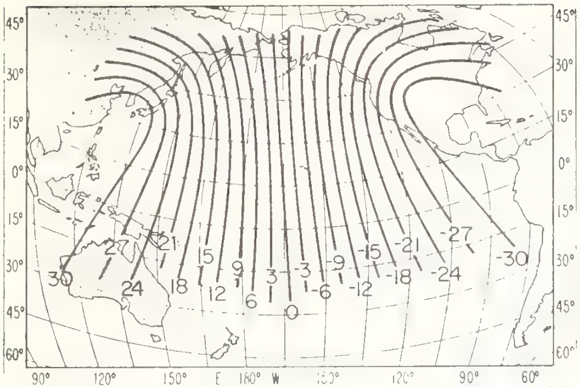

Fig. 5. Time difference in milliseconds (Lafayette minus Tottori).

secondary time standards reduced the accuracy of the time difference measurements to, perhaps, ±3 msec. Atmospheric sources located generally SE of Lafayette or SW of Tottori produced time differences approaching 32 msec, as can be seen in Figure 5. This fact was used during the analyses of data for most observation periods to check the accuracy of time difference measurements.

The approximate location of each slow-tail source was determined graphically by the direction of arrival and time difference of arrival of the VLF components. For a few cases where the VLF component was not measurable, it was necessary to measure time of arrival of the ELF component at the Tottori site and to correct for the separation times. The two parameters were quite compatible in that a crossed grid network was formed over the Pacific Ocean area and the errors in each measurement were of the same order of magnitude. The effect of location errors on the calculated propagation values will be discussed in the last section.

FORMULATION

The basic theoretical considerations for the radiation field propagated via the zero-order earth-ionosphere wave-guide mode have been developed by *Wait* [1960]. The use of atmospherics to determine single-mode propagation parameters has been reported by *Jean et al.* [1960, 1961] and *Taylor* [1960]. The attenuation rates for single wave-guide mode propagation using atmospherics observed in a two-station configuration can be expressed as

$$\alpha(\omega) = \left[20 \log \frac{|E_1(\omega, d_1)|}{|E_2(\omega, d_2)|} - 10 \log \frac{\sin d_2/a}{\sin d_1/a}\right] \cdot (d_2 - d_1)^{-1} \qquad (4)$$

and the corresponding phase velocities can be expressed as

$$\frac{V_p(\omega)}{c} = \left\{1 + \frac{[\Phi_2(\omega, d_2) - \Phi_1(\omega, d_1)]c}{\omega(d_2 - d_1)}\right\}^{-1} \qquad (5)$$

where $|E(\omega, d)|$ is the amplitude, $\Phi(\omega, d)$ is the phase of the Fourier spectrum for a single atmospheric, ω is the angular frequency ($2\pi f$), d_1 is the great circle distance to the near station (Tottori), d_2 is the great circle distance to the far station (Lafayette), a is the earth's radius, and c is the velocity of light.

These formulations are adequate when observations made at d_1 and d_2 are almost along the same great circle, in the same direction, and the propagation conditions along d_1 and d_2 are the same. We could devise formulations to include changes in ground conductivity along each path and variations in strength and direction of the earth's magnetic field, etc., but the present data determine only gross directional effects. They are still inadequate, however, for obtaining propagation parameters when paths are far removed from a great circle connecting the two observing stations. The effects of the geomagnetic field were such that directional effects could produce different propagation conditions along E–W and W–E paths. To account for gross directional effects additional formulations were required.

If we assume that propagation conditions can be calculated from (4) and (5) for W–E attenuation rates $\alpha(\omega)_{W-E}$ and phase velocities $V_p(\omega)_{W-E}/c$ using suitable data, then the attenuation rates for E–W propagation can be written

$$\alpha(\omega)_{E-W} = \alpha(\omega)_{W-E} \cdot \frac{d_4}{d_3} - \left[20 \log \frac{|E_3(\omega, d_3)|}{|E_4(\omega, d_4)|} - 10 \log \frac{\sin d_4/a}{\sin d_3/a}\right] d_3^{-1} \qquad (6)$$

and the phase velocities can be written

$$\frac{V_p(\omega)_{E-W}}{c} = \left\{\frac{c}{V_p(\omega)_{W-E}} \cdot \frac{d_4}{d_3} - \frac{d_4 - d_3}{d_3} \cdot \left[1 + \frac{(\Phi_4(\omega, d_4) - \Phi_3(\omega, d_3))c}{\omega(d_4 - d_3)}\right]\right\}^{-1} \qquad (7)$$

where the subscript 3 refers to the E–W path (Tottori) and the subscript 4 refers to the W–E path (Lafayette).

DATA ANALYSES RESULTS

The location of the lightning stroke producing each pair of slow tails was determined. Locations tended to cluster in certain areas. Figure 6 presents the six areas into which all sources were placed to simplify computations. The number of atmospherics in each group, the average direction of arrival at Lafayette, the average time difference in arrival between Lafayette and Tottori, and the computed distances from the source locations to each recording station are given in Table 1.

Attenuation rates and phase velocities were computed from the spectra of each wave-form pair; (4) and (5) were used for group A and B atmospherics, and (6) and (7) were used for the groups located in mid-Pacific Ocean areas. Average values for attenuation rates and phase velocities, as a function of frequency, were calculated for the 22 pairs in groups A and B. Results were assumed to represent W–E propagation. Direction of propagation relative to the geomagnetic field between each source area and Tottori was about 20° from magnetic north. The direction of propagation for the initial d_1 distance along the path toward Lafayette was about 25°. Over the remainder of the path to Lafayette, the direction of propagation increased from about 30° near Japan to about 100° over the United States; this results in an average direction of about 65° relative to magnetic north.

With the results from the A and B groups, average attenuation rates and phase velocities were calculated for the 18 pairs in groups C, D, E, and F. The geomagnetic propagation direction toward Japan varied between about 280° to 300° near the source areas and from about 245° to 280° near Japan; this gives an average of about 280°. The path direction toward the United States varied between about 40° to 60° near the source areas and between about 75° to 90° near Lafayette; this produces an average direction of about 70°.

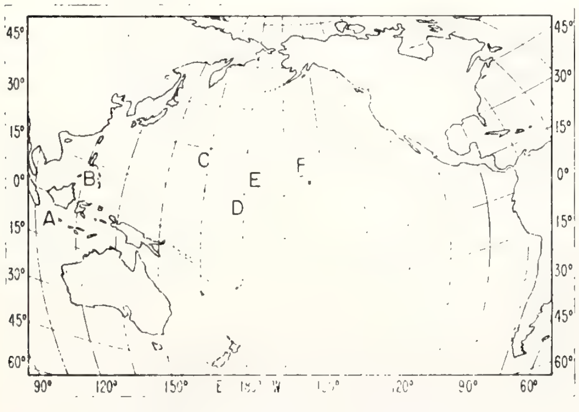

Fig. 6. Approximate location of slow-tail source areas.

TABLE 1. Summary of data

Group	Number	Azimuth at Lafayette	Time Diff., Lafayette to Tottori, msec	Distance to Tottori, Mm	Distance to Lafayette, Mm
A	18	305	31.0	5.7	15.0
B	4	310	32.0	3.0	12.5
C	2	292	16.0	3.3	8.0
D	6	270	10.0	5.2	8.3
E	6	275	7.5	5.0	7.2
F	4	272	−4.5	6.4	5.1

The results of the preceding computations are presented in Figure 7. Attenuation rates shown in the upper part of the figure were computed from smoothed amplitude-spectrum values at the frequencies indicated by the error bars and are presented in decibels per megameter. The lower part of the figure shows the phase velocities computed from smoothed phase-spectrum values and are presented as the velocity of the phase components relative to the velocity of light. Average values of propagation parameters are indicated by solid curves for W–E and by dashed curves for E–W. Error bars, shown slightly offset from the frequency at which computations were made, indicate the maximum excursions obtained from computations based on the spectra of each wave-form pair. The solid error bars and the dashed error bars correspond, respectively, to the W–E and the E–W curves.

As shown, attenuation rates vary from about 0.5 db/Mm at 20 Hz to 2.0 db/Mm at 300 Hz for W–E propagation and from about 0.8 db/Mm at 20 Hz to 2.8 db/Mm at 300 Hz for E–W propagation. The relatively slow increase of attenuation with frequency at lower frequencies is separated from the rather rapid increase of attenuation at the higher frequencies by a bend in the curves near 150 Hz.

Phase velocities, relative to the velocity of light, extend from about 0.7 and 0.8, for W–E and E–W propagation at about 20 Hz, to about 0.93 for either direction at 300 Hz as indicated. The increase in velocity with frequency is rapid at the lower frequencies but tends to increase slowly at frequencies above 70 to 100 Hz.

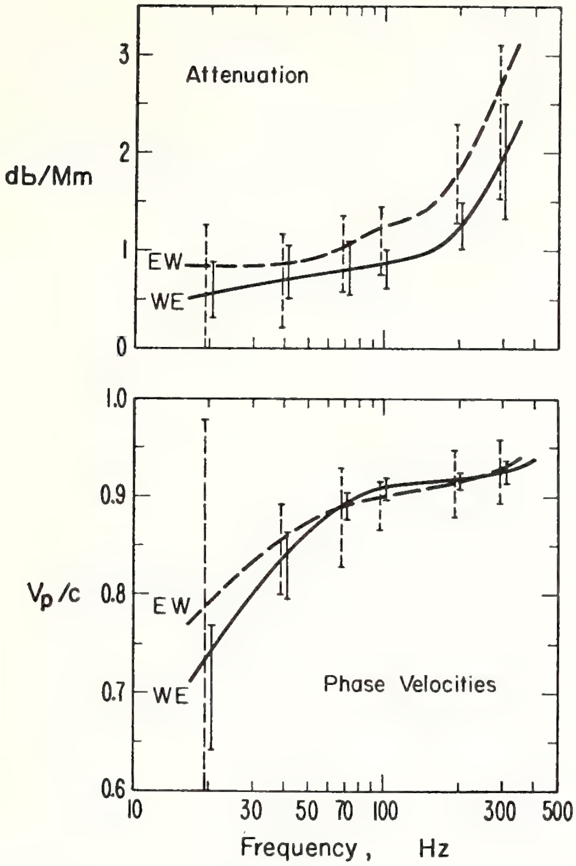

Fig. 7. Average attenuation rates and phase velocities. W–E propagation is shown by the solid-line curve; E–W propagation is shown by the dashed-line curve. W–E error bars are solid vertical lines; E–W error bars are dashed vertical lines.

DISCUSSION

Results presented here represent approximate W–E and E–W propagation conditions over the North Pacific area during all nighttime conditions. It would not be meaningful to assign statistical significance to these results because of the small number of samples and the complexities caused by various errors on the final results. It is important to know, however, the accuracy of these results as determined from expected errors in the over-all experimental techniques.

The effects of a location error on the W–E attenuation rate are proportional to changes in the second term of (4). The difference in distance $(d_2 - d_1)$ does not change with source location for the atmospherics assigned to groups A and B. An error of ±1000 km for all sources in both groups produces an error of ±0.13 db/Mm. This corresponds to an error of 25% at 20 Hz and only 7% at 300 Hz.

The calculation of changes in E–W attenuation rates for the four mid-Pacific areas is a much more complicated task. Errors of ±5° direction of arrival at Lafayette and of ±3 msec in time of arrival at both sites result in source locations that can change the distance to Tottori by ±500 km to Lafayette by ±1000 km. All terms in (6) are affected. If all sources in the mid-Pacific groups were changed in location by the maximum amount of distance error and in the same direction, the resulting E–W attenuation rates would change by about 19% the reported values over the entire frequency band (if we assume that errors in the W–E attenuation are independent of errors in the mid-Pacific atmospherics). Actually, an error of 10%, let us say, in the computed W–E attenuation values would result in an error in the E–W attenuation values of about 9% at 20 Hz and of 14% at 300 Hz. These errors are in the same direction (an increase in W–E attenuation would produce an increase in the computed E–W attenuation.)

Equipment sensitivities at each site were calibrated to a high degree of accuracy. Less than 1-db difference in relative equipment response between 30 Hz and 500 Hz was obtained. Yet, we have considerable doubt about the actual response of each site-equipment complex to an unperturbed signal propagating past each site. It is possible that absolute responses of our sites may be in error by as much as 3 db.

If we assume a 3-db error in actual equipment responses, an error of 0.32 db/Mm will result for the W–E attenuation rates, which corresponds to an error of 60% at 20 Hz and 16% at 300 Hz, relative to the computed values. The E–W attenuation rates, which are a function of the W–E attenuation rates, will vary by about 0.16 db/Mm; this variation corresponds to an error of about 19% at 20 Hz and only 8% at 300 Hz. These errors are in the opposite direction (an increase in W–E attenuation would produce a decrease in E–W attenuation).

There are no phase velocity errors caused by a source location uncertainty for the W–E computations, since only the difference in distance $(d_2 - d_1)$ is involved, as can be seen from (5). A value for the E–W phase velocity computation is greatly influenced, however, by changes in source locations, as indicated in (7). Changes in propagation distances for the mid-Pacific groups, ±500 km to Tottori and ±1000 km to Lafayette, would produce maximum errors of 5% in the computed E–W phase velocities.

Differences in relative phase responses of equipment at each recording site were found to be less than 10° between 50 and 500 Hz. The Tottori equipment phase led the Lafayette equipment phase by about 15° at 40 Hz and by, perhaps, 40° at 20 Hz. As with the equipment amplitude accuracy, it is not possible to determine absolute phase responses at these two sites. If we assume that these phase values actually represent the site-equipment response and correct the computed phase velocities accordingly, then the W–E values would increase to 0.85, while the E–W values would decrease to about 0.74 at 20 Hz. The error at 40 Hz would be about 2.5%, and, at frequencies above 50 Hz, the error would be less than 1% of the computed values shown in Figure 7.

Another error in phase velocity measurements, which does not affect the amplitude spectrum or the resultant attenuation values, is the uncertainty of establishing the zero time for spectrum analysis. Variations in the beginning time for the analysis, relative to each wave-form pair, change the relative delay of the corresponding frequency components and, thus, the computed phase velocity. It is believed that the zero time was determined with an error of less than 500 μsec relative to the arrival of the VLF component, which was assumed to propagate with the velocity of light. The error produced in the phase velocities caused by this relative time variation is less than 2%.

Note the errors for the limits of the error bars shown in Figure 7. The median error for the W–E attenuation error bars is about 33%; a slightly larger error exists for the E–W attenuation error bars. It is larger than expected, based on the discussion of errors above. It is quite likely that much of this additional variation for W–E error bars comes from the fact that the group A and B atmospherics are in an area where the locations are very poorly defined and may actually be in error by ±1500 km. The increased error for the E–W error bars, however, cannot be explained by assuming a larger source-location error. These larger errors for the mid-Pacific areas could be produced by sources with large variations in radiation as a function of direction. The wide angular difference in propagation direction toward Japan and the United States from these mid-Pacific areas could, through the combination of vertical, horizontal, and inclined dipole source effects (as suggested by *Wait* [1960]), produce large differences in the received signals at both sites. The median error for the W–E phase velocity error bar is 1.5%, whereas the median error for the E–W phase velocity error bar is 4.5%. Both these errors are commensurate with phase-error discussion.

The attenuation values reported here are in reasonably good agreement with the values of *Chapman and Macario* [1956], which are between the W–E and E–W values for frequencies above 100 Hz. Compared with the work of *Hughes* [1967], the present data result in less change in attenuation with frequency above 100 Hz and also less difference between W–E and E–W propagation. A recent work of *Galejs* [1968] indicates that, for a magnetic dip angle of 45° and with the use of a few closely related ionospheric profiles, the theoretical attenuation rates for both directions increased more rapidly with frequency. The phase velocities were consistently lower at all frequencies than the values obtained from the present data.

It is evident that more experimental work is needed, and a large number of additional observations have been made since the data for the present work were collected. The ELF slow-tail components of atmospherics recorded simultaneously at Tottori and Lafayette from sources throughout the Pacific Ocean area, south and southeast of Lafayette, and in the North Atlantic Ocean are to be subjected to analyses similar to that reported here. Additional values of ELF attenuation rates and phase velocities for many path configurations and for both day and night conditions will be reported.

Acknowledgments. We thank H. Jindo, K. Ohta, H. Burdick, and L. Eichacker for assisting with the observations, J. Leise for the computer program, and B. Boggs, M. Gregg, and C. Tombaugh for data analyses.

Partial financial support for this work was from the National Science Foundation in the United States and the Japan Society for the Promotion of Science as part of the United States-Japan Cooperative Science Program.

REFERENCES

Chapman, F. W., and R. C. V. Macario (1956), Propagation of audio-frequency radio waves to great distances, *Nature, 177,* 930–933.

Galejs, J. (1968), Propagation of ELF and VLF radio waves below an anisotropic ionosphere with a dipping static magnetic field, *J. Geophys. Res., 73,* 339–352.

Hepburn, F., and E. T. Pierce (1953), Atmospherics with very low frequency components, *Nature, 171,* 837–838.

Hughes, H. G. (1967), Nonreciprocal attenuation rates at

ELF from 'slow tail' measurements, *J. Geophys. Res., 72,* 5383–5388.

Jean, A. G., W. L. Taylor, and J. R. Wait (1960), VLF phase characteristics deduced from atmospheric wave forms, *J. Geophys. Res., 65,* 907–912.

Jean, A. G., A. C. Murphy, J. R. Wait, and D. F. Wasmundt (1961), Observed attenuation rate of ELF radio waves, *Radio Sci., J. Res. NBS, 65D,* 475–479.

Taylor, W. L. (1960), VLF attenuation for east-west and west-east daytime propagation using atmospherics, *J. Geophys. Res., 65,* 1933–1938.

Wait, J. R. (1960), Mode theory and the propagation of ELF radio waves, *Radio Sci., J. Res. NBS, 64D,* 387–404.

Reprinted from Radio Science 5, No. 1, 1-6, 1970.

The application of stationary phase to radio propagation for finite limits of integration

H. T. Dougherty

Radio Meteorology, Wave Propagation Laboratory, ESSA
Boulder, Colorado 80302

(Received July 28, 1969.)

The application of the stationary phase method is investigated for a dimensionless line integral encountered in wave propagation. Evaluation of the integral for a first-order point of stationary phase may be expressed, characteristically, by the Fresnel-Kirchhoff function or its derivative. A related function is found for the isolation factor required for finite limits of integration. Curves for evaluating this factor, $K(u_2\ u_1)$, are presented.

INTRODUCTION

Formulations of the problems of aperture radiation and surface scattering often contain line and surface integrals that permit an asymptotic evaluation by the stationary phase methods. The problem does arise, however, that the separation of the contributions due to individual points of stationary phase will usually involve integration between finite limits. Occasionally, Laplace's or Kelvin's method of stationary phase [*Copson*, 1943; *Erdelyi*, 1956] is still applied by assuming that there is negligible error in replacing the finite interval of integration by an infinite or semi-infinite interval. The same assumption is sometimes made in the method of steepest descent [*Schafer and Kouyoumjian*, 1967].

Correction for this assumption can be made by adding appropriate terms to the asymptotic evaluation of the infinite-interval integral [*Erdelyi*, 1956; *Jeffreys*, 1962], but this is not always convenient. When the infinite interval integral evaluation is available in closed form, it is convenient to express its modification to a finite interval as a correction factor. Here, we determine such a correction factor for points of stationary phase that are of first-order. The procedure should be applicable for higher-order points of stationary phase.

FORMULATION OF THE PROBLEM

Consider an integral of the form

$$I = \int_{l_1}^{l_2} \frac{g(l)}{h(l)} \exp\,[-isf(l)]\,dl \qquad (1)$$

Copyright © 1970 by the American Geophysical Union.

where g, h, and f are all real, well-behaved functions of the real variable l and have, at worst, only finite step discontinuities. The s is a large-valued parameter, and the l is a measure of length along a smooth contour that contains only one first-order point of stationary phase: at $l = 0$ in the interval between l_1 and l_2. We introduce the notation

$$\left[\frac{\partial^m A}{\partial_l{}^m}\right]_{l=0} = A_m \qquad (2)$$

so that, of course, $f_1 = 0$ and $f_2 \neq 0$. For radio wave difraction problems, the integrand can have a pole at the point of stationary phase. This difficulty is encountered, for example, in the case of the simple knife-edge and the infinite cylinder [*Ufimtsev*, 1958*a*, *b*]. *Rubinowicz* [1957] treats this situation (for $|l_1| = l_2 = \infty$) by factoring the phase function at $l = 0$ as $f_0 = Qh_0$ [*Rubinowicz*, 1957; *Karczewski*, 1963]. *Rubinowicz* defines an auxiliary integral

$$A(s) = \partial I/\partial s \qquad (3a)$$

and the integrand pole is removed by cancellation. The usual stationary phase method provides an evaluation of $A(s)$, and the original integral is then determined from

$$I = \int_{-i\infty}^{s} A(t)\,dt \qquad (3b)$$

Here, we shall apply Rubinowicz's method to arbitrary limits of integration $l_1 \leq 0$ and $l_2 \geq 0$, for $f_0 = Qh$. Then,

$$I = \frac{(f_0 f_2/2)^{1/2}}{2\pi} \int_{s}^{-i\infty} \int_{l_1}^{l_2} F(l) \exp\,[-itf(l)]\,dl\,dt \quad (4a)$$

where

$$F(l) = \frac{2\pi g(l)f(l)}{h(l)(f_0 f_2/2)^{1/2}} \tag{4b}$$

The normalization factor involving $f_0^{1/2}$ is merely a convenience here and may be omitted if $f_0 = 0$ creates any difficulties.

The phase function $f(l)$ may be expanded in a Taylor's series about the point $l = 0$ of stationary phase. For a first-order point of stationary phase, only the terms involving f_0 and f_2 are retained as exponents; the contributions involving higher derivatives are incorporated in an exponential series expansion. We write

$$I = \left(\frac{if_0}{4\pi}\right)^{1/2} \int_{s}^{-i\infty} \{ U_2(t) - U_1(t)\} \exp(-itf_0)\, dt \tag{5}$$

where, for $J = 1$ or 2,

$$U_J(t) = \left(\frac{if_2}{2\pi}\right)^{1/2} \int_0^{l_J} F(l) \cdot \sum_{p=0}^{\infty} \left[f(l) - f_0 - f_2 \frac{l^2}{2}\right]^p \frac{(it)^p}{p!} \exp(-itf_2 l^2/2)\, dl \tag{6}$$

The $U_J\ (t)$ may be evaluated by expanding $F(l)$ in a Maclaurin series and integrating (6) term-by-term.

THE FINITE INTERVAL

In the case of the finite interval of integration and a first-order point of stationary phase, $f_2 > f_n > f_m$ for $m = 3, 4, 5, \cdots$, but $m \neq n$ and $n \neq 2$. We define the value

$$\hat{l} = l_J(\alpha_J s)^{1/2} = \left|\frac{n!\ f_2}{2f_n}\right|^{(1/n-2)} \tag{7}$$

This is the value of l for which the terms containing f_2 and f_n make equal contributions to the Maclaurin series expansion of $f(l)$. Then

$$f(l) - f_0 - f_2 l^2/2 = \frac{f_2 l}{2}\left\{a_3 \frac{l^2}{\hat{l}} + \cdots + \frac{l^{n-1}}{\hat{l}^{n-2}} + \cdots + a_m \frac{l^{m-1}}{\hat{l}^{m-2}} + \cdots\right\} \tag{8a}$$

where

$$a_m = \frac{n!\ f_m}{m!\ f_n}\,\hat{l}^{n-m} = \frac{2f_m}{m!\ f_2}\,\hat{l}^{m-2} < 1.0 \qquad n \neq m \tag{8b}$$

For $n = 3$, the term containing a_3 is deleted from (8a). From (6), (7), and (8a), and(A1) through (A7) in the appendix, we determine

$$U_J(t) = \left\{ F_0 \frac{b_J}{(t)^{1/2}} + i^{3/2} \frac{F_1}{(2\pi f_2)^{1/2}} \frac{\exp(-itf_2 l_J^2/2) - 1}{t} + i^{3/2} \frac{F(l_J) - F_0 - F_1 l_J}{l_J(2\pi)^{1/2}} (f_2)^{1/2} \frac{\exp(-itf_2 l_J^2/2)}{t} \right\} [1 + O(t^{-1})] + \frac{1}{2}\left(\frac{if_2}{2\pi}\right)^{1/2} \frac{l_J F(l_J) \exp(-itf_2 l_J^2/2)}{(\alpha_J s)^{n/2-1}} [1 + O(\alpha_J^{-(m-n)/2} s^{-(m-n)/2})] \tag{9}$$

where b_J is the Fresnel integral given by (A1) for $m = 0$ or by (A2) and (A3). We insert (9) into (5) and carry out the integration with the aid of (A9) through (A16) to obtain

$$I = F_0 a(v, 0) K(u_2, u_1) \left\{ 1 - O\left(\frac{F_1}{F_0} [f_2 s]^{-1/2}\right) - O\left(\frac{F_2}{F_0} [f_2 s]^{-1}\right) + \cdots \right\} \tag{10}$$

where $a(v, 0)$ is the Fresnel-Kirchoff function defined by (A11a) and (A11b). For $f_2 > 0$,

$$u_J = l_J(sf_2/\pi)^{1/2} \tag{11a}$$

$$K(u_2, u_1) = K(u_2) + K(|u_1|) \tag{11b}$$

and, for $J = 1$ or 2,

$$K(u_J) = \frac{(if_0/4\pi)^{1/2}}{a(v, 0)} \int_{s}^{-i\infty} t^{-1/2} b_J \exp(-itf_0)\, dt \tag{11c}$$

For $f_2 < 0$, u_J is given by $-i$ times (11a), and $K(u_J)$ is given by its complex conjugate. Since s is a large-valued parameter, the integral (1) is given, asymptotically, by replacing the bracketed terms of (10) with unity. This requires that $F_1 F_0^{-1}(f_2 s)^{-1/2}$ and $F_2(F_0 f_2 s)^{-1}$ be of the order of $s^{-1/2}$ or less.

Some curves of the special function $K(u)$ are presented in Figure 1 (magnitude) and Figure 2 (phase) for selected values of the parameter v. As u goes to zero, $K(u)$ also approaches zero. For large values, that is, when $|u_J| \geq 3$, $K(u_2, u_1)$ is approximately unity, and (10) reduces to Rubinowicz's result. Therefore, we may describe $K(u_2, u_1)$ as the required modification of Rubinowicz's evaluation when his in-

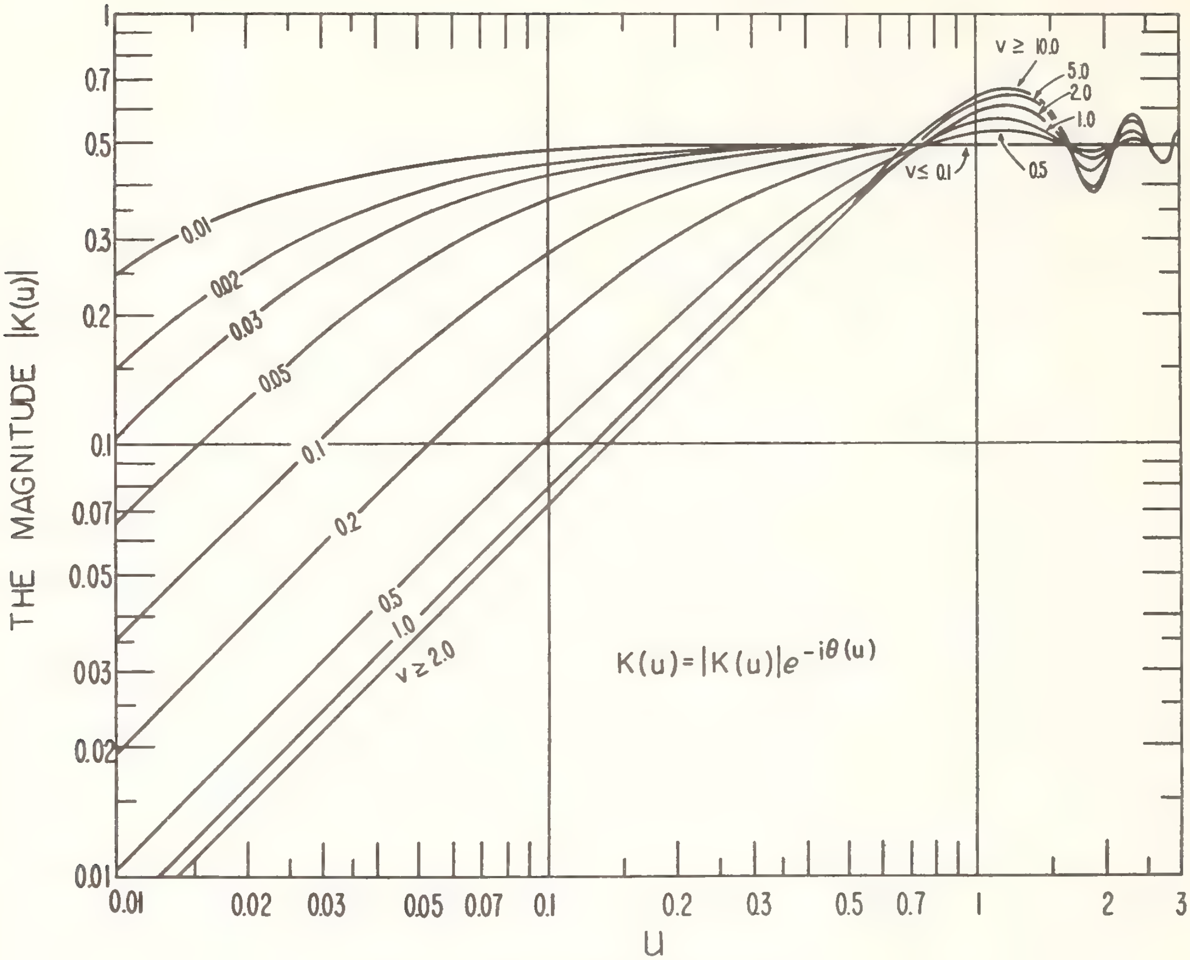

Fig. 1. The magnitude of the factor $K(u)$.

finite or semi-infinite interval of integration is replaced by a finite interval corresponding to

$$\mathfrak{a}_1/(s)^{1/2} = u_1 \leq u \leq u_2 = \mathfrak{a}_2/(s)^{1/2} \tag{12a}$$

where

$$\mathfrak{a}_J/(s)^{1/2} = \left(\frac{n!\,f_2}{2f_n}\right)^{(1/n-2)} (f_2/\alpha_J\pi)^{1/2} \tag{12b}$$

It should be noted that the form of the factor $K(u_2, u_1)$ results because the integrand of (1) can have a pole (i.e. $h(l) = 0$) at a first-order point of stationary phase. If we take $h(l)$ as unity, direct application of the stationary phase method to (1) yields the factor $b_2 - b_1$, a Fresnel integral. If the point of stationary phase were of second-order, the stationary phase method would retain the term involving f_3 as an exponent, and (1) could be expressed in terms of Airy functions [*Doherty*, 1952].

APPLICATION

The integral formulation of vector wave propagation [*Dougherty*, 1969] involves line integrals such as (1). The integrand encountered there appears quite basic to propagation theory, having appeared, at least in part, in earlier formulations of the problem [*Maggi*, 1888; *Rubinowicz*, 1917; *Kottler*, 1923]. The integrand functions for a spherical wave source are

$$f = (r_1 + r_2 - d)/(r_{10}r_{20})^{1/2} \tag{13a}$$

$$g = (d \sin \psi \cos \upsilon)/(4\pi r_1 r_2) \tag{13b}$$

$$h = 1 - \cos \psi \tag{13c}$$

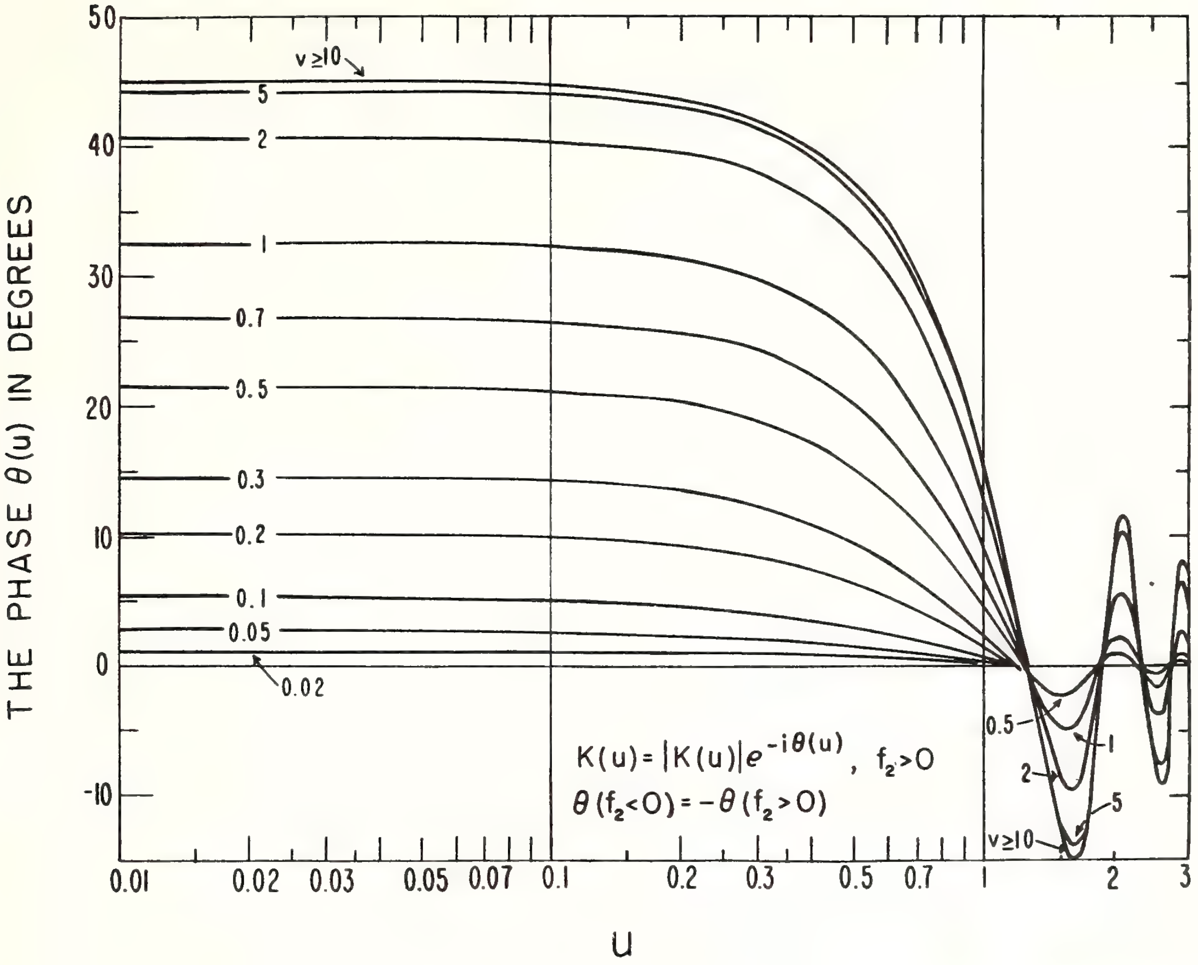

Fig. 2. The phase of the factor $K(u)$.

and

$$s = k(r_{10}r_{20})^{1/2} \tag{13d}$$

The d is the distance from the field source to the point of observation. The r_1 and r_2 are the distances measured from the source and observation points, respectively, to an arbitrary point on the curve or surface of interest. The ψ is the supplement of the angle formed by their directional vectors, and ν is the angle between the normal to the plane of r_1 and r_2 and the tangent to the path of integration C.

If the stationary phase point is taken as the origin of a Cartesian coordinate system, we can choose the unit vector in the x direction as tangent to C at the origin. The z direction is chosen so that the field source lies in the x–z plane. Let C be a portion of a plane conic curve with radius of curvature R_0 at the origin, and let us designate the acute angle between the y axis and the plane of C by σ. For the notation (2), the foregoing leads to

$$f_2 = [(r_{10} + r_{20}) \sin^2 \gamma_0/(r_{10}r_{20})^{3/2} T_C^2] \tag{14}$$

where

$$\frac{1}{T_C^2} = 1 - \frac{r_{10}r_{20} \sin \phi \cos \sigma}{R_0(r_{10} + r_{20}) \sin \gamma_0} \left(1 - \frac{\tan \sigma}{\tan \phi_0/2}\right) > 0 \tag{15}$$

The γ_0 is the angle between the directional vector of r_{10} and the x axis, and ϕ_0 is the projection of ψ_0 on the y–z plane. We observe that at $l = 0$ the phase function odd-order derivatives are small relative to those of even-order. The even-order derivatives, in tropospheric propagation applications, decrease with increasing order. Similarly, the amplitude function derivatives decrease with increasing order. For example,

$$F(l) = \frac{r_{10}r_{20}(r_{10} + r_{20} + d)}{r_1 r_2(r_1 + r_2 + d)} F_0 \tag{16}$$

and

$$F_0 = T_C \cos \phi_0/2 \left(\frac{2d^2/(r_{10} + r_{20})}{r_{10} + r_{20} + d}\right)^{1/2} \tag{17}$$

from combining (13*a*) through (13*c*) with (4*b*) and (14). Evaluating the derivatives of (16) at $l = 0$, we obtain

$$F_1/F_0 = \cos \gamma_0(r_{20} - r_{10})/r_{10}r_{20} \tag{18}$$

and

$$\frac{F_2}{F_0} = 2\frac{F_1^{\,2}}{F_0} - \frac{2}{r_{10}r_{20}} + O(d^{-2}) + O(d^{-1}R_0^{\,-1}) \tag{19}$$

In this case, $n = 4$ in (7) and $\hat{l}/2$ is closely approximated by the lesser of r_{10} and r_{20}. For applications where r_{10}, r_{20}, and R_0 are very much greater than the transmission wavelength, we can incorporate (14) through (19) in (10) to obtain

$$I \approx a(v, 0) \cos \phi_2/2\ T_C \left[\frac{2d^2/(r_{10} + r_{20})}{d + r_{10} + r_{20}}\right]^{1/2} K(u_2, u_1) \tag{20}$$

The first four factors of (20) are encountered for the diffracted field in the shadow of a curvilinear knife-edge that has only one point of stationary phase [*Dougherty*, 1969]. The $K(u_2, u_1)$ factor isolates that portion of the field attributable to the vicinity ($l_1 \leq l \leq l_2$) of the stationary point.

CONCLUSION

The application of the stationary phase method has been investigated for a dimensionless line integral encountered in wave propagation problems. We observe that application of the stationary phase method, for a first-order point, characteristically yields the familiar Fresnel-Kirchhoff function or its derivative. It is not surprising, therefore, that finite limits of integration yield an additional factor defined by (11*b*) and (11*c*) and presented in Figures 1 and 2 that is closely related to the Fresnel-Kirchhoff function.

In general, more than one point of stationary phase is encountered for curvilinear contours so that finite limits of integration may be chosen to isolate the contribution of the individual points. The resulting correction factors for the finite limits, $K(u_2, u_1)$, are perhaps more properly called isolation factors.

APPENDIX

The family of integrals

$$W_m = \int_0^{l_J} l^m \exp(-itf_2 l^2/2)\, dl \tag{A1}$$

$$m = 0, 1, 2, \cdots$$

may be evaluated by the change of variable

$$u_J = l_J(tf_2/\pi)^{1/2} \tag{A2}$$

for $f_2 > 0$. We define

$$b_J = b(u_J) = \left(\frac{i}{2}\right)^{1/2} \int_0^{u_J} \exp(-i\pi u^2/2)\, du \tag{A3}$$

This normalized Fresnel integral may be determined from the Cornu Spiral when u_J is real. For $f_2 < 0$, the u_J is given by $-i$ times (A2), and the b_J is given by the complex conjugate of (A3). Combining (A1), (A2), and (A3), we can carry out an integration by parts to determine

$$W_0 = (2\pi/if_2)^{1/2} b_J/(t)^{1/2} \tag{A4}$$

$$W_1 = (2\pi/if_2)^{1/2} i^{3/2}/(2\pi f_2)^{1/2} \cdot \{[\exp(-i\pi u_J^{\,2}/2) - 1]/t\} \tag{A5}$$

and, for $m \geq 2$,

$$W_m = \left(\frac{2\pi}{if_2}\right)^{1/2} \left\{ \frac{i^{3/2} \exp(-i\pi u_J^{\,2}/2)}{(2\pi f_2)^{1/2} t} l^{m-1}[1 + O(t^{-1})] + B_m \left(\frac{2}{if_2}\right)^{m/2} \frac{\Gamma\left(\frac{m+1}{2}\right)}{(\pi)^{1/2} t^{(m+1)/2}} \right\} \tag{A6}$$

where

$$B_m = \begin{cases} b_J, & \text{for } m \text{ even} \\ \frac{1}{2}[1 - \exp(-i\pi u_J^{\,2}/2)], & \text{for } m \text{ odd} \end{cases} \tag{A7}$$

For $l_J = \infty$, the W_m of (A1) may be evaluated by the limit technique of *Van Kampen* [1949]. That is, for $l_J = \infty$,

$$W_m = \left(\frac{if_2 t}{2}\right)^{-(m+1/2)} \frac{\Gamma\left(\frac{m+1}{2}\right)}{2} \tag{A8}$$

$$m = 0, 1, 2, \cdots$$

since B_m goes to ½.

There is another family of integrals

$$V_m(b) = \int_0^{-i\infty} t^{-m/2} \exp(-ibt)\, dt \tag{A9}$$

$$m = 0, 1, 2, \cdots$$

where, as in the text, s is a real large-valued parameter. For $m = 0$,

$$V_0(b) = -(i/b) \exp(-ibs) \tag{A10}$$

For $m = 1$ and 1 and $b = f_0$, we introduce a change of variable

$$v(t) = (2tf_0/\pi)^{1/2}, \qquad v(s) = v \tag{A11a}$$

and

$$\begin{aligned} V_1(f_0) &= \left(\frac{2\pi}{f_0}\right)^{1/2} \int_v^\infty \exp(-i\pi x^2/2)\, dx \\ &= \left(\frac{4\pi}{if_0}\right)^{1/2} a(v, 0) \end{aligned} \tag{A11b}$$

This $a(v, 0)$ is the familiar Fresnel-Kirchhoff function, and we note that $0.5 \geq a(v, 0) > 0.2$ for $0 \leq v < 1$, whereas $a(v, 0) = O(s^{-1/2})$ for $v \geq 1$. For $m = 2$, $V_2(b)$ is related to the integrals of $x^{-1} \sin x$ and $x^{-1} \cos x$[*Kreyszig*, 1963], and

$$V_2(b) = O(b^{-1}s^{-1}) \qquad \text{for} \quad bs > 1 \tag{A12a}$$

$$= -\ln bs + O(1.0) \qquad \text{for} \quad bs \leq 1 \tag{A12b}$$

For $m \geq 3$,

$$V_m(b) \leq V_1(b)O(s^{-1}) \tag{A13}$$

These integrals are associated in (9) of the text with specific coefficients we may identify as

$$C_0 = (if_0/4\pi)^{1/2} \tag{A14a}$$

$$C_1 = [(F_1/F_0)/4(\pi f_2)^{1/2}]v/s^{1/2} \tag{A14b}$$

$$C_2 = \frac{F_2 + F_3 l_J/3! + \cdots}{4f_2 F_0} \frac{vu_J}{s} \tag{A14c}$$

$$C_3 = \frac{F(l_J)/F_0}{8(\alpha_J)^{n/2-1}} \frac{vu_J}{s^{n/2}} \tag{A14d}$$

etc. From (A9) through (A14*d*), we observe that

$$C_1[V_2(f_0 + f_2 l_J^2/2) - V_2(f_0)] = O\left[\frac{F_1/F_0}{(f_2 s)^{1/2}}\right] \tag{A15a}$$

$$C_2 V_2(f_0 + f_2 l_J^2/2) = O\left(\frac{F_2/F_0}{f_2 s}\right) \tag{A15b}$$

and

$$C_3 V_0(f_0 + f_2 l_J^2/2) = O[F(l_J)F_0^{-1}s^{-(n-1)/2}] \tag{A15c}$$

relative to

$$C_0 \int_s^{-i\infty} b_J t^{-1/2} \exp(-if_0 t)\, dt = a(v, 0)K(u_J) \tag{A16}$$

in the determination of (10).

REFERENCES

Copson, E. T. (1943), The asymptotic expansion of a function defined by a definite integral or contour integral, *Rep. 12.29 ACS 26*, Admiralty Computing Service, Dept. of Scientific Research and Experiment, The Admiralty, London.

Doherty, L. H. (1952), Geometrical optics and the field at a caustic with applications to radio wave propagation between aircraft, *Res. Rep. EE 138*, Cornell University, Ithaca, N. Y.

Dougherty, H. T. (1969), Radio wave propagation for irregular boundaries, *Radio Sci.*, *4*(11), 997–1004.

Erdelyi, A. (1956), *Asymptotic Expansions*, Dover Pub., New York.

Jeffreys, H. (1962), *Asymptotic Approximations*, Oxford Press, New York.

Karczewski, B. (1963), The Fresnel field in Kottler's diffraction theory, *Can. J. Phys. 41*(10), 1623–1628.

Kottler, F. (1923), On the theory of diffraction by a black screen (in German), *Ann. Phys.*, *70*(6), 406–456.

Kreyszig, E. (1963), *Advanced Engineering Mathematics*, John Wiley, New York.

Maggi, G. A. (1888), Sulla propagazione libere e perturbata delle onde luminose in un mezzo isotropo, ***Anno i Math Pura Ed App. 16***, 21–48.

Rubinowicz, A. (1917), Die Beugungswelle in der Kirchhoffschen Theorie der Beugungsershenugen, *Ann. Phys.*, *53*, 258–278.

Rubinowicz, A. (1957), *Die Beugungswelle in der Kirchhoffschen Theorie der Beugung*, Polska Akademia Nauk, Warsaw.

Schafer, R. H., and R. G. Kouyoumjian (1967), Higher order terms in the saddle point approximation, *Proc. IEEE*, *55*(8), 1496–1497.

Ufimtsev, P. I. (1958*a*), Secondary diffraction of electromagnetic waves by a strip, *Sov. Phys.—Tech. Phys.*, *3*, 535–548.

Ufimtsev, P. I. (1958*b*), Approximate calculation of the diffraction of plane electromagnetic waves by a disk and by a finite cylinder, *Sov. Phys.—Tech. Phys.*, *3*, 2386–2396.

Van Kampen, N. G. (1949), An asymptotic treatment of diffraction problems, *Physica*, *14*(9), 575–587.

7

Reprinted from Radio Science 5, No. 1, 55-60, 1970.

Diffraction by irregular apertures

H. T. Dougherty

Radio Meteorology, Wave Propagation Laboratory, ESSA
Boulder, Colorado 80302

(Received July 28, 1969.)

This is a companion paper to two other papers, one of which developed an approximate, closed-form solution of the Stratton-Chu vectorial integral equation for irregular boundaries. That development involved the evaluation of several integrals by the stationary phase method and assumed that the points of stationary phase were well separated. A second paper presented the correction factor for definite integrals that are evaluated by the stationary phase method. Here, this correction factor is incorporated as a weighting function to permit a superposition of the closed-form solutions for irregular screens or apertures without limitation on the spacing between adjacent points of stationary phase. This extended solution is then applied to evaluate the diffraction effects for a bilinear screen and compared with experimental data.

INTRODUCTION

A previous paper [*Dougherty,* 1969*b*] presented an approximate, closed-form solution of the *Stratton and Chu* [1939] vectorial integral equation. The development involved the evaluation of several integrals by the stationary phase method for applications with only a single point of stationary phase. Here, we consider the application to an irregular screen whose transverse profile is sufficiently irregular to produce more than one point of stationary phase. As a result, we must provide for the superposition of the closed-form solutions for each point of stationary phase, correcting for the finite separation between adjacent points of stationary phase [*Dougherty,* 1970].

POINTS OF STATIONARY PHASE

The location of a point of stationary phase is given formally as the point at which the first derivative of the phase function is zero. For a simple knife-edge, this point is where the straight lines (directed from the transmitting point T and the receiving point R) form supplementary angles with a unit tangent vector along the straight edge. There is an alternative view of the point of stationary phase that includes the above, yet is more readily visualized, especially in the case of irregular screens.

For example, the above mentioned points T and R are also the focii of a family of confocal surfaces. Each surface is the locus of all points O for which the path-length difference $TOR - TR$ is constant, and each is also a surface of revolution about TR for a homogeneous medium. For a spherical wave source, these surfaces are Fresnel ellipsoids, surfaces of constant v for which the phase due to path-length difference $2\pi(TOR - TR)/\lambda$ is given by $\pi v^2/2$ or $n\pi$. The n is the order of the Fresnel ellipsoid; the TR line is the zeroth ($n = 0$) ellipsoid. For an incident plane wave, the confocal surfaces are paraboloids with focus at R and with major axis TR. For the case of monostatic radar and a homogeneous medium, they are spheres centered on the common TR point.

The points of stationary phase on a screen are, therefore, points at which the screen is tangent to a Fresnel ellipsoid. Points A, B, and C illustrate this in Figure 1. Ordinarily, the tangent plane at such points is also the plane of symmetry [*Dougherty,* 1969*b*] that is required by the definition of the secondary field polarization vector.

The foregoing suggests that an irregular screen may be said to consist, in effect, of a sequence of points of stationary phase, each with its apportioned interval of the total screen edge. In the vicinity of each point, the screen edge could be approximated by a section of a canonical screen, that is, by a relatively simple geometric shape, a straight edge, a plain curve, or an apex, such as at points A, B, and

Copyright © 1970 by the American Geophysical Union.

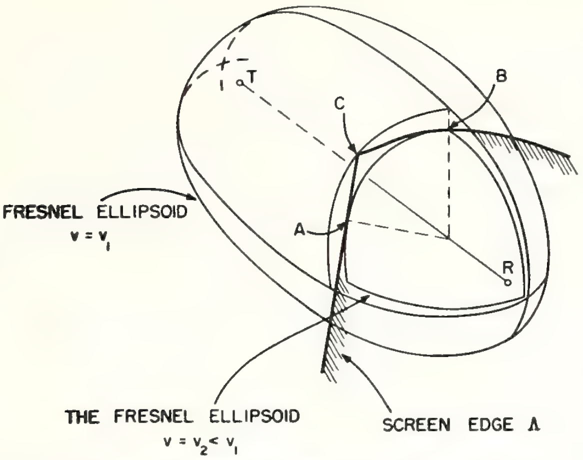

Fig. 1. Points of stationary phase and the Fresnel ellipsoids.

C in Figure 1. For an incident spherical wave, the contribution of each point of stationary phase to the total field (normalized to the incident source field at *R*) would be that of an equivalent knife edge $a_{KE}(R)$ multiplied by a transverse-profile factor T_c [*Dougherty,* 1969*b*] and a weighting factor $K(u_2, u_1)$ for an interval $l_1 \leq l \leq l_2$ about that point of stationary phase [*Dougherty,* 1970]. That is, for *N* points of stationary phase on an irregular screen, the total normalized field is

$$\mathbf{a}(R) = \sum_{n=1}^{N} \mathbf{a}_n(R)[1 + O(s^{-1/2})] + b_0(A \text{ or } B)\mathbf{u}_{10} \quad (1)$$

where

$$s = k(r_{10}r_{20})^{1/2} \quad (2)$$

$$\mathbf{a}_n(R) = [\mathbf{u}_2 a_{KE}(R) T K(u_2, u_1)]_n \quad (3)$$

$$a_{KE}(R) = \alpha_0 a(v, 0) \cos \frac{\phi_0}{2} \left[\frac{2d^2/(r_{10} + r_{20})}{d + r_{10} + r_{20}}\right]^{1/2} \quad (4)$$

$$T_c = \left[1 - \frac{r_{10}r_{20} \cos \sigma \sin \phi_0}{R_0(r_{10} + r_{20}) \sin \gamma_0}\left(1 - \frac{\tan \sigma}{\tan \phi_0/2}\right)\right] \quad (5)$$

and

$$v^2 = (2k/\pi)(r_{10} + r_{20} - d) \quad (6)$$

The *k* is the wave number $2\pi/\lambda$, $a(v, 0)$ is the Fresnel-Kirchhoff knife-edge diffraction function [*Dougherty,* 1969*a*], and α_0 is the diffraction constant or the reflection function at grazing [*Dougherty,* 1969*b*]. The geometrical quantities are illustrated in Figure 2. The *T* is unity for a simple knife edge, given by (5) for a plane curve and by T_Λ in (14) for a bilinear screen edge, such as for points *A, B,* and *C* in Figure 1.

Note that the nonlinearity of the screen edge is reflected in (1) through (5) in three ways: (*a*) it determines the number and location of the points of stationary phase, (*b*) the transverse radius of curvature R_0 at each point affects the value of T_c, and (*c*) both arc lengths, l_1 and l_2, and R_0 affect the values of u_2 and u_1 in the $K(u_2, u_1)$ factor (these u_J, $J = 1, 2$ were defined by *Dougherty* [1970] and are discussed in the next section). The effects of higher-order parameters of the screen edge are, however, masked in the $O(s^{-\frac{1}{2}})$ terms of (1).

THE BILINEAR SCREEN

Evaluating the integrals that determined (1) through (5), one would normally assume that the contour of integration is smoothly continuous. This assumption would not be true for the bilinear screen edge when the stationary phase point is at the apex. There, as illustrated at point *C* in Figure 1 and point *O* in Figure 2, the contour or edge is continuous in a piecewise manner; i.e., the slope has a finite, step discontinuity. This presents no real difficulty if we resort to an extended definition of the derivative based on Schwartz's theory of distributions, particularly as described by *Van Bladel* [1964] in ap-

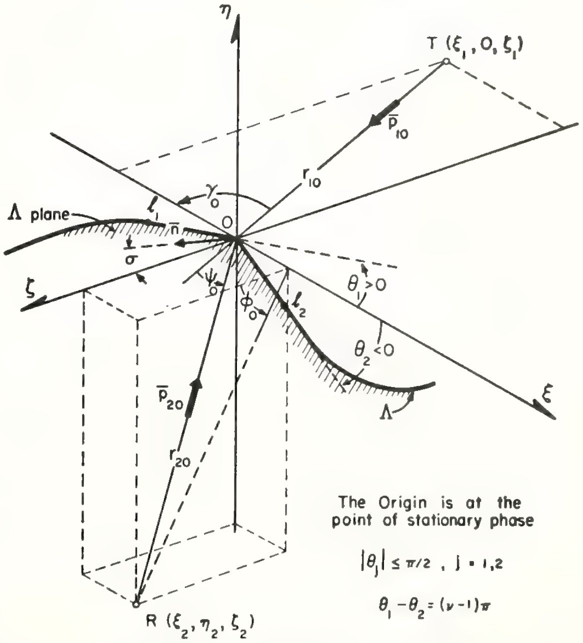

Fig. 2. Bilinear knife-edge geometry. The overbars indicate vectors.

pendix 6 of his text. Evaluation of the line integral for the scalar $a(R)$ is the same for an apex point of stationary phase as for a simple knife-edge, but a difference occurs in the evaluation of the line integral for the vector $\mathbf{a}(R)$ because of the secondary field polarization vector, $\mathbf{u}_2 = \mathbf{u}_{E2}$. This vector is defined from the primary field polarization vector $\mathbf{u}_{E1}$, the plane of symmetry (normal $\mathbf{n}_0$ and tangent $\mathbf{t}_2 = \mathbf{u}_\xi$), and the conditions [*Dougherty*, 1969*b*]:

$$\begin{aligned} \mathbf{t}_2 \cdot \{\mathbf{u}_{E1} + \mathbf{u}_{E2}\} &= 0 \\ \mathbf{t}_2 \times \mathbf{n}_0 \cdot \{u_{E1} + u_{E2}\} &= 0 \\ -\mathbf{p}_2 \cdot \mathbf{u}_{E2} &= 0 \end{aligned} \tag{7}$$

Ordinarily, the plane tangent to the ellipsoid and the diffracting screen at the point of stationary phase is also the plane of symmetry. Here, the apex point has a family of planes of symmetry that must be considered.

The field at the apex. We may consider the apex point as the limit condition of a curved edge when the transverse radius of curvature goes to zero. For example, when $\nu > 1$ (i.e., $\theta_2 \leq 0$, $\theta_1 \geq 0$, as in Figure 2), we may consider the screen edge to be semi-cylindrical with a radius R of curvature. The apex is then a spherical segment of radius R and of azimuthal width given by $(\nu - 1)\pi$, the constant ratio of apex arc length to radius. For $R > 0$ at a point $l = R\theta$ along Λ, the surface normal and tangent unit vectors of interest are given by

$$\begin{aligned} \mathbf{n}(\theta) &= \mathbf{n}(0) \cos \theta + \mathbf{t}_2(0) \sin \theta \\ \mathbf{t}_1(\theta) &= \mathbf{t}_1(0) \\ \mathbf{t}_2(\theta) &= \mathbf{n}(0) \sin \theta + \mathbf{t}_2(0) \cos \theta \end{aligned} \tag{8}$$

where the $\mathbf{n}(0)$, $\mathbf{t}_1(0)$, and $\mathbf{t}_2(0)$ are the unit vectors when $\theta = 0$. These, together with (7) and $a\mathbf{u}_{E1}$, will determine a family of secondary field components $\alpha(\theta)\mathbf{u}_{E2}(\theta)$ on the apex. This suggests that we integrate these to determine an enhanced secondary field component at the apex that we designate by

$$(T_\Lambda - 1)\alpha_0 \mathbf{u}_{E2} = \lim_{R \to 0} \left\{ \frac{1}{\pi} \int_{\theta_1}^{\theta_2} \mathbf{u}_{E2}(\theta) a(\theta)\, d\theta \right\} \tag{9}$$

An enhanced apex field seems reasonable for $\nu > 1$, if only to correspond to that required for the Meixner condition of integrable energy density in the vicinity of an edge [*Meixner*, 1949; *Van Bladel*, 1964]. The evaluation of (9), described in the appendix, results in

$$T_\Lambda = 2 - \nu \tag{10}$$

The bilinear points of stationary phase. The bilinear screen edge may have one, two, or three points of stationary phase at and in the vicinity of the apex. For an observation point in the shadowed region ($\psi_0 > 0$ and $\nu > 1$), there are three possible points of stationary phase: one at the apex, one on the left straight-edge portion of the screen, and one on the right straight edge. As ψ_0 is reduced to zero, these points on the straight edges approach and merge with the apex point; for $\psi_0 < 0$, they remain merged with the apex point. Their combined contribution to the observed field is, from (1) through (5) and (10), proportional to

$$(2 - \nu)\alpha_0 K(u_{2R}, u_{1L}) \qquad \nu > 1 \qquad \psi_0 \leq 0 \tag{11}$$

where u_{2R} and u_{1L} are proportional to l_2 and l_1, as illustrated in Figure 2. From their definition [*Dougherty*, 1970] it can be shown that these u_j are measures of path-length difference. For example, the u_{2R} proportional to the l_2 of Figure 2 is related to the path-length difference

$$\pi u_{2R}^2/2 = 2\pi(Tl_2R - TOR)/\lambda \tag{12}$$

where λ is the wavelength of interest.

When the point of observation is returned to the shadow region ($\psi_0 > 0$), the three points of stationary phase again separate so that the contribution of each is modified by its individual weighting factor. Their contributions to the total field are then proportional to

$$(1 - \nu)\alpha_0 K(u_{2A}, u_{1A}), \qquad \alpha_0 K(u_{2L}, u_{1L}) \tag{13}$$

and

$$\alpha_0 K(u_{2R}, u_{1R})$$

respectively, for $v > 1$ and $\Psi_0 > 0$. The u_{2A} and u_{1A} are proportional to $-R\theta_2$ and $-R\theta_1$; the sums $u_{1A} + u_{1R} + u_{2R}$ and $u_{2A} + u_{1L} + u_{2L}$ are proportional to l_1 and l_2. The straight-edge points of stationary phase are between l_1 and l_2 and the apex.

The situation is similar for $\nu > 1$; (11) then holds for $\psi_0 > 0$ (a shadowed point of observation) and (13) holds for $\psi_0 < 0$ (an illuminated point of observation). For the simple knife edge, $\nu = 1$, and the application of (11) and (13) would yield the same result. Comparing (9), (10), (11), and (13), we note

$$\begin{array}{lll} T_\Lambda = 2 - \nu & \nu > 1,\ \psi_0 \leq 0 & \nu < 1,\ \psi_0 \geq 0 \\ T_\Lambda = 1 & \nu > 1,\ \psi_0 > 0 & \nu < 1,\ \psi_0 < 0 \end{array} \tag{14}$$

Although this step-discontinuity form serves our immediate purpose, it has been derived as a limit condition, and further investigation would probably yield a continuous form.

COMPARISON WITH EXPERIMENTAL DATA

There appears to be no closed-form, extensive, theoretical solution for the bilnear diffracting screen, other than that presented here. There are some partial solutions, however, that are empirical and semi-empirical; some experimental data are also available. For example, the simple scalar Fresnel-Kirchhoff theory will predict the field due to a bilinear screen at exactly grazing conditions. The result, $\nu/2$, coincides with the present theory, (1) through (4) and (14), for $\psi_0 = 0$ and $b_0(S) = 1$. In addition, *Matsuo* [1950] gives an empirical solution for $\psi_0 > 0$ that approximates the present theory if $K(u_2, u_1)$ is arbitrarily taken as unity. Finally, *Bachynski and Kingsmill* [1962] present a partial, semi-empirical solution (for normal incidence upon a bilinear screen with $\nu > 1$ and $\psi_0 > 0$) that approximates the present theory when the straight-edge points of stationary phase are close to the apex $(0 < u < 0.5)$.

For this study, the extensive experimental investigations of Bachynski and his colleagues [*Neugebauer and Bachynski,* 1960; *Bachynski and Kingsmill,* 1962; *Bachynski,* 1963] provide a check on the present theory. Two arrangements of the bilinear screens were investigated; the diffraction loss, in decibels below free space, was measured for a field at normal incidence upon a symmetrical $(\theta_1 = |\theta_2| > 0)$ and nonsymmetrical $(\theta_1 = 0, \theta_2 < 0)$ screen. A comparison of the observed diffraction loss and the values provided by the present theory is plotted in Figure 3. The curves of the experimental data in Figure 3 were adapted from *Bachynski and Kingsmill* [1962, Fig. 3].

SAMPLE CALCULATIONS

For a wave incident normally upon a plane screen $(\gamma_0 = \pi/2, \psi_0 = \phi_0)$, where $r_{10} = 150\ \lambda$, and $r_{20} \cos \phi_0 = 113\ \lambda$, we obtain from (2) $s = [2\pi(150)\cdot(113)/\cos \phi_0]^{1/2}$ or $s \geq 810$ for $\phi_0 \leq 10°$. From the law of cosines and the binomial expansion from the above values, $d \cos \phi_0 \approx 150\ \lambda\ (\cos \phi_0 + 0.7533)$, so that (6) gives $v \approx 30 \sin (\phi_0/2)(\cos \phi_0 + 0.7533)^{-1/2}$. For the *apex knife-edge* and $\phi_0 = 6°$, $\hat{v} \approx 1.204$ and $a(\hat{v}, 0)$ is given by $0.177 \exp(-i\ 165.6°)$ or $A(v, 0) = 15$ decibels.

For the asymmetrical linear screen,

$$
\begin{aligned}
a_\Lambda(R) &= 1 - (2 - \nu)\hat{a}_{KE}(R) && \psi_0 \leq 0 \\
&= a_{KE}(R)K(\infty, u) + \hat{a}_{KE}(R)K(\infty, 0) && \psi_0 > 0
\end{aligned}
\tag{15}
$$

where $a_{KE}(R)$ and $\hat{a}_{KE}(R)$ are the diffraction losses for the equivalent knife-edge on, respectively, the inclined edge and the apex. The v for the inclined edge is given by $v = \hat{v} \cos (\nu - 1)\pi$, where $\hat{v}$ is the apex value above. The u is given by $u = \hat{v} \sin (\nu - 1)\pi$. For $\nu = 1.0833$, the v for the inclined edge is given by $v = \hat{v} \cos 15° = 1.16$, $a(v, 0) = 0.182 \exp (-i\ 156.4)$, and $u = \hat{v} \sin 15° = 0.31$. From *Dougherty* [1970], $K(u) = 0.25 \exp(i\ 26.5)$ and $K(\infty) = 0.5$, so that $K(u, \infty) = K(u) + K(\infty) = 0.71 \exp(i\ 8.2°)$. The asymmetrical screen loss for $\phi_0 = 6°$ is

$$
\begin{aligned}
a_\Lambda(R) = {} & 0.182(0.71) \exp(i148.2) \\
& + 0.177(0.5) \exp(i165.6)
\end{aligned}
$$

$$|a_\Lambda(R)| = 0.214 \text{ or } 13.4 \text{ decibels}$$

Similarly, for the symmetrical screen, the loss is given by

$$
\begin{aligned}
a_\Lambda(R) &= 1 - (2 - \nu)\hat{a}_{KE}(R) && \psi_0 \leq 0 \\
&= 2a_{KE}(R)K(\infty, u) && \psi_0 > 0
\end{aligned}
\tag{16}
$$

The v for the inclined edge is given by $v = \hat{v}$ cos

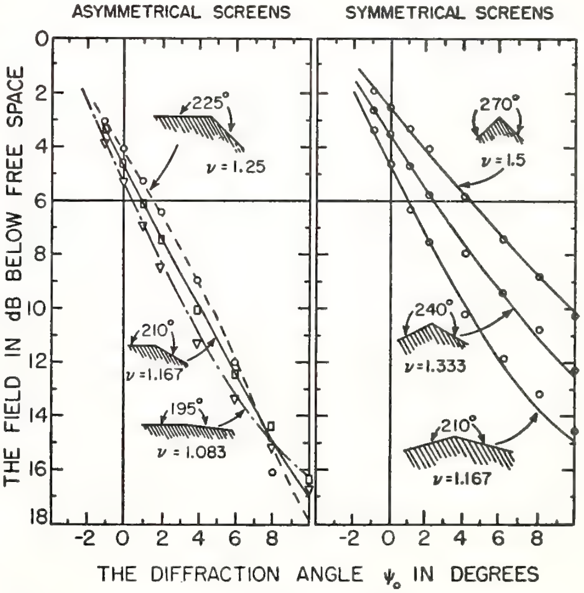

Fig. 3. The comparison of experimental data with theory. The measured data (adapted from *Bachynski and Kingsmill,* [1962]) are indicated by the curves. The indicated points are computed from the present theory.

$(\nu - 1)\pi/2$; u is given by $u = v \sin 15°$, $\nu = 1.1666$ and $\phi_0 = 6°$, the values of u and v are as above, and the symmetrical screen diffraction loss is $a_\Lambda(R) = 2(0.182)0.71 = 0.258$ or 11.8 decibels.

CONCLUSION

An alternative representation of the point of stationary phase and its location has been presented. The theoretical closed-form solution [*Dougherty,* 1969*b*] and the correction factor $K(u_2, u_1)$ [*Dougherty,* 1970] have been joined to provide a theoretical approximate method of solution for the diffraction loss of irregular screens. The method, in essence, is simply one of combining the exact solution for the two-dimensional problem (that for the infinite knife-edge), with allowance for the transverse profile (in terms of the transverse profile factor and the point of stationary phase weighting function), to obtain a three-dimensional approximate solution. The theory has been compared successfully with experimental data. The irregular screen problem is of interest because it is the limiting situation for the more general surfaces encountered in tropospheric propagation applications.

APPENDIX

Consider a vertically polarized source at T. At $l = -R\theta$,

$$\mathbf{u}_{E1}{}^{+} = \mathbf{u}_\eta = \mathbf{n}(0) \cos (\phi_0/2) - \mathbf{t}_1(0) \sin (\phi_0/2) \qquad \text{(A1)}$$

From (6),

$$\mathbf{u}_{E2}{}^{+}(\theta) = \mathbf{n}(\theta)[\mathbf{n}(\theta)\cdot\mathbf{u}_{E1}{}^{+}] - \mathbf{t}_1(\theta)[\mathbf{t}_1(\theta)\cdot\mathbf{u}_{E1}{}^{+}] - \mathbf{t}_2(\theta)[\mathbf{t}_2(\theta)\cdot\mathbf{u}_{E1}{}^{+}] \qquad \text{(A2)}$$

If we evaluate the components of (A2) from (8) and (A1), we can multiply the result by the coefficient $\alpha(l)$ and separate the field into components assocated with polarization in (+), and normal to (−), the local plane of incidence [containing $\mathbf{n}(\theta)$ and $\mathbf{t}_1(\theta)$]. That is,

$$\alpha\mathbf{u}_{E2}{}^{+}(\theta) = \alpha^{+}(l)\left[\mathbf{n}(\theta) \cos \frac{\phi_0}{2} \cos \theta + \mathbf{t}_1(\theta) A \sin \frac{\phi_0}{2}\right] + \alpha^{-}(l)\left[\mathbf{t}_1(\theta) B \sin \frac{\phi_0}{2} + \mathbf{t}_2(\theta) \cos \frac{\phi_0}{2} \sin \theta\right] \qquad \text{(A3)}$$

where

$$\alpha^{+}(l) A + \alpha^{-}(l) B \equiv 1 \qquad \text{(A4)}$$

Similarly, for the conditions

$$\begin{aligned} \mathbf{n}_0(\mathbf{u}_{H1} + \mathbf{u}_{H2}) &= 0 \\ -\mathbf{p}_2\cdot\mathbf{u}_{H2} &= 0 \end{aligned} \qquad \text{(A5)}$$

and

$$\mathbf{u}_{H1}{}^{+} = -\mathbf{u}_\xi = -\mathbf{t}_2(0) \qquad \text{(A6)}$$

we determine

$$\alpha\mathbf{u}_{H2}{}^{+}(\theta) = -\alpha^{+}(l)\mathbf{t}_2(\theta) \cos \theta + \alpha^{-}(l)\mathbf{n}(\theta) \sin \theta \qquad \text{(A7)}$$

We combine (A3) and (A7), grouping the components together as *locally* vertical or horizontal components, to obtain

$$\begin{aligned} [\alpha\mathbf{u}_{E2}{}^{+}(\theta)]^{+} &= \mathbf{n}(0) \cos \frac{\phi_0}{2} \cos^2 \theta + \mathbf{t}_1(0) \frac{\sin \phi_0/2}{2} + \left(\mathbf{t}_2(0) \cos \frac{\phi_0}{2} \sin \theta \cos \theta\right) \\ [\alpha\mathbf{u}_{H2}{}^{+}(\theta)]^{+} &= (\mathbf{n}(0) \sin \theta \cos \theta) - \mathbf{t}_2(0) \cos^2 \theta \end{aligned} \qquad \text{(A8)}$$

and

$$\begin{aligned} [\alpha\mathbf{u}_{E2}{}^{+}(\theta)]^{-} &= \mathbf{n}(0) \cos \frac{\phi_0}{2} \sin^2 \theta + \mathbf{t}_1(0) \frac{\sin \phi/2}{2} - \left(\mathbf{t}_2(0) \cos \frac{\phi_0}{2} \sin \theta \cos \theta\right) \\ [\alpha\mathbf{u}_{H2}{}^{+}(\theta)]^{-} &= -(\mathbf{n}(0) \sin \theta \cos \theta) - \mathbf{t}_2(0) \sin^2 \theta \end{aligned} \qquad \text{(A9)}$$

In arriving at (A8) and (A7) we observed that the magnitude of the secondary field component at the point of stationary phase on a knife edge ($\nu = 1$) is approximately unity [*Dougherty,* 1969*b*]. Implicitly, therefore, $\alpha_0{}^{+} \approx \pm 1$ at grazing incidence and vertical or horizontal (±) polarization. Hence, as R goes to zero, we obtain $A = \frac{1}{2}$ and $B = -\frac{1}{2}$ from (A4).

The components of (A8) and (A9) within the parentheses are not effective for propagation from 0 to R; the product $\mathbf{u}_{E2}{}^{+} \times \mathbf{u}_{H2}{}^{+}$ must be proportional to

$$-\mathbf{p}_{20} = -\mathbf{n}(0) \sin (\phi_0/2) + \mathbf{t}_1(0) \cos (\phi_0/2) \qquad \text{(A10)}$$

Substituting the sum of the effective portions of (A8) and (A9) into (9), we obtain

$$(T_\Lambda - 1)\mathbf{u}_{E2}{}^{+} = (1 - \nu)\{\mathbf{u}_\eta \cos \phi_0 + \mathbf{u}_\zeta \sin \phi_0\} \qquad \text{(A11)}$$

for the apex point of stationary phase. The term within the braces of (*A*11) is $\mathbf{u}_{E2}{}^{+}(0)$, since, from (7), (8), and (*A*1),

$$\begin{aligned} \mathbf{u}_{E2}{}^{+}(\theta) &= \mathbf{n}(0) \cos \frac{\phi_0}{2} + \mathbf{t}_1(0) \sin \frac{\phi_0}{2} \\ \mathbf{u}_{H2}{}^{+}(\theta) &= -\mathbf{t}_2(0) \end{aligned} \qquad \text{(A12)}$$

and T_Λ is given by $2 - \nu$. The same procedure may be applied for horizontal polarization to obtain the same factor $1 - \nu$ as in (A11). Similarly, the factor is also obtained for $\nu < 1$ (i.e., $\theta_1 < 0$, $\theta_2 > 0$).

REFERENCES

Bachynski, M. P. (1963), Scale model investigations of electromagnetic wave propagation over natural obstacles, *RCA Rev., 25*(1), 105–144.

Bachynski, M. P., and M. G. Kingsmill (1962), Effect of obstacle profile on knife-edge diffraction, *IRE Trans. Antennas Propagat., 10,* 201–205.

Dougherty, H. T. (1969*a*), An expansion of the Helmholtz integral and its evaluation, *Radio. Sci., 4*(11), 991–996.

Dougherty, H. T. (1969*b*), Radio wave propagation for irregular boundaries, *Radio Sci., 4*(11), 997–1004.

Dougherty, H. T. (1970), The application of stationary phase to radio propagation for finite limits of integration, *Radio Sci., 5*(1), this issue.

Matsuo, S. (1950), The method of calculating VHF field intensity and research on its variation, *Electrical Commun. Lab. Rep. 621.39.001.6 (047.3),* Tokyo, Japan.

Meixner, J. (1949), Die Kantenbedingung in der Theorie der beugung elektro-magnischer Wellen an volkommen leitenden ebenen Schirmen, *Ann. Phys., 6,* 2–9.

Neugebauer, H. E. J., and M. P. Bachnyski (1960), Diffraction by smooth conical obstacles, *J. Res. NBS, 64D* (4), 317–329.

Stratton, J. A., and L. J. Chu (1939), Diffraction theory of electromagnetic waves, *Phys. Rev., 56*(7), 99–107.

Van Bladel, J. (1964), *Electromagnetic Fields,* McGraw-Hill, New York.

8

Reprinted from Transactions of the IEEE, Communications Technology, COM-18, No. 3, 261-263, 1970.

Microwave Space and Frequency Diversity Performance under Adverse Conditions

RAYMOND E. McGAVIN, MEMBER, IEEE,
HAROLD T. DOUGHERTY, MEMBER, IEEE, AND
C. B. EMMANUEL

***Abstract*—An experimental study of the effects of meteorological conditions and irregular terrain upon the performance of an optimum diversity system showed that: 1) the refractive index departed appreciably from a linear profile and was not uniform along the propagation path, and 2) more than two field components were produced by the combination of irregular terrain and the nonlinear refractive index structure. These conditions violate the design assumptions so that the optimum space diversity system failed to provide the theoretical performance. Under such conditions, this same result would be expected for any of the present diversity design procedures.**

The deep fading experienced on line-of-sight microwave circuits due to multipath is usually countered by space and/or frequency diversity. Diversity schemes in which two received signals are combined typically yield some improvement. If certain idealized conditions exist, then a specified level of improvement can be achieved by utilizing available diversity design procedures [1]–[3]. These idealized conditions include a linear refractive index profile uniform over the propagation path and a multipath condition where only two dominant components are involved. Here we report a recent experiment where neither of these conditions was fulfilled with resultant degradation of diversity performance.

This study was carried out on a 48-km path across a bowl-like depression at Haswell, Colo. The terrain is rolling and covered with buffalo grass. The location was chosen because of unusual meteorological conditions which produce a variety of refractive index structures. On summer days the atmosphere is well mixed and exhibits the expected linear refractive index profile. At night under clear skies the ground cools rapidly, cooling the air adjacent

---

Paper 70TP3-COM, approved by the Radio Communication Committee of the IEEE Communication Technology Group for publication without oral presentation. Manuscript received July 10, 1969.

The authors are with the Wave Propagation Laboratory, ESSA, Boulder, Colo. 80302.

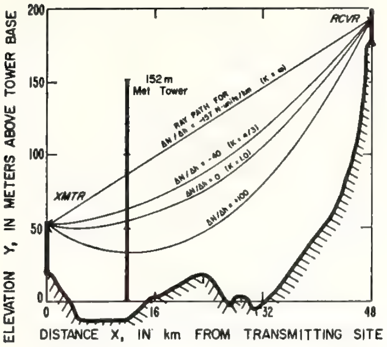
ELEVATION Y, IN METERS ABOVE TOWER BASE
200
150
100
50
0
DISTANCE X, IN km FROM TRANSMITTING SITE
0
16
32
48
XMTR
RCVR
152 m
Met Tower
RAY PATH FOR
ΔN/Δh = -157 N-units/km (K = ∞)
ΔN/Δh = -40 (K = 4/3)
ΔN/Δh = 0 (K = 1.0)
ΔN/Δh = +100

Fig. 1. Haswell terrain profile.

TABLE I
Characteristics of Haswell Radio Circuits — 1966

Transmitters			Receivers		
Frequency (MHz)	H^* (m)	$P^\dagger$ (dBm)	Frequency (MHz)	Antenna Number	H^* (m)
4985	54	44.7	4985	1	209.0‡
				2	201.0
				3	195.0‡
4855	54	45.3	4855		208.0
9330	157.5	28.4	9330	1	209.0§
				2	200.7§
9100	157.5	29.2	9100		208.2

* Height relative to the base of the meteorological tower.
† Effective radiated power. Half-power beamwidths exceed 3°.
‡ Optimum spatial diversity is between no. 1 and no. 3 antennas.
§ Optimum spatial diversity is between no. 1 and no. 2 antennas [1].

to it. This colder air flows into the "bowl" producing refractive index profiles markedly different from idealized linear profiles.

Fig. 1 illustrates the propagation path. The radio terminals were located asymmetrically to minimize the likelihood of atmospheric multipath [3]. A 150-m tower, located in the bowl, was furnished with a moveable instrumented carriage to measure refractive index, temperature, humidity, and wind. Table I contains the information on the radio circuit parameters. Both C-band and X-band signals were transmitted. Pairs of antennas were vertically spaced at the receiving terminal. For two of the pairs, the spacing was calculated from an "optimum" diversity design procedure [1], based on the average linear refractive index profile and the best quadratic fit to the terrain. This optimum diversity design, if applicable, would produce a combined signal level output which should always be greater than the median of either of the two signals. Three additional receiving antennas and an additional signal at both C band and X band were used, all separated at approximately one-half the optimum separation in space and frequency. These nonoptimum configurations were expected to exhibit poorer performance.

Continuous 24-hour-a-day recordings were made for one week in each of the months of February, March, and May of 1966. The resulting radio data were classified into two distinct types of signal: 1) essentially of constant amplitude, and 2) deeply fading. Although the former exhibited signal variations of only a few decibels and appeared to be of little interest as a fading phenomenon, they did establish ground reflections as the prevalent mechanism for multipath. For example, type 1) signals occurred during most afternoons and at times of high wind, when the atmosphere was well mixed and exhibited static linear refractive index structures. Further, these type 1) signal levels differed from the theoretical free-space value, as expected for the vector sum of direct- and ground-reflected components. Finally, continuous change of the receiving antenna height provided the expected height–gain lobing pattern of three or more received signal components.

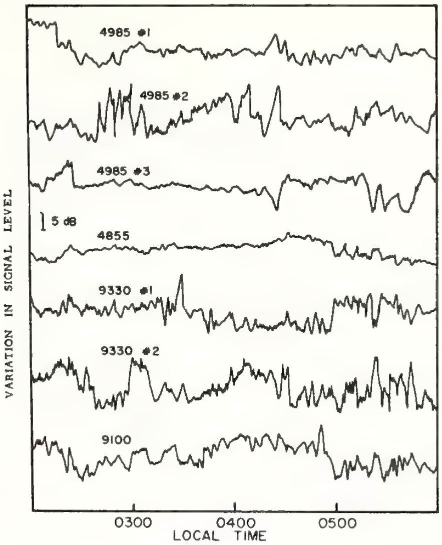

Fig. 2. Variation in signal level, Haswell, March 11, 1966 (frequency in MHz).

On the other hand, the deeply fading signals were observed for a dynamic but highly stratified atmosphere. This was prevalent during night-time hours when the ground radiated to the clear sky. The cooling ground created an adjacent layer of cool air with warmer air above [4]. This increase of temperature with height (temperature inversion) then became stronger and moved upwards as additional cool air flowed from the surrounding terrain into the bowl containing the meteorological tower. The resulting refractive index structure was sharply stratified; refractive index gradients were commonly measured across the temperature inversion as strong as -400 N units per kilometer over vertical extents of 50 meters. As the temperature inversion strengthened and moved upwards, the phase relationship between the direct- and ground-reflected components varied to provide fades commonly to 20 dB below the median (see Fig. 2). The periods of the fades were related to the rapidity of change in the refractivity structure. For example, whenever the refractive index structure was relatively static, the radio signals varied slowly, with periods of an hour or more. Whenever the refractive index structure changed drastically in periods of 10 to 15 minutes, the signal variation was rapid with periods of several minutes.

As a further indication of signal variability, the cross correlation between in-band signals was determined using an analog computer with an input time constant of 1 second. Fig. 3 illustrates the variability of the correlation coefficient when a 5-minute integration time was used. Notice that the coefficient might be highly positive or highly negative and remain so for periods as long as an hour, for any pair of either the space or frequency separated signals. This variability of the correlation coefficient was common, ranging from $+1.0$ to -1.0 when the atmosphere was stratified. If one were to consider a highly positive correlation coefficient as an indication of diversity failure, this experiment would indicate that such failure could be expected at some time for any of the pairs of signals.

To test the effectiveness of the diversity design, pairs of X-band and pairs of C-band signals were combined in an analog computer as if through a selection combiner. The hourly time distributions of

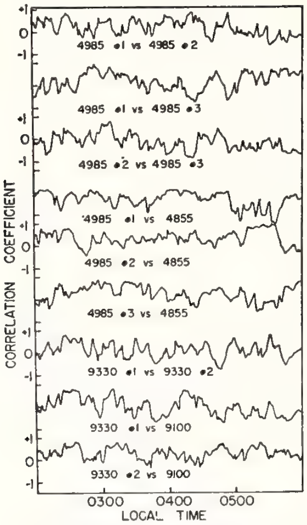

Fig. 3. Cross correlation coefficient between received signals, Haswell, March 11, 1966.

the combined output signal levels were then compared with the hourly time distributions of the input signal levels. Several representative samples of this comparison are shown in Table II, relative to the median of a single signal. In general, the combined output of any pair fell below the median of a single signal only 20 percent of the time; in one case (the fourth column) the combined output fell 10 dB below the single median for a short time. Although this demonstrates an improvement of the diversity over the nondiversity reception, it should be noted that the combined signal for the optimum pairs (the second and fourth column) were not supposed to fall below the median of the single signal. Not only did the design fail, but also no distinction can be made between the performance of the optimum and nonoptimum pairs.

TABLE II
PERCENTAGE OF TIME (ONE-HOUR SAMPLES) COMBINED SIGNAL IS BELOW INDICATED LEVEL (SELECTION COMBINING)

May 20, 1966	4985 no. 1 4985 no. 2	4985 no. 1* 4985 no. 3*	4985 no. 1 4855 no. 2	9330 no. 1* 9330 no. 2*	9330 no. 1 9100 no. 1
0600–0700					
10 dB above median†		72.0	72.0	72.4	72.4
median		19.9	23.0	21.8	15.2
10 dB below median		0	0	0.2	0
0700–0800					
10 dB above median	71.8	71.6	71.9	71.8	71.9
median	21.1	21.1	35.9	18.3	19.6
10 dB below median	0	0	0	0	0

* Optimum antenna spacing.
† Median level is the median of either signal.

These data indicate that the diversity designs which assume either linear or uniform refractivity profiles are only a partial answer to the problem of multipath fading. Our inability to differentiate between the optimum and nonoptimum systems demonstrates the limitations of such methods of calculating diversity design. Present designs can be modified to accommodate the additional ground-reflected components provided by irregular terrain, but the restriction to linear uniform refractivity profiles will still remain. Although any separation in space or frequency diversity will help, at present we have no assurance the degree of improvement will be sufficient. This suggests the need for efforts toward proper modeling of the refractive index structure.

REFERENCES

[1] K. A. Norton, G. A. Hufford, H. T. Dougherty, and R. E. Wilkerson, private communication.
[2] R. F. White, "Space diversity on line-of-sight microwave systems," *IEEE Trans. Communication Technology*, vol. COM-16, pp. 119–133, February 1968.
[3] H. T. Dougherty, "A survey of microwave fading mechanisms, remedies, and applications," ESSA, Tech. Rept. ERL 69-WPL4, March 1968.
[4] B. R. Bean and E. J. Dutton, *Radio Meteorology*. New York: Dover, 1968.

Reprinted from Proceedings of the AGARD/EWPP XVIth Symposium, No. 70, pp. 16-1 through 16-13, 1970.

REFLECTIONS FROM ELEVATED LAYERS IN TRANSHORIZON RADIO PROPAGATION

Gordon D. Thayer
U. S. Department of Commerce
Environmental Science Services Administration
Boulder, Colorado 80302
United States

SUMMARY

Computations of the power reflection coefficient R for some tropospheric elevated layers observed with radio refractometers show that the mean R varies as χ^{-1}, where $\chi \equiv 2\pi\theta h/\lambda$, θ being the grazing angle; h, the layer thickness; and λ, the radio wavelength. However, the values of R show fluctuations from the χ^{-1} dependence with standard deviations of from 3 to 14 dB, depending on the degree of smoothing assumed, predicting a scatter in the λ-dependence obtained from scaled frequency-diversity transhorizon radio experiments that agrees with published results. The mean λ-dependence derived from the χ^{-1} model ranges from λ^{-1} to λ^{+1}; the exact value depends on assumptions about the horizontal dimensions of individual layers compared with the size of effective Fresnel zones. Published results indicate that the atmosphere consists of a mixture of "large" and "medium" layers. The randomness of the χ-dependence of real tropospheric layers makes it difficult to separate layer and turbulence mechanisms in typical radio propagation experiments.

1. INTRODUCTION.

Partial reflections of electromagnetic waves occur wherever the refractive index changes appreciably over a distance that is not large compared with a wavelength. Thin layers -- ranging from roughly 1 m to 100 m thick -- with abnormally large refractive index gradients are common in the troposphere and are known to be an important transhorizon propagation mechanism[1-4].

In this paper we examine the results of calculations of the power reflection coefficient for some observed tropospheric layers which show that -- all other things being equal -- the power reflection coefficient of such layers is approximately proportional to the radio wavelength. In applying this to the theory of the wavelength dependence of transhorizon propagation, we take into account the horizontal size of the layers as compared with the size of a Fresnel zone. We find that this wavelength dependence varies between λ^{-1} when all the layers are small compared with a Fresnel zone to λ^{+1} when they are large compared with that zone. All intermediate wavelength dependencies -- between λ^{-1} and λ^{+1} -- should occur in nature.

Superimposed on the mean wavelength dependence of the reflection coefficients for individual layers is a random variation with a standard deviation of some 14 dB. A slightly reduced random variation is expected for actual propagation paths because of the averaging of layer fine-scale characteristics over a Fresnel zone. Thus, data from a frequency-diversity transhorizon propagation experiment would be expected to show a considerable variation in wavelength dependence as a function of time, even when layer reflections are the dominant mode of propagation at all times. Data from such experiments actually do show standard deviations in the diversity signal difference of from 3 to 11 dB, which agrees with our theoretical results.

We conclude that these effects, tending to mask the true nature of the propagation mechanism, render frequency diversity experiments of limited value for improving the theory of transhorizon propagation.

2. THEORY AND BACKGROUND.

Figure 1 shows the basic geometry of partial reflections, we assume flat earth geometry for calculating reflection coefficients. If the line-of-sight power that would be received at the receiver via a perfectly reflecting layer is given by P_0, then a tropospheric layer with a power reflection coefficient R will give a received power

$$P_R = P_0 R , \qquad (1)$$

provided the horizontal extent of the layer is large compared with the Fresnel zone. The Fresnel zone is approximately elliptical in shape, with a width perpendicular to the propagation path of $\sqrt{L\lambda}$ and a length along the path of $\sqrt{L\lambda}/\theta$, where λ is the radio wavelength, L is the path length, and θ is the grazing angle. When the layer is not large compared with the Fresnel zone, the reflected power can be obtained approximately by a Fresnel integral technique.[8]

If we assume that tropospheric layers have an approximately round horizontal shape (i.e., saucer-shaped, or "feuillets") and a mean diameter D, then for medium-sized layers, where

$$\tfrac{1}{2}\sqrt{L\lambda} < D < \tfrac{1}{2}\sqrt{L\lambda}/\theta \ , \qquad (2)$$

we have approximately

$$P_R \cong P_0 R \left[\frac{4D^2\theta^2}{\lambda L}\right] . \tag{3}$$

Where

$$D < \tfrac{1}{2}\sqrt{L\lambda} , \tag{4}$$

we have as a limiting case the "radar equation,"

$$P_R \cong P_0 R \left[\frac{16D^4\theta^2}{\lambda^2 L^2}\right] . \tag{5}$$

Thus, varying the size of the layers relative to the size of the Fresnel zone introduces a wavelength dependence into our results.[6]

We now need the value of the power reflection coefficient R to evaluate the received power. The theory of partially reflecting layers deals with the case given by (1), where the layer is considered a planar transition zone between two infinite half spaces of refractive index n and $n + \Delta n$, with a plane electromagnetic wave incident from below at angle θ (as defined in Figure 1). For weakly reflecting layers, i.e., when $R \ll 1$, the amplitude reflection coefficient r is adequately given in most instances by the WKB approximation[7]

$$r \cong \frac{1}{2\theta^2} \int_{z_1}^{z_2} \frac{dn}{dz} \exp\left\{-i2k\theta z\right\} dz , \tag{6}$$

where z_1 and z_2 are the vertical coordinates of the base and the top of the layer, k is the radio wavenumber $2\pi/\lambda$, and $i = \sqrt{-1}$. The problem can be parameterized by defining an effective layer thickness[8]

$$\chi = \frac{2\pi\theta h}{\lambda} , \tag{7}$$

where h is the actual layer thickness, and the integral can be simplified by defining a normalized gradient function[9]

$$g(y) \equiv (\Delta n)^{-1} \frac{dn}{dy} ,$$

where

$$y \equiv z/h, \text{ and } z_1 \equiv 0 . \tag{8}$$

The integral (6) is now reduced to

$$r \cong \frac{\Delta n}{2\theta^2} \int_0^1 g(y) \exp\left\{-i2\chi y\right\} dy . \tag{9}$$

This expression shows that the amplitude reflection coefficient is the product of the Fresnel coefficient $r_0 \cong \Delta n/2\theta^2$ and the complex Fourier transform, with argument 2χ, of the normalized gradient function g(y). The power reflection coefficient R is obtained as the square of the modulus of the complex number r, and hence is always a real number.

Figure 2 shows four tropospheric layer refractive index profiles for which power reflection coefficients have been calculated as a function of normalized thickness χ.[6] These profiles were obtained with airborne refractometers on flights through the Atlantic trade-wind inversion layer and are probably representative of the sort of fine detailed n-structure normally found in tropospheric layers.[10] The $R(\chi)$ function for each of the four profiles was calculated on a digital computer by a numerical integration technique applicable to (8) and (9). The results are shown in Figure 3, where the relative power reflection coefficients $R(\chi)/R_0$, in which $R_0 \equiv \Delta n^2/4\theta^4$, are plotted. The curve for layer 3 shows us that R for actual tropospheric layers may occasionally approach the Fresnel value $\Delta n^2/4\theta^4$ even when the layer is quite thick compared with the effective radio wavelength, i.e., when $\chi \gg 1$.

The very high and very low points on the curves in Figure 3 are caused by structuring of gradient changes in the layer profile that has a precise relationship to the effective radio wavelength; this is analagous to the Bragg condition for the maximum reflection of x-rays from a crystal lattice structure. However, in contrast with a crystal structure, the refractive index profile of a tropospheric layer cannot generally be expected to remain precisely uniform over a Fresnel zone; for a typical transhorizon propagation path with L = 300 km and $\theta \cong$ 17 mrad, the Fresnel zone will range from 800 m by 46 km for λ = 2 m to 80 m by 4.6 km for λ = 2 cm. The irregularities in the structure of actual layers, by smoothing over a Fresnel zone, will thus tend to reduce the extremes of the reflectivity function. We can see the effects of such smoothing by taking the geometric mean of the four reflectivity curves shown in Figure 3; the resulting reflectivity function is shown in Figure 4.

The average reflectivity curve for the four profiles shown in Figure 4 follows a χ^{-1} dependence rather well, as shown by the plot of the function $(1 + \chi)^{-1}$. The standard deviation of the data in Figure 4 from the $(1 + \chi)^{-1}$ curve is only 2.5 dB; the standard deviation of the data in Figure 3 from the $(1 + \chi)^{-1}$ curve is 11 dB. These deviations are not quite normally distributed , and when the standard deviations are evaluated as half the difference between the 16 and 84 percent levels of the cumulative distribution curves -- the percentage points for one standard deviation of a normal distribution -- the results are 3.5 dB and 14 dB for the smoothed and nonsmoothed data, respectively.

We can conclude that the probable power reflectivity of actual tropospheric layers is given by the function $(1 + \chi)^{-1}$, with a standard deviation of $\sim$ 14 dB or less, depending on the amount of Fresnel zone smoothing that may be present. Thus, we have a functional dependence for R in (1), (3), or (5), and are now in a position to interpret transhorizon propagation data in terms of reflection theory.

3. APPLICATION TO TROPOSPHERIC PROPAGATION AND COMPARISON WITH RADIO DATA.

3.1. Wavelength Dependence of Layer-Mechanism Propagation.

The solution in terms of Fresnel integrals for which (1), (3), and (5) are good approximations is

$$P_R = P_0 R\,[4F(Q)], \qquad (10)$$

where

$$Q \equiv \frac{D}{\sqrt{\lambda L}}, \quad F(Q) = F_1(u), \quad u \equiv \sqrt{2}Q,$$

and

$$F_1(u) = [S^2(u) + C^2(u)][S^2(u\theta) + C^2(u\theta)]. \qquad (11)$$

Here S(u) and C(u) are the usual Fresnel integrals, defined by

$$S(u) \equiv \int_0^u \sin\left\{\frac{\pi}{2}t^2\right\} dt,$$

and

$$C(u) \equiv \int_0^u \cos\left\{\frac{\pi}{2}t^2\right\} dt. \qquad (12)$$

The function $F_1(u) = F(Q)$ is plotted as a function of Q in Figure 5. Since the Fresnel integrals result in some high-frequency oscillations of F(Q) that are not pertinent to our problem, they are smoothed out in Figure 5 by the assumption that F(Q) for each Q is the mean of values obtained from a log-normally distributed population of layer sizes D that have a standard deviation of 15.5 percent of the mean value.

Combining (10) with our empirical result for R, we have

$$\left\langle\frac{P_R}{P_0}\right\rangle \cong \frac{(\Delta n)^2}{4\theta^4}(1 + \chi)^{-1}[4F(Q)], \qquad (13)$$

where χ is the effective thickness of the layer $2\pi\theta h/\lambda$, as previously defined; $\langle P_R/P_0\rangle$ is the expected or mean value of the ratio P_R/P_0, which is subject to fluctuation because of statistical variations in the χ dependence of R.

The wavelength dependence for layer-mechanism propagation is obtained from (13). Assuming that P_0 and θ are the same for two wavelengths, we obtain the ratio between the received powers P_1 and P_2:

$$\left\langle\frac{P_1}{P_2}\right\rangle \cong \frac{1 + \chi_2}{1 + \chi_1}\,\frac{F(Q_1)}{F(Q_2)}. \qquad (14)$$

If both χ_1 and χ_2 are large compared with 1, we have

$$\left\langle\frac{P_1}{P_2}\right\rangle \cong \frac{\lambda_1}{\lambda_2}\,\frac{F(Q_1)}{F(Q_2)}, \quad \chi_{1,2} >> 1. \qquad (15)$$

From Figure 5 we have three different wavelength dependences for F(Q), depending on the ratio of the approximate layer diameter to the Fresnel zone. For $Q = D/\sqrt{2L}$ larger than $1/2\theta$, F(Q) is independent of λ and (15) becomes

$$\left\langle\frac{P_1}{P_2}\right\rangle \cong \frac{\lambda_1}{\lambda_2}. \qquad (16)$$

We will refer to this as the "large layer" case. For Q intermediate between $\frac{1}{2}$ and $\frac{1}{2}\theta$, F(Q) varies as λ^{-1}, so that (15) becomes

$$\left\langle \frac{P_1}{P_2} \right\rangle \cong 1 \; ; \tag{17}$$

this is the "medium-sized layer" case. For Q smaller than $\frac{1}{2}$, F(Q) varies as λ^{-2}, and we have from (15)

$$\left\langle \frac{P_1}{P_2} \right\rangle \simeq \frac{\lambda_2}{\lambda_1} \; , \tag{18}$$

which is the case of small layer size.

The wavelength dependence of received power is usually expressed as λ^q; for the three cases treated above, the values of q are + 1, 0, and - 1, respectively. Intermediate values of q can result when Q for one of the wavelengths falls on one side of a dividing point ($1/2$ or $1/2\theta$) and Q for the second wavelength falls on the other side of the dividing point. Thus for layer-mechanism propagation, $\langle q \rangle$ may fall anywhere between - 1 and + 1, depending on the size of the layers involved.

3.2 Variability of the Wavelength Dependence for Layer-Mechanism Propagation.

In the preceding section we derived the mean or expected value of q, the exponent in the wavelength dependence factor λ^q, and we found that it was a function of the normalized layer size Q and the elevation angle θ at the reflection point. Thus, if we set up a scaled two-frequency experiment, i.e., where the line-of-sight powers P_0 are equal and the beams are coincident, and if we record, say, one-hour median values of P_1/P_2 at the receivers, we will get different values of q at different times if the layer sizes vary from time to time. Hence, we would expect to get a distribution of q-values.

There is an additional source -- probably more important than variable layer sizes -- of variability in measured values of q. Consider Figure 3. We can simulate the results for two wavelengths that are in a ratio of, say, 2 to 1 by picking χ values that differ by a factor 2. If the second wavelength is the smaller, we would expect to find, on the average, that R for that wavelength would be only half as large as for the first wavelength, since $\chi_2 = 2\chi_1$ for this particular case. However, it is obvious that for any two values χ and 2χ, the value of R_2 may be either larger or smaller than R_1.

Thus, in the course of an experiment, we would expect to get a distribution of q values even if the layers were all of one size category. For example, if we assume an experiment where all the layers are large compared with the Fresnel zones, i.e., $Q > 1/2\theta$ for both wavelengths, we would expect to get P_1/P_2 values distributed around a mean value of $10 \log_{10}(\lambda_1/\lambda_2)$dB with a standard deviation of between 3 and 14 dB. The actual standard deviation would depend on the amount of Fresnel-zone smoothing present in the actual layers, as discussed previously. Since we have no measurements of the horizontal variations in actual layer structure, we cannot predict what this degree of smoothing would be.

This variability in P_1/P_2 values introduced by the peculiarities of layer reflectivity functions is very important. For a typical experiment with $\lambda_1 = 2\lambda_2$, $10 \log_{10}(\lambda_1/\lambda_2)$ is 3.0 dB, a value that is not large compared with the estimated standard deviation of P_1P_2 of from 3 to 14 dB. Even for a frequency separation of 10 to 1, the standard deviation of the P_1/P_2 values is liable to be comparable to the mean value.

3.3 Comparison of Results with Radio Data.

As an example of hypothetical experimental results that can be obtained from our reflectivity curves, Figure 6 shows the cumulative distribution of 33 values of P_1/P_2 obtained by randomly selecting χ values in the range $2 < \chi < 18.2$ and reading the values for $R(\chi)$ and $R(5.49\,\chi)$ from Figure 4; then, if the layers are assumed larger than $\sqrt{\lambda L}/2\theta$, $P_1/P_2 = R_1/R_2$. The standard deviation for this sample, estimated as half the difference between the 16 and 84 percent levels, is 3.5 dB. The median value of q, i.e., for $P_1/P_2 = \lambda^q$, for the sample is 0.6. This shows that we require a rather large sample of P_1/P_2 values in order to accurately determine q; a curve of $(1 + \chi^{0.6})^{-1}$ drawn on Figure 4 would pass more than 1 dB above every point of the $R(\chi)$ curve for all $\chi > 2$; obviously then, $q = 0.6$ is not the correct λ-dependence for these data.

Figure 7 shows the P_1/P_2 distribution for a scaled, two-frequency propagation experiment conducted in the United States over a 302.5-km path between Round Hill, Massachusetts, and Crawford's Hill, New Jersey.[11] The median value of P_1/P_2 is 6.5 dB, or $q \cong 0.9$, and the standard deviation, taken from the 16 and 84 percent levels, is 5.0 dB. The observed distribution is consistent with the hypothesis that the received signals were reflected from layers that were mostly large compared with the effective Fresnel zone, i.e., $D > 14$ km. In an analysis of these same data,[12], hourly median values of P_1/P_2 for 76 winter hours in February and March showed a median of 6.5 dB or $q \cong 0.9$ -- the same as the total sample -- and a standard deviation of 4 dB; 80 summer values from June and July showed a median of 10 dB or $q \cong 1.35$ and a standard deviation of 7 dB. These seasonal data, if interpreted in terms of layer-mechanism propagation, suggest more well-developed and variable layer structure in the summer than in the winter. This is consistent with the higher level of atmospheric humidity observed in the summer, upon which strong refractive index gradients depend.

Figure 8 shows P_1/P_2 data for a more recent experiment.[3] These data are for a 259-km path between Stockholm and Mora in Sweden; the authors state that the crossover height is 1200 m, and the minimum grazing angle θ is approximately 17 mrad (1/2 of the minimum scatter angle). The elevated layers in that experiment would be considered "large" by our criterion if the mean horizontal diameter exceeded 8.2 km. The results in Figure 8 show during August a median of $q \cong 1$ and a standard deviation of P_1/P_2 of 4.0 dB, values that are consistent with an hypothesis that "large" layers are the dominant propagation mechanism. The value of q together with the standard deviation of P_1/P_2 decreases as the weather becomes colder. This, in turn, is consistent with either a decrease in the size of layers or a trend toward tropospheric forward scatter as the dominant propagation mechanism, for which theory indicates $q \cong -1/3$. Because the winter climate in Sweden is cold, absolute humidity levels are low, so that a decrease in the strength of elevated layers should be expected; this suggests that forward scatter might be expected to be the dominant winter propagation mechanism.

Results for these two experiments,[11,3] as well as three others,[13-15] are summarized in Table I.

Table I

Summary of Experimental Results for Wavelength Dependence

Path Length L km	Wavelengths λ_1, λ_2 cm	Min. Elev. Angle θ mrad	Q_L $\frac{\sqrt{\lambda_1 L}}{2}$ km	Q_U $\frac{\sqrt{\lambda_1 L}}{2\theta}$	Dates	q_{50}	$\sigma\left\{\frac{P_1}{P_2}\right\}$	References and Remarks
302.5	71.9, 13.1	17	233	14	2-7/57	0.9	5.0	Chisholm et al.[11]
302.5	71.9, 13.1	17	233	14	2-3/57	0.9	4.0	Bolgiano,[12] Winter
302.5	71.9, 13.1	17	233	14	6-7/57	1.35	7.0	Bolgiano,[12] Summer
108	35.7, 10.7	4.8*	196	41	8/60-7/61	0	6.5	Bolgiano,[13] Daytime
108	10.7, 3.3	4.8*	108	23	8/60-7/61	0.4	8.0	only: 1000-1600 LST.
108	35.7, 3.3	4.8*	196	41	8/60-7/61	0.2	11.0	only: 1000-1600 LST.
108	mean†	4.8*	- -	--	10/60-5/61	0.7	4.0	Winter: 1000-1600 LST.
108	mean†	4.8*	- -	--	9/60, 6-7/61	-0.5	3.5	Summer: 1000-1600 LST.
275	65.2, 7.3	13	212	16	4/56-12/57	0.9	4.0	Crawford et al.[14]
259	30, 10	17	140	8	8/66	1.0	4.0	Eklund & Wickerts[3]
259	30, 10	17	140	8	9/66	0.2	3.5	Eklund & Wickerts[3]
259	30, 10	17	140	8	12/66, 4/67	-0.1	2.5	Eklund & Wickerts[3]
306	24.0, 8.8	15	136	9	2/12/59	0.6	4.4	Ortwein et al.[15] "Layer" day.
306	24.0, 8.8	15	136	9	2/11/59	-0.2_5	2.6	"Turbulent" day.
306	8.8, 3.2	15	82	5.5	2/12/59	-0.2_5	2.6	"Layer" day.
306	8.8, 3.2	15	82	5.5	2/11/59	-0.1	3.1	"Turbulent" day.

*This path was asymmetric; calculations are for a layer tilted at 1.65 mrad.

†The hourly medians used were the average of the hourly median P_1/P_2 and P_2/P_3 values, where $P_1 \rightarrow 35.7$ cm, $P_2 \rightarrow 10.7$ cm, and $P_3 \rightarrow 3.3$ cm.

The results reported by Crawford et al.[14] are consistent with the large layer propagation mechanism. The results for Bolgiano's 1964 paper[13] are variable: the winter data are suggestive of the large layer propagation mechanism, whereas the summer data suggest either conventional troposcatter or a mixture of small and medium-sized layers. These data are confined to daylight hours and the crossover height was only about 150 m above the terrain; daytime layer formation in the summertime at this height is rather unlikely because of the strong convection expected near the ground. This may explain why Bolgiano's 1964 data[13] show a behavior opposite to some of the other experiments, in which the summer data show $q \cong 1$ and the winter data show $q \cong 0$. The data reported by Ortwein et al.[15] are only for a two-day period, carefully selected for the lack of a strongly layered atmosphere. The data for February 12, 1959, are suggestive of layer-mechanism propagation. Ortwein et al. state that "data from the morning of February 12 indicated a $\lambda^{0.4}$ dependence when there were slight irregularities in the profile, but a $\lambda^{0.9}$ dependence was observed in the afternoon when a turbulent layer had been more established." Their refractometer data could also be interpreted as indicating a sharply layered structure well above the surface, rather than a turbulent structure. For the 11th these authors state that "[this] followed passage of a frontal zone which left an unstable standard atmosphere with no layering." We can be reasonably certain that the data for February 11 represent a troposcatter propagation mechanism.

In total, the results shown in Table I do not indicate unambiguously any specific propagation mechanism; however, the results for many of the experimental periods are consistent with our estimates of the standard deviation of the P_1/P_2 power ratios -- if we assume a reasonable degree of Fresnel zone averaging -- and suggest that much of the time propagation is accomplished via layers of relatively large horizontal extent. This horizontal extent, as indicated by the values for Q_u in Table I, is on the order of 10 km or more. For an assumed average vertical thickness of 100 m, a 10-km diameter represents an aspect ratio of 100 to 1, which seems to be a reasonable figure when compared for example, with the normal ratio of vertical to horizontal refractive index gradients encountered in the atmosphere.

3.4. Angular Dependence of Layer-Mechanism Propagation.

The dependence of received power on the grazing angle θ can be obtained from (13). The function $(1 + \chi)^{-1}$ varies as θ^{-1} if λ and h are held constant in (7). For "large" layers F(Q) is independent of θ, and

$$P_R(\theta) \propto \theta^{-5}, \quad \theta > \frac{\sqrt{\lambda L}}{2D} \quad . \tag{19}$$

For "medium" and "small" layers F(Q) is proportional to θ^2, and

$$P_R(\theta) \propto \theta^{-3}, \quad \theta < \frac{\sqrt{\lambda L}}{2D} \quad . \tag{20}$$

The above is mainly of theoretical interest since it would apply only to radio paths with the same center point and crossover height but different path lengths -- and hence different θ -- whereas most experiments are set up with a common length and varying crossover heights to achieve varying θ. Layer characteristics tend to change markedly with the height of the layer.

3.5. Multiple Reflections and the "Whispering-Gallery" Mode of Propagation by Elevated Layers.

There are at least two elevated layer tropospheric propagation mechanisms other than the single partial reflection that we have considered thus far: multiple reflections and the "whispering-gallery" mode.

In this instance, multiple reflections refers to two or more partial reflections of a radio wave from an elevated layer; this mechanism has been treated by Hall.[4] The overall reflection coefficient is the product of the reflection coefficients at each point of reflection; the resulting decrease in efficiency may be offset by the decrease in layer height, and hence of grazing angle, that is required to satisfy the geometry. For two partial reflections, the wavelength and grazing angle dependence derived previously are presumably squared; they would be cubed for three reflections, etc. Otherwise, the mechanism behaves quite like the single reflection treated previously. Multiple reflections between an elevated layer and the ground have also been treated theoretically.[16]

Propagation by a "whispering-gallery" mode has been treated by Wait.[17] In this mechanism radio energy is guided in a waveguidelike mode along the undersurface of a sharp tropospheric layer, possibly with very low attenuation. The radio energy must first be introduced along the layer at a grazing angle very close to zero. The mechanism responsible for this introduction of energy is presumably a partial reflection from reflecting elements or facets of the layer that are slightly tilted from the horizontal; the tilt angle required is one-half of the actual grazing angle at the point where the main radio beam intersects the layer -- the required tilt angles are thus typically 0.5° or less.

Aside from the wavelength dependence of the attenuation in the "whispering-gallery" mode, the overall characteristics of this propagation mechanism are quite similar to the ordinary partial reflection process, and, except for a possible low frequency "cut-off" effect, it would probably be indistinguishable by ordinary experimental techniques from simple partial reflections.

4. SUMMARY OF RESULTS.

We have demonstrated several significant points regarding tropospheric radio propagation by partial reflections from elevated layers:

(1) The power reflection coefficient of elevated layers in the troposphere should, on the average, vary as χ^{-1}, where $\chi \equiv 2\pi\theta h/\lambda$; θ is the grazing angle, h is the vertical thickness of the layer, and λ is the radio wavelength.

(2) The wavelength dependence of beyond-the-horizon tropospheric transmissions when layer mode propagation is present may average between λ^{-1} and λ^{+1}, depending on the horizontal size of the layers compared with the size of the first Fresnel zone.

(3) Computed data on layer reflection coefficients indicate that experimental values of power ratios at two or more wavelengths on scaled tropospheric radio paths should show standard deviations of up to 14 dB when layer mode propagation exists. Experimental data for times when layer-mechanism propagation is believed to have occurred indicate that 4 to 7 dB are typical figures for this standard deviation of power ratios.

(4) The angular dependence of received power for layer-mechanism propagation is expected to be θ^{-5} for "large" layers and θ^{-3} for "medium" and "small" layers.

(5) The similarity of the wavelength dependence for a mixture of "small" and "medium" layers and the $\lambda^{-1/3}$ dependence expected for traditional troposcatter propagation, in addition to the expected scatter in the observed ratio of received powers, makes it difficult to separate these two mechanisms in experimental data without additional information, such as off-great-circle path received power measurements. Hence, frequency diversity experiments are of limited usefulness for revealing the nature of transhorizon propagation mechanisms.

(6) Comparison of theory with radio data indicates that elevated layers with horizontal dimensions on the order of tens of kilometers occur often in the troposphere.

Many other aspects of radio data can be interpreted in terms of layer-mechanism theory. For example, Eklund and Wickerts[3] found that the value of q in the wavelength dependence λ^q tended to increase as the level of received power at the longer wavelength increased. In terms of layer-mechanism theory, the higher values of received power on one of the wavelengths would tend to be associated with $R(\chi)$ values well above the mean $(1 + \chi)^{-1}$ dependence, as well as with layers having a high value of Δn or small thickness h. If the two frequencies are separated enough that the departures of the respective $R(\chi)$ values from the mean $(1 + \chi)^{-1}$ can be considered statistically independent, then the value of $R(\chi)$ for the shorter wavelength would tend to fall closer to the mean. Thus the observed power ratios in instances where P_1 is well above the long term median would be larger than normal, and the resulting values of q would also be larger than average. If this interpretation is correct, then the reverse should be true if q is plotted as a function of received power at the shorter wavelength, and q would be expected to at least show a lesser dependence on P_2 if not actually an inverse dependence. This is true for Eklund's and Wickerts' data;[3] the median value of q as a function of P_1(30 cm) varies from -0.3 to +1.7 between the 93 and 7 percent levels of P_1, but as a function of P_2(10 cm), q varies only from 0.2 to 0.6 between the 93 and 7 percent levels of P_2.

Finally, we can make a table of the expected characteristics of four tropospheric propagation mechanisms: partial reflections from elevated layers for the three size categories and troposcatter. The wavelength dependence of the "small" and "medium" layers is shown as variable since it depends on the number of individual layers occurring in a Fresnel zone, which is usually much smaller than the beam width. The standard deviation of P_1/P_2 is for scaled, multifrequency experiments, and the values are taken from Table I.

Table II

Characteristics of Four Tropospheric Propagation Modes

Mode	Description	Wavelength Dependence q	Angle Dependence	Std. Dev. P_1/P_2	Remarks
(1) "Large" layers	Coherent reflection	$\langle q \rangle \cong +1$	θ^{-5}	~ 4 to 7 dB	Rather common
(2) "Medium" layers	Incoherent reflection	$\langle q \rangle \simeq 0$ to $+\frac{1}{2}$	θ^{-3}	?	Difficult to separate from "troposcatter"
(3) "Small" layers	Anisotropic forward scatter	$\langle q \rangle \cong -1$ to 0	θ^{-3}	?	
(4) "Tropo-scatter	Quasi-isotropic forward scatter	$\langle q \rangle \cong -\frac{1}{3}$	$\theta^{-14/3}$ or $\alpha^{-14/3}$*	~ 2.5 to 3.5 dB	Difficult to isolate as a "pure" mechanism.

*α is the scattering angle, not necessarily in the vertical plane.

The "large" layer mechanism is described as coherent because the reflection is from a structure that is fairly uniform over the first Fresnel zone. The "medium" layer mechanism is described as "incoherent" because the reflections from several layers along the length of the Fresnel zone are random in phase and the powers are additive. The "small" layer mechanism consists of power reflected from many layers that are small compared with the first Fresnel zone but large compared with a wavelength; in this respect, the mechanism is similar to ordinary troposcatter, except that the layers may be confined to a rather narrow height interval (a "mother" layer) and the structures and hence the reflectivities are strongly anisotropic. Troposcatter is usually defined as a quasi-isotropic process -- the atmosphere being treated theoretically as a statistically stationary, homogeneous, isotropic medium -- and scattering from off-great-circle paths is assumed to be about as efficient as on great-circle paths at the same scattering angle. Mixtures of all four mechanisms may occur, resulting in mixed modes of propagation that are very difficult to separate experimentally.

5. REFERENCES.

1. Hardy, K. R., D. Atlas, and K. M. Glover, "Multiwavelength backscatter from the clear atmosphere," J. Geophys. Res. 71, 6, 1537 (1966).

2. Lane, J. A., "Radar echoes from tropospheric layers by incoherent backscatter," Electronics Letters 3, 4, 173 (1967).

3. Eklund, F., and S. Wickerts, "Wavelength dependence of microwave propagation far beyond the radio horizon," Radio Sci. 3 (New Series), 11, 1066 (1968).

4. Hall, M. P. M., "Further evidence of VHF propagation by successive reflections from an elevated layer in the troposphere," Proc. IEE 115, 11, 1595 (1968).

5. Thayer, G. D., "Radio reflectivity of tropospheric layers," to be published in Radio Sci. (1970).

6. Friis, H. T., A. B. Crawford, and D. C. Hogg, "A reflection theory for propagation beyond the horizon," Bell System Tech. J. 36, 3, 627 (1957)

7. Wait, J. R., "Electromagnetic Waves in Stratified Media," Pergamon Press, Oxford (1962).

8. du Castel, F., P. Misme, and J. Voge, "Sur le rôle des phénomènes de réflexion dans la propagation lointaine des ondes ultracourtes," in Electromagnetic Wave Propagation, 670-683, Academic Press, London (1960).

9. Wait, J. R., and C. M. Jackson, "Influence of the refractive index profile in VHF reflection from a tropospheric layer," IEEE Trans. Ant. Prop. AP-12, 4, 512 (1964).

10. Ament, W. S., "Airborne radiometeorological research," Proc. IRE 47, 5, 756 (1959).

11. Chisholm, J. H., J. F. Roche, and W. J. Jones, "Experimental investigations of angular scattering and multipath delays," paper presented at URSI-IRE Joint Meeting, Washington, D.C., May 1957. Results published by Bolgiano in reference 12.

12. Bolgiano, R., "A theory of wavelength dependence in ultrahigh frequency transhorizon propagation based on meteorological considerations," J. Res. NBS 64D, 3, 231 (1960).

13. Bolgiano, R., "A study of wavelength dependence of transhorizon radio propagation," Report CRSR 188, Cornell University, Ithica, N. Y., 15 June 1964.

14. Crawford, A. B., D. C. Hogg, and W. H. Kummer, "Studies in tropospheric propagation beyond the horizon," Bell System Tech. J. 38, 5, 1067 (1959)

15. Ortwein, N. R., R. U. F. Hopkins, and J. E. Pohl, "Properties of tropospheric scattered fields," Proc. IRE 49, 4, 788 (1961).

16. Paltridge, G. W., "Reflection from elevated layers in the troposphere," Proc. IEE 117, 1, 23 (1970).

17. Wait, J. R., "Whispering-gallery modes in a tropospheric layer," Electronics Letters 4, 18, 377 (1968).

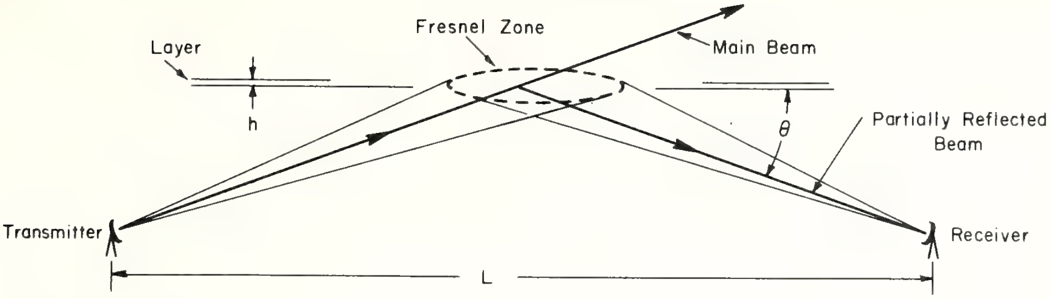

1. Geometry of partial reflection by a tropospheric layer.

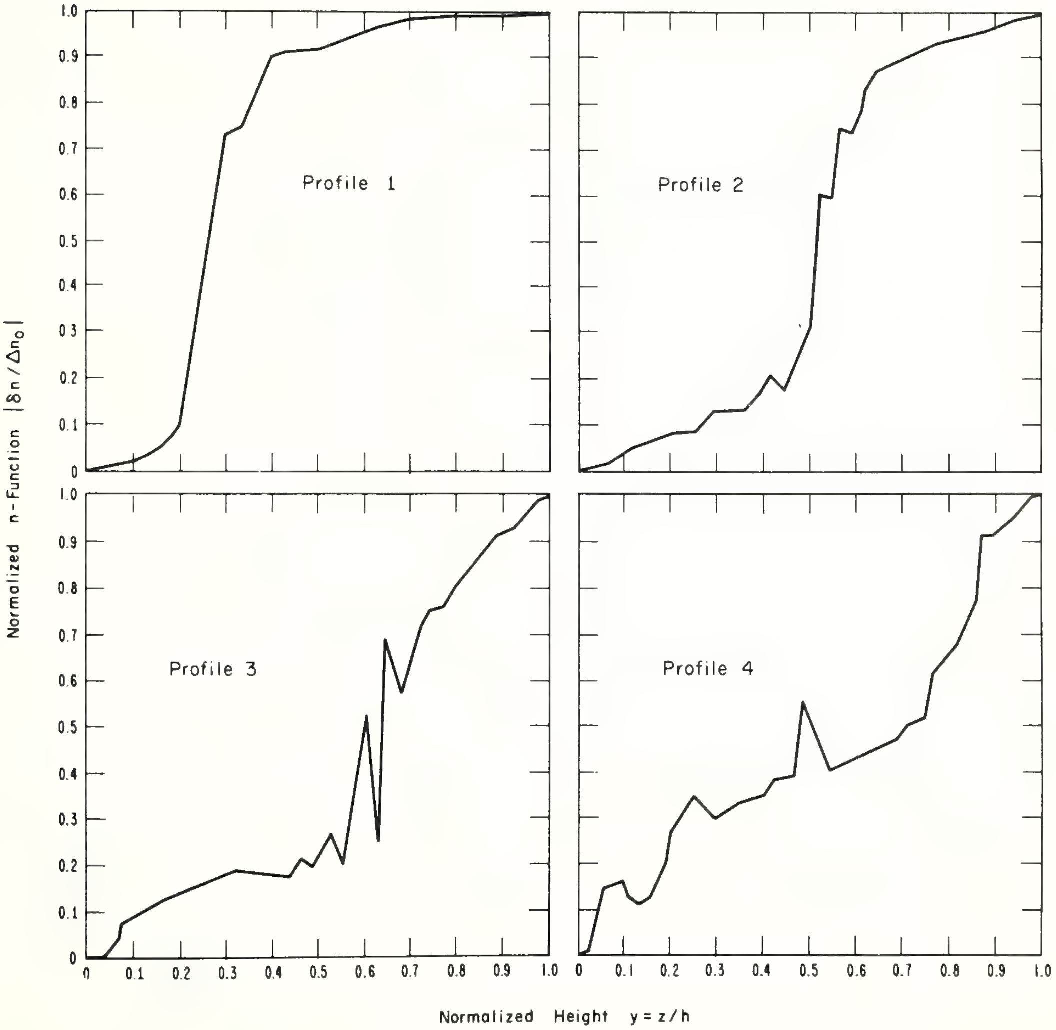

2. Normalized refractive index profiles for observed layers.

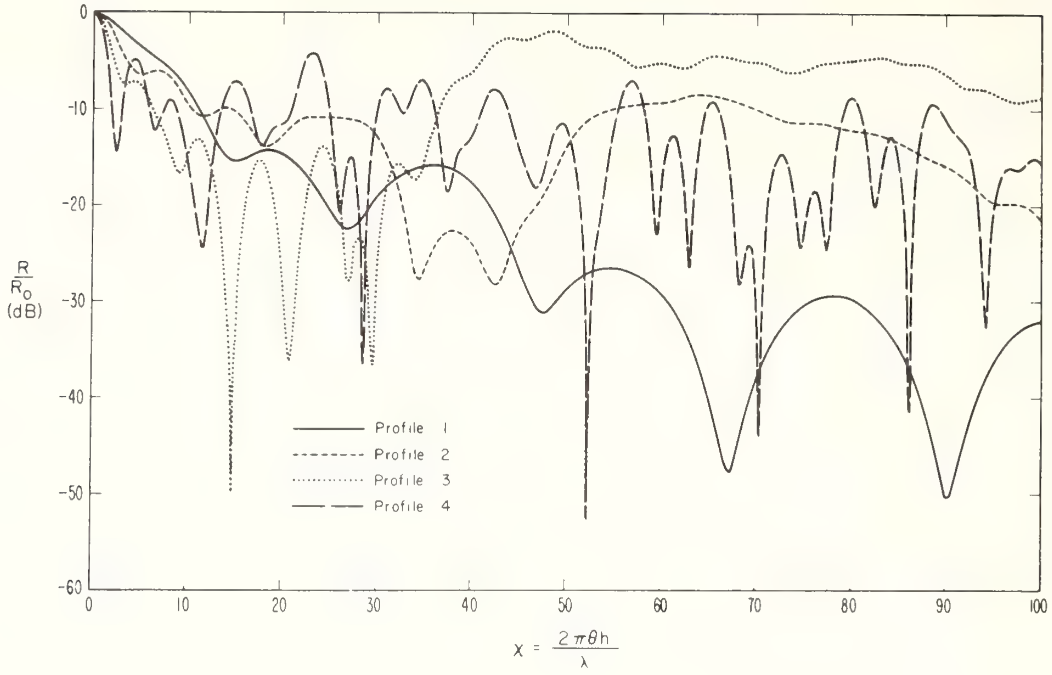

3. Relative power reflectivity for four observed layers.

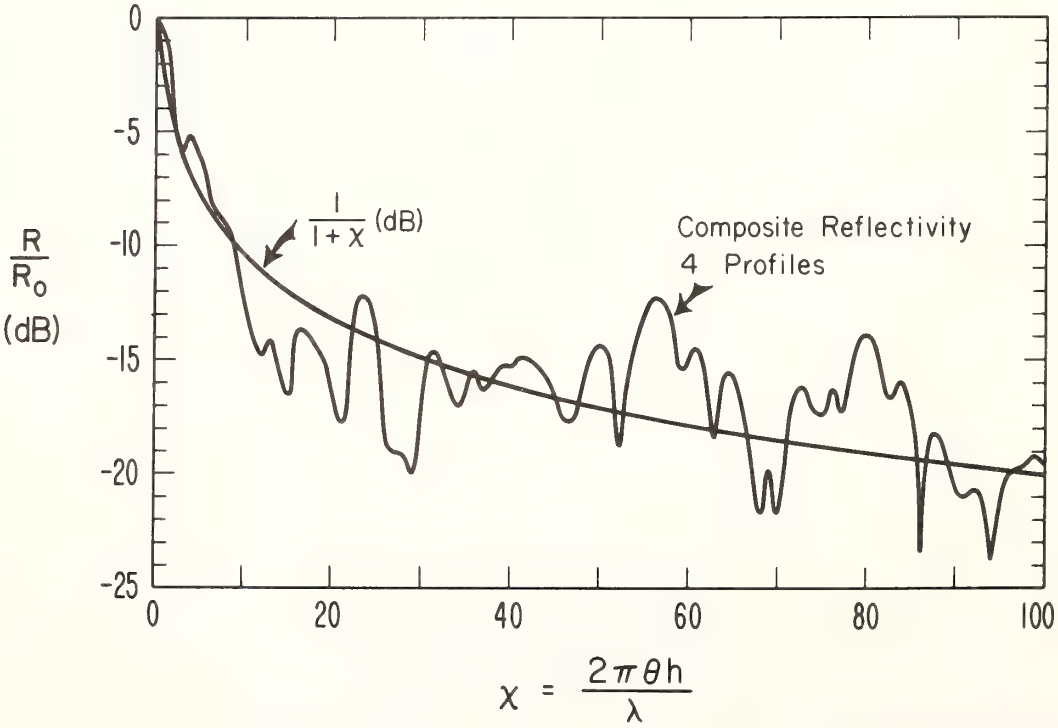

4. Composite power reflectivity curve - the geometric mean of four observed-layer reflectivity curves.

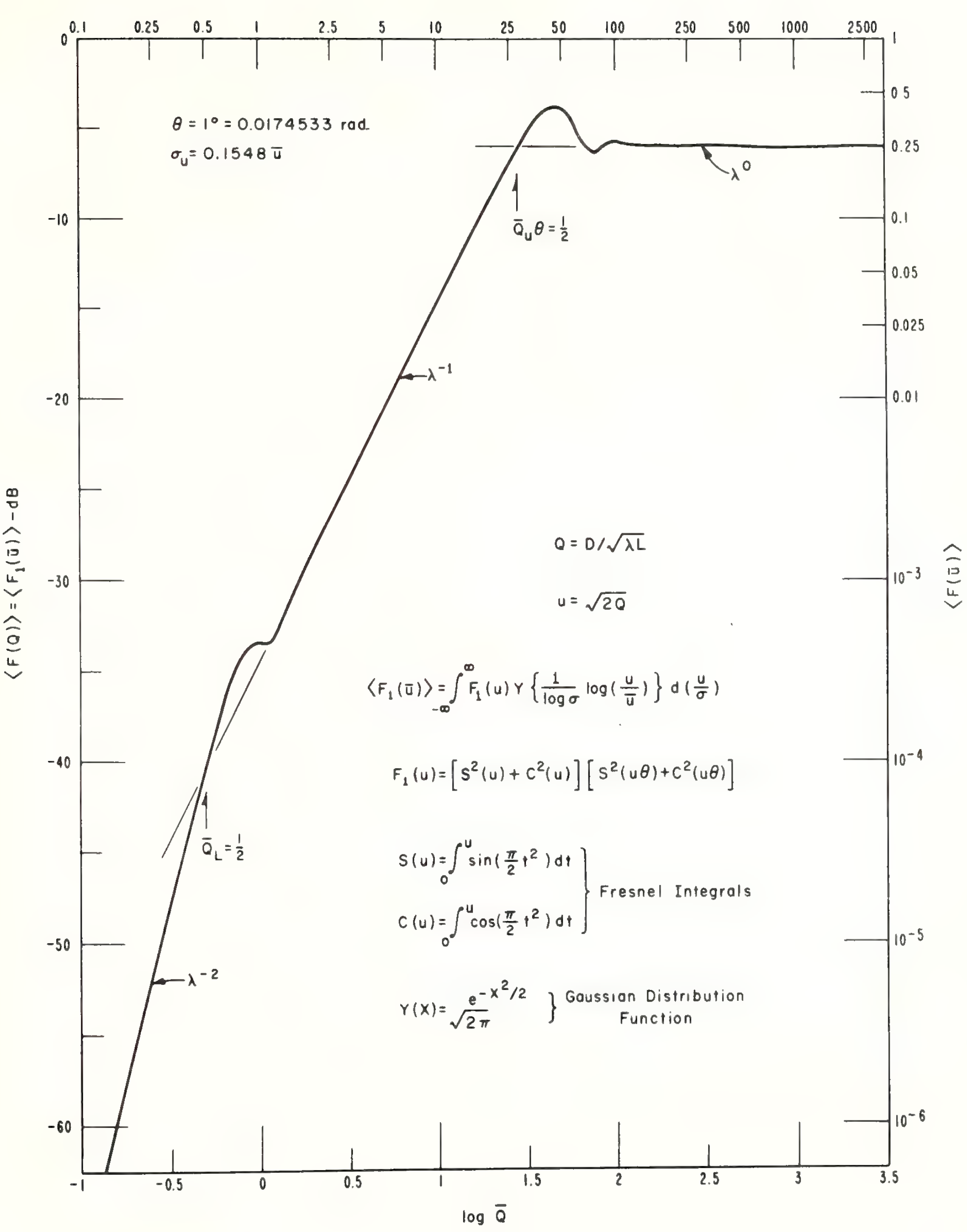

5. Fresnel integral function F(Q) for layer reflections.

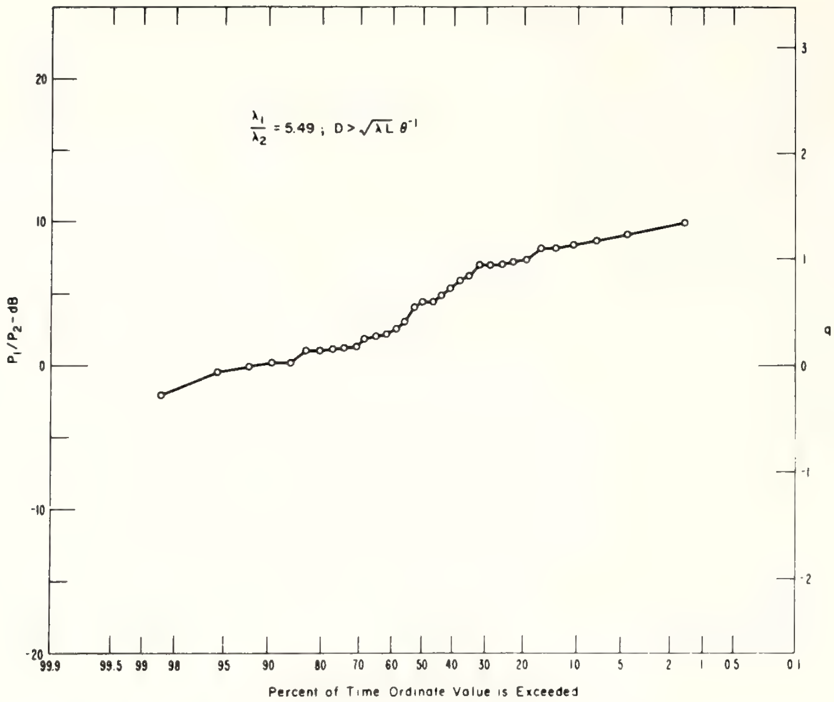

6. Simulated distribution of tropospheric propagation wavelength dependence for a scaled-antenna two-frequency experiment.

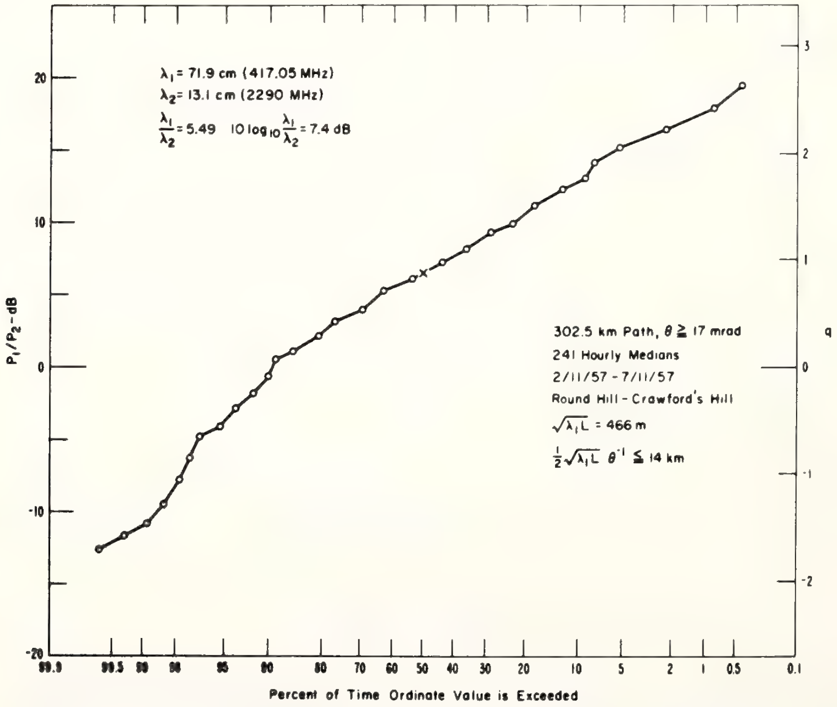

7. **Distribution of wavelength dependence for a scaled two-frequency tropospheric propagation path in the United States.**

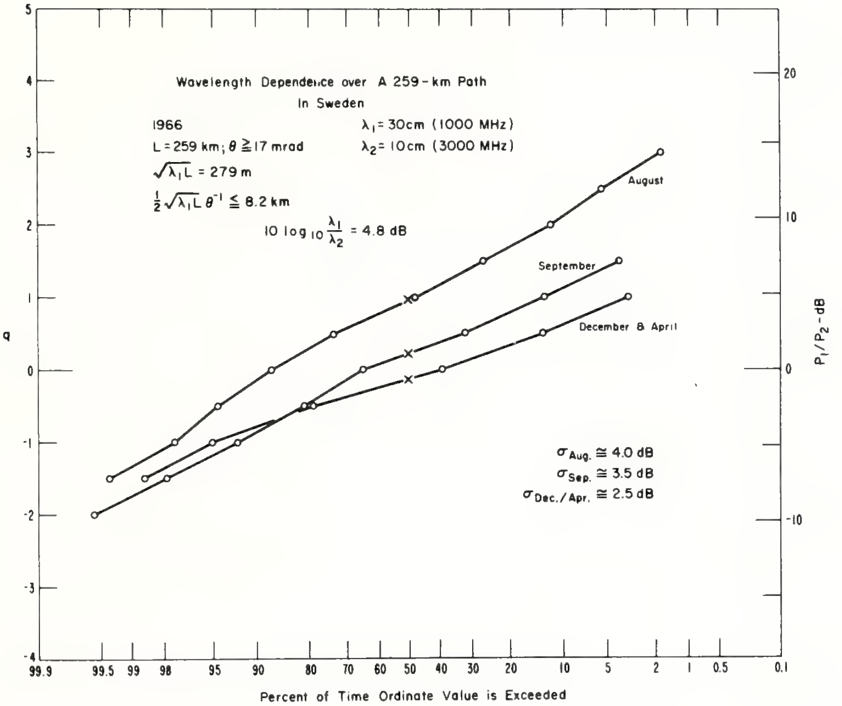

8. Distribution of wavelength dependence by seasons for a two-frequency tropospheric propagation path in Sweden

10

Reprinted from Radio Science 5, No. 11, 1293-1299, 1970.

Radio reflectivity of tropospheric layers

G. D. Thayer

ESSA Research Laboratories, Boulder, Colorado 80302

(Received February 9, 1970; revised May 25, 1970.)

Radio reflection coefficients for tropospheric elevated layers are examined as functions of the ratio of layer thickness to the effective radio wavelength and the refractive index structure of the layers. The layer reflectivity is shown to be nearly independent of the refractive index structure for small values of the thickness-wavelength ratio. Results for some layers observed with refractometers show that the reflectivities for large thickness-wavelength ratios are generally larger than those given by the simple linear or constant-gradient layer model.

INTRODUCTION

Partial reflections of electromagnetic waves are produced when the refractive index changes appreciably over a distance that is not large compared with a wavelength. Relatively thin layers containing abnormally large refractive index gradients are common in the troposphere and are known to be important as a trans-horizon propagation mechanism [cf. *Eklund and Wickerts,* 1968; *Hall,* 1968].

The reflection coefficients for tropospheric layers have been derived for various analytic models of the refractive index by several authors [*du Castel et al.,* 1960; *Wait and Jackson,* 1964]; their results show that the reflectivity depends critically on the refractive index model chosen for layers that are thick compared with the effective radio wavelength. For example, at typical grazing incidence and a layer-thickness/wavelength ratio of 150, the power reflection coefficients for the constant-gradient model and a typical 'smooth' function model differ by 40 to 50 db. This implies that the actual form of the refractive index structure in tropospheric layers will be important in determining their effectiveness as a propagation mechanism.

In this paper we calculate the theoretical reflection coefficients for some actual tropospheric layers derived from airborne refractometer data and show that the linear, constant-gradient model yields coefficients that are generally lower than the average of those obtained from these data.

BACKGROUND

The theoretical reflection coefficient for a tropospheric layer can be derived from solutions of the wave equation by considering the layer to be a planar transition zone between two infinite half-spaces of real refractive index n_0 and $n_0 + \Delta n_0$. A plane wave, of wave number $k = 2\pi/\lambda$, crossing the layer at an angle of incidence I produces both a refracted and a reflected wave. The reflection coefficient is found as the ratio of the magnitude of the **E** or **H** vector in the reflected wave to the magnitude of the corresponding vector in the incident wave. The simplest solution, one that is well suited to partially reflecting tropospheric layers, is the WKB series [*Wait,* 1962], in which the coefficient for single reflections is given approximately by

$$r \cong \frac{1}{2\cos^2 I} \int_{z_1}^{z_2} \frac{dn}{dz} \exp\{-i2k(\cos I)z\}\, dz \qquad (1)$$

Here the z axis is perpendicular to the layer, and z_1 and z_2 are the lower- and upper-layer boundaries, respectively. The reflection coefficient is evaluated at $z = z_1$, on the assumption that the incident wave is traveling in the positive z-direction. The theory of partial reflections in layered media, including the derivation of (1), has been thoroughly treated by several authors [*Brekhovskikh,* 1960; *Wait,* 1962].

In (1), multiple (internal) reflections are neglected. As the first-order reflected wave is generated in the downward direction it gives rise to a secondary reflected wave that travels upward through the layer, and that has no direct effect on the downward reflection coefficient. In turn, a third-order reflected wave traveling in the downward direction is generated by partial reflection of the second-order wave. It is this third-order wave (and all odd-order waves) that may affect the reflection coefficient. The

Copyright © 1970 by the American Geophysical Union.

third-order reflection coefficient can be arrived at through a triple integration involving three integrals each of which is similar to (1).

Criteria for neglecting higher-order reflections are difficult to define. Owing to the triple integration process, the third-order reflection coefficient will tend to have an order of magnitude close to $|r|^3$ for smooth dn/dz functions. Thus, for monotonic dn/dz it is generally sufficient that $|r|$ as given by (1) be small (say $|r| < 10^{-1}$), and multiple reflections can be neglected. For oscillatory or erratic dn/dz the situation is more complicated; it is usually sufficient that

$$\frac{1}{2\cos^2 I}\int_{z_1'}^{z_2'} \frac{dn}{dz} \exp\{-i2k(\cos I)z\}\, dz < |r| < 10^{-1} \tag{2}$$

for any $z_1 < z_1' < z_2' < z_2$ such that $z_2' - z_1' < z_2 - z_1$. This means that the reflection coefficient for any part of the layer taken alone should be smaller than that for the whole layer.

Reflectivity functions as given by (1) can be normalized by defining an effective layer thickness [*du Castel et al.,* 1960]

$$\chi = kh \cos I = kh \sin \theta \cong \frac{2\pi h\theta}{\lambda} \tag{3}$$

where h is the layer thickness $z_2 - z_1$, and θ is the elevation angle of the incident wave front. Since primarily small θ are of interest, the sine may be taken as being equal to the angle. We now define a normalized height variable

$$y \equiv z/h \cong k\theta z/\chi \tag{4}$$

and a gradient function [*Wait and Jackson,* 1964]

$$g(y) \equiv (\Delta n_0)^{-1}\frac{dn}{dy} = (\Delta n_0)^{-1}\frac{\chi}{k\theta}\frac{dn}{dz} \tag{5}$$

If we substitute these expressions into (1) we obtain

$$r \cong \frac{\Delta n_0}{2\theta^2}\int_0^1 g(y) e^{-i2\chi y}\, dy \tag{6}$$

where the limits correspond to $z_1 = 0$ and $z_2 = h$ in (1); we can set z_1 arbitrarily with no loss in generality. (Footnote: This is true for power reflection coefficients; it is not true if we must consider the phase of the reflected wave.) This expression shows that the reflection coefficient is the product of the Fresnel coefficient r_0 and the complex Fourier transform (with argument 2χ) of the normalized gradient function $g(y)$, if we assume $g(y) \equiv 0$ for $y < 0$ and $y > 1$.

The extension to continuous gradient functions is obvious; the limits in (1) and (6) become $-\infty$ and $+\infty$. However, the concept of the layer thickness h becomes somewhat ambiguous. Thus, in addition to the normalization

$$\int_{-\infty}^{\infty} g(y)\, dy = 1 \tag{7}$$

used by *Wait and Jackson* [1964], we require some further adjustment over the nominal layer thickness $y = 0$ to 1 if $z_1 \equiv 0$, such as

$$\int_0^1 g(ay)\, dy = P \qquad 0 < P < 1 \tag{8}$$

The choice of the value for P is arbitrary; the value chosen will have the effect of defining the layer thickness as that z interval over which $100P\%$ of the total change in the refractive index occurs, leaving the first and last $[100(1 - P)/2]\%$ of Δn_0 outside the layer. Experimentation shows that results are not very sensitive to the exact value of P that is chosen; values between 0.8 and 0.95 yield very similar results. (For determining the reflectivity of analytic profile models in this study we choose $P = 0.9$, since this corresponds to the 90% level used in many related applications.)

Figure 1 shows results for the same gradient functions used by *Wait and Jackson* [1964], but with layer-thickness normalization as described above with $P = 0.9$. The hyperbolic layers are defined by

$$g_m(y) = K_m \operatorname{sech}^m(ay) \tag{9}$$

and the Gaussian layer is defined by

$$g(y) = K \exp\{-a^2y^2\} \tag{10}$$

in all these, K is determined by (7) and a is determined by (8). The values of a for $P = 0.9$ are $2.326\cdots$ for the Gaussian layer and $5.084\cdots$, $2.944\cdots$, and $2.227\cdots$ for the hyperbolic layers for $m = 1$, 2, and 3, respectively. Also shown in Figure 1 is $|r/r_0|$ for the linear model

$$\begin{aligned} g(y) &= 1 \qquad 0 \leqq y \leqq 1 \\ g(y) &= 0 \qquad y < 0 \qquad y > 1 \end{aligned} \tag{11}$$

for which the relative reflectivity is given by

$$r/r_0 = (\sin \chi)/\chi \tag{12}$$

The layer-thickness normalization used here has reduced the dispersion in $|r/r_0|^2$ for the four-layer

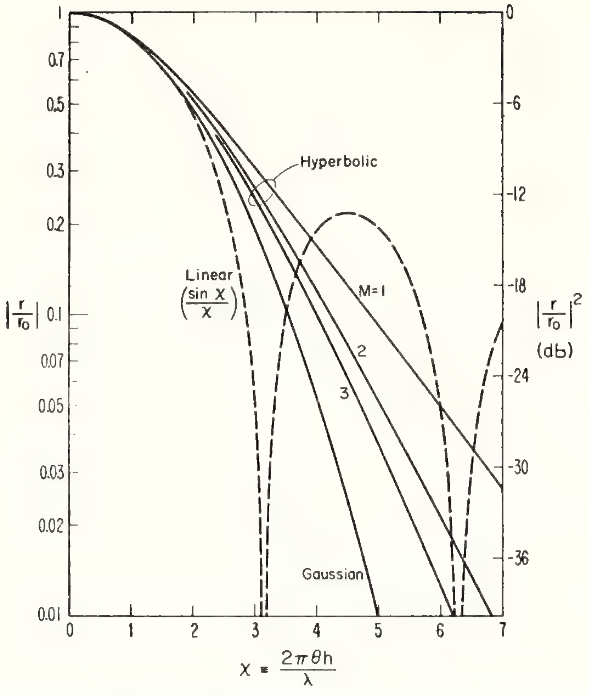

Fig. 1. Relative reflectivity for five normalized-layer refractivity profiles.

models when χ is small; for $\chi = 2$, *Wait and Jackson* [1964] found a maximum difference of 14 db between $|r/r_0|^2$ for the various layer models, whereas in Figure 1 we have a maximum difference of only 1 db. (Footnote: Wait and Jackson defined χ for the layer half-thickness. Hence there $\chi = 1$ corresponds to our $\chi = 2$; they did not treat the linear model.) Thus, with the modification indicated by (8), the results for the models treated by Wait and Jackson now agree with the conclusions of earlier investigators; that is, if the thickness of a layer is less than one-third of the effective radio wavelength, the reflectivity is independent of the form of the n profile. However, Figure 1 shows that even with layer-thickness normalization there are significant differences in the reflectivities of the various layer models for moderate values of χ.

The simple linear model (11) and (12) deserves further consideration; it is the simplest approximation to the form of actual tropospheric layers as they have been observed with conventional meteorological instrumentation such as the radiosonde. This model has been criticized in the past because there are discontinuities in the derivative of n (or in $g(y)$) at the layer boundaries. The general criticism against the model is that the large value of the reflection coefficient for large χ (as compared with continous models such as those in Figure 1) is caused by the discontinuities in $g(y)$ and that such discontinuities do not occur in nature. The criticism is legitimate, but it does not invalidate the use of the model, because any change in the n profile occurring over a distance that is small compared with the effective wavelength will have almost the same effect as a discontinuity. Indeed, *Brekhovskikh* [1960, p. 229] states that 'Using our results it can easily be shown that smoothing the discontinuity of dn/dz over an interval Δz which is small compared with the effective wavelength in the z direction, equal to [λ cosec θ], has no effect on the values of the reflection coefficient.'

We can easily demonstrate this effect by approaching the linear model (11) as the limit of a series of continuous models. If we define

$$g_N(y) = K_N/(1 + y^{2N}) \qquad (13)$$

where K_N is the normalization coefficient determined by condition (7), the linear model is represented by $g_\infty(y)$, which is defined by

$$g_\infty(y) = \lim_{N\to\infty} K_N/(1 + y^{2N}) \qquad (14)$$

The layer is considered to extend from $y = -1$ to $y = +1$; therefore, the definition of χ must be adjusted accordingly. The layer models $g_N(y)$ are continuous in all their derivatives everywhere along the axis of reals for all finite values of N.

Figure 2 shows the magnitude of the reflection coefficient for $N = 4$ and $N = 8$, and we see that the values are rapidly approaching the sin χ/χ curve of the linear model as N is increased. This is an important result, since we will next use the linear model as a basis for a numerical integration technique to obtain the reflection coefficients for some complicated tropospheric layer models.

REFLECTION COEFFICIENTS FOR SOME OBSERVED TROPOSPHERIC LAYERS

Shown in Figures 3 to 6 are four detailed examples of actual tropospheric layers obtained from airborne refractometers on flights through the Atlantic trade wind inversion [after *Ament*, 1959]. These profiles are displayed in the form of segmented linear approximations to the normalized height and gradient functions of the observed layers, with 100 equal segments used through the layer thickness. The resulting gradient function $g(y)$ is also shown for the

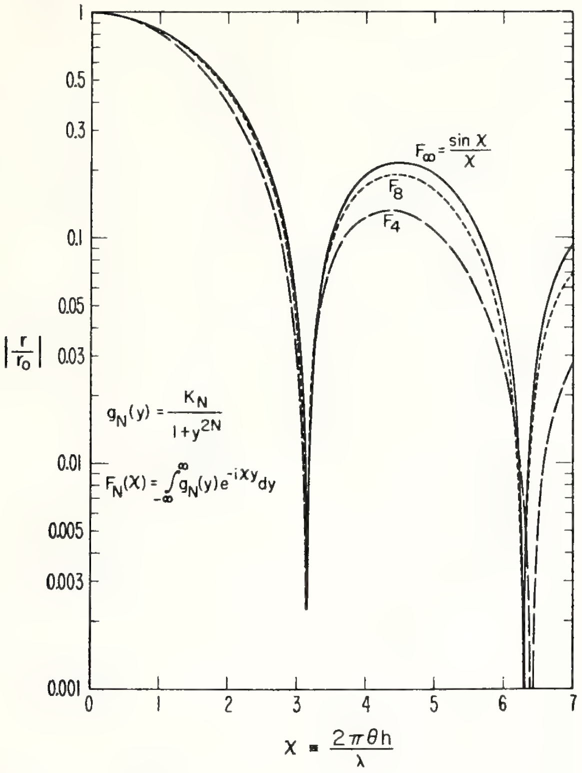

Fig. 2. Reflectivity curves for continuous approximations to the linear layer profile.

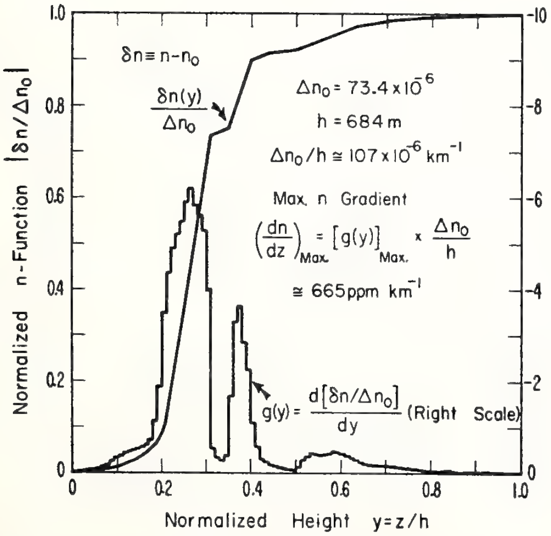

Fig. 3. Normalized refractivity and digitized refractivity gradient curves for observed layer profile 1.

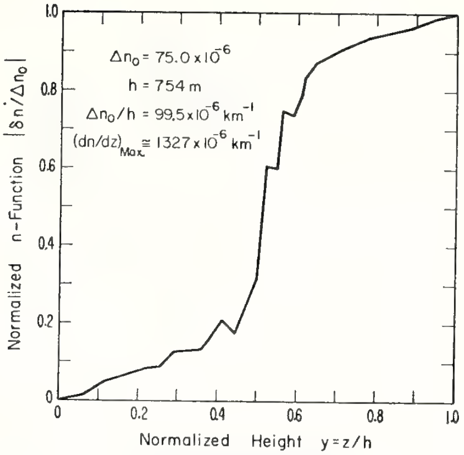

Fig. 4. Normalized refractivity curve for observed layer profile 2.

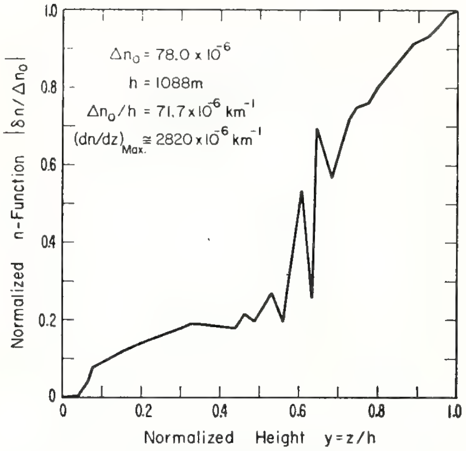

Fig. 5. Normalized refractivity curve for observed layer profile 3.

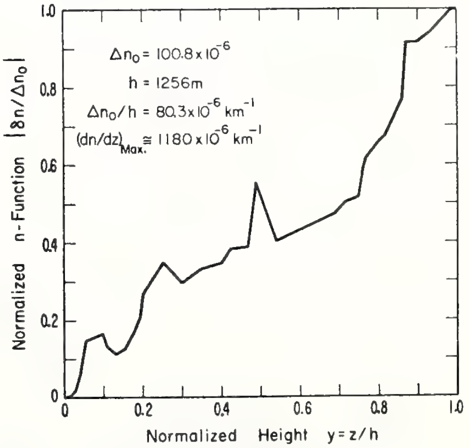

Fig. 6. Normalized refractivity curve for observed layer profile 4.

first layer (Figure 3). These four profiles are representative of some of the types of detailed fine structure found in actual tropospheric layers. The thickness of these observed layers ranged from 684 to 1256 meters, and, since n would be expected to decrease by roughly 25 to 50 parts per million over such intervals even in the absence of any unusual layer formation, we have adjusted the layer profiles by subtracting out the prevailing n gradient of about -40×10^{-6} km^{-1}. This procedure has very little effect on the regions of sharp n gradients that are responsible for most of the reflectivity of the layers; the maximum gradients of all four layers are seen to exceed 600×100^{-6} km^{-1}.

We wish to find the reflection coefficient functions $r(\chi)$ for these layers, for which we must evaluate

$$r(\chi) \cong r_0 \int_0^1 g(y) \exp\{i2\chi y\}\, dy \qquad (15)$$

where $r_0 \cong \Delta n_0/2\theta^2$. We rewrite (15) as

$$r(\chi) \cong r_0\left[\int_0^1 g(y) \cos(2\chi y)\, dy - i \int_0^1 g(y) \sin(2\chi y)\, dy\right] \qquad (16)$$

These observed layers have sharply defined end points; therefore, it is not necessary to use layer-thickness normalization such as was used previously for the analytic models.

Now we have each of the four profiles broken down into 100 sublayers, over each of which $g(y)$ is constant; if we reduce (16) into integrations over each of the 100 sublayers, the values of $g(y)$ can be taken outside the integrals, and the integration becomes elementary. If we denote the gradient function value over the kth sublayer as $g_k(y)$ and make the definitions

$$g_{101}(y) \equiv 0$$

$$\Delta g_k(y) \equiv g_k(y) - g_{k+1}(y) \qquad 1 \leqq k \leqq 100$$

then our solution may be written as

$$r(\chi) \cong \frac{r_0}{2\chi}\left[\sum_{k=1}^{100} \sin(2\chi y)\, \Delta g_k(y) + i\left\{\sum_{k=1}^{100} \cos(2\chi y)\, \Delta g_k(y) - g_1(y)\right\}\right] \qquad (17)$$

In (17) the value of y is understood to be appropriate to the upper end of the kth sublayer; that is,

$$y = k/100 \qquad 1 \leqq k \leqq 100 \qquad (18)$$

Interestingly, the changes in the gradient function, rather than in the absolute values, are significant in the integration; note, however, that, if a gradient change occurs over a small interval within which neither $\sin(2\chi y)$ nor $\cos(2\chi y)$ changes appreciably, further subdivision of the sublayers into smaller sublayers having smaller values of $\Delta g_k(y)$ will not alter the result. This agrees with the conclusions in the preceding section.

We can make a quantitative statement about the validity of our subdivided integration if we assign a separate value of χ to each sublayer. If the thickness of each sublayer is Δh and that of the main layer is h, then

$$\chi_\Delta \equiv \chi(\Delta h/h) \qquad (19)$$

From Figure 1 we may conclude that, if χ is less than approximately 2, the value of $r(\chi)$ will not be very different from the linear model for any functional dependence (except for a discontinuity in n), and our result should therefore be substantially accurate, provided that

$$\chi_\Delta < 2$$

or

$$\chi < h/\Delta h \qquad (20)$$

Since our $h/\Delta h$ is equal to 100 (the number of sublayers), we conclude that the result (17) should be valid for χ less than approximately 200.

We now require the power reflection coefficient function

$$R(\chi) = r(\chi) r^*(\chi) \qquad (21)$$

where $r^*(\chi)$ is the complex conjugate of $r(\chi)$. Hence

$$R(\chi) \cong \frac{r_0^2}{4\chi^2}\left[\left(\sum_{k=1}^{100} \sin(2\chi y)\, \Delta g_k(y)\right)^2 + \left(\sum_{k=1}^{100} \cos(2\chi y)\, \Delta g_k(y) - g_1(y)\right)^2\right] \qquad (22)$$

is the desired result.

Figure 7 gives the relative power reflectivity functions $R(\chi)/r_0^2$ for the four profiles shown in Figures 3 to 6. We note wide variations among the four functions; in particular, the function for profile 3 returns to a value only about 2 db below the value appropriate to a sharp discontinuity for a χ value of about 48 to 49 db. The actual thickness of layer 3 was 1088 meters; therefore, if we assume a graz-

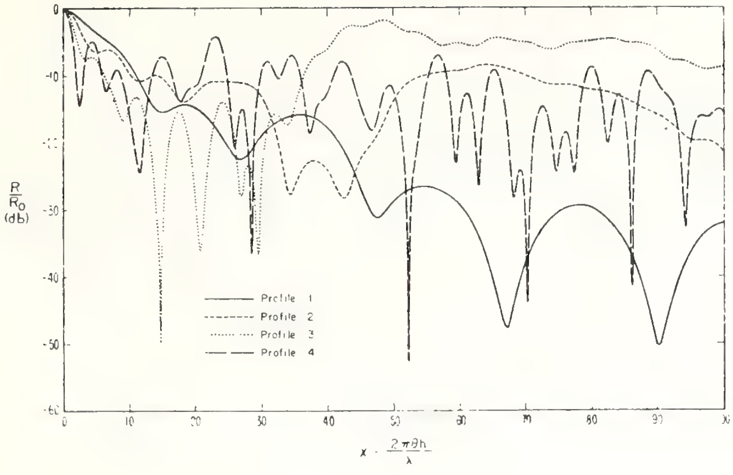

Fig. 7. Relative power reflectivity for four observed-layer refractivity profiles.

ing angle of about 15 mrad, the radio frequency that would have a χ value of 48.5 db for the layer is 142 MHz ($\lambda \cong 2.1$ meters).

Under actual conditions of propagation, the finite beamwidths of transmitting and receiving antennas would have the effect of smoothing out layer reflectivities over a Fresnel zone, and thus random horizontal irregularities that are certainly present in real layer structures would lead to a somewhat more well behaved relative reflectivity curve than any of those in Figure 7. We can estimate the typical effects of this smoothing by taking the geometric mean (the mean of the logarithms) of the four reflectivity curves in Figure 7; Figure 8 gives the results of the calculation. We see that the smoothed curve shows even higher reflectivity than the one given by the commonly assumed linear layer model.

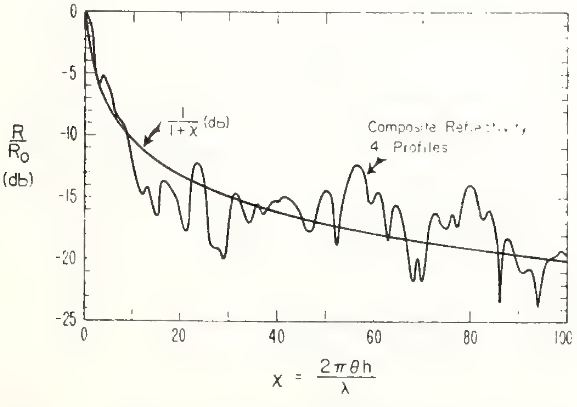

Fig. 8. Composite-layer power reflectivity curve (the geometric mean of four observed-layer reflectivity curves).

The composite curve agrees well with the function $(1 + \chi)^{-1}$, which is essentially the square root of the R/R_0 dependence for a linear layer model $(\sin \chi/\chi)^2$. Thus, the linear model (which has long been regarded as yielding overly optimistic estimates of tropospheric layer reflectivity) is apparently a rather conservative estimator of actual layer reflectivities.

However, we can conclude that the linear model is a reasonable order-of-magnitude estimator of the minimum reflectivity of real tropospheric layers.

CONCLUSIONS

We have demonstrated two significant points with respect to partial reflections from elevated tropospheric layers:

1. Power reflectivities calculated for tropospheric layers with known fine-scale gradient detail show generally greater values than those calculated from the simple linear layer model; in individual cases the reflectivities may differ by roughly -10 to $+30$ db from those for the linear model for large values of χ.

2. If the ratio of layer thickness to effective radio wavelength is moderately small (i.e., if the value of χ is between 0.5 and 2) the reflection coefficient, although reduced by 0.5 to 6 db from the Fresnel value appropriate to a discontinuity in $n(z)$, is to a good approximation independent of the form of $n(z)$. The reflectivity for a linear profile is the same as for a smooth analytic profile in this range of χ; this result allows the use of a segmented linear representation for obtaining accurate reflectivity values for detailed layer refractive index profiles.

The over-all conclusion we can draw is that the linear layer model is a useful tool for estimating minimal values of the reflectivity of tropospheric layers, although the most likely values appear to be given by the function $(1 + \chi)^{-1}$.

REFERENCES

Ament, W. S. (1959), Airborne radiometeorological research, *Proc. IRE, 47*(5), 756–761.

Brekhovskikh, L. M. (1960), *Waves in Layered Media,* 561 pp., Academic, London.

duCastel, F., P. Misme, and J. Voge (1960), Sur le rôle des phénomènes de réflexion dans la propagation lointaine des ondes ultracourtes, in *Electromagnetic Wave Propagation,* 670–683, Academic, London.

Eklund, F., and S. Wickerts (1968), Wavelength dependence of microwave propagation far beyond the radio horizon, *Radio Sci., 3*(11), 1066–1074.

Hall, M. P. M. (1968), Further evidence of VHF propagation by successive reflections from an elevated layer in the troposphere, *Proc. IEEE, 115*(11), 1595–1596.

Wait, J. R. (1962), *Electromagnetic Waves in Stratified Media,* 372 pp., Pergamon, London.

Wait, J. R., and C. M. Jackson (1964), Influence of the refractive index profile in VHF reflection from a tropospheric layer, *IEEE Trans. Antennas Propagation, 12*(4), 512–513.

Reprinted from Telecommunications Research Report,
OT/ITSRR 4, 1970.

AN EXPERIMENTAL STUDY OF THE ATMOSPHERIC CONDITIONS CONDUCIVE TO HIGH RADIO FIELDS

H. T. Dougherty, R. E. McGavin, and R. W. Krinks

The results are presented for a 13-month experimental investigation of anomalous propagation on two overland transhorizon paths at 185.75 MHz. The anomalous signals, 15 to 42 dB above the long-term median and persisting 1 to 6 hours, are described and their possible modes of propagation are reviewed. Surface search radar was found to be a most promising method for monitoring the surface refractivity conditions conducive to high fields. The extrapolation of the experimental results to other regions is discussed and recommendations for further study are included.

Key words: Troposcatter propagation, radar monitoring of meteorological conditions.

Reprinted from Transactions of the IEEE, Antennas and Propagation, AP-18, No. 2, 264-274, 1970.

The Theory of Microwave Line-of-Sight Propagation Through a Turbulent Atmosphere

STEVEN F. CLIFFORD AND JOHN W. STROHBEHN, MEMBER, IEEE

Abstract—**In this paper the covariance and spectra for amplitude and phase fluctuations for a microwave signal propagated over a line-of-sight path through a turbulent medium are calculated. It is shown that the results derived under the assumption that the wavelength is much smaller than the inner scale of turbulence l_0 are also valid when the wavelength is equal to or greater than l_0.**

Manuscript received September 2, 1969. This research was supported in part by the Atmospheric Sciences Section, National Science Foundation, under NSF Grant GA-1465.

S. F. Clifford was with the Radiophysics Laboratory, Thayer School of Engineering, Dartmouth College, Hanover, N. H. He is now with the Wave Propagation Laboratory, ESSA, Boulder, Colo. 80302.

J. W. Strohbehn is with the Radiophysics Laboratory, Thayer School of Engineering, Dartmouth College, Hanover, N. H. 03755.

I. INTRODUCTION

THIS paper is concerned with the amplitude and phase fluctuations of an electromagnetic wave as it propagates through a medium with random fluctuations in its refractive index. The major problem in which we are interested is line-of-sight propagation of microwave and millimeter waves through the troposphere, though the results are applicable to similar problems in other areas, e.g., acoustic propagation in the atmosphere [1]. The major theoretical effort in line-of-sight propagation through the lower atmosphere has been for optical wavelengths [2]–[4], although Barrows [5] and Lee and Harp [6] have considered the microwave problem. At optical wavelengths the means, variances, and covariance functions for the amplitude and phase fluctuations have been calculated by making the assumption that the wavelength is small compared with the smallest refractive index fluctuations. In this paper the above restriction has been removed. A more general result is derived which is valid independent of the relative size of the wavelength compared with the smallest refractive index inhomogeneity. It is shown that the more general results given here reduce to the optical results when the correct approximations are made. More importantly, for most practical propagation paths of interest in the millimeter and microwave region, the theoretical results for amplitude and phase fluctuations also reduce to the formulas derived earlier for optical wavelengths. Recently (while this paper was in review), Lee and Harp [6] published the same conclusion using an entirely different approach based on an ingenious scheme of decomposing the medium into phase screens. In our paper the results are derived directly from the wave equation, and the form of the results is presented directly in terms of the amplitude and phase spectra.

It is assumed that the fluctuations in the refractive index may be described in terms of a covariance function $C_n(r)$ and its associated spectrum $\Phi_n(\kappa)$:

$$n(r) = n_0 + n_1(r),$$

$$n_0 \equiv \langle n(r) \rangle$$

$$C_n(r) = \langle n_1(r_1) n_1(r_1 + r) \rangle$$

$$\Phi_n(\kappa) = 1/(2\pi)^3 \iiint_{-\infty}^{\infty} C_n(r) \exp(i\kappa \cdot r)\, dr.$$

The atmospheric model that is used for $\Phi_n(\kappa)$ is discussed elsewhere [3], [4], [7]. In general, it will have the form shown in Fig. 1. At wavenumbers greater than κ_m, where $\kappa_m = 2\pi/l_0$, there is no significant energy in the refractive index spectrum. The scale l_0, often called the inner scale of turbulence, is on the order of 1 to 10 mm. For the optical case the assumption that $\lambda \ll l_0$ is easily met. However, when dealing with microwave and millimeter wave propagation, the assumption that $\lambda \ll l_0$ is no longer true, and the question arises whether the results derived under the assumption $\lambda \ll l_0$ are still valid. In this paper we propose to show that the results derived for the optical case remain valid at wavelengths as long as microwave.

One other problem arises with respect to the form of the refractive index spectrum. For small wavenumbers the form of the spectrum is not known (nor predictable). It is known that at a wavenumber on the order of $\kappa = 2\pi/L_0$ the form of the spectrum will change. The value of L_0 varies depending on the height above the ground and other local conditions. At optical wavelengths the amplitude spectrum is only dependent on wavenumbers such that $\kappa \gg 2\pi/L_0$, but this is no longer true for the microwave case. The significance of this problem will be discussed later.

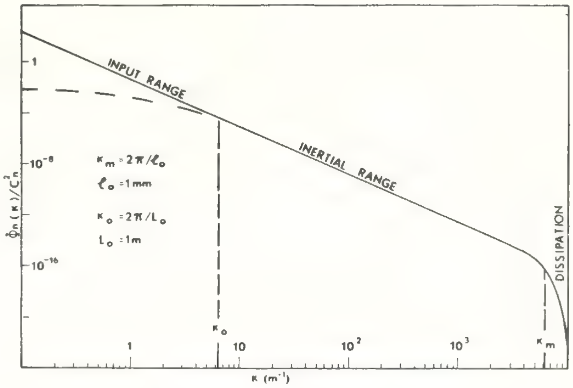

Fig. 1. A typical spectrum of the refractive index fluctuations. $\kappa_m \approx 2\pi/l_0$ corresponds to the inner scale of turbulence, and $\kappa_0 \approx 2\pi/L_0$ corresponds to the outer scale of turbulence.

In comparing the present results with the optical case, two other points should be mentioned. First, at optical frequencies the fluctuations in amplitude and phase are often very large, and there has been a great amount of discussion about the validity of the perturbation expansion approach to that problem (this approach is commonly called Rytov's method). In the longer wavelength case, the fluctuations are much smaller and the criticisms of the perturbation expansion method are no longer germane. Second, it is assumed in formulating the problem that the atmosphere is adequately described by the turbulence spectrum $\Phi_n(\kappa)$. Such a description omits the possibility of relatively large continuous layers which may affect the propagation. In the optical case, even if such layers exist, their large thickness relative to a wavelength precludes them from producing any large effect. At microwave wavelengths, the thickness of a layer may be on the order of a wavelength, and such a layer could cause significant fluctuations. We have ignored this situation, though we realize for some applications it may be the dominant mechanism inducing perturbations.

When examining the original derivations for the optical case, the assumption that $\lambda \ll l_0$ is applied in two ways. First, it is used to argue that the scalar wave equation instead of the vector wave equation may be used. It shall be shown that this approximation may still be made. Second, when $\lambda \ll l_0$, the effective scattering cone, i.e., that volume of the atmosphere from which there is significant energy scattered to the receiver, has a vertex angle on the order of λ/l_0. The assumption that this scattering cone is small is used to make several approximations, which result in simplifying the Green's function or, equivalently, the differential equation that is solved. Here we solve the more complex differential equation and show it leads to the same results.

The results derived here assume an incident plane wave; however, physical arguments imply that the basic conclusion is extendable to the spherical- or beam-wave case also. That is, the results derived on the basis that $\lambda \ll l_0$ are equally valid when $\lambda \gtrsim l_0$.

II. DERIVATION OF THE AMPLITUDE AND PHASE SPECTRA

The wave equation for the electric vector in a random medium with no free charges, zero conductivity, zero magnetic moment, and assuming exp $(i\omega t)$ time variations, is

$$\nabla^2 \boldsymbol{E} + k^2 n^2 \boldsymbol{E} + 2\nabla(\boldsymbol{E} \cdot \nabla \ln n) = 0 \qquad (1)$$

where n is the index of refraction and k is the wavenumber. It is assumed that n may be written as

$$n = \langle n \rangle + n_1 \cong 1 + n_1, \quad |n_1| \ll 1.$$

In the above the $\langle\ \rangle$ brackets indicate an ensemble average, and n_1 is the small fluctuation of the index of refraction about its mean value, here assumed to be 1. If the mean value is not 1, k may be replaced by $k\langle n \rangle$ to obtain valid results.

To solve (1), the method of small perturbations may be applied, where a solution is sought in the form

$$\boldsymbol{E} = \sum_i \boldsymbol{E}_i$$

the ith term being considered of order $n_1{}^i$. Substituting the above into (1), using

$$\nabla \ln n = \nabla \ln (1 + n_1) = \nabla\{\sum_{i=1}^{\infty} [-(-n_1)^i/i]\}$$

$$= \nabla n_1 \sum_{j=0}^{\infty} (-n_1)^j$$

we obtain

$$\nabla^2(\sum_{i=0}^{\infty} \boldsymbol{E}_i) + k^2(1 + n_1)^2 \sum_{i=0}^{\infty} \boldsymbol{E}_i$$

$$+ 2\nabla[\sum_{i=0}^{\infty} \boldsymbol{E}_i \cdot \nabla n_1 \sum_{j=0}^{\infty} (-n_1)^j] = 0.$$

Equating terms of the same order to zero yields

zero order:

$$\nabla^2 \boldsymbol{E}_0 + k^2 \boldsymbol{E}_0 = 0 \qquad (2)$$

first order:

$$\nabla^2 \boldsymbol{E}_1 + k^2 \boldsymbol{E}_1 + 2k^2 n_1 \boldsymbol{E}_0 + 2\nabla(\boldsymbol{E}_0 \cdot \nabla n_1) = 0 \qquad (3)$$

mth order:

$$\nabla^2 \boldsymbol{E}_m + k^2 \boldsymbol{E}_m + 2k^2 n_1 \boldsymbol{E}_{m-1} + k^2 n_1{}^2 \boldsymbol{E}_{m-2}$$

$$+ 2\nabla[\sum_{i=0}^{m-1} (-n_1)^i \boldsymbol{E}_{m-i-1} \cdot \nabla n_1] = 0. \qquad (4)$$

At this point it is helpful to discuss the geometry of the problem. We assume there is a wave with initial polarization in the z direction, traveling in the x direction, and incident on a boundary at $x = 0$. The volume $x > 0$ contains the random medium, and the wave enters from free space. The wave source is considered infinitely remote such that the incident wave may be taken as plane. (The spherical-wave case will be discussed below.)

Since we are primarily interested in the effects of the atmosphere on the incident polarized signal, we may write scalar equations for each of the higher order perturbations, where now E_i will represent E_{iz}. The other component equations represent the depolarized components of the original signal and have been discussed elsewhere in the optical case [8], [9]; and it has been shown in [1] that the effect of the depolarized terms remains small even in the microwave range. Under the above assumptions, (2)–(4) reduce to

zero order:

$$\nabla^2 E_0 + k^2 E_0 = 0 \qquad (5)$$

first order:

$$\nabla^2 E_1 + k^2 E_1 + 2k^2 n_1 E_0 + 2E_0(\partial^2 n_1/\partial z^2) = 0 \qquad (6)$$

mth order:

$$\nabla^2 E_m + k^2 E_m + 2k^2 n_1 E_{m-1} + k^2 n_1{}^2 E_{m-2}$$

$$+ 2(\partial/\partial z)[\sum_{i=0}^{m-1} (-n_1)^i E_{m-i-1}(\partial n_1/\partial z)] = 0. \qquad (7)$$

The solution to this set of equations may be obtained by a Fourier–Stieltjes integral representation of the locally homogeneous and isotropic random fields n_1 and E_1 [10]. To that end let

$$n_1(x,y,z) = n_1(x,0,0)$$

$$+ \iint_{-\infty}^{\infty} \{1 - \exp[i(\kappa_2 y + \kappa_3 z)]\}\, d\gamma(\kappa_2,\kappa_3,x)$$

$$E_1(x,y,z) = E_1(x,0,0)$$

$$+ \iint_{-\infty}^{\infty} \{1 - \exp[i(\kappa_2 y + \kappa_3 z)]\}\, d\epsilon_1(\kappa_2,\kappa_3,x).$$

Assuming $E_0 = e^{ikx}$, and following the procedure shown in Tatarski [3, ch. 7, sec. 3], (6) is transformed into a one-dimensional equation for the first-order variations in the field

$$d^2 d\epsilon_1/dx^2 + (k^2 - \kappa_2{}^2 - \kappa_3{}^2)\, d\epsilon_1$$

$$= -2(k^2 - \kappa_3{}^2)e^{ikx}\, d\gamma(\kappa_2,\kappa_3,x). \qquad (8)$$

The relationship between $d\epsilon_1(\kappa_2,\kappa_3,x)$ and Tatarski's $d\phi(\kappa_2,\kappa_3,x)$, where $d\phi$ is the random amplitude associated with the variations of the logarithm of the field, is given by (see Appendix I)

$$d\epsilon_1(\kappa_2,\kappa_3,x) = e^{ikx}\, d\phi(\kappa_2,\kappa_3,x).$$

The solution of (8) may be obtained directly by either Green's function techniques or by variation of parameters. However, there are two regions in which the solution differs substantially in form. These are for $(\kappa_2{}^2 + \kappa_3{}^2)^{1/2} > k$ and $(\kappa_2{}^2 + \kappa_3{}^2)^{1/2} < k$. It is therefore more convenient to generalize the equation slightly to the form

$$d^2 d\epsilon_1/dx^2 + \nu^2\, d\epsilon_1 = -2(k^2 - \kappa_3{}^2)e^{ikx}\, d\gamma(\kappa_2,\kappa_3,x)$$

$$\nu = (k^2 - \kappa_2{}^2 - \kappa_3{}^2)^{1/2}$$

where ν may be real or imaginary. It also permits us to generalize later to the case when k is complex, in which case ν will also be complex.

Under the above conditions, the solution for outgoing waves, ignoring the effects of backscattering, is

$$d\phi(\kappa_2,\kappa_3,x) = i(k^2 - \kappa_3^2)/\nu \cdot \int_0^x dx' \exp\left[-i(k-\nu)(x-x')\right] d\gamma(\kappa_2,\kappa_3,x'). \tag{9}$$

The backscatter term is neglected since most antennas in the microwave and millimeter range discriminate against the backscattered signal. The backscattered signal is sufficiently weak so that double scattering can be ignored.

If we note that

$$\ln(E_1/E_0) = \chi(x,y,z) + iS_1(x,y,z)$$

where $\chi \equiv \ln(A/A_0)$ and $S_1 \equiv S - S_0$, and assume expansions similar to those above are valid for χ and S_1, namely,

$$\chi(x,y,z) = \chi(x,0,0) + \iint_{-\infty}^{\infty} \{1 - \exp\left[i(\kappa_2 y + \kappa_3 z)\right]\}\, da(\kappa_2,\kappa_3,x)$$

$$S_1(x,y,z) = S_1(x,0,0) + \iint_{-\infty}^{\infty} \{1 - \exp\left[i(\kappa_2 y + \kappa_3 z)\right]\}\, d\sigma(\kappa_2,\kappa_3,x)$$

then we may obtain da and $d\sigma$ from [3, ch. 7, sec. 3]:

$$da(\kappa_2,\kappa_3,x) = (1/2)\left[d\phi(\kappa_2,\kappa_3,x) + d\phi^*(-\kappa_2,-\kappa_3,x)\right] \tag{10}$$

$$d\sigma(\kappa_2,\kappa_3,x) = (1/2i)\left[d\phi(\kappa_2,\kappa_3,x) - d\phi^*(-\kappa_2,-\kappa_3,x)\right]. \tag{11}$$

Performing the above operation on $d\phi$, noting that $d\gamma^*(-\kappa_2,-\kappa_3,x) = d\gamma(\kappa_2,\kappa_3,x)$, we obtain

$$da(\kappa_2,\kappa_3,x) = \frac{i(k^2-\kappa_3^2)}{2}\int_0^x dx' \left\{\frac{\exp\left[-i(k-\nu)(x-x')\right]}{\nu} - \frac{\exp\left[i(k-\nu^*)(x-x')\right]}{\nu^*}\right\} d\gamma(\kappa_2,\kappa_3,x') \tag{12}$$

$$d\sigma(\kappa_2,\kappa_3,x) = \frac{(k^2-k_3^2)}{2}\int_0^x dx' \left\{\frac{\exp\left[-i(k-\nu)(x-x')\right]}{\nu} + \frac{\exp\left[i(k-\nu^*)(x-x')\right]}{\nu^*}\right\} d\gamma(\kappa_2,\kappa_3,x') \tag{13}$$

which are the random amplitudes corresponding to the logarithm of the amplitude and the phase of the wave, respectively. Again the following relations from Tatarski are used:

$$\begin{aligned}
&\langle da(\kappa_2,\kappa_3,x)\, da^*(\kappa_2',\kappa_3',x)\rangle \\
&\quad = \delta(\kappa_2-\kappa_2')\delta(\kappa_3-\kappa_3')F_A(\kappa_2,\kappa_3,0)\, d\kappa_2 d\kappa_2' d\kappa_3 d\kappa_3' \\
&\langle d\sigma(\kappa_2,\kappa_3,x)\, d\sigma^*(\kappa_2',\kappa_3',x)\rangle \\
&\quad = \delta(\kappa_2-\kappa_2')\delta(\kappa_3-\kappa_3')F_s(\kappa_2,\kappa_3,0)\, d\kappa_2 d\kappa_2' d\kappa_3 d\kappa_3' \\
&\langle d\gamma(\kappa_2,\kappa_3,x')\, d\gamma^*(\kappa_2',\kappa_3',x'')\rangle \\
&\quad = \delta(\kappa_2-\kappa_2')\delta(\kappa_3-\kappa_3')F_n(\kappa_2,\kappa_3,x'-x'')\, d\kappa_2 d\kappa_2' d\kappa_3 d\kappa_3'.
\end{aligned} \tag{14}$$

We then find the two-dimensional spectra for the log-amplitude and phase, $F_A(\boldsymbol{\kappa},0)$ and $F_s(\boldsymbol{\kappa},0)$, respectively. The approximations involved in finding these spectra and a detailed derivation are contained in Appendix II. Letting $\kappa = (\kappa_2^2 + \kappa_3^2)^{1/2}$,

$$\left.\begin{matrix} F_A(\boldsymbol{\kappa},0) \\ F_s(\boldsymbol{\kappa},0) \end{matrix}\right\} = \frac{(k^2-\kappa_3^2)^2 L}{(k^2-\kappa^2)}\left[1 \mp \frac{\sin\{2[k-(k^2-\kappa^2)^{1/2}]L\}}{2[k-(k^2-\kappa^2)^{1/2}]L}\right] \cdot \int_0^L d\zeta F_n(\boldsymbol{\kappa},\zeta)\cos\{[k-(k^2-\kappa^2)^{1/2}]\zeta\}, \quad \kappa < k \tag{15}$$

$$F_A(\boldsymbol{\kappa},0) \cong F_s(\boldsymbol{\kappa},0) \le 2\frac{\exp\left[-(\kappa^2-k^2)^{1/2}L\right](k^2-\kappa_3^2)^2}{(\kappa^2-k^2)^{3/2}} \cdot \int_0^L d\zeta F_n(\boldsymbol{\kappa},\zeta)\cos k\zeta \sinh\left[(\kappa^2-k^2)^{1/2}(L-\zeta)\right], \quad \kappa > k. \tag{16}$$

Equations (15) and (16) are the two-dimensional spectra in the plane $x = L$ for the log-amplitude and phase fluctuations as a function of the two-dimensional permittivity spectrum $F_n(\kappa,\zeta)$. It is more instructive at this time to express these same results in terms of the three-dimensional spectrum $\Phi_n(\boldsymbol{\kappa})$. The relation between them is a simple Fourier transform [3, ch. 7, sec. 3]:

$$\Phi_n(\kappa_1,\kappa_2,\kappa_3) = \frac{1}{2\pi}\int_{-\infty}^{\infty} F_n(\kappa_2,\kappa_3,x)\cos(\kappa_1 x)\, dx. \tag{17}$$

Since $F_n(\boldsymbol{\kappa},\zeta)$ falls off rapidly to zero, we may extend the region of integration in (15) to infinity without appreciably affecting the result. Using (17), the fact that $F_n(\boldsymbol{\kappa},x)$ is even in x, and comparing with the integral involved in (15), we have

$$\left.\begin{matrix} F_A(\boldsymbol{\kappa},0) \\ F_s(\boldsymbol{\kappa},0) \end{matrix}\right\} = \frac{\pi(k^2-\kappa_3^2)^2 L}{(k^2-\kappa^2)}\left(1 \mp \frac{\sin\{2[k-(k^2-\kappa^2)^{1/2}]L\}}{2[k-(k^2-\kappa^2)^{1/2}]L}\right) \cdot \Phi_n[k-(k^2-\kappa^2)^{1/2},\kappa_2,\kappa_3], \quad \kappa < k. \tag{18}$$

In (16) it is considerably more difficult to relate the integral to $\Phi_n(\kappa)$, but, as will be seen below, we will require only upper bound information about this part of the spectrum. Therefore, noting that in the important region of integration (see Appendix II) $\zeta \ll L$, then we have

$$\sinh\left[(\kappa^2 - k^2)^{1/2}(L - \zeta)\right] \le \sinh\left[(\kappa^2 - k^2)^{1/2}L\right].$$

Substituting this into (16) and extending the region of integration as above, we have for a rough upper bound

$$F_A(\boldsymbol{\kappa},0) = F_s(\boldsymbol{\kappa},0) \le \frac{\pi(k^2 - \kappa_3^2)^2}{(\kappa^2 - k^2)^{3/2}}\,\Phi_n(k,\boldsymbol{\kappa}) \cdot\left\{1 - \exp\left[-2(\kappa^2 - k^2)^{1/2}L\right]\right\}, \quad \kappa > k. \tag{19}$$

The difficulty with the results (18) and (19) is readily apparent. The spectra increase without bound as $\kappa \to k$ when $\kappa_3 \neq k$. The physical interpretation of this infinity and possible methods for its removal are discussed in Section V.

III. The Optical Spectrum as a Limiting Case

In obtaining the results (18) and (19), no approximations were made that restrict the range of wavenumbers in which these equations are valid. Therefore, under the conditions of very short wavelengths (large wavenumbers) compared with the smallest inhomogeneity size, we should obtain the optical spectra due to Tatarski [3, eqs. (7.50) and (7.51)]. Assuming $(\kappa_2^2 + \kappa_3^2)^{1/2} = \kappa \ll k$, and expanding the square root in (15) as $(k^2 - \kappa^2)^{1/2} = k(1 - \kappa^2/2k^2)$, we obtain in the limiting case

$$\left.\begin{array}{l} F_A(\kappa,0) \\ \\ F_s(\kappa,0) \end{array}\right\} = \pi k^2 L\left(1 \mp \frac{\sin(\kappa^2 L/k)}{(\kappa^2 L/k)}\right)\Phi_n(\kappa)$$

which is the well-known optical result for the phase and amplitude spectra. The range $k > \kappa$ does not enter here since the inner scale of turbulence precludes consideration of the extremely small inhomogeneities in this range.

The objective of the remainder of this paper will be to show that the new results (15) and (16) differ in a negligible fashion from the optical spectrum found as a limiting case, and hence one may extend this optical result to wavenumbers found in the microwave range with negligible error.

IV. The Effects of Absorption on the Peak at $\kappa = k$

As was pointed out before, the results (15) and (16) increase without bound as κ approaches k. An explanation of this effect may be obtained by considering that for scatterers large with respect to a wavelength ($\kappa \ll k$), the signal energy is essentially forward scattered and the receiver receives most of the scattered energy from a small cone. As the inhomogeneities become smaller and approach $2\pi/k$ in size, the scattering becomes more isotropic and hence the received energy comes from a larger scattering volume. In the limit as κ approaches k the scattering volume becomes infinite and the small effects, spread over an infinite volume, contribute an infinite amount to the total scattered energy. It is possible that by retaining a sufficient number of higher order terms in the perturbation series, a convergent solution might be found. However, another approach to eliminate this peak is to limit the observable volume, either by introducing a realistic receiver into the problem, or by including the effects of atmospheric absorption to minimize the influence of scatterers as they become more and more remote from the receiver. This paper will take the latter approach in order to remove equipment considerations.

Proceeding with this in mind, we return to (32) in Appendix II which describes the exact result for the spectra assuming a complex wavenumber. Consequently, we assume a new incident wave given by $E_0' = A_0 e^{ikx - \alpha x}$, where α is the absorption coefficient, and we assume $\alpha \ll k$. With this change $\nu \cong (k^2 - \kappa^2 + 2ik\alpha)^{1/2}$, where $\kappa = (\kappa_2^2 + \kappa_3^2)^{1/2}$, and (32) becomes

$$\begin{aligned} \left.\begin{array}{l} F_A(\boldsymbol{\kappa},0) \\ \\ F_s(\boldsymbol{\kappa},0) \end{array}\right\} = {} & (k^2 - \kappa_3^2)^2\,\frac{e^{-bL}}{a^2 + b^2}\left\{\frac{1}{b}\int_0^L d\zeta F_n(\kappa,\zeta)\right. \\ & \cdot\cos\left[(k - a)\zeta\right]\sinh\left[b(L - \zeta)\right] \\ & \mp \frac{1}{\left[(k - a)^2 + 4b^2\right]^{1/2}} \\ & \cdot\Bigg[\cos\left[(k - a)L + \Phi_1 + \Phi_2\right] \\ & \cdot\int_0^L d\zeta F_n(\kappa,\zeta)\sin\left[(k - a)(L - \zeta)\right] \\ & \cdot\cosh\left[b(L - \zeta)\right] + \sin\left[(k - a)L + \phi_1 + \phi_2\right] \\ & \cdot\int_0^L d\zeta F_n(\kappa,\zeta)\cos\left[(k - a)(L - \zeta)\right] \\ & \left.\cdot\sinh\left[b(L - \zeta)\right]\Bigg]\right\} \end{aligned}$$

and

$$\begin{aligned} \nu &= a + ib \\ a &= (1/\sqrt{2})\left\{\left[(k^2 - \kappa^2)^2 + 4k^2\alpha^2\right]^{1/2} + (k^2 - \kappa^2)\right\}^{1/2} \\ b &= (1/\sqrt{2})\left\{\left[(k^2 - \kappa^2)^2 + 4k^2\alpha^2\right]^{1/2} - (k^2 - \kappa^2)\right\}^{1/2} \\ \phi_1 &= \tan^{-1}\left[2ab/(a^2 - b^2)\right] \\ \phi_2 &= \tan^{-1}\left[2b/(k - a)\right]. \end{aligned}$$

Rigorously, in order to derive the above equation we should return to the original wave equation and start over with a complex refractive index **n**, where the imaginary part represents absorption. However, it may be shown that the above equation is correct provided $\alpha \ll k$. It is obvious from the above expressions that α will significantly alter the results (15) and (16) only when κ is very close to k. In the region where κ is close to k, it can be shown that the term after the $\mp$ sign is at least $(\alpha/k)^{1/2}$ smaller than the first term. A somewhat simpler argument is to note that $F_A(\boldsymbol{\kappa},0)$ and $F_s(\boldsymbol{\kappa},0)$ are always greater than zero; therefore the magnitude of the term after the $\mp$ sign is never larger than the first term. Therefore, at worst, the expression for $F_A(\kappa)$ and $F_s(\kappa)$ is twice as large as the term we shall keep. Since we intend to show that the peak at $\kappa = k$ produced by the first term is always inconsequential when computing phase or amplitude covariance functions, dropping the last term will not effect our conclusion.

Therefore, for κ near k,

$$F_A(\boldsymbol{\kappa},0) \cong F_s(\boldsymbol{\kappa},0) \leq \frac{(k^2 - \kappa_3^2)^2 e^{-bL}}{(a^2 + b^2)b} \int_0^L d\zeta F_n(\kappa,\zeta) \cdot \cos[(k - a)\zeta] \sinh[b(L - \zeta)]. \tag{20}$$

Since $a,b \ll k$ throughout this region and $\sinh[b(L - \zeta)]$ is less than $\sinh(bL)$, we obtain

$$F_A(\boldsymbol{\kappa},0) = F_s(\boldsymbol{\kappa},0) \leq \frac{(k^2 - \kappa_3^2)^2 e^{-bL} \sinh(bL)}{(a^2 + b^2)b} \cdot \int_0^L d\zeta F_n(\kappa,\zeta) \cos(k\zeta).$$

Letting the upper limit on the integration go to infinity and replacing the integral by (17), its definition in terms of $\Phi_n(\kappa)$,

$$F_A(\boldsymbol{\kappa},0) = F_s(\boldsymbol{\kappa},0) \leq \frac{(k^2 - \kappa_3^2)^2 \pi (1 - e^{-2bL})}{2b(a^2 + b^2)} \Phi_n(\kappa,k). \tag{21}$$

By inspection, one can see that (21) approaches the upper bound of the spectra for $\kappa > k$ given in (19) as κ increases above k, and reduces to the limit of the spectra (18) as κ decreases below k; hence it is a reasonable representation for the spectra in this transition region.

Expressions (18), (19), and (21) represent the spectra throughout the range of κ. These may be further simplified by considering the effects of the polarization term κ_3^2 for different segments of the κ axis. As was shown in the last section, the amplitude spectrum in (18) contains a peak at $\kappa = (1.3k/L)^{1/2}$ which, for reasonable pathlengths, is very small compared with k. Therefore, in this region we may disregard the polarization effects and drop the κ_3^2 term. As κ now increases toward k, expression (18) is governed entirely by the falloff of the permittivity spectrum Φ_n and is very small until $\kappa \approx k$. At this point (21) shows that the κ_3^2 term in this region can only reduce the effect of the peak, since the gain function $1/[2b(a^2 + b^2)]$ falls off very rapidly for very small changes in κ (see next section). Hence, the only region in which the κ_3^2 term need be considered is for $\kappa \gg k$. To summarize these results, we finally have for the amplitude and phase spectra

$$\left.\begin{matrix} F_A(\boldsymbol{\kappa},0) \\ F_s(\boldsymbol{\kappa},0) \end{matrix}\right\} = \frac{\pi k^4 L}{(k^2 - \kappa^2)} \left[1 \mp \frac{\sin\{2[k - (k^2 - \kappa^2)^{1/2}]L\}}{2[k - (k^2 - \kappa^2)^{1/2}]L}\right] \cdot \Phi_n[k - (k^2 - \kappa^2)^{1/2}, \kappa_2, \kappa_3], \quad \kappa < k \tag{22}$$

$$\boldsymbol{\kappa} = (k_2, k_3)$$

$$F_A(\kappa,0) = F_s(\kappa,0) \leq \frac{\pi k^4 (1 - e^{-2bL})}{2b(a^2 + b^2)} \Phi_n(k,\kappa), \quad \kappa \simeq k \tag{23}$$

$$a = (1/\sqrt{2})\{[(k^2 - \kappa^2)^2 + 4k^2\alpha^2]^{1/2} + k^2 - \kappa^2\}^{1/2}$$

$$b = (1/\sqrt{2})\{[(k^2 - \kappa^2)^2 + 4k^2\alpha^2]^{1/2} - k^2 + \kappa^2\}^{1/2}$$

$$F_A(\kappa,0) = F_s(\kappa,0) \leq \frac{\pi(k^2 - \kappa_3^2)^2}{(\kappa^2 - k^2)^{3/2}} \Phi_n(k,\kappa) \cdot \{1 - \exp[-2(\kappa^2 - k^2)^{1/2}L]\}, \quad \kappa > k. \tag{24}$$

Expression (23) falls off rapidly to zero beyond $\kappa = k$. It appears that along the κ_3 axis (24) may become large and cause some difficulty for $\kappa_3 \gg k$. However, if we replace κ_3 by κ, which increases the upper bound, we find for $\kappa \gg k$

$$F_A(\kappa,0) = F_s(\kappa,0) \leq \pi\kappa\Phi_n(k,\kappa).$$

As long as $\Phi_n(k,\kappa)$ decreases rapidly enough there is no problem. Since $\Phi_n(\kappa)$ decreases at a rate of $\kappa^{-11/3}$ until close to κ_m, and then falls off even faster, this term will remain negligible.

V. The Effects of the New Peak on the Covariance Functions

In Section III it was shown that the amplitude and phase spectra, $F_A(\kappa)$ and $F_s(\kappa)$, respectively, reduce to Tatarski's optical results for $\kappa \ll k$, and for the rest of the range where $\kappa < k$, the spectra fall off very rapidly—essentially controlled by the rapid decay of the permittivity spectrum. In the region $\kappa \approx k$ a new peak appears in the spectra which is not integrable as it originally appeared in Section II. In Section IV, the infinite peak at $\kappa = k$ has been made finite by assuming some absorption in the medium. For $\kappa > k$ the spectra fall off very rapidly to zero. Fig. 2 illustrates these results for a path length of 1 km and a wavenumber $k = 210$ m^{-1} ($\lambda = 3$ cm), where it has been assumed that $\Phi_n(\kappa)$ is given by

$$\Phi_n(\kappa) = 0.033 C_n^2 \kappa^{-11/3}.$$

The second peak is not shown to scale and only the amplitude spectrum is shown.

One problem that arises in the microwave range that does not appear in the optical range is in the form of the refractive index spectrum. At high wavenumbers, for $\kappa > k_0$, the refractive index spectrum is normally assumed to be in the inertial subrange. In this range it is isotropic and follows a $\kappa^{-11/3}$ law. The wavenumber κ_0 is given by $\kappa_0 = 2\pi/L_0$, where L_0 is the outer scale of turbulence. The value of L_0 may typically vary from 1 meter close to the ground to possibly 100 meters or greater above the boundary layer of the atmosphere (approximately the first 50 meters of the atmosphere). For $\kappa \lesssim \kappa_0$ the form of the refractive index spectrum cannot be predicted, but is normally not isotropic and does not follow a $\kappa^{-11/3}$ law. It is apparent from Fig. 2, where a $\kappa^{-11/3}$ form and isotropy were assumed, that the first peak occurs at

$$\kappa = (1.3k/L)^{1/2} = 0.6 \text{ m}^{-1}.$$

However, at least near the ground, (see Fig. 1) this form of the spectrum is no longer valid for $\kappa < 1$ m^{-1}. Since in

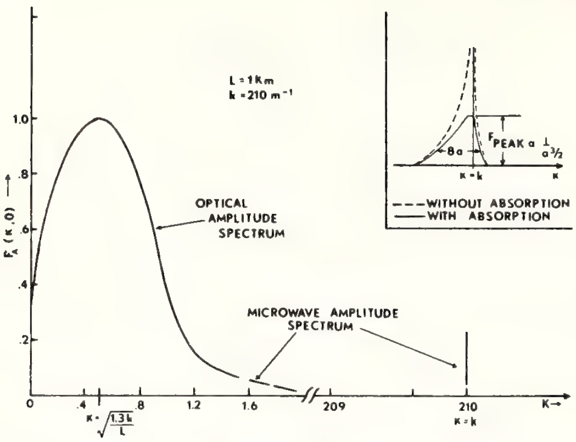

Fig. 2. Two-dimensional spectrum for the amplitude fluctuations of a line-of-sight microwave signal. The insert is an expansion of the narrow peak at $\kappa = k$.

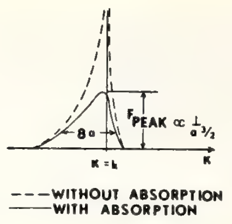

ABSORPTION TABLE * $E = E_0 e^{-\alpha x}$

f	γ (dB/m)	α (m^{-1})	k (m^{-1})
100 MHZ	2×10^{-7}	2.3×10^{-8}	2.1
3 GHZ	6×10^{-6}	6.9×10^{-7}	63
10 GHZ	1×10^{-5}	1.15×10^{-6}	2.1×10^{2}
50 GHZ	5×10^{-4}	5.75×10^{-5}	1.05×10^{3}

γ = ABSORPTION IN $\frac{dB}{m}$; $\alpha = 0.115\gamma$

Fig. 3. The peak at $\kappa = k$ with typical values for α at different frequencies. * Data from Bean and Dutton [10].

this section we are primarily interested in comparing relative sizes of different terms we shall use the $\kappa^{-11/3}$ spectrum and assume isotropy. In applying our results to specific propagation problems, it may be necessary to use a more accurate expression for the form of the refractive index spectrum.

It seems apparent from Fig. 2 that the influence of the peak at $\kappa = k$ will be negligible. However, one must consider the effects of the second peak on the variances of the amplitude and phase fluctuations, σ_χ^2 and σ_s^2, respectively. We will make the assumption that if the second peak contributes a negligible amount to the variances, then we may ignore it in the calculation of the covariance functions also.

The covariance functions $B_A(\rho)$ and $B_s(\rho)$ are obtained from the expressions

$$B_A(\boldsymbol{\varrho}) = \iint_{-\infty}^{\infty} d\kappa_2\, d\kappa_3 \cos(\boldsymbol{\kappa}\cdot\boldsymbol{\varrho}) F_A(\boldsymbol{\kappa},0)$$

$$B_s(\boldsymbol{\varrho}) = \iint_{\infty}^{\infty} d\kappa_2\, d\kappa_3 \cos(\boldsymbol{\kappa}\cdot\boldsymbol{\varrho}) F_s(\boldsymbol{\kappa},0).$$

Throughout the important region of integration the spectra are given by (22) and (23). Since isotropy has been assumed, the angular integration may be performed explicitly; this yields

$$B_A(\rho) = 2\pi \int_0^\infty J_0(\kappa\rho) F_A(\kappa,0)\, \kappa\, d\kappa \tag{25}$$

$$B_s(\rho) = 2\pi \int_0^\infty J_0(\kappa\rho) F_s(\kappa,0)\, \kappa\, d\kappa \tag{26}$$

where $\kappa = (\kappa_2^2 + \kappa_3^2)^{1/2}$. The variances are given by $B_A(0)$ and $B_s(0)$ for amplitude and phase, respectively. We are trying to show that the new peak at $\kappa = k$ will have a negligible influence on the covariance functions of the amplitude and phase compared to the spectrum at wavenumbers much less than k. Since the phase spectrum for $\kappa \ll k$ is much larger than the amplitude spectrum, and recalling that the phase and amplitude spectra in the region near $\kappa = k$ are approximately equal, it suffices to prove our point for the amplitude spectra alone. The result follows immediately for phase.

In calculating the importance of the different regions of the wavenumber spectrum, note that $B_A(\rho)$ depends on $\kappa F_A(\kappa,0)$. The quantity $\kappa F_A(\kappa,0)$, has two peaks: the first at $\kappa = (1.3k/L)^{1/2}$, which is the classical peak calculated for the optical case, and the second at $\kappa = k$.

The maximum height of the peak at $\kappa = k$, obtained from (23), is given by

$$\kappa F_A(k) \leq \frac{\pi k^5 \Phi_n(\sqrt{2}k)}{4(k\alpha)^{3/2}}. \tag{27}$$

Note that the height of the peak depends on both k and α, where α is the absorption coefficient. In order to evaluate the effect of the new peak, the value of α must be known. In Fig. 3, α is calculated from data given in Bean and Dutton [10]. As is well known, α is a function of the wavenumber k. Using the values for the absorption coefficient obtained from the table and the form given earlier for $\Phi_n(\kappa)$, one may plot $\kappa F(\kappa,0)$ versus wavenumber for the two peaks under consideration. Fig. 4 illustrates this and shows that for small wavenumbers, the peak at $\kappa = k$ becomes significantly larger than the optical spectrum peak.

In Fig. 5 the ratio of the contribution to the variance due to the new peak to the variance due to the optical peak is plotted versus wavenumber. The optical variance is well known and may be obtained from the short wavelength approximation discussed in Section III. Using the previous form for the refractive index spectrum we obtain for the optical variance [3, eq. (7.94)]

$$\sigma_\chi{}^2{}_{\text{opt}} = 0.31 C_n{}^2 k^{7/6} L^{11/6}. \tag{28}$$

In calculating the contribution to the variance due to the new peak, we note that the peak is very narrow, and mainly controlled by the function

$$G(\kappa) = \frac{1}{b(a^2 + b^2)} = \frac{\sqrt{2}}{[\{[(k^2 - \kappa^2)^2 + 4k^2\alpha^2]^{1/2} - k^2 + \kappa^2\}^{1/2} \cdot [(k^2 - \kappa^2)^2 + 4k^2\alpha^2]^{1/2}]}$$

in (23). To calculate the upper bound on the contribution of the new peak, we will use the fact that $\Phi_n(\kappa)$ varies slowly compared to $G(\kappa)$. Therefore we may evaluate the integral I where

$$I = 2\pi \int_0^\infty \kappa F_A'(\kappa)\, d\kappa \cong \pi^2 k^4 \Phi_n(\sqrt{2}k) \int_0^\infty \kappa G(\kappa)\, d\kappa$$

and $F_A'(\kappa)$ is the spectrum in the region near $\kappa = k$. After some algebra,

$$I = \pi^2 \frac{k^4 \Phi_n(\sqrt{2}k)}{(k\alpha)^{1/2}\{[1 + k^2/4\alpha^2]^{1/2} - k/2\alpha\}^{1/2}}$$

$$\cong \pi^2 (k^4/\alpha) \Phi_n(\sqrt{2}k)$$

assuming $\alpha \ll k$.

The ratio of the contribution to the variance from the new peak to the variance as calculated from the optical formula is

$$I/\sigma_{x\,\mathrm{opt}}^2 \simeq 0.29(1/k^{5/6}L^{11/6}\alpha).$$

As shown in Fig. 5 for $L > 10$ km, the effect of the new peak is entirely negligible. At $L = 1$ km it is possible the contribution of the new peak to the variance could be equal to the optical variance at wavenumbers as low as 5 m^{-1}. However, at these very low wavenumbers for paths as short as 1 km, the amplitude fluctuations as calculated from (28) are negligible for reasonable values of C_n^2. For example, at $k = 10$ m^{-1}, $L = 10$ km, and using $C_n^2 = 4 \times 10^{-14}$ m$^{-2/3}$, we obtain a calculated optical variance of $\sigma_x^2 = 5 \times 10^{-6}$. Since this variance is probably not measurable, there is no region in which the effect of the new peak need be considered.

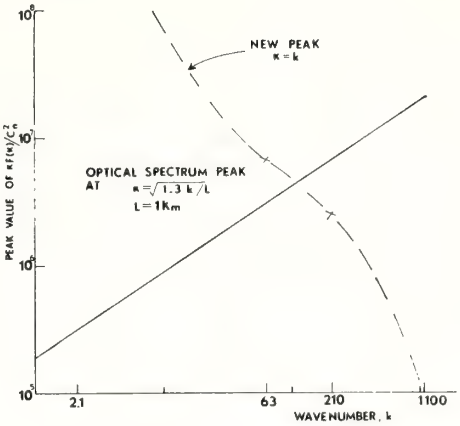

Fig. 4. The ratio of the peak of $\kappa F_A(\kappa)$ at $\kappa = k$ to the peak of the optical spectrum. The dashed curve is fitted to four points calculated from the data in Fig. 3.

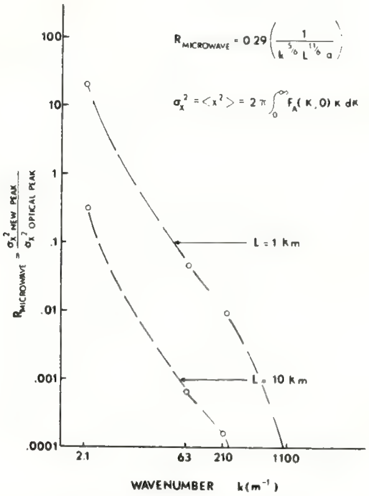

Fig. 5. The ratio of the contribution to the variance of the new peak of the microwave spectrum to the contribution from the peak calculated from optical formulas. The dashed curves are fitted to points calculated from the data in Fig. 3.

VI. Discussion

In the preceding analysis the restriction $\lambda \ll l_0$, normally used in deriving the spectra for the phase and amplitude fluctuations, has been removed. It has been shown that for almost all cases of practical interest in line-of-sight propagation at millimeter and microwave wavelengths, the results derived using the assumption that $\lambda \ll l_0$ are equally valid for $\lambda > l_0$. Formulas are presented which may be used in other situations to check when this approximation is valid. In those cases where the short wavelength formulas are not valid, the spectra for the long wavelength case are given.

Note that while the spectrum for $\kappa \ll k$ as given in (22) is strongly dependent on path length, the spectrum near $\kappa = k$ and the spectrum for $\kappa > k$ given in (23) and (24) are independent of path length. Physically, this result depends on the fact that for $\kappa \ll k$ the inhomogeneities, which are large compared to a wavelength, induce a scattered wave which propagates with little attenuation. Therefore, inhomogeneities over the entire path are important. When κ is close to or greater than k, the inhomogeneities produce evanescent waves which are rapidly attenuated as they propagate. Therefore, only inhomogeneities close to the receiver cause any appreciable contribution to the received signal. In this case, there is a local effect that does not depend on the total path length.

The results derived above were based on a plane wave incident on the random medium. However, the basic conclusion, that is, that the formulas derived on the assumption that $\lambda \ll l_0$ are equally valid for $\lambda > l_0$, should still apply to the cases when there is a spherical wave or finite antenna beam at the transmitter. Since, as we noted above, the contribution in the plane-wave case from the spectrum at $\kappa = k$ is a local effect only depending on the region near the receiver, the same type of effect must be true for spherical or beam waves. Therefore, the contribution must be approximately the same as computed for the plane-wave case, except multiplied by a factor that takes into account the attenuation of the free-space signal by the time it reaches the receiver. In spherical-wave propagation this is a factor of $1/L^2$, which will obviously attenuate the peak at $\kappa = k$ considerably more than in the plane-wave case. The optical variance $\sigma_x{}^2{}_{\text{opt}}$ for the spherical-wave case is down by a factor of 2.5 over the plane-wave case [3, eq. (9.43)]. Therefore, the ratio $I/\sigma_x{}^2{}_{\text{opt}}$, discussed in Section V for plane waves, will be even smaller for reasonable path lengths for spherical waves. A similar argument can be made for the case when there is an antenna with a finite beam at the transmitter.

Appendix I

Relation Between $d\epsilon_1(\boldsymbol{\kappa}, x)$ and $d\phi(\boldsymbol{\kappa}, x)$

Let $\Psi = \ln (E/E_0)$ where $E = E_0 + E_1 + E_2 + \cdots$. Substituting the first two terms of the perturbation series for E and expanding the logarithm to first order in E_1/E_0 yields

$$\Psi \cong \ln (1 + E_1/E_0) \approx E_1/E_0, \quad |E_2| \ll |E_1|. \tag{29}$$

Recalling the expansion for Ψ from Tatarski

$$\Psi = \Psi(x,0,0) + \iint [1 - \exp (i\boldsymbol{\kappa}\cdot\boldsymbol{\rho})]\, d\phi(\boldsymbol{\kappa},x) \tag{30}$$

and the expansion from Section II for E_1,

$$E_1 = E_1(x,0,0) + \iint [1 - \exp (i\boldsymbol{\kappa}\cdot\boldsymbol{\rho})]\, d\epsilon_1(\boldsymbol{\kappa},x). \tag{31}$$

By comparing (30) and (31) with the approximation (29), it is clear that $d\epsilon_1(\boldsymbol{\kappa},x) \cong E_0 d\phi(\boldsymbol{\kappa},x)$; and since E_0 is assumed to be e^{ikx} then

$$d\epsilon_1(\boldsymbol{\kappa},x) \cong e^{ikx} d\phi(\boldsymbol{\kappa},x).$$

The above illustrates that a first-order expansion in the logarithm of the field is approximately equal to a first-order expansion of the field itself.

Appendix II

Derivation of the Spectra $F_A(\boldsymbol{\kappa}, 0)$, $F_s(\boldsymbol{\kappa}, 0)$

A. Spectra for $\kappa < k$

Starting with (12) and (13),

$$\langle da(\kappa_2,\kappa_3,x)\, da^*(\kappa_2',\kappa_3',x) \rangle$$

$$= \frac{(k^2 - \kappa_3{}^2)(k^2 - \kappa_3{}'^2)}{4} \int_0^x dx' \int_0^x dx''$$

$$\cdot \left\{ \frac{\exp [-i(k - \nu_1)(x - x')]}{\nu_1} - \frac{\exp [i(k - \nu_1{}^*)(x - x')]}{\nu_1{}^*} \right\}$$

$$\cdot \left\{ \frac{\exp [i(k - \nu_2{}^*)(x - x'')]}{\nu_2{}^*} - \frac{\exp [-i(k - \nu_2)(x - x'')]}{\nu_2} \right\}$$

$$\cdot \langle d\gamma(\kappa_2,\kappa_3,x')\, d\gamma^*(\kappa_2',\kappa_3',x'') \rangle$$

$$\langle d\sigma(\kappa_2,\kappa_3,x)\, d\sigma^*(\kappa_2',\kappa_3',x) \rangle$$

$$= \frac{(k^2 - \kappa_3{}^2)(k^2 - \kappa_3{}'^2)}{4} \int_0^x dx' \int_0^x dx''$$

$$\cdot \left\{ \frac{\exp [-i(k - \nu_1)(x - x')]}{\nu_1} + \frac{\exp [i(k - \nu_1{}^*)(x - x')]}{\nu_1{}^*} \right\}$$

$$\cdot \left\{ \frac{\exp [i(k - \nu_2{}^*)(x - x'')]}{\nu_2{}^*} + \frac{\exp [-i(k - \nu_2)(x - x'')]}{\nu_2} \right\}$$

$$\cdot \langle d\gamma(\kappa_2,\kappa_3,x')\, d\gamma^*(\kappa_2',\kappa_3',x'') \rangle$$

where $\nu_1 = (k^2 - \kappa_2{}^2 - \kappa_3{}^2)^{1/2}$ and $\nu_2 = (k^2 - \kappa_2{}'^2 - \kappa_3{}'^2)^{1/2}$.

Noting the relation (14) given in the text, and performing the required integration, we have

$$\left. \begin{matrix} F_A(\kappa_2,\kappa_3,0) \\ \\ F_s(\kappa_2,\kappa_3,0) \end{matrix} \right\} = \frac{(k^2 - \kappa_3{}^2)^2}{4} \left\{ \frac{2 \exp [i(\nu - \nu^*)x]}{\nu\nu^*} \right.$$

$$\cdot \int_0^x dx' \int_0^x dx'' F_n(\boldsymbol{\kappa},x' - x'')$$

$$\cdot \exp [ik(x' - x'') - i(\nu x' - \nu^* x'')]$$

$$\mp \frac{\exp [-2i(k - \nu)x]}{\nu\nu} \int_0^x dx' \int_0^x dx''$$

$$\cdot F_n(\boldsymbol{\kappa},x' - x'') \exp [i(k - \nu)(x' + x'')]$$

$$\mp \frac{\exp [2i(k - \nu^*)x]}{\nu^*\nu^*} \int_0^x dx' \int_0^x dx''$$

$$\left. \cdot F_n(\kappa,x' - x'') \exp [-i(k - \nu^*)(x' + x'')] \right\}$$

where $\kappa = (\kappa_2{}^2 + \kappa_3{}^2)^{1/2}$ and the lower signs are the changes for the phase spectrum. The factor of 2 arises from the combining of two integrals which are equal due to the evenness of $F_n(\boldsymbol{\kappa},x' - x'')$ in $x' - x''$.

The above integrals may be simplified by a change of variables:

$$\zeta = x' - x''$$

$$\eta = \tfrac{1}{2}(x' + x'').$$

After making this substitution and replacing the variable x by the path length L, and again using the evenness of $F_n(\boldsymbol{\kappa},\zeta)$ in the variable ζ, we obtain

$$\left. \begin{matrix} F_A(\kappa_2,\kappa_3,0) \\ \\ F_s(\kappa_2,\kappa_3,0) \end{matrix} \right\} = \frac{(k^2 - \kappa_3{}^2)^2}{4} \left\{ \frac{4 \exp [i(\nu - \nu^*)L]}{\nu\nu^*} \right.$$

$$\cdot \int_0^L d\zeta F_n(\boldsymbol{\kappa},\zeta) \cos \left[\left(k - \frac{\nu + \nu^*}{2} \right) \zeta \right]$$

$$\cdot \int_{\zeta/2}^{L-\zeta/2} d\eta \exp [-i(\nu - \nu^*)\eta]$$

$$\begin{aligned}
&\mp \frac{2\exp[-2i(k-\nu)L]}{\nu\nu}\int_0^L d\zeta F_n(\kappa,\zeta)\\
&\cdot\int_{\zeta/2}^{L-\zeta/2} d\eta \exp[i2(k-\nu)\eta]\\
&\mp \frac{2\exp[2i(k-\nu^*)L]}{\nu^*\nu^*}\int_0^L d\zeta F_n(\kappa,\zeta)\\
&\left.\cdot\int_{\zeta/2}^{L-\zeta/2} d\eta \exp[-i2(k-\nu^*)\eta]\right\}.
\end{aligned}$$

The integration with respect to η may now be performed explicitly, yielding

$$\begin{aligned}
\left.\begin{matrix}F_A(\kappa_2,\kappa_3,0)\\ \\ F_s(\kappa_2,\kappa_3,0)\end{matrix}\right\} &= (k^2-\kappa_3^2)^2\left\{\frac{2\exp[i(\nu-\nu^*)L/2]}{(\nu-\nu^*)\nu\nu^*}\right.\\
&\cdot\int_0^L d\zeta F_n(\kappa,\zeta)\cos\left[\left(k-\frac{\nu+\nu^*}{2}\right)\zeta\right]\\
&\cdot\sin[(\nu-\nu^*/2)(L-\zeta)]\\
&\mp\frac{\exp[-i(k-\nu)L]}{2(k-\nu)\nu\nu}\int_0^L d\zeta F_n(\kappa,\zeta)\\
&\cdot\sin[(k-\nu)(L-\zeta)]\mp\frac{\exp[i(k-\nu^*)L]}{2(k-\nu^*)\nu^*\nu^*}\\
&\left.\cdot\int_0^L d\zeta F_n(\kappa,\zeta)\sin[(k-\nu^*)(L-\zeta)]\right\}.
\end{aligned}\tag{32}$$

At this point we recall that $\nu = (k^2 - \kappa_2^2 - \kappa_3^2)^{1/2}$ and find the spectra for $(\kappa_2^2 + \kappa_3^2)^{1/2} < k$. Under these conditions ν is real (for real k) and $\nu^* = \nu$. Therefore for $(\kappa_2^2 + \kappa_3^2)^{1/2} = \kappa < k$ we have

$$\begin{aligned}
\left.\begin{matrix}F_A(\kappa,0)\\ \\ F_s(\kappa,0)\end{matrix}\right\} &= \frac{(\kappa^2-\kappa_3^2)^2}{(k^2-\kappa^2)}\left\{\int_0^L d\zeta(L-\zeta)\right.\\
&\cdot F_n(\kappa,\zeta)\cos\{[k-(k^2-\kappa^2)^{1/2}]\zeta\}\\
&\mp\frac{\cos\{[k-(k^2-\kappa^2)^{1/2}]L\}}{k-(k^2-\kappa^2)^{1/2}}\\
&\left.\cdot\int_0^L d\zeta F_n(\kappa,\zeta)\sin\{[k-(k^2-\kappa^2)^{1/2}](L-\zeta)\}\right\}.
\end{aligned}$$

This result is exact and it is useful to obtain a reasonable approximation. To proceed, expand the

$$\sin\{[k-(k^2-\kappa^2)^{1/2}](L-\zeta)\}$$

term in the second integral by the multiple angle formula for sines and collect like terms:

$$\begin{aligned}
\left.\begin{matrix}F_A(\kappa,0)\\ \\ F_s(\kappa,0)\end{matrix}\right\} &= \frac{(k^2-\kappa_3^2)^2L}{(k^2-\kappa^2)}\\
&\cdot\left\{\int_0^L d\zeta F_n(\kappa,\zeta)\cos\{[k-(k^2-\kappa^2)^{1/2}]\zeta\}\right.\\
&\cdot\left[1-(\zeta/L)\mp\frac{\sin\{2[k-(k^2-\kappa^2)^{1/2}]L\}}{2[k-(k^2-\kappa^2)^{1/2}]L}\right]\\
&\pm\int_0^L d\zeta F_n(\kappa,\zeta)\sin\{[k-(k^2-\kappa^2)^{1/2}]\zeta\}\\
&\left.\cdot\frac{\cos^2\{[k-(k^2-\kappa^2)^{1/2}]L\}}{[k-(k^2-\kappa^2)^{1/2}]L}\right\}.
\end{aligned}$$

Noting that $F_n(\kappa,\zeta)$ falls off rapidly for $\kappa\zeta \geq 1$ [3, ch. 1, sec. 4], and since we are interested in inhomogeneities such that their scale $1/\kappa$ is much less than the path length L, we therefore conclude that $\zeta/L \ll 1$ in the important region of integration ($\zeta \leq 1/\kappa \ll L$), and we may disregard that term in the first integral. For $\kappa \gg 0$, the second integral is a factor $1/kL$ smaller than the first, and as $\kappa \rightarrow 0$ it becomes the same size as the ζ/L term. Hence we may disregard this term for the whole range of κ.

Taking the above considerations into account we have for the case $\kappa < k$ the spectra

$$\begin{aligned}
\left.\begin{matrix}F_A(\kappa,0)\\ \\ F_s(\kappa,0)\end{matrix}\right\} &\cong \frac{(k^2-\kappa_3^2)^2L}{k^2-\kappa^2}\left(1\mp\frac{\sin\{2[k-(k^2-\kappa^2)^{1/2}]L\}}{2[k-(k^2-\kappa^2)^{1/2}]L}\right)\\
&\cdot\int_0^L d\zeta F_n(\kappa,\zeta)\cos\{[k-(k^2-\kappa^2)^{1/2}]\zeta\}.
\end{aligned}\tag{15'}$$

B. *Spectra for $\kappa > k$*

Returning to (32) which is valid for the entire range of κ, and noting that ν is imaginary for $\kappa > k$, therefore, $\nu = i(\kappa^2 - k^2)^{1/2}$, i.e., $\nu^* = -\nu$. After substituting into (32) we obtain

$$\begin{aligned}
&\left.\begin{matrix}F_A(\kappa,0)\\ \\ F_s(\kappa,0)\end{matrix}\right\}\\
&= (k^2-\kappa_3^2)^2\left(\frac{\exp[-(\kappa^2-k^2)^{1/2}L]}{(\kappa^2-k^2)^{3/2}}\right.\\
&\cdot\int_0^L d\zeta F_n(\kappa,\zeta)\cos k\zeta\sinh[(\kappa^2-k^2)^{1/2}(L-\zeta)]\\
&\pm\frac{\exp[-(\kappa^2-k^2)^{1/2}L-ikL]}{2\kappa^2(\kappa^2-k^2)}[k+i(\kappa^2-k^2)^{1/2}]\\
&\cdot\int_0^L d\zeta F_n(\kappa,\zeta)\sin\{[k-i(\kappa^2-k^2)^{1/2}](L-\zeta)\}
\end{aligned}$$

$$\pm \frac{\exp\left[-(\kappa^2 - k^2)^{1/2}L + ikL\right]}{2\kappa^2(\kappa^2 - k^2)}\left[k - i(\kappa^2 - k^2)^{1/2}\right]$$

$$\left.\cdot \int_0^L d\zeta F_n(\kappa,\zeta) \sin\left\{\left[k + i(\kappa^2 - k^2)^{1/2}\right](L - \zeta)\right\}\right). \tag{33}$$

The second two integrals combine to give a real function. It may be shown that the last two integrals are small compared with the first except when $\kappa \rightarrow \infty$. However, a somewhat simpler argument is to note that $F_A(\kappa,0)$ and $F_s(\kappa,0)$ are always positive; therefore the terms after the ± signs can be at most the same size as the first. Hence we shall make an error of at most a factor of 2 in dropping these terms. Since we intend to show that the first term has virtually no effect when calculating amplitude and phase covariance functions, dropping the last two terms in (33) will not affect that conclusion.

To summarize the results for the spectra under the above approximations:

$$\left.\begin{matrix} F_A(\kappa,0) \\ \\ F_s(\kappa,0) \end{matrix}\right\} \cong \frac{(k^2 - \kappa_3^2)^2 L}{k^2 - \kappa^2}$$

$$\cdot\left(1 \mp \frac{\sin\left\{2\left[k - (k^2 - \kappa^2)^{1/2}\right]L\right\}}{2\left[k - (k^2 - \kappa^2)^{1/2}\right]L}\right)$$

$$\cdot \int_0^L d\zeta F_n(\kappa,\zeta) \cos\left\{\left[k - (k^2 - \kappa^2)^{1/2}\right]\zeta\right\}, \quad \kappa < k \tag{15'}$$

$$F_A(\kappa,0) = F_s(\kappa,0) \leq \frac{2\exp\left[-(\kappa^2 - k^2)^{1/2}L\right](k^2 - \kappa_3^2)^2}{\kappa^2 - k^2}$$

$$\cdot \int_0^L d\zeta F_n(\kappa,\zeta) \cos k\zeta \sinh\left[(\kappa^2 - k^2)^{1/2}(L - \zeta)\right], \quad \kappa > k. \tag{16'}$$

ACKNOWLEDGMENT

We would like to thank R. W. Lee for some informative discussions and Dr. L. E. Vogler for pointing out some corrections in the data from Bean and Dutton [10].

REFERENCES

[1] S. F. Clifford, "Wave propagation in a turbulent medium," Ph.D. dissertation, Thayer School of Engineering, Dartmouth College, Hanover, N. H.

[2] L. A. Chernov, *Wave Propagation in a Random Medium* (transl. from Russian). New York: McGraw-Hill, 1960, p. 168.

[3] V. I. Tatarski, *Wave Propagation in a Turbulent Medium* (transl. from Russian). New York: McGraw-Hill, 1961, p. 285.

[4] ——, *Propagation of Waves in a Turbulent Atmosphere* (in Russian). Moscow: Nauka, 1967, p. 548.

[5] E. C. Barrows, "Correlation matrix for radio waves in the troposphere," *Proc. 1962 Copenhagen Symp. on Electromagnetic Theory and Antennas*, vol. 2, pp. 743–746.

[6] R. W. Lee and J. C. Harp, "Weak scattering in random media, with applications to remote probing," *Proc. IEEE*, vol. 57, pp. 375–406, April 1969.

[7] J. W. Strohbehn, "Line-of-sight wave propagation through the turbulent atmosphere," *Proc. IEEE*, vol. 56, pp. 1301–1318, August 1968.

[8] J. W. Strohbehn and S. F. Clifford, "Polarization and angle-of-arrival fluctuations for a plane wave propagated through a turbulent medium," *IEEE Trans. Antennas and Propagation*, vol. AP-15, pp. 416–421, May 1967.

[9] A. M. Saleh, "An investigation of laser wave depolarization due to atmospheric transmission," *IEEE J. Quantum Electronics*, vol. QE-3, pp. 540–543, 1967.

[10] B. R. Bean and E. J. Dutton, *Radio Meteorology*. Washington, D. C.: U. S. Government Printing Office, 1966.

Reprinted from Journal of Optical Society of America *60*, *No. 6, 826-830, 1970.*

Measurements of Atmospheric Turbulence Relevant to Optical Propagation

R. S. Lawrence, G. R. Ochs, and S. F. Clifford
ESSA Research Laboratories, Boulder, Colorado 80302

(Received 28 November 1969)

The aspect of atmospheric turbulence of interest to optical-propagation studies is the variation of refractive index. We demonstrate the application of high-speed temperature sensors to the direct measurement of this variation at optically important scale sizes, as small as a few millimeters. The thermometers, used in pairs with spacings ranging from 3 mm to 1 m, disclose that the turbulence near the ground frequently differs substantially from the Kolmogoroff model, and that the temperature difference does not follow the gaussian probability-distribution function. A model of the turbulent atmosphere containing sharply bounded regions with stronger than average turbulence agrees well with our observations. We also demonstrate the use of a single sensor mounted on an airplane to observe refractive-index variations at heights up to 3 km.

Index Headings: Inhomogeneous media; Atmospheric optics.

Many theoretical predictions of the effects of atmospheric turbulence on the propagation of light can be checked only by measurements made in the open atmosphere. The open atmosphere, however, is notable for being statistically nonstationary and inhomogeneous. Accordingly, if outdoor optical measurements are to be useful in checking propagation theory, they must be supported by simultaneous direct measurements of the atmospheric turbulence. It is not sufficient to measure gross meteorological variables such as temperature gradient and wind velocity and from them try to deduce the properties of the turbulence. Available theories of the generation of turbulence are inadequate, and the complexity of the atmosphere precludes the use of simple models.

The aspect of atmospheric turbulence of interest to optical-propagation studies is, of course, the variation of refractive index or, what is equivalent, the variation of density of the air. Air density depends on both pressure and temperature, but only the latter need be measured to charcaterize the optical effects of the turbulence. Pressure fluctuations are rapidly dissipated, and their effect is miniscule compared to that of the longer-lasting temperature variations. Thus, for optical purposes, the word "turbulence" is synonymous with "temperature fluctuations" and is very different from the mechanical, velocity-fluctuation turbulence studied by the fluid dynamicist. In fact, if an adiabatic temperature gradient exists, it is quite possible to have strong mechanical turbulence with negligible optical effects.

The turbulent atmosphere contains temperature variations with scale sizes ranging from about a millimeter to several hundred meters or larger. Optical scintillations are caused primarily by irregularities having the size of a Fresnel zone, i.e., $(\lambda D)^{\frac{1}{2}}$ for a wavelength, λ, and a path length, D. Thus, for visible light and path lengths of a few kilometers, the scale sizes that cause scintillations are a few centimeters. The minimum scale size for very short paths is 1 or 2 mm, determined by the "inner scale" of turbulence—that region of the turbulent spectrum where viscous losses dissipate the turbulence. If we divide reasonable wind velocities by these scale sizes, we see that it is important to measure temperature fluctuations with a frequency response extending to several hundred hertz.

FINE-WIRE TEMPERATURE SENSORS

Ochs[1] described mounting and use of fine platinum wires as resistance thermometers. He used wires of various sizes for specific purposes, the most common being a 2.5-μ-diam wire having a resistance of 20 Ω/mm. The inner scale was measured with wires only one-tenth as large. The frequency response for the larger wire varies from 200 Hz in still air to 500 Hz in a wind with a velocity of 5 m/sec. Sensitivity in practice is about 0.02 K for the 2.5-μm-diam wire, and is deter-

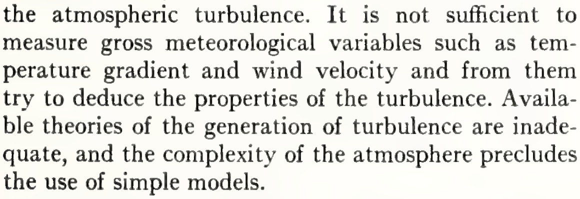

Fig. 1. Samples of high-speed temperature measurements made 1.5 m above the ground on a calm, sunny day. Noon, 23 September 1969.

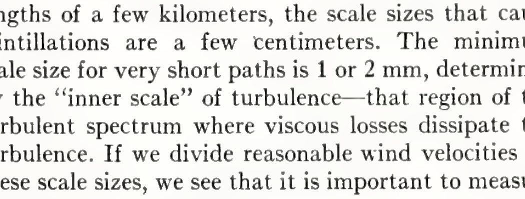

Fig. 2. Samples of temperature-difference measurements made on a clear, sunny day with sensors 1.5 m above the ground, spaced 10 cm apart. Noon, 23 September 1969.

mined by the input noise of the amplifier and the allowable measuring current for negligible self-heating of the wire. In a system limited only by the Johnson noise of the wire, the ultimate sensitivity would be about 0.002 K.

The "Wollaston process" wire is drawn inside a silver tube having a final outside diameter approximately 100 times greater than the diameter of the platinum wire. This heavy casing of silver facilitates the handling of the filament, permitting it to be attached with conducting glue to a supporting structure. Then nitric acid dissolves some of the silver, exposing a millimeter or so of the platinum wire.

The wires are used in pairs, separated by a distance of a few centimeters, so as to measure the temperature structure parameter,

$$C_T^2 = \langle (T_2 - T_1)^2 / r^{2/3} \rangle_{av} = D_T / r^{2/3}.$$

Here D_T is the temperature structure function, r is the separation of the sensors, and their individual temperatures are T_1 and T_2. According to the Kolmogoroff theory, C_T^2 is independent of r. It is related to the refractive-index structure parameter, C_n^2, by

$$C_n^2 = [(79p/T^2)10^{-6}]^2 C_T^2,$$

where p is the pressure in millibars, and T is the Kelvin temperature. The advantage of using the sensors in pairs is that the structure–function measurement acts as a spatial filter, discriminating against irregularities with scales larger than r. In this way it is possible to observe directly those irregularities that are most important in their optical effects. In fact, the slope of the turbulence spectrum can be determined from simultaneous measurements of D_T with various values of r.

In practice, it is more convenient to measure $\langle |T_2 - T_1| \rangle_{av}^2$ than $\langle (T_2 - T_1)^2 \rangle_{av}$. For a given probability density function of temperature fluctuations, these quantities are related by a known constant of proportionality.

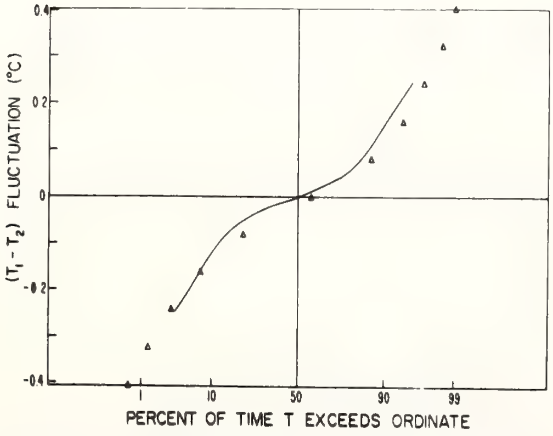

FIG. 3. The distribution function of temperature-difference measurements made with sensors separated vertically by 3 cm, placed 2 m above the ground, compared with a model consisting of a gaussian distribution modulated by a rectangular wave. Noon, 14 January 1969.

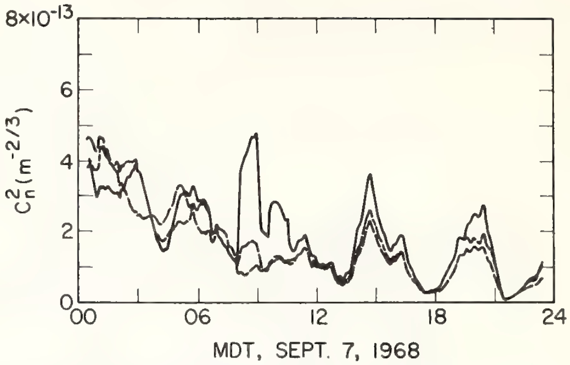

FIG. 4. The refractive-index structure parameter as measured with spaced temperature sensors having spacings of 1, 3, and 10 cm. 7 September 1968.

SAMPLE MEASUREMENTS

Figure 1 shows a typical measurement made with a single temperature sensor 2 m above the ground. The fluctuations, having peak values of several kelvins, are characterized by sharp discontinuities and relatively long quiescent periods. The variations are not symmetrical around the mean but tend to resemble hot patches, usually with sharp edges, superposed on a quiescent, cooler background.

Figure 2 shows typical temperature-difference records for sensors placed 1.5 m above the ground and separated by a spacing of 10 cm. Here, of course, the record is symmetrical about zero. However, the probability density function is definitely not gaussian. A typical distribution function is shown in Fig. 3, plotted on a distorted scale that would result in a straight line for a

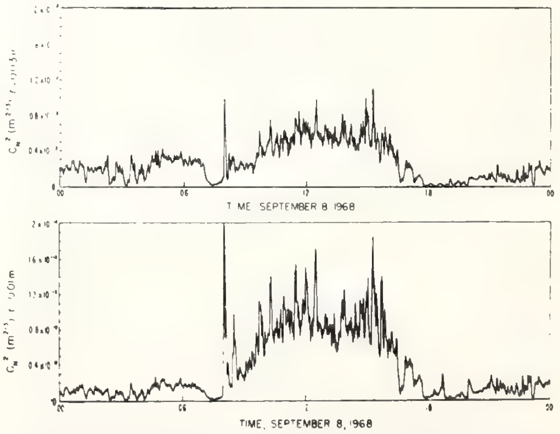

FIG. 5. The refractive-index structure parameter as measured with spaced temperature sensors having two different spacings. 8 September 1968.

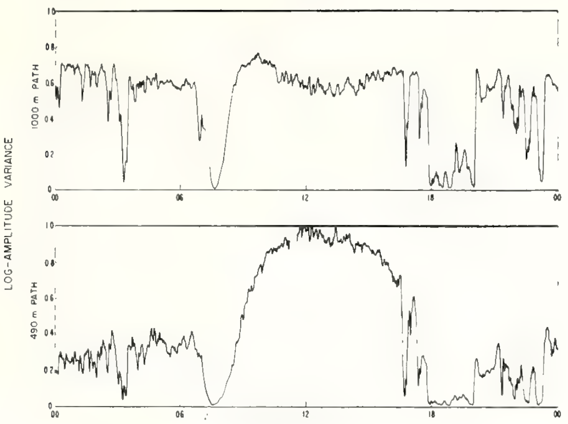

FIG. 6. The log-amplitude variance of laser-beam scintillations observed simultaneously with the refractive-index variations shown in Fig. 5.

normal distribution. The smooth curve in the figure is the theoretical distribution function of temperature difference that would result from multiplying a realization of gaussian temperature fluctuations by a train of rectangular pulses with random duration. The pulse train has an upper state of unity and a quiescent state of $\epsilon=0.2$, with a probability $p=0.45$ of being in the upper state. The product is sampled at two different times (representing spaced probes) and the statistics of the difference produce the curve shown in Fig. 3. The derivation requires the time interval representing sensor separation to be sufficiently small compared to the duration of a rectangular pulse so that the transition spikes are statistically insignificant. A possible physical meaning of this model is the existence of sharply bounded plumes of warm air, intercepting the temperature sensors approximately 45% of the time and containing normally distributed temperature fluctuations with a variance some 25 ($=1/\epsilon^2$) times greater than the fluctuations during the cool intervening periods. Straiton *et al.*[2] have reported similar distribution functions for radio refractive index.

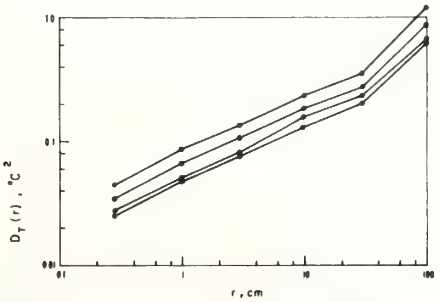

FIG. 7. Typical daytime observations of the temperature structure function (1-h averages). 24 April 1969.

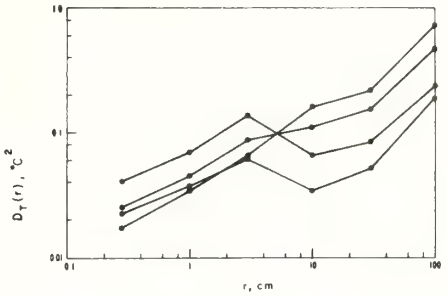

FIG. 8. Typical nighttime observations of the temperature structure function (1-h averages). 24 April 1969.

Figure 4 shows the variation, throughout a partly cloudy day, of C_n^2 as deduced from three pairs of temperature sensors placed 2 m above the ground and spaced at 1, 3, and 10 cm. A 1-h running average has been used to smooth these curves. Failure of the three curves to agree illustrates that the spectrum of turbulence near the ground is not always in agreement with the Kolmogoroff model. Similar records, smoothed with only a 100-sec time constant, for a sunny day and spacings 1 and 3 cm are shown in Fig. 5. The intensity of the corresponding optical scintillations, measured over paths of 0.5 and 1 km, is shown in Fig. 6. Notice the lack of scintillations in the evening and early morning, when the temperature gradient passes through adiabatic, and the pronounced midday saturation of the scintillations on the 1-km path.

Figures 7 and 8 show daytime and nighttime comparisons of 1-h averages of the temperature structure function observed with sensors 1.5 m above the ground and six different horizontal sensor spacings ranging from 3 mm to 1 m. A Kolmogoroff spectrum would produce straight lines with a slope of $\frac{2}{3}$ on these log–log plots. Figure 7 shows that the daytime turbulence for scale sizes smaller than 30 cm displays a slope of only 0.5. The nighttime situation displayed in Fig. 8 is much less regular, but the average slope is closer to $\frac{1}{2}$ than $\frac{2}{3}$. A possible explanation for the small slope of

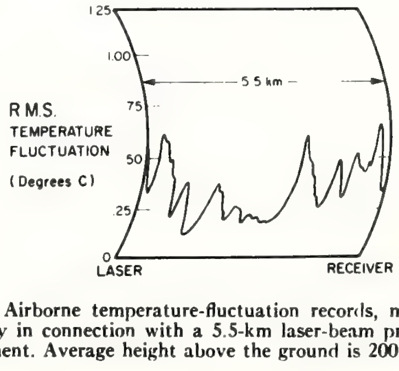

FIG. 9. Airborne temperature-fluctuation records, made on a sunny day in connection with a 5.5-km laser-beam propagation measurement. Average height above the ground is 200 ft. 3 July 1967.

the daytime turbulence is that, near the ground, there are energy inputs from all scale sizes rather than from only the largest scales, as assumed for the Kolmogoroff model.

Miniature, high-speed temperature sensors may also be used on aircraft following methods similar to those reported by Koprov and Tsvang.[3] A single sensor, arranged to respond to angular frequencies from ω_L to ω_H, is mounted on an aircraft traveling with velocity, v. Assuming that the spectrum of turbulence follows the Kolmogoroff law, Strohbehn[4] has shown that

$$C_T^2=\frac{2.68\langle T^2\rangle}{(v/\omega_L)^{\frac{2}{3}}-(v/\omega_H)^{\frac{2}{3}}},$$

where $\langle T^2\rangle_{\mathrm{av}}$ is the mean-square temperature fluctuation,

$$\langle T_2\rangle_{\mathrm{av}}=a(\langle\Delta T\rangle_{\mathrm{av}}{}^2-\bar{N}^2)=a(\langle T-\bar{T}\rangle_{\mathrm{av}}{}^2-\bar{N}^2).$$

Here $\bar{N}$ is the noise from all sources, principally that generated by the airplane propellor. In our experience, $\bar{N}$ is less than 0.02 K equivalent temperature. The scale factor has the value $a=\pi/2$ for a gaussian distribution of temperature. For the distribution that we actually observe 2 m above the ground, $a=2.48$. The temperature-difference model described above predicts a scale factor $a=\pi/2[p+(1-p)\epsilon^2]/[p+(1-p)\epsilon]^2$, which yields $a=2.36$ for $p=0.45$ and $\epsilon=0.2$. The airborne sensor consists of a platinum wire 6 μ in diameter, wound on an open square form 0.35 cm on a side and 2 cm long. Its resistance is 280 Ω. The aircraft velocity is usually about 60 m·sec^{-1}. The low-frequency cutoff is $\omega_L=31.4$ sec^{-1} (5 Hz), and the high-frequency limit is $\omega_H=2070$ sec^{-1} (330 Hz). The calibration of the airborne sensor has been checked by flying past the top of a 20-m tower on which was mounted a pair of sensors measuring C_T^2 in the more conventional manner.

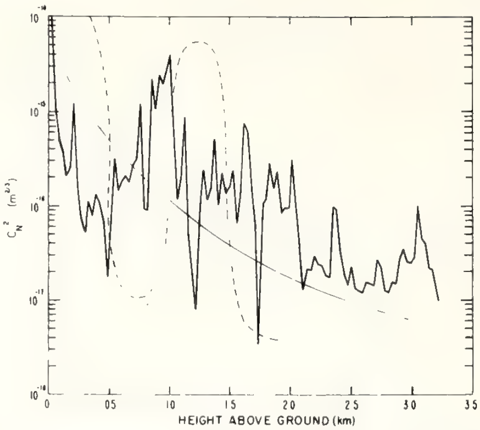

Fig. 11. Measurements, made in the afternoon of a sunny day with an airborne temperature sensor, of the variation of the refractive-index structure parameter in the first 3 km above the ground. Hufnagel's models for normal conditions (smooth curve) and disturbed layers (dashed curve) are shown for comparison. 1430–1500 MST, 26 November 1968.

Such airborne measurements clearly show the structure of the thermal plumes along a laser beam. Figure 9 is an example of such an observation. The structure of these plumes and their effect on optical propagation have been described in detail by Coulman.[5] Figures 10–12 show the vertical structure of C_N^2 observed at three different times during a day at a location about 40 km leeward of the Rocky Mountains. The dashed curve and the smooth solid curves show, for comparison, Hufnagel's model.[6] It is clear that no simple

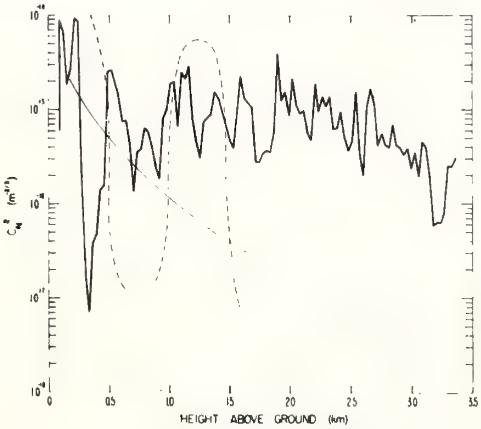

Fig. 10. Measurements, made in the forenoon of a sunny day with an airborne temperature sensor, of the variation of the refractive-index structure parameter in the first 3 km above the ground. Hufnagel's models for normal conditions (smooth curve) and disturbed layers (dashed curve) are shown for comparison. 1100–1130 MST, 22 October 1968.

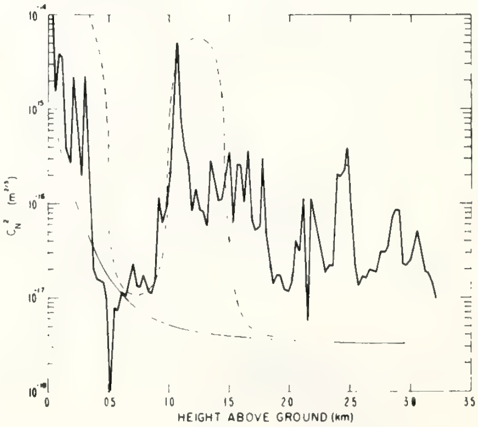

Fig. 12. Measurements, made on a clear evening with an airborne temperature sensor, of the variation of the refractive-index structure parameter in the first 3 km above the ground. Hufnagel's models for normal conditions (smooth curve) and disturbed layers (dashed curve) are shown for comparison. 2030–2100 MST, 26 November 1968.

model can accurately describe the violent variations of C_N^2, at least in the first 3 km above the ground. The irregularity and generally high level of the turbulence we observed may, of course, have been accentuated by the presence of the nearby mountains.

SUMMARY

We have emphasized the importance of high-speed temperature measurements as an aid to the interpretation of optical-propagation observations, and we have demonstrated the practicality of making such measurement both on the ground and from an aircraft. Noise levels are sufficiently low to permit measurement of C_N^2 at values less than 10^{-17} $\mathrm{m}^{-2/3}$.

REFERENCES

[1] G. R. Ochs, ESSA Tech. Rept. IER 47-ITSA 46 (U. S. Govt. Printing Office, Washington, D. C., 1967).

[2] A. W. Straiton, A. P. Deam, and J. L. Dodd, J. Geophys. Res. **72**, 4051 (1967).

[3] V. M. Koprov and L. R. Tsvang, Bull. (Izv.) Acad. Sci. USSR, Atm. Oceanic Phys. **2**, 1142 (1966).

[4] J. W. Strohbehn, private communication (1969).

[5] C. E. Coulman, Solar Phys. **7**, 122 (1969).

[6] R. E. Hufnagel, in *Restoration of Atmospherically Degraded Images* (Natl. Academy of Sciences, Washington, D. C., 1966), Vol. 2, p. 14.

14

Reprinted from Proceedings of the IEEE 58, No. 10, 1523-1545, 1970.

A Survey of Clear-Air Propagation Effects Relevant to Optical Communications

ROBERT S. LAWRENCE AND JOHN W. STROHBEHN, MEMBER, IEEE

Abstract—The theory and observations of the optical propagation effects of the clear turbulent atmosphere are reviewed, with particular attention to those characteristics most important to the designer of an optical communication system. Among the phenomena considered are the variance, probability distribution, spatial covariance, aperture smoothing, and temporal power spectrum of intensity fluctuations, and similar quantities for phase fluctuations and angle of arrival.

I. INTRODUCTION

THIS SURVEY treats the effects of the clear atmosphere upon light waves, with particular attention to the effects of turbulence. The results of atmospheric stratification and the normal variations with height of the atmosphere are also described, but we ignore any absorption by gaseous constituents and make no mention of scattering or absorption by aerosols or precipitation. Effects that are most important to the design of narrow-beam optical communications systems operating between two points on the ground or between the ground and space are emphasized. Much of our motivation in preparing this survey arises from the needs expressed clearly in the report [1] of a joint M.I.T.-NASA workshop. Rationalized MKS units are used, and the following symbols are employed.

A = amplitude of the electric vector of the optical wave
B = autocovariance or covariance function
b = normalized autocovariance or covariance function
b = separation of interferometer elements
C = curvature of a ray
C_n^2 = refractive-index structure parameter
D = aperture diameter
D_S = phase structure function
E = electric vector of the optical wave
F = two-dimensional spatial power spectrum
h = height above ground
$I = A^2$, intensity (or irradiance) of the optical wave
$k = 2\pi/\lambda$, wavenumber of the optical wave
L = path length, or distance to the turbulent layer
L_0 = outer scale of turbulence
$l = 2\pi/\kappa$, scale size of an irregularity
l_0 = inner scale of turbulence
$N = (n-1)\ 10^6$, refractivity in parts per million
n = refractive index
n_0 = ensemble average of n
$n_1 = n - n_0$
P = atmospheric pressure
R = autocorrelation function
R_0 = radius of curvature of a wavefront
S = phase of the electric vector of the optical wave
S = integrated intensity over an aperature
T = Kelvin temperature
$v_\perp$ = wind velocity component normal to the optical path
$v_\parallel$ = wind velocity component parallel to the optical path
W_0 = radius of an optical beam
w = temporal power spectrum
Z = zenith angle $(= \pi/2 - \theta_0)$
α = angle of arrival
α = angle between wind and direction of propagation
θ = aperture-averaging factor
θ_0 = apparent elevation angle above the horizon $(= \pi/2 - Z)$
$\kappa = 2\pi/l$, spatial wavenumber
$\kappa_m = 2\pi/l_0$
$\kappa_0 = 2\pi/L_0$
λ = optical wavelength
ν = ratio of specific heats, ≈ 1.4 for air
ρ = separation, parallel to the wavefront, of points of observation
ρ = ratio of receiver aperture radius to Fresnel-zone radius
$\sigma_{\ln I}^2$ = variance of log-intensity
σ_χ^2 = variance of log-amplitude
τ = astronomical refraction (total bending) of a ray
Φ = three-dimensional spatial power spectrum
$\chi = \log A$, the log-amplitude of the optical wave
$\Psi = \log E$
$\Omega = kW_0^2/2L$.

In Section II we briefly mention the magnitudes of the various effects and in later sections consider them in greater detail. Section III describes the atmospheric model we are using to derive the various optical results, Sections IV, V, VI, and VII discuss both theory and observations of optical intensity fluctuations, optical phase fluctuations, and angle-of-arrival effects, respectively.[1]

Manuscript received May 17, 1970. This work was supported in part by the Atmospheric Sciences Section, National Science Foundation, under Grant GA 1465.

R. S. Lawrence is with the ESSA Research Laboratories, Boulder, Colo. 80302.

J. W. Strohbehn is with the Department of Radiophysics, Dartmouth College, Hanover, N. H. 03755.

[1] After this manuscript had been prepared, we learned of a similar effort, at the time unpublished, by Brookner [95]. Many readers will find his work also of interest.

II. SUMMARY OF NUMERICAL VALUES

Optical Intensity Fluctuations

A smooth and featureless optical wave or beam traversing more than a few meters of ordinarily turbulent atmosphere has its energy redistributed and exhibits fluctuations in intensity known as "scintillations." The logarithm of the intensity of the distorted wave has a Gaussian probability density function, so the strength of the scintillations is described in terms of "log-intensity variance." Log-intensity variance increases with the strength of the turbulence and as the 11/6 power of the path length until it reaches a value of approximately 2.4, then it "saturates" and no longer increases. In fact, it slightly decreases. For paths a few meters above the ground, saturation may occur within a kilometer or two; for earth-to-space paths, saturation occurs only for elevation angles less than a few degrees. Formulas are given in Table I.

The instantaneous random pattern of scintillations, observed in a plane parallel to the wavefront, displays spatial Fourier components with a variety of scales, but the predominant scale size is the Fresnel-zone size $\sqrt{\lambda L}$, where λ is the optical wavelength and L is the path length or, for space-to-earth paths, the distance between the observer and the turbulent atmospheric layer. See Table II for formulas. Predominant scale sizes thus vary from about 1 cm for paths 1 km long to 7 or 8 cm for slant paths through the entire atmosphere. Since the scintillation pattern is random, if a receiving aperture receives a number N of statistically independent portions of the pattern corresponding to the predominant scale size, the log-intensity variance of the received signal will be reduced by a factor N. This effect is known as "aperture smoothing."

The temporal frequency of the variation of intensity observed at a fixed point depends upon the transverse component of wind that moves the turbulence across the beam. The predominant frequency is obtained by dividing wind velocity by Fresnel-zone size. For most paths it is usual for the important temporal frequencies to occupy the range from 1 to 100 Hz.

Until saturation occurs, the log-intensity variance of scintillations varies inversely as the 7/6 power of the optical wavelength. Although available observations are contradictory, the level of saturation probably varies little with wavelength. Details of the scintillation pattern are relatively broad-band, differing little with a wavelength change of a few tens of nanometers, but they become quite uncorrelated when the wavelength changes by a factor of 2.

Optical Phase Fluctuations

While the intensity scintillations are caused by turbulence with a scale near the Fresnel-zone size, phase fluctuations are produced by the largest scales in the turbulence and so depend on the "outer scale" of the turbulence and on the nature of the turbulence-generating mechanisms and the height above ground.

Until the size of the outer scale is reached, the mean-square difference of the phase observed at two points separated by distance ρ, parallel to the wavefront (the "phase structure function") $D_S(\rho)$, varies as $\rho^{5/3}$ and increases linearly with path length and with C_n^2, the strength of the turbulence. See Table III for formulas.

Angle of Arrival

Systematic bending of a ray passing through the entire atmosphere between earth and space depends strongly on the elevation angle θ_0 of the source as seen by the terrestrial observer. The sense is always such as to make the source appear higher above the horizon than it really is. For a sea-level observer with standard atmospheric pressure and temperature, the total bending (or "astronomical refraction") decreases from about 10 mrad when $\theta_0 = 0$ to zero at the zenith. For $\theta_0 > 170$ mrad, the astronomical refraction $\tau \approx 0.28 \cot \theta_0$ mrad. The value of τ decreases nearly linearly with pressure as the observer rises above sea level.

The downward bending of an optical beam on a ground-to-ground path is related to the vertical gradient of refractive index. For standard sea-level conditions, the curvature of a beam is

$$C = 32.6 + 0.93 \frac{dT}{dh} \mu\text{rad/km},$$

where dT/dh is the temperature lapse rate in K/km.

Short-term variation in the angle of arrival is best described in terms of the phase structure function, as shown quantitatively in [53]. The variation on earth-to-space paths typically amounts to a few microradians, while it may often be ten or more times greater on horizontal paths.

III. THE ATMOSPHERIC MODEL

This section describes the clear-air atmospheric properties most important when considering optical communications systems. Quite arbitrarily, we divide the discussion into "large-scale" and "small-scale" variations. We describe as large scale those phenomena that affect the average position of a light beam measured over a period of, say, 10 seconds; and we describe as small scale those irregularities that, for example, distort an image, broaden a laser beam, or cause rapid twinkling and dancing of a star. The dividing line between these scales is a meter or less.

Large-Scale Variations

The largest scales in the atmosphere are the general decrease with height of atmospheric density and the curvature of the atmospheric layer as it clings to the spherical earth. An optical ray arriving at the earth from a star bends downward as it passes through an atmosphere of steadily increasing refractive index. This effect is particularly significant for stars near the horizon or for near-horizontal ground-to-ground optical paths.

The variation of atmospheric refractive index with height above sea level can be computed from *The U. S. Standard Atmosphere* [2] adopted by the International Civil Aviation Organization (ICAO). The refractive index n of the atmosphere is conveniently and customarily described in terms of the refractivity N in parts per million. These N units are related to n by $N=(n-1)10^6$. For optical wavelengths,

$$N \approx 79\,P/T. \tag{1}$$

Here P is the atmospheric pressure in millibars and T is the temperature in Kelvin. N is roughly equal to 290 at sea level, varying with wavelength by about 10 percent over the visible band and with humidity by about 1 percent. The details of these variations have been reviewed by Owens [3]. In Section VI we discuss the application of these relationships and of the model atmosphere to the calculation of the systematic bending of an optical beam.

The actual atmosphere is usually less smooth than the ideal model of the U. S. Standard Atmosphere. Particularly characteristic are layers having great horizontal extent and and a vertical temperature gradient that changes abruptly. Their structure is usually measured with standard balloon-borne radiosonde equipment having time constants that limit the spatial resolution to about 15 meters. Thus we have only meager knowledge of how sharply defined such layers may be. We do know, however, that "looming" can occasionally occur, a phenomenon in which a light ray is refracted with a curvature equal to or greater than the curvature of the earth. We shall see in Section VI that a positive vertical temperature gradient of 134 K/km is required to produce such ducting. Thayer [4], while interpreting UFO sightings, displayed a number of radiosonde profiles which, when corrected for sensor lag, illustrate such sharp layers 1 or 2 km above ground. He infers that even sharper gradients must sometimes exist but points out the difficulty of making the necessary measurements. Lane [5], using a high-speed thermometer mounted on an airplane, measured an elevated layer at 2.6 km with a total temperature change of 4 K and a vertical temperature gradient that he estimates to be about 1000 K/km. Richter [6] has observed radar scattering layers less than 1 meter thick.

From such hints emerges the picture of thin sharp gradients of refractive index, often well above ground, extending horizontally for many kilometers and persisting for hours at a time. Visual observation from aircraft passing through the boundary of a haze layer occasionally discloses a more or less regular undulation of the layer. Ludlam [7] suggested that the breaking of such waves produces much of the turbulence that occurs a kilometer or more above ground.

Small-Scale Variations

Turbulence is almost always superposed on the large-scale variations of the atmosphere and produces random fluctuations in the density and therefore in the refractive index. If we are willing to neglect the minor optical Doppler shifts produced by the irregular turbulent velocities, we need consider only the spatial structure of the turbulence and may write the random variation of the refractive index as

$$n(\mathbf{r}) = n_0 + n_1(\mathbf{r}); \qquad n_0 = \langle n(\mathbf{r})\rangle,$$

where the sharp brackets denote an ensemble average.

For brevity and clarity, we define and work with spectra and covariance functions of $n(\mathbf{r})$, realizing all the time that the use of spectra requires the assumption of statistical homogeneity (or spatial stationarity) of the atmosphere. In fact, the atmosphere is notably nonstationary, i.e., the statistics of its fluctuations vary from time to time and from place to place. A method of analysis involving structure functions and the assumption of only locally homogeneous statistics has been devised and is partially successful in meeting this problem. Tatarski [8], [9] deals with this approach at length, and a summary of the pertinent formulas is given by Strohbehn [10]. Assuming stationarity and isotropy, we then define the autocovariance function $B_n(r)$ of the refractive index and its Fourier transform, the spectrum $\Phi_n(\kappa)$, as

$$B_n(r) = \langle n_1(r_1)n_1(r_1 + r)\rangle = \frac{4\pi}{r}\int_0^\infty \Phi_n(\kappa)\kappa \sin(\kappa r)\, d\kappa, \tag{2}$$

and

$$\Phi_n(\kappa) = \frac{1}{2\pi^2\kappa}\int_0^\infty B_n(r) r \sin(\kappa r)\, dr,$$

where $\kappa=2\pi/l$ is a spatial wavenumber and l is the corresponding scale size.

Refractive-index fluctuations are caused almost exclusively by fluctuations in temperature, since pressure variations are relatively small and are rapidly dispersed. The small-scale sizes and short lifetime of the temperature fluctuations ensure that they are adiabatic, so that

$$\frac{\delta P}{P} = \frac{\nu}{\nu - 1}\,\frac{\delta T}{T},$$

where the ratio of specific heats $\nu=c_p/c_v\approx 1.4$ for air. Differentiating (1) and eliminating δP, we see that the refractive-index fluctuations are proportional to the temperature fluctuations:

$$\delta N = \frac{-79}{\nu - 1}\,\frac{P}{T^2}\,\delta T.$$

The temperature fluctuations originate from large-scale phenomena, such as heating of the earth's surface, but are broken and mixed by the wind until they exist at all scales. Since wind velocity fluctuations control the temperature variations, we shall first briefly describe the statistics of the random velocity field. More detailed descriptions are available in many places [11], [12]; the two books by Tatarski [8], [9] cover aspects particularly relevant to propagation.

The kinetic energy of turbulence is usually introduced by such large-scale phenomena as wind shear or convection from solar heating of the ground. Therefore, it is reasonable to assume that the turbulent energy is introduced through the action of scale sizes larger than some minimum value L_0, called the outer scale of turbulence, which corresponds to a wavenumber $\kappa_0=2\pi/L_0$. For wavenumbers smaller than κ_0 the form of the energy spectrum cannot be specified in general, since it depends on surface geography and local meteorological conditions. Very likely, the turbulence is neither homogeneous nor isotropic in this range. Near the ground, the value of the outer scale is thought to be comparable with the height above ground. In the upper atmosphere L_0 is often 100 meters or more, but in the presence of stratified layers, perhaps as thin as a few meters. L_0 can not greatly exceed the layer thickness.

As the spatial wavenumber increases above κ_0 and the scale size becomes smaller than the distance to the ground or to the nearest inversion layer, the turbulence tends to become isotropic and homogeneous. Under these conditions, both theory and experiment indicate a $\kappa^{-11/3}$ dependence for the spectrum. The theory of this dependence, originally proposed by Kolmogorov [13] in 1941, is based on a number of assumptions: the energy is input at small wavenumbers and dissipated at much larger wavenumbers, the Reynolds number must be much greater than unity, and the scale sizes are small enough so that buoyancy effects are negligible. In this wavenumber range, the inertial subrange, the Reynolds number is so high for the large eddies that they are unstable and break apart. Thus they transfer energy to smaller scales (higher wavenumbers) down to the "inner scale of turbulence" l_0, a scale of only a few millimeters, where the Reynolds number approaches unity and the energy is dissipated into heat. The spectrum in the viscous dissipation region for which $\kappa > \kappa_m = 5.92/l_0$ is considerably steeper than in the inertial subrange, but its form is uncertain.

Temperature fluctuations which, as we have seen, are directly pertinent to optical propagation were considered by Obukhov [14], Corrsin [15], and Pond *et al.* [16]. They found that the temperature fluctuations obey the same spectral law as the velocity fluctuations. It should be remembered that while the forms of the spectra are identical, their magnitudes are not necessarily related. Strong mechanical turbulence tends to produce a well-mixed atmosphere with an adiabatic lapse rate so that the temperature fluctuations become very weak [17]. Conversely, a stable atmosphere with little wind may possess strong thermal gradients. Henceforth, we use the word "turbulence" to refer only to the temperature fluctuations, not to the velocity as in the usual fluid-dynamic sense.

Assuming that the form of the temperature spectrum, and hence the refractive-index spectrum, is the same as that of the velocity spectrum, Tatarski [9] used the following form for the refractive-index spectrum:

$$\Phi_n(\kappa) = 0.033\, C_n^2 \kappa^{-11/3} \exp(-\kappa^2/\kappa_m^2), \qquad (3)$$

with the following three conditions. 1) $\kappa_m l_0 = 5.92$. 2) The equation is a poor approximation for $\kappa \lesssim \kappa_0$, i.e., for large scales. 3) The equation is a reasonable approximation for $\kappa \gtrsim \kappa_m$, i.e., for small scales. The refractive-index structure parameter C_n^2 is a measure of the intensity of the refractive-index fluctuations. Tatarski's spectrum has a singularity at $\kappa = 0$, so it does not possess an autocovariance function, but this difficulty can be avoided [10].

The preceding spectra are reasonable approximations or models for the atmosphere under many conditions. They do not represent the actual atmosphere at all times or all places but it seems impossible to comment usefully on their range of validity. Bolgiano [18] predicted that the buoyancy effects that sometimes become important at low wavenumbers should produce a steeper spectrum. Lawrence, Ochs, and Clifford [19] observed flatter spectra near the ground, presumably caused by the direct introduction of turbulent energy at scale sizes smaller than L_0.

In contrast to the foregoing, a Gaussian spectrum and its corresponding Gaussian autocovariance function are frequently used for mathematical convenience. A serious problem is associated with the use of the Gaussian model for optical propagation; we believe its use should be discouraged. The Gaussian model contains only a single scale size, although at least two independent scales are important for optical effects. We shall see that the small-scale fluctuations are primarily responsible for intensity scintillation effects, and the large-scale fluctuations produce optical phase effects. A Gaussian model having too few adjustable parameters ties these together in an arbitrary and unrealistic way and engenders misleading and erroneous predictions.

So far we have discussed the form of the refractive-index spectrum of the turbulent atmosphere but have made only the most general references to the actual values of the parameters. The adjustable parameters of the model are as follows: 1) C_n^2, the refractive-index structure parameter (sometimes optimistically called the structure "constant") which is a measure of the intensity of the refractive-index fluctuations; 2) l_0, the inner scale of turbulence, below which viscous dissipation steepens the spectrum; 3) L_0, the outer scale of turbulence, above which the energy is presumed to be introduced into the turbulence. Between l_0 and L_0 lies the "inertial subrange" where the Kolmogorov model predicts a spectral slope of $-11/3$. The slope may be considered to be a fourth parameter if we wish to consider cases near the ground where the energy is introduced in a wide variety of scale sizes. Alternatively, and perhaps more properly, such a case may be described as one where the outer scale L_0 has decreased to nearly equal the inner scale l_0, thereby destroying the inertial subrange. Let us consider these parameters in turn.

The refractive-index structure parameter C_n^2 is measured in units of meters$^{-2/3}$. Its value varies from 10^{-17} or less when the turbulence is extremely weak, to 10^{-13} or more when the turbulence, generated near the ground in direct sunlight, is strong. Insufficient measurements exist to permit us to predict with confidence the mean value and variance of C_n^2 under specified meteorological and geographical conditions. Except for occasional individual measurements near the ground, estimates are based largely upon optical observations and, as we shall see, substantial uncertainty exists in the deduction of C_n^2 from such observations. A commonly used representation (Fig. 1) is the model of C_n^2 suggested by Hufnagel [20]. This model is derived from stellar scintillation measurements and from the few available direct temperature-fluctuation measurements, usually within 30 meters of the ground. Although Hufnagel's model

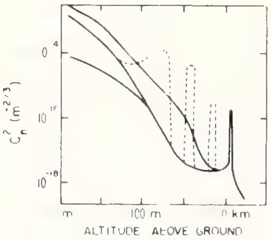

Fig. 1. Model of refractive-index structure parameter proposed by Hufnagel [20]. Solid lines represent normal atmospheric conditions for (in decreasing order) a sunny day, a clear night, and a dawn dusk minimum. The dashed line indicates typical (not average) effects to be expected from such meteorological disturbances as frontal activity.

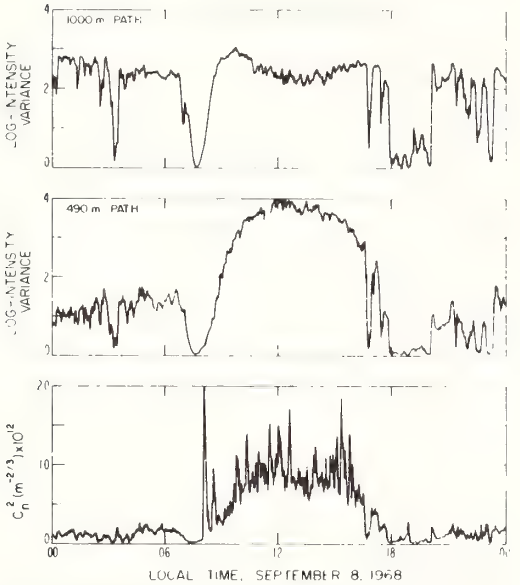

Fig. 2. Log-intensity variance versus time of day and its relationship to temperature fluctuations. The day was clear until approximately 1630, with alternate sunlight and shade from cumulus clouds for the remainder of the daylight hours. The middle curve a 490-meter path 1.6 meters above level ground, represents typical unsaturated diurnal behavior. The upper curve, a 1000-meter path, shows strong saturation during the middle of the day The lower curve is the temperature variance measured with high-speed sensors. From Ochs [94]

is commonly used, other workers have used the simpler exponential model with scale heights of from 2 to 8 km.

In Fig. 2 the bottom curve shows the typical diurnal variation of C_n^2 measured with temperature sensors 1.6 meters above the ground. Particularly notable are the increase in C_n^2 and its variability during the sunny hours of the day, and the very low values near sunrise and sunset when the temperature lapse rate near the ground was adiabatic.

The inner scale of turbulence l_0 can be calculated from the kinematic viscosity of air and from the rate of viscous dissipation of turbulent energy. From such calculations, l_0 is usually considered to be approximately 1 or 2 mm near the ground, increasing to about 1 cm at the tropopause. Direct measurements of l_0 with small temperature probes are unsatisfactory because of the uncertainty of the effect of the supporting structure. Gray and Waterman [21] and Strohbehn [22] have proposed measuring the inner scale by measuring light intensity fluctuations over a short path. Limited measurements by Gray and Waterman have given values of l_0 from 5 to 12 mm.

The outer scale L_0 is also uncertain. If we define L_0 to be that size above which the turbulence becomes nonisotropic and depends on the details of the generating mechanism, then certainly L_0 must not exceed some reasonable fraction of the distance from the ground. The value of L_0 may also depend on the strength of the turbulence. Values frequently used for L_0 are about 100 meters or 1/5 the height above the ground, whichever is less. Ochs [23] has measured the structure function of temperature fluctuations at 1.6 meters above flat ground and found the function to increase steadily up to spacings of about 60 cm, where it saturates. This observation suggests 1/3 the height above ground as a reasonable value for L_0.

IV. General Comments on the Theory

We do not attempt to present the derivations of the theoretical results in any comprehensive way. Instead, the final theoretical results are presented with a discussion of the assumptions and limitations involved. These results are then compared with observations, and we try to point out where we believe theory and experiment agree well, where theory and experiment disagree, or where there is insufficient information on either the observational or the theoretical side

In this section a brief review of the theoretical area is presented These comments are restricted to the fluctuations caused by small scale variations in the refractive index. From a theoretical viewpoint there are two features that cause difficulties in the problem of line-of-sight propagation of optical waves through the atmosphere. The first difficulty is that the atmospheric refractive index is a random function of both space and time; therefore, the best that we shall attempt is to relate the average properties of the optical wave to the average properties of the atmosphere. In general, the atmospheric properties are described by the spectral density function of the refractive-index fluctuation $\Phi_n(\kappa)$ which has been discussed in Section III. The second difficulty is that for a number of situations the linear theory based on applying a perturbation method to the wave equation is inadequate. At the present time there has been little progress in extending the linear theory.

There are several different theoretical approaches to the general problem of the propagation of waves in a random medium; excellent discussions of the mathematical aspects are given by Keller [24], [25] and Hoffman [26]. The approach that appears to be the most fruitful has been in directly solving the wave equation. This method is discussed in detail by Chernov [27] and Tatarski [8], [9]. Though there are a great many useful results in the monograph by Chernov and in the first monograph by Tatarski, their claims for the range of validity of some of the derived expressions are too liberal. The more recent work of Tatarski and a paper by Strohbehn [28] discuss the limitations in the theory of the earlier works. A different but extremely interesting approach has been introduced by Lee and Harp [29] based on phase screens. Their method leads to the same results but is more physical in its formulation.

We assume in the derivations that we are concerned with an atmosphere having no free charges, that the magnetic permeability is constant, and that the time dependence of the electrical field is given by $\exp(-i\omega t)$. With these assumptions the vector wave equation becomes

$$\nabla^2 \boldsymbol{E} + k^2 n^2 \boldsymbol{E} + 2\nabla(\boldsymbol{E} \cdot \nabla \log n) = 0, \tag{4}$$

where $k = 2\pi/\lambda$ and λ is the wavelength of the electromagnetic wave. The last term, which contains the interaction between orthogonal components of the field, produces depolarization effects. Strohbehn and Clifford [30] calculated the average power in the depolarized component and showed that it is typically 160 dB weaker than the power in the incident wave [10]. Saleh [31] was unsuccessful in his attempts to measure the depolarized signal with a sensitivity of 45 dB.

A practical possibility associated with the small depolarization of an optical signal when propagating through the "turbulent" atmosphere might be to use polarization modulation in optical communications systems. The amount of "polarization" noise introduced by the atmosphere is almost negligible, while there is very significant "amplitude modulation" and "phase modulation" noise. However, we are in no position to comment on other problem areas, such as the amount of depolarization caused by particle scattering or the technical problems in polarization modulation.

In any event, the lack of depolarization is a great theoretical advantage in that the vector wave equation (4) may be reduced to a scalar wave equation

$$\nabla^2 E + k^2 n^2 E = 0. \tag{5}$$

For simplicity in notation, we assume that the wave is plane polarized in the z direction, i.e., $E = E_z$, and is propagating in the x direction. We define $E = A \exp(iS)$, where A is the amplitude of the wave and S is the phase. Note that since the $\exp(-i\omega t)$ term has been eliminated, the amplitude and phase refer to quantities that would not change with time in a frozen medium. Further simplification would lead to a geometrical-optics approach that ignores diffraction effects. While that approach gives reasonable results for phase fluctuations, its results for amplitude fluctuations are valid only for $L \ll l_0^2/\lambda$, where l_0 is the inner scale of turbulence and L is the length of the propagation path. For typical parameters, this leads to restrictions of from 10 to 100 meters for the path length. For this reason we consider only the full-wave solution, which includes diffraction effects. The geometrical-optics results may be found as a limiting case.

Most of the literature since 1960 has followed the Russian approach of using the so-called Rytov method, which substitutes $E = \exp(\Psi)$ into the scalar wave equation (5). If we write $\Psi = \chi + iS$, where $\chi \equiv \log A$, then the real part of Ψ is called the log-amplitude and the imaginary part is the phase. With this substitution, the wave equation becomes

$$\nabla^2 \Psi(r) + \nabla\Psi(r) \cdot \nabla\Psi(r) + k^2 n^2(r) = 0. \tag{6}$$

The problem is to solve (6) for the fluctuations in log-amplitude and phase. Since a perturbation approach is used, the results are valid only if the perturbations are small.

The primary quantities that have been studied are the variances and the spatial covariance functions in a plane perpendicular to the direction of propagation. The major emphasis has been on phase and log-amplitude fluctuations, with some attention to angle-of-arrival, intensity, and coherence functions. For mathematical simplicity most of the work has dealt with plane-wave propagation; only recently have the spherical-wave and beam-wave cases been studied in much detail.

When a plane wave propagates through a statistically homogeneous random medium, there are certain symmetry properties that are mathematically convenient. In any plane perpendicular to the direction of propagation the statistics at any one point in the plane are the same as at any other. Therefore, the spatial covariance function depends only on the separation of the two points and not on their location in the plane. In this case, for an isotropic medium, the spatial covariance function may be written as a two-dimensional Fourier expansion, where

$$\begin{aligned} f &= \langle f \rangle + f_1 \\ B_f(\rho) &= \langle f_1(\rho_1) f_1(\rho_1 + \rho) \rangle \\ B_f(\rho) &= 2\pi \int_0^\infty F_f(\kappa) J_0(\kappa\rho)\kappa \, d\kappa \\ F_f(\kappa) &= \frac{1}{2\pi} \int_0^\infty B_f(\rho) J_0(\kappa\rho)\rho \, d\rho. \end{aligned} \tag{7}$$

Here $F_f(\kappa)$ is the two-dimensional spectral density of the fluctuations in f, where f might represent the log-amplitude or phase. For spherical-wave or beam-wave propagation, the expansion (7) is no longer valid since the symmetry has been destroyed. However, under the approximations that are usually made, expressions similar to (7) are often used. In a number of works the quantity derived is the two-dimensional spectral density function of the desired quantity, for example, log-amplitude fluctuations. Equation (7) is then used to find the covariance function or the variance $\sigma_f^2 = B_f(0)$.

The derivation of the spectral density functions of amplitude and phase from (6) is extremely involved and includes a number of approximations. The clearest derivations appear in the works of Tatarski [8], [9] and are not repeated here. In all the derivations a number of approximations are made. First, it is usually assumed that $\lambda \ll l_0$ and $\lambda^3 L/l_0^4 \ll 1$, where l_0 is the inner scale of turbulence. These are not important restrictions at optical wavelengths.

The only assumption that is definitely violated in some cases is the basic one that permits a perturbation expansion to be applied to the wave equation. As has been shown [32], [9], [33], there are cases of practical interest where the expansion converges very slowly and the perturbation method is no longer useful.

A major problem has been the difficulty in comparing theory with experiment. Until 1966 almost all of the theory centered on plane-wave propagation, for which the only applicable experimental arrangement involves stellar or satellite sources. For space-to-ground paths, the detailed distribution of refractive-index fluctuations is unknown and is certainly not uniform. The more recently proposed and less well-developed theories of spherical-wave and beam-wave propagation can, of course, be compared with ground-to-ground experiments over accessible paths. Even here, direct measurements of temperature fluctuations have seldom been supplied in adequate detail to permit critical tests of the theories.

V. Optical Intensity Fluctuations

Probability Distribution and Variance of Log-Intensity

Theory: Most of the theoretical investigations have concentrated on the fluctuations in the log-amplitude χ or the log-intensity (more properly, the log-irradiance). In applying Rytov's method, the scalar wave equation in the electric field E was transformed to an equation in $\Psi = \log E$. The solution of (6) for $\Psi_1 = \Psi - \langle \Psi \rangle$ can be written as an integral equation. Application of the central limit theorem to this integral equation leads to the prediction of a normal probability distribution for Ψ_1, i.e., for $\chi = \ln(A/A_0)$ and for S_1, the deviation of the phase from its mean value. If instead of transforming the scalar wave equation a perturbation expansion had been applied to E, the same procedure would have led to a normal probability distribution for E_1. This distribution leads to a Rice–Nakagami distribution for the amplitude A, in contrast to the log-normal distribution predicted by Rytov's method. For very small variances in χ the difference between the log-normal and Rice–Nakagami distributions is small. However, as the variance in χ becomes moderate or large, the difference between these distributions becomes easily recognizable.

The preceding comments are based on a theoretical approach valid when the variance of χ, denoted σ_χ^2, is small, i.e., less than 0.64. When σ_χ^2 exceeds 0.64, the theoretical results are rather scarce and quite controversial. DeWolf [34] originally predicted a Rice–Nakagami distribution in this region, but more recently [35] he seems to favor the log-normal. A physical discussion pointing out the differences is given by Strohbehn [10]. This argument tends to favor the log-normal distribution. Note that if the probability distribution of the amplitude is log-normal, so is the probability distribution of intensity. A Rice–Nakagami distribution describes an electric field E that contains a constant component plus a component with a normal probability distribution. In the limit where the constant component is zero, the amplitude obeys a Rayleigh distribution, and the intensity follows an exponential probability distribution.

Since intensity (or irradiance) is $I = A^2$, the variance of the log-intensity is equal to four times the variance of the log-amplitude:

$$\sigma_{\ln I}^2 = 4\sigma_\chi^2.$$

Normally, σ_χ^2 is calculated but $\sigma_{\ln I}^2$ is measured.

When we present the theoretical results, there are a number of different cases of interest, separated by the type of wave originally transmitted at the source. The three cases that we consider are an infinite plane wave; a spherical wave, i.e., a point source; and a beam wave. The beam wave that has been considered by almost all workers is the so-called Gaussian beam. At the transmitter the electric field is assumed to obey the formula

$$E_0(0, y, z) = A \exp\left\{-\left(\frac{1}{W_0^2} + i\frac{k}{2R_0}\right)(y^2 + z^2)\right\}, \quad (8)$$

where W_0 is the radius of the beam and R_0 is the radius of curvature of the wavefront. If $R_0 = \infty$, then the beam is collimated; if R_0 equals the path length, then the beam has its focal point at the receiver.

For each of the three cases we usually distinguish between two types of propagation conditions. First we assume that the atmosphere is statistically homogeneous and second that the medium is smoothly varying, i.e., at the spatial wavenumbers of interest the spectral shape remains constant along the path but the intensity of the fluctuations varies slowly along the path so

$$\Phi_n(x, \kappa) = C_n^2(x)\Phi_n^{(0)}(\kappa).$$

A further distinction is made: the first equations given are the general cases where the shape of the spectral density function of the refractive-index fluctuations is not specified. Where possible the results are also given for some specific form of the spectral density function, which is closely related to the forms discussed in Section III. In all cases we assume that the refractive-index fluctuations are isotropic. Though most of the equations could be generalized, there is very little known about the nonisotropic case.

The specific equations are given in Table I, assuming that the variance of the intensity fluctuations is measured by a point receiver. In practice a receiving aperture much smaller than $\sqrt{\lambda L}$ should adequately represent a point.

The most important restriction on these results is that $\sigma_{\ln I}^2$ must remain small for the equations to be valid. Based on plane-wave theory, Tatarski [32], [9] derives $\sigma_\chi^2 \ll 1$, or $\sigma_{\ln I}^2 \ll 4$, and claims experimental verification has shown good agreement if $\sigma_\chi^2 < 0.64$, or $\sigma_{\ln I}^2 < 2.5$. It is apparent that this type of restriction is placed on all the results, independent of the type of source; however, the numerical coefficient may differ depending on the source distribution. The only theoretical work has considered plane waves, while the experimental work has been primarily with spherical waves. Unfortunately, the restriction is not a minor one. For horizontal propagation paths close to the ground, where high values of C_n^2 are often observed, the theoretical expressions for $\sigma_{\ln I}^2$ may exceed 2.5 for paths as short as 500 meters. For vertical or slant paths, where the quantity C_n^2 varies along the path, there is less chance of exceeding this limit.

TABLE I

Variance of Log-Intensity

Case	General Random Medium	Locally Isotropic Random Medium*
Plane wave, homogeneous medium	$\sigma_{\ln I}^2 = 8\pi^2k^2L\int_0^\infty \left(1 - \frac{k}{\kappa^2L}\sin\frac{\kappa^2L}{k}\right)\Phi_n(\kappa)\kappa\,d\kappa$ (T1)	$\sigma_{\ln I}^2 = 1.23C_n^2k^{7/6}L^{11/6},\quad l_0^2/\lambda \ll L$ (T4)
	$\sigma_{\ln I}^2 = \frac{4}{3}\pi^2L^3\int_0^\infty \Phi_n(\kappa)\kappa^5\,d\kappa,\quad L \ll l_0^2/\lambda$ (T2)	$\sigma_{\ln I}^2 = 12.8C_n^2L^3l_0^{-7/3},\quad L \ll l_0^2/\lambda$ (T5)
Plane wave, smoothly varying medium	$\sigma_{\ln I}^2 = 16\pi^2k^2\int_0^L d\eta C_n^2(\eta)\int_0^\infty d\kappa\kappa\Phi_n^{(0)}(\kappa) \times \sin^2\left[\frac{\kappa^2(L-\eta)}{2k}\right]$ (T3)	$\sigma_{\ln I}^2 = 2.24k^{7/6}\int_0^L C_n^2(\eta)(L-\eta)^{5/6}\,d\eta,\quad l_0^2/\lambda \ll L$ (T6) $\sigma_{\ln I}^2 = 38.4l_0^{-7/3}\int_0^L C_n^2(\eta)(L-\eta)^2\,d\eta,\quad L \ll l_0^2/\lambda$ (T7)
Spherical wave, homogeneous medium	$\sigma_{\ln I}^2 = 8\pi^2k^2L\int_0^\infty \left\{1 - \left(\frac{2\pi k}{\kappa^2L}\right)^{1/2}\left[\cos\left(\frac{\kappa^2L}{4k}\right)C\left(\left(\frac{\kappa^2L}{2\pi k}\right)^{1/2}\right) + \sin\left(\frac{\kappa^2L}{4k}\right)S\left(\left(\frac{\kappa^2L}{2\pi k}\right)^{1/2}\right)\right]\right\}\Phi_n(\kappa)\,\kappa\,d\kappa$ (T8)†	$\sigma_{\ln I}^2 = 0.50C_n^2k^{7/6}L^{11/6},\quad l_0^2/\lambda \ll L$ (T10)
	$\sigma_{\ln I}^2 = \frac{2}{15}\pi^2L^3\int_0^\infty \Phi_n(\kappa)\kappa^5\,d\kappa,\quad L \ll l_0^2/\lambda$ (T9)	$\sigma_{\ln I}^2 = 1.28C_n^2L^3l_0^{-7/3},\quad L \ll l_0^2/\lambda$ (T11)
Spherical wave, smoothly varying medium	$\sigma_{\ln I}^2 = 16\pi^2k^2\int_0^L d\eta C_n^2(\eta)\int_0^\infty d\kappa\kappa\Phi_n^{(0)}(\kappa) \times \sin^2\left[\frac{\kappa^2\eta(L-\eta)}{2kL}\right]$ (T12)	$\sigma_{\ln I}^2 = 0.56k^{7/6}\int_0^L C_n^2(\eta)\left(\frac{\eta}{L}\right)^{5/6}(L-\eta)^{5/6}d\eta,\quad l_0^2/\lambda \ll L$ (T13) $\sigma_{\ln I}^2 = 46.7l_0^{-7/3}\int_0^L C_n^2(\eta)\left(\frac{\eta}{L}\right)^2(L-\eta)^2\,d\eta,\quad L \ll l_0^2/\lambda$ (T14)
Beam wave, homogeneous medium	$\sigma_{\ln I}^2 = 8\pi^2\int_0^L d\eta\int_0^\infty d\kappa\kappa\left[J_0(i2\gamma_2\kappa\rho) - \cos\left(\frac{\gamma_1(L-\eta)}{k}\kappa^2\right)\right]\lvert H\rvert^2\Phi_n(\kappa)$ (T15) where $\gamma_1 = \frac{1-\alpha_2L+\{(\alpha_1^2+\alpha_2^2)L-\alpha_2\}\eta}{(1-\alpha_2L)^2+(\alpha_1L)^2}\qquad \gamma_2 = \frac{\alpha_1(L-\eta)}{(1-\alpha_2L)^2+(\alpha_1L)^2}$ $\alpha_1 = \lambda/(\pi W_0^2)\qquad \alpha_2 = 1/R_0$ $\alpha = \alpha_1 + i\alpha_2\qquad \rho = (y^2+z^2)^{1/2}$ = distance from beam center $\lvert H\rvert^2 = \kappa^2\exp\left\{-\frac{\gamma_2(L-\eta)}{k}\kappa^2\right\}$	$\sigma_{\ln I}^2 = 4\pi^2(0.033\,C_n^2)\Gamma(-5/6)k^{7/6}L^{11/6}\left\{\frac{\alpha_1L}{1+(\alpha_1L)^2}\right\}^{5/6} \cdot \left\{\frac{3}{8}\,{}_1F_1\left(-5/6, 1; \frac{2\rho^2}{W_0^2[1+(\alpha_1L)^2]}\right) - g(\alpha_1L)\right\}$ (T17)‡ where ${}_1F_1(a, c; z) = \Phi(a, c; z)$ is the Kummer function $g(\alpha_1L) = \int_0^1 \mathrm{Re}\left[(1-x)^2 - i\frac{[1+(\alpha_1L)^2x](1-x)}{\alpha_1L}\right]^{5/6}dx = \mathrm{Re}\left\{\frac{6}{11}\left(\frac{1+i\alpha_1L}{i\alpha_1L}\right)^{5/6}{}_2F_1\left(-\frac{5}{6}, 1; \frac{17}{6}; i\alpha_1L\right)\right\}$ ${}_2F_1(a, b; c; z)$ is a hypergeometric function
Beam wave, smoothly varying medium	$\sigma_{\ln I}^2 = 8\pi^2\int_0^L d\eta C_n^2(\eta)\int_0^\infty d\kappa\kappa\left[J_0(i2\gamma_2\kappa\rho) - \cos\left(\frac{\gamma_1(L-\eta)}{k}\kappa^2\right)\right]\lvert H\rvert^2\Phi_n^{(0)}(\kappa)$ (T16)	$\sigma_{\ln I}^2 = 4\pi^2(0.033)[-\Gamma(-5/6)]k^{7/6}L^{11/6}\int_0^1 d\eta C_n^2(\eta)G_A(\eta)$ where $G_A(x) = \mathrm{Re}\left[(\gamma_2+i\gamma_1)(1-x)+S_m^2\right]^{5/6} - \left[\gamma_2(1-x)+S_m^2\right]^{5/6}$ $S_m = (k/L)^{1/2}l_0/5.92$ (T18)‖

---

* For the locally isotropic random medium $\Phi_n(\kappa) = 0.033C_n^2(x)\kappa^{-11/3}\exp(-\kappa^2/\kappa_m^2)$. For the homogeneous medium $C_n^2(x)$ is a constant independent of x.

† $C(x) = \int_0^x \cos(\pi t^2/2)\,dt$, $S(x) = \int_0^x \sin(\pi t^2/2)\,dt$.

‡ Results according to Ishimaru [39], [40]. Receiver a distance ρ from beam center, beam collimated ($R_0 = \infty$).

‖ Receiver at beam center, any value of R_0.

The results for plane and spherical waves have been derived by a number of different workers and are well accepted. For locally isotropic turbulence it is apparent that the functional form of the equations for the two cases is the same. However, the numerical coefficients differ by a factor of about 2.5, i.e., a spherical wave has smaller variance. The beam-wave problem has been attacked more recently, and the expressions are considerably more complex. For this reason the different results have not been carefully compared. The first comprehensive paper on beam-wave propagation was by Schmeltzer [36], who gave some reasonably general expressions for the mean value of the electromagnetic field and for the covariance functions of log-amplitude and phase. These results were left as double integrals that were not evaluated. His derivation uses the approximation that the observation point is in the far field, i.e., the path length

$$L >> \frac{k|R_0|W_0^2}{(4R_0^2 + k^2W_0^4)^{1/2}}, \tag{9}$$

where W_0 is the width of the Gaussian beam at the transmitter and R_0 is the curvature of the wavefront. With this approximation, the terms in his expressions are only weakly dependent on the position of the observation point relative to the center of the beam; therefore, the dependence is dropped, i.e., all calculations are done on the beam axis. For a collimated beam, where $R_0 = \infty$, (9) becomes $L >> kW_0^2/2$. For a 1-cm beam, L must exceed 1 km; for a 5-cm beam, $L >> 12$ km at optical wavelengths. Therefore, for a number of cases of interest this approximation is not met. Fried and Seidman [37] and Fried [38] have taken Schmeltzer's expressions and evaluated specific cases. Since in the beam-wave case there are additional parameters, the beam width and its wavefront curvature, it is difficult to portray the results in any general manner. They assumed a $\kappa^{-11/3}$ form for $\Phi_n(\kappa)$ and investigated the two specific cases where the beam is collimated ($R_0 = \infty$) and where the beam is focused at the receiver ($R_0 = L$). They introduced a parameter $\Omega = kW_0^2/(2L)$, which is the ratio of the distance to the far field divided by the path length. Note that Schmeltzer made the approximation $\Omega << 1$ in deriving his formulas which would appear to limit Fried and Seidman's results to $\Omega << 1$ also. However, though it is not specifically stated, it appears that the above restriction can be removed if we are interested in effects only on the beam axis. For a collimated beam and a given source diameter, the variance $\sigma^2_{\ln I}$ starts out being equal to that of a plane wave for $L << kW_0^2/2$, i.e., for short paths where the beam appears as a plane wave (see Fig. 3). When $L >> kW_0^2/2$, i.e., the observation point is well into the far field, the variance becomes very close to that of a spherical wave, which is reasonable. For the focused case in the near field the calculations give a sharp decrease in $\sigma^2_{\ln I}$. As the path length increases and goes into the far field of the transmitter, the variance of the log-intensity again approaches that of a spherical wave. One point of caution should be given, however. These results would seem to indicate that one method of reducing the scintillations ($\sigma^2_{\ln I}$) would be to use a focused beam and a large aperture; however, in the case where the reduction would be most useful, i.e., high values of $\sigma^2_{\ln I}$, it is doubtful that it would occur. In this case, in a very short distance the phase front of the wave is so perturbed that the concept of a focused beam becomes meaningless.

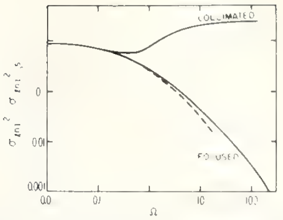

Fig. 3. Dependence of normalized log-intensity variance $\sigma^2_{\ln I}$ $\sigma^2_{\ln I\,s}$ (where the subscript s denotes the variance calculated for a spherical wave) on normalized transmitter size Ω. Solid curves represent a homogeneous path and, for them, $\Omega = kW_0^2\,(2L)$. The dashed curve represents slant propagation through the entire atmosphere. In the slant case, $\Omega = kW_0^2/(2h_0 \csc \theta_0)$, where h_0 is the "scale height" of the atmosphere and θ_0 is the angle from the horizon. From Fried and Seidman [37], [38].

One way to look at this problem is to compare the phase fluctuations introduced by the atmosphere with the difference in phase that distinguishes between a collimated beam and a focused beam. For a beam focused at a point at some distance L, the difference in phase at the transmitter compared with a collimated beam is $\delta S \cong \frac{1}{2}k\rho^2/L$, where ρ is the transverse distance from the beam axis. Clearly, phase fluctuation introduced by the atmosphere must be much less than δS for the concept of a focused beam to hold. The phase fluctuations may be estimated from the phase structure function $D_S(\rho)$ (see Section VI); therefore, $D_S(\rho) < \delta S^2$. Using (T35) ("T" means the equation appears in a table) for a plane wave, we have

$$2.92C_n^2k^2L\rho^{5/3} < \tfrac{1}{4}\rho^4k^2/L^2.$$

Therefore,

$$C_n^2 < \tfrac{1}{12}\rho^{7/3}/L^3.$$

For a 5-cm beam and a 1-km path, C_n^2 must be less than 10^{-13} meters$^{-2/3}$ to consider focusing a beam. Notice that the permissible value of C_n^2 decreases as L^3.

Fried [38] also considered the reduction in scintillation for a collimated Gaussian beam propagating from the ground to a receiver in space and its dependence on zenith angle and aperture size. His results are plotted as the dashed line in Fig. 3. In this case, as the optics size increases, the predicted scintillations decrease substantially. This is a distinct contrast to a uniform path where the scintillations increase, a difference that seems somewhat hard to reconcile.

Ishimaru's approach [39], [40] is somewhat different than Schmeltzer's in that he extends the idea of spectral representations. His final equations also include the effect of the observation point being off the center of the beam. However, a quantitative evaluation of the magnitude of this effect is not given. Ishimaru also predicts a strong reduction in the scintillations when the beam is focused. Fig. 4 is a graph from Ishimaru showing the dependence of $\sigma^2_{\ln I}$ as a func-

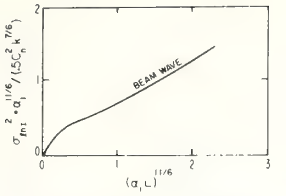

Fig. 4. Variance of log-intensity as a function of $(\alpha_1 L)^{11/6}$, where $\alpha_1 = \lambda/(\pi W_0^2)$ and W_0 is the beam radius [39]. The vertical scale was added after private correspondence.

tion of $\alpha_1 L)^{11/6}$. For a given aperture size, i.e., a constant value of $\alpha_1 = \lambda/(\pi W_0^2)$, the curve shows how the variance should increase with path length. Again, we urge a note of caution in using these curves. When C_n^2 is reasonably high, it seems that the phase fluctuations would be large enough to seriously affect the beam parameters.

As indicated previously, the equations for the variance of the log-intensity fluctuations are valid only when $\sigma_{\ln I}^2 \ll 4$. Attempts at verifying experimentally (T4) or (T10) have shown that for small values of $\sigma_{\ln I}^2$ there is good agreement between theory and experiment. However, when $\sigma_{\ln I}^2$ is greater than about 2.5, as predicted by the preceding equations, the experimental value of $\sigma_{\ln I}^2$ appears to saturate and remain almost constant. Therefore, the theoreticians know not only that the above expressions are of limited validity but also what type of relation they should expect to find. Despite this insight, very little progress has been made theoretically as of this writing. A number of workers have tried using the renormalization techniques of field theory [41]–[45], [34], [35], which approach is exceedingly complex mathematically, involving the selective summing and neglecting of very complicated terms in a series representation. There is still no general agreement among workers over which terms must be kept. The only worker that appears to derive a saturation-like curve for the variance of the log-intensity fluctuations using this method is deWolf, and his results are controversial. In his second paper [34] he predicted a saturation effect but also concluded that the probability distribution of the amplitude fluctuations should follow a Rice–Nakagami curve. The experimental evidence does not seem to bear this out, and in a more recent paper [35] he favors a log-normal distribution while keeping his saturation curve. His work leads to the following expression for the variance of the log-intensity:

$$\begin{aligned}\sigma_D^2 &= \sum_{n=0}^{\infty} \frac{1}{(n+m)^2}\\ m &= 1/[1 - \exp(-\sigma_R^2)]\\ \sigma_R^2 &= 1.23 C_n^2 k^{7/6} L^{11/6},\end{aligned} \tag{10}$$

where σ_R^2 is the variance calculated by the first-order perturbation theory. This curve, which leads to a saturation value of 1.65, is plotted in Fig. 5.

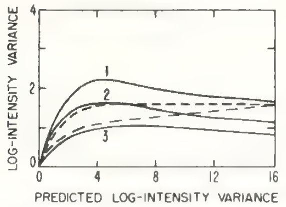

Fig. 5. Theory and observation of saturation of scintillations compared with values predicted from temperature fluctuations using (T4) or (T10). The lower dashed curve is the theoretical result from Tatarski [9] [$\sigma_{\ln I}^2$ from (11)]; the upper dashed curve is the theoretical result from deWolf [35] [σ_D^2 from (10)]. Solid curves are averaged observations replotted from Gracheva, Gurvich, and Kallistratova [50]. Curve 1, spherical wave; curve 2, plane wave (50-cm-diam collimator); curve 3, white light. The shaded area includes all the observations by Ochs [94] over a 1000-meter path. If Ochs' measurements are restricted to times of moderate wind (2 to 6 m/s), the mean of his observations agrees well with curve 1.

Tatarski has tried two other approaches toward predicting saturation. In [46] he tried a rather crude approach that gave a saturation curve, but the final value was an undetermined constant. In another attempt [9] he used a geometrical-optics approach that also led to saturation despite the neglect of diffraction effects. In this case his final equation was

$$\begin{aligned}\sigma_{\ln I}^2 &= 4\left[1 - \left(1 + \frac{3}{2}\sigma_G^2\right)^{-1/6}\right]\\ \sigma_G^2 &= \frac{4}{3}\pi^2 L^3 \int_0^{\infty} \Phi_n(\kappa)\kappa^5\, d\kappa.\end{aligned} \tag{11}$$

This curve is also plotted in Fig. 5.

In summary, at this time there is no well-accepted general theory for amplitude fluctuations in the saturation region. Though there are some results for the variance of the log-intensity, no method has yet predicted other quantities of interest, such as the amplitude covariance function or phase fluctuations.

Experimental Observations Compared with Theory: We have grouped the experimental observations into two categories. First, there are those measurements that we believe may be meaningfully compared with theory. In those experiments the optical configuration is close enough to the theoretical models, and the meteorological parameters are known well enough so that such a comparison should either prove or disprove the theory. Second, the bulk of the measurements are those that have been taken under such conditions that a comparison is meaningless, but they do provide numerical values showing the magnitude of the effects.

The only experimental configuration for which the meteorological parameters can be obtained is a short horizontal path close to the gound. A number of experiments of this type have been conducted, originally in the U.S.S.R. [47]–[50], [28], and more recently in the West [51]–[54]. These experiments attempt to verify (T4) or (T10). Fig. 5 shows some experimental data [52], [50] indicating a decrease in the measured variance after the onset of saturation. On the horizontal axis is the value $\sigma_{\ln I}^2$ calculated from (T4) or (T10), where C_n^2 was measured with high-speed temperature sensors. On the vertical axis is the experimental value of $\sigma_{\ln I}^2$. As is apparent, there is good agreement for $\sigma^2_{\ln I} < 2.5$, but the variance saturates near 2.5. Different saturation values are quoted by different workers, but these values appear the most reliable. The two theoretical curves of Tatarski and deWolf are shown for comparison. Gurvich *et al.* [49] have measured the ratio of the log-intensity variance of a plane wave and a spherical wave, obtaining a value of 2.3 compared to the theoretical value of 2.4. Numerous measurements [47]–[53] of the probability distribution of the intensity have shown good agreement with a log-normal distribution over short paths and fairly good agreement even in the saturation region. Fitzmaurice *et al.* [55] compared scintillations at 0.632 and 10.6 μm and found good agreement with the wavelength effects predicted in Table I.

Experimental attempts to verify Fried and Seidman's predictions [37] about the difference between a focused and a collimated beam led Khmelevtsov and Tsvyk [56] to conclude that there was no difference. Their measurements were in the weak-scattering region and, although their paper lacks the details required to judge the quality of the work, their result seems to agree with our contention that the concept of a focused beam is not very meaningful for optical propagation.

General Observations: Fig. 2 shows a one-day sample of the log-intensity variance at 490 and 1000 meters on a path close to the ground, compared with the measured value of C_n^2. The typical diurnal variation of scintillation consists of a broad maximum throughout daylight hours, sharp minima near sunrise and sunset, and highly variable effects at night. The daytime maximum reaches a broad smooth peak soon after noon, but cloud cover, either intermittent or continuous, produces a sharp drop in scintillation activity. Activity increases with wind velocity for light winds but decreases again as the wind becomes strong, mixing the air to produce an adiabatic lapse rate. Sharp minima at sunrise and sunset occur when the lapse rate, changing because of the rapidly varying solar radiation, passes through the adiabatic condition. The middle curve in Fig. 2 is typical of the diurnal behavior of scintillation. Along a 1000-meter path, during the middle of the day, the variance has become saturated and is actually smaller at 1000 meters than at 490 meters! For paths longer than 1000 meters it is difficult to calculate the expected variance since the meteorological parameters are rarely statistically homogeneous. Where most of the path is not close to the ground, the variance tends to be much lower. This may be attributed to two facts. First, the turbulence normally decreases sharply with distance above the ground. Second, for spherical waves it is only near the middle of the path that turbulence is effective in producing scintillations [see (T13)]. Measurements by Ochs *et al.* [57] over a 45-km path at night gave values of $\sigma^2_{\ln I} \approx 1.2$.

Spatial Covariance Functions for Irradiance and Log-Amplitude

Theory: Theoretically the spatial covariance function normally calculated is for log-amplitude fluctuations $B_\chi(\rho)$, but experimentally there is more interest in the covariance function for irradiance fluctuations $B_I(\rho)$. Fortunately, if we accept the log-normal probability distribution for the amplitude fluctuations, discussed in some detail previously, the relationship between $B_I(\rho)$ and $B_\chi(\rho)$ is reasonably straightforward. Let

$$\chi \equiv \ln (A/A_0) = \bar{\chi} + \chi_1, \quad \bar{\chi} = \langle \chi \rangle$$
$$I = A^2 = A_0^2 \exp (2\bar{\chi} + 2\chi_1)$$
$$B_\chi(\boldsymbol{\rho}_1, \boldsymbol{\rho}_2) = \langle \chi_1(\boldsymbol{\rho}_1)\chi_1(\boldsymbol{\rho}_2)\rangle, \tag{12}$$

where we have assumed that the mean value of χ is not zero (A_0 could be chosen such that $\bar{\chi}=0$). Then if χ follows a normal probability distribution,

$$\langle I(\boldsymbol{\rho})\rangle = A_0^2 \exp [2\bar{\chi}(\boldsymbol{\rho})] \exp [2\langle \chi_1^2(\boldsymbol{\rho})\rangle]$$
$$\langle I(\boldsymbol{\rho}_1)I(\boldsymbol{\rho}_2)\rangle = A_0^2(\boldsymbol{\rho}_1)A_0^2(\boldsymbol{\rho}_2) \exp [2\bar{\chi}(\boldsymbol{\rho}_1) + 2\bar{\chi}(\boldsymbol{\rho}_2)]$$
$$\cdot \exp \{2[\langle \chi_1^2(\boldsymbol{\rho}_1)\rangle + \langle \chi_1^2(\boldsymbol{\rho}_2)\rangle + 2B_\chi(\boldsymbol{\rho}_1, \boldsymbol{\rho}_2)]\}. \tag{13}$$

Defining the covariance function as

$$B_I(\boldsymbol{\rho}_1, \boldsymbol{\rho}_2) = \langle I(\boldsymbol{\rho}_1)I(\boldsymbol{\rho}_2)\rangle - \langle I(\boldsymbol{\rho}_1)\rangle\langle I(\boldsymbol{\rho}_2)\rangle, \tag{14}$$

we have

$$B_I(\boldsymbol{\rho}_1, \boldsymbol{\rho}_2) = A_0^2(\boldsymbol{\rho}_1)A_0^2(\boldsymbol{\rho}_2) \exp [2\bar{\chi}(\boldsymbol{\rho}_1) + 2\bar{\chi}(\boldsymbol{\rho}_2)]$$
$$\cdot \exp [2\langle \chi_1^2(\boldsymbol{\rho}_1)\rangle + 2\langle \chi_1^2(\boldsymbol{\rho}_2)\rangle]\{\exp [4B_\chi(\boldsymbol{\rho}_1, \boldsymbol{\rho}_2)] - 1\}. \tag{15}$$

Defining a normalized covariance function by

$$b_I(\boldsymbol{\rho}_1, \boldsymbol{\rho}_2) = \frac{B_I(\boldsymbol{\rho}_1, \boldsymbol{\rho}_2)}{[\langle I^2(\boldsymbol{\rho}_1)\rangle\langle I^2(\boldsymbol{\rho}_2)\rangle]^{1/2} - \langle I(\boldsymbol{\rho}_1)\rangle\langle I(\boldsymbol{\rho}_2)\rangle},$$

we have

$$b_I(\boldsymbol{\rho}_1, \boldsymbol{\rho}_2) = \frac{\exp [4B_\chi(\boldsymbol{\rho}_1, \boldsymbol{\rho}_2)] - 1}{\exp [2\langle \chi_1^2(\boldsymbol{\rho}_1)\rangle + 2\langle \chi_1^2(\boldsymbol{\rho}_2)\rangle] - 1}. \tag{16}$$

If the transmitted wave is plane, or if the statistics at $\boldsymbol{\rho}_1$ and $\boldsymbol{\rho}_2$ are the same, then the formula reduces to

$$b_I(\rho) = \frac{\exp [4B_\chi(\rho)] - 1}{\exp [4\langle \chi_1^2\rangle] - 1}. \tag{17}$$

If $\langle \chi_1^2\rangle \ll 1$, then (16) and (17) become

$$b_I(\boldsymbol{\rho}_1, \boldsymbol{\rho}_2) = \frac{2B_\chi(\boldsymbol{\rho}_1, \boldsymbol{\rho}_2)}{\langle \chi_1^2(\boldsymbol{\rho}_1)\rangle + \langle \chi_1^2(\boldsymbol{\rho}_2)\rangle} \tag{18}$$

and

$$b_I(\rho) = \frac{B_\chi(\rho)}{\langle \chi_1^2\rangle} = \frac{B_\chi(\rho)}{\sigma_\chi^2} \equiv b_\chi(\rho). \tag{19}$$

Since the equations derived theoretically are for $B_\chi(\rho)$, or $B_\chi(\boldsymbol{\rho}_1, \boldsymbol{\rho}_2)$, and since these equations are valid whether or not the amplitude distribution is log-normal, these are the equations given in Table II. In comparing Table II with experimental observations, which are usually of the covariance of intensity (irradiance) fluctuations, we may use the formulas, recognizing the assumptions made when they were derived.

The approximations involved in deriving the equations of Table II are essentially the same as those used in deriving

TABLE II

COVARIANCE OF LOG-AMPLITUDE

Case	General Random Medium	Locally Isotropic Random Medium
Plane wave, homogeneous medium	$B_\chi(\rho) = 2\pi^2 k^2 L \int_0^\infty \left(1 - \frac{k}{\kappa^2 L} \sin \frac{\kappa^2 L}{k}\right) \Phi_n(\kappa) J_0(\kappa\rho) \kappa \, d\kappa$ (T19) $B_\chi(\rho) = \frac{1}{3}\pi^2 L^3 \int_0^\infty \kappa^4 \Phi_n(\kappa) J_0(\kappa\rho)\, \kappa \, d\kappa, \quad L \ll l_0^2/\lambda$ (T20)	For $l_0^2/\lambda \ll L$, $b_\chi(\rho) = \begin{cases} 1 - 12.3 \frac{\rho^2}{(\lambda L)^{5/6} l_0^{1/3}}, & \rho \ll l_0 \\ 1 - 2.36\left(\frac{k\rho^2}{L}\right)^{5/6} + 1.71 \frac{k\rho^2}{L} - 0.024 \left(\frac{k\rho^2}{L}\right)^2 + \cdots, & l_0 \ll \rho \ll (\lambda L)^{1/2} \\ - 0.0242\left(\frac{k\rho^2}{4L}\right)^{-7/6}, & (\lambda L)^{1/2} \ll \rho \end{cases}$ (T22)* $b_\chi(\rho) = {}_1F_1(7/6, 1, -\kappa_m^2\rho^2/4), \quad L \ll l_0^2/\lambda$ (T23)*
Plane wave, smoothly varying medium	$B_\chi(\rho) = 4\pi^2 k^2 \int_0^L d\eta C_n^2(\eta) \int_0^\infty d\kappa \kappa J_0(\kappa\rho) \Phi_n^{(0)}(\kappa) \times \sin^2\left[\frac{\kappa^2(L-\eta)}{2k}\right]$ (T21)	$B_\chi(\rho) = 4\pi^2 \cdot 0.033\, k^2 \int_0^L d\eta C_n^2(\eta) \int_0^\infty d\kappa \kappa J_0(\kappa\rho) \times \kappa^{-11/3} \exp(-\kappa^2/\kappa_m^2) \sin^2\left[\frac{\kappa^2(L-\eta)}{2k}\right]$ (T24)* $B_\chi(\rho) = 9.6 l_0^{-7/3} {}_1F_1(7/6, 1, -\kappa_m^2\rho^2/4) \int_0^L C_n^2(\eta)(L-\eta)^2 d\eta, \quad L \ll l_0^2/\lambda$ (T25)*
Spherical wave, homogeneous medium	$B_\chi(\rho) = 4\pi^2 k^2 \int_0^\infty d\kappa \kappa \Phi_n(\kappa) \int_0^L d\eta J_0\left(\frac{\rho\kappa\eta}{L}\right) \times \sin^2\left[\frac{\kappa^2\eta(L-\eta)}{2kL}\right]$ (T26)	$b_\chi(\rho) = 1 - 2.2\left(\frac{k\rho^2}{L}\right)^{5/6} + 1.71 \frac{k\rho^2}{L} + 0.050\left(\frac{k\rho^2}{L}\right)^{17/6} - 0.080\left(\frac{k\rho^2}{L}\right)^2,$ $l_0^2/\lambda \ll L, \quad l_0 \ll \rho \ll (\lambda L)^{1/2}$ (T28)†
Spherical wave, smoothly varying medium	$B_\chi(\rho) = 4\pi^2 k^2 \int_0^\infty d\kappa \kappa \Phi_n^{(0)}(\kappa) \int_0^L d\eta C_n^2(\eta) J_0\left(\frac{\rho\kappa\eta}{L}\right) \times \sin^2\left[\frac{\kappa^2\eta(L-\eta)}{2kL}\right]$ (T27)	$B_\chi(\rho) = 4\pi^2 0.033 k^2 \int_0^L d\eta C_n^2(\eta) \int_0^\infty d\kappa \kappa J_0\left(\frac{\rho\kappa\eta}{L}\right) \times \kappa^{-11/3} \exp(-\kappa^2/\kappa_m^2) \sin^2\left[\frac{\kappa^2\eta(L-\eta)}{2kL}\right]$ (T29)
Beam wave, homogeneous medium	$B_\chi(\rho) = \pi^2 \int_0^L d\eta \int_0^\infty d\kappa \kappa [\{J_0(\kappa P) + J_0(\kappa P^*)\} \lvert H \rvert^2 + J_0(\kappa Q) H^2 + J_0(\kappa Q^*) H^{*2}] \Phi_n(\kappa)$ (T30)‡ where $P^2 = [(\gamma_1 y_d - i2\gamma_2 y_c)^2 + (\gamma_1 z_d - i2\gamma_2 z_c)^2]$ $Q^2 = (\gamma y_d)^2 + (\gamma z_d)^2$ $y_d = y_1 - y_2, \quad z_d = z_1 - z_2$ $y_c = \frac{1}{2}(y_1 + y_2), \quad z_c = \frac{1}{2}(z_1 + z_2)$ $H^2 = -k^2 \exp\left\{-i \frac{\gamma(L-\eta)}{k} \kappa^2\right\}$ $\gamma = \gamma_1 - i\gamma_2$	No cases worked out.
Beam wave, smoothly varying medium	Let $\Phi_n(\kappa) = C_n^2(\eta)\Phi_n^{(0)}(\kappa)$ in (T30). (T31)	No cases worked out.

* $\Phi_n(\kappa) = 0.033\, C_n^2(x) \kappa^{-11/3} \exp(-\kappa^2/\kappa_m^2)$. For homogeneous medium, $C_n^2(x) =$ constant.

† $\Phi_n(\kappa) = 0.033\, C_n^2(x) \kappa^{-11/3}$

‡ $\rho_1 = (y_1, z_1)$, $\rho_2 = (y_2, z_2)$ are the observation points referred to the center of the beam. Other symbols defined in Table I.

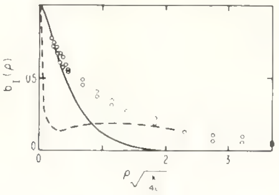

Fig. 6. Observed covariance function of a mountaintop-to-mountaintop path (dashed line) [57] and for saturation conditions over a uniform path (circles) [94] as compared with the solid curve calculated from (T28).

the expressions for the variance of the log-intensity. Again, the most critical restriction is that $\sigma_{\ln I}^2$ must be less than 2.5, or σ_χ^2 less than 0.64. Note that for values of $\sigma_{\ln I}^2 \gtrsim 2$ there may be considerable error in using (19) in place of (17). The expressions for the log-amplitude covariance function for plane and spherical waves are reasonably well accepted. In the beam-wave case, to our knowledge, there are no examples worked out for the case of locally isotropic turbulence. The major differences between the plane-wave and the spherical-wave log-amplitude covariance functions are in the point of the zero crossing and in the depth of the minimum. In the beam-wave case it seems reasonable to expect that if $W_0^2 \gg \lambda L$ and the wave is collimated or diverging, then the covariance function for the beam-wave case will be similar to the cases presented.

For spherical or plane waves it is often easier to evaluate the integrals numerically. This can be done even in the smoothly varying medium if the model is mathematically reasonable. Specific cases for light propagating through the atmosphere have been worked out by Tatarski [8], [9] and Fried and Cloud [58]. In the beam-wave case there are double integrals to evaluate, unless some reasonable approximations are found. No theoretical results now exist for the log-amplitude covariance function in the saturation region.

Experimental Observations Compared with Theory: The most striking prediction of the equations for the covariance function of log-intensity is that the covariance will fall to zero in a distance given by the Fresnel-zone size $(\lambda L)^{1/2}$. The validity of these equations when the variance is not saturated has been shown by Tatarski [8], [9] over 500- to 2000-meter paths and by Ochs *et al.* [57] on 5.5-km and 15-km paths. Fitzmaurice *et al.* [55] in a two-wavelength experiment also indicated good agreement with the wavelength dependence. Most of these measurements use a spherical wave, and no experimental work has been reported which specifically relates to beam-wave effects. There are no theoretical predictions and very few measurements of the covariance function in the saturation region. Fig. 6 shows data collected by Ochs [52] over a 1-km path when saturation existed. Similar experiments by Gracheva [48] show an increasing broadening of the covariance curves as the theoretical value for $\sigma_{\ln I}^2$ increases.

General Observations: Over nonuniform paths the character of the covariance function may change markedly; a typical example for a 45-km path, taken from Ochs *et al.* [57], is plotted in Fig. 6. This covariance curve may be duplicated by (T29) only through the use of a nonuniform distribution of turbulence, specifically by assuming all the turbulence to be concentrated near the ends of the path, a reasonable situation for the mountaintop-to-mountaintop path that was used.

Deitz [59] has published photographs of the scintillation pattern produced by a ground-to-ground laser beam, which demonstrate the striking variation and complexity of the patterns. Sometimes the patterns consist of amorphous areas of random sizes and shapes, but frequently they have a reticulated appearance with sharp lines bounding large polygonal areas.

Observations of spatial covariance are also available for starlight. Both Gaviola [60] and Mikesell *et al.* [61] have published photographs of "shadow bands," the intensity variations of light incident on the earth's surface from a single star. The shadow bands tend to be elongated rather than isotropic random variations. The width of the bands is sometimes as small as 3 or 4 cm but is more often 7 or 8 cm. Thus, if one's eyes are slightly converged by focusing on a nearby object, the two images of a star are often seen to scintillate independently. Interpreting the width of the shadow band as the width of the covariance function, we see from (T22) that the distance from the ground-based observer to the effective midpoint of the turbulent path is about 2 km for 3-cm shadow bands and 12 km for 8-cm bands. Even if the stellar-scintillation observations were made at angles of 50° or 60° from the zenith, the scintillation must have arisen from elevated layers high in the atmosphere.

Aperture Smoothing

Theory: The preceding results are appropriate only when the intensity is measured by a point receiver. If the receiving aperture is less than some critical size, such that the intensity fluctuations are correlated over its area, then the aperture will behave as a point detector. As the aperture size increases so that the intensity fluctuations are uncorrelated over the aperture, then the intensity is a spatial average over some finite region of space, and the fluctuations tend to decrease. This is a well-known experimental effect in astronomical observations with a telescope. Tatarski considered the problem in his first monograph [8] but he revised his work in his later manuscript [9] and his results agree with those of Fried [62].

The pertinent parameter in these calculations is defined in terms of the quantity

$$S \equiv \iint dy\,dz\,W(y,z)\,I(y,z), \tag{20}$$

where I is the intensity of the light falling on a point (y, z), and $W(y, z)$ is the weighting function over the aperture. Both Tatarski and Fried have used the simple assumption that $W(y, z)$ is equal to one over a circle of diameter D and zero elsewhere. Using S, we may define the aperture-averaging factor θ by

$$\theta = \frac{\sigma_S^2(D)}{\left(\frac{\pi D^2}{4}\right) B_I(0)}, \tag{21}$$

which is the ratio of the actual variance of S to the variance if the intensity were perfectly correlated over the aperture. They find

$$\theta = \frac{16}{\pi D^2} \int_0^D d\rho b_I(\rho)\rho \left\{ \cos^{-1}\left(\frac{\rho}{D}\right) - \frac{\rho}{D}\left[1 - \left(\frac{\rho}{D}\right)^2\right]^{\frac{1}{2}} \right\}. \tag{22}$$

If we assume the intensity follows a log-normal distribution, we may use (17) to get

$$\theta = \frac{16}{\pi D^2} \int_0^D \mathrm{d}\rho \frac{\exp\left[4B_\chi(\rho)\right] - 1}{\exp\left[4B_\chi(0)\right] - 1} \cdot \rho \left\{ \cos^{-1}\left(\frac{\rho}{D}\right) - \left(\frac{\rho}{D}\right)\left[1 - \left(\frac{\rho}{D}\right)^2\right]^{1/2} \right\}. \tag{23}$$

Fig. 7 is a graph from Tatarski who assumed that $\langle \chi^2 \rangle \ll 1$ and so used (19) for $b_I(\rho)$. An equation similar to (T22) was used for $B_\chi(\rho)$. Fried presents a family of curves by working with (23); but since the expressions he used for $B_\chi(\rho)$ are not valid for $\langle \chi^2 \rangle \gg 1$, some of his curves are misleading. He evaluated the space-to-ground case, but the only curves that are meaningful are for $\langle \chi^2 \rangle \ll 1$. (In Fried's paper, $C_l(0)$ corresponds to $\langle \chi^2 \rangle$.) Note that (22) and (23) are reasonably general for a circular aperture as long as the log-normal distribution for the intensity is correct, and therefore may be used in any case where $B_\chi(\rho)$ is known.

Lutomirski and Yura [63] have attempted to extend the range of the results in Fried's paper by a curve-fitting procedure. Since Fried's calculations are valid only in the region of weak fluctuations, they extend his results by assuming $B_I(\rho, L)$ is given by

$$B_I(\rho, L) = I_0^2[1 - \exp\{-2[B_\chi^R(\rho, L)]^{1/2}\}]^2, \tag{24}$$

where $B_\chi^R(\rho, L)$ is given by expression equivalent to (T22). Although (24) was chosen so that it fit the experimental results for $\rho = 0$, there is no evidence that it is a reasonable model for the covariance function, i.e., for $\rho \neq 0$.

Gracheva and Gurvich [64] used a heuristic approach based on Gracheva's measurements [48] of $B_I(\rho)$ in the saturation region. Using the measured values, they integrated (22) numerically to estimate the aperture-averaging effects. Their results for a given aperture size indicate that as the theoretical value of $\sigma_{\ln I}^2$ increases, the amount of smoothing decreases.

Experimental Observations Compared with Theory: We know of no definitive experiments over homogeneous paths concerned with aperture averaging.

General Observations: Fried *et al.* [65] used a slightly diverging laser beam over an 8-km path and found the log-amplitude variance to decrease nicely as the aperture increased from 1 mm to 10 cm, but further increase of the aperture to 89 cm produced no further decrease in scintillation and no change in the log-normal distribution of received signal. As Fried *et al.* point out, this result implies a covariance function that falls sharply in the first 10 cm but then fails to decrease further for spacings as large as 1 meter. They attribute this effect to some unexplained feature of beam-wave propagation, as opposed to spherical-wave propagation for which the theory was developed. We suspect it is simply the result of the concentration of the turbulence near the ends of the path, the only places where the beam approached within 15 meters of the ground. This would then be the same effect as seen by Ochs *et al.* [57] on their 45-km path (see Fig. 6).

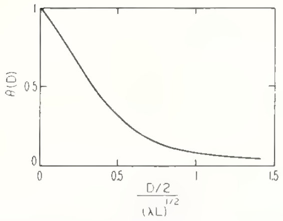

Fig. 7. Relative decrease in the variance of intensity fluctuations of a plane wave when received by an aperture of diameter D, assuming $l_0 \ll (\lambda L)^{\frac{1}{2}} < L_0$. From Tatarski [9, p. 374].

Höhn [66] used 4.5-km and 14.5-km paths and observed little or no smoothing for apertures up to 8 cm. Here again, the explanation may be that the path was not uniform or that saturation existed. The resulting large-scale covariance function would prevent aperture smoothing for modest apertures.

There have been numerous papers concerned with the dependence of stellar scintillations on zenith angle. As shown by Tatarski [8], [9], this dependence is strongly related to the aperture size used. For large apertures, i.e., $D \gg (\lambda h)^{1/2}$ (h is the scale height of the atmosphere), the variance of scintillations should vary as $(\sec Z)^3$. For $D \ll (\lambda h)^{1/2}$, the prediction for the dependence is $(\sec Z)^{11/6}$.

Probably the theories would adequately describe most observed scintillations of starlight, given detailed information about the distribution of turbulence and winds throughout the atmosphere. However, since the atmospheric parameters are not known in detail and since the signal-to-noise ratio for starlight observations is poor, comparisons between observation and theory can be only qualitative and statistical.

Poor seeing has always plagued astronomers and a huge volume of literature has accumulated to describe and interpret the effects. Meyer-Arendt and Emmanuel [67] have surveyed this literature and present more than 300 references with a brief discussion of each topic. Astronomical "seeing" is an ill-defined function of scintillation, image quality, and image motion, and its effects depend on the aperture of the optical telescope. As a result, only a small portion of the literature on astronomical seeing is useful to our discussion of scintillation. Some of the most pertinent are mentioned in the following.

In accord with theory, Megaw [68] reported that rms fluctuations vary as $(\sec Z)^{3/2}$ for zenith angles less than about 60°. He presented some data to show a weaker variation nearer the horizon. Siedentopf [69] found a variation as $(\sec Z)^{1/2}$ at zenith angles greater than about 60°, but very near the horizon he observed deviations from this law and referred to the effect as "saturation," particularly evident at the high-frequency end of the scintillation spectrum.

Observations of scintillations for propagation in the opposite direction, from earth to space, are only just becoming available. Minott [70], observing with the satellite GEOS-II a ground-based laser at a wavelength of 488 nm, found the irradiance to be log-normally distributed and to have a variance comparable with that of stellar scintillations.

Many attempts have been made to determine the height of the turbulent region responsible for scintillations by observing balloon-borne lights and comparing their scintillations with those of nearby stars. For example, Mikesell [71] observed such lights 3 mm in diameter and found them to scintillate only 1/3 to 1/10 as much as adjacent stars, even though the lights were carried to heights of 8 km. Proper interpretation of this observation demands attention to (T13) which shows that even though the balloon may have risen above all the turbulent atmosphere, the scintillations could not be expected to become fully developed. Thus the atmospheric structure is only weakly determined by such an experiment.

Temporal Power Spectrum of Scintillations

Theory: The frequency spectra of both intensity fluctuations and log-amplitude fluctuations are of interest, but since the theoretical work has been concerned with log-amplitude fluctuations, we shall concentrate on them. Whenever the conditions are such that (19) holds, then the frequency spectrum for intensity and log-amplitude fluctuations will be the same. When (19) does not hold, but reasonable expressions for $B_\chi(\rho)$ are known, the expression for the frequency spectrum of the intensity fluctuations should be obtainable using (17) and numerical techniques.

The frequency spectrum of the intensity or log-amplitude fluctuations is caused by the motion of the atmosphere. For our purposes this motion may be separated into three groups: 1) mean motion of the wind, 2) changes in wind direction, and 3) internal "mixing" motions of the atmosphere due to the evolution of turbulence. Tatarski [8], [9] appears to be the only author to have studied these effects theoretically in any detail. The most straightforward approximation involves the use of Taylor's hypothesis of "frozen" turbulence, which assumes that the temporal variations of some quantity measured at a point are caused by the uniform motion of the atmosphere past the point, and that internal motions of the atmosphere may be neglected. For propagation problems, it is assumed that the only motion of interest is perpendicular to the path.

Under the assumption of Taylor's hypothesis,

$$\chi(\boldsymbol{r}, t+\tau) = \chi(\boldsymbol{r} - \boldsymbol{v}_\perp \tau, t), \tag{25}$$

where $\boldsymbol{v}_\perp$ is the average velocity component perpendicular to the path. The time autocorrelation function is

$$R_\chi(\tau) = \langle \chi(\boldsymbol{r}, t+\tau)\chi(\boldsymbol{r}, t)\rangle \tag{26}$$

$$= B_\chi(v_\perp \tau). \tag{27}$$

The definition of the frequency spectrum,

$$\begin{aligned} w_\chi(f) &= 4\int_0^\infty \cos(2\pi f\tau) R_\chi(\tau)\, d\tau \\ &= 4\int_0^\infty \cos(2\pi f\tau) B_\chi(v_\perp \tau)\, d\tau, \end{aligned} \tag{28}$$

gives the general relation between the spatial covariance function $B_\chi(\rho)$ and the frequency spectrum $w_\chi(f)$ under the assumption of "frozen" turbulence.

Tatarski [8], [9] has evaluated the frequency spectrum for a plane wave propagating through a medium with a refractive-index spectrum given by (3). He finds

$$\begin{aligned} w_\chi(f) = 2\pi \cdot 0.033 C_n^2 k^{7/6} L^{11/6} \frac{\Omega^{-8/3}}{f_0} & \\ \cdot \Bigg\{ 1.69 - \operatorname{Im} \frac{\pi^{1/2}\exp(i\Omega^2)}{\Omega^2} \Bigg[\frac{\Gamma(7/3)}{\Gamma(17/6)} & \\ \cdot {}_1F_1(1/2, -4/3, -i\Omega^2) + (-i\Omega^2)^{7/3} \frac{\Gamma(-7/3)}{\pi^{1/2}} & \\ \cdot {}_1F_1(17/6, 10/3, -i\Omega^2) \Bigg] \Bigg\}, \quad l_0^2/\lambda \ll L & \end{aligned} \tag{29}$$

where $f_0 = v_\perp/(2\pi\lambda L)^{1/2}$, $\Omega = f/f_0$, and ${}_1F_1$ is a hypergeometric function (the Kummer function). As can be seen, the frequency spectrum depends on the characteristic frequency f_0, which is the ratio of the perpendicular component of the wind velocity to the width of the first Fresnel zone. The scale sizes of the inhomogeneities primarily responsible for the amplitude fluctuations are about the width of the first Fresnel zone. Defining $T_0 = 1/f_0$, we find that the characteristic time T_0 is equal to the time required for an inhomogeneity of size $(2\pi\lambda L)^{1/2}$ to cross the path. For $\Omega \ll 1$ or $\Omega \gg 1$, (29) is approximately equal to

$$w_\chi(f) = 0.44\,\langle\chi^2\rangle \frac{1}{f_0}\left[1 + 0.27\Omega^{4/3} + \cdots\right], \quad \Omega \ll 1 \tag{30}$$

or

$$w_\chi(f) = 1.14\langle\chi^2\rangle \frac{\Omega^{-8/3}}{f_0}, \quad \Omega \gg 1 \cdot \tag{31}$$

The dimensionless quantity $F(\Omega) = f_0 w_\chi(f)/\langle\chi^2\rangle$ is plotted in Fig. 8 where it is labeled $F(\Omega, 0)$.

Let us consider the conditions Tatarski requires for the above expressions to hold. Denote $v_\perp$ as the perpendicular and $v_\parallel$ as the parallel component of the average wind velocity. Since the fluctuations in the direction of the wind are about 0.1, if $v_\perp \sim 0.1 v_\parallel$, then the fluctuating portion of the perpendicular component is of the same order as the mean, and Taylor's hypothesis does not hold. Let v equal the magnitude of the average wind speed, $\sigma_\perp$ and σ the standard deviations of the perpendicular component and of the

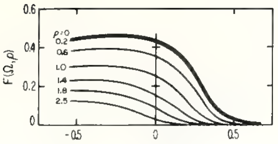

Fig. 8. Frequency spectrum of intensity fluctuations as a function of receiving aperture diameter $\rho \equiv \pi D^2/(4\lambda L)$. From Tatarski [9, p. 378].

magnitude of the wind speed, respectively, and α the angle between the wind direction and the direction of propagation. From the turbulence theory of Tatarsk: [9], $\sigma_\perp^2 = \frac{2}{3}\sigma^2$. Then

$$\frac{\sigma_\perp}{v_\perp} = \frac{0.8\,\sigma}{v \sin\alpha}.$$

Usually $\sigma/v \sim 0.1$; therefore, for $\alpha = \pi/2$, $\sigma_\perp/v_\perp \sim 10$ percent. For $\alpha \lesssim 50°$, $\sigma_\perp/v_\perp \gtrsim 1$ and the frozen hypothesis must be considered questionable.

In the limit when $\alpha = 0$, however, Tatarski [9] has estimated the frequency spectrum by considering the fluctuations in the diffraction pattern of the wave, where the perpendicular component of the velocity is considered to have a normal distribution with variance σ^2. He calculates an average spectrum, again assuming the same form for $\Phi_n(\kappa)$, as

$$\langle w_\chi(f)\rangle = \frac{4\pi(2\pi)^{1/2}\cdot 0.033k^2LC_n^2}{\sigma}\left(\frac{\pi f}{\sigma}\right)^{-8/3} \cdot \int_0^\infty \left[1 - \frac{x^2}{\Omega_1^2}\sin\frac{\Omega_1^2}{x^2}\right] e^{-x^2}\cdot K_0(x^2)x^{5/3}\,dx, \qquad l_0^2/\lambda \ll L, \qquad (32)$$

where

$$f_1 = \frac{\sigma}{\pi}(k/L)^{1/2},$$

$$\Omega_1 = \pi f(L/k)^{1/2}/\sigma = f/f_1,$$

$K_0(x) =$ a modified Bessel function.

If $\Omega \gg 1$, then

$$\langle w_\chi(f)\rangle = 0.32\frac{\langle\chi^2\rangle}{f_1}\Omega^{-8/3}, \qquad l_0^2/\lambda \ll L. \qquad (33)$$

For both cases considered (constant motion and completely random motion) for $f \gg f_1, f_0$, the spectrum decreases as $f^{-8/3}$; however, the coefficient in the second case is smaller. Since

$$\int_0^\infty \langle w_\chi(f)\rangle\,df = \int_0^\infty w_\chi(f)\,df = \langle\chi^2\rangle,$$

this implies that the spectrum in the low-frequency region must be higher for the completely random motion than for the constant motion (frozen turbulence).

In summary, Tatarski concludes that for $\sigma \ll v_\perp$, (29), (30), and (33) hold, and the spectral peak is at $f = f_0$. For $\sigma \sim v_\perp$ the maximum of the spectrum begins to move toward zero, and for $\sigma \gg v_\perp$ this maximum begins to grow.

These calculations have not considered the influence of the random motions of the medium caused by the evolution of the turbulence. Such random motion may be ignored if

$$v_\perp \gg \left[\varepsilon(\lambda L)^{1/2}\right]^{1/3}, \qquad (34)$$

where ε is the energy dissipation rate of the turbulence. Or if $v_\perp \approx 0$, $v_\perp$ is replaced by $\sigma_\perp \approx (\varepsilon L_0)^{1/3}$, leading to

$$L_0 \gg (\lambda L)^{1/2}. \qquad (35)$$

Normally this last condition is always satisfied.

Tartarski [9] also calculates the frequency spectrum for a receiver with a finite aperture. He determines the frequency spectrum of the quantity S defined in (20). Let

$$S_1 = \iint dy\,dz\,W(y,z)I_1(y,z) \qquad (36)$$

where the subscript denotes the fluctuating component. Defining

$$w_S(f) = 4\int_0^\infty \cos(2\pi f\tau)R_S(\tau)\,d\tau,$$

he then defines a relative spectrum

$$w_{S/\langle S\rangle}(f) = \frac{w_S(f)}{\langle S\rangle^2} = \frac{w_S(f)}{\left(\frac{\pi D^2}{4}\langle I\rangle\right)^2}, \qquad (37)$$

and shows that, in general, if $f \gg v_\perp/(\pi D)$, i.e., for high frequencies, the effect of the aperture is to average a number of inhomogeneities and hence to reduce substantially the spectrum compared with that of a point aperture. For $f \ll v_\perp/(\pi D)$, if the important spatial wavenumber $\kappa \ll 2/D$, the spectrum is approximately equal to that for a point aperture, but if the important spatial wavenumber $\kappa \gg 2/D$, the spectrum will also decrease substantially.

For weak fluctuations, where (19) holds, and assuming $\Phi_n(\kappa) = 0.033C_n^2\kappa^{-11/3}$, Tatarski finds for the plane-wave case

$$w_{S/\langle S\rangle}(f) = 0.67\frac{\langle\chi^2\rangle}{f_0}\int_0^\infty \left[\frac{2J_1[\rho(z+\Omega^2)^{1/2}]}{\rho(z+\Omega^2)^{1/2}}\right]^2 \cdot \left[1 - \frac{\sin(z+\Omega^2)}{z+\Omega^2}\right](z+\Omega^2)^{-11/6}z^{-1/2}\,dz, \qquad (38)$$

where

$f_0^2 = kv_\perp^2/(4\pi^2L)$
$\Omega^2 = (f/f_0)^2$
$\rho^2 = \pi D^2/2\lambda L$
$z = L\kappa^2/k$
$D =$ aperture diameter.

Note that ρ is the ratio of the aperture radius to the radius of the first Fresnel zone. Fig. 8 is a plot of

$$F(\Omega,\rho) = f_0 w_{S/\langle S\rangle}(f)/\langle\chi^2\rangle$$

as ρ is varied.

Experiments Compared with Theory: Experimental measurements verifying the theory have been discussed by

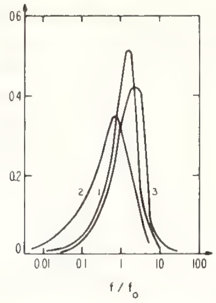

Fig. 9. Normalized frequency spectrum $u(f)=fw(f)/\int_0^\infty w(f)\,df$ for intensity fluctuations. Curve 1, plane wave; curve 2, spherical wave; curve 3, theoretical curve for plane wave. The spectra are averages of about ten different samples $[f_0=v_\perp/(2\pi\lambda L)^{\frac{1}{2}}]$. From Gurvich et al [48] .

Tatarski [8], [9] and Gurvich *et al.* [49]. Fig. 9 shows the normalized frequency spectrum for both plane and spherical waves as obtained by Gurvich. These measurements show that the predicted normalization frequency $f_0=v_\perp/(2\pi\lambda L)^{1/2}$ is very close to the actual peak, and they appear to agree well with theory for short homogeneous paths. No theoretical predictions exist for the spectrum in the saturation region, but Gracheva's measurements [48] show much more energy in the low-frequency region when compared with Fig. 9.

General Observations: We have already mentioned the discrepancies between the spatial covariance functions observed on long paths and the functions expected for ideal conditions. Similarly, we must expect that measurements of temporal power spectra will frequently differ significantly from the ideal forms given above. Thus, it may not be surprising that Ryznar [72] reports that the peak frequency of the spectrum is independent of path length, or that Höhn [73] finds the spectra unaffected by variations in receiving aperture diameter from 5 to 80 mm and states that the expected variation with $(\lambda L)^{1/2}$ does not hold. On the other hand, Gilmartin and Horning [74] observed the peak of the $fw(f)$ curve to be $f_p=Kv_\perp(\lambda L)^{-1/2}$ with K assuming values of 2.5 to 2.8. Chu [75] measured the power spectrum at three wavelengths (0.63, 3.5, and 10.6 μm) and found an essentially exponential spectrum at each wavelength, the width of the spectrum decreasing with wavelength but more slowly than $\lambda^{-1/2}$.

Temporal power spectra of stellar scintillations have been measured by many observers [71], [76]. Scintillations observed through telescopes with aperture less than about 10 cm display spectra that are nearly constant from 0.1 to 100 Hz and decrease steadily into the noise level at about 500 Hz. As the telescope aperture increases, the intensity of the scintillations is reduced at all frequencies in agreement with Fig. 8. Above about 25 Hz the reduction proceeds faster than the reciprocal of the aperture diameter. Low frequencies are enhanced as the star approaches the horizon.

Mikesell found that the higher frequencies of scintillation are enhanced when the wind speed at heights of 8 to 14 km increases. There is no evidence in his observations that the wind exactly at the tropopause is more closely related to scintillation frequency than wind at other heights in the 8-km to 14-km range. Young [77] prepared a computer program to calculate power spectra of stellar and planetary scintillations for various apertures and source sizes and used arbitrary vertical profiles of turbulence and wind velocity. He obtained good agreement with Mikesell's observed spectra [71] without invoking thin turbulent layers high in the atmosphere.

Minott [70] observed a light source carried aboard the GEOS-II satellite and found spectra similar to those of stellar scintillations. There was no evidence of a "pseudowind" caused by the motion of the line of sight across the turbulent structure of the upper atmosphere because the satellite moved so slowly that the actual winds aloft were comparable with the pseudowind.

Variation of Scintillations with Wavelength

It is common knowledge that stars near the horizon scintillate with different colors at different times, while stars higher in the sky show no such effect. Therefore, we might conclude that weak scintillations are correlated over a wavelength ratio of at least 2:1, while stronger scintillations show less correlation. Neglecting saturation effects, Fried [78] calculated that the correlation of log-amplitude should drop to 0.5 for wavelengths differing by an octave. Fitzmaurice [79] has recently measured the correlation of intensity for various wavelength separations of from 10 to 50 percent and found the correlation to be about 0.6.

VI. PHASE FLUCTUATIONS

Introduction

In general, the same considerations arise when studying phase fluctuations as when studying intensity fluctuations, though there are a few important differences. We start with (6), where the imaginary part of ψ is equal to S. For intensity fluctuations the important scale sizes of the refractive-index inhomogeneities are about the width of a Fresnel zone; for phase fluctuations the longer scales are more important. As a result, a geometrical-optics approach leads to results that are very similar to those of a diffraction theory. The importance of the large scales poses a problem since this portion of the refractive-index spectrum does not have a universal shape. Therefore, attempts to predict the variance of the phase fluctuations for the general case are meaningless. For this reason, much attention has been focused on the "phase structure function" $D_S(\rho)$ which is less sensitive to large scales, defined as follows:

$$D_S(\rho) = D_S(|\boldsymbol{\rho}|) = \langle[S_1(\boldsymbol{r}) - S_1(\boldsymbol{r} + \boldsymbol{\rho})]^2\rangle. \qquad (39)$$

Because of less theoretical and less experimental attention, the range of validity of the expressions for phase fluctuations is not as well understood as for intensity fluctuations, though there is some indication that the expressions should be valid for longer paths [10].

The probability distribution for phase fluctuations, based on the same arguments as for log-intensity, should be normal, at least where linear perturbation theory is valid. Note, however, that the fluctuations in phase about the mean value will be much greater than 2π. Therefore, while the total phase deviation from the mean has a normal distribution, the phase referred to a zero-to-2π band has a distribution that is practically uniform.

Spatial Structure Function of Phase

Table III shows equations for the phase structure function for the same cases as before, i.e., plane wave, spherical wave, and beam wave. Again we give no derivations, only references. Except for the numerical coefficients, the phase structure functions for plane waves and spherical waves are similar. It seems reasonable to expect that the beam-wave case will lie somewhere between the two but, to our knowledge, no such case has been worked out. Specific cases for a spherical wave propagating vertically through the atmosphere have been published for the wave structure function [80], [81]. The wave structure function is related to the phase and log-amplitude structure functions by the relation

$$D(\rho) = D_S(\rho) + D_\chi(\rho) \tag{40}$$

where

$$D_\chi(\rho) = 2[B_\chi(0) - B_\chi(\rho)].$$

Since the phase structure function is usually larger than the log-amplitude structure function, the wave structure function is dominated by the phase term. Therefore, the results for specific cases for the wave structure function give some insight into the behavior of the phase structure function.

The difficulties involved in optical interferometry through the open atmosphere have tended to discourage direct measurements of the phase structure function. Bertolotti *et al.* [82] and Moldon [83] observed phase differences over 4-km urban paths 25 meters or more above the ground and concluded that the phase structure function could not be construed to increase as $\rho^{5/3}$ for any $\rho > 3$ cm. Measurements of the modulation transfer function (a function of the wave structure function) by Djurle and Bäck [84] and by Coulman [85] also failed to verify the $\rho^{5/3}$ dependence, but the effect of scintillations confuses the interpretation of these measurements in terms of phase structure function.

By contrast, Bouricius and Clifford [86] observed phase structure function over a folded 50-meter path only 1.6 meters above ground and verified an increasing power-law dependence on ρ, though the exponent may be less than 5/3.

Temporal Power Spectrum of Phase

The procedure for finding the frequency spectrum of the phase fluctuations is similar to that for finding the log-intensity frequency spectrum, except that the formulas involve the structure function instead of the covariance function. Again, the simplest approach is to use Taylor's hypothesis, so that

$$S_1(\mathbf{r}, t + \tau) = S_1(\mathbf{r} - \mathbf{v}_\perp \tau, t). \tag{41}$$

Defining a time structure function $H_S(\tau)$, we get

$$H_S(\tau) \equiv \langle [S_1(\mathbf{r}, t + \tau) - S_1(\mathbf{r}, t)]^2 \rangle = D_S(\mathbf{v}_\perp \tau).$$

The structure function may be written as a spectral representation, where the frequency spectrum $w_S(f)$ is equal to the frequency spectrum defined in terms of covariance functions, provided the covariance function exists. The spectral representation is

$$H_S(\tau) = 2 \int_0^\infty [1 - \cos(2\pi f \tau)] w_S(f)\, df. \tag{42}$$

Using this approach, Tatarski [9] found for the general case

$$w_S(f) = \frac{8\pi}{v_\perp} \int_0^\infty F_S\left[\left(\kappa^2 + \frac{4\pi^2 f^2}{v_\perp^2}\right)^{1/2}, L\right] d\kappa, \tag{43}$$

where

$$F_S(\kappa, L) = \pi k^2 L \left(1 + \frac{k}{\kappa^2 L} \sin \frac{\kappa^2 L}{k}\right) \Phi_n(\kappa).$$

Assuming $\Phi_n(\kappa) = 0.033 C_n^2 \kappa^{-11/3} \exp(-\kappa^2/\kappa_m^2)$, he finds

$$\begin{aligned} w_S(f) = {} & 2\pi \cdot 0.033 C_n^2 k^{7/6} L^{11/6} \frac{\Omega^{-8/3}}{f_0} \\ & \cdot \left\{ 1.69 + \operatorname{Im} \frac{\pi^{1/2} \exp(i\Omega^2)}{\Omega^2} \left[\frac{\Gamma(7/3)}{\Gamma(17/6)} \right.\right. \\ & \cdot {}_1F_1\left(\frac{1}{2}, -\frac{4}{3}, -i\Omega^2\right) + (-i\Omega^2)^{7/3} \frac{\Gamma(-7/3)}{\pi^{1/2}} \\ & \left.\left. \cdot {}_1F_1\left(\frac{17}{6}, \frac{10}{3}, -i\Omega^2\right)\right]\right\}, \quad l_0^2/\lambda \ll L \end{aligned} \tag{44}$$

where $\Omega = f/f_0$ and $f_0 = v_\perp/(2\pi\lambda L)^{1/2}$. As one can see by comparing (44) with (29), the expression for the frequency spectrum for the phase fluctuations is the same as for log-amplitude fluctuations except for a minus sign. For $\Omega \ll 1$ and $\Omega \gg 1$, (44) becomes

$$w_S(f) = 3.28 \cdot 10^{-2} C_n^2 k^2 L v_\perp^{5/3} f^{-8/3}, \qquad \Omega \ll 1, \tag{45}$$

$$w_S(f) = 1.64 \cdot 10^{-2} C_n^2 k^2 L v_\perp^{5/3} f^{-8/3}, \qquad \Omega \gg 1. \tag{46}$$

Note that for $\Omega \gg 1$, the spectra $w_S(f)$ and $w_\chi(f)$ agree. For the two regions $\Omega \ll 1$ and $\Omega \gg 1$, the values of $w_S(f)$ differ only by a factor of 2. However, in the low-frequency region, the form for $\Phi_n(\kappa)$ is not known in general; therefore, (45) must be applied cautiously at frequencies less than $v_\perp/L_0$, where L_0 is the outer scale of turbulence.

For many applications the quantity of interest is not the frequency spectrum of the phase fluctuations but the spectrum of the fluctuations of the phase difference measured at two points separated by a distance ρ. If we define the phase difference as

$$\delta_\rho S(t) = S_1(\mathbf{r}, t) - S_1(\mathbf{r} + \boldsymbol{\rho}, t), \tag{47}$$

Tatarski [9] shows that the covariance function of the phase difference is

$$\begin{aligned} R_{\delta S}(\tau) &= \langle \delta_\rho S(t) \delta_\rho S(t + \tau) \rangle \\ &= \tfrac{1}{2}\{D_S(\boldsymbol{\rho} - \mathbf{v}_\perp \tau) + D_S(\boldsymbol{\rho} + \mathbf{v}_\perp \tau) - 2D_S(\mathbf{v}_\perp \tau)\}, \end{aligned} \tag{48}$$

using once more the frozen-turbulence hypothesis. If ρ and $v_\perp$ are parallel, then Tatarski calculates

TABLE III

STRUCTURE FUNCTION OF PHASE

Case	General Random Medium	Locally Isotropic Random Medium*
Plane wave, homogeneous medium	$D_s(\rho) = 4\pi^2 k^2 L \int_0^\infty [1 - J_0(\kappa\rho)] \times \left[1 + \frac{k}{\kappa^2 L} \sin \frac{\kappa^2 L}{k}\right] \Phi_n(\kappa)\kappa \, d\kappa$ (T32) $D_s(\rho) = 8\pi^2 k^2 L \int_0^\infty [1 - J_0(\kappa\rho)] \Phi_n(\kappa)\kappa \, d\kappa, \quad L \ll l_0^2/\lambda$ (T33)	For $l_0^2/\lambda \ll L$, $D_s(\rho) = \begin{cases} 1.64 C_n^2 k^2 L l_0^{-1/3}\left[1 + 0.87\left(\frac{l_0^2}{\lambda L}\right)^{1/6}\right]\rho^2 + \cdots, \rho \ll l_0 \\ 1.46 C_n^2 k^2 L \rho^{5/3}, \quad l_0 \ll \rho \ll (\lambda L)^{1/2} \\ 2.92 C_n^2 k^2 L \rho^{5/3}, \quad (\lambda L)^{1/2} \ll \rho \end{cases}$ For $L \ll l_0^2/\lambda$, $D_s(\rho) = 0.132\pi^2 \frac{6}{5} \Gamma\left(\frac{1}{6}\right) k^2 L C_n^2 \kappa_m^{-5/3}$ (T35) $\times \left[{}_1F_1\left(-\frac{5}{6}, 1, -\frac{\kappa_m^2 \rho^2}{4}\right) - 1\right]$ (T36)
Plane wave, smoothly varying medium	$D_s(\rho) = 8\pi^2 k^2 \int_0^L d\eta C_n^2(\eta) \int_0^\infty d\kappa\kappa [1 - J_0(\kappa\rho)] \times \Phi_n^{(0)}(\kappa) \cos^2\left[\frac{\kappa^2(L - \eta)}{2k}\right]$ (T34)	$D_s(\rho) = 8\pi^2 \cdot 0.033 k^2 \int_0^L d\eta C_n^2(\eta) \int_0^\infty d\kappa\kappa [1 - J_0(\kappa\rho)] \times \kappa^{-11/3} \exp(-\kappa^2/\kappa_m^2) \cos^2\left[\frac{\kappa^2(L - \eta)}{2k}\right]$ (T37) $D_s(\rho) = 2.92 k^2 \rho^{5/3} \int_0^L C_n^2(\eta) \, d\eta, \quad (\lambda L)^{1/2} \ll \rho$ (T38) For $L \ll l_0^2/\lambda$, $D_s(\rho) = 0.132\pi^2 \frac{6}{5} \Gamma\left(\frac{1}{6}\right) k^2 \kappa_m^{-5/3} \times \left[{}_1F_1\left(-\frac{5}{6}, 1, -\frac{\kappa_m^2 \rho^2}{4}\right) - 1\right] \int_0^L C_n^2(\eta) d\eta$ (T39)
Spherical wave, homogeneous medium	$D_s(\rho) = 8\pi^2 k^2 \int_0^\infty d\kappa\kappa \Phi_n(\kappa) \int_0^L d\eta \left[1 - J_0\left(\frac{\rho\kappa\eta}{L}\right)\right] \times \cos^2\left[\frac{\kappa^2 \eta(L - \eta)}{2kL}\right]$ (T40)	$D_s(\rho) = 1.089 k^2 C_n^2 \rho^{5/3} L - 2[B_\chi(0) - B_\chi(\rho)]$ (T42)†
Spherical wave, smoothly varying medium	$D_s(\rho) = 8\pi^2 k^2 \int_0^\infty d\kappa\kappa \Phi_n^{(0)}(\kappa) \int_0^L d\eta C_n^2(\eta) \left[1 - J_0\left(\frac{\rho\kappa\eta}{L}\right)\right] \times \cos^2\left[\frac{\kappa^2 \eta(L - \eta)}{2kL}\right]$ (T41)	$D_s(\rho) = 8\pi^2 k^2 \int_0^L d\eta C_n^2(\eta) \int_0^\infty d\kappa\kappa \left[1 - J_0\left(\frac{\rho\kappa\eta}{L}\right)\right] \times \kappa^{-11/3} \exp(-\kappa^2/\kappa_m^2) \cos^2\left[\frac{\kappa^2 \eta(L - \eta)}{2kL}\right]$ (T43)
Beam wave, homogeneous medium	$D_s(\rho) = 2\pi^2 \int_0^L d\eta \int_0^\infty d\kappa\kappa [\{J_0(i2\gamma_2\kappa\rho_1) + J_0(i2\gamma_2\kappa\rho_2) - J_0(\kappa P) - J_0(\kappa P^*)\}\lvert H\rvert^2 - \{1 - J_0(\kappa Q)\}H^2 - \{1 - J_0(\kappa Q^*)\}H^{*2}]\Phi_n(\kappa)$ (T44)‡	No cases worked out.
Beam wave, smoothly varying medium	Let $\Phi_n(\kappa) = C_n^2(\eta)\Phi_n^{(0)}(\kappa)$ in (T44). (T45)	No cases worked out.

* $\Phi_n(\kappa) = 0.033\, C_n^2(x)\kappa^{-11/3} \exp(-\kappa^2/\kappa_m^2)$ except as noted. For homogeneous medium, $C_n^2(x) =$ constant.

† $\Phi_n(\kappa) = 0.033\, C_n^2 \kappa^{-11/3}$. Also, $B_\chi(\rho)$ given by (T26) and (T28).

‡ Symbols defined in Tables I and II. Same comments as (T15) and (T30).

$$w_{\delta S}(f) = 4\sin^2\left(\frac{\pi\rho f}{v_\perp}\right) w_S(f). \tag{49}$$

Using (45) and (46), we find that (49) becomes

$$w_{\delta S}(f) = 0.132 C_n^2 k^2 L v_\perp^{5/3} \sin^2\left(\frac{\pi\rho f}{v_\perp}\right) f^{-8/3}, \quad (\lambda L)^{1/2} \ll \rho \tag{50}$$

$$w_{\delta S}(f) = 0.066 C_n^2 k^2 L v_\perp^{5/3} \sin^2\left(\frac{\pi\rho f}{v_\perp}\right) f^{-8/3}, \quad \rho \ll (\lambda L)^{1/2}. \tag{51}$$

In the low-frequency region for $f \ll v_\perp/\rho$, $w_{\delta S}(f) \sim f^2 w_S(f)$, and if ρ does not exceed L_0, then $w_{\delta S}(f) \sim f^{-2/3}$. Although there is a singularity at $f=0$, Tatarski shows that it does not contribute much energy to the spectrum of the fluctuations. Another point to note is that (49) predicts zeros or nulls in the phase-difference spectrum. These nulls result from assuming a constant wind speed, and fluctuations in wind speed smear them out. If $f > \frac{1}{2}(v_\perp^2/\sigma_v \rho)$, then the $\sin^2$ factor can be replaced by $\frac{1}{2}$, so that

$$w_{\delta S}(f) = 2 w_S(f), \qquad f > \frac{1}{2}\frac{v_\perp^2}{\sigma_v \rho}. \tag{52}$$

Note that all the specific cases for the above spectra are calculated assuming plane-wave propagation. Though we do not know of any calculations for spherical-wave or beam-wave cases, the approach is straightforward, but the mathematics may become cumbersome.

The only measurements of the spectrum of fluctuations of phase are those made incidentally to the structure function measurements of Bouricius and Clifford [86] who, for wind velocities of about 1 $\text{m}\cdot\text{s}^{-1}$ and $L=50$ meters, observed no contribution from frequencies above 15 Hz. Phase-difference spectra have not yet been measured directly but are intimately related to the angle-of-arrival spectra described in Section VII.

VII. ANGLE-OF-ARRIVAL FLUCTUATIONS

Introduction

In considering angle-of-arrival fluctuations, we must distinguish carefully among the different definitions of angle of arrival, remembering that the angle of arrival is closely tied to the equipment involved. Attempting to remove equipment considerations, Strohbehn and Clifford [30] used the direction of the wave normal at the receiving point. With this definition, the angle of arrival is proportional to the spatial derivative of the phase fluctuations. However, if one is using an interferometer, then the angle of arrival is the phase difference measured at two points separated by some distance, call it b. Obviously, the parameter b affects the measurements. If a telescope is used, the angle of arrival is closely related to the average tilt of the wave across the aperture of the telescope. In this case spatial variations in phase tend to average out if they are smaller than the diameter D of the aperture.

Variance of Angle-of-Arrival Fluctuations

Most of the theoretical work has been done by Tatarski [8], [9]; the second work is more complete. For an interferometer with separation b, the variance of the angle of arrival α is

$$\langle \alpha^2 \rangle = \sigma_\alpha^2 = \frac{D_S(b)}{k^2 b^2}, \tag{53}$$

where it has been assumed that α is small so that $\sin\alpha \approx \alpha$. Thus, the variance of the angle of arrival may be obtained from the appropriate expressions for the phase structure function given in Table III.

Tatarski [9] derives the angle-of-arrival variance for a telescope of diameter b, and the result differs from (53) by only 3 percent. For spherical-wave propagation, Gurvich *et al.* [49] give

$$\sigma_\alpha^2 = 1.05 C_n^2 b^{-1/3} L, \qquad (\lambda L)^{1/2} \ll 2b. \tag{54}$$

In (53) and (54), α corresponds to one component of the angle-of-arrival fluctuations; (54) is valid only as long as the expressions used for $D_S(\rho)$ are valid.

Gurvich and Kallistratova [87] measured the variance of angle-of-arrival fluctuations under conditions where the intensity fluctuations were saturated and not saturated. Using a telescope with a constant aperture size, they verified that (54) was correct over paths 125 and 500 meters long. The maximum values of σ_α were 15 and 25 μrad, respectively. Over a 1750-meter path the predictions were still quite good, but the measured values were somewhat lower than predicted. Similar measurements by Gurvich *et al.* [49] gave $\sigma_\alpha \sim 5$ to 20 μrad for a 650-meter path and 15 to 45 μrad for a 6500-meter path during daytime. These measurements indicate that the theoretical expressions for the phase structure function appear to be valid even when the expressions for intensity are not. More comparisons of this type are needed. Gurvich *et al.* also measured $\sigma_{\alpha,\text{pl}}^2/\sigma_{\alpha,\text{sp}}^2$ (the ratio of the plane-wave to spherical-wave variance) and found a ratio of 2.42 compared with a theoretical value of 2.75.

Kerr [88] has tabulated theoretical values for various cases.

The Covariance Function and Spectrum of Angle-of-Arrival Fluctuations

Strohbehn and Clifford [30] calculated the angle-of-arrival covariance function assuming that the angle of arrival corresponds to the normal to the wavefront. Their results are of questionable practical value since most measurement techniques do considerable averaging over the phase front.

The temporal power spectrum of angle-of-arrival fluctuations may be estimated by using some of the previous results. We have mentioned that the variance of angle-of-arrival fluctuations of an interferometer is almost identical to that of a telescope. Assuming that the same similarity holds for the spectrum, we must only find the frequency spectrum for

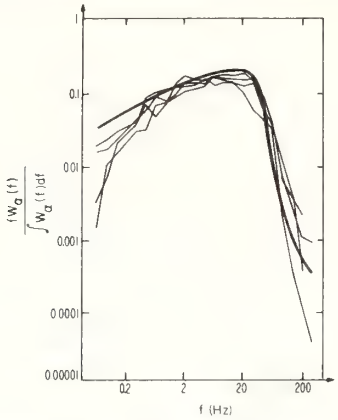

Fig. 10. Normalized frequency spectrum for angle-of-arrival fluctuations over a 650-meter path; $v_\perp = 2$ m/s. The heavy curve is theoretical From Gurvich *et al.* [49, p. 1368].

an interferometer. When considering phase fluctuations, however, we described the spectrum of the difference of the phase fluctuations at two receivers separated by distance ρ. Setting $\rho = b$ makes the spectrum $w_{\delta S}(f)$ found in Section VI also the spectrum of the angle-of-arrival fluctuations of an interferometer, provided the expressions for $w_{\delta S}(f)$ are divided by k^2; i.e., in (49) through (52), let

$$w_\alpha(f) = \frac{1}{k^2} w_{\delta S}(f).$$

Gurvich *et al.* [49] measured the frequency spectrum of angle-of-arrival fluctuations over a 650-meter path when $v_\perp$ was 2 m · s^{-1}. Fig. 10 compares their results with theory. The value of $\sigma_{\ln I}^2$ for these measurements varied between 1 and 2.2; therefore, they were not in saturation. Excellent agreement is shown.

Astronomical Refraction and Beam Wander

A ray of starlight traveling to the earth's surface undergoes a total bending τ that depends on the refractive-index profile of the atmosphere and on the elevation angle of the star above the observer's horizon. This bending is known as "astronomical refraction." For a grazing ray where the elevation angle of arrival $\theta_0 = 0$, at sea level, a typical value for τ is 10 mrad (34 minute of arc, or slightly more than the apparent angular diameter of the sun). For a surface refractivity N_s and for $\theta_0 > 170$ mrad, the approximate formula $\tau \approx N_s \cot \theta_0$ μrad is valid to within 0.1 mrad.

Garfinkel [89] prepared a computer program for calculating the astronomical refraction through an arbitrary atmospheric profile, including the U. S. Standard Atmosphere, applicable to all cases for $-\pi/2 \leq \theta_0 \leq \pi/2$. More approximate and more convenient methods for estimating astronomical refraction are discussed and tabulated by Bean and Dutton [90]. They fitted an exponential function of height to the model atmosphere and made appropriate corrections to permit the inclusion of the initial refractive-index gradient observed within the first 100 meters above ground. Their interest is the refraction of radio waves, but their methods, tables, and graphs, with the humidity taken as zero, all apply directly to the optical case. This arises from the fact that the refractive index for radio waves is the same as that for light waves, except that for the radio case a term must be added to account for a strong water-vapor effect. They have compared in detail the results of the exponential model that was corrected for surface observations with actual ray tracings through observed radiosonde profiles of the atmosphere. For elevation angles θ_0 greater than about 10 mrad the simplified method can be trusted to yield accuracies in total bending τ of a small fraction of a milliradian.

Downward bending of an optical ray also occurs on ground-to-ground paths. The curvature C of the ray is given by the transverse gradient of refractive index or, for nearly horizontal rays, by the vertical refractive-index gradient. Adopting a sign convention that downward curvature is positive and using N units so that curvature is measured in μrad/km, we can differentiate (1) to obtain

$$C = -\frac{dN}{dh} = -\frac{79}{T}\frac{dP}{dh} + \frac{79P}{T^2}\frac{dT}{dh}.$$

For sea-level conditions, where the pressure is 1013.25 mbar, the vertical pressure gradient is -121 mbar · km^{-1}, and the temperature is 20°C; the ray curvature is related to the temperature lapse rate (°C · km^{-1}) by

$$C = 32.6 + 0.93\frac{dT}{dh}\ \mu\text{rad} \cdot \text{km}^{-1}.$$

Under these conditions the temperature gradient needed to prevent bending ($C = 0$) is -35°C · km^{-1}. Although this temperature lapse rate is much greater than that for a normal atmosphere (-6°C · km^{-1}) or an adiabatic atmosphere (-10°C · km^{-1}), even greater lapse rates can occur for a short distance above a hot surface. Such conditions produce upward curvature and cause a *mirage*. On the other hand, if the vertical temperature gradient becomes strongly positive, exceeding about 134°C · km^{-1} as may happen above a cold surface, the normal downward curvature of the ray may exceed 157 μrad · km^{-1}, the curvature of the earth's surface. This produces another kind of mirage known as *looming*. The corresponding phenomenon in radio-wave propagation is known as "ducting." A review of the theory and observation of mirages, with an extensive bibliography, was recently prepared by Viezee [91].

Since the curvature of a light ray depends so strongly on the vertical temperature gradient of the atmosphere, the apparent position of a distant object or, what is equivalent, the spot produced at a distance by a fixed laser, will vary from time to time. Ochs and Lawrence [92] measured the variations of beam curvature over paths from 5 to 45 km long. A typical 24-hour measurement showed a diurnal variation of 30 μrad · km^{-1} on a 15-km path. A laser beam wanders sufficiently over long paths to exceed the minimum beamwidth permitted by the turbulent atmosphere. Thus optical systems using minimum beamwidth must employ a servo pointing system to remove variable refraction. Ochs and Lawrence [92] tracked their beams at a maximum angular rate of 7.5 μrad $\cdot$ s^{-1} and were usually, but not always, able to maintain lock. When occasionally the nearly horizontal beam passes through an elevated inversion layer of the kind described in Section III, the vertical deflections are greatly enhanced. In these cases nearly periodic vertical oscillations are common. The maximum required tracking rate is unknown; the spot position at the receiving plane may, in fact, sometimes be discontinuous. More observations are required to permit predicting the reliability of a laser-beam tracking system.

Motion of stellar images can be measured either with small apertures and long exposures, in which case the motion results in a blurred image indistinguishable from defocusing, or with large apertures and short exposures, in which case the aperture-averaging effects produce multiple overlapping images. Measurements of the latter type were made by Lese [93] with a fixed 0.9-meter telescope and exposure times of a few milliseconds. Multiple exposures produced images lying more or less on a straight line, and deviations from the straight line were caused by random atmospheric fluctuations. The mean value of such deviations was 3 μrad for zenith angles $\theta_0 \leq 1$ rad. Maximum excursions of about 5.5 μrad occurred for the largest zenith angles.

References

[1] R. S. Kennedy and S. Karp, Eds., "Optical space communications," U. S. Govt. Printing Office, NASA Rept. SP-217, Washington, D. C., 1969.

[2] *The U. S. Standard Atmosphere.* Washington, D. C.: U. S. Govt. Printing Office, 1962.

[3] J. C. Owens, "Optical refractive index of air: Dependence on pressure, temperature and composition," *Appl. Opt.*, vol. 6, no. 1, pp. 51–59, 1967.

[4] G. D. Thayer, "Optical and radar analysis of field cases," in *Scientific Study of Unidentified Flying Objects*, E. U. Condon, Ed. New York: Bantam Books, 1968, ch. III-4.

[5] J. A. Lane, "Some investigations of the structure of elevated layers in the troposphere," *J. Atmos. Terr. Phys.*, vol. 27, pp. 969–978, 1965.

[6] J. H. Richter, "High resolution tropospheric radar sounding," *Radio Sci.*, vol. 4, no. 12, pp. 1261–1268, 1969.

[7] F. H. Ludlam, "Characteristics of billow clouds and their relation to clear-air turbulence," *Quart. J. Roy. Meterorol. Soc.*, vol. 93, pp. 419–435, 1967.

[8] V. I. Tatarski, *Wave Propagation in a Turbulent Medium.* New York: McGraw-Hill, 1961 (transl. by R. S. Silverman).

[9] ——, *Propagation of Waves in a Turbulent Atmosphere.* Moscow: Nauka, 1967 (in Russian).

[10] J. W. Strohbehn, "Line-of-sight wave propagation through the turbulent atmosphere," *Proc. IEEE*, vol. 56, pp. 1301–1318, August 1968.

[11] G. K. Batchelor, *The Theory of Homogeneous Turbulence.* London: Cambridge University Press, 1959.

[12] J. L. Lumley and H. A. Panofsky, *The Structure of Atmospheric Turbulence.* New York: Wiley, 1964.

[13] A. Kolmogorov, in *Turbulence, Classic Papers on Statistical Theory*, S. K. Friedlander and L. Topper, Eds. New York: Interscience, 1961, p. 151.

[14] A. M. Obukhov, "Structure of the temperature field in a turbulent flow," *Izv. Akad. Nauk SSSR, Ser. Geogra. Geofiz.*, vol. 13, p. 58, 1949.

[15] S. Corrsin, "On the spectrum of isotropic temperature fluctuations in an isotropic turbulence," *J. Appl. Phys.*, vol. 22, pp. 469–473, 1951.

[16] S. Pond, S. D. Smith, P. F. Hamblin, and R. W. Burling, "Spectra of velocity and temperature fluctuations in the atmospheric boundary layer over the sea," *J. Atmos. Sci.*, vol. 23, pp. 376–386, 1966.

[17] B. R. Bean, "Meteorological factors affecting the fine-scale structure of the radio and optical refractive index," in *Tropospheric Wave Propagation*, Conf. Publ. 48. London: IEE, 1968.

[18] R. Bolgiano, Jr., "A theory of wavelength dependence in ultrahigh frequency transhorizon propagation based on meteorological considerations," *J. Res. Nat. Bur. Stand.*, vol. 64D, pp. 231–237, 1960.

[19] R. S. Lawrence, G. R. Ochs, and S. F. Clifford, "Measurements of atmospheric turbulence relevant to optical propagation," *J. Opt. Soc. Amer.*, vol. 60, no. 6, pp. 826–830, 1970.

[20] R. E. Hufnagel, "An improved model turbulent atmosphere," in *Restoration of Atmospherically Degraded Images.* Washington, D. C.: National Academy of Sciences, July 1966, vol. 2, pp. 14–18.

[21] D. A. Gray and A. T. Waterman, Jr., "Measurement of fine-scale atmospheric structure using an optical propagation technique," *J. Geophys. Res.*, vol. 75, no. 6, pp. 1077–1083, 1970.

[22] J. W. Strohbehn, "The feasibility of laser experiments for measuring the permittivity spectrum of the turbulent atmosphere," *J. Geophys. Res.*, vol. 75, no. 6, pp. 1067–1076, 1970.

[23] G. R. Ochs, ESSA Res. Lab., Boulder, Colo., private communication, 1970.

[24] J. B. Keller, "Wave propagation in random media," in *Proc. Symp. in Applied Mathematics*, G. Birkhoff, R. Bellman, and C. C. Lin, Eds. Providence, R. I.: American Mathematical Society, 1962, vol. 13, pp. 227–246.

[25] ——, "Stochastic equations and wave propagation in random media," in *Proc. Symp. in Applied Mathematics*, R. Bellman, Ed. Providence, R. I.: American Mathematical Society, 1964, vol. 16, pp. 145–170.

[26] W. C. Hoffman, "Wave propagation in a general random continuous medium," in *Proc. Symp. in Applied Mathematics*, R. Bellman, Ed. Providence, R. I.: American Mathematical Society, 1964, vol. 16, pp. 117–144.

[27] L. A. Chernov, *Wave Propagation in a Random Medium.* New York: McGraw-Hill, p. 168, 1960.

[28] J. W. Strohbehn, "Comments on Rytov's method," *J. Opt. Soc. Amer.*, vol. 58, pp. 139–140, 1968.

[29] R. W. Lee and J. C. Harp, "Weak scattering in random media, with applications to remote probing," *Proc. IEEE*, vol. 57, pp. 375–406, April 1969.

[30] J. W. Strohbehn and S. F. Clifford, "Polarization and angle-of-arrival fluctuations for a plane wave propagated through a turbulent medium," *IEEE Trans. Antennas Propagat.*, vol. AP-15, pp. 416–421, May 1967.

[31] A. A. M. Saleh, "An investigation of laser wave depolarization due to atmospheric transmission," *IEEE J. Quantum Electron.*, vol QE-3, pp. 540–543, November 1967.

[32] V. I. Tatarski, "The second approximation in the problem of wave propagation in media with random inhomogeneities," *Izv. Vyssh. Ucheb. Zaved. Radiofiz.*, vol. 5, pp. 490–507, 1962.

[33] W. P. Brown, Jr., "Validity of the Rytov approximation in optical propagation calculations," *J. Opt. Soc. Amer.*, vol. 56, pp. 1045–1052, 1966.

[34] D. A. deWolf, "Saturation of irradiance fluctuations due to turbulent atmosphere," *J. Opt. Soc. Amer.*, vol. 58, pp. 461–466, 1968.

[35] ——, "Are strong irradiance fluctuations log-normal or Rayleigh distributed?," *J. Opt. Soc. Amer.*, vol. 59, pp. 1455–1460, 1969.

[36] R. A. Schmeltzer, "Means, variances and covariances for laser beam propagation through a random medium," *Quart. Appl. Math.*, vol. 24, pp. 339–354, 1967.

[37] D. L. Fried and J. B. Seidman, "Laser beam scintillation in the atmosphere," *J. Opt. Soc. Amer.*, vol. 57, pp. 181–185, 1967.

[38] D. L. Fried, "Scintillation of a ground-to-space laser illuminator," *J. Opt. Soc. Amer.*, vol. 57, pp. 980–983, 1967.

[39] A. Ishimaru, "Fluctuations of a beam wave propagating through a locally homogeneous medium," *Radio Sci.*, vol. 4, pp. 295–305, 1969.

[40] ——, "Fluctuations of a focused beam wave for atmospheric turbulence probing," *Proc. IEEE*, vol. 57, pp. 407–414, April 1969.

[41] V. I. Tatarski and M. E. Gertsenshtein, "Propagation of waves in a medium with strong fluctuation of the refractive index," *Sov. Phys.—JETP* (English transl.), vol. 17, pp. 458–463, 1963.

[42] V. I. Tatarski, "Propagation of electromagnetic waves in a medium with strong dielectric constant fluctuations," *Sov. Phys.—JETP* (English transl.), vol. 19, pp. 946–953, 1964.

[43] W. P. Brown, Jr., "Coherent field in a random medium—Effective refractive index," in *Modern Optics*, J. Fox, Ed. Brooklyn, N. Y.: Polytechnic Press, 1967, pp. 717–742.

[44] ——, "Propagation in random media—Cumulative effect of weak inhomogeneities," *IEEE Trans. Antennas Propagat.*, vol. AP-15, pp. 81–89, January 1967.
[45] D. A. deWolf, "Multiple scattering in random continuum," *Radio Sci.*, vol. 2, pp. 1379–1392, 1967.
[46] V. I. Tatarski, "On strong fluctuations of light wave parameters in a turbulent medium," *Sov. Phys.—JETP* (English transl.), pp. 1083–1088, 1966.
[47] M. E. Gracheva and A. S. Gurvich, "On strong fluctuations of the intensity of light when propagating in the lower layer of the atmosphere," *Izv. Vyssh. Ucheb. Zaved. Radiofiz.*, vol. 8, pp. 717–724, 1965.
[48] M. E. Gracheva, "Research into the statistical properties of the strong fluctuations of light when propagated in the lower layer of the atmosphere," *Izv. Vyssh. Ucheb. Zaved. Radiofiz.*, vol. 10, pp. 775–787, 1967.
[49] A. S. Gurvich, M. A. Kallistratova, and N. S. Time, "Fluctuations of the parameters of a laser light wave propagating in the atmosphere," *Radiofizika*, vol. 11, pp. 1360–1370, 1968.
[50] M. E. Gracheva, A. S. Gurvich, and M. A. Kallistratova, "Measurements of the variance of 'strong' intensity fluctuations of laser radiation in the atmosphere," *Izv. Vyssh. Ucheb. Zaved. Radiofiz.*, vol. 13, pp. 55–60, 1970.
[51] G. E. Mevers, M. P. Keister, Jr., and D. L. Fried, "Saturation of scintillation," *J. Opt. Soc. Amer.*, vol. 59, no. 4, pp. 491–492, 1969.
[52] G. R. Ochs and R. S. Lawrence, "Saturation of laser-beam scintillation under conditions of strong atmospheric turbulence," *J. Opt. Soc. Amer.*, vol. 59, pp. 226–227, 1969.
[53] W. B. Johnson, "Turbulence-induced 'supersaturation' of laser scintillation observed over a 3.5-kilometer horizontal range," *Trans. Amer. Geophys. Union*, vol. 50, no. 4, p. 158, 1969 (abstract only).
[54] P. H. Deitz and N. J. Wright, "Saturation of scintillation magnitude in near-earth optical propagation," Ballistic Res. Labs., Aberdeen Proving Ground, Md., Memo. Rept. 1941, 1968.
[55] M. W. Fitzmaurice, J. L. Bufton, and P. O. Minott, "Wavelength dependence of laser-beam scintillation," *J. Opt. Soc. Amer.*, vol. 59, no. 1, pp. 7–10, 1969.
[56] S. S. Khmelevtsov and P. Sh. Tsvyk, "Intensity fluctuations of a laser beam propagating in a turbulent atmosphere," *Izv. Vyssh. Ucheb. Zaved. Radiofiz.*, vol. 13, pp. 146–148, 1970.
[57] G. R. Ochs, R. R. Bergman, and J. R. Synder, "Laser-beam scintillation over horizontal paths from 5.5 to 145 kilometers," *J. Opt. Soc. Amer.*, vol. 59, pp. 231–234, 1969.
[58] D. L. Fried and J. D. Cloud, "Propagation of an infinite plane wave in randomly inhomogeneous medium," *J. Opt. Soc. Amer.*, vol. 56, pp. 1667–1676, 1966.
[59] P. H. Deitz, "Optical method for analysis of atmospheric effects on laser beams," Ballistic Res. Labs., Aberdeen Proving Ground, Md., Memo. Rept. 1840, 1967.
[60] E. Gaviola, "On seeing, fine structure of stellar images, and inversion layer spectra," *Astron. J.*, vol. 54, no. 6, pp. 155–161, 1949.
[61] A. H. Mikesell, A. A. Hoag, and J. S. Hall, "The scintillation of starlight," *J. Opt. Soc. Amer.*, vol. 41, no. 10, pp. 689–695, 1951.
[62] D. L. Fried, "Aperture averaging of scintillation," *J. Opt. Soc. Amer.*, vol. 57, no. 2, pp. 169–175, 1967.
[63] R. F. Lutomirski and H. T. Yura, "Aperture averaging factor of a fluctuating light signal," *J. Opt. Soc. Amer.*, vol. 59, no. 9, pp. 1247–1248, 1969.
[64] M. E. Gracheva and A. S. Gurvich, "The averaging effect of the receiving aperture on light intensity fluctuations," *Izv. Vyssh. Ucheb. Zaved. Radiofiz.*, vol. 12, pp. 253–255, 1969.
[65] D. L. Fried, G. E. Mevers, and M. P. Keister, "Measurements of laser beam scintillation in the atmosphere," *J. Opt. Soc. Amer.*, vol. 57, no. 6, pp. 787–797, 1967.
[66] D. H. Höhn, "Effects of atmospheric turbulence on the transmission of a laser beam at 6328 Å. I—Distribution of intensity," *Appl. Opt.*, vol. 5, no. 9, pp. 1427–1431, 1966a.
[67] J. R. Meyer-Arendt and C. B. Emmanuel, "Optical scintillation; a survey of the literature," U. S. Govt. Printing Office, Washington, D. C., NBS Tech. Note 225, 1965.
[68] E. C. S. Megaw, "Interpretation of stellar scintillation," *Quart. J. Roy. Meteorol. Soc.*, vol. 80, pp. 248–251, 1954.
[69] H. Siedentopf, "Scintillation and photometric accuracy," in *Astronomical Optics and Related Subjects*, Z. Kopal, Ed. Amsterdam: North-Holland, 1956, pp. 317–322.
[70] P. O. Minott, Goddard Space Flight Ctr., Greenbelt, Md., private communication, 1969.
[71] A. H. Mikesell, "The scintillation of starlight," *Publ. U. S. Naval Obs.*, vol. 17, pp. 139–191, 1955.
[72] E. Ryznar, "Dependency of optical scintillation frequency on wind speed," *Appl. Opt.*, vol. 4, no. 11, pp. 1416–1418, 1965.
[73] D. H. Höhn, "Effects of atmospheric turbulence on the transmission of a laser beam at 6328 Å. II—Frequency spectra," *Appl. Opt.*, vol. 5, no. 9, pp. 1433–1436, 1966.
[74] T. J. Gilmartin and R. R. Horning, "Spectral characteristics of intensity fluctuations on a laser beam propagating in a desert atmosphere," *IEEE J. Quantum Electron.*, vol. QE-3, pp. 254–256, June 1967.
[75] T. S. Chu, "On the wavelength dependence of the spectrum of laser beams traversing the atmosphere," *Appl. Opt.*, vol. 6, no. 1, pp. 163–164, 1967.
[76] W. M. Protheroe, "Stellar scintillation," *Science*, vol. 134, no. 3490, pp. 1593–1599, 1961.
[77] A. T. Young, "Photometric error analysis. VIII—The temporal power spectrum of scintillations," *Appl. Opt.*, vol. 8, no. 5, pp. 869–885, 1969.
[78] D. L. Fried, Autonetics Div., North American Aviation, Inc., Anaheim, Calif., private communication, 1967.
[79] M. W. Fitzmaurice, Goddard Space Flight Ctr., Greenbelt, Md., private communication, 1970.
[80] D. L. Fried, "Limiting resolution looking down through the atmosphere," *J. Opt. Soc. Amer.*, vol. 56, pp. 1380–1384, 1966.
[81] F. P. Carlson and A. Ishimaru, "Propagation of spherical waves in locally homogeneous random media," *J. Opt. Soc. Amer.*, vol. 59, pp. 319–327, 1969.
[82] M. Bertolotti, M. Carnevale, L. Muzii, and D. Sette, "Interferometric study of phase fluctuations of a laser beam through the turbulent atmosphere," *Appl. Opt.*, vol. 7, no. 11, pp. 2246–2251, 1968.
[83] J. C. Moldon, "Imaging of objects viewed through a turbulent atmosphere," M.I.T. Res. Lab. Electron., Cambridge, Mass., Tech. Rept. 469, 1969.
[84] E. Djurle and A. Bäck, "Some measurements of the effect of air turbulence on photographic images," *J. Opt. Soc. Amer.*, vol. 51, no. 9, 1029–1030, 1961.
[85] C. E. Coulman, "Dependence of image quality on horizontal range in a turbulent atmosphere," *J. Opt. Soc. Amer.*, vol. 56, no. 9, pp. 1232–1238, 1966.
[86] G. M. B. Bouricius and S. F. Clifford, "Experimental study of atmospherically-induced phase fluctuations in an optical signal," *J. Opt. Soc. Amer.*, 1970 (to be published).
[87] A. S. Gurvich and M. A. Kallistratova, "Experimental investigations of fluctuations of arrival angle of light under the conditions of strong fluctuations of intensity," *Radiofizika*, vol. 11, pp. 66–71, 1968.
[88] J. R. Kerr, P. J. Titterton, A. R. Kraemer, and C. R. Cooke, "Atmospheric optical communications systems," *Proc. IEEE*, this issue, pp. 1691–1709.
[89] B. Garfinkel, "Astronomical refraction in a polytropic atmosphere," *Astron. J.*, vol. 72, no. 2, pp. 235–254, 1967.
[90] B. R. Bean and E. J. Dutton, *Radio Meteorology*. New York: Dover 1968.
[91] W. Viezee, "Optical mirage," in *Scientific Study of Unidentified Flying Objects*, E. U. Condon, Ed. New York: Bantam Books, 1968, ch. VI-4.
[92] G. R. Ochs and R. S. Lawrence, "Measurements of laser beam spread and curvature over near-horizontal atmospheric paths," U. S. Govt. Printing Office, Washington, D. C., ESSA Tech. Rept. ERL 106-WPL 6, 1969.
[93] W. G. Lese, Jr., "Stellar image excursions caused by random atmospheric refraction," Ballistic Res. Labs., Aberdeen Proving Ground, Md., Memo. Rept. 2014, 1969.
[94] G. R. Ochs, "Measurements of 0.63 μm laser-beam scintillation in strong atmospheric turbulence," U. S. Govt. Printing Office, Washington, D. C., ESSA Tech. Rept. ERL 154- WPL 10, 1970.
[95] E. Brookner, "Atmospheric propagation and communication channel model for laser wavelengths," *IEEE Trans. Commun. Technol.*, vol. COM-18, pp. 396–416, August 1970.

Reprinted from the PROCEEDINGS OF THE IEEE
VOL. 58, NO. 10, OCTOBER, 1970
pp. 1523–1545

COPYRIGHT © 1970—THE INSTITUTE OF ELECTRICAL AND ELECTRONICS ENGINEERS, INC.
PRINTED IN THE U.S.A.

Reprinted from JOURNAL OF THE OPTICAL SOCIETY OF AMERICA, Vol. 60, No. 11, 1484–1489, November 1970

Experimental Study of Atmospherically Induced Phase Fluctuations in an Optical Signal

G. M. B. BOURICIUS AND S. F. CLIFFORD
ESSA Research Laboratories, Boulder, Colorado 80302

(Received 12 February 1970)

We present the results of measurements of the optical phase variations on a short line-of-sight path through the turbulent atmosphere. A helium–neon laser (6328 Å) propagates along a folded 50-m path that is one arm of a Michelson interferometer, and its interference fringes are observed. A measured time-lagged structure function, found by using Taylor's hypothesis, compares well with the theoretical predictions of Tatarski for a broad range of effective separations, in contrast with earlier observations. Simultaneous measurements of C_n^2 are made to facilitate comparison with theory. Values of the outer scale, deduced from temperature measurements at a different time at the same location, indicate excellent agreement with the spacing corresponding to the knee of the observed phase structure function, a result predicted by Tatarski's theory and not previously observed.

INDEX HEADINGS: Inhomogeneous media; Coherence; Atmospheric optics.

When a light beam traverses the turbulent atmosphere it suffers distortion due to random refractive-index variations. We concern ourselves here with the fluctuations that the refractive turbulence produces in the received optical phase. These fluctuations limit the maximum useful aperture for optical heterodyne receivers and have detrimental effects on the resolution of imaging systems. Hence, a study of the signal degradation due to the atmospherically induced phase perturbations is relevant to both communications and optics.

Many authors[1–4] consider theoretical predictions of the various statistical properties of the phase. However, there are few direct optical-phase measurements. Gurvich *et al.*,[5,6] while measuring angle-of-arrival variance, have effectively observed the behavior of the phase structure function as a function of path and intensity of turbulence at a single separation. There exists, to our knowledge, only one direct experimental measurement of the phase structure function,[7] for variable separations, although others have measured it indirectly through the modulation transfer function.[8–10] These measurements, especially the work of Bertolotti *et al.*,[7] have raised serious questions about the theoretical prediction of the form of the phase structure function advanced by Tatarski. One goal of our research is to resolve some of the questions raised by their measurements.

Tatarski predicted that the phase structure function of an initially plane wave passing through locally homogeneous and isotropic turbulence, measured at a given position along the propagation path, will have the form

$$D_\phi(\rho)=2.91k^2LC_n^2\rho^{5/3};\quad \rho=|\boldsymbol{\rho}_1-\boldsymbol{\rho}_2|. \qquad (1)$$

Here $\kappa=2\pi/\lambda$ is the wavenumber, L the path length, and C_n^2 a parameter representing the intensity of the refractive turbulence. The vectors $\boldsymbol{\rho}_1$ and $\boldsymbol{\rho}_2$ represent points in the plane perpendicular to the axis of propagation. The form of Eq. (1) is expected to be valid for separations, ρ, greater than a Fresnel zone, $(\lambda L)^{\frac{1}{2}}$, up to the outer scale of turbulence, L_o. In another paper Tatarski[11] discusses the limitations of Eq. (1) and states that its range of validity is restricted to the condition $D_\phi(\rho)\ll\pi$. Strohbehn,[12] using this restriction, found that, for strong turbulence ($C_n^2\geq 4\times10^{-14}$ m$^{-\frac{2}{3}}$) and a path length of 100 m or more, Eq. (1) would be valid for separations of only a few centimeters. However, in his later work Tatarski dropped the restriction and implied that the phase results have broader validity.

The measurements of Bertolotti *et al.*[7] indicated that the phase structure function does not follow the 5/3 law for separations greater than a few centimeters. They assumed that the law holds below that value but presented no experimental verification. There are at least three interpretations of Bertolotti's result: (1) The outer scale of turbulence is only a few centimeters instead of a few meters, as is generally believed, or (2) Tatarski's original contention that his phase results are not valid for $D_\phi>\pi$ is correct, or (3) the meteorological situation over Bertolotti's path did not satisfy the conditions for homogeneous turbulence. If the second interpretation were true, the phase theory would have a range of validity for strong refractive turbulence that would be about as limited as that of the theory for log-amplitude fluctuations.

In order to resolve the status of the phase theory, we must have careful measurements of the phase structure function for different path lengths under a wide variety of meteorological conditions, and supporting meteorological data consisting of temperature, humidity, pressure, and wind information. We report here the initial results of such a measurement program.

EQUIPMENT CONFIGURATION AND MEASUREMENTS

Our measurements were made at the ESSA Table Mountain Research Facility, located 10 miles north of Boulder, Colorado. The terrain is flat and the semiarid vegetation is less than 60 cm in height. We placed a Michelson-type interferometer on a 1.6-m concrete pillar with its movable mirror on a similar pillar at a distance of 25 m. We installed a differential temperature sensor near the midpoint of the light path, 0.5 m off the beam axis and at the same 1.6-m height as the collimated laser beam. This sensor, described by Ochs,[13] contains two resistance thermometers, made from 2-μm-diam platinum wire, spaced 10 cm vertically. A propeller-driven anemometer was located about 5 m from the midpoint of the path. The data used in this paper were all obtained between 5 and 6 h after sundown.

The laser beam propagates along the 25-m path and returns while the transverse wind speed, v_n, and the intensity of the refractive-index fluctuations are monitored. The interferometer has a conventional movable mirror that may be located at an arbitrary distance (we used 25 m) from the rest of the instrument. A highly stabilized He–Ne laser provides the light. As is shown in Fig. 1, a small portion of the laser power is extracted from the beam by a plain-glass beam splitter and monitored by detector D_3. The beam then passes through the plane-of-polarization rotator that sets the polarization plane about 45° to the horizontal. This angle may be adjusted to obtain maximum fringe visibility. The beam splits at the next beam splitter into approximately equal portions. The reference beam passes through the retardation plate, R, is reflected by first-surface mirrors, M, and arrives at the next beam splitter where it combines with the returning long-path beam, to produce the observed interference fringes. Detector D_4 monitors the returning beam flux.

Although a single detector can reliably count fringes, it is necessary to use a second detector, out of phase with the first, in order to determine unambiguously the direction of fringe motion. It is most convenient for the two signals to be 90° out of phase. To obtain two such signals in quadrature, we use a retardation plate to delay the horizontally polarized component 90° relative to the vertically polarized component of the reference beam. The Wollaston prism separates the two polarized components and detectors D_1 and D_2 measure their fluxes as functions of time.

Amplifiers with adjustable bias and gain settings and adder–subtracter circuits compose a real-time analog computer that uses the signals from the four detectors as inputs and furnishes two output voltages,

$$E_x(t) = AF\cos\phi, \qquad (2)$$

and

$$E_y(t) = BAF\sin\phi. \qquad (3)$$

The constant B is determined while adjusting the instrument, A is the measured laser power, and F^2 is the measured returning beam flux. The phase angle, $\phi(t)$, is the difference of phase between the reference beam and the returning long-path beam.

The output voltages, Eqs. (2) and (3), are recorded on an analog magnetic tape. Simultaneously with these tape recordings, we record, on a paper chart,

(1) wind speed and direction,

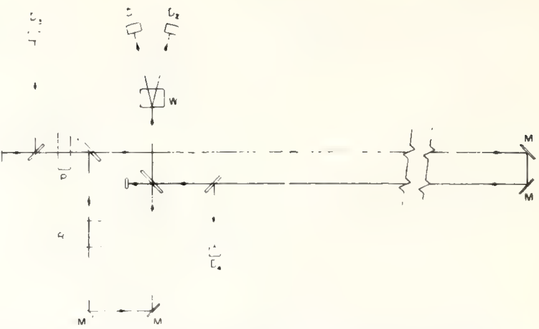

FIG. 1. The optical-phase-measuring instrument, illustrating the relative position of half-wave plate, P, retardation plate, R, Wollaston prism, W, photodetectors, D_i, and mirrors, M.

(2) relative laser power. This signal comes from interferometer detector D_3, Fig. 1, and

(3) root-mean-square temperature difference between two vertically spaced probes.

While these data are being recorded, the mean air temperature, barometric pressure, and humidity are observed and recorded from time to time.

DATA REDUCTION

As part of our analysis of the phase data, we wish to relate its fluctuations to the variations of some local measure of atmospheric conditions. Only the variations of temperature affect the propagation of visible light. We measured the temperature at two points separated vertically by 10 cm. The rms difference of these values, as a function of time, is read directly from the paper-chart recording.

The temperature difference, $(T_2 - T_1)$, is related to the temperature structure parameter, $C_T{}^2$, by

$$C_T{}^2 = \frac{\langle (T_2 - T_1)^2 \rangle_{\text{av}}}{\rho^\nu}, \qquad (4)$$

where ρ^ν is the power law of the temperature structure function. We assumed $\upsilon = \frac{2}{3}$ for our work. To obtain the refractive-index structure parameter, $C_n{}^2$, we use[14]

$$n = 1 + (77.6P/T)(1 + 0.00753/\lambda^2) \times 10^{-6}. \qquad (5)$$

Here n is the refractive index, λ is the wavelength of the light, and P is the barometric pressure. Taking the partial derivative of Eq. (5) with respect to temperature and noting the definitions of $C_n{}^2$ and $C_T{}^2$, we obtain for our wavelength 0.6328 μm,

$$C_n{}^2 = [(79P/T^2) \times 10^{-6}]^2 C_T{}^2.$$

We determine $C_T{}^2$ from Eq. (4). Experimentally, it is more convenient to measure $\langle T_2 - T_1 \rangle_{\text{av}}{}^2$ than $\langle (T_2 - T_1)^2 \rangle_{\text{av}}$. They are related by a constant factor for a given probability distribution of the temperature fluctuations. Lawrence *et al.*[15] have determined this

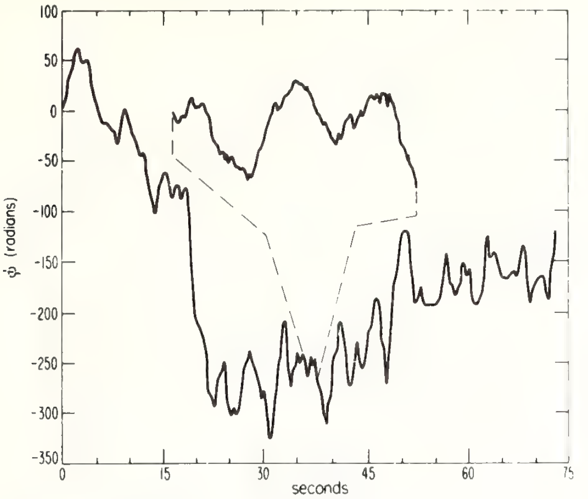

FIG. 2. A typical run of phase as a function of time. The expanded section has been magnified 5× in the vertical direction and 20× in the horizontal direction.

factor to be 2.48 for temperature variations at 2 m above the ground for a wide range of atmospheric conditions. Thus, in the absence ot noise, we use

$$C_n{}^2=2.48\left[\frac{79P}{T^2}\times10^{-6}\right]^2\frac{\langle|T_2-T_1|\rangle^2{}_{\text{av}}}{\rho^{\frac{2}{3}}}\tag{6}$$

as a measure of the strength of the refractive inhomogeneities. The measured values of P and T were 831.2 mb and 279°, respectively. Equation (6) was used directly, along with the probe spacing ($\rho=0.1$ m), to determine the refractive-index structure parameter, $C_n{}^2$, for each of our nine runs. The wind speed and direction, read from a chart recording, were used to estimate the average transverse wind component.

The two signals, $E_x(t)$ and $E_y(t)$ [see Eqs. (2) and (3)], containing the time-varying phase information, along with the necessary calibration signals, were played back from the magnetic tape through an analog-to-digital converter, the output being recorded on digital magnetic tape. From this tape, a computer program calculated

$$\phi(t)=\tan^{-1}[(E_y/B)/E_x],$$

and the relative returning beam flux,

$$I(t)=[E_x{}^2+(E_y/B)^2]/A^2=F^2.$$

Figure 2 shows the phase as a function of time for a typical data run of 73 s.

During the analog-to-digital conversion, the analog data were sampled at the rate of 137 samples/s. The power spectrum of the time series of phase samplings was obtained to determine whether our sampling rate, with a Nyquist frequency of 68.5 Hz, had been sufficiently rapid. In obtaining the power spectrum, we used deviations from a running average over a 4-s time interval, therefore the frequencies below 0.25 Hz are highly attenuated. The spectrum exhibits a rapid decrease and no important contributions beyond 15 Hz. Because the spectrum exhibits no significant amplitude near the Nyquist frequency, we conclude that the sampling rate was more than adequate.

The power spectrum appears to decay somewhat slower than the $f^{-8/3}$ predicted by Tatarski.[16] This is consistent with our observation (see below and Ref. 15) that the temperature structure function rises more slowly for our experimental conditions than the usually assumed $\frac{2}{3}$ law of Kolmogorov.

From the decay of the phase power spectrum, it is apparent that any laser frequency noise, arising from wind-induced acoustic vibrations at frequencies above 15 Hz, did not affect our results. To check laser noise at the lower end of the spectrum, the system was tested in an enclosure relatively free from temperature gradients. The laser was subjected to acoustic noise and simulated wind from a blower. We observed no fringe blurring, caused by high frequencies, but a low-frequency fringe motion of less than one tenth of a fringe was detected. This would cause less than a 1-rad^2 error in the measured structure function.

The phase data generated as described above are used to obtain a time-lagged structure function. The time interval between phase values is 0.0073 s. The time lags for obtaining the phase structure function are thus restricted to multiples of this unit,

$$D_\phi(n)=\frac{1}{m}\sum_{i=1}^{m}[\phi_i-\phi_{i+n}]^2,$$

where m is the total number of phase samples used and varies between 2000 and 10 000 for each run. No significant changes of the shape of the structure function occurred for values of m greater than 2000. The final results were based on $m=10\,000$.

ANALYSIS OF THE MEASURED STRUCTURE FUNCTION

The experimental results we describe below are based on the assumption that the temperature field does not change appreciably in a time interval τ and is merely carried across the path by the mean transverse wind, $\bar{v}_n$. Then the random field representing the phase fluctuations at a point $\boldsymbol{\rho}$ and time $t+\tau$ coincides with the field at a point $\boldsymbol{\rho}-\mathbf{v}_n\tau$ at the time t, and therefore $D_\phi(\rho)=D_\phi(\bar{v}_n\tau)$. This assumption, called Taylor's hypothesis, has several obvious difficulties. First, it requires that the significant time changes in the atmospheric variables are due to translational motions of the air and not to thermodynamic processes such as convection or decay of turbulence. Second, it assumes that the wind velocity is uniform along the path, an assumption that severely limits the range of path lengths for which this method is applicable. The major advantage of this measuring technique is that it produces a large number of data points without a corresponding increase of experimental complexity, as would be the case if the structure function were measured directly, by use of a large number of spacings either simultaneously or in rapid sequence.

The validity of Taylor's hypothesis strongly depends upon the optical parameter being measured. Each parameter of the optical beam is sensitive to different regions of the spectrum of turbulence. Tatarski shows that for amplitude fluctuations, the validity of this assumption requires that $(\lambda L)^{\frac{1}{2}} \ll L_0$. However, the turbulence scales most effective in producing phase variations are approximately the size of the outer scale. Tatarski[1] indicates that, for phase measurements, Taylor's hypothesis should be valid for delays as long as a few seconds. Direct measurements of Ochs at ESSA Laboratories, who obtained the time-lagged cross correlation of two temperature sensors spaced along the wind and used the criterion that a maximum correlation of less than 0.5 implies failure of this hypothesis for that separation, indicated validity for time delays greater than 1.5 s (The wind velocity was steady at 3 m/s during his observations.) Ochs's measurement weighted equally the contributions from all turbulence scales, to give an effective eddy lifetime. Since the lifetime is proportional to eddy size,[1] we expect that an even longer lag would result if larger scales in the spectrum of turbulence were emphasized. We arbitrarily chose to use a time delay of 3 s to account for the large scales that are most effective in producing phase perturbations. This we assumed to be the maximum allowable time lag for computing the phase structure function, and our analysis has been conducted accordingly. The results below indicate that our approach was sound because a failure of Taylor's hypothesis would have caused a premature saturation of the measured phase structure function, an effect that did not occur.

Our experiment was conducted on a total path of 50 m. Nine runs were made, of which three were discarded because of inadequate transverse winds. Of the six remaining runs, the first and last groups of three were consecutive, with 30 min between each group.

Table I. Transverse wind speed and intensity of turbulence for each run.

Run No.	Transverse wind speed (cm sec^{-1})	$C_n^2(\mathrm{m}^{-\frac{2}{3}})$
1	57	4.8×10^{-13}
2	37	2.6×10^{-13}
3	39	3.0×10^{-13}
4	29	9.2×10^{-13}
5	72	5.9×10^{-13}
6	82	4.3×10^{-13}

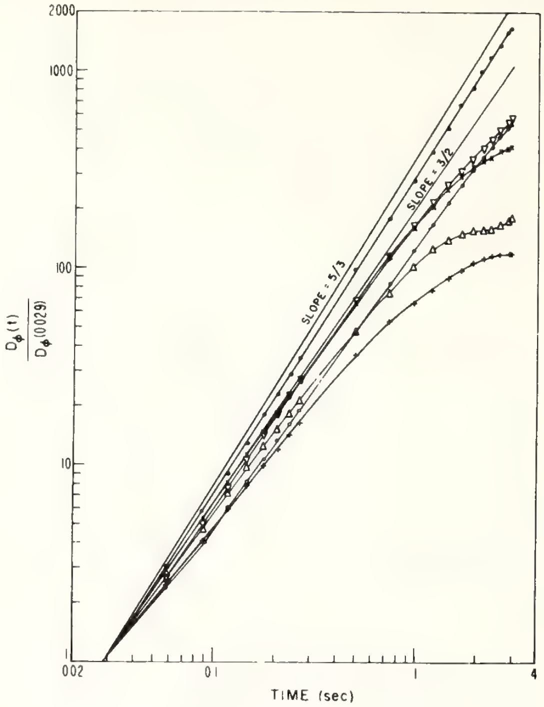

Fig. 3. The time-lagged phase structure function normalized to its value at 0.029 s for each of six runs. The labeled straight lines are theoretical curves. The run numbers and associated symbols are, 1—×, 2—△, 3—+, 4—○, 5—▽, 6—●.

Figure 3 illustrates the measured phase structure function vs time lag for each of the six runs. The curves are all normalized to their value at a time lag of 0.029 s to facilitate comparison of slopes. From these results it appears that the structure functions may not follow the predicted 5/3 power law. They rise more slowly, possibly in agreement with the temperature data reported by Lawrence *et al.*[15] whose daytime observations indicated a slope on a log–log plot much closer to $\frac{1}{2}$ than the predicted $\frac{2}{3}$. For such a case, the phase structure function would have a slope of $\frac{3}{2}$. Their nighttime observations show a much more variable set of curves, most of which exhibit slopes less than $\frac{2}{3}$. The curves of Fig. 3 were drawn vs time lag in order to avoid the uncertainty that would have been introduced by use of the average wind along the path to compute the equivalent value of the spacing according to the formula $\rho=\bar{v}_n\tau$. The minimum transverse wind speed for all runs was 29 cm/s; therefore, all the curves in the figure extend to at least 87-cm effective spacing.

Table I shows the values of transverse wind speed and intensity of turbulence, C_n^2, for each of our six runs. Using the measured transverse winds and the values of the time-lagged structure function, we obtain the curves in Fig. 4. (Taylor's hypothesis must certainly apply for our data in all but runs 4 and 5. Except for these runs the measured variance of the normal wind

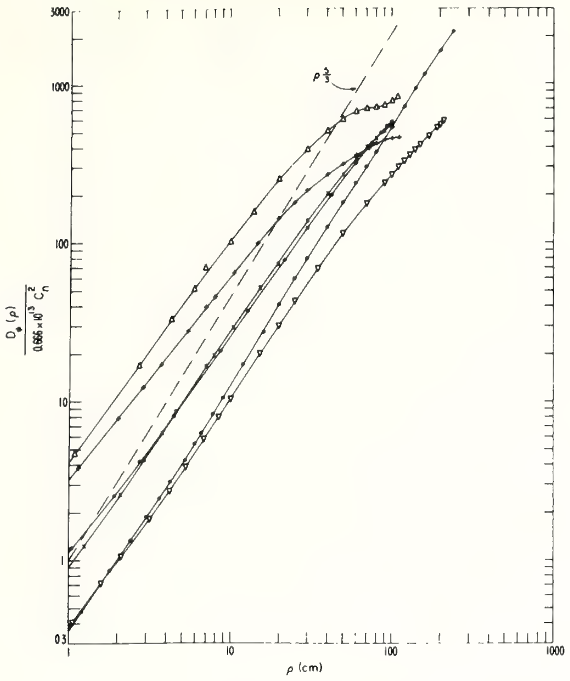

FIG. 4. The phase structure function, normalized by the coefficient of the theoretically predicted power law using the observed temperature structure parameter, is plotted vs separation. The dotted line is a theoretical curve that applies for all six runs.

component was much less than 10% of the normal wind.) The curves were normalized by inserting the path length, $L=50$ m, and the wavelength of light, $\lambda=6328$ Å, into Eq. (1). Then

$$D_\phi(\rho)=6.66\times10^{12}C_n^2\rho^{5/3},$$

where ρ is now given in centimeters. Using the values listed in Table I for C_n^2, each run shown in Fig. 4 was normalized by the factor $6.66\times10^{12}\ C_n^2$ to make the curves independent of the changes in the level of turbulence and therefore easier to compare. The curves follow a power law quite closely until separations on the order of 1 m. This compares well with a nighttime measurement of the outer scale by Ochs at the same location and the same height above the ground, inferred from the knee of the temperature structure function measured by separating two sensors until saturation occurred.

It is apparent from Fig. 4 that our results are significantly different from those of Bertolotti *et al.*[7] The phase structure function follows a power law for a large range of separations up to and sometimes exceeding 1 m, instead of saturating at distances of less than 3 cm as was true for their work. The results appear to correlate well with the measured temperature structure function according to the theoretical prediction [Eq. (1)].

CONCLUSIONS AND PLANS FOR FUTURE WORK

Our experimental results are well predicted by Tatarski's theory over a large range of spacings if, close to the ground, we allow for a reasonable departure of the spectrum of turbulence from the usual Kolmogorov spectrum. This conclusion disagrees with the results of Bertolotti *et al.* who found disagreement with the theory at separations greater than a few centimeters. Differences between our experimental arrangement and theirs should be noted. Our propagation path of 50 m is over a uniform flat terrain with the beam about 1.6 m above and parallel to the ground. Their paths were longer (0.5–3.5 km) and were 25–30 m above a city. It is difficult to argue the relative merits of the two experimental locales, but it is certain that ours contained fewer extraneous atmospheric variables.

We indicated previously that there are several possible explanations of their results. It is interesting to consider the results of our work in that light. Measurements of the outer scale, taken in conjunction with our experiments, show excellent agreement with the phase data. The knee of the phase structure functions occur at separations on the order of 1 m, and this compares well with the measured outer scale. As for uncertainties of our wind measurements, they would have had to be in error by a factor of 10 to move the saturation point of the phase structure function down to a few centimeters. It therefore appears very unlikely that juggling the size of the outer scale affords much insight into the results of Bertolotti *et al.* The other possibility, mentioned above, was that of exceeding the range of validity of the phase theory. In the plan of our experiment, a path length of 50 m was chosen, sufficiently short to be within the range $D_\phi(\rho)<\pi$ for spacings up to the outer scale of turbulence. However, the particular night that data were taken, C_n^2 indicated very strong turbulence, as is seen in Table I. For such strong turbulence, the restriction $D_\phi(\rho)<\pi$ implies that Eq. (1) should be valid only for separations less than a few centimeters.[12] However, the measured phase agrees with the theory for separations up to 1 m! Apparently the condition $D_\phi(\rho)<\pi$ may be relaxed considerably, as was thought by Tatarski, and the phase theory is adequate, at least for distances up to 50 m, for propagation near the ground.

More work needs to be done to compare the theory with measurements at different heights above the ground, at different path lengths, and under a wide variety of atmospheric conditions. We intend to take measurements on a 1-km path, instrumented with anemometers and temperature sensors. Using the resulting wind and temperature-structure profiles along the path, we hope to determine the relation between the observed temperature and wind data and the measured phase. We are also completing a multiple-aperture interferometer which has several spacing stops and will measure the structure function directly. Comparing the two techniques, we shall be able to test directly the validity of Taylor's hypothesis for optical phase, and perhaps take advantage of its simplifications in future phase measurements at different heights and under more variable atmospheric conditions.

REFERENCES

[1] V. I. Tatarski, *Wave Propagation in a Turbulent Medium* (McGraw-Hill, New York, 1960).

[2] R. A. Schmeltzer, Quart. Appl. Math. **24**, 339 (1967).

[3] D. L. Fried, J. Opt. Soc. Am. **57**, 175 (1967).

[4] P. Beckmann, Radio Sci. **69D**, 629 (1965).

[5] A. S. Gurvich and M. A. Kallistratova, Radiofizika **11**, 66 (1968).

[6] A. S. Gurvich and M. A. Kallistratova, N. S. Time **11**, 1360 (1968).

[7] M. Bertolotti, M. Carnevale, L. Muzii, and D. Sette, Appl. Opt. **7**, 2246 (1968).

[8] E. Djurle and A. Bäck, J. Opt. Soc. Am. **51**, 1029 (1961).

[9] C. E. Coulman, J. Opt. Soc. Am. **56**, 1232 (1966).

[10] J. D. Gaskill, J. Opt. Soc. Am. **59**, 308 (1969).

[11] V. I. Tatarski, Radofizika **5**, 490 (1962).

[12] J. W. Strohbehn, Proc. IEEE **6G**, 1301 (1968).

[13] G. R. Ochs, ESSA Tech. Rep. IER47-ITSA46 (U. S. Govt. Printing Office, Washington, D. C., 1967).

[14] *Handbook of Geophysics and Space Environments*, edited by S. L. Valley (McGraw-Hill, New York, 1965).

[15] R. S. Lawrence, G. R. Ochs, and S. F. Clifford, J. Opt. Soc. Am. **60**, 826 (1970).

[16] V. I. Tatarski, *Propagation of Waves in a Turbulent Atmosphere* (Nauka, Moscow, 1967).

Reprinted from The Review of Scientific Instruments 41, No. 12, 1800-1803, 1970.

An Optical Interferometer Using Polarization Coding to Obtain Quadrature Phase Components

G. M. B. Bouricius and S. F. Clifford
ESSA Research Laboratories, Boulder, Colorado 80302

(Received 20 August 1970)

We have demonstrated the feasibility of using polarization coding in an interferometric measurement of optical phase. Phase variations can be followed continuously, relative to the beginning of any desired time interval. Typical phase fluctuations of a laser beam traversing the open turbulent atmosphere are presented.

INTRODUCTION

THE phase of a light beam propagated through the free atmosphere will vary with time because the optical path length is time dependent. To test theories of the statistical properties of phase variations or establish design parameters for optical systems, it is necessary to study the optical phase fluctuations experimentally. Previous workers, all using laser sources, have employed various devices for obtaining absolute phase measurements. Buck[1] used a Michelson interferometer. Because of laser frequency instability, an equal arm arrangement was needed that called for one arm to be shielded from atmospheric effects. (The shielding becomes unwieldly for long path lengths.) To obtain two signals with a 90° phase difference for determining direction of fringe motion, he adjusted two photomultipliers to view different parts of the fringe system. Unfortunately, variations in fringe spacing render that method impractical in the open atmosphere. Other experimenters have obtained the relative phase of two open air optical paths rather than the phase variations of a single path. Burlamacchi *et al.*[2] used a grating interferometer and a rotating mirror to display a portion of the fringe system on a cathode ray oscilloscope. The display was then photographed for analysis. Moldon[3] moved a Ronchi ruling back and forth to modulate the optical signal. In this system the useful observation time interval is limited because the signal phase is lost each time the motion of the ruling is reversed. Bertolotti *et al.*[4] obtained interference patterns on a screen and photographed them with a continuously recording camera to produce pictures for data analysis.

Our instrument has several advantages over the previous methods: No long path shielding is needed because of improved lasers, no photography is involved, and no rotating machinery is used. We obtain continuous phase measurements using only one portion of a polarization coded fringe system.

THEORY

We have constructed a two-beam interferometer with a long arm containing an atmospheric path of many meters and a reference path of 60 cm. A photomultiplier detector monitors the fringe pattern. While a single detector observing the fringe pattern can reliably count the passage of fringes, it is necessary to add a second detector which produces a signal out of phase with the first to obtain unambiguous direction of fringe motion and, thus, phase. We have used a single aperture so that both detectors view the same portion of the fringe system. It turns out to be most convenient for data reduction purposes if the two signals have 90° phase difference. To obtain two such signals in quadrature, we employ perpendicular polarizations of the laser output and place a retardation plate in the reference arm of one of the polarizations; thus, the light input to the detectors comes from two fringe patterns, one from each polarized component, 90° out of phase, but otherwise identical.

Figure 1 is a block diagram of the optical assembly. The half-wave plate P rotates the laser output to a plane about 45° to the horizontal. This angle may be adjusted to obtain maximum fringe visibility. We now consider the system using the horizontal and vertical components of the polarized input to the first beam splitter. If the input beam amplitude is A, it has complex components A_x and A_y. As the input light beam strikes the various elements, each has its own transmission, reflection, and phase changing properties. The following convention will be followed: Components of light vibrating in a plane parallel to or perpendicular to the plane of the optical assembly (Fig. 1) will be called x components or y components, respectively.

Since the laser emits polarized light, it is permissible to use Jones' matrices for the optical elements. Assuming ideal optical alignment, each element may be represented by a diagonal matrix containing either a reflection or transmission amplitude factor and an accompanying phase change. With the exception of the atmospheric path, all optical elements are constants. Suppose the fast axis of the retardation plate, having retardation angle θ, is oriented along the x axis. The reference beam amplitude A' arriving at beam splitter B4 is

$$\begin{bmatrix} A_x' \\ A_y' \end{bmatrix} = \begin{bmatrix} K_x \exp(-i\alpha_x) & 0 \\ 0 & K_y \exp(-i\alpha_y) \end{bmatrix} \times \begin{bmatrix} 1 & 0 \\ 0 & \exp(-i\theta) \end{bmatrix} \begin{bmatrix} A_x \\ A_y \end{bmatrix},$$

where the first matrix represents all optical elements in the reference beam except the retardation plate, and the second matrix represents the phase retardation in the y polarization. The amplitude A'' of the beam traversing the atmosphere and arriving at beam splitter B4 is

$$\begin{bmatrix} A_x'' \\ A_y'' \end{bmatrix} = \begin{bmatrix} L_x \exp(-i\beta_x) & 0 \\ 0 & L_y \exp(-i\beta_y) \end{bmatrix} \times \begin{bmatrix} F \exp(-i\Phi) & 0 \\ 0 & F \exp(-i\Phi) \end{bmatrix} \begin{bmatrix} A_x \\ A_y \end{bmatrix},$$

where the first matrix represents all the constant optical elements in the atmospheric beam, and the second matrix represents the atmospheric effects.

We make the assumption that the atmosphere treats both polarizations alike. Φ and F are the time varying phase and amplitude perturbations introduced by the atmospheric refractive turbulence. At beam splitter B4 the beams combine to produce two signals that are separated by the Wollaston prism and detected by D1 and D2 as quadrature intensities, given by

$$I_x = A_x^2[K_x^2 + F^2L_x^2 + 2K_xL_xF \cos(\Phi + \beta_x - \alpha_x)],$$
$$I_y = A_y^2[K_y^2 + F^2L_y^2 + 2K_yL_yF \cos(\Phi + \beta_y - \alpha_y - \theta)].$$

The angle θ is an assignable constant. The only time dependent angle is Φ, a characteristic of the atmospheric path. The statistics of the fluctuating part of the above phase angles are unaffected by additive constants; therefore, let $\phi = \Phi + \beta_x - \alpha_x$ and adjust the retardation angle θ so that

$$\theta = (\beta_y - \beta_x) - (\alpha_y - \alpha_x) + \pi/2,$$

and the two output signals arriving at the detectors become

$$\left.\begin{matrix} I_x \\ I_y \end{matrix}\right\} = A_i^2\left[K_i^2 + F^2L_i^2 + 2K_iL_iF \begin{Bmatrix} \cos\phi \\ \sin\phi \end{Bmatrix}\right] \tag{1}$$

$$i = x,\ y.$$

Off-diagonal terms in the matrix representation of the optical elements will produce additional scintillation dependent terms in Eq. (1) which will not be eliminated by the procedure discussed below. If these terms are sufficiently large they may cause significant errors in the measurement of phase.

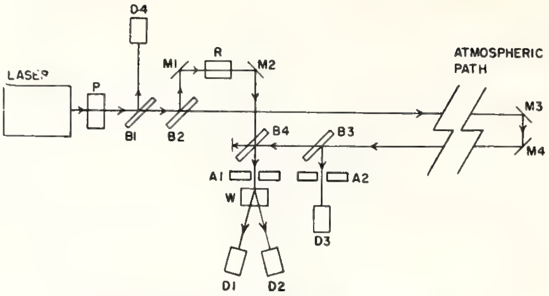

FIG. 1. The optical phase measuring instrument.

EXTRACTION OF PHASE

In order to extract $\phi(t)$, the additive terms in Eq. (1) must be removed. A fraction of the laser output power I_1 is diverted by beam splitter B_1 into detector D4. The returning atmospheric beam intensity is monitored by the detector D3, which receives a small fraction I_2 of the light intensity diverted by beam splitter B3. These four signals (I_x, I_y, I_1, and I_2) are used to obtain $\phi(t)$.

Each of the four optical intensities illuminates an electron multiplier phototube. Each phototube output current is an input to an amplifying circuit whose output is a voltage proportional to the input current. The amplifier biases are adjusted for a zero output with the laser extinguished. This removes phototube dark currents and offset biases. Let the channel gain factors be G_i. Then the output voltages will be

$$E_1 = G_1I_x, \quad E_2 = G_2I_y, \quad E_3 = G_3I_1, \quad E_4 = G_4I_2,$$

and

$$E_5 = G_5I_1,$$

where I_x and I_y are given in Eq. (1). The relative values of the gains are adjusted by blocking first the reference beam and then the atmospheric beam with the system in operation. With the reference beam blocked, $K_x = K_y = 0$. The gains G_1, G_2, and G_4 are adjusted so that $E_1 = E_2 = E_4$;

thus, we have

$$G_1A_x^2L_x^2=G_2A_y^2L_y^2=G_4(I_2/F^2). \tag{2}$$

Restoring the reference beam and interrupting the beam passing through the atmosphere makes $F=0$. Gain G_3 is subsequently adjusted so that $E_3=E_1$; thus, we have

$$G_3I_1=G_1A_x^2K_x^2. \tag{3}$$

Gain G_5 is next adjusted so that $E_5=E_2$; then,

$$G_5I_1=G_2A_y^2K_y^2. \tag{4}$$

Dividing Eq. (4) by Eq. (3) yields

$$\frac{G_5}{G_3}=\frac{G_2}{G_1}\left(\frac{A_yK_y}{A_xK_x}\right)^2.$$

The relative gains G_3 and G_5 are measured by introducing a common input to the amplifiers and measuring the output with a digital voltmeter having an accuracy better than 0.1%. Using the measured ratio of G_5/G_3 and the ratio of G_2/G_1 from Eq. (2), we obtain the gain ratio B^2, where

$$B^2=G_5/G_3=(L_xK_y/L_yK_x)^2.$$

Now the interrupted beam is restored. The value of B is inserted into the output equations which become

$$E_1=G_1A_x^2(K_x^2+F^2L_x^2+2K_xFL_x\cos\phi),$$
$$E_2=G_1A_x^2(B^2K_x^2+F^2L_x^2+2K_xFL_xB\sin\phi),$$
$$E_3=G_1A_x^2K_x^2,$$
$$E_4=G_1A_x^2F^2L_x^2, \text{ and}$$
$$E_5=G_1A_x^2K_x^2B^2.$$

To conserve data recording channels, these five signals are fed into a simple real time analog computer to add and subtract them in a suitable manner. One computer circuit forms $E_1-E_3-E_4$ and another $E_2-E_4-E_5$. Their respective output voltages, E_x and E_y, are

$$E_x=J\cos\phi(t), \tag{5}$$

$$E_y=JB\sin\phi(t), \tag{6}$$

where

$$J=2G_1A_x^2K_xL_xF;$$

E_x and E_y are then recorded on analog tape at the field site.

Subsequently these data are transcribed to digital tape for computer processing. The phase angle often changes by hundreds of radians during an experimental run. The assumption is made that the digitizer has a sufficiently rapid sampling rate so that the phase does not change more than $\pm\pi$ rad between consecutively sampled sets of values of E_x and E_y. The computer program uses $E_x=J\cos\phi$, $E_y=BJ\sin\phi$, B, and the sampling assumption to produce the phase angle as a function of time for an experimental run of any desired length.

If the time variation of the relative intensity of the returning beam is desired in addition to the phase, another signal voltage must also be recorded, digitized, and used in computations. The returning beam intensity is F^2. Since E_x and E_y are already necessary, only one more signal, e.g., E_3, need be recorded. The intensity F^2 is then found to be

$$F^2=(K_x/2L_xB)^2[(B^2E_x^2+E_y^2)/E_3^2].$$

Since K_x/L_x is not known, only the relative intensity is obtainable.

ERROR ESTIMATES

As mentioned above, B in Eq. (6) is measured with an accuracy of 0.1%. The uncertainty this produces in the measured phase is given by

$$\frac{\Delta\phi}{\phi}=\frac{\Delta B}{B}\frac{\sin 2\phi}{2\phi}.$$

Hence, the error in ϕ will be bounded by the 0.1% error in B.

The off-diagonal terms previously mentioned will tend to alter the form of Eqs. (5) and (6) and return them to a form similar to Eq. (1). If these signals are displayed on the X and Y axes of an oscilloscope with suitably adjusted gains, the resulting average locus will not be a circle as would be the case if Eqs. (5) and (6) were valid. There would be additional scintillation-induced modulation of the circle radius and a random precession of the center. The latter effect would seriously inhibit the ability to determine the quadrant of the phase at a given instant. Average circularity may be assured in the alignment procedure by linearly changing the phase along the atmospheric path in the laboratory and adjusting the relative position of the optical elements. However, a check for motion of the center of the circle must be made under the actual atmospheric conditions or with simulated scintillations to determine the magnitude of the undesirable effects of the off-diagonal elements. We have not observed any motion of the center of the circle.

DESIGN AND CONSTRUCTION

The optical elements are rigidly mounted on a 1.9 cm thick by 38 cm by 76 cm aluminum baseplate placed in a horizontal plane. The mirrors M1 and M2 located on the baseplate, the mirrors M3 and M4 located on the remotely placed dihedral reflector, and the beam splitter B4 are adjustable in angle. The apertures A1 and A2 are adjustable vertically and laterally so that the intensity monitor D3 and the detectors D1 and D2 all view the same portion of the returning beam. Because of the vastly unequal lengths of the two arms of the instrument, a highly stabilized He–Ne laser[5] is used as the light source. The returning light beam is prevented from entering the laser and disturbing the stability of the source by using beam splitter B2 to separate the beam and a second beam

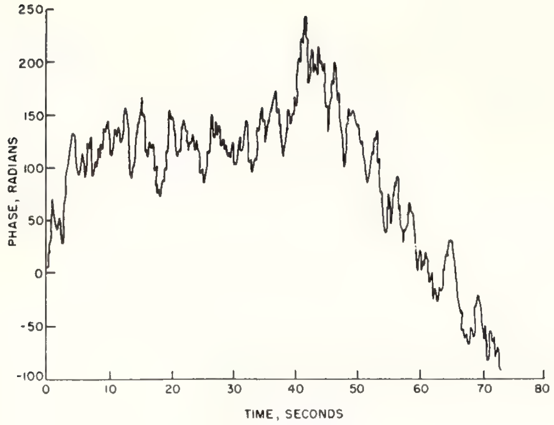

FIG. 2. A typical measurement of absolute optical phase as a function of time.

splitter B4 to recombine the beams. All signal and power leads on the assembly are rigidly fastened to the baseplate. The baseplate itself is supported on 15 flattened balls of putty to provide vibration damping. While recording data, it is necessary that vibration be held to a minimum. Thus no power supplies or electronic equipment are located on the same platform on which the instrument is mounted. All cables leading from the instrument assembly to the electronic equipment are firmly fastened to prevent wind induced vibration.

RESULTS AND DISCUSSION

A typical plot of absolute optical phase as a function of time is shown in Fig. 2. This curve is a computer generated graph of 10 000 successive values of ϕ taken in a 73 sec time interval. The sampling rate for these data was 137 sec^{-1}. A Fourier analysis of the data shows negligible contribution for frequencies higher than about 15 Hz, indicating a sufficiently rapid sampling rate. Laboratory tests of vibration sensitivity carried out in a quiet atmosphere showed that winds below about 5 m·sec^{-1} blowing directly upon this laboratory model instrument have negligible effect on the signals.

---

[1] A. L. Buck, Appl. Opt. **6**, 703 (1967).

[2] P. Burlamacchi, A. Consortini, and L. Ronchi, Appl. Opt. **6**, 1273 (1967).

[3] J. C. Moldon, M.I.T. Tech. Rep. 469 (1969).

[4] M. Bertolotti, M. Carnevale, L. Muzii, and D. Sette, Appl. Opt. **7**, 2246 (1968).

[5] Spectra-Physics, Inc., model 119 gas laser.

Reprinted from Journal of Optical Society of America 60, No. 12, 1695-1697, 1970.

Measurements of the Wavelength Dependence of Scintillation in Strong Turbulence*

R. H. KLEEN† AND G. R. OCHS
ESSA Research Laboratories, Boulder, Colorado 80302

(Received 2 July 1970)

INDEX HEADINGS: Atmospheric optics; Scintillation.

It is now generally agreed that the scintillation of an optical beam does not increase indefinitely as the refractive-index turbulence of the atmosphere increases but tends to saturate for sufficiently strong turbulence and sufficiently great path length. Several workers have verified the existence of this saturation region.[1–6]

Additionally, Mevers *et al.*[6] have made observations in this region at several wavelengths. Their results indicated that the maximum saturation level was markedly wavelength dependent, decreasing with increasing wavelength. This unexpected result encouraged us to perform a similar experiment, comparing the scintillation of two wavelengths at a fixed distance but over a wide range of turbulence conditions. Our results show little, if any, variation of the maximum scintillation level with wavelength.

The measure of scintillation that we use is log-amplitude variance, $C_l(0)$, defined as

$$C_l(0)=\langle(\ln v-\langle\ln v\rangle_{\mathrm{av}})^2\rangle_{\mathrm{av}},$$

where v is the amplitude of the vector of the optical wave. Because the irradiance, I, over a small aperture is actually measured, $C_l(0)$ can be obtained from the expression

$$C_l(0)=\tfrac{1}{4}\langle(\ln I-\langle\ln I\rangle_{\mathrm{av}})^2\rangle_{\mathrm{av}}.$$

The refractive-index structure constant, C_n^2, is derived from temperature measurements by using small, high-speed, platinum resistance thermometers.[7]

All measurements were made on a 1-km optical path 2 m above the grass-covered surface of Table Mountain, a very flat mesa 12 km north of Boulder, Colorado. Two continuous-wave He–Ne lasers were used with single-mode outputs at 0.6328 and 1.084 μm, respectively. The experimental conditions are summarized in Table I.

At the lasers, the beams were separated 4 cm (horizontally) by a mirror in one of the optical paths. The receivers were separated by 30 cm horizontally. The relatively large receiving apertures, scaled as $\lambda^{1/2}$, were used so that a sufficient signal-to-noise (S/N) ratio was available at 1.084 μm. Occasionally, the analog circuitry following the photomultiplier tubes was interchanged, and results were compared to insure that the two circuits were performing identically.

TABLE I. Summary of experimental conditions.

Wavelength	0.6328 μm	1.084 μm
Laser output	3 mW	5 mW
Laser aperture	5 mm	2 mm
Laser divergence	2 mrad	1 mrad
Receiver	EMI 9558	RCA 7102 at dry-ice temperature
Receiver aperture	5 mm	6.4 mm
Receiver acceptance angle	5 mrad	5 mrad
Optical-filter bandpass	10 Å	25 Å
Electrical filter	0–3 kHz	0–3 kHz

Recorded variables were preprocessed with analog equipment, and mean values of quantities of interest were recorded digitally, once each minute, for later computer processing. (Analog methods of computation have been described by Ochs *et al.*[7]) These techniques for the measurement of log-amplitude variance might have lacked sufficient dynamic range for values of $C_l(0)$ such as were

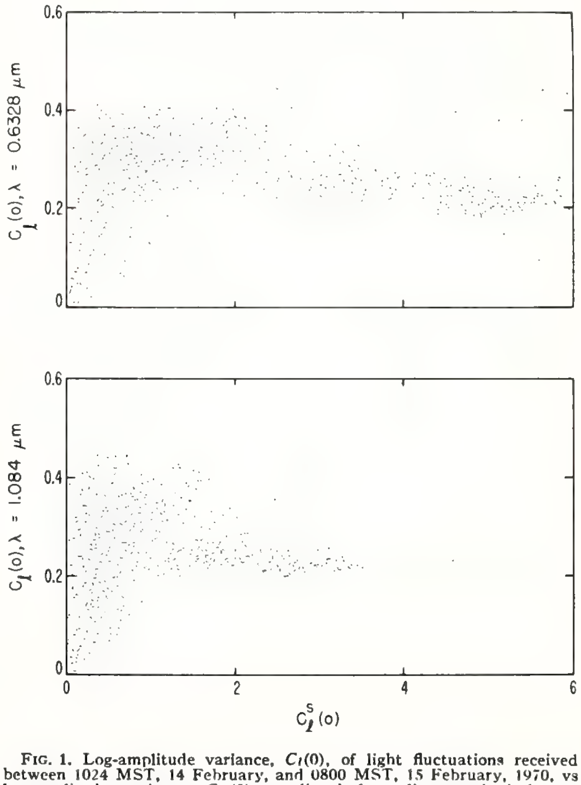

FIG. 1. Log-amplitude variance, $C_l(0)$, of light fluctuations received between 1024 MST, 14 February, and 0800 MST, 15 February, 1970, vs log-amplitude variance, $C_{l^s}(0)$, predicted from linear spherical-wave propagation theory. $C_{l^s}(0)$ is determined from a temperature structure–function measurement made near the receiving end of the path. Each point represents a 1-min average of the variables. The upper graph is for λ = 0.6328 μm; the lower is for λ = 1.084 μm.

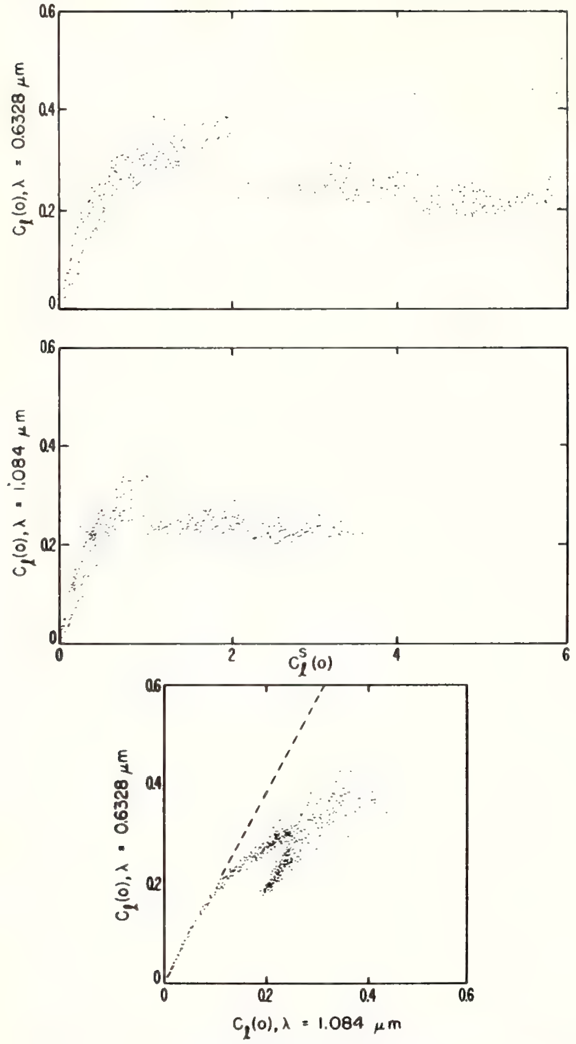

FIG. 2. The upper two graphs display only that data of Fig. 1 obtained when the wind speed was in the range 2–6 m/s. The lower graph is log-amplitude variance, $C_l(0)$, at $\lambda = 0.6328$ μm vs that at $\lambda = 1.084$ μm, for the wind-velocity range 2–6 m/s.

encountered in the saturation region; hence an occasional check, consisting of an amplitude-distribution analysis, was made when the optical scintillations were saturated. From the portion of the amplitude plot having the best S/N ratio, $C_l(0)$ was determined and used to check the calibration of the analog equipment.

In Fig. 1, we show a comparison of our observed scintillation levels with those predicted by Fried's[8] spherical-wave-propagation theory, developed from Tatarski's earlier work, which does not predict a saturation of scintillation. According to Fried's theory,

$$C_l^s(0) = 0.124(2\pi/\lambda)^{7/6} Z^{11/6} C_n^2,$$

where λ is the wavelength of the light, Z is the path length, and C_n^2 is the refractive-index structure parameter derived from our temperature-fluctuation sensors, separated 10 cm vertically. Although there is considerable scatter in the data, the optical scintillation displays a general tendency to rise, reach a peak, and then diminish somewhat with increasing turbulence. Most of the scatter occurs when, because of low wind velocity, the path becomes extremely nonuniform. At such times, a 1-min average may be expected to have large statistical fluctuations and, in addition, the atmosphere is less likely to be described adequately by a Kolmogorov theory of turbulence.

In Fig. 2, we show only that portion of the data taken when the wind velocity was between 2 and 6 m/s. The scatter in the upper two plots is noticeably less than in Fig. 1. Below saturation, the measured scintillation is somewhat less than that predicted by spherical-wave propagation theory. There is considerable scatter in the region of maximum scintillation. Farther into the saturation region, there is a decrease of the scintillation at both wavelengths. Because of aperture smoothing, the variance at which the 0.6328-μm scintillations saturate is less than that reported earlier by Ochs and Lawrence.[5] A 1-mm-diam aperture was used in the early experiments. The aperture-averaging effect was measured at 0.6328 μm, where the S/N ratio for a 1-mm aperture was adequate. These experiments indicated a 40% reduction of log-amplitude variance with the 5-mm-diam aperture.

Some features of the wavelength comparison become more

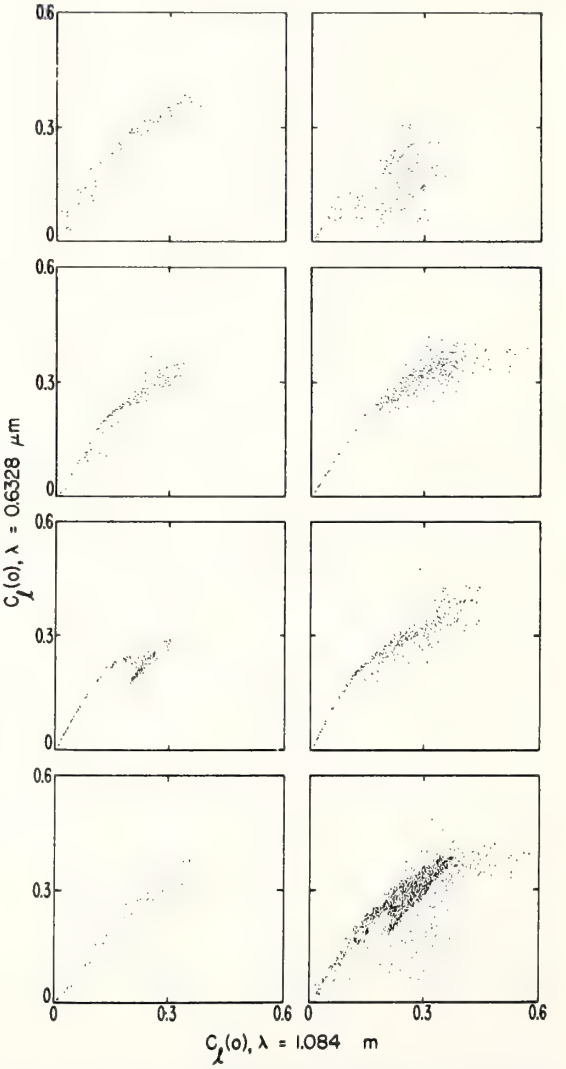

FIG. 3. A series of scatter plots of log-amplitude variance, $C_l(0)$, at 0.6328 μm vs that at $\lambda = 1.084$ μm. Each point is a 1-min average and the first seven graphs contain 8 h of data each, beginning with 0001–0800 MST, 13 February and ending with 0001–0800 MST, 15 February 1970. The sequence is by rows from upper left to lower right. The last graph contains all 56 h of data.

evident if the scintillation at $\lambda = 1.084$ μm is plotted vs that at 0.6328 μm, as shown in the lower graph of Fig. 2. The agreement with the predicted wavelength-scaling law (dotted line) is good at low variance, in agreement with the findings of Fitzmaurice *et al.*,[9] over a greater wavelength range. Also there is less scatter in this plot than in the upper two plots of Fig. 2.

The scatter in the upper two plots is principally due to two causes: First, there is a variation in the spectrum of turbulence; second, there is a statistical fluctuation resulting from a 1-point turbulence measurement being used to represent turbulent conditions along a 1-km path. The lower plot is affected only by turbulence-spectrum variations, so the relative magnitudes of the two effects can be seen.

All of the data in Fig. 2 were taken when the wind velocity ranged between 2 and 6 m/s. In Fig. 3, no such restriction has been applied, and comparisons of scintillation at $\lambda = 0.6328$ and 1.084 μm are shown for consecutive 8-h segments of a 56-h observing period. The last plot contains all of the data taken during the period. The most striking feature of Fig. 3 is the great variation from segment to segment, even though each includes 8 h of data. It is clear that the nonstationary nature of the turbulent atmosphere near the ground necessitates long periods of measurement to obtain stable (or representative) results. Such nonstationarity undoubtedly explains some of the differences reported in the results of various experiments. An additional source of error lies in the difficulty, pointed out by Fitzmaurice and Bufton,[10] in measuring accurately high log-amplitude variances. In Fig. 4, the data of Fig. 3 have been sorted in 2-m/s wind-speed ranges. Again, most of the scatter appears to occur in those data taken when the wind speed was less than 2 m/s.

It appears that the atmosphere is more nearly statistically stationary and most closely approximates a Kolmogorov spectrum of turbulence, when the speed exceeds about 2 m/s. The lower graph of Fig. 2 and the two lower graphs of Fig. 4 were taken under these conditions, and they show less scatter. At low variances, the wavelength-scaling laws are obeyed. With increasing turbulence, the shorter wavelength begins to saturate first, and the slope of the curve begins to decrease. When the log-amplitude variances at both wavelengths have reached their maximum values, they appear to be about equal, although it could be argued that the maximum scintillation of the shorter wavelength is a little greater. By contrast, Mevers *et al.*[6] reported a pronounced decrease of saturation with increasing wavelength, using measurements made over a wider wavelength range.

After the scintillations at the two wavelengths saturate, further increase of atmospheric turbulence decreases the scintillation of each. The scintillation seems to be independent of wavelength at this stage, although at the highest turbulence levels there is some indication that the scintillation of the shorter wavelength decreases more rapidly.

In summary, our observations below saturation indicate good agreement with the predicted wavelength dependence. With increasing turbulence, the scintillations for both wavelengths saturated at nearly the same level and then decreased, the shorter wavelength tending to decrease more rapidly.

We wish to acknowledge the helpful discussions with S. F. Clifford, and the computational assistance of M. J. Hallenbeck.

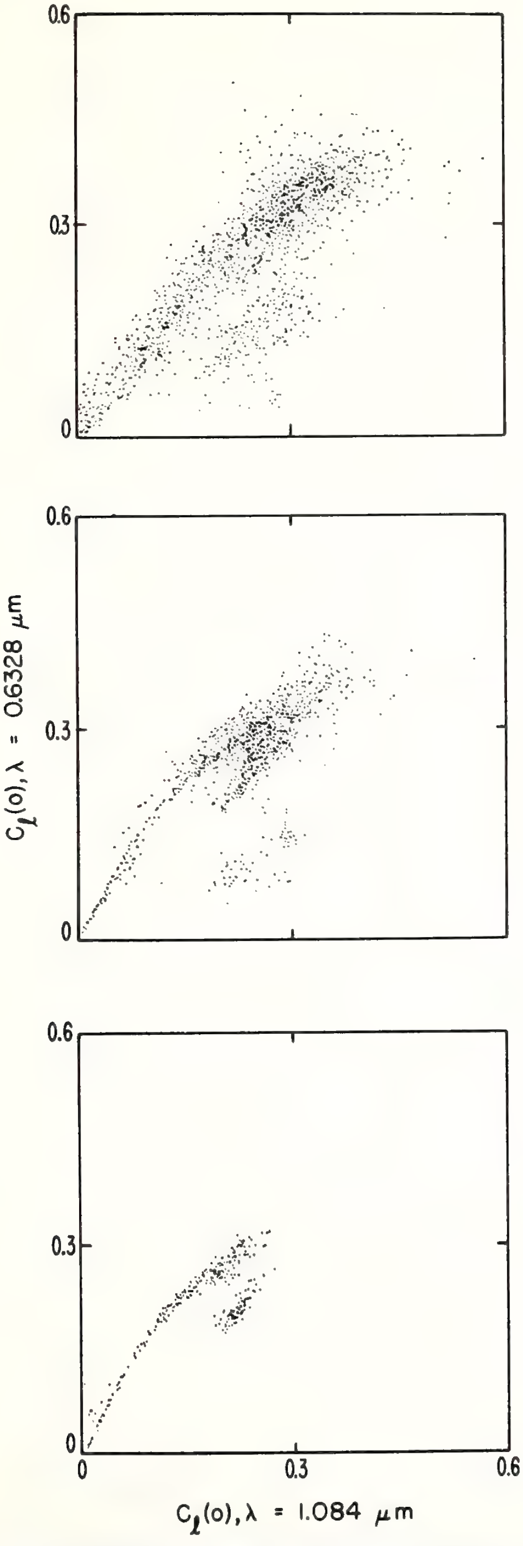

FIG. 4. The data of Fig. 3, log-amplitude variance, $C_l(0)$, for $\lambda = 0.6328$ μm, sorted as a function of wind speed. From top to bottom, the scatter plots contain only those observations made when the wind speed was in the ranges 0–2, 2–4, and 4–6 m/s, respectively.

---

* Paper presented at Fall 1970 Meeting, Optical Society [J. Opt. Soc. Am. **60**, 1549A (1970).

† Present address: R. H. Kleen, Lockheed Electronics Company, Houston, Tex. 77058.

[1] M. E. Gracheva and A. S. Gurvich, Izv. Vuz. Radiofiz. **8**, 717 (1965).

[2] M. E. Gracheva, Izv. Vuz. Radiofiz. **10**, 775 (1967).

[3] P. H. Deitz and N. J. Wright, J. Opt. Soc. Am. **59**, 462 (1969).

[4] W. B. Johnson, Trans. Am. Geophys. Union **50**, 158 (1969) (abstract only).

[5] G. R. Ochs and R. S. Lawrence, J. Opt. Soc. Am. **59**, 226 (1969).

[6] G. E. Mevers, M. P. Keister, Jr., and D. L. Fried, J. Opt. Soc. Am. **59**, 491 (1969).

[7] G. R. Ochs, R. R. Bergman, and J. R. Snyder, J. Opt. Soc. Am. **59**, 231 (1969).

[8] D. L. Fried, J. Opt. Soc. Am. **57**, 175 (1967).

[9] M. W. Fitzmaurice, J. L. Bufton, and P. O. Minott, J. Opt. Soc. Am. **59**, 7 (1969).

[10] M. W. Fitzmaurice and J. L. Bufton, J. Opt. Soc. Am. **59**, 462 (1969).

Reprinted from Journal of Optical Society of America 61, No. 10, 1285-1292, 1971.

Temporal-Frequency Spectra for a Spherical Wave Propagating through Atmospheric Turbulence

S. F. Clifford
National Oceanic and Atmospheric Administration, Environmental Research Laboratories, Boulder, Colorado 80302

(Received 26 March 1971)

Tatarski has found the frequency spectra for the amplitude, phase, and phase-difference fluctuations of an infinite plane wave propagating through turbulence. Many practical optical beams, used in atmospheric studies, closely resemble point sources, for which the spherical-wave theory is more applicable. The same spectra, calculated for spherical waves, reveal contributions at higher frequencies for amplitude scintillations, nearly identical phase results, and a phase-difference spectrum with no nulls, in contrast with the plane-wave results. Comparison with recent data is shown.

Index Headings: Scintillation; Inhomogeneous media; Atmospheric optics; Turbulence.

In a recent paper, Lawrence and Strohbehn[1] considered the temporal-frequency spectrum of the amplitude, phase, and phase-difference fluctuations of a plane, monochromatic wave propagating through atmospheric turbulence. A similar calculation for spherical waves is easily tractable as they imply and contain some interesting features not found in the plane-wave results.

A propagating wave's amplitude and phase are modulated in a complex manner by the temporal and spatial behavior of the atmosphere's turbulent fields. These effects are usually modeled by means of a variable refractive index, $n(x,y,z,t)$, a function of both position and time.[2–5] The function n has a mean value, $\langle n\rangle$ (angle brackets indicate an ensemble average), independent of coordinates and time, and a random component, $n_1(x,y,z,t)$, with zero mean. Time variations of n are due to motion of the atmosphere. These motions are either random, such as those produced by individual turbulent-eddy decay, or large-scale mean motions involving the entire spectrum of turbulence scales, such as those produced by the wind. Taylor's hypothesis, that the effects of the mean motion dominate, producing time changes in n_1 by transporting frozen-in spatial variations of refractive index past the point of observation, allows the determination of the power spectra most directly. Then, simultaneous knowledge of the spatial statistics of the wave parameters and the wind velocity permits a transformation to temporal statistics. In propagation problems, the component of the wind perpendicular to the path produces the most important variations.

Following Tatarski[6] we define the temporal power spectrum of the function $g(\mathbf{r},t)$ as

$$W_g(f)=4\int_0^\infty d\tau\cos(2\pi f\tau)R_g(\tau), \qquad (1)$$

where $R_g(\tau)$ is the time-lagged autocorrelation of g given by

$$R_g(\tau)=\langle g(\mathbf{r},t)g(\mathbf{r},\,t+\tau)\rangle. \qquad (2)$$

Assuming the mathematical existence of $R_g(\tau)$ and applying the transformation implied in Eq. (1), we easily solve the problem posed above. Taylor's hypothesis aids in the determination of $R_g(\tau)$, given the spatial covariance function, $B_g(\boldsymbol{\rho})$, where

$$B_g(\boldsymbol{\rho})=\langle g(\mathbf{r},t)g(\mathbf{r}+\boldsymbol{\rho},\,t)\rangle. \qquad (3)$$

The assumption of statistical homogeneity allows writing B_g as a function of $\boldsymbol{\rho}$ alone. If g is a wave parameter, such as amplitude or phase, and $\boldsymbol{\rho}$ the position vector representing a displacement in the plane perpendicular to the propagation path at the point of observation, $R_g(\tau)$ is easily determined, if the wave is initially plane. A refracting eddy of size l, passing through the beam with a velocity $\mathbf{v}$, parallel to the unperturbed phase front, produces a disturbance at the receiver with the same spatial size and with a characteristic frequency, $f\sim v/l$. Clearly, the effect of this eddy motion is to produce variations of g with the property that the behavior of the function at previous positions determines its future. Therefore,

$$g(\mathbf{r},\,t+\tau)=g(\mathbf{r}-\mathbf{v}\tau,\,t). \qquad (4)$$

[Equation (4) also requires that the disturbances are persistent and coherent[6] for times up to the maximum time lag of interest.] If we assume a statistically homogeneous spectrum of eddies, distributed uniformly along the path, Eq. (2) becomes

$$R_g(\tau)=\langle g(\mathbf{r},t)g(\mathbf{r}-\mathbf{v}\tau,\,t)\rangle=B_g(\mathbf{v}\tau).$$

If g is statistically isotropic, i.e., $B_g(\mathbf{v}\tau)=B_g(v\tau)$, Eq. (1) becomes

$$W_g(f)=4\int_0^\infty d\tau\cos(2\pi f\tau)B_g(v\tau). \qquad (5)$$

Equation (5) relates the power spectrum of the temporal fluctuations in the plane-wave parameters to the two-dimensional covariance of their spatial variations. The spherical-wave calculation proceeds in the same manner, with some interesting complications due to the divergence of a point source.

AMPLITUDE AND PHASE POWER SPECTRA

Consider the following problem. A spherically divergent, monochromatic wave propagates along the z axis from $z=0$, through a region of refracting irregularities, moving across the path, to a receiver at $z=L$. The wind velocity, $\mathbf{v}$, perpendicular to the z direction, and the strength of the refractive-index fluctuations are uniform along the entire path. We wish to derive the expressions for the temporal power spectra of the received amplitude and phase fluctuations using their spatial covariance functions and Taylor's hypothesis.

The spatial covariance functions for a spherical wave of wavenumber, $k=2\pi/\lambda$, if we assume a homogeneous and isotropic refractivity spectrum, $\Phi_n(K)$, are[3]

$$B_{\chi,S}(\rho)=2\pi^2k^2\int_0^L dz\int_0^\infty dKK\Phi_n(K)J_0\left(\frac{K\rho z}{L}\right)\times\left\{1\mp\cos\left[\frac{K^2z(L-z)}{kL}\right]\right\}, \quad (6)$$

where the upper sign applies for log amplitude, χ, and the lower for phase, S. Equation (6) contains the spacing, $\boldsymbol{\rho}$, and the two-dimensional spatial wavenumber, K, both defined in the plane perpendicular to the z axis, J_0 is a zero-order Bessel function, and $\Phi_n(K)$ is the isotropic form of the Fourier transform

$$\Phi_n(\mathbf{K})=\frac{1}{(2\pi)^3}\int d^3\mathbf{r}B_n(\mathbf{r})e^{i\mathbf{K}\cdot\mathbf{r}}$$

of the three-dimensional refractive-index covariance function defined by

$$B_n(\mathbf{r})=\langle n_1(\mathbf{r}_1)n_1(\mathbf{r}_1+\mathbf{r})\rangle.$$

In contrast to the plane-wave case, a receiver observing the motion of an eddy of size, l, drifting through the diverging bundle of rays from a point source, sees a magnified disturbance of size, $l_{\text{dist}}=l(L/z)$, moving with velocity, $\mathbf{v}_{\text{dist}}=\mathbf{v}(L/z)$. (Note, however, that the characteristic frequency, $f=v_{\text{dist}}/l_{\text{dist}}$, is the same as for plane waves, $f\sim v/l$. The relative strengths of the contribution at this frequency depend on the different path-weighting functions in the plane- and spherical-wave cases, i.e., the relative effectiveness of the eddy in producing phase or amplitude variations at the receiver.) Because the observed disturbance propagates with a velocity $\mathbf{v}L/z$, the expression for spherical waves equivalent to Eq. (4) is

$$g(\mathbf{r},t+\tau)=g[\mathbf{r}-\mathbf{v}(L/z)\tau,t].$$

Generalizing to a spectrum of eddies located between z and $z+dz$ leads directly to the definition of a differential time-lagged autocorrelation. With $\mathbf{v}$ perpendicular to the z direction and assuming statistical homogeneity in this plane, we find

$$R_g(\tau,z)dz=\langle g(\mathbf{r},t)g[\mathbf{r}-\mathbf{v}(L/z)\tau,t]\rangle=dB_g[\mathbf{v}(L/z)\tau]. \quad (7)$$

If we assume that effects of different portions of the path on g are uncorrelated, then the entire covariance function is the path integral of Eq. (7). (This is a good assumption because we require only that contributions from the same-size eddies at different positions along the path be uncorrelated. The assumption of homogeneous turbulence forces different eddy sizes to be uncorrelated.[3] For a weakly scattering medium with an outer scale of turbulence equal to L_0, this assumption restricts our solutions to the case $L\gg L_0$.)

$$R_g(\tau)=\int_0^L dzR_g(\tau,z)=\int_{B_g(\infty)}^{B_g(\mathbf{v}\tau)}dB_g\left(\frac{\mathbf{v}L\tau}{z}\right). \quad (8)$$

If $B_g(\infty)=0$, Eq. (8) becomes[7]

$$R_g(\tau)=B_g(\mathbf{v}\tau).$$

If the two-dimensional spectrum of eddies in consecutive z-axis planes results from the projection of a three-dimensional refractivity field that is statistically homogeneous and isotropic, then, for amplitude and phase fluctuations, Eq. (6) with $\rho=vL/z$ is equivalent to $B_g(v\tau)$ above, and we may write

$$R_{\chi,S}(\tau)=B_{\chi,S}(v\tau)=2\pi^2k^2\int_0^L dz\int_0^\infty dK\times K\Phi_n(K)J_0(Kv\tau)\left\{1\mp\cos\left[\frac{K^2z(L-z)}{kL}\right]\right\} \quad (9)$$

for the time-lagged autocorrelations of χ and S. To proceed, substitute Eq. (9) into Eq. (1) and integrate with respect to τ to obtain[8]

$$W_{\chi,S}(f)=8\pi^2k^2\int_0^L dz\int_{2\pi f/v}^\infty dK\times K\Phi_n(K)[(Kv)^2-(2\pi f)^2]^{-\frac{1}{2}}\times\left\{1\mp\cos\left[\frac{K^2z(L-z)}{kL}\right]\right\} \quad (10)$$

for the temporal power spectra of the spherical-wave amplitude and phase.

For the particular case of a Kolmogorov refractivity spectrum,[6]

$$\Phi_n(K)=0.033C_n{}^2K^{-11/3}, \quad (11)$$

assumed valid in the inertial subrange of turbulence between some minimum scale l_0 and some maximum scale L_0, Eq. (10) assumes a particularly useful form for atmospheric-propagation problems. ($C_n{}^2$ is the structure constant of the index of refraction, a quantity related to the magnitude of the refractive-index fluctuations.) Changing the variables of integration to $(u+1)/2=z/L$ and $q=(Kv/2\pi f)^2-1$ after inserting Eq. (11) into

TABLE I. Comparison between the plane- and spherical-wave asymptotic forms of the log-amplitude, phase, and phase-difference temporal power spectra.[a]

	Plane wave	Spherical wave
log amplitude—$W_\chi(f)$, $l_0 \ll (\lambda L)^{\frac{1}{2}} \ll L_0$, $f > v/L_0$		
$\Omega \ll 1$	$0.85 k^{\frac{2}{3}} L^{7/3} C_n^2 v^{-1}(1+0.27\Omega^{4/3})$	$0.191 k^{\frac{2}{3}} L^{7/3} C_n^2 v^{-1}[1+0.119\Omega^{4/3}]$
$\Omega \gg 1$	$2.19 k^{\frac{2}{3}} L^{7/3} C_n^2 v^{-1} \Omega^{-8/3}$	$2.19 k^{\frac{2}{3}} L^{7/3} C_n^2 v^{-1} \Omega^{-8/3}$
In terms of log-amplitude variance		
	$\langle \chi^2 \rangle_p = 0.308 k^{7/6} L^{11/6} C_n^2$,	$\langle \chi^2 \rangle_s = 0.124 k^{7/6} L^{11/6} C_n^2$,
$\Omega \ll 1$	$0.44 \langle \chi^2 \rangle_p (1/f_0)(1+0.27\Omega^{4/3})$	$0.245 \langle \chi^2 \rangle_s (1/f_0)[1+0.119\Omega^{4/3}]$
$\Omega \gg 1$	$1.14 \langle \chi^2 \rangle_p (1/f_0) \Omega^{-8/3}$	$2.81 \langle \chi^2 \rangle_s (1/f_0) \Omega^{-8/3}$
phase—$W_S(f)$, $l_0 \ll (\lambda L)^{\frac{1}{2}} \ll L_0$, $f > v/L_0$		
$\Omega \ll 1$	$4.38 k^{\frac{2}{3}} L^{7/3} C_n^2 v^{-1} \Omega^{-8/3}$	$4.38 k^{\frac{2}{3}} L^{7/3} C_n^2 v^{-1} \Omega^{-8/3}$
$\Omega \gg 1$	$2.19 k^{\frac{2}{3}} L^{7/3} C_n^2 v^{-1} \Omega^{-8/3}$	$2.19 k^{\frac{2}{3}} L^{7/3} C_n^2 v^{-1} \Omega^{-8/3}$
phase difference—$W_{\delta S}(f)$, $l_0 \ll (\lambda L)^{\frac{1}{2}} \ll L_0$, $f > v/L_0$		
$\rho \ll (\lambda L)^{\frac{1}{2}}$	$0.033 k^2 L C_n^2 v^{5/3}[1-\cos(2\pi\rho f/v)] f^{-8/3}$	$0.033 k^2 L C_n^2 v^{5/3}\left[\dfrac{1-\sin(2\pi\rho f/v)}{(2\pi\rho f/v)}\right] f^{-8/3}$
$\rho \gg (\lambda L)^{\frac{1}{2}}$	$0.066 k^2 L C_n^2 v^{5/3}[1-\cos(2\pi\rho f/v)] f^{-8/3}$	$0.066 k^2 L C_n^2 v^{5/3}\left[\dfrac{1-\sin(2\pi\rho f/v)}{(2\pi\rho f/v)}\right] f^{-8/3}$

[a] Symbols used in the table: λ = wavelength, $k = 2\pi/\lambda$; v = wind speed perpendicular to $\mathbf{k}$; ρ = separation in plane perpendicular to $\mathbf{k}$; L = path length; C_n^2 = strength of refractive turbulence; f = frequency, $\Omega = f/f_0$, $f_0 = v/(2\pi\lambda L)^{-1/2}$; χ = log amplitude; S = phase; l_0 = inner scale, L_0 = outer scale.

Eq. (10) yields

$$W_{\chi,S}(f) = 0.132\pi^2 k^{\frac{2}{3}} L^{7/3} C_n^2 v^{-1} \Omega^{-8/3} \int_0^1 du \times \int_0^\infty \frac{d\sigma\sigma^{-\frac{1}{2}}}{(\sigma+1)^{11/6}} \{1 \mp \cos[-\tfrac{1}{4}\Omega^2(\sigma+1)(1-u^2)]\}, \quad (12)$$

where $\Omega = f/f_0$ and $f_0 = v(2\pi\lambda L)^{-\frac{1}{2}}$. The equation is subject to the constraints $l_0 \ll (\lambda L)^{\frac{1}{2}} \ll L_0$ and $f > v/L_0$, both arising from the requirement that the important region of integration be in the range of validity of Eq. (11). The former constraint allows setting the upper limit of the σ integration to infinity. Equation (12), integrated in Appendix A with no additional restriction, yields

$$W_{\chi,S}(f) = 2.19 k^{\frac{2}{3}} L^{7/3} C_n^2 v^{-1} \Omega^{-8/3} R_e \times [1 \mp {}_2F_2(1, -\tfrac{5}{6}; \tfrac{3}{2}, -\tfrac{1}{3}; i\tfrac{1}{4}\Omega^2) \mp (4/11)\Gamma(-\tfrac{4}{3})(-i\tfrac{1}{4}\Omega^2)^{\frac{4}{3}} {}_1F_1(\tfrac{1}{2}, 17/6, i\tfrac{1}{4}\Omega^2)], \quad (13)$$

where ${}_2F_2$ is defined as

$${}_2F_2(a_1,a_2;b_1,b_2;z) = \sum_{n=0}^{\infty} \frac{\Gamma(a_1+n)\Gamma(a_2+n)\Gamma(b_1)\Gamma(b_2)}{\Gamma(b_1+n)\Gamma(b_2+n)\Gamma(a_1)\Gamma(a_2)} \frac{z^n}{n!}$$

and the obvious relation,

$${}_2F_2(a_1,a; b_1,a; z) = {}_1F_1(a_1,b_1,z),$$

applies in Eq. (13).

Equation (13), valid for $f > v/L_0$, has the asymptotic forms listed in Table I. Tatarski's original low-frequency, plane-wave asymptote for W_χ is in error. The corrected form is in Table I.

Figures 1 and 2 illustrate the complete spherical-wave log-amplitude and phase power spectra plotted versus $\log\Omega$, using Eq. (13). Shown for comparison are the same spectra for plane waves. All curves are normalized to the appropriate log-amplitude variance. This peculiar normalization for the phase is necessary because of the impossibility of defining the variance of the phase fluctuations without introducing other parameters, such as the outer scale. The shapes of the curves for $f > v/L_0$ are universal, changes in the experimental parameters λ, L, C_n^2, and v merely modify the vertical and horizontal scales. Figure 3 contains the same curves as Fig.

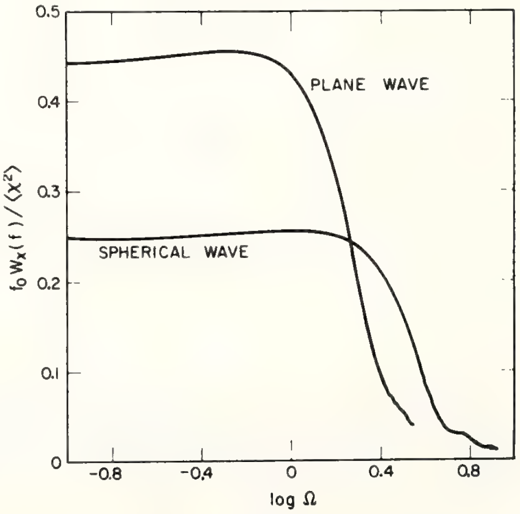

FIG. 1. Temporal power spectrum of the log-amplitude fluctuations for both plane- and spherical-wave propagation. Each curve is normalized to the applicable log-amplitude variance, $\langle \chi^2 \rangle$, and plotted vs frequency ratio $\Omega = f/f_0$, with $f_0 = v(2\pi\lambda L)^{-\frac{1}{2}}$.

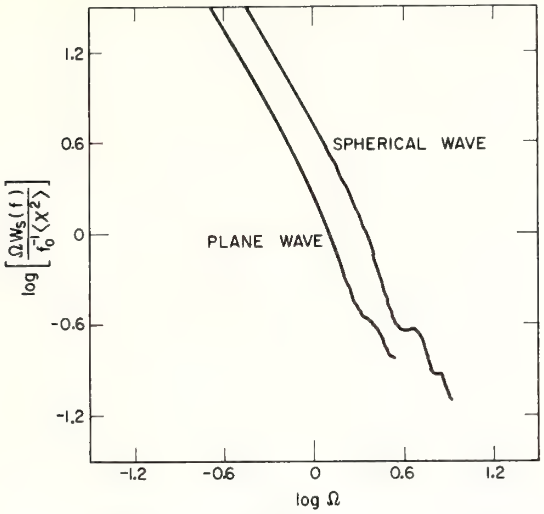

FIG. 2. Temporal power spectrum of the phase fluctuations times frequency ratio, $\Omega=f/f_0$, for both plane- and spherical-wave propagation. Each curve is normalized to the applicable log-amplitude variance, $\langle\chi^2\rangle$. $f_0=v(2\pi\lambda L)^{-\frac{1}{2}}$.

1, replotted to show the true relative distribution of power versus frequency.

A simple geometrical argument explains the predominance of higher frequencies for the spherical-wave amplitude scintillations (Fig. 3). For a given position along the path, the optimum-size eddy for producing amplitude fluctuations will have extreme ray paths that differ in length by $\lambda/2$ at the receiver, causing complete cancellation. These most effective eddy sizes are $l_p\sim[\lambda(L-z)]^{\frac{1}{2}}$ and $l_s\sim[\lambda z(1-z/L)]^{\frac{1}{2}}$ for plane and spherical waves, respectively. (If $l\sim 2\pi/K$, these results also come directly from the maxima of the $\{1-\cos[K^2z(L-z)/(kL)]\}$ filter function in Eq. (10) and the corresponding function, $\{1-\cos[K^2(L-z)/k]\}$, for plane waves, provided that we assume that the decay of the refractive-index spectrum suppresses the effects of the smaller eddies at the same position and that only the first maximum contributes.) Recalling that the characteristic frequency for a given wind, v, and a scale size, l, is the same for both cases, $f\sim v/l$, and noting that $l_s\leq l_p$ for $z>0$, we find that the smaller most effective eddies for spherical waves will contribute higher-frequency amplitude fluctuations than the larger, most effective eddies for plane waves.

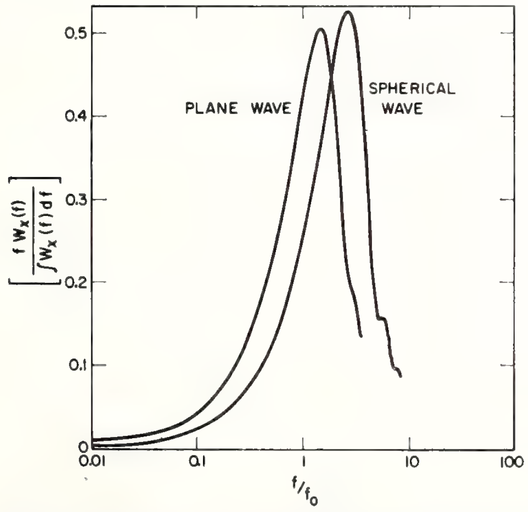

FIG. 3. Normalized frequency spectrum for intensity or log-amplitude fluctuations vs $\log(f/f_0)$, $f_0=v(2\pi\lambda L)^{-\frac{1}{2}}$. The plane- and spherical-wave cases are normalized to their appropriate log-amplitude variance $\langle\chi^2\rangle=\int W_\chi(f)df$.

The phase results, Fig. 2, are easily understood. Apart from the different normalization for the two curves, the gross features (see the asymptotes, Table I) are identical. Only the minor ripple in the tails, showing larger fluctuations about the asymptotic line in the spherical-wave case, differentiates them. Large-scale irregularities simply modulate the phase by changing the optical path length. Diffraction effects dominate for small scales and reduce their contribution to the phase variance at the high frequencies from that determined by simple geometric optics considerations. This reduction of effectiveness of the small eddies is clearly shown by the 50% reduction of the high-frequency asymptote.

PHASE-DIFFERENCE POWER SPECTRUM

For measuring the structure function of phase, i.e., the mean-square phase deviation at two points separated by a distance, $\boldsymbol{\rho}$, the phase-difference frequency spectrum is of most interest. The derivation follows essentially that for the phase or amplitude spectrum but with some additional complications that arise from the introduction of a new degree of freedom, the spacing $\boldsymbol{\rho}$.

We define the phase difference in the receiving plane as

$$\delta_\rho S(t)=S(\mathbf{r},t)-S(\mathbf{r}+\boldsymbol{\rho},\,t),\tag{14}$$

and again seek the time-lagged autocorrelation function

$$R_{\delta S}(\tau)=\langle\delta_\rho S(t)\delta_\rho S(t+\tau)\rangle.$$

[This derivation parallels the calculations leading to Eqs. (7)–(9).] A spectrum of turbulent irregularities, drifting through the beam at some position, z, produces a received differential correlation function of the form

$$R_{\delta S}(\tau,z)dz=\left\langle\left[S\left(\mathbf{r}-\mathbf{v}\frac{L}{z}\tau,t\right)-S\left(\mathbf{r}+\boldsymbol{\rho}-\mathbf{v}\frac{L}{z}\tau,t\right)\right]\right.$$
$$\left.\times[S(r,t)-S(\mathbf{r}+\boldsymbol{\rho},t)]\right\rangle.\tag{15}$$

The drift velocity, $\mathbf{v}$, assumed in the plane of $\boldsymbol{\rho}$, is perpendicular to the z axis. If the refractivity spectrum is homogeneous in this plane, Eq. (15) simplifies to

$$R_{\delta S}(\tau,z)dz$$

$$=2dB_S\left(\mathbf{v}\frac{L}{z}\tau\right)-dB_S\left(\boldsymbol{\rho}-\mathbf{v}\frac{L}{z}\tau\right)-dB_S\left(\boldsymbol{\rho}+\mathbf{v}\frac{L}{z}\tau\right),\quad(16)$$

where dB_S is the spatial phase-covariance function for a spherical wave propagating through a differential slab of turbulent refractive-index variations. Again assuming uncorrelated effects from parallel planes, valid for $L\gg L_0$, the entire autocorrelation function, $R_{\delta S}(\tau)$, is the path integral of Eq. (16),

$$R_{\delta S}(\tau)=\int_0^L R_{\delta S}(\tau,z)dz$$

$$=[2B_S(\mathbf{v}\tau)-B_S(\boldsymbol{\rho}-\mathbf{v}\tau)-B_S(\boldsymbol{\rho}+\mathbf{v}\tau)$$

$$+2B_S(\infty)-B_S(-\infty)-B_S(\infty)].\quad(17)$$

For a three-dimensionally homogeneous and isotropic refractivity spectrum and a well-behaved phase-covariance function, i.e., $B_S(\infty)=B_S(-\infty)=0$,[7] Eq. (17) with $\boldsymbol{\rho}$ and $\mathbf{v}$ parallel becomes

$$R_{\delta S}(\tau)=2\pi^2k^2\int_0^L dz$$

$$\times\int_0^\infty dKK\Phi_n(K)\left\{1+\cos\left[\frac{K^2z(L-z)}{kL}\right]\right\}$$

$$\times\left[2J_0(Kv\tau)-J_0\left(\frac{K\rho z}{L}-Kv\tau\right)\right.$$

$$\left.-J_0\left(\frac{K\rho z}{L}+Kv\tau\right)\right].\quad(18)$$

The form of Eq. (18) results from the insertion of $B_S(\rho)$ from Eq. (6) into Eq. (17). Substituting Eq. (18) into the definition of the temporal power spectrum, Eq. (1), we finally obtain

$$W_{\delta S}(f)=32\pi^2k^2\int_0^L dz\sin^2\left(\frac{\pi\rho fz}{vL}\right)\int_{2\pi f/v}^\infty dK$$

$$\times\left(K\Phi_n(K)[(Kv)^2-(2\pi f)^2]^{-\frac{1}{2}}\right.$$

$$\left.\times\left\{1+\cos\left[\frac{K^2z(L-z)}{kL}\right]\right\}\right).\quad(19)$$

The τ integration (see Appendix B), although involved, is straightforward. Note the $\sin^2[\pi\rho fz/(vL)]$ term is the same filter function obtained in the plane-wave case[1] with the exception that in Eq. (19) we must integrate over the propagation path or, equivalently, over the spectral components in the received pattern which, owing to the geometric magnification of the velocity, $v(L/z)$, are moving at different speeds.

Equation (19) may be cast in a form similar to Eq. (12) with the substitutions $(u+1)/2=(z/L)$, $\sigma=[Kv/(2\pi f)]^2-1$, and using the Kolmogorov spectrum defined in Eq. (11). Then

$$W_{\delta S}(f)=0.264\pi^2k^{\frac{1}{3}}L^{7/3}C_n{}^2v^{-1}\Omega^{-8/3}$$

$$\times\int_0^1 du\left[1-\cos\left(\frac{\pi\rho fu}{v}\right)\cos\left(\frac{\pi\rho f}{v}\right)\right]$$

$$\times\left(\int_0^\infty\frac{d\sigma\sigma^{-\frac{1}{2}}}{(\sigma+1)^{11/6}}\{1+\cos[-\tfrac{1}{4}\Omega^2(\sigma+1)(1-u^2)]\}\right),$$

$$(20)$$

where $\Omega=f/f_0$ as before. The inside integral may be written as follows.

$$W_{\delta S}(f)=4.38k^{\frac{1}{3}}L^{7/3}C_n{}^2v^{-1}\Omega^{-8/3}$$

$$\times\int_0^1 du\left[1-\cos\left(\frac{\pi\rho f}{v}\right)\cos\left(\frac{\pi\rho fu}{v}\right)\right]$$

$$\times[1+G(\tfrac{1}{4}\Omega^2u^2)],\quad(21)$$

where

$$G=\frac{\Gamma(11/6)}{\pi^{\frac{1}{2}}\Gamma(\frac{4}{3})}\operatorname{Re}\left\{\exp[-i\tfrac{1}{4}\Omega^2(u^2-1)]\right.$$

$$\left.\times\int_0^\infty\frac{d\sigma\sigma^{-\frac{1}{2}}}{(\sigma+1)^{11/6}}\exp[-i\tfrac{1}{4}\Omega^2(u^2-1)]\right\}.\quad(22)$$

Equation (22), solved explicitly in Appendix A, upon substitution into Eq. (21), causes the u integration to become extremely cumbersome. The interesting behavior of Eq. (21) may be elicited from asymptotic solutions.

The function $G(\frac{1}{4}\Omega^2u^2)$ is bounded by a sinusoid

$$G\leq\cos[\tfrac{1}{4}\Omega^2(u^2-1)].$$

Using this bound in Eq. (21), we obtain four terms, the last two involving

$$I_3\leq\int_0^1\cos[\tfrac{1}{4}\Omega^2(u^2-1)]du$$

and

$$I_4\leq\cos\left(\frac{\pi\rho f}{v}\right)\int_0^1\cos\left(\frac{\pi\rho fu}{v}\right)\cos[\tfrac{1}{4}\Omega^2(u^2-1)]du.$$

In the region $\Omega\gg\pi\rho f/v$, $\cos[\frac{1}{4}\Omega^2(u^2-1)]$ oscillates rapidly over the u integration compared to $\cos(\pi\rho fu/v)$ (also rapidly compared to unity in I_3) and, from a stationary-phase approximation, valid for large Ω, both the I_3 and I_4 contributions are of order Ω^{-1} times the

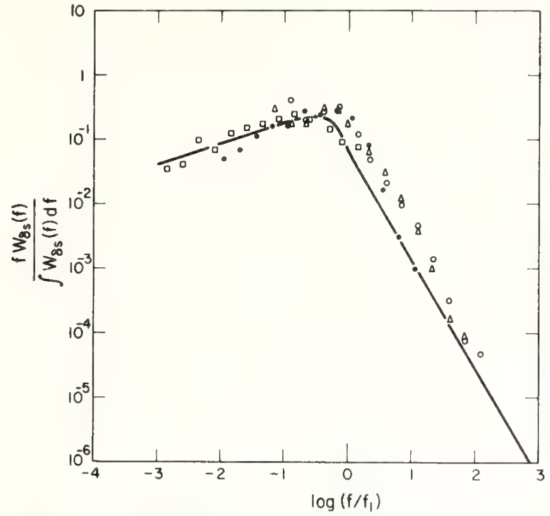

FIG. 4. Theoretical spherical-wave frequency spectrum of the phase-difference fluctuations (solid line) vs log of the frequency ratio f/f_1, where $f_1=v/\rho$, v is the transverse wind, and ρ the spacing of two sensors. The curve is normalized such that it also represents the normalized angle-of-arrival spectrum. Also shown are recent data for four different spacings. □—$\rho=0.3$ cm, ●—$\rho=3$ cm, △—$\rho=15$ cm, and ○—$\rho=30$ cm.

integral of the first two terms; therefore

$$[I_1+I_2+I_3+I_4]\approx\int_0^1 du\left[1-\cos\left(\frac{\pi\rho f}{v}\right)\cos\left(\frac{\pi\rho f u}{v}\right)\right]$$

$$=\left[1-\frac{\sin(2\pi\rho f/v)}{(2\pi\rho f/v)}\right],\quad \Omega\gg\pi\rho f/v. \quad (23)$$

For $\Omega\ll\pi\rho f/v$, G oscillates very slowly in I_4 compared with $\cos(\pi\rho f u/v)$ and we may use its asymptotic form from Eq. (22), i.e., $G\rightarrow 1$ as $\Omega\rightarrow 0$, in the important region of u integration. Therefore,

$$[I_1+I_2+I_3+I_4]\approx 2\int_0^1 du\left[1-\cos\left(\frac{\pi\rho f}{v}\right)\cos\left(\frac{\pi\rho f u}{v}\right)\right]$$

$$=2\left[1-\frac{\sin(2\pi\rho f/v)}{(2\pi\rho f/v)}\right],\ \Omega\ll\pi\rho f/v. \quad (24)$$

Substituting Eqs. (23) and (24) and rewriting the Ω constraints by use of the formula, $\Omega=f/f_0$, $f_0=v(2\pi\lambda L)^{-\frac{1}{2}}$, gives for the asymptotic forms,

$$W_{\delta S}(f)=0.033C_n{}^2k^2Lv^{5/3}$$
$$\times\left[1-\frac{\sin(2\pi\rho f/v)}{(2\pi\rho f/v)}\right]f^{-8/3},\quad \rho\ll(\lambda L)^{\frac{1}{2}}, \quad (25)$$

$$W_{\delta S}(f)=0.066C_n{}^2k^2Lv^{5/3}$$
$$\times\left[1-\frac{\sin(2\pi\rho f/v)}{(2\pi\rho f/v)}\right]f^{-8/3},\quad \rho\gg(\lambda L)^{\frac{1}{2}}. \quad (26)$$

Equations (25) and (26) are the desired results. (Of course, the restriction $f>v/L_0$ applies to these and all results of this paper.) The comments following Eqs. (50) and (51) of Ref. 1 apply directly, with the interesting exception that Eqs. (25) and (26) do not predict nulls in the spectrum as was the case for plane waves. Lawrence and Strohbehn removed the nulls by noting that variations of the wind along the path would tend to smear them out and produce a smooth high-pass filter with a breakpoint at $f\approx\frac{1}{2}v_\perp{}^2/(\sigma_v\rho)$, where σ_v is the standard deviation of the transverse wind, $v_\perp$. In the derivation of Eqs. (25) and (26) the assumption of a point source with its accompanying spherical divergence produced a multiplicity of scale velocities in the pattern instead of a single velocity corresponding to the transverse wind as in the plane-wave case. These different pattern motions smeared out the nulls in a fashion analogous to that described by Lawrence and Strohbehn, resulting in a $[1-(\sin x)/x]$ high-pass filter with a break point at $f\sim v/\rho$, independent of wind variations along the path. For the asymptotic regions $\rho\ll(\lambda L)$ and $\rho\gg(\lambda L)$, the plane- and spherical-wave results are the same, with the exception of this effect.

ANGLE-OF-ARRIVAL SPECTRUM

Tatarski[6] indicates that the angle-of-arrival spectrum of a plane wave is related to the phase-difference spectrum. By setting $\rho=b$ in $W_{\delta S}$ for an interferometer of separation b, he implies that $W_\alpha(f)\approx(1/k^2)W_{\delta S}(f)$, where α is the angle-of-arrival. Assuming the same relation applies for spherical waves, using Eqs. (25) and (26), we have

$$W_\alpha(f)=0.033C_n{}^2k^2Lv^{5/3}\left[1-\frac{\sin(2\pi bf/v)}{(2\pi bf/v)}\right]f^{-8/3},$$
$$b\ll(\lambda L)^{\frac{1}{2}}, \quad (27)$$

$$W_\alpha(f)=0.066C_n{}^2k^2Lv^{5/3}\left[1-\frac{\sin(2\pi bf/v)}{(2\pi bf/v)}\right]f^{-8/3},$$
$$b\gg(\lambda L)^{\frac{1}{2}}, \quad (28)$$

for the temporal power spectrum of the angle-of-arrival fluctuations. This result also applies to about the same order of approximation for a telescope of diameter b.[1]

CONCLUSIONS

The formulas developed for the spherical-wave scintillation spectrum, plotted in Figs. 1 and 3, indicate power at higher frequencies, less relative power in the low frequencies, and a central frequency approximately a factor of 2 higher than the equivalent plane-wave results. There is no essential difference of the plane- and spherical-wave phase power spectrum (Fig. 2). Table I contains all of the asymptotic results for these spectra, the corresponding results for plane waves, and includes a corrected form of Tatarski's low-frequency asymptote for $W_\chi(f)$.

Figure 4 illustrates some recent optical phase-difference measurements, taken at four different spacings on a uniform propagation path of 70 m ($\lambda = 0.6328\ \mu$m). The power spectrum was found by using the fast Fourier transform directly on the time series of the sampled phase-difference data. Each point illustrated represents an average of the quantity $fW_{\delta S}(f)$ over many adjacent points contained in evenly spaced $\log f$ intervals about the frequency shown. The solid line is the theoretical curve [Eqs. (25) and (26)] normalized to the appropriate phase structure function.

The data were plotted in terms of the characteristic frequency, $f_1 = v/\rho$, a function of the measured transverse wind, v, and the spacing, ρ. At each of the four spacings, $\rho = 0.3$, 0.15, 0.03, and 0.003 m; the measured mean-square phase difference was used as the normalization factor. The transverse wind speed averaged 0.72 m/s.

The theoretical curves for phase difference [Eqs. (25) and (26)] were normalized to the mean-square phase deviation at each spacing, i.e., the phase structure function. Tatarski[6] gives the spherical-wave phase structure function as

$$D_S(\rho) = 0.54k^2LC_n^2\rho^{5/3}, \quad l_0 \ll \rho \ll (\lambda L)^{\frac{1}{2}},$$

and

$$D_S(\rho) = 1.09k^2LC_n^2\rho^{5/3}, \quad \rho \gg (\lambda L)^{\frac{1}{2}}.$$

With this as a normalization factor, we obtain the theoretical curve in the form

$$\frac{fW_{\delta S}(f)}{\int W_{\delta S}(f)df} = 16.5\left[1 - \frac{\sin(2\pi f/f_1)}{(2\pi f/f_1)}\right]\left(\frac{f}{f_1}\right)^{-5/3}, \quad (29)$$

valid for both $l_0 \ll \rho \ll (\lambda L)^{\frac{1}{2}}$ and $\rho \gg (\lambda L)^{\frac{1}{2}}$. Equation (29), plotted as the solid line in Fig. 4, also applies, using Eqs. (27) and (28) for the angle-of-arrival-fluctuation spectrum. It is interesting to note that the breakpoint in Fig. 4 depends only on the mean wind velocity and the spacing and not on the standard deviation of the wind as in the plane-wave case. Good agreement with the data is shown.

ACKNOWLEDGMENT

The author gratefully acknowledges the valuable contributions of M. H. Ackley for carefully checking the equations, computing all the curves, and pointing out the error in Tatarski's equation.

APPENDIX A

In order to evaluate Eq. (12) in the text, we write the σ integral in the form

$$I = \mathrm{Re}\left(\int_0^\infty \frac{d\sigma\sigma^{-\frac{1}{2}}}{(\sigma+1)^{11/6}} \times\{1 \mp \exp[-i\tfrac{1}{4}\Omega^2(\sigma+1)(u^2-1)]\}\right), \quad (A1)$$

where Re means take the real part of the result in the boldface parentheses. With the aid of tables,[9] the first integral is easily performed in terms of gamma functions

$$\int_0^\infty \frac{d\sigma\sigma^{-\frac{1}{2}}}{(\sigma+1)^{11/6}} = \frac{(\pi)^{\frac{1}{2}}\Gamma(\frac{4}{3})}{\Gamma(11/6)}. \quad (A2)$$

From Erdelyi *et al.*,[10] the second integral is[11]

$$(\pi)^{\frac{1}{2}}[i\tfrac{1}{4}\Omega^2(u^2-1)]^{1/6}\exp[-i\tfrac{1}{8}\Omega^2(u^2-1)] \times W_{2/3,-2/3}[i\tfrac{1}{4}\Omega^2(u^2-1)], \quad (A3)$$

where $W_{m,n}$ is the Whittaker[12] function. It is convenient to express Eq. (A3) in terms of the confluent hypergeometric function, ${}_1F_1$, where

$${}_1F_1(a,b,x) = \sum_{n=0}^{\infty} \frac{\Gamma(a+n)\Gamma(b)}{\Gamma(b+n)\Gamma(a)} \frac{x^n}{n!}. \quad (A4)$$

From the NBS Handbook,[12] we find that Eq. (A3) may be written

$$\frac{(\pi)^{\frac{1}{2}}\Gamma(\frac{4}{3})}{\Gamma(11/6)}\exp(-x)\left[{}_1F_1(\tfrac{1}{2}, -\tfrac{1}{3}, x) + \frac{\Gamma(-\frac{4}{3})\Gamma(11/6)}{(\pi)^{\frac{1}{2}}\Gamma(\frac{4}{3})}x^{\frac{4}{3}}{}_1F_1(11/6, 7/3, x)\right], \quad (A5)$$

where $x = i\Omega^2\frac{1}{4}(u^2-1)$. Noting also that

$$e^{-x}{}_1F_1(a,b,x) = {}_1F_1(b-a, b, -x)$$

and substituting Eqs. (A2) and (A5) into Eq. (A1) yields

$$I = \frac{(\pi)^{\frac{1}{2}}\Gamma(\frac{4}{3})}{\Gamma(11/6)}\mathrm{Re}\left[1 \mp {}_1F_1(-\tfrac{5}{6}, -\tfrac{1}{3}, -x) \mp \frac{\Gamma(-\frac{4}{3})\Gamma(11/6)}{(\pi)^{\frac{1}{2}}\Gamma(\frac{4}{3})}x^{\frac{4}{3}}{}_1F_1(\tfrac{1}{2}, 7/3, -x)\right]. \quad (A6)$$

Inserting Eq. (A6) into Eq. (12) yields

$$W_{\chi,S}(f) = 0.132\pi^2k^{\frac{1}{3}}L^{7/3}C_n^2v^{-1}\Omega^{-8/3}\frac{(\pi)^{\frac{1}{2}}\Gamma(\frac{4}{3})}{\Gamma(11/6)}R_e\left\{\int_0^1 duI\right\}.$$

The integral in the curly brackets is most easily evaluated by substituting $z = -\Omega^2\frac{1}{4}(u^2-1)$ and $t = \frac{1}{4}\Omega^2$; then

$$\int_0^1 duI = \frac{1}{2(t)^{\frac{1}{2}}}\int_0^t dz(t-z)^{-\frac{1}{2}}\left[1 \mp {}_1F_1(-\tfrac{5}{6}, -\tfrac{1}{3}, iz) \mp \frac{\Gamma(-\frac{4}{3})\Gamma(11/6)}{(\pi)^{\frac{1}{2}}\Gamma(\frac{4}{3})}(-iz)^{\frac{4}{3}}{}_1F_1(\tfrac{1}{2}, 7/3, iz)\right].$$

By use of tables,[13] these integrals yield Eq. (13).

APPENDIX B

Obtaining Eq. (19) in the text required evaluation of the integral

$$\int_0^\infty d\tau \cos\gamma\tau[J_0(\beta+\alpha\tau)+J_0(\beta-\alpha\tau)]. \quad \text{(B1)}$$

Using the addition formulas for Bessel functions[14]

$$J_0(\beta+\alpha\tau)+J_0(\beta-\alpha\tau)$$
$$=\sum_{k=-\infty}^{\infty} J_{-k}(\beta)J_k(\alpha\tau)+\sum_{k=-\infty}^{\infty} J_k(\beta)J_k(\alpha\tau),$$

noting that $J_{-k}=(-1)^k J_k$, and simplifying yields

$$J_0(\beta+\alpha\tau)+J_0(\beta-\alpha\tau)$$
$$=2J_0(\beta)J_0(\alpha\tau)+4\sum_{k=1}^{\infty} J_{2k}(\beta)J_{2k}(\alpha\tau). \quad \text{(B2)}$$

Substituting Eq. (B2) into Eq. (B1) and integrating[15] yields

$$2J_0(\beta)(\alpha^2-\gamma^2)^{-\frac{1}{2}}+4\sum_{k=1}^{\infty}(-1)^k$$
$$\times J_{2k}(\beta)T_{2k}(\gamma/\alpha)(\alpha^2-\gamma^2)^{-\frac{1}{2}}, \quad 0<\gamma<\alpha, \quad \text{(B3)}$$

and

$$0, \quad \alpha<\gamma<\infty,$$

where $T_{2k}(z)=\cos[2k\cos^{-1}(z)]$. Noting that Eq. (B3) is related to the series representative of $\cos(\beta\gamma/\alpha)$,[16] we write Eq. (B3) as

$$2(\alpha^2-\gamma^2)^{-\frac{1}{2}}\cos(\beta\gamma/\alpha), \quad 0<\gamma<\alpha,$$

and (B4)

$$0, \quad \alpha<\gamma<\infty.$$

Equation (B4) is the result desired and gives the $\sin^2[\pi\rho fz/(vL)]$ spectral-filter term in Eq. (19) for $\gamma=2\pi f$, $\beta=K\rho z/L$, and $\alpha=Kv$.

REFERENCES

[1] R. S. Lawrence and J. W. Strohbehn, Proc. IEEE **58**, 1523 (1970).

[2] Formulas derived here in the context of optical propagation, where n is function of the random temperature field, extend directly to microwave or acoustic propagation with n interpreted as a function of the humidity fields or temperature and wind fields, respectively (see Refs. 3–5).

[3] R. W. Lee and J. C. Harp, Proc. IEEE **57**, 375 (1969).

[4] S. F. Clifford and J. W. Strohbehn, Proc. IEEE **AP-18**, 264 (1970).

[5] S. F. Clifford and E. H. Brown, J. Acoust. Soc. Am. **48**, 1123 (1970).

[6] V. I. Tatarski, *Wave Propagation in a Turbulent Atmosphere* (Nauka, Moscow, 1967) (in Russian).

[7] The phase fluctuations, because they are most sensitive to the largest turbulent eddy scales, have an undefined spatial covariance function for a Kolmogorov spectrum of turbulence. Therefore, the phase power spectrum should be defined in terms of structure functions (Ref. 1) that are less sensitive to large scale variations. The two definitions give the same spectrum when the covariance function exists.

[8] *Tables of Integral Transforms*, edited by A. Erdelyi (McGraw-Hill, New York, 1959), Vol. 1, p. 43, No. 1.

[9] Reference 8, Vol. 1, p. 311, No. 30.

[10] Reference 8, Vol. 2., p. 234, No. 12.

[11] The integral in Ref. 9 converges for $\lambda-\rho\geq 2$ if $\mathrm{Re}(a)=0$, a condition satisfied by Eq. (A1).

[12] *Handbook of Mathematical Functions*, edited by M. Abramowitz and I. A. Stegun (U. S. Govt. Printing Office, Washington, 1964; Dover, New York, 1965).

[13] Reference 8, Vol. 2, p. 200, No. 95.

[14] Reference 12, p. 363, No. 9.1.75.

[15] Reference 8, Vol. 1, p. 43, No. 2.

[16] Reference 12, p. 361, No. 9.1.44.

Reprinted from Journal of Optical Society of America 61,
No. 10, 1279-1284, 1971.

Phase Variations in Atmospheric Optical Propagation

S. F. Clifford, G. M. B. Bouricius, G. R. Ochs, and Margot H. Ackley
National Oceanic and Atmospheric Administration, Environmental Research Laboratories, Boulder, Colorado 80302

(Received 26 March 1971)

Temperature structure in the atmosphere, transported by the wind across a laser beam, produces time variations in the optical path length. Using a He–Ne laser (0.6328 μm) on a 70-m propagation path, we measured the optical phase variations at four different spacings, $\rho \leq 30$ cm. Simultaneously, a midpath measurement of wind velocity and temperature structure parameter, C_T^2, provided the necessary meteorological measurements to compare the observed phase structure function with Tatarski's theoretical curve. We obtained excellent agreement between theory and experiment. Direct measurements of the outer scale of turbulence, taken continuously over a 24-h period at a height of 1.6 m, indicated an average outer scale of 1.3 m with diurnal variations of ±20%. The frequency spectrum of the received phase difference at each of the four spacings is plotted and its implications for the data-sampling rate are examined. The curves obtained exhibit excellent agreement with the predicted spherical-wave phase-difference frequency spectrum.

Index Headings: Inhomogeneous media; Coherence; Atmospheric optics.

The received phase of an optical beam propagated through the atmosphere varies with time due to turbulent temperature variations in the intervening medium. Many studies, both theoretical[1–4] and experimental,[5–9] have been undertaken. The major thrust of some of these[5,6] is to propose extremely small values (3–10 cm) of the outer scale of turbulence, derived from phase-difference measurements, for both long and short paths (3 m–3.5 km) and almost independent of height above the ground (1–30 m). These experiments contain only the most qualitative statements about meteorological conditions and hence cannot reasonably be compared with theory.

The theoretical result of Tatarski[1] that directly bears on our phase-difference measurements is his derivation of the phase structure function. The phase of a wave, after propagating through a region of refractive-index variations, will vary randomly as a function of coordinates in the receiving plane. The structure function is defined as the mean-square variation of the received phase φ between two observation points separated by a distance ρ, i.e.,

$$D_\varphi = \langle [\varphi(\mathbf{r}+\boldsymbol{\rho}) - \varphi(\mathbf{r})]^2 \rangle. \tag{1}$$

The angle brackets indicate an ensemble average. The physical utility of the structure function is that, as a measure of the phase deviation in the receiving plane, it defines phase coherence. A length derived from the separation at which the structure function exceeds a certain value, say π^2, is related to the maximum usable aperture diameter for optical heterodyne receivers. Therefore, measurements of the phase structure function have important practical significance.

Specifically, for a wave of wavelength λ propagating a distance L in a homogeneous and isotropic turbulent medium, Tatarski obtains, for plane waves

$$D_\varphi(\rho) = 2.91 k^2 L C_n^2 \rho^{5/3}, \quad \sqrt{(\lambda L)} \lesssim \rho < L_o \tag{2}$$

and for spherical waves

$$D_\varphi(\rho) = 1.09 k^2 L C_n^2 \rho^{5/3}, \quad \sqrt{(\lambda L)} \lesssim \rho < L_o, \tag{3}$$

where L_o is the outer scale of turbulence. The quantity C_n^2 is a measure of the magnitude of the refractive-index fluctuations and for $\lambda = 0.6328$ μm is related directly to C_T^2, the temperature structure parameter, by the formula[7]

$$C_n^2 = [(79P/T^2) \times 10^{-6}]^2 C_T^2. \tag{4}$$

Here P is the barometric pressure in millibars and T the temperature in Kelvin. [Equations (2) and (3) may be looked upon as the limiting formulas for the more accurate beam-wave[3] approach.]

Our present work consists of direct measurements of all the variables pertinent to a complete description of

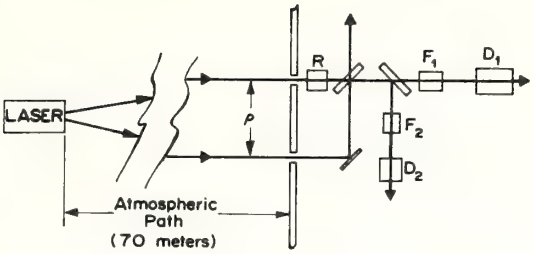

FIG. 1. Schematic diagram of the optical-phase experiment, illustrating configuration of laser, retardation plate R, optical filters F_1 and F_2, and signal detectors D_1 and D_2.

the statistics of the phase-difference fluctuations. We then compare the observed data with existing theory.

EXPERIMENT DESCRIPTION

The site of the experiment was the National Oceanic and Atmospheric Administration (NOAA) Table Mountain Research Facility described earlier.[7] A highly stabilized, spatially filtered, laser beam initially 5 cm in diameter illuminates a 2-m-diam area at the receiver 70 m away. The beam, polarized at an angle of 45° to the horizontal, propagates to the interferometer shown schematically in Fig. 1. Different portions pass through two 2-mm apertures separated by a distance ρ. The phase of the horizontally polarized component of signal 1 is retarded 90° at R with respect to the same component of signal 2, before they interfere at the following beam splitter. The vertical components interfere directly. The beams pass through analyzers F1 and F2, which are polarized in the vertical and horizontal directions, respectively. The signals detected at D_1 and D_2 will then be in quadrature, proportional to the sine and cosine of the phase difference of the two paths. (The detailed construction and more elaborate analysis of the essentials of this interferometer may be found elsewhere.[10]) A series of apertures and mirror arrangements with the same retardation arm permit the acquisition of data with a single set of photomultiplier detectors by rapidly sequencing different spacings. The output voltages S_1 and S_2 are recorded on magnetic tape. Because the phase-difference data at different spacings are obtained sequentially, a typical 20-s run at each separation requires a total experiment time of 80 s to cycle through the four separations. We have observed that steady winds of at least 1 m/s are required to produce reasonably stationary atmospheric conditions over this 80-s period.

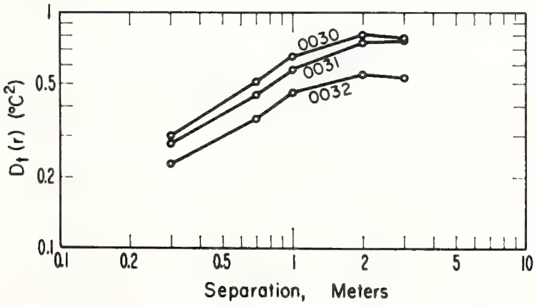

FIG. 2. Plot of temperature structure function vs separation measured on 2 June 1970.

A differential temperature sensor,[11] 0.5 m off the beam axis and at the same 1.6-m height as the He–Ne laser, is placed near the middle of the optical path. The temperature-sensor measurements, using a separation of 40 cm, provided an estimate of the refractive-turbulence parameter, C_n^2, for each run. C_n^2 is derivable via C_T^2 as described in Eq. (4). A simple analog circuit computes C_T^2 continuously from the temperature-difference measurements. A propellor-driven anemometer, 5 m up-wind, monitored the wind speed and direction. The temperature and wind data were recorded on a paper chart.

The data reduction consisted of digitizing the sine and cosine of the phase difference (with careful attention to proper sampling rate, as discussed below) and using a digital computer to find the phase difference, along with its mean-square fluctuation, statistical distribution, and temporal power spectrum. The digitizing was very important because we sampled the sine and cosine functions of the phase difference and then retrieved the phase-difference information by use of an arctangent computer routine. Hence, an insufficient sampling rate (one with less than two samples a period of the highest significant frequency in the data) would produce peculiar results, far removed from the true phase. From a plot of the deduced phase difference vs time it becomes obvious whether the sampling rate is sufficiently rapid. Severe trends in the normally zero-mean phase difference and interesting geometric figures are generated by sampling too slowly when the phase difference exceeds 360°.

OUTER-SCALE MEASUREMENTS

On 2 June 1970, the first evening of phase-data acquisition, we attempted to coordinate our experiment with simultaneous temperature-sensor measurements of the outer scale. Unfortunately, the phase data taken on that occasion were useless. We include those temperature-sensor measurements here and assume that they give representative values of the outer scale of turbulence along our path for the evenings when we did obtain valid phase data.

Using five sets of platinum-resistance-thermometer probes[11] (2.5-μm diameter, 2 mm long) at horizontal spacings of 0.3, 0.7, 1.0, 2.0, and 3.0 m, continuous 24-h measurements of temperature fluctuations at 1.6 m above the ground supplied information about the temperature structure function.

Assuming that the temperature fluctuations are statistically homogeneous and isotropic, Tatarski[1] shows that the structure function is

$$D_T(r)=2\langle T_r^2\rangle(1-R_r), \tag{5}$$

where R_r is the normalized covariance of the temperature fluctuations at two points separated by a distance, r. We measure $\langle T_r^2\rangle$, the mean-square temperature fluctuation, and the normalized covariance as a function of separation using 100-s averages for each quantity. (The normalized covariance was measured using a 1-bit correlator[12] with a 100-s cutoff.) The averaging time was varied from 10 to 100 s with no change of $\langle T_r^2\rangle$ or the normalized covariance.

Figure 2 illustrates three such temperature structure functions on log–log scales. If we assume a Kolmogorov spectrum of turbulence, the slope of the line drawn through the points should be $\frac{2}{3}$ until the outer scale is reached. The curves should then change slope at a spacing corresponding to the outer scale. The curves appear to obey the $\frac{2}{3}$ law up to separations of about 1–2 m.

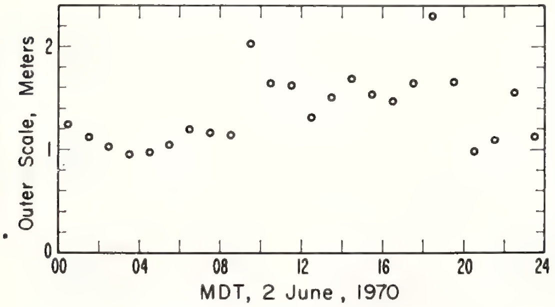

Fig. 3. Outer scale, measured at 1.6 m above the ground, vs time.

Figure 3 uses the somewhat arbitrary definition of the outer scale as the intersection of the lines drawn through the two extreme pairs of data points, to illustrate the behavior of hourly mean outer scale for a 24-h period. The average of these points illustrates that the outer scale measured over our uniform path is of the order of 1.3 m±20%. This is somewhat higher than the value suggested by Tatarski,[13] $L_o{}^t=Kh$, where K is von Karman's constant, roughly equal to 0.4, and somewhat lower than that suggested by Fried,[14] $L_o{}^f=\sqrt{(4h)}$. For $h=1.6$ m, $L_o{}^t=0.64$ m, $L_o{}^f=2.5$ m.

ANALYSIS

The useful phase-difference data consisted of runs in July and August of 1970—in each case 3–4 h after sunset. Our measurement technique demands that the medium be stationary for 1–2 min. A relatively uniform wind of 2 m/s provided excellent results for the July data and a lighter wind somewhat less so for August.

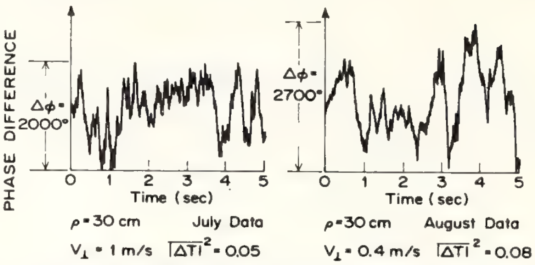

Fig. 4. Phase difference vs time for July and August 1970, illustrating the variability of the data as a function of transverse wind v and average rectified temperature difference $\langle|\Delta T|\rangle^2$.

Figure 4 illustrates a comparison between the conditions of July and August for the same 30-cm spacing. Using $\langle|\Delta T|\rangle^2$ as an indicator of the strength of turbulence[7] on our 70-m path, we observe the higher peak-phase difference corresponding to the more turbulent August conditions and note the predominance of lower frequencies to the lighter transverse winds on that occasion.

Figure 5 shows a typical set of phase-difference data, $\Delta\varphi$, taken consecutively at each of our four spacings. Note how the frequency content varies with spacing. This was well predicted by Tatarski[13] and is a function of the transverse wind (here, less than 1 m/s) and the spatial-filtering action of the phase-difference operation [see Eq. (8)]. The data were retrieved by digitizing $\sin\Delta\varphi$ and $\cos\Delta\varphi$, which are proportional to fringe intensity at fixed positions. The arctangent operation was subsequently performed in the digital computer, resulting in the curves of Fig. 5. The rate of change of the sampled function, e.g., $\cos\Delta\varphi$, is determined not only by the frequency content of $\Delta\varphi$ but also by the peak-phase deviation. We found that our sampling rate (1000 samples/s), sufficient to prevent aliasing, was determined primarily by the large peak-phase

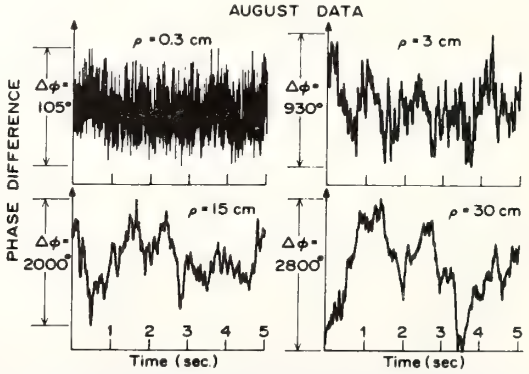

Fig. 5. Typical data, phase difference vs time, taken at each of four spacings, $\rho=0.3$, 3, 15, 30 cm, illustrating predominance of lower frequencies and higher peak-to-peak variations as spacing increases.

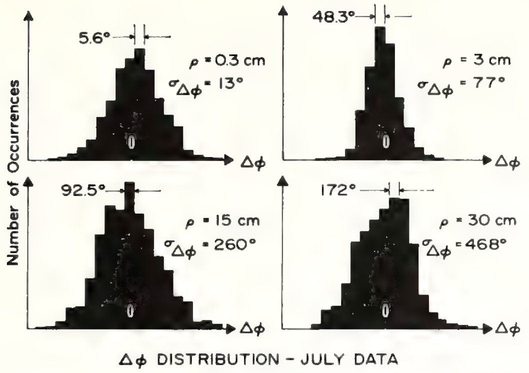

FIG. 6. Probability distribution of the received phase difference for each of four spacings, $\rho = 0.3$, 3, 15, and 30 cm. $\sigma_{\Delta\varphi}$ is the standard deviation of the phase difference at each point, $\sigma_{\Delta\varphi} = \sqrt{D_\varphi}$.

deviations at the wider spacings and not by the high-frequency variations of $\Delta\varphi$.

There is an insidious effect associated with this phenomenon. Any sampling rate will produce the correct mean-square phase deviation (or equivalently, phase-difference variance) provided that the phase difference does not exceed 2π rad, i.e., as long as the fluctuation remains within this bound, it is not possible to lose track of entire cycles and hence err in the variance calculation. Once a full cycle is exceeded, however, the aliased result (caused by too slow a sampling rate) will increase slowly and saturate prematurely at less than $(2\pi)^2$ as the spacing is changed. The properly digitized phase-difference variance will continue to increase as it does for small separations.[15] We experimented with aliased data and found, for our 70-m path and rather large C_n^2, that the variance saturated at approximately 3-cm spacing, the point where the phase difference first exceeded 2π rad a significant percentage of the time.

Figure 6 shows typical statistical distributions obtained from one run in July. (Note that a large part of the data analysis was done on the July data only. Then the wind was steady and the turbulent conditions, as reflected by our meteorological measurements, were stationary over 10-min periods. The August data exhibited light and variable winds.)

The points on the structure function presented in Fig. 7 are the result of several runs on 2 July. The data are uncorrected for measured C_n^2 variations and nevertheless exhibit a rather close clustering along the 5/3 line, shown for comparison. (The $\rho^{5/3}$ line was drawn without any regard to its intercept. It is merely to indicate slope.) The spread of the points at a specific spacing indicates the stability of the turbulent conditions during our runs. Some points at 3-cm spacing, for example, are separated by more than 40 min. Each point represents a 20-s average of the square of the phase deviation at that separation. Data were taken for longer runs, up to 2 min, to test the stability of the average, with excellent repeatability. This 20-s averaging time is at least 20 times the integral scale of the process, i.e., 20 times the duration needed for the largest (≈ 1 m) eddy to pass a single sensor at the observed wind speed. Figure 8 shows the same data corrected for the measured C_n^2 variations and averaged over all runs. (C_n^2 varied from 5.3×10^{-14} to 1.9×10^{-13} $\text{m}^{-2/3}$ for the duration of the experiment.) Here the data points were all normalized to a C_n^2 value of 1.0×10^{-13} $\text{m}^{-2/3}$ and the solid line is the plot of the spherical-wave theoretical curve from Eq. (3),

$$D_\varphi(\rho) = [1.09\times10^{-13}k^2L\rho^{5/3}](57.3)^2, \text{ (degrees)}^2 \quad (6)$$

or, for $k \sim 10^7$ m^{-1} and $L = 70$ m,

$$D_\varphi(\rho) = 2.5\times10^6\rho^{5/3}, \text{ (degrees)}^2. \quad (7)$$

The circled figure indicates the number of data points contained in the average. There is excellent agreement with the theory, Eq. (7), and no pronounced reduction of slope up to separations of 30 cm, in agreement with our outer-scale measurements.

Figure 9 illustrates, we believe for the first time, the temporal-frequency spectrum of the phase difference vs frequency f for each of our four spacings. [Figure (5) is a picture of the first 5 s of these same data and Fig. (6) its statistical distribution.] After sampling approximately 16 s of the phase difference for each

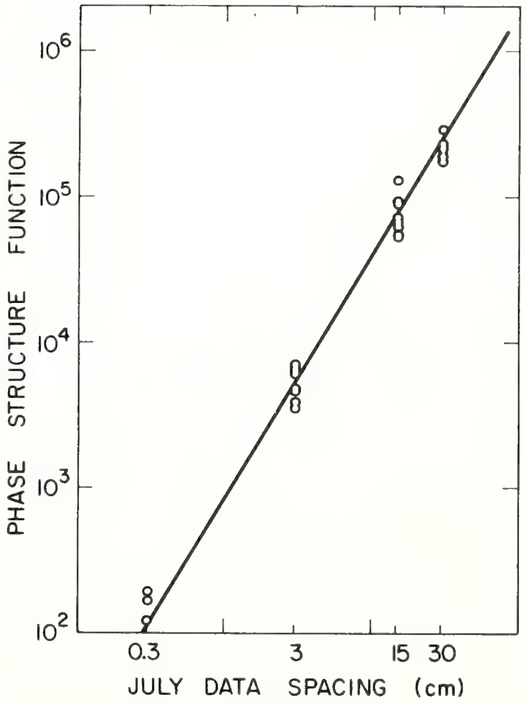

FIG. 7. Phase structure function (degrees squared) vs spacing (cm). Data uncorrected for C_n^2 variations and shown with a $\rho^{5/3}$ curve for comparison.

spacing at a rate of 1000 samples/s, we obtained 2^{14} data points that were directly used as input to a fast Fourier-transform routine. The output was 2^{13} values representing the contribution to the variance of $\Delta\varphi$, at equally spaced intervals in frequency. To obtain a representative set of points equally spaced in $\log f$ for our curve, we averaged $fW_{\delta\varphi}(f)$ over all points found in an interval of ± 0.125 in $\log f$ about each frequency selected. Each symbol in Fig. 9 is the result of this averaging process. Recently,[16] the spherical-wave phase-difference power spectrum was obtained. The solid lines represent the plot of this spherical-wave spectrum,

$$W_{\delta\varphi}(f)=0.066C_n{}^2k^2Lv^{5/3}\left(1-\frac{\sin(2\pi\rho f/v)}{(2\pi\rho f/v)}\right)f^{-8/3}. \quad (8)$$

Equation (8) is valid for $\rho \gg \sqrt{(\lambda L)}$. The result for $\rho \ll \sqrt{(\lambda L)}$ is 50% smaller. The value of the experimental parameters used in obtaining the plot were $C_n{}^2=1.1\times 10^{-13}$ $\mathrm{m}^{-2/3}$ (found from the paper-chart recording), the measured transverse wind $v=0.72$ m/s, $k\sim 10^7$ m^{-1}, $L=70$ m, and the four spacings $\rho=0.3$, 3, 15, and 30 cm. For our path and wavelength, $\sqrt{(\lambda L)}$ ~ 0.6 cm, so that all but the 0.3-cm case are clearly in the region $\rho \gg \sqrt{(\lambda L)}$. Our average measured wind velocity during this run was 1.7 m/s at an angle of 25° to our path. We were unable to read the paper chart any closer than ±5° which makes our transverse-wind value $v=0.72\pm 0.15$ m/s due to this uncertainty alone. However, this variation would not make much difference in our curves, and the data and theory are in good agreement.

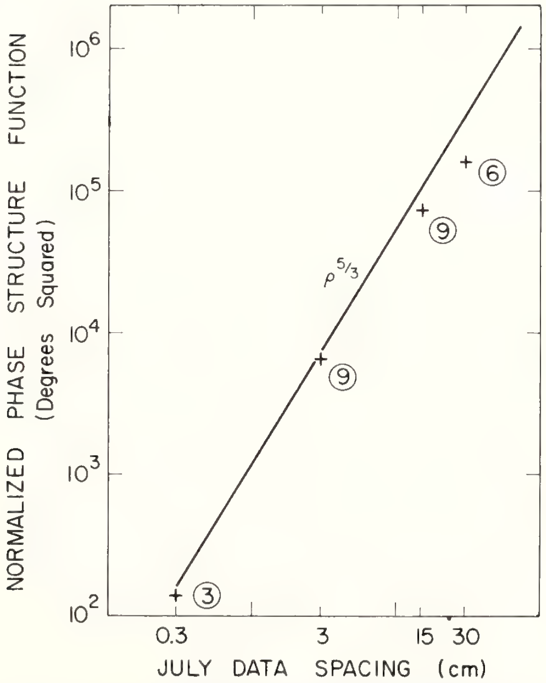

FIG. 8. Normalized phase structure function (degrees squared) vs spacing (cm). Each point represents the average value over the circled number of points. The solid line is the theoretical curve, $D_\varphi(\rho)=1.09\ k^2LC_n{}^2\rho^{5/3}$.

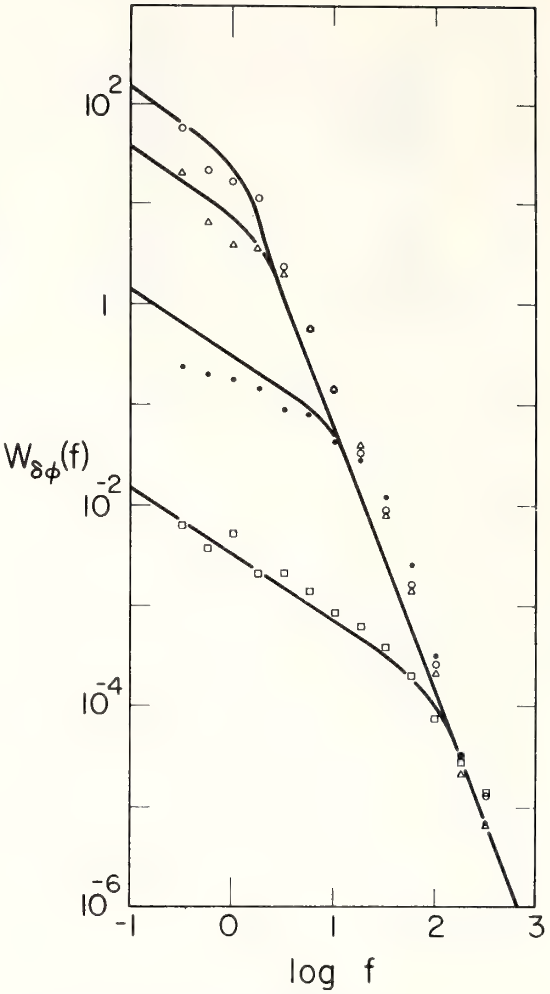

FIG. 9. Phase-difference temporal power spectrum $W_{\delta\varphi}(f)$ plotted vs frequency for four different spacings, ρ. □—$\rho=0.3$ cm, ●—$\rho=3$ cm, △—$\rho=15$ cm, and ○—$\rho=30$ cm. The solid lines are the corresponding theoretical curves plotted from Eq. (8).

CONCLUSIONS

Measurements of the phase structure function have shown direct correspondence with the predicted 5/3 law of Tatarski, persisting to spacings of 30 cm without significant bending, in agreement with outer-scale measurements taken at the same location at a different time. We have included effects, previously neglected, of transverse wind and spacing of the sensors. Noting the obvious importance of the eddy-transport velocity to the received frequency spectrum, and the high-pass filtering by the difference operation [see Eq. (8)], we have considered the effects of wind and spacing on the digitizing rate and discussed the effects of data aliasing on the derived structure-function power law. The phase-difference power spectrum, measured possibly for the first time, has well defined asymptotes and break points, and exhibits good correspondence to the spherical-wave theory.[16]

The agreement of these multiple-aperture measurements with our earlier single-aperture measurements,[7] with the results of Tatarski, and with each other, implies that a single-sensor measurement of phase using Taylor's hypothesis is a feasible and reliable way of studying the phase variations of a laser beam. The advantages of the single-sensor method are: simplicity of design, the large number of data points per run without interruption, and power requirements at only one end of the path. However, the technique requires a laser with extremely long coherence length (on the order of the path length) and, over long paths, can be sensitive to laser-frequency noise. The multiple-aperture technique allows propagation experiments over longer paths (provided scintillation effects are properly removed) and requires only short coherence lengths of the order of the maximum spacing.

ACKNOWLEDGMENTS

We gratefully acknowledge the computing assistance of N. M. Kohn and the extremely helpful discussions with R. S. Lawrence and J. W. Strohbehn.

REFERENCES

[1] V. I. Tatarski, *Wave Propagation in a Turbulent Medium* (McGraw–Hill, New York, 1960).

[2] A. Consortini and L. Ronchi, Nuovo Cimento **2**, 683 (1969).

[3] A. Ishimaru, Radio Sci. **4**, 295 (1969).

[4] D. L. Fried, J. Opt. Soc. Am. **57**, 175 (1967).

[5] M. Bertolotti, M. Carnevale, L. Muzii, and D. Sette, Appl. Opt. **7**, 2246 (1968).

[6] P. Burlamacchi, A. Consortini, L. Ronchi, and G. Toraldo di Francia, *Phase and Frequency Instabilities in Electromagnetic Wave Propagation* (Technivision Services, Slough, England, 1970).

[7] G. M. B. Bouricius and S. F. Clifford, J. Opt. Soc. Am. **60**, 1484 (1970).

[8] R G. Buser and G. K. Born, J. Opt. Soc. Am. **60**, 1079 (1970).

[9] M. Bertolotti, M. Carnevale, B. Crosignani, and P. D. Porto, Appl. Opt. **8**, 1111 (1969).

[10] G. M. B. Bouricius and S. F. Clifford, Rev. Sci. Instr. **41**, 1800 (1970).

[11] G. R. Ochs, ESSA Tech. Rept. IER 47-ITSA 46, U. S. Govt. Printing Office, Washington, D. C. (1967).

[12] G. R. Ochs, ESSA Tech. Rept. ERL 63-WPL 2, U. S. Govt. Printing Office, Washington, D. C. (1968).

[13] V. I. Tatarski, *Wave Propagation in a Turbulent Atmosphere* (in Russian) (Nauka, Moscow, 1967).

[14] D. L. Fried, Proc. IEEE **55**, 57 (1967).

[15] M. Bertolotti, M. Carnevale, L. Muzii, and D. Sette, Appl. Opt. **9**, 510 (1970).

[16] S. F. Clifford, J. Opt. Soc. Am. **61**, 1285 (1971).

20

Reprinted from Journal of Optical Society of America 60, No. 8, 1035-1037, 1970.

Relative Power Losses at the Mirrors of an Asymmetric, Confocal, Laser Interferometer

G. T. McNice and V. E. Derr
ESSA Research Laboratories, Boulder, Colorado 80302

(Received 7 January 1970)

The asymmetric, confocal, laser interferometer with output coupling apertures is considered. The diffraction losses at the two mirrors are shown to be equal, regardless of differences in mirror sizes or the existence of coupling apertures in one or both mirrors.

Index Headings: Interferometer; Laser; Mirrors; Diffraction.

The diffraction losses[1] of an asymmetric laser interferometer (one with geometrically dissimilar mirrors) are generally divided unequally between the two mirrows, depending on the interferometer geometry. The purpose of this analysis is to show that, within the conditions of the Fox and Li formulation,[2] the confocal asymmetric interferometer with circular or rectangular mirrors is an exception to the rule. Its diffraction losses are shown to occur equally at the two mirrors, regardless of differences of mirror sizes or the existence of coupling apertures in one or both mirrors. This result is useful in calculations associated with asymmetric, aperture-coupled laser interferometers.[3]

Assuming, then, that the interferometer is confocal (concave spherical mirrors separated by their common radius of curvature), that the mirrors are of circular or rectangular cross section with perfectly reflecting surfaces, and that the conditions of validity[4] of the Fox and Li interferometer theory are satisfied, the electric fields of a normal mode incident on the mirror surfaces are proportional to the eigenfunctions of a coupled set of integral equations of the form

$$\gamma_2\mu_2(\xi_2)=e^{i\alpha}\int_{f(a_1)}^{f(b_1)} K(\xi_2,\xi_1)\mu_1(\xi_1)d\xi_1 \qquad (1)$$

$$\gamma_1\mu_1(\xi_1)=e^{i\alpha}\int_{f(a_2)}^{f(b_2)} K(\xi_1,\xi_2)\mu_2(\xi_2)d\xi_2, \qquad (2)$$

where γ_1 and γ_2 are the eigenvalues associated with the eigenfunctions $\mu_1(\xi_1)$ and $\mu_2(\xi_2)$, and the kernels are real and symmetric[5]; that is,

$$K(\xi_1,\xi_2)=K(\xi_2,\xi_1)=K^*(\xi_1,\xi_2)=K^*(\xi_2,\xi_1). \qquad (3)$$

In these equations and the ones that follow, the mirrors are identified by the subscripts. The ξ's represent field positions on the mirror surfaces, the $f(b)$'s represent the outer dimensions of the mirrors, the $f(a)$'s represent the aperture sizes, and α is a constant. Explicit expressions for these quantities are given in Appendix A for both circular and rectangular mirrors.

If the eigenfunctions are normalized so that

$$\int_{f(a_1)}^{f(b_1)} |\mu_1(\xi_1)|^2 d\xi_1=\int_{f(a_2)}^{f(b_2)} |\mu_2(\xi_2)|^2 d\xi_2, \qquad (4)$$

it is shown in Appendix B that $|\gamma_1|^2$ and $|\gamma_2|^2$ may be interpreted as effective power reflection coefficients associated with the diffraction losses at mirrors 1 and 2, so that the fractional power loss at the two mirrors is $1-|\gamma_1|^2$ and $1-|\gamma_2|^2$. The fractional power loss per two-way transit is $1-|\gamma_1\gamma_2|^2$, regardless of the normalization of the eigenfunctions.

To determine the power losses of one mirror relative to the other, a relation between γ_1 and γ_2 is required. Such a relation can be obtained by multiplying both sides of Eq. (1) by $e^{-i\alpha}\mu_2^*(\xi_2)$, integrating over ξ_2, and interchanging the order of integration on the right side to produce

$$\gamma_2 e^{-i\alpha}\int_{f(a_2)}^{f(b_2)} |\mu_2(\xi_2)|^2 d\xi_2 = e^{i\alpha}\int_{f(a_1)}^{f(b_1)} \left[e^{-i\alpha}\int_{f(a_2)}^{f(b_2)} K(\xi_2,\xi_1)\mu_2^*(\xi_2)d\xi_2\right] \times\mu_1(\xi_1)d\xi_1. \qquad (5)$$

Applying Eq. (3), we see that the quantity in brackets is the complex conjugate of the right side of Eq. (2), so that Eq. (5) reduces to

$$\gamma_2 e^{-i\alpha}\int_{f(a_2)}^{f(b_2)} |\mu_2(\xi_2)|^2 d\xi_2=\gamma_1^* e^{i\alpha}\int_{f(a_1)}^{f(b_1)} |\mu_1(\xi_1)|^2\xi_1, \qquad (6)$$

and finally to the required relation

$$\gamma_2 e^{-i\alpha}=\gamma_1^* e^{i\alpha} \qquad (7)$$

under the normalization of Eq. (4). From Eq. (7) it follows that

$$|\gamma_1|^2=|\gamma_2|^2; \qquad (8)$$

thus the diffraction losses at the two mirrors are equal, regardless of differences of mirror or aperture sizes.[6]

Note that Eq. (8) does not imply that the power losses of the interferometer are independent of the mirror or aperture sizes. On the contrary, a change of any of these dimensions generally produces a corresponding change of the fractional power loss per transit of the interferometer, but the losses at the two mirrors change by the same factor, so that Eq. (8) remains valid. This result has been numerically substantiated for several asymmetric, confocal systems with circular mirrors and circular apertures, by solving Eqs. (1) and (2) with the numerical-integration technique of Fox and Li.[2] The possibility that these results might have wider validity than their proof has also been considered and discarded. Numerical solutions have shown Eq. (8) to be invalid for several asymmetric, nonconfocal systems.

APPENDIX A: EXPLICIT EXPRESSIONS FOR $K(\xi_i,\xi_j)$, $f(a_i)$, $f(b_i)$ AND α FOR CIRCULAR AND RECTANGULAR MIRRORS

The confocal interferometer with circular mirrors and apertures is shown in Fig. 1. The quantities in Eqs. (1) and (2) appropriate to this interferometer are

$$\left.\begin{aligned} K(\xi_i,\xi_j)&=\pi J_n[2\pi(\xi_i,\xi_j)^{\frac{1}{2}}]\\ \xi_i&=r_i^2/(\lambda d)\\ f(a_i)&=a_i^2/(\lambda d)\\ f(b_i)&=b_i^2/(\lambda d)\end{aligned}\right\}\begin{matrix} i,j=1,2\\ i\neq j,\end{matrix}$$
$$\alpha=(\pi/2)(n+1-4d/\lambda),$$

where λ is the wavelength, the r's are the radial coordinates of the field points, $J_n(x)$ is the nth order Bessel function of the first kind with argument x, and the remaining quantities are defined in the figure.

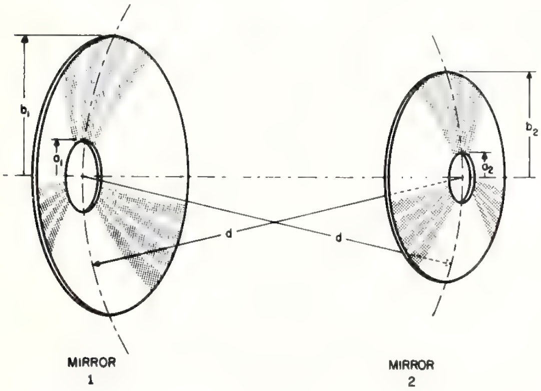

Fig. 1. Asymmetric confocal interferometer with circular mirrors and apertures.

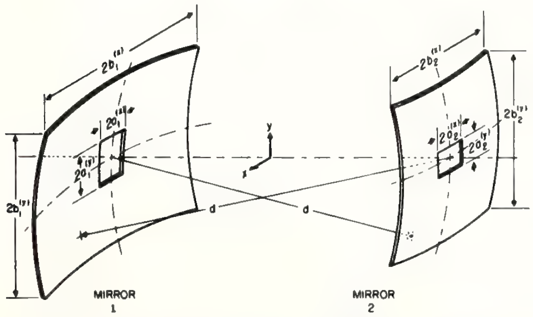

Fig. 2. Asymmetric confocal interferometer with rectangular mirrors and apertures.

The confocal resonator with rectangular mirrors and apertures is shown in Fig. 2. Here the integral equations separate into two sets, one associated with an infinite strip in the x direction, and the other with an infinite strip in the y direction. The eigenvalue associated with a mirror is the product of the eigenvalues obtained with the x and y solutions for that mirror; that is, $\gamma_i=\gamma_i^{(x)}\times\gamma_i^{(y)}$, $i=1,2$. Because both infinite-strip equations have the same form, only the quantities required for the x solutions are given. These are

$$\left.\begin{aligned} K(\xi_i,\xi_j)&=\begin{cases} 2(\lambda d)^{-\frac{1}{2}}\cos[2\pi\xi_i\xi_j/(\lambda d)] \\ \qquad\text{for even symmetric modes}\\ 2(\lambda d)^{-\frac{1}{2}}\sin[2\pi\xi_i\xi_j/(\lambda d)]\\ \qquad\text{for odd symmetric modes}\end{cases}\\ \xi_i&=x\\ f(a_i)&=a_i^{(x)}\\ f(b_i)&=b_i^{(x)}\end{aligned}\right\}\begin{matrix} i,j=1,2\\ i\neq j\end{matrix}$$
$$\alpha=\begin{cases}(\pi/4)(1-4d/\lambda)\text{ for even symmetric modes}\\ (\pi/4)(3-4d/\lambda)\text{ for odd symmetric modes,}\end{cases}$$

where the x's are the cartesian coordinates of the field points, and the remaining quantities are defined in the figure.

APPENDIX B: CALCULATION OF EFFECTIVE REFLECTION COEFFICIENTS

Following Gordon and Kogelnik,[7] we consider a traveling wave launched from mirror 1 with electric-field distribution $e^{i\alpha}\mu_1(\xi_1)$. Since the right side of Eq. (1) is a Fresnel–Kirchhoff integral and the mirror surfaces are perfectly reflecting, the field distribution of the wave on reflection from mirror 2 is $\gamma_2\mu_2(\xi_2)$. The power in the wave leaving mirror 1 is proportional to

$$\int_{f(a_1)}^{f(b_1)}|\mu_1(\xi_1)|^2d\xi_1,$$

and the power in the reflected wave at mirror 2 is proportional to

$$|\gamma_2|^2\int_{f(a_2)}^{f(b_2)}|\mu_2(\xi_2)|^2d\xi_2,$$

so that the effective reflection coefficient representing the diffraction loss at mirror 2 is

$$D_2=|\gamma_2|^2\int_{f(a_2)}^{f(b_2)}|\mu_2(\xi_2)|^2d\xi_2\bigg/\int_{f(a_1)}^{f(b_1)}|\mu_1(\xi_1)|^2d\xi_1,\quad\text{(B1)}$$

and, similarly, at mirror 1 it is

$$D_1=|\gamma_1|^2\int_{f(a_1)}^{f(b_1)}|\mu_1(\xi_1)|^2d\xi_1\bigg/\int_{f(a_2)}^{f(b_2)}|\mu_2(\xi_2)|^2d\xi_2.\quad\text{(B2)}$$

If the eigenfunctions are normalized so that

$$\int_{f(a_1)}^{f(b_1)} |\mu_1(\xi_1)|^2 d\xi_1 = \int_{f(a_2)}^{f(b_2)} |\mu_2(\xi_2)|^2 d\xi_2,$$

the reflection coefficients reduce to $D_1 = |\gamma_1|^2$ and $D_2 = |\gamma_2|^2$.

REFERENCES

[1] We follow the convention of the literature and define diffraction loss to be the energy lost from an interferometer by propagation through the apertures and around the edges of the mirrors.

[2] A. G. Fox and T. Li, Bell System Tech. J. **40**, 453 (1961); Proc. IEEE **51**, 80 (1963).

[3] G. T. McNice and V. E. Derr, IEEE J. Quantum Electron. **QE-5**, 569 (1969).

[4] These conditions are essentially those required by the Fresnel–Kirchhoff theory of diffraction. See, for instance, S. Silver, *Mircowave Antenna Theory and Design* (Dover, New York, 1965), pp. 167.

[5] It is this condition that restricts the validity of this analysis to the confocal interferometer.

[6] The normalization of Eq. (4) is not necessary for this derivation; it is employed only to simplify the form of the result and to provide a simple physical interpretation of $|\gamma_1|^2$ and $|\gamma_2|^2$ which is otherwise unavailable. The unnormalized expressions for the reflection coefficients [Eqs. (B1) and (B2) of Appendix B] can also be shown to be equal by squaring the modulus of both sides of Eq. (6) and dividing by the product

$$\left[\int_{f(a_1)}^{f(b_1)} |\mu_1(\xi_1)|^2 d\xi_1\right] \times \left[\int_{f(a_2)}^{f(b_2)} |\mu_2(\xi_2)|^2 d\xi_2\right].$$

[7] J. P. Gordon and H. Kogelnik, Bell System Tech. J. **43**, 2873 (1964).

Reprinted from NOAA Technical Report, ERL 211-WPL 15, 1971. **21**

A NOTE ON TERMINOLOGIES USED IN GASEOUS ABSORPTION PROCESSES

R. F. Calfee

The relationships among the many systems of units for absorption coefficients, optical paths, and intensities for gaseous processes are discussed. A table showing the interconnecting factors is presented.

22
Reprinted from Meteorological Monographs 11, No. 33, 397-404, 1970.

ACOUSTIC SOUNDING OF THE LOWER ATMOSPHERE[1]

C. Gordon Little

ESSA Research Laboratories, Boulder, Colo.

ABSTRACT

The refractive index of air to sound waves is a function of the three primary meteorological parameters of the lower atmosphere, i.e., wind, temperature and humidity. It is therefore of interest to consider to what extent the propagation of sound waves can be used to derive quantitative information on these atmospheric parameters.

It is shown that the fluctuations in acoustic refractive index may be expected to be about one thousand times stronger than in the radio case; hence, the scatter of acoustic waves may be expected to be roughly one million times stronger than for radio waves. In addition, the million-fold ratio between the velocities of electromagnetic and acoustic waves results in an acoustic system requiring one million times less bandwidth to interrogate a given atmospheric volume. This results in an overall reduction in interfering noise power for the acoustic case of about a factor of one million. For a single pulse, the acoustic signal-to-noise ratio from a given scattering region is likely to be some twelve orders of magnitude stronger than in the radio case.

The system parameters required to achieve an effective acoustic sounder are discussed. It is concluded that the acoustic sounding technique could be developed to monitor (to heights of at least 1500 m) the vertical profile of wind speed and direction, the vertical profile of humidity, the location and intensity of temperature inversions, the three-dimensional spectrum of mechanical turbulence, and the three-dimensional spectrum of temperature inhomogeneity (i.e., of optical refractive index fluctuation).

Typical time and height resolutions for the proposed acoustic echo-sounders could be of the order of 10 sec and 10 m; the spatial wavenumber explored could range from about 0.01 to ~400 m^{-1}.

Limitations to the acoustic technique include its limited range (to perhaps 10 km) and the probability of serious loss of sensitivity due to increased noise level during periods of strong wind, hail or rain. Other difficulties include the low information rate [of the order 1 pulse $(10\ \mathrm{sec})^{-1}$] and the strong refraction effects due to wind and temperature gradients.

1. The refractive index of air to sound waves

The phase velocity of sound in air is affected by three primary meteorological parameters: wind, temperature and humidity. It is therefore of some interest to consider to what extent acoustic waves can be used to sense these parameters remotely.

In dry air the velocity of sound ($\mathrm{m\ sec}^{-1}$) is given by

$$C_d = 20.05\sqrt{T}, \tag{1}$$

i.e., the phase velocity C_d relative to [dry] air is proportional to the square root of the air temperature T.

If water vapor is present, the phase velocity is slightly increased, since water molecules are lighter than oxygen or nitrogen molecules, and travel faster at a given temperature. For moist air the phase velocity C_m is increased by an amount proportional to the partial pressure of water vapor, and is given by

$$C_m = C_d[1 + 0.14\,(e/p)], \tag{2}$$

where e/p is the ratio of the partial pressure of water vapor e, to the total pressure p. The total contribution of water vapor to the phase velocity of sound is typically less than $\sim 1\ \mathrm{m\ sec}^{-1}$ ($\sim 0.3\%$). For frequencies higher than ~ 100 Hz, however, the primary result of the water's presence in the atmosphere lies not in its effect on the phase velocity (the real component of the refractive index) but on the attenuation, i.e., on the imaginary component. Fig. 1, due to C. M. Harris (1966), shows how the exponential decay exponent varies with relative humidity at 20C for several frequencies in the kHz range.

In the presence of wind, the phase velocity of sound observed by a stationary observer is given by

$$V = C + W\cos\phi, \tag{3}$$

where C is the phase velocity of sound through the air, W the wind and ϕ the angle between the wave normal and the wind direction.

The lower atmosphere is, of course, a somewhat turbulent, inhomogeneous medium, and the phase velocity of sound is therefore a fluctuating quantity, varying in both time and space. Following radio

---

[1] This manuscript is largely based on a paper published in the April 1969 issue of the *Proceedings of the Institute of Electrical and Electronic Engineers.*

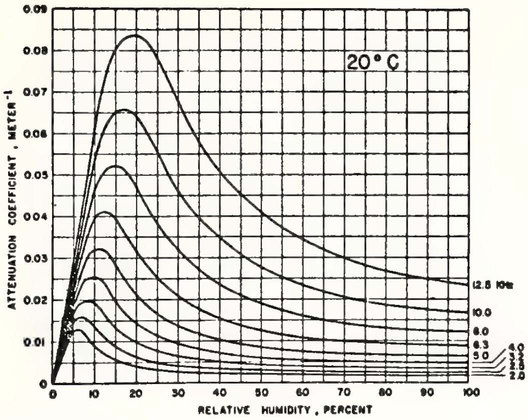

FIG. 1. Total attenuation coefficient m vs percent relative humidity for air at 20C and normal atmospheric pressure, for frequencies between 2.0 and 12.5 kHz at one-third octave intervals. To obtain the attenuation in dB per meter, multiply the ordinate by 4.34 (from C. M. Harris, 1966).

practice, it is convenient to express these fluctuations in terms of N units, where $N = (\Delta n/n)\ 10^6$, i.e., N is the fractional change in refractive index n, expressed in parts per million.

Table 1 compares the refractive index changes in N units associated with given changes in temperature, humidity and wind for acoustic, radio and optical frequencies.

Acoustic waves are shown to be very much more sensitive to atmospheric fluctuations than are electromagnetic waves. Analysis indicates that normal fluctuations in the refractive index in the boundary layer are (roughly) 1000 times stronger for acoustic waves than for electromagnetic waves. Since the power scattered by refractive index irregularities is proportional to $(\Delta n/n)^2$, the scattering efficiency of atmospheric turbulence is on the order of one million times greater for acoustic waves than for electromagnetic waves.

The sensitivity of sound velocity to changes in wind, temperature and humidity is such that the humidity fluctuations can almost always be ignored. For remote probing purposes one is therefore left with the problem of being able to identify separately the effects of wind and temperature fluctuations. This can readily be done since the wind is a vector quantity, while the temperature is scalar. Measurements of the time of arrival of a pulse, or of the phase of a received cw acoustic signal, taken on a ring of microphones surrounding a central loudspeaker, could be used to measure both the mean temperature (from the average time delay around the ring) and the mean wind and wind direction (from the variation of time delay around the ring). These values are averaged over the diameter of the ring and hence are more representative of the ambient atmosphere than the rapidly fluctuating measurements taken at a single point. The data from the various microphones could also be used to derive information on spatial scales of turbulence and on power spectra in the time domain. With a cw system, considerable sensitivity in measurements of mean wind speed and temperature could be achieved. A 100 m radius circle around which the relative phase of a 100-Hz acoustic signal could be measured to an accuracy of $(1/100)\lambda \equiv 3.6°$ would give mean wind speeds to ~ 10 cm sec^{-1}. Temperature measurements to an accuracy of 0.2C could be made, provided the partial pressure of water vapor was known to an accuracy of ~ 1 mb.

TABLE 1. Sensitivity of refractive index of the lower atmosphere to changes in atmospheric temperature, wind and humidity, for acoustic, radio and optical waves.

Parameter	Change of	ΔN		
		Acoustic	Radio	Optical
Temperature	1K	~1700	~1	~1
Humidity	1 mb	~ 140	~4	~0.04
Wind	1 m sec^{-1}	~3000	~2×10^{-6}	~2×10^{-6}

Measurements of the mean humidity of the air could be made from studies of the variation of received power around the ring of microphones as the transmitted frequency is varied. Since the variation of absorption with acoustic frequency, relative humidity and temperature is well known, a circular ring of microphones operated in a multi-frequency mode should provide sufficient information to permit unambiguous derivation of the mean humidity, even in the presence of unknown refraction effects in the vertical plane due to vertical gradients in wind and/or temperature.

The discussion above relates to the measurement of atmospheric parameters at the surface of the earth. For many years, the rocket grenade technique (Strand *et al.*, 1956) has proven to be of value in the derivation of wind and temperature profiles to heights on the order of 90 km. It is also possible that aircraft could be used as elevated sources of sound, using either the broadband noise radiated by the aircraft engines, or specially installed cw sources. In either case, one could take advantage of the very strong Doppler frequency shifts which occur with modern aircraft. The author has not conducted any acoustic ray-tracing analyses, but it would appear likely that useful profiles of wind, temperature and relative humidity could be derived from such observations.

2. Echo-sounding of the atmosphere, using acoustic scatter

Experimentally, the scatter of sound by irregularities in the atmospheric wind or temperature field has been investigated by several workers. One of the earliest of these was Tyndall (1874), who concluded that the echo, which he obtained occasionally when using a fog siren on the south coast of England, could be attributed to the "flocculent" nature of the atmosphere. Gilman *et al.* (1946) of the Bell Telephone Laboratories reported the detection of acoustic echoes of unexpectedly high intensity from the lowest few hundred feet of the atmosphere. Kallistratova (1959a, b), and Kallistratova and Tatarsky (1960), conducted experimental tests of the theory of the scatter of sound by atmospheric irregularities. Kelton and Bricout (1964) showed that the scattered acoustic signals were of sufficient intensity to permit Doppler measurements of wind velocity. Studies by Bellamy *et al.* (1958) of scattering from considerably greater heights were inconclusive, and it remained for McAllister (1968) to show that these echoes could readily be obtained and studied.

The theory of the scatter of sound by turbulent atmospheric velocity fluctuations or by fluctuations in scalar atmospheric properties such as temperature has been investigated by several authors. Thus, Lighthill (1953) and Kraichnan (1953) dealt with the case of scatter by turbulent velocity fluctuations, while Batchelor (1957) treated the scatter of sound by temperature inhomogeneities. The broadening of the spectrum of scattered energy due to the Doppler shifts associated with turbulent velocity fields was discussed by Kraichnan (1953), and by Ford and Meecham (1960). The scatter of sound by both temperature and velocity fluctuations has also been treated by Tatarsky (1961), Kallistratova (1961) and Monin (1961). Experimental checks of the theory have been made in the field by Kallistratova and in the laboratory by Baerg and Schwarz (1966).

Following Monin (1961), we have, for the scatter of sound inhomogeneities in dry air

$$d\sigma_s = 2\pi k^4 V \cos^2\theta\left[(1/C^2)\,E\,(K)\cos^2(\theta/2) + (\tfrac{1}{4}T^2)\,\varphi\,(K)\right]d\Omega, \quad (4)$$

where $d\sigma$ is the fraction of the incident acoustic power which is scattered by irregularities in volume V through an angle θ into a cone of solid angle $d\Omega$; $k = 2\pi/\lambda$ and is the wavenumber of the acoustic wave; and $K = 2k\,(\sin\theta/2)$ is the effective wavenumber at which an acoustic radar scattering through angle θ interrogates the medium. The parameters C and T are the mean velocity of sound and the mean temperature of the scattering volume, and $E(K)$ and $\varphi\,(K)$ are, respectively, the spectral intensity of the wind fluctuations and the temperature fluctuations at wavenumber K.

Eq. (4) is not complete, since it does not include the Doppler effects due to transportation of the small scattering eddies by larger scale eddies, as discussed by Ford and Meecham (1960). This omission is equivalent to the assumption that echo power is measured with a receiver bandwidth several times broader than the Doppler broadening (assumed small) due to larger scale turbulence. Other limitations of this equation include the omission of any term to cover scatter by humidity fluctuations (this term would typically be two or three orders of magnitude lower than the wind or temperature terms and therefore can safely be ignored) and the inherent assumption that the wind and temperature fluctuations are uncorrelated. This latter assumption appears to have been made in all the acoustic scattering theories to date, and probably warrants critical evaluation, especially under conditions of strong convection. Despite these limitations, the equation is adequate for a first-order discussion and calculation of the scatter of sound by atmospheric irregularities.

It is very important to note the different angular dependences of the scatter from mechanical turbulence [proportional to $\cos^2\theta\cos^2(\theta/2)$] and the scatter from temperature fluctuations [proportional to $\cos^2\theta$]. The additional $\cos^2(\theta/2)$ factor in the turbulence scatter term results in a null in the backscatter direction, i.e., when $\theta = 180°$. In other words, backscattered echoes are produced only by temperature fluctuations; at all other scatter angles (except $\theta = 90°$, where both terms go to zero because of the $\cos^2\theta$ term) the scatter will be caused by the sum of the effects of both temperature and wind fluctuations. By taking measurements of scattered power as a function of scatter angle, it should therefore be possible to determine the intensities of $E(K)$ and $\varphi(K)$ separately. In this way profiles of the variation with height of mechanical turbulence, and of temperature inhomogeneity, could be obtained.

3. Acoustic Doppler measurements of wind and turbulence

Additional information can be derived from the Doppler frequency shifts of the echoes. The Doppler spectrum of an acoustic signal scattered from isotropic turbulence has been discussed theoretically by Ford and Meecham (1960) and investigated experimentally by Kelton and Bricout (1964). Ford and Meecham showed that the maximum of the scattered power spectrum is shifted from the incident frequency by an amount determined by the Doppler shift due to the radial component of the mean flow, and that the half-width of the spectrum is proportional to the turbulence Mach number (see Fig. 2). The velocity-azimuth type of display, originally developed for Doppler radar studies of the wind field (Lhermitte and Atlas, 1961), can be used to determine the complete

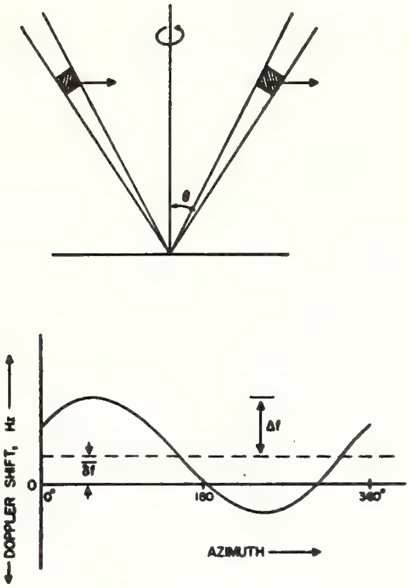

FIG. 2. The velocity-azimuth display Doppler radar system: a., the Doppler radar beam, sweeping in azimuth at fixed zenith angle, and b., the Doppler shift at a given height, as a function of azimuth. Note that 1) the amplitude of Δf of the sine wave is proportional to the mean horizontal wind, 2) the phase of the sine wave is determined by the azimuthal direction of the mean wind, and 3) the mean displacement $\overline{\delta f}$ of the sine wave is proportional to the mean vertical velocity.

velocity vector. In this technique, the sounding beam is rotated in azimuth at a fixed zenith angle. The direction of the horizontal component of the mean wind is deduced from the phase of the sinusoidal variation of Doppler frequency with azimuth, the magnitude of the mean horizontal component of the wind from the amplitude of the sine wave, and the mean vertical velocity from the mean value of the Doppler shift around a full 360° azimuthal rotation (see Fig. 3). By comparing the mean radial velocities of pulse volumes observed essentially simultaneously at different spacings along the beam, the intensity of turbulence at scales larger than the pulse length could also be explored. Since pulse lengths as short as 3 m could be used, this implies that the spectrum of turbulence could be measured for spatial wavenumbers $k = 2\pi/\lambda$ in the range 2 to 0.01 m^{-1}. Note that the turbulence spectrum at shorter spatial wavelengths could be measured by determining $E(K)$ as a function of K from the measurements of total echo power (as opposed to echo spectrum) proposed in Section 2.

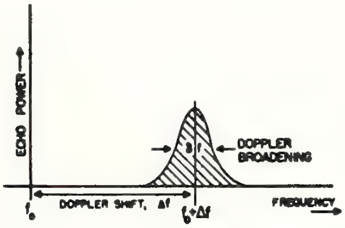

FIG. 3. The ability of the Doppler radar to measure the mean radial component of velocity (proportional to Δf) and the fluctuation in that component (proportional to δf).

4. A possible technique for the measurement of humidity profiles

The scattering cross section for acoustic waves in the inertial subrange of the Kolmogorov spectrum of turbulence varies as $\lambda^{-1/3}$ (Kallistratova, 1961), i.e., rather weakly with wavelength. The molecular absorption of the sound, however, varies quite strongly with the acoustic wavelength and with humidity (see Fig. 1). This fact suggests that measurements of the received echo strength as a function of frequency and height could be used to derive information on the variation of humidity with height. A possible method is outlined below.

Consider the case in which two acoustic radars are used in the backscatter mode to obtain echoes successively from the same volume of space on two frequencies, say, 4 and 8 kHz. Let us suppose that the same peak power, antennas, transducer efficiencies, etc., apply to each radar. In the absence of any atmospheric attenuation, the 8-kHz radar echoes should be 1 dB stronger than the 4-kHz echoes at all heights, because of the $\lambda^{-1/3}$ increase in effective scattering cross section. The classical absorption of acoustic energy would result in a weakening of the 8-kHz echoes relative to those at 4 kHz by a known amount [~ 1 dB (100 m)$^{-1}$ increase in height]. Any additional decrease in the ratio of 8 to 4 kHz echo power with height could be attributed to molecular absorption due to water vapor; the known dependence of this absorption upon humidity could be used to derive the humidity profile. Thus, Fig. 4 indicates that a 5.75 dB increase in the ratio of 8 to 4 kHz echo power, per 100 m increase in height, implies a 50% relative humidity if the temperature is 20C. The double-valued nature of the curve, however, could result in unreasonable ambiguities near the peak; thus, values near a 12 dB change in echo ratio per 100 m could be interpreted as a relative humidity of either 12 or 30%. This ambiguity could be fully resolved if the radar could also operate at 2 kHz. In this case the right-hand scale shows that the change in ratio of the 4 and 2 kHz echoes would either be 7 dB (100 m)$^{-1}$ for a 12% relative humidity or 2.8 dB (100 m)$^{-1}$ for a 30% relative humidity, a difference which could presumably be detected.

One obvious weakness of this method is the assumption of an isotropic homogeneous Kolmogorov spectrum of turbulence. However, the effect of temperature inversions could be identified and avoided by using different elevation angles; and checks of the spectrum of turbulence could also be made using bistatic systems.

5. On the feasibility of acoustic echo-sounding

The above discussion indicates that acoustic sounding offers considerable potential for remote measurement of atmospheric parameters. We therefore proceed to estimate the system requirements for an effective acoustic sounder.

For a Kolmogorov spectrum of turbulence, Eq. (4) reduces to

$$\sigma(\theta) = 0.03\, k^{1/3} \cos^2\theta \left[(C_v^2/C^2) \cos^2(\theta/2) + 0.13\, (C_T^2/T^2) \right] (\sin\theta/2)^{-11/3}, \quad (5)$$

where $\sigma(\theta)$ is now the scattered power, per unit volume, per unit incident flux, per unit solid angle at an angle θ from the initial direction of propagation. The values of C_v and C_T may be obtained from measurements of the corresponding structure functions

$$\left. \begin{aligned} D_W &= \overline{[W(x) - W(x+r)]^2} = C_v^2\, r^{2/3} \\ D_T &= \overline{[T(x) - T(x+r)]^2} = C_T^2\, r^{2/3} \end{aligned} \right\},$$

where $W(x)$ and $T(x)$ are the instantaneous wind speed and temperature at point x, and $W(x+r)$ and $T(x+r)$ are the corresponding instantaneous values at point $(x+r)$. Thus, C_v and C_T are, respectively, the rms differences in velocity, or in temperature, for two points separated by unit distance.

The radar equation, applied to the monostatic case (i.e., co-located transmitter and receiver), gives the received power P_r as

$$P_r = P\, \sigma\, (C\tau/2)\, A_r\, (1/R^2) L, \quad (6)$$

where P is the radiated acoustic power, σ the scattering cross section of Eq. (1) with $\theta = 180°$, C the velocity of sound in the scattering region, τ the pulse length, A_r the collecting area of the receiving antenna, R the range to the scattering region, and L an attenuation factor which takes into account antenna and transducer inefficiencies and any atmospheric attenuation along the double path to and from the scattering region.

Assuming, for the moment, that

$$\begin{aligned} P &= 10\ \text{W}, \\ \tau &= 10^{-2}\ \text{sec (3.3 m pulse)}, \\ R &= 150\ \text{m}, \\ A_r &= 1\ \text{m}^2, \end{aligned}$$

then

$$P_r = 7.3 \times 10^{-4}\, \sigma L \ [\text{mks units}].$$

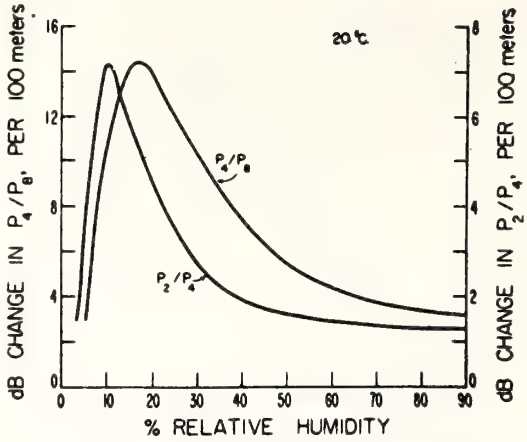

FIG. 4. The variation with relative humidity of the increase, per 100 m increase in height, of the ratio of echo powers, P_2/P_4 and P_4/P_8, for acoustic radars operating at 2, 4 and 8 kHz. The atmospheric temperature is assumed to be 20C.

For the backscatter case, Eq. (5) reduces to

$$\sigma = 0.0039\, (2\pi/\lambda)^{1/3}\, (C_T/T)^2.$$

Taking $\lambda = 2\pi \times 10^{-2}$ m ($f \approx 5$ kHz), $C_T = 4.6 \times 10^{-2}$ deg m$^{-1/3}$ and $T = 300$K, then

$$\sigma = 4.4 \times 10^{-10}\ \text{m}^2\ \text{m}^{-3}.$$

Using this value of σ, we have

$$P_r = 3.2 \times 10^{-13} L.$$

In considering the detectability of this received power, we must first estimate L and then estimate the the interfering noise power against which the signal must be detected.

The attenuation factor L is made up of the efficiency factor of the receiving antenna (i.e., the ratio of output electrical power from the microphone transducer to the acoustical power incident upon the geometrical area of the receiving antenna) and the absorption of acoustical energy occurring on the propagation path.

The efficiency factor of a loudspeaker at the focus of a paraboloid is likely to be of the order 0.05, based on an effective collecting area of about 0.5 of the geometrical area and a transducer efficiency of about 0.1.

The absorption of sound by the atmosphere is a strong function of frequency. It is conventional to divide this into two components: a classical absorption due to the sum of viscoscity, conduction, diffusion and radiation terms; and a non-classical component due to the presence of water vapor. In the frequency range 1–10 kHz, the classical absorption is usually the smaller, and can be well predicted; at 5 kHz it is about 1.0 dB for the round trip path to a height of 150 m.

From Fig. 1 we see that the total attenuation at a frequency of 5 kHz would be about 10 dB for the round trip to a height of 150 m. This figure would decrease with increasing temperature and with increasing relative humidity.

Using the above values of receiving antenna efficiency and of atmospheric attenuation, we have

$$L = 5 \times 10^{-8},$$

whence

$$P_r = 1.6 \times 10^{-15}\ \mathrm{W}.$$

This electrical signal is now to be compared with the interfering noise level existing at the input to the preamplifier.

Five potential sources of noise must be considered in identifying the signal-to-noise ratio to be expected on an acoustic radar. The ultimate ineluctable limit, to be achieved only under ideal conditions, will be set by the random pressure fluctuations experienced by the microphone due to the random thermal motion of the atmospheric molecules. The available acoustic noise power is given by

$$P_a = kTB,$$

where k is Boltzmann's constant, T the absolute temperature of air, and B the observing bandwidth. For a bandwidth of 100 Hz and normal atmospheric temperature, this thermal acoustic noise power would be about 4.2×10^{-19} W.

Electron shot noise in the receiving preamplifier must also be considered. At audible frequencies there should, however, be no difficulty in building a preamplifier which generates no more noise than that of a resistor at room temperature. For a 100-Hz bandwidth, this noise power also is $\sim 4.2 \times 10^{-19}$ W.

Wind noise on the receiving microphone is likely to prove a more serious limit to the sensitivity of the radar. This noise can, however, be greatly reduced by placing the microphone as close to the surface of the earth as practicable, by using an array of microphones (since the wind noise will not be correlated on microphones more than a wavelength apart), and by screening the microphone from the wind. A combination of these techniques may be expected to reduce this problem until it is no longer limiting, at least under low wind conditions.

In addition to wind-induced noise created at the microphone itself, atmospheric turbulence may create pressure fluctuations which propagate as sound waves of natural atmospheric origin. Pressure fluctuations of sub-audible frequencies attributable to the jet stream, severe storms, etc., have been detected at considerable ranges; it is believed that the intensity of these pressure fluctuations drops off rapidly with frequency. It is not known to what extent acoustic noise generated by atmospheric turbulence may at times limit the sensitivity of an acoustic radar, but if this should occur, it should be recognized that the technique may provide a new passive method of sensing atmospheric turbulence.

The final noise limitation to be considered is that of acoustic energy from non-atmospheric sources such as vehicles, insects, etc. This may be estimated from data, as summarized by Stevens and Baruch (1957). They show that the ambient acoustic noise power at a quiet site is on the order of 20 dB above 10^{-16} W cm^{-2} for an octave band centered at 1 kHz and decreases by about 5 dB per octave increase in frequency. From these figures, an acoustic noise power of about 8 dB per octave at 5 kHz would be expected; for a 100-Hz bandwidth at 5 kHz, the noise power flux would be of the order of -9 dB relative to 10^{-16} W cm^{-2} or 1.25×10^{-17} W cm^{-2}. If we assume that the noise is isotropic in origin, the effective collecting area for this noise will be $\lambda^2/(4\pi) = 3$ cm^2, leading to an acoustic noise power of 3.75×10^{-17} W. This acoustic noise power is, however, reduced to 3.75×10^{-18} W because of the transducer inefficiency. This result suggests that even at a quiet site the electrical noise level due to 5-kHz acoustical interference is likely to be some 10 dB above the equivalent electrical noise input due to the preamplifier noise.

The expected received signal power of 1.6×10^{-15} W exceeds the predicted interference noise power of about 4×10^{-18} W by a factor of 400, or 26 dB; that is, for the conditions postulated, the signal-to-noise ratio would be 26 dB.

6. Choice of the optimum frequency range for an acoustic radar

The optimum frequency for an acoustic radar will be chosen as a compromise between the increase in directivity, the improved Doppler resolution and the reduced interference potentially available at the higher frequencies, and the undesired increase in attenuation with increasing frequency. The optimum frequency will be a strong function of the range over which the radar is to work, and will be lower for the larger ranges. Thus, the calculations above give a predicted 26 dB signal-to-noise ratio for a range of 150 m and a frequency of 5 kHz. At ten times the range, the atmospheric absorption would be 100 dB instead of 10 dB, making it imperative to use a lower frequency. Computations similar to the above indicate that a backscattered signal-to-noise ratio of 20 dB could still be obtained at a range of 1.5 km, but would require 100-W, 100-msec, 1-kHz acoustic pulses radiated and received on a 10 m^2 acoustic antenna. By reducing the frequency to 100 Hz, increasing the pulse length to 1 sec and narrowing the receiver bandwidth to a few Hz, it should be possible to get acoustic echoes from a height of 10 km.

7. Some limitations of the echo-sounding technique

The above discussion of the acoustic echo-sounding technique indicates that it offers great promise for remote acoustic probing of the atmospheric boundary layer. It is therefore important to identify some of the probable limitations of the technique.

The primary limitation of the acoustic sounding technique is likely to be one of range. If round trip attenuations due to anomalous absorption are to be less than 10 dB, ranges will have to be limited to (roughly) 150 m at 5 kHz and 1.5 km at 1 kHz, depending upon humidity. A second limitation may arise due to the strength of the interaction of the acoustic waves with the atmospheric irregularities. The theory presented earlier is a single-scatter theory, and assumes that the acoustic beam remains essentially unaffected by the atmosphere, except for the very small fraction of the energy which is scattered. In other words, the attenuation or broadening of the beam by the scatter process is assumed to be negligible. This assumption warrants further investigation, since multiple scatter is likely to degrade the performance of the echo-sounder at long ranges, or under conditions of strong turbulence.

Tatarsky (1961) has discussed the propagation of sound in an inhomogeneous medium. For the case of a spherical wave propagating through a region in which the inhomogeneities are characterized by the Kolmogorov spectrum of turbulence, he derives

$$\overline{\chi^2} = 0.13\ C_n^2\, k^{7/6}\, L^{11/6},$$

where $\overline{\chi^2} = \overline{[\log_e (A/A_0)]^2}$ is the mean square fluctuation of the logarithm of the ratio of the instantaneous amplitude of the wave to the mean amplitude, C_n a structure constant of the (acoustic) refractive index, $k = 2\pi/\lambda$ where λ is the acoustic wavelength, L the length of acoustic path, and $C_n = C_T/(2T)$. For the case already considered ($\lambda = 6 \times 10^{-2}$ m, $C_T = 4.6 \times 10^{-2}$ m$^{-1/3}$, $L = 150$ m), we have

$$\chi \approx 0.04,$$

from which we see that the acoustic beam will propagate to a 150 m height with only minor amplitude scintillation. For $\lambda = 0.3$ m, $C_T = 4.6 \times 10^{-2}$ m$^{-1/3}$ and $L = 1500$ m,

$$\chi \approx 0.13,$$

and the amplitude scintillations are still not fully developed.

We may conclude, for the experimental conditions used as examples in this paper, that multiple scatter will not be a serious factor. However, for more turbulent conditions, or for longer paths or shorter wavelengths, a multiple scatter theory may be required.

A third limitation arises from the susceptibility of the receiving system to adverse weather conditions, such as strong winds, rain or hail. These would tend to enhance the ambient noise level. Other difficulties include the relatively low information rate (one pulse per second to a height of 150 m, less frequently for greater heights) and the effects of beam refraction due to wind or temperature gradients. In addition, the problems of the susceptibility of the radar to man-made noise, and of man to the acoustic signals from the sounder have not been adequately investigated; some preliminary tests by the author of a low-side-lobe acoustic antenna suggest that these need not be a serious problem.

8. Conclusion

Despite the somewhat unknown magnitude of these limitations, it is concluded that the acoustic echo-sounding technique could be developed to measure (to heights of up to at least 1500 m): 1) the vertical profile of wind speed and direction (by utilizing a Doppler system); 2) the vertical profile of humidity (by means of a multi-wavelength system); 3) the location and intensity of temperature inversions (by using a monostatic system to study the echo power and frequency spectrum, as a function of elevation angle, range and wavelength); 4) the three-dimensional spectrum of temperature inhomogeneity (by using a monostatic system to study the echo power as a function of wavelength, azimuth, and elevation); and 5) the three-dimensional spectrum of mechanical turbulence (by using both monostatic and bistatic systems to study the echo power as a function of scatter angle, wavelength and direction).

Typical height resolutions attainable would be on the order of one-half of the pulse length, i.e., about 10 m if a 60-msec pulse is used. Spatial wavenumbers could be explored over the range from $4\pi/\lambda_{\min}$ (about 400 m^{-1}) to about 10^{-2} m^{-1} in the case of mechanical turbulence, and from 400 m^{-1} to 40 m^{-1} for the temperature inhomogeneities. The difference is due to the ability of the Doppler radar to measure the radial velocities at different points along a beam simultaneously. Time resolutions for successive independent measurements to heights of 1500 m would be about 10 sec.

The above potentialities suggest that the acoustic sounding technique will prove a uniquely valuable remote sensing concept for atmospheric boundary-layer studies. In particular, the author suggests that active consideration be given to its application to the meteorological aspects of air pollution, and to such airport problems as the measurement of low-level wind shear and the detection of wake turbulence. In lower atmospheric research, its strongest contribution is likely to be in the field of atmospheric turbulence and the measurement of vertical fluxes of heat, momentum and water vapor. If necessary, it would seem likely that a large array of loud-speakers and/or microphones on the ground could be used with a holographic technique, to make "visible" the atmospheric structure responsible for the scattering of the sound waves. Electromagnetic propagation research will also benefit as the acoustic sounder makes apparent the atmospheric structure responsible for the fluctuations in microwave and optical propagation.

REFERENCES

Baerg, W., and W. H. Schwarz, 1966: Measurements of the scattering of sound from turbulence. *J. Acoust. Soc. Amer.*, **39**, 1125–1132.

Batchelor, G. K., 1957: Wave scattering due to turbulence. *Proc. Symp. Naval Hydrodynamics*, NAS-NRC Publ. 515, 409–430.

Bellamy, J. C., R. F. Bosshart *et al.*, 1958: Investigation of the feasibility of acoustic soundings of the atmosphere. Final Rept., Skokie, Ill., Cook Res. Labs.

Ford, G. W. and W. C. Meecham, 1960: Scattering of sound by isotropic turbulence of large Reynolds number. *J. Acoust. Soc. Amer.*, **32**, 1668–1672.

Gilman, G. W., H. B. Coxhead and F. H. Willis, 1946: Reflection of sound signals in the troposphere. *J. Acoust. Soc. Amer.*, **18**, 274–283.

Harris, C. M., 1966: Absorption of sound in air versus humidity and temperature. *J. Acoust. Soc. Amer.*, **40**, 148–159.

Kallistratova, M. A., 1959a: An experimental investigation into the scattering of sound in a turbulent atmosphere. *Dokl. Akad. Nauk, SSSR*, **125**, No. 1, 69–72.

——, 1959b: Procedure for investigating sound scattering in the atmosphere. *Akust. Zh.*, **5**, 496–498 (Also, *Soviet Phys. Acoust.*, **5**, 512–514).

——, 1961: Experimental investigation of sound wave scattering in the atmosphere. *Tr. Inst. Fiz. Atmos.*, No. 4, 203–256.

——, and V. I. Tatarsky, 1960: Accounting for wind turbulence in the calculation of sound scattering in the atmosphere. *Akust. Zh.*, **6**, 503–505 (Also *Soviet Phys. Acoust.*, **6**, 503–505).

Kelton, G., and P. Bricout, 1964: Wind velocity measurements using sonic techniques. *Bull. Amer. Meteor. Soc.*, **45**, 571–580.

Kraichnan, R. H., 1953: The scattering of sound in a turbulent medium. *J. Acoust. Soc. Amer.*, **25**, 1096–1104.

Lhermitte, R. M., and D. Atlas, 1961: Precipitation motion by pulse Doppler radar. *Proc. Ninth Weather Radar Conf.*, Boston, Amer. Meteor. Soc., 218–223.

Lighthill, M. J., 1953: On the energy scattered from the interaction of turbulence with sound or shock waves. *Proc. Cambridge Phil. Soc.*, **49**, 531–555.

McAllister, L. G., 1968: Acoustic sounding of the lower troposphere. *J. Atmos. Terr. Phys.*, **30**, 1439–1440.

Monin, A. S., 1961: Characteristics of the scattering of sound in a turbulent atmosphere. *Akust. Zh.*, **7**, 457–461 (Also *Soviet Phys. Acoust.*, **7**, 370–373).

Stevens, K. N., and J. J. Baruch, 1957: *Handbook of Noise Control.* New York, McGraw-Hill, 35-1 to 35-17.

Strand, W. G., W. Nordberg and J. R. Walsh, 1956: Atmospheric temperatures and winds between 30 and 80 km. *J. Geophys. Res.*, **61**, 45–56.

Tatarsky, V. I., 1961: *Wave Propagation in a Turbulent Medium.* New York, McGraw-Hill.

Tyndall, J., 1874: On the atmosphere as a vehicle of sound. *Phil. Trans. Roy. Soc. London*, **164**, 183–244.

23

Reprinted from Proceedings of FAA Turbulence Symposium, March 22, 1971.

ABSTRACT

Acoustic Radar Detection Techniques

by

D. Beran
Wave Propagation Laboratory
NOAA, Environmental Research Laboratories
Boulder, Colorado 80302

Following a brief introduction to the theory of sound scattering by turbulence and a description of an acoustic sounder, examples of currently feasible measurements are given. These include records of inversion height, intensity of temperature fluctuations, the height and intensity of thermal plumes and vertical wind velocities. Measurements which are possible, but have not yet been made, are also discussed along with the use of detectable features other than scattering such as ray bending and scintillation.

Based on the established ability of an acoustic sounder to monitor low level meteorological parameters a system is proposed for use in an airport environment. This system would be capable of providing a real time output of the mean wind profile, the height of inversion layers and the turbulence intensity along runway approach paths.

Acoustic Radar Detection Techniques

D. Beran

This paper describes a new approach, acoustic sounding, to the detection of atmospheric phenomena which may constitute a hazard to low-level aircraft operations.

It has been realized for some time that acoustic waves interact strongly with the medium through which they are transmitted and the early work of Lighthill (1953), Kraichnan (1953), Batchelor (1957), Ford and Meecham (1960), Tatarski (1961), Kallistratova (1961) and Monin (1962) resulted in an equation describing the scatter of sound waves by turbulent inhomogenities (both temperature and wind).

This equation,

$$\sigma(\theta) = 0.03k^{\frac{1}{3}} \cos^2\theta \left[\frac{C_v^2}{C^2} \cos^2 \frac{\theta}{2} + 0.13 \frac{C_t^2}{T^2} \right] \left(\sin \frac{\theta}{2}\right)^{-\frac{11}{3}}, \quad (1)$$

relates σ the scattered power, per unit volume, per unit incident flux, per unit solid angle at an angle θ from the initial direction of propagation, to the wave number k of the sound wave and structure constants of wind C_v and temperature C_t. The ambient speed of sound and the temperature are represented by C and T respectively. Values of C_v and C_t can be obtained from the structure functions for wind and temperature fluctuations and are functions of the root mean square difference in longitudinal velocity, or in temperature, for two points separated by a unit distance.

Equation 1 shows that: a) the scattered acoustic power is only a weak function of the wave length of the illuminating frequency, b) the scattered power is the sum of two terms, one due to wind fluctuations and one due to temperature fluctuations, c) both wind and temperature scattering terms are multiplied by $\cos^2\theta$, which means that no power will be scattered at an angle of 90°, d) the wind term includes a $\cos^2(\theta/2)$ multiplying term, which means that the wind fluctuations produce no scatter in the backward direction ($\theta = 180^\circ$) and e) both the wind and temperature components of the scatter are multiplied by a $(\sin\theta/2)^{-\frac{11}{3}}$ factor, i.e., most of the scatter is in the forward hemisphere.

By sensing the scattered power as a function of wave number and scatter angle a wide variety of direct and inferred measurements of low level atmospheric phenomena are possible. The RMS intensity of both temperature and wind fluctuations at a scale determined by the carrier frequency and as a function of time and height are available through the dual use of a monostatic and bistatic system. The radial velocity of the wind along a receiver beam can be determined by using doppler techniques. A monostatic system operated in the velocity-azimuth display mode, or a bistatic system with orthogonally oriented receivers could give a profile of the total wind component at any height within the range of the sounder. (The present WPL sounder has a range of 1 km or more.) In addition, the inherent pattern of turbulence fluctuations associated with various temperature lapse rates makes it possible to detect strong returns from horizontal stratifications in the atmosphere. This same pattern of differing turbulence intensities also makes the structure of thermal plumes easy to monitor.

Many of these same measurements can and have been made with other types of remote sensors, including electromagnetic radar, both pulsed and CW-FM systems and lidar; however, it is important to note the rather striking differences in the degree of interaction with the atmosphere of acoustic, radio and optical waves. Little (1969) makes this point very well by expressing the magnitude of the fluctuations in refractive index of the medium, i.e., the phase velocity of the wave in the medium relative to the phase velocity for standard conditions (vacuum for electromagnetic waves, 1 atm pressure of dry air at 0^{o}C for acoustic waves) and then comparing the expected N unit change for both types of wave. (1 N unit equals 1 part in 10^{6}).

Table 1 gives the comparison for different parameters based on Little's (1969) analysis.

TABLE 1

Magnitude of Parameter Deviation	Change in Refractive Index (N units)		
	Acoustic	Radio	Optical
1^{o}C fluctuation in temperature	1700	1	1
1 meter-per-sec variation in wind speed	3000	negligible	negligible
1 m bar change in water vapor pressure	140	4	0.04

The very large difference, shown in Table 1, for the various types of wave are an indication of the potential of acoustics as a remote sensor of atmospheric processes. The overall picture is of course not without some disadvantages. For one thing, the desirable strong interaction of the acoustic wave with the atmosphere also produces a large attenuation of the power, leading to a relatively short useful range for the system. An examination of the radar equation which relates the power returned P_r to various equipment parameters, losses and the scattering strength suggests possible steps which could be taken to increase the range.

This equation is

$$P_r = P\sigma \frac{C\tau}{2} A_r \frac{1}{R^2} L \qquad (2)$$

where P_r is the power returned from range R to a system which has a transmitted power P, antenna area A_r and pulse width τ. The scattering cross section σ can be obtained from Equation 1, and L includes equipment parameters such as transducer and antenna efficiency as well as the loss due to atmospheric attenuation. It is clear that an increase in power, antenna area, and pulse width will all result in stronger return from a given range, however, limitations imposed by the state of transducer technology, the physical dimensions of the system and loss of resolution at longer pulse widths combine to make the range of operational systems something on the order of 2 km. Echoes from as high as 9 km have been received during experiments in Australia, (Beran 1970), but these were observed during unusual propagation conditions with a 15 m antenna using a pulse width of nearly 1 sec (making the vertical resolution something of the order of 160 meters). While future advances may increase the useful range of acoustic sounders to something approaching 3 or 4 km their greatest potential will probably remain as a sensor of boundary layer phenomena under 1 km in height.

Acoustic sounders now being used for research comprise rather simple and inexpensive systems, the essential components of which are shown in Fig 1. Various configurations have been constructed both in the U. S. (Wescott, Simmons and Little, 1970) and in Australia (McAllister et al, 1968; Beran, 1970) at costs ranging from $3,000.00 to $12,000.00 depending on the degree of sophistication.

The feasibility of acoustic sounders, established during the past 3 years, is demonstrated by the following examples:

1. The height-time history of inversion surfaces. The record in Fig 2 shows an oscillating inversion surface associated with the top of a stratus cloud deck which produced intermittent snow and reduced ground level visibility.
2. The intensity, height and spacing of thermal plumes. Fig 3 shows a time section of C_t (the intensity of temperature fluctuations taken from a sounder record of thermal plumes.
3. The vertical velocity field. Fig 4 shows the vertical velocities measured during thermal plumes and Fig 5 those under a nocturnal inversion containing waves. (Beran, Little and Willmarth, 1971).

Experiments now in progress are testing the feasibility of measuring components of the wind other than vertical, a procedure which will make possible the monitoring of mean horizontal wind profiles as a function of height.

The potential applications for these measurements are at present a matter of speculation but the proven ability of an acoustic sounder to monitor low level atmospheric phenomena in addition to its relatively low per unit cost suggests that more effort should be directed toward the development of operational systems which could provide the following real-time information at an airport.

1. A single sounder with a vertically oriented beam monitoring the height of an inversion surface, could provide a possible indication of cloud formation at an inversion, the top surface of visibility reducing polluted air, and the layers where strong wind shear is likely to be present.
2. Information on the intensity of thermal plume activity - a factor of interest to approaching and departing aircraft - is also available from a simple monostatic sounder.
3. The actual strengths of vertical wind velocities can be derived by analysis of the Doppler frequency shifts from a monostatic system, a procedure which is feasible in real time.
4. The addition of two receivers, looking at, and programmed to sweep up and down along the vertically pointing beam would provide the information necessary for monitoring the low level wind profile, indicating the strength and location of strong wind shears.
5. A bistatic system with the receiver and transducer located on opposite sides of a runway and with the common volume of their beam overlap located above the runway could be used to monitor the turbulence in the approach path produced by both ambient background turbulence and the presence of wake vortices. In this connection it should be pointed out that the present scattering theory assumes random homogeneous turbulence, clearly not the case in the early stages of a wake vortex. Before quantitative measurements of vortex strength can be made it

will therefore be necessary to develop the theoretical aspects of sound scattering by a vortex; however, the present theory seems adequate for simply monitoring the location of vortices and for indicating the strength of the turbulence resulting after the vortex breaks up.

Operation of an acoustic sounder in an airport environment will of course require that the receiver be well shielded from aircraft noise. While this problem needs more study, present indications are that the use of narrow receiver bandwidth, higher frequencies (4000 to 5000 Hz) and the installation of anechoic shielding to suppress side lobes will make it possible to monitor a volume within less than 5 sec after a jet aircraft passes overhead.

In addition the very strong scattering produced by a vortex reduces the need for an extremely high gain system, thus reducing the effect of ambient background noise in the side lobes. Tests have also shown (A. Proudian, private communication) that the scatter from temperature fluctuations in a vortex are much stronger than would normally be expected, probably due to the entrainment of jet exhaust, indicating that monostatic detection of vortices is feasible.

So far only the scatter of acoustic waves has been suggested as a method of detecting atmospheric phenomena. Other characteristics of the interaction between the atmosphere and sound waves are equally intriguing and deserve mention as possible mechanisms for monitoring of low level turbulence. One of these is the ray bending found when sound is transmitted through a vortex. Dr. T. M. Georges of NOAA's Wave Propagation Laboratory has recently developed a computer model for simulating ray paths through a vortex. Some of his early results, (see Fig 6) show intense concentrations of rays as well as shadow zones occurring after sound waves have passed through the vortex. The vortex model, shown at the bottom of the figure, represents a combination of a viscous core, rotating as a solid body and, outside the core, the $\frac{1}{r}$ velocity is only about 30 m/sec, probably near the upper limit for the velocities found in aircraft wakes. How this interaction of sound waves with a vortex could be used to detect wake vorticies is not entirely clear, however, an understanding of the phenomena is important when other methods such as scatter and amplitude scintillation (discussed below) are considered.

A second characteristic of the interaction of sound and the atmosphere is the amplitude and phase scintillation produced when the wave passes through turbulence (Clifford and Brown, 1970). These scintillations are a function of the eddy size and intensity of the turbulent fluctuations, suggesting that a system designed to monitor say the log amplitude of the acoustic wave after it has passed through a turbulent region could be used to provide a continual picture of the averaged turbulence along the path between a transmitter and receiver. By using two receivers, one placed at a position on the opposite side of a runway from the transmitter, and the second placed along a line parallel to the runway both the ambient background turbulence at any given time and the increased turbulence produced by aircraft movement could be monitored. This type of system is limited to regions where line of sight transmission can be made, however this difficulty might be overcome by incorporating the bistatic approach and monitoring the scintillation of the scattered signal.

The various techniques described above might be incorporated into a single system which would provide information on the mean wind profile, turbulence intensity and inversion height either along or in the vicinity of an airport approach path. Fig 7 shows a sketch of such a proposed system using the vertically pointing antenna in a monostatic mode to collect information on the inversion height and vertical wind velocities. The doppler shift observed by the other two orthogonally positioned antennas would provide the required components of the mean wind and, by scanning along the vertical beam, a mean wind profile could be measured. Finally the amplitude scintillation of the signal transmitted from the vertically pointing antenna to either of the orthogonally positioned receivers would provide a measure of the turbulence intensity along the path, or by gating the received signal the turbulence in a volume along the path could be monitored.

Acknowledgments:

The author wishes to thank Dr. F. Hall and Mr. J. Wescott for their helpful comments during the preparation of the manuscript. The ray diagram used in Fig 7 was supplied by Dr. T. M. Georges, his cooperation in supplying this information is gratefully acknowledged.

References

Batchelor, G. K. (1957) Wave scattering due to turbulence, Symp. on Naval Hydrodynamics, F. S. Sherman, ed., NAS-NRC Publ. 515, pp. 409-430.

Beran, D. W. (1970) Project EAR (Environmental Acoustic Research) Vol. I, Univ. of Melbourne, Meteorology Dept. Pub. no. 15.

____________ C. G. Little and B. C. Willmarth (1971) Acoustic Doppler Measurements of Vertical Velocities in the Atmosphere. To be published in Nature.

Clifford, S. F. and E. H. Brown (1970) Propagation of sound in turbulent atmospheres, J. Acoust. Soc. Am., Vol. 48, pp 1123-1127.

Ford, G. W. and W. C. Meecham (1960) Scattering of sound by isotropic turbulence of large Reynolds number, J. Acoust. Soc. Am., Vol. 32, pp. 1668-1672.

Kallistratova, M. A. (1961) Experimental investigation of sound wave scattering in the atmosphere, Trudy Inst. Fiz. Atmos., Atmos Turbulentnost, no. 4, pp 203-256.

Kraichnan, R. H. (1953) The scattering of sound in a turbulent medium, J. Acoust Soc. Am., Vol 25, pp. 1096-1104.

Lighthill, M. J. (1953) On the energy scattered from the interaction of turbulence with sound or shock waves. Proc. Cambridge Phil. Soc. Vol. 49, pp. 531-555.

Little, C. G. (1969) Acoustic methods for the remote probing of the lower atmosphere. Proc. IEEE, Vol. 57, no. 4. pp 571-578.

McAllister, L. G., J. R. Pollard, A. R. Mahoney, and P.J.R. Shaw (1969) Acoustic sounding - a new approach to the study of atmospheric structure, Proc. IEEE, Vol. 57, 579-587.

Monin, A. S. (1962) Characteristics of the scattering of sound in a turbulent atmosphere. Akust. Zh., Vol. 7 pp 457-461 (Sov. Phys.-Acoustics, Vol. 7 pp 370-373).

Tatarski, V. I. (1961) Wave propagation in a turbulent medium (R. A. Silverman, transl.) New York: McGraw-Hill.

Wescott, J. W., W. R. Simmons and C. G. Little (1970) Acoustic echo-sounding measurements of temperature and wind fluctuations, ESSA Tech. Memo. ERLTM-WPL5.

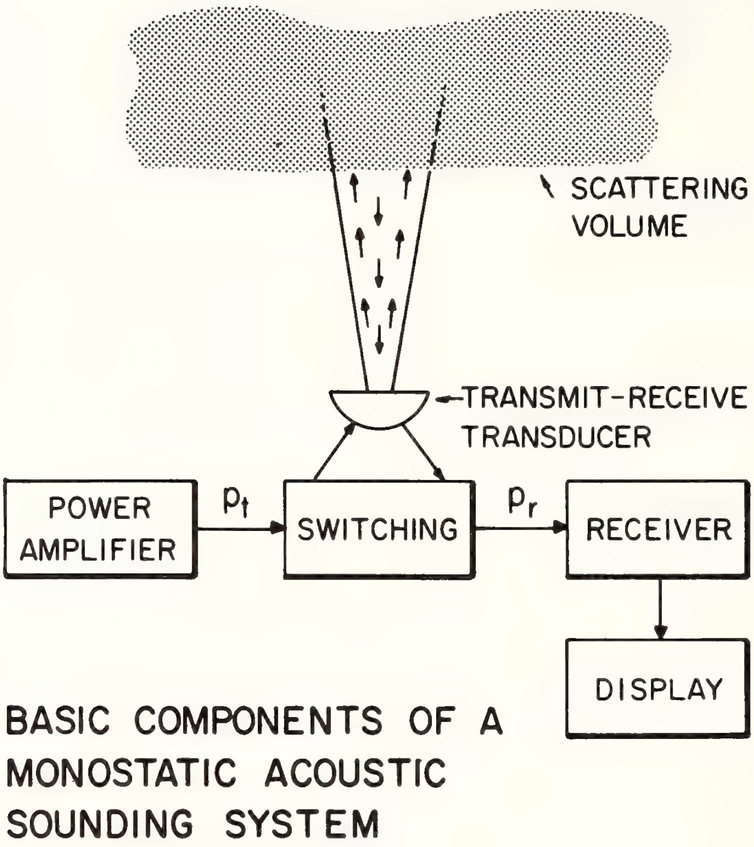
SCATTERING VOLUME
TRANSMIT-RECEIVE TRANSDUCER
POWER AMPLIFIER
p_t
SWITCHING
p_r
RECEIVER
DISPLAY
BASIC COMPONENTS OF A MONOSTATIC ACOUSTIC SOUNDING SYSTEM

Figure 1. Block diagram of monostatic sounder

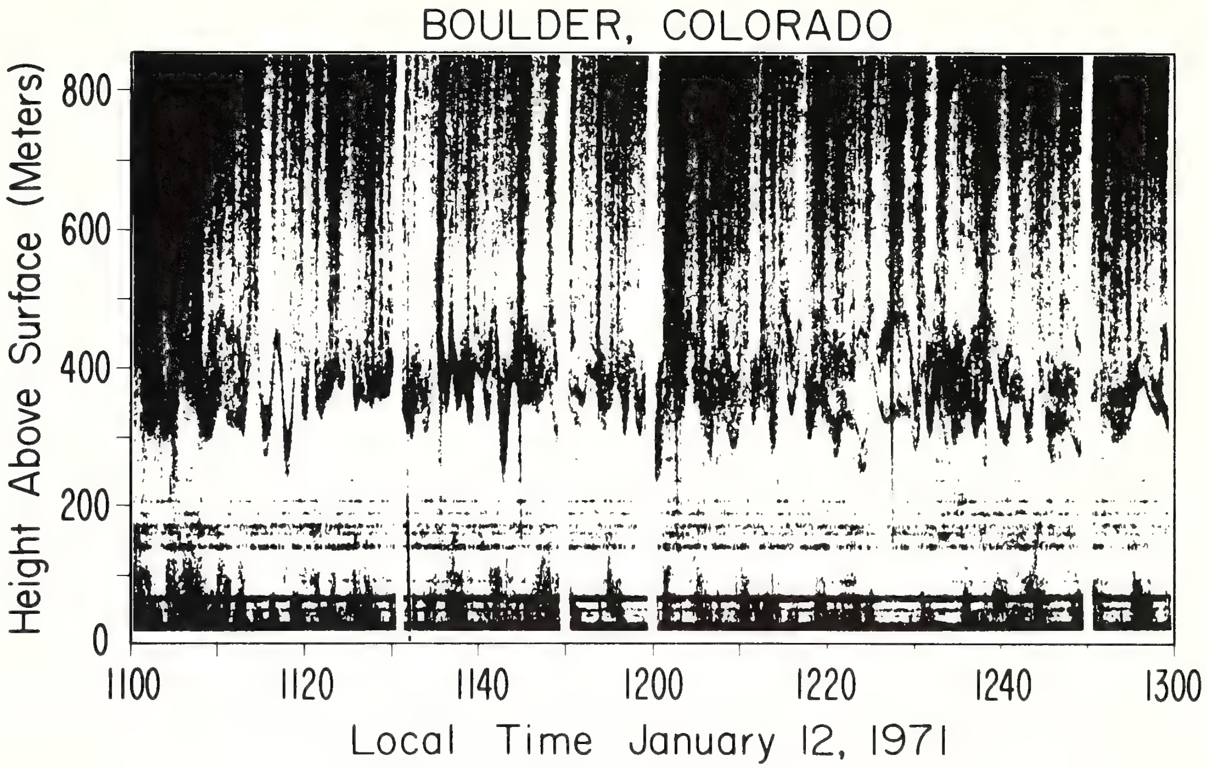

Figure 2. Facsimile recording of the backscatter from an inversion surface.

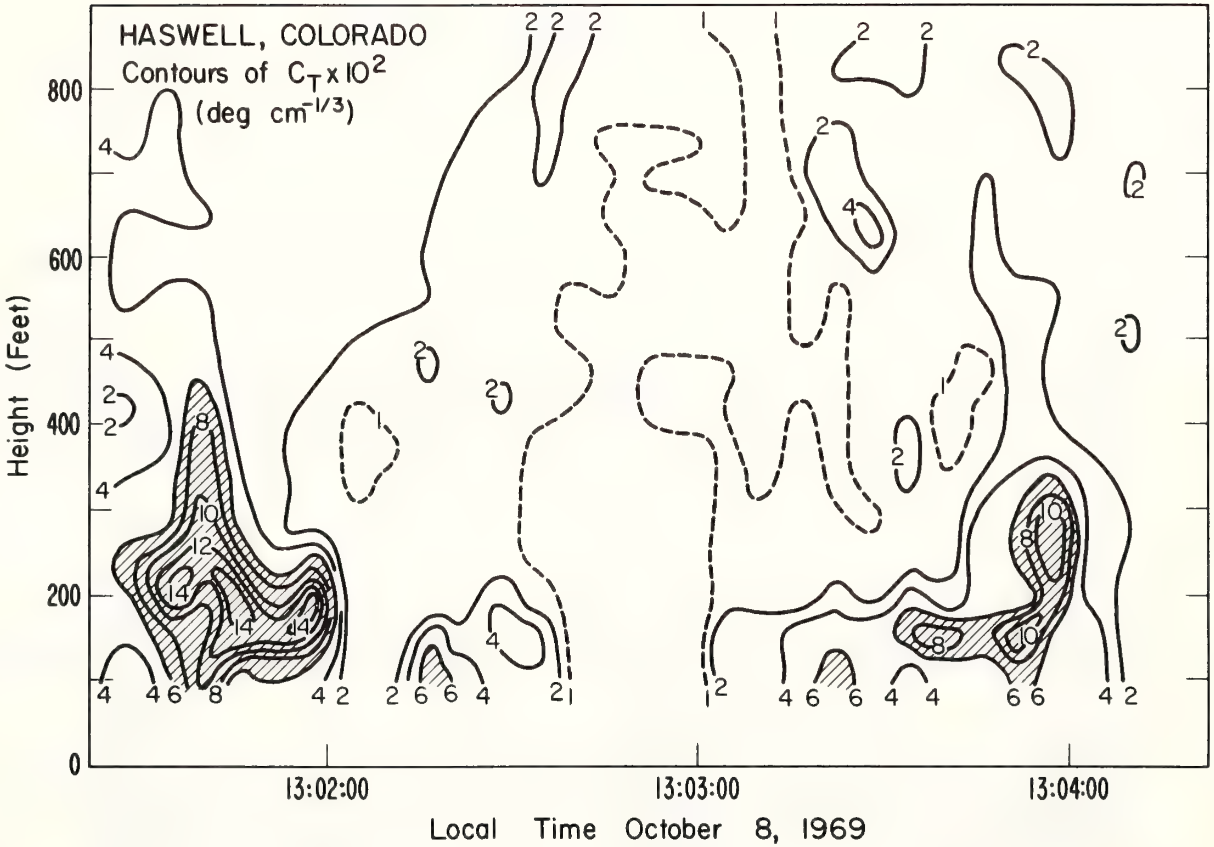

Figure 3. Time section of the field of C_T (a measure of the intensity of turbulent fluctuations) derived from sounder records made during moderate low level convection. Note the clear indication of thermal plumes.

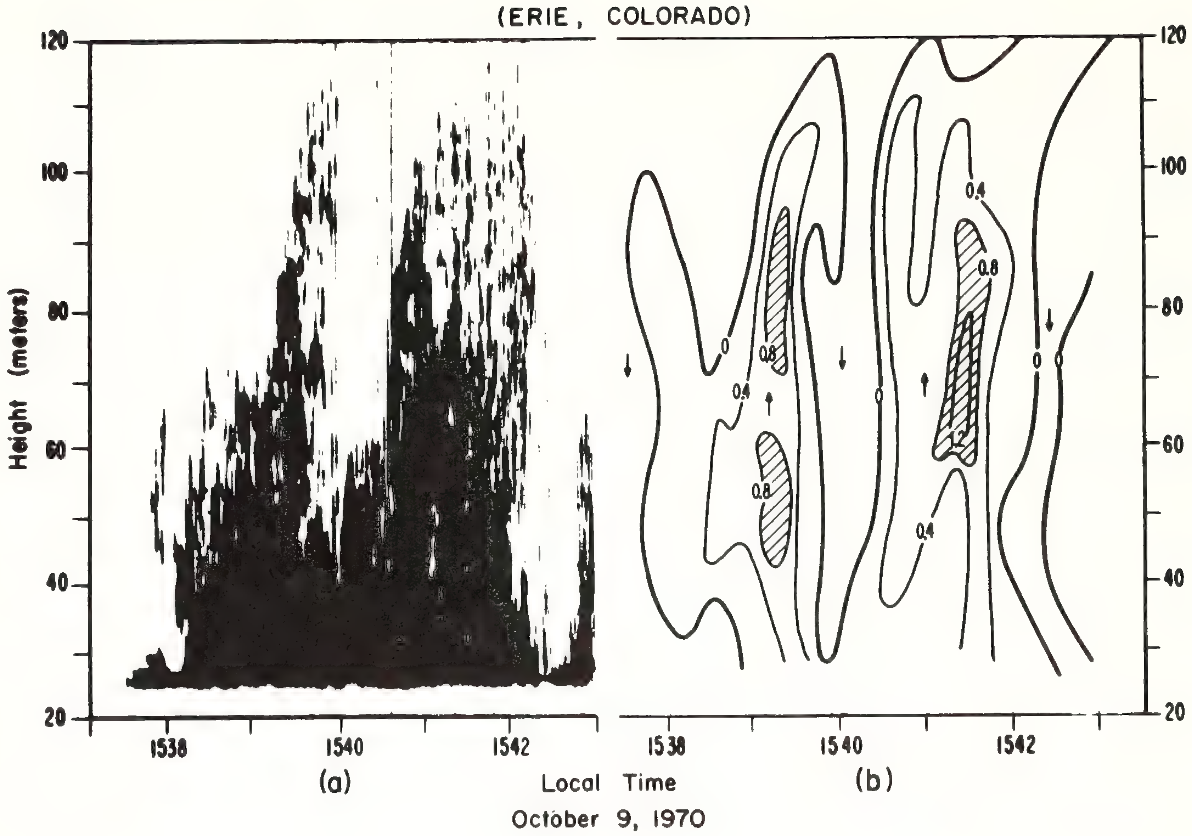

Figure 4. Acoustic echoes (left) and Doppler derived vertical velocity field during thermal plume activity. Contour interval is 0.4 m/sec, regions of vertical velocity >0.8 m/sec are shaded, arrows indicate direction of vertical component.

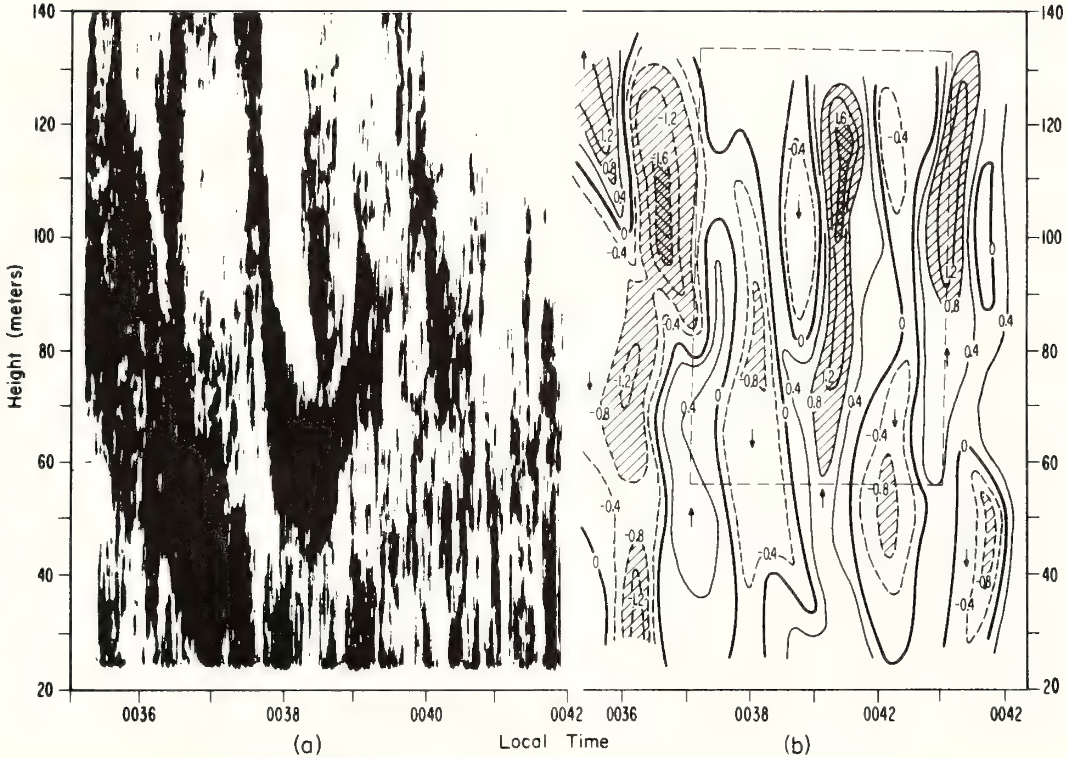

Figure 5. Acoustic echoes (left) and Doppler derived vertical velocity field under a nocturnal inversion which was exhibiting wave motions. Contour interval is 0.4 m/sec, velocities >0.8 m/s (single hatching), >1.6 m/sec double hatching, upward vertical velocities (solid lines), downward vertical velocities dashed lines.

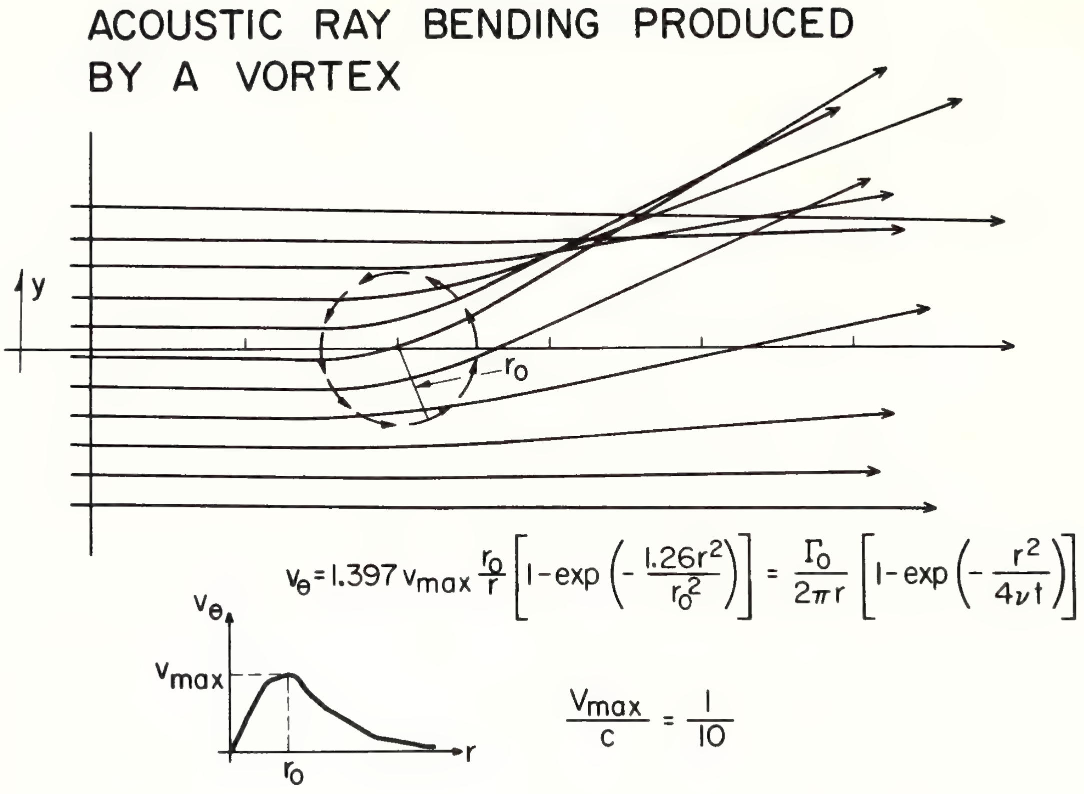

$$v_\theta = 1.397\, v_{max} \frac{r_0}{r}\left[1-\exp\left(-\frac{1.26r^2}{r_0^2}\right)\right] = \frac{\Gamma_0}{2\pi r}\left[1-\exp\left(-\frac{r^2}{4\nu t}\right)\right]$$

$$\frac{V_{max}}{c} = \frac{1}{10}$$

Figure 6. Acoustic ray paths through a vortex. The scale is arbitrary, ray bending being a function of V_{max}/C only. Data supplied by Dr. T. M. Georges.

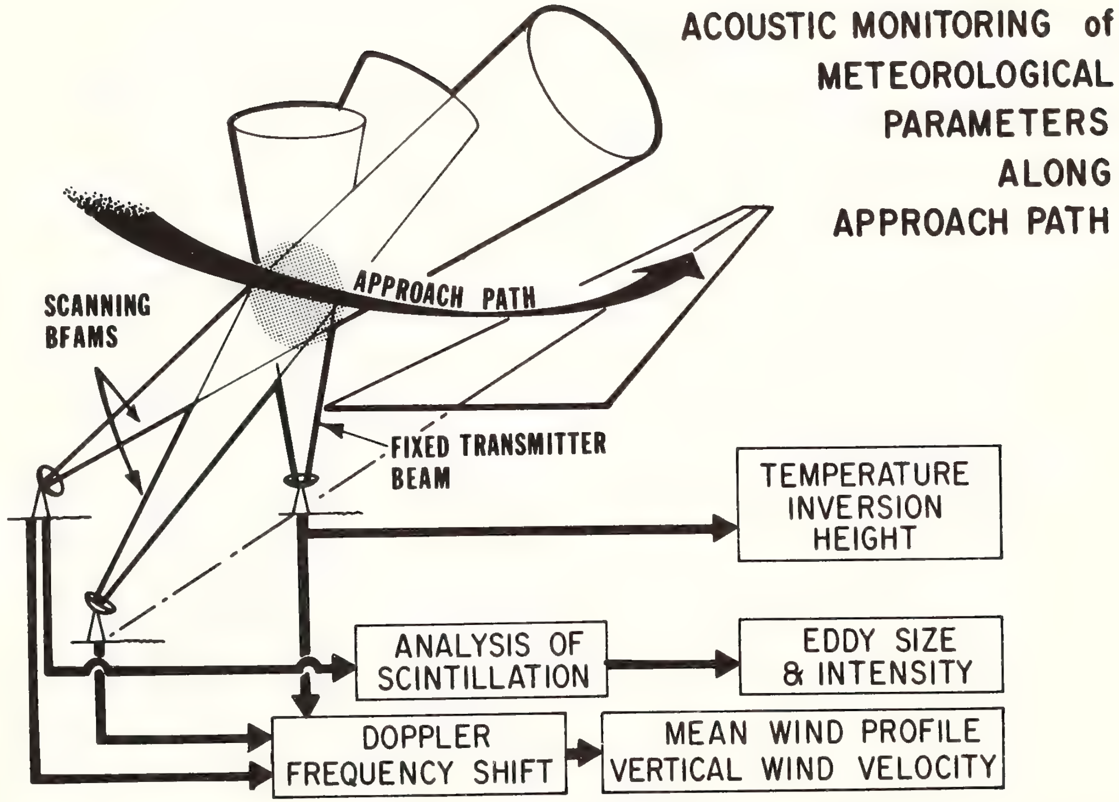

Figure 7. Schematic of proposed approach path monitoring system using one vertically pointing monostatic acoustic sounder and two orthogonally positioned receivers programmed to sweep the vertical beam.

24

Reprinted from American Institute of Aeronautics and Astronautics, Journal of Aircraft 8, No. 11, 934-936, 1971.

Acoustics: A New Approach for Monitoring the Environment near Airports

D. W. Beran*

Wave Propagation Laboratory, Environmental Research Laboratories NOAA, Boulder, Colo.

THE introduction of much larger aircraft to commercial and military fleets has focused attention on the need for more complete coverage of the meteorological environment at airports. Of immediate concern to those responsible for flight safety, and indeed to every pilot who may encounter one, are the intense vortices shed from the wings of large aircraft. This problem is especially critical near the ground where momentary loss of control could prove fatal. Concern over this new safety aspect has lead to a concerted effort by the FAA to learn more about the nature of vortices and their effect on other aircraft, and to a search for ways of reducing their residence time in the atmosphere or of determining their location in order that other aircraft can be advised of the potential hazard.

This effort has lead to a potpourri of suggested methods for monitoring the affected airspace, ranging from pulsed lidar to various acoustic devices. A common weakness found in most of the proposed monitoring systems is that they concentrate only on vortex detection and overlook other equally important, if less spectacular, environmental factors which affect low-level aircraft operation. For example, the effect on a planned glide slope of strong low-level wind shear or of turbulence produced by strong thermal activity can be of great importance to aircraft safety. This Note describes a relatively new device, an acoustic echo sounder, which has the potential to not only indicate the presence or absence of wake vortices, but to act as a continuous monitor of other important meteorological parameters.

In 1962, Monin[1] following contributions from many others, formulated the basic relationship describing the scatter of sound waves by turbulent wind and temperature fluctuations. More recently following a summary of this work, Little[2] outlined the potential applications of this principle which has been applied in the development of acoustic echo sounders used in remote sensing of low-level atmospheric phenomena.[2-4]

Because an acoustic wave is dependent on the medium being measured (the atmosphere) for its transmission, its

---

Received August 12, 1971. Taken from a talk given by the author at the FAA Sponsored Symposium on Turbulence held in Washington, D. C. during March of 1971.

* Research Meteorologist.

interaction with changes in structure are far stronger than for other types of waves (radio or light) used for remote sensing.[2] This strong interaction also limits the useful range of the echo sounder to regions within the Earth's boundary layer. For these reasons, an acoustic echo sounder is ideally suited for minitoring the immediate environment of an airport.

The mode of operation which has been successfully used in sounders designed for research purposes consists of sending a sound pulse, on the order of 50 msec long, into the atmosphere and then monitoring the acoustic power scattered from atmospheric inhomogenities along the path traversed by the pulse. This has been done for both colocated and separated transmitters and receivers, an important consideration because of the different scattering intensity for the two modes.

The sounder is sensitive to turbulent eddies on a scale which is equal to one half the wavelength of the acoustic wave, i.e., at a carrier frequency of 2000 Hz, eddies having dimensions of about 0.08 m produce the strongest scatter. While this portion of the turbulence spectra is of little aeronautical interest, information relevant to larger scale motions can be inferred. Assuming a Kolmogorov turbulence spectrum, having a well defined energy cascade rate, the intensity of the fluctuations at the smaller scale are directly related to the intensity of the eddies at all other scales within the inertial subrange. Perhaps more important, however, is the influence of much larger motions on regions or layers of strong, small scale, turbulence.

The regions of intense scatter are displaced by the larger scale flow and serve as tracers of phenomenon which are large enough to affect the flight of aircraft. This influence of large scale motion on smaller tracer is clearly shown in Fig. 1, a typical example of the output from an acoustic sounder reproduced on a facsimile recorder. Each vertical trace of the facsimile corresponds with a single pulse from the sounder, the dark line along the bottom of the record showing the end of each active pulse and the remaining portion, above this level, the period of time when the sounder was in a passive mode, "listening" for the scattered returns. The single vertically pointing antenna used during this field test provided the data necessary for monitoring a temperature inversion surface, the dark oscillating line between 200 and 450 m. This inversion marked the boundary between clear air and a low-level stratus deck, a valuable input to ILS operations. The ability to continually monitor the height of such low-level inversions would be of value also in regions where visibility reducing air pollution might accumulate.

The evolution from stable horizontally stratified structures to vertically oriented unstable structure (thermal plumes) after the breakup of a low-level inversion is equally vivid in acoustic sounder records and can also be monitored with a single antenna. A typical record produced by a thermal plume is shown on the left side of Fig. 2, where the ascending portion of the plume creates the dark vertically oriented structure.[5]

The actual vertical velocities within the plume can be determined from the Doppler frequency shift of the scattered signal. This was done for the plume shown in Fig. 2 and resulted in the vertical velocity field shown on the right side of the figure.

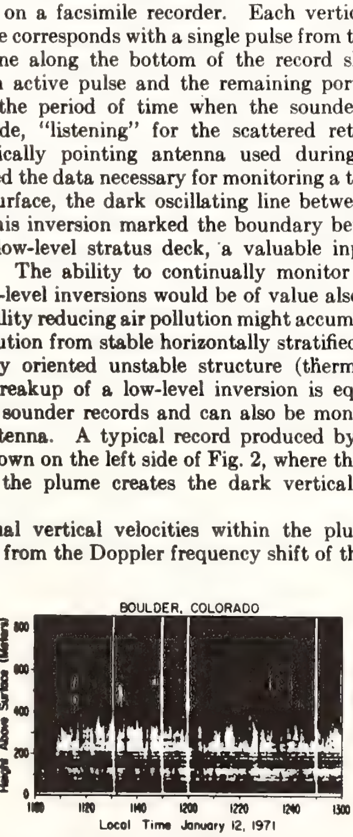

Fig. 1 Facsimile recording of the backscatter from an inversion surface.

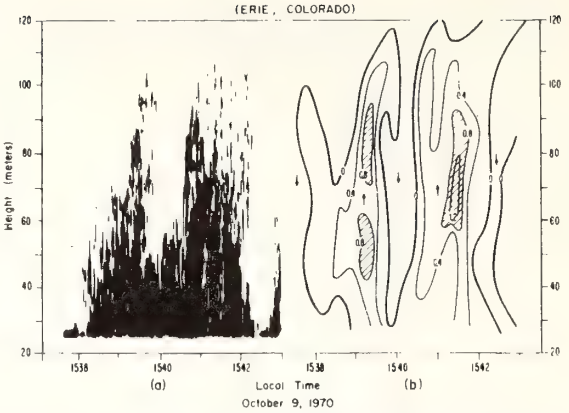

Fig. 2 Acoustic echoes (left) and Doppler derived vertical velocity field during thermal plume activity. Contour interval is 0.4 msec^{-1}; regions of vertical velocity >0.8 msec^{-1} are shaded; arrows indicate direction of vertical component.

By adding a second antenna separated from the first, but pointing at a volume common to both antenna beams, a second wind component in the plane formed by the two beams can be measured. This type of measurement has also been carried out successfully,[6] demonstrating the feasibility of adding a third antenna orthogonal to the plane of the first two in order to resolve the total wind vector at the intersection of the three beams.

From here, it should be a relatively simple matter to incorporate phased steerable antennas capable of sweeping up and down the vertically pointing beam and to process the information in a small on-line computer for real time display of a vertical profile of the total wind vector up to heights of about 1 km. This technique could then be incorporated into a complete monitoring system, such as that shown in Fig. 3, where a terminal forecaster or air controller would have a display of the vertical wind profile, inversion height, and information on the ambient turbulence intensity. This amount of continually updated detail wind information would certainly improve the air controllers ability to advise aircraft, considering that present information at airports at best consists of a constant output of surface wind and a vertical sounding every 6 hr.

It should be noted that the information discussed above is derived entirely from the ambient background scattering of sound in the atmosphere, no additional tracer is required. Very high velocities found in wake vortices coupled with entrained engine heat result in an increase of scatter from both velocity and temperature fluctuations. The scattering strengths associated with this increased activity should be orders of magnitude greater than those which result from ambient turbulence. The presence of a wake vortex will be readily detectable by the increased signal amplitude and its range or height above the ground can be fixed by the delay time between each pulse and the return signal. Methods of vortex detection similar to this are already being tested,[7,8] and preliminary results support the speculation that scatter from a vortex is much stronger than that from the ambient atmosphere. In addition, these tests have demonstrated that an acoustic sounder can be successfully operated in an environment containing extremely high-intensity noise sources, such as would be present at an airport.

Other characteristics of the interaction of sound waves with vortices may also prove useful as detectable phenomenon. One of these is the ray bending which results as a sound wave passes through a strong vortex. Georges,[9] has demon-

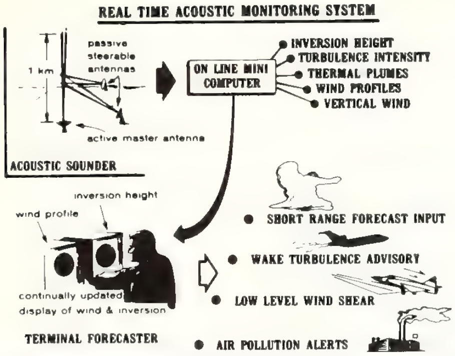

Fig. 3 Schematic of monitoring system which could provide real time information about meteorological conditions near an airport.

strated that this bending can be of very large magnitude and can result in high concentrations of sound pressure or complete nulls depending on the locations of the receivers. Because of the requirement that the transmitter and receiver must be located at just the right spot to receive the enhanced signal this approach would appear to have limited operational value. A better understanding of the phenomenon, however, will certainly aid in the interpretation of data collected by the scattering method.

A second approach, as yet untested, might be to interpret the amplitude or phase scintillation of the received signal as a measure of the turbulence intensity along the path of the sound wave. It is known that the intensity of such scintillations is a function of the turbulence intensity and eddy size[10,11] and a real time analysis of this parameter could provide information on the intensity of both the ambient background turbulence and the turbulence when a vortex is present. While more theoretical study and experimentation are needed to establish the functional relationship between sound wave scintillation and a vortex or ambient turbulence this approach would seem to provide exactly the type of information that a pilot making an approach would be interested in knowing. It would also be possible to make this type of measurement with the same equipment used for measuring the wind profile.

With any operational monitoring system the question of cost must certainly be considered, and it is here that acoustics has a decided advantage over the use of other types of waves. Thanks to the high level of interest in providing quality sound eqipment for the general public, many of the components needed for an acoustic sounder have already been developed and are being mass produced. This factor alone reduces the over-all cost of the system to a level which would allow the building and installation of sounders at most major airports. This, added to the versatility of a system which can monitor not only wake vortices but also provide real time information on the ambient environment, makes the acoustic sounder an attractive prospect.

To summarize, recent studies have shown that the strong interaction of acoustic waves with the atmosphere can be used to remotely sense a variety of details about the structure and motions within the boundary layer. The need for more complete information on both the ambient and man induced structure of the environment near airports can be fulfilled by the practical application of this relatively new monitoring technique. Based on confirmed measurements and an extension of these ideas one can envision systems similar to that shown in Fig. 3. Here a fixed, vertically pointing antenna, in conjunction with two orthogonally positioned scanning antennas could provide a continual real time record of the inversion height, the turbulent intensity, an indication of the presence of wing tip vortices, and the vertical profile of the total wind vector.

References

[1] Monin, A. S., "Characteristics of the Scattering of Sound in a Turbulent Atmosphere," *Akusticheskii Zhural*, Vol. 7, pp. 457–461; also *Soviet Physics Practice*, Vol. 7, April 1962, pp. 370–373.

[2] Little, C. G., "Acoustic Methods for the Remote Probing of the Lower Atmosphere," *Proceedings of IEEE*, Vol. 57, 1969, pp. 571–578.

[3] McAllister, L. G., Pollard, J. R., Mahoney, A. R., and Shaw, P. J. R., "Acoustic Sounding—A New Approach to the Study of Atmospheric Structure," *Proceedings of IEEE*, Vol. 57, 1969, pp. 579–587.

[4] Beran, D. W., "Project EAR (Environmental Acoustic Research)," Rept. 17, March, 1970, Meteorology Dept., Univ. of Melbourne, Melbourne, Australia.

[5] Beran, D. W., Little, C. G., and Willmarth, B. C., "Acoustic Doppler Measurements of Vertical Velocities in the Atmosphere," *Nature*, Vol. 230, 1971, pp. 160–162.

[6] Beran, D. W. and Willmarth, B. C., "Doppler Winds from a Bistatic Acoustic Sounder," *Proceedings of the Seventh International Symposium*, Univ. of Michigan, 1971.

[7] Kodis, R. D., *FAA Sponsored Symposium on Turbulence*, Washington, D. C., March 1971.

[8] Proudian, A., private communication, Xonics Inc., Van Nuys, Calif. March 1971.

[9] Georges, T. M., "Acoustic Ray Paths Through a Model Vortex with a Viscous Core," to be published, *Journal of the Acoustical Society of America*, Nov. 1971.

[10] Clifford, S. F. and Brown, E. H., "Propagation of Sound in a Turbulent Atmosphere," *Journal of the Acoustical Society of America*, Vol. 48, Nov. 1970, pp. 1123–1127.

[11] Mandics, P. A., "Line-of-Sight Acoustical Probing of Atmospheric Turbulence," TR 4502-1, 1971, Stanford Electronics Laboratories, Stanford Univ., Stanford, Calif.

25

Reprinted from Proceedings of NATO Advanced Study Institute, Statistical Methods and Instrumentation in Radio Meteorology, April 15-22, 1971, 167-180, 1971.

5.1 ACOUSTIC REMOTE SENSING OF TEMPERATURE AND VELOCITY STRUCTURE IN THE ATMOSPHERE

Freeman F Hall Jr, Wave Propagation Laboratory, NOAA
Environmental Research Laboratories, Boulder, Colorado,
USA.

INTRODUCTION

Acoustic echo sounding of atmospheric structure is one of the newest and yet one of the oldest remote sensing techniques. It was in 1873 that John Tyndall detected acoustic backscatter from thermal and wind structure in the atmosphere. He attributed the scattering to "acoustic clouds". The effect was discovered while investigating the propagation of acoustic energy from a large fog horn [1]. He was even able to demonstrate that air, heated by a flame, could attenuate the direct propagation of sound and lead to backscattering. A sensitive flame detector was used in this laboratory experiment. After Tyndall's initial investigation, the technique lay dormant for over 70 years before being studied again as an atmospheric probe.

Shortly before the end of World War II, Gilman, Coxhead and Willis [2] used acoustic backscatter to study the structure of low level temperature inversions as they affected the propagation in microwave communication links. A loud-speaker source and microphone in a 60 cm parabolic dish were used as source and receiver, and the backscatter echoes displayed on an oscilloscope, which was photographed with a time-lapse camera. The surprising amount of atmospheric structure displayed under inversions was noted. Strong correlation was found between the acoustic inversion echo and microwave fading over a low level, 64 km path. The breakup of nocturnal

Published in: "Statistical Methods and Instrumentation in Geophysics," A. G. Kjelaas, ed., Teknologisk Forlag A/S, Oslo (1971).

thermal inversions was monitored, and the change to typical daytime convective echoes could be observed. The authors were not able to explain completely the reason why such echoes were obtained. The publication of these results in the Journal of the Acoustical Society of America may explain why meteorologists were not attracted to the advantages of acoustic remote sensing at an earlier date.

During the late 1950's acoustic scattering from the atmosphere was investigated experimentally in the Soviet Union by Kallistratova [3, 4, 5] but it was the studies by McAllister [6] which showed that echoes could be reliably obtained to heights of several hundred meters. McAllister also showed the value of the facsimile recording media for illustrating the temporal structure of atmospheric scatter for both stable and unstable lapse rates.

The analytical study of the capabilities of acoustic echo sounding by Little [7] was the first step on which the NOAA Atmospheric Acoustics Program was based. In this paper it is shown that $\sigma(\theta)$, the acoustic power of wavelength λ scattered, per unit volume, per unit incident power is given by

$$\sigma(\theta) = 0.06\lambda^{-1/3}\cos^2\theta \left(\frac{C_v^2}{C^2} \cos^2\frac{\theta}{2} + 0.13 \frac{C_T^2}{T^2} \right) \left(\sin\frac{\theta}{2} \right)^{-\frac{11}{3}} \qquad (1)$$

where θ is the scattering angle measured from the original incident direction, C_v^2 is the velocity structure parameter, C_T^2 is the thermal structure parameter, C is the velocity of sound, T is the mean absolute temperature of the atmosphere, and a Kolmogorov spectrum of turbulence is assumed. The values of the two atmospheric structure parameters are defined by

$$C_v^2 = \overline{\left(\frac{u(x) - u(x+r)}{r^{1/3}} \right)^2} , \quad C_T^2 = \overline{\left(\frac{T(x) - T(x+r)}{r^{1/3}} \right)^2} \qquad (2)$$

where u is the wind speed at x in the positive x direction and r is measured along the x axis. It is seen that the scattered acoustic power is only a weak function of acoustic wavelength varying as $\lambda^{-1/3}$, that direct backscatter for $\theta = \pi$ is a function of the thermal structure only, that because sound is a longitudinal vibration there is no scattering at $\pi/2$, and that there is strong scattering in the forward direction because of the final factor in equation (1). Obviously the equation is a simplification and cannot be applied for extremely small values of θ. More details and discussion of the scattering are given by Little [7].

Expressing the interaction of acoustic waves in terms of the sonic refractive index where 1 N unit is one part in 10^6, one can compare the interaction of acoustic waves with radio and optical waves for a given change in atmospheric temperature, velocity, or absolute humidity. The results from Little are shown in Table 5.1.1. The reason for the strong interaction of acoustic energy with the atmosphere is essentially because the atmosphere is the transmitting vehicle for the longitudinal pressure vibrations with the velocity of sound given by

$$C = 331\sqrt{\frac{T}{273}} \quad \mathrm{m\,s^{-1}} \tag{3}$$

for dry air.

The atmosphere is but a perturbation for the propagation velocity of electro-magnetic energy.

Magnitude of Parameter Change	Change in Refractive Index, N units *		
	Acoustic	Radio	Optical
1°K fluctuation in temperature	1700	1	1
1 m s^{-1} variation in wind speed	3000	2×10^{-6}	2×10^{-6}
1 mb change in water vapour pressure	140	4	0.04

* One N unit equals one part in 10^6

Table 5.1.1. Comparison of refractive index change for acoustic, radio, and optical waves for small changes in atmospheric parameters.

THE ACOUSTIC ECHO SOUNDER SYSTEM

A typical sounding system will employ an acoustic source to insonify the atmosphere with short pulses of sound, and a means to collect the scattered acoustic power. The acoustic power must be converted to an electrical signal, amplified, and recorded or displayed for operator evaluation. Fig 5.1.1

illustrates a schematic block diagram for the NOAA Mark I Acoustic Echo Sounder. Most of the components were purchased as off-the-shelf electronic sub-systems. It was found to be prudent to purchase the highest quality equipment available to insure reliable low noise operation of the completed system. The acoustic carrier frequency, pulse repetition rate, pulse length, receiver turn-on and turn-off time, receiver gain, receiver bandwidth, and receiver amplifier gain sweep are all controllable parameters of the system. It has been found desirable to have this number of controllable parameters variable over a wide range to insure a flexible system to match the varying atmospheric conditions.

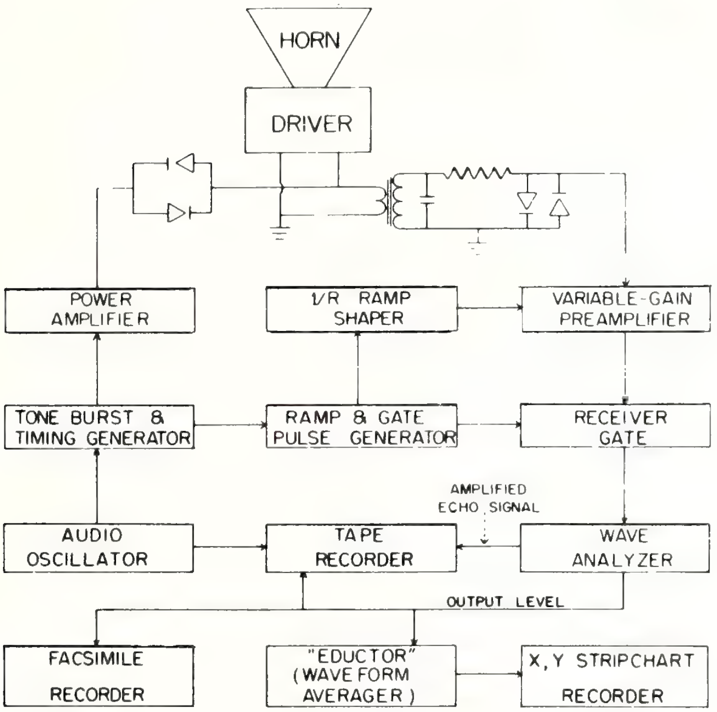

ACOUSTIC RADAR BLOCK DIAGRAM

Fig 5.1.1. The NOAA Mark I Echo Sounder, illustrating the flow of transmitted signal, control functions, and received signal.

The operation of the sounder can be followed from the block diagram, further details are given in the report by Wescott, Simmons and Little [8]. The tone burst and timing generator is ster control center of the system. The tone burst is -acting electronic switch. When closed, it passes the signal output of the audio oscillator to the input of the power amplifier. The duration of this switch closure is adjustable. Typical settings range from 20 to 200 ms and are accurate to a small fraction of a microsecond. The timing generator controls the repetition rate of the tone bursts. Typical repetition rates range from 0.1 to 0.5 Hz. During each burst, the power amplifier delivers 40 W through the back-to-back diodes of the transmit-receive circuit to the acoustic transducer or driver. The driver is coupled acoustically to a reflector-horn antenna, which then radiates a tone burst pulse of acoustic energy into the atmosphere. As soon as the pulse is completed, the sub-threshold high impedence of the back-to-back diodes prevents low-level hum and noise of the power amplifier from reaching the acoustic transducer. During the tone burst, another set of back-to-back diodes in the transmit-receive circuit shorts out the input of the receiver variable-gain preamplifier to prevent overload and damage to this extremely sensitive component. At the completion of the pulse, the sub-threshold impedance of this set of diodes comes into play and they act as an open circuit (no load) across the very small echo signal about to be received.

During reception of echoes, the acoustic transducer acts as a microphone, transformer coupled to the variable-gain preamplifier. The transformer has a high step-up ratio and increases the microphone Johnson noise voltage to a level that exceeds the input self-noise of the preamplifier. This insures that the receiving system does not degrade the ultimate signal-to-noise ratio at the microphone terminals.

The gain of the preamplifier is electronically controlled by the $1/R$ ramp shaper to compensate for the spherical divergence of acoustic echoes as they are received from progressively longer ranges. The voltage gain is varied inversely with range $(1/R)$ rather than as the inverse square of range $(1/R)^2$ because the voltage signal developed by the receiving transducer is proportional to acoustic pressure rather than acoustic power.

The output of the variable-gain preamplifier is applied to a receiver gate. This gate is opened and closed by rectangular pulses from the ramp and gate pulse generator. Pulse timing is controlled by the tone burst and timing generator. The purpose of the receiver gate is to suppress the small amount of signal that leaks through the transmit-receive circuit during the transmitted tone burst and would otherwise reach the wave analyzer. Since the driver and antenna "ring" for some 50 ms after termination of the high power tone burst, the opening of the receiver gate is delayed for a controllable time (typically about 100 ms) until the ringing has stopped and the driver has fully recovered its sensitivity as a microphone. As soon as the receiver gate has opened, amplifier echo signals from the preamplifier are able to reach the wave analyzer.

The wave analyzer operates as a receiver tuned to the carrier frequency of the acoustic tone burst radiated into the atmosphere. Its bandwidth is set to accommodate the radiated bandwidth and is therefore determined by the duration of the tone burst. A 100 Hz bandwidth generally has been used to accommodate the major sideband frequencies generated by tone bursts lasting 20 ms. The wave analyzer has two types of output signal, both of them tape recorded. One of the signals is an amplified version of the received carrier and sidebands. This is the type of signal that is used for determining Doppler shifts of frequency between a transmitted signal and its received echo. The other signal is the detected level of the received echo and is displayed as functions of altitude and time of day by means of the facsimile recorder.

An alternate display of receiver output level is indicated by the blocks labeled "eductor" and X-Y stripchart recorder. The "eductor" is an electronic instrument that obtains the waveshape of a repetitive signal obscured by noise. It does so by sampling and accumulating the signal level at corresponding points along consecutive sweeps of a noisy waveform. Selecting an accumulation time not appreciably longer than the time in which the repetitive waveshape of the original signal changes significantly yields an optimum combination of improved signal-to-noise ratio without substantial loss of time resolution.

The improved echo signal from the "eductor" can be applied to the X-Y stripchart recorder that plots signal level (proportional to echo strength) along the Y-axis and time (proportional to height above local terrain) along the X-axis. The incrementally advancing stripchart of the recorder permits nesting of consecutive traces at regular intervals of real time. The advantage of this display over facsimile recording is that it is quantitative rather than qualitative, allowing direct and accurate reading of echo signal strength.

The acoustic antenna is an important component of the system since it serves to collimate the transmitted power into a narrow beam in the transmit mode, and serves as a highly directional microphone in the receive mode. The NOAA sounder uses a cone paraboloid antenna originally designed for microwave use. The electro-dynamic transducer is bolted to the cone section in place of the microwave conical wave guide. The only other modification of the antenna found desirable is to coat it with an acoustical dampening material to limit reverberation time after the transmitting pulse is turned off. The antenna is shown in Fig 5.1.2. Other types of antennas which have been used in acoustic sounders include arrays of electrodynamic speakers, and transducers mounted at the focus of parabolic dishes.

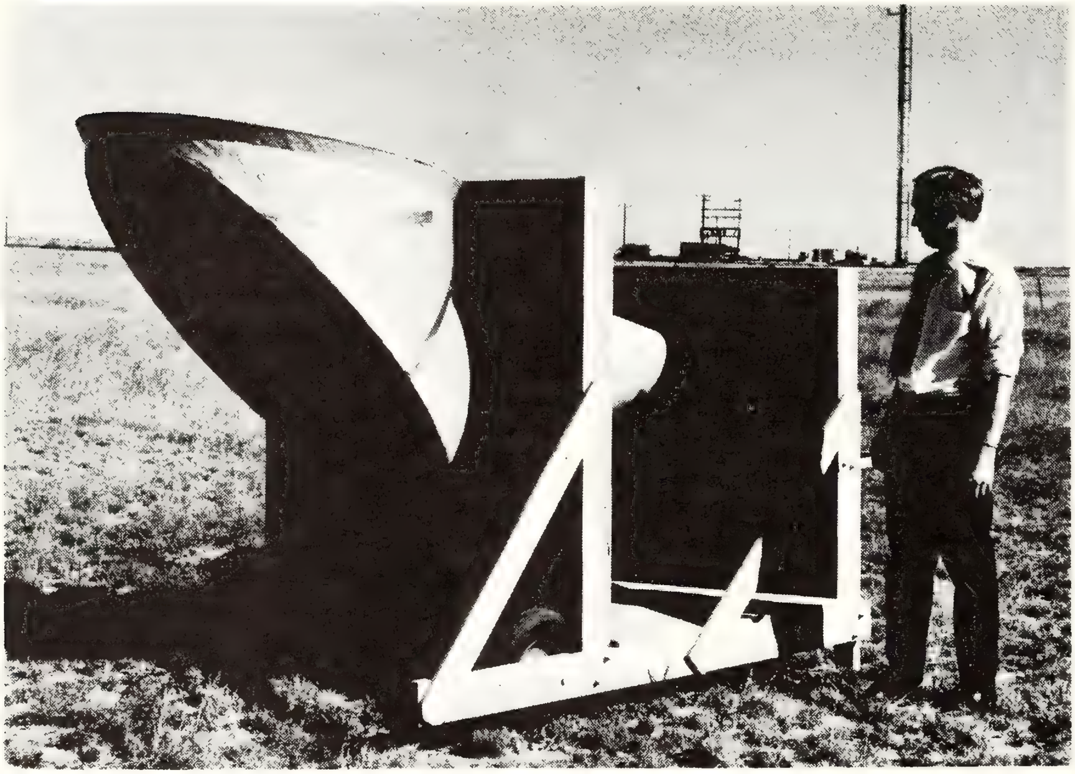

Fig 5.1.2. Cone-paraboloid antenna adapted for acoustic echo sounding.

A desirable feature of any antenna is the limitation of side lobes so that unwanted acoustic power is not directed elsewhere and so that noise in the environment surrounding the sounder does not affect sounder performance. The measured side lobe characteristics of the NOAA cone paraboloid antenna are shown in Fig 5.1.3 for different acoustic frequencies. It will be seen that at a frequency of 1 kHz, the half power beam width is about 16°, whereas at 5 kHz the main beam is measured to be only 3 or 4 degrees wide to the half power points. Note also that the 90° sidelobe is 38 dB below the main beam at 1 kHz and nearly 50 db below the main beam at 5 kHz.

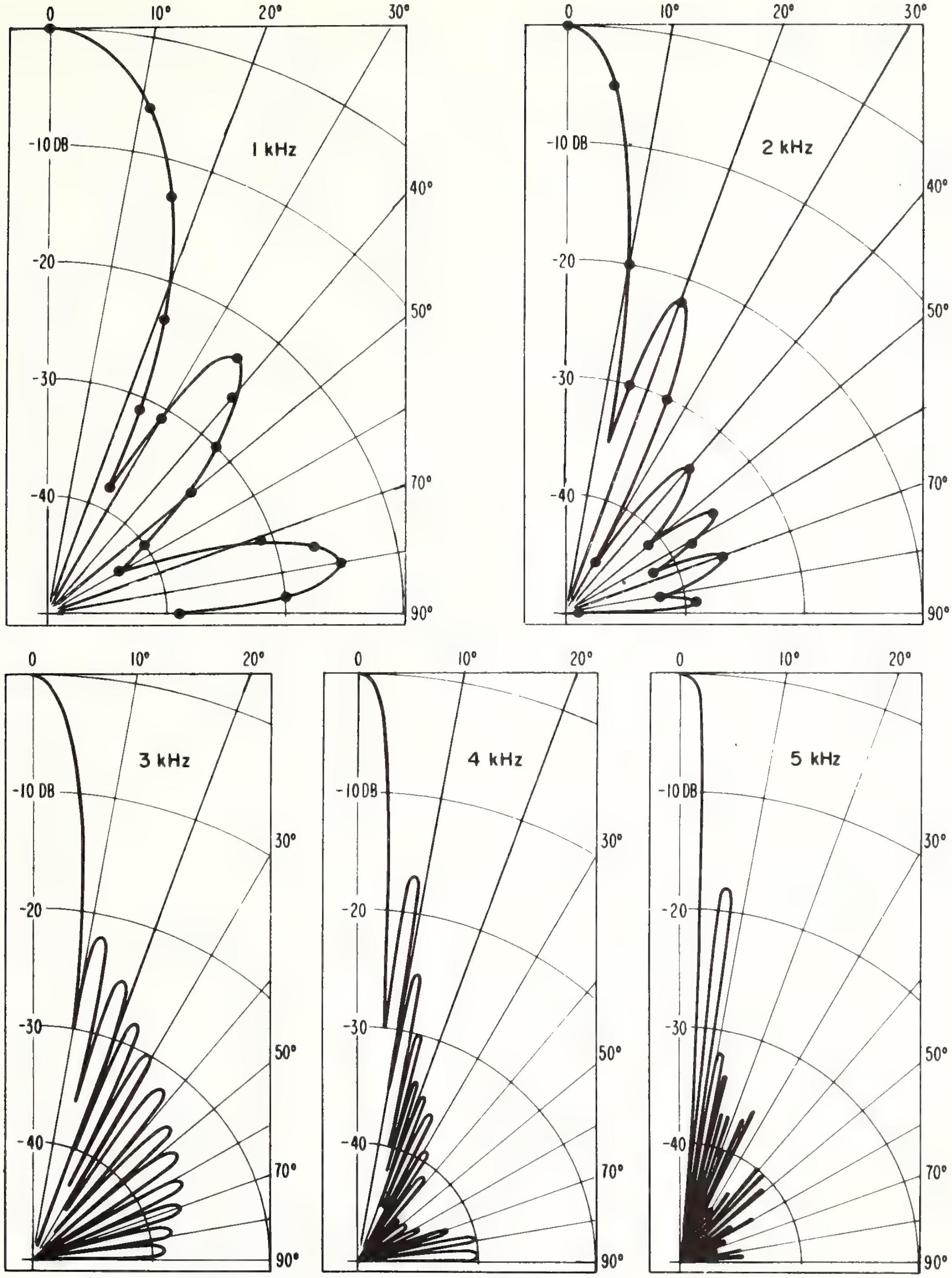

Fig 5.1.3. Measured antenna patterns for the cone-paraboloid antenna for the range of acoustic frequencies used in echo sounding.

One easy way to improve sidelobe rejection is to surround the antenna with an absorbing cuff. For a vertically pointed antenna it has been found that an open cylinder of hay bales is an effective absorber. If the cylinder aperture is several times that of the antenna and the height several times the antenna aperture, 20 - 30 dB additional 90° sidelobe attenuation is obtained. An analysis of this absorbing cuff has been performed by Strand [9] and the theoretical improvement closely checks with that experimentally measured in the field. Further improvements should be possible with internal attenuators in the horn to achieve the effect of a tapered feed in the microwave case. The present antenna acts nearly like a perfect piston source, but by decreasing the amplitude of the pressure fluctuations near the edge of the aperture, less energy will be diffracted at the edge, further improving the sidelobe rejection.

Our interest in improving the antenna characteristics is strongly motivated by the desire to utilize the acoustic echo sounder for studying boundary layer meteorology of interest in urban air pollution situations. While the unshielded antenna will be entirely adequate to achieve performance limited only by the Johnson noise from the ohmic resistance in the transducer in a quiet rural environment, the background noise in typical urban or industrial environments will not be so easy to live with. Based on analysis of typical noise levels of built up areas, it was found that a desirable side lobe attenuation varied from 70 dB for the urban environment to 100 dB for a noisy downtown location, if transducer Johnson noise was to be the fundamental limitation on systems performance.

Another consideration when operating the sounder in built up areas is the avoidance of noise pollution which might be aggravating to nearby inhabitants. We have analyzed the masking effect of background noise in typical urban and industrial environments. Based on the Fletcher [10] masking criterion, wherein sound levels comparable to the background noise are not readily discernible, we find that with 50 - 60 dB side lobe rejection, it should be possible to operate the present NOAA sounder, with an output of 8 acoustic watts, within several hundred meters of a suburban residence without being annoying. In the typical downtown noise levels, the sounder would be undetectable by persons within just a few meters, because of the masking noise from traffic, industrial activity, or building airconditioning noise. With proper attention to design detail then, it appears that the sounder should be operable within most environments without being troubled by nominal environmental noise and without contributing to noise pollution from acoustic pulses.

OPERATIONAL RESULTS WITH A MONOSTATIC ACOUSTIC SOUNDER

We noted earlier that with a co-located transmitter and receiver, the backscatter from the atmosphere is caused only by thermal structure. It is not surprising that considerable thermal structure is observed when the atmosphere is convectively unstable. The typical pattern observed on the facsimile recording showing backscattered intensity with height, as a function of time, is shown in Fig 5.1.4. This is the thermal plume structure, indicating the non-uniform rise of heated and thermally non-uniform parcels from the ground due to surface heating from solar radiation. That the upwelling air is characterized by variation in temperature is well known from investigations with fast response temperature sensors on aircraft, such as the study by Myrup [11].

Myrup also shows how the variation of C_T with height may be used to differentiate between different convective models. With a well calibrated acoustic sounder, and if the atmospheric acoustic attenuation is known, it is possible to measure C_T as a function of height and compare results with the Townsend convective theory, where a variation as the -0.6 power with height is predicted, or with similarity theory where a -0.33 power law is found. We are just to the stage where it should be possible in the near future to perform such studies. By comparing the acoustic sounder measurements of C_T with temperature differences recorded by fast response thermometers, spaced one-half of the acoustic wavelength apart, on a nearby micro-meteorological tower, we are now

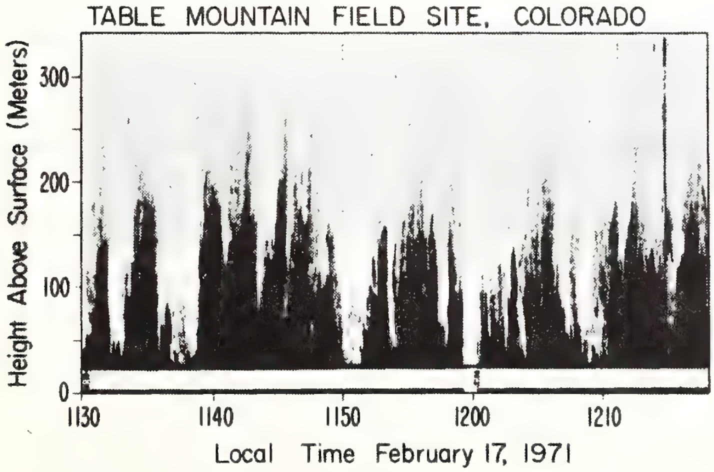

Fig 5.1.4. Facsimile recording of backscatter acoustic intensity from convective thermal plumes.

studying the accuracy of the acoustic measurements. Preliminary results indicate rather good agreement between the sounder and tower measurements of mean C_T, and even in the variance of this parameter. The great advantage in using the sounder over tower or aircraft measurements is that the entire spatial structure of the plume is visible, instead of one or several finite horizontal slices through the structure.

The sounder facsimile record clearly shows the vertical organization of the convective plumes, seemingly putting to rest the controversy over the existence of plumes as opposed to isolated heated bubbles of rising air. One improvement which we were striving to add to our sounder is to enable the detection of echoes from lower levels in the atmosphere than the present minimum of 30 m. It is in these lower levels that wind shear frequently produces a marked slope in the plume structure as observed by Kaimal and Businger [12]. We have observed such plume slopes occasionally in the levels above 30 m, but at our present location do not have wind instrumentation above 15 m to verify wind shear at higher levels. Occasionally the plumes seem to slope in a direction opposite to that to be expected from wind shear in the lower levels, or backward into the wind. Without knowledge of the wind profile with height it is not possible to explain this observation. We look forward in the future to tests with tethered balloon sounding systems to obtain better wind profile data.

Although backscatter at $\theta = \pi$ is caused only by thermal structure, the frequency of the scattered sound will depend upon the velocity of the scattering parcel along the line-of-sight. The Doppler shift produced by vertical winds has been sensed acoustically as reported by Beran, Little and Willmarth [13]. It is possible to resolve line-of-sight velocities to several tenths ms^{-1} when the sounder is operated at a carrier frequency of 4 kHz. We are now experimenting with bistatic Doppler wind detection wherein two monostatic systems are used with beams intersecting in a common volume. Wind velocity components along each beam are then obtained which may be resolved into an orthogonal wind field in the plane defined by the beams. Three sounders would allow remote detection of three dimensional wind in the intersecting volume.

A second class of acoustic sounder returns is found under stable conditions in the boundary layer during nocturnal radiation temperature inversions. Fig 5.1.5 shows a typical record of inversion taken on a night when considerable wind shear existed above the inversion layer. Evidently the wind shear at the top of the inversion was sufficient to cause Kelvin-Helmholtz instabilities in the layer which propagated as gravity waves in the stable, cold, trapped air. The large excur-

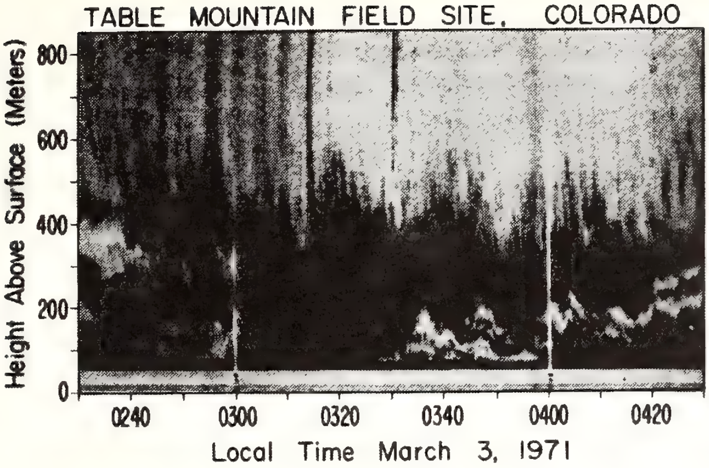

Fig 5.1.5. Facsimile recording of backscatter acoustic intensity from a nocturnal inversion, showing gravity wave structure.

sions in height of these waves, shown in Fig 5.1.5, could also be detected with an array of infrasound microphones. We are presently studying more carefully the correlation between infrasound detected pressure excursions, of the order of a few microbars, with the structure revealed from acoustic sounding.

Another class of breaking wave phenomenon is revealed in Fig 5.1.6, with the braiding structure in the center of the figure typical of the clear air radar returns from Kelvin-Helmholtz breaking waves detected by Hardy, Glover, and Ottersten [14].

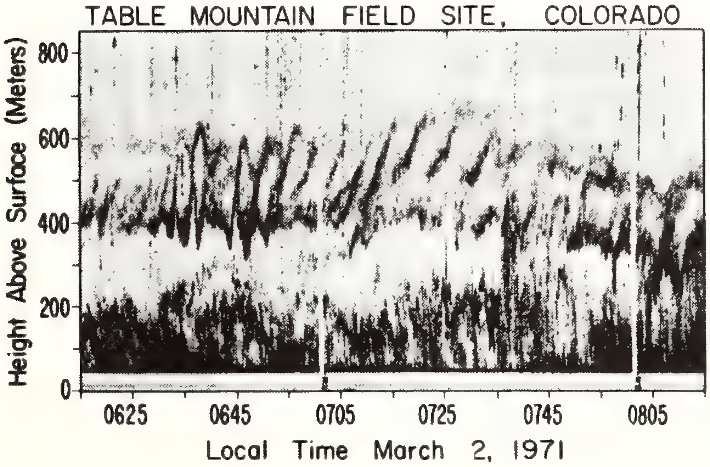

Fig 5.1.6. Breaking wave structure revealed by thermal irregularities in the turbulent air, leading to acoustic backscatter.

CONCLUSIONS

Acoustic echo sounding has been found to provide a new and valuable tool for sensing temperature and velocity structure in the earth's boundary layer. The ability to measure quantitatively these variables, at the same time providing pictorial displays of the organization of convective structures, inversions, and waves is already providing new insights into boundary layer dynamics. The simplicity and relatively low expense of fabricating an acoustic system, as compared with radar or lidar devices, makes it probable that acoustic techniques will find wider application in the future.
(Not subject to copyright.)

ACKNOWLEDGEMENT

The program in atmospheric acoustic echo sounding reported here is a group effort at the NOAA Wave Propagation Laboratories. The contributions of D W Beran, J W Wescott, W R Simmons, B C Willmarth, W D Neff and WPL Director C G Little are greatfully acknowledged.

REFERENCES

(1) Tyndall, J, Sound, Appleton Co, London, 3 ed, ch 7 (1875)

(2) Gilman, G W, H B Coxhead and F H Willis, Reflection of sound signals in the troposphere, J Acoust Soc Amer 18, 274-83 (1946)

(3) Kallistratova, M A, An experimental investigation into the scattering of sound in a turbulent atmosphere, Dokl Acad Nauk SSSR 125, 69-72 (1959)

(4) Kallistratova, M A, Procedure for investigating sound scattering in the atmosphere, Sov Phys - Acoust 5, 512-4 (1959)

(5) Kallistratova, M A and V I Tatarski, Accounting for wind turbulence in the calculation of sound scattering in the atmosphere, Sov Phys - Acoust 6, 503-5 (1960)

(6) McAllister, L G, Acoustic sounding of the lower troposphere, J Atmos Terr Phys 30, 1439-40 (1968)

(7) Little, C G, Acoustic Methods for the remote probing of the lower atmosphere, Proc IEEE 57, 571-8 (1969)

(8) Wescott, J W, W R Simmons and C G Little, Acoustic sounding measurements of temperature and wind fluctuations, ESSA Technical Memorandum ERLTM-WPL 5, Boulder, Colorado (1970)

(9) Strand, O N, Numerical study of the gain pattern of a shielded acoustic antenna, J Acoust Soc Amer 49, 1698-1703 (1971)

(10) Fletcher, H, Auditory patterns, Rev Mod Phys 12, 47-65 (1940)

(11) Myrup, L O, Temperature and vertical velocity fluctuations in strong convection, Quart J Roy Meteorol Soc 93, 350-60 (1967)

(12) Kaimal, J C and J A Businger, Case studies of a convective plume and a dust devil, J Appl Meteorol 9, 612-20 (1970)

(13) Beran, D W, C G Little and B C Willmarth, Acoustic doppler measurements of vertical velocities in the atmosphere, Nature 230, 160-2 (1971)

(14) Hardy, K R, K M Glover and H Ottersten, Radar investigations of atmospheric structure and CAT in the 3 to 20 km region. In: Clear Air Turbulence and its Detection, edited by Y H Pao and A Goldburg, Plenum Press, New York, 402-16 (1969)

26

Reprinted from Proceedings of the 7th International Symposium on Remote Sensing of Environment 1, No.. 10259-1-X, May 17-21, 1971, 1699-1714, 1971.

PROCEEDINGS of the SEVENTH INTERNATIONAL SYMPOSIUM

on

REMOTE SENSING OF ENVIRONMENT

17-21 May 1971

Sponsored by

Center for Remote Sensing Information and Analysis
Willow Run Laboratories, Institute of Science and Technology
The University of Michigan

Water Quality Office
Environmental Protection Agency

Office of Space Science and Applications
National Aeronautics and Space Administration

Federal Highway Administration
U. S. Department of Transportation

U. S. Geological Survey
U. S. Department of Interior

Air Force Cambridge Research Laboratories
Air Force Systems Command
U. S. Air Force

Agricultural Research Service
U. S. Department of Agriculture

Infrared and Optics Laboratory
Willow Run Laboratories
INSTITUTE OF SCIENCE AND TECHNOLOGY
THE UNIVERSITY OF MICHIGAN
Ann Arbor, Michigan

DOPPLER WINDS FROM A BISTATIC ACOUSTIC SOUNDER

D. W. Beran and B. C. Willmarth

Wave Propagation Laboratory
NOAA Environmental Research Laboratories
Boulder, Colorado

ABSTRACT

Acoustic echo sounding has been shown to have considerable promise as a remote sensor of various low level atmospheric phenomena. The feasibility of one application, the derivation of vertical winds from the Doppler shift on a monostatic acoustic sounder, was demonstrated in an earlier experiment by the authors. This paper describes a more complex arrangement involving the use of bistatic acoustic sounding to measure a component of the horizontal wind. The feasibility of this approach is demonstrated and found to be superior to a monostatic system. The results also suggest that refraction due to temperature or wind gradients along the tilted beam of a bistatic sounder can result in an incorrect estimate of the real wind.

DOPPLER WINDS FROM A BISTATIC ACOUSTIC SOUNDER

In an earlier experiment (Beran, Little and Willmarth, 1971) the Doppler shift of monostatic acoustic sounder returns was used to derive the vertical motion of the echo volume. The Doppler information made it possible to produce a height-time section of the vertical velocity field in a breaking gravity wave and in a thermal plume (see Fig. 1).

This paper describes a more complex experiment in which a second acoustic receiver is employed to test various bistatic techniques for obtaining a horizontal component of the wind. The results of this work will help to determine the feasibility of complete determination of the wind vector by complementing a monostatic sounder with two bistatic links.

The optimum arrangement of antennas for measuring Doppler winds must take into consideration the basic scattering equation, developed from contributions by Lighthill (1953), Kraichnan (1953), Batchelor (1957), Ford and Meecham (1960), Tatarski (1961), Kallistratova (1961) and Monin (1962). The scatter of sound by turbulent wind and temperature inhomogenities, represented by the structure constant for wind C_v^2 and temperature C_t^2, can be represented by;

$$\sigma(\theta) = 0.03k^{\frac{1}{3}} \cos^2\theta \left[\frac{C_v^2}{C^2} \cos^2 \frac{\theta}{2} + 0.13 \frac{C_t^2}{T^2} \right] (\sin \frac{\theta}{2})^{-\frac{11}{3}} , \qquad (1)$$

where σ is the scattered power, per unit volume, per unit incident flux, per unit solid angle θ measured from the initial direction of propagation. The wave number of the sound wave is k and the ambient speed of sound and temperature are represented by C and T respectively.

It is clear from Equation 1 that: a) the scattered acoustic power is only a weak function of the wave length of the illuminating frequency, b) the scattered power is the sum of two terms, one due to wind fluctuations and the other to temperature fluctuations, c) both wind and temperature scattering terms are multiplied by $\cos^2\theta$, which means that no power will be scattered at an angle of 90°, d) the wind term includes a $\cos^2(\frac{\theta}{2})$ multiplying term, which means that the wind fluctuations produce no scatter in the backward direction ($\theta = 180^\circ$) and, e) both the wind and temperature components of the scatter are multiplied by a $(\sin \frac{\theta}{2})^{-\frac{11}{3}}$ factor, i.e. most of the scatter is in the forward hemisphere.

For bistatic acoustic measurements it is important to avoid configurations where the beams will intersect at right angles because of the lack of scatter at 90°. In addition, because of the enhanced scatter at angles other than 180° and 90°, the bistatic configuration should have a range advantage over a monostatic system.

Keeping these differences in mind, we now turn to the Doppler shift produced by motion of the scattering volume (the mean wind). Consider the scattering geometry shown in Fig. 2. Sound transmitted from T at a frequency f_o and having the wave vector $\bar{K}_o$ is incident on the scattering volume at 0, moving with a mean velocity $\bar{V}$. The scattered sound, having frequency f_s and wave vector $\bar{K}_s$ is received at R and a difference frequency $\Delta f = f_s - f_o$ is observed. This Doppler shift Δf is given to the first order by

$$\Delta f = \frac{1}{2\pi} (\bar{K}_s - \bar{K}_o) \cdot \bar{V}$$

$$\approx \frac{2v}{\lambda_o} \sin (\frac{\theta}{2}) \cos \beta \qquad (2)$$

where θ is the scattering angle defined in Equation 1, β is the angle, in the plane formed by the two beams, between the wind vector $\bar{V}$ and $(K_s - K_o)$ and λ_o is the wavelength of the original carrier frequency. Replacing λ_o with C/f_o, where C is the speed of sound in the scattering volume, and solving for the magnitude of the wind component being measured, we have

$$v = \frac{C}{2 \sin \frac{\theta}{2}} \left[\frac{\Delta f}{f_o} \right] . \qquad (3)$$

From Equation 2 we see that the magnitude of the Doppler shift is also a function of scattering angle, becoming larger as the scatter angle increases. The direction of the measured component is the same as the direction of the vector $(\overline{K}_s - \overline{K}_o)$, or the direction of the bisector of the angles formed by the intersection of the two beams, in the following termed the radial vector*. Clearly if we wish to derive a horizontal wind component from this radial vector, it must be kept as close to the horizontal as possible.

The above derivation does not consider the effect of a time-varying average refractive index along the path from the transmitter to the volume, a factor which would produce phase changes and a false Doppler shift. A potentially more serious effect is the bending of the beam due to spatial changes of refractive index along the beam produced by a temperature or wind gradient. If horizontal homogeneity is assumed, and one beam is pointing vertically and the second tilted at some angle, refraction will cause the second beam to bend. The effect of this bending is illustrated in Fig. 3 where the active sounder, A, is transmitting in the vertical and the passive sounder, B, is receiving the signal scattered from point 0. If the refractive index is constant along the sloping beam the ray paths will follow the straight solid line from A to 0 and back to B, and the component of the wind which is measured will be the vector $\overline{R}$ directed along the bisector of the angle formed by the two beams. When a refractive index gradient, produced by a wind profile such as that shown in Figure 3 is introduced, the ray which eventually reaches the passive sounder will follow the curved dashed line from 0′ to B. This ray leaves the scattering volume at an angle which is greater then AOB, and the measured wind component is at an angle defined by the bisector of the tangent to the curved path at 0′ and the line A 0′. Thus, the vector which is calculated from the observed Doppler shift will have the direction of $\overline{R}'$ and a length determined by the real wind $\overline{V}'$. If refraction is not accounted for when this component is used to derive the horizontal wind, the observed value $\overline{R}'$ will be erroneously directed along $\overline{R}$ and the derived horizontal wind will have the value $\overline{V}$, an overestimate of the real value $\overline{V}'$. If either the direction of propagation or the direction of wind shear is reversed the opposite effect will occur and the real wind will be underestimated.

To test the feasibility of bistatic Doppler wind measurements, the following experiment was conducted. Two acoustic-echo sounders were located on a broad flat mesa north of Boulder, Colorado. The two sounders were electronically independent except for timing functions which controlled the pulse repetition rates, pulse lengths and gate times. Table 1 lists the sounder parameters used during the experiment.

The general layout of the antennas and meteorological tower is shown in Fig. 4. The two antennas were positioned along a line (azimuth 108°) 80 meters apart with sounder A fixed and pointing vertically and sounder B gimbal mounted so its angle of tilt could be varied to receive the forward scatter at different elevations along the beam produced by A. For the purposes of this experiment three tilt angles (measured from horizontal), were selected. Table 2 lists the scatter angles, angle of the wind component measured, the equation for the magnitude of the measured wind component and the altitude of the measurement for the three tilt angles selected.

A form of ground truth for the Doppler measured winds was provided by a Boundary Layer Profiler (BLP) designed and operated by the Field Facilities section of the National Center for Atmospheric Research (NCAR). The BLP system consists of a tethered balloon which can be positioned at any height up to about 700 m where the attached sensors measure wind speed, temperature, humidity and pressure. Unfortunately the BLP does not provide wind direction, a critical factor as only one component of the horizontal wind (108°/288°) could be determined by two antennas. As a partial solution to this problem, the wind direction measured on top of the 15 meter meteorological tower (see Fig. 4) was used to estimate the wind direction at the balloon altitude, a less than satisfactory arrangement considering the possible magnitude of directional shear between 15 meters and the three heights at which measurements were made (see Table 2).

---

*Use of the term radial vector is not strictly accurate in the bistatic context, however, since both monostatic (which does measure a true radial vector) and bistatic systems are discussed the term is applied to both, and always means the component of the wind which is measured by the Doppler shift.

Experimental procedures consisted of fixing the angle of tilt for antenna B at one of the predetermined angles, θ_r, and pulsing one sounder at a carrier frequency of 2750 Hz while receiving the forward scatter at the other antenna for periods ranging from 10 to 15 min. During this time the BLP was tethered at the level of the beam intersection, but not directly in the beam as the acoustic echoes from a helium filled balloon are strong enough to obliterate all other information. Additional runs were made with both echo sounders operating in the monostatic mode and aimed at a common volume in order to assess the difference between monostatic and bistatic operation. When both systems were operated in the monostatic mode it was necessary to separate the carrier frequencies to prevent contamination of the individual records by forward scatter from the other beam.

While schemes for real-time determination of the acoustic Doppler shift are in the development stage, none were operational at the time of this experiment and it was necessary to record the signals for later computer analysis. This processing resulted in frequency spectrum plots for the carrier and echo at gated times corresponding to the distance between the antennas and the scattering volume. The peak of the two spectra, each determined as the average of 30 spectra for 30 successive pulses (one minute), was then compared to determine the Doppler shift. For a more detailed account of the analysis procedure see Beran, Little and Willmarth (1971).

Wind speed during the experiment ranged from calm to 10 m/s and the direction was highly variable. A total of eight runs were completed, two of which were made with both systems operating monostatically and the remainder with a dual bistatic-monostatic configuration. Table 3 lists the time of each run, the frequencies used, and the configuration of the two echo sounders. The column headed "tilt" indicates the angle, measured from horizontal, at which the antennas were aimed and the transmitter and receiver columns indicate whether the system was transmitting or receiving the signal. Where both columns are checked, the system was operated in the monostatic mode.

Two radial wind components in the plane formed by the antenna beams were measured in each of the configurations. During monostatic operation the vertical component was derived from sounder A while sounder B provided a component directed along its beam. In the bistatic mode where one sounder was active and receiving its own backscatter, and the second was receiving the forward scatter from the first, one component was directed along the beam receiving backscatter and the other along the bisector of the angle formed by the two beams. In each case the two components were resolved into the total wind vector in the plane of the sounders (108° Azimuth) and then the horizontal component in the same plane was derived from the total wind vector (see Fig. 5).

As anticipated, the results of the experiment support using the bistatic configuration in favor of a monostatic sounder with a tilted antenna for continuous monitoring of the horizontal wind. This is true despite the advantage of smaller angles between the radial component and the horizontal for a monostatic system having the same tilt as a bistatic. The intermittency of strong echoes, characteristic of monostatic operation, would severely limit its use in an operational sense. For the two monostatic runs only one had consistently strong enough echoes to derive the Doppler winds. The thermal structure (weak erratic thermal plumes) during Run 1 was such that little confidence could be placed in the averaged spectra and for this reason it was eliminated from the final analysis. Run 4, on the other hand, was made during a period characterized by stronger and more persistent thermal echoes, and the majority of the spectra on this run were easily interpreted.

Before further discussion of the individual runs, let us turn our attention to the overall comparison between the Doppler measured winds and those measured by the BLP system. This comparison is represented in Fig. 6 as a scatter diagram of the winds measured by both systems. The derived value of horizontal wind based on the Doppler shifts (see Fig. 5) is plotted against the 108°/288° component of the horizontal wind measured by the BLP, both for one minute averages. Positive winds are from 288° and negative from 108° azimuth. Data points for individual runs are plotted with different symbols defined in the figure. The correlation coefficient for the total of 39 points is .94 and the regression coefficient for the line of best fit is .67 with 95% confidence limits having slopes of .58 and .75. Considering the possibilities for error in determining the direction of the wind measured by the BLP, the high correlation coefficient is encouraging.

A second notable feature of the scatter diagram in Fig. 6 is the tendency for the Doppler measurements to be overestimates of the wind (.67 regression coefficient as opposed to 1 for a perfect fit). As suggested earlier, this tendency to overestimate might be partially explained by the effect of refractive index gradient along the tilted beam. Calibration error or incorrect angles between the wind vane and the antenna axis should be considered as possible sources of the consistent displacement of the data from a 45° slope.

Separation of the data into individual runs (see Fig. 7) helps to shed light on possible sources of error. The scatter diagram for Run 4, the only monostatic run analyzed, shows a cluster of points between +1 and +2 m/s, all lying very near the line of perfect fit (dashed line) with two values in the negative quadrant which deviate markedly from the best fit line. Examination of the records indicate that the points in the negative quadrant correspond to times when the echo strength may have been too weak to derive a good frequency spectrum. This in addition to the fact that the wind was changing direction at this time,might explain the large deviation of the two negative winds on Run 4. The good fit of the cluster of points in the positive quadrant does suggest that when strong signals are assured,the monostatic mode of operation can provide good results.

During Run 5 the tilted sounder B was active and the vertical system A was passive (see Table 3). In this configuration,the two radial components were directed at 45° and 67.5° respectively. For the remaining bistatic runs (6, 7 and 8),the role of the sounders was reversed with A operating in the active mode and B in the passive, providing radial components in the vertical and at an angle along the bisector of the two beams (as shown in Fig. 5).

While the slope of the linear regression line through the data points from Run 5 is close to 1 the scatter of the points is quite large. A possible explanation for the scatter might be the light and highly variable wind which made it difficult to extract the BLP component along the axis of the antennas. The wind velocity increased during the last three Runs (6, 7, 8) and despite a reversal of direction, which occurred during Run 7, the scatter of points is much less than was observed earlier.

It is interesting to note that all of the bistatic runs (5, 6, 7 and 8) showed a tendency for the Doppler winds to be an overestimate of the wind measured by the BLP. If we assume that the wind speed increased with height for each of these runs, in such a way as to produce a refractive index gradient along the sloping beam, it is possible to check the sense of the error that might be introduced by bending of the beam (see Fig. 3). This simplified approach indicates that Run 5, 8 and the negative portion of 7 would all have been overestimates of the real wind. Run 6 and the positive portion of Run 7 should be underestimates of the real wind. Elimination of Run 5 from this analysis can be justified by the observation that the light and variable winds would have little if any shear. Much stronger shear was present during the last three runs (as indicated by the BLP winds and those recorded at 2 and 15 meters). If we now compare the slopes of the regression curves for the last 3 runs (slopes for Run 7 were calculated separately for the positive and negative sides of the distribution) we find .80 for Run 6 and .44 for the positive side of 7 opposed to .41 for Run 8 and .42 for the negative side of 7. The statistical significance of the difference on Run 7 is doubtful, however, Run 8 shows a much greater tendency than Run 6 for the Doppler winds to be overestimated. A possible explanation for this pattern might be that the effect of refractions has been superimposed on a constant error arising from any of several sources. While more data is clearly needed to confirm this speculation it does appear that refraction could be responsible for some of the observed error.

This experiment was only part of a continuing program to develop acoustic Doppler wind measuring techniques to their full potential and as such its aims were necessarily limited. To reiterate, the purpose of the work reported on here was to demonstrate the feasibility of using a bistatic approach to measure the acoustic Doppler shift. While achieving this goal,the authors have also speculated on the possible reasons for less than perfect agreement between the Doppler measured winds and the ground truth, keeping in mind that providing verification for this kind of measurement is extremely difficult. The results are of benefit in highlighting areas where more study and careful measurements are required and will serve as a basis for the continued development of an acoustic Doppler wind measuring system.

To summarize, the following conclusions and recommendations can be made:

1. The bistatic approach to Doppler wind measurements is feasible.

2. For an operational system, the bistatic approach has the advantage over a tilted monostatic system in that continually strong echoes are more likely and can be received from greater altitude. For special applications where the presence of strong thermal echoes can be assumed, and for shorter ranges, a monostatic tilted beam might be used to advantage, because of the inherent smaller angle between the radial component being measured and the horizontal component of the wind.

3. Refraction of the sloping antenna beam may produce an error in the resolved horizontal wind component. In an operational system employing scanning antennas it should not be difficult to use iteration techniques to calculate the wind shear for use in correcting this effect.

4. Because of the relatively low number of data points used in this analysis and the wide variety of possible errors, the significance of the apparent constant overestimate on the bistatic Doppler runs is questionable. When a third sounder is introduced and the total horizontal wind can be measured and its magnitude compared directly with that measured by the BLP, the need for resolving the total ground truth wind into components based on rather tenuous direction measurements will be less important.

5. The close spacing of the antennas (80 m) during this exercise made it impossible to determine the maximum altitude at which the horizontal wind might be measured. The 60° tilt angle does; however, appear to be approaching the maximum usable limit. The trade off between tilt angle, the angle of the measured component to the horizontal and the varying intensity of returns at different scatter angles in order to achieve best results at a given range of altitudes must be based on the requirements for each application and an optimum arrangement for all cases cannot be predicted. The signal strength at a tilt of 60° (an altitude of 139 meters) during this experiment was more than ample for determining the frequency spectra, and, for the equipment used, the winds at altitudes of at least 500 meters should be within reach.

ACKNOWLEDGMENTS

The authors wish to express their sincere thanks to Dr. H. Baynton, Mr. R. McBeth and Mr. D. Call of NCAR for providing and operating the BLP system. The invaluable aid provided during the preparation of this experiment, and in data reduction by Dr. F. Hall, Mr. J. Wescott, Lt. W. Neff and Mr. R. Dickason are gratefully acknowledged. Special thanks are also due Mr. H. Ottersten and Dr. S. Clifford for their critical review and suggested improvements to the manuscript.

REFERENCES

(1) Batchelor, G. K. (1957) Wave scattering due to turbulence, Symp. on Naval Hydrodynamics, F. S. Sherman, ed., NAS-NRC Publ. 515, pp. 409-430.

(2) Beran, D. W., C. G. Little and B. C. Willmarth (1971), Acoustic doppler measurements of vertical velocities in the atmosphere, Nature, Vol 230, pp. 160-162.

(3) Ford, G. W. and W. C. Meecham (1960), Scattering of sound by isotropic turbulence of large Reynolds number, J. Acoust. Soc. Am., Vol 32, pp. 1668-1672.

(4) Kallistratova, M. A. (1961), Experimental investigation of sound wave scattering in the atmosphere, Trudy Inst. Fiz. Atmos., Atmos Turbulentnost, no. 4, pp. 203-256.

(5) Kraichnan, R. H. (1953), The scattering of sound in a turbulent medium, J. Acoust. Soc. Am., Vol 25, pp. 1096-1104.

(6) Lighthill, M. J. (1953), On the energy scattered from the interaction of turbulence with sound or shock waves. Proc. Cambridge Phil. Soc., Vol 49, pp. 531-555.

(7) Monin, A. S. (1962), Characteristics of the scattering of sound in a turbulent atmosphere. Akust. Zh., Vol 7, pp. 457-461 (Sov. Phys. Acoustics) Vol 7, pp. 370-373.

(8) Tatarski, V. I. (1961), Wave propagation in a turbulent medium (R. A. Silverman, transl.) New York: McGraw-Hill.

Acoustic Echo Sounder Parameters Used for Bistatic Doppler Experiment

Peak Power	7.5 watts (acoustic)
Pulse Width	100 ms
Pulse Repetition Frequency	2 $\sec^{-1}$
Maximum Range	340 meters
Carrier Frequencies	2750 and 3750 Hz
Antenna Diameters	122 cm
Antenna Beam Width	± 2° to 3 db points
Beam Directions	vertical, 30°, 45° and 60°
Receiver Bandwidth	100 Hz (vertical antenna) 1000 Hz (tilted antenna)
System Noise Level in 100 Hz Bandwidth	$\sim 10^{-18}$ watts
Scattering Volume at 100 Meter Altitude	intersection of two cylinders ~7 meters diameter

TABLE II

Parameters needed for calculating the Doppler wind component for a bistatic system with a fixed vertically pointing antenna and a second antenna scanning at angle θ_r

Tilt Angle	Scatter Angle	Angle of Radial Component to Horizontal	Magnitude of Radial Component	Height of Observation Above Sounder B
θ_r	θ	β_h	v_r (m/s)	m
30°	120°	60°	$=196\left[\frac{\Delta f}{f_o}\right]$	46
45°	135°	$67^\circ 30'$	$=184\left[\frac{\Delta f}{f_o}\right]$	80
60°	150°	75°	$=176\left[\frac{\Delta f}{f_o}\right]$	139

TABLE III

LIST OF RUNS AND THE ECHO SOUNDER CONFIGURATIONS
USED FOR DOPPLER EXPERIMENT CONDUCTED ON MARCH 1971

RUN	TIME (MST)	SOUNDER (See Fig. 4)	FREQ (Hz)	TILT (θr) (deg)	TRANS	REC
1	0923	A	2750	90	X	X
	0933	B	3750	30	X	X
2*	0943	A	2750	90		X
	0953	B	2750	30	X	X
3*	1001	A	2750	90	X	X
	1012	B	2750	30		X
4	1017	A	2750	90	X	X
	1028	B	3750	45	X	X
5	1031	A	2750	90		X
	1041	B	2750	45	X	X
6	1044	A	2750	90	X	X
	1059	B	2750	45		X
7	1100	A	2750	90	X	X
	1111	B	2750	30		X
8	1113	A	2750	90	X	X
	1123	B	2750	60		X

*Equipment malfunctions on Runs 2 and 3 rendered the data at these times of questionable value and they were eliminated from the final analysis.

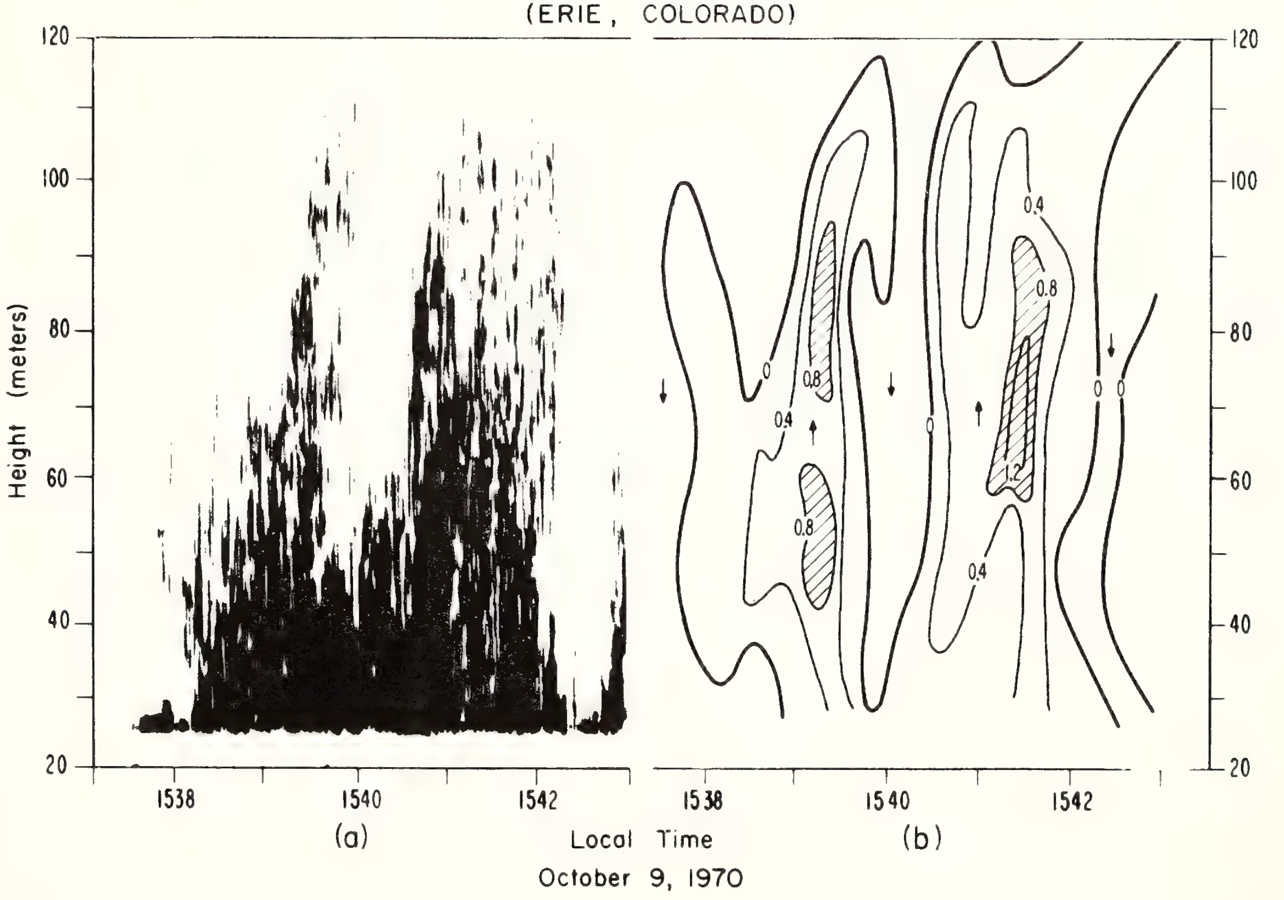

FIGURE 1 -Acoustic echoes (left) and Doppler derived vertical velocity field during thermal plume activity. Contour interval is 0.4 ms^{-1}; regions of vertical velocity > 0.8 ms^{-1} are shaded; arrows indicate direction of vertical component.

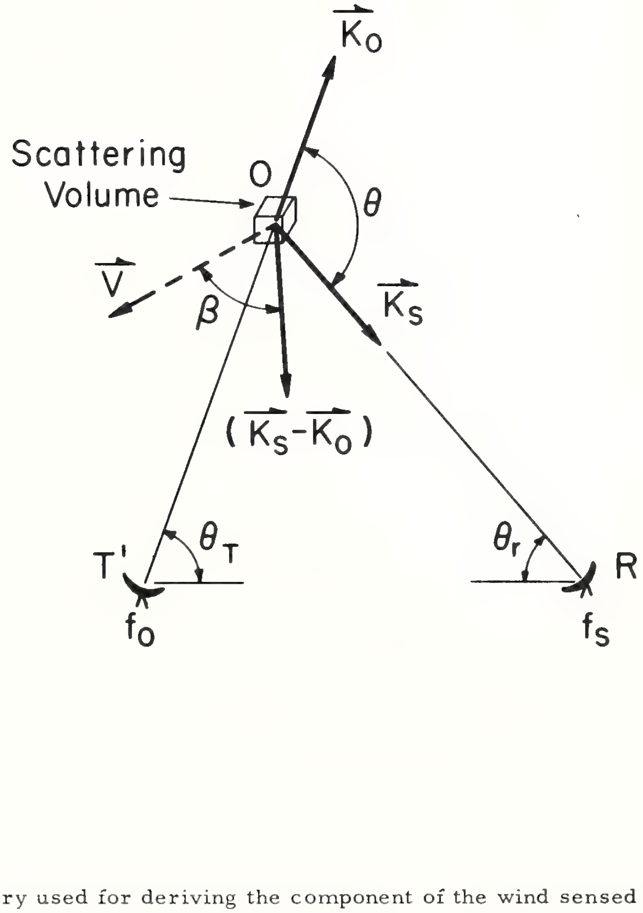

FIGURE 2 - Geometry used for deriving the component of the wind sensed by a bistatic acoustic sounder.

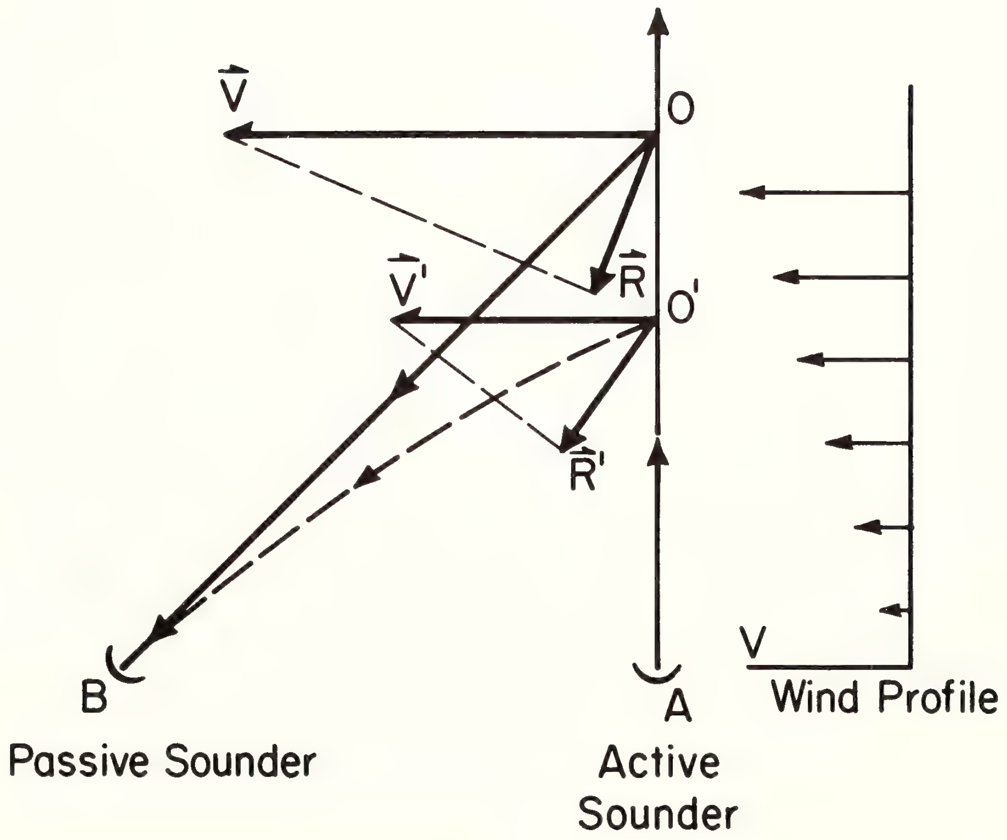

FIGURE 3 - Geometry demonstrating the effect of refraction on a sloping acoustic beam. For the case shown the Doppler derived horizontal wind would be an overestimate.

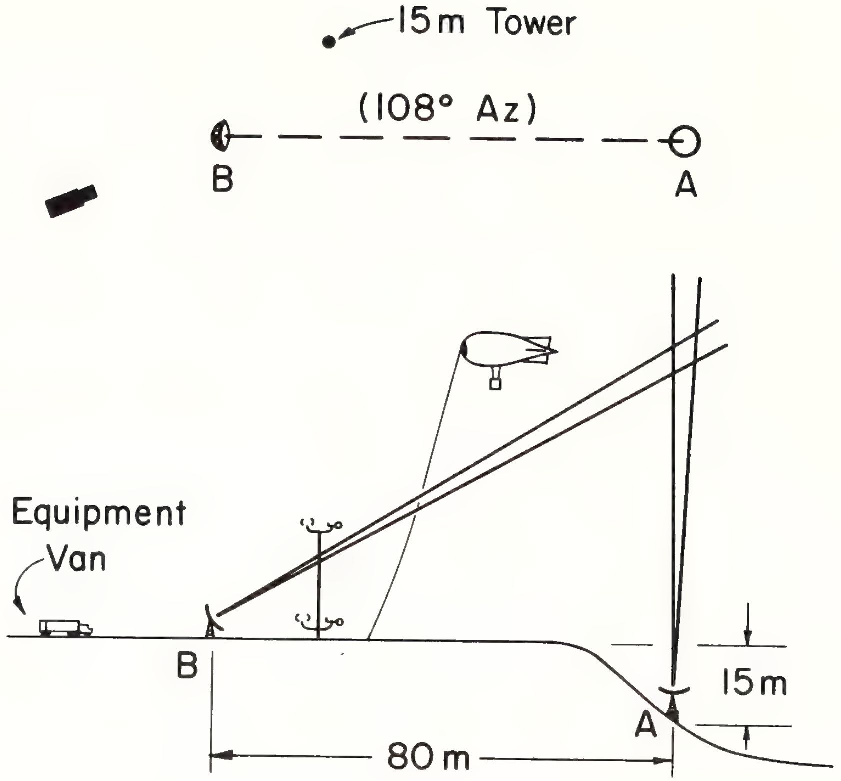

FIGURE 4 - Plan and elevation view of the site layout.

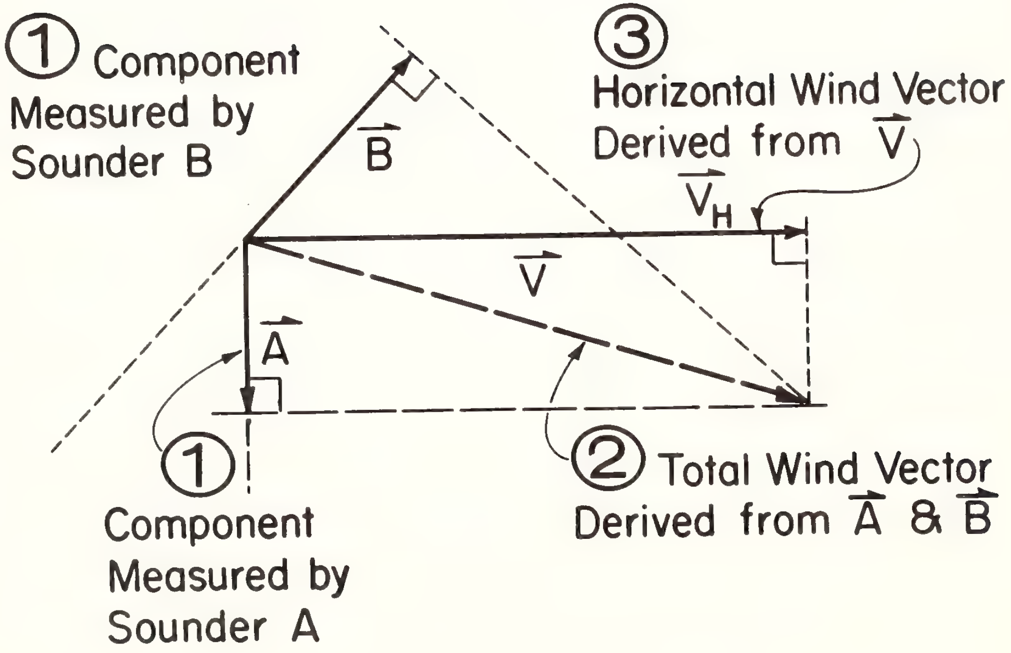
① Component Measured by Sounder B
$\vec{B}$
③ Horizontal Wind Vector Derived from $\vec{V}$
$\vec{V}_H$
$\vec{V}$
$\vec{A}$
① Component Measured by Sounder A
② Total Wind Vector Derived from $\vec{A}$ & $\vec{B}$

FIGURE 5 - Diagram of the steps involved in deriving the horizontal wind vector $\vec{V}_H$ from two components measured by the bistatic-monostatic sounder system. The total wind vector is the component in the plane of the two antenna beams.

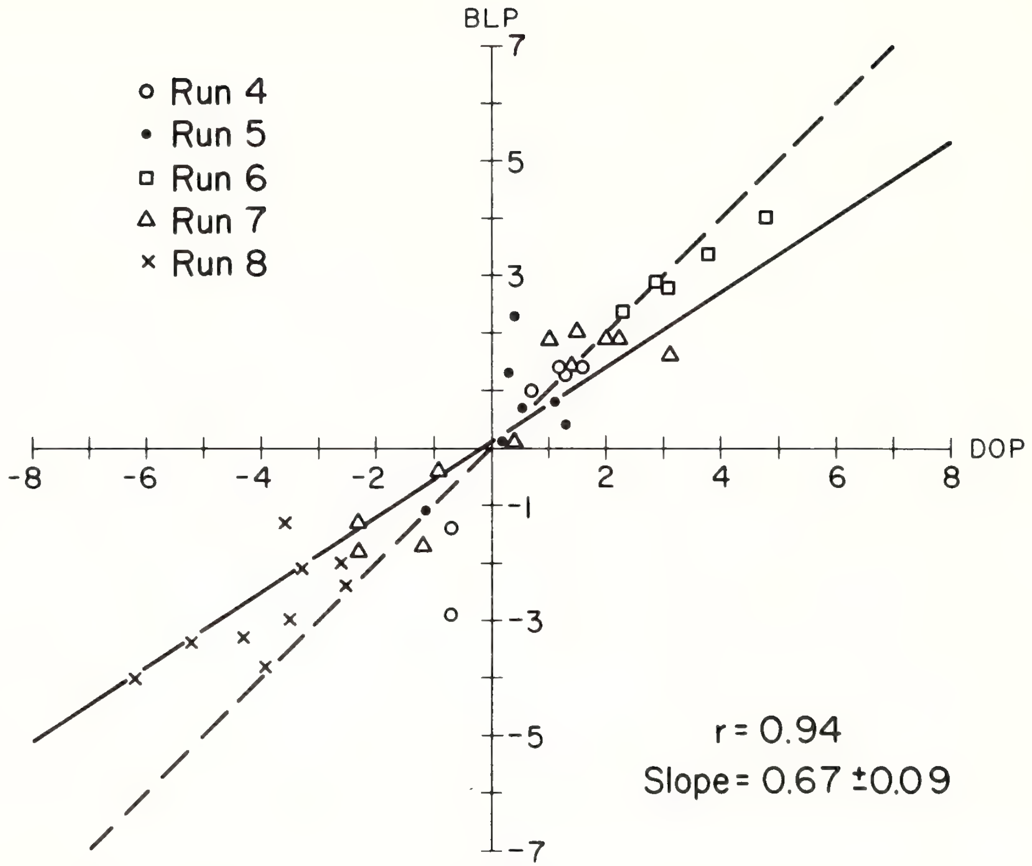

FIGURE 6 - Scatter diagram of all measured winds (1 min averages) for the 5 runs shown. The Boundary Layer Profile Winds are plotted on the BLP axis and the Doppler winds on the DOP axis.

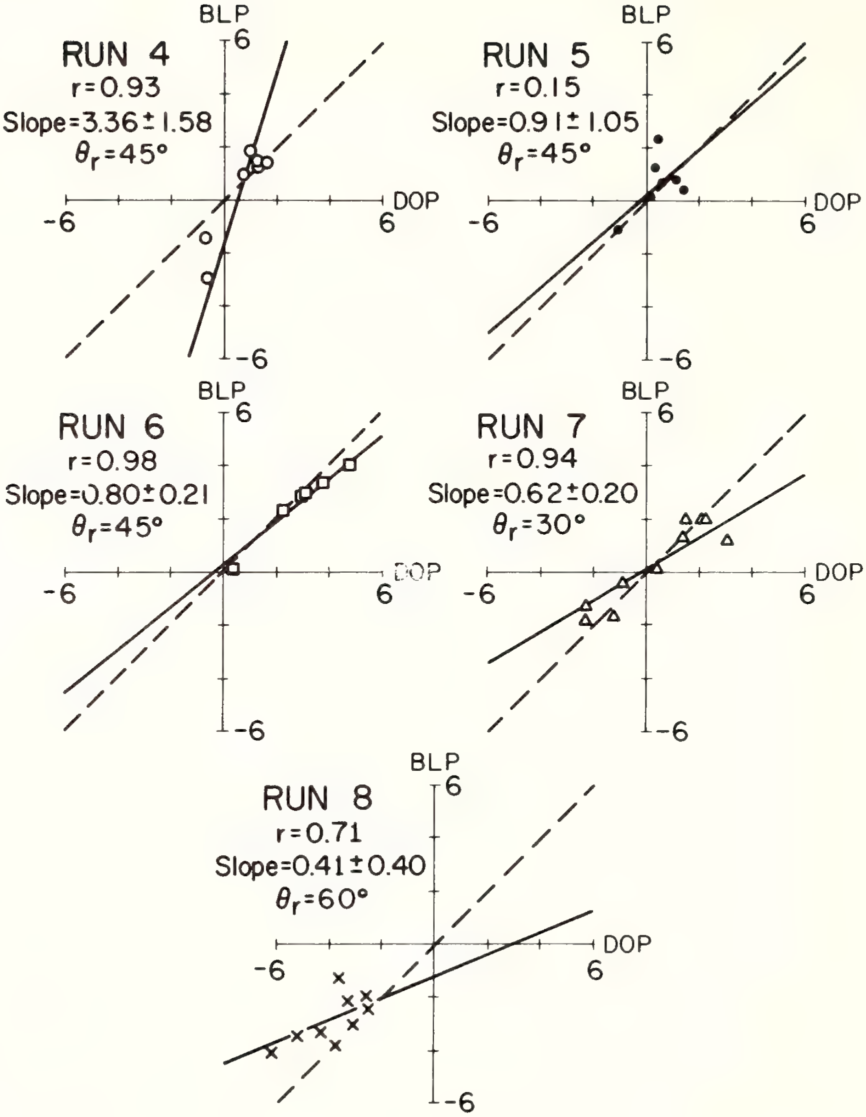

FIGURE 7 - Individual scatter diagrams for the winds measured on each of the 5 runs shown in Fig 6. The Boundary Layer Profile Winds are plotted on the BLP axis and the Doppler winds on the DOP axis. Correlation coefficient=r; slope of linear regression curve = slope. Antenna tilt = θ_r.

Reprinted from Proceedings of the 7th International Symposium on Remote Sensing of Environment 1, No. 10259-1-X, May 17-21, 1971, 1715-1732, 1971.

Sponsored by

Center for Remote Sensing Information and Analysis
Willow Run Laboratories, Institute of Science and Technology
The University of Michigan

Water Quality Office
Environmental Protection Agency

Office of Space Science and Applications
National Aeronautics and Space Administration

Federal Highway Administration
U. S. Department of Transportation

U. S. Geological Survey
U. S. Department of Interior

Air Force Cambridge Research Laboratories
Air Force Systems Command
U. S. Air Force

Agricultural Research Service
U. S. Department of Agriculture

Infrared and Optics Laboratory
Willow Run Laboratories
INSTITUTE OF SCIENCE AND TECHNOLOGY
THE UNIVERSITY OF MICHIGAN
Ann Arbor, Michigan

ACOUSTIC ECHO SOUNDING OF ATMOSPHERIC THERMAL AND WIND STRUCTURE

F. F. Hall, Jr., J. W. Wescott and W. R. Simmons*

Wave Propagation Laboratory
NOAA Environmental Research Laboratories
Boulder, Colorado

ABSTRACT

The scatter of acoustic waves in the atmosphere is caused by variability in the temperature and wind structure and to a lesser extent by humidity fluctuations. Frequently the air trapped under nocturnal radiation inversions exhibits considerable thermal structure, providing strong acoustic echoes to a sounding system operating in the monostatic mode. The breakup dynamics of temperature inversions can be studied by monitoring the interaction of thermal plumes rising from the earth's surface. The potential usefulness of acoustic sounders in studying air pollution situations suggests that the ability to operate a sounder in urban and industrial environments be studied. It is concluded that sounders can be operated in most environments except those close to airports without being severely affected by environmental noise and without contributing to noise pollution. The operation of the present NOAA equipment is described and an analysis of thermal plume rise as a function of local meteorological conditions is given.

---

*Present address: Interactive Technology, Inc., Santa Clara, Calif.

INTRODUCTION

This paper is a progress report on the Atmospherics Acoustics Program at the Wave Propagation Laboratory of NOAA/ERL. The program has been operational for almost two years and is concerned primarily with investigating active acoustic echo sounding in the atmosphere. At the 6th International Symposium on Remote Sensing of the Environment, McAllister and Pollard[1] described the fundamentals of acoustic echo sounding and showed that interesting atmospheric structures could be studied through facsimile recordings of echoes from monostatic or bistatic scattering. Based on the earlier tests of McAllister[2] and the analysis by Little[3] of the potential for boundary layer studies with acoustics, the NOAA program was initiated in the middle of 1969.

We are interested primarily in exploiting the acoustic echo sounder to better understand atmospheric boundary layer phenomena. Because of the capability of sounders to monitor the structure of temperature inversions it is also relevant to inquire if such equipment will be useful in air pollution studies. If the analysis of sounder records provides a better understanding of inversion formation and breakup dynamics, it may be possible to predict more accurately the height and strength of inversions. Operation of sounders in populated areas could be useful for a routine determination of inversion heights to permit a continuous estimation of the volume of atmosphere available for the dispersion of pollutants.

In this paper we will consider first the NOAA progress in sounder system design. We have progressed from an initial Mark I System to a more flexible Mark II design, and its operation is explained. Then studies of the feasibility of sounder operation in urban and industrial environments will be described. Finally some new data on the characteristics of thermal plumes as determined through the use of the echo sounder will be presented.

ECHO SOUNDER DESIGN

The NOAA Mark II Echo Sounder is a second generation system embodying many worthwhile engineering improvements while carrying on the general design philosophy of the Mark I Sounder.[4] As much of the system as possible was built with the laboratory quality, commercially available electronic instruments.

The operation of the equipment can be followed from the block diagram, Figure 1. All timing functions are regulated by a crystal stabilized clock in the time code generator. Timing logic consists of a configuration of diode gates which pass a pulse only when a particular combination of zero and plus binary coded decimal levels occur that correspond to a desired pulse repetition frequency (PRF). Timing logic gates are currently provided for PRF's of 0.5, 0.2, 0.1 Hz corresponding to maximum echo ranges of approximately 330, 825, and 1650 m.

The PRF signal is used to trigger a digital timing generator which in turn passes a tone burst of carrier frequency from the receiver BFO, generates a gate pulse coincident with the tone burst, and generates two additional pulses having start and stop times that may be delayed independently by desired amounts from the start of the tone burst. Tone burst durations ranging from 10 milliseconds to 1 second are normally used with the Mark II sounder depending upon whether maximum resolution, or maximum range is desired.

As Figure 1 shows, the tone burst from the timing generator is gated a second time as it passes through a transmit gate on the way to the transmitting power amplifier. The transmit gate is an FET solid-state switch with ON and OFF modes controlled by the gate pulse from the timing generator. The need for redundant gating of the tone burst is necessary because the digital timing generator provides only 60 db of carrier frequency attenuation between gate pulses. The resulting carrier leakthrough was enough to create a very low level "false echo" signal during the echo sounder receive mode.

The tone burst from the transmit gate is applied to the input of the power amplifier at a level of 1 volt rms. The gain of the power amplifier is adjusted to deliver 40 watts rms of electrical power through a pair of back-to-back diodes to a 16-ohm acoustic transducer for the duration of the tone burst. The transducer is coupled acoustically to a reflector-horn antenna. The overall transmitting efficiency of the transducer-antenna configuration is about 20% so that the antenna radiates about 8 watts rms of acoustic energy into the atmosphere during the tone burst.

Between tone bursts the power amplifier produces less than a millivolt of hum and instrument noise. This noise is nonetheless more than an order of magnitude larger than some of the voltages produced by weak atmospheric echoes. Back-to-back silicon diodes were therefore placed between the power amplifier and the acoustic transducer. These diodes readily conduct large-amplitude transmit tone bursts, but are virtual open circuits to signals of less than 300 millivolts rms. In order for the diode isolation circuit to work reliably, however, it is essential that the power amplifier have a well regulated power supply. Otherwide power line surges will produce voltage fluctuations at the amplifier output large enough to pass through the diodes, and receiver overload will occur.

During transmission it is necessary to isolate and protect the extremely sensitive receiver circuits of the echo sounder from overload and possible damage. This is done in three stages, and the circuit elements involved (mostly silicon diodes as shown in Figure 1) perform a task equivalent to that of a radar 'T-R" device. The first stage is a set of back-to-back diodes in series with resistor R1. The second stage is a diode bridge shorting gate. The action of this gate is controlled by the polarities of a pair of equal but opposite receiver gate pulses. When the polarities of these pulses are as shown in Figure 1, all diodes of the bridge conduct, and the receiver preamplifier input terminal is thereby clamped to ground. When the polarities of the pulses are reversed, as they are throughout the receiver ON time, all diodes of the bridge are biased beyond cutoff, and the gate has no effect on the receiver circuit.

The pulses that control the action of the diode bridge shorting gate are obtained from the gate pulse amplifier. The start time of these pulses is chosen to delay the turn on of receiver circuits until the ringing or reverberation in the acoustic antenna caused by the powerful transmit tone burst has decayed to a negligible level. This is about 100 msec from the end of the tone burst for the fiberglass horn-reflector antenna now in use, and is equivalent to about the first 16 m of echo range. It should be possible to reduce the reverberation time and subsequent loss of close-range echoes by future improvements in acoustic antenna design. The stop time of the pulses from the gate pulse amplifier is set to turn off the receiver circuits a few msec before the start of the next transmit tone burst. This is done as a precaution to insure against possible damage to the receiver circuits by the initial transient of the transmit signal.

During reception of echoes the gating actions described earlier enable the acoustic transducer to act as a microphone which is transformer coupled to a variable-gain preamplifier as shown in Figure 1. The coupling transformer has a 30 to 1 step-up turns rationwhich serves to increase the irreducible Johnson noise voltage of the microphone to a level that substantially exceeds the input self-noise of the preamplifier.

The preamplifier is located remotely at the antenna-transducer site in order to increase echo signal levels to about 1 volt rms before transmission through over 100 m of cable to the rest of the receiver system. For this reason the preamplifier includes a calibrated, remote gain control subsystem and a balanced, low-impedance, differential output stage. Preamplifier gain may be varied from 60 db to 0 db by varying a dc gain control signal from 0 to +5 volts. The differential output signal of the preamplifier is delivered through the long, multiconductor cable to the differential amplifier of the receiver system. This amplifier converts the balanced and therefore relatively hum-free signal from the preamplifier to a single-ended signal for subsequent passage through an 800 Hz highpass filter. The purpose of the highpass filter is to eliminate strong, low-frequency wind noise, man-made noise and other low-frequency components of background noise that might otherwise overload subsequent stages of the receiver system.

The output of the highpass filter is applied to the receiver gate. This is a redundant gate that operates in unison with the previously described diode bridge shorting gate. Both gates are controlled by the output pulse from the receiver gate logic section. The purpose of the receiver gate is to block a small leakthrough signal that develops during the transmit tone burst. The leakthrough path is in the multi-conductor cable that interconnects the remotely located antenna, transducer and preamplifier sections of Figure 1 to the rest of the sounder system. The cable consists of separately shielded pairs of conductors to minimize cross-coupling effects among transmit, receiver and gate control signals. Since up to 300 m of cable may be used, however, there is still enough cross-coupling to warrant the use of the redundant receiver gate.

The echo signal from the receiver gate is applied to one of the two inputs of the 1/R analog multiplier. The other input to the multiplier is a linear ramp signal generated by the gain ramp integrator. The output of the 1/R analog multiplier at any time is simply one tenth the product of the applied echo signal and the instantaneous amplitude of the linear ramp. The linear ramp from the integrator always starts at zero volts dc and grows with time at the rate of 1 volt/sec. This causes the multiplier to act as an echo signal amplifier the gain of which periodically starts at zero and increases linearly with time at the rate of 0.1/sec. By the end of a 10 second echo receiving period, for example, the gain of the 1/R analog multiplier has been swept from zero to unity. This type of gain sweep compensates for the spherical divergence or spreading loss of acoustic echoes as they are received from progressively longer ranges. The gain is varied inversely with range (1/R) rather than as the inverse square of range ($1/R^2$) because the output signal of the receiving transducer is proportional to acoustic pressure rather than acoustic power.

The range-compensated echo signal from the 1/R analog multiplier is applied to the input of the tuned receiver. The receiver is constructed so that the center of its pass band automatically coincides with the frequency of an integral BFO that is the source of carrier frequency for the Mark II sounder. The receiver tuning is thus locked to the mean frequency of the echo signal. Receiver bandwidth is adjustable, and normally is set to accommodate just the major sidebands of the transmitted tone burst in order to achieve an optimum S/N with minimal loss of resolution. For example, a bandwidth of 100 Hz generally has been used for tone bursts lasting 20 msec, whereas a bandwidth of 10 Hz has been used for tone bursts of 200 msec and longer.

The tuned receiver has two outputs. One of these is an amplified replica of the echo signal as bandwidth-limited by the receiver tuned circuits. This is the type of signal that is used for determining Doppler shifts of frequency between a transmitted tone burst and its received echo. It is planned to digitize this signal (and others) before recording in order (1) to eliminate frequency errors associated with analog tape recorder wow and flutter, and (2) to shorten the number of steps required for subsequent digital data analysis. The digital recording scheme, though not yet completed, is shown connected to the echo signal output of the tuned receiver on Figure 1. The other output of the tuned receiver is the detected level of the echo signal. This is a fluctuating dc signal the amplitude of which is proportional to the acoustic pressure of echoes received after correction for spherical divergence. This signal is displayed as functions of range and time of day by means of the facsimile recorder.

The acoustic antenna is an important component of the system since it serves to collimate the transmitted power into a narrow beam in the transmit mode, and serve as a highly directional microphone in the receive mode. The NOAA sounder uses a cone paraboloid antenna originally designed for microwave use. The electro-dynamic transducer is bolted to the cone section in place of the microwave conical wave guide. The only other modification of the antenna found desirable is to coat it with an acoustical dampening material to limit reverberation time after the transmitting pulse is turned off. The antenna is shown in Figure 2. Other types of antennas which have been used in acoustic sounders include arrays of electro-dynamic speakers, and transducers mounted at the focus of parabolic dishes.

A desirable feature of any antenna is the limitation of side lobes so that unwanted acoustic power is not directed elsewhere and so that noise in the environment surrounding the sounder does not effect sounder performance. The measured sidelobe characteristics of the NOAA cone paraboloid antenna are shown in Figure 3 for different acoustic frequencies. It will be seen that at a frequency of 1 kHz, the half power beam width is about 16°, whereas at 5 kHz the main beam is measured to be only 3 or 4 degrees wide to the half power point. Note also that the 90° sidelobe is 38 db below the main beam at 1 kHz and nearly 50 db below the main beam at 5 kHz.

One easy way to improve sidelobe rejection is to surround the antenna with an absorbing cuff. For a vertically pointed antenna it has been found that an open cylinder of hay bales is an effective absorber. If the cylinder aperture is several times that of the antenna and the height several times the antenna aperture, 20-30 db additional 90° sidelobe attenuation is obtained. An analysis of this absorbing cuff has been performed by Strand[5] and the theoretical improvement closely checks with that experimentally measured in the field. Further improvements should be possible with internal attenuators in the horn to achieve the affect of a tapered feed in the microwave case. The present antenna acts nearly like a perfect piston source, but by decreasing the amplitude of the pressure fluctuations near the edge of the aperture, less energy will be diffracted at the edge, further improving the sidelobe rejection.

OPERATION OF SOUNDERS IN URBAN OR INDUSTRIAL ENVIRONMENTS

Our interest in improving the antenna characteristics is strongly motivated by the desire to utilize the acoustic echo sounder for studying boundary layer meteorology of interest in urban air pollution situations. While the unshielded antenna will be entirely adequate to achieve performance limited only by the Johnson noise from the ohmic resistance in the transducer in a quiet rural environment, the background noise in typical urban or industrial environments will not be so easy to live with. The environmental ambient noise data used to study this problem were obtained from noise surveys found in the literature. Table 1 lists the locations and conditions under which the surveys were taken, the location numbers that will be referenced in later figures, and a reference to the publications from which the data were taken.

Although the surveys considered here were made in specific locations, they represent a rather complete cross-section of the types of populated areas into which the acoustic echo sounder might be placed. Consequently, the noise data taken from these surveys provide a representative basis for predicting the interaction of the echo sounder with its potential environment. The analysis results will be indicative of what can be expected in any future application.

The data published in each survey were in the form of sound pressure levels in db (referred to the threshold of hearing or 0.0002 dynes/cm^2) for octave bands of the audible spectrum, usually up to 10,000 Hz. Many of the surveys gave more than one sound pressure level in db for each octave band. This spread of data is the result of statistical analyses, representing values above or below which a percentage of the levels in the octave band occurred. For the purposes of this study only the minimum and maximum values given were used. The former were used in the study to determine the effect of the acoustic-echo sounder on the inhabitants in the surrounding community and the latter were used for the study on the amount of environmental noise received by the acoustic echo sounder antenna. This purposefully conservative approach was used in order to provide a margin of safety against falsely optimistic conclusions on the feasibility of acoustic echo sounding in urban environments.

The acoustic antenna is a directional device, but because of diffraction it has sensitivity in directions other than the main lobe. As a result, the amount of environmental noise received by the echo sounder will depend not only on the noise levels existing at the antenna, but on the antenna sensitivity in the direction of incidence. The evaluation that follows will present a relation between the environmental noise and the antenna sidelobe suppression necessary for operating the acoustic echo sounder in the various environments.

Johnson noise or thermal noise generated in the transducer element of the acoustic antenna represents the absolute minimum of background noise that can be realized by the acoustic sounder[11]. This limiting level of noise provides the basis to which the environmental noise is referred, determining the signal-to-noise ratios. We define an ambient noise figure F as the ratio of environmental to Johnson noise powers,

$$F = 20 \log \frac{V_a(\upsilon,\theta)}{V_j} \quad . \tag{1}$$

Here $V_a(\upsilon, \theta)$ is the rms voltage developed at the acoustic sounder transducer terminals by the spectral component υ of the noise incident on the antenna from the direction θ. V_j is the thermal or Johnson noise voltage developed at the same terminals. The ambient noise figure F relates the environmental noise spectrum levels incident on the antenna to the sidelobe suppression required for satisfactory performance. Consequently when the signal to Johnson noise ratio is known, the amount of sidelobe suppression necessary for successful operation can be determined for each possible environment.

When the explicit expressions for $V_a(\upsilon, \theta)$ and V_j are substituted into (1), the noise figure can be written as

$$F - 20 \log \varepsilon(\upsilon, \theta) = 137 + SL_a + 20 \log \alpha(\upsilon) - 10 \log T \quad . \tag{2}$$

We define the quantity on the left of (2) as the noise suppression figure. The second term on the left is the antenna sidelobe attenuation factor relative to the main beam in decibels, and it is determined experimentally as discussed earlier. The value to be used will be determined by the direction of incidence of the noise on the antenna. SL_a is the sound pressure spectrum level (or noise level per hertz) in decibels of the incident environmental noise, T is the absolute temperature of the atmosphere, and $\alpha(\upsilon)$ is the antenna-transducer efficiency expressed in millivolts per dyne per square centimeter.

The important characteristic of the echo sounder that will determine acceptable ambient noise levels when operating in various environments will be the suppression of the environmental noise by the antenna sidelobes. A realistic estimate of the total range of the sidelobe suppression factors ($20 \log \varepsilon(\upsilon, \theta)$) required can be obtained by using a measured value for the antenna-transducer efficiency (α) in (2) and determining the sidelobe suppression necessary for each locality listed in Table 1. The value of $\alpha(\upsilon)$ that will be used in the discussion that follows is 25 millivolts per dyne per square centimeter; this value was measured at an operational frequency of 2000 Hz on the Wave Propagation Laboratory's Mark I acoustic echo sounder.

When the measured value for α is substituted into (1), the relation reduces to

$$F - 20 \log \varepsilon(\theta) = 80 + SL_a \text{ (Frequency = 2000 Hz)} \tag{3}$$

Implicit in this expression is an atmospheric temperature of 20°C.

Sound pressure spectrum levels (SL_a) for 2000 Hz were obtained from the noise surveys listed in Table 1. The surveys published their data in sound pressure levels (re. 0.0002 dynes cm^{-2}) in octave band widths. In order to determine the values of SL_a at 2000 Hz, it was necessary to reduce the published octave band sound pressure levels (SPL) to sound pressure spectrum levels (SL) at the octave band center frequency by

$$SL = SPL - 10 \log \Delta\upsilon_a \quad , \tag{4}$$

where $\Delta\upsilon_a$ is the octave band width in hertz. The values of SL_a existing at the considered frequencies of operation of the echo sounder were obtained by interpolation. Since the possible frequencies of operation being considered are 1, 2, 3, 4, and 5 kHz, the reducing-interpolation procedure was carried out for each frequency for the sake of future reference and the results are shown in Figure 4.

The localities listed in Table 1 have been arranged in Figure 4 by ascending order of SL_a at 1000 Hz. Each locality is identified with a circled location number along with a brief description of the conditions under which the survey was made and the numbers adjacent to the SL_a value bars refer to the frequency in kilohertz.

It must be emphasized that these values of the sound pressure spectrum levels (SL_a) were derived from the maximum levels of noise published in the surveys. They therefore represent the most stringent conditions that would be imposed on the acoustic echo sounder if it were required to operate in any of the listed or similar localities.

When the values for the environmental noise spectrum levels at 2000 Hz are substituted into (3), the results represent the difference between the ambient noise figure and the sidelobe suppression factor. These results are shown in Figure 5. The values shown in this level graph represent the noise suppression figure $F - 20 \log \varepsilon(\theta)$ (the difference between the ambient noise figure F and the sidelobe suppression) for each locality. Thus if the sidelobe suppression of the antenna is known, the amount of noise that will be received at each locality can be determined.

Conversely if the ambient noise figure has been determined from the expected signal-to-Johnson noise figure, the sidelobe suppression that will be necessary for operation in the various localities can be found. Based on analysis of typical noise levels of built up areas, Figure 5 shows that a desirable sidelobe attenuation varies from 70 db for the urban environment to 100 db for a noisy downtown location, if transducer Johnson noise is to be the fundamental limitation on systems performance.

Another consideration when operating the sounder in built up areas is the avoidance of noise pollution which might be aggravating to nearby inhabitants. We have analyzed the masking effect of background noise in typical urban and industrial environments. Based on the Fletcher[12] masking criterion, wherein sound levels comparable to the background noise are not readily discernible, we find that with 50-60 db sidelobe rejection, it should be possible to operate the present NOAA sounder, with an output of 8 acoustic watts, within several hundred meters of a suburban residence without being annoying. In the typical downtown noise levels, the sounder would be undetectable by persons within just a few meters, because of the masking noise from traffic, industrial activity, or building airconditioning noise. With proper attention to design detail then, it apperas that the sounder should be operable within most environments without being troubled by nominal environmental noise and without contributing to noise pollution from acoustic pulses.

ATMOSPHERIC STUDIES WITH A MONOSTATIC ACOUSTIC SOUNDER

The analytical study of the capabilities of acoustic echo sounding by Little[3] was the first step on which the NOAA Atmospheric Acoustics Program was based. In Little's paper it is shown that $\sigma(\theta)$, the acoustic power of wavelength λ scattered, per unit volume, per unit incident power is given by

$$\sigma(\theta) = 0.03\,\lambda^{-1/3} \cos^2\theta \left[\frac{C_v^2}{C^2} \cos^2\frac{\theta}{2} + 0.13\,\frac{C_T^2}{T^2} \right] \left(\sin\frac{\theta}{2} \right)^{-\frac{11}{3}} \qquad (5)$$

where θ is the scattering angle measured from the original incident direction, C_v^2 is the velocity structure parameter, C_T^2 is the thermal structure parameter, C is the velocity of sound, T is the mean absolute temperature of the atmosphere, and a Kolmogorov spectrum of turbulence is assumed. The values of the two atmospheric structure parameters are defined by

$$C_v^2 = \overline{\left[\frac{u(x) - u(x+r)}{r^{1/3}}\right]^2}\,, \quad C_T^2 = \overline{\left[\frac{T(x) - T(x+r)}{r^{1/3}}\right]^2} \qquad (6)$$

where u is the wind speed at x in the positive x direction and r is measured along the x axis. It is seen that the scattered acoustic power is only a weak function of acoustic wavelength varying as $\lambda^{-1/3}$, that direct backscatter for $\theta = \pi$ is a function of the thermal structure only, that because sound is a longitudinal vibration there is no scattering at $\pi/2$, and that there is strong scattering in the forward direction because of the final factor in equation (1). Obviously the equation is a simplification and cannot be applied for extremely small values of θ. More details and discussion of the scattering are given by Little[3].

With a co-located transmitter and receiver, the backscatter from the atmosphere is caused only by thermal structure. It is not surprising that considerable thermal structure is observed when the atmosphere is convectively unstable. The typical pattern observed on the facsimile recording showing backscattered intensity with height, as a function of time, is shown in Figure 6. This is the thermal plume structure, indicating the nonuniform rise of heated and thermally nonuniform parcels from the ground due to surface heating from solar radiation. That the upwelling air is characterized by variation in temperature is well known from investigations with fast response temperature sensors on aircraft, such as the study by Myrup[13]. Myrup also shows how the variation of C_T with height may be used to differentiate between different convective models. With a well calibrated acoustic sounder, and if the atmospheric acoustic attenuation is known, it is possible to measure C_T as a function of height and compare results with the Townsend convective theory, where a variation as the -0.6 power with height is predicted, or with similarity theory where a -0.33 power law is found. We are just to the stage where it should be possible in the near future to perform such studies. By comparing the acoustic sounder measurements of C_T with temperature differences recorded by fast response thermometers, spaced one-half of the acoustic wavelength apart, on a nearby micro-meteorological tower, we are now studying the accuracy of the acoustic measurements. Preliminary results indicate rather good agreement between the sounder and tower measurements of mean C_T, and even in the variance of this parameter. The great advantage in using the sounder over tower or aircraft measurements is that the entire spatial structure of the plume is visible, instead of one or several finite horizontal slices through the structure.

The sounder facsimile record clearly shows the vertical organization of the convective plumes, seemingly putting to rest the controversy over the existence of plumes as opposed to isolated heated bubbles of rising air. One improvement which we are striving to add to our sounder is to enable the detection of echoes from lower levels in the atmosphere than the present minimum of 30 m. It is in these lower levels that wind shear frequently produces a marked slope in the plume structure as observed by Kaimal and Businger[14]. We have observed such plume slopes occasionally in the levels above 30 m, but at our present location do not have wind instrumentation above 15 m to verify wind shear at higher levels. Occasionally the plumes seem to slope in a direction opposite to that to be expected from wind shear in the lower levels, or backward into the wind. Without knowledge of the wind profile with height it is not possible to explain this observation. We look forward in the future to tests performed in cooperation with tethered balloon sounding systems to obtain better wind profile data.

With the calibration of the sounder well understood to an estimated accuracy of 3 db, the facsimile recordings of plume structure can be used to study the diurnal and seasonal variation of plume height. We define a plume as being that volume of the atmosphere where the thermal structure parameter $C_T > 4 \times 10^{-2}$ °K cm$^{-1/3}$. In Figure 6, the darkest areas in the plumes correspond to C_T values as large as 14×10^{-2} °K cm$^{-1/3}$. By overlaying the records of plumes with a transparent grid, it is possible to count off the percentage of time when the plume is discernable as a shade of light grey or darker, corresponding to the discriminating C_T value defined above. The results of such an analysis are shown in Figure 7 where the increase in plume height from early morning hours to a maximum shortly after noon is documented by the three curves drawn. This data was taken at Haswell, Colorado, a flat prairie site 200 km southeast of Boulder, on a sunny day with light and variable winds below 2 ms^{-1}.

After the plumes reach a maximum height shortly after noon, the heights begin to decrease but on a slower time scale than the rise in height during the morning hours. The 1400-1500 plume height characteristic is nearly the same as the 1000-1100, and the 1600-1700 late afternoon plumes have nearly the same characteristic as the 0900-1000.

Turbulent mixing at the edges of the plume, and turbulence within the plume, reduces the C_T with height as shown in Figure 6. The lower regions of the plume are clearly a darker grey on the facsimile record than the upper regions. It must be emphasized, however, that C_T is a class of atmospheric variable about which we have much to learn. The thermal structure parameter does not exactly correspond with plume vertical velocity, as verified by acoustic Doppler measurements of vertical winds. Therefore low values of C_T do not necessarily delimit the convective zone in the boundary layer, but there is a clear correlation between convection and the C_T. Further theoretical and experimental work will be required to determine how the unstable convective region interacts with thermal inversions.

A second way to study the characteristics of thermal plumes is to investigate seasonal effects on plume height. In Figure 8, the 1200-1300 plume height characteristics are examined for three dates in the summer, fall, and winter months. All data were taken over Colorado prairie land on sunny days with winds 0-2 ms^{-1}. Figure 8 shows surprising little variation in plume characteristic with season. This somewhat surprising result needs further study, for the angles of solar radiation incidence differ by more than 50° between the extreme seasonal cases. Surface temperature gradients, or in other words the lapse rate in the lowest few tens of centimeters does not change greatly with season[15], and this may be the explanation.

CONCLUSIONS

Acoustic echo sounding has been found to provide a new and valuable tool for sensing temperature and velocity structure in the earth's boundary layer. As with any new tool, initial results may prove surprising and even contradictory, and this is certainly true with the initial studies of thermal plume structure. The ability to measure quantitatively plume structure and vertical velocity is providing new insight into plume dynamics, especially as they modify the structure of inversions and influence fluxes of heat and water vapor in the boundary layer. The simplicity and relatively low expense of fabricating acoustic echo sounder systems, as compared with radar or lidar devices, make it probable that acoustic techniques will find even wider application in boundary layer studies in the future.

ACKNOWLEDGMENT

The program in atmospheric acoustic echo sounding reported here is a group effort at the NOAA Wave Propagation Laboratories. The contributions of D. W. Beran, B. C. Willmarth, W. D. Neff, and WPL Director, C. G. Little are gratefully acknowledged. The data gathered at the October, 1969 Haswell, Colorado experiment was part of a joint effort with the Australian team from the Weapons Research Establishment and the discussions with L. G. McAllister and his group were extremely useful. This work was supported both by NOAA research funds and by the Air Pollution Control Office, EPA.

REFERENCES

(1) L. G. McAllister and J. R. Pollard, "Acoustic sounding of the lower atmosphere", Proc. 6th Int. Symp. Remote Sens. Env., U. Mich (1969) pp. 436-450.

(2) L. G. McAllister, "Acoustic sounding of the lower troposphere", J. Atmos. Terr. Phys. 30, 1439-1440 (1968).

(3) C. G. Little, "Acoustic methods for the remote probing of the lower atmosphere", Proc. IEEE 57, 571-578 (1969).

(4) J. W. Wescott, W. R. Simmons, C. G. Little, "Acoustic echo-sounding measurements of temperature and wind fluctuations", ESSA Tech. Mem. ERLTM-WPL 5, Boulder, Colorado, Jan., 1970, 24 pp.

(5) O. N. Strand, "Numerical study of the gain pattern of a shielded acoustic antenna", to be publ., J. Acoust. Soc. Amer. (June, 1971).

(6) G. L. Bonvallet, "Levels and spectra of traffic, industrial, and residential area noise", J. Acoust. Soc. Amer. 23, 435-439 (1951).

(7) W. E. Blazier, Jr. "Criteria for control of community noise", Sound and Vibration, 2 (5), 11-18 (May 1968).

(8) P. B. Ostergaard and R. Donley, "Background-noise levels in suburban communities", J. Acoust. Soc. Amer. 36, 409-413 (1964).

(9) W. F. Bateman and E. Ackerman, "Some observations on small-town noise", Noise Control 1 (6), 40 (Nov., 1955).

(10) R. D. Berendt, G. E. Winzer, and C. B. Burroughs, "A guide to airborne, impact, and structure borne noise-control in the multi-family dwellings", U. S. Dept. Housing & Urban Dev., Wash. D. C., pp C5-C12 (Sept., 1967).

(11) H. Nyquist, "Thermal agitation of electric change in conductors", Phys. Rev. 32, 110-113 (1928).

(12) H. Fletcher, "Auditory patterns", Rev. Mod. Phys. 12, 47-65 (1940).

(13) L. O. Myrup, "Temperature and vertical velocity fluctuations in strong convection", Quart. J. Roy. Meteorol. Soc. 93, 350-360 (1967).

(14) J. C. Kaimal and J. A. Businger, "Case studies of a convective plume and a dust devil", J. Appl. Meteorol. 9, 612-620 (1970).

(15) W. C. Whitman and G. Wolters, "Microclimatic gradients in mixed grass prairie", in Ground Level Climatology, ed. by R. H. Shaw. Amer. Assn. Adv. Sci., Wash., D. C. 1967, pp. 165-185.

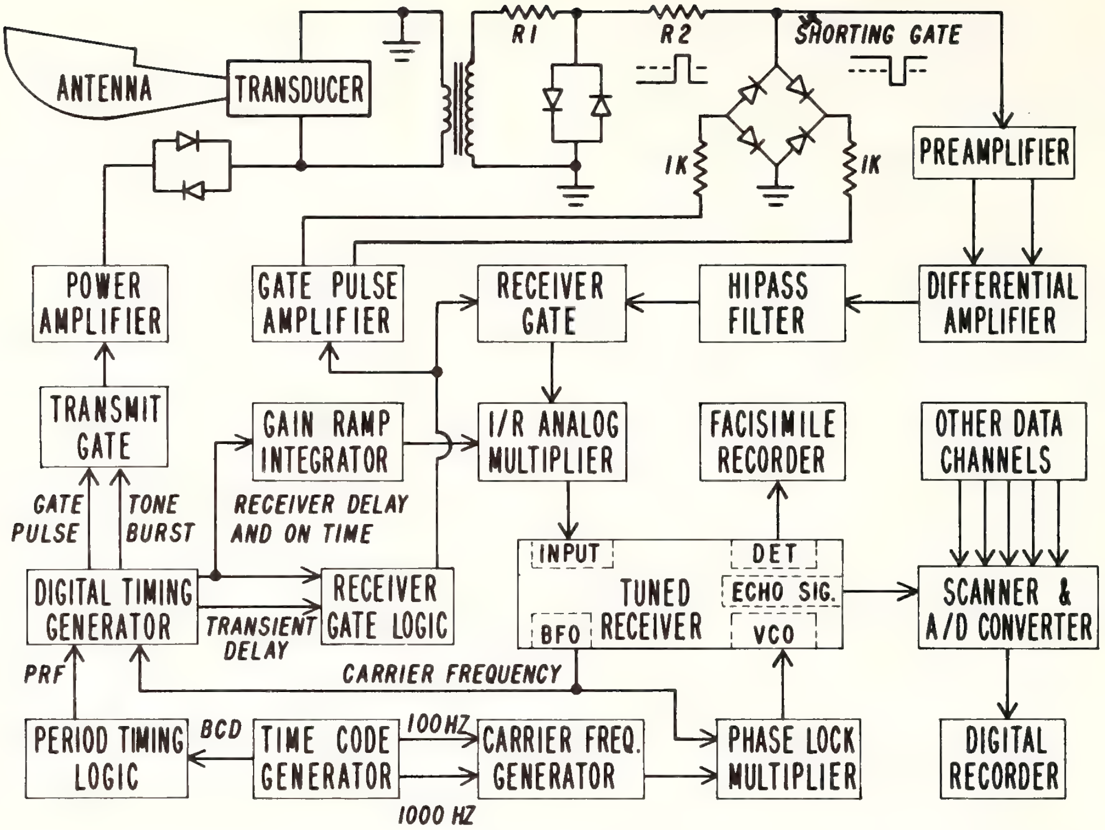

Figure 1 - The NOAA Mark II Echo Sounder Block Diagram, illustrating the flow of transmitted signal, control functions, and received signal.

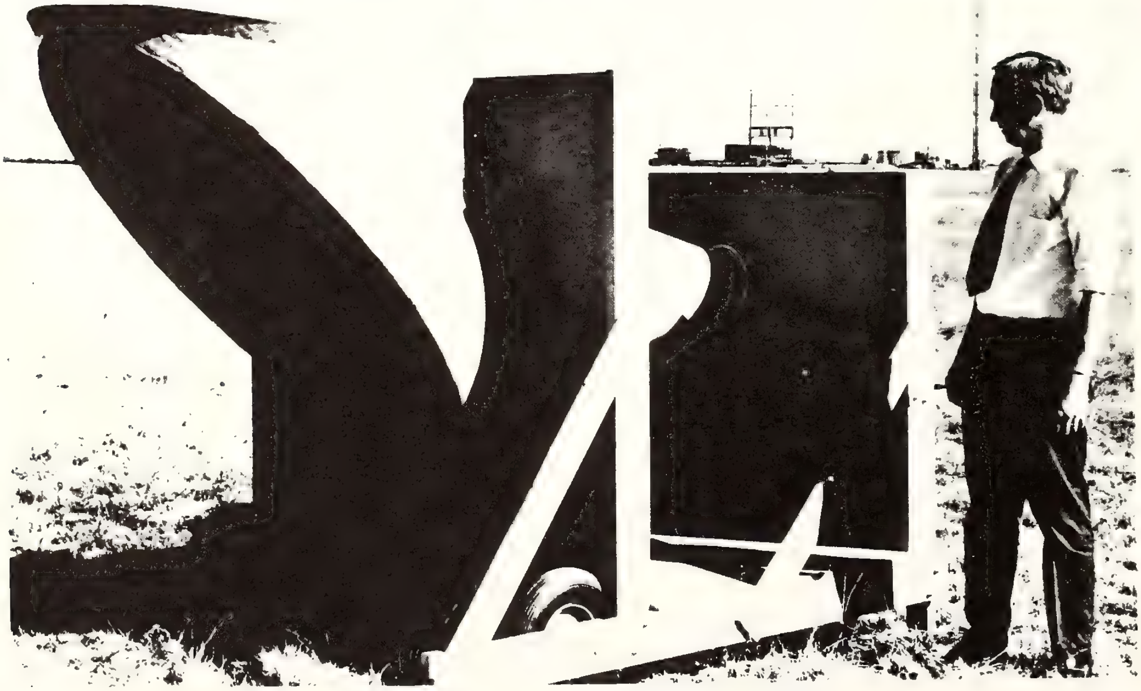

Figure 2 - Cone-paraboloid antenna adapted for acoustic echo sounding.

Table I. Locations and Conditions Under Which Environmental Noise Data Were Recorded

Location Number	Location	Conditions	Reference
2	Chicago, Ill. (1950)	Residential; minimum night	Bonvallet (6)
6		Residential; and commercial areas with little or no traffic	
7		Residential; unidentifiable backgrounds	
14		Commercial areas; fast auto traffic, light truck and commercial traffic	
16		Residential; industrial backgrounds	
18		Industrial area	
19		Commercial areas, busy downtown heavy traffic	
4	Coral Gables, Florida (1968)	Residential; ambient, no air conditioners operating	Blazier (7)
9		Residential; 15 feet from 11 window or wall air conditioners	
10		Residential; 15 feet from 28 central air conditioners	
13		Residential; 20 feet from 22 central and room air conditioners	
5	New Jersey (1963)	Residential; spring, 9:00-11:00 p.m., heavily wooded suburban and parks	Ostergaard & Donley (8)
8	State College (1955)	Residential; late summer, one family houses, daytime	Bateman & Ackerman (9)
12		Residential; late fall, duplex dwellings, daytime	
11		Campus, during class hours	
15		Commercial, noisy downtown sidewalk, 5:00 p.m.-12 midnight	
17		Commercial, noisy downtown sidewalk, 8:00 a.m. - 5:00 p.m.	
3	Rural area	Daytime-near highway	Berendt et al. (10)
1		Daytime-no highway noise	
20	Suburban	Near large metropolitan airport	
21	Jet Aircraft Takeoff	One mile slant height both sides	
22		1500 feet slant height both sides	
23		2-3 miles in front	
24		200 feet in front	
25		200 feet in back	

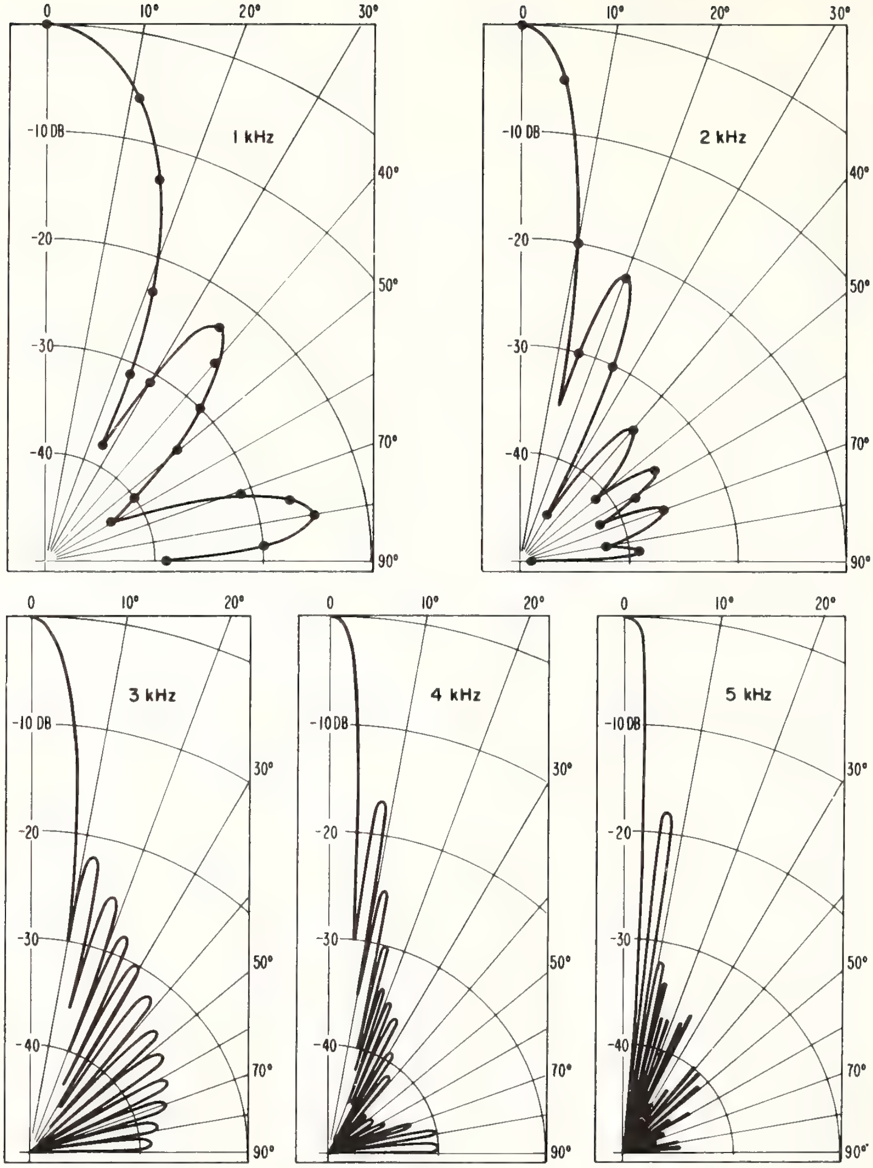

Figure 3 - Measured antenna patterns for the cone-paraboloid antenna for the range of acoustic frequencies used in echo sounding.

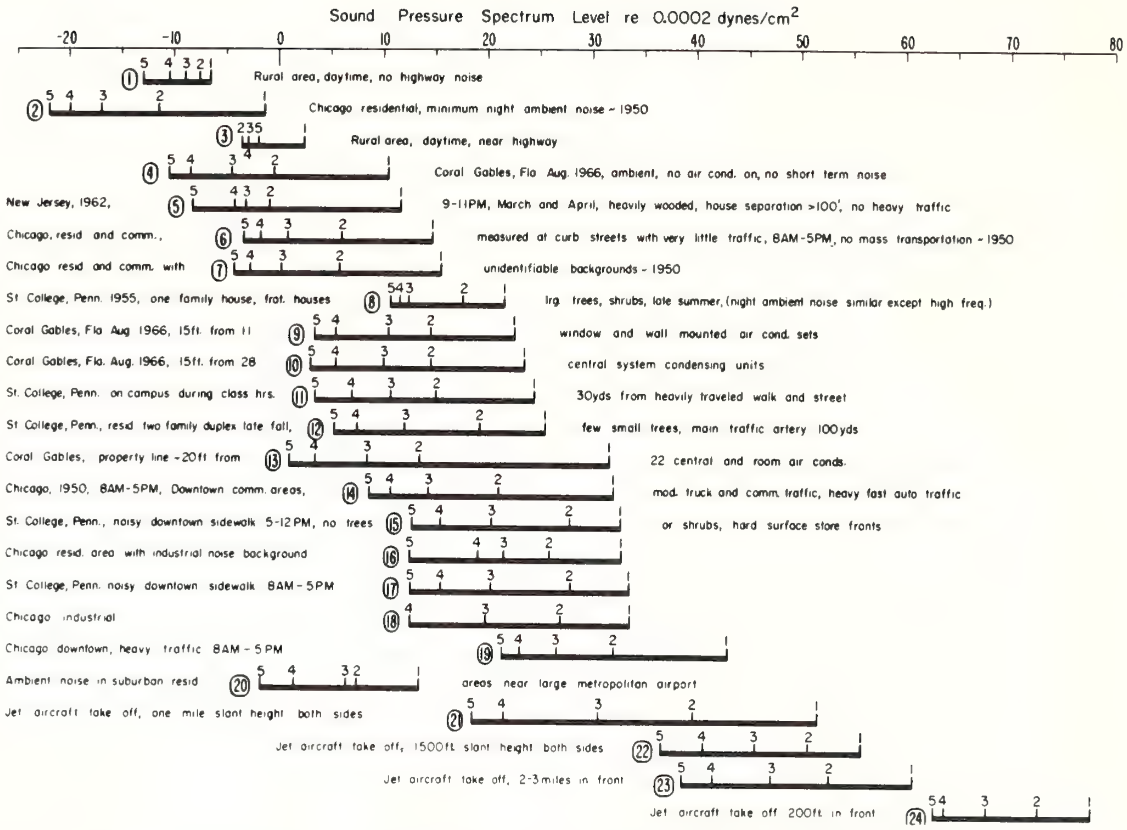

Figure 4 - Ambient noise sound pressure spectrum levels for a number of environments for frequencies of 1, 2, 4, 4, and 5 kHz. Circled location reference numbers are identified in Table I.

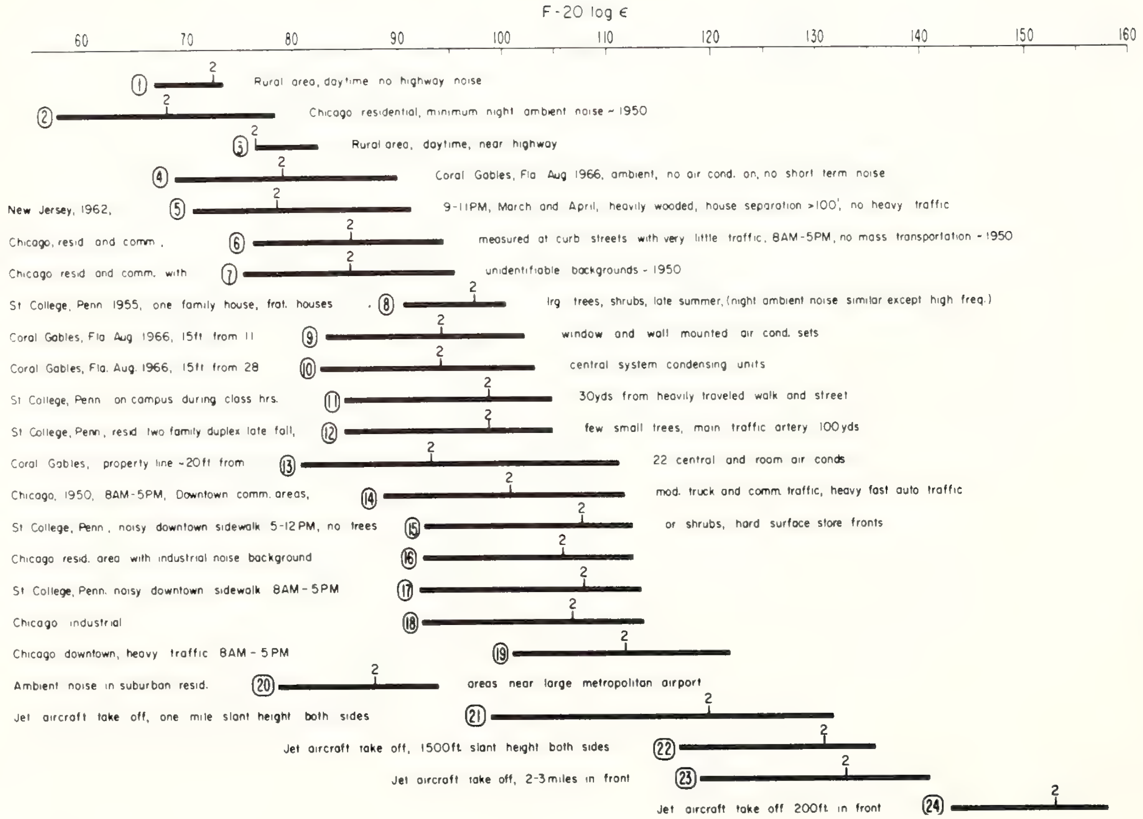

Figure 5 - Noise suppression figure required for various environments of obtain a pre-determined value of the ambient noise figure F.

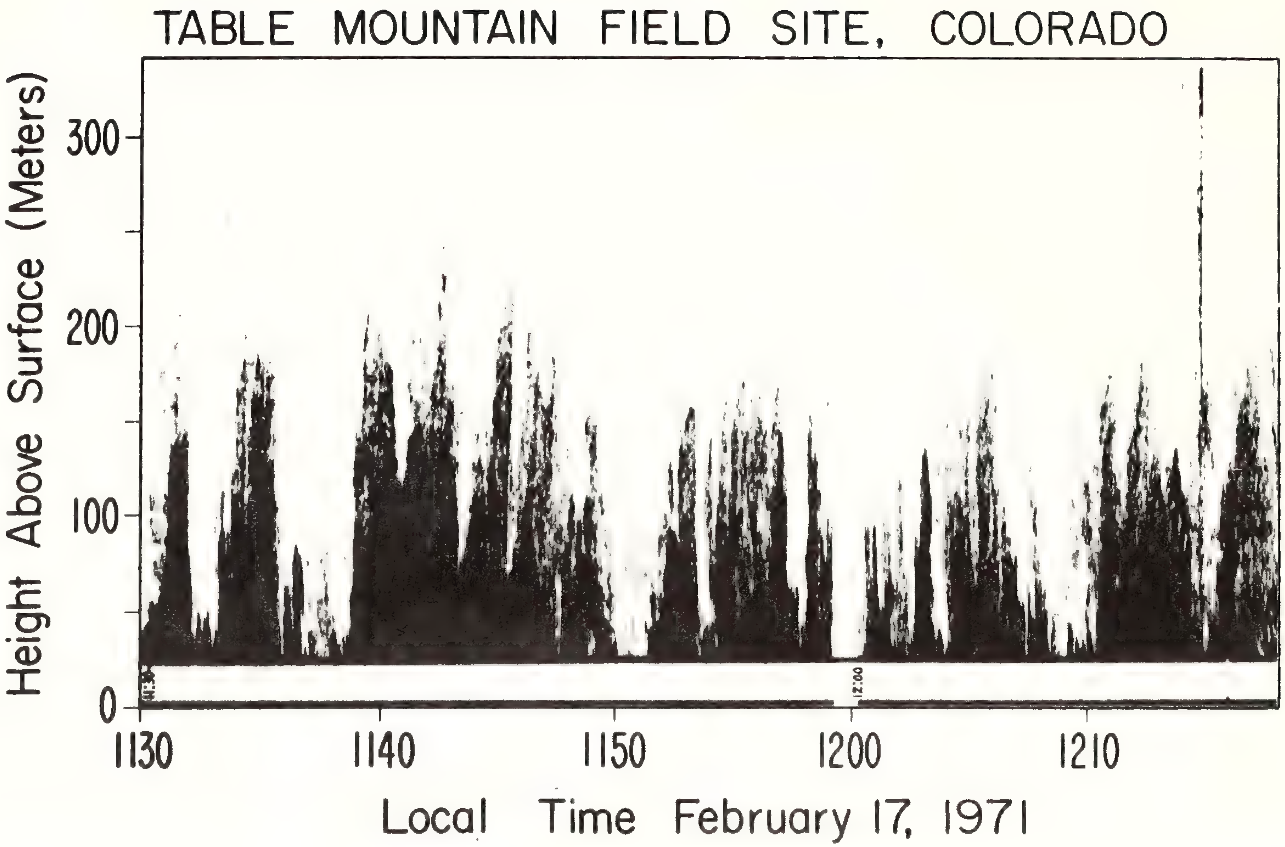

Figure 6 - Facsimile recording of backscatter acoustic intensity from convective thermal plumes.

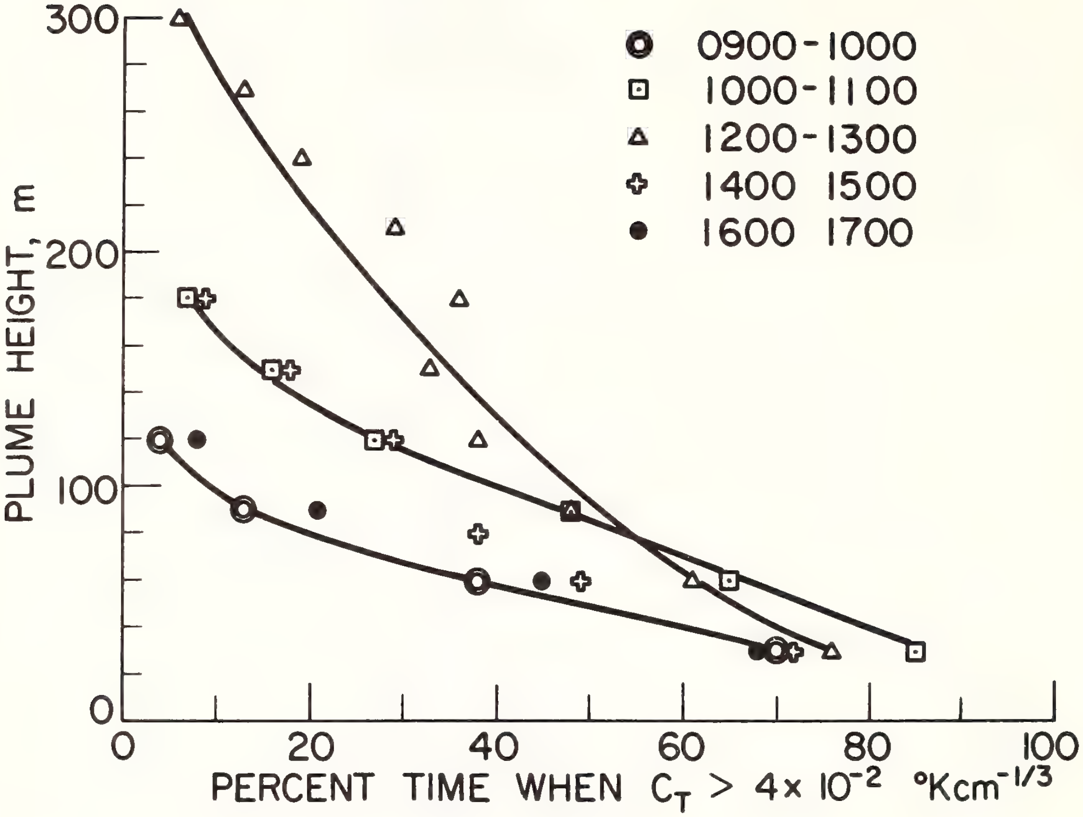

Figure 7 - Diurnal variation of thermal plume height statistics, Haswell, Colorado, 8 October 1969.

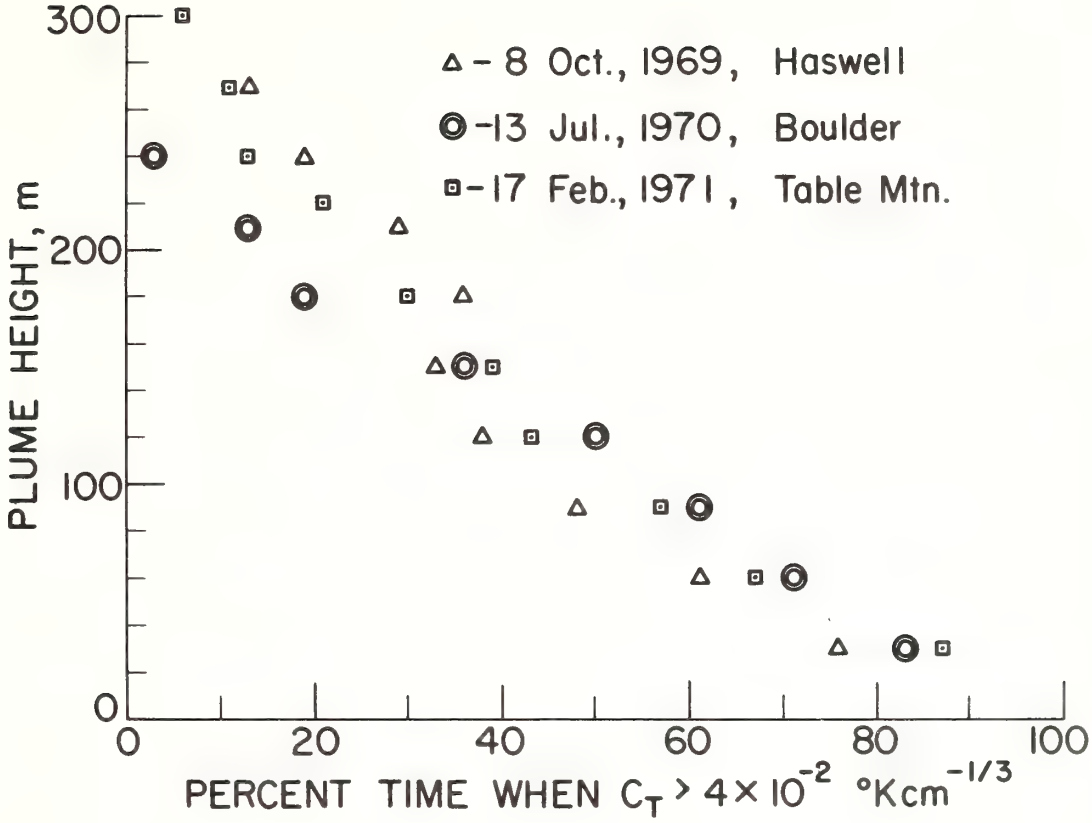

Figure 8 - Seasonal influence on thermal plume height, 1200-1300 hr, sunny days, dry Colorado prairie, winds 0-2 ms^{-1}.

28

Reprinted from Proceedings of Air Pollution, Turbulence, and Diffusion Symposium, December 7-9, 1971, New Mexico State University, 66-72, 1971.

APPLICATION OF AN ACOUSTIC SOUNDER TO AIR POLLUTION MONITORING

D. W. Beran, F. F. Hall, Jr., J. W. Wescott, W. D. Neff*

Wave Propagation Laboratory
NOAA, Environmental Research Labs.
Boulder, Colorado

INTRODUCTION

Control measures for air pollution in most large cities, are more in the nature of an effort to lessen the pain, rather than to cure the patient. In this unhappy state, the role of monitoring devices, which make possible some prediction of hazardous conditions, becomes even more important.

Effective monitoring requires instruments which provide information on the concentration of both gaseous and particulate matter, and instruments for monitoring meteorological conditions which control the dissipation of the noxious elements. This paper concentrates on a relatively new device, the Acoustic Echo Sounder, which is particularly well suited for the task of monitoring those meteorological parameters required for making intelligent decisions concerning the degree of hazard during a particular event.

It is common knowledge that the low level temperature structure is a prime factor in the creation of air pollution events. Severe problems are associated with the low level capping inversion off the coast of California and the Los Angeles basin, an area where quantities of polluted air can be trapped under the advected inversion. While Los Angeles may claim pride of place for these conditions, it is not, unfortunately, unique and many other cities can be found where similar topography - temperature structure interaction leads to severe pollution conditions.

While the temperature lapse rate is of prime concern in air pollution meteorology, secondary, and at times equally important, effects can be attributed to the wind pattern over a city. Clearly, wind direction plays an important role in determining the path pollutants will take after emission. In addition, the strength of the wind is important in determining how rapidly effluents will be carried away; a necessary input when determining if a given emission rate will produce critical concentration levels over a region. Other meteorological parameters, such as the presence of humidity and solar radiation, (both of which induce chemical reactions of certain pollutants) are important, but to a lesser degree.

A monitoring system which could provide a continuous detailed picture of the wind and temperature structure in the lowest 1 km over a city would be of much more value than the in situ meteorological sensors presently used. In general, most forecasters must rely on instrumentation designed to sample the larger synoptic scale, and as such, provide continual data only on surface parameters, upper air soundings being made, at most, four times daily. In addition, aviation requirements have often dictated the location of these sensors, a situation not necessarily in the best interests of the urban meteorologist.

It is suggested that the acoustic sounder is a device which could collect continuous mesoscale measurements in critical regions at a cost significantly below other proposed methods. The remainder of this paper will present a brief discussion of the theory of acoustic sounding followed by the results from recent field tests which demonstrate the potential of the device for measuring wind and temperature structure. In addition, problems relating to operating in the urban environment under all types of conditions will be covered.

THE ACOUSTIC ECHO SOUNDER

The acoustic echo sounder is, in principle, not unlike Sonar. A sound wave is transmitted into the medium to be interrogated, the atmosphere. Turbulent wind and temperature fluctuations scatter some of this wave energy, a part of which can then be collected at a receiver. This process is described by the radar equation

$$P_r = P_t \, \sigma \, \frac{c\tau}{2} \, \frac{A^2}{R^2} \, L \quad , \qquad (1)$$

---

*Assigned to NOAA/ERL from the NOAA Commissioned Officer Corps.

where the acoustic power returned P_r, is a function of the power transmitted, P_t, the speed of sound, C; the length of pulse, τ; the area of the receiving antenna, A; the range to the area where the return is generated, R; the losses, L due to absorption and equipment efficiences, and, finally, the scattering cross section, σ. Theoretical work[1,2,3] has established the relationship of the scattering cross section per unit volume, σ, to the turbulence parameters. The final form of the scattering equation is,

$$\sigma(\theta) = 0.03k^{1/3} \cos^2\theta \left[\frac{C_v^{\,2}}{C^2} \cos^2\frac{\theta}{2} + 0.13 \frac{C_t^{\,2}}{T^2}\right] \left(\sin\frac{\theta}{2}\right)^{-\frac{11}{3}} , \qquad (2)$$

where σ (θ) is the scattered power, per unit volume, per unit incident flux, per unit solid angle at an angle, θ, from the initial direction of propagation. The wave number of the acoustic wave is represented by $k = 2\pi/\lambda$; C and T are the mean speed of sound and temperature in the scattering volume and $C_v^{\,2}$ and $C_t^{\,2}$ are the structure constants for velocity fluctuation and temperature fluctuations respectively.

The potential of acoustic echo sounding, first analyzed by C. G. Little[4], has been demonstrated by the work of several investigators[5,6,7] concentrating mainly on vertically pointing monostatic (colocated transmitter and receiver) systems. This early work clearly showed one of the possible roles that the acoustic echo sounder might play in air pollution monitoring[8]. One of these records made by the repeating traces of a facsimile recorder, synchronized with the pulses from the sounder is shown in Figure 1. This type of record gives a height time cross section of the low level boundary layer structure. Absolute temperature and gradients cannot be directly determined from this type of presentation, but the known interaction of C_T with various stability parameters i.e., temperature gradient and Richardson's number does make it possible to derive a qualitative assessment of the low level temperature structure. For example, regions which are dark (i.e. showing strong echoes) can, in general, be associated with either stable or unstable lapse rates and white areas are produced where conditions are neutral.

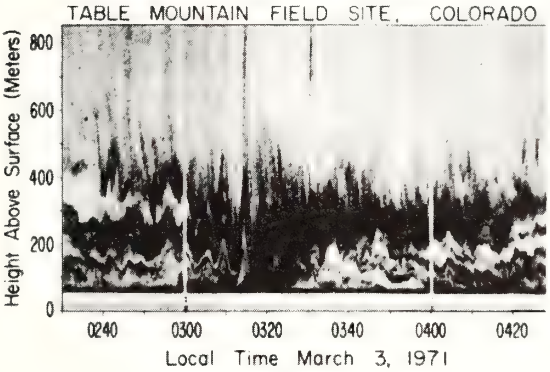

Figure 1 - Acoustic sounder record taken under stable conditions.

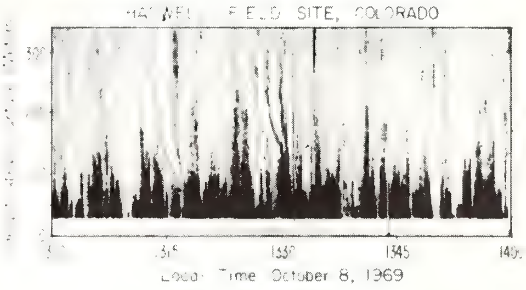

Figure 2 - Acoustic sounder record taken under unstable conditions.

It is then logical to ask, how stable regions can be distinguished from those which are unstable? Here, experience has shown that distinctive patterns are associated with the two stability regimes. When acoustic returns are generated in a stable region, the pattern will be horizontally stratified, usually with a wave structure superimposed on the layers. Conversely, when unstable conditions are present, the record will contain predominantly vertically oriented structure. Figure 1 is an example of the return from a stable atmosphere. This can be compared with an unstable case shown in Figure 2. During the morning transition periods, when surface heating after sunrise starts to lift an inversion surface, both patterns can be observed during the same time period. An example of this is shown in Figure 3 where the quasi-horizontal dark region is associated with the remains of the surface based nocturnal inversion. This layer is progressively lifted as the low level lapse rate becomes more unstable. Later the unstable lapse rate predominates, and all remnants of the inversion layer are gone.

Where a particular application requires only that the presence and depth of an inversion are known, this type of system, consisting of a single monostatic antenna and receiver, would suffice. As indicated earlier, however, the wind structure under the inversion is also a major concern. The acoustic echo sounder can be used to provide this type of information through a slightly more complex configuration.

A component of the total wind can be sensed by analyzing the Doppler shift of the returned signal at a single receiver. For monostatic configurations, this component is directed along the axis of the beam and for bistatic systems, the component is along the bisector of the angle formed by the intersections of the two beams. Recent work[9,10,11] has tested many different configurations and assessed the accuracy with which the wind can be measured with the Doppler technique. The most recent of these experiments used three antennas, one pointing vertically and the other two positioned along orthogonal axes through the first, and tilted in such a way that the three beams intersected at some height above the ground (see Figure 4). In tests with this configuration, the wind measured by the Doppler system was compared with that measured by a Boundary Layer Profiler (BLP), a kytoon mounted anemometer supplied by the field facilities group of NCAR. Results of this comparison are given in the scatter diagram shown in Figure 5. For comparable 30 minute samples, the average value for the Doppler method was 2.33 m/s and that for the BLP was 2.43 m/s. The observed very close agreement indicates the ability of the acoustic Doppler to measure the total wind vector at any height within range of the system.

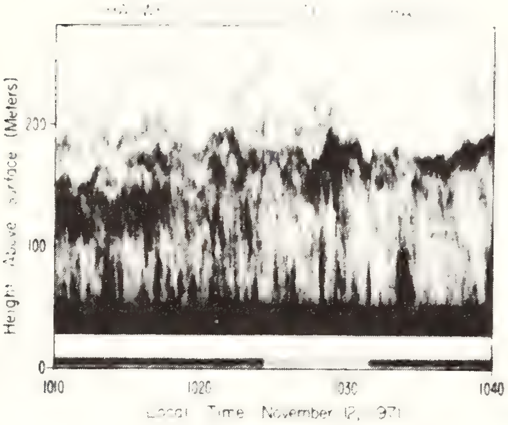

Figure 3 - Acoustic sounder record taken during the transition from stable to unstable conditions. The stable layer is associated with the upper portion of the dark areas: Unstable conditions are forming vertical convective elements below the stable layer.

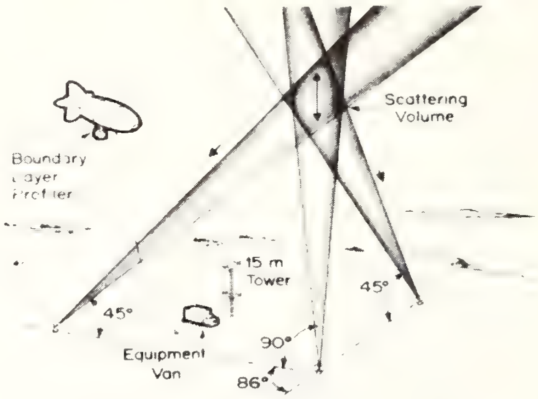

Figure 4 - Antenna configuration used to measure total wind vector.

By using the same configuration as that shown in Figure 4, but with all three systems operating in the monostatic mode, it is possible to measure a vertical profile of the total wind vector. This is done by gating the signal from each of the systems at distances which correspond to the same height above the terrain. The components measured at each of the three gates at a given level are then averaged for periods of the order of 1 or 2 minutes. The resulting components are then resolved into the total wind vector at that height. (The averaging process, assuming Taylor's Hypotheses is valid, minimizes the error that might be produced because of the spatial separation of volumes along the beams away from the point of intersection.) An example of winds measured in this way is shown in Figure 6, a height time section of the horizontal isotachs derived from the total wind vector at ten elevations.

Where absolute temperature information is required, it is at least conceptually feasible to use the wind information and boundary layer theory to calculate the temperature gradient. Greater refinements might also be possible if the measured intensity of C_v^2 and C_t^2, the structure constant for wind and temperature fluctuations are incorporated. These parameters and the measured wind profile can be combined through empirical boundary layer expressions of stability to estimate lapse rates between very unstable and neutral, and very stable and neutral. These concepts show promise, but have not yet been field tested.

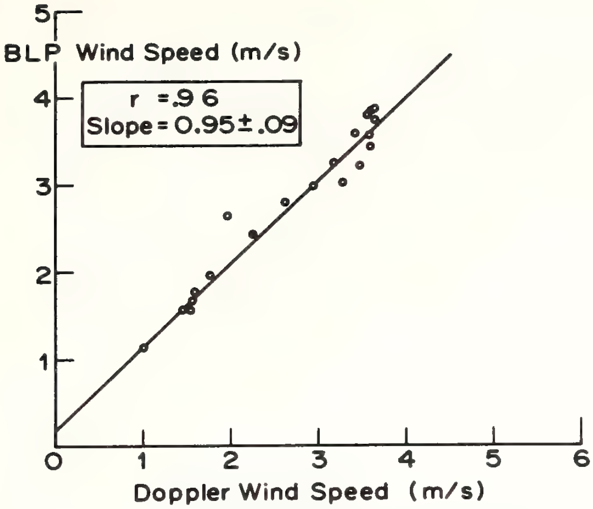

Figure 5 - Scatter diagram of winds measured by Doppler (DOP) and Boundary Layer Profiler Anemometer (BLP).

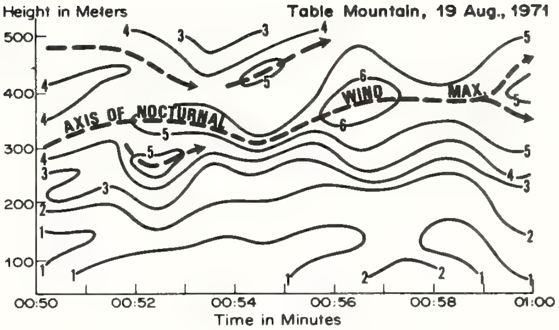

Figure 6 - Isotachs of horizontal wind derived from acoustic Doppler measurements.

A second approach, also untested, would use the dependence of sound absorption on the frequency of the carrier wave and on temperature and humidity. If it can be assumed that all absorption is due to the classical and molecular portions of the attenuation coefficient, this method should work well, and would require only that 2 or 3 separate frequencies be generated; the difference in signal strength at each frequency is used to derive the temperature and humidity profiles. The assumption of no excess absorption(i.e. that due to processes other than molecular or classical) may prove to be limiting[12,13] and more information on the nature of the attenuation is needed before the method can be demonstrated.

MONITORING DURING AN AIR POLLUTION EVENT

Our best example, to date, of the potential of an acoustic sounder for monitoring meteorological structure during an air pollution event was obtained during April of 1971. The acoustic sounder was located at Table Mountain, a field site some 50 km northwest of downtown Denver. It was being operated on a round-the-clock basis in a monostatic mode with the antenna pointed vertically.

Fortuitously, the sounder recorded the low level pattern of C_T^2, indicative of the temperature structure on the 13th and 14th of April, a period when effluent concentrations in Denver reached the "pollution alert" level. The 24 hour long acoustic record for this period is shown in Figure 7.

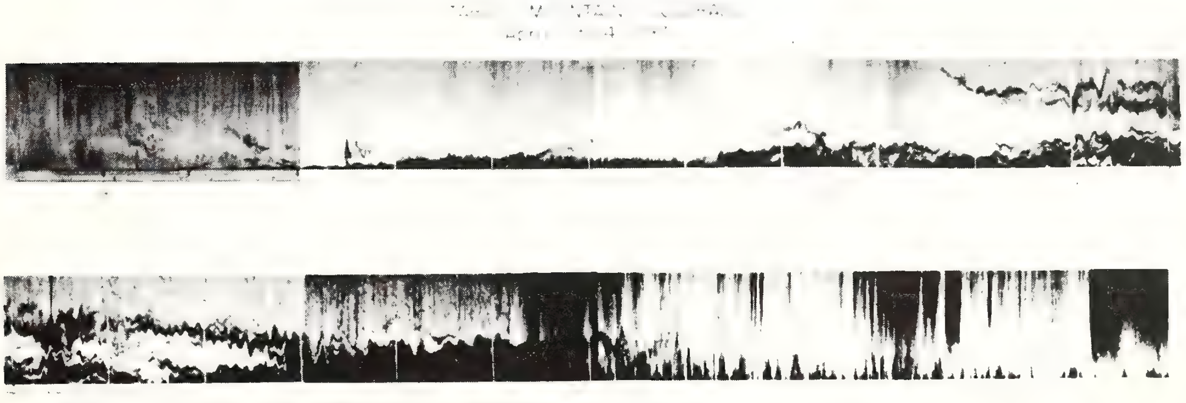

Figure 7 - Acoustic sounder record showing the evolution of the boundary layer structure before, during and after an air pollution alert.

The late afternoon portion, 1700 to 2000 (local time) on the 13th, shows the typical pattern which occurs after thermal plume activity has subsided and the lapse rate is near neutral. Following 2000, we see evidence of a surface based radiation inversion starting to form and deepen. This process continues throughout the nocturnal hours. Other layered structure, probably the result of advected inversion layers, also appear throughout the night. These layers all show the typically horizontally stratified structure with a variety of wave modes superimposed. Of particular interest is the subsiding layer which appears at about 800 meters shortly before 0300 on the 14th. This layer continues to descend until just before 0800 where it merges with the other lower layers and a very strong surface based inversion results. Shortly after this time, surface heating begins to have an effect and the lower regions start to take on the vertically oriented structure indicative of convective activity. This process tends to lift and intensify the capping inversion which was responsible for the air pollution alert. By 1200 on the 14th. the convective activity has destroyed the inversion layer and deep mixing has started. Two hours later at 1400, the air pollution alert was cancelled in Denver.

The temperature structure during this period was recorded by conventional radiosonde soundings at Denver's Stapleton Airport. The temperature, T, and dew point, T_d, profiles for 1700 LT on the 13th, and 0500 LT on the 14th are shown in Figure 8.

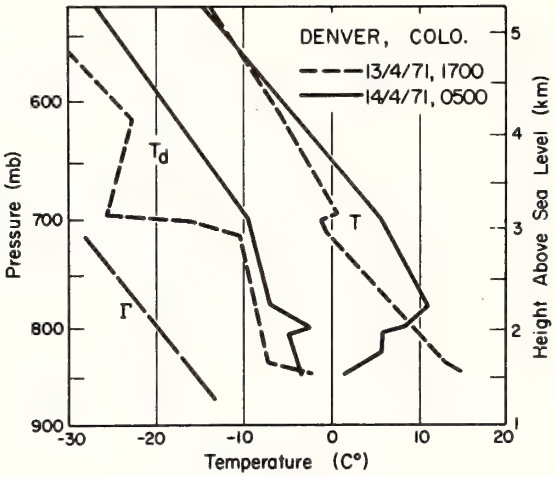

Figure 8 - Denver radiosonde records corresponding to the record shown in Figure 7.

The temperature and dew point profiles taken at 1700 LT on 13 April, 1971 show the typical subsidence inversion associated with a large high pressure region. These profiles, shown as dashed lines in Figure 8, were taken near the beginning of the record shown in Figure 7. The second set of profiles (solid lines) were taken at 0500 on the 14th, near the right side of the top portion of the 24 hour record. Looking at the radiosonde records alone, one can only speculate that the elevated inversion, near 3.3 km above sea level (1700 meters above the ground) at 1700 on the 13th had lowered and helped to intensify the inversion at 2.4 km on the 14th. The acoustic sounder record, on the other hand, clearly shows this evolution with the subsidence inversion entering the picture just before 0300 and lowering to about 600 meters above the ground. It is difficult to make a direct comparison of the inversion height at the two locations in question. However, the difference of less than 200 meters at 0500 LT appears very good despite such factors as the variation in surface elevations, local flow patterns and ground cover.

While this record does not tell the entire story, i.e., the concentration level of pollutants and the low level winds are absent, it is a simple matter to trace the events, even with data taken at a point far removed from downtown Denver. Using only this basic type of display, the air pollution meteorologist would have far more information than the present four per day temperature soundings provide.

Before placing an acoustic sounder in the urban environment, it is important to address certain practical questions relating to the ambient background noise in a city. The issue is really two sided; 1) can the sounder be successfully operated in the high noise environment of an urban area, and 2) will the operation of the sounder in this environment prove to be an annoyance to the inhabitants?

The first problem has been extensively analyzed with the conclusion reached that proper sidelobe suppression can be achieved by shielding the antennas[14]. It is also interesting to note that acoustic systems designed for other purposes, but essentially operating on the same basic principle, are now being successfully used in the extremely high noise environment of major airports.

Solution of the first part of this problem also eliminates the worst aspect of the second part, the annoyance factor. As most of the sound which might bother people is transmitted in the sidelobe of the antenna, shielding for sidelobe suppression will also greatly reduce the annoyance factor.

CONCLUSIONS

While full scale testing in an urban environment remains to be completed, the results to date clearly indicate the potential of an acoustic sounder as a monitor of important meteorological parameters that contribute to undesirable air pollution situations. At present it appears that the worst effect of a high noise environment on the operation of a sounder will be periodic losses of of record, a factor which can be significantly reduced by improved anechoic shielding and proper selection of operating frequencies. In the unlikely event that as much as half of the record is lost, the amount of usable information would still be orders of magnitude greater than is available from conventional measuring techniques. This point is well amplified by comparing the information in Figures 6 and 7 of the previous section.

The importance of knowing the low level winds associated with an inversion also suggests that the Doppler capability should be incorporated into any operational system. The alternative would be to produce a backlog of acoustic records taken under various types of boundary layer structure and then use a pattern recognition technique to relate the observed records to conditions which might produce hazardous air pollution events. The Doppler capability would require slightly more complex equipment, but the additional information would seem to be worth the extra investment. Analog techniques, now under development, will allow rapid extraction of the Doppler shift at predetermined intervals above the ground. This information can then be converted into a real time display of the wind profile, updated every two or three minutes.

The number and location of monitoring stations in an urban environment must be a function of such factors as, the local terrain, the pattern of residential vs. commercial zoning, and the mesoscale climatology of the city, each case being analyzed individually. If, for example, convergence into the urban heat island is a factor, stations could be placed at strategic locations around the perimeter of a city and the rate of inflow monitored continuously. In the final analysis, especially when compared with other types of remote sensors, the inexpensive acoustic sounder, combining its wind and temperature measuring capability, seems well suited to the task of monitoring the mesoscale urban environment.

REFERENCES

1. Tatarski, V. I. (1961), Wave Propagation in a Turbulent Medium (R. A. Silverman, transl.) New York: McGraw-Hill, 1961.

2. Kallistratova, M. A. (1961), Experimental investigation of sound wave scattering in the atmosphere, Trudy Inst. Fiz. Atmos, Atmos. Turbulentnost, 4, pp. 203-256.

3. Monin, A. S. (1962), Characteristics of the scattering of sound in a turbulent atmosphere, Akust. Zh., 7, pp. 457-461, (Sov. Phys - Acoust. 7, pp. 370-373).

4. Little, C. G. (1969), Acoustic methods for the remote probing of the lower atmosphere. Proc. of the IEEE, 57, pp. 571-578.

5. McAllister, L. G., J. R. Pollard, A. R. Mahoney, and P.J.R. Shaw (1969), Acoustic sounding - a new approach to the study of atmospheric structure. Proc. IEEE, 57, pp. 579-587.

6. Beran, D. W. (1970), Project EAR (Environmental Acoustic Research) Vol. I, Univ. of Melbourne, Meteorology Dept. Pub. No. 15.

7. Wescott, J. W., W. R. Simmons, and C. G. Little (1970), Acoustic echo sounding measurements of temperature and wind fluctuations, ESSA Tech. Memo. ERLTM-WPL-5.

8. Beran, D. W., G. H. Clark, and U. Radok (1969), Meteorological aspects of air pollution in the Geelong region, Proceedings of the Third Clean Air Conference, Sydney, Australia, May 1969.

9. Beran, D. W., C. G. Little, and B. C. Willmarth (1971), Acoustic Doppler measurements of vertical velocities in the atmosphere, Nature, 230, pp. 160-162.

10. Beran, D. W., and B. C. Willmarth (1971), Doppler winds from a bistatic acoustic sounder, Proc. Seventh Int. Symp. on Remote Sensing of the Environment, Univ. of Mich., Ann Arbor, Vol. III, pp. 1699-1714.

11. Beran, D. W., and S. F. Clifford (1972), Acoustic Doppler measurements of the total wind vector, Proc. of American Met. Soc. Second Symp. on Met. Observations and Inst. To be held in San Diego, Calif. March 1972.

12. Delsasso, L. P., and R. W. Leonard (1953), The attenuation of sound in the atmosphere, Rept. for USAF Cont. W-28-099-AC-228.

13. Beran, D. W., R. M. Reynolds, and J. T. Gething (1970), Sound attenuation in the free atmosphere, Project EAR Rept. No. 5, Publ. No. 17, Univ. of Melbourne, Dept. of Meteorology.

14. Simmons, W. R., J. W. Wescott, and F. F. Hall (1971), Acoustic echo sounding as related to air pollution in urban environments, NOAA Tech. Rept. ERL 216-WPL 17.

Reprinted from Nature 230, 160-162, 1971.

Acoustic Doppler Measurements of Vertical Velocities in the Atmosphere

D. W. BERAN, C. G. LITTLE & B. C. WILLMARTH

Atmospheric Acoustics Group, Wave Propagation Laboratory, National Oceanic and Atmospheric Administration, Boulder, Colorado 80302

Acoustic echo sounding techniques have been used to determine vertical velocities in the atmosphere during thermal plume activity and a nocturnal inversion. The existence of breaking wave formations within the inversion has been clearly established.

EXPERIMENTS during the past few years[1,2] have clearly demonstrated the potential of acoustic echo sounding as a means of monitoring atmospheric structure and motions. This work, although striking in detail, does not provide quantitative measurements and the interpretation of the patterns has been based chiefly on speculation about the associated velocity and temperature fields. In this article we describe how Doppler information from acoustic echoes was used to derive vertical velocities both during daytime thermal plumes and during the occurrence of breaking waves within a nocturnal inversion.

The scattering of sound waves by turbulent temperature and wind fluctuations has been described by Tatarski[3], Kallistratova[4], Monin[5] and others. The potential of this scattering process for remote sensing of atmospheric structure and motion has been fully documented elsewhere[4,6,7], but we wish to point out that for the monostatic case (that is, using collocated transmitting and receiving antennas) only temperature fluctuations contribute to the received acoustic echo power.

Doppler Shifts

The radial velocity, v, of a scattering target is given by

$$v = \frac{c}{2}\left(\frac{f_0}{f_d} - 1\right) \qquad (1)$$

where c is the phase velocity of the acoustic wave in the radial direction, f_0 is the original carrier frequency, and f_d is the frequency of the returned signal. Second order velocity terms are neglected in the derivation of equation (1), but although this simplification can readily be made for electromagnetic waves, caution must be exercised when making the same simplification for the acoustic case, especially if very high wind speeds are to be measured. We were measuring vertical velocities less than 2 m s^{-1} so the second order terms are unimportant.

The much slower speed of acoustic waves compared with electromagnetic waves can introduce some errors into the Doppler measurements. If the medium along the path to the target is varying with time, which is usually the case in the atmosphere, additional frequency shifts may be added to the true Doppler shift produced by the radial motion of the target. Fluctuations in the vertical velocity of the air along the path do not, however, produce spurious frequency shifts, provided that the vertical velocity field does not change between the upward and the downward traverse of the medium. On the other hand, temperature fluctuations, which produce phase changes of equal magnitude and sign in both propagation directions, will not cancel out. This spurious propagation-induced frequency shift should not produce errors in derived vertical velocities of more than about 0.1 m s^{-1} for the heights which concern us.

Table 1 Acoustic Echo Sounder Parameters used during the Doppler Experiment

Peak power	6.4 W (acoustic)
Pulse width	100 ms
Pulse repetition frequency	1 s^{-1}
Maximum range	170 m
Carrier frequency	4,000 Hz
Antenna diameter	122 cm
Antenna beam width	±2° to 3 db points
Beam direction	Vertical
Receiver band width	100 Hz
System noise level in 100 Hz band width	$\sim 10^{-18}$ W
Scattering volume at 100 m altitude	Cylindrical, ~7 m diameter by 17 m deep

The frequency spectrum of the returned signal is compared with that of the original transmitted pulse to obtain the Doppler frequency shift. The method of obtaining the spectra differs slightly in the acoustic and electromagnetic cases, primarily because of the characteristically much higher pulse repetition rate used with electromagnetic radar. The final spectrum generated from a radar return is extracted from information contained in each of many separate pulses and it is this spectrum which is used to reproduce the Doppler frequency; in the acoustic case, a spectrum can be generated for each pulse. The higher pulse repetition rate of the radar does not increase the accuracy if the signal-to-noise ratios and overall duty cycles (fraction of time that the transmitter is on) are equal in the two cases. A further improvement can be made by averaging the acoustic spectra from succeeding pulses, although this reduces the horizontal resolution (by increasing the size of the total volume being considered) because of the ambient air motion during the time required to collect the sample.

Resolution

Vertical resolution is much higher for the acoustic Doppler method because of the difference in the speed of the acoustic and electromagnetic wave. Standard pulse radars have range resolutions of about 100 m, but acoustic sounders readily attain resolutions of the order of 10 m, and can be further improved by using shorter pulse lengths. The vertical resolution is then only limited by the length of the transmitted pulse, suggesting that a very short pulse length would be optimum. The selection of optimum pulse length must be a compromise, however, in order to reduce the transmitted band width and to increase the signal-to-noise ratio. In both cases, FM–CW or other broad band modulation techniques can be used to obtain better range resolution if necessary.

The relevant parameters of our equipment are shown in Table 1. The pulse repetition rate was fixed at 1 s^{-1} and gives a maximum usable range of 170 m. The carrier frequency was increased to such a value that echoes were obtained at approximately the maximum range with a minimum of return from higher levels; this ensured that echoes from preceding pulses would not contaminate the returns—the strong dependence of atmospheric attenuation on frequency makes this a suitable method for limiting the range of an acoustic sounder. The antenna beam width becomes narrower at higher frequencies, and so the spatial (horizontal) resolution of the system also improves as the frequency is increased.

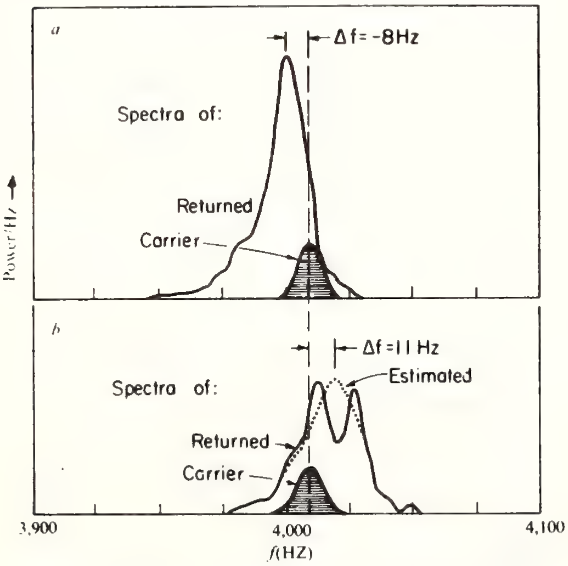

Fig. 1 Example of spectra used to determine the Doppler shift. Amplitudes of spectra are not plotted on the same scale.

The data were reduced in a two channel digital processor which derived the frequency spectra of the returned signal at predetermined range gates corresponding to selected heights. The stability of the estimate was increased by taking spectra from each of ten succeeding pulses and then averaging them together. The power spectra for transmitted pulses and the return echoes were then plotted on a linear scale of frequency against power; the Doppler shift was determined by visual inspection and it was therefore necessary to limit the number of spectra by using only alternate groups of ten pulses at a given height and alternating the groups of ten from level to level, thus creating a checkerboard pattern of sampled volumes in time and height. The best fit curve through the computed spectrum was estimated and the peak taken as its first moment. The mean vertical velocity of the volume was determined from equation (1). The spectra were fair approximations to a Gaussian curve (see Fig. 1*a*). A few of the spectra had bimodal shapes (see Fig. 1*b*) suggesting that two or more separate velocity regions were contained within the volume sampled by the sounder during the 10 s averaging period.

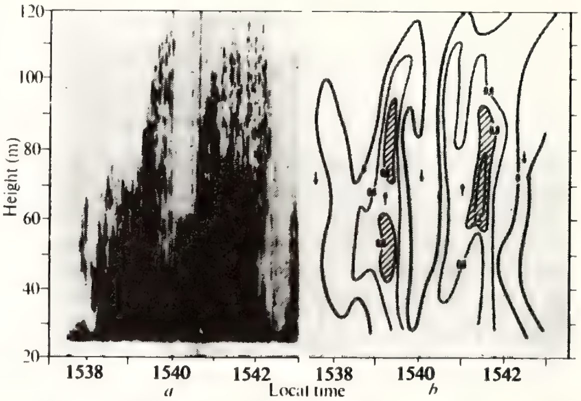

Fig. 2 Acoustic echoes (left) and Doppler derived vertical velocity field during thermal plume activity. Contour interval is 0.4 m s^{-1}; regions of vertical velocity <0.8 m s^{-1} are shaded; arrows indicate direction of vertical component.

Plumes and Inversions

Two cases were analysed which represented distinctly different vertical velocity regimes. The first set of data was taken during the afternoon of October 9, 1970, when convective thermal plume activity was present. A portion of the facsimile record for this time (see Fig. 2*a*) shows the characteristic strong returns from the ascending air and weaker or nonexistent returns from the surrounding region; the derived vertical velocity field is shown in Fig. 2*b*. The strongest acoustic echoes do not correspond exactly with the regions of maximum vertical velocity, but are displaced slightly in a downwind direction and arrive first at the sounder. This implies that the strongest temperature fluctuations are associated with the region of maximum shear between the rising warm air and the descending cooler air, as would be expected. The vertical or even slightly upwind slope of both the echoes and the vertical velocity field seems to be in disagreement with results of previous thermal plume studies in which it has been shown that the slope of the plume is a function of the vertical shear of the horizontal wind[8]. Conventional wind data associated with the two cases were available only at a height of 5 m, and there is no way to correlate the slope of the plume with actual measured wind shear. Also, because of equipment limitations, the lowest echoes occur at about 25 m and the slope of the plume between this level and the ground—the region where most previous tower measurements have been made—is not available for comparison. For a well mixed atmosphere, which characteristically accompanies thermal plumes, the wind profile would contain strong shear in the lowest few metres, but vertical momentum transfer would tend to eliminate shear at higher levels. This leads to the conclusion that the observed slopes are realistic; the apparent inconsistency with previous studies seems principally due to the different height ranges investigated.

Data for the second case were taken from acoustic measurements made between 0035 : 40 and 0042 : 00 h on October 12, 1970, just before passage of a cold front. During the time before and including this example, the nocturnal inversion exhibited large oscillations with amplitudes of about 100 m and a period of 15 to 20 min. Fig. 3*a* shows a portion of the last oscillation before the complete breakdown of the structure, which is accompanied by an abrupt increase in the surface wind velocity from 3 m s^{-1} to 12 m s^{-1}. Smaller oscillations are clearly visible within the larger one and are interpreted as the return from a breaking gravity wave. The Doppler derived vertical velocity field (see Fig. 3*b*) shows the alternating up and down motion as these smaller waves pass the acoustic sounder with the region of downward velocity ahead of the breaking wave in the centre and top half of the picture. The "spillover" from the breaking gravity wave is seen just before 0039 h at heights between 90 and 100 m.

A slightly different presentation of the breaking wave is shown in Fig. 4; the wind speed at a height of 5 m was used to estimate the horizontal translation of the air. Assuming that the values recorded at this height are representative for all heights, it is possible to interpret a streamline pattern through the breaking wave by using the measured vertical velocity components. Although the assumption of constant wind speed through the layer is rather extreme, the procedure does reverse the order of events from right to left and produces a pattern which is more easily recognized as a breaking wave.

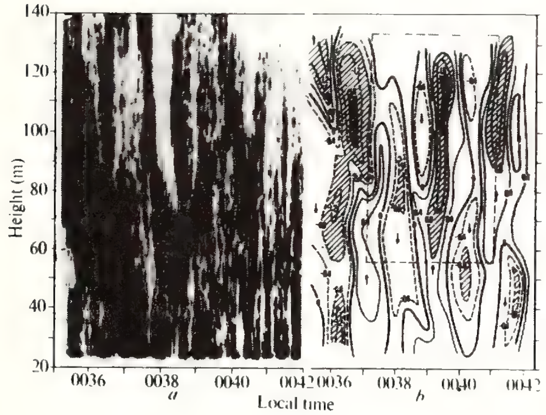

Fig. 3 Acoustic echoes (left) and Doppler derived vertical velocity field under a nocturnal inversion which was exhibiting wave motions. Contour interval is 0.4 m s^{-1}; velocities <0.8 m s^{-1}, single hatching; <1.6 m s^{-1}, double hatching; upward vertical velocities, solid lines; downward vertical velocities, dashed lines. Derived streamlines for area within box are shown in Fig. 4.

It is difficult to assess the accuracy of the Doppler velocity measurements because of the method of determining the first moment of the spectra; the remarkable consistency of the velocity field suggests, however, that the accuracy of the velocities is about ± 0.2 m s^{-1}. A further accuracy estimate for the velocity measurements can be obtained from the vertical displacement of identifiable portions of the acoustic echoes. The vertical velocity deduced for the descending layer near 0032 h was -1.6 m s^{-1}. This compares with ~ -1.0 m s^{-1} measured by the Doppler method, and is in reasonable agreement considering that the Doppler velocities are spatially averaged over 10 s.

Only the first moment of the frequency spectrum was required for determining the Doppler shift but a more complete analysis of the individual spectra, including the extraction of higher moments, should help to develop a clearer picture of the turbulent structure within a given scattering volume.

Refinements

Other refinements in the technique are, of course, still needed, for example digitization of the acoustic records and on-line data processing. It would also be desirable to have a better understanding of the processes producing spectra which are not normally distributed and which might lead to improved methods of determining the true Doppler shift caused by the vertical motions. A component of the horizontal wind could be measured with improved scanning techniques, including beam tilting.

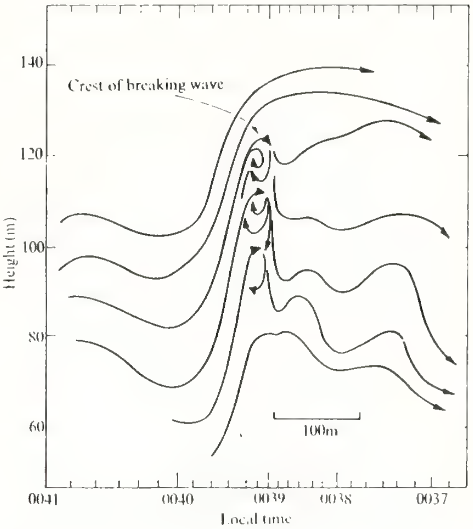

Fig. 4 Derived streamline pattern for region outlined in Fig. 3.

The potential of the acoustic Doppler approach as a method of measuring velocity fields in the Earth's boundary layer is clearly demonstrated. With the help of relatively inexpensive equipment it should now be possible for the meteorologist to gain new insight into such problems as low level heat flux, air–sea interaction and exchange processes, and the structure and motion of wave phenomena. As was stressed earlier[6], it should also be possible to determine the variation with height and time of the temperature structure constant, C_T (that is, of the r.m.s. difference in atmospheric temperature at two points unit distance apart). This parameter is of importance in the field of optical communications, because it is linearly related to the structure constant C_n, which describes the intensity of small scale fluctuations of optical refractive index.

Received December 4, 1970.

[1] McAllister, L. G., Pollard, J. R., Mahoney, A. R., and Shaw, P. J. R., *Acoustic Sounding—A New Approach to the Study of Atmospheric Structure*, Tech. Note CPD(T), 160 (Weapons Research Establishment, Salisbury, South Australia, 1968).

[2] Beran, D. W., thesis, Univ. Melbourne (1970).

[3] Tatarski, V. I., *Wave Propagation in a Turbulent Medium* (trans. by Silverman, R. A.) (McGraw-Hill, 1961).

[4] Kallistratova, M. R., *Study Instituta Fizika at Atmosfery, Atmosfernoya Turbulentnost*, 4, 203 (1961).

[5] Monin, A. S., *Soviet Phys. Acoust.*, 7, 4, 370 (1962).

[6] Little, C. G., *Proc. I.E.E.E.*, 57, 4, 571 (1969).

[7] Derr, V. E., and Little, C. G., *Appl. Optics*, 9, 9, 1976 (1970).

[8] Kaimal, J. C., and Businger, J. A., *J. Appl. Meteor.*, 9, 4, 612 (1970).

30 *Reprinted from ESSA Technical Memorandum, ERL TM-WPL 5, 1970.*

ACOUSTIC ECHO-SOUNDING MEASUREMENTS OF TEMPERATURE AND WIND FLUCTUATIONS

J. W. Wescott, W. R. Simmons, and C. G. Little

This report describes the Wave Propagation Laboratory Mark I acoustic echo-sounding system and illustrates its performance with results obtained during observations alongside a 500-ft meteorological tower at Haswell, Colorado.

Reprinted from NOAA Technical Report, ERL 216-WPL 17, 1971.

ACOUSTIC ECHO SOUNDING AS RELATED TO AIR POLLUTION IN URBAN ENVIRONMENTS

W. R. Simmons, J. W. Wescott, and F. F. Hall, Jr.

The feasibility of operating an acoustic echo sounder in an urban or industrial environment, without serious degradation in performance and without contributing to noise pollution, is confirmed. Anechoic absorbers placed about the acoustic antenna are the key to improving the sounder performance. Optimum operating frequencies are between 1 and 2 kHz. The design and operation of the all solid state circuitry is described.

Key words: Atmospheric acoustics, acoustic echo sounder, urban noise

Reprinted from AGARD Conference Proceedings No. 33, 729-744, 1970.

58

Electromagnetic Phase Variability as a Measure of Water Vapor and Temperature Variations over Extended Paths

B.R. BEAN, R.E. McGAVIN
Environmental Science Services Administration Research Laboratories, Boulder, Colorado, U.S.A.

Summary

In many applications the value of the water vapor density and of temperature would be more meaningful if the measurement is integrated over an area or along a path rather than being made at a fixed point. With the development of radio and optical distance measuring techniques, integrated measurements are becoming practical over paths of tens of km. Accuracy to be expected from commercially available two-frequency methods indicates that the absolute value of the integrated water vapor density can be determined to within approximately 2.75%, that of integrated temperature to within approximately 0.6%. The resolution to be expected is .02 gm/m^3 in water vapor density, 0.1°K in temperature. With the expected improvement of available equipment the uncertainties in the absolute values are expected to be reduced to considerably less than 1%. Added improvement can be achieved by avoiding approximations. The ultimate accuracy depends on the accuracies in the coefficients in the equations for refractive index.

Introduction

Until recently the atmospheric scientist has been limited to point measurements of pertinent meteorological parameters. It is known that the probes used disturb the environment and that the point measurement itself is not necessarily characteristic of the region or even of another point not far removed from the observing point. For many applications values of such parameters integrated over an area or along a path would be a more useful quantity. With the development of accurate electrical distance measuring techniques, a promising method has become available for measuring water vapor and temperature over paths tens of kilometers long. The development of these techniques is the result of increased interest in accurate geodesy. The literature on this subject has been growing steadily during the past decade. Review papers are now available where state-of-the-art techniques and expected accuracies are discussed. The reader is referred to these papers and to their bibliographies for detailed discussion (1) (2) (3).

The electromagnetic path length can be shown to be a function of the refractive index which in turn is a function of temperature, water vapor and pressure. In this chapter we will analyze first the possibility of estimating water vapor density from radio path length measurements alone, and then the possibility of estimating both water vapor density and temperature using a radio-optical system. The discussion here has been confined to a dual frequency system (1 microwave and 1 optical), with the realization that a three-frequency system would produce a significant increase in accuracy.

Attention will be concentrated on the uncertainty in the measurement of the water vapor density and temperature integrated over the path. These uncertainties arise due to limitation in instrumental capabilities, experimental evaluation of constants and from what is considered to be reasonable approximations. Uncertainty here is defined as the range of values which should contain the true value of the quantity desired. Where random errors(in absence of systematic errors)are encountered, the uncertainty is defined as one standard deviation. Bias errors due to approximations are combined in a root sum square (rss) fashion with the standard deviations of random errors to provide an estimate of the possible percent departure from the true value.

Atmospheric Effects on the Radio Path Length

Theory

The radio path length (L_R) is related to the geometric path length (S) by:

$$L_R = \int_0^S n_R \, dS, \qquad \text{(Eq. 58-1)}$$

where n_R is the refractive index at radio frequencies. This can be written:

$$L_R = \langle n_R \rangle S , \qquad \text{(Eq. 58-2)}$$

where $\langle n_R \rangle$ is the space average of the refractive index over the path. (Usually n_R is expressed in terms of N_R where $N_R = (n_R - 1)10^6$. The constants in equation 58-3 yield accuracies in N_R on the order of 0.1%.) In radio distance measuring this relationship is utilized to determine the geometric distance from the radio path length. The measured radio path is corrected for the average value of the refractive index calculated from meteorological measurements at each terminal to provide an estimate of the geometric path length (S is not the exact straight line distance since the path is slightly curved due to refraction). If the problem is inverted, i.e., if S is known from other sources, then the mean values and fluctuations of L_R will yield the mean value and fluctuations of the refractive index averaged over the path.

Now from (4):

$$n_R = 1 + K_1 \frac{P}{T} + K_2 \frac{\rho_w}{T} \qquad \text{(Eq. 58-3)}$$

where:

K_1 = 7.76×10^{-5} °K/mb

K_2 = 1.72×10^{-3} °K/gm/m³

P = total pressure in mb

T = temperature in °K

ρ_w = water vapor density in gm/m³

and then performing the space averaging and assuming $\langle \frac{x}{y} \rangle \approx \frac{\langle x \rangle}{\langle y \rangle}$

$$L_R \approx S \left[1 + K_1 \frac{\langle P \rangle}{\langle T \rangle} + K_2 \frac{\langle \rho_w \rangle}{\langle T \rangle} \right] \qquad \text{(Eq. 58-4)}$$

or:

$$\langle\rho_w\rangle = \left[\frac{L_R}{S} - 1\right]\frac{\langle T\rangle}{K_2} - \frac{K_1}{K_2}\langle P\rangle \qquad \text{(Eq. 58-5)}$$

If some estimates of $\langle T\rangle$ and $\langle P\rangle$ are available, then L_R will provide a measure of the integrated water vapor density over the path. Variations in the average water vapor density are given by:

$$\Delta\langle\rho_w\rangle = \frac{\partial\langle\rho_w\rangle}{\partial\langle T\rangle}\,\Delta(\langle T\rangle) + \frac{\partial\langle\rho_w\rangle}{\partial\left(\frac{L_R}{S} - 1\right)}\,\Delta\left(\frac{L_R}{S} - 1\right) + \frac{\partial\langle\rho_w\rangle}{\partial\langle P\rangle}\,\Delta P \qquad \text{(Eq. 58-6)}$$

Then assume that for average conditions:

$$\langle\bar{T}\rangle = 300^\circ\,\mathrm{K}$$

$$\frac{\bar{L}_R}{S} - 1 = 3 \times 10^{-4} \quad \text{(equivalent to } \langle n\rangle = 1.000300\text{)}$$

$$\langle\bar{P}\rangle = 1000\ \mathrm{mb}$$

(where the overbar denotes a time average); equation 58-16 becomes:

$$\Delta\langle\rho_w\rangle = 0.174\,\Delta(\langle T\rangle) + 1.74 \times 10^5\,\Delta\left(\frac{L_R}{S} - 1\right) - 0.045\,\Delta(\langle P\rangle) \qquad \text{(Eq. 58-7)}$$

which indicates the sensitivity of the measured integrated water vapor density to changes in integrated temperature and pressure as well as to radio path length variations. The contribution from pressure variations is very small since P is not expected to change by more than a tenth of a millibar. However, the contribution of uncertainties in the assumed mean temperature is significant. If one uses a time average of the temperature at a point as an estimate of the integrated temperature, an error will be introduced. For example, from a recent experiment on a 1.65 km over-water path, the rms fluctuations in the temperature as measured at the center of the path were compared to those measured by optical path variations. The average over a number of 10-min samples indicated an rms variability of 0.2° C in the point measurements whereas the rms variability in the optical path measurements was only a few hundredths of a degree (5). Hence the use of a point measurement of temperature in equation 58-5 over this path could contribute an uncertainty of as much as 4% in $\langle\rho_w\rangle$ due only to temperature variability. (The contribution from the pressure was less than 0.1%). It is evident that if the radio path length alone is to furnish an accurate estimate of the integrated water vapor over a path, some better method must be used to obtain an estimate of the integrated temperature.

Experimental Estimates

A direct test of how well the radio path length alone can yield estimates of water vapor density was made using data from six paths taken from the literature (6)(7). These paths represented two diverse climates and terrain settings: Boulder, Colorado (a dry climate and mountainous region) and Cape Kennedy, Florida (a moist climate and flat terrain). A synopsis of the path characteristics is given in Table 1.

Unfortunately, these data yield only relative values of $(\overline{L_R}/S)-1$ and not absolute values, but for this test this is not important. We assume initial values of $(\overline{L_R}/S)-1$ and $\bar{\rho}_w$ and measure variations of $\hat{\bar{\rho}}_w$ using equation 58-5. Estimates of the average temperature and pressure were obtained from measurements at both ends of the path. A comparison was made on samples of 10-sec averages taken every half hour. Figures 58-1, 58-2, and 58-3 illustrate these comparisons between $\hat{\bar{\rho}}_w$ determined by path length measurements, and $\tilde{\bar{\rho}}_w$ determined by psychrometric measurements. The bias between samples is due to the initial assumption in L_R. But there is surprisingly good agreement between $\hat{\bar{\rho}}_w$ and $\tilde{\bar{\rho}}_w$. The 17.1 km Cape Kennedy path yielded the highest correlation coefficient (r), of (0.983) while the 7.7 km path at the same location produced the lowest correlation (0.622). (It is interesting to note that even for point measurements most of the short term variability in the refractive index is caused by variations in water vapor (8).)

Measurement of Water Vapor Density and Temperature by Microwave-Optical Techniques

Theory

Microwave phase systems have been under continuous development since 1955 (9). Recently, comparable optical systems have been enjoying similar growth (3)(10). The use of both microwave and optical techniques should provide estimates of both integrated water vapor density and integrated temperature. The microwave system is sensitive to both temperature and water vapor, whereas the optical system while sensitive to temperature is only weakly influenced by water vapor.

The optical path length can be expressed as:

$$L_o \approx S\left[1 + K_3 \frac{< P >}{< T >} + K_4 <\rho_w>\right] \qquad \text{(Eq. 58-8)}$$

where if the optical wavelength is 6328 Å:

$$K_3 = 8.09 \times 10^{-5}\,{}^\circ\mathrm{K/mb}$$

$$K_4 = -5.33 \times 10^{-8}/\mathrm{gm/m}^3$$

If this is combined with equation 58-4:

$$\frac{L_R - L_0}{S} = [K_1 - K_3]\frac{<P>}{<T>} + K_2 \frac{<\rho_w>}{<T>} - K_4 <\rho_w> \qquad \text{(Eq. 58-9)}$$

For convenience define a new parameter K_5 by:

$$\frac{K_2}{<T>} - K_4 = \frac{K_5}{<T>}$$

which for $<T> = 293°$:

$$K_5 = 1.74 \times 10^{-3}\,{}^\circ\mathrm{K/gm/m}^3 \qquad \text{(Eq. 58-10)}$$

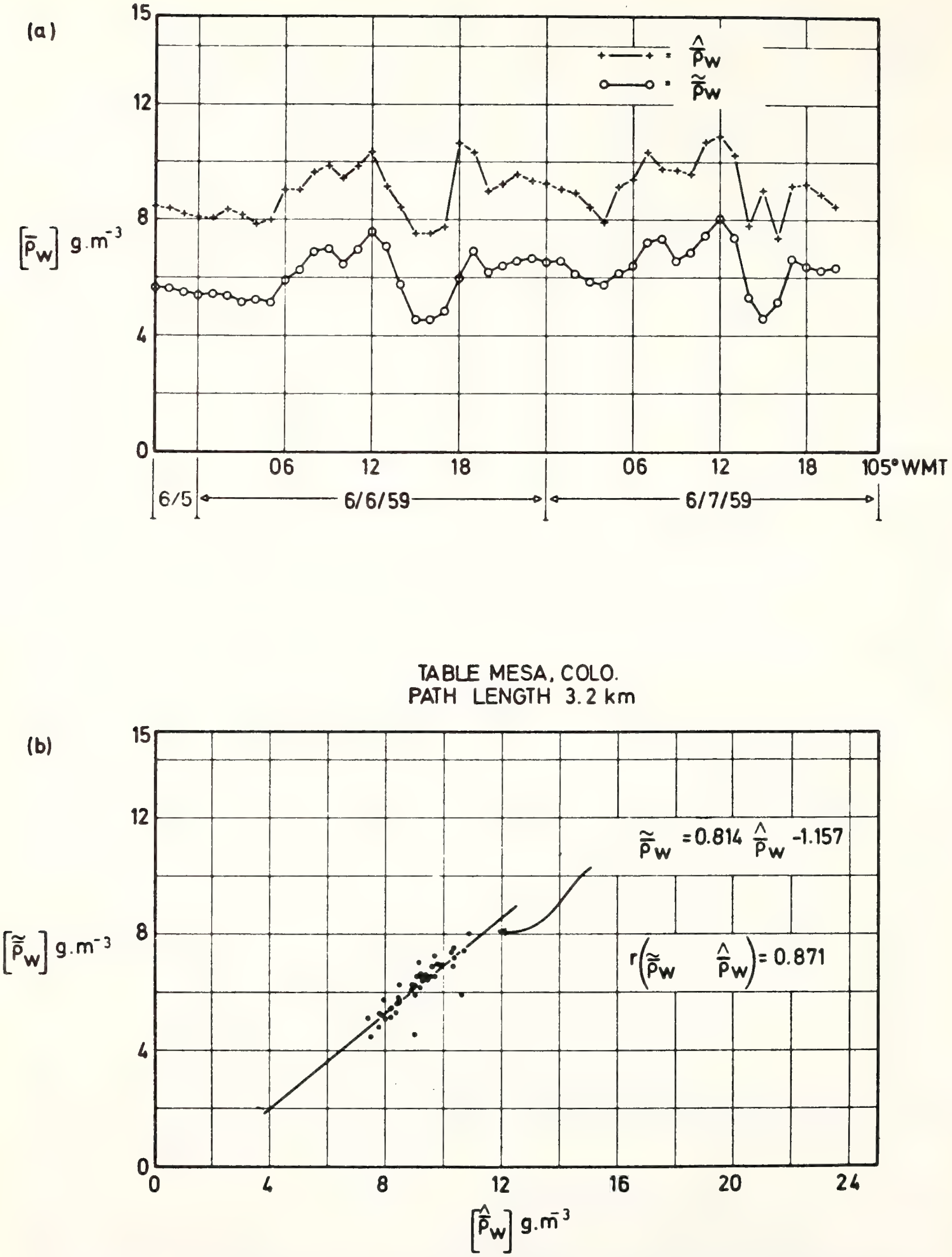

Fig. 58-1 Comparison between water vapor density $\hat{\bar{\rho}}_w$ as measured by the radio path length and $\tilde{\bar{\rho}}_w$ as measured by psychrometric means at the path terminals

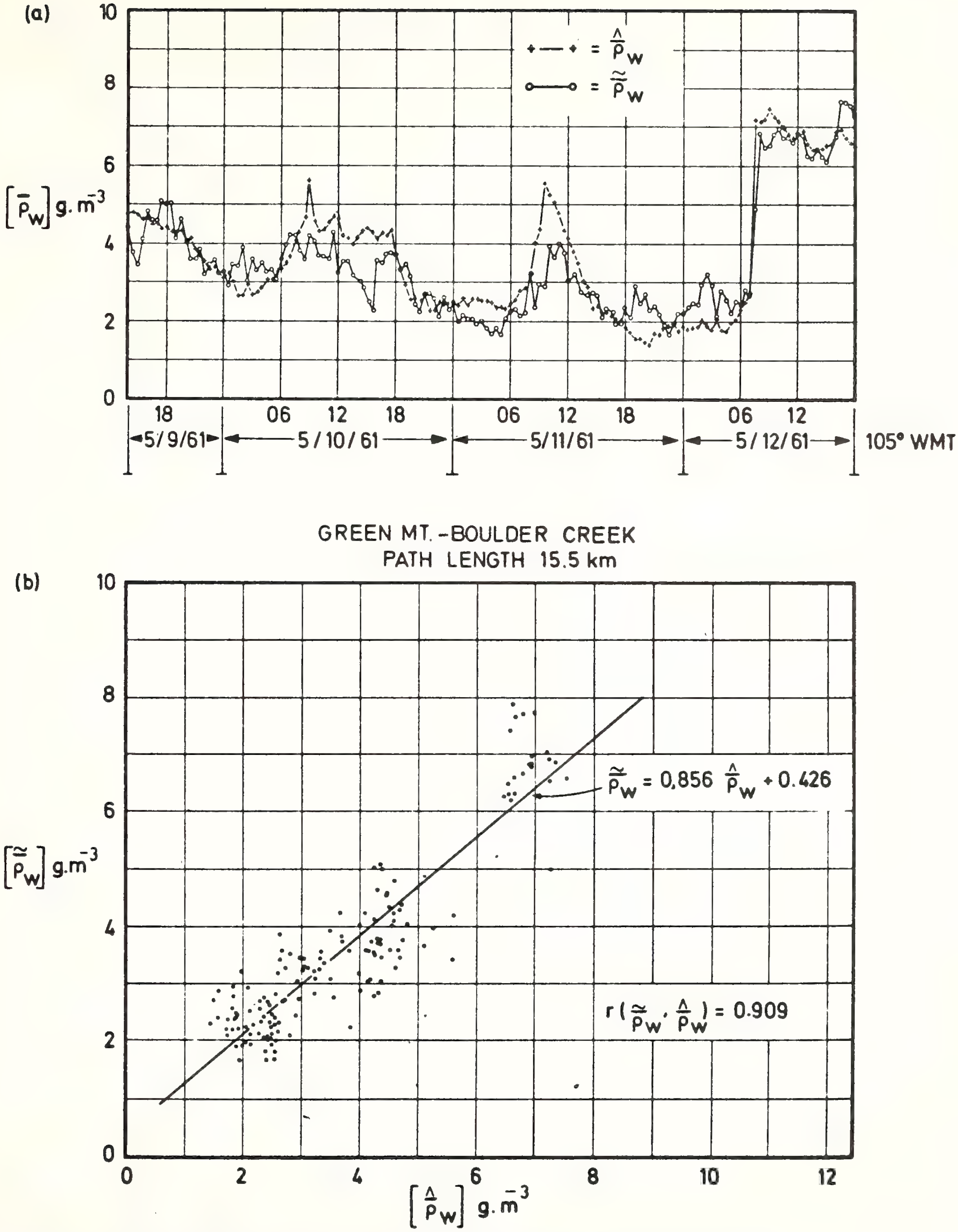

Fig. 58-2 Comparison between water vapor density $\hat{\rho}_w$ as measured by the radio path length and $\tilde{\rho}_w$ as measured by psychrometric means at the path terminals

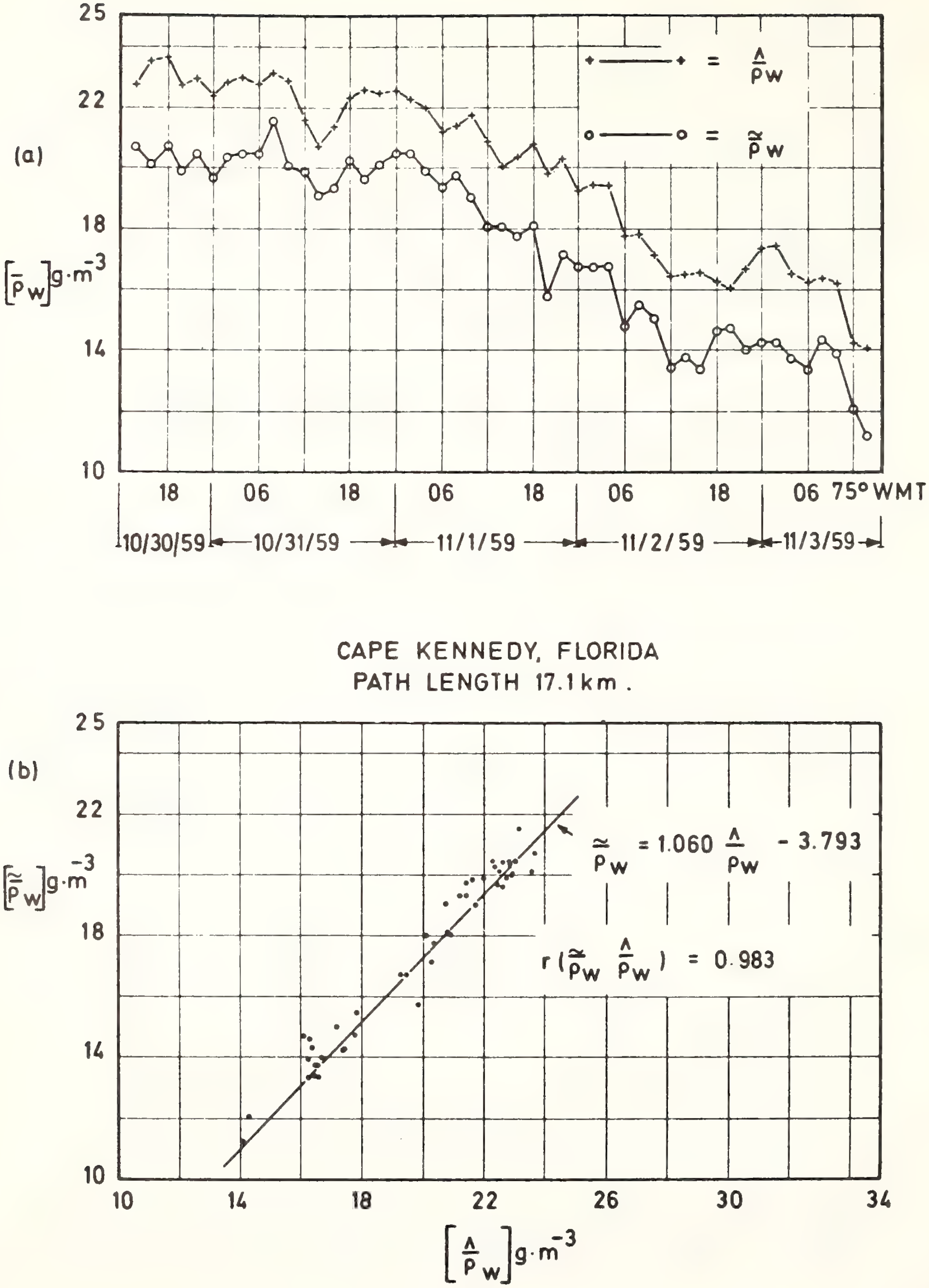

Fig. 58-3 Comparison between water vapor density $\hat{\rho}_w$ as measured by the radio path length and $\tilde{\rho}_w$ as measured by psychrometric means at the path terminals.

Using this constant value of K_5 will result in a maximum possible error of 0.1 % compared to equation 58-9 for a temperature range of 233°K to 303°K. Hence

$$\frac{L_R - L_0}{S} = -3.3\times10^{-6}\,\frac{\langle P\rangle}{\langle T\rangle} + 1.74\times10^{-3}\,\frac{\langle \rho_w\rangle}{\langle T\rangle} \qquad \text{(Eq. 58-11)}$$

and:

$$\langle \rho_w\rangle = 575\left(\frac{L_R - L_0}{S}\right)\langle T\rangle + 0.0019\,\langle P\rangle \qquad \text{(Eq. 58-12)}$$

where $\langle \rho_w\rangle$ is now a linear function of $\langle T\rangle$ and $\langle P\rangle$.
The average temperature is found from equation 58-8 to be:

$$\langle T\rangle = \frac{8.09\times10^{-5}\,\langle P\rangle}{\left(\frac{L_0}{S} - 1\right) + 5.33\times10^{-8}\,\langle \rho_w\rangle} \qquad \text{(Eq. 58-13)}$$

A further approximation can be made in equation 58-12 for the average value of $\langle \rho_w\rangle$ If average conditions are again assumed to be $\langle \overline{P}\rangle = 1000$ mb, $\langle \overline{T}\rangle = 293°$K, and $\langle \overline{RH}\rangle = 70\%$, then:

$$\langle T\rangle = \frac{8.09\times10^{-5}\,\langle P\rangle}{\left(\frac{L_0}{S} - 1\right) + 4.80\times10^{-7}} \qquad \text{(Eq. 58-14)}$$

where the increase in the maximum possible error will be less than 0.2% over a reasonably expected range of humidity and temperature. Using equation 58-14, equation 58-12 now becomes:

$$\langle \rho_w\rangle = 4.65\times10^{-2}\left[\frac{\frac{L_R - L_0}{S}}{\frac{L_0}{S} - 1 + 4.80\times10^{-7}} + .041\right]\langle P\rangle \qquad \text{(Eq. 58-15)}$$

If $\langle P\rangle$ does not vary by more than a few tenths of a millibar and if there are no instrumental errors, the total uncertainty in $\langle \rho_w\rangle$ should not exceed 0.6% and that in ΔT should not exceed 0.3% except when there are extreme changes in temperature or humidity. These coefficients can be determined for the particular location and season, and hence an accuracy of approximately 0.5% should be achievable.

In addition, these expressions can be simplified to:

$$\langle T\rangle = 8.09\times10^{-5}\left(\frac{S}{L_0 - S}\right)\langle P\rangle$$

and: (Eq. 58-16)

$$\langle \rho_w\rangle = 4.65\times10^{-2}\left(\frac{L_R - L_0}{L_0 - S} + 0.041\right)\langle P\rangle$$

where the uncertainty due to the approximations and to the coefficients in the equation for refractive index is 0.3%, root sum square (rss), in $< T >$ and 0.65% (rss) in $<\rho_w>$.

Instrumental Limitations

Up to this point it has been assumed that L_R, L_O and S are known exactly. It remains to find the uncertainty in $<\rho_w>$ due to inaccuracy in L_R, L_O and S. Consider the finite differential of equation 58-16 under the assumption of $< \overline{P} > = 1000$ mb, S = 1 km, $< \overline{T} > = 293° <\overline{\rho}_w> = 10$ gm/m³.

$$\begin{aligned} \Delta(<T>) &= 0.29\Delta(<P>) - 10.6\Delta L_O + 10.6\Delta S \\ \Delta(<\rho_w>) &= 0.009\Delta(<P>) - 1.97\Delta L_O + 1.69\Delta L_R - 0.287\Delta S \end{aligned} \qquad \text{(Eq. 58-17)}$$

If L_O and L_R can be measured with an uncertainty of no more than 1 ppm (i.e. 0.1 cm in 1 km), then the uncertainties in $< T >$ and $<\rho_w>$ will be 0.33% and 2%, respectively. It is also evident that if S can be measured with an equivalent accuracy (i.e. 1 ppm) then it likewise will give rise to an uncertainty of 0.33% in $< T >$ and approximately 0.3% in $<\rho_w>$.

An indirect method of determining S was tested in the aforementioned overwater experiment. Forty-two determinations of L_R were made over the 1.65 km path during a 5½-day period. The refractive index was measured at both ends of the path at the times of these measurements. Over the entire period L varied 8 cm, but when corrected for the refractive index as measured at the terminals, the range was reduced to 2 cm. The mean value of the 42 determinations of S was 164, 982.3 cm; the standard deviation was 0.52 cm. Hence, the standard error of the mean was less than 0.1 cm representing an uncertainty of about 1 ppm.

Summary

The accuracy in $<\rho_w>$ and $< T >$ expected under these measurement conditions yields an uncertainty in the absolute values of 2.6% (rms) in $<\rho_w>$ and less than 0.5% (rms) in $< T >$. When all the uncertainties are considered, i.e., accuracies of the constants in the equations for refractive index, approximations used, and the measurement accuracies, the overall uncertainty in $<\rho_w>$ is approximately 2.75% (rss), that in $< T >$ approximately 0.6% (rss). Most of this uncertainty in $<\rho_w>$ is due to measurement capabilities which probably can be improved. The remainder of the uncertainty is divided between the accuracies in the coefficients in the refractive index equations and the approximations used.

If ΔL_R, and ΔL_O and S exhibited uncertainties of 1 part in 10^7, then the uncertainty in $<T>$ would be .05%, and that in $<\rho_w>$ would be 0.3% due only to measurement capability. There are experimental systems which exhibit these capabilities today but it may be some time before such devices are commercially available. Further improvement in the residual uncertainty of approximately 0.5% would require more exactitude in the coefficients in the equations for the refractive index.

Measurement of Fluctuations

This process can be simplified if only small variations about an arbitrary mean are of interest. The total differentials in finite form of equations 58-4 and 58-7 yield expressions of the form:

$$\begin{aligned} \Delta(<\rho_w>) &= \frac{A}{S}\,[\Delta L_R - B\Delta L_O] - C\Delta(<P>) \\ \Delta(<T>) &= \frac{D}{S}\,[\Delta L_R - E\Delta L_O] - F\Delta(<P>) \end{aligned} \qquad \text{(Eq. 58-18)}$$

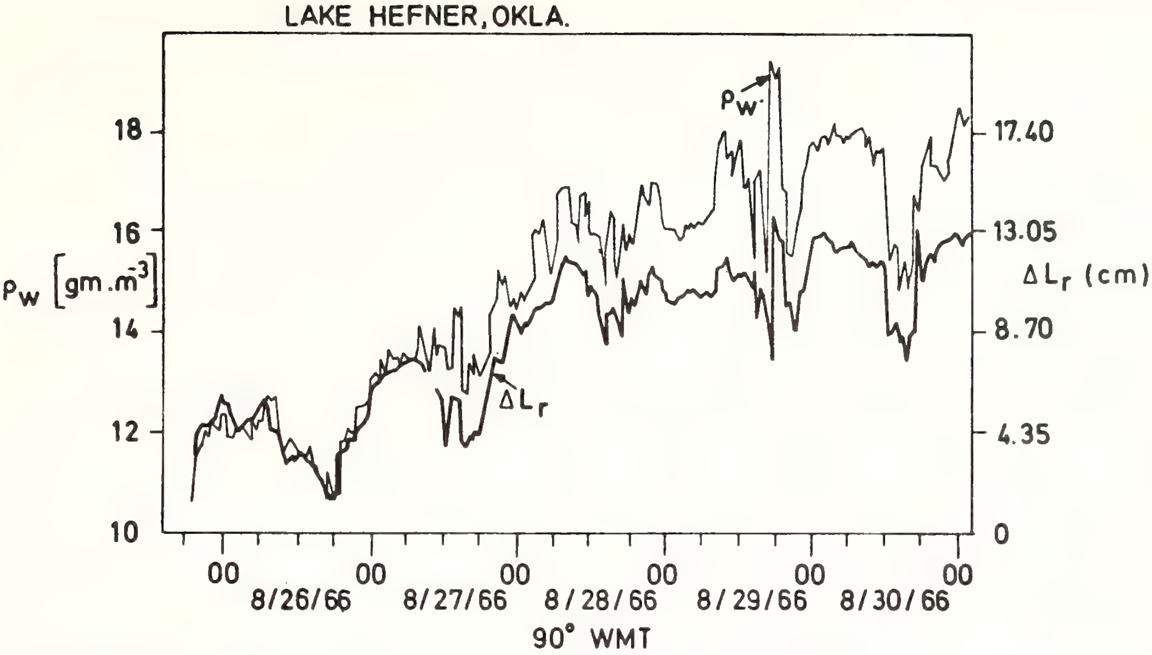

Fig. 58-4 The change of radio path length and the change of the point measurement of the water vapor density at the center of the path. (1.65 km path)

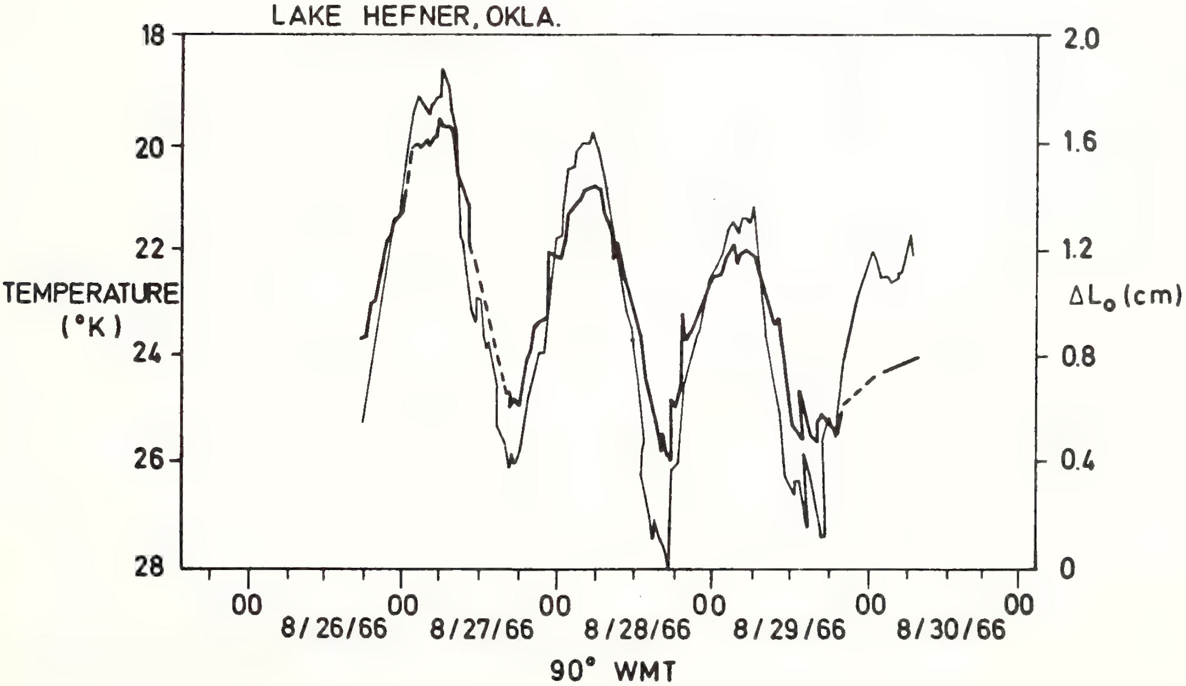

Fig. 58-5 The change of optical path length and the change of the point measurement of the temperature at the center of the path. (1.65 km path)

where the coefficients in equation 58-18 involve the constants K_1 to K_4 and the average values of the temperature, pressure and water vapor density. These coefficients are sensitive to the average conditions selected and can change appreciably. Graphs can be constructed so that appropriate coefficients can be chosen. For assumed values of:

$$<\bar{P}> \; = \; 1000 \text{ mb}$$

$$<\bar{T}> \; = \; 293°\text{K}$$

$$<\bar{\rho}_w> \; = \; 10 \text{ gm/m}^3 \; (\text{RH} \; = \; 58\%)$$

$$\Delta<\rho_w> = \frac{1.69 \times 10^5}{S}[\Delta L_R - 1.17\Delta L_O] + 0.009\Delta<P>$$

$$\Delta<T> = \frac{1.05 \times 10^6}{S}[-0.0091\Delta L_R - \Delta L_O] + 0.292\Delta<P> \qquad \text{(Eq. 58-19)}$$

which is of course similar to equation 58-17. It is seen that $\Delta<\rho_w>$ is only weakly dependent upon pressure changes whereas $\Delta <T>$ is significantly influenced. The sensitivity of the coefficients in these expressions can be appreciated when it is realized that a change in the mean value of $<\rho_w>$ of 2 gm/m^3 (a change of 12% in relative humidity at 293°K) produced negligible change in either $\Delta<\rho_w>$ or $\Delta <T>$; a change of 10 mb in the pressure reflected a change of less than 1% in the amplitude of $\Delta<\rho_w>$ or $\Delta <T>$; a change of 5°C in the mean value of the temperature will cause approximately 3.5% change in the apparent amplitude of both $\Delta<\rho_w>$ and $\Delta <T>$. Hence the degree of accuracy desired in the estimation of fluctuations of $<\rho_w>$ or $<T>$ about an arbitrary mean will determine the range over which these coefficients can be assumed constant. This is, more or less, under the control of the experimenter.

Consider how these perturbations are affected by the precision in ΔL_R and ΔL_O. ΔL_R and ΔL_O should have a precision of approximately 1 part in 10^7. Then from equation 58-19 the resolution in $\Delta<T>$ would be approximately 0.1°C and that of $\Delta<\rho_w>$ would be 0.02 gm/m^3.

An Initial Experimental Investigation of the Use of a Microwave-Optical System to Measure Water Vapor Density Variability

An initial investigation of this technique was made for a 5½ day period at Lake Hefner Oklahoma, in August of 1966. A microwave phase system (11) as well as an optical distance measuring system (10) were installed on a 1.65 km path over the lake. Meteorological measurements were made at both terminals and on a tower at the center of the path. Since evaporation suppressing films were spread from time to time on the surface of the lake, a large range of humidities were provided. (107 samples of 10-sec averages taken every half hour were used). The initial results have been published by Bean and Emmanuel (12). Figure 58-4 illustrates the comparison between the fluctuations in the radio path length and the variations in the water vapor density measured at the center of the path. Figure 58-5 shows the relationship between variations in the optical path length, L_O and temperature variations at the center of the path. The correlation coefficients between these variables are shown in Table 2.

It can be seen that the correlation between the radio path length (an integrated measurement) and the water vapor density (a point measurement) is quite good; however, a definite improvement results when the radio path is corrected by the optical path. The correction applied here was a first approximation since it was assumed that the effect of the air density was the same at both radio and optical frequencies.

It is noted that, on the average, quite good agreement is found between water vapor fluctuations and radio and optical path length variations. One can also compare the variance of water vapor density as measured at a point and that of the radio path length. Twenty-three ten minute samples (sampling rate = 1 sample/sec) were selected of the variance of the radio path length, and of the variances of both water vapor density and the radio refractive index at the center of the path.

The correlation between the variance of the refractive index and the variance of water vapor density both measured at the center of the lake is as expected, quite high (0.920). The correlation between the variance of the point measurement of the refractive index and the variance of the radio path length is lower (0.732) and that between the variances of water vapor density and the radio path even lower (0.554). Again one may wish to know how these variances are distributed and hence compare the spectrum of the water vapor density at the center of the path to the spectrum of the radio path length. Figure 58-6 shows the spectrum of the water vapor density at the path for daytime and nighttime conditions in the presence and in the absence of the evaporation suppressing film. Figure 58-7 is the spectrum of the radio path during the same times.

Conclusions

The use of the measurement of both the radio and optical path lengths to determine integrated water vapor density and temperature over a path appears to be a useful technique. The absolute value of $<\rho_w>$ can be measured with an uncertainty of approximately 2.75% while that of $<T>$ reflects an uncertainty of approximately 0.6%. Under average temperate conditions such techniques can resolve variations in $<\rho_w>$ of approximately 0.02 gm/m^3, and can resolve variations in $<T>$ of approximately 0.1°K.

With expected improvements in these techniques, it is possible that the uncertainties due to measurement capabilities can be reduced to several tenths of a percent. When such expected improvements are available, the applicability of the approximations used here would be questionable. Ultimately the precision of the coefficients in the equations for refractive index would be the limiting factor. This is particularly true in the case of the coefficient for the water vapor term.

References

1. **Bender, P.L.,** Proc. IEEE 55, 1039, 1967.

2. **Owens, J.C.,** 'The use of atmospheric dispersion in optical distance measurements', Rep., XIV Gen. Ass., IUGG, Lucerne, Switzerland, 1967.

3. **Thompson, M.C.,** 'A summary of progress in problems related to terrestrial electronic distance measuring in the U.S. since 1963', AGU Rept., IUGG Gen. Assy., Geodesy Section, 1967.

4. **Bean, B.R., Dutton, E.J.,** Radio Meteorology, NBS Monograph 92, Washington, D.C., U.S. Govt. Printing Office, 1966.

5. **Owens, J.C.,** private communication, 1967.

6. **Thompson, M.C., Janes, H.B.,** J. Res. NBS 63D (Radio Prop.), 45, 1959.

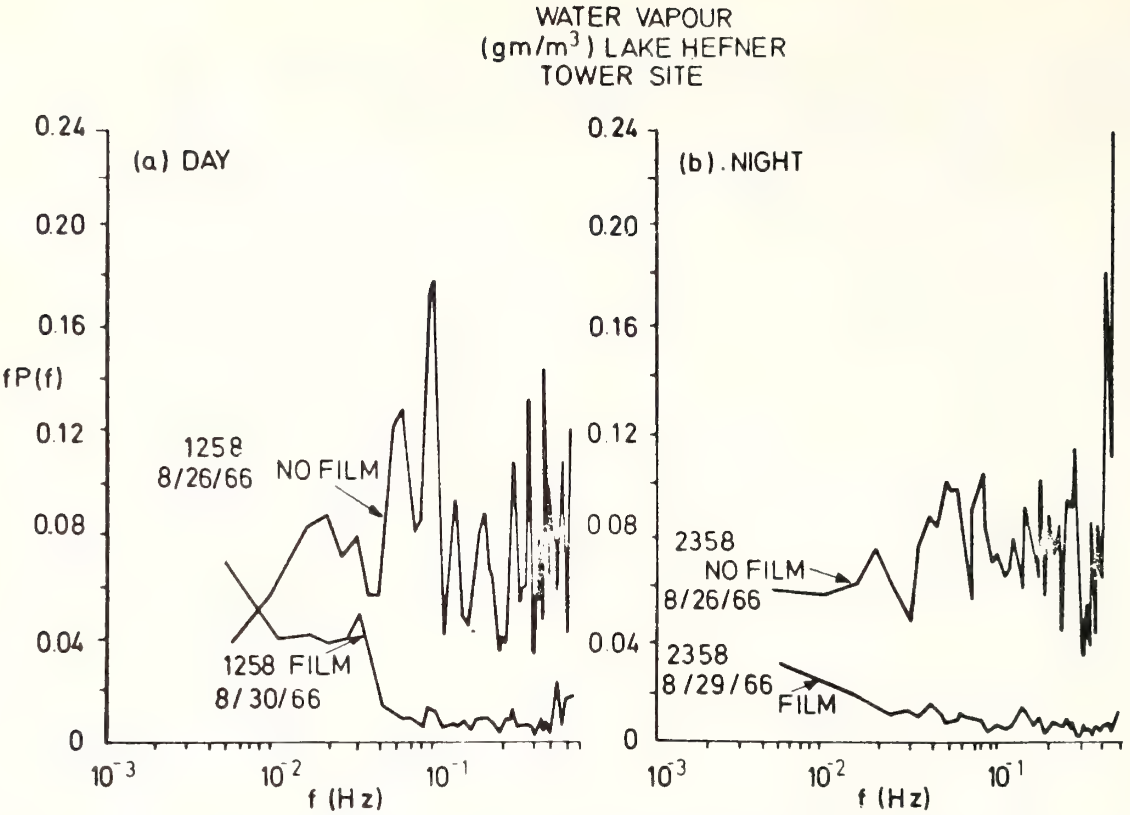

Fig. 58-6 Spectrum of water vapor density measured at the centre of a 1.65 km path in the presence and absence of an evaporation suppression film

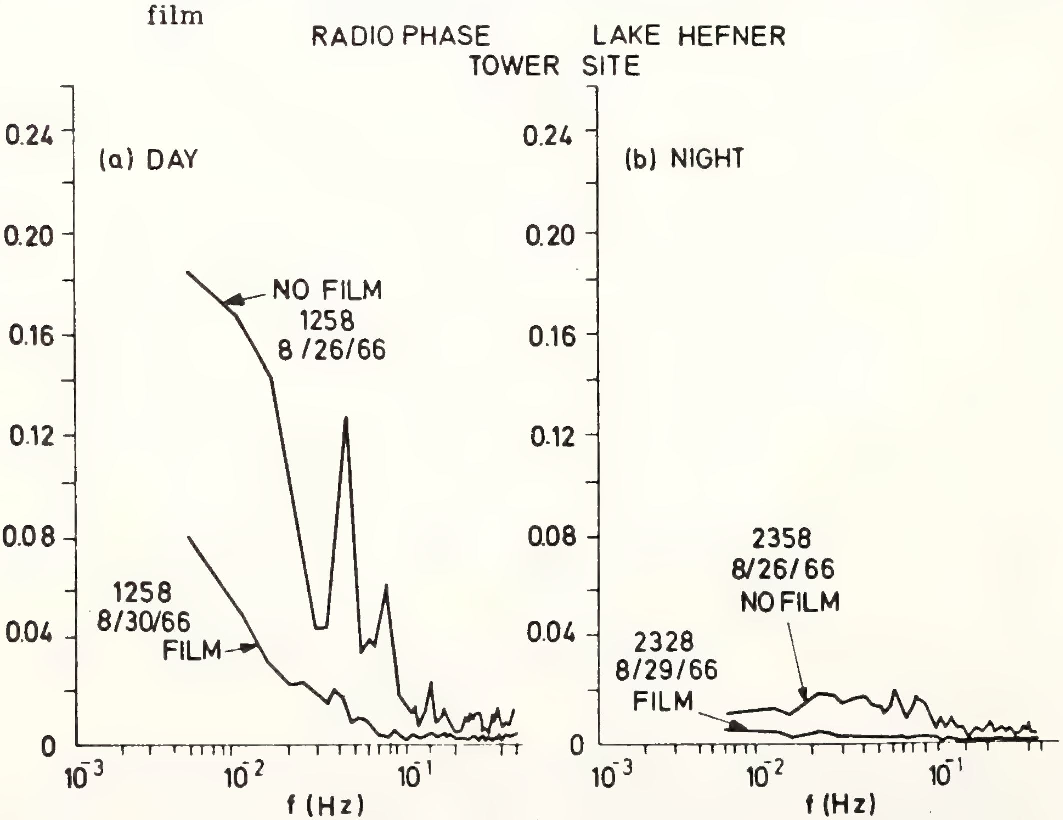

Fig. 58-7 Spectrum of the radio path length measured over a 1.65 km overwater path in the presence and absence of an evaporation suppression film

7. **Thompson, M.C., Janes, H.B.,** 'Radio path length stability of ground-to-ground microwave links', NBS Tech. Note No. 219, 1964.

8. **Bean, B.R., McGavin, R.E.,** 'The use of the radio refractometer to measure water vapor turbulence', Proc. Internat. Symp. on Humidity and Moisture, 1965.

9. **Herbstreit, J.W., Thompson, M.C.,** Proc. IRE 43, 1391, 1955.

10. **Earnshaw, K.B., Owens, J.C.,** IEEE J. Quantum Electron. QE-3, 544, 1967.

11. **Gilmer, R.O., Waters, D.M.,** 'A solid state system for measurement of integrated refractive index', ESSA Tech. Rept. IER-40/ITSA-40, Washington, D.C., U.S. Govt. Printing Office, 1967.

12. **Bean, B.R., Emmanuel, C.B.,** 'Application of radio and optical path length measurements to studies of low-level turbulence', Proc. Tech. Exchange Conf. Air Weather Service, USAF, 294, 1967.

Table 1 Radio path data and path average water vapor densities; Carrier frequency 9.4 GHz

Path	Date	Location	Site elevation and radio path morphology	Path length (km)	$\overset{\simeq}{\rho}_w$, g . m^{-3}	r($\overset{\simeq}{\rho}_w$, $\hat{\bar{\rho}}_w$)
1.	2/59	Boulder, Colo.	1667 & 1676 m Flat terrain	0.7	2.38	0.803
2.	6/59	Boulder, Colo.	1667 & 1714 m Flat terrain, low antenna heights.	3.2	6.18	0.871
3.	10/59	Cape Kennedy, Fla.	7 & 16 m Flat terrain, path at approximately grazing incidence to foliage.	7.7	21.60	0.622
4.	9/58	Boulder, Colo.	1760 & 1715 m Path over two valleys separated by a flat mesa containing a small lake.	15.2	6.10	0.890
5.	5/61	Boulder, Colo.	2240 & 1554 m Mountain top to relatively flat terrain with creek running by lower site.	15.5	3.61	0.909
6.	10, 11/59	Cape Kennedy, Fla.	3 & 9 m. Path crossed the Banana and Indian rivers with approximately half the path length over water.	17.1	17.30	0.983

Table 2

Variables	Correlation
L_O vs T	-0.915
L_O vs ρ	0.923
L_R vs ρ_w	0.956
$T(L_R - L_O)$ vs ρ_w	0.978

where ρ is the air density.

744

List of Mathematical Symbols

c	speed of light
d	transmission grating line width
n	numerical constant
prf	pulse repetition frequency
R	aircraft range to turbulence
u	aircraft range-rate
v	transverse gust velocity
v_m	maximum expected transverse gust velocity
w	average lobe width in diffraction pattern
γ	ratio of average lobe width to grating line width
θ	effective laser beamwidth
λ	wavelength of laser radiation
λ'	Doppler-shifted wavelength
ϕ	single lobe average angular beamwidth of backscattered light

Reprinted from Proceedings of the 14th Radar Meteorology Conference, November 17-20, 1970, 111-116, 1971.

RADAR OBSERVATIONS OF THE TURBULENT STRUCTURE IN SHEAR ZONES IN THE CLEAR ATMOSPHERE

Hans Ottersten*

CIRES, University of Colorado & ESSA Research Laboratories
Boulder, Colorado

1. INTRODUCTION

I want to disseminate some new ideas on the detailed spatial and temporal structure of the turbulent breakdown of shear flows in a stably stratified atmosphere. These concepts were conceived in an effort to explain the evolution of clear-air structures observed with sensitive radars in the statically stable atmosphere. Supporting evidence has been secured after detailed studies of radar images of vertical cross-sections of the clear atmosphere.

After specifying the atmospheric region of interest and describing its conditions for turbulence generation, we examine how radar observations of the structure in the clear atmosphere may be used to infer the structure of the streamlines in order to follow the progression of a turbulent breakdown. A new concept of turbulence generation emerges from such observations. The overturning is observed to occur initially at small scales and to be oriented in rows of laterally extended roll-instabilities (billows). In increasing turbulence the breakdown reiterates itself at discrete scales in successively larger vortex-rolls. The vortices also appear to lose their energy in discrete steps by transfer to smaller, secondary instabilities. Radar observations are discussed with evidence from studies of the destabilization and turbulent transition of shear flows in other media. Some of the implications of the new turbulence concept are pointed out.

2. THE STRUCTURE OF THE STABLE ATMOSPHERE

In the major part of the atmosphere, horizontal stratification and hydrostatic stability prevail. Local static stability is primarily determined by the vertical structure of potential temperature, which tends to suppress turbulent motion and preserve almost horizontal flow. Local vertical motion and turbulence is induced by mechanical energy extracted from the mean flow. The mean vertical gradient of the horizontal vector wind, or vertical wind shear, is the main source for the turbulent energy production.

These conditions apply typically in the free atmosphere, removed from the influence of topographical features or clouds and convective activity. They also closely describe situations in stratified clouds when radiative cooling or release of latent heat thermodynamically are of secondary importance, and in atmospheric zones under weak topographical influence, implying modification of the mean flow without strong interaction with the turbulent scales. Regions of strong topographical influence (boundary layer turbulence, lee wave rotors) and with dominant convective instability (plumes, thermals, convective clouds, Bénard cells) are left out. Finally, we recognize and exclude an interaction zone where positive buoyancy and mechanical forces are coupled, resulting in complex three-dimensional flow configurations (cloud and convective cell streets, sea-breeze fronts, precursor lines).

The fine-scale multi-layered character of the horizontally stratified, stable atmosphere has been revealed by sensitive radars capable of detecting fluctuations in water vapor and temperature of clear air. The layers correspond to zones of enhanced static stability, generally with evidence of accentuated vertical wind shear. Conventional rawinsondes are unable to depict this fine-scale vertical temperature structure and are even more inadequate for delineation of the wind profile. It is only after laborious experiments with high-resolution direct sensing techniques that the fine-scale structure has become evident. Increased variability in the parameters due to turbulent mixing in the layers is an additional complication in the determination of the mean profiles.

The detailed picture that emerges from the combined evidence of radar and direct sensing shows a multitude of thin, very stable layers imbedded between intervening regions of much less static stability. The layers are horizontally extensive and often accompanied by humidity gradients. Generation of such thin, very stable layers has been described by Scorer (1969). The vertical distribution of horizontal velocity appears to be related to the stability, resulting in accentuated vertical wind shears in very stable layers and weaker shears in less stable regions, much as predicted by Woods (1969a) on the basis of observations in the oceanic thermocline. Although more evidence from fine-scale atmospheric measurements is necessary to confirm this conjecture, we may intuitively accept it because we suspect that developing shears in regions of weak static stability soon would lead to hydrodynamic instability and redistribution of velocity, resulting in accentuated shears over the layers. We also expect the turbulence in the intervening regions of weak gradients to be weak, while in the layers we may expect outbursts of stronger turbulence when the energy stored in concentrated shear is released through dynamic instability. Further, tilting of very stable layers due to internal fronts, gravity waves or mountain waves will result in accentuated vertical shear inducing additional vorticity. Actually, such tilting due to internal waves has been shown to modulate turbulence generation on thin stable "sheets" within the thermocline (Woods, 1969a). The tilting process offers an explanation to strongly dynamical situations when shears increase rapidly and produce violent outbursts of turbulence.

---

*Formerly with Air Force Cambridge Research Laboratories, Bedford, Massachusetts

Preprints of the Fourteenth Radar Meteorology Conference, November 17-20, 1970, Tucson, Arizona.
American Meteorological Society, Boston, Massachusetts

The predominant mechanism producing dynamic instability in stable shear layers generates wavelike disturbances that grow and overturn into roll-like vortices, or billows, which extend horizontally in parallel rolls across the shear vector. Scorer (1969) has deduced some of their properties from observations of cloud billows. Billows are believed to be manifestations of Kelvin-Helmholtz instability and are probably the main cause of bumpiness and violent accelerations experienced in aircraft flight and reported as CAT (clear-air turbulence). Billows also generate eddies of smaller scales and of more random nature by static instability in their interior and, possibly, by secondary dynamic instabilities along their boundaries.

3. RADAR IMAGES OF THE CLEAR STABLE ATMOSPHERE

During the last few years studies with sensitive radars have revealed structures in clear air which closely resemble the patterns generated by billow-type roll-instabilities. Radar echoes from such structures have been found to be associated with CAT. The echoes originate from regions of enhanced static stability and strong vertical wind shear.

3.1. Clear-Air Backscattering

The clear-air echoes are caused by backscattering from the small-scale refractive-index fluctuations resulting from mixing of strong mean gradients in water vapor and/or temperature. In the lower atmosphere, the water vapor contributions to the refractive-index variability generally dominate. In the highest layers temperature variations may be the main cause. (The polar molecules of water vapor interact strongly with high-frequency radio fields, and, therefore, the influence of water vapor variability on radio refractive-index fluctuations is amplified several orders of magnitude compared to its fairly weak effect on density variations.)

The backscattering process is selective in as much as only refractive-index inhomogeneities with scale sizes of half the radar wavelength and oriented in surfaces orthogonal to the radar beam contribute significantly to the returning signal. This implies that clear-air structures showing no appreciable angular dependence in radar reflectivity contain a three-dimensional distribution of refractive-index irregularities without strong anisotropy. Almost isotropic radar reflectivity, although selective in scale size, indicates the degree of general variability in the refractive-index field because the backscattering small-scale irregularities result from the breakdown of inhomogeneities of larger scale. It may then be inferred that these irregularities, and the resulting radar returns, evidence the presence of velocity perturbations, small-scale turbulence and larger, possibly anisotropic, whirls (Ottersten, 1969). An alternative, but unsubstantiated, interpretation is that the irregularities are "fossil turbulence," the three-dimensional microstructure of temperature and humidity produced by a turbulent field that has since decayed (Woods, 1969b).

3.2. Flow Visualization by Radar

In Figure 1 are shown photos of range-height indicator (RHI) displays that represent vertical cross-sections through the clear atmosphere. The tracing on the right brings out the structural details that are observed in clear-air layers. The radar reflectivity from such layers show no appreciable angular dependence, and it is concluded that the enhanced refractive-index variability in the layers is almost isotropic at the cm-scales, which are responsible for the backscattering.

Small-scale refractive-index irregularities serve as tracers for radar and outline the general structure of the clear atmosphere on radar displays. Moreover, if care is exercised, motions in the clear air may be deduced from radar images. Identification of structural features in RHI sequences through clear-air layers reveal that turbulent patches and associated refractive-index structure are advected with velocities that agree well with rawinsonde determinations of the mean flow. Similarly, vertical motions caused by traveling waves or local instabilities in shearing layers are revealed by displacements of the layers, and the streamlines may be inferred from the patterns outlined on radar images. This is permissible provided that the interpretation of the patterns accounts for the fact that the velocity perturbations also may modify the small-scale refractive-index variability and thus modulate the intensity of the radar return.

The three-dimensional configuration of the streamlines may be deduced from RHI's in various azimuths. RHI sequences in the up- or downwind direction allow identification of evolutionary changes in the structures that are advected with the wind toward or away from the radar. Such radar images compiled into motion pictures with a speeded up time scale give a vivid display of the motions in the clear air and allow the eye to readily follow the advection of perturbations in the flow.

Hicks (1968) and Hicks and Angell (1968) examined radar observations of large-scale wavelike disturbances, such as those perturbing the clear-air layers in Figure 1, and concluded that they were caused by breaking waves in stable regions characterized by vertical wind shear. They noted the considerable lateral extent of the structures and the

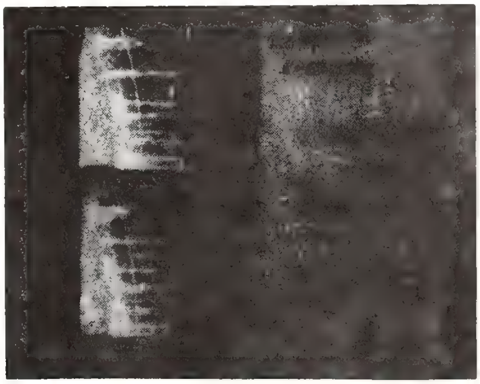

Fig. 1. RHI photos in 120° azimuth taken at 1515 EST (top picture 4.5 minutes earlier) on Jan. 9, 1969 with the 10.7-cm radar at Wallops Island, Va. Azimuth is about 35° off downwind direction; directional shears are weak. Tracings on the right demonstrate the ubiquity of wave-like perturbations of various scales in clear-air layers. Tracings of individual perturbations throughout a time period identify them as rolls of considerable lateral extension across the flow, which are advected through the observation plane with the mean flow.

preference for the wave crests to be aligned nearly normal to the vertical shear vector. The wavelike disturbances grew into a vortex-stage resulting in overturning and probable turbulence. The description is consistent with the characteristics of developing billows due to hydrodynamic instability forming rows of laterally extended vortex-rolls.

A dilemma seems to present itself at the interpretation of radar observations of clear-air billows. The turbulent breakdown process is generally visualized as a generation of large, anisotropic whirls at an outer scale followed by a continuous cascade of kinetic energy through successively smaller and more isotropic eddies, to the eventual frictional dissipation at the smallest scales. The turbulence draws energy from the vertical wind shear, which is diminished. Refractive-index inhomogeneities are produced when the overturning perturbs the boundaries between air streams and turbulence breaks up the vertical contrasts in temperature and water vapor between adjacent air layers.--Obviously, some of the wavelike instabilities in Figure 1 are too young to cascade but are outlined by pre-existing small-scale refractive-index tracers.--The concept of a turbulence cascade probably triggered the idea of "fossil turbulence" in the clear atmosphere: "If the initial stages of the overturning is revealed by the radar, the small-scale refractive-index tracers, known to be nearly isotropic, must be remnants of some earlier turbulence process, which has decayed, leaving three-dimensional structure only in the scalars to outline a new breakdown, if suitably located."

4. A NEW CONCEPT OF TURBULENCE GENERATION

The idea of "fossil turbulence" in clear-air layers does not conform with the experience from simultaneous investigations of CAT with radar and aircraft (Glover et al., 1969). Such joint soundings reveal at least perceptible turbulence even in thin radar layers, apparently destitute of perturbations. Consequently, a concept emerged of initial small-scale turbulent breakdown in substrata within atmospheric shear zones. In strongly dynamical situations of rapid shear enhancement, successive large-scale breakdown was conceivable since the initial turbulence could be unable to accomplish completely the shear destabilization because of the limited momentum-distributing capability of the small eddies induced by the initial instability. Subsequently, detailed analysis of RHI sequences of improved spatial and temporal resolution secured evidence of small-scale instabilities in all clear-air layers and revealed the existence of consecutive turbulent breakdown at successively larger scales.

Although the cascading process may be a basic element in all turbulence generation, detailed radar observations of the turbulent structure in shear zones in the clear atmosphere reveal a more complex breakdown procedure with simultaneous or successive generation of vortices at several discrete scales. These whirls are distinctly separate in size and are not connected by any intermediate-size eddies. Moreover, there is clear evidence that the turbulence is initially generated at small scale sizes and that additional and separate breakdown occurs at successively larger scales for turbulence of increasing intensity. It is not necessary to postulate the existence of "fossil turbulence" to explain radar observations of clear-air billows, because it appears that large-scale instability is always preceded by small-scale turbulence and associated refractive-index variability.

The initial breakdown occurs in thin friction layers and is organized in rows of laterally extended roll-instabilities (Figure 2 a). In increasing turbulence, second and possibly higher generations of larger, but similar, roll-instabilities develop (Figure 2 b). These instabilities have a larger vertical extent and may enroll one or several friction layers (Figure 2 c). Three-dimensional flow configurations may result. The radar returns from the layers outline the higher generation instabilities, and the patterns resemble the structures that have been observed in clouds (Ludlam, 1967; Scorer, 1969), in the ocean (Woods, 1969a), and in the laboratory (Thorpe, 1969), and that have been interpreted as manifestations of Kelvin-Helmholtz instability.

The radar reflectivity of the friction layers intensifies when the layers are perturbed by higher generations of roll-instabilities. This implies that the small-scale, three-dimensional variability in refractive index is enhanced by the flow imposed by the larger rolls. This may be the result of the initial friction-layer turbulence mixing the enhanced local gradients at the boundaries of the larger rolls. There is also some evidence that small, secondary instabilities develop locally along the boundaries and produce the enhanced refractive-index variability (Figure 2 d). Again, the secondary instabilities are clearly separated in size from their parent roll and are essentially confined to its boundaries. It is not clear whether the secondary instabilities are oriented.

It appears that the parent roll sometimes never overturns before it loses its energy to these secondary instabilities or to the preceding friction-layer turbulence. Thus, not only is the formation of turbulence initially confined to several discrete

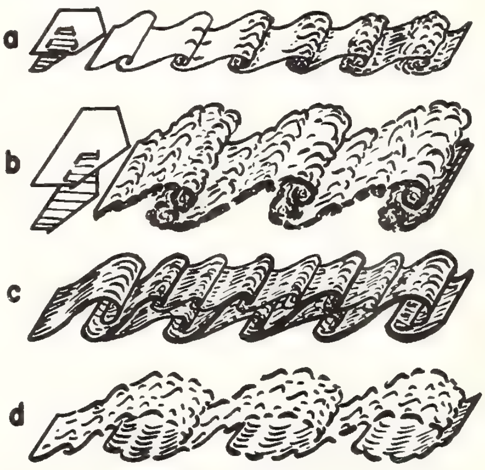

Fig. 2. The successive generation of vortices at several discrete scales. (a) The initial breakdown forms small billows in thin friction layers. (b) In increasing turbulence higher generations of rolls form. (c) Several friction layers may join in large instabilities. Three-dimensional flow configurations may result (not shown). (d) Secondary instabilities perturb the boundaries of the parent rolls.

sizes of vortices, but these parent vortices also transfer their energy in discrete steps to smaller instabilities. A continuous cascading process through successively smaller eddies does not occur, except possibly during complete overturning within individual billows, when convective instability may produce motions on a range of scales. This process does not lend itself to radar study because of the weak refractive-index contrasts in the interior of rolls. (Buoyancy-induced mixing strives to annihilate refractive-index contrasts, as opposed to mechanical mixing, which creates refractive-index variability by intensifying local contrasts at the expense of large scale inhomogeneity).

4.1. The Initial Turbulent Breakdown

The size of the roll-instabilities, observed with radar in clear air, varies from layer to layer. Evidence of quite small rolls is often seen in the regular RHI's (Figure 1) obtained with the 10.7-cm radar (0.48°) at Wallops Island, Virginia. When the returns are sufficiently strong, the 3.2-cm radar at the same location confirms this observation. This radar has a better angular resolution (0.21°) but is not sufficiently sensitive to show much of the clear-air backscattering. The angular resolution of the 71.5-cm radar at Wallops Island is poor (2.9°). Only very large roll-instabilities are indicated on this radar. It shows thick stratified clear-air returns from shear zones that, when viewed at better resolution, are revealed to consist of multiple layers with interior perturbations.

For detailed analysis of clear-air structures RHI's were obtained every 30 seconds in extended sequences, generally in the up- or downwind direction. The pulse of the 10.7-cm radar was shortened to provide a spatial resolution better than 75 m within 9 km range, compared to the 200-300 m of the regular RHI's. Temperature and wind data matching the temporal and spatial resolution of the radar data was not available. Figure 3 shows two RHI's, 2.5 minutes apart, excerpted from a 90-minute sequence in the upwind direction. On the right, tracings every 30 seconds follow the mean flow toward the radar (top to bottom) to show the evolution in the friction layer at 2.3 km altitude.

With improved spatial radar resolution multiple layers become increasingly evident within shear zones coarsely outlined on radar images of poor resolution. Five layers or more may be distinguished within a 1 km altitude interval. The thickness of these fine layers often appears to be less than 75 m. We interpret this as evidence for a vertical substructure in temperature and wind with locally increased vertical shears at substrata of enhanced static stability, often accompanied by water vapor gradients, the main source of refractive-index variability. Fine-scale meteorological profiles to verify this conjecture are not available but stratified radar layers in general correspond to zones of enhanced static stability with vertical wind and vapor gradients (Ottersten, 1969). The overturning observed in individual fine layers substantiates presence of vertical shear.

In each and every one of the fine layers a granular structure is obvious from time to time. We interpret this as evidence of overturning, since in the more clear cases horizontal rows of separate elements develop in previously echo-free space, advect with the mean flow, and merge into fine layers or disperse. The individual elements have been shown to be cylinders with lateral extensions up to several hundred meters, considerably exceeding their dimensions in vertical section. (Identification for several minutes of individual elements during advection is sufficient evidence when the plane of observation not quite coincides with the wind direction). On the radar the vertical dimension of these rolls is about 75 m. The actual scale of the overturning may be considerably less. The horizontal separation between the rolls is about 200-400 m when a regular spacing is evident.

Whether these rolls are manifestations of the initial overturning or if they actually are preceded by even smaller instabilities cannot be determined conclusively. It is conceivable that they are structures of the type in Figure 2a which do not become visible to the radar until the individual billows burst because of convective instability. The resulting eddies would form a "friction layer" with a marked increase in momentum distribution and frictional dissipation when the laminar flow breaks down. The radar studies indicate that this process often is sufficient to diminish the shear. The roll-instabilities merge, and the layers disperse or are maintained by continued or new instability without any visible increase in the size of the generating eddies. We believe that this is the ordinary progression of turbulent breakdown in shear flows, which goes on intermittently in various thin layers everywhere in the stable atmosphere, apparently at scales of a few tens of meters.

4.2. Consecutive Instability at Successively Larger Scales

At times friction layers are perturbed by larger roll-instabilities. These have horizontal separations from 0.5 km up to a few km and vertical dimensions from about 200 m up to 1 km in rare instances. Hicks and Angell (1968) have given more

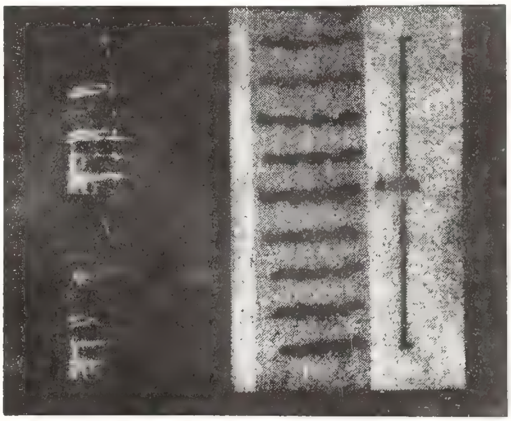

Fig. 3. RHI photos 2.5 minutes apart taken at about 1105 EST on October 20, 1969, with the 10.7-cm radar at Wallops Island, Virginia, in 245° azimuth, no more than 15° off upwind direction which varies little. Tracings every 30 seconds of fine layer at 2.3 km altitude follow the mean flow toward the radar and show initial small-scale roll-instabilities merging while larger rolls develop (top to bottom). Top tracing is from top picture, sixth from top traces bottom picture. Spatial resolution is better than 75 m within 9 km range.

details on these instabilities. Figure 3 traces an apparent second generation instability deforming one single friction layer. The large rolls in Figure 1 at an altitude of 5 km enroll two or more friction layers and may be of third generation, since they were preceded by intermediate instabilities in two different layers, which presumably were outlined by previous friction layers. The large rolls seemed to overturn completely and left two vertically separated layers dissipating, one of which later produced new intermediate instabilities. Occasionally, one single large roll has been observed in layers with intermediate instabilities. Other times the structures are entangled, and the situation appears too complex to resolve. Common denominators of the higher generation instabilities, appear to be previous turbulent activity of smaller scale and local increase in radar reflectivity in the new perturbations.

Also the large perturbations appear to be advected with the mean flow and are therefore better characterized as roll-instabilities than as traveling waves that break. It is probable, however, that the pre-existing flow configuration in the friction layers influences the higher generation breakdown and that the analogy with Kelvin-Helmholtz instability has deficiencies. Tilting of stable zones, reported by Woods (1969a) to trigger roll-instabilities in the thermocline, is observed in the clear atmosphere too and is probably the mechanism responsible for the rapid shear enhancement required for consecutive instability. Sloping layers and indications of true, long waves have been observed by radar in the clear atmosphere. Boucher (1970) has described a well-documented case of moderate CAT in a sloping subsidence inversion with presence of large clear-air billows on radar. Internal fronts with steep slopes are known to be associated with CAT.

4.3. Secondary Instability

The increase in radar reflectivity evident in the upward slopes of developing roll-instabilities implies an intensifying of cm-scale refractive-index variability. As explained by Scorer (1969), the vorticity advection in developing billows results in a thickening of the original stable layer toward the vortices, while the gradients are enhanced in the thinned tilted layer between vortices. This process will operate also in consecutive instabilities although the preceding friction layer turbulence will feed on enhanced shear in the tilted parts of the layer and transfer refractive-index contrasts to small-scale inhomogeneity. This may not diminish the shear sufficiently fast, however, since there is some radar evidence that small, secondary instabilities develop in the slopes. Small protuberances are often evident along the boundaries of large clear-air billows. These could be manifestations of secondary instabilities responsible for enhancement of refractive-index variability and radar reflectivity. Secondary instabilities may also operate in the billows formed during the initial overturning (Figure 2 a) and these instabilities, rather than the bursting billows, may be responsible for the first radar echo.

The possibility of secondary instabilities in the tilted layer between vortices and evidence of such instability in various media have been recognized by many investigators. It is not clear if these small instabilities are oriented or if they are responsible for a three-dimensional flow at small scales. The radar images can just barely point to the existence of secondary instabilities, much less answer the question of their flow configuration. It appears probable, however, that these small instabilities produce three-dimensionality in the maximum property-inhomogeneity structure along the boundaries of the parent roll. The instructive tilted tube experiments by Thorpe (1968) with fluids of different densities for the visualization of shear flow destabilization support this conclusion. In Figure 4, from one of Thorpe's experiments, small whirls riding upon large rolls evidence secondary instability along the boundaries of the parent rolls. The progression of this particular experiment also gives evidence of consecutive instability at successively larger scales (Thorpe, priv. comm.). Initial roll-instabilities in the accelerating shear flow have paired and amalgamated in a second generation of instabilities of larger scale, the large parent rolls in Figure 4. Thorpe (1968) also notes the tendency toward three-dimensional flow when the first generation rolls start winding around each other during the amalgamation. With the development of secondary instabilities the boundaries of the entire flow configuration are outlined by small-scale inhomogeneity in a pattern that strongly resembles the "rope-like" structures observed by radar in completely overturned clear-air layers.

Developing roll-instabilities in the clear atmosphere do not always proceed to complete overturning. Presumably, the supply of vertical wind shear is not sufficient to overturn the rolls in presence of friction layer turbulence which continuously drains energy out of the higher generation instabilities. If secondary instabilities develop at an early stage, they may also inhibit the overturning of their parent roll. In these instances the higher generation rolls extract energy from the mean flow but transfer this energy in discrete steps to small vortices without a cascade through intermediate eddies.

5. CONCLUSIONS AND IMPLICATIONS

Radar observations of shear zones in a clear stable atmosphere reveal substrata of enhanced static stability, where vertical wind shears are accentuated and produce small-scale overturning and turbulence in friction layers separating the air streams. The

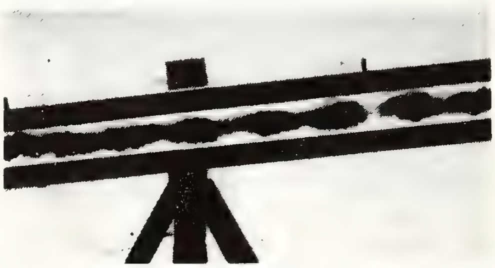

Fig. 4. Shear flow destabilization in a tilted tube experiment with a colored fluid of intermediate density between two clear fluids, the lower heavier. Initial instabilities in the accelerating shear flow have paired and amalgamated in a second generation of instabilities, visible here as large rolls. Small whirls riding upon the rolls evidence secondary instability and three-dimensionality in the maximum property-inhomogeneity structure along the interface. (Courtesy S. A. Thorpe. See Thorpe, 1968).

initial overturning is organized in rows of laterally extended roll-instabilities. Resulting eddies distribute momentum and diminish the shear, and the layers disperse. The process repeats itself intermittently. This is probably the ordinary progression of turbulent breakdown of shear flows in the stable atmosphere. The largest scales involved in the overturning motion appear to be a few tens of meters. In the dry parts of the atmosphere, this process will be difficult to detect even with sensitive radars.

When vertical wind shears are accentuated rapidly, the initial small roll-instabilities are unable to accomplish completely the destabilization and turbulent transition of the shear flow. The turbulence intensity increases by consecutive roll-instability at successively larger scales. These instabilities are always preceded by one or more friction layers which participate in the new roll-up. The higher generations of roll-instabilities produce substantial CAT and are more readily detected by radar because of the associated increase in cm-scale refractive-index variability. Tilting of very stable layers by internal fronts, gravity waves, and mountain waves is believed to be the dynamical process which accentuates the vertical wind shear and triggers consecutive instability. The local increase in cm-scale refractive-index variability, associated with development of higher generations of roll-instabilities, is the result of enhanced gradients in the thinned tilted layer between vortices, probably in combination with secondary instabilities along the boundaries of the large rolls. The turbulence in the boundaries feeds on enhanced shear in the tilted layer and transfers refractive-index contrasts to small-scale inhomogeneity. Friction layer turbulence and secondary instabilities drain energy from the large rolls and may prohibit their complete overturning.

Large-scale overturning and formation of hazardous turbulence is unveiled by radar because refractive-index contrasts generated by the preceding smaller roll-instabilities are accentuated when subsequent higher generation rolls form. The success of radar detection of CAT is, therefore, mainly a question of the sensitivity and resolution of the radars employed. In the lower humid atmosphere, strong echoes may originate from weakly turbulent regions associated with strong water vapor gradients. Identification of the largest scale of the overturning can resolve these cases.

Formation of wave clouds and cloud billows depends on the condensation levels in the atmosphere. Flow visualization by radar is not as radically dependent on the water vapor distribution. Tilting of very stable layers in mountain waves will continually generate friction layers, and sensitive radars could delineate the flow even prior to large-scale overturning and formation of lee wave rotors. Incorporation of a mountain-wave radar in lee wave investigations will be the most prolific effort for furthering the understanding of motions in the clear atmosphere. In addition, radar detection of CAT may be tested in the environment where operational applications are foreseen.

The spectral distribution of kinetic energy in turbulent components is of considerable interest in aeronautical design and in studies of the turbulent energy budget. The new concept of turbulence generation points to the existence of several "spectral gaps," intermittency and "self-similarity" in the turbulent structure, and an interplay at various scales between organized overturning and more random and isotropic motions. Resolution of these issues will require a deterministic approach, which avoids statistical compiling of turbulence data and promotes subtle analysis of carefully selected time histories of overturning in order to explain the structure in the context of a physical process evolving in a changing environment. It is inconceivable to me how hydrodynamic experiments in the atmosphere can be conducted intelligently without the aid of a radar capable of resolving the three-dimensional structure in clear air for direction of interrogating aircraft. "Wavelengths" measured by aircraft during traverses of anisotropic structures cannot be attributed any significance unless they are interpreted in relation to the existing three-dimensional structure. Identification of the wind shear vector as a unique direction already in the data-taking-phase may conceivably assist the analysis.

6. ACKNOWLEDGEMENT

I am deeply indebted to my former colleagues of the Weather Radar Branch, Air Force Cambridge Research Laboratories, and particularly to its chief, Dr. Kenneth Hardy, for continuous exchange of results and ideas. The radar data were obtained through the cooperative efforts by Mr. Jack Howard and his crew at the JAFNA radar facility. The research conducted at Wallops Island has been supported in part by the National Aeronautics and Space Administration, Wallops Station.

7. REFERENCES

Boucher, R. J., 1970: CAT at a subsidence inversion: A case study. J. Appl. Meteor., 9, 534-537.

Glover, K. M., R J. Boucher, H. Ottersten, and K. R. Hardy, 1969: Simultaneous radar, aircraft and meteorological investigations of clear air turbulence. J. Appl. Meteor., 8, 634-640.

Hicks, J. J., 1968: Radar observations of gravitational waves in a clear atmosphere. Proc. 13th Radar Meteor. Conf., Boston, Amer. Meteor. Soc. 258-261.

Hicks, J. J., and J. K. Angell, 1968: Radar observations of breaking gravitational waves in the visually clear atmosphere. J. Appl. Meteor., 7, 114-121.

Ludlam, F. H., 1967: Characteristics of billow clouds and their relation to clear-air turbulence. Quart. J. Roy. Meteor. Soc., 93, 419-435.

Ottersten, H., 1969: Atmospheric structure and radar backscattering in clear air. Radio Sci., 4, 1179-1193.

Scorer, R. S., 1969: Billow mechanics. Radio Sci. 4, 1299-1307.

Thorpe, S. A., 1968: A method of producing a shear flow in a stratified fluid. J. Fluid Mech., 32, 693-704.

Thorpe, S. A., 1969: Experiments on the stability of stratified shear flows. Radio Sci., 4, 1327-1331.

Woods, J. D., 1969a: On Richardson's number as a criterion for laminar-turbulent-laminar transition in the ocean and atmosphere. Radio Sci., 4, 1289-1298.

Woods, J. D., 1969b: Fossil turbulence. Radio Sci., 4, 1365-1367.

34

Reprinted from Proceedings of the 1971 International Symposium on Antennas and Propagation, Japan, Vol. 2-IV B2, 237-238, 1971.

2-IV B2

REMOTE PROBES FOR THE STUDY OF ATMOSPHERIC SOURCES OF FADING ON OPTICAL AND MICROWAVE LINE-OF-SIGHT PATHS

B. R. Bean*, H. T. Dougherty†, and R. E. McGavin*
U. S. Department of Commerce
*National Oceanic and Atmospheric Administration
†Office of Telecommunications
Boulder, Colorado, U.S.A.

Fading on microwave or optical line-of-sight paths may be due to either ground-reflection multipath, atmospheric multipath, or defocusing. The identification of the particular mechanism involved has been hampered by the lack of rapid fine-scale meteorological measurements in the immediate vicinity of the propagation path.

As early as 1968, acoustic radars had been developed[1] which could detect fluctuations of temperature (effectively fluctuations in the optical refractivities) in the lower atmosphere. The characteristics of these radars are amply described in the literature[2,3].

Recently a new tool, the FM-CW Radar[4,5] was developed which has the capability of detecting small fluctuations of the radio refractivity in the atmosphere. This is particularly appropriate for the microwave region where both temperature and water vapor fluctuations can play significant roles. Herein is described a study made in eastern Colorado where the propagation medium was monitored by each of these radars particularly at times when fading occurred over a line-of-sight path.

This experiment was conducted at Haswell, Colorado where a large bowl-like depression produces a variety of extreme refractivity structures by nocturnal radiative cooling with the attendant pooling of cool air. After sunrise, solar heating results in vertical motion. A 23 km microwave-optical path was established across the bowl to provide near grazing intersection with the atmospheric layers to maximize the effects of forward scattering during turbulent conditions and "specular" reflection during inversion conditions. The microwave antennas were tilted upward so that ground reflections would be minimized under well-mixed conditions. Standard surface meteorological measurements were made at each terminal. At midpath measurements were made at fixed points and on an instrumented carriage of a 150-meter meteorological tower.

At midpoint and near the meteorological tower (250 meters away in the direction of the prevailing wind) the radar was located to monitor the propagation medium. In the fall of 1969 the acoustic radar (950 Hz) was used, in the fall of 1970 the FM-CW Radar (3 GHz) was used.

In 1969, the phase of the microwave signal (9.5 GHz) and the modulation of the optical signal (3.2 GHz), the amplitudes and the angle of arrival of the optical signal were recorded. In 1970, the modulation on the optical signal was replaced by the relative phase between microwave signals recorded from two vertically spaced (4.25m) antennas. At the tower the radio refractivity and its structure function, and the three-dimensional wind were recorded at several fixed elevations as well as on the movable carriage. The FM-CW Radar provided a continuous measurement of the fluctuations of radio refractivity as a function of height. The acoustic radar provided a similar measurement of the temperature fluctuations. This permitted measurement of the atmospheric structure for vertical motion too rapid to be observed by the carriage on the meteorological tower.

Calibration of the FM-CW Radar returns in terms of meteorological parameters was conducted at a time when the atmospheric structure appeared to be stationary and when the line-of-sight signals were steady.

Comparison between the FM-CW Radar returns and the refractivity structure on the tower was surprisingly good. Agreement was obtained to within a factor of two between the reflectivities calculated from the radar and those calculated from the tower even though both varied from 10^{-13} to 10^{-15}. The radar sees fluctuations particularly at scales of approximately one-half the transmitted wavelength. These fluctuations occur in the region where there are sharp breaks in the vertical profile, and hence the radars can detect layers.

In most cases the layer was first detected by the FM-CW Radar which then permitted the operator at the tower to place the carriage in the appropriate location.

Both radars illustrated the difficulty of applying point measurements or tower measurements to line-of-sight paths. The atmospheric structure changes rapidly with time; layers form and move with surprisingly large vertical velocities. Very thin but very intense layers were noted by the radars and confirmed by the carriage on the tower; such layers could easily be missed by conventional tower measurements. Such layers have a strong influence on signal characteristics on a line-of sight path. Fades as deep as 30 db were noted at times when these layers were moving and crossed the zero angle of incidence region.

At times, particularly at sunup, considerable fluctuations of the amplitude and phase were observed over the microwave-optical path. On one occasion three distinct images of the laser beam were noted at the receiving terminal; concurrent observation at mid-path indicated that the optical path was incident upon the temperature inversion at a shallow angle.

On the occasions when rapid microwave amplitude and phase fluctuations occurred, both the radar and the tower indicated the presence of a layer intersecting the line-of-sight path at a shallow angle. When the layer rose well above the microwave optical path, the fluctuations on the line-of-sight path ceased.

From measurements made at midpath and from the surface meteorological measurements at the path terminals, various atmospheric models were constructed.

Ray tracing techniques were then applied to these model structures to obtain estimates of the received signal behavior for comparison with the observed fields.

This comparison indicated that the atmospheric layers were often tilted along the line-of-sight path. Although this was consistent with the radar observations, the radar does not definitively distinguish, at this time, between wave motion on the layers and a vertical motion of horizontal stratification.

The radio and optical refractivity structures introduced multiple-imaging or atmospheric multipath with appreciable variation of the take-off angles and angles-of-arrival and, in the case of the microwave path, a shifting of the centers of reflection on the terrain. These marked changes in the angles-of-arrival interfered with beam-tracking on the optical path and caused signal variation on the microwave path attributable to the effect of the antenna patterns.

These effects were most pronounced when the refractivity layers observed at midpath were positioned between the elevations of the line-of-sight path terminals; the effects disappeared when the layers dropped below the elevation of the lower terminal or rose above that of the higher terminal.

References

1. McAllister, L.G., J.R. Pollard, A.R. Mahoney, and P.J.R. Shaw. Proc. IEEE 57, 4, Apr. 1969.
2. McAllister, L.G. J. Atmos. Terr. Phys. 30, 1968.
3. Little, C.G. Proc. IEEE 57, 4, Apr. 1969.
4. Richter, J.H. Radio Sci. 12, 1969.
5. Bean, B.R., R.E. McGavin, R.B. Chadwick, and B.D. Warner. Boundary Layer Met., 4, Apr. 1971.

Reprinted from Boundary Layer Meteorology 1, No. 4, 466-473, 1971.

PRELIMINARY RESULTS OF UTILIZING THE HIGH RESOLUTION FM RADAR AS A BOUNDARY-LAYER PROBE

B. R. BEAN and R. E. McGAVIN
NOAA, Boulder, Colo., U.S.A.

and

R. B. CHADWICK and B. D. WARNER
Institute for Telecommunication Sciences, Boulder, Colo., U.S.A.

(Received 14 december, 1970)

Abstract. Comparison of meteorological tower measurements with a high resolution CW-FM radar indicates that the device is applicable to studies of structure of temperature inversions, stable and unstable waves upon such inversions, thermal plumes and convective processes within the boundary layer. The radar also appears to follow the transport of insects by such processes.

1. Introduction

The introduction of the 10-cm CW-FM radar technique by Richter (1969) for studies of clear-air fluctuations of refractivity has rapidly led to studies of elevated inversions (Richter, 1969), gravity waves on these inversions (Gossard and Richter, 1970) and to a detailed discussion by Atlas *et al.* (1970) on the possibility that the breaking of these waves is a cause of clear-air turbulence.

We will report here on the adaption of Richter's technique to probe the clear air over the high plains of eastern Colorado. The vertically pointing radar used here differs insignificantly, for the present study, from that of Richter. The experiment was performed at our 150-m micrometeorological tower at Haswell, Colorado. The site is sparsely covered with 15-cm high clumps of buffalo grass for a minimum of 3 km in any direction from the tower. The site is at an elevation of 1307 m and displays a characteristic high-plain meteorological regime with strong solar heating during the day and radiative cooling at night. The radar was placed 240 m from the base of the tower in the direction of the prevailing wind. The 150-m tower is instrumented to measure fluctuations in wind, temperature, and radio refractive index utilizing a microwave refractometer at several fixed levels as well as a similarly equipped carriage that travels the height of the tower in 10 min. The carriage was also equipped to measure the difference in radio refractive index over a 20-cm vertical spacing. Thus, the carriage allowed the placing of the meteorological probes within the region of radar returns. Further, the characteristic radar return from the tower at 225–295 m (see Figure 1) not only serves as a reference but also can be used to track the carriage motion within the tower echo from a height of approximately 65 m to the top of the tower. A reference line is placed at 150 m to indicate tower height.

Boundary-Layer Meteorology **1** (1971) 466–473. *All Rights Reserved*
Copyright © 1971 by D. Reidel Publishing Company, Dordrecht-Holland

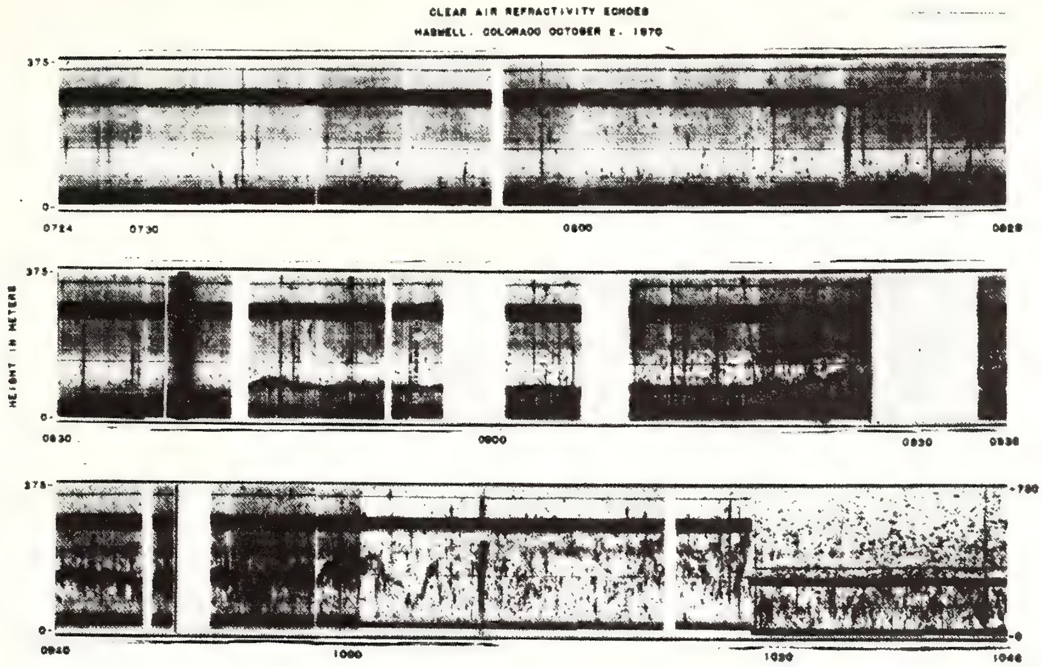

Fig. 1. Radar record of clear air returns of October 2. The (range)$^{-2}$ variation of radar return for volume scattering has been removed electronically. The record was obtained from photographs of an intensity-modulated oscilloscope face. The radar operates on 10-cm wavelength with a power of 200 W. The beamwidth is 4.5 deg.

2. Comparison of Tower and Radar Returns

The data from the morning of October 2, 1970 were utilized to compare radar reflectivities obtained from the tower with those obtained by radar. As can be seen in Figure 1, the region of strong radar returns lifted slowly and nearly uniformly from 0800 through approximately 0930 corresponding to the growth of a well-mixed layer below the inversion. The dots that appear throughout the record are attributed to insects. The blanks in the record correspond to times when the reflectivity of the atmospheric returns was monitored. The tower data were converted to radar reflectivity by assuming that the scales of interest corresponding to the radar wavelength λ (10 cm) lie within the '$\frac{5}{3}$' region of the spectrum. In our case we measure the refractive index difference Δn over 20 cm so that when the structure function is given by (Ottersten, 1969)

$$\overline{\Delta n_{20}^2} = C_n^2 (0.2)^{2/3}, \tag{1}$$

where C_n^2 is the structure-function constant, one may obtain the radar cross-section in $\mathrm{m}^2/\mathrm{m}^3$ by substitution into

$$\eta = 0.38\,\lambda^{-1/3} C_n^2 \tag{2}$$

where η is the radar reflectivity, to obtain

$$\eta = 2.4\,\overline{\Delta n_{20}^2}\,.$$

Examination of both sets of data for the height of the meteorological carriage when stationary within the layer of radar returns yields the results as given in Table I.

TABLE I

Time	$\eta(\mathrm{m}^{-1})$ radar	$\eta(\mathrm{m}^{-1})$ tower
0844	1×10^{-15}	1.1×10^{-15}
0907	3×10^{-13}	0.7×10^{-13}
0930	1×10^{-13}	0.7×10^{-13}
0948	1×10^{-14}	2.8×10^{-14}

The agreement of the reflectivities measured by the radar and computed from the tower data is excellent considering the several unknowns involved in this kind of comparison.

The major unknown in the numerical comparison is the effect of the 240-m separation of the radar and tower sites. This separation was chosen to keep the tower echo from appearing within the height of the tower as seen by the radar. Therefore, it was impossible to obtain collocated measurements of radar reflectivity, refractivity, temperature, and wind. This initial attempt at comparing radar and tower data has been hand reduced. Every effort was made to obtain either time or height coincidences between the two sets of data, depending upon whether or not the tower carriage was stationary.

The vertically-pointed radar antennas were set into separate earth excavations two meters deep and no subsequent measurements were made of the resultant antenna patterns. This type of antenna configuration is required to keep the leakage power from the transmitter below the saturation level of the receiver. A recent study of similarly configured acoustic antennas (Strand, 1971) has shown that this shielding technique may be utilized to reduce the side lobes of the antennas in the 30°–90° zenith angle region with little noticeable effect upon the main lobe pattern. Hence, it was assumed that the main lobe pattern of the sunken antennas was substantially unchanged from the free-space pattern.

The sytem performance of the radar was continuously monitored during the course of reflectivity measurements. The transmitted power was measured with a thermistor element and did not vary by more than ±0.5 dB. Frequent calibration of the power meter indicated that most of this variation is the effect of ambient temperature changes upon the thermistor element, implying that the transmitted power is sensibly constant. In addition, some of the transmitted power was continuously leaked into the receiver through a 2.5-μsec delay line providing a continuous system echo at 375-m range. Thus, the total electronic system is essentially self-monitored and self-calibrated with reference to a single power meter.

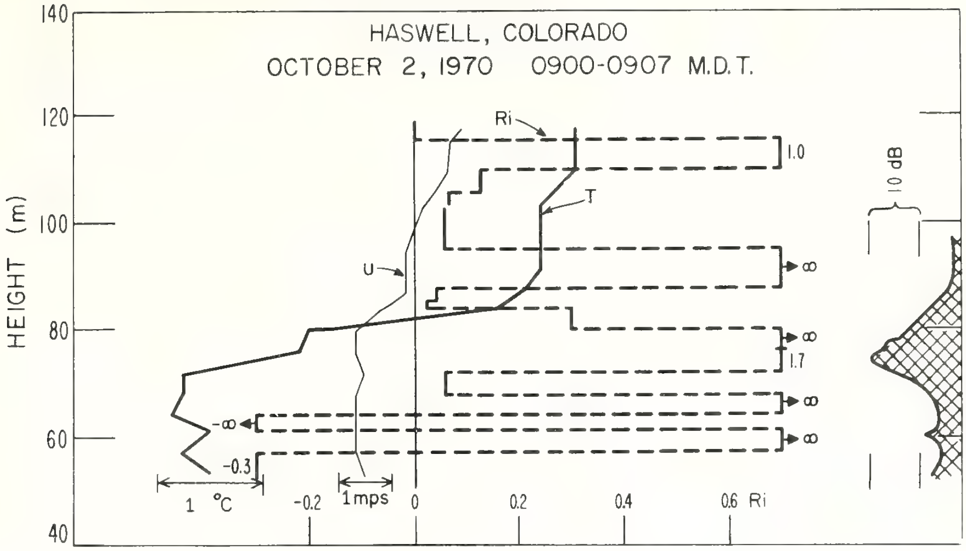

Fig. 2. Comparison of temperature and horizontal wind speed profiles taken 0900–0906, the resulting Richardson's number and a 3.2-sec average of radar return taken at 0907.

We now examine in more detail the correspondence between the profiles of the meteorological parameters and the radar returns. The period 0900–0907 MDT was analyzed in some detail. The radar return shown on the right side of Figure 2 displays two peaks at 60 and 75 m which closely correspond to the occurrence of inversions in the temperature profile. The return at 60 m is not reflected in the wind profile while a wind maximum is observed above the 75-m inversion. Richardson's number, *Ri*, was calculated from

$$\mathrm{Ri} = g \frac{\partial \ln \theta}{\partial z} \bigg/ \left(\frac{\partial \bar{u}}{\partial z}\right)^2 ,$$

where θ is the potential temperature, g the acceleration of gravity, and $\bar{u}$ the horizontal wind. Infinite values of *Ri* would correspond to regions of zero wind shear. Although there has been much speculation that regions of large ΔN and strong radar returns correspond to regions where $Ri = \frac{1}{4}$ (Atlas *et al.*, 1970), our data do not show this. We do note, however, that the radar return region is one of large changes of *Ri* with no obvious critical value of *Ri*. Figure 3 compares the profiles of N, $\overline{\Delta N_{20}^2}$ with the radar returns (N is the refractivity: $N = (n-1) \times 10^6$). One notes maxima in $\overline{\Delta N_{20}^2}$ corresponding to those in the radar returns as well as in the edges of the temperature inversions. The difference between the observed maxima is 11 dB while that calculated from the ΔN data is 8 dB, i.e., within a factor of two. Again this agreement is taken to be good considering the time and space separations of the measurements.

The N profile is mostly controlled by the T profile, especially across the main in-

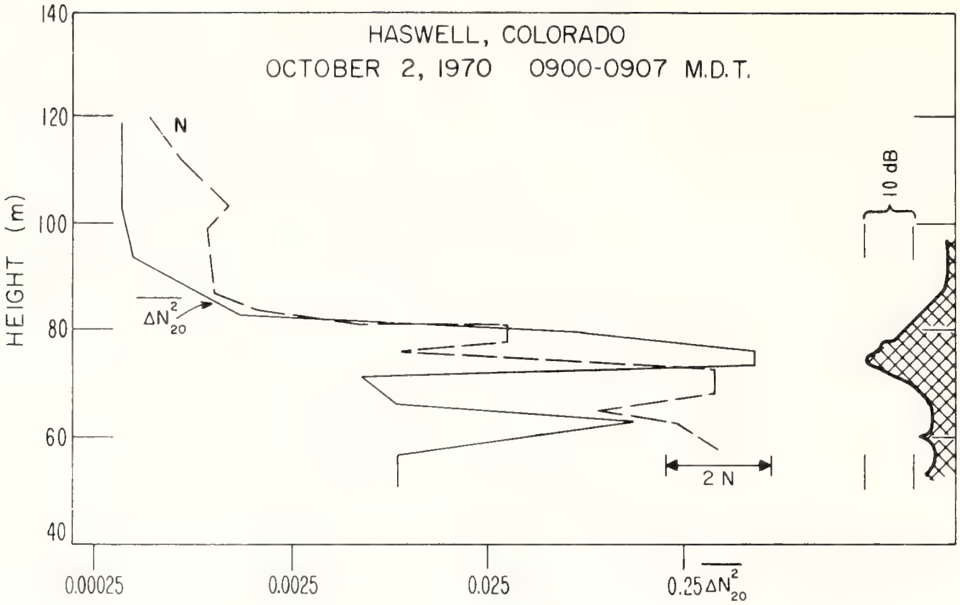

Fig. 3. Comparison of refractivity and refractivity fluctuation profiles taken 0900–0906 and a 3.2-sec average of radar return (represented by the crosshatched curve) taken at 0907. The refractivity, N, is defined by $N=(n-1)\times 10^6$, where n is the refractive index. N is measured directly with a microwave refractometer, but may also be determined from $N=77.6\,(P/T+4810\,e/T^2)$ where P is total atmospheric pressure in millibars, T is in degrees Celsius and e is water vapor pressure in millibars. $\Delta N^2{}_{20}$ is determined from two microwave refractometer cavities separated 20 cm in the vertical.

version at 80 m. If we write (Bean and Dutton, 1968)

$$\Delta N = -\,1.08\Delta T + 4.75\Delta e$$

where ΔT, Δe are the differences in temperature and vapour pressure, respectively, then

$$\Delta e = \frac{\Delta N + 1.08\,\Delta T}{4.75}.$$

If we take $\Delta T=3.25\,^\circ\mathrm{C}$ and $\Delta N=-4.75$ from Figures 2 and 3, then

$$\Delta e = \frac{-\,4.75 + 3.51}{4.75} = -\,0.26\ \mathrm{mb}\,.$$

This, by coincidence, represents 26% of the total change in N across the inversion, indicating the dominant role of temperature in this case. Normally, fluctuations of humidity will dominate those of N, which is why the microwave refractometer is often used as a high-speed humidity probe.

3. Other Examples

INSECTS, CONVECTIVE ELEMENTS, INVERSIONS AND WAVES

A large number of insects were observed in the radar returns during this experiment.

We concluded this from the presence of gulls, apparently feeding during these periods, and from the reports of pilots who were having difficulty in keeping their windshields clear of insects while flying past the tower. We (RBC and BDW) also observed that when standing in the shadow of an object just shielding the sun's disk, the insects become quite visible. At 10-cm wavelength a radar is quite sensitive to insects. For example, our system mdb (minimum-discernable-bug) is 2.0 mm in diam at a range of 1 km. We see on Figure 4 that insects are observed to a 1500-m height during the entire period from 1227 to 1517 MDT on October 2, 1970. By this time the morning inversion is completely destroyed. The insects appear to act as tracers of an oscillatory flow. One presumes that the 'rising' portions of the record are convective elements since the air in the boundary layer is slightly unstable at this time due to solar heating of the ground. The rising portion appears darker, indicating a filling in of the background by mixing of the leading edge of the element with the ambient air while the descending portion displays only the insects, indicating well-mixed air. This is in keeping with the convective plume model of Kaimal and Businger (1970) determined from the data in the first 30 m of the atmosphere. *Note well*, that the plumes rise with time, indicating, since we only see that which the wind carries past us, that the plume is bent *backwards* in space relative to the air flow. This is just the opposite of Kaimal and Businger's observations. This discrepancy could be explained by the presence of a wind maximum above tower height. Verification of this conjecture must await subsequent observations. The vertical velocities of these insects are also quite large. For example, at 1530 it is quite easy to follow a single insect rising over 450 m in 3 min with an average velocity of 2.5 m sec^{-1}.

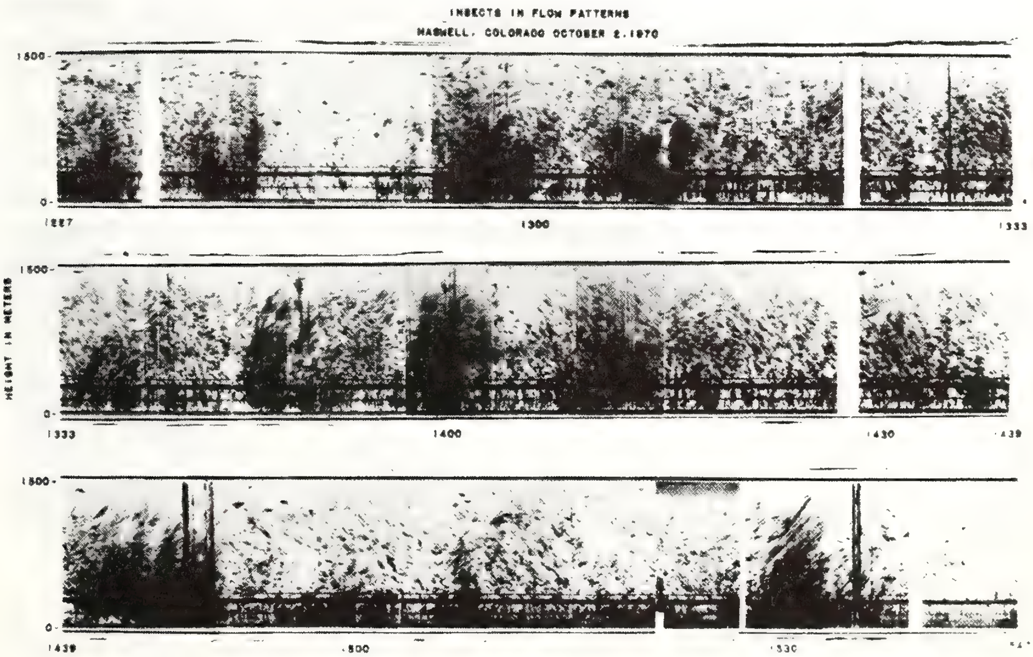

Fig. 4. Radar record of insect returns of October 2.

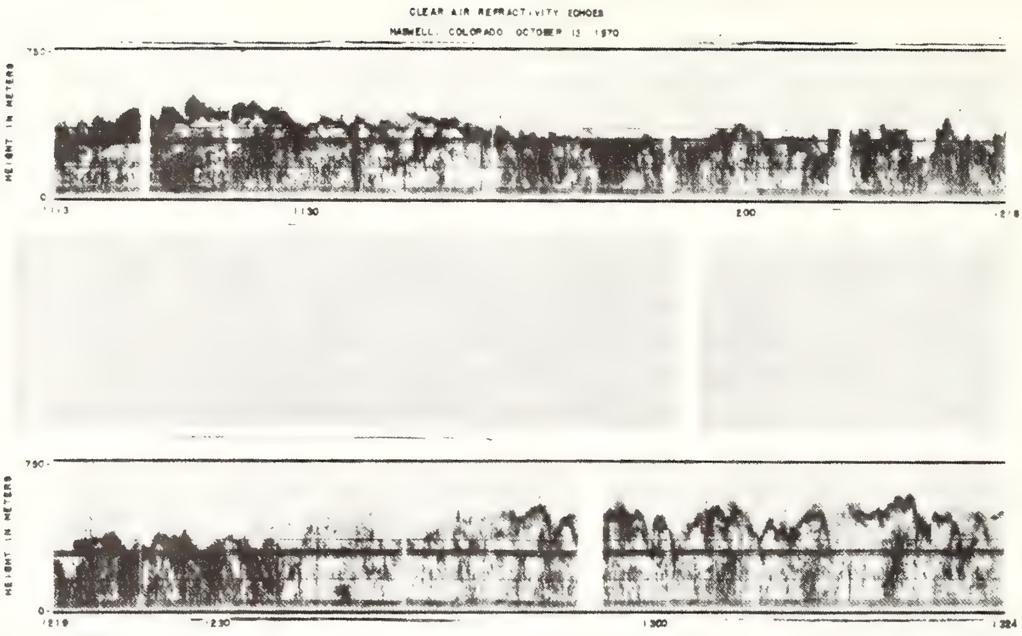

Fig. 5. Radar record of clear air and insect returns of October 12.

A further example, shown in Figure 5, illustrates thermal plume modulation of an elevated inversion during the late morning of October 12, 1970. With few exceptions the insects are confined under the inversion and within the mixing layer. Again, where a convective plume is clearly delineated, such as near 1320, the insect returns indicate that the plume is bent backwards in space relative to the air flow. The period before 1235 does not show such clear-cut convective activity but rather undulations on the inversion with some mixing of insects. The period from 1200–1235 shows structures reaching to the ground that are spatially tilted *forward* with the wind. These are assumed to be instability waves on the inversion that break to produce trailing wakes. Such waves are the object of much research within our laboratories. Although they are not Kelvin-Helmholtz waves, their physical cause has not yet been explained.

Waves of the Kelvin-Helmholtz (K-H) variety are shown in Figure 6 for the morning of October 22, 1970. The record starts at 0800 with faint echoes of high amplitude internal gravity waves of the characteristic shape that Gossard and Richter (1970) attribute to non-linear third-order Stokes waves. The inversion then rises slowly until just before 0900 when a large-amplitude wave appears. The characteristic braided return of K-H instability appears from 0901–0904; mixing presumably occurs, thus weakening both the contrast in N across the layer and the resultant radar returns. The layer remains relatively weak until about 0925 when wave action again commences. The long wave at 0945 crests with a roll that captures clear ambient air in its center. Some instability is indicated by the diffuse returns on the downward side of the wave. Note that the returns from this wave are as strong as those from the tower.

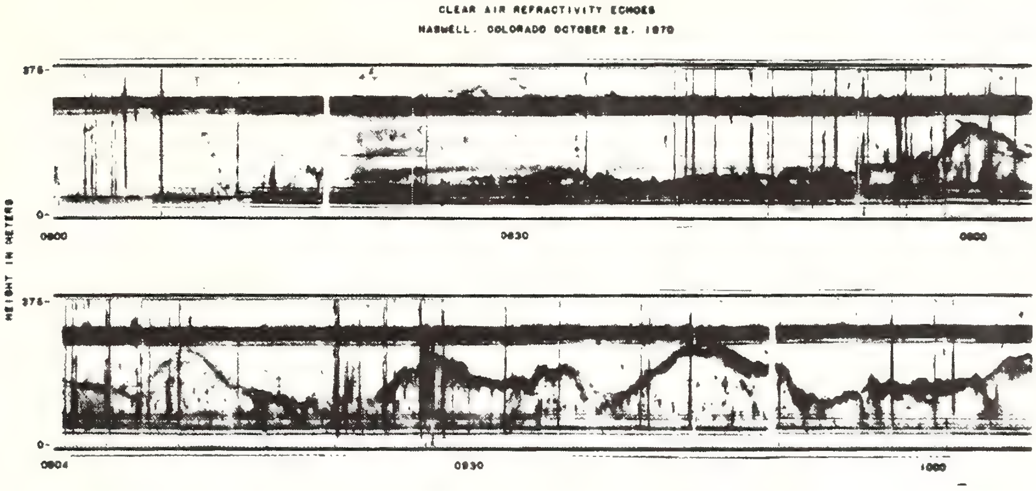

Fig. 6. Radar record of clear air returns of October 22.

4. Conclusions

This first field expedition with the CW-FM radar indicates that the device is applicable to studies of the structure of temperature inversions, stable and unstable waves upon such inversions, thermal plumes and convective processes within the boundary layer. The radar also appears to follow the transport of insects by such processes.

Perhaps the most important of our conclusions is that many boundary-layer studies would be enhanced by the use of a clear-air radar. For example, the present authors are concerned with the budgets of heat, momentum and water vapor as determined from the 150-m tower. In such budgets one must determine the flux quantities as well as the profile characteristics, i.e., averages and covariances must be determined over some representative averaging time. The radar indicates that many intervals are not as stationary as they appear to the eye and can serve to delineate those periods most suitable for the analysis of particular phenomena such as instability waves and convective processes.

References

Atlas, D., Metcalf, J. I., Richter, J. H., and Gossard, E. E.: 1970, 'The Birth of "CAT" and Microscale Turbulence', *J. Atmospheric Sci.* **27**, 903–913.

Bean, B. R. and Dutton, E. J.: 1968, *Radio Meteorology*, Dover Publications, Inc., New York, 435 pp.

Gossard, E. E. and Richter, J. H.: 1970, 'The Shape of Internal Waves of Finite Amplitude from High-Resolution Radar Sounding of the Lower Atmosphere', *J. Atmospheric Sci.* **27**, 971–973.

Kaimal, J. C. and Businger, J. A.: 1970, 'Case Studies of a Convective Plume and a Dust Devil', *J. Appl. Meteorol.* **9**, 612–620.

Ottersten, H.: 1969, 'Radar Backscattering from the Turbulent Clear Atmosphere', *Radio Sci.* **12**, 1251–1255.

Richter, J. H.: 1969, 'High Resolution Tropospheric Radar Sounding', *Radio Sci.* **12**, 1261–1268.

Strand, O. N.: 1971, 'Numerical Study of the Gain Pattern of a Sunken Acoustic Antenna', to be published in *J. Acoust. Soc. Am.*

36 *Reprinted from Proceedings of Symposium on Advances in Instrumentation for Air Pollution Control, Atmospheric Environment, Vol. 5, 691-702, 1970.*

MEASUREMENT OF WIND AND WIND FIELD BY MICROWAVE DOPPLER RADAR TECHNIQUES*

ROGER M. LHERMITTE

Environmental Science Services Administration, Wave Propagation Laboratory,
Boulder, Colorado, U.S.A.

(*First received* 6 *February* 1970 *and in final form* 23 *April* 1970)

Abstract—This paper is a survey of the applicability of microwave Doppler radar techniques to the observation of clear air motion. Emphasis is placed on discussion of the methods required for analyzing wind and turbulent motion by observing the velocity of man-made radar targets used as tracers for the air motion.

1. INTRODUCTION

MICROWAVE Doppler radar techniques have been widely applied to the study of wind field in precipitation conditions by using precipitation particles as tracers for the air motion. Similar methods can be applied to observing cloud-free air motion if suitable targets, acting as tracers for air motion, are in the region probed by radar. Such targets might occur in a dense smoke plume or in the clear atmosphere ("angels"), but the presence and reliability of natural targets detectable by microwave radars in clear air will often be questionable; thus, release of man-made targets will be needed at times to provide required air motion tracers. Such targets designed for this purpose have low inertia, small terminal speed, and can be dispersed in large quantities ("chaff"). They are thin aluminum-coated fiberglass needles which are cut to one-half the radar wavelength for maximum radar cross section.

This paper reviews and discusses microwave Doppler radar methods and techniques applicable to studying clear air motion—and its time variability—in three dimensions by release of chaff targets. The method, using two Doppler radars that probe the same region in space, should lead to three-dimensional observation of well-organized features of the wind field, such as local convergence or vorticity, as well as their relation to the smaller-scale wind variability.

2. THE DOPPLER RADAR SPECTRUM

Numerous discussions of the Doppler radar method applied to the study of atmospheric phenomena have been presented (LHERMITTE, 1964, 1966; ATLAS, 1964). It appears necessary here only to mention briefly the basic principles of the method. Only pulse Doppler radar techniques having the same ranging capabilities as conventional radars are discussed.

In addition to the same capability of a conventional radar, e.g., observing backscattered signal amplitude, pulse Doppler radar provides information on rate of change of the phase, ϕ, of the backscattered signal returned by the radar-detected target. With appropriate design of Doppler circuits, the phase difference between transmitted and received signals, which is observed by the coherent radar, is a function only of the distance between the target and the radar. The rate of phase change,

---

* Presented at the Symposium on Advances in Instrumentation for Air Pollution Control, sponsored by National Air Pollution Control Administration, U.S. Department of Health, Education and Welfare, Cincinnati, Ohio, 26–28 May 1969.

$d\phi/dt$, will therefore provide knowledge of the radial velocity, dR/dt, of the target. We can then write

$$\frac{d\phi}{dt} = \frac{4\pi}{\lambda}\frac{dR}{dt},$$

where λ is the wavelength of the transmitted signal. This expression shows that there is a complete cycle of phase change every time the target moves by $\lambda/2$. The pulse Doppler radar is thus an accurate ranging device that measures the rate of change of target range, i.e., the radial velocity. If the target is approaching the radar, the phase of the signal is increasing as a function of time, which makes $d\phi/dt$ a positive quantity equivalent to an effective increase of the transmitted frequency. On the other hand, if the target is receding, $d\phi/dt$ becomes negative, which is equivalent to an effective decrease of the transmitter frequency. The sign of $d\phi/dt$ is opposite to the sign of motion derived from the convention that kinematic divergence is a positive quantity. It therefore appears that it is more appropriate in meteorological work to consider that receding targets have positive velocity. If the target moves in a direction different from the radar beam axis, only the radial velocity, i.e., the component of the target's vectorial velocity along the axis of the radar beam, is measured. This statement reveals the ambiguities of dealing with radial velocities, which can partially or completely be overcome in certain ways described in this paper.

Since we are discussing the application of Doppler techniques to studying atmospheric phenomena, we are dealing with volume scattering from an extended or "distributed" target composed of large numbers of scatterers.

The classical analysis of the backscattered signal received by conventional pulse radars from distributed targets, such as a cloud of chaff dipoles used as tracers for air motion, shows that signal amplitude at any selected point in the radar range is due to the contribution of signals re-radiated by scatterers inside a scattering volume, defined by the cross section of the radar beam and the pulse length of the radar. In addition to observing signal amplitude, pulse Doppler radar techniques also provide information on signal phase.

If we assume that the signal backscattered from scatterer, j, has constant amplitude, a_j, and phase, ϕ_j, the total backscatter signal, $A(t)$, is given by

$$A(t) = \sum_{j=1}^{N} a_j \, e^{-i(\omega_0 t + \phi_j)}, \qquad (1)$$

$\omega_0 = 2\pi f_0$; f_0 is the transmitted signal frequency. The signal phase, ϕ, can be split into a component, ϕ_0, corresponding to some conditions at the origin and a variable term $\omega_d t$, where $\omega_d = d\phi/dt$ (Doppler shift); therefore, we can write

$$A(t) = e^{-i\omega_0 t} \sum_{j=1}^{N} a_j \, e^{-i(\omega d_j t + \phi_{0_j})}. \qquad (2)$$

The above relationship implies statistical independence of motion between scatterers and no collision process between scatterers. It also relies on scatterers moving freely for several radar wavelengths, therefore leading to a clear definition of the Doppler shift. If the scatterers are submitted to a random displacement limited to a small fraction of the radar wavelength, a different and more complicated expression of $A(t)$ is needed.

For pulse radars, the time function $A(t)$ is sampled at the radar pulse repetition rate. Selecting the signal at any radar range can be done with conventional range-sampling units assisted by signal-holding circuits, which restore the time continuity of the signal between pulses and, therefore, provide a time function of the form of equation (1). However, sampling and propagating the $A(t)$ signal in the radar circuits slightly modifies its spectral characteristic, especially for frequencies approaching half of the pulse repetition rate. These effects are well known and usually corrected by appropriate means.

Equation (1) shows that the power density spectrum of $A(t)$ is the probability density function for the backscattered power expressed as a function of the Doppler shift, and is called the Doppler spectrum. If the radar cross section of the individual scatterers exhibits time variations, the spectrum of $A(t)$ includes the Fourier components generated by amplitude modulation due to this effect (BROOK and LATHAM, 1968).

3. COHERENT RADAR DESIGN

Radar equipment capable of observing the phase difference between backscattered and transmitted signals is called phase-coherent, or simply "coherent".

The simplest method for comparing phases is based on mixing the signal returned from a moving target with the signal reflected by a fixed target at the same range. This "external-coherence" method, which is often used in airborne navigational Doppler radars, has been applied to the study of motion of precipitating particles (LHERMITTE, 1960). However, the usefulness of this method is seriously limited by the need for a fixed target to be at exactly the same range as the moving target under study. The transmitter pulse signal can also be stored in microwave cavities, but this technique is limited to short ranges by the fast time decay of the stored signal.

The most effective and accurate way to generate microwave phase coherent signals relies on the use of a primary stable microwave source called a STALO (Stable Local Oscillator). The microwave signal generated by the STALO is amplified, pulsed by a phase-coherent amplifier, and radiated by the antenna. The scattered signal coming from a moving target is compared to the STALO signal, and the signal phase is analyzed by systems sensitive to the phase difference, $\Delta\phi$, between successive pulses. The quality of this system depends upon frequency stability of the microwave oscillator during the time interval between radiation of a pulse and return of the scattered signal. Therefore, it involves only "short-term" frequency instabilities of the STALO. Relative frequency stabilities of 10^{-10} can be easily achieved for longer than 1 ms and with Doppler phase jitter smaller than 5×10^{-3} rad.

System performance can be analyzed in terms of these estimated random phase instabilities occurring from pulse to pulse. If these phase instabilities are uncorrelated and limited to a small fraction of 2π, they produce a radar-sampled white spectrum superimposed on the signal Doppler spectrum. The Doppler signal-to-noise ratio is given by the ratio between the signal phase variance (Doppler) and the contribution of the variance caused by random phase instabilities (LHERMITTE and KESSLER, 1964). If this is due to STALO phase instabilities, this ratio is typically better than 50 dB. We must emphasize that small STALO frequency instabilities do not limit the ability of the radar to observe very slow target motion, which is only limited by the signal dwell time and the stability of the mean index of refraction along the path. The instabilities only generate a phase noise that limits the dynamic range of the Doppler spectrum and thereby inhibits the clear definition of the spectrum boundaries. The STALO contribution to phase instability increases systematically with target distance. In a well designed, fully coherent system, the STALO contribution to phase instabilities largely exceeds other contributions.

The need for a coherent microwave amplifier can be overcome by using a conventional (but stable) magnetron microwave oscillator assisted by a transmitter phase-locked system (COHO) that stores the phase of the transmitter signal. This is the classical MTI radar, which has been known and used for years. Phase locking is usually done at intermediate radar frequency and basic requirements for the STALO remain the same as they are for fully coherent systems. High quality, commercially available magnetron oscillators have acceptable frequency stability. However, there is more phase noise generated by the magnetron and phase-locking instabilities in the COHO circuits than in a system using a STALO and a microwave coherent amplifier. The ratio of signal phase to phase noise, which reaches more than 50 dB for fully coherent systems, is reduced to 30–35 dB for the MTI system. This phase noise contribution is independent of the radar range.

4. DOPPLER RADAR SIGNAL PROCESSING

The backscattered time signals returned by the moving targets must be frequency analyzed before any other manipulation of the Doppler data. The following methods have been used in the past:

(a) Range-gating associated with either a signal-crossing technique that provides the spectrum's second moment (LHERMITTE, 1962) or a velocity tracking system that essentially processes the spectrum median frequency (TRIPP, 1964). This technique has the advantage of simplicity but does not provide information on the spectrum width and shape and is only applicable for narrow or, at least, symmetric spectra for which only the knowledge of the average frequency is required.

(b) Range gating associated with the use of a multifilter frequency analyzer which leads to acceptable knowledge of spectrum shape, especially if integration means are provided for the signal at the output of every filter. It is, however, a slow process that does not match the requirements of studying atmospheric phenomena.

(c) Coherent memory filter of velocity-indicator coherent integrator (VICI) applied to meteorological work, which was first proposed by CHIMERA (1960) and allows quick display of the distribution of the Doppler velocity as a function of radar range (range velocity indicator, RVI). The device is extremely fast but suffers from restricted range and velocity resolutions due to practical limitations of the system. The VICI is also unable to provide or display the signal power spectral density quantitatively and, therefore, fails to indicate the Doppler spectrum shape. In its present form, the coherent memory filter also fails to produce data in a digital format, which seems to be the only way to cope with the information provided by this system. Extending its use for PPI display has recently been proposed by DONALDSON *et al.* (1969).

(d) Digital time compression of the Doppler signal which essentially allows quick analysis of the spectra by fast scanning filters. The system can be associated with range

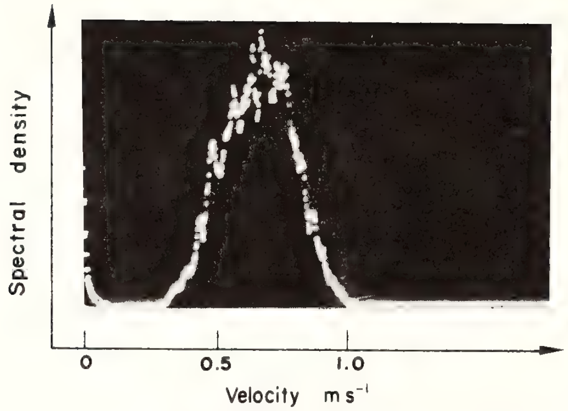

FIG. 1. Doppler spectrum observed with a vertically pointing radar beam on falling snow.

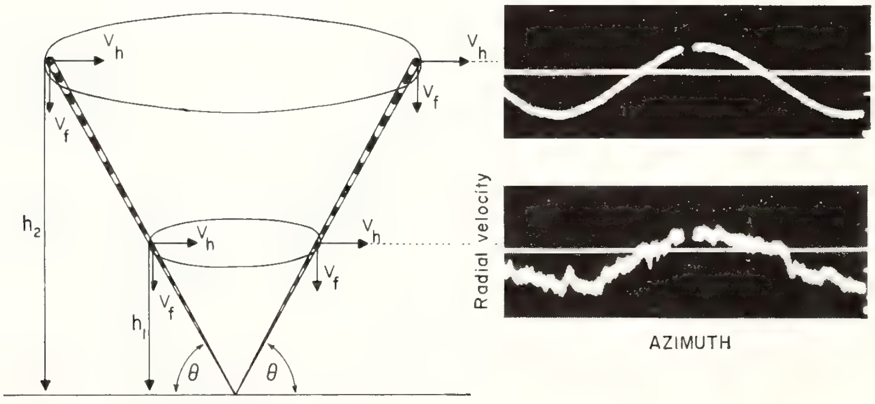

$$V_R = V_h \cos\theta \cos(\beta - \beta_o) + V_f \sin\theta$$

FIG. 3. Velocity–azimuth display showing the difference between VAD patterns obtained for smooth and turbulent flow.

(*Facing p.* 694)

multiplexing and is capable of analyzing the Doppler information at 10 range gates in a time on the order of a few seconds.

(e) If real-time operation is unnecessary, recording the Doppler signal by aid of a multitrack magnetic tape recorder offers a high rate of data acquisition, which matches most of the requirements. Complementary information can also be recorded on a separate track. Processing the recorded signals can be done with the aid of specialized digital devices that provide a digital output.

Recently, signal and data processing methods have drastically improved through the use of advanced general purpose digital computers and special purpose processing systems based on the use of modern digital hardware, such as integrated circuits. The meteorological Doppler radar system, with its high rate of information flow, can benefit drastically from modern digital circuitry and methods for processing and storing of Doppler information. The following is devoted to analyzing problems and predicting solutions, which are expected to take place in the next few years, for the treatment of Doppler radar information so that the potential of the method will be fully realized.

As mentioned above, the transformation to be performed on the Doppler signal is that of a conventional Fourier transform or its equivalent, such as processing the signal with an analog type frequency analyzer.

Although digital computations of the Doppler signal power density spectrum had been involved in some early experiments (BATTAN, 1964), they have not been widely used because of the time consuming nature of the operation. However, substantial progress has now been achieved for computing power density spectrum by digital computers, and efficient algorithms are available that provide fast Fourier transforms of sampled time series (COOLEY and TUKEY, 1965). This fast Fourier method substantially reduces the time required for the digital computations of Fourier transforms.

The digital Fourier transform is based on the availability of digitized time samples of the signal to be analyzed. The spectral power density estimates, S_j, are computed from the following equations:

$$C_j = \sum_{k=1}^{N} C_k \, \mathrm{e}^{-i2\pi kj/N}$$

$$S_j = C_j^2$$

where $C_k = a_k + ib_k$, with a_k the real and b_k the imaginary part of the backscattered signal.

The method provides N non-redundant frequency samples from N time samples, thus requiring that N^2 multiplications be done per complete spectrum. Five hundred time samples are fairly representative of the spectral information in a time signal, requiring that 250,000 complex multiplications be done for each conventional Fourier transform. With modern, fast digital computers, computing time will be on the order of, or less than, 1 s, which does not much exceed the signal dwell time required to build an acceptable knowledge of the spectrum. Therefore, real-time digital computations by conventional Fourier algorithms are, at least, as effective as the filter bank method. Also, the digital computer offers complete flexibility in the choice of appropriate frequency coverage that is controlled by the signal sampling rate, see BLACKMAN and TUKEY (1958). Since it is based on the unambiguous Fourier transform mathematical expression, the digital frequency analyzer provides a well defined answer for the spectral density estimate, which is easier to use in the analysis of the data.

Fast Fourier transform algorithms decrease the required number of multiplications to $N \log_2 N$ instead of N^2. This considerably reduces computation time to much less than signal dwell time and thereby makes it feasible to process several radar ranges in less than a few seconds. The method involves using a high speed, elaborate system for multiplexing and an analog-to-digital conversion of the Doppler signal. It also requires core memories that are organized in sequence so the Fourier transforms can be easily computed, range after range, from the stored digital data. Such systems can be built at an acceptable cost by use of modern integrated circuit digital hardware. The expected rate of data that can be processed is about 10,000 (200 ranges, 50 velocities) samples every second. By using a logarithmic scale, only one 7-bit character is necessary to represent the spectral density with sufficient accuracy at a given range-velocity address. Storing Doppler data with range-velocity addresses can be done on magnetic tape with a format compatible with requirements of general purpose digital computers (used for assembling the radar data.in space). FIGURE 2 illustrates the capabilities of the digital method for reducing and even presenting a three-dimensional display of Doppler radar information. Such displays can be quickly

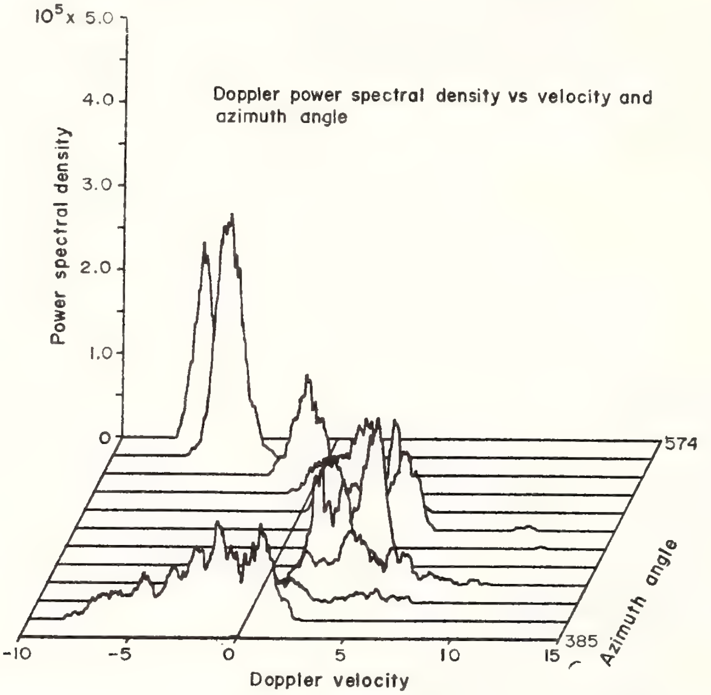

FIG. 2. Three-dimensional display showing Doppler spectra at the same distance for selected azimuths inside a convective storm. Doppler velocity range is from -10 m s^{-1} (approaching) to 15 m s^{-1} (receding). Spectrum width ranges from 2 to 12 m s^{-1}. Azimuth steps are separated by 2 degrees. Range gating is at 25 km.

obtained by using output devices usually associated with large computers. Of course, the effectiveness of such a fast data acquisition rate relies on our ability to cover large regions of the atmosphere with chaff dipoles.

Note that if better time or space resolution is needed, the Doppler data acquisition speed can be increased well beyond the limits expressed above. The expected availability of large scale integration (LSI) digital hardware and the increasing speed of integrated circuits can increase the data acquisition rate expressed above by one order of magnitude. The capability of the system will still be limited by the scanning speed capabilities of radar antennas, although this, too, may ultimately be overcome by the development of electronic beam scanning techniques; but, isn't it dreaming??

5. THE RADIAL VELOCITY SPECTRUM AND ITS METEOROLOGICAL SIGNIFICANCE

The nature of Doppler information obtained from the backscattering of pulse radar signals has been widely discussed in various articles (i.e., see Atlas, 1964; Lhermitte, 1964, 1966). Information on the radial velocity of the targets, which is contained in the phase of the backscattering signal, is observed not at a point in space but more precisely inside a range-selectable scattering region defined by the radar beam cross section and half the radar pulse length in space. Frequency analysis of the backscatter signal provides a spectrum of velocity representing radial velocities of the detected targets weighted by a possible relationship between their radar cross section and their velocity. This "Doppler spectrum" can be reduced to an expression of average velocity (first moment of the spectrum) and spectrum variance (second central moment).

If the targets exhibit a large range of sizes and shapes, which in turn influences their motion relative to the air, the interpretation of the Doppler spectrum requires an assumption of the relationship between the target radar cross section and the velocity. However, if the targets have a uniform size (chaff dipoles) or if they respond to air motion similarly, regardless of their size, the Doppler spectrum can be interpreted in terms of the statistics of the air radial velocity inside the scattering region. For targets moving under the influence of air speed only, average Doppler velocity is the mean air velocity, and Doppler spectrum variance is caused by the three-dimensional spectrum of turbulent air motion integrated from wave numbers that correspond to the smallest scale of the scattering region, which can be reproduced by spacing the targets.

The Doppler radar measures only the targets' radial velocity, V_R, which can be expressed as

$$V_R = v \cos\beta \cos\theta + u \sin\beta \cos\theta + w \sin\theta, \tag{3}$$

where β and θ, respectively, are the azimuth angle (relative to north) and the elevation angle of the radar beam; v, u, respectively, are the N–S and E–W components of the target's horizontal motion, and w is the target's vertical velocity; V_R is positive for motion away from the radar, v is positive from S to N, u is positive from W to E, and w is positive upwards. The expression of the Doppler spectrum variance, $\sigma^2{}_R$, indicated by the spectrum width, is given from equation (3) by:

$$\begin{aligned}\sigma^2{}_R = {} & \sigma^2{}_v \cos^2\beta \cos^2\theta + \sigma^2{}_u \sin^2\beta \cos^2\theta + \sigma^2{}_w \sin^2\theta \\ & + \cos^2\theta \sin 2\beta \operatorname{cov}(uv) + \cos\beta \sin 2\theta \operatorname{cov}(vw) \\ & + \sin\beta \sin 2\theta \operatorname{cov}(uw),\end{aligned} \tag{4}$$

where $\sigma^2{}_v$, $\sigma^2{}_u$, $\sigma^2{}_w$, respectively, are the variances for v, u, and w; cov(uv) etc. ... the covariance between v and u etc. ....

Note that the relative contribution of the v, u, w variances (and their covariances) to the radial velocity variance as expressed in equation (4) is modified significantly by varying azimuth and elevation angles of the radar beam.

For instance, if the Doppler data are acquired by directing the radar beam along the mean wind at the selected altitude (upwind and downwind regions) the method is sensitive only to V_l, the longitudinal component of the wind, and the vertical motion, w. We then express the upwind, V_U, and the downwind, V_D, Doppler velocities by the following equations:

$$\text{Upwind} \qquad V_U = V_l \cos\theta + w \sin\theta \tag{5}$$
$$\text{Downwind} \qquad V_D = -V_l \cos\theta + w \sin\theta, \tag{6}$$

where V_U and V_D are positive for motion away from the radar, and w is positive upwards, with the variances

$$\text{Upwind} \qquad \sigma^2{}_U = \sigma^2{}_l \cos^2\theta + \sigma^2{}_w \sin^2\theta + \text{cov}(V_l w) \sin 2\theta \tag{7}$$
$$\text{Downwind} \qquad \sigma^2{}_D = \sigma^2{}_l \cos^2\theta + \sigma^2{}_w \sin^2\theta - \text{cov}(V_l w) \sin 2\theta. \tag{8}$$

Since only the sign of the covariance changes from downwind to upwind, the difference between the Doppler spectrum upwind and downwind variances is a measure of the covariance between V_l and w. The covariance has a great importance in the boundary layer since it is related to the shearing stresses due to friction. To remove the contribution due to time or space variability of the above quantities, equations (7) and (8) should involve time averages of $\sigma^2{}_U$ and $\sigma^2{}_D$. The upwind-downwind method has been discussed for Doppler data obtained during a snowstorm (LHERMITTE, 1968), where it was shown that the calculated cov($V_l w$) is on the same order of magnitude as the Doppler spectrum variance.

6. VAD METHODOLOGY

If chaff dipoles are uniformly released in a large region surrounding the radar site, and if we assume statistical homogeneity of the wind field in the area, it is appropriate to observe several radial components of the motion of the tracers, obtained in different directions by means of azimuth scanning of the radar beam and display of the velocity azimuth function (Velocity-Azimuth-Display). With appropriate programming of the radar beam elevation angles and the selected ranges, the data can represent a range of altitudes in the storm, thereby leading to a definition of the vertical distribution of the properties of the motion field.

The method was first proposed (LHERMITTE and ATLAS, 1961) for measuring the wind vertical profiles within a snowstorm but can be extended to measuring clear air motion by use of suitable targets released over large areas. An example of the method's capability is shown in FIG. 3. The tracers' radial velocity, V_R, at a certain altitude is continuously recorded as a function of radar beam azimuth, β. V_R is expressed as a function of the horizontal motion speed, V_h; and direction, β_0; the radar beam elevation angle, θ; and the particle vertical velocity, V_f; by the following equation:

$$V_R = V_h \cos\theta \cos(\beta - \beta_0) + V_f \sin\theta. \tag{9}$$

V_R is, in fact, a spectrum whose variance is due to the contribution of V_h variance, $\sigma^2{}_h$; V_f variance, $\sigma^2{}_f$ (due mainly to the distribution of dipole terminal speed); and the covariance between V_f and V_h. The estimate of the mean velocity, V_R (spectrum first moment), collected as a function of radar beam azimuth, offers means to determine a least square fit of equation (9), which permits a prediction of the average quantities: $\bar{V}_h$, $\bar{V}_f$, and β_0.

There is, however, an ambiguity in the prediction of $\bar{V}_f$ that is due to the possible presence of wind convergence in the wind field. This is easily shown by integrating V_R as a function of β. We have

$$\int_0^{2\pi} V_R(\beta)\, d\beta = \cos\theta \int_0^{2\pi} V_h \cos(\beta - \beta_0)\, d\beta + \sin\theta \int_0^{2\pi} V_f\, d\beta. \tag{10}$$

The term $\int_0^{2\pi} V_h \cos(\beta - \beta_0)\, d\beta$ is null only if there is no wind convergence. We then can write

$$\int_0^{2\pi} V_R(\beta)\, d\beta = \sin\theta \int_0^{2\pi} V_f\, d\beta \tag{11}$$

and therefore estimate $\bar{V}_f$. However, if there is wind convergence the term $\int_0^{2\pi} V_h \cos(\beta - \beta_0)\, d\beta$ is not zero and contributes to the term on the right of equation (10). By further manipulating the equations, we can estimate the wind divergence, $\text{div}_2 V$ by the following expression:

$$\text{div}_2\, V = \frac{1}{\pi r} \int_0^{2\pi} \frac{V_R(\beta)\, d\beta}{\cos\theta} - \left(\frac{2V_f \tan\theta}{r}\right). \tag{12}$$

In this equation, r is the radius of the circle scanned by the radar beam at the selected range or altitude. The method is capable of an accurate estimate of the wind divergence if θ is small and if the fall speed of chaff dipoles can be estimated accurately. For instance, if $\theta = 10°$, a change of the estimate of V_f by 0.25 m s^{-1} modifies the convergence estimate by 10^{-5} s^{-1} at $r = 15$ km.

This method of measuring wind convergence was first proposed and applied by CATON (1963) for precipitation particles observed by a Doppler radar. It reliably applies only to air motion tracers whose fall velocity either is small or is accurately estimated. Deformation of the wind field can also be derived from the data, but vorticity cannot be observed with a single Doppler radar since it requires that the tangential component of the motion be known.

Wind fluctuations of smaller scale can also be estimated by classical Fourier analysis of the $V_R(\beta)$ function and the Fourier components expressed in the following equation:

$$C_n = \int_0^{2\pi} V_R(\beta)\, e^{-in\beta}\, d\beta. \tag{13}$$

C_n is indeed a complex quantity containing information of phase and amplitude of the Fourier components.

Mesoscale wind properties as well as eddy dissipation rate can be observed and analyzed by this method if the data are simultaneously acquired at a high rate and at different altitudes. However, the method is used to its full capabilities only if the data are produced in digital form for efficient reduction by digital computers.

7. THE TWO DOPPLER RADAR METHOD

Using two Doppler radars, installed at different locations and simultaneously observing the same region where air motion tracers have been released, drastically improves the capability of the Doppler method. FIGURE 4 illustrates this concept.

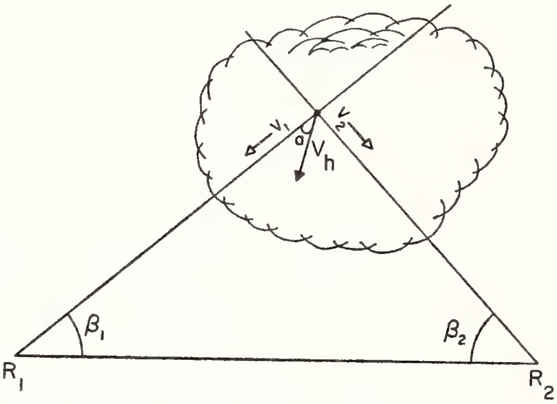

FIG. 4. The dual radar system from which velocities of the targets are obtained from two different directions. R_1 and R_2 are the positions of the two radars.

The same region is observed by two radars, R_1 and R_2, installed at different locations, thereby providing two radial components of the targets' motion, V_1 and V_2. The two components, V_1 and V_2, can be expressed by the following equations:

$$V_1 = V_h \cos\alpha \cos\theta_1 + (V_t + w)\sin\theta_1 \tag{14}$$

$$V_2 = -V_h \cos(\beta_1 + \beta_2 + \alpha)\cos\theta_2 + (V_t + w)\sin\theta_2. \tag{15}$$

In these equations θ_1 and θ_2 are elevation angles for R_1 and R_2; β_1 and β_2 are the inside angles shown in FIG. 4; V_h is horizontal motion speed; α is the angle between the direction of horizontal motion and β_1; $V_t + w$ is the targets' vertical velocity (V_t is the targets' terminal speed and w is the air vertical motion). If the contribution to the Doppler caused by vertical motion can be neglected, i.e., $(V_t + w)\sin\theta \simeq 0$, equations (14) and (15) can be solved for V_h and α according to the following expressions:

$$V_h = \frac{1}{\sin^2(\beta_1 + \beta_2)}\left[\frac{V_1^2}{\cos^2\theta_1} + \frac{V_2^2}{\cos^2\theta_2} + \frac{2V_1V_2\cos(\beta_1 + \beta_2)}{\cos\theta_1\cos\theta_2}\right], \tag{16}$$

$$\tan\alpha = \frac{1}{\sin(\beta_1 + \beta_2)}\left[\frac{V_2\cos\theta_1}{V_1\cos\theta_2} + \cos(\beta_1 + \beta_2)\right]. \tag{17}$$

This method offers excellent potential for easy mapping of the horizontal air motion field for nearly horizontal radar beams. However, radar beam elevation angles smaller than 5°–10° can be accepted, allowing the observation of the horizontal motion field up to 10,000–15,000 ft. For targets outside the line of sight between the two radars, the method offers accurate and unambiguous results that should clearly reveal convergence and vorticity patterns of the wind field.

If we add the equation of continuity of mass applying to noncompressible fluid,

$$\frac{\partial u}{\partial x} + \frac{\partial v}{\partial y} + \frac{\partial w}{\partial z} = 0, \qquad (18)$$

to equations (14) and (15), we can solve the system of three equations for u, v, and w, provided that V_t is a known quantity. For chaff, V_t is easily estimated, therefore making the method capable of probing three-dimensional wind fields at any altitude where air motion tracers have been released. The method will therefore offer the unique opportunity, for instance, to observe the three-dimensional motion field in the boundary layer. Since the smaller-scale air motion variability can be derived from the variance of the Doppler spectra that are obtained at numerous points in space, the interaction between small-scale variability and organized features of the wind field can be derived from the data.

CONCLUSION

This note emphasizes the potential of microwave Doppler radar techniques for the study of wind fields and smaller-scale turbulent air motion. We believe that the present state of the technique presented in this discussion can and will provide a significant contribution to the study of boundary layer and turbulent diffusion processes.

REFERENCES

ATLAS D. (1964) Advances in radar meteorology. *Adv. Geophys.* **10,** 317–478.

BATTAN L. J. (1964) Some observations of vertical velocities and precipitation sizes in a thunderstorm. *J. appl. Meteor.* **3,** 415–520.

BLACKMAN R. B. and TUKEY J. W. (1958) *The Measurement of Power Spectra*, 190 pp. Dover Publications, New York.

BROOK M. and LATHAM D. (1968) The fluctuating radar echo. I. Modulation by vibrating drops *13th Radar Meteor. Conf.* pp. 2–7. Am. Meteor. Soc., Boston, Mass.

CATON P. G. G. (1963) The measurement of wind and convergence by Doppler radar. *Proc. Tenth Weath. Radar Conf.*, pp. 290–296. Am. Meteor. Soc., Boston, Mass.

CHIMERA A. J. (1960) Meteorological radar echo study. Buffalo, N.Y., *Cornell Aeronautical Rept.* No. 1327, p. 1.

COOLEY J. W. and TUKEY J. (1965) An algorithm for the machine calculation of complex Fourier series. *Math. Comput.* **19,** 297–301.

DONALDSON R. J., JR., ARMSTRONG G. M., CHMELA A. C. and KRAUS M. J. (1969) Doppler radar investigation of air flow and shear within severe thunderstorms. *Proc. Sixth Conf. on Severe Local Storms*, pp. 146–154. Am. Meteor. Soc., Boston, Mass.

LHERMITTE R. M. (1960) The use of a special pulse Doppler radar in measurement of particles' fall velocities. *Proc. Eighth Weath. Radar Conf.*, pp. 269–275. Am. Meteor. Soc., Boston, Mass.

LHERMITTE R. M. (1962) Note on wind variability with Doppler radar. *J. atmos. Sci.* **19,** 343–346.

LHERMITTE R. M. (1964) Doppler radars as severe storm sensors. *Bull. Am. meteor. Soc.* **45** (9) 587–596.

LHERMITTE R. M. (1966) Application of pulse Doppler radar technique to meteorology. *Bull. Am. meteor. Soc.* **47** (9), 703–711.

LHERMITTE R. M. (1968) Turbulent air motion as observed by Doppler radar. *13th Radar Meteor. Conf.*, pp. 498–503. Am. Meteor. Soc., Boston, Mass.

LHERMITTE R. M. and ATLAS D. (1961) Precipitation motion by pulse Doppler radar. *Proc. Ninth Weath. Radar Conf.*, pp. 218–223. Am. Meteor. Soc., Boston, Mass.

LHERMITTE R. M. and KESSLER E. (1964) An experimental pulse Doppler radar for severe storm investigations. *World Conf. on Radio Meteor.*, pp. 304–309. Am. Meteor. Soc., Boston, Mass.

TRIPP, R. (1964) The CAL pulse Doppler radar. *World Conf. on Radio Meteor.*, pp. 330–337. Am. Meteor. Soc., Boston, Mass.

Reprinted from Proceedings of the 14th Radar Meteorology Conference, November 17-20, 1970, 139-144, 1971.

DUAL-DOPPLER RADAR OBSERVATION OF CONVECTIVE STORM CIRCULATION

Roger M. Lhermitte

ESSA Research Laboratories
Boulder, Colorado

1. INTRODUCTION

Pulse Doppler radars provide information on the radial velocity of precipitation particles. This information has the form of a spectrum of radial velocities related to the distribution of particle motion in the radar pulse volume. The first moment, $\bar{V}_r$, of the spectrum (mean Doppler) can be expressed by:

$$\bar{V}_r = \bar{u} \sin\beta \cos\theta + \bar{v} \cos\beta \cos\theta + (\bar{w} + \bar{V}_t)\sin\theta \,, \qquad (1)$$

where β and θ, respectively, are the azimuth and elevation angles of the radar beam, and $\bar{u}$, $\bar{v}$, and $\bar{w}$ are the three orthogonal components of the mean air motion. $\bar{V}_t$ is the mean Doppler related to particle terminal velocity alone for a vertically pointing beam. Equation (1) is based on the assumption that precipitation particles are good tracers of mean air motion (Wilson, 1970) regardless of their size.

Equation (1) also shows that the $\bar{u}$, $\bar{v}$, and $\bar{w} + \bar{V}_t$ terms can be separated only if several observations of $\bar{V}_r$ at a given point in space are obtained by three radars installed at different locations. The resolution of the u and v components of two-dimensional horizontal motion can be realized by use of only two radars, if the contribution from the $\bar{w} + \bar{V}_t$ term can be assessed. This paper discusses results obtained by such a method applied to the observation of convective storm circulation.

2. DUAL RADAR CONCEPT

The dual-Doppler radar method is based on simultaneous observations of two mean radial velocities, $\bar{V}_1$ and $\bar{V}_2$ as provided by Radars 1 and 2, leading to two expressions analagous to (1) at a given point in a storm.

Solving these equations for u and v gives:

$$\bar{u} = \frac{1}{\sin(\beta_1 - \beta_2)} \left[\frac{\bar{V}_1 \cos\beta_2}{\cos\theta_1} - \frac{\bar{V}_2 \cos\beta_1}{\cos\theta_2} \right] - (\bar{w} + \bar{V}_t) \left[\frac{\cos\beta_2 \tan\theta_1 - \cos\beta_1 \tan\theta_2}{\sin(\beta_1 - \beta_2)} \right]; \qquad (2)$$

$$\bar{v} = \frac{1}{\sin(\beta_1 - \beta_2)} \left[\frac{\bar{V}_2 \sin\beta_1}{\cos\theta_2} - \frac{\bar{V}_1 \sin\beta_2}{\cos\theta_1} \right] - (\bar{w} + \bar{V}_t) \left[\frac{\sin\beta_1 \tan\theta_2 - \sin\beta_2 \tan\theta_1}{\sin(\beta_1 - \beta_2)} \right] \qquad (3)$$

If θ_1 and θ_2 are small, the last term in equations (2) and (3) can be neglected.

For precipitation in a liquid form, $\bar{V}_t$ can be estimated from radar reflectivity, Z, with reasonable accuracy (Rogers, 1964; Lhermitte, 1970). The term $\bar{w}$ can then be estimated through the equation of continuity:

$$\frac{\partial\bar{u}}{\partial x} + \frac{\partial\bar{v}}{\partial y} + \frac{\partial\bar{w}}{\partial z} = -\frac{1}{\rho}\frac{d\rho}{dt} \;. \qquad (4)$$

where $\frac{1}{\rho}\frac{d\rho}{dt}$ can be neglected through the assumption of an incompressible fluid.

If $\bar{V}_t$ is estimated from a $\bar{V}_t$/Z mean relationship, $\bar{u}$, $\bar{v}$, and $\bar{w}$ are evaluated from an interation process using (2), (3), and (4), leading to a solution satisfying these three equations.

Acceptable estimates of $\bar{u}$ and $\bar{v}$, as derived from (2) and (3), are only obtained in a limited region determined by the separation of the radars (Lhermitte and Miller, 1970).

Although coordinated scanning of the radar beams provides a much better solution to the problem (Lhermitte and Miller, 1970), this paper presents and discusses data which were obtained by two independent, simultaneous three-dimensional scannings of the radar beams with a preprogrammed sequence of elevation angles. One radar only was fully equipped with a digital recording system, allowing easy, accurate processing of the Doppler information by digital computer. The other radar was operated in a coordinated mode, recording additional radial velocity data in analog form.

The two-dimensional velocity data acquired in this manner at small elevation angles, with the contributions from $\bar{w} + \bar{V}_t$ lead to the presentation of well-organized and consistent horizontal motion fields resolved at a scale never attained before, therefore justifying the presentation and discussion of the material in this paper.

3. RADAR METHOD AND CHARACTERISTICS

Dual-Doppler observations of a convective storm were obtained by two Doppler radars installed in the area of Boulder, Colorado. Figure 1 illustrates the geometry of the radar system. The separation between the two radars is 15 km; the mean distance of the storm for this selected case is on the order of 20 km. The two pulse Doppler radars have identical characteristics:

Operating Frequency	9.31	GHz
Peak Power	20	kw
Antenna Beam Width	0.9	degrees
Pulse Width	0.3	μsec
Pulse Repetition Period	512	μsec

The radar receiver provides complex phase-coherent signals (in-phase and quadrature) which are both necessary to provide the sign of the Doppler frequency shift.

One radar was designed for recording Doppler signals by analog means. The other radar was operated with an improved system digitally recording receiver signals in a format compatible with direct processing of the tape by a digital computer. The data were recorded at a rate of 16,000 12-bit samples sec^{-1}, as imposed by the maximum capabilities of the digital tape recorder. Each record leading to the expression of one Doppler spectrum is composed of 512 complex samples (in-phase and quadrature), sufficient to allow an accurate evaluation of a Doppler spectrum at a given point in space. The signals are recorded at 24 selected ranges in 1.7 sec. After their digital recording on magnetic tape, the Doppler signals are processed by the digital computer programmed with fast Fourier transform algorithms for the calculation of the Doppler spectra. Additional computations are included, such as the evaluation of the first and second central moments of the Doppler spectrum and the signal power from which radar reflectivity of the medium is derived.

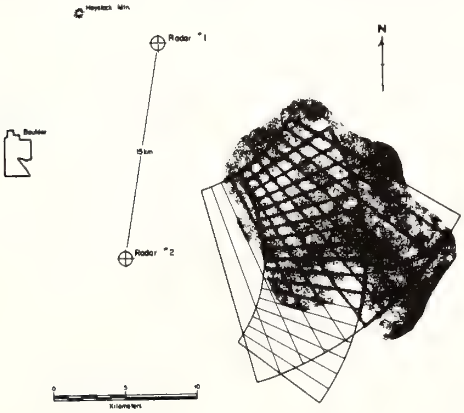

Figure 1. Plan view of the radar locations showing the scanning regions covered by the two radars related to the storm's boundaries.

The sample size mentioned above provides a standard deviation of the mean Doppler estimate, $\bar{V}$, of about 0.2 m sec^{-1} for a Doppler spectrum standard deviation of 1 m sec^{-1} (total width 5 m sec^{-1}), which is typical for the data discussed here (Lhermitte and Miller, 1970). Since the largest spectrum width observed in the data discussed in this paper was 15 m sec^{-1}, the maximum standard deviation of the $\bar{V}$ estimate is about 0.35 m sec^{-1}.

The processing system also includes frequency smoothing of the spectra and a printout of smoothed spectral density estimates at 64 points equally spaced in the velocity range. An example of results obtained by use of such a computer method has been shown elsewhere (Lhermitte and Miller, 1970). Since sign discrimination is allowed by the complex expression of the backscattered signal, frequency folding at half the radar pulse repetition rate is avoided. Therefore, if a positive Doppler frequency shift exceeds half of the pulse repetition rate, it will appear in the negative channel. The unambiquous velocity range is ± 16 m sec^{-1} as determined by the sampling of the Doppler signal at the radar pulse repetition rate.

The scanning of the antenna involves a radar beam stepping mode, synchronized with the operation of a tape recorder which records the data digitally. For each fixed position of the antenna, which lasts 1.7 sec, the Doppler signals are recorded at 24 different points in the radar range. The antenna is then stepped to a new position. The process is repeated every 2 sec with a stepping time of 0.3 sec, during which the signal recording operation is inhibited.

The azimuth stepping allows observation and presentation of radial velocity fields in a two-dimensional range-azimuth coordinate system. After each complete azimuth scan, the antenna moves to a new elevation angle position, so a three-dimensional scanning of the region of interest is acheived.

The stepping action for antenna scanning is required by the relatively low speed at which data are acquired. The antenna remains at a fixed position during the recording of the signals so that the Doppler data are assigned to clearly determined points in space. The stepping action, combined with the fixed position of the 24 range gates, provides fixed grid points in space and allows systematic treatment of the data by computer means.

The second radar utilized in this work was operated in the same manner, establishing grid points in space by digital stepping of the radar beam at selected range gates. However, the radar signals were recorded in analog form and processed by analog means.

4. ANALYSIS OF THE DATA

The observations of a convective storm's circulation reported in this paper were acquired on August 29, 1969 in the area of Boulder, Colorado, while the storm was consistently moving from 230° at a speed of 9 m sec^{-1}.

Considerable effort has been devoted in the past to study translation and rotation of convective storms. These studies were mostly concerned with the observation of trajectories and evolution of radar cells with occasional splitting and rotation. The investigations were severely limited by the lack of detailed information about the wind field structure inside the storm and in the storm environment. This paper is concerned with observations of both the wind field and the precipitation-echo patterns at a time during which translation of the storm was a significant feature of its behavior.

Inspection of the radar data obtained for altitudes ranging from 150 to 2500 m above ground level, in the subcloud region, shows that the moving storm is effectively composed of two cells, the more intense one being in the southwestern part of the storm system. Although significant changes in the reflectivity pattern were evident during the time the storm was observed, the basic structure characterized by the presence of two cells remained unchanged. Detailed studies of the motion of the patterns reveal a systematic translation of the echoes toward the northeast with slight acceleration of the storm movement (from 8 m sec^{-1} to 9 m sec^{-1} in 20 min) while the data were obtained. A slight cyclonic rotation of the echo pattern, a few degrees in 20 min, was also observed. The motion of the echo cells (230°, 9 m sec^{-1}) remains constant at all altitudes at which the data were acquired (150 to 2500 m) and is in agreement with the environmental wind at an altitude higher than 10,000 ft above terrain.

The radial velocity field pattern, derived from Doppler data, also advects consistently, although in a different direction (245°) which is in agreement with the environmental wind at lower levels. The deviation of the direction toward the west is increasing with lower altitudes, which strongly suggests that wind pattern advection is more sensitive to environmental wind than precipitation echo translation. This is consistent with the expectation that precipitation echo motion is only controlled by the air movement at the altitude where precipitation particles are formed.

It remains that both the radial velocity and the reflectivity patterns exhibit systematic translation and also a negligible evolution of their structure for several minutes. The overall stationarity of these features justifies evaluation of a field at a given time on the basis of data acquired at slightly different times.

Examples of the wind fields derived from the application of this method are presented in figures 2a, 2b, and 2c, which show the two-dimensional wind presented in planes with inclination angles of 1°, 2°, and 6° as related to the Radar #1 coordinate

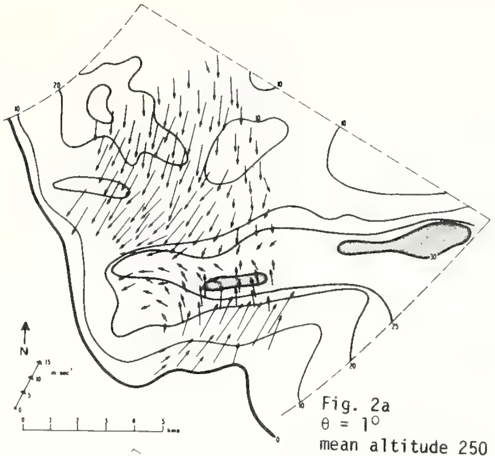

Fig. 2a
θ = 1°
mean altitude 250 m

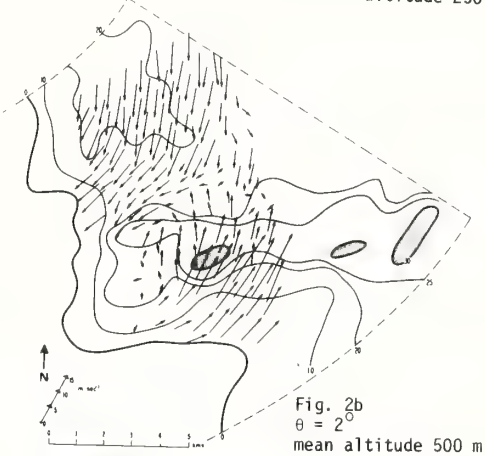

Fig. 2b
θ = 2°
mean altitude 500 m

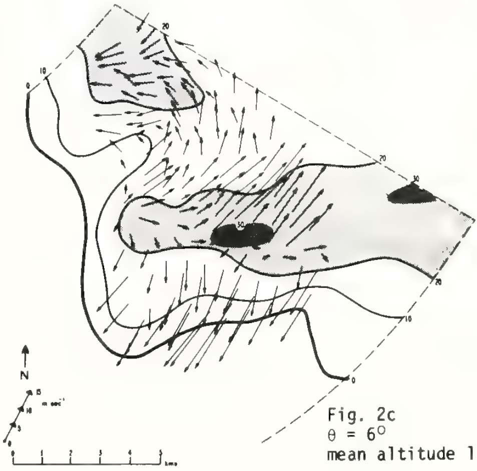

Fig. 2c
θ = 6°
mean altitude 1500 m

Figure 2a-c. Two-dimensional wind field observed inside a convective storm on August 29, 1969 at 1414 MST as derived from dual-Doppler radar data. Data are presented at different mean altitudes, thereby showing the three-dimensional structure of the storm in the subcloud layer. Storm reflectivity is also shown.

system. The altitude coverage corresponds to 150 m for the closest region at the smallest elevation angle, to 2500 m for the farthest region at the largest elevation angle.

The wind field displays in figures 2a, 2b, and 2c show that the observational data provided by Radar #1 cover a region of the storm larger than the restricted area where observations from both radars were available (see figure 1). Since the two-dimensional horizontal motion field is already determined in the major portion of the radar cells from the dual-Doppler radar observations, acceptable estimates of velocities can be obtained in a region where only Doppler measurements from Radar #1 are available, by matching an extrapolation of the two-dimensional wind field to actual radial velocity observations.

Such treatment of the wind fields is presented in figures 3a through 3d where estimated streamlines, as well as the main features of the radar cells, are shown for tilt angles of 1°, 2°, 4°, and 6°.

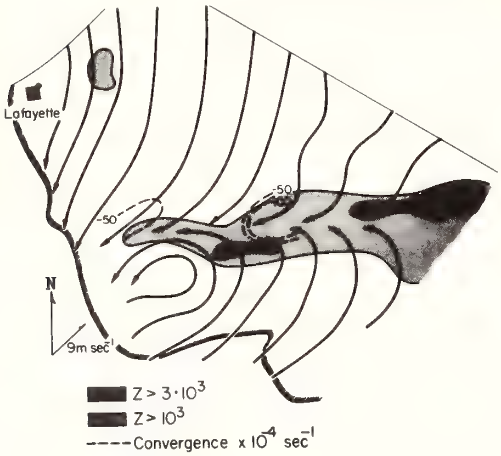

Fig. 3a
$\theta = 1^\circ$
mean altitude 250 m

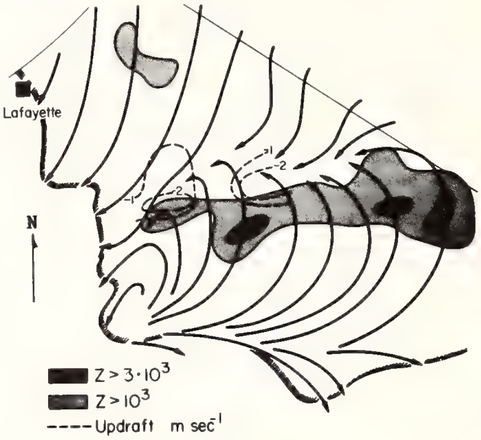

Fig. 3b
$\theta = 2^\circ$
mean altitude 500 m

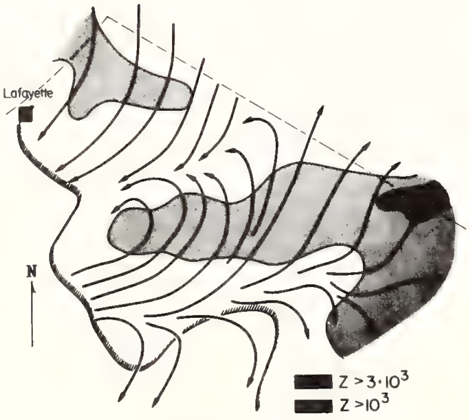

Fig. 3c
$\theta = 4^\circ$
mean altitude 1000 m

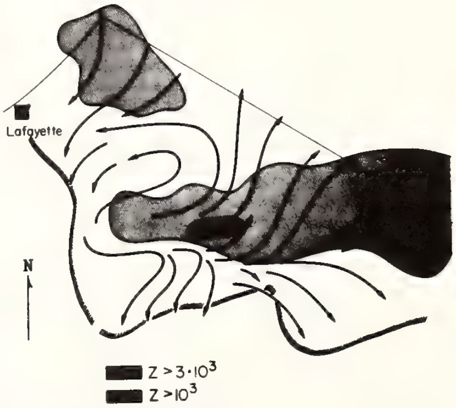

Fig. 3d
$\theta = 6^\circ$
mean altitude 1500 m

Figures 3a-d. Streamline analysis from dual-Doppler radar data obtained on August 29, 1969, at 1414 MST. The data are shown for several mean altitudes. Figure 3a includes computation of convergence from the wind field, and Figure 3b includes an estimate of vertical air motion from the wind field shown in Figures 2a and 2b. Note the vorticity and confluence regions and their displacement towards the northwest with increasing altitudes. Echo advection (230°, 9 m sec^{-1}) is also indicated.

The wind field and streamline analyses presented in figures 2a through 3d clearly show the importance of the dual-Doppler method in revealing the three-dimensional structure of storm circulation. Although the Doppler observations only cover a limited altitude in the subcloud layer of the storm (maximum altitude 2500 m), the well-defined and organized structure of the wind field reveals significant features of storm circulation and justifies a discussion of their importance as related to storm processes.

The most striking feature of the wind field is the presence of a strong vortex at all altitudes. The vorticity is strongest at the lower levels (10^{-2} sec^{-1} average in 4 km^2) and decreases as a function of altitude. There is also a zone of convergence ahead of the vorticity region and a region of divergence behind it. Although the radar echoes have vertical boundaries, the structure of the velocity pattern in a vertical plane exhibits a strong tilt with height in the general direction of motion. This characteristic is presented in figure 4 which shows a significant displacement of wind field features, such as the vorticity region, toward the northwestern part of the storm for observations made at increasing altitudes (3 km for a mean altitude change of 1250 m). The region of convergence ahead of the vortex region is also displaced in a consistent manner, as well as the divergence region, which only appears for 2° tilt and not below. It appears that the divergence region is not observed at lower altitudes, which can be explained by assuming that at lowest altitude levels this region extends outside the precipitation and is not "seen" by the radar.

Divergence of the wind field has been computed in the region covered by the two radars. The results are shown in figure 3a for data acquired with 1° tilt. One sees that convergence reaches a maximum of 10^{-2} sec^{-1}. There is no dual-Doppler radar data obtained in the southeastern part of the storm, but streamline analysis, as derived from Radar #1 data and also shown in figure 3a, suggests that the convergence region extends well beyond the limits shown to the southeastern part of the storm.

The same evaluation has been done for data obtained for different tilts of the radar beam. The results show that, for a 4° tilt (figure 3c), the convergence region is still ahead of the stronger cell but extends in the gap region which is always noticeable between the two cells.

The maximum convergence at this level decreases to less than 5×10^{-3} sec^{-1}. The divergence region appearing for tilts larger than 2° reaches 10^{-2} sec^{-1} at an altitude on the order of 1000 m. The presence of such a divergence region and its inclination suggests the existence of a strongly tilted downdraft in the backside of the moving storm extending outside of the radar cell at the low levels.

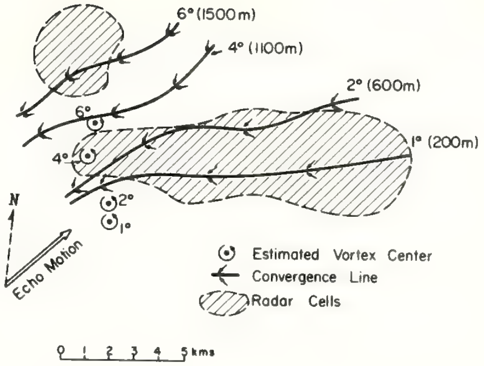

Figure 4. Displacement of the vortex center and the confluence line with increasing altitudes.

Vertical air motion can be numerically evaluated from the equation of continuity applied to wind fields obtained at selected altitudes. Such a method has been applied to wind fields obtained in two layers at 1° and 2° tilt for which Doppler data were acquired at the same time. The results, which show the vertical velocity estimated as a field at the top of the 2° tilt layer, are presented in figure 3b for velocities larger than 1 m sec^{-1}. The main feature of the field is an updraft region which is located ahead of the large cell. The computations also show a weak downward motion in the extreme southern part of the storm, which is not shown in figure 3b and possibly indicates the presence of the downdraft, in the backside of the storm, mentioned above. Although the method has not been applied to other layers for this preliminary work, it is suggested from the very strong tilt of the convergence region that the updraft region is also very strongly tilted.

5. CONCLUSIONS

The data presented in this paper clearly show that the dual-Doppler radar method has enormous capabilities for observing convective storm circulation in precipitation regions. The tilt of the circulation patterns in the low layer of the storm presented in this paper is consistent with observations of the strongly tilted distribution of electric charges in a moving thunderstorm reported by Ogawa and Brook (1969). The data presented here show striking details of the low-level storm circulation and seem to indicate strong interaction between storm dynamics and boundary layer processes. This suggests that storm development might be very sensitive to slight changes in the boundary layer, such as the presence of small terrain features. For instance, waterspouts often dissipate upon reaching a shoreline. Also, it has been noted that tornado paths can be greatly affected by small variations of terrain.

Observations presented in this paper are restricted to low altitudes; however, such observations can be extended to higher regions of a storm by use of better assumptions about particle mean terminal velocity. One method is to use the V_t/Z relationship proposed by Rogers (1964), which, of course, applies only in the case of liquid water. It is expected that the three-dimensional structure of the wind field and its continuity would provide even better analysis and treatment of the data, without relying on specific assumptions quantitatively formulated.

The COPLAN scanning proposed by Lhermitte and Miller (1970) certainly extends the method to almost all three-dimensional storm structures, since it essentially provides a more appropriate method of dealing with vertical velocity contributions.

6. ACKNOWLEDGMENTS

The author is indebted to Dr. James Fankhauser and Mr. Dean A. Wilson for reviewing the manuscript.

7. REFERENCES

Lhermitte, R. M. (1970), Probing of atmospheric motion by airborne pulse Doppler rada techniques, ESSA, Boulder, Colorado, unpublished.

Lhermitte, R. M. and L. J. Miller (1970), Doppler radar methodology for the observation of convective storms, Proc. 14th Radar Meteorol. Conf., forthcoming.

Ogawa, T. and M. Brook, (1969), Charge distribution in thunderstorm clouds, Quart. J. Roy. Meteorol. Soc. 95, No. 405, 513-525.

Rogers, R. R. (1964), An extension of the Z-R relationship for Doppler radar, Proc. World Conf. Radar Meteorol. and the 11th Weather Radar Conf., 158-160.

Wilson, D. A. (1970), The kinematic behavior of spherical particles in an accelerating environment, ESSA, Boulder, Colorado, unpublished.

Reprinted from Proceedings of the 14th Radar Meteorology Conference, November 17-20, 1970, 191-196, 1971.

DOPPLER RADAR STUDIES OF BOUNDARY LAYER WIND PROFILE AND TURBULENCE IN SNOW CONDITIONS

Dean A. Wilson

ESSA Research Laboratories
Boulder, Colorado

1. INTRODUCTION

The budget of turbulent kinetic energy (TKE) applying to boundary layer processes can be expressed schematically (after Badgley, 1969) as follows:

$$\begin{aligned}\begin{bmatrix}\text{LOCAL RATE OF}\\ \text{CHANGE OF TKE}\\ A\end{bmatrix} &= \begin{bmatrix}\text{WIND SHEAR}\\ \text{PRODUCTION RATE}\\ B\end{bmatrix}\\ &+ \begin{bmatrix}\text{TKE CONVERTED TO OR}\\ \text{FROM POTENTIAL ENERGY}\\ C\end{bmatrix} - \begin{bmatrix}\text{TKE DISSIPATION}\\ \text{BY VISCOSITY}\\ D\end{bmatrix}\\ &- \begin{bmatrix}\text{TKE FLUX DIVERGENCE}\\ \text{BY EDDY MOTION}\\ E\end{bmatrix} + \begin{bmatrix}\text{TKE ADVECTED BY}\\ \text{THE MEAN FLOW}\\ F\end{bmatrix}\\ &+ \begin{bmatrix}\text{TERMS INVOLVING THE DIVERGENCE OF THE}\\ \text{MEAN FLOW AND PRESSURE FLUCTUATIONS}\\ G\end{bmatrix}\end{aligned} \qquad (1)$$

There is substantial evidence that, under steady-state conditions when the term A is zero, the energy produced locally by B and/or C tends also to be dissipated locally through D, creating a balance between these terms. Under unstable or strongly stable thermal conditions, the term E can be significant, and this term may even approach the magnitude of the production terms (i.e., see Lumley and Panofsky, 1964, p. 128). Terrain effects in the boundary layer may produce local gradients of eddy energy, which implies that the term F and, consequently, A may be of some importance. The terms involved in G are generally thought to be of minor importance; although, to the author's knowledge, this hypothesis has not been substantiated by experimental measurements.

Until recently, estimates of the terms in (1) were derived almost entirely from wind measurements on towers and a few airplane measurements. Doppler radar now provides additional methods for observing the mean and variance of turbulent air motion over large regions of space in a short period of time, if targets capable of tracing air motion are present in the region of interest. This paper proposes such a method of measuring the rate at which the TKE grows at the expense of wind shear given by term B in (1) by observing the space variability of snowflake motion. The common assumption of a horizontally homogeneous boundary layer results in the following expression for B:

$$B \approx -\overline{u'w'}\,\frac{\partial \bar{u}}{\partial z} - \overline{v'w'}\,\frac{\partial \bar{v}}{\partial z} \ . \qquad (2)$$

u, v, and w are velocities in the x, y, and z directions, and u', v', and w' are their fluctuations around their means, $\bar{u}$, $\bar{v}$, $\bar{w}$. B can be estimated from the Doppler measurements, provided that the Reynolds' stresses $\overline{u'w'}$ and $\overline{v'w'}$ can be evaluated in the wavenumber range where energy input is expected.

Once (2) is calculated and if the vertical structure of temperature is known, a common and useful procedure is to determine the ratio of buoyant energy input to production of TKE from wind shear given by the quantity C/B derived from (1). With the coordinate system defined above, C consists of only one term and the ratio C/B becomes the flux form of the Richardson number.

$$Ri_F = \frac{g}{\bar{\Theta}}\,\frac{\overline{w'\Theta'}}{\left(\overline{u'w'}\,\frac{\partial \bar{u}}{\partial z} + \overline{v'w'}\,\frac{\partial \bar{v}}{\partial z}\right)} \ , \qquad (3)$$

where $\bar{\Theta}$ and Θ' are the mean and fluctuating potential temperature, respectively, and g is gravity. Expression (3) reduces to the familiar gradient form of the Richardson number:

$$Ri = \frac{K_m}{K_H}\,Ri_F = \frac{g}{\bar{\Theta}}\,\frac{\partial \bar{\Theta}/\partial z}{\left(\frac{\partial \bar{u}}{\partial z}\right)^2 + \left(\frac{\partial \bar{v}}{\partial z}\right)^2} \ , \qquad (4)$$

where K_m and K_H are exchange coefficients for momentum and heat, respectively.

2. METHOD

Doppler radar information is typically provided as a spectrum of radial velocities observed in a backscattering region defined by the pulse length and radar beam cross section. Such a spectrum is represented by a mean, V_R, and a variance, σ_D^2, related to spectrum width. This paper, however, is only concerned with the mean Doppler, V_R, which effectively removes contributions to motion variance due to scales smaller than the radar pulse volume.

For a radar operated in a VAD (Velocity Azimuth Display) mode (Lhermitte and Atlas, 1961), the variation of V_R as a function of azimuth angle, β, measured from north, is given by:

$$V_R(\beta) = u \cos \theta \sin \beta + v \cos \theta \cos \beta + (w + V_T) \sin \theta \, , \tag{5}$$

where θ is the radar beam elevation angle; u, v, and w are orthogonal components of the mean air motion in the scattering volume, and V_T is the mean Doppler vertical speed for target terminal velocity. Assuming that V_T is constant and that u, v, and w have stationary means $\bar{u}$, $\bar{v}$, and $\bar{w}$ in the region scanned by the radar defines a mean radial velocity, $\bar{V}_R$, given by:

$$\bar{V}_R(\beta) = \bar{u} \cos \theta \sin \beta + \bar{v} \cos \theta \cos \beta + (\bar{w} + V_T) \sin \theta \, , \tag{6}$$

where $\bar{u}$, $\bar{v}$, and $(\bar{w} + V_T)$ are estimated by use of a method described by Browning and Wexler (1968). Any deviation, V_R', of a V_R sample with respect to the predicted mean, (6), is caused by local velocity variations related to the turbulent motion spectrum. These fluctuations of V_R can be represented by the variance of this quantity, σ_R^2, and are related to the variances σ_u^2, σ_v^2, and σ_w^2 of the u, v, and w components of the mean air motion (and their covariances) by the following expression (Lhermitte, 1968):

$$\sigma_R^2(\beta) = \sigma_u^2 \cos^2 \theta \sin^2 \beta + \sigma_v^2 \cos^2 \theta \cos^2 \beta + \sigma_w^2 \sin^2 \theta + \mathrm{cov}(uv) \cos^2 \theta \sin 2\beta + \mathrm{cov}(uw) \sin 2\theta \sin \beta + \mathrm{cov}(vw) \sin 2\theta \cos \beta \, . \tag{7}$$

It can be shown (Lhermitte, 1968) that by observing σ_R^2 in the upwind and downwind directions at low elevation angles, the variance of the longitudinal velocity, σ_L^2, and covariance, $\mathrm{cov}(v_L w)$, between the longitudinal velocity and the vertical velocity can be estimated, provided that σ_L^2 and $\mathrm{cov}(v_L w)$ remain identical in the upwind and downwind directions (horizontal homogeneity).

This method can be extended to a more general treatment of the Doppler data acquired in all azimuths for a complete VAD scan. Assuming the variance of the actual V_R samples with respect to their predicted mean given by (6) is observed for all values of β allows that the following expressions be evaluated:

$$I_1 = \int_0^{\pi/2} \sigma_R^2(\beta) d\beta \; ; \qquad I_2 = \int_{\pi/2}^{\pi} \sigma_R^2(\beta) d\beta \; ;$$
$$I_3 = \int_{\pi}^{3\pi/2} \sigma_R^2(\beta) d\beta \; ; \qquad I_4 = \int_{3\pi/2}^{2\pi} \sigma_R^2(\beta) d\beta \, . \tag{8}$$

Assuming space and time stability of the variance and covariance terms contained in (7) leads to:

$$I_1 + I_2 + I_3 + I_4 = \pi \cos^2 \theta (\sigma_u^2 + \sigma_v^2) + 2\pi \sin^2 \theta (\sigma_w^2) \, , \tag{9}$$

$$(I_1 + I_2) - (I_3 + I_4) = 4 \sin 2\theta \, \mathrm{cov}(uw) \, , \tag{10}$$

$$(I_4 + I_1) - (I_2 + I_3) = 4 \sin 2\theta \, \mathrm{cov}(vw) \, , \tag{11}$$

$$(I_1 + I_3) - (I_2 + I_4) = 4 \sin 2\theta \, \mathrm{cov}(uv) \, . \tag{12}$$

It can be readily seen that the method effectively allows separation of the variance terms from the covariance terms in (7) and also leads to an evaluation of individual covariances. At low elevation angles the vertical component in (9) is small, and the contribution from σ_w^2 becomes negligible; therefore, the quantity $(\sigma_u^2 + \sigma_v^2)$, which is proportional to the horizontal turbulent kinetic energy, can be estimated from (9). Note that expressions (10, 11, and 12) only contain covariance terms and thus allow an estimation of the individual Reynolds' stresses required in the evaluation of B in (1).

In practice, a single VAD scan only provides one sample of V_R at each selected azimuth angle. The square of the V_R deviation, $V_R'^2$, can be considered as only an estimate of the variance, σ_R^2, at the selected azimuth. However, the processing of successive $V_R'^2$ samples obtained for different β's effectively leads to an expression of the form $\sum v_R'^2 \Delta\beta$, which is an acceptable approximation of the integral terms in (8). Therefore the exact expressions (9 through 12) can be approximated by replacing the variance and covariance terms with means of the quantities u'^2, v'^2, w'^2, $u'v'$, $u'w'$, and $v'w'$ evaluated from samples acquired during the VAD scan.

The TKE and momentum fluxes, as derived from (9 through 12), apply to air motion variability in a wavenumber range bounded by K_1 and K_2. These bounds vary with the slant range at which data are acquired. K_1 is inversely proportional to the dimension of the area scanned by the radar, and K_2 is limited by the size of the backscattering region as discussed above. The V_R samples (mean Doppler) are effectively related to mean motion taken over the pulse volume. Therefore, air motion variance caused by spectral contributions of wavenumbers greater than $K_2 = 10^{-2}$ cpm, corresponding to a typical dimension of the pulse volume, is effectively suppressed. At altitudes above 100 m, considered in this paper, this value of K is expected to be within the turbulent spectrum inertial subrange so that no energy input through the term B in (1) is expected to take place at wavenumbers greater than K_2. Since the diameter of the region scanned by the radar is typically 2 km or larger, the evaluation of the TKE and momentum fluxes by the above method applies to that part of the energy spectrum where significant input through the term B is expected.

K_1 is inversely proportional to the size of the scanning circle, which is in turn controlled by the range at which observations are made. Therefore the variances and covariances evaluated at different altitudes should be normalized to the same wavenumber, K. This requires knowledge of the spectrum shape in the K range considered above.

The method requires that K_1 be outside the inertial subrange to justify the existence of significant covariance terms. However, there is experimental evidence that the $K^{-5/3}$ spectrum form, initially derived from the inertial subrange concept, extends to low wavenumbers well beyond that range. For instance, Vinnichenko (1969) found that such spectrum shape exists for wavelengths extending to 10 km. Accepting the $K^{-5/3}$ form and noting that $K_2 \geq 20K_1$, provides the following expression for the normalized variance, σ_R^{2*}:

$$\sigma_R^{2*} \approx \sigma_R^2 (L_n/L)^{2/3} , \qquad (13)$$

where $L = 2H/\tan\theta$ is the wavelength corresponding to the height, H, at which σ_R^2 is measured and L_n is a wavelength taken as a reference.

3. EXPERIMENTAL RESULTS

The method described in section 2 is applied to data acquired with a radar operated in a VAD mode in steady, light snow conditions. The radar was located northeast of Boulder, Colorado, 8 mi from the foothills of the Rocky Mountains. The main radar characteristics are: wavelength - 3.2 cm; peak power - 25 kw; beamwidth - 0.9°, pulse length - .25 μsec; pulse repetition frequency 2 kHz.

The data presented in this paper were acquired on March 10, 1970, during a total time of 6 min with signals gated at 24 fixed ranges and a sequence of elevation angles of 10°, 15°, and 20°. Each complete VAD scan requires 1 min, during which the signals pertaining to 720 spectra were recorded.

The detailed temperature profile shown in figure 1 and used in this analysis was derived from a radiosonde released at the National Center for Atmospheric Research, Marshall field site, located 10 mi south of the radar, 10 min prior to the time at which the VAD data were recorded.

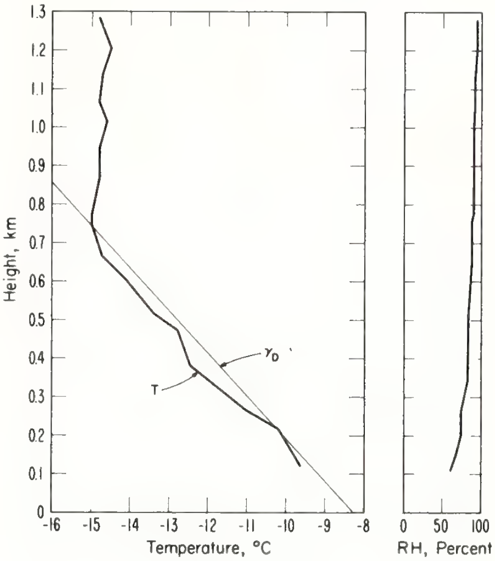

Figure 1. Vertical structure of temperature and humidity obtained from a "slow-ascent" radiosonde released at 1140 MST, March 10, 1970. The lapse rate is near neutral below 700 m and isothermal above that level. Data are plotted as a function of altitude above the radar.

The snow conditions were associated with typical eastern Colorado upslope conditions with a large-surface high-pressure system centered over the northern plains and southern Canada, producing an easterly flow of moist air over Colorado. At the upper levels, there was a trough located west of the continental divide in Utah and western Colorado with associated southwesterly flow over the Boulder area above 10,000 ft MSL or 4600 ft above the radar. Continuous light snow fell in the area from about 1800 MST on March 9 until 1200 MST on March 11, 1970.

The temperature profile shown in figure 1 indicates that the lapse rate varies from a slightly stable to a slightly unstable condition from the surface to 670 m and there was a very stable condition above that level. Since the relative humidity measurements indicate that saturation is never reached, it is expected that small-scale turbulence exchanges, at least below the inversion level, would only involve dry adiabatic processes.

The mean u and v components of the wind for elevation angles of 10°, 15°, and 20° were computed from the Doppler radial velocity through evaluation of (6), assuming the mean velocity field was horizontally uniform in the region where observations were made and time stationary over the 1 min period required to complete a single VAD scan. Vertical profiles of $\bar{u}$ and $\bar{v}$, derived from these results, are presented in figure 2. Note that the mean wind is indeed very stable during the entire 6-min period of observation.

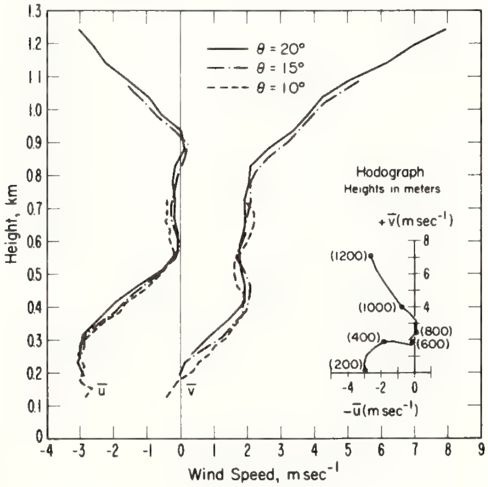

Figure 2. Vertical wind profiles for the period 1151-1157 MST, March 10, 1970, as determined from the Doppler measurements. The hodograph is derived from a mean of the three profiles. Note the excellent time stability of the wind at 600 m associated with a region of very weak shear.

The turbulent kinetic energy was calculated from (9) for the three elevation angles with the results, shown in figure 3, normalized to a circle of 10-km diameter by use of (13). In general, the turbulent energy decreases with height up to an altitude where the vertical wind shear is minimal, and then it increases again. No sharp gradients of turbulent kinetic energy are evident at the inversion level.

Notice that the profiles for 15° and for 20° are nearly identical in shape and very similar in magnitude, except at the lowest altitudes. This suggests that the turbulence is essentially time stationary during the period for which these data were acquired. Therefore, calculations of the covariances, $\overline{u'w'}$ and $\overline{v'w'}$, from (10) and (11) can be made with reasonable confidence. B is estimated by multiplying the covariances, normalized according to (13), by the mean vertical wind shear obtained from mean wind profiles. This procedure effectively estimates the rate at which turbulent eddies are gaining or losing energy from interaction with vertical shear.

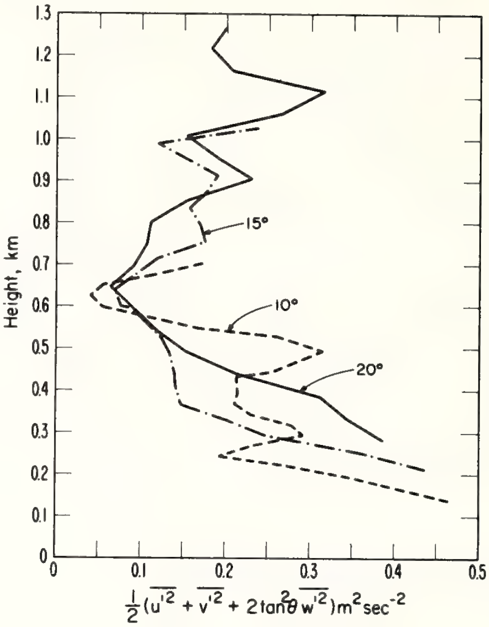

Figure 3. Turbulent energy profiles normalized to $\frac{2H}{\tan\theta} = 10$ km, as derived from the variance of the Doppler velocity. Notice the decrease of turbulent energy with height in the neutral boundary layer and the subsequent increase in the stable air above 700 m.

The quantity B is presented as a function of height in figure 4 where noticeable fluctuation of the unsmoothed data can be seen. At levels below 500 m, where the turbulent energy is decreasing with height and the mean wind is an increasing function of altitude, the term B is generally negative. This suggests that some of the energy at low wave numbers may contribute to mean wind shear enhancement in this layer. Such negative values of B (countergradient of momentum flux) have recently been predicted by Deardorff (1970) in a numerical model of the boundary layer.

From 600 to 800 m, where the turbulent energy is minimal, B becomes very small. Such a result could be predicted by the presence of weak shear in this layer, regardless of the magnitude of momentum fluxes. Examination of the $\overline{u'w'}$ and $\overline{v'w'}$, however, shows that these quantities are also very small, suggesting that this layer is characterized by a minimum of turbulent exchanges.

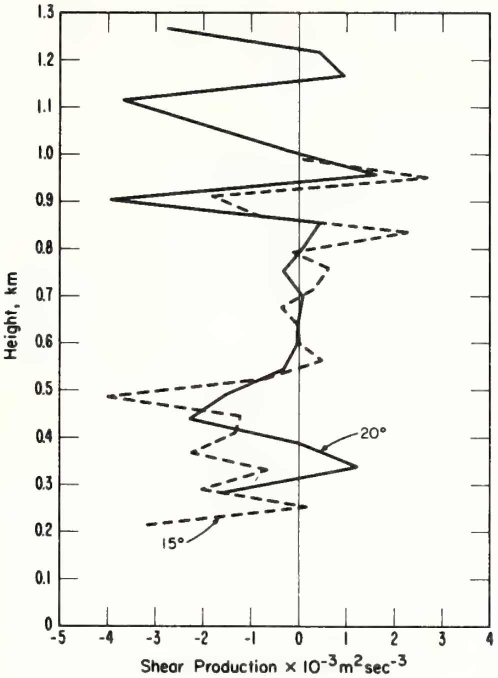

Figure 4. Rate of change of turbulent kinetic energy as a result of breakdown of vertical wind shear. The "production" rate is negative in the low levels and near zero near the top of the neutral layer, $\overline{u'w'}$ and $\overline{v'w'}$ have been normalized to $\frac{2H}{\tan\theta} = 10$ km.

The layer from 800 to 1200 m, where the lapse rate is stable and the turbulent energy increases with height, is characterized by considerable fluctuation of B with altitude. However, these variations appear to be stable with time, possibly indicating the presence of persistent layers. Note that B is again mainly negative in this layer.

In order to estimate the importance of buoyant energy production qualitatively, the gradient Richardson number is calculated according to (4). Ri is determined using 50-m averages of temperature and mean wind gradients shown in figures 1 and 2. The results are plotted as a function of height in figure 5. Ri generally increases with height from negative values in the lowest layers to about +3 near 600 m where the turbulent energy is at a minimum. This might suggest that the turbulent energy in the layer between 200 and 500 m is almost entirely maintained by conversion of potential energy to kinetic energy. The shallow layer of large positive Richardson numbers from 700 to 800 m is attributed to the increase of stability in the lower part of the thermal layer (see fig. 1) associated with very weak shear. Note that such high values of Ri could result from uncertainties in estimating the height of the inversion at the radar location. Above this layer, the Richardson number ranges from +2.8 to +0.7 with a general decrease with height. This compares favorably with the increase of turbulent energy in the same altitude range (see fig. 3). However, the relationship between turbulent energy and Richardson number is different below and above the inversion.

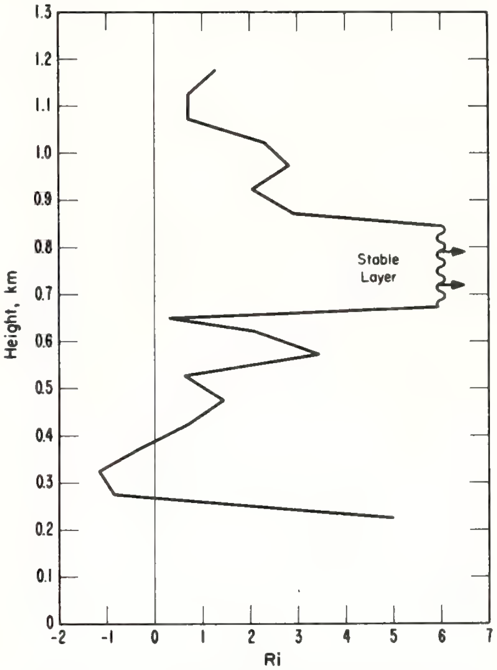

Figure 5. Richardson number as a function of height as determined from the Doppler winds.

Figure 6 shows the normalized turbulent kinetic energy versus the Richardson

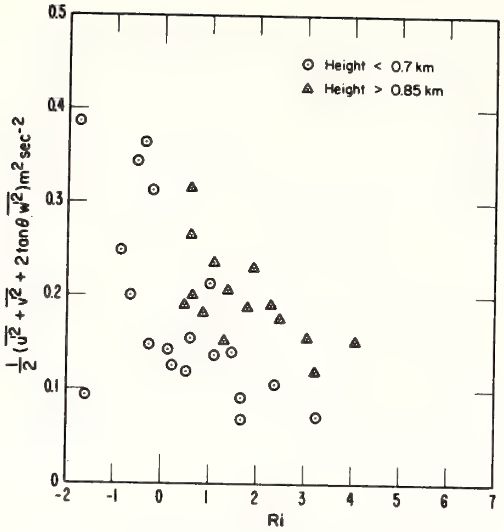

Figure 6. Dependence of the turbulent energy on Richardson number. Turbulence increases with decreasing Richardson number, but there appears to be a dependency on the thermal stability also.

number. These data suggest that the relationship between Ri and the turbulent energy depends on stability. Such dependence can be qualitatively explained by the smaller ratio of K_H/K_m expected in stable air. However, more accurate knowledge of the actual spectrum shape is required before any meaningful calculation of $K_H K_m$ can be made. Even if the limited number of points shown in figure 6 fails to indicate the existence of a critical Richardson number, it still reveals a definite dependence between Ri and TKE.

4. CONCLUSION

This paper demonstrates how Doppler radar techniques are applicable to the evaluation of the turbulent kinetic energy budget in the boundary layer. The experimental results are derived from observations of space motion variability of snowflakes, which restricts the scope of this present study to an assessment of boundary layer structure in precipitation conditions. Also, since the experiment was conducted in close proximity to mountains, the results derived from such observational conditions should not be considered as representative of a typical boundary layer. Consequently, it would be desirable to conduct similar experiments over flat terrain or over water and also to include supplemental information, such as tower wind and temperature measurements, to extend the analysis of the processes to the lowest layers.

The Doppler method could also lead to an assessment of other terms involved in the energy budget, (1). For example, radar observations of long-term time variations of V_R at given points in space can provide estimates of the terms A and F. The term D can be estimated from the width of the Doppler spectrum as proposed by Melnichuk et al. (1968). Finally, recalling that the momentum fluxes were derived in this paper through consideration of the variance of the Doppler mean, it can be shown that the flux divergence, given by E in (1), can be estimated by similar considerations applied to space variability of the third central moment of V_R.

5. ACKNOWLEDGEMENTS

The author is indebted to Dr. W. C. Swinbank and Dr. E. Kraus for their helpful discussions on boundary layer processes. The radiosonde data was acquired through the cooperation of Mr. Roy Eis and Dr. Harold Baynton of the National Center for Atmospheric Research. Diana Grunig assisted in the data reduction and editing. This work was performed under the general supervision and guidance of Dr. Roger Lhermitte, Chief of the Doppler Radar Program, Wave Propagation Laboratory, ESSA. Dr. Lhermitte also provided the Doppler radar data used in the analysis.

6. REFERENCES

Badgley, F.I. 1969: Large scale processes contributing energy to clear air turbulence, Clear Air Turbulence and Its Detection, New York, Plenum Press, 109-123.

Browning, K.A., and R. Wexler, 1968: The determination of kinematic properties of a wind field using Doppler radar, J. Appl. Meteorol. 7, 105-113.

Deardorff, J.W., 1970: Preliminary results from numerical integrations of the unstable planetary boundary layer, Natl. Center for Atmospheric Research, Boulder, Colorado, unpublished.

Lhermitte, R.M., 1968: Turbulent air motion as observed by Doppler radar, Proc. 13th Radar Meteorol. Conf., 498-503.

Lhermitte, R.M., and D. Atlas, 1961: Precipitation motion by pulse Doppler radar, Proc. 9th Weather Radar Conf., 218-223.

Lumley, J.L., and H.A. Panofsky, 1964: The Structure of Atmospheric Turbulence, New York, Interscience Publ. and Wiley & Sons, 239 pp.

Melnichuk, Yu. V., G. A. Smirnova and A. A. Chernikov, 1968: Radar measurements of the rate of turbulent energy dissipation in clouds, Proc. 13th Radar Meteorol. Conf., 488-489.

Vinnichenko, N.K., 1969: Recent Investigations of Clear-Air Turbulence and Its Detection, New York, Plenum Press, 246-270.

Reprinted from Journal of Applied Meteorology 10, No. 2, 234-246, 1971.

Probing of Atmospheric Motion by Airborne Pulse-Doppler Radar Techniques[1]

ROGER M. LHERMITTE[2]

Rosentiel School of Marine and Atmospheric Science, University of Miami, Coral Gables, Fla.

(Manuscript received 21 September 1970, in revised form 1 December 1970)

ABSTRACT

The paper discusses the use of airborne pulse-Doppler techniques for the sensing of particle motion inside convective storms. A downward-looking beam method providing observations of particle vertical velocity distributed in a vertical plane generated by the aircraft's motion is presented in detail. The possible use of a horizontal beam, which is perpendicular to the aircraft's trajectory and senses horizontal motion, is briefly mentioned. Included is a discussion of the application of the method to the probing of vertical air motion in convective storms and the observation of drop-size distributions in widespread rain. The real-time processing and recording of the Doppler signals by an on-line digital computer installed aboard the airplane is also described. The paper discusses the accuracy of the velocity measurements as related to radar system parameters and the aircraft ground speed.

1. Introduction

Observations of precipitation particle motion by ground-based, microwave, pulse-Doppler radars has been demonstrated to be an efficient means for the study of the physical and dynamical processes inside convective storms (Atlas, 1964; Lhermitte, 1966). This method relies on the assumption that precipitation particles effectively trace horizontal motion. The Doppler information is available in the form of a spectrum of radial velocities of the targets distributed in a small scattering volume which can be selected at practically any location in the atmospheric region effectively covered by the radar equipment.

Multi-Doppler radar systems, which have been recently proposed, are capable of observing and mapping the three-dimensional field of particle motion inside storms, leading to a much better understanding of their dynamics (Lhermitte, 1968). The use of a vertically pointing radar beam, providing observations of the vertical velocity of the precipitation particles above the radar equipment, has often been utilized and has contributed significantly to the knowledge of vertical air-motion structure within convective storms.

The ground-based Doppler radar method is expected to provide an effective means for probing motion inside storms; thus, it is anticipated that the method will generate a renewal of interest in the modeling of the three-dimensional circulation of convective storms based on observational data. The method, however, only applies to the observation of storms in the area covered by the radars. Although the radars can be installed in mobile vans and readily moved to locations where convective storms are likely to occur, the method still lacks the flexibility of observing storms found in remote regions, over water, etc., where there is also considerable interest in observing convective phenomena. A typical example is the tropical belt, where the study of convective storms over the ocean would definitely improve the design of general circulation models by better assessment of the vertical transport processes due to widespread convective activity.

If the radars are installed on mobile platforms such as ships or airplanes, they become very flexible tools capable of being moved to practically any region of interest. Airplanes are certainly the most flexible platforms, providing a means of access to any geographical area. There is, therefore, a definite interest in exploring the capability of airborne Doppler radars as a means of probing air motion within storms. The purpose of this paper is to investigate the concept of airborne Doppler, to discuss the efficiency of the method, and to estimate the design parameters required in such a system.

In ground-based radar systems, beam-scanning techniques are used for acquiring and mapping the Doppler radar information in three-dimensional space. Radar beam-scanning techniques can be duplicated in airborne systems; however, beam scanning in the direction of flight is not appropriate since in this case a Doppler frequency shift is produced by the airplane motion itself. This additional Doppler shift, which is produced by a radar beam that is not precisely perpendicular to the airplane motion, is discussed in the following section. It is therefore imperative to keep the radar beam perpendicular to the airplane trajectory and use the airplane movement to translate the beam through the storm. It must be noted, when combined with the aircraft movement, that additional scanning of the radar beam in the plane perpendicular to the aircraft's direction of flight can supply effective three-dimensional scanning of the region centered on the aircraft's trajectory.

---

[1] Contribution No. 1308 from the Rosentiel School of Marine and Atmospheric Science, University of Miami.

[2] Former affiliation: NOAA Research Laboratories, Boulder, Colo.

The most convenient scheme is based on the design of a vertically pointing beam, carried by an airplane flying above the storm to be observed. This method, which provides observation of the fall motion of precipitation particles in the vertical plane generated by the trajectory of an aircraft, will be discussed in detail in this paper.

Although it is more appropriate to conduct preliminary experiments with a vertically pointing radar beam, which has fewer logistical problems, it is proposed for later experiments that the radar beam be also used in a side-looking mode, thereby providing a means for observing the radial component of the horizontal motion of storm particles. Information concerning two-dimensional, horizontal wind fields must then be derived from two airborne Doppler radars being flown at the same altitude and scanning the same region of a storm from two different flight trajectories (see Fig. 8).

This paper includes a discussion of the radar design and the Doppler signal processing techniques suggested for optimizing the usefulness of the tool. Real-time processing of the Doppler radar signals, which offers the capability of displaying the radial velocity in real time aboard an airplane, will also be discussed.

2. Radar design and signal processing

The Doppler radar transmitter is a phase-coherent system composed of a very stable microwave source (STALO) and a phase-coherent microwave pulse amplifier which delivers a high-power signal which is then applied to the radiating antenna. It must be noted that since the airplane can be positioned close to the storm, the radar transmitted power can be maintained at a relatively low power level (1 – 20 kW) and still provide adequate sensitivity. The antenna beam axis must always be perpendicular to the direction of flight to minimize the contribution to the Doppler signal due to airplane motion. The joint contribution of the finite size of the antenna and the airplane's motion produces a smearing of the Doppler spectra which is discussed later in the paper. Investigation of this effect indicates that the beam size must be limited to less than 1° in the direction of the airplane's flight.

Since a narrow beam is needed, it will only be practical to consider short wavelengths, i.e., X band ($\lambda = 3.2$ cm) or K_u band ($\lambda = 1.7$ cm). Such a decision allows antenna sizes which are not prohibitive for airborne equipment. It must also be noted that the use of shorter wavelengths is associated with a significant increase of signal absorption by precipitation particles as well as an increase of the Doppler frequency shift for the same particle radial velocity. Therefore, even if K_u band optimizes the antenna size, it may be preferable to decide on X band equipment for easier interpretation of the data; in addition, radar components for that wavelength are more readily available. At X band, an antenna size of 8 ft by 5 ft, providing a 1°–2° beam, is an acceptable solution.

The pulse repetition frequency (PRF), which controls the rate of sampling of the radar signal, is dictated by the Doppler frequency coverage required by the anticipated maximum radial velocity and the radar wavelength. For instance, at 3.2 cm wavelength a PRF of 2 and 4 kHz provides a velocity coverage of ± 16 and ± 32 m sec^{-1}, respectively. It must be noted that full velocity coverage for a given PRF will be obtained only if Doppler sign discrimination is allowed by the signal processing scheme. This feature of the system is discussed later. Radar pulse duration should be maintained at less than 0.5 μsec to limit the duty cycle, and thereby the average transmitted signal power, and also to provide adequate range resolution.

The signal backscattered by the precipitation particles is detected by a phase-coherent receiver sensitive to pulse-to-pulse changes of the Doppler signal phase and amplitude. The receiver signal is phase-compared with a reference signal to show only the Doppler frequency shift. In order to obtain discrimination of the Doppler frequency sign, the phase-coherent receiver delivers two orthogonal signals, in-phase and quadrature, which are both necessary for a complete description of the radar signal. Those components are the real and imaginary parts of a complex receiver signal, thus containing information on the sign of the frequency shift, which thereby allows discrimination between approaching (positive Doppler shift) or receding (negative Doppler shift) targets. It must also be noted that the availability of complex receiver signals also permits the effective removal of folding processes at zero frequency in the Fourier transform operation, leading to the estimate of Doppler frequency spectra in a manner discussed below.

Such coherent radar systems have been used extensively for ground-based equipment and have demonstrated a capability of resolving radial velocity to within less than 0.1 m sec^{-1}, depending on the signal dwell time. If the radar transmitter operates at a low peak power level (~ 5 kW), the transmitter-receiver system can be kept very simple and compact. Solid state electronic components are used throughout the design with the exception of the power transmitter tube. An X band radar system based on this concept should not weigh more than 100 lb.

It is necessary that the radar signal available at the output of the radar receiver be processed in real time aboard the aircraft to provide readily available information on the radial velocity of the particles which are observed by the radar. The radial velocity information can then be presented in real time on displays which are

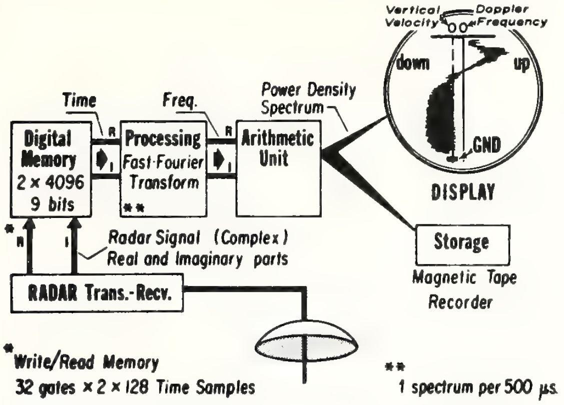

FIG. 1. Doppler radar signal real-time processing system. The radial velocity is continuously displayed on a cathode ray tube at the same time as the first and second moments of the Doppler spectra are recorded on magnetic tape. Note the ground return spectrum which indicates the zero Doppler.

installed aboard the aircraft, therefore providing means for better monitoring and control of the experiments. Since the expression of radial velocity spectra requires a Fourier transform operation on the radar signal selected at a given range, a specialized digital computer must be designed and built for this purpose. Fig. 1 illustrates this concept. The two radar signals (in phase R and quadrature I) selected at a given range are applied to an analog-digital converter capable of digitizing the amplitude of the coherent signals in a time less than 1 μsec, or preferably 0.5 μsec.

The digitized radar signals are then sorted in a digital memory array arranged in the form of an x, y matrix. The samples are stored along the x dimension for range-gate-to-range-gate information and along the y dimension for pulse-to-pulse data. It must be noted that each transmitter pulse is associated with a maximum number of range bins equal to the possible number of pulse widths in the range interval where targets occur. With a pulse width of 0.5 μsec (75 m resolution) and a maximum range of 15 km (altitude of the airplane, for example), the maximum number of non-redundant range gates is 200. In order to cover such a large number of range gates, a sequential operation for the storing and processing of the signals might be needed. This is discussed below.

The time signals available at each range gate must be recorded for a time long enough so that the spectral information obtained from the Fourier transform of the signal is meteorologically acceptable. The processing of N time samples provides N separate spectral density estimates with two degrees of freedom. Discussion of the effectiveness of the method, however, relies on discussion of the stability of the estimate of the spectral moments and is beyond the scope of this paper. The reader is referred to specialized treatment of the subject (e.g., see Blackman and Tukey, 1958).

For instance, the variance $\sigma^2/\bar{V}$ of the estimate of the first moment $\bar{V}$ of the Doppler spectrum can be derived from the calculation proposed by Miller and Rochwarger (1970) and expressed by

$$\frac{\sigma^2}{V}=\frac{\sigma_V\lambda}{4nT},$$

where σ_V is the standard deviation of the Doppler spectrum itself, T the signal dwell time, λ the radar wavelength, and n the number of independent estimates of the first moment which are used to calculate $\bar{V}$. If $\lambda=3.2$ cm, $T=0.2$ sec, then $\sigma_{\bar{V}}=0.12$ m sec^{-1} for $\sigma_V=1$ m sec^{-1}, and $\sigma_{\bar{V}}=0.37$ m sec^{-1} for $\sigma_V=10$ m sec^{-1}. Therefore, at a PRF of 2 kHz, a few hundred time samples provide a satisfactory estimate of the mean Doppler signal.

The real-time signal processing system proposed in this paper involves the use of hardware-implemented fast Fourier transform algorithms, requiring that the number of samples for each time series, N, be of the form $N=2^m$, where m is an integer.

Although it is recognized that increasing the number of time samples always increases the quality of the spectrum, it also increases the signal dwell time, thereby slowing the data acquisition rate and requiring better assumptions about the time stationarity of the scattering processes which might be critical for a fast-moving airplane. Also, the cost of the memory will drastically increase with its size. It is therefore suggested that the memory size be limited to 64 gates by 128 time samples, i.e., capable of storing 8192, 18-bit, complex samples (9-bit for in-phase and 9-bit for quadrature samples). The time required to fill the memory at a 2-kHz pulse repetition rate is 64 msec. The processing of the samples by the Fourier transform system will only start when the writing cycle has been completed and will then be done by reading the data stored in the memory for each range gate. A detailed description of the Fourier transform system is beyond the scope of this paper. It must be noted, however, that the system design is based on hardware implementation of a slightly modified fast Fourier transform (FFT) algorithm (Cooley and Tukey, 1965). The FFT requires that 7×128 complex multiplications be performed for the evaluation of each spectrum. The complex multiplication is effectively a rotation of coupled samples, which is obtained from four elementary multiplications between a complex signal (in-phase and quadrature components) and the sine and cosine terms which determine the rotation of the sample. Four parallel multipliers are required to bring the complex multiplication time down to approximately 0.5 μsec, which can be easily met with modern MSI (medium scale integration) integrated circuits. It will then take ~0.4 μsec for a Fourier transform of 128 points to be obtained.

Subsequent operation must be done after the Fourier transform process to evaluate spectral density. This will bring the whole spectrum processing time to ~1 msec, including the evaluation of the first moment and the variance of the spectra and the transfer of the data to a tape recording system and a cathode ray tube (CRT) display. The total time for processing 64 gates will be equal to the time required for the loading of the 128 samples (64 msec), at the rate mentioned earlier. If the system includes two separate memory units with alternate write and read functions, the system will be used 100% of the time.

The spectral information delivered by the system can then be displayed on a cathode ray tube to show range-velocity functions, thereby providing real-time monitoring of the experiment. The concept is illustrated in Fig. 1. If only one memory unit is available, the 64-gate Doppler information will be upgraded every 128 msec. During this time an airplane flying at 100 m sec^{-1} will move 12.8 m, which is a dimension comparable to the size of the radar beam at a mean range. If two memory units are used, the acquisition rate of the system will be increased to 1 msec per gate. The 64 gates can also be scanned and the Fourier operation done by steps to increase the number of range gates processed by the system at the sacrifice of the total time needed to display and record the range-velocity information.

The availability of a real-time monitoring capability constitutes a definite advantage of the system, since it provides effective means for optimizing the experiment through the monitoring of particle velocity conditions during the flight. The information which is displayed on the CRT can be recorded photographically, thereby showing the continuity of the velocity information from gate to gate. This capability is assisted by the simultaneous processing and digital recording of the moments of the spectra. The first moment, the second central moment (variance), and perhaps the third and fourth moments are sufficient to characterize the Doppler information in a quantitative manner, since the detailed information on the spectrum will still be recorded photographically on the CRT.

3. Vertical beam method

The method, which is illustrated in Fig. 2, relies on the use of a vertically pointing beam produced by a Doppler radar installed aboard an airplane. Since it deals with particle vertical velocity, this concept is very similar to the vertically pointing mode which has been used for years in ground-based equipment (Battan, 1963, 1964; Donaldson and Chmela, 1968; Donaldson and Wexler, 1969; Probert-Jones and Harper, 1961). The Doppler spectrum observed with such a method [a joint probability function $p(V_f,\sigma)$ for the vertical velocity V_f] and the radar cross section of the detected targets σ can be considered as the distribution, $S(V)=dp/dV_f$, of the target backscattered signal intensity with radial—in this case vertical—velocity. The spectrum $S(V)$ is evaluated from a Fourier transform operation on the backscattered signal selected at a given range. Thus, we have

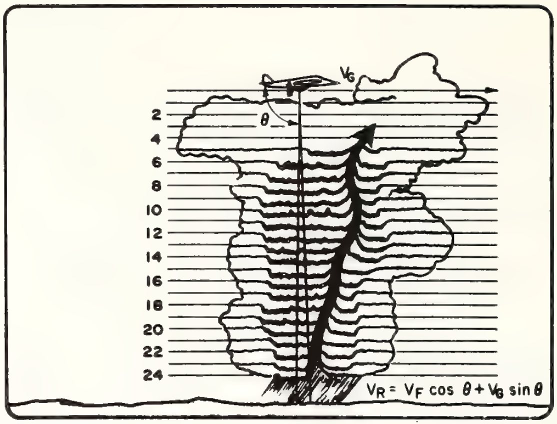

Fig. 2. Vertical beam method. The presence of an updraft can be seen from the organized distribution of the vertical velocity in the two-dimensional plane generated by the beam motion. The same scheme can apply to an upward-looking beam.

$$S(V)=C d\eta/dV_f, \tag{1}$$

where η is the reflectivity of the medium and the constant C is conventionally determined from the radar signal mean intensity, the characteristics of the radar, and the range of the target.

The spectrum $S(V)$ can be described by its moments as follows:

$$\bar{V}_f{}^n = \int_{-\infty}^{+\infty} S(V) V_f{}^n dV \Big/ \int_{-\infty}^{+\infty} S(V) dV, \tag{2}$$

where the first moment $\bar{V}_f$ is the mean Doppler velocity and the second central moment, $\overline{(V_f-\bar{V}_f)^2}$, is the spectrum variance. Although the mean Doppler velocity and spectrum variance provide most of the needed meteorological information which is discussed in this paper, the third moment (skewness) and the fourth moment (kurtosis) can be useful in more detailed meteorological interpretation of the Doppler radar data.

It must be noted that in the application discussed here of a vertical beam which is moving at the high speed of the airplane, an additional variance, σ^2_G, to the Doppler spectrum will be generated by the airplane's ground speed, V_G, combined with the finite size of the radar beam, $\Delta\beta$. For a beam with Gaussian shape, we have

$$\sigma_G{}^2 = (7\times 10^{-3}\Delta\beta V_G)^2, \tag{3}$$

where $\Delta\beta$ is the total 3-dB beamwidth in degrees, $\sigma_G{}^2$ is in m^2 sec^{-2} and V_G in m sec^{-1}.

This effect is illustrated by Fig. 3 which also shows that a departure β_0 of beam axis from a position perpendicular to the airplane's trajectory produces a shift,

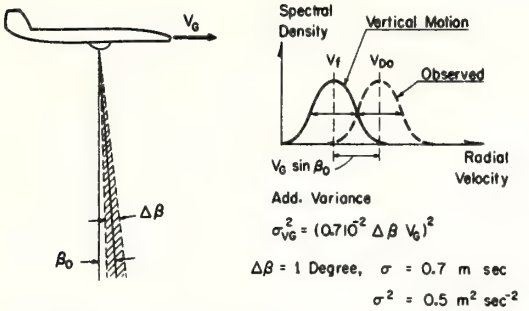

FIG. 3. Contribution to shift and variance of the Doppler spectrum due to the tilt of the beam in the direction of motion and its finite size.

$\Delta V = 1.7\times 10^{-2}\beta_0 V_G$, of the mean Doppler speed, where β_0 is in degrees. This effect can be overcome practically by recording and processing the signal returned by the ground so that the mean Doppler evaluated from the ground return can be used for estimating the zero vertical velocity position in the Doppler velocity scale (see Fig. 1). This procedure will also provide means for correcting Doppler shifts caused by the possible occurrence of airplane vertical motion.

In the case of a vertically pointing radar beam, both vertical air velocity w and particle terminal speed V_t contribute to the Doppler velocity V_f of the targets. Assuming that all particles have reached their terminal speeds and further assuming that the air velocity can be neglected leads to $V_f = V_t$. If, in addition, there is a known relationship between particle size and terminal velocity, as well as between particle size and radar cross section, the Doppler spectrum $S(V)$ can be derived from a given particle-size distribution, $n(D)$, from

$$dn/dV_f = [n(D)\sigma(D)] \bigg/ \left[\frac{dV_f}{dD}\right], \tag{4}$$

where $\sigma(D)$ is the radar cross section of the targets as a function of their diameter and dV_f/dD the derivative of the relationship between the target diameter D and terminal velocity.

The assumption of spherical raindrops falling at their terminal speed provides the required condition, since the particle radar cross section can be evaluated as a function of its diameter, and the relationship between V_t and D can be derived from experimental data. The experimental data on the terminal speed of raindrops are derived from ground-level measurements and must be adjusted to account for the change of air density at the altitude at which the observations are made. For water spheres smaller than the radar wavelength, the radar cross section $\sigma(D)$ is closely approximated by $\sigma(D) = \pi^5 D^6/\lambda^4$. Evaluating $\sigma(D)$ for larger particles requires the application of the more complex Mie scattering theory, still leading to an accurate solution except in the case of significant departures of drop shape from sphericity.

The possible contribution of significant vertical air motions, discussed below in more detail, also affects the accuracy of the estimate of drop-size distributions derived from this method. An uncertainty of vertical velocity of ±0.5 m sec^{-1}, for instance, modifies the estimated diameter by ±0.1 mm for a mean diameter of 1 mm and ±0.25 mm for a mean diameter of 2 mm. Thus, the method is most attractive for probing mean drop-size distributions in large meteorological systems in which the contribution of vertical air motion can be assessed from synoptic conditions. Widespread precipitation systems, such as are associated with large tropical cyclones, can be probed efficiently by the method with enhanced potential, due to the excellent mobility of the airplane.

In the case of convective storms, the applicability of the method for the probing of precipitation particle-size distributions becomes more questionable because of the probable occurrence of significant, unknown vertical air motions. Since knowledge of the updraft/downdraft structure of a convective storm is of paramount importance for assessing storm processes, it is more appropriate in this case to use the vertical Doppler beam method as a means of deriving vertical air velocity from observations of the Doppler spectra. The presence of significant vertical air motions modifies both the Doppler mean velocity $\bar{V}_f$ and the spectrum variance σ_d^2.

The mean Doppler velocity is expressed by

$$\bar{V}_f = \bar{V}_t + \bar{w}, \tag{5}$$

where $\bar{V}_t$ is the mean Doppler velocity due solely to particles falling at their terminal velocity and $\bar{w}$ is the mean vertical motion of the air. If the random processes V_t and w are independent, the variance of the Doppler spectrum is given by

$$\sigma_f^2 = \sigma_t^2 + \sigma_w, \tag{6}$$

where σ_t^2 is the variance for terminal velocity alone and σ_w^2 is the air motion variance.

Let us assume a known exponential drop-size distribution of the form

$$n(D)dD = N_0 e^{-\Lambda D} dD, \tag{7}$$

where $n(D)dD$ is the number of drops per unit volume in the diameter interval dD, and N_0 and Λ are parameters of the distribution adjusted for best fit to actual data.

The mean velocity $\bar{V}_t$, the rain intensity R, and the reflectivity factor Z can all be expressed within the above drop-size distribution assumption by the following expressions:

$$\bar{V}_t=\int_0^{+\infty} n(D)\sigma(D)V(D)dD \bigg/ \int_0^{+\infty} n(D)\sigma(D)dD, \quad (8)$$

$$R=(\pi/6)\int_0^{+\infty} n(D)D^3V(D)dD, \quad (9)$$

$$Z=\int_0^{+\infty} n(D)D^6dD. \quad (10)$$

The parameter N_0 disappears in the expression for $\bar{V}_t$ but is still contained in R and Z equations; therefore, the value of N_0 contributes significantly to the $\bar{V}_t$-Z relationship derived from (8) and (10) as discussed below.

By assuming an exponential distribution of the form (7) and also assuming that N_0 is a constant, we obtain the familiar Marshall-Palmer distribution. By further assuming a Rayleigh radar cross section for the raindrops of the form $\sigma \propto D^6$ and the approximation proposed by Spilhaus (1948) for the function $V(D)$, we have

$$V(D)=KD^{1/2}. \quad (11)$$

Substituting (11) in expressions (8)–(10), we obtain the solutions:

$$\bar{V}_t=\frac{259}{(42)^{1/2}}KR^{1/9}, \quad (12)$$

$$\Lambda=42R^{-2/9}, \quad (13)$$

$$Z=213R^{14/9}, \quad (14)$$

where Λ is in cm^{-1}, R in mm hr^{-1} and K is the constant proposed by Spilhaus to fit the Laws (1941) and Laws and Parsons (1943) raindrop terminal velocity data. Expression (12) was first proposed by Chimera (1960), and a different form, involving the relationship between $\bar{V}_t$ and Z, was discussed by Rogers (1964). The relationship proposed by Rogers, which can be derived from (12) and (14), is

$$\bar{V}_t=3.8Z^{1/14}. \quad (15)$$

A different expression for $V(D)$ can be derived which provides a more realistic fit for the experimental data on the terminal velocity of raindrops published by Gunn and Kinzer (1949). This expression, which has the same form as that proposed by Best (1950) to fit the Davies (1942) raindrop terminal velocity data, is

$$V(D)=V_{\max}[1-e^{-(aD^2+bD)}], \quad (16)$$

where $V_{\max}=920$ cm sec^{-1}, $a=11$ cm^{-2}, and $b=3.3$ cm^{-1} were determined for best fit to the Gunn and Kinzer data.

The functions $\bar{V}_t$ vs Z, derived from (8) and (16), and the Chimera-Rogers relationship are shown in Fig. 4, where they can be compared with estimates of $\bar{V}_t$ obtained from numerical computations based on actual drop-size distributions reported by Cataneo and Stout (1968). One sees, at least in the domain of Z shown in Fig. 4, that the curve labeled Frank/Best [the more realistic expression of terminal velocity proposed in (16)] is a better fit to the computations of $\bar{V}_t$ evaluated from actual drop-size distributions. It must be noted, however, that the evaluation of $\bar{V}_t$ based on experimental drop-size distributions still assumes a Rayleigh radar cross section. The use of a different $\sigma(D)$ function will modify the relationship between $\bar{V}_t$ and Z. It is interesting to note also that the departure from an exponential shape, which is noticeable in all drop-size distributions, does not affect the results significantly. However, on the basis of this limited selection of actual drop-size distributions, which underestimates $\bar{V}_t$ for small values of Z and overestimates $\bar{V}_t$ for large values of Z, the empirical relationship

$$\bar{V}_t=2.0Z^{1/11.5} \quad (17)$$

is a better fit for the experimental data, and provides a means of estimating the mean vertical air motion to within ±0.3 m sec^{-1} when rain is present. It is therefore suggested that vertical air motion can be observed from (5) with reasonable accuracy by use of an assumed $\bar{V}_t$-Z relationship, if the scattering medium is composed of raindrops at all levels such as in the case of precipitation from "warm" clouds or below the melting level in widespread precipitation conditions.

The Doppler velocity variance for terminal velocity alone, σ_t^2, the second central moment of the Doppler spectrum mentioned earlier, can be evaluated within the same assumptions involved in the computations of $\bar{V}_t$ above. Chimera (1960) calculated σ_t^2 from the expression

$$\sigma_t^2=\frac{\int_0^{\infty} n(D)D^6[V(D)-\bar{V}_t]^2dD}{\int_0^{\infty} n(D)D^6dD}. \quad (18)$$

By assuming the Spilhaus relationship (11) for $V(D)$ and the Marshall-Palmer drop-size distribution for $n(D)$, we have

$$\sigma_t^2=0.036\bar{V}_t^2. \quad (19)$$

Expression (19), proposed by Chimera,[3] is shown in Fig. 4 as a function of Z [making use of (14)], as are calculations of σ_t^2 made by assuming the more realistic expression (16) for $V(D)$. The numerical evaluations of σ_t^2, derived from the same selected experimental drop-size distributions used in the computations of $\bar{V}_t$ discussed above, are also shown in Fig. 4 for assessment of the significance of the theoretical estimates of σ_t^2. One sees that the theoretical expression proposed by

---

[3] Chimera originally proposed $\sigma_t^2 = 0.04(\bar{V}_t)^2$ which is slightly incorrect.

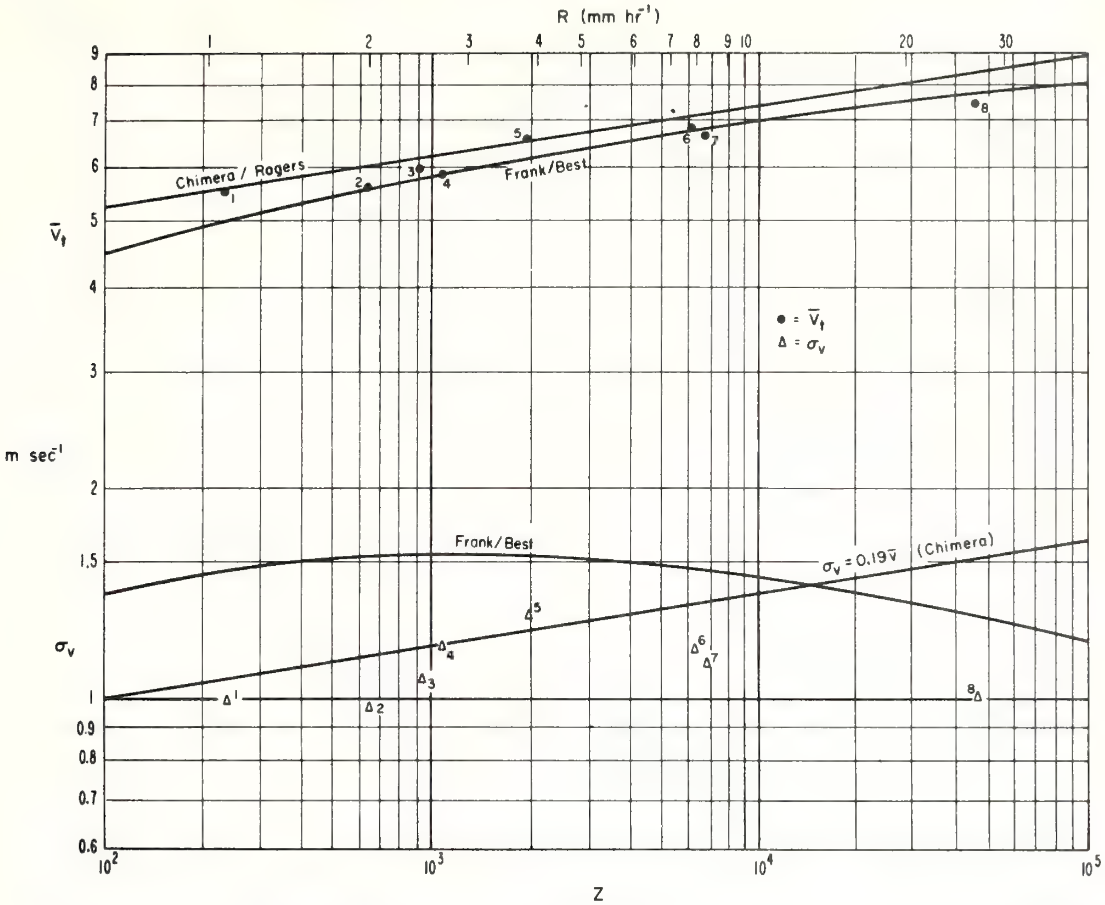

FIG. 4. The functions $\bar{V}_t$ and σ_v shown as a function of radar reflectivity Z for a medium exclusively composed of raindrops. Theoretical estimates shown by the curves are based on the Marshall-Palmer drop-size distribution. The Spilhaus relationship for terminal velocity is used for the curve labeled Chimera/Rogers; a more refined velocity assumption applies to the curve labeled Frank/Best. Open triangles and solid circles are experimental values calculated from actually observed drop-size distributions.

Chimera overestimates σ_t^2 and does not reveal its actual variation with Z. The same evaluation using the assumption (16) for $V(D)$ also overestimates σ_t^2 but still shows its variation with Z, i.e., the presence of a weak maximum in the vicinity of $Z=10^3$ and its systematic decrease for large Z's. It is obvious, from inspection of experimental drop-size distributions, that the exponential function overestimates the number of drops for both very small and very large sizes, thus causing an increase of the variance of the distribution and resulting in an increase of the theoretical estimate of the Doppler spectrum variance. For both large and small values of Z, the spectrum variance computed from experimental data is always in the vicinity of 1 m^2 sec^{-2}. This result was shown in an earlier paper (Lhermitte, 1963). There is only a slight maximum of σ_t^2 for $10^3<Z<10^4$. Since any experimental drop-size distribution known to the author always exhibits the same shape characterized by a maximum of the distribution for a drop diameter in the vicinity of 1–2 mm, it is practically correct from the results discussed above to expect that the variance of the vertical Doppler spectrum obtained in rain conditions will always be near 1 m^2 sec^{-2}. Note that σ_t^2 varies more with slight changes of the shape of the drop-size distribution than with the radar reflectivity Z. Also, if the particles are falling in a wind shear environment, there is a sorting of drop sizes which can cause a drastic reduction of the drop-size distribution, thereby upsetting the $\bar{V}_t$-Z relationship. In this case, however, σ_t^2 is also reduced, which offers the possibility of recognizing the presence of such an unusual drop-size distribution.

The particle vertical velocities which have been used above for the evaluation of $\bar{V}_t$, for example, are derived from actual measurements of the terminal velocities of raindrops, such as those published by Gunn and Kinzer (1949). However, terminal velocity can be expressed theoretically, since it results from a balance condition between gravitational drag forces represented by

$$(m-m_a)g=\frac{SC_d\rho_aV^2}{2}, \qquad (20)$$

where m is the particle mass, S its cross section normal to the direction of movement, g the acceleration of gravity, ρ_a the surrounding air density, m_a the displaced air mass and C_d the drag coefficient. For a water particle, we have that $m-m_a\approx m$.

If we are concerned with spherical particles

$$m=\frac{\pi D^3}{6}\rho_s, \quad S=\frac{\pi D^2}{4},$$

where ρ_s is the sphere density. In this case V^2 is then expressed by

$$V^2(D)=\frac{4}{3}\frac{Dg\rho_s}{C_d\rho_a}, \qquad (21)$$

where C_d can be derived from experimental data showing the relationship between C_d and the Reynolds number Re for spherical bodies. We express the Reynolds number in the form

$$\mathrm{Re}=\frac{LV\rho_a}{\mu}, \qquad (22)$$

where L is the characteristic length (diameter in the case of spheres), and μ the air dynamic viscosity.

In the case of nonspherical particles, if the particle mass m, its cross section S, and drag coefficient C_d are specified, V can still be evaluated theoretically from (20). It must be noted, however, that any departure from the spherical shape modifies the relationship between m and S with respect to that applying to a sphere and that there will also be a modification of the C_d-Re relationship. If we write (20) in the form proposed by Genève (1959), we have

$$C_d=\frac{2g}{V^2}\frac{\rho_s}{\rho_a}\frac{v}{S}, \qquad (23)$$

where v is the volume of the particle.

In the case of a spherical particle, $v/S=\frac{2}{3}D$, and C_d is evaluated correctly from (21).

In the case of a nonspherical particle of mass m, we define an equivalent diameter D_0 determined from

$$\frac{\pi D_0^3}{6}=v, \qquad (24)$$

and a particle cross section defined by

$$S=\frac{\pi}{4}D_0^2\alpha^2, \qquad (25)$$

where the adjusted diameter, $D_0\alpha$, is derived from a parameter α which characterizes the particle's nonsphericity. If we evaluate v/S for a nonspherical particle, we have

$$\frac{v}{S}=\frac{2}{3}D_0\frac{1}{\alpha^2}, \qquad (26)$$

and by substituting in (23), we obtain

$$C_d\alpha^2=\frac{2g\rho_s}{V^2\rho_a}\left(\tfrac{2}{3}D_0\right)=\hat{C}_d. \qquad (27)$$

Therefore, the estimate of $\hat{C}_d$ (implicitly assuming a spherical condition), shown in Fig. 5 as derived from data published by Gunn and Kinzer (1949) and Foote and Du Toit (1969) for actually nonspherical particles, effectively leads to the estimate of the quantity $C_d\alpha^2$, involving both the drag coefficient and the departure of the drop from sphericity.

The quantity α^2 can be evaluated from the particle shape: for a hemispherical particle, $\alpha^2=\sqrt[3]{4}$, while a prolate ellipsoid gives $\alpha^2=\sqrt[3]{\beta^2}$, where β is the ratio between major and minor axes.

For the nonspherical particles discussed above, Re must be expressed by

$$\frac{\mathrm{Re}}{\alpha}=\frac{D_0V\rho_a}{\mu}. \qquad (28)$$

For a small deviation from spherical shape, it is probable that the C_d-Re relationship does not appreciably differ from that applying to a sphere, offering the means to estimate α^2 and therefore to assess raindrop flatness from terminal velocity observations. Indeed, Piat (1960) has shown that even for very flat spheroids, C_d does not exceed 0.6 for $10^3<\mathrm{Re}<10^5$, compared to $C_d=0.45$ for rigid spheres at the same Reynolds number. Such a procedure applied to the Gunn and Kinzer data provides an estimate of α^2 ranging from 1 for small spheres to 1.6 for large drops (5 mm diameter). Since the drag coefficient is expected to increase with departure of a particle from sphericity, the above estimates constitute an upper limit for α^2. This procedure must be supported by actual observations of the shape of the raindrops. A very complex structure of the drop, the occurrence of internal circulations in the drop, i.e., the presence of small-scale motion variability in the boundary layer around the drop, will render the above discussion only marginally acceptable.

The change of air density with altitude modifies the expression of the terminal velocity given by (20). For the terminal velocities at two selected levels, we thus have

$$\frac{V_1^2}{V_0^2}=\frac{C_{d0}S_0\rho_0}{C_{d1}S_1\rho_1}, \qquad (29)$$

where subscripts 0 and 1 refer to two different levels.

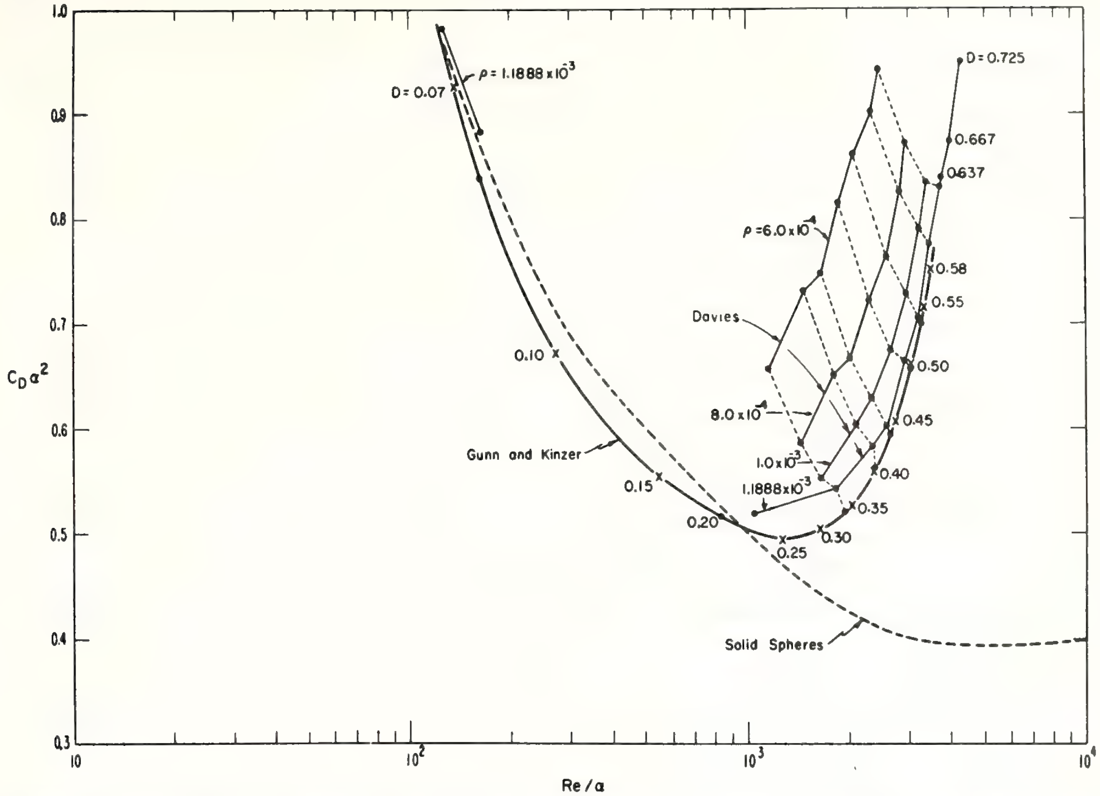

FIG. 5. Estimate of $C_d\alpha^2$ as a function of Re/α for raindrops as derived from experimental data on terminal velocity from the Gunn and Kinzer experiments. The C_d-Re relationship for solid spheres is also shown, as well as the experimental data from Davies obtained in a medium of lower air density ρ.

By substituting the expression (25) for S in (29) and assuming particles of the same mass, we have

$$\frac{V_1^2}{V_0^2}=\frac{C_{d0}\alpha_0^2\rho_0}{C_{d1}\alpha_1^2\rho_1}. \tag{30}$$

If $C_d\alpha^2$ does not vary from level 0 to level 1, implying no change of either C_d or the particle shape, we have

$$\frac{V_1}{V_0}=\left(\frac{\rho_0}{\rho_1}\right)^{\frac{1}{2}}. \tag{31}$$

If the drop retains its shape at the two levels, only an adjustment of C_d is necessary to reach the correct solution; this is required by the variation of Re due to the change of terminal velocity. The evaluation of V therefore requires an iteration process converging to a solution which fits both (20) and the C_d value derived from the C_d-Re relationship. This procedure is easier for spheres for which the C_d-Re relationship is known.

It must be noted that Re will effectively decrease with smaller values of ρ, since the change of velocity cannot exceed the $\sqrt{\rho}$ function. Therefore, for smaller particles for which C_d is expected to decrease with an increase of Re, (31) overestimates the variation of terminal velocity with the decrease of ρ. The behavior of the relationship for particle diameters >3 mm cannot be predicted without knowledge of the particle shape.

The only actual observations of the terminal velocities of raindrops in a low density medium were made by Davies (1942) and reported and discussed by Best (1950). The evaluation of the quantity $C_d\alpha^2$ obtained from these data by use of (27) is presented in Fig. 5 and shows that the $(C_d\alpha^2)$-(Re/α) relationship varies with with change of ρ. This variation can be attributed to a change of the drop shape or to internal circulations and also to a change of C_d. No physical explanation is offered for this effect at this time.

Since the Davies' observations were effectively made in low air density conditions corresponding to altitudes extending to 6000 m, they can be used almost directly to access or estimate the terminal velocity of liquid raindrops in actual atmospheric conditions. The procedure still requires taking into account the actual change of temperature which influences μ in (28) and therefore C_d. Therefore, an empirical fit of these data may represent an appropriate solution to the problem.

Although the Davies' data exhibit slight dependence of the V_1/V_0 ratio with particle size, Best proposed a mean relationship applying to particles 0.3–6 mm in diameter. Best also proposed an exponential fit for the dependence of V with altitude of the form

$$V_1 = V_0[\exp(-bz)], \tag{32}$$

which can be derived from a standard atmosphere assumption. However, because of the limited applicability of the standard atmosphere concept for a given convective storm situation, it is preferable to resort to the fit for the Davies' data proposed by Foote and Du Toit (1969), i.e.,

$$V_\rho(D) = V_{\rho 0}(D) 10^y [1 + 2.3 \times 10^{-3} (1.1 - \rho/\rho_0)(T - T_0)], \tag{33}$$

with

$$y = 0.43 \log_{10}(\rho_0/\rho) - 0.4 \log_{10}(\rho_0/\rho)^{2.5}, \tag{34}$$

and where ρ_0 and T_0, respectively, refer to density and temperature at 20C and 1013 mb.

It must be noted that this solution applies only to a domain of ρ_0/ρ limited to less than 2 and leads to an incorrect answer above this value of ρ_0/ρ. A somewhat simpler expression,

$$V_\rho(D) = V_{\rho 0}(D)(\rho_0/\rho)^{0.4}, \tag{35}$$

has also been proposed by Foote and Du Toit and has been found an acceptable fit to the Davies' data. Expression (35) also applies to a much larger domain of ρ_0/ρ than (33). It must be noted that any solution of the form (35), where the corrective term does not contain the particle size, allows an easy adjustment of such Doppler spectrum moments as mean velocity and variance.

Solving (8), we can thus write

$$\overline{V_\rho(D)} = \overline{V_{\rho 0}(D)} f(\rho_0/\rho, T). \tag{36}$$

Similarly, for the variance, we have

$$\sigma_\rho{}^2 = \sigma_\rho{}^2 [f(\rho_0/\rho, T)]^2. \tag{37}$$

Best proposed a slightly different fit for particles with diameters <0.3 mm, but still outside of the Stokes' regime, and particles of larger sizes extending to 6 mm. It is interesting to note, however, that small diameters do not contribute significantly to the estimate of mean Doppler velocity or variance because of the presence of the D^6 term in the spectrum resulting from the radar cross section/diameter relationship. Indeed, the evaluation of V_t and Z from actual drop-size distributions discussed in this section shows that there is no significant contribution from particles <0.5 mm.

The method discussed above offers the best means for estimating the vertical air velocity in the case of a known relationship between V_t and Z. It can be replaced by a different method proposed by Probert-Jones and Harper (1961) and Battan (1964), where the lower boundary of the spectrum is related to a known particle size and shape and, therefore, to a known terminal velocity. The Battan/Harper method is certainly appropriate in the absence of a known relationship between V_t and Z. It must be noted, however, that the lower boundary of the spectrum cannot be assigned to a specific particle diameter until the spectrum dynamic range is specified (Lhermitte, 1964). Furthermore, the method is very sensitive to slight changes of the drop-size distribution in the small diameter region. However, this is contrary to the effect discussed above, i.e., that there is no significant contribution to $\bar{V}_t$ due to small particles.

The presence of frozen particles does not allow a similar theoretical determination of the relationship between $\bar{V}_t$ and Z. The mean vertical Doppler ranges from 0.25 m sec^{-1} for ice crystals to 1.5 m sec^{-1} in the case of large snowflakes, and Z ranges from approximately 10^{-2} to 10^{+3}, depending on the snow density. The spectrum variance expected in this case is considerably smaller than that for rain, ranging from 0.04 to 0.2 m^2 sec^{-2} depending on the shape and size of the particle. Thus, the presence of snowflakes and ice crystals can be identified on the basis of the observation of very narrow spectra if, however, there is no air velocity variance. The presence of small-scale air motion variability, which controls spectrum width, will always be associated with a larger scale variability of the spectrum mean; it can therefore be identified on this basis in the velocity-time pattern.

Since the relationship between $\bar{V}_t$ and Z will be drastically different for snowflakes and ice crystals, we have an additional means of recognizing the presence of snow and of accessing the contribution due to air motion variance. However, the occurrence of graupel or melting snowflakes will cause larger terminal velocities and, therefore, complicate the interpretation of the data.

The presence of hailstones will greatly increase both $\bar{V}_t$ and the Doppler variance since the terminal velocities will substantially exceed those of other particles. The terminal velocity V of hailstones can be derived from (23) in the form

$$V^2 = \frac{2g\rho_s}{C_d\rho_a}\frac{v}{S}, \tag{38}$$

where ρ_s is now the hailstone density, v the hailstone volume, and S its cross section normal to the direction of fall. The ratio v/S characterizes the hailstone nonsphericity and is equal to $\frac{2}{3}$D for spheres of diameter D.

The assumption of spherical hailstones leads to an easy evaluation of their terminal speed based on (38) [or in a simplified form on (21)] and the C_d-Re relationship applying to spheres. The computation can be made for any value of ρ_a provided that the air dynamic viscosity μ is also specified so that the Reynolds number can be evaluated. The Reynolds numbers for hailstones are large, falling in a region of the relationship of

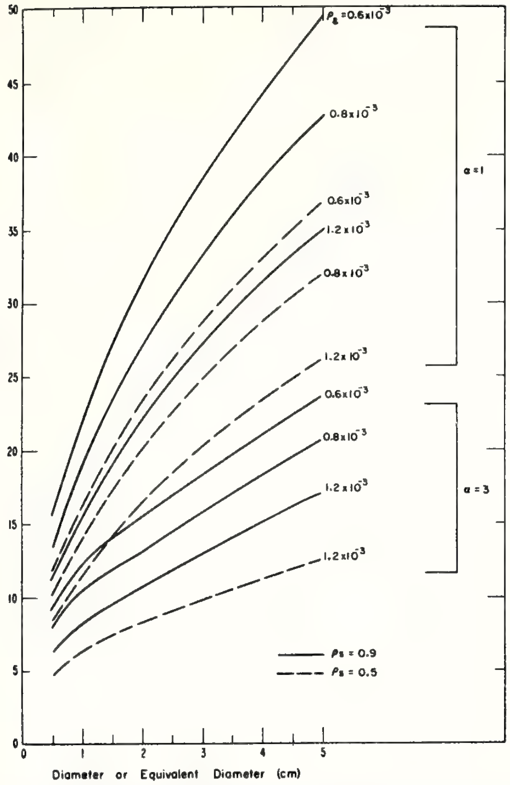

FIG. 6. Estimated terminal velocity of hailstones of different sizes and shapes falling in different air densities ρ_a. The hailstone density is ρ_s while α is a nonsphericity index derived from V/S (V and S being the hailstone volume and cross-sectional area, respectively).

$C_d = f(\text{Re})$ where there is only a small variation of C_d as a function of Re. In such a case, the extrapolation of the terminal velocity of hailstones, falling in a fluid of density ρ_{a_1} can be derived from the terminal velocity of hailstones falling in the fluid of density ρ_{a_0} from (31). This procedure is justified only if C_d does not vary appreciably with Re. This is not so for very large hailstones, since the Reynolds number in this case can reach its critical value.

Terminal velocity can also be evaluated for nonspherical hailstones, since, as shown by Piat (1960), we have $C_d \approx 0.45$ for conical hailstones; for flattened bodies $C_d \approx 0.6$ for Re in the vicinity of 10^3–10^4, increasing to $C_d = 0.75$ for $\text{Re} > 3 \times 10^4$. Fig. 6 shows terminal velocities for hailstones of different densities and shapes as well as for different air densities evaluated according to the above discussion.

Assuming the $V(D)$ relationship and an exponential distribution of hailstone sizes permits the computation of $\bar{V}_t$ in essentially the same manner as described in (8).

Computations of $\bar{V}_t$ and the variance σ_t^2 for a scattering medium composed exclusively of hailstones have been reported by Donaldson and Wexler (1969) and Boston and Rogers (1969). These authors used an exponential distribution for hailstone sizes of the form $n(D) = N_0 e^{-\beta D}$ where β varies from 2.93 (Donaldson and Wexler) to 3.9 (Boston and Rogers). The moments $\bar{V}_t$ and σ_t^2 were then evaluated from (8) and (18) as a function of maximum hail size adopted in the exponential distribution for observations made at an altitude of 4 km.

The complete Mie scattering coefficients were evaluated by Boston and Rogers at different wavelengths for both dry and wet hailstones. The results show that at the short wavelength ($\lambda = 3.2$ cm) discussed in this paper, $\bar{V}_t$ increases to ~ 20 m sec^{-1} in the case of dry hail and to ~ 15 m sec^{-1} in the case of wet hail. The variance σ_t^2 increases to ~ 18 m^2 sec^{-2} for dry hail and to ~ 8 m^2 sec^{-2} for wet hail. There is almost no change of these quantities for hailstone sizes > 2 cm. A Doppler spectrum due to hail was also presented by Lhermitte (1964) showing a spectrum width reaching 20 m sec^{-1}.

Since radar reflectivity increases with the presence of hailstones even at the radar wavelength proposed here, we must use a $\bar{V}_t$-Z relationship other than that used for raindrops.

The presence of a significant vertical air motion complicates the interpretation of the data as shown by the ground-based application of the method. However, in the airborne application of the technique, spectra can be displayed with excellent continuity as a function of space coordinates. This capability provides better observation of the details of the Doppler-space coordinate pattern, leading to an easier detection of striking features. Fig. 7 is an attempt to show the differences between a sharp discontinuity of vertical air motion, the presence of turbulence characterized by random deviations of the motion with respect to a mean, and the

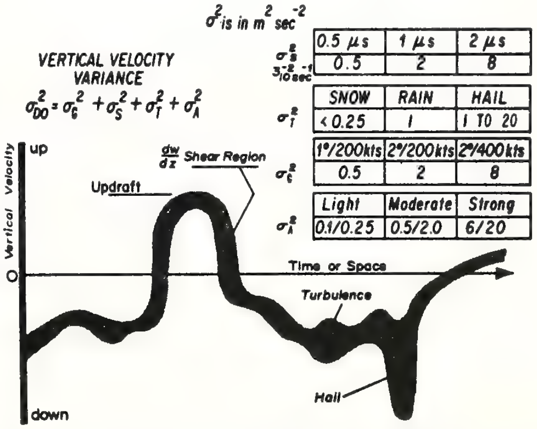

FIG. 7. Estimated velocity-time pattern obtained at a given altitude where an updraft, turbulence and hail are present. Several contributions to the Doppler spectrum variance are indicated: σ_G^2, airplane motion; σ_S^2, wind shear; σ_T^2, particle terminal velocities; and σ_A^2, air turbulence.

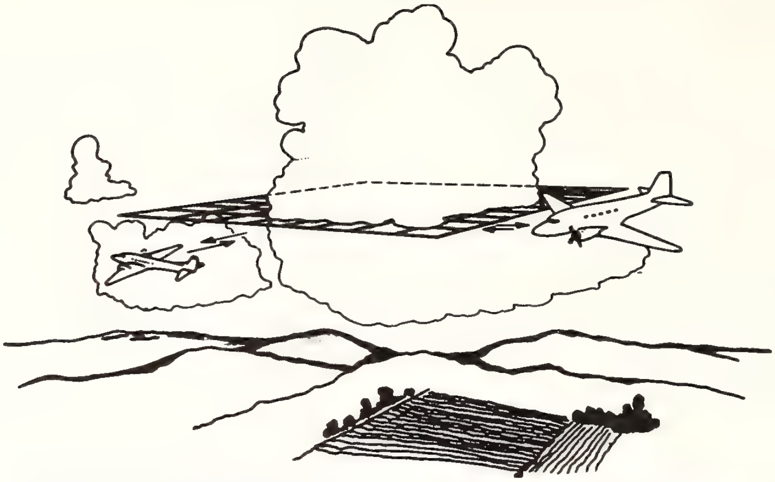

Fig. 8. Observing two-dimensional horizontal velocities in a plane defined by the trajectories of two aircraft simultaneously probing the same storm. Only one aircraft is needed if the storm processes are stationary for several minutes.

presence of hail. All these effects contribute to an increase of the variance of the Doppler spectrum as shown in the equations presented in the figure. However, the presence of an updraft leads to an easily detected velocity pattern, turbulence increases the width but does not change the mean of the spectrum, and the presence of hail will drastically change the spectrum width as well as the spectrum mean.

For an airplane flying above a convective storm, the hail region can be reasonably close to the radar, leading to a small cross section of the radar beam and excellent space resolution; this is allowed by the fast real-time signal processing system capable of upgrading the Doppler information every 1/10 of a second corresponding to the average displacement of the airplane of only 15–20 m. This feature should enhance the details in the Doppler-space relationship and provide better means for their interpretation.

4. Conclusion

The description of the airborne pulse-Doppler radar method presented in this paper clearly shows that the technique is capable of providing observational data on particle velocities inside convective and tropical storms, thereby offering drastic improvement in the knowledge of the processes which take place in those storms.

The excellent mobility of the airplane permits the experiments to be conducted according to free choice of the best region of interest. This constitutes a definite advantage over the use of ground-based facilities for the same purpose, since observations which are made by equipment installed at fixed locations are possible only in the limited region determined by the location of the radar system.

The airborne vertical beam method allows rapid scanning of a vertical plane generated by the aircraft's trajectory. Vertical particle motions and their spectra can be observed and mapped in such planes with excellent continuity. Since the airplane is moving at high speed, it is appropriate to assume that the processes in the storm are stationary during the time required to make the scans. This leads to a continuous mapping of the wind in space coordinates determined by the scanning of a vertical beam by the airplane motion. It must be noted that this is not the case with ground-based equipment, which always deals with time-altitude relationships leading to a space coordinates expression only if an assumption can be formulated involving advection of a non-evolving storm.

The method is particularly attractive for the mapping of vertical motion inside convective storms. Vertical planes can be scanned at the rate of one plane every 2 min, for instance, thereby leading to the observation of vertical velocity in three-dimensional space. The updraft and downdraft structure of a storm can then be effectively observed in the precipitating region of the storm.

The lateral beam method shown in Fig. 8 is also attractive. Two airplanes flying at the same altitude are needed to map horizontal particle motions from two radial velocity components as proposed in the dual-Doppler radar method (Lhermitte, 1968). If the wind field is stationary for a period of several minutes, only one airplane is needed. Since the velocity is evaluated from two independent Doppler observations, the logistical and navigational problems will be more serious than in the case of a vertically pointing beam.

It is therefore suggested that a feasibility study of the vertical beam method be conducted to assess its potential and allow development of the techniques involved, including a real-time signal processing system. It is the opinion of this author that such a feasibility test would supply definite assurance that the method offers one of the best opportunities to study convective and tropical storm processes.

Acknowledgments. This paper resulted from earlier discussions on the interests and applicability of the airborne pulse-Doppler radar method with Dr. J. P. Kuettner, ERL, Mr. B. B. Phillips, ERL, Dr. S. A. Rossby, NCAR, Dr. P. MacCready, MRI, and Dr. D. Atlas, University of Chicago. Mr. D. A. Wilson contributed significantly to the discussion of terminal velocities of precipitation particles. Mr. H. W. Frank, Mr. L. J. Miller and Miss D. Grunig of ERL calculated some of the V_f-Z relationships. Mrs. J. Watts had the difficult task of editing and typing the manuscript.

REFERENCES

Atlas, D., 1964: Advances in radar methodology. *Advances in Geophysics*, Vol. 10, New York, Academic Press, 317–478.

Battan, L. J., 1963: Some observations of vertical velocities and precipitation sizes in a thunderstorm. *Proc. 12th Weather Radar Conf.*, Norman, Okla., Amer. Meteor. Soc., 303–308.

——, 1964: Some observations of vertical velocities and precipitation sizes in a thunderstorm. *J. Appl. Meteor.*, **3**, 415–420.

Best, A. C., 1950: Empirical formulae for terminal velocity of water drops falling through the atmosphere. *Quart. J. Roy. Meteor. Soc.*, **76**, 302–311.

Blackman, R. B., and J. W. Tukey, 1958: *The Measurement of Power Spectra.* New York, Dover Publ., 190 pp.

Boston, R. C., and R. R. Rogers, 1969: Hail detection by Doppler radar. *J. Appl. Meteor.*, **8**, 837–840.

Cantaneo, R., and G. E. Stout, 1968: Raindrop-size distributions in humid continental climates and associated rainfall rates—radar reflectivity relationships. *J. Appl. Meteor.*, **7**, 901–907.

Chimera, A. J., 1960: Meteorological radar echo study. Cornell Aeronautical Laboratories, Rept. UB-1327-P-1, Buffalo, N. Y.

Cooley, J. W., and J. Tukey, 1965: An algorithm for the machine calculation of complex Fourier series. *Math. Comput.*, **19**, 297–301.

Davies, C. N., 1942: Unpublished Ministry of Supply reports. Quoted by Sutton in Air Ministry Rept. MRP 40.

Donaldson, R. J., Jr., and A. C. Chmela, 1968: Distribution of vertical velocity mean and variance in a thunderstorm. *Proc. 13th Radar Meteor. Conf.*, Montreal, Amer. Meteor. Soc., 492–496.

——, and R. Wexler, 1969: Flight hazards in thunderstorms determined by Doppler velocity variance. *J. Appl. Meteor.*, **8**, 128–133.

Foote, G. B., and P. S. Du Toit, 1969: Terminal velocity of raindrops aloft. *J. Appl. Meteor.*, **8**, 249–253.

Genève, R., 1959: La vitesse de chute des grêlons. Notes de L'Etablissement d'Études et de Recherches Météorologiques, No. 23, Paris, France.

Gunn, R., and G. D. Kinzer, 1949: The terminal velocity of fall of water droplets in stagnant air. *J. Meteor.*, **6**, 243–248.

Laws, J. O., 1941: Measurements of the fall-velocity of water drops and rain drops. *Trans. Amer. Geophys. Union*, **22**, 709–721.

——, and D. A. Parsons, 1943: The relation of raindrop size to intensity. *Trans. Amer. Geophys. Union*, **24**, 452–460.

Lhermitte, R. M., 1963: Motions of scatterers and the variance of the mean intensity of weather radar signals. SRRC-RR-63-57, Sperry Rand Res. Center, Sudbury, Mass., 43 pp.

——, 1964: Doppler radars as severe storm sensors. *Bull. Amer. Meteor. Soc.*, **45**, 587–596.

——, 1966: Application of the pulse Doppler radar technique to meteorology. *Bull. Amer. Meteor. Soc.*, **47**, 703–711.

——, 1968: New developments in Doppler radar methods. *Proc. 13th Radar Meteor. Conf.*, Montreal, Amer. Meteor. Soc., 14–17.

Miller, K. S., and M. M. Rochwarger, 1970: On estimating spectral moments in the presence of colored noise. *IEEE Trans. Information Theory*, **IT-16**, 303–309.

Piat, D., 1960: Mésures en soufflerie due coneficient de trainée de quelques modèles de grêlons. Notes de L'Etablissement d'Etudes et de Recherches Météorologiques, No. 32, Paris, France.

Probert-Jones, J. R., and W. G. Harper, 1961: Vertical air motion in showers as revealed by Doppler radar. *Proc. 9th Weather Radar Conf.*, Kansas City, Mo., Amer. Meteor. Soc., 225–232.

Rogers, R. R., 1964: An extension of the Z-R relationship for Doppler radar. *Proc. World Conf. Radar Meteor.*, Boulder, Colo., Amer. Meteor. Soc., 158–160.

Spilhaus, A. F., 1948: Drop size, intensity and radar echo of rain. *J. Meteor.*, **5**, 161–164.

Reprinted from Proceedings of the 14th Radar Meteorology Conference, November 17-20, 1970, 133-138, 1971.

DOPPLER RADAR METHODOLOGY FOR THE OBSERVATION OF CONVECTIVE STORMS

Roger M. Lhermitte and L. Jay Miller

ESSA Research Laboratories
Boulder, Colorado

1. INTRODUCTION

Meteorological Doppler radars have been used for years for the observation of precipitation particle motion inside storms and have demonstrated their usefulness for the study of storm processes. Although a substantial amount of early work deals with vertically pointing radar beam methods, that lead to the observation of particle vertical velocities, emphasis is now placed on methods capable of scanning a storm and providing the Doppler information in three-dimensional space coordinates. However, the unambiguous observation of three-dimensional particle motion from radial velocity data requires simultaneous use of three radars, installed at different locations, providing three separate radial velocity estimates at the same point in space.

The less complex dual-Doppler radar method is a reasonable step towards this goal and still represents a drastic improvement of the meteorological application of Doppler techniques, since the method provides two-dimensional wind field information capable of showing details of storm circulation in a manner never attained before (Lhermitte, 1970).

When applied to the probing of convective storms, the method requires that data provided by the two radars be separately evaluated and presented in the form of scalar fields of radial velocity expressed in a plane common to the two radars. The dual-Doppler concept, therefore, requires complex solutions for the coordinated scanning of the radar beams and the acquisition and processing of the data. The ultimate development of the method will include signal and data processing systems operating in real time for better monitoring of storm processes and the assessment of storm modification attempts.

This paper outlines the concepts involved and the design parameters required for optimizing the effectiveness of the dual-Doppler method. The accuracy of two-dimensional velocity estimates, as controlled by radar signal dwell time and data processing, and the method required to optimize this accuracy are also discussed.

2. SIGNAL PROCESSING AND SPECTRAL ACCURACY

It is well known that processing of the Doppler radar signal requires frequency analysis of time functions recorded at selected ranges that must be accomplished prior to any further treatment of the data. A substantial number of Doppler signal processing systems have used analog treatment of the signals. However, it is the opinion of the authors that the only acceptable solution for an optimum processing of Doppler radar data should be based on the use of digital techniques, with the radar signals digitized in real time by an analog-to-digital converter (ADC) and then processed by arithmetic manipulations of the digital samples. The availability of fast analog-digital converters and new LSI (large-scale integration) components, as well as the availability of fast Fourier transform (FFT) algorithms well-suited for binary calculations, make the digital technique optimum for the processing of radar signals. The common requirement for the simultaneous recording of radar signals at a multitude of selected ranges, which apply to distributed targets, can be met by storing the digital samples in digital memory units.

For reasons of convenience, Doppler radar signals are usually frequency-shifted in heterodyne circuits so that a zero Doppler frequency shift will indeed be a zero frequency. This manipulation of the signal generates a frequency sign and requires that the receiver signal be thus represented by a complex expression, C_k, involving two orthogonal components (real, and imaginary). The numerical evaluation of the spectrum is derived from a time series of complex time samples from the following expression:

$$C_j = \sum_{k=1}^{k=N} c_k W_k e^{-\frac{i2\pi kj}{N}} . \qquad (1)$$

The total number of samples is N; W_k is a weighting function, and j is an index which characterizes the frequency points. The numerical expression produces estimates of spectral density with 2 degrees of freedom evaluated at frequency points spaced by 1/T, where T=Nτ; τ is the time interval between samples. The frequency range effectively covered by the numerical computations extends from -1/2τ to 1/2τ. Note that the availability of the signal in a complex form effectively removes frequency folding at 1/2τ, since this folding is really caused by lack of frequency sign discrimination resulting from processing of real signals alone (folding at zero frequency). If complex signals are used, there is no frequency folding when the spectrum width is within the total unambiguous frequency coverage of 1/τ.

In practice, expression (1) is replaced by the more systematic FFT, suitable for binary computation as originally proposed by Cooley and Tukey (1965). Fast Fourier transforms can easily be implemented in hardware design by sequential treatment of the samples and their rotation by a complex multiplier. With standard TTL (transistor-transistor logic) integrated circuits, each complex multiplication, which is indeed four multiplications done in parallel, can be performed in less than 0.5 μsec. Since the required number of complex multiplications (rotations) is equal to $N\log_2 N$, the evaluation of a Fourier spectrum based on 256 time samples, for instance, can be done in approximately 1 msec, less with high-speed hardware. The system should be used in conjunction with suitable data recording facilities. The spectra can be displayed on a cathode ray tube showing RVI (range velocity indicator) patterns at a rate of five complete RVI displays, composed of 200 spectra, each second. Only moments of the spectrum, such as the mean signal power, the first moment (mean Doppler), second central moment (Doppler variance), normalized third moment (skewness) and fourth moment (kurtosis), need to be recorded. Such a system, combined with coordinated radar beam scanning schemes, can lead to real-time display of two-dimensional velocity information and is well within the present capabilities of digital hardware.

Figure 1 shows an example of computer treatment of data digitally recorded on magnetic tape. One sees that spectra are displayed in 3-dB quantized levels to show the general shape of the spectrum. The signal mean intensity, as well as the first, second, third and fourth moments of the spectra, are also shown in the printout and recorded on punched cards. This system, which is presently used in our dual-Doppler work, is still slow (24 spectra recorded every 2 sec) but is very accurate. Indeed, 512 complex samples

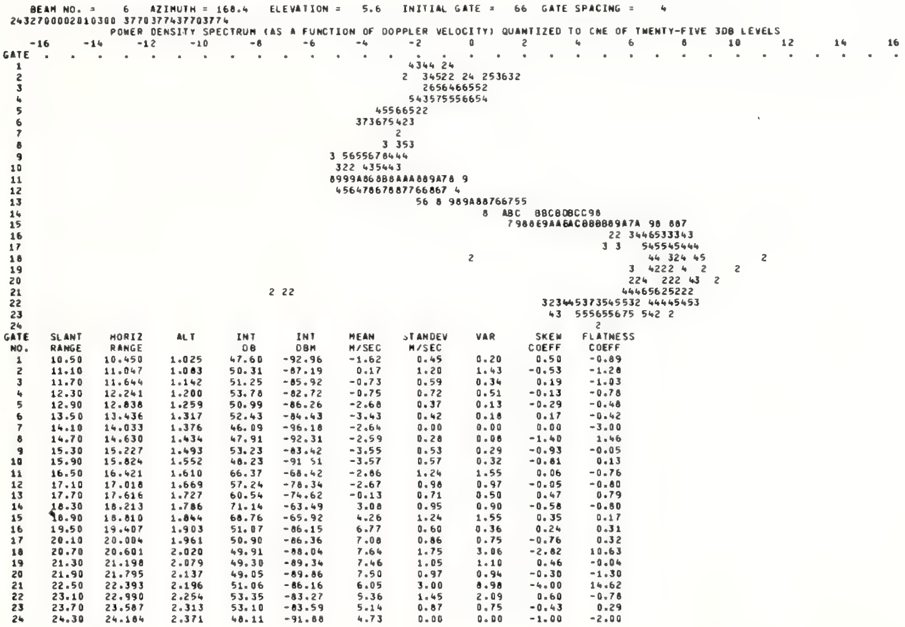

```
    BEAM NO. =    6   AZIMUTH = 168.4   ELEVATION =   5.6   INITIAL GATE =   66  GATE SPACING =    4
 2432700002010300 3770377437703774
                POWER DENSITY SPECTRUM (AS A FUNCTION OF DOPPLER VELOCITY) QUANTIZED TO CNE OF TWENTY-FIVE 3DB LEVELS
    -16     -14     -12     -10      -8      -6      -4      -2       0       2       4       6       8      10      12      14      16
GATE  .   .   .   .   .   .   .   .   .   .   .   .   .   .   .   .   .   .   .   .   .   .   .   .   .   .   .   .   .   .   .   .   .
  1                                                          4344 24
  2                                                         2  34522 24 253632
  3                                                            2656466552
  4                                                          543575556654
  5                                                     45566522
  6                                                  373675423
  7                                                          2
  8                                                        3 353
  9                                                3 5655678444
 10                                                 322 435443
 11                                                8999A868B8AAA889A78 9
 12                                                 456478678877668 67 4
 13                                                              56 8 989A88766755
 14                                                                        8  ABC  88C8D8CC98
 15                                                                            7988E9AA6AC888889A7A 98 887
 16                                                                                           22 3446533343
 17                                                                                          3 3   545545444
 18                                                                    2                          44 324 45        2
 19                                                                                              3  4222 4  2    2
 20                                                                                              224  222 43  2
 21                                        2 22                                                 44465625222
 22                                                                                 323445373545532 44445453
 23                                                                                  43  555655675 542 2
 24                                                                                         2
GATE   SLANT    HORIZ      ALT      INT      INT     MEAN   STANDEV     VAR      SKEW  FLATNESS
 NO.   RANGE    RANGE                DB      DBM    M/SEC    M/SEC              COEFF    COEFF
  1    10.50   10.450    1.025    47.60   -92.96    -1.62      0.45    0.20     0.50    -0.89
  2    11.10   11.047    1.083    50.31   -87.19     0.17      1.20    1.43    -0.53    -1.28
  3    11.70   11.644    1.142    51.25   -85.92    -0.73      0.59    0.34     0.19    -1.03
  4    12.30   12.241    1.200    53.78   -82.72    -0.75      0.72    0.51    -0.13    -0.78
  5    12.90   12.838    1.259    50.99   -86.26    -2.68      0.37    0.13    -0.29    -0.48
  6    13.50   13.436    1.317    52.43   -84.43    -3.43      0.42    0.18     0.17    -0.42
  7    14.10   14.033    1.376    46.09   -96.18    -2.64      0.00    0.00     0.00    -3.00
  8    14.70   14.630    1.434    47.91   -92.31    -2.59      0.28    0.08    -1.40     1.46
  9    15.30   15.227    1.493    53.23   -83.42    -3.55      0.53    0.29    -0.93    -0.05
 10    15.90   15.824    1.552    48.23   -91 51    -3.57      0.57    0.32    -0.81     0.13
 11    16.50   16.421    1.610    66.37   -68.42    -2.86      1.24    1.55     0.06    -0.76
 12    17.10   17.018    1.669    57.24   -78.34    -2.67      0.98    0.97    -0.05    -0.80
 13    17.70   17.616    1.727    60.54   -74.62    -0.13      0.71    0.50     0.47     0.79
 14    18.30   18.213    1.786    71.14   -63.49     3.08      0.95    0.90    -0.58    -0.80
 15    18.90   18.810    1.844    68.76   -65.92     4.26      1.24    1.55     0.35     0.17
 16    19.50   19.407    1.903    51.07   -86.15     6.77      0.60    0.36     0.24     0.31
 17    20.10   20.004    1.961    50.90   -86.36     7.08      0.86    0.75    -0.76     0.32
 18    20.70   20.601    2.020    49.91   -88.04     7.64      1.75    3.06    -2.82    10.63
 19    21.30   21.198    2.079    49.30   -89.34     7.46      1.05    1.10     0.46    -0.04
 20    21.90   21.795    2.137    49.05   -89.86     7.50      0.97    0.94    -0.30    -1.30
 21    22.50   22.393    2.196    51.06   -86.16     6.05      3.00    8.98    -4.00    14.62
 22    23.10   22.990    2.254    53.35   -83.27     5.36      1.45    2.09     0.60    -0.78
 23    23.70   23.587    2.313    53.10   -83.59     5.14      0.87    0.75    -0.43     0.29
 24    24.30   24.184    2.371    48.11   -91.88     4.73      0.00    0.00    -1.00    -2.00
```

Figure 1. Computer printout of the Doppler data. Twenty-four spectra quantized in 3-dB levels indicated by the alpha-numeric scale are displayed for signals recorded at 24 selected ranges when the radar beam is in a fixed position. The spectrum moments are also evaluated. Flatness is kurtosis normalized to Gaussian spectrum shape.

corresponding to a 0.25-sec signal dwell time are recorded for each spectrum, leading to the evaluation of spectral density estimates spaced by 6.4 sec^{-1}. The variance of the first moment estimate for such a sample size is discussed below. Data are recorded at 24 selectable points in the radar range. The radar beam is stepped automatically every 2 sec, but data are recorded only when the beam is in a fixed position. This beam-scanning method, combined with the presence of selected ranges, effectively generates grid points evenly distributed in the scanned plane.

3. ERROR DUE TO SIGNAL QUANTIZATION

Quantization of the radar signal produces a certain amount of noise caused by random adjustments of the true signal to the nearest quantization level. Following Larson and Singleton (1967), let us assume a probability density for this noise, uniform between $-\Delta X/2$ and $\Delta X/2$, where ΔX is the interval between two adjacent quantization levels. The power, P_N, of this quantization noise is:

$$P_N = \frac{(\Delta X)^2}{12} . \qquad (2)$$

Note that when a random Gaussian signal is digitized, quantization noise is white. The total amplitude X_0, covered by the digitizing process is: $X_0 = \Delta X \cdot 2^N$, where N is the number of binary bits. Let us assume now that the radar signal, which has a Gaussian probability distribution with standard deviation σ_s, is adjusted so that $X_0 = a\sigma_s$. We have:

$$\beta = 6N + 10.79 - 20 \log_{10} a \ , \qquad (3)$$

where β is the ratio of signal-to-noise expressed in decibels. One sees that each additional bit increases β by 6 dB. For a Gaussian radar signal covering the full range of the ADC with a = 5, 7 bits (6 bits + sign for bipolar signals) provide a signal-to-noise ratio of approximately 40 dB.

If we want to maintain the same condition for weaker signals, one more bit will be required for each 6-dB decrease of the signal power, if no adjustment of the signal amplitude takes place. For instance, 12 bits still provide β = 40 dB for signal amplitudes 30 dB below the maximum allowed by the ADC coverage. Such dynamic range capabilities should be matched by the radar circuits themselves.

The dynamic range of the spectrum is enhanced by F_m/B, where B is the signal equivalent bandwidth, and F_m is the total frequency coverage, $1/\tau$, defined above.

Figure 2 illustrates this reduction in spectral dynamic range caused by signal quantization. These results were produced by a computer-generated narrow-band Gaussian signal with a Gaussian spectrum designed so that $\sigma_f = F_m/8$, with σ_f being the frequency standard deviation and F_m the total frequency coverage. The signal was then quantized and signal spectrum evaluated with the number of bits ranging from 2 to 12. It was found, as shown in figure 2, that each additional bit decreased the quantized noise by 6 dB, as predicted by (3). Note also that, for 8 bits and a=6, the observed spectral dynamic range is 50.5 dB, which compares reasonably well with the theoretical estimate of 43-dB signal-to-noise, to which 8 dB due to F_m/B must be added.

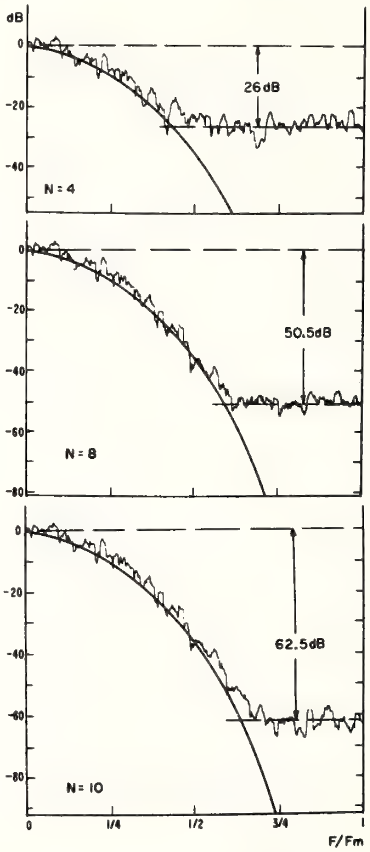

Figure 2. Effect of quantization noise on the dynamic range of a narrow-band Gaussian spectrum. N is the number of bits used in the quantization process, a=6 (see text). Note that each additional bit increases the dynamic range by 6 dB. The solid line indicates spectrum before signal quantization.

4. ACCURACY OF SPECTRAL MOMENTS

Except in the case where spectral shape or spectral boundaries must be specified, the quality of the meteorological information provided by the Doppler radar is effectively discussed in terms of the stability of spectral moment estimates. These quantities can be expressed in two-dimensional fields and used in the processing of dual-Doppler radar information. The stability of the spectral zero moment, which is the signal mean intensity, has often been discussed in the literature; i.e., Marshall and Hitschfeld (1953), Lhermitte (1963).

The first moment, which can be identified within assumptions with the mean particle radial velocity or even the mean radial air flow, if particle terminal speed is neglected, is of greatest importance in the treatment of the dual-Doppler radar information. Indeed, this information can lead to the mapping of two-dimensional mean velocities, indicating the mean flow in a convective storm (Lhermitte, 1970).

The estimate of the first moment, $\overline{V}$, of the Doppler spectrum has a Gaussian probability distribution evaluated from a large number of spectral density estimates. The variance, $\sigma^2_{\overline{V}}$, of the $\overline{V}$ estimate is controlled by the signal sampling rate, the signal dwell time, T, and the variance, σ^2_V, of the spectrum itself. Assuming that the sampling rate is much higher than $1/\sigma_V$ leads to the following expression derived from Miller and Rochwarger (1970):

$$\sigma^2_{\overline{V}} = \frac{\lambda\sigma_V}{4T}\left(1 + \frac{1.6}{\rho} + \frac{3}{\rho^2}\right) . \qquad (4)$$

In this equation, λ is the radar wavelength and ρ is the signal-to-noise power ratio. Note that the expression applies only to colored noise with a bandwidth equal to three times the signal bandwidth. Expression (4) is shown in figure 3 for $\rho = \infty$ (no noise).

5. COPLAN SCANNING

If conventional radar methods are used in the dual-Doppler radar system, a three-dimensional scanning sequence based on both azimuth and elevation angle stepping must be completed before the data can be expressed in a coordinate system common to the two radars. The velocity fields must be stationary during the total time required for the acquisition of the three-dimensional Doppler data so that two radial velocities estimated from this process at the same point in space can be combined for calculation of two-dimensional velocity estimates. It is therefore more appropriate to replace the conventional independent scanning of two radar beams by a coordinated operation designed so that the two radar beams stay in the same plane during a given time interval (COPLAN scanning). Stationarity assumptions now apply only to the time interval for the scanning of one plane. Interpolation procedures are reduced to only two-dimensional expressions, thereby greatly simplifying data analysis and allowing easy presentation of the fields in two-dimensional planes.

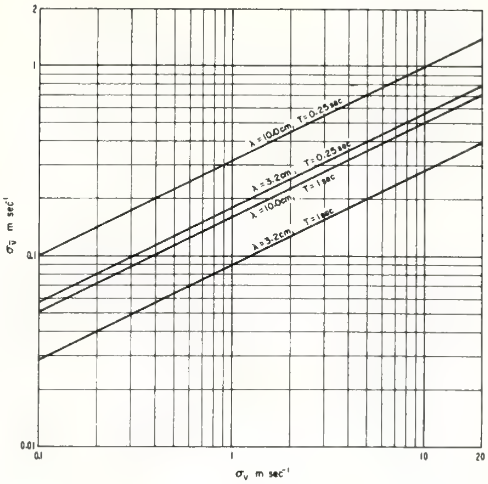

Figure 3. Standard deviation, $\sigma_{\overline{V}}$, of the estimate of Doppler spectrum first moment versus spectrum standard deviation, σ_V, for various radar wavelengths, λ, and signal dwell times, T.

This condition of COPLAN scanning is realized with conventional PPI scanning when the radar beams are perpendicular to their vertical rotation axes, the common plane being horizontal. If the two rotation axes of the radar beams are tilted in exactly the same manner, still keeping beams perpendicular to these new axes, the same conditions of COPLAN scanning will be realized for a tilted plane whose inclination is controlled by the tilt of the vertical rotation axes. In practice, it is more appropriate to introduce a relationship between the azimuth angle, β, and the elevation angle, θ, of each radar beam, designed so that the beams stay in the same plane.

Two beams produced by two radars installed at different locations will lie in the same plane that intersects the baseline between the two radars, provided that the following condition is realized:

$$\frac{\tan \theta_1}{\cos \beta_1} = \frac{\tan \theta_2}{\cos \beta_2} = \tan \alpha . \qquad (5)$$

Subscript 1 and 2, respectively, refer to radar #1 and radar #2; β is taken from a perpendicular to the baseline joining the two radars; α is the tilt of the common plane. The solution leading to θ's < 0 is eliminated by taking the absolute value of $\tan\theta$ in (5). Note that for small angles α, (5) reduces to: $\alpha \approx \theta_1/\cos\beta_1 \approx \theta_2/\cos\beta_2$.

Figure 4 illustrates this concept. The radar beams are effectively scanned independently, with the constraint that for both radars, β and θ are related by (5) for a given α. Then the radial velocities from the dual-Doppler data can be readily combined in the two-dimensional plane with tilt α. This reduces the problem of processing radial velocity information to that of two-dimensional interpolation of two scalar fields, which are assumed to be stationary during the time needed to scan the plane.

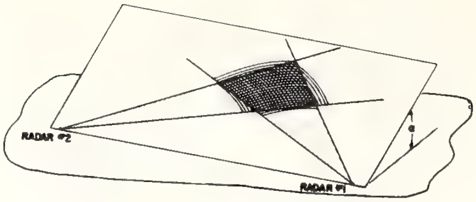

Figure 4. COPLAN scanning. The azimuth and elevation angles of the two radar beams are controlled so that coplanar scanning is realized in a plane with tilt α.

The two radial velocities, V_1 and V_2, provided by the two radars, are expressed as a function of the u and v components of the horizontal air motion and with u parallel to the radars' baseline, the vertical air motion component, w, to which the particle terminal velocity, V_t, must be added, by the following equations:

$$V_1 = u \sin\beta_1 \cos\theta_1 + v \cos\beta_1 \cos\theta_1 + (w + V_t)\sin\theta_1 \tag{6}$$

$$V_2 = u \sin\beta_2 \cos\theta_2 + v \cos\beta_2 \cos\theta_2 + (w + V_t)\sin\theta_2 \ . \tag{7}$$

Solving for u and v leads to:

$$u = \frac{1}{\sin(\beta_1 - \beta_2)} \left[\frac{V_1 \cos\beta_2}{\cos\theta_1} - \frac{V_2 \cos\beta_1}{\cos\theta_2} \right] - (w + V_t) \left[\frac{\cos\beta_2 \tan\theta_1 - \cos\beta_1 \tan\theta_2}{\sin(\beta_1 - \beta_2)} \right], \tag{8}$$

$$v = \frac{1}{\sin(\beta_1 - \beta_2)} \left[\frac{V_2 \sin\beta_1}{\cos\theta_2} - \frac{V_1 \sin\beta_2}{\cos\theta_1} \right] - (w + V_t) \left[\frac{\sin\beta_1 \tan\theta_2 - \sin\beta_2 \tan\theta_1}{\sin(\beta_1 - \beta_2)} \right] . \tag{9}$$

For data acquired by COPLAN scanning, we can substitute (5) in the term involving $w + V_t$ in (8) and (9), obtaining:

$$u = \frac{1}{\sin(\beta_1 - \beta_2)} \left[\frac{V_1 \cos\beta_2}{\cos\theta_1} - \frac{V_2 \cos\beta_1}{\cos\theta_2} \right], \tag{10}$$

$$v = \frac{1}{\sin(\beta_1 - \beta_2)} \left[\frac{V_2 \sin\beta_1}{\cos\theta_2} - \frac{V_1 \sin\beta_2}{\cos\theta_1} \right] - (w + V_t)\tan\alpha \ . \tag{11}$$

Equations (10) and (11) show that the presence of a significant $w + V_t$ term does not modify the expression of u but still produces a shift of v proportional to $\tan\alpha$. This constitutes an additional advantage of COPLAN scanning compared to conventional radar methods, since, for a given common plane, the shift of the estimate will only vary with $w + V_t$ and will not be a function of the location, in the common plane, at which the estimates of u and v are made.

6. ACCURACY OF TWO-DIMENSIONAL VELOCITY ESTIMATES

Equations (10) and (11) provide the solution for u and v. Assuming that the term $(w + V_t)\tan\alpha$ is neglected and that angles are accurately measured, the only possible source of error in the calculation of u and v arises from random uncertainties in the estimates of the Doppler first moments, V_1 and V_2, discussed in section 4.

Assuming independent distributions for the estimates of V_1 and V_2, the variances σ_u^2 and σ_v^2 of the u and v components can be readily derived from the linear equations (10) and (11), leading to:

$$\sigma_u^2 = \frac{\cos^2\beta_1\left(\dfrac{\sigma_2^2}{\cos^2\theta_2}\right) + \cos^2\beta_2\left(\dfrac{\sigma_1^2}{\cos^2\theta_1}\right)}{\sin^2(\beta_1-\beta_2)}, \quad (12)$$

$$\sigma_v^2 = \frac{\sin^2\beta_1\left(\dfrac{\sigma_2^2}{\cos^2\theta_2}\right) + \sin^2\beta_2\left(\dfrac{\sigma_1^2}{\cos^2\theta_1}\right)}{\sin^2(\beta_1-\beta_2)}. \quad (13)$$

Note that σ_u^2 and σ_v^2 are functions of the Doppler first moment variances, σ_1^2 and σ_2^2, but also vary with β and θ and, therefore, with the location of the point in space where the u and v estimates are evaluated. If we assume $\sigma_1^2 = \sigma_2^2$ and $\theta_1 = \theta_2 = 0$, we can define the region of the horizontal plane scanned by the two radars for which the condition σ_u^2 or $\sigma_v^2 \leq a\sigma_1^2$. This is shown in figure 5 for a = 2. We can also limit, with the same assumption as above, the σ_u^2 and σ_v^2 terms by the following condition :

$$\sigma_u^2 + \sigma_v^2 = \frac{2}{\sin^2(\beta_1-\beta_2)} \leq b\sigma_1^2 . \quad (14)$$

The region of the plane with boundaries imposed by this condition (locus of two circles) is also shown in figure 5 for b = 4. The above discussion is useful for specifying the region covered by the dual-Doppler system in which reasonable estimates for u and v are obtained.

7. CONCLUSION

This paper is an attempt to outline the practical concepts and limitations involved in the dual-Doppler radar method. COPLAN scanning is a substantial improvement of the method, offering major advantages such as: shorter time requirement for stationarity of the wind fields; easier implementation of real-time processing of two-dimensional wind fields; use of two-dimensional interpolation method only; easier treatment of vertical velocity contamination, and three-dimensional representation possible from a set of true tilted planes as opposed to conical surfaces.

8. ACKNOWLEDGEMENTS

J. W. Cateora designed the computer program leading to the estimate of noise due to quantization processes.

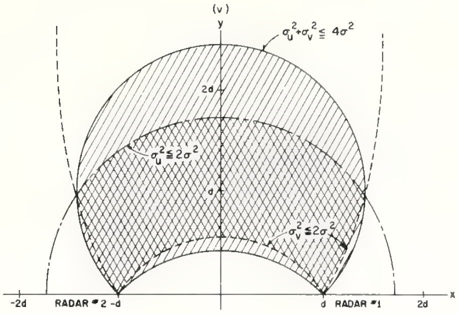
(v)
y
$\sigma_u^2+\sigma_v^2 \leq 4\sigma^2$
2d
$\sigma_u^2 \leq 2\sigma^2$
d
$\sigma_v^2 \leq 2\sigma^2$
-2d
RADAR #2 -d
d RADAR #1
2d
x

Figure 5. Horizontal area effectively covered by a dual-Doppler radar system for a given upper limit of the variance σ_u^2 and σ_v^2, of the u and v components of the motion taken along the x and y coordinate system, as evaluated from the Doppler data. σ^2 is the variance of the mean Doppler velocity estimate. The symmetric solution for negative y is not shown.

9. REFERENCES

Cooley, J. W. and J. Tukey (1965), An a rithm for the machine calculation of complex Fourier series, Mathematics Computation 19, 297-301.

Larson, A. G. and R. C. Singleton (1967 Real-time spectral analysis on a sma general-purpose computer, Fall Joint Computer Conf., AFIPS Proc. 31, Washington, D.C.: Thompson, 1967, 665-674.

Lhermitte, R.M. (1963), Motions of sca terers and the variance of the mean intensity of weather radar signals, SRRC-RR-63-57, 43 pp., Sperry Rand Research Center, Sudbury, Mass.

Lhermitte, R. M. (1970), Dual Doppler o servation of convective storm circul tion, to be published Proc. 14th Rad Meteorol. Conf.

Marshall, J. S. and W. Hitschfeld (195 The interpretation of the fluctuatir echo for randomly distributed scatte ers, Part I, Canadian J. Phys. 31, 962.

Reprinted from Journal of Atmospheric Sciences 27, No. 5, 785-790, 1970.

Radiometric Observations of Liquid Water in Thunderstorm Cells

Martin T. Decker and Evan J. Dutton

ESSA Research Laboratories, Boulder, Colo.

(Manuscript received 27 January 1970, in revised form 15 May 1970)

ABSTRACT

An estimate of the integrated liquid water content along radio rays passing through a thunderstorm has been made by using the thermal emission from the storm at 10.7 GHz. The radiometric data, together with supplementary radar, radiosonde, and surface meteorological data are used to determine absorption in the storm, which in turn is used to determine the liquid water content. The results of the technique are illustrated by contour diagrams showing liquid water content of a small storm system and its changes over a period of 2 hr.

1. Introduction

Microwave thermal emission from condensed water in the atmosphere is a potential source of significant information about that water. In the case of thunderstorm cells the emission is easily observed with simple radiometer systems. This remote sensing technique can be used to deduce various properties of the radiating cell of interest both to communication system designers and to cloud physicists. Quantities that can be measured or estimated include noise degradation of sensitive communication systems, total attenuation of an electromagnetic wave passing through the cell, and the integrated liquid water content. The last is emphasized in this paper and is illustrated by observations made of thunderstorm cells during the summer of 1967. Briefly, the procedure consists of the following steps: 1) measuring the emission from the thunderstorm and the clear sky in terms of brightness temperatures, 2) separating the absorption of the storm from the combined absorption of atmospheric gases and the storm, and 3) estimating the integrated water content from this absorption and certain properties of water drop absorption cross sections.

2. Observations

During the summer of 1967, frequent observations of thunderstorms were made from the ESSA Table Mountain site near Boulder, Colo. These storms were generally small and isolated, typical of the high-plains thunderstorms that build immediately east of the Rocky Mountains during summer afternoons. The isolated nature of the storms is particularly advantageous since it allows a reference observation of essentially clear sky near the storm.

Typical data obtained 18 July 1967 were chosen for examination in this paper. A compact storm system was observed for about 2 hr at distances ranging from 50–75 km from the radiometer. Storm cells were located with a radar operating at 9-cm wavelength.

A conventional Dicke-switching radiometer (Dicke, 1946) operating at 10.7 GHz (2.8 cm) was used for brightness temperature measurement. The principal equipment parameters for the conditions of this experiment are given in Table 1. The reference arm of the radiometer used an ambient temperature termination. The system was operated near the balanced condition by the addition of noise from a gas discharge tube to the signal arm. The antenna was a parabolic reflector 18.3 m in diameter with the horn feed (and the radio frequency portion of the radiometer) mounted at the prime focus. In the usual mode of operation the antenna beam was scanned across the storm at a fixed initial elevation angle from the clear sky on the one side of the storm to the clear sky on the other. The basic measurement then was the difference in noise temperature at the antenna terminals for the two conditions of measurement, i.e., the beam directed toward the clear sky background and then directed toward the storm. A separate gas discharge tube was used to calibrate this change. The scan was repeated in 0.5° increments of elevation angle until all of the storm that could be observed from the radiometer site had been covered. This technique allowed us to draw contour diagrams of the storm; thus, repetitive observations showed changes in storm characteristics with time.

The antenna directivity pattern and main beam gain were measured with the aid of a target transmitter at a distance of 29 km from the 18.3 m antenna. Considerable effort was expended in arranging the target trans-

Table 1. Radiometer equipment parameters.

Frequency	10.7 GHz
Wavelength	2.8 cm
Antenna diameter	18.3 m
Antenna half-power beamwidth	0.15°
Azimuthal scan rate	~27 deg min^{-1}
Bandwidth (double side-band)	10 MHz
Integration time (RC)	1 sec
Radiometer noise temperature	~3000K
Minimum detectable temperature change	2K

mitter to produce a field over the radiometer antenna aperture that was uniform to about ±1 db. The pattern and gain data were used to derive the beam efficiency (Kraus, 1966), computed here as a function of conical angle measured from the axis of the main beam. This efficiency is defined as the percent of the total energy radiated by the antenna that would be directed into the solid angle described by a cone whose axis coincides with the main beam axis. As the half-angle of the cone increases from 0 to π, this efficiency increases from 0 to 100%.

Meteorological data included surface observations of temperature and relative humidity at the radiometer site and radiosonde data from Denver, the Denver station being ~50 km southeast of the radiometer site. Two radiosonde flights were made for most of the days on which storm measurements were made.

In summary, we now have available for analysis 1) the change in antenna noise temperature as the antenna beam is moved from clear sky to storm, 2) the antenna beam efficiency, 3) the location of the storm cell, and 4) radiosonde and other meteorological data.

3. Analysis

The brightness temperature T_{bcs} observed in the direction of the storm is the sum of emission contributions from the atmosphere between the observer and the storm, from the storm itself, from sources beyond the storm, and from energy scattered by particles within the cloud. Using the microwave equation of radiative transfer (Shklovsky, 1960), these four terms are written

$$\begin{aligned} T_{bcs} = & \int_0^{r_1} T(r)\beta_s(r)e^{-\tau(r)}dr \\ & + \int_{r_1}^{r_2} T(r)[\beta_s(r)+(1-\omega)\beta_c(r)]e^{-\tau(r)}dr \\ & + \int_{r_2}^{\infty} T(r)\beta_s(r)e^{-\tau(r)}dr + \int_{r_1}^{r_2} T_{bg}(r)\omega\beta_c(r)e^{-\tau(r)}dr, \quad (1) \end{aligned}$$

where the symbols are defined as follows:

T	kinetic temperature of the absorbing medium along the observed ray path
β_s	extinction (or absorption) coefficient of atmospheric gases
β_c	extinction coefficient of liquid particles
τ	total attenuation
ω	single-scattering albedo defined as the ratio of scattering coefficient to extinction coefficient
T_{bg}	mean brightness temperature of the sphere surrounding the scattering elements which are assumed to scatter isotropically
r_1, r_2	distances from the observer to the near and far boundaries of the storm

If we assume that "mean radiating temperatures" are known[1] for the first three terms of (1) and are designated T_1, T_2 and T_3, respectively, and that ω and T_{bg} are constant through the storm, then (1) may be solved for the absorption of the liquid particles, τ_c. The result is

$$\begin{aligned} \tau_c = & -(1-\omega) \\ & \times \ln\left\{\frac{T_1(1-e^{-\tau_1})+T_2(1-\omega)e^{-\tau_1}-T_{bcs}+T_{bg}\omega e^{-\tau_1}}{[T_2(1-\omega)-T_3(1-e^{-\tau_3})+T_{bg}\omega]e^{-\tau_1}}\right\} \\ & -(1-\omega)\tau_2, \quad (2) \end{aligned}$$

where τ_1, τ_2 and τ_3 are the gaseous attenuations from 0 to r_1, r_1 to r_2 and r_2 to ∞, respectively.

In some observational situations it is possible to simplify (2), and two cases will be considered. First, if the wavelength of observation is long enough with respect to the drop sizes, scattering may be neglected, and $\omega=0$. At our measurement frequency $\omega\approx 0.05$, i.e., the scattering is only ~5% of the total attenuation in precipitating clouds (Crane, 1966); thus, we have neglected ω in the results shown here. Second, for cloud heights and ranges great enough so that the total gaseous absorption may be approximated by the absorption between the observer and the storm, τ_3 is set equal to zero. With these two simplifications (2) becomes

$$\tau_c = -\ln\left[1-\frac{T_1(T_{bcs}-T_{bs})}{T_2(T_1-T_{bs})}\right], \quad (3)$$

where T_{bs} is the sky brightness temperature in the absence of cloud. This clear-sky brightness temperature was determined from five years (248 soundings) of Denver radiosonde data for a summer month, using the Van Vleck formulas for atmospheric gaseous absorption (Van Vleck, 1951). The arithmetic mean of data at a given elevation angle is used to represent T_{bs} at that elevation angle. The possibility of improving this estimate by a regression of the calculated T_{bs} vs surface temperature was considered, but the standard deviation of T_{bs} was not large (<5% of T_{bs}) and the regression analysis did not improve the estimate appreciably. A plot of the resulting T_{bs} vs elevation angle is shown in Fig. 1.

The five years of radiosonde data used determine T_{bs} were also used to estimate T_1. A regression of the 248 resulting values of T_1 with their corresponding surface temperatures and the surface temperature observed at the radiometer site was then used to obtain an estimate of T_1 for the time of observation. Values of T_1 are shown in Fig. 2.

---

[1] That is to say, for example,

$$\int_0^{r_1} T(r)\beta_s(r)e^{-\tau(r)}dr = T_1\int_0^{r_1}\beta_s(r)e^{-\tau(r)}dr = T_1(1-e^{-\tau_1}).$$

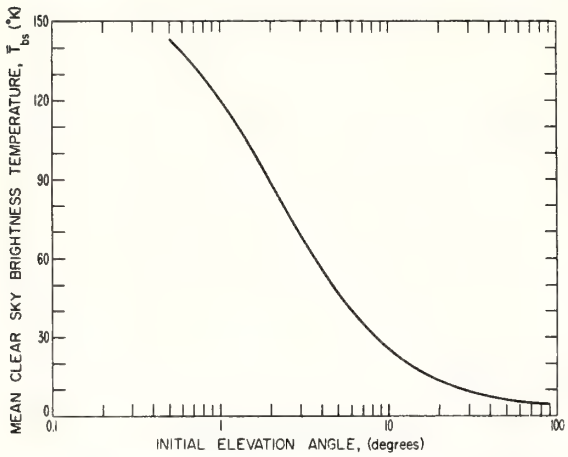

Fig. 1. Clear sky brightness temperature at 10.7 GHz as a function of radiometer elevation angle as obtained from five summers of Denver, Colo., radiosonde data.

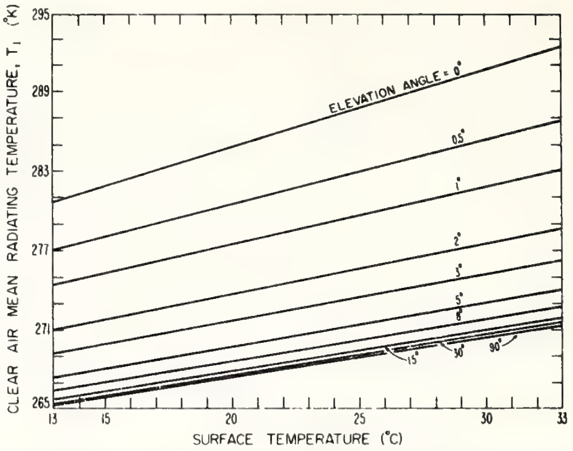

Fig. 2. Linear regressions of clear air mean radiating temperature vs surface temperature using 248 summer radiosonde profiles from Denver, Colo.

The value of T_2 is assumed to be equal to the kinetic temperature at the height at which the ray passes through the storm. This temperature is estimated from the surface temperature at the radiometer site and the average of the two temperature lapse rates taken from that day's 1200 and 1800 MDT Denver radiosondes.

The brightness temperature T_{bcs} in the direction of the storm is derived from the radiometer measurements from

$$T_{bcs}=\frac{\Delta T_a}{\epsilon}+T_{bs},$$

where ΔT_a is the difference in antenna temperature measured by the radiometer as it moves from clear sky to storm. An example of a chart recording of this temperature difference is shown in Fig. 3. The antenna beam efficiency ϵ is computed for a conical angle of 0.5° with a value of 0.62 resulting for ϵ. This choice of beam angle is a compromise; it is chosen to be large enough so that the contribution of noise sources outside the beam does not change much as the antenna is moved horizontally, and small enough so that the brightness temperature as weighted by the beam pattern and integrated over the beam will represent the brightness temperature in the direction of the main beam.

Having obtained values for integrated liquid absorption, we proceed to estimate the corresponding line integral of liquid water L, given by

$$L=\int_{r1}^{r2} M(r)dr,$$

where M is liquid water content (gm m^{-3}). For very small drop-size-to-wavelength ratios, i.e., non-precipitating clouds in the microwave region, the absorption coefficient at a given temperature is proportional to liquid

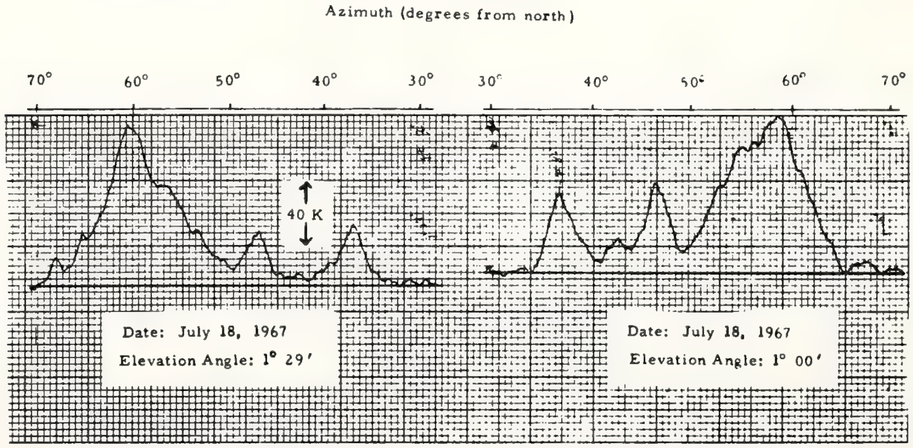

Fig. 3. Example of chart recording of radiometer sweeps across a thunderstorm.

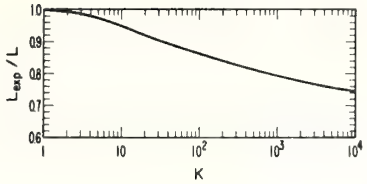

FIG. 4. Ratio of L_{exp} to L vs the shaping factor K of the exponential liquid water distributions used to determine L_{exp}.

water content, so that

$$\tau_c=\int_{r1}^{r2}\beta_c(r)dr=\int_{r1}^{r2}aM(r)dr,$$

or

$$L=\frac{\tau_c}{a}.$$

However, precipitating storms contain drop sizes large enough so that we cannot use this simple relation, and we modify it as follows. Crane (1966) has computed attenuation coefficients β_c for a large sample of drop size distributions and at a number of frequencies. At each frequency he has plotted attenuation coefficient vs liquid water content M and computed a fit to the data of the form

$$\beta_c=aM^b. \tag{4}$$

Letting $(1-\omega)\beta_c\approx\beta_c$ as before, we have

$$\tau_c=a\int_{r1}^{r2}[M(r)]^b dr. \tag{5}$$

Eq. (5) implies that we must have a knowledge of the spatial distribution of M in order to solve for the total liquid water content. However, Hölder's inequality (Munroe, 1953) can be used to show that

$$\int_{r1}^{r2}M(r)dr\leqslant(r_2-r_1)^{(b-1)/b}\left\{\int_{r1}^{r2}[M(r)]^b dr\right\}^{(1/b)},$$

or

$$L\leqslant(r_2-r_1)^{(b-1)/b}\left(\frac{\tau_c}{a}\right)^{(1/b)}, \tag{6}$$

with the restrictions that $b>1$ and that $M(r)>0$, both of which are true in our case. The equality in (6) occurs when $M(r)$ is a constant, i.e., the liquid water is uniformly distributed between r_1 and r_2. Since $M(r)$ is undoubtedly not a constant, L will be somewhat less than the maximum, depending on the value of b. For our frequency of 10.7 GHz, a simple linear interpolation between Crane's computations at 9.35 and 15.5 GHz results in constants $a=0.12$ and $b=1.28$ for (4), where β_c is in nepers per kilometer and M in grams per cubic meter. Since b is not very much greater than 1, L is rather close to the right-hand side of (6), as can be seen by taking some simple distributions of $M(r)$ for comparison. For a "triangular" distribution that is symmetrical about the center of the ray path between r_1 and r_2, the L resulting here is 95% of the maximum given by (6). A second example is a symmetrical exponential distribution of the form

$$M(l)=M_0\exp\left(-\frac{l}{l_e}\ln K\right),$$

where M_0 is the liquid water density at the "center" of the storm, l the distance from this point, l_e the distance to the edge of the storm, and K the ratio of M_0 to the density at the edge of the storm. Fig. 4 shows the ratio of integrated liquid water, L_{exp}, from this model to the maximum L of (6) as a function of K. The figure shows that for a very large value of K, indicating almost a spiked distribution, L is reduced by only ~25% from the maximum.

Eq. (6) also requires an estimate of r_2-r_1. This estimate of storm size is made from the location of relative "hot spots" (maximum L value, estimated) and the outer edge (zero contour) of the storm. The outer boundary of the storm is taken to be a semicircle in a plane perpendicular to the contour diagram and containing the line from the hot spot through the measurement point to the zero contour. The radius r_0 of this semicircle is the distance from the hot spot to the zero contour. If the distance from the hot spot to the data point (in the contour plane) is d, then

$$r_2-r_1=2\sqrt{r_0{}^2-d^2}.$$

Since b in (6) is near 1, the solution for L is not very sensitive to errors in this quantity, again indicating that the measurement is not strongly dependent on the spatial distribution of M.

4. Results

The relationship (6) is used to plot the contours of L shown in Fig. 5. The contours are plotted on an azimuth angle-elevation angle grid as seen from the radiometer site. The horizontal scans necessary to produce the contour diagrams were made during the time interval indicated. The units of (6) are grams of liquid water per cubic meter times kilometers, which is equivalent to the number of kilograms of liquid in a column 1 m² in cross section along the entire path through the storm. Alternatively, one can estimate the average liquid water density (gm m⁻³) over the path length by dividing the contour values by an estimated length (km) through the storm.

Eq. (6) is used with the implicit assumption that (4) is applicable at all cloud temperatures encountered in addition to the 0C for which it was determined. It can be shown that this is a rather good assumption at our

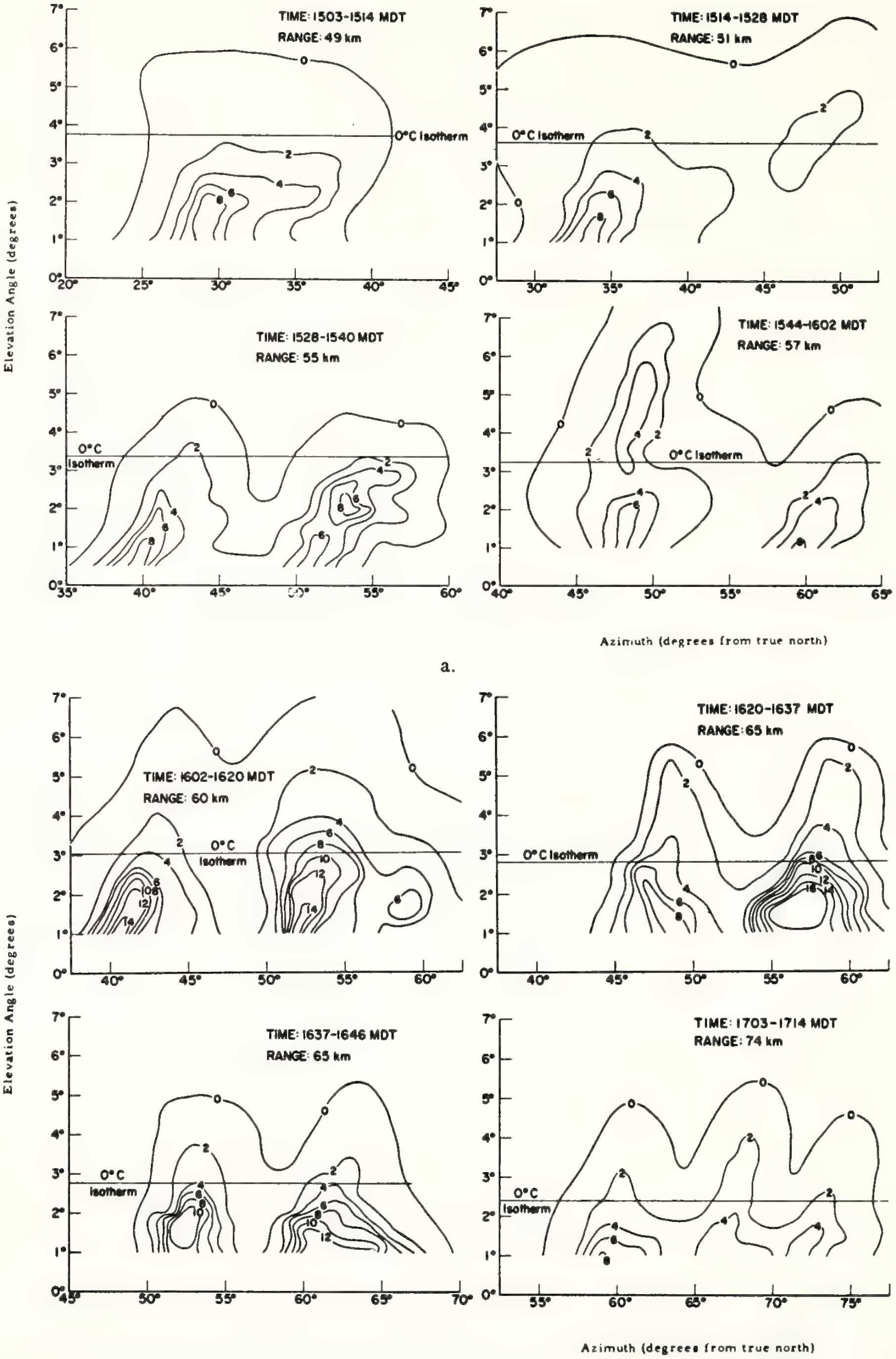

a.

b.

FIG. 5. Liquid water content (kg m^{-2} column) of an 18 July 1967 thunderstorm near Boulder, Colo., from 1503–1602 MDT, a., and from 1602–1714 MDT, b.

frequency for typical drop size distributions encountered in rainfall. This results from the fact that for small drops the absorption coefficient decreases with increasing temperature; for drops of ~1 mm in radius the absorption is essentially independent of temperature, and for larger drops the temperature dependence is reversed.

The analysis presented here contains another implicit assumption. In using the absorption cross section, we assume that the emission does indeed originate from liquid rather than ice. Since thunderstorms are generally mixtures of ice and water particles it is difficult to say which is dominant. To aid in judging in which regions of the storm the assumption may be valid, we have indicated the 0C isotherm (freezing level) on the contour diagrams and note that no hail reports from the 18 July storm were known to us. It seems likely that quantitative radar reflectivity data would be very useful in determining the validity of this assumption.

5. Conclusions

The technique described here shows promise as a tool for studying liquid water in clouds, although some further experimental work is needed to delineate its limitations. In addition to an estimate of integrated liquid water per unit area encountered by a radio ray, it provides a partial picture of how the liquid is distributed and some idea of the flux of liquid water in a particular volume. This information could be useful in predicting the amount of water available for precipitation and in observing the changes produced by storm modification experiments. In such a study, the method would, of course, be used with other techniques, especially radar. Measurement of attenuation in the storm is also an important use of the technique for the communication engineer, although this has not been elucidated here in detail.

Acknowledgments. We express our gratitude to J. M. Pepio for his valuable contributions, both to the experiments and to the data reduction procedure.

REFERENCES

Crane, R. K., 1966: Microwave scattering parameters for New England rain. M.I.T. Lincoln Laboratory, Tech. Rept. 426, 73 pp (DDC AD 647 798).

Dicke, R. H., 1946: The measurement of thermal radiation at microwave frequencies. *Rev. Sci. Instr.*, **17**, 268–275.

Kraus, J. D., 1966: *Radio Astronomy.* New York, McGraw-Hill, 212–223.

Munroe, M. E., 1953: *Introduction to Measure and Integration.* Cambridge, Mass., Addison-Wesley Publ. Co., p. 238.

Shklovsky, I. S., 1960: *Cosmic Radio Waves.* Harvard University Press, 141–142.

Van Vleck, J. H., 1951: *Theory of Absorption of Uncondensed Gases, Propagation of Short Radio Waves.* New York, McGraw-Hill, 646–664.

42

Reprinted from Proceedings of the 7th International Symposium on Remote Sensing of Environment 1, No. 10259-1-X, May 17-21, 1971, 585-594, 1971.

PROCEEDINGS of the SEVENTH INTERNATIONAL SYMPOSIUM
on
REMOTE SENSING OF ENVIRONMENT

17-21 May 1971

Sponsored by

Center for Remote Sensing Information and Analysis
Willow Run Laboratories, Institute of Science and Technology
The University of Michigan

Water Quality Office
Environmental Protection Agency

Office of Space Science and Applications
National Aeronautics and Space Administration

Federal Highway Administration
U. S. Department of Transportation

U. S. Geological Survey
U. S. Department of Interior

Air Force Cambridge Research Laboratories
Air Force Systems Command
U. S. Air Force

Agricultural Research Service
U. S. Department of Agriculture

Infrared and Optics Laboratory
Willow Run Laboratories
INSTITUTE OF SCIENCE AND TECHNOLOGY
THE UNIVERSITY OF MICHIGAN
Ann Arbor, Michigan

MICROWAVE DETERMINATION OF LOW ALTITUDE TEMPERATURE PROFILES[1]

Ed R. Westwater

National Oceanic and Atmospheric Administration
Boulder, Colorado

ABSTRACT

Passive ground-based radiometric measurements of thermal emission by oxygen can provide significant information about low altitude temperature structure. Theoretical results indicate that rms accuracies of 1 K can be obtained up to 2 km by inversion of fixed-frequency, angular-scan radiometer data with noise levels of 1 K. Statistical inversion techniques are applied to angular scan data to recover various types of temperature profiles.

1. INTRODUCTION

The remote sensing of low altitude vertical temperature profiles is of great interest to studies of air pollution which require methods of determining atmospheric stability. Primary quantities of interest during stable conditions are the mixing depth associated with elevated thermal inversions, the height of ground-based "radiation" inversions, and the intensities of both of these types of inversions. During unstable and neutral conditions, the lapse rate is of primary interest. To monitor these quantities with accuracies desired by air pollution forecasters requires determination of mixing depths to within 10 percent and intensities with an accuracy comparable to that obtained by conventional radiosondes [Hosler, 1]. Ground-based passive remote sensing of temperature profiles by microwave radiometry can satisfy many of the above requirements.

2. THEORY

The clear air atmospheric contribution to the frequency and the angular variation of microwave radiometric intensities is a function of the spatial distribution of pressure, water vapor, and temperature [Staelin, 2]. Ground-based passive measurements of downward thermal emission at well chosen frequencies in the 5-mm band of oxygen, coupled with easily obtainable surface pressure observations, result in a measured brightness temperature that depends mainly on the spatial temperature distribution. The contribution of an isothermal layer to the brightness is a function of its kinetic temperature, its emissivity, and the transmittance between the layer and the receiver. The contribution from various layers to the total observed emission is a function of both elevation angle and frequency. The resulting information that can be generated about the temperature structure by angular and frequency variation is described by the so-called "weighting functions," which are numerically equal to the negative of the spatial

---

[1] This work has been partially funded by the Air Pollution Control Office of the Environmental Protection Agency.

derivative of the transmittance function [Meeks and Lilley, 3]. A typical set of ground-based temperature weighting functions for a fixed-frequency variable angle technique is given in Fig. 1. As shown, information about temperature layers of 100 to 200 m thick is obtained at low elevation angles; higher elevation angles result in averages over increasingly thicker layers. Corresponding zenithal weighting functions for different frequencies are given by Gaut and Reifenstein [4]. In section 3 we discuss the important problem of recovering the vertical temperature profiles from observations of their weighted spatial averages.

Ground-based remote sensing of vertical temperature profiles can use either multi-spectral or multi-angle measurements. An angular system, such as used by Sperry Rand Research Center [Mount, 5] requires the assumption of horizontal stratification over distances of the order of 1 km. With present radiometer sensitivities and with a single antenna, used in either a continuous scan or a discrete angle mode, time resolution of about 20 to 30 minutes is achieved with a receiver integration time of 60 sec. To achieve the spatial resolution shown in Fig. 1, antennas with good angular resolution are required. In addition to the stratification assumption, the principal disadvantage of angular measurements is the difficulty of eliminating ground effects at low elevation angles. Multi-frequency observations at a fixed elevation angle can give a line profile in a given direction, and the technique does not require a stratification assumption. With a multichannel radiometer, the time resolution is limited only by the receiver integration time. Spatial resolution along the line of sight is determined principally by the possible range of absorption coefficient -- roughly from 0.1 to 3 km^{-1} in the 50-60 GHz region.

3. INVERSION OF RADIOMETRIC OBSERVATIONS

The difficult problem of recovering atmospheric profiles from indirect observations has received much attention in the past. Application of statistical estimation techniques to the inversion problem [Rodgers, 6; Westwater and Strand, 7] has led to successful retrieval of temperature profiles from satellite observations [Wark, 8], and from ground-based measurements [Westwater, 9]. Below, we discuss the application of this technique to ground-based microwave inference of temperature profiles.

Statistical inversion techniques require knowledge of the statistical characteristics of temperature profiles to construct a physically significant and stable solution to the inverse problem of radiative transfer. The estimation of the required statistical matrices can be formed from a past history of directly measured profiles, such as a backlog of radiosonde observations. The a priori knowledge is then combined with weighting functions and radiometer noise levels to yield a minimum-variance data processing scheme. In Fig. 2, an example is given of the predicted achievability in temperature sensing by applying statistical techniques to microwave radiometer data. The curve labeled σ_T represents the a priori standard deviation in temperature which could be achieved by using only the measured surface temperature as a statistical predictor. The three dashed curves represent the residual standard deviation when the indicated angular scan measurements are used. Thus, for this climatology, angular measurements of the given noise levels and frequencies, can infer temperature profiles with a rms error of less than 1 K up to about 3 km.

Applying statistical inversion techniques to profile inference assumes that the a priori mean profile and covariance matrix are representative of the local environment of the radiometer. Since it is frequently desired to place radiometers in locations where a priori data have not been gathered, it is quite important to determine the sensitivity of inversion results to errors in estimating the representative statistics. Examples are given in the next section of reasonable profile recoveries using statistical information gathered 50 to 60 miles from the radiometer location.

4. RESULTS

Below we present examples of temperature profiles inferred from microwave radiometric data.

For two 2-week periods in April and July-August 1968, the Environmental Radiometry Program Area of the Wave Propagation Laboratory, N.O.A.A., conducted microwave radiometer experiments at Upolu Point, Hawaii, Hawaii. Discrete angular measurements of sky brightness at

52.5 GHz were taken every 3 hours during the 2-week intervals. The radiometer measurements were supplemented by simultaneous radiosonde soundings. Twenty-five radiometer-radiosonde pairs were selected at random from the entire ensemble of data for later use in inversion; the remainder of the data were used to compute the relevant statistical quantities needed for inversion. Inversion of the 25 piece data sample resulted in a 1.27 K average rms departure of the inferred profile from the radiosonde measured temperature profile up to 10 km. The total vertical water content was simultaneously estimated with a relative accuracy of about 10 percent. Fig. 3 shows an example of these inversion results and illustrates the improvement obtained when using measured surface parameters as constraints. The inferred profile is typically a smoothed version of the true profile with a loss of detail that is determined by the radiometer noise level, by the weighting functions, and, to an extent, by the a priori statistics.

The application of microwave radiometry to remote probing of low altitude temperature profiles is being investigated by Sperry Rand Research Center [Mount, 5]. To further test statistical inversion techniques on microwave data, data from several of their field tests were procured.

The first data analyzed were taken at Salt Lake City, Utah, on August 15 and 16, 1968, during clear daytime conditions. Null balance radiometer measurements of thermal emission at discrete elevation angles ranging from horizontal to zenith were taken at 54.0, 54.5, and 55.0 GHz. The field site was at the Salt Lake City airport, a location for which a history of radiosonde observations were readily available. Mean profiles and covariance matrices were calculated from 5 years of August soundings. The complete set of inversion results for these 2 days is shown in Fig. 4. An average rms error of less than 1 K was achieved below 3 km with a resulting reduction in variance of 25 to 1 over a priori constrained statistics. The above results from the Hawaiian and Salt Lake City field tests are described in much greater detail by Westwater [10].

Emission data from a field test in Cincinnati, Ohio, were also inverted. The data collection and subsequent analysis differed in two respects from the procedure described above: (a) the emission data were obtained from a 54.5 GHz angular scan rather than from data at discrete angles. An attempt to estimate the brightness corresponding to a discrete angle was made by using knowledge of the radiometer time constant and two-point numerical derivatives of the data; (b) the a priori statistics were obtained from Dayton, Ohio, which was roughly 50 miles away. In addition, every sounding during a 5-year period was used to compute the means and covariances, and no attempt was made to compute monthly or seasonal statistics. An example of a Cincinnati profile recovery during a fairly intense ground-based inversion is shown in Fig. 5. Note that both the height and the intensity of the ground-based inversion are well determined, but that the details of the elevated inversion at 2.5 km are lost.

The final example of a profile retrieval that we present here was inferred from 54.5 GHz angular scan data taken at the Raleigh-Durham airport in North Carolina. Statistical quantities were estimated from 5 years of October radiosonde soundings taken at Greensborough, North Carolina, roughly 60 miles away. The station elevations differed by 135 m. An example of a retrieval of an elevated inversion is shown in Fig. 6. Note that the inferred profile clearly indicates the existence of an elevated inversion, and that the depth of the mixing layer can be estimated by the lowest vertical tangent of the inferred curve. It is also clear that very little information is obtained about either the intensity or the thickness of the elevated layer. This illustrates the inherent difficulty of recovering profiles that oscillate at a higher spatial frequency than that of the weighting functions.

In addition to the above inversions of data, we performed inversions of several sets of simulated angular brightness containing rms gaussian noise of 1 K. This test was to determine the improvement in recovering elevated inversions that could be achieved by a more judicious selection of a priori statistics. The profiles selected for brightness calculation and subsequent inversion were mainly of the elevated inversion type from Greensborough, North Carolina, during August. Average profiles and covariance matrices were based on selected statistical samples containing (a) both ground-based and elevated inversions, and (b) only elevated inversions. Although the retrievals using selected statistics differed slightly from those based on heterogenous statistics, there was no marked improvement in the quality of the results. This rather surprising result seems to reflect that although the selected statistics contained only thermal inversions, there was a large dispersion of the heights at which the inversions occurred.

5. CONCLUSIONS

Analysis of several sets of fixed-frequency variable angle radiometer data has indicated the potential use of ground-based microwave measurements in air pollution forecasting. Statistical inversion of radiometer data has yielded successful retrievals of lapse and ground-based inversion temperature profiles. The existence of elevated inversions has been inferred from the data, but with poor height resolution. The mixing depth associated with an elevated inversion can be estimated to within about 10 percent, but retrieval of more detailed information is difficult.

Further experiments are being conducted to compare the variable angle vs. the variable frequency technique. A four-channel radiometer, operating between 52.5 and 55.5 GHz, is now being tested by N.O.A.A. Environmental Research Laboratories, Boulder, Colorado.

6. REFERENCES

1. Hosler, Charles R. (1971), Private communication.

2. Staelin, D. H. (1969), Passive remote sensing at microwave wavelengths, Proceedings of the IEEE 57, No. 4, pp. 427-439.

3. Meeks, M. L., and A. E. Lilley (1963), The microwave spectrum of oxygen in the earth's atmosphere, J. Geophys. Research 68, No. 6, pp. 1683-1703.

4. Gaut, N. E., and E. C. Reifenstein, III (1971), Interaction of microwave energy with the atmosphere, Technical Report, Environmental Research and Technology, Inc., Waltham, Massachusetts.

5. Mount, W. D. (1969), Use of millimeter wave radiometry to remotely measure atmospheric stability, Proceedings of the Sixth International Symposium on Remote Sensing of Environ., Vol. 1, pp. 469-490.

6. Rodgers, C. D. (1966), Satellite infrared radiometer - A discussion of inversion results, Memorandum No. 66.13, Clarendon Laboratory, Oxford University, 31 pp.

7. Westwater, E. R., and O. N. Strand (1968), Statistical information content of radiation measurements used in indirect sensing, J. Atmospheric Sciences 25, No. 5, pp. 750-758.

8. Wark, D. Q. (1970), SIRS, an experiment to measure the free air temperature from a satellite, Applied Optics 9, No. 8, pp. 1761-1766.

9. Westwater, E. R. (1970), Ground-based determination of temperature profiles by microwaves, PhD Thesis, Dept. of Physics, University of Colorado, Boulder, Colo., 121 pp.

10. Westwater, E. R. (1971), Ground-based determination of low altitude temperature profiles by microwaves, submitted for publication.

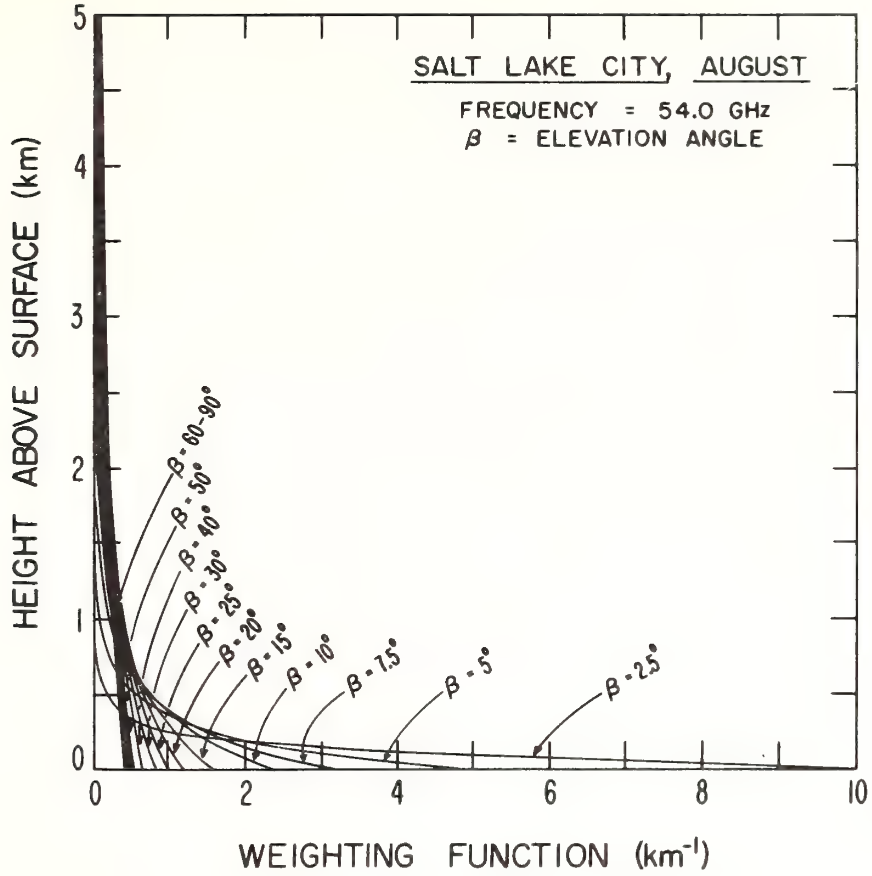

FIGURE 1. WEIGHTING FUNCTIONS FOR ANGULAR PROBING

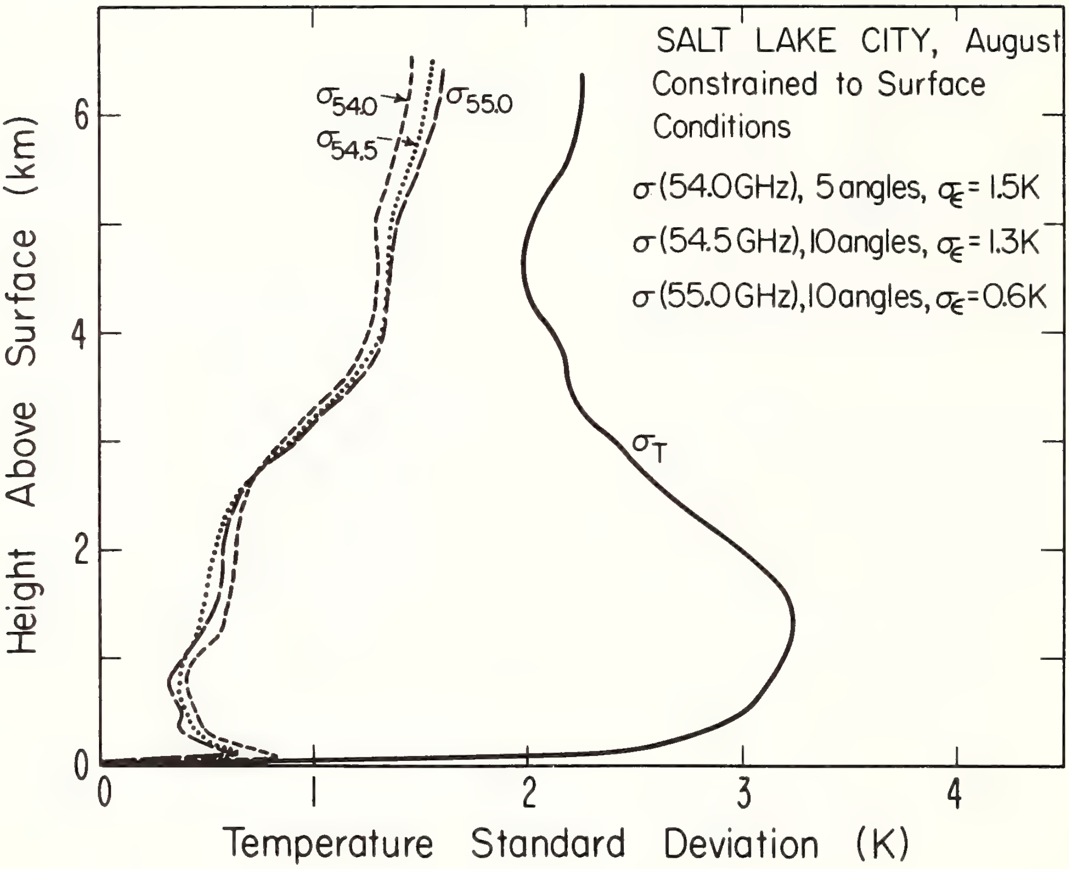

FIGURE 2. PREDICTED ACHIEVABILITY in determining vertical temperature profiles by inversion of microwave radiometer data.

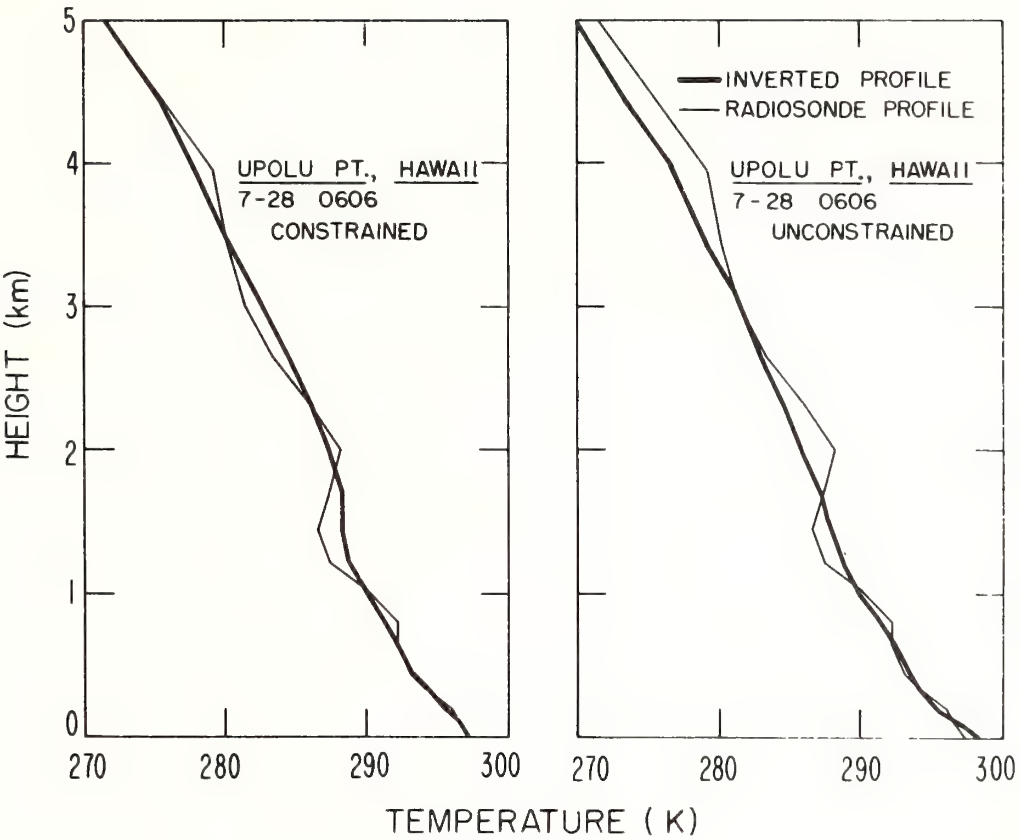

FIGURE 3. TEMPERATURE PROFILE derived from radiometer measurements at 52.5 GHz.

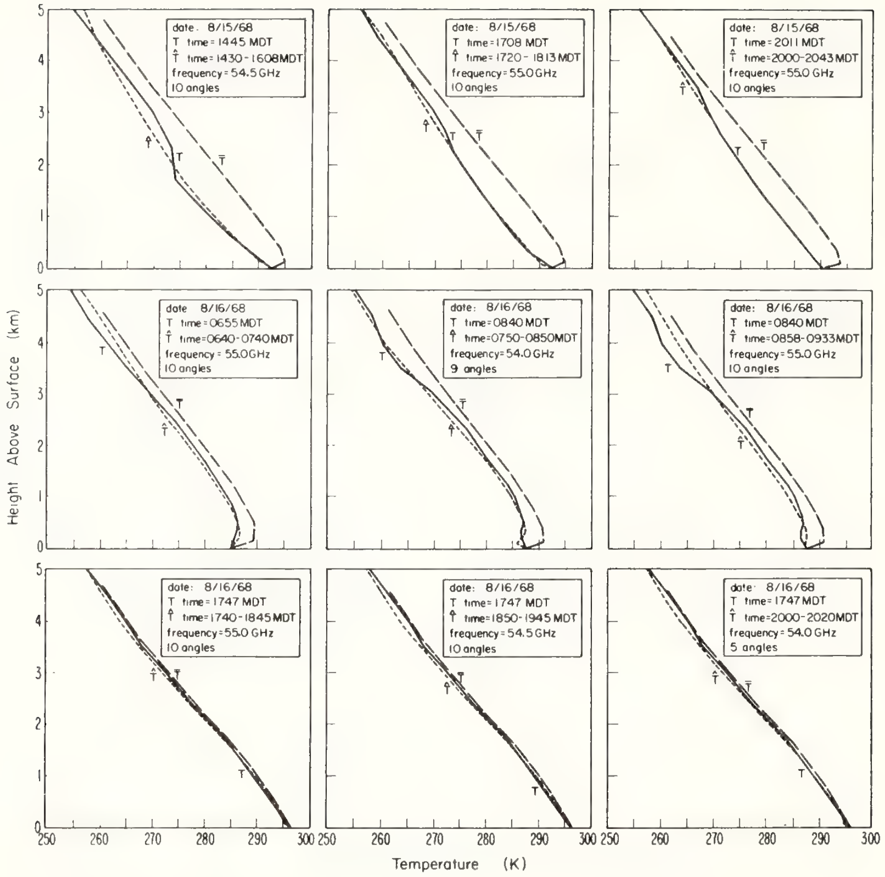

FIGURE 4. TEMPERATURE PROFILES derived from radiometer measurements at Salt Lake City, Utah.

T = radiosonde profile
$\overline{T}$ = mean profile constrained to surface conditions
$\hat{T}$ = inferred profile

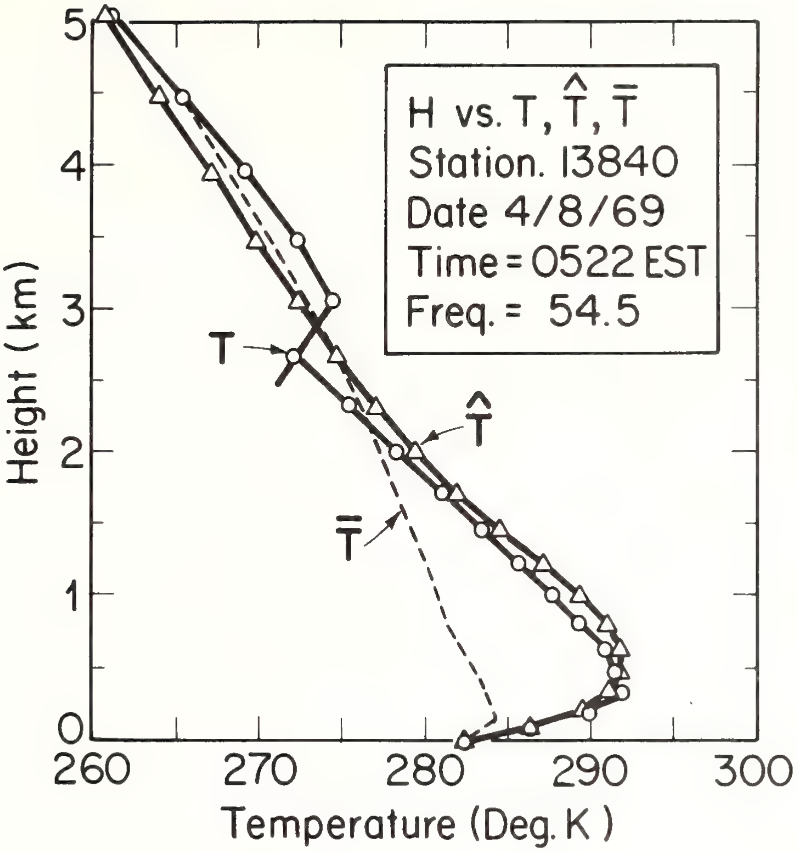

FIGURE 5. TEMPERATURE PROFILE derived from radiometer measurements at Cincinnati, Ohio. *A priori* statistics from Dayton, Ohio.
$\underline{T}$ = radiosonde profile
$\underset{\wedge}{T}$ = mean profile constrained to surface conditions
T = inferred profile.

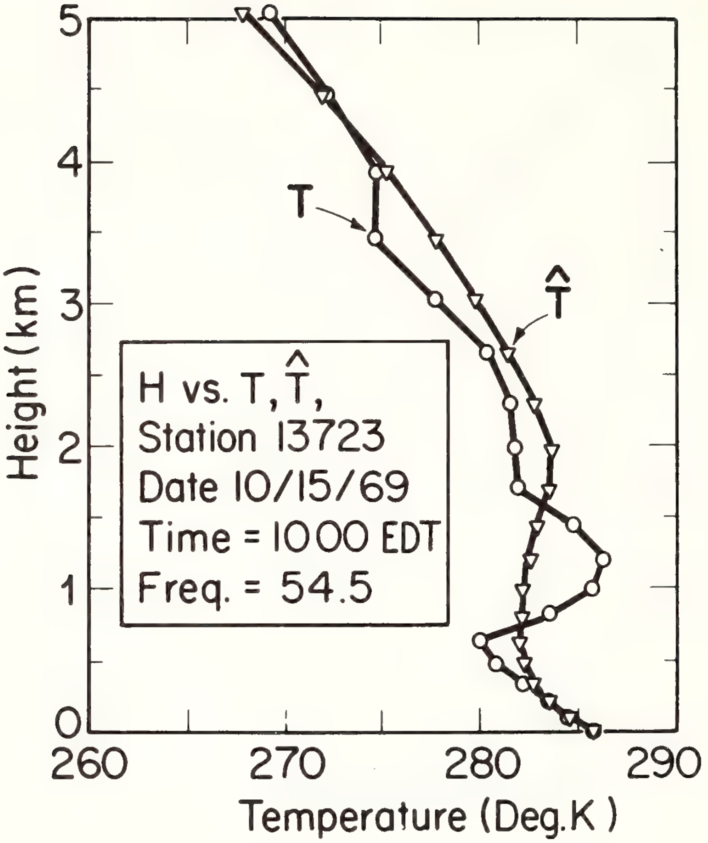

FIGURE 6. TEMPERATURE PROFILE derived from radiometer measurements at Raleigh, Durham, North Carolina. *A priori* statistics from Greensborough, North Carolina.

T = radiosonde profile
$\hat{T}$ = inferred profile.

Reprinted from Proceedings of Symposium on Air Pollution, Turbulence, and Diffusion, December 7, 1971, 56-65, 1971.

RECENT RESULTS IN GROUND-BASED SENSING OF ATMOSPHERIC TEMPERATURE PROFILES

J. B. Snider
Wave Propagation Laboratory
Environmental Research Laboratories
National Oceanic and Atmospheric Administration
Boulder, Colorado 80302

INTRODUCTION

The application of ground-based radiometric measurements of emission from atmospheric oxygen to the problem of estimating the variation of temperature with height has been discussed in recent literature.(1-3) In the majority of measurements reported, temperature profiles have been determined by inverting single frequency measurements of brightness temperature as a function of elevation angle. An alternate technique consists of inverting observations of brightness temperature as a function of frequency at either a fixed or variable elevation angle. The second technique has received relatively little attention.

An obvious advantage in favor of the first, or angular scan method, is that the instrumentation is fairly simple, consisting of a single frequency radiometer with an antenna that is steerable in elevation; however, conversion of antenna to brightness temperature may be complicated and subject to error since the stray radiation into antenna back and side lobes changes with elevation angle. In the second, or multi-spectral method, the antenna is not moved with the result that stray radiation is relatively constant thus simplifying the determination of brightness temperature.

In principle, the multi-spectral system offers the advantage that a profile can be measured in a time period set mainly by the radiometer time constant. With present radiometer sensitivities, the angular scan method requires 15 to 30 minutes to complete a temperature profile measurement. The major disadvantage of the multi-spectral system is that the instrumentation is complicated and relatively expensive.

This paper describes instrumentation developed to permit experimental evaluation of both techniques and presents the results of an experiment performed to compare quantitatively the relative merits of the two techniques.

THEORY

In this section we briefly consider the theory of the estimation of temperature profiles from measurements of microwave emission by oxygen. Emission by oxygen is utilized because this gas is well-mixed in the atmosphere and its absorptive properties in the microwave region are reasonably well understood. Absorption of electromagnetic energy by O_2 occurs in a series of resonant lines centered at 60 GHz and in a single line near 118 GHz; here we consider only the 60 GHz absorption complex. At the earth's surface the individual absorption lines merge into an absorption continuum due to pressure broadening and a ground-based radiometer observes a smooth variation of brightness with frequency. The brightness temperature, T_b, measured at frequency, ν, and elevation angle, θ, is given by(4)

$$T_b(\nu,\theta) = T_b^{ext}(\nu,\theta)\exp(-\int_0^\infty \alpha_\nu \csc\theta\ dh) + \int_0^\infty T(h)\alpha_\nu[\exp(-\int_0^h \alpha_\nu \csc\theta\ dh')]\csc\theta\ dh \qquad (1)$$

where T_b^{ext} = brightness temperature caused by a source external to the earth's atmosphere,

$T(h)$ = absolute temperature as a function of height, h, above the earth's surface, and

α_ν = absorption coefficient at frequency ν.

Here we assume that the absorption is a function of oxygen, water vapor, temperature, and pressure only and that scattering is negligible; these assumptions are valid except when clouds or precipitation is present. The problem at hand is to estimate the quantity, $T(h)$, from measurements of the quantity, $T_b(\nu,\theta)$.

Study of (1) shows that input data may be generated in three ways:

1. Angular scan, i.e., measurements of T_b at a given frequency versus elevation angle,
2. Multi-spectral, i.e., measurements of T_b versus frequency at a fixed elevation angle,

and 3. A combination of angular-scan and multi-spectral techniques.

The method employed to invert the radiative transfer equation (1) has been described in detail by Westwater$^{(1)}$ and will only be briefly described here. The method involves replacing (1) with a Fredholm integral equation of the first kind. The Fredholm equation is then solved by means of a statistical estimation technique that yields estimates of the atmospheric temperature structure based upon a priori knowledge of the temperature, pressure, and humidity statistics for the particular measurement location and the given set of brightness temperature measurements. The solution is the set of atmospheric temperature versus height values that results in the minimum departure (in a least-squares sense) from the expected value.

MULTI-FREQUENCY RADIOMETER

We now describe the instrument developed to compare the relative usefulness of the methods described above in making accurate estimates of atmospheric temperature profiles. Major objectives in the design of the radiometer were capability of operation in both angular-scan and multi-spectral modes, simultaneous operation on 3 or 4 frequencies from a common antenna, high angular resolution in the antenna system, good spectral resolution, and the greatest possible sensitivity consistent with the other design goals.

A block diagram of the final radiometer design is given in Figure 1. The basic system is the well known Dicke radiometer in which the receiver is switched between the antenna and a temperature-controlled reference termination. In the present system, the Dicke switch (modulator) is a rotating vane attenuator that alternately transmits and absorbs the energy from the antenna. The components located between the antenna and rotary modulator serve the following functions: during calibration the radiometer is connected to one of the temperature controlled terminations through the waveguide switch to establish a known temperature reference. (At 0° elevation angle and in the 60 GHz spectral region the atmosphere is essentially a blackbody having an effective temperature very nearly equal to the surface temperature; hence, atmospheric emission may also be used as a calibration reference point.) Incremental calibration of the radiometer output is accomplished by injecting noise from the gas discharge noise source into the signal channel via the precision attenuator and auxiliary arm of the directional coupler. During measurements, the antenna is connected to the radiometer and noise is injected into the signal channel to allow operation in a "semi-balanced" condition. Since a true balance cannot be obtained at more than a single frequency, an appropriate amount of noise is injected to obtain an approximate balance at all frequencies.

The first mixer translates a 4 GHz band of frequencies in the 50 GHz region to a 4-8 GHz first intermediate frequency. After a stage of amplification, separation into four individual channels takes place in a strip-line multiplexer; center frequencies are 4.5, 5.5, 6.5, and 7.5 GHz. A second conversion to a 60 MHz center frequency follows the multiplexer; the noise bandwidth of the 60 MHz IF amplifiers is approximately 30 MHz to achieve a fair degree of spectral resolution. Following the second IF amplifiers are four identical stages of video detection, synchronous detection using a lock-in amplifier, and analog output recording.

All components before the lock-in amplifiers are located in an equipment enclosure mounted at the antenna. The waveguide compartment is heated to maintain the ambient temperature reasonably constant. Since ohmic losses in the waveguides generate noise, waveguide temperatures are measured by thermistor probes located at several points and remotely recorded for subsequent use in computing the antenna temperature.

The radiometer enclosure and its 1.2 m diameter conical horn antenna are installed on an elevation over azimuth antenna mount which provides the capability of angular scan operation. The antenna position is read out remotely at the data recording position. A relatively large antenna aperture was employed to obtain the high angular resolution mentioned earlier, while the conical horn configuration was selected to minimize stray radiation into the back and side lobes and thereby simplify the conversion of antenna temperature to brightness temperature.

A summary of the essential radiometer characteristics is presented in Table 1.

Table 1. Multi-frequency radiometer characteristics

Operating frequency	- 52.5, 53.5, 54.5, 55.5 GHz
Antenna characteristics	- 1.2 meter diameter conical horn, 3 dB beamwidth 0.3°
Receiver type	- Dicke switching radiometer, dual-conversion superheterodyne 1st IF: 4 to 8 GHz 2nd IF: 60 MHz center frequency, noise bandwidth approx. 30 MHz
Sensitivity	- Approx. 1K for 60 s integration time

TABLE MOUNTAIN EXPERIMENT

During April 1971, an experiment was conducted at Table Mountain near Boulder, Colorado, primarily to evaluate the performance of several radiometric systems in yielding atmospheric temperature profiles; however, as the planning for the experiment evolved, it became clear that additional sensors could not only benefit from but supplement the basic objectives of the main experiment. As a result, the final scope of the program greatly exceeded the original plan. The list of participants along with their respective measurements follows:

Participant	Equipment
Air Pollution Control Office	54.5 GHz radiometer, angle-scan mode
Sperry Rand Corporation	54.5 GHz radiometer, angle-scan mode
Wave Propagation Laboratory, NOAA	4-frequency radiometer, angle-scan and multi-spectral modes
	Acoustic sounder
	Infra-sound array
	Lidar
	Infrared radiometer
	Radiosonde data
	Aircraft temperature measurements
	Surface T, RH, P, Sky photographs
National Center for Atmospheric Research	Boundary layer profiler (tethered balloon with radiosonde)

In the remainder of this paper, we shall limit our discussion to the WPL radiometric observations to provide temperature profiles and a comparison of the inversion results with the temperature profiles measured by the radiosondes.

Data were recorded three times daily beginning at 0400, 0900, and 1500 during a one-week period in April 1971. These observation times were selected in order to acquire data for a variety of profiles. The radiometric observations were made at a series of 10 discrete antenna elevation angles ranging from 0° to 90°; a ccmplete run required about one hour. During the radiometer measurements, a radiosonde was released and data were recorded to an altitude of about 10 km; the aircraft also recorded temperature-height variations to an altitude of 3 km. Before and after recording of the radiosonde data, the boundary layer profiler made a sounding from the surface to about 500 meters and back to the surface. In addition to these supporting data, sky photographs were made at each antenna elevation angle so that possible contamination of data by clouds could be detected.

The majority of measurements recorded showed lapse temperature profiles; however, 3 temperature inversions were present. We shall now examine a few sets of data from two viewpoints:

1. What is the optimum set of input data?, and
2. What are the relative effects of different statistics upon the final inversion result?

INVERSION RESULTS

The theoretical accumulated standard deviation of the estimated difference in inferred and actual (measured) temperature profiles is shown in Figures 2 and 3; the two figures illustrate the effects of using different statistics as well as different sets of input data. Figure 2 is based upon the 5 year mean all month radiosonde data for Denver, Colorado, while Figure 3 is calculated using the 5 year mean April radiosonde data. The various curves are plotted for different sets of input data; the symbol for a particular set is shown in the legend. Combinations 1A, 1, and 2 refer to the multi-spectral input data combinations listed in Table 2. Combinations 1A and 1 are equivalent except that 1A is computed for a simulated measurement accuracy of 0.1K while combination 1 is based upon the actual observed differences between radiometric measurements and the brightness temperature calculated from radiosonde information. Angle scan designations are simply measurements of brightness temperature versus elevation angle at the frequency indicated.

The curve labeled a priori is the theoretical inversion accuracy that would be obtained if only the long-term statistics and the surface temperature were known. In all the results presented here, the measured surface temperature is used as a constraint. The theoretical curves for spectral combinations 1 and 4 are nearly identical; the curves for combination 4 have been omitted from Figures 2 and 3 for clarity.

Table 2. Explanation of spectral combinations employed to estimate temperature profiles

Combination No.	Input Data	
	Elevation Angle (deg)	Frequency (GHz)
1	5	54.5, 55.5
	10	54.5, 55.5
	15	54.5, 55.5
	30	53.5, 54.5, 55.5
	60	52.5, 53.5, 54.5
	90	52.5, 53.5, 54.5
2	90	52.5, 53.5, 54.5, 55.5
3	60	52.5, 53.5, 54.5, 55.5
4	5	53.5, 54.5
	10	at all angles
	15	
	20	
	30	
	60	
	90	

Several important points are brought out in Figures 2 and 3. First, it is clear that spectral combination 1 results in the smallest standard deviation over the full 10 km height interval. Second, the accumulated error in the angular scan mode is about the same at both 53.5 and 54.5 GHz and is smaller than for multi-spectral measurements at a fixed elevation angle, i.e., combination 2. Thus we reach the not surprising conclusion that a combination of angular scan and multi-spectral input data yields a better inversion result than either set of input data alone. It is somewhat surprising that a fairly large reduction in measurement error (from approx. 2.5K to 0.1K) does not result in a substantial decrease in accumulated error for combination 1. This result may indicate that multi-spectral angular scan measurements need not be extremely accurate to give good inversion results except during serious departures from horizontal stratification.

The rather poor performance of the multi-spectral inversion method may be partly caused by measurement error; however, the main reason is believed to be the smaller number of input measurements in the multi-spectral case. It is also possible that a more optimum selection of frequencies would result in a smaller difference between inferred and actual profiles.

As for the comparative merits of the statistics used to invert the data, it appears that all-month and April statistics produce comparable results over the first 3 or 4 km for all input combinations. Above 4 km, use of April statistics results in a slightly smaller error when angular scanning or spectral combination is used. Thus, for this rather limited sample at least, the inversion result is rather insensitive to the statistics employed.

We shall now examine some of the actual inversion results and compare the measured and inferred profiles for a few samples. Figure 4 is an example of a profile containing a surface based temperature inversion. The curves are the profile measured by the radiosonde and the profile inferred from the radiometric data; inversion results are shown for four different combinations of input data. All sets of data, except for spectral combination 2, show the presence of the temperature inversion. Although the magnitude of the inversion is slightly underestimated in this example, the height of inflection is fairly well defined. As predicted by theory, spectral combination 1 gives the best overall agreement with the radiosonde profile. Note that combination number 4, for which a theoretical curve is not shown, results in agreement comparable to that obtained with combination 1 and the angular scans at both frequencies. This trend was observed consistently in all the samples considered in this study which suggests that a two-frequency radiometer operated in the angular scan mode yields results comparable in accuracy with those obtainable with a 4-frequency device; however, it does not necessarily follow that this behavior would be true for all geographic areas.

Figures 5 through 7 show inversion results for three other samples using spectral combination 1 and April statistics to illustrate recovery of several different types of profiles. The radiosonde data in Figure 5 show an elevated temperature inversion at about 500 m altitude: the inversion is also seen in the aircraft and boundary layer profile recordings. The inferred profile does not detect the intensity of the elevated inversion although there is a change in the estimated profile lapse rate in the vicinity of the temperature inversion. This inability to detect elevated temperature inversions has also been observed in angular scan measurements.(3) In both instances, it is believed that the temperature structure is smoothed out because of integration effects and/or overlapping of weighting functions. In principle, the multi-spectral approach should be more successful in recovering elevated inversions if the frequencies of operation are chosen so as to cause the weighting function to give more information in the vicinity of the elevated inversion. It is clear that the optimum frequency problem should receive additional study.

CONCLUSIONS

Based upon the very limited sample available for this study, it is concluded that a combination of angular scan and multi-spectral input data produces more accurate inferred profiles than do other input data combinations. It further appears that the angular scan method is superior to multi-spectral techniques especially when detecting surface based temperature inversions. However, the possibility exists that a more optimum selection of frequencies would result in improved accuracy for the multi-spectral method. For the measurements reported here, a 2 frequency-angular scan combination yields results nearly as good as those obtained with the 4 frequency angular scan combination. The implication regarding simplification of equipment is obvious; thus, the extent to which this result applies to other geographic areas should be carefully evaluated.

REFERENCES

1. Westwater, E. R. (1970): Ground-based determination of temperature profiles by microwaves, Ph.D. Thesis, Dept. of Physics, University of Colorado, Boulder, Colorado, 121pp.

2. Staelin, D. H. (1969): Passive remote sensing at microwave wavelengths, Proceedings of the IEEE 57, No. 4, 427-439.

3. Westwater, E. R. (1971): Microwave determination of low altitude temperature profiles, Proceedings of 7th International Symposium on Remote Sensing of Environment, Ann Arbor, Michigan, May 17-21, 1971.

4. Meeks, M. L., and A. E. Lilley (1963): The microwave spectrum of oxygen in the earth's atmosphere, J. Geophys. Res. 68, No. 6, 1683-1703.

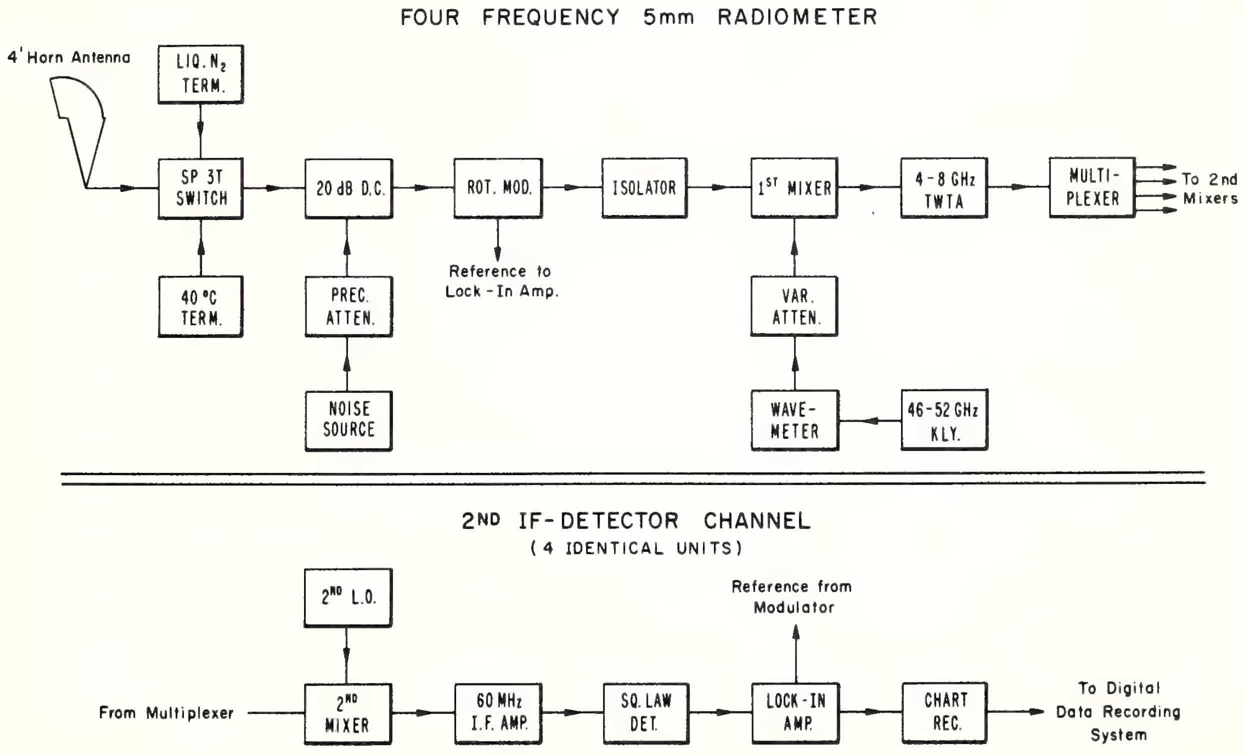

Figure 1. Block diagram of multi-frequency radiometer.

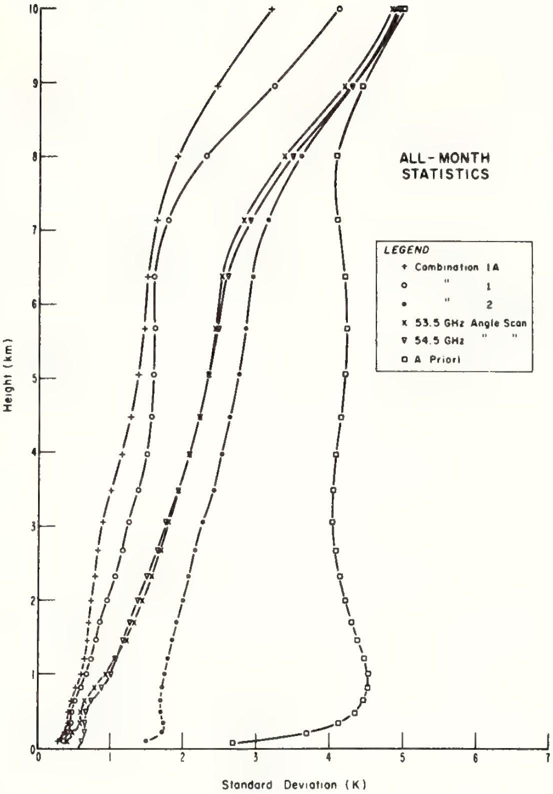

Figure 2. Theoretical accumulated standard deviation of estimated profile using all-month statistics.

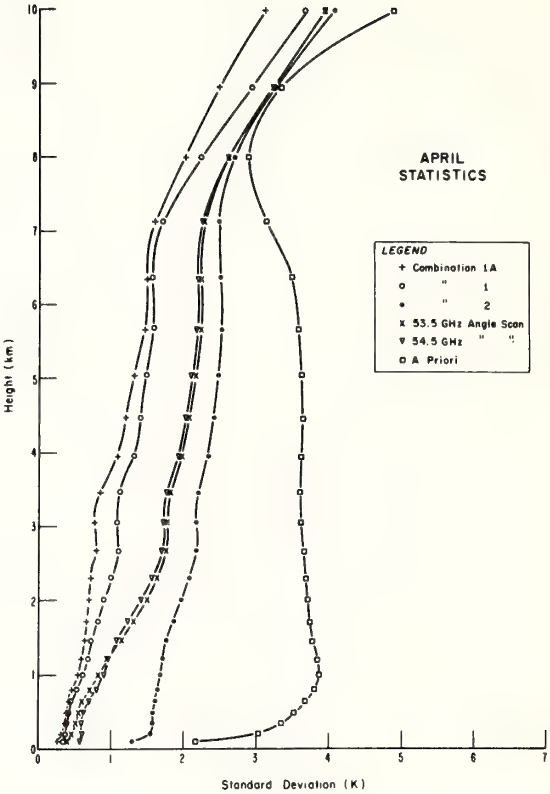

Figure 3. Theoretical accumulated standard deviation of estimated profile using April statistics.

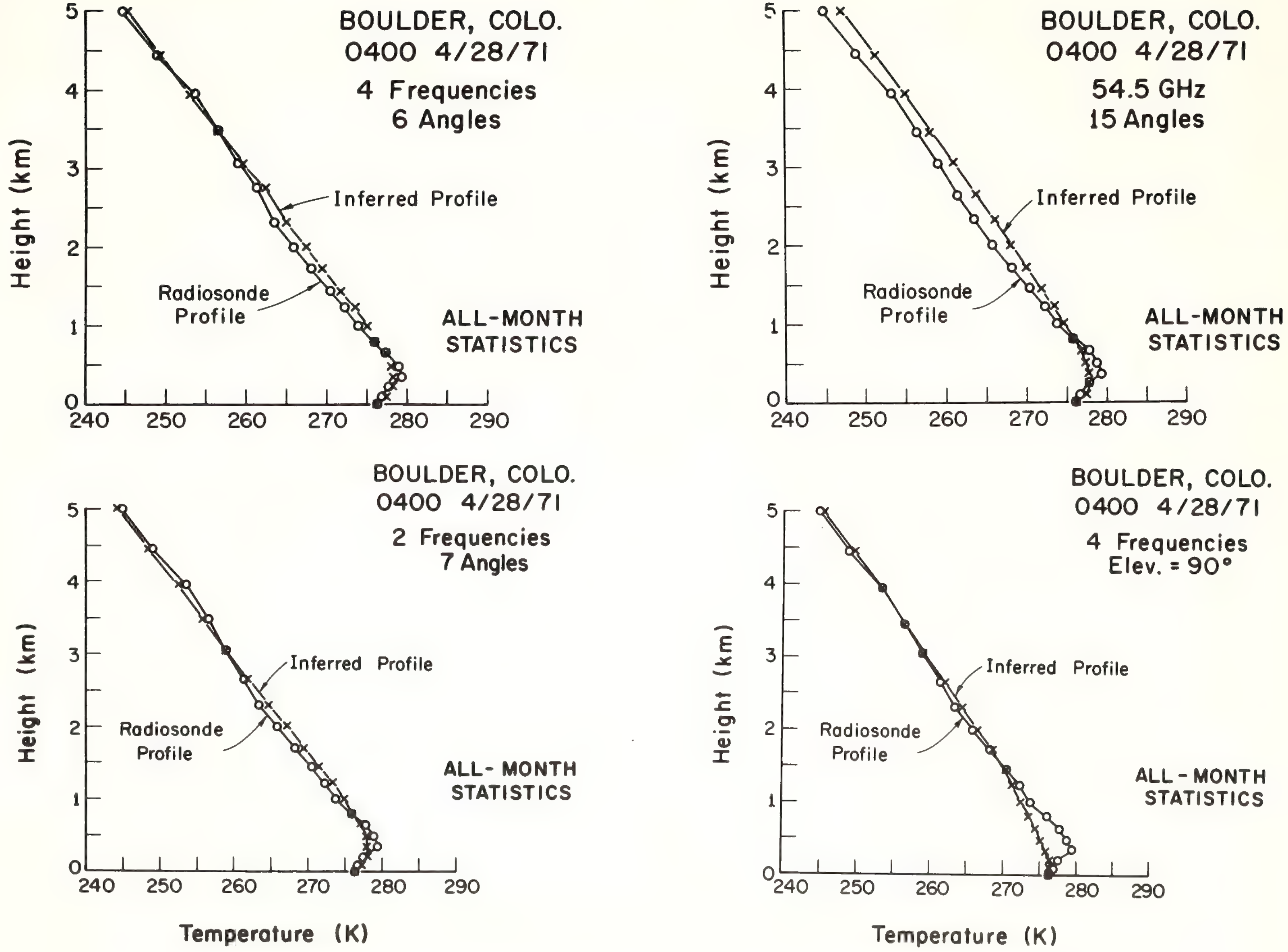

Figure 4. Inferred and measured temperature profiles using four different combinations of input data.

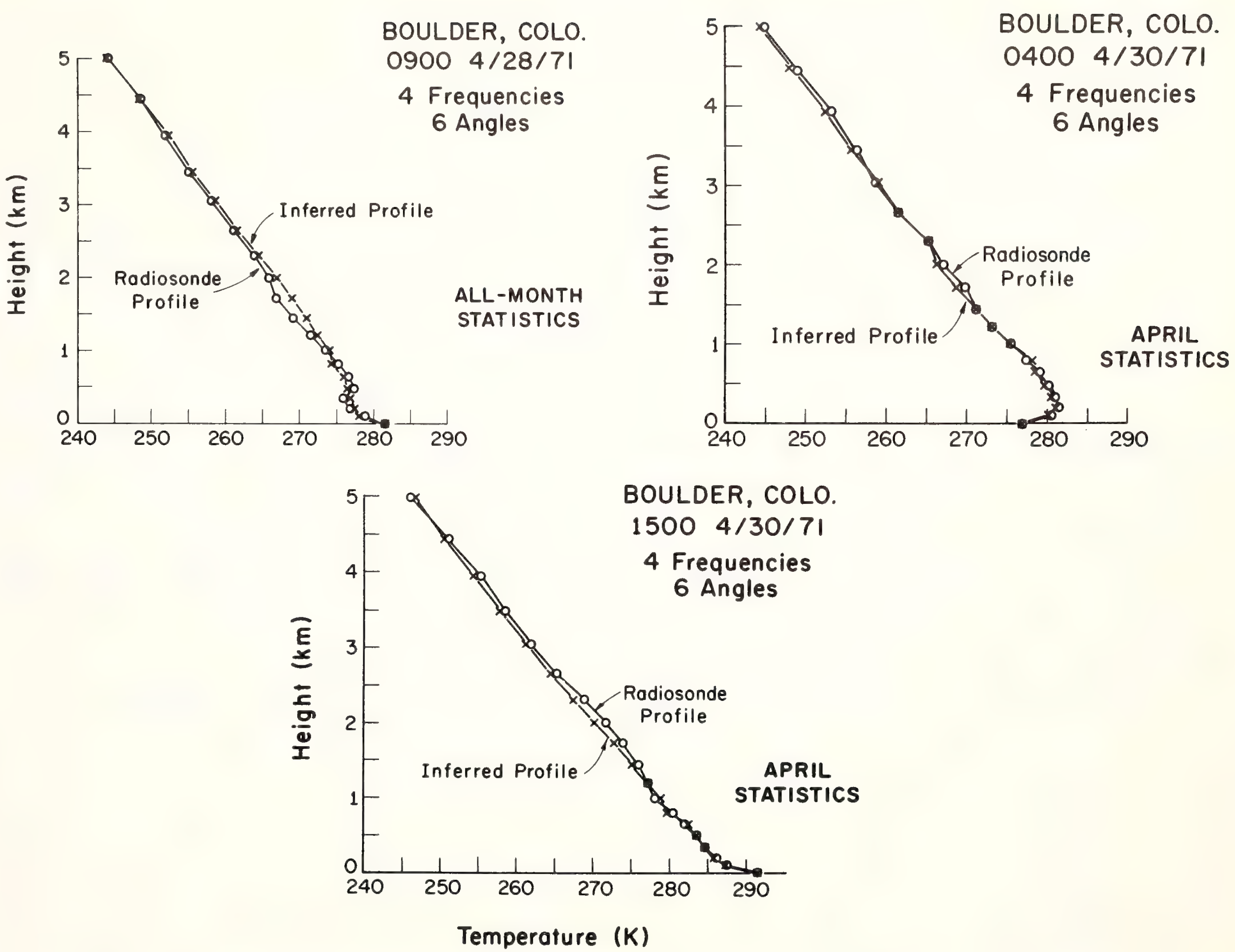

Figures 5, 6, 7. Inferred and measured temperature profiles using combination of angle-scan and multi-spectral input data.

Reprinted from NOAA Technical Report, ERL 202-WPL 14, 1971.

OPTIMIZATION OF FREQUENCIES USED IN INDIRECT SENSING BY INVERSION

Otto Neall Strand

An expression for the expected mean-square error in the statistical estimation of tropospheric temperature profiles by the inversion of microwave thermal emission measurements has been derived in the literature. A semi-probabilistic computer search technique has now been devised to determine the frequencies that minimize this expected mean-square error for a given (small) number of microwave frequencies. Although a specific problem is solved here, the methods are general, and can be applied to any situation involving optimum linear estimation of the solution of a Fredholm integral equation of the first kind with specified *a priori* mean and covariance data on the unknown function.

Key words: Optimization, inversion, Fredholm integral equation.

45

Reprinted from NOAA Technical Memorandum, ERL WPL-6, 1971.

REVIEW OF ELECTROMAGNETIC RADIATION DATA FROM SEVERE STORMS IN OKLAHOMA DURING APRIL 1970

William L. Taylor

The rate of occurrence of atmospherics in the 10 kHz to 10 MHz frequency range was examined for 6 severe storms and 8 non-severe thunderstorms during April 1970. Rates often exceeded 500/s in the VLF channels and 100,000/s in the HF channels for short time periods. The general characteristic of the rate data during non-severe conditions was that of a low background of atmospherics with occasional individual bursts of high rates produced by discrete discharges. Atmospheric activity greatly increased during severe conditions producing many more bursts per unit of time and resulting in an enhanced background of almost continuous high rate with little or no large individual bursts.

Reprinted from Journal of Geophysical Research 75, No. 9, 1629-1632, 1970.

A Raman Scattering Method for Precise Measurement of Atmospheric Oxygen Balance

R. L. SCHWIESOW AND V. E. DERR

ESSA Research Laboratories, Boulder, Colorado 80302

Quantitative measurements of Raman scattering intensities from N_2, O_2, and CO_2 under ambient atmospheric conditions are given. The atmosphere was illuminated with 20,489 cm^{-1} Ar^+ laser radiation. These scattering intensities are sufficiently strong to allow measurement of O_2/N_2 and CO_2/N_2 concentration ratios in the atmosphere to a precision of 0.3 and 0.006 ppm total atmosphere, respectively, by means of scattered photon counting over a 174-hour integration period. The Raman technique represents an improvement in precision over existing techniques by almost two orders of magnitude, and a substantial but less easily determined improvement in accuracy by using the transition probabilities of a monomolecular reference gas as a standard, rather than the properties of a mixed gas standard as is done in current measurements.

Because the potential reduction of atmospheric oxygen and the increase of atmospheric carbon dioxide could have important nonlinear effects, especially if abetted by a decrease of marine life responsible for oxygen production, the worldwide precision measurement of oxygen–carbon-dioxide–nitrogen ratios is important [*Berkner and Marshall*, 1965]. Precision of the order of 1 part in 10^6 for these ratios is essential.

Existing measurements do not provide this precision; they are limited to ratio precision of about 2 parts in 10^4 for O_2 [*Hughes et al.*, 1968] and 1 part in 10^3 for CO_2 [*Pales and Keeling*, 1965], corresponding to 40 and 0.3 ppm atmospheric concentration uncertainty, respectively. These measurements compare the mole percentage of O_2 and CO_2 in the atmosphere with primary standards of O_2 in N_2 and CO_2 in N_2 mixed on the basis of volume ratios. New mixed standards based on weight ratios are being prepared. Comparison with the atmosphere and interpolation between standards are performed by means of a magnetic susceptibility measurement for O_2 and a nondispersive infrared absorption measurement for CO_2. Although these measurements are highly developed and carefully applied, some inherent limitations exist. The use of a standard mixture is based on the assumption that the composition will remain fixed over a period of years; however, informal reports indicate that CO_2 standards at Scripps Institute and Stockholm have drifted 3.5 ppm apart in recent years. To compare atmospheric and standard samples accurately, pressure ratios between the two mixtures must be measured to at least the accuracy desired in the O_2/N_2 ratio.

Results from the commercial Beckman E2 magnetic susceptibility oxygen analyzer are reproducible to 30 ppm under ideal conditions [*Beckman Instruments*, 1969]; the analyzer sets the limit of precision on determination of O_2 atmospheric concentration by the present

Copyright © 1970 by the American Geophysical Union.

method. The pollutant NO, which is almost one-half as paramagnetic as O_2, must be recognized as an interferer in high-precision work. Results from the nondispersive infrared carbon dioxide analyzer [*Smith,* 1953] are practically reproducible to about 0.5 ppm [*Keeling et al.*, 1965] if the atmospheric sample is carefully dried. Nonresonant N_2-N_2 collision-induced absorption, peaking at about 4.3 μ [*Shapiro and Gush,* 1966], is a previously unrecognized and perhaps important interferer in this measurement and must be considered.

Other methods of analysis such as mass spectrometry for CO_2 [*Hughes and Dorko,* 1968] and gravimetric determination after alkali metal reaction for O_2 [*Hughes,* 1968] are good to at best 0.1 mole % and are not suitable for highly precise atmospheric measurements.

A method of precise analysis that is highly applicable to the oxygen balance problem involves the study of Raman scattering. Raman spectroscopy has become a practical method for gaseous analysis both in the field and in the laboratory, following the increased flexibility and sensitivity provided by laser sources [*Porto et al.*, 1966; *Leonard,* 1967; *Cooney,* 1968].

The purpose of this paper is to report recent quantitative results on Raman spectra of N_2, O_2, and CO_2 taken under experimental conditions similar to those suited to a precise measurement of $O_2/CO_2/N_2$ ratios in the atmosphere. Figure 1 shows the strongest lines of the vibrational spectra of N_2, O_2, and CO_2 obtained from an air sample in the laboratory under ambient atmospheric conditions. The detection system was an uncooled Bendix 754 photomultiplier. An Ar^+ laser with 1-watt output at 20,489 cm^{-1} (4880 A) was focused into the scattering volume by a 5-cm focal length lens. A Spex 1401 spectrometer was used with 500-μ slits ($\approx$10-cm^{-1} resolution).

The significant feature of these traces is the peak count rates of approximately 10^4 counts/sec for N_2, 4×10^3 counts/sec for O_2, and 10 counts/sec for CO_2 per incident watt. If the principle source of inaccuracy in measuring O_2 density is shot noise, as is achievable in a properly designed ratio system, an accuracy of 1 part in 10^6 in the O_2/N_2 ratio, for example, would require recording 10^{12} O_2 counts.

Extrapolating from the results quoted above, we note that a power level of 100 watts is avail-

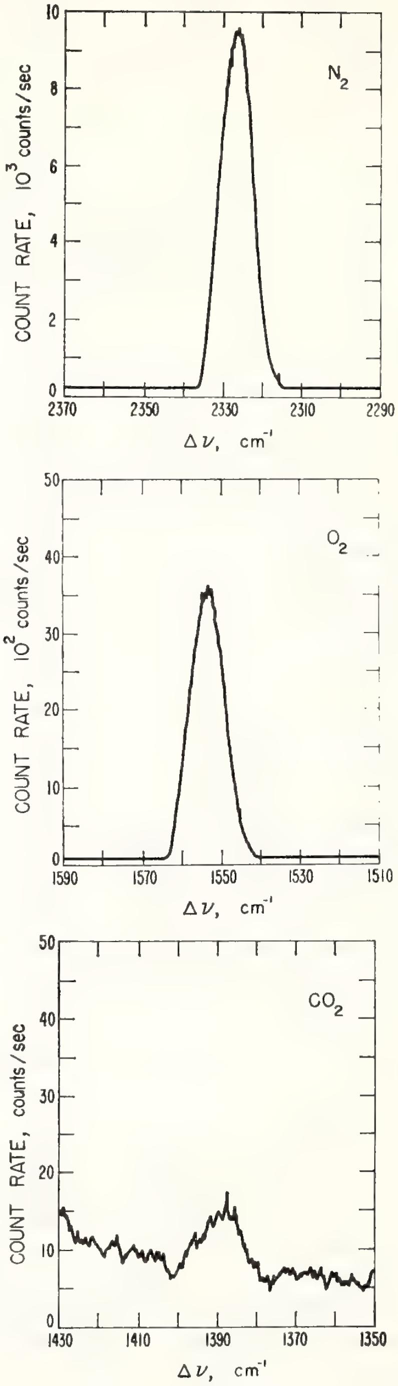

Fig. 1. Vibrational Raman spectra of N_2 (*top*), O_2 (*middle*), and CO_2 (*bottom*) with wave number shift measured from the laser line at 20,489 cm^{-1} (in air). Laser power 1 watt; instrumental bandwidth 10 cm^{-1}; station pressure 628 torrs; time constant 0.5 sec (*top* and *middle*) and 10 sec (*bottom*).

able inside the resonant cavity of current Ar^+ lasers. A factor of 2 in spectrometer transmission and a factor of 2 in scattered photon collection efficiency are conservatively available over the experimental apparatus used for the reported traces. From these extrapolations and our data, 10^{12} counts for O_2 would require an integration time of 6.25×10^5 sec, or approximately 7.2 days. The same integration time would result in the accumulation of 2.5×10^9 counts for CO_2 and 2.5×10^{12} counts for the N_2 reference. Thus the O_2/N_2 ratio would have a precision of 1.6 parts in 10^6 and the CO_2/N_2 ratio a precision of 2 parts in 10^5. In terms of atmospheric concentration, the expected precision is within 0.3 ppm for O_2 and 0.006 ppm for CO_2.

The precision of a Raman scattering analyzer is two orders of magnitude greater than the precision of present comparison techniques. The sensitivity of the proposed system may also be compared with annual variations in CO_2 concentration of 10 ppm and a long-term increase thought to be 0.7 ppm/year [*Pales and Keeling*, 1965]. Analogous long-term variations in O_2 concentration have not been observed with the apparatus now being used. The advantage, in principle, of the Raman technique is obvious.

In practice, count rates larger than the values extrapolated for present lasers are possible from higher-power lasers now being developed and from multiline laser operation. Integration times of the order of a few days are reasonable in terms of the oxygen balance problem and will eliminate the question of when discrete samples should be taken during the diurnal cycle [*Bischof*, 1960]. By recording count totals at frequent intervals, concentration data can be processed to yield both moderately precise information on short-term atmospheric variations and highly precise figures for long-term concentration changes averaged over larger seasonal differences.

The Raman measuring method could be implemented by a polychromator with multiple photomultipliers. Variations in atmospheric pressure, laser intensity, and optical alignment have no effect on O_2/N_2 and CO_2/N_2 ratios. Systematic uncertainties are reduced to small perturbations due to possible differential thermal effects on Raman cross sections of the molecules of interest and to differential changes in photocathode spectral quantum efficiency. Thermal cross-section effects, if present, can be eliminated by adjusting sample air temperature. Photocathode changes may be reduced by proper aging. By measuring the Raman intensity of the 918-, 2249-, and 2942-cm^{-1} lines of the CH_3 CN molecule [*Schrötter and Bernstein*, 1964] to 10^{12} counts, any relative change in detector quantum efficiency can be determined and possibly corrected for. This spectral reference gas is monomolecular, and so spectral intensities depend only on transition probabilities, in contrast to methods using a mixture of gases as a primary standard. Similarly, by photon counting and digital processing, inaccuracies due to photomultiplier and amplifier gain, zero drift, leakage currents, and limited dynamic range are eliminated. Since Raman energy shifts are discrete and sharply defined, the atmospheric spectrum is remarkably free of interference, in contrast to the methods discussed earlier. The underlying assumption in measuring ratios is that the amount of N_2 in the atmosphere is constant on a scale in which O_2 and CO_2 are presumed to vary. Present methods based on a mixed-gas standard utilize the same assumption.

From these results, we conclude that highly accurate measurements of O_2/N_2 and CO_2/N_2 ratios in the atmosphere are possible with current Raman spectroscopic techniques. The inherent advantage of the Raman scattering method in avoiding the interfering background signals by means of optical frequency selection and the wide separation between Raman-shifted frequencies of atmospheric constituents must be emphasized. A suitable number of alternate or simultaneous measurements of less than 10 days' duration each, over the continental shelf and over inland areas, should allow a definitive study of the atmospheric oxygen balance by means of quantitative Raman spectroscopy.

Acknowledgment. This research was conducted under an NRC-ESSA Postdoctoral Research Associateship (R.L.S.).

REFERENCES

Beckman Instruments, Inc., Beckman laboratory oxygen analyzers, *Bulletin 7159*, 1969.

Berkner, L. V., and L. C. Marshall, On the origin and rise of oxygen concentration in the earth's atmosphere, *J. Atmos. Sci.*, *22*, 225–261, 1965.

Bischof, W., Periodical variations of the atmospheric CO_2 content in Scandinavia, *Tellus*, *12*(2), 216–226, 1960.

Cooney, J. A., Measurements on the Raman component of laser atmospheric backscatter, *Appl. Phys. Lett., 12,* 40–42, 1968.

Hughes, E. E., A simple technique for the absolute determination of atmospheric oxygen, *Environmental Sci. Technol., 2,* 201–203, 1968.

Hughes, E. E., and W. D. Dorko, Direct mass spectrometric determination of atmospheric carbon dioxide, *Anal. Chem., 40,* 866–869, 1968.

Hughes, E. E., W. D. Dorko, and J. M. Ives, Microchemical analysis section: Summary of activities, *NBS Tech. Note 455,* 15–18, Oct. 1968.

Keeling, C. D., N. W. Rakestraw, and L. S. Waterman, Carbon dioxide in surface waters of the Pacific Ocean, 1, Measurements of the distribution, *J. Geophys. Res., 70,* 6087–6097, 1965.

Leonard, D. A., Observation of Raman scattering from the atmosphere using a pulsed nitrogen ultraviolet laser, *Nature, 216,* 142–143, 1967.

Pales, J. C., and C. D. Keeling, The concentration of atmospheric carbon dioxide in Hawaii, *J. Geophys. Res., 70,* 6053–6076, 1965.

Porto, S. P. S., L. E. Cheesman, A. Weber, and J. J. Barrett, Photoelectric recording of laser-excited Raman spectra of gases, *J. Opt. Soc. Amer., 56,* 551, 1966.

Schrötter, H. W., and H. J. Bernstein, Intensity in the Raman effect, *J. Mol. Spectrosc., 12,* 1, 1964.

Shapiro, M. M., and H. P. Gush, The collision-induced fundamental and first overtone bands of oxygen and nitrogen, *Can. J. Phys., 44,* 949–963, 1966.

Smith, V. N., A recording infrared analyzer, *Instruments, 26,* 421–427, 1953.

(Received October 7, 1969;
revised December 15, 1969.)

Reprinted from Proceedings of Workshops on Research Problems in Air and Water Pollution, August 3-15, 1970, University of Colorado, 309-321, 1971.

RESEARCH PROBLEMS IN THE USE OF LIDAR IN ANTI-POLLUTION STUDIES

V. E. Derr
ESSA Research Laboratories
Boulder, Colorado

Introduction

The purpose of this workshop is to present discussions of the research problems remaining in the understanding, measurement and control of air and water pollution. These research problems can then be studied where appropriate knowledge and facilities exist.

One of the earliest uses of lidar was in the determination of the presence of aerosols, but it also has direct application to the specific task of remote detection and measurement of gaseous pollutants when Raman scattering and fluorescence are employed. These radiative interactions produce an output at a frequency that differs from the irradiating frequency. The frequency of the scattered radiation is usually uniquely related to the scattering molecule, allowing identification. Thus lidar can be used in the remote measurement of water profiles by Raman scattering, and also in the remote measurement of wind profiles by the use of Mie scattering. Wind and water vapor profiles are important in the prediction of weather conditions leading to pollution trapping or dissemination conditions. The use of lidar in the measurement of aerosols, smoke stack constituents, humidity profiles, and wind velocities will be discussed, and the limitations of present systems that are potentially removable through research will be pointed out. More detailed consideration of the use of lasers may be found in references 1, 2, and 3, with extensive literature references in reference 1.

Use of lidar in aerosol determination and wind sensing

Atmospheric aerosols scatter laser radiation so strongly that the location of aerosol layers is only prevented when the attenuation due to atmospheric loading is very high. Indeed aerosols have been detected above 90 km by lidar. However important limitations occur in the interpretation of lidar signals from aerosols since the information received is usually not sufficient to allow the determination of an unknown distribution of sizes and shapes by solution of the radar equation. Since the product of the backscattering coefficient and the attenuation factor occur in the system equation (Reference 1) they cannot be separately determined by examining the Mie scattering alone, at a single frequency.

Two additional pieces of information aid in distinguishing between molecular and aerosol scattering, the specifically molecular information inherent in Raman scattering, and the Doppler spectrum of the on-frequency backscattering. The latter method depends on the difference in the Doppler spectrum of air molecules and the much heavier and, on the average, slower, aerosol particles. With this information, the knowledge of the presence and opacity of atmospheric aerosol layers can be supplemented by further details of the nature of the aerosols, reducing the requirements on the specifications of the atmosphere model, although it appears that some limitations on the possible aerosol constitution will always have to be assumed. In practice, this is probably not a serious limitation since aerosols are very frequently of known origin, and their distributions are often known by prior observation within broad limits.

In the real atmosphere, passive additives that are carried along by the prevailing wind are inhomogeneous. To the extent that the structure of the turbulent eddies persists as they travel with the wind, they can be observed at two points separated by a known distance. Even in strong mixing conditions, the eddy structure remains recognizable over useful distances. Thus, by a pattern recognition process, such as cross correlation, we can compare the signals at two points in the wind stream, determining velocity from the passage time of eddies (Reference 1).

Active and passive correlation methods have been effective in wind tunnels. Passive methods have been used in the field, but their signal-to-noise ratio is unfavorable (Reference 3). Active wind sensing methods using lasers to illuminate the atmosphere have been used by V.E. Derr and R.G. Strauch at ESSA Research Laboratories. Fig. 1 shows a simple scheme used to test the method. (It is too cumbersome to use in practice, since the wind direction changes frequently.) A coaxial transmitter and receiver (or closely coupled parallel axes) may be used as in Fig.2. The beam is conically scanned at so rapid a rate that no turbulence crosses the cone unilluminated, and with sufficiently high pulse repetition frequency that the turbulent spectra is sampled. The cone may be divided into elements and cross correlation between elements may be used to detect the drift of turbulence across the cone, while the height is determined by ranging. The data rate is high and would require special purpose data processing equipment, especially if off-frequency backscattering is also examined by a scanning monochromator. (The later device would allow the simultaneous determination of water vapor profiles by Raman backscattering as described below.)

Fig. 1 shows a typical output of two laser illuminated cells of the atmosphere examined by two telescopes. The output of receiver B is delayed by an average of one second with respect to receiver A. Parts of the record require a cross correlation analysis to determine wind speed, but large fluctuations which allow determination of wind velocity from visual examination of the record occur with great frequency when the wind is steady. The record above was taken under light, variable wind conditions, from 0 to 10 mph in the configuration shown in Fig. 1.

Research areas in aerosol and wind determination

The determination of the presence of aerosols is easily done by present lidar systems to great altitudes. The major problems remaining are the determination of size and shape distributions and the determination of composition by remote means. Better statistics of atmospheric aerosol composition are required in order to set limitations on possible distributions in nature. The size and shape distribution can be partially determined by the scattered signal amplitude recorded as a function of frequency; thus the development of lasers tunable over wide frequency ranges is important. The most likely approaches appear to be in dye lasers and in parametric devices.

Thus far, insufficient attention has been given to the depolarization effects of Mie particles and both theoretical and experimental investigations are needed here. The composition can be obtained only by off-frequency backscattering and probably only by either Raman scattering or fluorescence. The field of shifted frequency scattering from aerosols has not received very much attention and may be very fruitful. It has been noted by researchers that an ultraviolet laser does produce strong fluorescence in some dust particles and not in others; also some insects are observed to fluoresce strongly.

Further, the use of Doppler lidar methods for wind measurement should be explored. These have been used at short ranges. They require the development of highly stable, high power lasers, but may be eventually the best method of wind velocity measurement. The Doppler method is limited to the measurement of radial components while correlation methods measure transverse components.

Raman and fluorescent scattering in laser ranging

In addition to the radiation scattered by atmospheric constituents at the frequency of the lidar transmitter, frequency-displaced signals are also received, either from Raman scattering or fluorescence. As mentioned above, the spectral frequency of the Raman or fluorescence signal is specific to the molecules interacting with the lidar radiation and is a means of identification, unlike Rayleigh or Mie scattering. Specific cases of Raman scattering by atmospheric constituents are summarized in Fig. 3. The number of signal photons received is shown as a function of range. Sky background noise appears on the same ordinate scale. The rms values of the sky noise are the most significant, in the absence of saturation, since the average level can be suppressed. The right side shows the detector dark noise from some selected photomultiplers. The graph can be used to determine the SNR of any gas with the same backscattering cross section as N_2 by reference to the ppm curves. The graph has been computed for one pulse; the lidar is capable of 100 pulses per second. Integration times of several hundred seconds are not unreasonable in applications. The transmitter characteristics shown are those of a commercially available pulsed nitrogen laser; the receiver has very modest dimensions, and could be improved. The cross sections listed are estimated for the graph and should not be construed as accurate to closer than an order of magnitude.

Water vapor in the atmosphere has been detected and a humidity profile determined to several thousand meters with ruby laser systems by a few minutes integration, and this could also be done with the system described above. With such a system only short ranges may be achieved in daylight because of the sky background. Of course the receiver may be improved by a larger collector; this helps only a little since when background limited, the increase in signal is partially offset. The increase in SNR would be a factor of the square root of the collector area increase, or by the increase in linear dimensions. A significant increase in SNR could be obtained by operating in the spectral region below 2900 Å, where the strong solar absorption by stratospheric ozone lowers the background noise to a level below that of the best detectors. At short range, pollutants such as SO_2 have been detected by Raman lidar, as well as impurities in water.

Research areas in Raman and fluorscent lidar

The use of backscattered off-frequency radiation has important potential uses in remote identification of atmospheric, oceanic and terrestrial constituents, in the study of atmospheric statistics, in cloud height and wind velocity measurement and in precise measurement of the ratios of atmospheric constituents[2]. Some of these, such as the measurement of humidity profiles, have essentially been proven. The extension of the method to other problems depends very strongly on the results in achieved in research areas relating to the components, and the basic spectroscopic properties of the atmosphere.

For tropospheric use, transmitters in the ultraviolet below 2900 Å would be preferable because the intensity of Raman scattering is generally proportional to the fourth power of the frequency of the irradiating source, and solar background noise is largely eliminated by the strong absorption by ozone in the upper atmosphere. The wavelength chosen must be short of the oxygen absorption beginning at 1800 Å. The development of suitable lasers in the 2000 Å to 2900 Å range would have important consequences in pollution measurement.

At this time field-worthy laser transmitters below 2900 Å are unavailable. The closest to realization is the quadrupled neodymium laser near 2650 Å, but the efficiency is low and the adjustment is tedious. Ideally, a tunable pulsed laser below 2900 Å with 10^6W peak power, 10 ns pulse width, and 1000 pulses per second, could perform most of the tasks outlined above; no such equipment is in the field at present. Probably pulsed gas lasers offer the most likely future possibility. An additional important factor in a laser transmitter is the brightness of beam divergence. Indeed the greatest single source of loss in lidar systems is usually found in the mismatch of transmitter and receiver apertures. Greater brightness is always an advantage; a beam with no greater divergence than 2 mr is a good design goal. Finally, the laser output should be free of fluorescence or any radiation other than the laser output.

The optics of the receiver must be treated for high reflectivity (mirrors) or transmission (lenses) in the ultraviolet. The techniques of interference filters could be applied here. There is an additional problem observed by workers in the field, - almost everything fluoresces under short ultraviolet radiation. Lenses, filters, windows, the dust of the atmosphere, black paint and water droplets all fluoresce. At present very pure quartz is one of the few materials which can be used. The problem can be alleviated by a judicious placement of the components of the optical train, but new non-fluorescing materials of optical quality would be very welcome. It has been observed that some plastics fluoresce much less than other materials and purification of them might be profitable.

The use of wavelengths below 2900 Å requires a careful measurement of the attenuation coefficient of the atmosphere in the wavelength range 2000-3000 Å and a distance up to 10 km. Further, more exact measurements of solar absorption in this part of the spectrum are necessary in order to determine system range capability.

Until recently, the manufacturers of photomultipliers have paid very little attention to the needs of lidar systems; the principal developments in phototubes have accommodated the nuclear scintillation counting art. Phototubes of higher quantum efficiency, solar blind, with high gain and rise times of a few nanoseconds are needed. The cathode should be solid, for high efficiency, the envelope should be of ultraviolet transmitting material, and the gain should be at least 10^8. The tube should be end-on so that a low silhouette can be obtained in use at the Coudé focus. The tube base should be left off so resistors and a small transistorized preamplifier can be soldered directly to the leads. The effective sensitive area should not be less than an inch in diameter to prevent vignetting the field. The dark count, uncooled, should not be more than 100 per second.

Although improvements in system components can be expected to increase the effectiveness of lidar in pollution measurement, it will probably be limited to lower atmospheric uses for constituents with the presently known cross sections. Even the use of the highest lidar frequency available will not substantially change this estimate. It is necessary to examine to what extent we may hope for larger cross sections. Aside from the fourth power frequency dependence of cross sections, there is a dependence on resonance denominators.

The intensity of Raman lines, when the molecule makes a transition from state m to state n, is given by

$$I = \frac{2^7 \pi^5}{3^2 c^4} I_0 (\nu_o - |\nu_{mn}|)^4 \sum_{\rho\sigma} |\alpha_{\rho\sigma,mn}|^2 ,$$

where $\alpha_{\rho\sigma,mn}$ is the $\rho\sigma$(=X,Y,Z) component of the scattering dyadic

$$\alpha_{mn} = \frac{1}{h} \sum_r \frac{\vec{\mu}_{rn} \vec{\mu}_{mr}}{\nu_{rm} - \nu_o + i\gamma_r} + \frac{\vec{\mu}_{mr} \vec{\mu}_{rn}}{\nu_{rn} + \nu_o + i\gamma_r} .$$

Here c is the velocity of light, h is Planck's constant, I_0 is the incident plane-polarized intensity of frequency ν_0, r is an intermediate state, and $\vec{\mu}_{rn}$ and $\vec{\mu}_{mr}$ are the transition moments of the dipole moment operator μ, and γ_r is the damping constant of state r. When the denominators of α are not small, it can be seen that the intensity varies as the fourth power of the output frequency, making higher frequency lasers advantageous.

When the incident radiation is at a frequency close to any of the transition frequencies, ν_{rm}, the scattered intensity can be greatly increased. Although few experiments have been performed on gases, other than alkali metal vapors, experiments on liquids have indicated several orders of magnitude increase in intensity for resonance Raman scattering. If such increases could be obtained in gases or aerosols the range-sensitivity product of lidars could be greatly increased and their utility in pollutant measurement and atmospheric studies magnified. The problem of the nature of the transition in resonance effects must be examined to determine whether the process remains essentially one of scattering or becomes more like a fluorescence. In the latter case, at atmospheric pressure, the effect would be at least partially quenched by collisions and the intensity increase could only be found high in the atmosphere.

Conclusions

Lidar is presently a useful device at short ranges for pollutant measurement, humidity profile determination and wind sensing. The optimization that can be achieved by research on the problems listed above will probably extend its useful range to the whole troposphere, and to greater distances if resonance effects can be found.

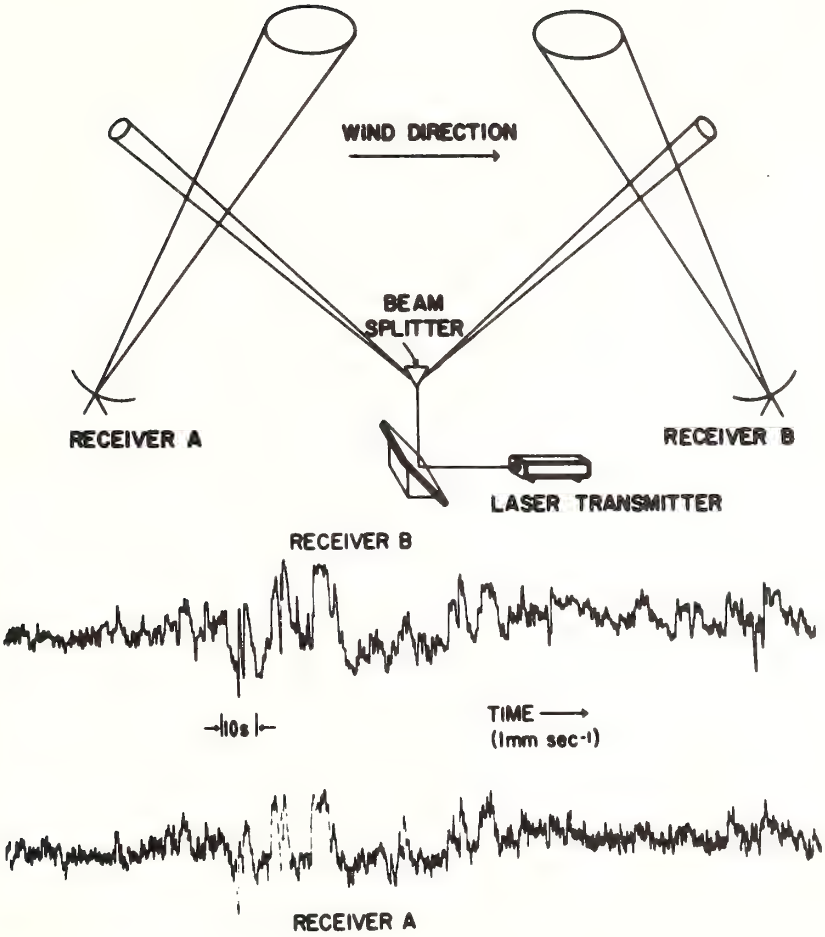
WIND DIRECTION
BEAM SPLITTER
RECEIVER A
RECEIVER B
LASER TRANSMITTER
RECEIVER B
10s
TIME
(1mm sec-1)
RECEIVER A

Figure 1

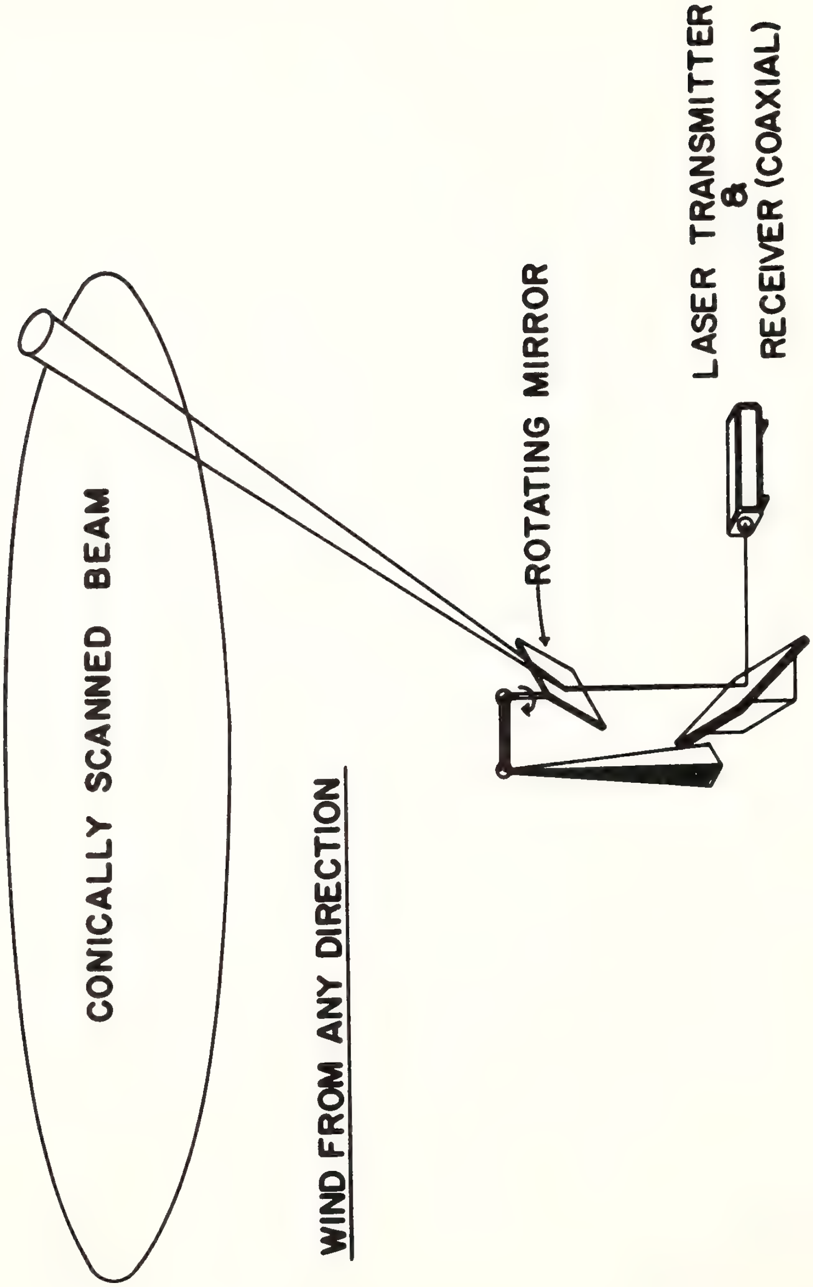
CONICALLY SCANNED BEAM
WIND FROM ANY DIRECTION
ROTATING MIRROR
LASER TRANSMITTER & RECEIVER (COAXIAL)

Figure 2

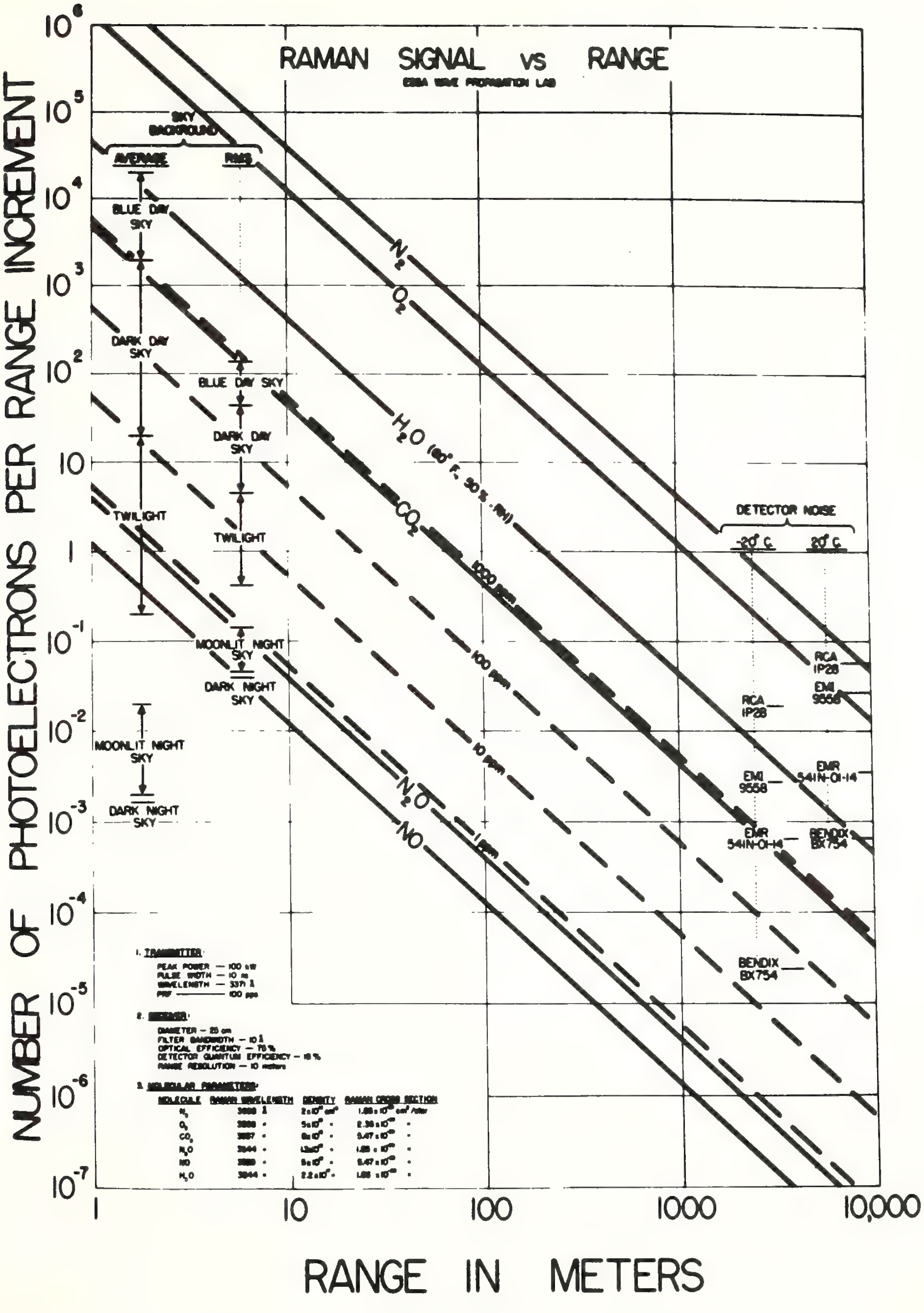
RAMAN SIGNAL vs RANGE
NUMBER OF PHOTOELECTRONS PER RANGE INCREMENT
RANGE IN METERS
10^6
10^5
10^4
10^3
10^2
10
1
10^{-1}
10^{-2}
10^{-3}
10^{-4}
10^{-5}
10^{-6}
10^{-7}
1
10
100
1000
10,000
SKY BACKGROUND
AVERAGE
RMS
BLUE DAY SKY
DARK DAY SKY
TWILIGHT
MOONLIT NIGHT SKY
DARK NIGHT SKY
N_2
O_2
H_2O (60° F, 30 % RH)
CO_2
1000 ppm
100 ppm
10 ppm
1 ppm
N_2O
NO
DETECTOR NOISE
-20° C
20° C
RCA IP28
EMI 9558
EMR 541N-01-14
BENDIX BX754
1. TRANSMITTER
PULSE WIDTH — 10 ns
WAVELENGTH — 3371 Å
2. RECEIVER
FILTER BANDWIDTH — 10 Å
DETECTOR QUANTUM EFFICIENCY
RANGE RESOLUTION — 10 meters
3. MOLECULAR PARAMETERS
MOLECULE
RAMAN WAVELENGTH
DENSITY
RAMAN CROSS SECTION
N_2
O_2
CO_2
N_2O
NO
H_2O

Figure 3

LEGEND

FIGURES

1. Wind velocity measurement configuration and typical signals
2. Conical scan configuration for wind sensing
3. Raman signal vs. range

REFERENCES

1. Derr, V.E. and C.G. Little, "A comparison of remote sensing of the clear atmosphere by optical, radio and acoustic radar techniques," Appl. Opt. 9, 1976, (Sept. 1970).

2. Schwiesow, R.L. and V.E. Derr, "A Raman scattering method for precise measurement of atmospheric oxygen balance," J. Geophys. Res., 75, No. 9, 1629, (March 20, 1970).

3. Krause, F.R., V.E. Derr, et al., "Remote probing of wind and turbulence through cross-correlation of passive signals," Proc. of the Sixth International Symposium on Remote Sensing of the Environment, Vol II, 327, (Oct. 1969).

Reprinted from Proceedings of Air Pollution, Turbulence and Diffusion Symposium, December 7-9, 1971, New Mexico State University, 93-99, 1971.

THE SIZE SPECTRUM DETERMINATION OF SPHERICAL AEROSOLS BY LIGHT SCATTERING
PART I: METHOD

Ariel Cohen
Wave Propagation Laboratory
Environmental Research Laboratories
National Oceanic and Atmospheric Administration
Boulder, Colorado 80302

INTRODUCTION

The scattering functions for spherical particles with size parameters $\alpha = 2\pi r/\lambda \gtrsim 1$ are given by the Mie theory.(1,2) The theory shows that unless the scattering medium is composed of mono-dispersed particles, the fluctuation of the scattering intensities with the variation of either the incident wavelength or with the radius of the particles cannot be easily predicted.(3) The usual method to overcome this difficulty is to assume an experimentally-based size spectrum function (such as the Junge distribution) with, normally, two parameters.(4) These parameters are then calculated from the behavior of the scattering or the extinction of light as a function of wavelength by the examined particles.(5) Polarization properties of the scattered light as compared with the degree of polarization of the incident light can also be used for the size spectrum definition but their use requires certain assumptions, among others - the number densities - and usually does not have a unique solution.(6)

In this article a method will be described for the determination of the size spectrum of spherical particles with a distribution of indices of refraction, which are present in an atmospheric volume containing aerosol particles (possibly both spherical and unspherical) of unknown nature *a priori* based on the properties of the scattering intensity as a function of α. The method does not require any assumption on the size spectrum function, nor does it demand any knowledge of the type (refractive index) of the scattering spheres.

Method

The scattering intensity of unpolarized light by a spherical particle having a size parameter $\alpha = 2\pi r/\lambda$ and a known index of refraction $n = f(\lambda)$ can be calculated by the use of Mie scattering functions.(2) For this calculation, the polarized component ($I_{||}$) of the scattered light at $\theta = 90°$ by a water droplet normal to the scattering plane, was chosen as an example (see Figure 1). In Table I a series of α_i values is given for which $I_{||,i}$ have maximal values. A corresponding series of α_i values for which $I_{||,i}$, have minimal values can also be given (13 pairs of minimal and maximal values are given in Table II).

Let us now assume that the relative number densities ($\rho_1^{(n)}$; $\rho_2^{(n)}$) of spherical particles having radii r_1;r_2 and refractive index n (out of many other particles) may be defined by measuring the dependence of $I_{||}$ ($\theta = 90°$) on λ (wavelength). The method suggested here is as follows: each $\alpha_i^{(n)}$ determines two values $\lambda_i^{(n)}(r_1)$; $\lambda_i^{(n)}(r_2)$, for the above mentioned spheres:

$$\lambda_i^{(n)}(r_1) = 2\pi r_1/\alpha_i^{(n)};\ \lambda_i^{(n)}(r_2) = 2\pi r_2/\alpha_i^{(n)}$$

We now measure the scattering intensities of the sample as a continuous function of wavelength, and, thus for each of the above calculated $\lambda_i^{(n)}$, the measured intensity $I_{||}^{(n)}(\lambda_i^{(n)}[r])$ is found. (In this work, the measured intensities are divided by λ_i^2, see Example.)

If we define:

$$A_n(r) = \sum_{i=1}^{N} I_{\parallel}^{(n)}(\lambda_i^{(n)}(r)) - \sum_{i=1}^{N} I_{\parallel}^{(n)}(\lambda_i'^{(n)}(r)) \qquad (1)$$

$$A_n(r_1) = \sum I_{\parallel}^{(n)}(\lambda_i^{(n)}(r_1)) - \sum I_{\parallel}^{(n)}(\lambda_i'^{(n)}(r_1)) \qquad (1a)$$

$$A_n(r_2) = \sum I_{\parallel}^{(n)}(\lambda_i^{(n)}(r_2)) - \sum I_{\parallel}^{(n)}(\lambda_i'^{(n)}(r_2)) \qquad (1b)$$

(where N is the chosen number of the $\alpha_i^{(n)}$ and $\alpha_i'^{(n)}$ values* for which the theoretical $I_{||}(\alpha)$ have maximum [and minimum] values), then $A_n(r_1)/A_n(r_2) = \rho_1^{(n)}/\rho_2^{(n)}$ with an increased accuracy with the increasing of N. The function $A_n(r)$ is therefore, proportional to the size spectrum of the particles with refractive index n, acting as a filter with 100 percent transmission for one particle and almost zero percent transmission for any other particle.

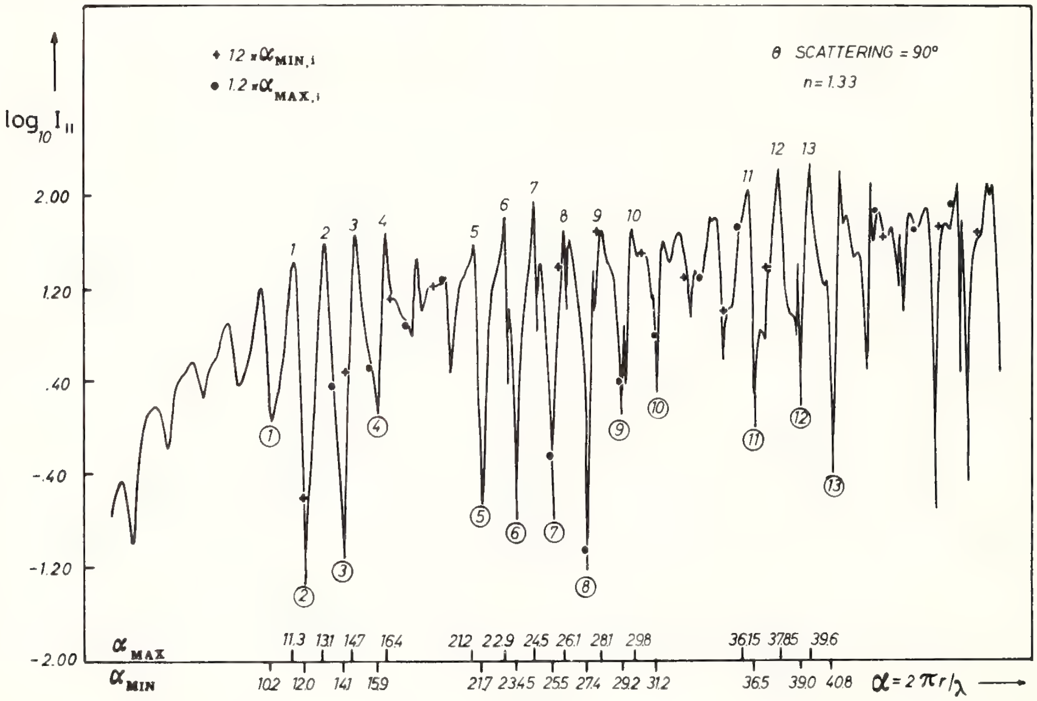

Fig. 1. Computer plotting of $\log_{10} I_{||}$ ($I_{||}$ = the polarized light, normal to the scattering plane), as a function of α. The α for 13 of the maximum values of $I_{||}$ are noted on the abcissa. Dots and plus signs on the graph correspond to the above α values multiplied by 1.2. It can be seen that their ordinate values are "random" with respect to the maxima and minima of the curve.

To prove this assertion, one has to check the contribution of any other particle in the two summations appearing in the definition of $A_n(r)$ (Equation 1) and to show that it can be approached to zero. For example, the contribution of the particles having radius r_2 in Equation 1a, depends on the $\alpha_i^{(n)}(r_2)$ values corresponding to the $\lambda_i^{(n)}(r_1)$ and $\lambda_i'^{(n)}(r_1)$:

---

*Within a range defined by the measuring system, i.e. if the measurements can be made only in the visible range, the α_i values are limited: $2\pi r_j/0.7 \leq \alpha_i \leq 2\pi r_j/0.4$ (r_j is the radius of the sphere, the number density of which is to be defined).

$$\alpha_i^{(n)}(r_2) = 2\pi r_2/\lambda_i^{(n)}(r_1) = (r_2/r_1) \times \alpha_{\mathrm{MAX},i}^{(n)} \tag{2a}$$

$$\alpha_i'^{(n)}(r_2) = (r_2/r_1) \times \alpha_{\mathrm{MIN},i}'^{(n)} \tag{2b}$$

It can be seen from Table I, that the ratio $\alpha_{i,\mathrm{MAX}}^{(n)}/\alpha_{i+1,\mathrm{MAX}}^{(n)}$ is not constant. Nor is the ratio of $\alpha_{i,\mathrm{MAX}}^{(n)}/\alpha_{i+j,\mathrm{MAX}}^{(n)}$, for any j.

It follows that the particles with radii r_2 contribute to the first summation of Equation 1a, practically random values in respect to the appearance of maxima and minima in Figure 1. Since the same effect of "randomization" appears in the second summation in Equation 1a, the submmations** for the r_2 particles can be approached to the same value

$$A_n(r_1) = \underbrace{\sum_i I_{\parallel,r_1}^{(n)}(\lambda_i(r_1)) - \sum_i I_{\parallel,r_1}^{(n)}(\lambda_i'(r_1))}_{\text{Contribution of particle having radius } r_1} + \underbrace{\sum_i I_{\parallel,r_2}^{(n)}(\lambda_i(r_1)) - \sum_i I_{\parallel,r_2}^{(n)}(\lambda_i'(r_1))}_{\text{Contribution of particle having radius } r_2} \tag{3}$$

$$\cong \sum_i I_{\parallel,r_1}^{(n)}(\lambda_i(r_1)) - \sum_i I_{\parallel,r_1}^{(n)}(\lambda_i'(r_1)) \underset{\mathrm{Df}}{=} \Sigma_{\mathrm{MAX},r_1} - \Sigma_{\mathrm{MIN},r_1}$$

(see example, Section III). In the case that N (- the number of maxima and minima values), derived from Figure 1, is not sufficient in order to achieve a desired accuracy, this number can be approximately doubled by repeating the experiment at a different scattering angle or at a different polarization angle; or even by extinction measurements.

Now:

$$\Sigma_{\mathrm{MAX},r_1} - \Sigma_{\mathrm{MIN},r_1} = V \times \rho_1 \times (\Sigma_{\mathrm{MAX},r_1} - \Sigma_{\mathrm{MIN},r_1})_{\text{per one particle}} \tag{4}$$

where V is the scattering volume.

Also, we surely have:

$$(\Sigma_{\mathrm{MAX},r_1} - \Sigma_{\mathrm{MIN},r_1})_{\text{per one particle}} = F \times \sum_i (I_{\parallel}(\alpha_{\mathrm{MAX},i}) - I_{\parallel}(\alpha_{\mathrm{MIN},i})) \underset{\mathrm{Df}}{=} F \times \Sigma = F \times \text{Constant} \tag{5}$$

where $I_{\parallel}(\alpha)$ is the theoretical (relative) Mie scattering intensity and F is a factor of the specific experimental system for rationalizing the units of intensity.

By elimination between (4) and (5), and substitution into (3), we get:

$$A_n(r_1) = V \times \rho_i \times F \times \Sigma \Rightarrow \rho_1 = A_n(r_1)/(V \times F \times \Sigma) \tag{6}$$

or dropping the index 1, we get

$$\rho_r = A_n(r)/(V \times F \times \Sigma) \tag{6a}$$

If the incident light intensity I_0, is a function of the wavelength so that $I_0 = \int_0^\infty f(\lambda)d\lambda$ one would have to weigh the $I_{\parallel}^{(n)}(\lambda)$ values (appearing in Equation 1) by the factors $f(\lambda)$

Example

To illustrate the method, let us assume that we have a sample of molecular air containing spherical water particles of only two sizes $r_1 = 2.0$ μm and $r_2 = 2.4$ μm. In Table III, the

---

**Each recorded scattering intensity at a specific wavelength ($I_{\parallel}(\lambda_i)$) is the summation of the scattering intensities of the individual particles having radii r_1 and r_2:

$$A_n(r_k) = \sum_i \sum_j (I_{r_j}(\lambda_i) - I_{r_j}(\lambda_i'))$$

This example indicates that for a sample of water particles with the above mentioned sizes having a size distribution varying within one order of magnitude, 13 maxima and 13 minima are sufficient for determining the size distribution to a high degree of accuracy. When the size distribution covers a variation of more than one order of magnitude, the more maxima and minima values, the better precision is achieved.

$I_{||}(\alpha)$, with $\alpha_{MAX,i}$ and $\alpha_{MIN,i}$, were calculated on the CDC 6400 computer, at the Hebrew University of Jerusalem.

Conclusions

The method described above requires, in principle, only experimental facilities of recording (preferably, by means of a multi-channel recorder) scattering (or extinction) intensities as a function of wavelengths. It can be seen from Table III, that for water droplets with radii varying between 1.0 μm and 5.0 μm, the α_{MAX} and α_{MIN} values, given as an example in this work (Figure 1, Table II) correspond to wavelengths near and within the visual range. Since the experimental methods of wavelength-scanning are limited, it is suggested that other α_{MAX} and α_{MIN} values be selected (not appearing in Figure 1) rather than change the wavelength range for droplets with radii> 5.0 μm. The only requirement on the selection of these α values is that the Mie scattering intensities corresponding to the $\alpha_{MAX,i}$ or $\alpha_{MIN,i}$ should not vary by more than an order of magnitude (preferably much less).

(2.0 μm) $\lambda_{MAX,i}$ Å	11120	9590	8550	7660	5930	5490	5130	4820	4470	4220	3470	3320	3170
(2.4 μm) $\lambda_{MAX,i}$ Å	13340	11510	10260	9200	7110	6580	6160	5780	5370	5060	4160	3980	3810
(2.0 μm) $\lambda_{MIN,i}$ Å	12320	10470	8910	7900	5790	5360	4930	4590	4300	4030	3440	3220	3080
(2.4 μm) $\lambda_{MIN,i}$ Å	14780	12570	10700	9480	6950	6430	5910	5500	5160	4830	4130	3870	3700

Table III. Wavelengths used in the determination of the number densities of water droplets of radii 2.0 μm and 2.4 μm.

Note: Since any random size distribution may be devided into sets of two radii each (r_{i1},r_{i2}) so that $r_{i1}/r_{i2} = 1.2$, the respective λ values appearing above multiplied by the factor $(r_{i1}/2.4)$ can be used for the determination of the number densities of any random sample. In case of the available aparatus not covering the required range of λ values, see Conclusions.

The required accuracy in the definition of the scattering angle, for this purpose, was calculated to be within ± 0.2 degrees.

It would be well to note that since no theoretical limitations are imposed on the accuracy in calculating the values α_{MAX} and α_{MIN}, it is always possible to calculate these values to an accuracy compatible with the wavelength resolution of the experimental system.

corresponding λ_i and λ_i' values are listed for the calculation of $A(r_1)$ and $A(r_2)$, respectively. Since $I(\alpha = 2\pi r_1/\lambda_1)/\lambda_1^2 = I(\alpha = 2\pi r_2/\lambda_2)/\lambda_2^2$ when $r_1/\lambda_1 = r_2/\lambda_2$, the experimental values are assumed to be divided by λ^2 (see Figure 2a, b). This is done to permit the use of one set of $I = f(\alpha)$ values for all wavelengths and radii of particles. 13 maxima and 13 minima were chosen for both the calculation of $A(r_1)$ and $A(r_2)$; $A(r)$ was calculated for a single particle. It can be seen from Table II that the contribution of the particle with radius r_2(= 2.4 μm) in the value of $A(r_1 = 2.0\ \mu m)$ is less than two percent.

The same calculations for the contribution of the particle with radius r_1 (= 2.0 μm) in the value of $A(r_2 = 2.4\ \mu m)$ show that it is less than 1.3 percent.

The first contribution was calculated for

$$\alpha_i = \frac{2.4}{2.0}\alpha_{MAX,i} \ ; \ \alpha_i' = \frac{2.4}{2.0}\alpha_{MIN,i}' \ ,$$

and the second for

$$\alpha_i = \frac{2.0}{2.4}\alpha_{MAX,i} \ ; \ \alpha_i' = \frac{2.0}{2.4}\alpha_{MIN,i}' \ .$$

Figure 2a.

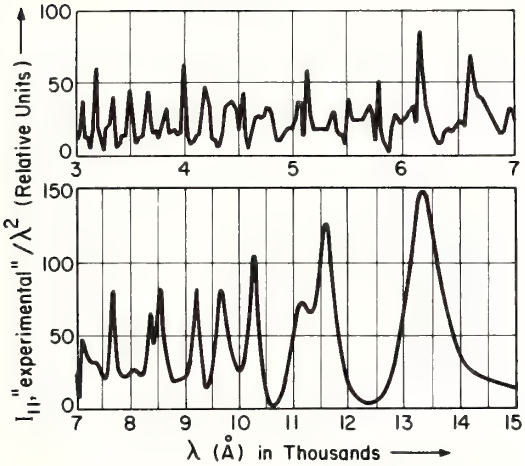

Figure 2. The expected 90° scattering intensities measured as a function of wavelength (3000 Å ≤ λ ≤ 15000 Å) of the component normal to the scattering plane, by a sample including water droplet particles having radii r_1 = 2.0 μm and r_2 = 2.4 μm (2a). In Figure 2b all "measured" values are multiplied by $(7000/\lambda)^2$.

Figure 2b.

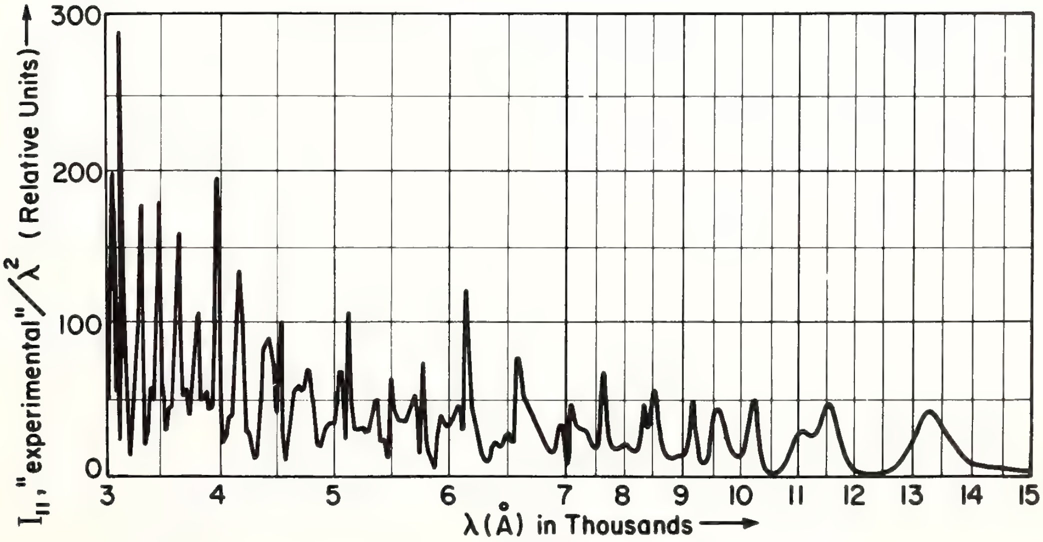

i	$\alpha_{MAX,i}$	Log $I_{\parallel}$	1.2 α	$1.2^{-1}\alpha$
1	2.0	-.456	2.4	1.7
2	3.8	.177	4.6	3.2
3	5.9	.599	7.1	4.9
4	7.8	.904	9.4	6.5
5	9.6	1.202	11.5	8.0
6	11.3	1.428	13.6	9.4
7	13.1*	1.583	15.7	10.9
8	14.7*	1.665	17.6	12.3
9	16.4*	1.673	19.7	13.7
10	18.1	1.467	21.7	15.1
11	18.8	1.219	22.6	15.7
12	19.6	1.296	23.5	16.3
13	21.2*	1.579	25.4	17.7
14	22.9*	1.844	27.5	19.1
15	23.1	1.026	27.7	19.3
16	24.5*	1.964	29.4	20.4
17	24.8	1.418	29.8	20.7
18	26.1*	1.794	31.3	21.8
19	26.4	1.631	31.7	22.0
20	27.7	1.362	33.2	23.1
21	28.1*	1.710	33.7	23.4
22	29.8*	1.702	35.8	24.8
23	30.5	1.532	36.6	25.4
24	31.0	1.140	37.2	25.8
25	31.5	1.601	37.8	26.3
26	32.4	1.675	38.9	27.0
27	33.2	1.345	39.8	27.7
28	34.1	1.818	40.9	28.4
29	34.4	1.798	41.3	28.7
30	36.2*	2.047	43.4	30.2
31	37.3	1.389	44.8	31.1
32	37.9*	2.224	45.5	31.6
33	38.9	1.396	46.7	32.4
34	39.6*	2.290	47.5	33.0
35	40.5	1.291	48.6	33.8
36	41.2	2.209	49.4	34.3
37	41.6	1.814	49.9	34.7
38	42.1	1.500	50.5	35.1
39	42.9	2.114	51.5	35.8
40	43.3	1.888	52.0	36.1
41	44.0	1.708	52.8	36.7
42	44.5	1.662	53.4	37.1
43	45.1	1.851	54.1	37.6
44	45.9	1.887	55.1	38.3
45	46.9	1.753	56.3	39.1
46	47.7	2.115	57.2	39.8
47	47.9	1.785	57.5	39.9
48	49.3	2.119	59.2	41.1
49	49.6	2.087	59.5	41.3

Table I. Maxima of scattering function $I_{\parallel}$, as a function of size parameter α(θ scattering = 90°, n = 1.33).

*(see Figure I and Table II)

	α_{MAX}	$I(\alpha_{MAX})$	$I(1.2\alpha_{MAX})$	α_{MIN}	$I(\alpha_{MIN})$	$I(1.2\alpha_{MIN})$
1	11.3	26.4	2.3	10.2	1.09	0.24
2	13.1	38.4	3.2	12.0	0.04	3.02
3	14.7	46.0	7.7	14.1	0.07	12.8
4	16.4	47.0	18.4	15.9	1.25	16.5
5	21.2	37.8	0.57	21.7	0.21	23.7
6	22.9	70.0	0.087	23.45	0.15	47.0
7	24.5	94.2	2.5	25.5	0.16	31.6
8	26.1	58.3	6.2	27.4	0.06	19.0
9	28.1	52.4	19.7	29.2	1.27	9.9
10	29.8	50.6	52.4	31.2	1.95	23.7
11	36.15	114.3	70.0	36.5	1.00	43.7
12	37.85	172.6	52.4	39.0	1.51	54.3
13	39.6	199.5	80.9	40.8	0.40	47.0
	ΣI_i =	1007.5	316.4	ΣI_i =	9.16	332.4

$$\sum_i I_i(\alpha_{MAX}) - \sum_i I_i(\alpha_{MIN}) = 998.3 \simeq \sum_i I_i(\alpha_{MAX}) \equiv A$$

$$\sum_i I_i(1.2\ \alpha_{MAX}) - \sum_i(1.2\ \alpha_{MIN}) = 16.0 \equiv a \ll A$$

Table II. Demonstration of the validity of the assertion that $A(r_1) \cong \Sigma_{MAX,r_1} - \Sigma_{MIN,r_1}$ (Equation 3) for 2 water droplets of radii r_2/r_1 = 1.2 with a randomly chosen set of 13 pairs of α_{MAX}, α_{MIN}. ($I_{\parallel}$ - relative units)

ACKNOWLEDGEMENT

I wish to thank Professor J. Neumann and Professor Y. Gallily of the Department of Meteorology of the Hebrew University, Jerusalem, and Dr. Vernon E. Derr of the Wave Propagation Laboratory, ERL, NOAA, Boulder, Colorado, for their helpful discussions, Mr. M. Graber for assisting with the computer analysis, and Mr. M. Berman for his assistance.

This research was completed while the author held a National Research Council Postdoctoral Research Associateship supported by the National Oceanic and Atmospheric Administration.

References

1. G. Mie, Ann. Phys., 25, 377 (1908).
2. H. C. van de Hulst, Light Scattering by Small Particles (Wiley, New York, 1957).
3. A. Cohen, Tellus XXI, 5 (1969).
4. C. Junge, J. Meteorology 12, 13 (1955).
5. G. Yamamoto and T. Masayuhi, Appl. Opt. 8, 447 (1969).
6. A. Cohen, M. Graber and J. Neumann, The Effect of Double-Scattering by Water Droplet Clouds on the Polarization of Laser Pulses. Presented at the International Conference on Meteorology, IMS-AMS, Nov. 30 - Dec. 4, (1970).

Reprinted from Applied Optics 10, No. 12, 2665-2669, 1971.

Atmospheric Temperature Measurement Using Raman Backscatter

R. G. Strauch, V. E. Derr, and R. E. Cupp

A ground-based method of measuring atmospheric vertical temperature profiles using Raman backscatter from N_2 is discussed. Experimental measurement of temperature fluctuations at tower heights is described.

Introduction

Atmospheric probing with laser radar (lidar) is becoming an increasingly useful tool for gathering data that enables the meteorologist to better understand atmospheric processes. The potentials of lidar have been discussed[1] and experiments have been conducted using Mie scattering to study aerosols,[2] fluorescent scattering to study the sodium layer,[3] and Raman scattering to study vertical water vapor profiles up to several kilometers.[4,5] The potential of Raman lidar in pollutant detection has been studied theoretically and experimentally.[6] The relatively weak Raman signals present considerable experimental difficulty, and only limited success has been reported for pollution detection in the atmosphere.[7] In this paper, we discuss the measurement of the vertical temperature profile using Raman backscatter from nitrogen and report the results of experiments that indicate the feasibility of the method.

The most widely used method of obtaining a remote measurement of the vertical temperature profile with a ground-based instrument utilizes the absorption line of oxygen near 60 GHz to vary the transmission distance for received energy in a radiometer. The radiometer temperature measurements require an integral inversion to determine an atmospheric temperature profile. A radar-type determination offers improved resolution and simplicity of data analysis, and allows the measurement of temperature fluctuations at known altitudes of specific interest as well as a determination of a long-term average profile. In addition to water vapor profile measurement and pollution detection, temperature information can be obtained directly from the Raman signal intensity.

The concept of using molecular density measurements to derive temperature profiles is not new. Elterman,[8,9] using searchlights, has measured temperature profiles from 10 km to 67.6 km by assuming that the scattering from above 10 km is due only to molecular scattering. Accurate temperature and pressure meaurements were made at the lowest altitude that the scattering could be assumed to be Rayleigh. Below about 10 km the scattering is from molecules and aerosols and very accurate measurements of particulate scattering would have to be made to separate out the molecular scattering component. Methods of separating the scattering components have not been perfected. Aerosol density measurements rely on using an assumed Rayleigh density. Raman backscatter can be used to measure molecular density because the Raman component of backscatter is shifted in wavelength from aerosol or Rayleigh scattering. The relatively weak Raman backscatter can be used for density measurements in the lower atmosphere to complement density measurements made by Rayleigh scattering from the higher clean air.

A lidar backscatter measurement is a measurement of the product of the volume backscatter and the two-way extinction. In the case of on-frequency lidar, both the volume backscatter and the extinction are the sum of molecular and aerosol terms, whereas the volume backscatter for the Raman component involves only the molecular density. The total extinction must be measured for the Raman determination of density. For example, suppose that a 3400-Å lidar measurement of the backscatter at 1-km altitude is being made. Suppose that the total extinction from aerosol scattering is the same as that from Rayleigh scattering and assume that the total extinction can be measured to within 5%. Then the Raman backscatter can be used to determine a molecular density to within 1.4%, whereas the on-frequency backscatter would not give a useful density measurement.

The authors are with the Environmental Research Laboratories, National Oceanic and Atmospheric Administration, Boulder, Colorado 80302.

Received 3 May 1971.

Theory

The use of the ideal gas law in the form

$$P(h) = \rho(h)T(h)R/M, \qquad (1)$$

where h is the altitude, P is the pressure, ρ is the density, R is the universal gas constant, and M is the molecular weight leads to

$$\Delta P(h)/P(h) = [\Delta\rho(h)/\rho(h)] + [\Delta T(h)/T(h)].$$

For a fixed altitude h, where the pressure can usually be taken as constant for the duration of a measurement,

$$\Delta\rho(h)/\rho(h) = -\Delta T(h)/T(h).$$

The signal received by a lidar system measuring Raman backscatter from nitrogen would indicate, for constant pressure (altitude),

$$\Delta S_{N_2}(h)/S_{N_2}(h) = -\Delta T(h)/T(h),$$

where $S_{N_2}(h)$ is the backscattered Raman signal and is proportional to $\rho_{N_2}(h)$. Thus, at any altitude where the partial pressure of nitrogen is approximately constant, the Raman backscatter gives a direct indication of temperature fluctuations. The results of experiments demonstrating this capability of Raman lidar will be discussed later.

The measurement of a temperature profile using nitrogen density measurements is not as direct as the measurement of temperature fluctuations.[1] From the ideal gas law and the hydrostatic relationship, it follows that

$$\begin{aligned} T(h) &= P_{N_2}(h)/[\rho_{N_2}(h)R/M] \\ &= \left[P_{N_2}(h_0) - g\int_{h_0}^{h} \rho_{N_2}(z)dz\right][\rho_{N_2}(h)R/M], \qquad (2) \end{aligned}$$

where $P_{N_2}(h_0)$ is the partial pressure of N_2 for a reference altitude. The integral in the numerator indicates that in order to measure temperature at any altitude, using density measurements, the density must be measured as a function of altitude from h_0 to h. The lidar measures $\rho_{N_2}(h)$, using the lidar equation[1]

$$N_r = (N_t\eta_t\sigma_{N_2}\rho_{N_2}{}^*LA_r\eta_r\eta_q/h^2) \exp \int_{h_0}^{h} -(B_t + B_r)dz, \qquad (3)$$

where the number of received signal photons counted per transmitted lidar pulse is N_r, N_t is the number of laser photons per pulse, η_t is the transmitter efficiency, σ_{N_2} is the Raman scattering cross section for N_2 for the transmitted wavelength, $\rho_{N_2}{}^*$ is the number density of N_2 at height h, L is the length of the atmospheric column observed by the gated lidar receiver, A_r is the receiver aperture, η_r is the receiver optical efficiency, η_q is the detector quantum efficiency, B_t is the atmospheric extinction coefficient for the transmitted wavelength, and B_r is the extinction coefficient for the Raman wavelength. B_t and B_r are the Rayleigh extinction coefficients (neglecting aerosol attenuation) and are proportional to ρ_{N_2}, so the measurement of $\rho_{N_2}(h)$ as well as $P_{N_2}(h)$ requires the evaluation of

$$\int_{h_0}^{h} \rho_{N_2}(z)dz.$$

There are two ways to approach the evaluation of the integral; an *a priori* statistical model of the atmosphere can be used or the integration can be performed using the lidar measurements.

Consider first the statistical approach. An *a priori* statistical model based on the statistics of radiosonde measurements at a nearby station can be used to approximate $P_{N_2}(h)$ in Eq. (2) and the extinction term in Eq. (3). The statistical model has the important constraint that accurate measurements of $P_{N_2}(h_0)$ and $T(h_0)$ can be made. The statistical model can also be constrained by time of day, date, and ground measurements of meteorological data of immediately preceding days at the local site and surrounding sites. One of the approaches to performing the temperature inversion for microwave radiometer data utilizes this approach for the pressure term.[10] If the pressure and density measurement errors of $P_{N_2}(h)$ and $\rho_{N_2}(h)$ are independent, then

$$(\mathrm{Var}T)^{\frac{1}{2}}/\bar{T} = [(\mathrm{Var}P_{N_2}/\bar{P}_{N_2}{}^2) + (\mathrm{Var}\rho_{N_2}/\bar{\rho}_{N_2}{}^2)]^{\frac{1}{2}}.$$

The bar denotes the mean value of an ensemble of measurements and $\mathrm{Var}X = \bar{X}^2 - \bar{X}^2$. The measurement errors are not completely independent in this case, since $\rho_{N_2}(h)$ also depends on the statistical model to obtain the Rayleigh attenuation. However, the optical thickness for wavelengths and altitudes of interest here is less than 1, so that covariance terms can be neglected.

As an example of the statistical approach, consider the model using only the constraint of pressure at ground level, $P(o)$. Westwater[10] has analyzed the yearly data from radiosondes taken near sunrise and sunset at Denver, Colorado. The results are shown in Table I. The unconstrained variances $\mathrm{Var}[P]$ are about 30 (mbar)^2 for all altitudes, but the constrained variances $\mathrm{Var}[P|P(o)]$ [variance of P, given $P(o)$] are much less at low altitude because of the strong correlation between $P(h)$ and $P(o)$ for the yearly average data. Additional constraints, particularly $T(o)$, will further reduce the variances and make the statistical approach applicable to wider ranges of meteorological conditions. If the pressure is found from the statistical model with uncertainty $\{\mathrm{Var}[P|P(o)]\}^{\frac{1}{2}}/\bar{P}$ as in Table I, and the uncertainty in the lidar measurement $(\mathrm{Var}\rho_{N_2})^{\frac{1}{2}}/\bar{\rho}_{N_2}$ is numeri-

Table I. Atmospheric Pressure Measurements at Denver, Colo.

h (km)	$\bar{P}$ (mbar)	$\mathrm{Var}[P]$ (mbar)^2	$\mathrm{Var}[P\ P(h_0)]$ (mbar)^2	$\{\mathrm{Var}[P\ \bar{P}(h_0)]\}^{\frac{1}{2}}/\bar{P}$
$0.00 = h_0$	837	35.2	0	0
0.35	802	31.7	0.85	1.14×10^{-3}
0.648	773	30.1	2.27	1.94×10^{-3}
1.013	739	28.9	4.55	2.88×10^{-3}
5.040	437	39.8	28.62	1.22×10^{-2}
10.000	210	20.9	19.28	2.08×10^{-2}

Table II. Signal Intensity Required for Temperature Measurement

h (km)	$(\text{Var. } T)^{\frac{1}{2}}/\bar{T}$	S (photon counts)	Observation time required (sec)
0	0	0	0
0.35	1.61×10^{-3}	7.69×10^{5}	20.2
0.648	2.74×10^{-3}	2.66×10^{5}	25.6
1.013	4.07×10^{-3}	1.21×10^{5}	30.8
5.040	1.72×10^{-2}	6.72×10^{3}	95.0
10.000	2.94×10^{-2}	2.31×10^{3}	317

$(\text{Var}T)^{\frac{1}{2}}/\bar{T} = \{2\text{Var}[P|P(o)]/\bar{P}^2\}^{\frac{1}{2}}$

Table III. Lidar Characteristics

N_t,	photon transmitted per pulse	$= 1.7 \times 10^{16}$
η_t,	transmitter efficiency	$= 80\%$
σ_{N_2},	cross section for N_2	$= 1.86 \times 10^{-33}$ m^2/sr[a]
L,	range resolution	$= 50$ m
A_r,	receiver aperture	$= 0.36$ m^2
η_r,	receiver optical efficiency	$= 25\%$
η_q,	detector quantum efficiency	$= 25\%$
PRF,	pulse repetition rate	$= 100$ sec^{-1}
λ_t,	transmitter wavelength	$= 3371$ Å

[a] Calculated by D. A. Leonard Avco-Everett (private communication).

cally the same, then the temperature uncertainty is that shown in Table II. Also listed in Table II are the number of photon counts required to obtain this accuracy for a lidar system where the Poisson statistics of the signal determine the lidar signal-to-noise ratio. The fourth column in Table II lists the observation time required for a lidar system having the characteristics listed in Table III. (The attenuation term was calculated for a standard atmosphere.) Table II indicates that present lidar systems can make temperature profile measurements using an *a priori* statistical model of the atmosphere to obtain pressure profiles and using the lidar to measure $\rho_{N_2}(h)$. A pressure model with sufficient constraints will make the temperature uncertainty depend only on the lidar measurement of ρ_{N_2} for a wide range of conditions.

The second approach to making a temperature profile measurement utilizes the measured density from h_0 to h to find the pressure and the Rayleigh extinction. In this case, the inaccuracy of the temperature measurement depends on the inaccuracy of $\rho_{N_2}(h)$. The temperature uncertainty is given by

$$(\text{Var}T/\bar{T}^2) = (\text{Var}\rho_{N_2}/\bar{\rho}_{N_2}{}^2) + (\text{Var}P_{N_2}/\bar{P}_{N_2}{}^2) - [2\text{Cov}(P_{N_2},\rho_{N_2})/\bar{P}_{N_2}\bar{\rho}_{N_2}].$$

Since P_{N_2} is found from ρ_{N_2} through the hydrostatic relationship, VarP_{N_2} is the variance of the spatial average of $g\rho_{N_2}$. The covariance term depends on the correlation between the density measurement at h and the spatial average of the density measurements from h_0 to h. If the lidar contains no systematic errors, the covariance term becomes negligible (except for the low altitudes where the density measurement will be most accurate), because the lidar system must have sufficient bandwidth (i.e., spatial resolution) to make the measurement of $\rho_{N_2}(z)$ independent of the measurement of $\rho_{N_2}(z + \Delta z)$. The variance of the spatial average of ρ_{N_2} from h_0 to h is the variance of a sum of independent measurements, and if the lidar contains no systematic errors, this variance will be much less than the variance of $\rho_{N_2}(h)$. Hence, the main contribution to the temperature uncertainty at h will be the uncertainty in the measurement of $\rho_{N_2}(h)$ for lidar systems with no systematic error. The applicability of this method depends on the development of a Raman lidar system free of systematic error.

Lidar measurement of temperature profiles presents a major practical problem not found in water vapor profile measurements. Effects of aerosol attenuation, laser beam misalignment, $1/h^2$ corrections, etc. can be accounted for in water vapor measurements by measuring the mixing ratio instead of the water vapor density. A nitrogen profile measurement, however, would require a careful calibration of the laser system and a measurement of attenuation. An absolute measurement of $\rho_{N_2}(h)$ is not necessary for the profile measurement of temperature if the minimum altitude of the lidar system is h_0 where $\rho(h_0)$ or $T(h_0)$ can be measured with meteorological instruments.

Experimental Results

An experiment was devised to check the feasibility of using Raman backscatter to observe temperature fluctuations using a high pulse repetition rate laser. A lidar system with parameters similar to those in Table III was used. The range was reduced to tower height (30.5 m) so that temperature could be precisely monitored and compared with the Raman backscatter. The length of the backscatter volume was 5 m and was determined by the geometry of the transmitting and receiving beams. Thermistors were placed near the center and near both ends of the 5-m observation length. The laser beam passed vertically approximately 2 m from the thermistors. A pressure indicator located at ground level continuously monitored total pressure. The atmospheric pressure change during any observation time was less than 0.2 mbar so that $\Delta P/P_{N_2}$ is negligible compared to $(\Delta T/T)$ for temperature changes of 1°C or greater. Since $(\Delta T/T) \approx 0.35\%$ per °C, the stability of the laser output power becomes important for monitoring fluctuations of atmospheric N_2 density. (For profile measurements where the backscatter from each range increment is measured for each laser pulse, the laser power stability is not as important.) During these experiments the S/N ratio was sufficient to allow observations of Raman signal fluctuations of 0.35% with a 3-sec time constant, but the long-term record contained random fluctuations of approximately 1%. These changes were traced to laser power variations, temperature effects on the transmission of optical filters, and mechanical instability.

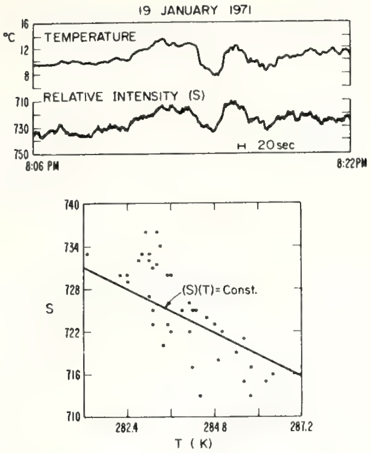

Fig. 1. Raman backscatter intensity vs temperature.

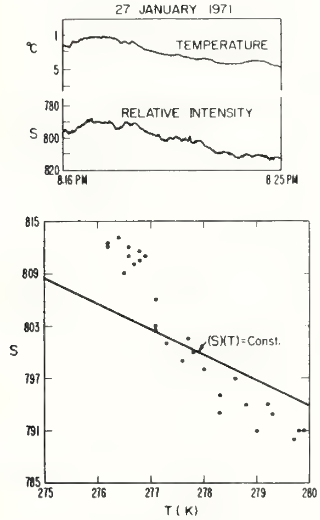

Fig. 2. Raman backscatter intensity vs temperature.

The total extinction due to Rayleigh scattering of the transmitted and backscattered laser energy is about 0.7%, and fluctuations of the Rayleigh extinction will be negligible. Fluctuations of the total aerosol extinction were also shown to be negligible by monitoring the laser power output with a 10-m transmission path.

The Raman backscatter signal was recorded using a fast sample and hold gate to measure a voltage level proportional to the number of backscattered photons received from the 5-m interaction region after each pulse. The steplike signal was filtered and recorded on a zero-suppressed strip chart.

Figures 1–4 show the examples of data in which temperature changes of several degrees were recorded by the thermistors. Only the center thermistor temperature is shown; the other two thermistors indicated the same temperature. In Figs. 1–3, data points were read every 20 sec and a plot of relative Raman backscatter (S) vs T is shown with the data. The theoretical curve $(S)(T)$ = constant is shown for reference. This curve is approximately a straight line over the range of values measured in these experiments. Fluctuations other than temperature are recorded on the Raman channel, but temperature changes are clearly recorded by the Raman lidar. In Fig. 3, compensation for the change in laser power was made in the S-T graph. Figure 4 shows a 23-min segment of data during which T changes by approximately 2 degrees. Data points were read every 4 sec and a cross-correlation of the S-T data was performed. No corrections were made to the raw data. The peak

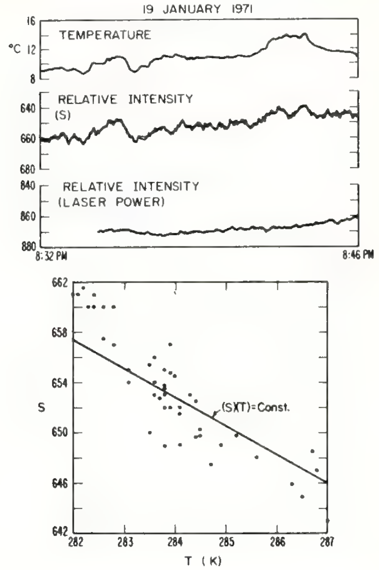

Fig. 3. Raman backscatter intensity vs temperature.

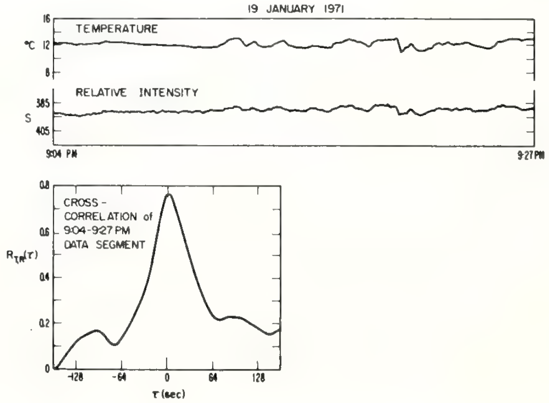

Fig. 4. Cross-correlation of Raman backscatter intensity and temperature.

correlation, at zero time lag, was 0.76 and the correlation decreases to 0.2 with about 1-min time lag. Laser power variations and mechanical instability also contribute to short-term signal fluctuations. The noise on the signal channel and uncertainty in chart reading contribute approximately three divisions of uncertainty to the relative Raman signal level (S) in Figs. 1–3. The rms deviation of the Raman signal from the theoretical curve is 4.14, 3.58, and 2.28 divisions for Figs. 1–3. The other major factor that prevents perfect correlation of the data is that the Raman signal is a volume measurement and the thermistor is essentially a point measurement. The temperature variations move with the wind and an abrupt change in T can be recorded by the point sensor, whereas the volume sensor will record the total abrupt change only when it fills the entire volume.

Conclusion

The correlation between the Raman scattering of nitrogen and the temperature measured by thermistors shows that lidar can measure temperature fluctuations. Detailed study of temperature fluctuations can be made with the narrow pulse and high pulse repetition rate of available lasers. Temperature profiles in the clear atmosphere can be measured with acceptable accuracy if the lidar is calibrated. Available laser equipment can be utilized for studying the temperature structure of the atmosphere to several kilometers altitude. Pressure information can be obtained if the lidar system is free of systematic error. Data processing equipment capable of measuring the backscatter from each range increment for each laser pulse is needed for efficiency of operation and to eliminate practical problems encountered in field operation.

References

1. V. E. Derr and C. G. Little, Appl. Opt. **9**, 1976 (1970).
2. E. W. Barrett and O. Ben-Dov, J. Appl. Meteorol. **6**, 500 (1967).
3. M. R. Bowman, A. J. Gibson, and M. C. W. Sanford, Nature **221**, 456 (1969).
4. J. Cooney, J. Appl. Meteorol. **9**, 182 (1970).
5. S. H. Melfi, J. D. Lawrence, and M. P. McCormick, Appl. Phys. Lett. **15**, 295 (1970).
6. T. Kobayasi and H. Inaba, Nature **224**, 170 (1969).
7. T. Kobayasi and H. Inaba, Appl. Phys. Lett. **17**, 139 (1970).
8. L. Elterman, J. Geophys. Res. **58**, 519 (1953).
9. L. Elterman, J. Geophys. Res. **59**, 351 (1954).
10. E. R. Westwater, Ph.D. Thesis, University of Colorado (1970).

Reprinted from Applied Optics 9, No. 9, 1976-1992, 1970.

A Comparison of Remote Sensing of the Clear Atmosphere by Optical, Radio, and Acoustic Radar Techniques

V. E. Derr and C. G. Little

The considerable utility of ultrasensitive microwave radar in atmospheric studies can now be augmented by lidar and acoustic echo-sounding techniques. The current and potential capabilities, and limitations, of these methods of remote atmospheric probing are discussed and the techniques are compared. From this analysis the conclusion emerges that a remote sensing facility consisting of these instruments probing the same volume of the atmosphere can measure many of the meteorologically significant parameters necessary to increase our understanding of the structure and dynamics of the clear lower atmosphere, and provide the spatial and temporal density of measurements necessary for weather forecasting.

Introduction

The rapidly expanding concern for environmental conservation and control requires an immediate acceleration in attempts to increase our understanding of the atmosphere. Such problems as short- and long-range weather prediction, the prediction and control of severe storms, maximum allowable pollution concentrations, and oxygen regeneration cycles remain without solution because of the lack of basic understanding of atmospheric and other environmental processes. The fundamental physical, chemical, and mathematical knowledge is presumably available, but the particular phenomena involved in atmospheric interactions are not readily deducible from first principles. Rather, an interleaving of observation and theory is necessary before we may arrive at an atmospheric science that can measure, predict, confirm, modify, and control. Even for those atmospheric processes for which a sufficiently complete theory is available, the prediction of cycles and variations from norms is very uncertain. Failures in forecasting are frequently due to insufficient data from areas where rapid development of storms occurs, with strong convergence of air masses having large differences of temperature or humidity.

Theoretical and experimental progress on these and associated problems has been impeded by the lack of direct measurements of atmospheric parameters in three dimensions, over large volumes, and with sufficient resolution in time and space to allow the study of composition and dynamical structure in time evolution. This article discusses a special set of remote sensing methods, selected because of their applicability to these problems. The methods selected all use the principle of active echo-sounding, because this offers the unique advantage of precise identification of the atmospheric volume being interrogated. The three different radar techniques considered—optical, radio, and acoustic—are selected because the different radars are sensitive to different parameters of the atmosphere. The discussion illuminates the separate potentials of the methods, and anticipates their power in atmospheric experiments in which two of them or all three may be combined to attack specific problems.

By scanning in angle, it is possible to derive three-dimensional fields of measurable scalar atmospheric parameters. (Since doppler methods measure only the radial velocity, it is necessary to use three separate systems to obtain three-dimensional velocity fields.) Three-dimensional mapping is essential to an understanding of the structure and dynamics of the atmosphere. Such phenomena as inversion, layering, breaking waves, and gravity waves are strongly dependent on boundary conditions for stability, and a knowledge of their structure over a large volume is essential for gaining an understanding of the conditions of their formation. Coupling the geometrical precision of the radar with sensitivity to composition, temperature, turbulence, and wind velocity results in a precise and comprehensive, yet flexible, system for atmospheric studies. The discussion will emphasize tropospheric applications of the echo-sounding techniques.

Scattering and Absorption Processes in the Clear Atmosphere

The success of remote sensing by radar techniques depends on the strength of the interaction of the electromagnetic and mechanical radiation with the atmospheric constituents, and on the magnitude of the scattered radiation, particularly the backscattered component. Two quite different types of interaction play

---

The authors are with the Wave Propagation Laboratory, ESSA, Boulder, Colorado 80302.

Received 18 June 1970.

principal roles in the probing of the atmosphere. The first, which we may call spectroscopic, is an absorption and reradiation, or a scattering process in which the radiation reacts with individual molecules. The cross section for these events is dependent on the specific molecule, i.e., on its state, its energy level diagram, its environment (pressure, temperature), and on the frequency of irradiation.

The second principal type of interaction is with the fluctuations of refractive index. This classical electromagnetic or acoustic scattering is dependent on the atmospheric parameters of density, temperature, humidity, and wind velocity which determine the electromagnetic and acoustic refractive indexes. This scatter is much less frequency dependent than the spectroscopic interactions. Because Mie scattering is associated with particles and is to some extent frequency dependent, it is here treated as a spectroscopic interaction. Rayleigh scattering, often treated as scattering by individual molecules, is caused by the fluctuations of atmospheric density. Because calculation on a molecular basis (the phase cancellation due to random scatterers being neglected) yields the same numerical results as calculation based on fluctuation theory, it is here considered spectroscopic.[1] This result holds only for dilute media, but the refinements of the theory are unnecessary for our purposes. The next sections contain a more detailed discussion of both types of interaction.

Optical Interactions

We can determine meteorologically significant facts concerning the atmosphere by means of electromagnetic and acoustic radiation only if the interaction is sufficiently strong. In this section we summarize the absorption, scattering, and re-emission processes of importance in tropospheric remote sensing with optical waves. We consider these processes in the frequency range from near infrared to the oxygen absorption at approximately 180 nm.

The atmosphere consists of a turbulent mixture of gases and aerosols. Electromagnetic radiation interacts with the atmospheric constituents in a variety of ways. The incident radiation may be characterized by amplitude or power, frequency (or spectrum), phase, direction, polarization, and coherence and speed of the event. Any of these characteristics may be changed in the process of absorption, scatter, or reradiation.

Typical cross sections per particle for the various electromagnetic scattering processes are given in Table I. The values apply in the visible range.

Table I. Typical Optical Scattering Cross Sections (per Particle)

Process	Cross section (cm²/sr)
Mie	10^{-27} to 10^{-8}
Rayleigh	10^{-27}
Raman	10^{-28}
Resonance Raman	10^{-22}
Fluorescence	10^{-16} and smaller

In the troposphere, the aerosol content is highly variable, but ordinarily, due to it, the strongest electromagnetic scattering process is the Mie scattering from such particulate matter. Such scattering is rarely absent even after rain-washing of air. Radii of aerosols range from 10^{-7} mm to 10^{-1} mm under most conditions, being highly variable. Smoke accounts for most particles with radii less than 10^{-4} mm. Particles larger than 10^{-4} mm are often dust or ocean spray. Detailed discussion of the distribution of aerosols is given by Junge[2] and by Elterman.[3] Typical volume backscatter and extinction coefficients range from approximately 10^{-4} m^{-1} for light haze to 10^{-1} m^{-1} for dense water clouds at the ruby laser frequency (Collis[4]).

Mie scattering is normally evaluated by a classical calculation based on electromagnetic scattering theory.[1] The results depend critically on the shape and size of the particle. Even a sphere shows a very complex angular dependence. In the case of a water droplet with a radius of 10^{-3} mm, the scatter is strongest in the forward direction, decreasing by a factor of 300 at $\pi/2$, with a slight increase in the direction of $\theta = \pi$. Thus, forward scatter and direct backscatter are the most favorable observing angles. Mie scattering is on-frequency and the scattered radiation from a single particle is in phase with the incident radiation. However, since the particles are randomly distributed, there is a loss of coherence. The polarization of the scattered light is a complex function of $2\pi a/\lambda$, where a is the particle radius and λ the incident wavelength, but the degree of polarization is generally smaller than in Rayleigh scattering. Compared with other scattering modes the intensity of scattered light and its other characteristics are only weakly dependent on frequency ($\propto 1/\omega^2$); hence, the source frequency is not critical. The time averaged radiant flux[1] of Rayleigh scattering is:

$$\bar{S} = \frac{\pi c(1 + \cos^2\theta)}{16R^2N\lambda^4}\,(n^2 - 1)^2(\mathbf{E}^\circ)^2, \tag{1}$$

i.e., $\bar{S}$ is the scattered energy per unit time per unit perpendicular area to the direction of scattered light, at a distance R from the scattering particle, at an angle θ with the incident radiation, assumed unpolarized. The $1/\lambda^4$ dependence on wavelength λ must be modified slightly when the dispersion of air is taken into account. N is the number of particles per unit volume, $\bar{E}^\circ$ the electric field, n the index of refraction, c the velocity of light.

Fluorescent scattering can occur only when the frequency of the incident radiation is in an absorption line or band in the sample material. Transition to a state of higher energy may then occur, followed by relaxation and emission of light at frequencies equal to or less than the incident frequency. This is called Stokes fluorescence; anti-Stokes fluorescence, in which the light of higher frequency is emitted, is weaker by a factor of 10^{-3}. The emitted (and absorbed) radiation frequencies are dependent on the detailed structure of the molecular energy level diagram and hence are characteristics of the molecule. Since the absorbed light is required to be at a frequency fixed by the molecular characteristics, the source of illumination must, barring lucky accidents, be tunable. The emitted radiation can then be used to identify uniquely the molecule responsible for the scattering. Fluorescence has characteristic re-emission times of the order of 10^{-8} sec to 10^{-1} sec. The mean time between air molecule collisions in the troposphere is usually so short ($\approx 10^{-9}$ sec) that the fluorescent emission is quenched or perturbed, and it is rarely observed at atmospheric pressure. Fifteen kilometers is, with few exceptions, a lower limit on the observation of fluorescence. Two exceptions[5,6] are NO_2 and SO_2, which have been observed at atmospheric pressure in mixtures with N_2 and with air. The cross sections for fluorescent interactions can be much larger than Rayleigh cross sections—as large as 10^{-16} cm^2/sr.

Raman scattering, although the weakest of the phenomena considered here, is useful because it is a means of identifying scattering molecules, and because it occurs regardless of the irradiating frequency. The radiation frequency need not be matched with molecular resonances to allow transitions of the molecule; thus it can be used with fixed frequency laser sources. If the incident radiation is of frequency ν, Raman lines occur at a series of frequencies $\nu \pm \nu_1, \nu \pm \nu_2 \cdots$; the lower frequencies are called Stokes lines, the higher anti-Stokes lines. The latter are not considered here because they are weaker under tropospheric conditions. The frequency displacement is related to the rotation–vibration spectrum of a molecule, but selection rules differ from those operating in infrared spectra. The detailed calculation and listing of Raman lines may be found in Herzberg[7] and Mizushima.[8] Here we will review briefly the quantities important in atmospheric probing.

The intensity of Raman lines, when the molecule makes a transition from state m to state n, is given by Behringer[9] as

$$I = \frac{2^7\pi^5}{3^2c^4} I_0(\nu_0 - |\nu_{mn}|)^4 \sum_{\rho\sigma} |\alpha_{\rho\sigma,mn}|^2, \tag{2}$$

where $\alpha_{\rho\sigma,mn}$ is the $\rho\sigma(= X,Y,Z)$ component of the scattering dyadic

$$\alpha_{mn} = \frac{1}{h} \sum_r \left(\frac{\boldsymbol{\mu}_{rn}\boldsymbol{\mu}_{mr}}{\nu_{rm} - \nu_0 + i\delta_r} + \frac{\boldsymbol{\mu}_{mr}\boldsymbol{\mu}_{rn}}{\nu_{rn} + \nu_0 + i\delta_r} \right).$$

Here c is the velocity of light, h Planck's constant, I_0 is the incident plane-polarized intensity of frequency ν_0, r is an intermediate state, $\boldsymbol{\mu}_{rn}$ and $\boldsymbol{\mu}_{mr}$ are the transition moments of the dipole moment operator μ, δ_r is the damping constant of state r. When the denominators of α are not small, the intensity varies as the fourth power of the output frequency, making higher frequency lasers advantageous.

The dependence of the Raman intensity on the angle of observation θ is, when the molecule is isotropic, the same as for the Rayleigh scattering in Eq. (1). A more complete discussion is given in the text edited by Szymanski.[9]

Interaction of Radio and Acoustic Waves with an Atmosphere Containing Weak Fluctuations in Refractive Index

The interaction of electromagnetic and acoustic waves with a spatially nonhomogeneous atmosphere has been treated extensively in the literature, notably by Tatarski.[10] The turbulent structure of the atmosphere results in weak fluctuations in atmospheric parameters such as temperature, humidity, and velocity; these produce corresponding variations in the local refractive index for electromagnetic or acoustic waves. These fluctuations have many size scales and are neither necessarily statistically homogeneous in distribution nor isotropic in nature. A radar wave traversing such a medium is weakly scattered by the fluctuations in the refractive index, the fraction of power scattered in a given direction being a function of the intensity of the refractive index fluctuations, the angle of scatter, and the wavelength and polarization of the radar. In effect, the radar waves are sensitive only to the fourier component of the three-dimensional spectrum of refractivity that meets the Bragg condition[11] for reflection from periodic structures. For energy backscattered to the radar, the radar cross section per unit scattering volume (radar reflectivity η) is given by

$$\eta = 8\pi^2k^4\varphi_n(4\pi/\lambda), \tag{3}$$

where k is the wavenumber of the radar wavelength, $2\pi/\lambda$, and φ_n $(4\pi/\lambda)$ is the spectral intensity of the refractivity fluctuations at a spatial wavelength equal to one half the radar wavelength in the direction of the radar beam. A measurement of η therefore is a measurement of the intensity of the refractivity fluctuations at this particular wavenumber. Variations of this intensity with height can be used as indicators of the internal structure of the atmosphere; also, since the small scale refractivity fluctuations typically are transported with the speed of the mean wind, the velocity field can often be explored by studying the motion of these weakly scattering atmospheric targets.

Although the refractivity structure may not be isotropic and homogeneous, the acoustic and radio frequencies usually used for radar studies of clear air refractivity returns are such that this assumption is often valid locally. For a Kolmogorov spectrum of turbulence, using radar wavelengths corresponding to the inertial subrange of turbulence (i.e., wavelengths in the range roughly 1 cm to a few meters), it is often convenient to express the refractivity fluctuations in terms of the structure parameter of the refractivity, C_n, defined by

$$D_n(r) = \langle |n(x) - n(x + r)|^2 \rangle_{\text{av}} = C_n^{\,2} r^{2/3}, \tag{4}$$

where $D_n(r)$ is the structure function of the refractivity, dependent upon the spacing r between two points. For a Kolmogorov inertial subrange of turbulence, C_n is the rms difference in refractivity at two points unit distance apart.

The relationship between the radar cross section per unit volume, and the corresponding value of C_n for a

Kolmogorov spectrum of turbulence is[10]

$$\eta(\lambda) = 0.38C_n{}^2\lambda^{-\frac{1}{3}}. \tag{5}$$

For radio waves, the refractive index of air is given by[12]

$$N = (77.6/T)[P + (4810e/T)], \tag{6}$$

where $N = (n - 1)10^6$, n = refractive index, T = absolute temperature in kelvins, e = partial pressure of water vapor, and P = total pressure in millibars. For acoustic waves propagating in a stationary atmosphere, the phase velocity of sound in dry air is given by

$$C_d = 20.05 \times T^{\frac{1}{2}}\ \mathrm{msec}^{-1}. \tag{7}$$

In stationary moist air, the phase velocity of sound is given by

$$C_m = C_d(1 + 0.14e/P)\ \mathrm{msec}^{-1}. \tag{8}$$

Unlike electromagnetic waves, the phase velocity of sound waves is increased by the component of the wind velocity in the direction of the wave normal. Thus the second velocity is

$$C = C_{d,m} + V\cos\varphi, \tag{9}$$

where φ is the angle between the wind direction and the phase normal.

It is important to recognize that, because the wind is a vector rather than a scalar quantity, the refractivity change for an acoustic wave is a function of direction of propagation relative to the mean wind.

For scatter through angles other than 180°, the expressions required for electromagnetic and acoustic scatter are slightly different because of the difference in polarization. For the transversely polarized plane electromagnetic waves, the scattering cross section as a function of angle is given by

$$\sigma_r(\theta) = 2\pi k^4 \sin^2\chi \cdot \varphi_n(2k\sin\tfrac{1}{2}\theta),$$

where $\sigma(\theta)$ is the fraction of the incident power scattered per unit volume, per unit solid angle, in a direction θ relative to the incident direction and at a polarization angle χ. (The polarization angle is the angle between the scattered wave direction and the electric field vector in the incident wave.)

For the longitudinally polarized acoustic waves, the corresponding expression is

$$\sigma_a(\theta) = 2\pi k^4 \cdot \cos^2\theta \cdot \varphi_n(2k\sin\tfrac{1}{2}\theta).$$

If we assume a Kolmogorov spectrum of turbulence,[10] and assume that $2k\sin\frac{1}{2}\theta$ lies within the inertial subrange, these equations reduce to

$$\sigma_r(\theta) = 0.016k^{\frac{1}{3}} \cdot \sin^2\chi \cdot (\sin\tfrac{1}{2}\theta)^{-11/3}C_n{}^2, \tag{10}$$

and

$$\sigma_a(\theta) = 0.016k^{\frac{1}{3}} \cdot \cos^2\theta \cdot (\sin\tfrac{1}{2}\theta)^{-11/3}$$
$$[1.85\ C_v{}^2/C^2 \cos^2\tfrac{1}{2}\theta + C_T{}^2/4T'^2], \tag{11}$$

where C_V and C_T are the strictive parameters for velocity and temperature, respectively, and C and T are the mean values.

These two equations show that there will be no scatter of electromagnetic waves for a polarization angle of 0°, and that for acoustic waves, no scatter will occur through an angle 90°. Note also that the first term inside the square bracket, which gives the acoustic power scattered from the velocity field, is zero for $\theta = 180°$; i.e., the backscattered power will be entirely due to the temperature field. At all other angles (except $\theta = 90°$, where both contributions are zero) the scattered powers will be the sum of the powers scattered from the temperature fluctuations and from the velocity fields.

Table II summarizes the relative values of C_n for acoustic, radio, and optical waves for values of C_T, C_e, and C_V such as that the rms difference in temperature, humidity, and wind velocity at two points 1 m apart are respectively 1°, 1 mbar, and 1 msec^{-1}. Note that in the case of velocity fluctuations the values of C_n are a function of the scatter angle [see Eq. (11)].

Mean temperatures of 288 K, mean total pressure of 1013 mbar, and mean humidity of 10 mbar are assumed for the background levels. The mean radial component of wind is assumed to be zero.

Assuming that the temperature, humidity, and velocity eddies are uncorrelated on the scale of half a radar wavelength, the scattered signals from each component of the refractivity field will add incoherently, i.e., the powers add.

Table II, together with Eq. (5), shows that the radar cross section (depending on $C_n{}^2$) of typical atmospheric irregularities and turbulence are some six or seven orders of magnitude larger for acoustic waves than for radio waves. Under normal atmospheric conditions, the ratio of humidity fluctuations to temperature fluctuations is such that the acoustic power scattered from the humidity field is about two orders of magnitude below that from the temperature field. For radar waves, on the other hand, the scattered power from the humidity fluctuations is usually larger than that from the temperature fluctuations by about one order of magnitude.

Remote Measurement Capabilities and Limitations

Lidar

The use of lasers in atmospheric scattering studies began with the work by Fiocco and Smullin.[13] Lasers have been used as atmospheric illuminators in preference to lamps because the monochromaticity of the laser allows discrimination against background noise by the use of narrow band filters. In addition, the high peak power and narrow pulses yield good signal-to-noise ratios (SNR) and range resolution, even for low cross section scatterers. Practical field laser systems now

Table II. Relative Values of C_n for Acoustic, Radio, and Optical Waves[a]

Atmospheric condition	Acoustic $C_n \times 10^6$	Radio $C_n \times 10^6$	Optical $C_n \times 10^6$
C_T = 1 K	1720	1.26	0.93
C_e = 1 mbar	138	4.50	0.04
C_V = 1 m sec^{-1}	0–4000	(0–2) × 10^{-6}	(0–2) × 10^{-6}

[a] The very small values of C_n indicated for the velocity fluctuations in the electromagnetic cases are those due to Fizeau drag.

range in peak pulse power up to several hundred megawatts. Pulse widths are as short as 10^{-8} sec, and pulse repetition frequencies are as high as 1000 pulses $\sec^{-1}$. The spectral range extends from the 10.6-μm CO_2 laser to the frequency quadrupled 1.06-μm Nd laser, with another group of frequencies available from the HCN and other molecular lasers at 311-μm 337-μm, and longer wavelengths. Not all the desired characteristics of frequency, power, pulse width, pulse repetition frequency, coherence, beam divergence, efficiency, and compact size are available in the same laser. Tunable dye and parametric lasers are now in field operation, offering increased flexibility in the choice of optimum frequencies for resonance effects and in differential modes of operation. Tunable lasers exist also in the infrared at present, unfortunately without the convenience necessary for field operation.[14]

The basic radar equation for the calculation of scattered signal returns applies to both lidar and acoustic radar. It has been presented in many sources and will be given here only briefly to define the terms of reference. Using the geometry of Fig. 1 and assuming a pulsed transmitter, we let N_t be the number of photons transmitted per pulse. (If $d = 0$ in the figure, we have the frequently used monostatic arrangement.) If ρ is the number density of scattering centers in the effective volume V_e, S is the transmitter to cell distance, R the distance from cell to receiver, α_1 and α_2 the respective absorption coefficients, $\sigma_\theta(\Omega)$ the angle dependent cross section per solid angle, then the number of received photons is

$$N_r = N_t \exp\left(-\int_0^S \alpha_1(s)ds\right)\cdot \sigma_\theta(\Omega)\Omega_r \rho V_e \times \exp\left(-\int_0^R \alpha_2(r)dr\right)\Big/\Omega_t S^2. \quad (12)$$

Here the absorption coefficients α_1 and α_2 are different not only because of the displacement of outgoing and returning paths, but also because the return signal may be at a different frequency from the transmitted signal. ρ is assumed constant over the effective volume. The area of the receiver is A; $\Omega_r = A/R^2$. We may let $\beta_\theta = \sigma_\theta(\Omega)\rho$, where β_θ, the radar scatter coefficient, has dimensions $m^{-1}sr^{-1}$. The area of the cell of interest is $A_b = \Omega_t S^2$, hence $V_e = \Omega_t S^2 L$; its size depends on the pulse width relative to L. In the monostatic case, the effective volume is $A_b c\tau/2$, where τ is the pulse length and c the velocity of light. We will use L to represent the effective length of the illuminated volume even in the monostatic case.

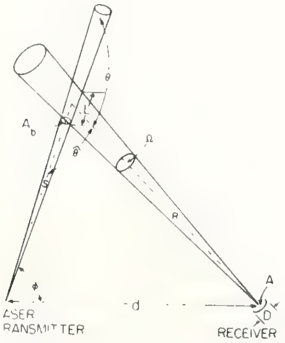

Fig. 1. Lidar configuration.

With these substitutions, we have

$$N_r = N_t \exp\left(-\int_0^S \alpha_1(s)ds\right) A\epsilon\beta_\theta L \exp\left(-\int_0^R \alpha_2(r)dr\right)\Big/R^2, \quad (13)$$

where ϵ is the receiver fractional efficiency. In many tropospheric situations the integrals in the exponential attenuation factors can be replaced by $\alpha_1 S$ and $\alpha_2 R$. Further, since the attenuation coefficients are small for many cases of interest, the exponentials may be replaced by 1. Figure 2 shows the fraction of photons received when N_t are transmitted, as a function of range, with the volume backscattering coefficient $\beta(m^{-1})$ as a parameter. No exponential absorption factor was used in the computation. In Fig. 3 on the other hand, the factor $\exp(-2\beta R)$ was included. By comparing the figures for the ranges of interest, we see that the attenuation of the atmosphere is of significance in the backscattered signal only for values of β larger than $10^{-4}\ m^{-1}$, that is, when haze is moderate or dense. For these figures we have assumed $A = 0.05\ m^2$, $L = 10$ m, $\epsilon = 0.75$.

The detector (photomultiplier) current is composed of the signal current i_s, the dark current (or current in the absence of illumination), i_d, and the current arising from background noise, i_b. The effective rms noise current at the photocathode is

$$N = \left(\eta P + m\tau\frac{(\eta B_\lambda A \Omega_r \lambda \Delta\lambda)}{hc} + \frac{I_d}{eG}\right)^{\frac{1}{2}}, \quad (14)$$

where P = number of signal photons arriving in time γ, η = photocathode efficiency, m = number of pulses of width τ, B_λ = background radiant flux (W $cm^{-2}\ sr^{-1}$ Å^{-1}), A = receiver aperture (cm^2), λ = wavelength (cm), Δ_λ = optical filter bandwidth (Å), e = electronic charge (1.6×10^{-19}C), G = photomultiplier gain, h = Planck's constant (6.6×10^{-34}J-sec) and c = velocity of light (3×10^{10}). (The units are chosen for convenience in the use of published data.)

For any active probing method to be successful, the variations introduced by passage from the transmitter to the cell of interest and by passage from the cell to the receiver must be much smaller than the fluctuations of the signal from the cell. Two factors allow us to evaluate the effect of the intervening atmosphere, the mean power absorbed and the fluctuations of the illumination of the cell of interest caused by scintillation. The mean absorbed power can be obtained from the extinction coefficient assuming it is equal to the radar backscattering coefficient. Thus the fractional power absorbed is $1 - e^{-\alpha R}$. When this fraction is small, the beam illuminating a cell of interest is essentially unperturbed, and the scattering from the cell is characteristic of the cell. When an appreciable fraction of the

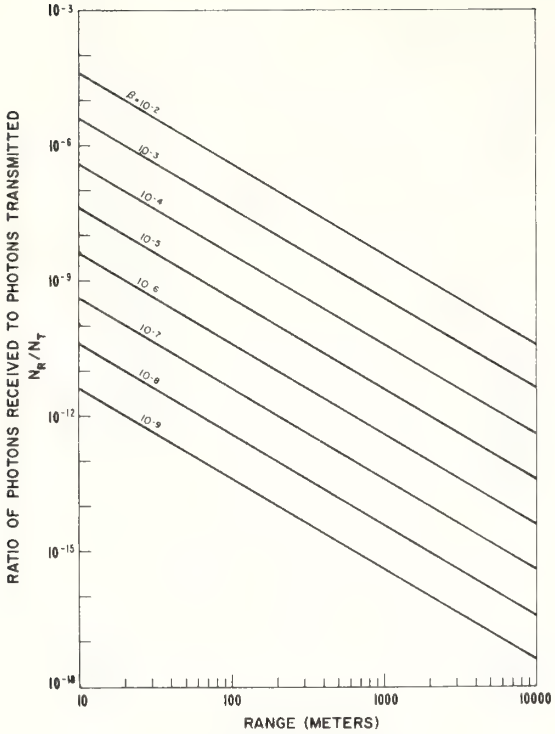

Fig. 2. Ratio of received to transmitted lidar signal as function of range, for various values of the radar backscatter coefficient β (m^{-1}). No atmospheric attenuation.

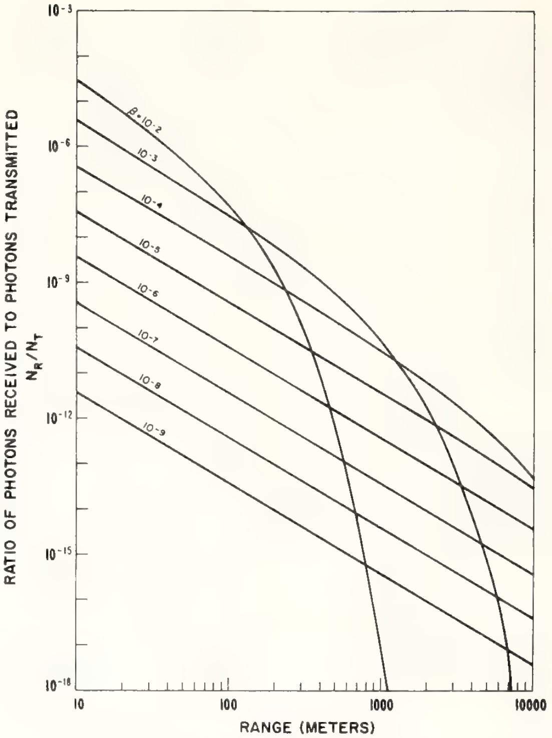

Fig. 3.
Same as Fig. 2 with exponential atmospheric attenuation.

beam has been absorbed, the fluctuations of the absorption of the intervening atmosphere may introduce a randomness on the signal not characteristic of the cell of interest. The range at which the illuminating beam becomes insufficiently steady will depend strongly on the atmospheric structure functions for the component of interest.

The fluctuations caused by scintillation depend in a complex way on the geometry of the lidar beams and the strength of the temperature fluctuations in the turbulent atmosphere along the path,[15] but we can estimate for visible wavelengths the worst case. Let us suppose the illumination volume is a cube of side S, the illuminating wavelength is λ and the length of laser-to-volume path is D. Then the correlation distance of scintillations in the illuminated volume is $r = \lambda D^{\frac{1}{2}}$. If, for example, $\lambda = 0.489\ \mu m$ and $D = 100$ m, then $r = 7 \times 10^{-3}$ m. In the worst case of a 90° scattering angle, the number of independently illuminated areas is

$$N = (S/r)^2 = (10/7 \times 10^{-3})^2 = (1500)^2.$$

The log amplitude is defined as $\chi = (\frac{1}{2}) \log_e(I/I_0)$, where I is the irradiance in the scattering, and I_0 is the average I. From field data the maximum possible saturated variance of χ in the scattering volume is $\sigma_\chi^2 = 0.6/2.25 \times 10^6 = 2.7 \times 10^{-7}$ for the total light in the volume. The corresponding variance for I is $\sigma_I^2 = I_0^2\ [\exp(4\ \sigma_\chi^2) - 1] \approx 1.12 \times 10^{-6}\ I_0^2$. The maximum possible relative fluctuation of the intensity is then

$$\frac{\sigma_I}{I_0} = (1.12 \times 10^{-6})^{\frac{1}{2}} = 1.06 \times 10^{-3} = 0.10\%.$$

In practice this maximal estimate of the noise seldom occurs. It is reduced by two effects. First, the path is normally not horizontal, but nearly vertical. Since the turbulence diminishes rapidly with increasing height, the important middle portion contains too little turbulence to produce saturated scintillations. Second, in winds of interest the fading rate of the scintillation will be of the order of $V_T/(D\lambda)^{\frac{1}{2}}$, where V_T = transverse wind velocity. It will usually be of the order of a few hundred Hz. Since most of the information sought in atmospheric studies lies below 10 Hz, a large percentage of the scintillation-caused noise will be removed by smoothing. The exact diminution is dependent on the experiment situation, but we can expect for frequently occurring situations that the fluctuation of the illuminating intensity on the cell of interest will be lowered by a factor of 10^3 or have a value $\sigma_I I = 1.06 \times 10^{-6}$.

Determination of the presence of aerosols was the earliest use of lidar in the atmosphere.[13,16] The signals as a function of range for a specific aerosol content can be determined from Figs. 2 and 3. However, the principal limitations lie in the interpretation of the lidar return signals since they do not give a unique solution of the lidar equation for the backscattering coefficient and the attenuation coefficient when they arise from an unknown distribution of size and shapes.[16]

Two additional pieces of information have been investigated to aid in distinguishing between molecular and aerosol scattering, viz., the specifically molecular information inherent in Raman scattering and the doppler spectrum of the on-frequency backscattering, as pointed out by Schotland.[4] The latter method depends on the difference in the doppler[4] spectrum of air molecules and the much heavier and, on the average, slower, aerosol particles.

With these developments, the knowledge of the presence and opacity of atmospheric aerosol layers can be supplemented by further details of the nature of the aerosols, reducing the number and stringency of assumptions needed in an atmospheric model used to interpret the data.

In the real atmosphere, the variation of temperature, humidity, and composition observed by use of a point sensor shows inhomogeneity of passive additives that are carried along by the prevailing wind. To the degree that the structure of the eddies persists, they can be observed at two points separated by a known distance. Even in strong mixing conditions, the eddy structure remains recognizable for useful distances. Thus, by some kind of pattern recognition process, such as cross correlation, we can compare the signals at two points in the wind stream, determining velocity from the passage time of eddies.

Active and passive correlation methods have been effective in wind tunnels,[17,18] passive methods have been used in the field,[19] and active methods with searchlights have been studied by Newstein. Active wind sensing methods using lasers are under investigation by Derr and Strauch at ESSA Research Laboratories. There are many possible geometrical configurations of the crossed beam technique. Figure 4 shows a simple scheme used to test the method. It is, however, too cumbersome to use in practice, since the wind direction changes constantly. An alternative method is to use a coaxial transmitter and receiver (or closely coupled parallel axes) as in Fig. 5. The beam is conically scanned with sufficient frequency so that no turbulence crosses the cone unilluminated and with sufficiently high pulse repetition frequency so that the turbulent spectrum is properly sampled. The cone is divided into elements, and cross correlation between elements is used to detect the drift of turbulence across the cone. The height is determined by range gates. Obviously the data rate is high and would require special purpose data processing equipment, especially if off-frequency backscattering is also examined by a scanning monochromator. The latter device would allow the simultaneous determination of water vapor profiles by Raman backscattering as described below.

The simplest pattern recognition method is the cross correlation of the outputs of two sensors. However, examination of many records of passive and active signals from the atmosphere show that the interesting signals often occur in bursts[20] separated by long intervals of poor SNR. These signals occur when significant eddies pass through the beams and they represent the best indications of the mean wind. The cross correlation function is diluted by the intervening high noise record and the accuracy of its indication of wind speed is diminished. As a result an observer of the dual trace output of correlation crossed beam receivers can frequently, by eye, pick out the delayed signals and determine the delay and, hence, the wind speed (under circumstances where the truncated correlation function used as an estimate of the correlation function) has a very large uncertainty. A simple threshold has been found to be effective, but more sophisticated methods must be developed to optimize determination of wind speed under nonstationary conditions. Figure 6 shows some typical records of active, laser illuminated, cross-beam outputs. It can be seen in the part of the record containing the largest fluctuations that the output of receiver *B* is delayed by an average of 1 sec with respect to receiver *A*. Other parts of the record require a cross correlation analysis to determine wind speed, but such large fluctuations occur with great frequency when the wind is steady. This record was taken under light, variable wind conditions, from 0 km h^{-1} to 16 km h^{-1} in

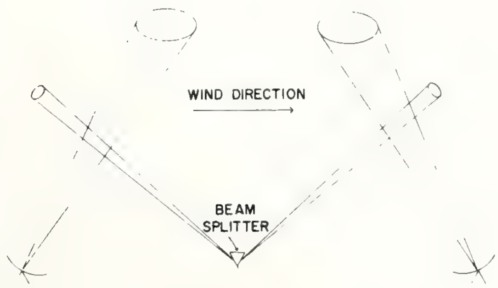

Fig. 4. Crossed beam wind sensing test configuration.

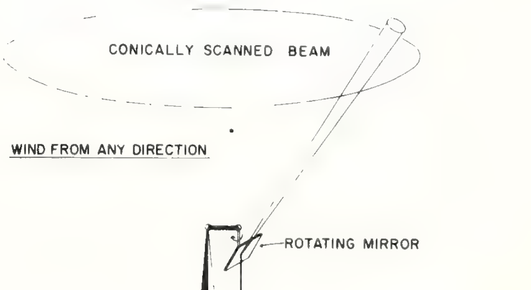

Fig. 5. Conically scanned wind sensing configuration.

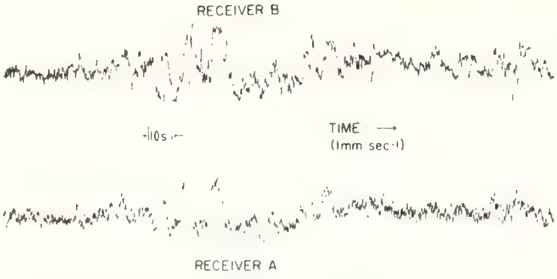

Fig. 6. Typical output of two receivers in the configuration of Fig. 2. Laser: Ar^+, 2 W at 488 nm, separation between cells, 4 m, wind 0–24 km h^{-1}.

the configuration of Fig. 4. The conditions when few features correlate by eye generally are almost calm.

The wind speed in the cross correlation method is determined by small fluctuations on the return signals caused by fluctuations in the atmospheric passive additives. This places severe restrictions on the tolerable power variation of the laser. These restrictions can be met by existing lasers. When it is nearly but not quite met, a differential system of comparison of output with return can be devised, although it is preferable to avoid this complexity. As has been pointed out above, an ultimate limitation on the range at which wind can be measured by correlation techniques arises from the unavoidable random fluctuations on the signal current of a photomultiplier. Even in the absence of background noise and dark current, if the signal is small (photon counting), the Poisson shot noise of the signal may mask the fluctuations of the atmosphere.

From Eqs. (13) and (14), we may determine the SNR and the maximum range on the assumption that S/N = 1:

$$R_{\max} = (\epsilon \eta N_t L A \beta')^{\frac{1}{2}}.$$

For three cases of interest see Table III.

The results in Table III are for a single pulse, with assumed values $\epsilon = 0.5$, $\eta = 0.2$, $N_t = 1.7 \times 10^{15}$ (10^5 W peak power, $\tau = 10$ nsec), $L = 10$ m, and receiver area $A = 2.84 \times 10^{-2}$ m^2. With integration of 100 pulses sec^{-1}, and somewhat larger collecting optics, it is clear that the chief limitation for tropospheric wind sensing will be background noise and noise of the intervening atmosphere, rather than signal shot noise. The discussion above of the effect of the intervening atmosphere is applicable to this case.

Owens[21] has reviewed the optical doppler measurement of wind velocity and has concluded that remote temperature measurement by doppler means is impossible, but that a 1-WAr^+ laser at 4880 Å would make it possible to measure the velocity of natural aerosols, smokes, and fogs from a few tens to a few hundreds of meters. Additional range can be achieved with more powerful cw lasers such as the CO_2 laser and Nd^{3+} laser. However, this method is too limited in range. Remote sensing by doppler means must probably await the creation of phase-coherent pulsed lidars. Developments along the lines of stable cw lasers with pulsed amplifiers may be the solution to the problem. Huffaker[22] has discussed laser doppler systems. The above analyses of signal and noise, and the discussion of doppler radar below, apply here with only minor modification.

Table III. Maximum Range for Wind Sensing

$R_{\max}$(m)	β' (m^{-1})	Interaction
1.3×10^3	3.72×10^{-8}	Raman (N_2)
3.1×10^3	2×10^{-7}	Rayleigh (N_2)
3.5×10^4	2.5×10^{-6}	Mie (sea level)

Besides the radiation scattered by atmospheric constituents at the frequency of the lidar transmitter, frequency-displaced signals are also received. These result from either Raman effects or fluorescence. As mentioned above, the spectral frequency of the Raman or fluorescence return signal is specific to the molecules interacting with the lidar radiation and can be used as a means of identification, unlike Rayleigh or Mie scattering. Specific cases of Raman scattering are summarized in Fig. 7. Here the number of signal photons received is shown as a function of range for several atmospheric components, and at the left side the sky background noise appears on the same ordinate scale. The rms values are the most significant, in the absence of saturation, since the average level can be filtered. The right side of the figure shows the detector dark noise from some selected photomultipliers. The graph can be used to determine the SNR of any gas with the same backscattering cross section as N_2 by reference to the ppm curves. The number of photoelectrons received is from a 10-m range increment. Thus one photoelectron per range increment is a counting rate of approximately 20 MHz. The graph has been computed for one pulse. Integration times of several hundred seconds are not unreasonable in applications. The transmitter characteristics shown are those of a commercially available pulsed nitrogen laser; the receiver has very modest dimensions, and could be improved.

An immediately obvious application of Raman lidar is to short range (~100 m) examination of the plumes of industrial smoke stacks. Several hundred ppm could be detected in a few minutes.

Water vapor in the atmosphere has been detected and a humidity profile determined to several thousand meters with ruby laser systems by a few minutes integration,[23,24] and this could also be done with the system described above. Figure 7 shows the importance of solar background noise in the lidar systems, which is not true for radar or acoustic sounding. Indeed with such a system only short ranges may be achieved in daylight. Of course the receiver may be improved by a larger collector; this helps only a little since, when background limited, the increase in signal is partially

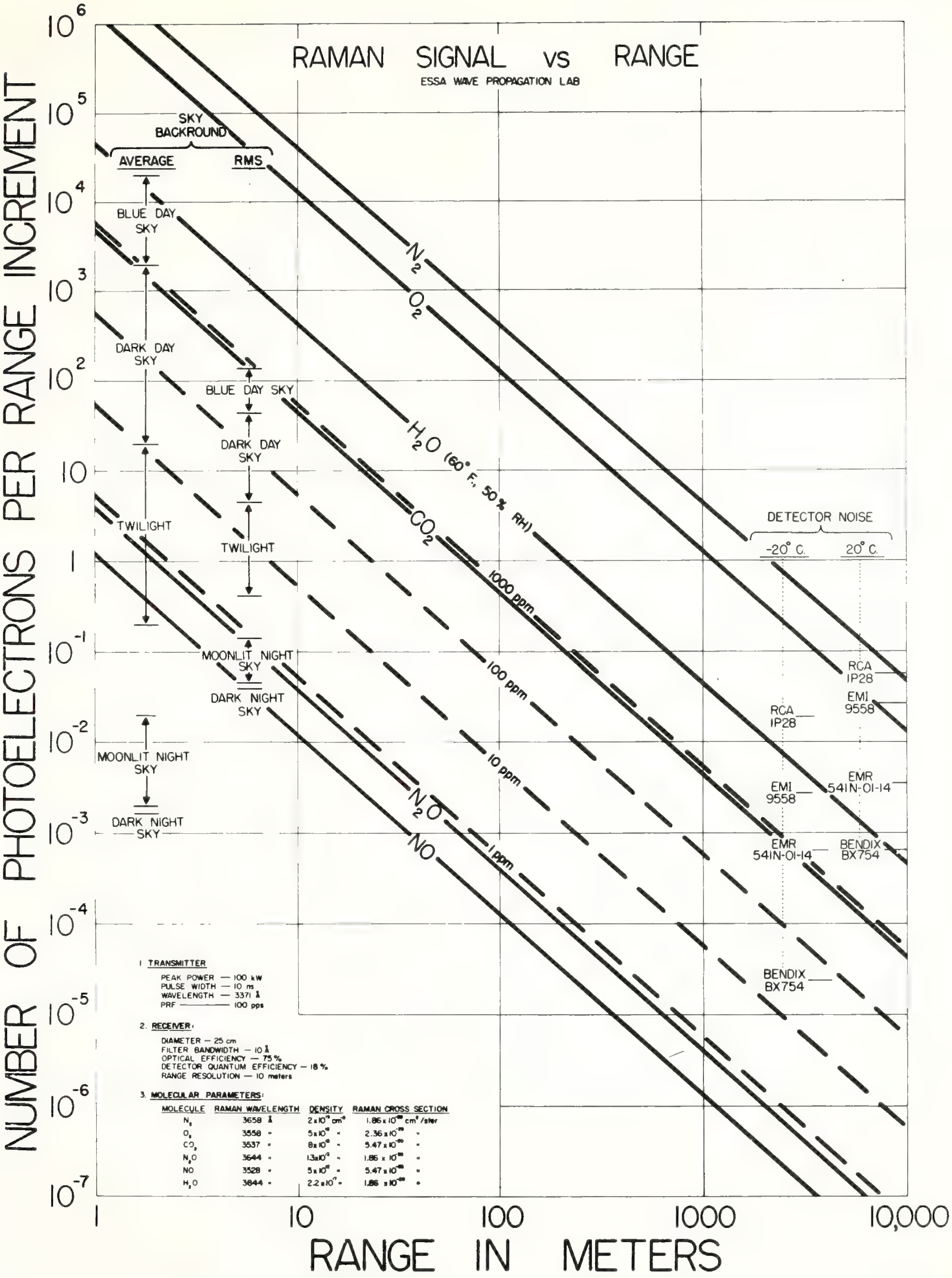

Fig. 7. Raman lidar signal vs range, and background and detector noise magnitudes. (Graph courtesy of G. T. McNice.)

offset by the increase in background noise. By Eqs. (13) and (14), the increase in SNR would be by a factor of the square root of the collector area increase, or by the increase in linear dimensions. A significant increase in SNR could be obtained by operating in the spectral region below 2900 Å, where the strong solar absorption by stratospheric ozone lowers the background noise to a level below that of the best detectors. This fact shows the importance for tropospheric sounding of the development of powerful, efficient lasers in the ultraviolet region below 2900 Å. Although now of great usefulness in tropospheric probing, the lidar will probably reach its ultimate usefulness only after such a development. The only alternative to use of short wavelengths is the production of very narrow-band filters, used in conjunction with stable, single-line lasers. It is not clear how to produce sufficiently narrow filters without the penalty of loss of throughput. Optical superheterodyne receivers may be an ultimate, but probably not an immediate, answer.

The use of the differential absorption of scattered laser energy to determine the vertical distribution of H_2O, and other atmospheric constituents has been discussed by Schotland.[4] By his technique, the difference in the returns from an absorption line and a nearby spectral region of low absorption is used. Shotland shows that the vertical profile of the atmospheric constituent can be calculated from

$$\rho(z) = \frac{1}{2\alpha}\frac{\partial}{\partial z}\ln\frac{N_r(\lambda_1,\beta,z)}{N_r(\lambda_2,\beta,z)},$$

where α is the absorption coefficient at the center of the abosrption line and $N_r(\lambda_1,\beta,z)$ is the number of photons received from range z at wavelength i. He also shows that the principal error arises from uncertainty in the line strength and shape and from the frequency instability of the tunable ruby laser. The noise from background and signal generated shot noise would be as discussed above in Eqs. (13) and (14).

The uncertainty in line strength and shape is not a trivial spectroscopic problem to solve, but will not be discussed here since it can, in principle, be entirely removed. The problem of the frequency stability of the laser is solvable by careful engineering of ruby lasers or the use of gas lasers. It is probable, however, that the tunable dye or parametric lasers, which can give much more information, should receive maximum effort. Thus, as these problems are solved, the differential technique will be useful for obtaining density profiles. A complete analysis of the comparison of this method with the Raman lidar is desirable, but not yet available. A special case of difference between returns for strongly absorbing regions in comparison with windows can be seen by comparing Figs. 2 and 3, in which the principal difference is the exponential absorption factor.

Figure 7 shows the futility of extending the Raman lidar systems to great ranges, such as would be required in satellite-to-ground observations where several hundred kilometers range would be needed. It is reasonable to inquire to what extent such systems can be improved. Improvements in peak power, average power, and pulse repetition frequencies will be achieved as a matter of course. Factors of twenty to one hundred are possible in laboratory designs. As has been pointed out, larger aperture receivers could be built, especially considering that precise image formation is not necessary. However, aside from these considerations, only the cross section for scattering might be improved.

The intensity of the Raman scattering is given by Eq. (2). This expression shows that aside from the frequency to the fourth power dependence of the intensity, there is a frequency dependence of the resonant denominators. In those cases where favorable frequencies may be used for illumination, considerable increase in cross section may be expected. The increase in the past has only been noted in the case of liquids, but recently a resonance has been found in water vapor, which increases the cross section several times over the ω^4 law. Resonances can only be effective near absorption lines. The pressure dependence of resonance Raman and the possible quenching at atmospheric pressure requires further study. Raman resonance studied in liquids has shown intensity increases of several orders of magnitude, but very little data are available for resonances in gases except for Cs_2, Rb_2, and Na_2.

The principal contribution to atmospheric pressure is from the oxygen and nitrogen content. Water vapor accounts for less than 1% of the mass in a column through the atmosphere. In a static atmosphere the pressure at ground level is due to the total mass of gas, and the minor departures from this in nonstatic situations can usually be ignored. The perfect gas law, $p = \rho RT/M$, where p is the pressure, ρ is the density, R is the universal gas constant, M is the molecular weight, and T is the absolute temperature, is locally applicable, but if ρ and p are known as functions of height then T is also known as a function of height h. But $p(h)$ can be obtained from the hydrostatic equation

$$P(h) = P_g - \int_0^h g\rho(z)dz,$$

if $\rho(z)$ can be obtained from the Raman lidar data. Thus we can calculate the temperature profile.

$$T(h) = \left[p_g - g\int_0^h \rho(z)dz\right] \Big/ (\rho(h)R/M),$$

where g is the acceleration due to gravity. The pressure at ground level p_g, can be obtained from a local barometer reading.

Since the errors of range measurement can be made small, the important source of error in determining the temperature arises from the errors in $\rho(z)$. Random and systematic errors in $\rho(z)$ will contribute in different ways to temperature errors. Random errors, assumed of zero mean, are serious when the term $\rho(h)$ in the denominator is small. Systematic errors will contribute to the integral of the density more than to the density term in the denominator. As a measure of the error in the calculated temperature, we can calculate the variance of the temperature, σ_T^2. The variance of

$$I = \int_0^h \rho(z)dz$$

can be shown to be much less than the variance of $\rho(z)$ under time–bandwidth conditions normally true for lidar systems, and hence can be ignored. Under this condition it is easily shown that

$$\sigma_T^2/\langle T\rangle^2 = \sigma_\rho^2/\langle\rho\rangle^2,$$

where σ_ρ^2 is the variance of ρ and the brackets indicate ensemble averages. Each of the quantities in this equation is a function of time (or range). We may most easily obtain some numerical results by assuming an exponential falloff for the density, i.e., $\rho(z) = \rho_0 e^{-\lambda z}$. If we choose $p_g = 1.013 \times 10^6$ dyn cm^{-2}, $\rho_0 = 1.77 \times 10^{-3}$ g cm^{-3}, then for $z = 1$ km, $T = 295.6$ K. Simulating an inaccuracy in ρ, if we replace $\rho(z)$ by $\rho(z) + 10^{-2} \times \rho(z)$, T changes to 292.3 K; if $\rho(z)$ is replaced by $\rho(z) + 0.09\ \rho(z)$, T changes to 268.2 K. Only if the measurement of ρ is accurate to better than a few percent is this method of temperature measurement very useful in tropospheric probing.

Introducing the determination of composition by absorption and by Raman scattering above, we did not include the effects of aerosols. When aerosols, producing Mie scattering, are present, there are more unknowns than equations, and the composition can be determined only by approximation or by the assumption of a relation between the unknown, based on an atmospheric model. Ignoring the Rayleigh scattering in comparison with aerosol scattering, we have

$$\frac{N_r}{N_\epsilon} = \sigma_A\rho_A(R)\cdot\epsilon\cdot\frac{A}{R^2}\cdot\exp\left\{-2\left[\int_0^R \rho_A(z)K_A dz\right]\right\}, \quad (15)$$

where σ_A is the average cross section of particles, $\rho_A(R)$ their number density as a function of range, and K_A is the total attenuation cross section of the particles. We do not know, *a priori*, the cross section of the aerosols as we do the cross sections of molecules; part of the problem is to determine the distribution, and hence the average cross section. Thus even if a relation between K_A and σ_A were available Eq. (15) contains two unknowns. A relation assumed between K_A and σ_A would allow the determination of $\sigma_A\rho_A(R)$. The possible variation of K_A with respect to σ_A is small and little error would occur in assuming such a relation. Figures 2 and 3 show that in ranges less than 10 km, the deviation from the correct scattered Raman return begins to occur only when the value of β_A is greater than 10^{-4} m^{-1}. That is, under conditions of light haze or worse, the aerosol will affect the Raman measurement. Further discussion of this point is given by Barrett and Ben-Dov[16] and Collis.[4] Cooney[25] has discussed the use of Raman lidar in distinguishing between gaseous and aerosol constituents.

The lidar permits us to determine the vector wind, to determine the presence and partly the composition of aerosol layers, cloud ceilings and their velocities, to determine the humidity and temperature profiles, and to specifically measure pollutant concentrations. The vector wind measurement has been demonstrated only to a few hundred meters but almost certainly can be extended to 4 km. Aerosol layers have been observed to 90 km and perhaps further. Humidity profiles have been determined to 2 km and can be extended to at least 5 km. Temperature profiles depend on the accuracy of Raman returns. Pollutants have been observed in smoke stacks at the 100-ppm level at ranges of several hundred meters. The ultimate potential of the lidar remote sensing methods is not completely known, partly because of the uncertainty in laser development, but mostly because the necessary knowledge of atmospheric characteristics, particularly fluctuations, is not available. Indeed, the methods of remote sensing are probably the only practicable means to obtain the data necessary for a final evaluation.

An efficient method of using the many advantages of lidar systems is to mount the transmitter and receiver coaxially or with parallel axes and to scan conically as in Fig. 5. By cross correlation between elements of the cone, the vector wind could be determined. Range gating determines the altitude, and examination of the spectrum can determine composition. Since range, angular, and spectral data will be obtained at a high rate, it will be desirable to perform data analysis and information compression at such a device before its output is sent to a central computer.

Radar Capabilities

Many years of development effort on ultrasensitive radars in the wavelength range from 0.86 cm (T PQ-11) to 71.5 cm (Wallops Island) have resulted in systems that can detect single targets with cross sections smaller than 10^{-5} cm^2 (TPQ-11) at ranges of 1 km. In this section, since adequate references exist, we briefly review the capabilities of three types of radar: the ultrasensitive pulsed radar,[26] the ultrahigh resolution FM-cw radar described by Richter,[27] and the doppler radar system under development by Lhermitte.[4] Because of the advancement of the science of radar meteorology, it is now possible to describe applications to meteorological problems. Characteristic cross sections of echoes can be obtained by calibrated radars, allowing a partial identification of targets. Use of multifrequency radar increases the certainty of identification by observation of the frequency dependence of the cross sections. Extensive studies of dot angles, the point targets on PPI radar scopes, has shown they are almost certainly due to insects, birds, and particles of equivalent radar cross section. These tracer targets may be of importance in investigating jet streams and other phenomena. They can also serve to confuse measurements since the presence of relatively few insects may increase the backscattering by orders of magnitude.

Of major importance are radar measurements to determine the validity of the theory of clear-air echoes arising from variations of refractive index. The relationship between the radar reflectivity and the spectrum of turbulence in Eq. (3), and its relation to the refractivity structure constant in Eq. (5), has been well verified. Thus the radar reflectivity can be calculated for strong mechanical turbulence, from[26]

$$\eta = 0.38\alpha^2\epsilon^{\frac{2}{3}}\beta^{-2}\langle(dn/dz)^2\rangle\lambda^{-\frac{1}{3}},$$

where α is a constant, ϵ the rate of energy dissipation, β the vertical gradient of the mean horizontal wind, $\langle dn/dz\rangle$ is the mean vertical gradient of refractive index. These reflectivities are usually in the range 10^{-16} to 10^{-14} cm^{-1} for high gradient inversion.

The FM-cw radar described by Richter and Atlas *et al.*[29] has very high range resolution, of the order of 1 m, compared with the 100–200 m of the Wallops Island radars. For this range resolution the minimum detectable value of C_n at a range of 1 km is 7×10^{-9} m$^{-\frac{1}{3}}$, corresponding to a value of C_T of 7.5×10^{-3}km$^{-\frac{1}{3}}$, or value of C_e of 4.6×10^{-3} mbar m$^{-\frac{1}{3}}$. With this sensitivity and range resolution, thin scatter layers may be precisely probed.

This unique radar achieves its high resolution by the use of a sweeping frequency and a narrow band receiver which detects the beat frequency between the previous radiated and reflected frequency f_1, and the frequency f_2 of the transmitter at the time of the return. The spectrum analysis of the beat frequency is performed by a narrow bandwidth spectrum analyzer. It has been shown by Richter that the resolution is inversely proportional to the bandwidth of the transmitted signal. The high sensitivity is achieved because of the very narrow bandwidth of the receiver. The noise $KT\Delta f$ is limited in the system described by Richter by $\Delta f = 30$ Hz instead of the several megahertz needed by pulsed radars. An important characteristic of FM-cw radars is their relatively low cost, many millions of dollars less than high power pulsed radars. Their chief disadvantages are the loss of resolution in long range operation and their insensitivity to particles below 10 μm in diameter.

In addition to conventional radar techniques that have been used in the study of atmospheric phenomena, doppler radar techniques have been developed in recent years for the study of atmospheric microscale and mesoscale atmospheric phenomena.[28,30] The pulsed doppler radar provides both ranging and radial velocity information from distributed targets consisting of randomly distributed scatterers, such as raindrops, snow, hail, or chaff. Thus, the radial velocity field can be mapped in radial space with altitude, azimuth, and time as parameters. As pointed out by Lhermitte,[4] the use of a multi-unit doppler radar system will allow the investigation of the three-dimensional field of particle motion inside convective storms. Thus, the fundamental dynamic inner processes of the storm can be observed as a function of time. By the detection of the large velocities associated with tornadoes the doppler radar gives promise of early warning. Sufficiently powerful transmitters would offer the possibility of mapping hurricanes and other tropical disturbances over wide areas in order to observe the large-scale processes associated with their formation and motion. Since the doppler radar depends strongly on the presence of hydrometeors or other target matter, its principal uses are not in the clear atmosphere. However, aerosols and insects in the clear atmosphere occur with sufficient frequency to make it a useful instrument for clear air research, or on those many occasions when the atmosphere is partly clear and partly stormy.

Atlas[30] and Lhermitte* have reviewed the basic theory and meteorological applications of the doppler radar; hence only a summary will be presented here. Lhermitte[28] has shown that the amplitude of the doppler radar return is proportional to

$$A(t) = \sum_i a_i \cos(\omega + \omega_i)t,$$

and that its intensity is proportional to

$$I(t) = \sum_i a_i^2 = 2\sum_{ij} a_i a_j \cos(\psi_{ij}t),$$

where $\Sigma_i a_i^2$ is the sum of the intensities of the individual scatterers and is proportional to the total reflectivity. The time-varying term contains the difference frequencies $\omega_i - \omega_i = \Psi_{ij}$. The difference in velocity of the two scatterers $V_i - V_j = (f_i - f_j)\lambda/2$, where λ is the radar wavelength. If, as is the case in a coherent radar, some portion of a stable local oscillator of frequency ω is heterodyned with the return from the target, the difference frequencies $(\omega_1 - \omega)$ will give a measure of the absolute (radial) velocity. In practice the spectra of the radar returns are obtained and the velocity spectrum deduced therefrom. If $f = 2\,v/\lambda$, then the spectra are related by $S(f)df = S(v)dv$, giving the radial velocity distribution within the resolution cell, an estimate of the number of particles in a velocity interval, and the intensity of the return by particles of velocity v. Lhermitte has applied fast fourier transform alogrithms to produce the spectrum of the radar signals and has shown that acceptable observational speed can be obtained from range resolution of a few hundred meters, with a 1° beam width, and a beam dwell time of 0.5 sec.

The doppler radar technique has potentially excellent SNR characteristics. Within tropospheric distances, its minimum detectable cross sections may be as low as 10^{-6} cm^2. However, portable field units will sacrifice some power and antenna size. The phase noise due to the stable local oscillator may be so small that the doppler SNR may easily exceed 50 dB (Lhermitte[4]).

Measurement Potential of Acoustic Echo Sounding

The monostatic radar equation for acoustic waves may be written as

$$P_r = P_T\sigma_{180}(C_T/2)(A_r/R^2)\alpha_T\alpha_R \exp[-2\int \alpha(r)dr],$$

---

* See additional references in Lhermitte, Ref. 4.

where P_r is the received electrical power, P_T is the input electrical power to the transmitting element, α_T is the transducer transmission efficiency for the conversion of electrical power to acoustic power and α_R the transducer reception efficiency for the conversion of acoustic power to electrical power, τ is the pulse length, C is the velocity of sound, R is the range, A_r is the effective collecting area of the antenna, and $\alpha(r)$ is the acoustic attenuation at the radar frequency as a function of range, r, and σ_{180} is the radar cross section* per unit volume per unit solid angle in the backscatter direction (i.e., scatter angle $\theta = 180°$).

The noise level against which the acoustic echoes have to be detected depends strongly on location and frequency. Under favorable circumstances, with a directional acoustic antenna aimed overhead from a low noise site, noise levels of about 15 dB above the minimum theoretical noise level of KTB (K = Boltzmann's constant, T = absolute temperature, and B = observing bandwidth) have been measured by Wescott (private communication) at a frequency of 2000 Hz. With reasonable system components, e.g., $P_T = 10$ W, $\alpha_T = \alpha_R = 0.25$, $\tau = 100$ msec, $A_r = 1$ m^2, $B = 10$ Hz, and $R = 1000$ m, and assuming that the round trip absorption is 10 dB, a SNR of unity would occur for a $\sigma_{180} = 3.1 \times 10^{-13}$ m^2/m^3.

The corresponding value of C_n for $f = 1000$ Hz, $\lambda = 0.34$ m given by Eq. (5) is

$$C_n = 2.6 \times 10^{-6}\ \mathrm{m}^{-\frac{1}{3}}.$$

From Eq. (7) we see that for acoustic waves (assuming only temperature fluctuations are present)

$$C_n = C_T/2T.$$

Using this fact, we see that the value of C_T required to give unity signal to noise at a range of 1 km is

$$C_T = 2TC_n \approx 1.6 \times 10^{-3}\ \mathrm{K\ m}^{-\frac{1}{3}}.$$

In other words, unity SNR or higher would be expected, provided the echo volume (of depth $\sim$ 17 m) was filled with turbulent temperature fluctuations so that the rms difference for two points 1 m apart was 1.6×10^{-3} K. This almost certainly would be the case, and therefore echoes would be expected more or less continuously in time, out to a range of at least 1 km. This very high sensitivity is attributable both to the relatively strong interaction of acoustic waves with the atmosphere (see Table II) and the fact that the narrow receiving bandwidth permits detection of about one part in 10^{19} of the radiated power.

The above acoustic echo sounder sensitivity refers to the scatter from the temperature field only, as is appropriate for a monostatic system. For a bistatic system, the scatter from the turbulent velocity field is usually dominant, and it is therefore important to compute the value of C_v which would be required to give an echo just equal to noise.

If we assume that the effective scattering volume is still given by $C\tau/2$ (an approximation which tends to underestimate the echo strength actually received) a bistatic system having the above characteristics will receive an echo power given by

$$P_r = 4.25 \times 10^{-6}\sigma(\theta).$$

If we further assume that the temperature fluctuations are negligible, Eq. (11) reduces to

$$\sigma(\theta) = 0.030k^{\frac{1}{3}} \cos^2\theta \cos^2\tfrac{1}{2}\theta(\sin\tfrac{1}{2}\theta)^{-\frac{11}{3}}/(C_v/C)^2.$$

For $\theta = 60°$ and $\theta = 120°$, we obtain

$$\sigma(60°) = 0.090k^{\frac{1}{3}}(C_v/C)^2.$$

and

$$\sigma(120°) = 0.053k^{\frac{1}{3}}(C_v/C)^2.$$

Based on the same effective receiver noise power (15 dB above KTB), the background noise power against which the echo must be detected is given by $P_n = 1.33 \times 10^{-18}$ W.

Equating the received echo power with the background noise power (the condition for a just detectable echo), we have

$$C_v = 6\ \mathrm{mm\ sec^{-1} m^{-\frac{1}{3}}} (\theta = 120°),$$

and

$$C_v = 3.5\ \mathrm{mm\ sec^{-1} m^{-\frac{1}{3}}} (\theta = 60°).$$

In other words, unity SNR or higher would be expected provided the common echo volume is filled with turbulence so that the rms difference in velocity for two points 1 m apart exceeded 3.5 mm/sec (for a scatter angle of 60°) or 6 mm/sec (for a scatter angle of 120°). This almost certainly would be the case, and on a bistatic system (except for the $\theta \approx 90°$) one would therefore expect echoes from the velocity field more or less continuously in time, out to a range of at least 1 km.

Given, then, that acoustic echoes can be obtained more or less continuously in height and in time out to a range of about 1 km, we may ask what atmospheric information can be derived from these echoes. This point has already been discussed[31]; it is elaborated on below.

Measurement of Vertical Profiles of the Intensity of Small Scale Temperature Fluctuations, i.e, of the Intensity of Optical Refractivity Fluctuations

Profiles of the intensity of small-scale temperature eddies can be automatically obtained with a vertically directed monostatic echo sounder. In this case, $\theta = 180°$ and Eq. (11) reduces to

$$\sigma_a(\theta) = 3.9 \times 10^{-3}k^{\frac{1}{3}}(C_T/T)^2.$$

Measurement of echo power vs height, after correction for the (range)^2 divergence of the beam and the atmospheric absorption of the acoustic waves, will therefore permit us to derive $(C_T{}^2/T^2)$ as a function of height. But the structure function of optical refractive index C_n is given by

---

* The symbol is changed from that used for the equivalent quantity in previous sections to conform to the terminology frequently used by meteorologists.

$$C_n^2 = (79P/T \cdot 10^{-6})^2 C_T^2/T^2.$$

Since the variation of pressure and temperature with height can usually be well estimated from climatological records, the measurements of $(C_T/T)^2$ as a function of height may therefore be immediately translated into measurement of $C_n^2(h)$. This capability is of considerable potential importance to optical propagation, since the sensitivity of the measurement ($C_n^2 \geq 2 \times 10^{-18}\ \mathrm{m}^{\frac{2}{3}}$) and the scale sizes involved (one-half the acoustic wavelength) are directly relevant to the optical scintillation problem.

Measurement of Verticle Profiles of the Mean Wind

Acoustic echo sounding offers the potential of three independent methods of measuring the wind profile. These methods are independent because they make use of three different parameters of the echoes: the frequency spectrum, the angle of arrival, and the temporal distribution of the echo pattern across the ground.

The first method relies on the transport by the mean wind of the fluctuations in the refractive index responsible for the acoustic echoes. The component of this motion along the phase normal will result in a doppler frequency shift given by $\Delta f = 2V_r/\lambda$, where V_r is the radial component of the wind speed and λ is the acoustic wavelength. By measuring in different directions, the mean horizontal and vertical velocities can be deduced, as shown for short ranges by Kelton and Bricout.[32]

A second method relies on the refraction or bending of the acoustic beam as it traverses a region of changing wind speed. The received echo in general will return from a direction somewhat different than the transmitted beam; it can be shown that measurements of the angle of arrival of the received signal relative to that transmitted are proportional to the transverse component of the wind, integrated up to the height of the echoing region. To obtain the height profile of the mean wind, it would be necessary to differentiate these angle measurements with height; this feature is likely to reduce the accuracy of the method relative to the doppler technique which measures the radial component of the velocity directly.

The third method makes use of time-lagged cross correlation analysis of spaced sounding measurements. Preliminary examination of such measurements, taken by Little and Wescott during a cooperative experiment with the Australian workers McAllister and Pollard, indicate that the time lags between spaced soundings can be clearly identified, suggesting that this method should be directly applicable. By studying the variation of the time delays for optimum cross correlation as a function of height, it should be possible to derive the height profile of wind speed and direction.

Measurement of the Turbulence Profile, and the Spectrum of Turbulence

Three different approaches to the measurement to height profiles of the intensity of turbulence appear feasible, and once again these are also essentially independent.

With the doppler technique the mean radial component of scatterers within the pulse volume is measured. The variability of this velocity at a fixed range is a measure of the intensity of the turbulence at that height. Moreover, comparisons of the radial velocities of different pulse volumes along the acoustic beam could be used to derive the structure function of the velocity, given by

$$D_{rr}(r) = \langle [V_r(r_1) - V_r(r_1 + r)]^2 \rangle_{\mathrm{ar}}.$$

A second approach is to make use of both monostatic and bistatic measurements simultaneously. As indicated above, bistatic measurements include contributions from both the velocity (turbulence) field and from the temperature field, while monstatic measurements are indicators of the temperature field only. Simultaneous monostatic and bistatic measurements should therefore permit us to identify the height variation of the intensity of both temperature and velocity fluctuations.

A third method relies on the detailed analysis of spaced sounding data. As shown by Briggs *et al.*[33] it is possible to derive information on the relative magnitude of the mean and the fluctuating components of the velocity from a detailed comparison of the fading records at spaced receivers. With different spacings of receivers, it should be possible to derive information on the magnitude of the turbulence of different scale sizes. Further discussion of spaced soundings is given by Gossard and Sailors.[34]

Measurement of Humidity Profile

The possibility of using multifrequency echo sounding to derive the vertical profile of humidity has been pointed out by Little.[31] The method makes use of the known dependence of acoustic absorption on humidity and temperature, and like the angle-of-arrival method of determining the wind profile requires the differentiation of what are basically integral measurements in order to derive the height profile.

Measurement of the Internal Structure and Dynamics of the Boundary Layer

As shown by McAllister[35] and his colleagues, acoustic echo sounding may be used to study the dramatic changes in the structure of the boundary layer of the atmosphere. Thermal plumes, radiation inversions, gravity waves, and breaking waves may all be identified and studied in this way.

The acoustic echo-sounding technique has several inherent limitations, where magnitude is not yet known, but whose existence should be mentioned.

The most fundamental limitation is that of absorption of the acoustic waves by the atmosphere, and especially the anomalous absorption due to water vapor. The primary effect of this absorption is to limit the useful range of echo sounding, especially at the higher frequencies. This limitation is a function of both frequency and atmospheric conditions, and to a major extent excessive anomalous absorption can be compensated for by the use of lower frequencies. Operation to ranges of the order 1 km are certainly feasible; however, ranges of the order 10 km are not likely to be attainable except under unusual circumstances.

A second limitation is the effect of adverse weather conditions upon the ambient acoustic noise level. Strong winds, hail, and rain will increase the noise level registered by the receiving antenna, with resultant degradation of system performance. Careful design of the antenna housing could presumably reduce these effects.

The problem of excessive interference to, or from, human activity in the area around the sounder does not at this time appear to be a serious problem. While it is obvious that optimum performance will always be obtained in very low noise environments; the use of very directional acoustic antennas, with excellent sidelobe rejection, will greatly reduce adverse interactions with surrounding activities.

Other difficulties perhaps unique to acoustic echo sounding include the refraction of the beam by wind or temperature gradients. In general, it should be possible to compute the effects of such refractions, and so the net effect is likely to be one of increased analytical complexity rather than one of serious limitations. Similarly, the interaction of acoustic waves with the turbulent atmosphere is so strong that scintillation effects set in rapidly, and narrow beams will tend to diffuse into wider and wider cones. Again, these effects should be calculable (at least to the first order) and should not present a primary limitation.

Summary of Capabilities and Limitations

The three remote clear atmosphere probing techniques discussed above have the greatest potential of any known active monostatic methods for revealing new information on the clear atmosphere and aiding in the development of the science of its structure and dynamics. Because of their unique features they form an almost complete means of tropospheric probing. Not only do they offer us the ability to measure vertical profiles of the three primary meteorological parameters of wind, temperature, and humidity, but as the full potential of these remote sensing techniques is realized the temporal and spatial variation of the spectrum of these variables should become available. In addition to studying the properties of the gaseous components of the atmosphere, the distribution, intensity, and dynamics of precipitation, clouds, and aerosol particles are also potentially available for study.

Because of specific molecular interaction, lidar has the unique capability of identification of atmospheric gases. As tunable lasers become available it will be possible to discriminate against increasingly dense aerosol conditions. The wind sensing capability of lidar has been demonstrated, but, at present, the ultimate range is uncertain. Since it depends on aerosol concentration it is particularly useful in polluted atmospheres. Whether optical doppler methods will provide extended range is unclear at this time. Lidar wind sensing and acoustic doppler wind sensing are both under development, and the most practical method in clear air is uncertain.

Turbulence measurement by lidar depends on the presence of aerosols. The lidar has good range and volume resolution but little interaction with the clear air. On the other hand, acoustic and radar techniques are most sensitive to the index of refraction variations of the atmosphere and are useful in detailed studies of layering, instabilities, and wavelike structures of the atmosphere insofar as these are accompanied by refractive variations. The index of refraction in the radio region is affected principally by water vapor; in the acoustic regime the main effect is due to temperature. Thus simultaneous measurements of the same phenomena by these two techniques would separate temperature and humidity turbulence.

Absolute temperature and pressure profiles are possible by lidar probing, since the density profiles can be determined. Neither radar nor acoustic probing offer this opportunity.

The maximum ranges of each method are adequate for tropospheric probing. The range resolution of the lidar is due to its very short pulse width; these can be shortened to considerably less than 1 m if desirable. Among the radars, the FM-cw has the bandwidth to achieve 1-m resolution and the acoustic echo-sounder can also achieve that.

The lidar is at present seriously limited by background noise from scattered sunlight, but development of higher frequency lasers will solve this for the troposphere. Acoustic techniques are hampered by the natural noise of the atmosphere and man-made interference. Careful choice of location and antenna sidelobe reduction are required. The radars are little affected by background noise other than ground clutter.

In cloud ceiling measurement the lidar is the best choice. Radar, at properly chosen wavelengths can be used. The acoustic technique probably is not useful. Radar and acoustic sounding have significant cloud penetration capability, the lidar has little in thick clouds. Acoustic sounding could locate the top of fog banks from within, by observation of temperature discontinuities.

Use of the Three Methods in Large-Scale Meteorological Experiments

The objective of large-scale meteorological experiments is to gain greater insight into the dynamical and physical processes of the atmosphere by the concerted application of a variety of experimental means and theoretical analysis. In the past the collection of the large volume of detailed tropospheric data has been entrusted to sondes, rockets, balloons, aircraft, and to passive radiometry. Economic limitations have prevented, and doubtless always will prevent, the most desirable density of coverage. Radarlike devices can perform nearly point measurements or volume measurements with sufficiently high scanning frequency that essentially continuous data can be obtained. Programming the scan so that portions of the coverage in which little change occurs are scanned less frequently than portions in which interesting events occur can lead to great economy of data processing.

The variability of some atmospheric data can cause deceptive averages. In an ocean or wherever much evaporative flux is being balanced by precipitation over wide areas, the determination of the net flux has been best achieved by aircraft flying set patterns. However, the net flux can be very small compared with the local variation of flux. Thus, large volume accurate measurements are a necessity, for definitive large scale meteorological experiments. As these methods develop, their use in such experiments can be expected to grow.

Conclusions

Large scale meteorological experiments such as the Bomex experiment have shown that data obtained in great density over large areas can lead to important new knowledge of the atmosphere and the ocean. The value and efficiency of such experiments can be greatly enhanced by the use of remote sensing methods. The development of radar, acoustic radar, and lidar to their ultimate potential is justified by their current status and by the need for their use in atmospheric studies. The present advanced state of development of radar has been the result of thirty years of effort. Even a small portion of such effort on acoustic echo-sounding and lidar will undoubtedly result in substantial progress. With regard to lidar, the development, by analogy with radar, of the techniques of great stability, heterodyning, and tunability of sources are certain to add to potential uses. The most pressing immediate needs for the lidar technique are tunable lasers operating below 2900 Å and receivers capable of spectral discrimination with large apertures. The development of doppler velocity measuring methods and more efficient directional antennas are the most pressing needs for the acoustic echo-sounding techniques.

Aside from a few atmospheric scientists interested in remote probing, the development of remote sensing methods, electromagnetic and acoustic, has been, in the main, the interest of those involved in wave propagation studies and the interaction of the atmosphere with radiation. As the trustworthiness of the remote sensing methods is demonstrated, significant experiments must be designed and priorities established.

It is apparent from the preceding analysis that the combination of radio, optical, and acoustic sounding techniques offers a very effective facility for the study of atmospheric problems.

The authors wish to thank G. T. McNice, R. G. Strauch, B. Bean, R. Lawrence, R. M. Lhermitte, S. Clifford, and R. Schwiesow, ESSA Research Labs., for many enlightening discussions on the subject matter of this article, and to thank D. Leonard, AVCO Everett, for data on cross sections and discussions of the use of Raman lidar in smoke stack gas analysis. J. Cooney, National Center for Atmospheric Research, has been especially helpful in discussions of the techniques of lidar.

References

1. K. Ya. Kondratyev, *Radiation in the Atmosphere* (Academic, New York, 1969).
2. C. Junge, *Air Chemistry and Radioactivity* (Academic, New York 1963).
3. L. Elterman, Environmental Research Papers, No. 46 (Air Force Cambridge Research Laboratories, AFCRL-64-740 1964).
4. Final Report of the Panel on Remote Atmospheric Probing to the Committee on Atmospheric Sciences, *Atmospheric Exploration by Remote Probes, Vol. 2* (National Academy of Sciences, Washington, D.C., 1969).
5. K. Sakurai and H. P. Broida, J. Chem. Phys. **50,** 2404 (1969).
6. D. Leonard, AVCO Corp., Everett, Mass. (private communication).
7. G. Herzberg, *Molecular Spectra and Molecular Structure, Vol. 2 Infrared and Raman Spectra of Polyatomic Molecules* (Van Nostrand, Princeton, N. J., 1960.)
8. S. Mizushima, in *Handbuch der Physik*, 26–27, S. Flügge, Ed. (Springer-Verlag, Berlin, 1958).
9. H. A. Szymanski (Ed.), *Raman Spectroscopy* (Plenum Press, Inc., New York, 1967).
10. V. I. Tatarski, *Wave Propagation in a Turbulent Medium,* (Dover Publ., Inc., New York, 1967).
11. R. Bolgiano, Jr., Proc. IRE **47,** 331 (1959).
12. B. R. Bean and E. J. Dutton, *Radio Meteorology* (Dover Publ., Inc., New York, 1966).
13. G. Fiocco and L. D. Smullin, Nature **199,** 275 (1963).
14. C. K. N. Patel, Bull. Amer. Phys. Soc. **15,** 505 (1970).
15. R. S. Lawrence and J. W. Strohbehn, Proc. IEEE, to be published Sept. 1970.
16. E. W. Barrett and P. Ben-Dov, J. Appl. Meteorol. **6,** 500 (1967).
17. F. R. Krause and M. J. Fisher, Proc. ASME Symp. 171, (1966).
18. M. J. Fisher and F. R. Krause, J. Fluid Mech. **28,** 705 (1967).
19. F. R. Krause, V. E. Derr, N. L. Abshire, and R. G. Strauch, Proc. 6th Int. Symp. Remote Sensing Environ. **1,** 327 (1969).
20. J. A. Dutton, J. A. Lane *et al.* Radio Science **3,** 1357 (1969).

21. J. C. Owens, Proc. IEEE **57,** 530 (1969).
22. R. M. Huffaker, Appl. Opt. **9,** 1026 (1970).
23. J. Cooney, J. Appl. Meteorol. **9,** 182 (1960).
24. S. H. Melfi, J. D. Lawrence, and M. P. McCormick, Appl. Phys. Lett. **15,** 295 (1969).
25. J. A. Cooney, Appl. Phys. Lett. **12,** 40 (1968).
26. K. R. Hardy and I. Katz, Proc. IEEE **57,** 468 (1969).
27. J. H. Richter, Radio Science **4,** 1261 (1969).
28. R. M. Lhermitte, in *Proc. 8th Weather Radar Conf.* (Amer. Meteorol. Soc., Boston, 1960), p. 269.
29. D. Atlas, J. H. Richter, and E. E. Gossard, Tech. Rep. No. 13, Laboratory for Atmospheric Probing, Dept. of Geophysical Sciences (University of Chicago Press, Chicago, 1969).
30. D. Atlas, Advan. Geophys. **10, 317** (1964).
31. C. G. Little, Proc. IEEE **57,** 571 (1969).
32. G. Kelton and P. Bricout, Bull. Amer. Meteorol. Soc. **45,** 571 (1964).
33. B. H. Briggs, G. J. Phillips, and D. H. Shinn, Proc. Phys. Soc. **63,** 106 (1950).
34. E. E. Gossard and D. B. Sailors, J. Geophys. Res., Space Phys. **75,** 1324 (1970).
35. L. G. McAllister, J. R. Pollard, A. R. Mahoney, and P. J. R. Shaw, Proc. IEEE **57,** 579 (1969).
36. C. M. Harris, J. Acoust. Soc. Amer. **40,** 148 (1966).

51

Reprinted from ESSA Technical Report, ERL 168-WPL 12, 1970.

REMOTE SENSING OF THE WIND PROFILES IN THE BOUNDARY LAYER

C. G. Little, V. E. Derr, R. H. Kleen, R. S. Lawrence,
R. M. Lhermitte, J. C. Owens, and G. D. Thayer

The present report is an analysis, with recommendations, of the various remote-sensing concepts that could be used for the sensing of wind profiles in the boundary layer. The report is divided into four main sections. The first of these deals with the Doppler "radar" technique as it might be utilized with acoustic, radio, and optical waves; a hybrid system involving the (spatially) resonant interaction between radio waves and powerful acoustic waves is also discussed. The second section deals with acoustic, radio, and optical forward-scatter or line-of-sight propagation techniques. The third technical section deals with the so-called crossed-beam eddy correlation technique (using either passive or active sensing of the eddies).

The report then turns to a summary of the relative potential of each of these techniques for wind-sensing in the boundary layer and concludes with recommendations relative to the two techniques considered most promising.

Reprinted from Radio Science 5, No. 7, 1017-1028, 1970.

D-region electron temperatures at the northern auroral zone

G. M. Lerfald and C. G. Little

ESSA Research Laboratories, Boulder, Colorado 80302

(Received February 19, 1970.)

To determine the approximate temperatures of free electrons in the sunlit ionospheric *D* region an experiment was conducted at a site near College, Alaska, during the summer and fall of 1960. A dual polarized antenna whose beam was directed at the zenith was used to observe alternately the incident radio noise fluxes in the ordinary and extraordinary polarizations at the frequency 2.89 MHz. The 2.89-MHz radio noise flux measured on a vertical dipole antenna was used to check for propagated interference from low elevation angles. The results show that, during the five-month observing period, the extraordinary-mode antenna registered a median daytime temperature of 260°K, with a standard deviation of about ±23°K, which indicates that the electrons in the *D* region are approximately in thermal equilibrium with the neutral gas, even at the auroral zones. The theoretically anticipated antenna temperatures, based on assumed ionospheric parameters, agree fairly well with the observed experimental values. In particular, the observed variations of antenna temperature with solar zenith angle can be matched by use of reasonable theoretical models.

INTRODUCTION

Pawsey et al. [1951] used zenith-directed antennas at frequencies near 2 MHz to observe the thermal noise emitted by the lower ionosphere and demonstrated that *D*-region electron temperatures can be derived from such measurements made during the daytime. *Gardner* [1954] conducted additional observations and strengthened the conclusion of *Pawsey et al.* [1951] that, at least at temperate latitudes, the electron temperatures remained approximately equal to the neutral-gas temperatures. Other results, such as the radio-wave interaction experiments by *Smith et al.* [1965], have given additional strength to the latter conclusion.

It was natural to question whether or not the electron temperatures could be elevated above the neutral-gas temperatures by particle bombardment at the auroral zones. Two independent experiments were conducted to test this possibility: *Dowden* [1960] conducted observations on Macquarie Island near the southern auroral zone (geographic latitude 55°S, geomagnetic latitude 62°S), and *Little et al.* [1961] reported on measurements taken at College, Alaska, at the southern edge of the northern auroral zone (geomagnetic latitude 65°N, geomagnetic latitude 65°N). *Dowden*'s [1960] results showed that most of the derived electron temperatures were between 200° and 300°K, i.e., approximate equilibrium existed with the neutral gas. Some elevated temperatures during wintertime were attributed to leakage of cosmic radio noise that might have penetrated the *F* region near the south pole, where nighttime conditions prevailed, and propagated to the receiving site. The latter possibility was substantiated by *Little et al.* [1961], who observed during winter months at a geographic latitude about 10° higher than the latitude of Dowden's measurements. *Little et al.* [1961] measured higher noise temperatures on a vertical dipole than on a horizontal dipole with its nulls directed north–south.

Copyright © 1970 by the American Geophysical Union.

A cross-modulation experiment by *Rumi* [1962] at College, Alaska, yielded an electron temperature of 1200°K at a height of 40 km. *Belrose and Hewitt* [1964], using partial-reflections data, observed enhanced electron-collision frequency values correlated with solar activity at a 60-km height and suggested electron temperatures up to about twice the gas temperature as a possible explanation. *Belrose et al.* [1967] have since reported that electron collision frequencies at Ottawa were quite variable, and the cause for the variability was attribtued to meteorological pressure changes. [See also *Belrose,* 1967]. *Sears* [1963] has presented a theoretical paper with assumptions that support the possibility that electron temperatures higher than 1000°K could be maintained in the lower *D* region during auroral events.

On the other hand, *Dalgarno and Henry* [1965] give a theoretical analysis of the question and conclude that any large (say, a factor of 2 or more) enhancement of the lower *D*-region electron temperatures over the ambient gas temperature would require a larger influx of energy than is expected during even the most intense auroral events. Other experimental evidence indicating that temperature equilibrium exists at the auroral zones is the result obtained by a number of rocket experimenters, including *Jespersen et al.* [1964], *Kane* [1961], and *Landmark and Lied* [1961], that collision frequencies in the 60–90 km height range are not enhanced, even during auroral absorption events. *Thrane and Piggott* [1966] and *Belrose and Bourne* [1967] have pointed out that the collision frequencies measured by aforementioned above rocket experiments agree well with those expected from meteorological rocket pressure data; this implies that electron temperatures remain in equilibrium with the neutral-gas temperatures.

The present paper describes observations taken at College, Alaska, during the summer and fall of 1960. The principal incentive for publishing the results now, more than 9 years after the data were taken, is the belief that they represent valid experimental evidence that bears on the 'not-quite-settled' question of electron temperatures in the *D* region at the auroral zones.

OBSERVATIONAL METHODS AND DATA REDUCTION

The observations were conducted at a low-noise site about 30 miles west of College, Alaska. The measurements were made with a circularly polarized 'turnstile' antenna connected so as to cause the receiver to sample alternately the right and left circular polarizations.

In addition, records were obtained by using a vertical antenna to test for the presence of low-angle propagated interference, especially cosmic noise that had penetrated nighttime areas of the polar ionosphere. (For a detailed discussion of this problem, see *Little et al.* [1961].) During the summer, propagated cosmic noise of this type was not observed.

Two records were obtained on each of the three polarizations: one through a minimum-level circuit, the second through a peak-detecting circuit. The latter channel was used to help identify the presence of impulsive interference, such as that due to atmospherics.

Figure 1 shows a typical record in which the antenna-noise temperatures in the two circular polarizations are displayed in sequence, together with calibration values at 310° and 410°K. A daily calibration was performed with a diode noise generator to give the sensitivities of the systems in degrees Kelvin per chart division over the range 310°–500°K. Occasionally a calibration point was made at 194.5°K by cooling a resistor with solid CO_2. Considerable care was taken to ensure that all antenna and calibrating resistor impedances, as seen by the receiver input circuit, were maintained equal to within a few tenths of an ohm.

Because of cable losses, the noise temperature T_a produced at the output of the antenna will be related to the recorded receiver input temperature T_r by the following relation:

$$T_r = (1 - \alpha)T_a + \alpha T_c \tag{1}$$

where α is the fractional power loss in the antenna cable, and T_c is the cable temperature. The cable losses were about 16% for the extraordinary mode and 22% for the ordinary mode. Under these conditions, an error of 5°K in the assumed cable temperature will introduce an error of about 1°K in the derived temperature. During the summer, the cable temperature assumed was the recorded noontime temperature at the observing site; for the late fall observations, the cable temperature was taken as 273°K, since it was buried by several inches of snow. A ground mesh with dimensions 1λ by 1λ was used below the 'turnstile' antenna.

Despite the presence of the wire-mesh ground plane, the effective ground reflectivity, and hence the antenna efficiency, may have been somewhat less than unity. The relation between the antenna temperature and the apparent ionospheric (integrated) temperature T' is given by the relation

$$T_a = \eta T' + (1 - \eta)T_g \tag{2}$$

where η is the antenna efficiency, and T_g is the ground temperature. Since the observed antenna temperature is usually within 40°K of the ground temperature (273°K), there is only about a 4°K error introduced in the derived antenna temperature by an error of 10% in the estimate of the efficiency. An antenna efficiency of 90% was assumed. The estimated total error (due to the simultaneous effect of uncertainties in the cable losses, antenna efficiencies, and calibration errors) in the derived ionospheric-noise temperatures is <20°K and is <10°K for temperatures in the range 250°–300°K.

During daylight hours, the ionospheric absorption was usually found to be sufficiently intense to permit continuous measurements of antenna-noise temperatures that were unaffected by distant atmospherics. Occasionally, transmitter interference was observed, and at times local weather conditions such as thunderstorm activity and precipitation static affected the records; whenever it was apparent that such interference was present, the records were rejected. All other daytime data were scaled and tabulated, even though unexpectedly high antenna temperatures (> 300°K) were sometimes recorded. Careful aural and oscilloscope monitoring and scrutiny of the records from the minimum and peak detectors showed that at least some of these high-level signals were indistinguishable from thermal noise, and, for these reasons, the values were included in our analysis.

A numerical value for the apparent (daytime) antenna-noise temperature on each circular polarization was obtained during each 12-minute cycle of the polarization switch by scaling the lowest temperature recorded during each cycle on each mode. Equations 1 and 2 were then used to correct the circularly polarized antenna temperatures for ground and cable losses. Hourly average values (average of the five corrected minimum temperatures recorded during each hour) were then obtained. The vertically polarized records showed relatively little variability during daylight hours, and, for this polarization, uncorrected hourly minimum values were obtained by direct scaling of the records.

A turnstile antenna displays truly circular polarization only in the zenith direction; in other directions its polarization is elliptical. Computations show that, if the entire sky is characterized by a uniform temperature, the resultant antenna temperatures consist approximately of $\frac{4}{5}$ of the wanted mode temperature and $\frac{1}{5}$ that of the unwanted mode. The hourly apparent ionospheric temperatures obtained from the turnstile antenna were corrected for leakage between the modes by the use of the relationships

$$T_x = \tfrac{1}{3}(4T_x' - T_o') \qquad (3a)$$

and

$$T_o = \tfrac{1}{3}(4T_o' - T_x') \qquad (3b)$$

where T_o' and T_x' are the apparent temperatures in the ordinary and extraordinary modes, and T_o and T_x are the corrected ionospheric temperatures. This procedure inherently assumes that the sky temperature is the same in all directions. This assumption is not strictly satisfied in practice, and its implications will be discussed in the next section.

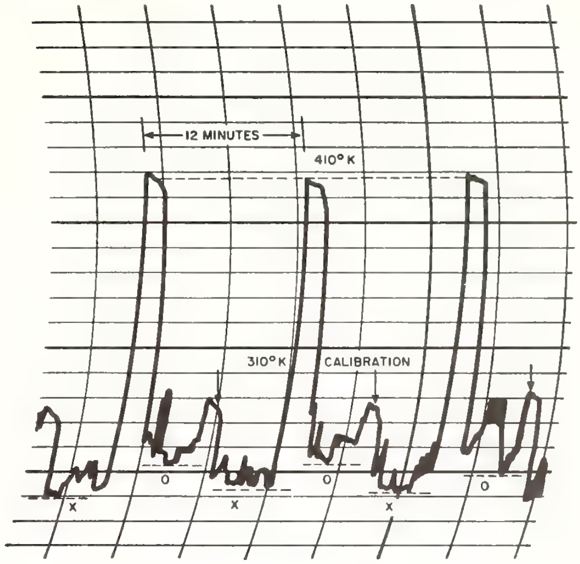

Fig. 1. Record showing *O*-mode and *X*-mode antenna signal levels and calibration levels.

DISCUSSION OF THEORY

The conditions that must be satisfied to permit the valid interpretation of temperatures registered by a ground-based antenna in terms of the thermal radiation of electrons in the *D* region have been discussed in the various references given in the introductory section of this paper. Among these requirements are a strongly absorbing *D* region (at the radio wavelength being used); the absence of local and propagated interference; and, in order to exclude cosmic noise, an *F*-region critical frequency that is greater than the frequency at which the antenna temperatures are measured. It is believed that the latter two conditions were usually satisfied at the frequency 3 MHz during daytime for the observing period (July–November 1960). We wish here to investigate in some detail the anticipated results from model ionospheres in terms of radio frequency absorption and the consequent equivalent antenna temperatures.

A narrow-beam antenna directed into an ionized region will register an equivalent temperature

$$T_n = \int_{s=0}^{s=\infty} T_e(s)\cdot \exp\left[-\int_0^s \alpha(s)\, ds\right] ds \qquad (4)$$

where T_e is the electron temperature, s is the distance along the ray path with the antenna at $s = 0$, and α

is the absorption in nepers per unit distance. For a broad-beam antenna, it is necessary to compute the temperature T_n as a function of the aximuth angle φ and elevation angle ϵ and to integrate over the entire sky, with appropriate functions applied to take into account the antenna radiation pattern. For a circularly polarized antenna, the wanted and the unwanted modes have different radiation patterns, [$G_w(\epsilon, \varphi)$ and $G_u(\epsilon, \varphi)$], and the equation for the apparent antenna temperature of the wanted mode takes the form

$$T_w' = \frac{\int_0^{\pi/2}\int_0^{2\pi} T_w(\epsilon, \varphi)G_w(\epsilon, \varphi) \cos \epsilon \, d\epsilon \, d\varphi + \int_0^{\pi/2}\int_0^{2\pi} T_u(\epsilon, \varphi)G_u(\epsilon, \varphi) \cos \epsilon \, d\epsilon \, d\varphi}{\int_0^{\pi/2}\int_0^{2\pi} [G_w(\epsilon, \varphi) + G_u(\epsilon, \varphi)] \cos \epsilon \, d\epsilon \, d\varphi} \tag{5}$$

where T_w' can pertain to the temperature of either the ordinary or the extraordinary mode, and T_w (ϵ, φ) and T_u (ϵ, φ) are the narrow-beam ionospheric temperatures as a function of direction. If it is assumed that the equivalent sky temperatures of the wanted and unwanted modes are each independent of direction, (3*a*) and (3*b*) are obtained from (5) for the case of a turnstile antenna.

Each incremental volume element along the ray path both emits and absorbs radio frequency energy. The radio wave absorption per unit distance at any point along the ray path is a function of the electron-collision frequency and electron density in the medium, the frequency of the radio wave concerned, and the angle between the magnetic-field vector and the instantaneous direction of the ray path. Ray tracings were performed with a computer program developed by J. W. Finney (private communication, 1964). The computations of absorption along each ray path were done by using the *Sen and Wyller* [1960] magnetoionic theory, which takes into account the energy dependence of electron-neutral collision frequency. Computations were made on models of the ionosphere that assumed the following values for the physical parameters:

1. The electron temperatures in the ionosphere are assumed to be equal to the neutral-gas temperatures; the height profile of gas temperature assumed to be up to 80 km is the average of the winter and summer values given by Nordberg in the COSPAR International Reference Atmosphere (CIRA) [see *Kallman-Bijl et al.*, 1961] for Ft. Churchill, Canada. Above 80 km, the average values quoted in Table 1 of CIRA are used.

2. The electron-collision frequency versus height profile assumed is computed from the atmospheric pressure data given in the tables of the CIRA mentioned above.

3. The electron density versus height profiles $N(h)$ considered are (a) those for aurorally quiet periods when $N(h)$ is a function of the solar zenith angle χ and (b) those that occur during disturbances, such as auroral absorption events and polar cap absorption events.

Even at the auroral zone, quiet conditions prevail in the *D* region much of the time. Figure 2 shows electron density profiles for different values of χ, where it is assumed that no auroral activity is present. The $N(h)$ values up to 90 km are based on theoretically determined profiles that fit 10-MHz cosmic-noise absorption data from quiet periods, whereas those above 100 km were determined from ionogram scalings by the method of *Paul and Wright* [1963]. The profiles represent average values for the period of observation; considerable variability from day to day does in fact occur, especially above 100 km.

By using the above assumptions, computations were made of the incremental and accumulated absorption of 2.89-MHz radio waves for both the ordinary (*O* mode) and extraordinary (*X* mode) polarizations for ray paths with take-off (elevation) angles ranging from 0° to 90°. Figure 3*a* and *b* shows examples of accumulated absorption and temperature for the *O* and *X* modes, respectively, during a quiet period when $\chi = 70°$, for a vertical ray. The height regimes that contribute appreciably to the net narrow-beam antenna temperature are designated by capital letters on each figure and are identified in the table inserted in Figure 3. It is necessary to continue the computation by using (4) along the ray path until the integrated absorption becomes large; a value of $\int \alpha \, ds \geq 7$ nepers ($\simeq$ 30 db) was found to be large enough for these computations, since electron temperatures are in all cases <1000°K. It was, therefore, necessary in many cases to continue the computation downward after reaching the reflection height. In a few cases, it was also necessary to continue the computation after the first ground reflection

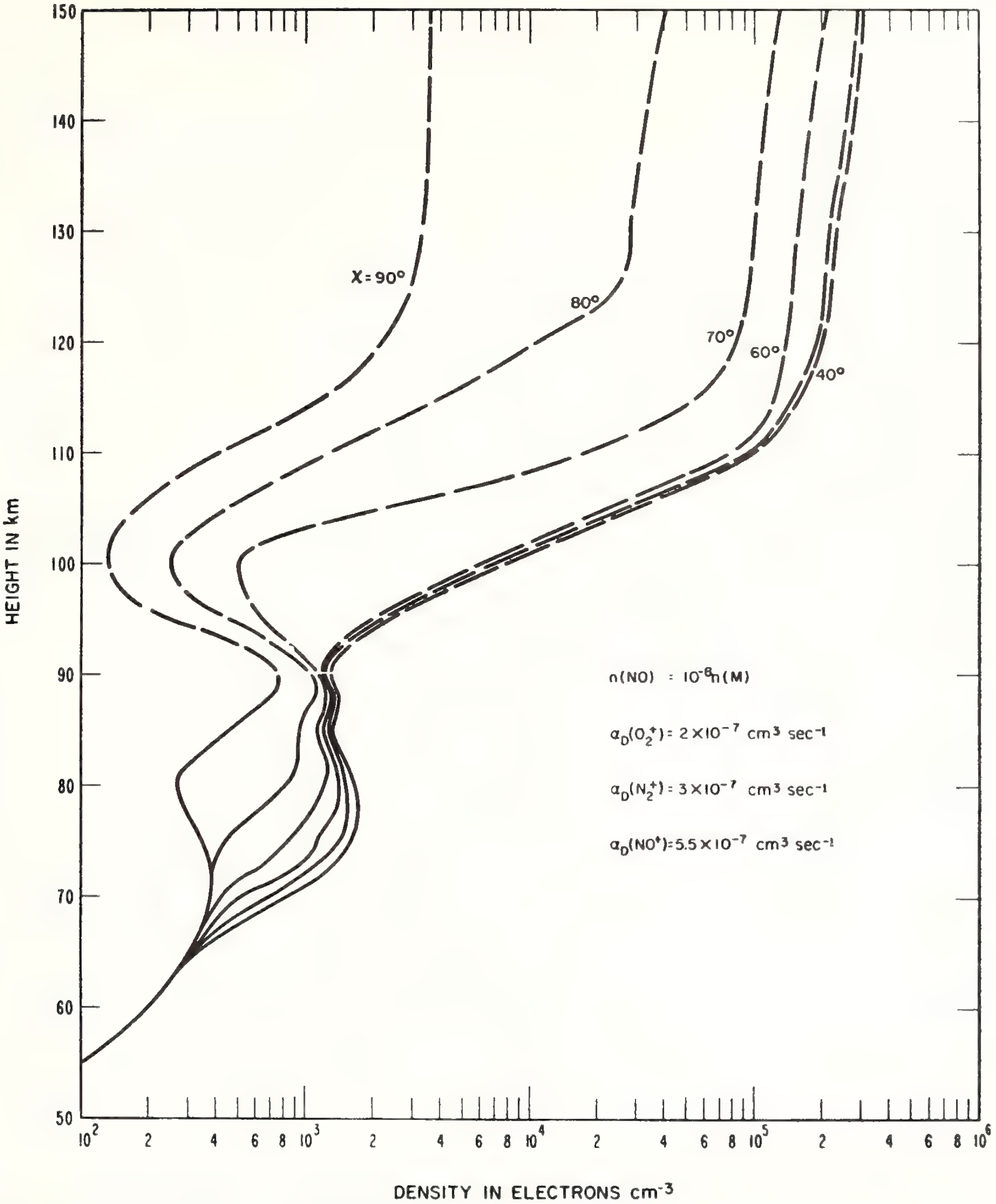

Fig. 2. Electron density versus height profiles for various solar zenith angles χ during undisturbed periods. The solid portion of the curve corresponds to computed values; the dashed portion is derived from ionosonde scalings. The n(NO) is the assumed number density of nitric oxide molecules; $n(M)$ is the total atmospheric number density; $\alpha_D(O_2+)$, $\alpha_D(N_2+)$, and $\alpha_D(NO+)$ are the assumed rate coefficients for the dissociative recombination of electrons with the respective ions.

(where a loss of 3 db was assumed to occur, and the ground temperature was assumed to be 273°K).

A number of interesting features are illustrated by Figure 3*a* and *b:*

1. The attenuation of the vertically directed *O* mode ray is only about 5 db by the time it reaches the 100-km level.

2. The *O*-mode ray is reflected in the *E* region where the temperature has a rapid gradient with height. The losses near the reflection height are con-

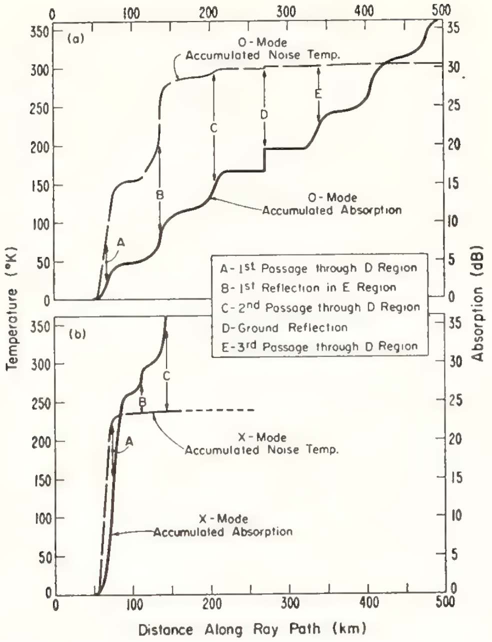

Fig. 3. (*a*) Accumulated absorption and equivalent noise temperature along a vertical ray path (for quiet conditions, $\chi = 70°$) starting from the antenna as origin for the *O* mode. (*b*) Same as 3(*a*) but for the *X* mode.

siderable, resulting in a substantial contribution to the net *O*-mode antenna temperature ($\approx$ 100°K for the vertical-incidence case shown) emanating from this region.

3. In contrast, the *X*-mode ray experiences at least about 15 db of absorption by the time it has penetrated the *D* region; this fact, together with the lower reflection height (where the temperature is approximately the same as that in the lower regions), results in a sky temperature which is close to the averaged *D*-region temperature.

The conclusion, therefore, is that *the 2.89 MHz X-mode sky temperatures can safely be interpreted in terms of D-region thermal emission, whereas the O-mode temperatures cannot,* at least during quiet periods.

Figure 4 shows the variation of equivalent temperature with elevation angle for $\chi = 70°$. Integration over the hemisphere by using (5) yields the *O*- and *X*-mode antenna temperatures shown in column I of Figure 4. Application of the corrections of (3) yields the derived sky temperatures shown in column II.

Computations of the type described above will be used in the next section to compare the expected results with those actually observed.

ANALYSIS OF DATA

The data used were essentially restricted to the daylight hours of observation during the period July through November 1960. Since the geographic latitude of College is 65°N, the seasonal variation in the useful daily observing periods is large: from approximately 16 hours per day during July to only about 4 hours by the end of November. The monthly means of the midday antenna temperatures as measured on the different antennas during the entire course of the observations (November 1959 to November 1960) are shown in Figure 5. *Little et al.* [1961] showed that cosmic radio noise propagating through the nighttime region of the polar ionosphere was responsible for the higher temperatures, particularly on the vertically polarized antenna, during the winter months. Note that during the 1960 summer and fall months, the vertically polarized antenna temperatures were comparable with or lower than those observed on the circularly polarized antennas. For this reason, we may be confident that the data described in the present paper are not significantly contaminated by ionospherically propagated cosmic noise or atmospherics arriving from low elevation angles.

Figure 6 shows hourly antenna temperatures (average of five samples taken during each hour) for a 12-day period in July. On some days, the antenna-noise temperatures remained within a narrow range

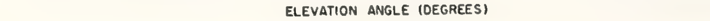

Fig. 4. Equivalent sky temperature as a function of ray-path elevation angle when the solar zenith angle is 70° and when magnetically quiet conditions prevail.

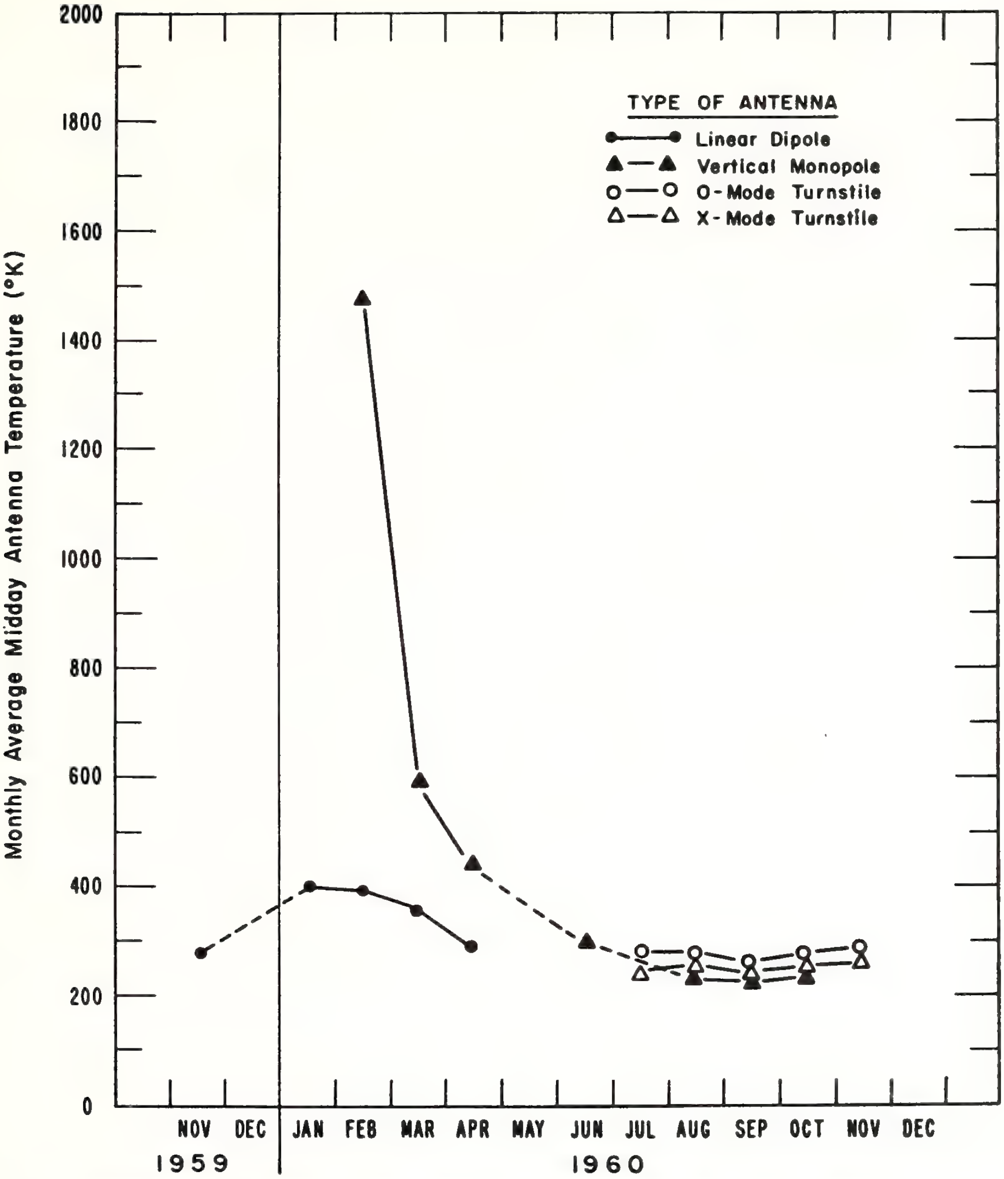

Fig. 5. Monthly means of midday antenna temperatures as measured on the different antennas (Nov. 1959 to Nov. 1960).

(say ±5°K) for several hours consecutively. On other days, the antenna-noise temperatures varied by as much as several tens of degrees from hour to hour. This variability was particularly noticeable on the *O*-mode circularly polarized antenna. It is likely that fluctuations of this sort were caused principally by variations of the electron density profile near the reflection height of the *O*-mode signal. The large temperature-height gradient at these levels and the effect of the electron density-height gradient dN/dh on deviative losses near the reflection point could readily account for changes of this magnitude. The observed relative stability of the vertically polarized antenna temperatures is consistent with and indeed supports this thesis, since oblique rays derive almost all of their temperature from the *D* region. (See Figure 3*b*, for example).

Figure 1 shows short-term fluctuations typical of

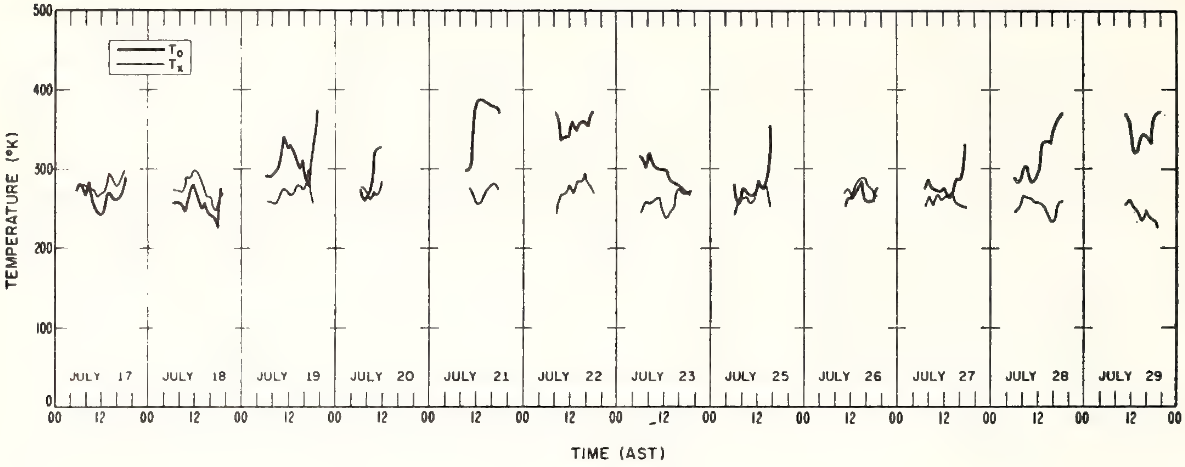

Fig. 6. Hourly antenna temperatures for a 12-day period in July.

the records in general. There are frequent noise 'spikes' of a few degrees Kelvin, which are usually caused by operation of other electrical equipment, (such as relays and motors) at the receiving site. Somewhat slower changes with time constants of a few minutes are believed due to short-term receiver gain fluctuations resulting from temperature variations of the receiver. Note that there are fluctuations of the calibration levels of a few degrees Kelvin from one calibration period to the next (12 minutes apart). The magnitude of the uncertainties imposed by these short-term variations is generally less than ±10°K. Statistical analysis of the data for the month of October 1960 reveals that the average standard deviation of the five samples used to determine hourly values was about 9°K for the *O* mode and about 6°K for the *X* mode, respectively.

The daytime hourly sky temperatures (corrected by using relationships 3) for the entire observing period have the occurrence distributions shown by Figure 7*a* and *b*. It is seen that the *X*-mode temperatures are more closely grouped and have a modal value about 15°K lower than that of the *O*-mode temperatures. Also, normal curves fitted to the temperature values below the modal value show that the *O*-mode temperatures display a greatly enhanced skewness toward higher values, whereas the *X*-mode temperatures show a relatively symmetrical distribution.

Figure 8*a* and *b* show the median (open circles) and the third and seventh decile values (end of bars) of the antenna temperatures as a function of solar zenith angle. Note that the *X*-mode temperatures decrease with increasing zenith angle out to $\chi > 90°$, while the *O*-mode temperatures begin to rise with $\chi > 75°$. The expected variations of antenna temperature were computed at 10-degree intervals of χ by using the method and assumptions given in the preceding section. These are shown connected by dashed lines in Figure 8*a* and *b*. The probable reasons for the differences between the measured and computed antenna temperatures will be discussed later.

Additional *D*-region ionization due to an influx of energetic particles, such as those associated with auroral and polar cap absorption events, might be expected to change the observed antenna temperatures. Figure 9*a* and *b* shows the median and third and seventh decile values of antenna temperature versus the absorption measured at College by a 27.6-MHz riometer. The number of hourly data points is also indicated for each interval of 27.6-MHz absorption. Antenna temperatures were computed by assuming uniform ionization layers over the entire visible hemisphere. But since this is not a realistic model for some auroral absorption events, this limitation should be kept in mind. The *D*-region electron concentration profiles used were based on multifrequency absorption measurements made during absorption events [*Parthasarathy et al.*, 1963; *Lerfald et al.*, 1964]. These profiles are illustrated in Figure 10. Each of these $N(h)$ profiles satisfies the relation $A \propto f^{-n}$, where A is the absorption of cosmic radio noise at effective radio frequency f, and n is an index whose range of values was determined from experimental data. The calculations were carried out by using each of these profiles normalized so as to yield an integrated absorption at 27.6 MHz ranging from 0.2 to 25 db. The results are shown in Figure 9*a* and *b* and can be seen to be fairly insensitive, both to the profile used and to the magnitude of the absorption. The reason for this insensitivity lies in the fact that for 27.6-MHz absorption values in excess of 1 or 2 db, the largest contribution to the observed temperature originates in the altitude region from 40 to 60 km, which is close to the stratopause where the normal variation of temperature with height is small.

The most important conclusion derived from the absorption calculations centers on the data at 2.89 MHz where the *X*-mode antenna signals from the ionosphere emanate almost wholly from the *D* region, whereas the *O*-mode signals may partially come from the higher ionospheric regions. We will therefore restrict our attention mainly to the *X*-mode results. Figure 8*b* shows a systematic difference of 20°–30°K between the observed and computed antenna temperatures; the observed values being higher. Figure 9*b* shows a similar systematic difference at low absorption values ($A < 3$ db at 27.6 MHz), but for heavy absorption, the observed temperatures are in fact just a few degrees *below* the computed ones. This good agreement under conditions of large absorption is encouraging because optimum conditions prevail at these times; i.e., the thermal emission will emanate from a narrow height range, and any propagated interference will be strongly absorbed. Nearly all the instances of 27.6-MHz absorption >6 db occurred during the polar cap absorption events of November 12–20, 1960, and the antenna temperature results are consistent with the inferred presence of a large quantity of abnormally low-lying ionization during these events.

The lack of precise agreement between the observed and computed temperatures shown in Figures 8 and 9 could be due to one or more of the following:

1. actual enhancements of electron temperatures over neutral-gas temperatures,
2. unrecognized natural or manmade radio interference,
3. the assumption of inappropriate physical parameters such as atmospheric temperature and pressure and electron-concentration profiles when making the computations, or
4. the approximations inherent in equations 1, 2, 3, and 5.

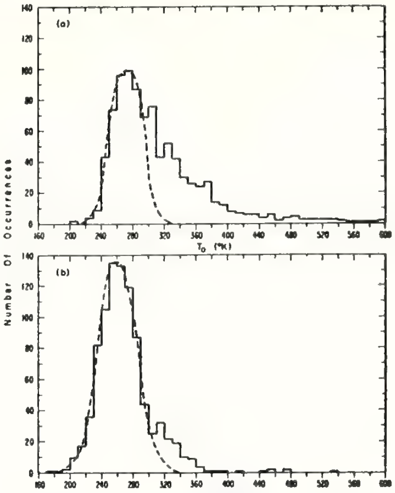

Fig. 7. Occurrence distributions of *O*-mode (*a*) and *X*-mode (*b*) antenna temperatures corrected by use of (3*a*) and (3*b*).

It is difficult to assess the relative importance of the above factors in explaining the differences between the observed and computed antenna temperatures. If the assumed values of one or more of the physical parameters of item 3 above were significantly different from the actual value, a systematic difference

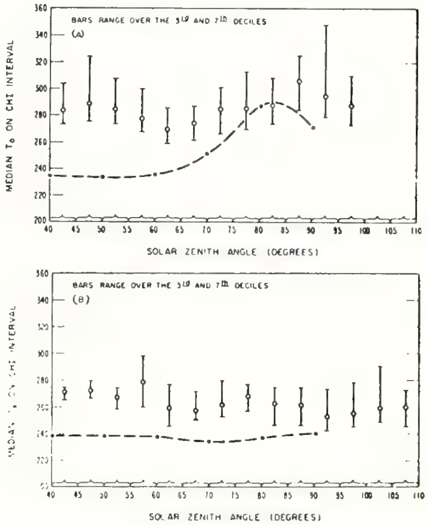

Fig. 8. Median (open circles) and third and seventh decile values (ends of bars) of antenna temperatures versus solar zenith angle (*A*, *O*-mode; *B*, *X*-mode) and values (black circles connected by dashed line) computed from model ionospheres.

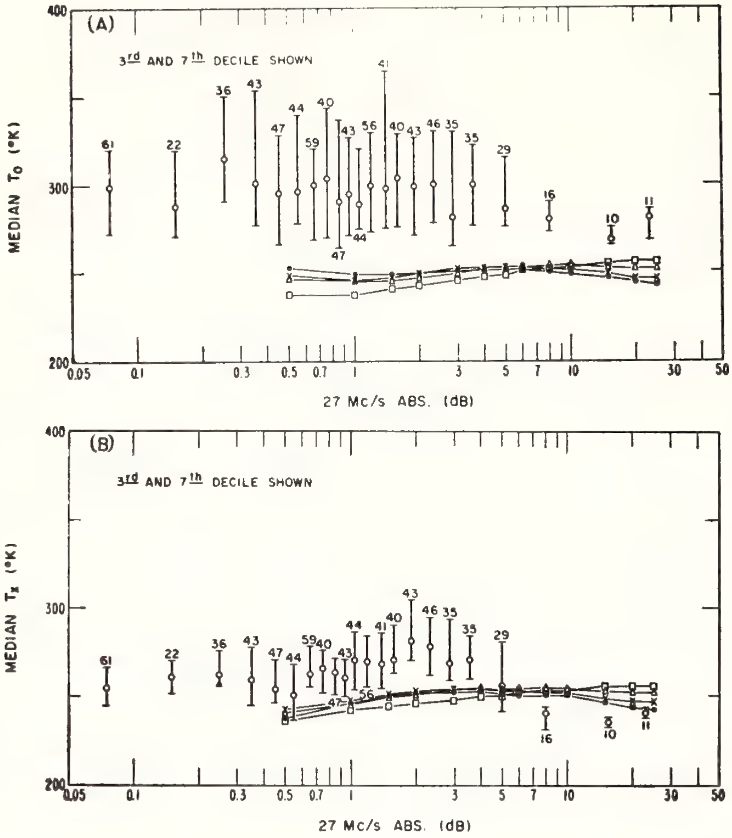

Fig. 9. Median values (open circles) and third and seventh decile values (ends of bars) of antenna temperature as a function of 27.6-MHz absorption (*A*, *O*-mode; *B*, *X*-mode); the number of data points for each interval is given. Also shown are the results of antenna temperature computations when the $N(h)$ profile shapes of Figure 10 are assumed (dot for $n = 1.3$, × for $n = 1.5$, triangle for $n = 1.7$, and box for $n = 1.9$).

would be expected. Item 4 should not be important unless the antenna efficiency was quite different from the assumed one or unless there were serious errors in the measurement of transmission-line losses.

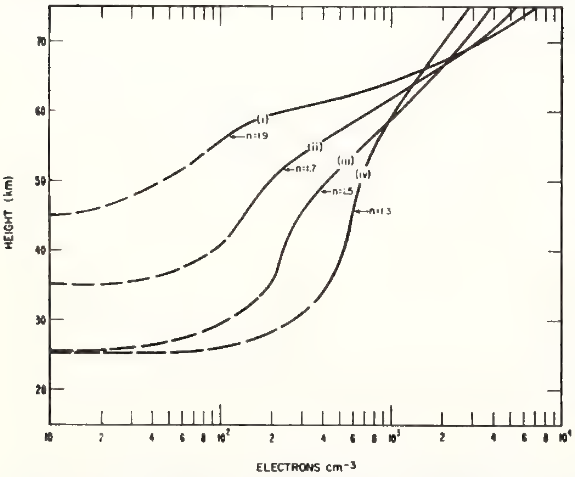

Fig. 10. Four assumed electron density height profiles. Each of these profiles will produce an absorption whose frequency dependence is given by f^{-n}, where n is given in the text.

Regarding item 2, several tests were made to check for possible contamination of the antenna-temperature data by radio frequency noise from the local diesel-electric power plant by operating the equipment solely from batteries, with our diesel power unit shut down. The results of these tests showed that less than 5°K of equivalent noise was contributed by the local power generator. However, it was not possible to make any conclusive tests of the interference that might have come from power lines in the College and Fairbanks areas about 20 or 30 miles away. The possible influence of propagated signals from radio transmitters is also difficult to assess. We think it likely that a considerable portion of the instances of high antenna temperature resulted from weather-associated effects. This supposition is based on a study of Weather Bureau records from the Fairbanks, Alaska, meteorological station, which reveal that most of the *X*-mode antenna temperatures >300°K occurred during days when there was persistent rain, low-level clouds, or wind, or a combination of these.

CONCLUSIONS

1. The most important conclusion drawn from the experiment is that electron temperatures in the *D* region remained at or near the expected gas temperature at the auroral zone during both aurorally disturbed and quiet periods.

2. During the winter months, a significant amount of cosmic noise at 3 MHz penetrates the arctic ionosphere and is detectable even at local noon, as evidenced by observations on horizontal and vertical dipoles during January, February, and March 1960 [reported in *Little et al.*, 1961]; see also Figure 5 of this paper. The summer and fall months including November 1959 and November 1960 show no systematic evidence of such contamination. It is not known whether this apparent asymmetry about the winter solstice is an annual effect due to changes in the *F*-region critical frequencies or is a function of the amount of auroral activity.

3. The use of a lower operating frequency (say, in the range 1.0–2.0 MHz) would probably make the experimental results more amenable to interpretation, i.e., the absorption integrated up to a given height would be greater, and the *O*-mode antenna temperatures would thus originate at a lower height; hence the variations of sky temperature with elevation angle would be reduced, and the uncertainties inherent in the use of approximations 3*a* and 3*b* would be lessened.

4. The electron-temperature values derived are likely to be upper limiting values, since interfererence of whatever source will raise the apparent antenna temperature rather than lower it.

Acknowledgments. The contributions of R. Parthasarathy (Geophysical Institute, University of Alaska) to the observational program and to the early analysis and interpretive phases of the program are gratefully acknowledged. The extensive computational program was carried out by Mr. Louis Puls, Mr. William Retallack, and Mrs. Irene Lowenbach. Mr. Douglas Williams performed much of the data processing.

REFERENCES

Belrose, J. S. (1967), Epilogue, in *Proc. Conf. Ground-Based Radio Wave Propagat. Studies Lower Ionos.*, pp. 671–685, Defence Research Board, Ottawa, Canada.

Belrose, J. S., and I. A. Bourne (1967), The electron distribution and collision frequency height profile for the lower part of the ionosphere (the *D* and lower *E* regions): A review of observational data, in *Proc. Conf. Ground-Based Radio Wave Propagat. Studies Lower Ionos.*, pp. 79–96, Defence Research Board, Ottawa, Canada.

Belrose, J. S., I. A. Bourne, and L. W. Hewitt (1967), A preliminary investigation of diurnal and seasonal changes in electron distribution over Ottawa, Churchill, and Resolute Bay, in *Proc. Conf. Ground-Based Radio Wave Propagat. Studies Lower Ionos.*, pp. 176–188, Defence Research Board,, Ottawa, Canada.

Belrose, J. S., and L. W. Hewitt (1964), Variation of collision frequency in the lowest ionosphere with solar activity, *Nature, 202,* 267–269.

Dalgarno, A., and R. J. W. Henry (1965), Electron temperatures in the *D* region, *Proc. Roy. Soc. London, A, 288,* 521–530.

Dowden, R. L. (1960), Ionospheric thermal radiation at radio frequencies in the auroral zone, *J. Atmos. Terr. Phys., 18,* 8–19.

Gardner, F. F. (1954), Ionospheric thermal radiation at radio frequencies, 2, further observations, *J. Atmos. Terr. Phys., 5,* 298–315.

Jespersen, M., O. Petersen, J. Rybner, B. Bjelland, O. Holt et al. (1964), Electron density and collision frequency observations in the lower *D* region during auroral absorption, in *Electron Density Distribution in Ionosphere and Exosphere,* edited by E. Thrane, pp. 22–35, North-Holland, Amsterdam.

Kallmann-Bijl, H., R. L. F. Boyd, H. LaGow, S. M. Poloskov, and W. Priester (1961), *COSPAR International Reference Atmosphere,* pp. 12–27 and 56.

Kane, J. A. (1961), Re-evaluation of ionospheric electron densities and collision frequencies derived from rocket measurements of refractive index and attenuation, *J. Atmos. Terr. Phys., 23,* 338–347.

Landmark, B., and F. Lied (1961), Observations of the *D* region from a study of ionospheric cross modulation, *J. Atmos. Terr. Phys., 23,* 92–100.

Lerfald, G. M., C. G. Little, and R. Parthasarathy (1964), *D*-region electron density profiles during auroras, *J. Geophys. Res., 69,* 2857–2860.

Little, C. G., G. M. Lerfald, and R. Parthasarathy (1961), Some observations of 2.89 Mc/s equivalent antenna temperatures at the auroral zone, *J. Atmos. Terr. Phys., 23,* 275–286.

Parthasarathy, R., G. M. Lerfald, and C. G. Little (1963), Derivation of electron density profiles in the lower ionosphere using radio absorption measurements at multiple frequencies, *J. Geophys. Res., 68,* 3581–3588.

Paul, A. K., and J. W. Wright (1963), Some results of a new method for obtaining ionospheric *N*(*h*) profiles and their bearing on the structure of the lower *F* region, *J. Geophys. Res., 68,* 5413–5420.

Pawsey, J. L., L. L. McCready, and F. F. Gardner (1951), Ionospheric thermal radiation at radio frequencies, *J. Atmos. Terr. Phys., 1,* 261–277.

Rumi, G. (1962), Experiment Luxembourg: cross modulation at high latitude, low height, 1, Theoretical aspects, *IRE Trans. Antennas Propagat. 10,* 594–607.

Sears, R. D. (1963), Contribution of energetic photoelectrons to *D*-region nonequilibrium electron temperatures, *J. Geophys. Res.*, *68*, 5135–5142.

Smith, R. A., I. A. Bourne, R. G. Loch, C. S. G. K. Setty, T. N. R. Coyne, et al. (1965), Radio wave interaction using gyro-waves, *AFCRL Sci. Rep. 65-460*, Air Force Cambridge Research Laboratories, Bedford, Mass.

Sen, H. K., and A. A. Wyller (1960), On the generalization of the Appleton-Hartree magnetoionic formulas, *J. Geophys. Res.*, *65*, 3931–3950.

Thrane, E. V., and W. R. Piggott (1966), The collision frequency in the *E* and *D* regions of the ionosphere, *J. Atmos. Terr. Phys.*, *28*, 721–737.

Reprinted from Journal of Molecular Spectroscopy 35, No. 3, 494-495, 1970.

Copyright © 1970 by Academic Press, Inc.

LETTER TO THE EDITORS

Water Vapor Spectrum Near 600 GHz

This letter is a report on the observation of absorption lines of H_2O and D_2O at frequencies near 600 GHz. In H_2O we have measured the frequency of the strong $1_{1,0} \leftarrow 1_{0,1}$ line shown in Fig. 1 to be 556935.8 ± 1.0 MHz (*1*). In D_2O we have measured the frequency of the $1_{1,1} \leftarrow 0_{0,0}$ line as 607349.6 ± 0.2 MHz and have observed the relatively weak $3_{1,2} \leftarrow 3_{0,3}$ line at approximately 555.33 GHz (*2*). The measurement of this transition frequency in H_2O allows a better determination of the microwave spectrum of H_2O because only 5 lines had been measured previously. In D_2O, where about 30 transitions have already been measured, our measurements confirm the prediction of Benedict and Clough (*2*).

The measurements were made with the second harmonic of a carcinotron backward wave oscillator operating near 300 GHz. A block diagram is shown in Fig. 2. The second harmonic was generated in an RG/138-by-RG/98 cross-guide mixer with an adjustable point contact diode. The mixer was used in an unusual configuration, with the fundamental input on the RG/138 waveguide for better matching to the diode and the second harmonic output on the RG/98 waveguide. The absorption cell was a 15 cm long section of RG/98 waveguide with mica windows. A K-band by RG/98 point contact diode mixer was used to generate a beat between the carcinotron fundamental and a phase-locked Ku-band klystron. When this beat signal was strong enough, it was used to phase lock the carcinotron, otherwise it was used to give a frequency marker. The 600 GHz signal was allowed to pass through the harmonic mixer by removal of back RG/98 tuning plunger. A directional coupler could not be used on the carcinotron input to monitor frequency and to phase lock because the increased fundamental loss greatly attenuated the second harmonic output. A 9-Hz chopper was used behind the mixer. The signal was detected by a Golay-cell infrared detector. The 300 GHz fundamental was prevented from entering the detector by a waveguide filter with a cutoff of about 400 GHz. Near-infrared radiation from the chopper was blocked by a quartz filter.

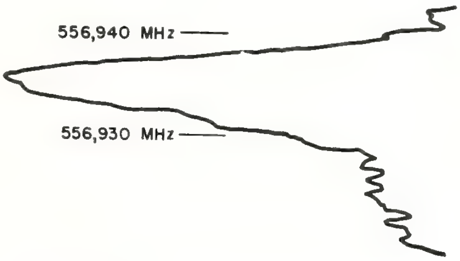

FIG. 1. Recorder trace of $1_{0,1} \leftarrow 1_{0,1}$ transition in H_2O at a pressure of 0.02 Torr with a 10-sec time constant.

For the D_2O line at 607 GHz, we had sufficient power to phase lock the carcinotron and to frequency modulate it at 20 Hz. We were then able to observe a derivative presentation of

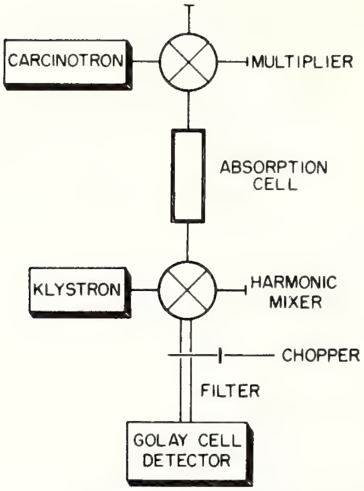

FIG. 2. Block diagram of 600 GHz spectrometer

the absorption line without using the chopper. By tuning for the zero of the derivative curve, the center of the line could be determined quite precisely. A small pressure shift was observed but could not be adequately studied because of the poor signal-to-noise ratio. The quoted uncertainties are large enough to include these pressure shifts.

We are now acquiring a liquid helium-cooled bolometer that should be 1000 times more sensitive than the Golay cell. With this new detector we plan to measure more of the H_2O and D_2O lines in the neighborhood of 600 GHz, and to investigate line shapes, pressure dependence, and the Stark effect.

REFERENCES

1. V. E. DERR, private communication, ESSA Research Laboratories.
2. W. S. BENEDICT AND S. A. CLOUGH, private communication.

ESSA Research Laboratories,
Boulder, Colorado 80302
Submillimeter Wave Program Area,
Wave Propagation Laboratory

D. A. STEPHENSON[1]

R. G. STRAUCH

Received: April 20, 1970

---

[1] NRC-ESSA Postdoctoral Research Associate.

Reprinted from Proceedings of the NATO Advanced Study Institute, August 29-September 6, 1969, 139-155, 1970.

TURBULENCE AND IRREGULARITIES OF THE ATMOSPHERE

B. R. Bean

U. S. Department of Commerce
Environmental Science Services Administration
Research Laboratories
Boulder, Colorado 80302

Abstract

Both the classical exchange coefficient and the more modern statistical theories of turbulence are examined. It is emphasized that active turbulence may mix passive parameters such as the radio refractive index or atmospheric water to such an extent that the fluctuations of the latter may essentially vanish. Experimental evidence for this apparent paradox is presented for both point in-situ measurements and sharpening of a laser beam produced by mixing of refractive index irregularities over a 15 kilometer path by a "chinook" wind.

1. INTRODUCTION

This lecture is concerned with the measurement of refractivity, N, at a point, or a series of points. Thus it starts with a brief background treatment of the theory of passive parameters and how this theory could be applied to N and/or water vapor. Experimental results are then examined to shed light upon the structure of water vapor turbulence.

The small-scale fluctuations of temperature, humidity and refractive index are all treated as dynamically passive parameters in the absence of phase changes (i.e., condensation, etc.). This is not to say that the large-scale variations of these parameters do not affect turbulence, but only that in the region of eddy sizes sufficiently removed from both the input and viscous scales, these parameters do not modify the flow. In this case one would expect that the statistics of these parameters would be controlled by the vertical wind. Thinking for example, of humidity, one would expect little variation during calm periods of stratification such as in a nocturnal radiation inversion, but rather large variations during the convective break-up of the inversion.

The study of atmospheric turbulence is that of the variation of some property of the atmosphere about its mean value and the dependence of that departure upon the mean value itself, as well as the properties of any bounding surfaces. We may adopt a working definition of turbulence as those irregular motions which transport atmospheric properties (momentun, heat, water vapor, etc.) across the mean flow rather than down the mean flow.

Early studies of turbulence aimed at describing the average flux of some parameter, say x, away from, or towards the earth's surface. For transport, or flux, of x in the vertical direction (z) with vertical velocity (w) leads to an expression

$$\text{vertical flux of } x = F_x = \overline{xw}$$

where the overbar denotes a time average over a convenient period of time, usually an hour or less. If we now introduce the concept that x and w are composed of time invariant means, $\bar{x}$ and $\bar{w}$, plus departures from the means, x' and w' then

$$\overline{xw} = \overline{(\bar{x} + x')\,(\bar{w} + w')}$$

or

$$\overline{xw} = \overline{\bar{x}\bar{w}} + \overline{\bar{x}w'} + \overline{x'\bar{w}} + \overline{x'w'}$$

which becomes

$$\overline{xw} = \bar{x}\,\bar{w} + \overline{x'w'} ,$$

since by definition:

$$\overline{\bar{x}} \equiv \bar{x}, \quad \overline{w'} \equiv 0$$

so that

$$\overline{\bar{x}w'} = \bar{x}\overline{w'} = 0 \quad ,$$

Similarly

$$\overline{x'\bar{w}} = 0 \quad .$$

Further, since the average vertical velocity is customarily taken to be zero ($\bar{w} = 0$,

$$\overline{xw} = \overline{x'w'} \quad .$$

(The experimental conditions reported later in this lecture were such that any systematic bias introduced by the slope of the terrain is usually contained within the error in determining $\bar{w}$.) It is now natural to make the additional assumption that the average vertical transport of x is proportional to the gradient of the mean of x

$$F_x = \overline{x'w'} = -K_x \frac{\partial \bar{x}}{\partial z}$$

where K_x is the austausch or exchange coefficient for x. The flux equation for water vapor takes the form

$$\frac{F_\gamma}{\rho} = -K_\gamma \frac{\partial \bar{\gamma}}{\partial z}$$

where ρ is the air density and γ the humidity mixing ratio. For the vertical flux of heat H,

$$\frac{F_\theta}{\rho} \equiv \frac{H}{\rho} = -K_\theta c_p \frac{\partial \bar{\theta}}{\partial z}$$

where θ is the potential temperature and c_p the specific heat of air at constant pressure. Finally, for horizontal momentum per unit mass

$$-\frac{F_m}{\rho} \equiv \frac{\tau}{\rho} = -\overline{u'w'} = K_m \frac{\partial \bar{u}}{\partial z}$$

where us is the horizontal velocity of the uni-directional flow. The horizontal shearing stress is designated by τ and

$$\frac{\tau}{\rho} = u^{*2}$$

is the so-called friction velocity. A good deal of research has gone into the study of the behavior of K_θ and K_m in the boundary layer, (the boundary layer is here defined as the layer of frictional influence of the earth's surface) where both τ and H may be taken as invariant with height. The general result of these studies is that the exchange coefficients are not equal, and the inequality is a function of thermal and mechanical stability of the boundary layer: the observation that

$$K_\theta / K_m > 1$$

is perhaps attributable to the radiative flux of heat adding to that of the mechanical flux associated with w.

STATISTICAL CONSIDERATIONS

The above discussion is concerned with the time average of turbulent flux. Considerable insight may be gained by examining the variability of a turbulent parameter, such as wind, with frequency or scale length, in that rapid variations may be treated statistically while slow variations may be studied for their physical cause.

If, following Kolmogorov, the spectral density of a turbulent parameter is plotted as a function of frequency, then three distinct frequency ranges become apparent. These are: the input region where thermal buoyancy or mechanical wind shear initiates the turbulent motion that cascades down through the inertial subrange and is finally dissipated as heat in the viscous subrange. These regions will now be discussed separately.

The consideration of the small scales of turbulence, i.e., those so much smaller than the input scales that they no longer bear the imprint of their origin, have been treated by Kolmogorov under the assumption that the statistical properties of such small eddies are the same. From considerations of the conservation of energy, and provided the mean level of turbulent energy is constant, the small eddies must convert to heat all of the energy that is passed down to them by the break up of larger eddies. Thus Kolmogorov's first similarity hypothesis:

> "The average properties of the small-scale components of any turbulent motion at large Reynolds number are determined uniquely by the kinematic viscosity of the fluid (ν) and the average rate of dissipation of energy per unit mass of the fluid (ϵ)."

The first similarity hypothesis applies to the viscous subrange mentioned earlier. Kolmogorov's second hypothesis treats those small scales that are sufficiently removed from the viscosity dissipation scales that the energy distribution is independent of viscosity, i.e.,

> "For sufficiently large Reynolds numbers there is a subrange of the range of small eddies in which average properties are determined solely by the average rate of dissipation of energy per unit mass of the fluid."

This second sypothesis applies to the inertial subrange.

The most common coordinate system used in micrometeorology is the Cartesian, where the space variables are x, y, and z. The direction of the mean horizontal wind is taken as x, y as the cross-wind component. The vertical coordinate, z, is positive upwards. The wind velocities in the x, y, and z directions are designated as u, v, and w, respectively. As before it is assumed that the flow can be described by mean and eddy terms:

$$v_i = \overline{v_i} + v_i'; \quad i = x, y, z .$$

The mean values are defined by

$$\overline{v_i} = \lim_{T \to \infty} \frac{1}{T} \int_0^T v_i(t)\, dt .$$

The variances, or mean square deviations are defined as

$$\sigma^2(v_i) = \lim_{T \to \infty} \frac{1}{T} \int_0^T [v_i'(t)]^2\, dt .$$

Early work in turbulence concentrated on the Reynolds stresses,

$$\tau_{ij} = -\rho\, \overline{v_i' v_j'}$$

which represents the mean rate of transfer of momentum across a surface due to velocity fluctuations, and on $I_i = \overline{v_i'^2}$ which is proportional to the kinetic energy of the turbulent energy. I is called the intensity of turbulence.

Although τ_{ij} and I_i provide a description of turbulent fluctuations, they are insufficient to define the flow since identical values may be obtained from widely differing spectral distributions. Thus more restrictive statistical definitions have been adopted under the assumption that the individual record is that of a random process. Frequently further restrictions to the random process are involved so that the statistics be:

stationary - invariant in time coordinate translation,
homogeneous - invariant in any one space coordinate translation,
isotropic - invariant in rotation or translation of the space-coordinate system.

Thus in stationary, isotropic flow

$$\sigma^2(v) = \sigma^2(u) = \sigma^2(w) \text{ for all time.}$$

For a stationary random process the correlation function, R, for a given velocity component is a function only of the time separation, r:

$$R_{v_i v_i}(r) = \overline{v_i'(t) v_i'(t+r)} / \overline{\left[v_i'(t)\right]^2} .$$

Cross-correlation between different velocity components can be defined by

$$R_{v_i v_j}(r) = \overline{v_i'(t)\, v_j'(t+r)} / \sigma(v_i)\sigma(v_j) .$$

The power spectrum is defined as

$$P_{v_i}(f) = 2\int_0^\infty R(r)_{v_i v_i} \cos 2\pi f r dr$$

where f is the frequency in cycles per second. The power spectrum is so defined that a plot of P(f) versus f represents the relative contribution to the total variance ($\sigma^2(v_i)$) by individual frequency intervals.

Similarly the cross spectrum of two velocity components is defined by

$$C_{v_i v_j}(f) = \int_{-\infty}^{\infty} R_{v_i v_j}(r) \exp(-i2\pi f r)\, dr .$$

The cross spectrum is a complex quantity where the real part, called the cospectrum, represents the correlation of the in phase energy of the two velocity components, and the imaginary part, called the quadrature spectrum, represents the correlation of the out of phase components.

The cross spectrum allows a definition of the correlation of two random time series as a function of frequency in terms of the coherence COH:

$$\mathrm{COH}(f) = \frac{\left| C_{v_i v_j}(f) \right|^2}{P_{v_i v_i}(f)\, P_{v_j v_j}(f)} .$$

The numerical value of COH lies between 0 and 1 and is similar to the square of the correlation coefficient.

DIMENSIONAL CONSIDERATIONS

In studying the turbulent characteristics of the boundary layer one naturally strives to relate the vertical distribution of mean potential temperature and wind with the constant fluxes of heat and momentum, height, and gravity. Monin and Obukhov (1954) argue that if one wishes to obtain non-dimensional, and thus universal, equations of motion for the boundary layer under conditions of horizontally uniform turbulence then the only parameters of concern are g, z, $u_* = \sqrt{\overline{u' w'}}$, $\overline{w' T'} = H/\rho c_p$ and the buoyancy force $(g/T)T'$ per unit mass of air. Since the fractional variation of the mean temperature over the layer is small, g/T is taken as constant. To normalize the equations of motion, any lengths, velocities or temperatures used should be functions of u_*, $H/\rho c_p$, and g/T. The only velocity from this set is u_*, the only length

$$u_*^3 / \left(\frac{g}{T} \frac{H}{\rho c_p}\right)$$

and the only temperature

$$H/\rho c_p u_* .$$

Thus we define

$$L \equiv -u_*^3 / k \left(\frac{g}{T} \frac{H}{\rho c_p}\right)$$

$$T^* \equiv -\frac{H}{\rho c_p u_*}$$

where von Kármán's constant k has been introduced for later convenience. In stable layers the heat flow is downwards

$$H < 0, \ L > 0, \text{ and } T* > 0 .$$

For unstable layers

$$H > 0, \ L < 0, \text{ and } T* < 0 .$$

Starting with the log-law for wind in neutral conditions Monin and Obukhov note that the dimensionless expression

$$\frac{z}{u*} \frac{\partial v}{\partial z} = \frac{1}{k} \quad \text{(a pure number)}$$

must be replaced by a non-dimensional variable. The only dimensionless constant that one can construct from $H/c_p \rho$, g/T, $u*$ and z is z/L. It follows then that:

$$\frac{kz}{u*} \frac{dv}{dz} = \phi_1(z/L)$$

and, similarly

$$\frac{kz}{T*} \frac{d\theta}{dz} = \phi_2(z/L)$$

where ϕ_1 and ϕ_2 are undetermined, but universal functions of z/L. Much of the work of the Soviet school of turbulence in recent years has been devoted to the empirical determination of ϕ_1 and ϕ_2. One notes that with the introduction of these universal functions the exchange coefficients for heat and momentum may be written

$$K_\theta = \frac{ku*z}{\phi_2(z/L)} \quad \text{and} \quad K_m = \frac{ku*z}{\phi_1(z/L)} .$$

If, as is often assumed, $K_\theta = K_m$ then

$$\phi_1 = \phi_2 = \phi$$

and θ and v will follow similar profiles. Although Sheppard (1952) finds no systematic difference of form of profiles of v and θ on a height range of 0.5 to 8.0 m, Senderikhina (1961) surveyed a large number of observations and concludes that $K_\theta/K_m \sim 1.3$. Quite in contrast to this result is that of Petterssen and Swinbank (1947) who, by examining more than 1500 radiosonde observations selected for the free atmosphere (900-300 mbs) $K_\theta/K_m \sim 0.65$. These last data indicate a systematic decrease of K_θ/K_m with height, indicating a ratio of 0.75 for the layer 900-850 mbs and 0.64 for the layer 350-300 mbs. For the present study, being unable to shed more light on the question of this ratio, we shall assume $K_\theta/K_m = 1$.

To clarify the role of z/L we now examine the flux Richardson's number, R_f, (Reiter, 1963)

$$R_f = \frac{K_\theta}{K_m} R_i = \frac{K_\theta g}{K_m \bar{\theta}} \frac{\frac{d\bar{\theta}}{dz}}{\left(\frac{d\bar{u}}{dz}\right)^2}$$

which, upon substitution from the expressions for ϕ_1 and ϕ_2 (and assuming $\phi_1 = \phi_2$ and thus $K_\theta = K_m$)

and

$$R_f = R_i = \frac{gk}{T} \frac{T^* z}{u^{*2} \phi(\frac{z}{L})}$$

$$R_i = \frac{z}{L} \cdot \frac{1}{\phi(\frac{z}{L})}$$

i.e., the dependence of Richardson's number upon height can be expressed as a function of the single variable z/L.

SPECTRAL VARIATION OF TEMPERATURE, HUMIDITY AND REFRACTIVE INDEX IN THE INERTIAL SUBRANGE

The Kolmogorov statistical theory of turbulence hypothesizes the presence of an inertial sub-range of small eddies in which average properties of the flow are determined solely by the average rate of dissipation of energy per unit mass of the fluid (ϵ). A consequence of this hypothesis is that the structure function, $D_u(r)$, for wind, u, measured at a distance r from the origin but referenced to r_0,

$$D_u(r) = \overline{[u(r_0) - u(r_0 + r)]^2}$$

must, by dimensional arguments, take the form

$$D_u(r) = a^2 \epsilon^{2/3} r^{2/3} \quad ,$$

where a is a constant. Similar arguments lead to the conclusion that the structure functions for temperature, T, and radio refractivity, N, are of the form

$$D_T(r) = a^2 \epsilon^{-1/3} G_T r^{2/3}$$

$$D_N(r) = a^2 \epsilon^{-1/3} G_N r^{2/3}$$

G_T and G_N are, respectively, the average rate of dissipation of temperature and refractive index fluctuations per unit mass. The presence of these additional dissipation terms in $D_T(r)$ and $D_N(r)$ accounts for a fundamental difference in their spectral behavior compared to $D_u(r)$. We, therefore, now examine expressions for ϵ, G_T, and G_N in terms of mean winds, gradients, etc.

Writing the equation for the time rate of change of kinetic energy, E, Lumley and Panofsky (1964) obtain:

$$\frac{d\overline{E}}{dt} = -\overline{u'w'} \frac{\partial \overline{u}}{\partial z} + g \frac{\overline{w'T'}}{T} - \frac{\partial \overline{w'E}}{\partial z} - \epsilon \, , \qquad (1)$$

where t is time, u is the wind in the direction of flow and w that in the vertical direction, z. The primes denote departure from the average as denoted by an over bar, i.e. $u' = u - \overline{u}$. Gravity is denoted by g. $\frac{d\overline{E}}{dt}$ is usually small. The first term on the right hand side of (1) is a measure of mechanical generation of kinetic energy. Since $\overline{u'w'}$ has the opposite sign to the gradient the total term is positive. The flux divergence is normally assumed small (as were the other divergence terms in the derivation of (1). Further, if we restrict our attention to those conditions where buoyance effects, $\overline{gw'T'/T}$, are small compared to the mechanical ones, then

$$\epsilon \approx \overline{u'w'} \frac{\partial \bar{u}}{\partial z} \quad . \tag{2}$$

One may obtain similar expressions for temperature,

$$\frac{1}{2} \frac{\overline{d(T')^2}}{dt} = -\overline{w'T'} \frac{\partial \bar{\theta}}{\partial z} - \frac{1}{2} \frac{\overline{\partial w'(T')^2}}{\partial z} - G_T$$

and refractivity,

$$\frac{1}{2} \frac{\overline{d(N')^2}}{dt} = -\overline{N'w'} \frac{\partial \bar{N}_*}{\partial z} - \frac{1}{2} \frac{\overline{\partial w'(N')^2}}{\partial z} - G_N \quad .$$

Utilizing similar arguments to those used to derive (2) one may obtain

$$G_T \approx \overline{w'T'} \frac{\partial \bar{\theta}}{\partial z}$$

$$G_N \approx \overline{w'N'} \frac{\partial N_*}{\partial z} \quad , \tag{3}$$

where one notes that the potential temperature, θ and potential refractivity, $N*$, enter. Remembering that

$$\frac{\partial \theta}{\partial z} = \frac{\partial T}{\partial z} + \Gamma \ ,$$

where Γ is the adiabatic lapse of temperature ($\Gamma \approx -10^{\circ}C/km$) one notes that it is entirely possible for $\partial\theta/\partial/z \rightarrow 0$ and thus $G_T \rightarrow 0$ with the result that $D_T(r) \rightarrow 0$. The same is true for the gradient of potential refractivity with similar implications for $D_N(r)$. This is due to θ and $N*$ being assumed dynamically passive parameters in the generation of mechanical turbulence. The physical interpretation is that the mechanical turbulence will mix temperature and refractive index inhomogeneities until each assumes the appropriate adiabatic height distribution. Thus, although there might be active vertical mixing, the fluctuations of T and N, T' and N', have been effectively smoothed out. Several specific examples of this effect will now be examined.

EXPERIMENTAL EXAMPLES

The first example is that of the fluctuations of temperature and wind measured at 50 feet above ground at Gunbarrel Hill, Colorado. The instrumentation described elsewhere (Bean, Emmanuel and Krinks,

1967) has adequate bandwidth to delineate fluctuations over the frequency range of figure 1. P(f) is the spectral density at a given frequency f. The coordinates f P(f) versus log f are used to maintain equal area - equal spectral contribution over the wide frequency range of meteorological fluctuations observed. Two hours were selected for study; 0650-0750 and 1300-1400 on November 24, 1964. The early morning, run 1, was characterized by stable conditions with temperature increasing with height, a light wind of 2.84 mps, practically no fluctuations of vertical wind but relatively large fluctuations of temperature at low frequency ($f \approx 0.002$ cps). The temperature fluctuations of figure 1, run 1, are perhaps associated with the "undulance" observed under stable conditions (Lunley and Panofsky, 1964). By 1300, run 2, a cold front had passed the observing tower with a resultant increase of wind to 15.6 mps and Richardson's number near zero. The observed temperature gradient was within measurement error of the adiabatic lapse of T. The rapid fluctuations of the vertical wind experienced by an observer on the tower left no doubt that the atmosphere was in a condition of strong mechanical turbulence. Note, however, that temperature fluctuations are low at all frequencies as one would expect from (3). This, then, is one illustration of conditions where $D_u(r) \not\to 0$ whilst $D_T(r) \to 0$.

The second example chosen is that of the variability of spectral density of the radio refractive index with changes in atmospheric stability. The radio refractive index is strongly affected by humidity and, to a lesser extent, by temperature fluctuations. The data presented in figure 2 were taken during July and August of 1963 with a multi-cavity microwave refractometer sampled at several levels on a 150-foot tower. Details of the experiment are given by Bean, Emmanuel and Krinks (1967). Although there is a wide spread in the experimental data, it is again observed that regions of relatively spectral density occur where $\partial\theta/\partial z \to 0$ and thus $R_i \to 0$.

The third example is drawn from the observations of propagation characteristics of optical beams made by the author's colleague, G. R. Ochs (Ochs and Little, 1968). The particular meteorological condition

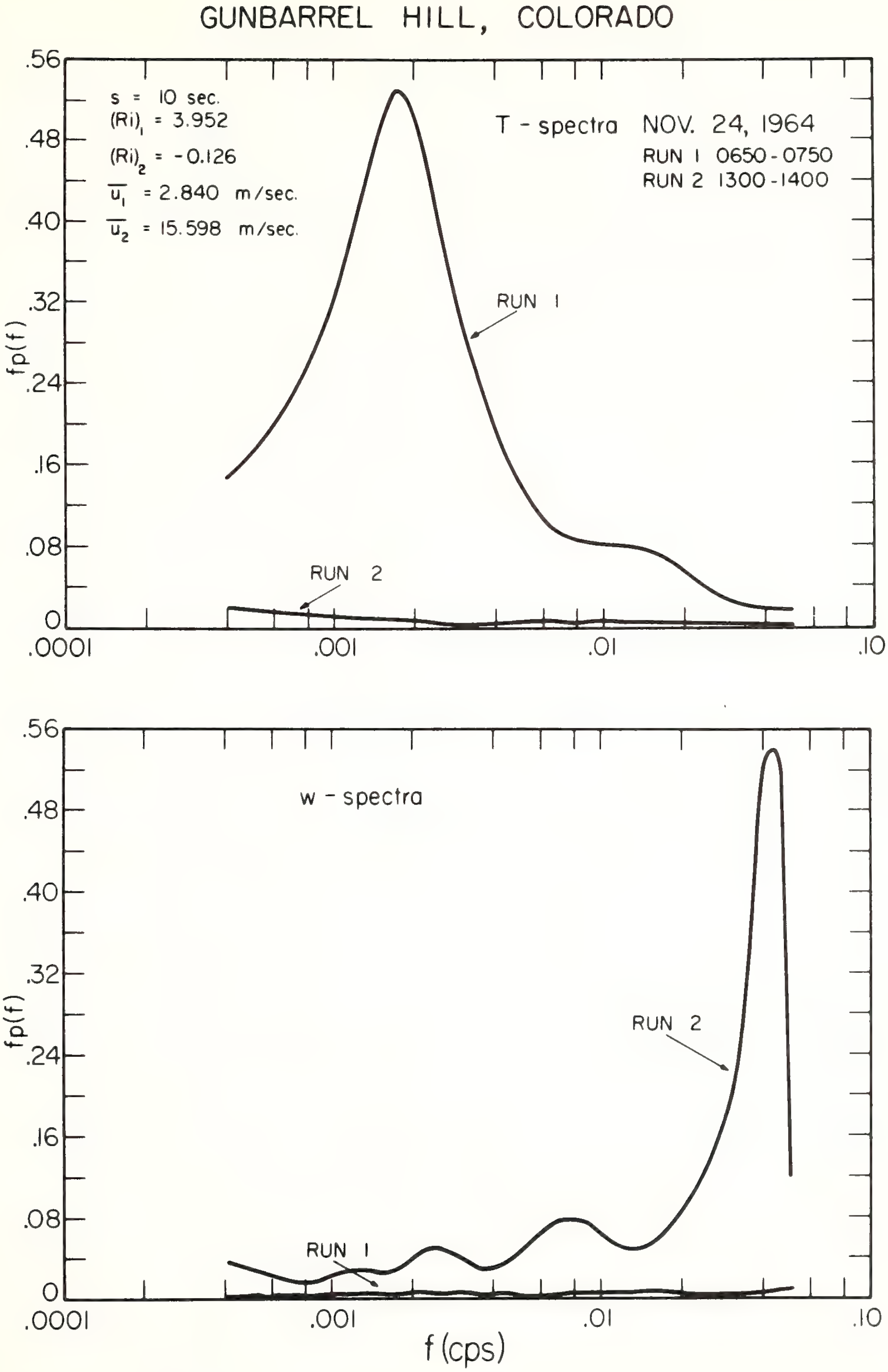

FIGURE 1. Spectra of temperature and vertical wind fluctuations; Gunbarrel Hill Tower, 50 foot level - November 24, 1964.

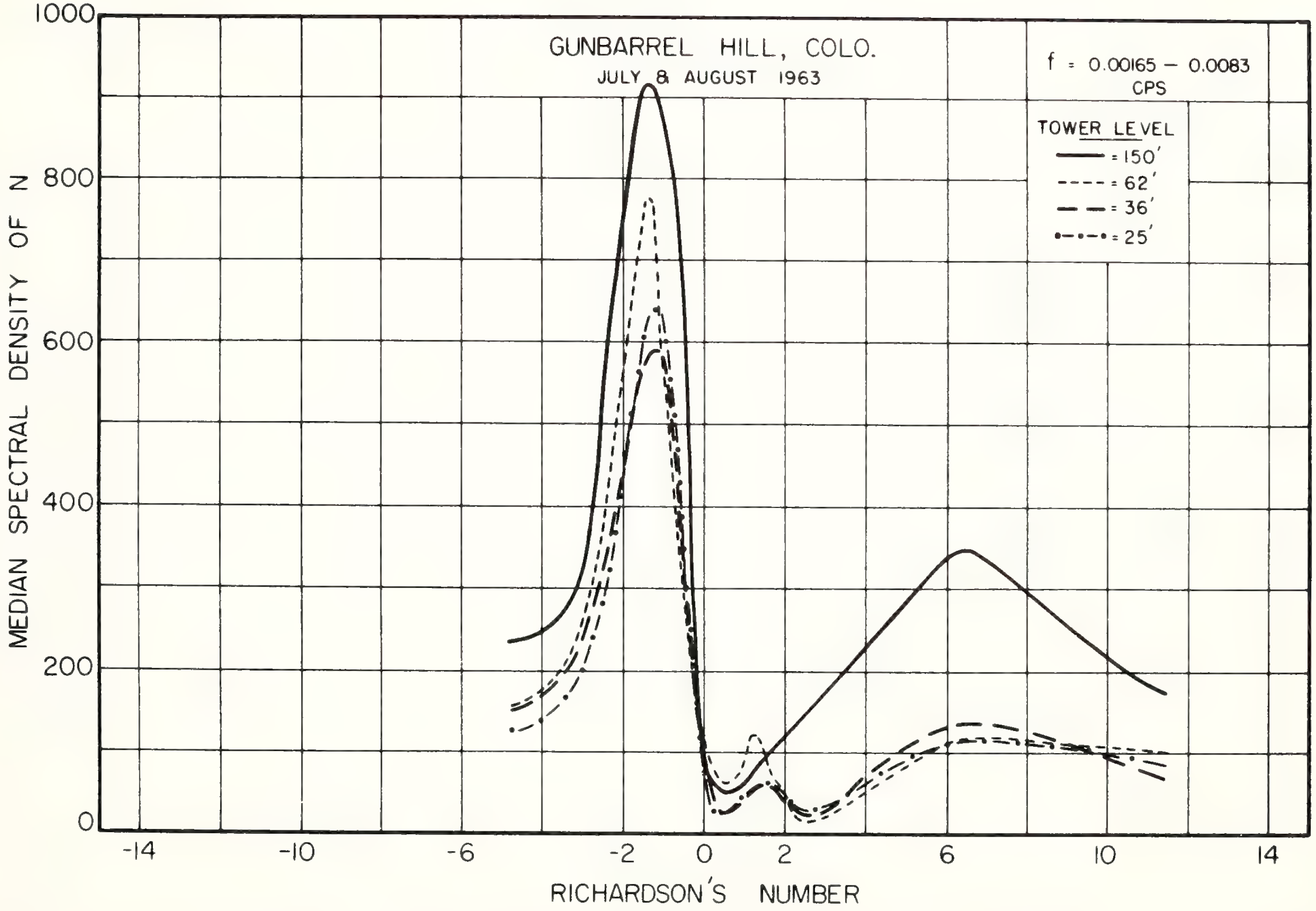

FIGURE 2. Height and stability dependence of median spectral density of N for the frequency range of $0.00165 < f < 0.0083$ cps.

for the observations of figure 3 is that of the chinook or föhn wind which is a warm, dry wind on the lee side of a mountain range, the warmth and dryness of the air being due to adiabatic compression upon descending the mountain slopes (Glossary of Meteorology, 1959). On this particular day the chinook started about 0500 when the wind increased from a few miles per hour to over 30 mph. The optical beam width, which is strongly affected by temperature inhomogeneities along the propagation path (15 km in length with a vertical drop of 80 meters) decreased from about 125 to 25 μradians. This decrease in beam width is consistant with what one would expect under chinook conditions, i.e. $\partial\theta/\partial z \rightarrow 0$ and $D_T(r) \rightarrow 0$. Quite consistent with this decrease in beam width is the increase in vertical beam wander, or change in apparent elevation angle. Recalling that the optical refractive index, n, is proportional to air density, then the increase in temperature lapse from, say, the normal -6°C/km to the adiabatic lapse of -10°C/km would tend to lessen the normal density gradient and thus produce less bending and a rise in the beam position (the "autoconvective" or constant density lapse rate of -34.3°C/km would produce straight rays). The change in total bending under these assumed conditions would lessen atmospheric bending by some 80μ radians, a number not inconsistent with that observed. The vertical beam wander remains high and the beamwidth low through 1600 hours, indicating that the air along the path remains well mixed even though the wind, which is recorded only at the lower terminal, decreases.

CONCLUSIONS

Theoretical and experimental evidence indicates that wind-induced mixing near the ground may so thoroughly mix parameters such as the radio and optical refractive index that their normal short-term variability effectively vanishes. It is evident, from both the many assumptions of the theoretical development and the lack of supporting meteorological observations during the optical experiments, that simultaneous combined radio, optical and meteorological measurements are required to further explore these preliminary conclusions.

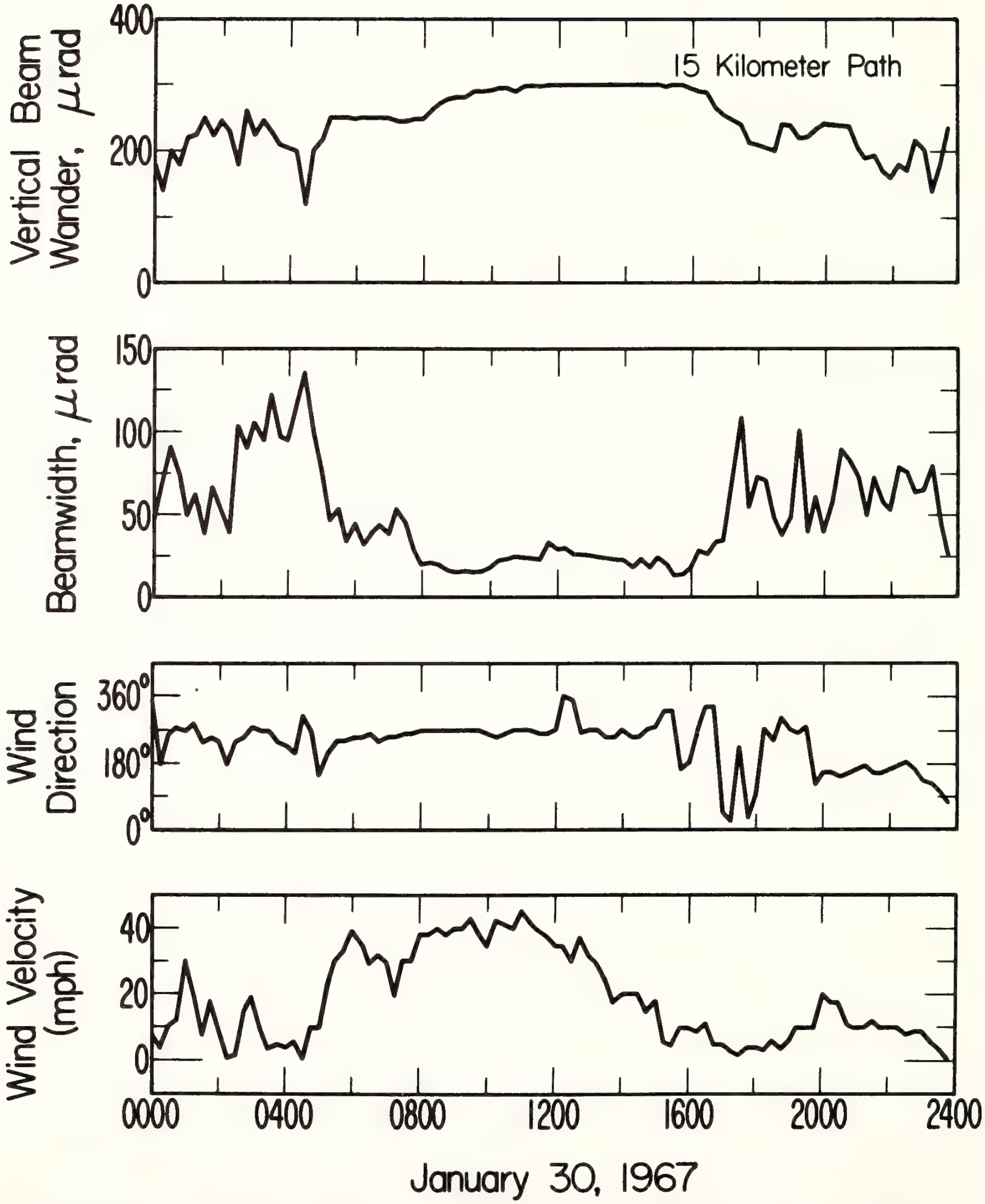

FIGURE 3. Optical propagation characteristics. Green Mountain - Table Mountain, Colorado, January 30, 1967.

B- 73894

REFERENCES

Bean, B. R., C. B. Emmanuel and R. W. Krinks (1967), Some spectral characteristics of the radio refractivity in the surface layer of the atmosphere, Radio Science, 2, No. 5, 503-510.

Glossary of Meteorology (1959), American Meteorological Society, Boston, Mass.

Lumley, J. L. and H. A. Panofsky (1964), The Structure of Atmospheric Turbulence, John Wiley and Sons, New York.

Monin, A. S. and A. M. Obukhov (1954), Basic regularity in turbulent mixing in the surface layer of the atmosphere, Trudy Geophys. Inst. ANSSSR, No. 24, 163.

Ochs, G. R. and C. G. Little (1968), Studies of atmospheric propagation of laser beams on 5.5, 15, 45, and 145 km paths, To be presented at the Conference on "Tropospheric Wave Propagation", London, England.

Petterssen, S. and W. C. Swinbank (1947), On the application of the Richardson criterion to large-scale turbulence in the free atmosphere, QJRMS 73:335-345.

Reiter, Elmar R. (1963), Jet-Stream Meteorology, The university of Chicago Press, Chicago, Ill.

Senderikhina, I. L. (1961), On the relationship among the coefficients of turbulent transport of momentum, heat and matter in the surface layer of the atmosphere, Trudy Glav. Geofiz. Obs., 121, 1.

Sheppard, P. A. (1952), Discussion of paper by Taylor (1952), QJRMS 73, 647.

Reprinted from Proceedings of the AGARD/EWPP XVIth Symposium, 3-1 through 3-13, 1970.

WORLDWIDE CHARACTERISTICS OF REFRACTIVE INDEX AND CLIMATOLOGICAL EFFECTS

G. D. Thayer, B. R. Bean, and B. A. Hart
Environmental Science Services Administration
Boulder, Colorado 80302
United States

SUMMARY

The development and present status of radio climatology -- the study of characteristics of the radio refractive index as they are related to climatic and meteorological variables -- is reviewed, from Newton's use of the exponential atmosphere to recent work on the climatology of radio refractive index turbulence. The results of work in four areas of radio climatology are discussed.

(1) Development of models of the general vertical structure of the refractive index has culminated in a three-part exponential profile, which is adequate in most parts of the world except where low-level subsidence inversions are common. Further work is needed to incorporate layers with unusual refractive index gradients into the exponential models.

(2) The general refractive index gradient, elevated layers with strong refractive index gradients, and winds in the common volume region have all been established as significant to the performance of transhorizon radio propagation systems. Elevated layers, which are perhaps the most important of these three factors, have been neglected in radio climatology surveys.

(3) Studies of the climatology of the initial gradient of the radio refractive index have revealed that the tropical areas of the world experience the most severe conditions; however, the data base is insufficient to properly define the radio climates of these regions, which are in the locales of most of the developing nations.

(4) The likelihood of turbulence of the radio refractive index can be determined from the gradient of the potential refractive index -- defined by an adiabatic process -- as calculated from conventional meteorological soundings of the atmosphere, but virtually no work has been done on the climatology of this gradient.

1. INTRODUCTION.

The manner in which radio waves propagate over and around the earth is determined in large part by the refractive index structure of the atmosphere through which the waves must travel. Thus, radio climatology -- the study of worldwide characteristics of the refractive index as they are related to climatic and meteorological variables -- is of fundamental importance in advancing our understanding of radio propagation within or through the atmosphere.

Radio-climatic theory has evolved in two primary fields. The first is the study of the general vertical structure of the refractive index -- its rate of decrease as a function of height -- and its relationship to the various climates of the world. This vertical structure affects both the diffraction of radio fields beyond the geometric horizon and the refraction of radio beams as they pass through the atmosphere. The second main field of study concerns the perturbations of the systematic, quasi-homogeneous refractive index structure -- specifically, ground-based layers (including ducts), elevated layers, small-to-medium-scale horizontal inhomogeneities of the refractive index, and turbulence of the refractive index. One or more of these perturbations will affect the stability of radio tracking system data, fading on line-of-sight paths, such as microwave relay systems, and the strength of radio signals over transhorizon paths of medium length operating in the so-called troposcatter mode.

In the sections that follow we shall review four areas:

(1) The development of radio-climatic models of the vertical refractive index structure and their applications.

(2) The climatology of refractive index gradients in the first kilometer of the atmosphere and of elevated layers and their importance to the problem of estimating troposcatter system performance.

(3) The radio climatology of unusual ground-based layers as applied to line-of-sight radio links and the reliability of radio tracking system data at low elevation angles.

(4) The climatology of radio refractive index turbulence.

2. THE CLIMATOLOGY OF VERTICAL REFRACTIVE INDEX STRUCTURE.

The general decrease of the refractive index with height is apparent in any vertical profile covering 10 km or more, such as the one shown in Figure 1. The overall exponential character of the height dependence of the refractive index is also evident whenever a vertical n-profile is plotted on a semi-logarithmic graph, as is done in Figure 1. This general exponential characteristic was, however, deduced by Sir Isaac Newton long before any vertical profile data were available.[1] Newton reasoned that

(a) the refractivity, n-1, of air, at optical wavelengths, is proportional to the density of the air; (b) the density is proportional to the pressure divided by the absolute temperature of the air; and (c) the pressure of the air is caused by the weight of all the air above it. The air pressure thus ought to behave exponentially, since it is proportional to the weight of all air above it; hence, if the absolute temperature were roughly constant with height -- and Newton had no data available that would have indicated a better assumption -- the optical refractivity should also follow an exponential law with height. Newton's rather accurate estimates of astronomical refraction were based on this simple model.

Although various exponential models were commonly used for calculating astronomical refraction effects by the early 1900's,[1] the first widely used model for radio refractive index was, interestingly enough, an essentially linear model introduced in the early 1930's in a now classic paper by Schelleng et al.[2] This is the well-known effective earth's radius model, and there are a number of reasons why it was a good choice at the time.

Compared with optical propagation theory, atmospheric radio propagation theory was still in its infancy in 1933. What was needed at that time particularly was a model that would allow calculations of diffracted radio fields beyond the horizon and that would supply corrections for refraction effects on line-of-sight paths between two points on the earth's surface; in the paper cited above[2] the approach was aimed at the latter need, although the effective earth's radius treatment subsequently proved to be very powerful in attacking a whole class of problems related to the diffracted field (see especially references 3 and 4).

The nearly linear refractive index profile of the effective earth's radius treatment did not adequately depict the normal refractive index structure through the entire atmosphere, but this was not an important failure in 1933; tracking radar and large radio telescopes requiring accurate refraction corrections for targets well within or beyond the earth's atmosphere had not yet been developed. With the increasing use of highly precise radio tracking systems in the 1940's and 1950's came the need for a more accurate model of the vertical refractive index.

A simple exponential model of the radio refractive index structure was first proposed in connection with the refraction problem.[5] Shortly thereafter a whole family of exponential profiles was proposed, with the decay constant given as a function of the initial, or surface, refractivity,[6] where the exponential reference atmosphere from the latter publication was defined by

$$N(z) = N_s \exp\left\{ \log\left[\frac{N_s - 7.32 \exp\{0.005577\, N_s\}}{N_s}\right] z \right\} \quad . \qquad (1)$$

Here N(z) is the radio refractivity $N \equiv (n-1) \times 10^6$ as a function of height z above the surface in kilometers, and N_s is the surface value of N at z = 0.

Early investigators felt that this model, being a simple exponential function of height for any given N_s, would be easy to handle analytically, but this proved not to be the case; not only is the exponential model very difficult to handle in mode theory for diffracted fields beyond the horizon, but even the simple integrals for refraction cannot be solved in closed form, although some good analytical approximations can be derived.[7,8] Nevertheless, the simple exponential model is a useful tool for making refraction corrections to radio tracking data, for example in computerized reduction of range tracking data based on a number of trackers.[9]

Recently, more sophisticated refractive index models have been introduced in which the "dry" and "wet" terms of the radio refractivity are treated separately; these terms are defined by

$$D = 77.6 \frac{P}{T} ,$$

$$W = 3.73 \times 10^5 \frac{e}{T^2} , \qquad (2)$$

where N = W + D, P is the air pressure in millibars, e is the partial pressure of water vapor in millibars, and T is the temperature in degrees Kelvin. Figure 2 shows the same data as Figure 1, but with the wet and dry terms presented separately; these data are typical in that the wet and dry terms are each approximately exponentially distributed with height but with different slopes. There is also a noticeable change in the slope of the dry-term distribution as one passes from the troposphere -- where the temperature generally decreases with height -- to the nearly-isothermal stratosphere; this change is evident in Figure 2 at about 13.5-km altitude.

Studies of the distribution with height of the wet and dry terms at many locations from the equatorial regions to the arctic and antarctic led to the formulation of a three-part exponential model of $\overline{N(z)}$.[10] The resulting model, with separate exponentials for the wet term, the tropospheric dry term, and the stratospheric dry term adequately represents the mean N(z) climate in most regions of the world.

For certain regions of the world, however, this model or any other simple analytic model, is totally or partly inadequate. This was first pointed out as a criticism of the simple, single-exponential model.[11] These regions, shown in Figure 3, are primarily the domains of the semipermanent subtropical high pressure systems, especially the tradewind zones along their eastern and equatorward margins.

The meteorology of these systems reveals pronounced low-level subsidence of potentially warm, dry air. The large temperature inversions that result from this subsidence result in a marked depression of the mean wet-term curves at low altitudes, as exemplified by the May profile for Dakar, Senegal, shown in Figure 4. Here the mean wet-term value drops from 93 at the surface to 37 at 500 m, a gradient of -112 N km^{-1}. Note that the wet-term value recovers at about $z = 4$ km to approximately the value it would have reached had there been a smooth exponential decrease from the surface.

How to deal with this type of $N(z)$ profile remains one of the unsolved problems of radio climatology. It may prove possible, for example, to construct a model of the subsidence-zone layer that could then be superimposed on the overall exponential model. Such a layer model would have to include as climatic/geographic-dependent variables the thickness and $N(z)$ gradient of the inversion zone, and the thickness of the transition layer that accomplishes the return to the normal profile.

3. THE RADIO CLIMATOLOGY OF TROPOSCATTER SIGNALS.

Early experimental work at radio frequencies above 40 MHz showed that the signals received at distances far beyond the optical horizon -- roughly 80 to 700 km from the transmitter -- were much stronger than could be accounted for by the simple diffraction of radio waves around a smooth, spherical earth of normal effective radius ~ 8,500 km.[12-16] In 1948, Norton[17] suggested that these high fields were caused by reflections from many small discontinuities in the refractive index of the atmosphere. The subsequent elaboration of this theory became known as tropospheric forward scatter, and Wheelon[18,19] showed that describing the process by use of the power wavenumber spectrum of the atmospheric dielectric irregularities was a powerful way to attack the problem theoretically. Thus, the field of atmospheric turbulence and diffusion has become closely enmeshed with the field of radio propagation. In most theories of tropospheric forward scatter, the idea developed is that the intensity of atmospheric dielectric fluctuations is a direct function of the prevailing vertical gradient of the refractive index and that the received troposcatter signal therefore would also be a direct function of the N-gradient. Thus, one of the simplest radio-climatic estimators of troposcatter signal strength is a measure of the average refractive index gradient in the lower atmosphere.

A widely used variable is ΔN, the average gradient of N between the surface and 1 km above the surface.[20] Because the correlation between monthly median signal strength and monthly mean ΔN at the path midpoint is useful at most locations throughout the world, the adequate mapping of ΔN on a monthly mean basis for all the countries of the world is a current goal of the CCIR.[21]

ΔN is also correlated with the surface refractivity N_s[6], which therefore can be used as a field-strength estimator for troposcatter systems in the absence of vertical refractive index data. Such predictions are, of course, less useful than those made from good vertical profile data; in particular, for those areas of the world where ΔN and N_s are not well correlated -- basically the regions shown in Figure 3 -- N_s is almost useless for this purpose.[22] However, since the inversions in the regions shown in Figure 3 are generally below 1 km in altitude, ΔN includes their effects and can still be of use in estimating troposcatter fields.

During the past fifteen years evidence has accumulated that some of the variability of troposcatter signal strengths -- especially the highest levels -- is produced by partial reflections from elevated layers of a sharp refractive index gradient along the path.[23-25] In 1956, a paper by Friis et al.[26] presented at a meeting of the IRE showed the connection between the purely statistical forward scatter theory and the simple theory of partial reflection from an elevated layer. This paper served to stimulate interest in the reflection mechanism of tropospheric propagation, and to be noted also is that the theory it presents is much closer to the original concept advanced by Norton[17] than is the conventional forward-scatter theory.

Only layers located within the common volume can provide direct, single, specular reflections, which are required by most reflection mechanism theories. Surprisingly, the most recent evidence indicates that layers located below the common volume are far more effective in producing strong signals on transhorizon paths than are layers located within the common volume,[25] a situation shown in Figure 5. Layers located below this point can provide multiple specular reflections; there is strong evidence that this is sometimes the case.[27-29] Nevertheless, there is considerable evidence in these and other published results that strong contributions to signal strength are made by layers that are at heights not satisfying the constraints* imposed by the multiple-reflection process.[25,27,29]

We can only conjecture what the propagation mechanism is for these layers. A likely process might involve reflections from facets or "feuillets" in the layer that are tilted with respect to the horizontal. Part of the transmitted power, reflected by such facets into a near-horizontal trajectory, could propagate along the main layer interface in a sort of one-sided waveguide mode called a "whispering gallery mode."[30] Continuous leakage of power from the whispering gallery mode would result from partial reflections by other tilted facets in the layer, which would eventually direct energy to the receiver. Although such a process sounds inefficient, it can, in fact, be highly efficient compared with the ordinary forward-scatter mechanism.

---

*The propagation ray path must form part of an inscribed polygon with respect to the layer, which is assumed to be circular (horizontal). Multiple reflections are therefore only possible from layers located at certain discrete heights over any particular path.

The climatology of elevated layers has thus become an important factor in assessing the expected performance of troposcatter systems. Recent work in Sweden has shown some of the conditions, e.g. lower frequencies, summertime, under which layer-mode propagation is dominant over conventional forward-scatter.[31] However, our knowledge of the climatology of elevated layers is sorely limited. Besides knowledge of the probability of occurrence of elevated layers at given locations, we need statistics on the height, vertical thickness, and N-gradient of such layers when they do occur. Other than some reports on a few special areas, notably one on the Atlantic trade wind system,[32] information of this sort is almost nonexistent.

Qualitative investigations show that strong elevated layers are found at many locations throughout the world, and, except for a marked persistence of such layers in the subsidence zones shown in Figure 3, are not much more common in the tropics than in some of the more temperate climatic zones. Further work on the climatology and meteorology of elevated layers is badly needed.

Data from some troposcatter paths at times when elevated layers are absent indicate that the cross-path component of wind just above the crossover height, e.g. as measured by a rawinsonde, is related to the strength of the received signal.[25] When these winds are strong -- over 25 knots-- the received signals are low, but when they are light the signals are often considerably stronger. This phenomenon may be connected with the differences between mechanical and refractive index turbulence.[33] Strong vertical wind shear induces mechanical turbulence and vertical mixing that tend to produce an adiabatic layer; however, such a well-mixed adiabatic layer will show only small irregularities in the refractive index, and hence a low level of N-turbulence -- a severely depressed power spectrum of N. Thus, the results reported by Fengler[25] may be an indication that, in the absence of elevated layers, a conventional forward-scatter mechanism is dominant. This phenomenon clearly deserves further study.

4. THE RADIO CLIMATE NEAR THE GROUND.

The gradient of the refractive index near the surface of the earth has a direct influence on the performance of such systems as radio relay links and radars used for tracking targets at low altitudes or low elevation angles; at a zero elevation angle about 15% of the total refraction of a radio ray is experienced in the first 100 m above the transmitter in average conditions, and with superrefraction this figure increases to 20% or more. The study of initial N-gradients is therefore a significant aspect of radio climatology.

There are two extremes of initial gradient behavior: subrefraction and superrefraction. Subrefraction, as usually defined, occurs when the initial gradient of N is positive, $dN/dz > 0$; superrefraction has been variously defined as dN/dz less than -80, -100, or -120 N km^{-1}. We will use -100 N km^{-1} as the limit since it is twice the average worldwide initial gradient value of -50 N km^{-1} and conveniently sets the superrefractive and subrefractive boundaries equally above and below the average. A superrefractive layer with a gradient sufficiently strong to bend an initially-horizontal radio ray along the curved surface of the earth -- a phenomenon called "trapping," since the ray cannot penetrate the top of the layer -- is called a "radio duct." The ducting gradient is defined mathematically as that which will cause a radio ray at a zero elevation angle to be refracted downward with a radius of curvature equal to that of the earth; this condition is shown to be

$$\frac{dn}{dz} = -\frac{1}{a}$$

$$\cong -157 \times 10^{-6} \text{km}^{-1}, \qquad (3)$$

where a is the radius of the earth.

Radio ducting has been studied in great detail, especially during and immediately after World War II in connection with tracking radar.[34] Although not yet fully understood, ducting is a well-known phenomenon in radio climatology; it often results in microwave radio energy propagating many hundreds or even thousands of kilometers beyond the normal horizon.[34] At the same time, signals from a transmitter located above the ducting layer may show deep fading or a total loss of signal at a receiver located on the ground.[35]

The opposite phenomenon, subrefraction, has received much less attention. The probability of strong subrefraction at a particular location is critical to the design of microwave relay links, since economy dictates the use of the largest feasible separation between antennas. For example, in a radio link designed for a maximum gradient of $dN/dz = 0$ the receiver will be just above the horizon of the transmitter for an effective earth's radius of ~ 6370 km; if the gradient now increases to + 100 N/km, the effective earth's radius will decrease to ~ 3900 km and the receiver will be well below the transmitter's horizon. This phenomenon is known as diffraction-fading, because it is produced by having the receiver below the radio horizon, where it can receive only diffracted (and scattered) signals.

Subrefractive gradients at optical wavelengths are rare; since the optical refractive index is insensitive to water vapor, a subrefractive gradient must be produced by a super-autoconvective lapse rate -- a decrease of temperature with height at a rate exceeding 3.4°C/100 m. Although super-autoconvective lapse rates are observed often under sunny weather conditions, especially in desert areas and sometimes to heights of 200 + m above the surface, the lapse rate seldom exceeds the critical value of 3.4°C/100 m by very much, except in restricted layers close to the ground. Maximum optical subrefractive gradients are therefore usually restricted to values of no more than + 20 or + 30 N km^{-1}. The very strong subrefractive gradients observed for the radio refractive index -- up to + 300 N km^{-1} over 100 m or stronger -- are produced by humidity inversions (an increase of absolute humidity with height). Thus there is little correlation between the optical and radio behavior over a line-of-sight path during conditions favorable to subrefraction.

The occurrence of super-autoconvective lapse rates of temperature is interesting in itself. Because such lapse rates result in absolute mechanical instability of the air, they were formerly believed to occur only in very thin layers, or under extreme conditions, such as in tornadoes or "dust devils." Data from the tropical desert areas of the world show that this is not true. For example, at Colomb-Bechar, Algeria, data taken by radiosonde at 1200 local time from May 1 to September 30, 1964 and 1965, show a lapse rate in the surface layer exceeding 3.4°C/100 m on 24% of the days included; Figure 6 shows these data. The lapse rate was superadiabatic (over 1°C/100 m) on all but 23 days; the mean lapse rate for all the days was 2.6°C/100 m over a mean layer thickness of 246 m. The strongest cases of autoconvection found were a lapse rate of 9.4°C/100 m over a layer 68 m thick and a lapse rate of 7.8°C/100 m over a 97-m layer; the N-gradient for the latter case was +77 N km^{-1}, or $k = 2/3$.

The strongest subrefraction occurred when a humidity inversion was also present. Such inversions are frequently found under strongly convective conditions, because the density of moist air is less than that of dry air at the same temperature and pressure, and thus the available moisture tends to be transported to the top of the convective layer. At Colomb-Bechar, for the periods mentioned above, the dewpoint increased with height on 67 of the 153 days; the strongest subrefraction was a gradient of + 259 N km^{-1} ($k \cong 3/8$) for a layer 104 m thick. The temperature lapse rate was only 1.3°C/100 m for this case, but there was a water vapor inversion of 7 mb from the base to the top of the layer.

Subrefraction is also found in many locations during nighttime with a temperature inversion; the subrefraction occurs when moisture carried aloft during the daytime becomes trapped in the warm air at the top of the temperature inversion. The low level of eddy diffusivity under such stable temperature inversion conditions prevents the redistribution of the water vapor. This type of subrefraction can logically be called "residual subrefraction."

Both types of subrefraction are commonly found in warmer climates, especially the tropical areas of the world. At Aden, Arabia, for example, during nighttime the refractivity gradient over the first 50 m exceeds + 300 N km^{-1} for 1 to 2% of the time, resulting in an effective earth's radius factor k of 1/3 or less, i.e., 1/4 the "normal" 4/3 value.

In fact, one of the chief problems in tropical radio climatology is the large variability of the initial N-gradients as compared with the temperate zones. Some extreme examples of tropical N-gradients are as follows:

(1) A subrefractive layer 50 m thick with a gradient of + 1024 N km^{-1} observed at Darwin, Australia, in November.

(2) A radio duct 867 m thick observed at Bahrain Island, Persian Gulf, in August.

(3) Numerous gradients stronger than - 1000 N km^{-1} over layers 100 m thick, observed at Bahrain Island, Dakar, Senegal, and other locations, at many different times.

(4) A superrefractive layer 1421 m thick with a gradient of - 127 N km^{-1} observed at Calcutta, India, in the month of May.

The extremes listed above are virtually unheard of in temperate locations, such as western Europe. The radio climatology of the tropics is therefore an important field for future study; this is especially true because most of the developing nations of the world, which seek to establish a telecommunication technology, are located within or near the tropics. The first priority should be to increase the data base for refractive index profiles, which at the present is miniscule compared with the data base for Europe, North America, and some of the other more developed areas of the world.

5. THE CLIMATOLOGY OF RADIO REFRACTIVE INDEX TURBULENCE.

As pointed out by Bean,[33] the term "turbulence" may have different meanings for the radio scientist and the atmospheric scientist. To the atmospheric scientist, the atmosphere is turbulent when the mechanical turbulence is high; strong mechanical turbulence enhances, for example, the rate of diffusion of passive atmospheric constituents, such as pollutants. However, the radio scientist considers the atmosphere as turbulent when it contains a spectral hierarchy of eddies or "blobs" of differing radio refractive index; this may or may not occur under conditions of strong mechanical turbulence.

In the analysis that follows we must make use of the concept of potential meteorological variables. The potential value of a meteorological variable is the value that variable would attain if a parcel of air from the level under consideration were to be transferred "adiabatically" to some specific reference level. We exclude any changes that would involve condensation of water vapor -- the so-called psendo-adiabatic process -- as beyond the scope of our treatment.

The likelihood of strong mechanical turbulence is indicated by a Richardson number less than 1/4; the Richardson number is given by[36]

$$\mathrm{Ri} = \frac{g\left(\frac{\partial\overline{\theta}}{\partial z}\right)}{\overline{\theta}\left(\frac{\partial\overline{v}}{\partial z}\right)^2} \quad , \tag{4}$$

where g is the acceleration of gravity, θ is the potential temperature, v is the wind velocity, and z is height. The overbars denote mean values over the layer under consideration.

When the vertical gradient of temperature is 1°C/100 m, the potential temperature is constant with height, and $d\theta/dz = 0$; this temperature gradient is called the adiabatic lapse rate. With an adiabatic lapse rate, strong convection and mechanical turbulence often occur; however, turbulence of optical refractive index, which depends almost entirely on the density of the air, is at a minimum because the potential density is constant with height. Thus, a parcel of air transported by mechanical turbulence to a different level in the atmosphere will arrive there -- with an adiabatic lapse rate -- at the same density, and hence the same refractive index, as the air around i.e.[33] From a propagation standpoint, the atmosphere under these conditions is described as "well mixed."

Two conditions are necessary therefore to allow a turbulent refractive index structure to develop in the atmosphere: the presence of mechanical turbulence and a sufficiently strong vertical gradient of the potential refractive index. Some mechanical turbulence is necessary to transport parcels of air to different heights; a strong vertical gradient of potential refractive index then insures that these parcels of air will arrive at their new heights with a markedly different refractive index than the air around them. This process produces an atmospheric structure consisting of many different-sized parcels, or eddies, of air with contrasting refractive index values; such a turbulent refractive index structure is capable of scattering radio waves and is the mechanism responsible for troposcatter propagation when layering or stratification of the atmosphere is not present.

The potential refractive index of the atmosphere can be calculated from the potential refractive modulus Φ,[37] which is given by

$$\Phi = \frac{77.6\,P_0}{\theta} + 3.73 \times 10^5\,\frac{e_0}{\theta^2} \quad , \tag{5}$$

where P_0 is the pressure at an arbitrary reference level, θ is the potential temperature at the reference level, and e_0 is the potential water vapor partial pressure at the reference level. The potential temperature is given by

$$\theta = T\left(\frac{P_0}{P}\right)^{0.288} \quad , \tag{6}$$

and the potential water vapor partial pressure is given by

$$e_0 = e\left(\frac{P_0}{P}\right) \quad . \tag{7}$$

In these equations we assume there is no addition or subtraction of water vapor from a parcel of air if it is lifted, i.e., a dry adiabatic process is considered.

The derivative of Φ with respect to height is

$$\frac{d\Phi}{dz} = -\frac{77.6\,P_0}{\theta^2}\,\frac{d\theta}{dz} + \frac{3.73 \times 10^5}{\theta^2}\,\frac{de_0}{dz} - \frac{7.46 \times 10^5\,e_0}{\theta^3}\,\frac{d\theta}{dz} \quad , \tag{8}$$

where P_0 is a constant. If we define W_0 as the potential wet term

$$W_0 \equiv \frac{3.73 \times 10^5\,e_0}{\theta^2} \quad , \tag{9}$$

then (8) becomes

$$\frac{d\Phi}{dz} = -\frac{(\Phi + W_0)}{\theta}\,\frac{d\theta}{dz} + \frac{W_0}{e_0}\,\frac{de_0}{dz} \quad . \tag{10}$$

Refractive index turbulence will be at a low level whenever $d\Phi/dz$ is close to or equal to zero, as demonstrated earlier. The condition $d\Phi/dz \simeq 0$ can be satisfied either by $d\theta/dz$ and de_0/dz both being close to zero, or by

$$\frac{de_0}{dz} \simeq \frac{e_0}{W_0}\,\frac{(\Phi + W_0)}{\theta}\,\frac{d\theta}{dz} \quad . \tag{11}$$

Condition (11) can be simplified to

$$\frac{de_0}{dz} \cong \left[2 \times 10^{-4} P_0 + \frac{2e_0}{\theta} \right] \frac{d\theta}{dz} , \tag{12}$$

where the units are millibars and degrees Kelvin. The equations involving de_0/dz can be written in terms of the specific humidity q or the mixing ratio w by noting that

$$q \cong w \cong 0622 \frac{e}{P} , \tag{13}$$

while, from (7),

$$\frac{de_0}{dz} = P_0 \frac{d}{dz} \left(\frac{e}{P} \right) \cong 1.6 \, P_0 \frac{dq}{dz} \cong 1.6 \, P_0 \frac{dw}{dz} . \tag{14}$$

Thus, the first condition for low refractive index turbulence, $d\theta/dz \cong 0$ and $de_0/dz \cong 0$, will be satisfied whenever the potential temperature and the specific humidity or mixing ratio are approximately constant with height, while the second condition given by (12) becomes

$$\frac{dq}{dz} \cong 1.2 \times 10^{-4} \left[1 + 1.6 \frac{q_0}{\theta} \times 10^4 \right] \frac{d\theta}{dz} . \tag{15}$$

Finally, for q or w in the usual units of parts per thousand, e.g., $g(kg)^{-1}$, which we shall denote as q^* or w^*, (15) becomes

$$\frac{dq^*}{dz} \cong 0.12 \left[1 + 16 \left(\frac{q_0^*}{\theta} \right) \right] \frac{d\theta}{dz} . \tag{16}$$

Since the potential temperature normally increases with height, the specific humidity must also increase with height in order to satisfy (16); an increase of q with height is often found in temperature inversion layers, but q ordinarily decreases with height. When the potential temperature decreases with height, i.e., when the temperature lapse rate exceeds the dry adiabatic rate, the specific humidity or mixing ratio must also decrease with height to satisfy (16), a situation more likely to be encountered in nature. Because strong mechanical turbulence will usually be found when the temperature lapse rate is superadiabatic, (16) is most important at these times as an indicator of the unlikeliness of refractive index turbulence.

Figure 7 shows the combinations of dq/dz and dT/dz that will satisfy condition (16) for various values of q_0^*/θ. Figure 7 is plotted in terms of dT/dz, and

$$\frac{d\theta}{dz} = \left(\frac{P_0}{P} \right)^{0.288} \left[\frac{dT}{dz} + \Gamma \right] , \tag{17}$$

where Γ is the dry adiabatic lapse rate, i.e., about 1°K/100 m. We have assumed the factor $(P_0/P)^{0.288}$ to be equal to 1; thus the values of $d\theta/dz$ used will be correct within a 5% error, provided P_0/P does not exceed 1.185. If P_0 is 1000 mb, then this 5% error in $d\theta/dz$ will not be exceeded until P is less than 850 mb, or about 1500 m above the reference level. Figure 7 is therefore valid throughout the atmospheric boundary layer.

The climatology of radio refractive index turbulence can be determined by applying the criteria for mechanical instability, e.g., Richardson number, and refractive index potential turbulence, e.g., a high value of potential refractive modulus height gradient or a negative criterion such as (16), to the climatic data on winds, temperature, and humidity for a particular area. This could be done with conventional rawinsonde data. Apparently, no studies of this sort have been done, and radio refractive index turbulence climatology appears to be a fertile field for work along these lines.

6. CONCLUSIONS.

We have reviewed the progress to date in four major fields of radio climatology and have found that although much has been learned, a great deal remains to be accomplished.

Relatively sophisticated models of the vertical distribution of the radio refractive index have been developed, yet a method of handling problem areas, which have abnormal N-profiles, remains to be discovered.

The most recent work on problems of transhorizon radio propagation shows that elevated layers in the troposphere are of fundamental importance as a propagation mechanism, but very little is known of the climatology of such layers.

The importance in many radio propagation problems of the initial refractive index gradient is well known, and existing theory is sufficient to obtain useful results from climatological data. However, the most highly variable of such radio climates occur in the tropical areas of the world, and we are not now able to accurately define most of these tropical radio climates, largely because of an insufficient data base.

Finally, although we have seen that the climatology of radio refractive index turbulence can be objectively defined, we find that virtually no work has been done on this important aspect of radio climatology.

7. REFERENCES.

1. Garfinkel, B., An investigation in the theory of astronomical refraction, Astron. J. 50, 8, 169 (1944).

2. Schelleng, J. C., C. R. Burrows, and E. B. Ferrell, Ultra-short-wave propagation, Proc. IRE 21, 3, 427 (1933).

3. Bremmer, H., On the theory of wave propagation through a concentrically stratified troposphere with a smooth profile, J. Res. NBS 64D, 5, 467 (1960), and pt. II J. Res. NBS 66D, 1, 31 (1962).

4. Wait, J. R., Electromagnetic Waves in Stratified Media, Pergamon Press, London (1962).

5. Bauer, J. R., W. C. Mason, and F. A. Wilson, Radio refraction in a cool exponential atmosphere, Tech. Rept. 186, Lincoln Laboratory, Massachusetts Institute of Technology, Cambridge, Mass., (1958).

6 Bean, B. R., and G. D. Thayer, CRPL Exponential Reference Atmosphere, Natl. Bur. of Standards Monograph 4, U. S. Govt. Printing Office, Washington, D.C. (1959).

7. Thayer, G. D., A formula for radio ray refraction in an exponential atmosphere, J. Res. NBS 65D, 2, 181 (1961).

8. Freeman, J. J., Range-error compensation for a troposphere with exponentially varying refractivity, J. Res. NBS 66D, 6, 695 (1962).

9. Gardner, C., Determination of elevation and slant range errors due to atmospheric refraction, Pacific Missile Range Tech. Note No. 3280-6(1962).

10. Bean, B. R., B. A. Cahoon, C. A. Samson, and G. D. Thayer, A World Atlas of Atmospheric Radio Refractivity, ESSA Monograph 1, U.S. Govt. Printing Office, Washington, D.C. (1966).

11. Misme, P., B. R. Bean, and G. D. Thayer, Models of the atmospheric radio refractive index, Proc. IRE 48, 8, 1498 (1960).

12. van der Pol, B., and H. Bremmer, The diffraction of electromagnetic waves from an electrical point source round a finitely conducting sphere, with applications to radio telegraphy and the theory of the rainbow, Phil. Mag. Ser 7, 24, 141 and 825 (1937); also 25, 817 (1938), 27, 261 (1939).

13. Marconi, G., Radio communication by means of very short electric waves, Proc. Roy. Inst. Great Britain, Dec. 1932.

14. Hull, R. A., Air-wave bending of ultra-high-frequency waves, QST 21, 5, 16 (1937).

15. Englund, C. R., A. B. Crawford, and W. W. Mumford, Ultra-short wave transmission and atmospheric irregularities, Bell System Tech. J. 17, 4, 489 (1938).

16. Maclean, K. G., and G. S. Wickizer, Notes on the random fading of 50 mc signals over nonoptical paths, Proc. IRE 27, 8, 501 (1939).

17. Norton, K. A., Propagation in the FM broadcast band, in Advances in Electronics, Academic Press, 1, 381 (1948).

18. Wheelon, A. D., Relation of radio measurements to the spectrum of tropospheric dielectric fluctuations, J. Appl. Phys. 28, 6, 684 (1957).

19. Wheelon, A. D., Radio-wave scattering by tropospheric irregularities, J. Res. NBS 63D, 2, 205 (1959).

20. Bean, B. R., and F. M. Meaney, Some applications of the monthly median refractivity gradient in tropospheric propagation, Proc. IRE 43, 10, 1419 (1955).

21. Reports and Recommendations of the Plenary Meeting of the CCIR, New Delhi, 1969; I.T.U., Geneva, 1969.

22. Misme, P., Quelques aspects de la radiométéorologie et de la radioclimatologie, Ann. Telecomm. 15, 11-12, 266 (1960).

23. du Castel, F., P. Misme, and J. Voge, Sur le rôle des phenomènes de réflexion dans la propagation lointaine des ondes ultracourtes, in Electromagnetic Wave Propagation, 670-683, Academic Press, London (1960).

24. Bean, B. R., V. R. Frank, and J. A. Lane, A radiometeorological study, Part II. An analysis of VHF field strength variations and refractive index profiles, J. Res. NBS 67D, 6, 597 (1963).

25. Fengler, G., Dependence of 500 Mc/s field strength values and fading frequencies on meteorological parameters, Proc. 1964 World Conf. on Radio-Meteorology, Boulder, Colo., Sept. 14-18, 1964, p. 84, A.M.S., Boston, Massachusetts.

26. Friis, H. T., A. B. Crawford, and D. C. Hogg, A reflection theory for propagation beyond the horizon, Bell System Tech. J. 36, 3, 627 (1957).

27. Lane, J. A., and P. W. Sollum, VHF transmission over distances of 140 and 300 km, Proc. IEE 112, 2, 254 (1965).

28. Hall, M. P. M., VHF radio propagation by double-hop reflection from a tropospheric layer, Proc. IEE 115, 4, 503 (1968).

29. Hall, M. P. M., Further evidence of VHF propagation by successive reflections from an elevated layer in the troposphere, Proc. IEE 115, 11, 1595 (1968).

30. Wait, J. R., Whispering-gallery modes in a tropospheric layer, Electronics Letters 4, 18, 377 (1968).

31. Eklund, F., and S. Wickerts, Wavelength dependence of microwave propagation far beyond the radio horizon, Radio Sci. 3 (New Series), 11, 1066 (1968).

32. Dougherty, H. T., L. P. Riggs, and W. B. Sweezy, Characteristics of the Atlantic trade wind system significant for radio propagation, ESSA Tech. Rept. IER 29-ITSA 29, April 1967.

33. Bean, B. R., Meteorological factors affecting the fine-scale structure of the radio and optical refractive index, Proc. Conf. on Tropospheric Wave Prop., 30 Sept.-2 Oct. 1968, IEE Conf. Publ. No. 48, London.

34. Kerr, D. E. (editor), Propagation of Short Radio Waves, in MIT Radiation Laboratory Series, McGraw-Hill, New York (1951).

35. Bean, B. R., Prolonged space wave fadeouts at 1046 Mc observed in Cheyenne Mountain propagation program, Proc. IRE 42, 5, 848 (1954).

36. Any standard text on dynamic meteorology. The authors particularly recommend: S. L. Hess, Introduction to Theoretical Meteorology, H. Holt and Co., New York 1959.

37. Kerr, D. E., op. cit., p. 199.

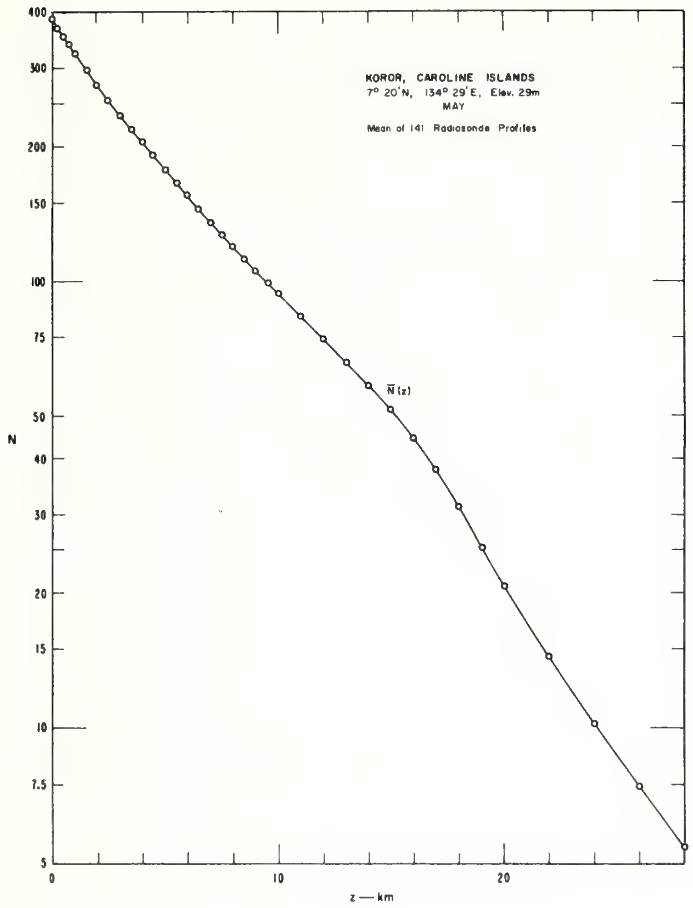

Fig. 1 Five-year mean N-profile for Koror, Caroline Islands, in May

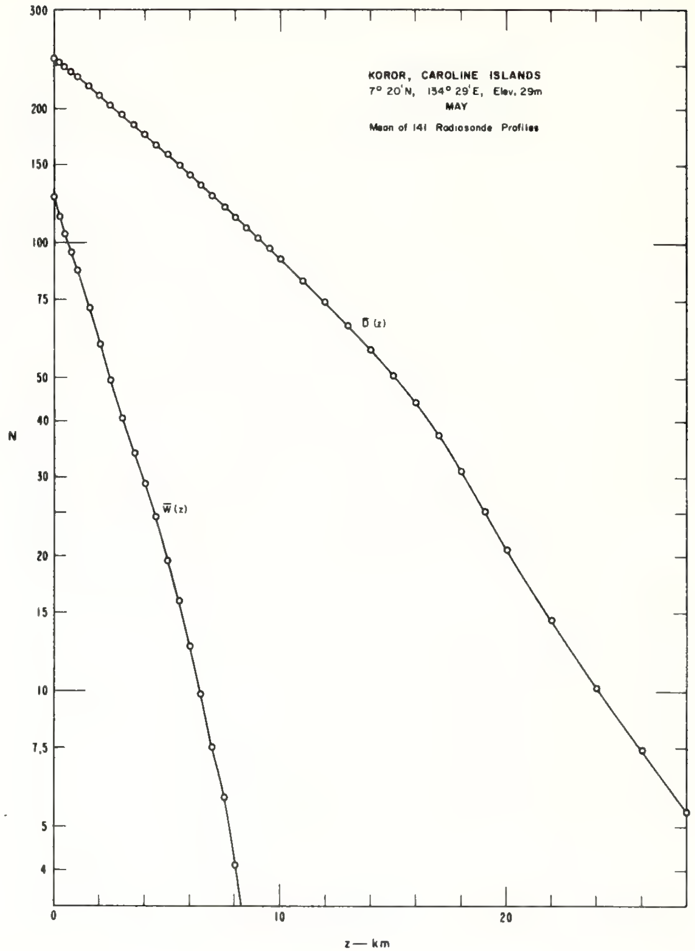

Fig. 2 Five-year mean wet- and dry-term profiles for Koror in May

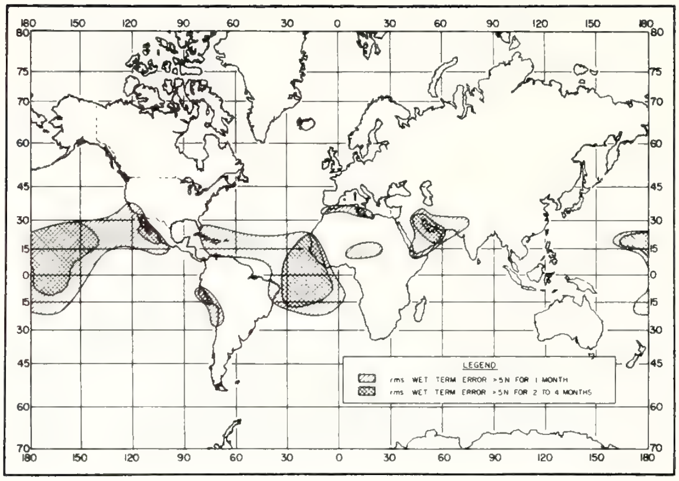

Fig.3 Areas of the world where the three-part exponential model of N(z) fails

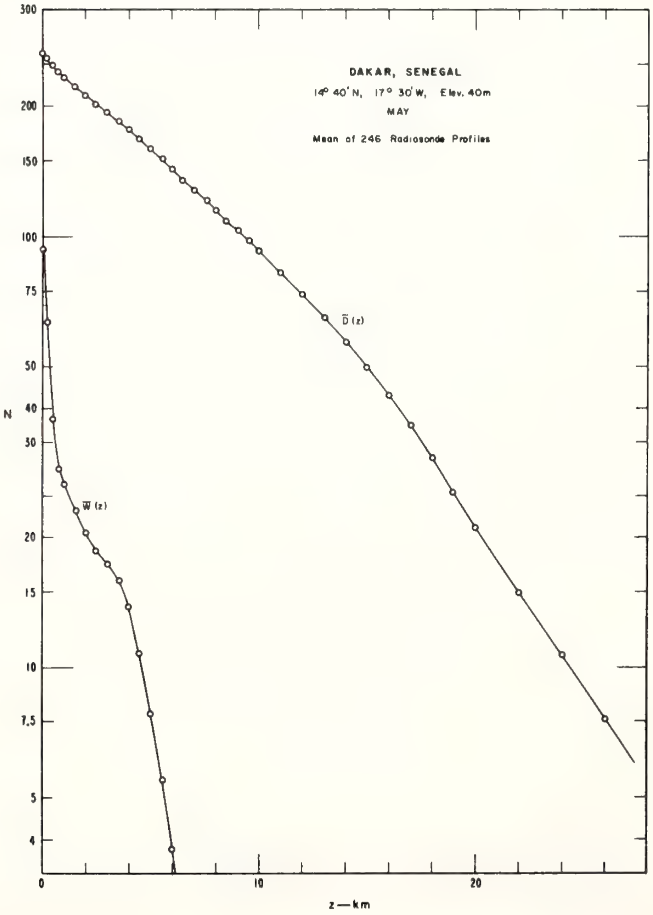

Fig.4 Five-year mean wet- and dry-term profiles for Dakar, Senegal, in May

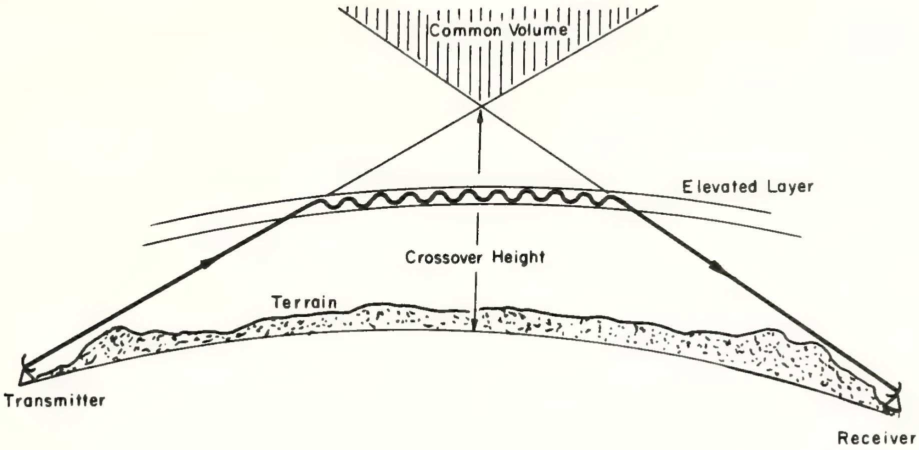

Fig.5 Tropospheric propagation by a layer located below the common volume

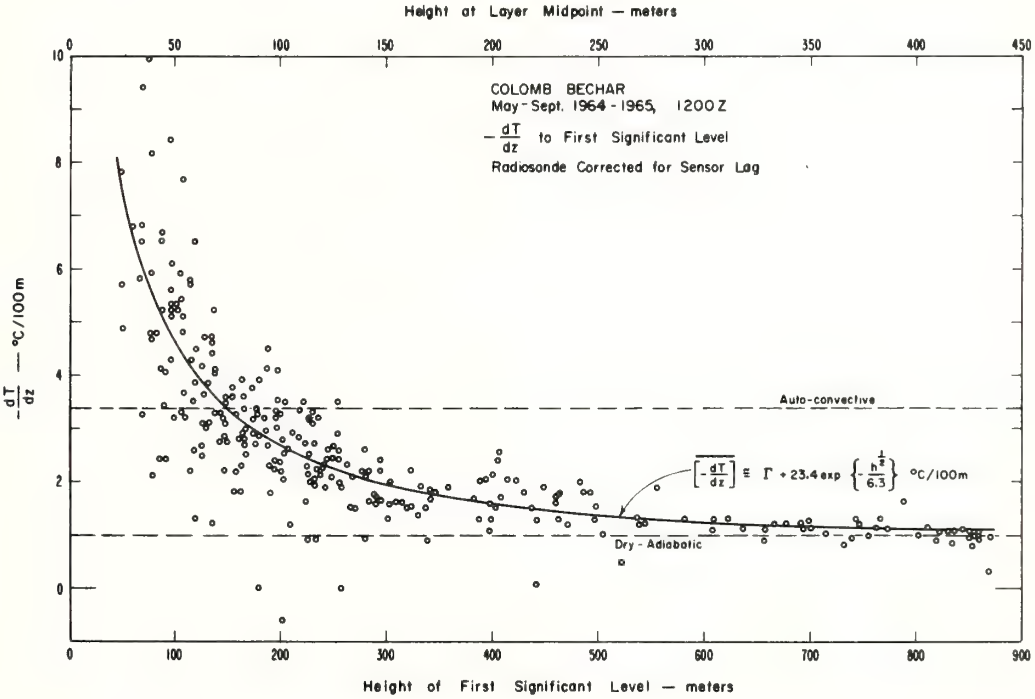

Fig.6 Temperature lapse rates observed at Colomb-Bechar, Algeria, during the summers of 1964 and 1965

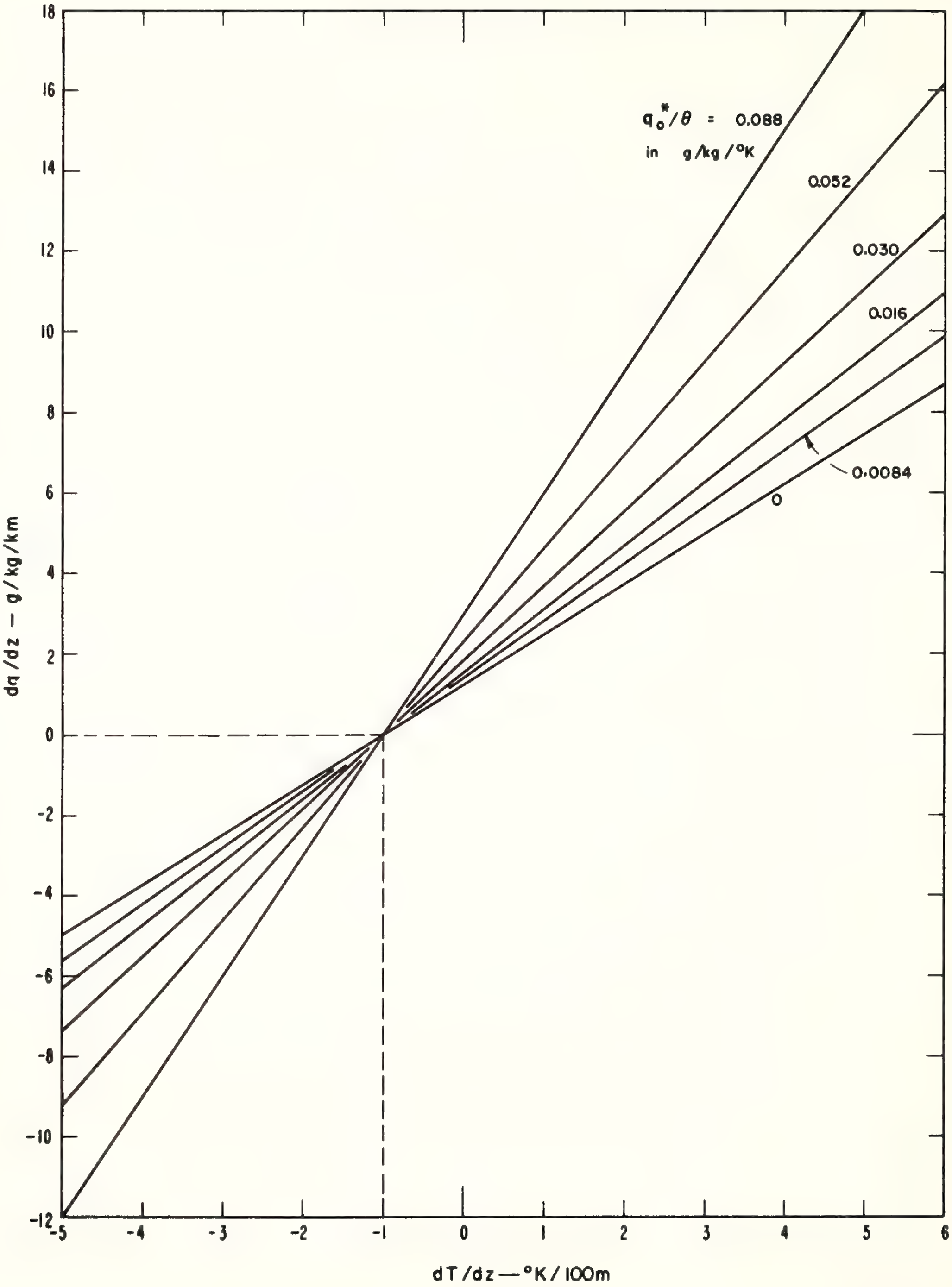

Fig.7 Temperature gradient and specific humidity gradient combinations that result in a potential refractive modulus gradient of zero

Reprinted from Journal of Geophysical Research, Space Physics
75, No. 28, 5535-5544, 1970.

The Ionospheric Response to Internal Gravity Waves

1. The F_2 Region Response

William H. Hooke

Institute for Telecommunication Sciences, ESSA Research Laboratories,
Boulder, Colorado 80302

The F_2 region ionospheric response to individual internal gravity waves is calculated as a function of the azimuth of wave propagation. This response is shown to be highly anisotropic, with the anisotropy itself depending on the wave parameters, the geomagnetic dip, and the prevailing ionization density gradient. Because the ionization density gradient changes with time of day and season, the ionospheric response and hence the traveling ionospheric disturbance statistics themselves should exhibit corresponding diurnal and seasonal variations. The physical basis for the anisotropy of the ionospheric response is discussed.

Earlier theoretical work [*Hooke*, 1968*a*] has shown that internal gravity waves produce traveling ionospheric disturbances (TID's) through a variety of photochemical and dynamical means in such a way that the ionospheric response to the waves should be anisotropic and subject to diurnal and seasonal variations. In other words, two internal gravity waves that have the same periods, wavelengths, and amplitudes and are alike in all respects except their directions of travel over the face of the globe or the times of their propagation could produce fractional perturbations in ionospheric electron density of quite different magnitude. The ionospheric response to the waves should also vary with geomagnetic and geographic latitude. In the same paper, this author suggested that the ionospheric response should therefore contribute to the observed [*Munro*, 1950, 1958; *Price*, 1955] diurnal and seasonal variations in TID occurrence frequency and statistically preferred directions of travel.

The earlier theoretical work stopped short, however, of explicitly calculating the ionospheric response to representative waves as a function of the azimuth of wave propagation for given ionospheric conditions. This paper (and a later companion paper) presents the results of such more detailed calculations. They reveal rather vividly certain features and intricacies of the ionospheric response that appear to have previously escaped explicit notice in the literature, though they have always been implicit in the governing equations. Consider, for example, the situation at F_2 region heights, where the ionospheric response to the waves is simplest, because ion lifetimes are long in comparison to the wave periods and the waves produce TID's solely by moving the preexisting ionization back and forth along the geomagnetic field lines [*Hooke*, 1968*a*]. One finds, as expected, that some azimuthal directions of wave propagation are preferred in terms of the ionospheric response evoked. One also finds that *which* azimuths are preferred depends on the wave parameters, the geomagnetic dip, and the prevailing ionospheric conditions as well; thus any simple theoretical interpretation of the observed diurnal and seasonal variations in directions of TID travel is precluded. The situation is even more complicated at lower F region heights, where ion lifetimes are comparable to, or shorter than, the wave periods and wave-associated photochemical effects are important in TID production. There the azimuthal directions of wave propagation preferred in terms of the ionospheric response evoked are generally those for which the sun's rays lie nearly in surfaces of constant wave phase, for reasons explained earlier [*Hooke*, 1968*a*]. For a given wave, location, and time of day and season, there may be two azimuthal directions, as much as 180° apart, one direction, or none at all satisfying this condition.

Because the nature of wave-associated TID

Copyright © 1970 by the American Geophysical Union.

production is so different at the two F region levels, it seems useful to treat the two levels separately. This paper considers the F_2 region ionospheric response to the waves, which is purely dynamical, as mentioned earlier. Though not directly relevant to the statistical observations that pertain to TID's at heights below 200 km [*Heisler*, 1958], it does provide insight into the mechanism of TID production at work in the individual events observed at higher altitudes by *Thome* [1964, 1968], *Georges* [1967], and *Vasseur and Waldteufel* [1969]. It also serves as useful background for a later paper, which considers the lower F region ionospheric response to internal gravity waves, because here wave-associated photochemical and dynamical effects are both active, and compete with (or complement) each other.

CALCULATIONS

The calculations of this paper assume that the lifetimes of the dominant ionospheric ions greatly exceed the wave periods of interest, so that the wave-associated photochemical effects can be legitimately ignored. For waves having periods of less than about 1 hour, this should be true at F_2 region heights of 250 km and above [*Hooke,* 1968*a*]. At F_2 region heights, then, internal gravity waves produce ionospheric irregularities solely because they set the neutral upper atmosphere into motion. These atmospheric motions, which can be determined from the wave parameters, in turn induce motions of the ionization through collisions. Geomagnetic constraints modify the resulting ion motion in a manner specified by the orientation of the geomagnetic induction field and the ratio of ion-neutral collision frequency to the ion gyrofrequency. In consequence, the (nearly) divergence-free neutral atmospheric motions produce ion motions that are in general divergent, creating ionospheric irregularities as dictated by the equation of continuity for the ionization.

Thus consider an inviscid, plane-stratified, isothermal atmosphere and ionosphere, stationary in the absence of internal gravity waves. Now allow an internal gravity wave, having angular frequency ω, wave vector $\mathbf{k}$, and energy density per unit mass E at the altitude of interest, to perturb this atmosphere. It produces neutral atmospheric motions

$$\mathbf{u} \propto \exp(z/2H) \exp i(\omega t - \mathbf{k}\cdot\mathbf{r}) \qquad (1)$$

where z is the height, H is the neutral atmospheric scale height, t is the time, and $\mathbf{r}$ is a position vector. The horizontal and vertical components of $\mathbf{u}$ are related in amplitude and phase by equations 25 and 26 of *Hines* [1960]. These relations depend not only on ω, $\mathbf{k}$, and H, but also on the neutral-gas ratio of specific heats γ and the acceleration of gravity g. The magnitude of $\mathbf{u}$ can be determined from the wave energy per unit mass E by equation 45 of *Hines* [1960]. The wave vector $\mathbf{k}$ is related to the angular frequency ω by the wave dispersion equation (21) of *Hines* [1960] (that equation contains a typographical error; the second k_x of the formula should be k_z).

Through collisions the neutral atmosphere sets the ionization into motion. This ion motion is given by [*MacLeod*, 1966]

$$\mathbf{u}_i = (1 + \rho_i^2)^{-1}[\rho_i^2\mathbf{u} + \rho_i(\mathbf{u}\times\mathbf{1}_b) + (\mathbf{u}\cdot\mathbf{1}_b)\mathbf{1}_b] \qquad (2)$$

where $\rho_i \equiv \nu_i/\omega_i$ is the ratio of the ion-neutral collision frequency ν_i to the ion gyrofrequency ω_i and $\mathbf{1}_b$ is a constant unit vector directed parallel to the geomagnetic induction. In the calculations it is assumed that

$$\rho_i \propto \exp(-z/H) \qquad (3)$$

In general, this wave-produced ion motion is divergent, which gives rise at F_2 region heights to small periodic departures or perturbations N_e' of the electron density N_e from its unperturbed value N_{e0} that are given to first order by

$$N_e' = -(i\omega)^{-1}\nabla\cdot(N_{e0}\mathbf{u}_i) \qquad (4)$$

the production and loss terms of this equation of continuity being neglected here.

Equations 1 through 4, together with the cited equations from *Hines* [1960], can be used to calculate the amplitude of the instantaneous electron density fluctuations N_e'/N_{e0} in terms of given values of the parameters λ, g, H, ρ_i, z, $\mathbf{k}$, E, $\mathbf{1}_b$ and $d(\ln N_{e0})/dz$. In all the calculations presented here, γ is taken to be 1.4, g to be 8.9325 m/sec², H to be 50 km, and ρ_i to be 0.005, corresponding to a choice of approximately 300 km as the height of interest. The logarithmic ionization density gradient is taken to be either zero (F_2 layer peak conditions), or 4×10^{-5} m^{-1}, for reasons discussed later. The vector $\mathbf{1}_b$, specified in the figures by the geomagnetic inclination I (here taken to be positive in the southern hemisphere) and the azimuthal orientation of **k** relative to geomagnetic north–south vary from computation to computation. Wave phase propagation is taken to be downward, in agreement with observation [*Munro*, 1950]

In order to compare differences in the ionospheric response to the different waves, it is assumed in all the calculations that the wave energy per unit mass $E = 40$ m²/sec² at the level of interest, corresponding to atmospheric motions there ~6 m/sec. This value agrees in order of magnitude with observational estimates of the internal gravity wave amplitudes at these heights [e. g., *Vasseur and Waldteufel*, 1969]. Note that this method of wave amplitude normalization is purely arbitrary. The waves could have been normalized instead to a constant vertical energy flux, or to a constant horizontal, vertical, or total velocity, or to some other condition, with a corresponding influence on the final results.

Since at F region heights $\rho_i \ll 1$, equation 2 reduces approximately to

$$\mathbf{u}_i \doteq (\mathbf{u}\cdot\mathbf{1}_b)\mathbf{1}_b \tag{5}$$

so that equation 4 becomes

$$N_e' \doteq -(i\omega)^{-1}\nabla\cdot[N_{e0}(\mathbf{u}\cdot\mathbf{1}_b)\mathbf{1}_b] \tag{6}$$

In terms of the parameters used in the calculations, equation 6 can be written as

$$\frac{N_e'}{N_{e0}} \doteq \left(\frac{\mathbf{u}\cdot\mathbf{1}_b}{\omega}\right)\left\{(\mathbf{k}\cdot\mathbf{1}_b) + i(\mathbf{1}_b\cdot\mathbf{1}_z)\cdot\left[\frac{1}{2H} + \frac{d}{dz}(\ln N_{e0})\right]\right\} \tag{7}$$

Obviously, in determining the instantaneous N_e'/N_{e0} fluctuations, one uses the real part of this expression. The accurate results were used in the computer calculations, so that the computer programs would have a greater range of validity, but these approximations are useful in showing the physics behind the computations. In connection with this particular problem, the approximations have appeared in one form or another in a number of papers [*Georges*, 1967, 1968; *Hooke*, 1968*a*; *Nelson*, 1968; *Thome*, 1968].

Equations 5 through 7 show that at the F_2 layer peak the fractional perturbations in electron density are proportional to the product of two factors. The first is the component $(\mathbf{u}\cdot\mathbf{1}_b)$ of the wave-associated motions **u** parallel to the geomagnetic field lines; the second is the variation $[(\mathbf{k}\cdot\mathbf{1}_b) + i(\mathbf{1}_b\cdot\mathbf{1}_z)/2H]$ of the motions parallel to the field lines. This variation in turn arises from two sources. The first is the variation $(\mathbf{k}\cdot\mathbf{1}_b)$ in wave phase from point to point along geomagnetic field lines that occurs unless these lines happen to lie in surfaces of constant wave phase (i. e., unless $\mathbf{k}\cdot\mathbf{1}_b = 0$). The second is the exponential increase $(1/2H)$ in wave amplitude with height, which translates into a change of wave amplitude along the field lines except at the geomagnetic dip equator $(\mathbf{1}_b\cdot\mathbf{1}_z = 0)$. For waves whose vertical wave number k_z satisfies the condition $4k_z^2 \gg 1/H^2$, however, this second term usually has little relative significance. The requirements that both $(\mathbf{u}\cdot\mathbf{1}_b)$ and $(\mathbf{k}\cdot\mathbf{1}_b)$ be large if the ionospheric response is to be large often work against one another, because internal gravity waves are very nearly transverse [*Hines*, 1960].

At heights where there exists a steep ambient ionization density gradient, however, the $d(\ln N_{e0})/dz$ term of equation 7 contributes significantly to N_e', at least at sufficiently high geomagnetic dip latitudes. In these circumstances N_e'/N_{e0} is large provided that $(\mathbf{u}\cdot\mathbf{1}_b)$ is large; **u** need not vary along the field lines to produce a significant ionospheric response.

Note that, when $d(\ln N_{e0})/dz$ is negative upward rather than positive, it is canceled to some extent by the growth in wave amplitude with height, represented by the factor of $1/2H$ in equation 7. At heights well above the F_2 peak, where diffusive equilibrium obtains, $d(\ln N_{e0})/dz = -1/2H$ [Hines *et. al.*, 1965], and these two terms should exactly cancel (however, see the concluding remarks of this paper). It should also be noted that because $d(\ln N_{e0})/dz$ varies with height, and because this contribution and the $(\mathbf{k}\cdot\mathbf{1}_b)$ contribution to N_e' are not in phase (equation 7), the N_e' variations will not exhibit the same phase variations in the vertical as the internal gravity waves. Depending on the sense of the variations in the ambient ionization density gradient and the sign of $\mathbf{k}\cdot\mathbf{1}_b$, this effect will result in either upturns or downturns of the apparent TID phase surfaces. The maximum phase shifts available are ±90°.

Physically, the phases of the $(\mathbf{k}\cdot\mathbf{1}_b)$, $i(\mathbf{1}_b\cdot\mathbf{1}_z)/$

$2H$, and $i(\mathbf{1}_b \cdot \mathbf{1}_z)\, d(\ln N_{e0})/dz$ contributions to N_e'/N_{e0} arise as follows: In each case N_e'/N_{e0} is a maximum one-quarter of a wave cycle after the time of maximum convergence. For the $(\mathbf{k} \cdot \mathbf{1}_b)$ contribution to N_e'/N_{e0}, which represents a convergence of ionization due to the variation of wave phase along geomagnetic field lines, the convergence is greatest where the change of $\mathbf{u}$ along $\mathbf{1}_b$ is greatest, namely at $\mathbf{u} = 0$. The maximum perturbation N_e'/N_{e0} then occurs a quarter of a wave cycle later, where $|\mathbf{u}|$ is also a maximum, and N_e' and $(\mathbf{u} \cdot \mathbf{1}_b)$ are either in phase or antiphase, depending on the sign of $\mathbf{k} \cdot \mathbf{1}_b$. The $i(\mathbf{1}_b \cdot \mathbf{1}_z)/2H$ contribution to N_e'/N_{e0} represents a convergence of ionization due to the variation of wave amplitude along geomagnetic field lines. This convergence is greatest where $|\mathbf{u}|$ is greatest, and the maximum of N_e' occurs a quarter of a wave cycle later; hence, we have the factor i. The $i(\mathbf{1}_b \cdot \mathbf{1}_z)\, d(\ln N_{e0})/dz$ contribution represents a convergence of ionization due to the displacement of a preexisting ionization density gradient. This displacement occurs a quarter of a wave cycle after $|\mathbf{u}|$ is a maximum, and again we have the factor i.

RESULTS

The results of this paper take the form of polar coordinate plots such as the one shown in Figure 1. Each curve shows the amplitude of the fractional perturbations in electron density (proportional to the radial distance from the curve to the plot origin) produced by a specified wave as a function of the azimuth of wave propagation (measured circumferentially) for given ionospheric conditions. Thus the curves of Figure 1 show the response of the F_2 region ionosphere at $I = 55°$ to an internal gravity wave having a 50-km horizontal wavelength λ_h and a 100-km vertical wavelength λ_z (phase propagation is taken to have a downward component, as mentioned earlier). In the model atmosphere considered here, this wave has a period $\tau = 16.4$ min and a horizontal phase velocity $v_{ph} = 50.8$ m/sec. Its energy per unit mass $E = 40$ m^2/sec^2 at this height implies a horizontal component $u_h = 2.84$ m/sec. The solid curve of Figure 1 shows the ionospheric response at heights where $d(\ln N_{e0})/dz = 0$, as, for instance, at the height of the F_2 layer peak, whereas the dashed curve shows the response where $d(\ln N_{e0})/dz = 4 \times 10^{-5}$ m^{-1}.

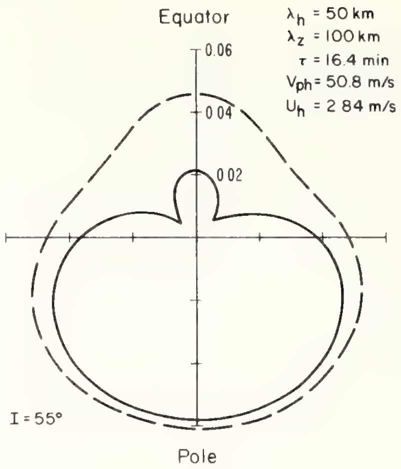

Fig. 1. The response of the F_2 region ionosphere (geomagnetic inclination $I = 55°$) to an internal gravity wave having the parameters shown, as a function of the azimuth of wave propagation. The radial distance from the points of the curves to the plot origin gives the amplitude of the fractional electron density perturbations N_e'/N_{e0} occurring during wave passage. The solid curve shows the response at heights where $d(\ln N_{e0})/dz = 0$, as, for instance, at the height of the F_2 peak, whereas the dashed curve shows the response at heights where $d(\ln N_{e0})/dz = 4 \times 10^{-5}$ m^{-1}.

Such large ambient ionization density gradients may or may not be attained at F region heights; this value is chosen merely to illustrate the effects of such gradients on the ionospheric response under conditions where they dominate. The ambient ionization density gradient has been chosen to be positive upward since this is the case of greatest interest for observations at heights below the height of the F_2 peak.

Figure 1 shows that this particular internal gravity wave produces a TID of 6% amplitude at both heights in the $I = 55°$ F_2 layer ionosphere when it propagates poleward. When propagating within 45° of equatorward, this same wave produces a TID of 4 to 5% amplitude at heights where $d(\ln N_{e0})/dz = 4 \times 10^{-5}$ m^{-1}, but only 1 to 2% amplitude at the height of the F_2 layer peak. For purposes of comparison, it might be noted that fractional fluctuations in electron density of a few per cent constitute the detectability threshold for many radio sounding techniques. As a result, an observer monitoring TID activity at the height of the F_2 layer peak might detect the wave if it were traveling toward the pole but would fail to notice it if it were traveling equatorward. On the other hand, if he were monitoring a height where a steep ambient ionization density gradient existed, he might detect the wave regardless of its direction of propagation.

The anisotropy in ionospheric response revealed by Figure 1 is readily explained in terms of the discussion at the end of the second section, as illustrated by Figure 2. It shows that in this example the factor $(\mathbf{u}\cdot\mathbf{1}_b)$ is relatively large when the wave is propagating equatorward, but for equatorward propagation the geomagnetic field lines lie nearly in surfaces of constant wave phase, so that $(\mathbf{k}\cdot\mathbf{1}_b)$ is small. When the wave is propagating poleward, $(\mathbf{u}\cdot\mathbf{1}_b)$ is smaller, but $(\mathbf{k}\cdot\mathbf{1}_b)$ is so much larger that the ionospheric response is much greater. Thus it is the wave front tilt (related to the wave period τ, as discussed above) relative to the geomagnetic inclination I that is primarily responsible for determining the shape of the ionospheric response pattern. The absolute magnitude of the ionospheric response depends on the magnitude of $\mathbf{k}$ (for fixed E), but the variation with azimuth does not, provided that $4k_z^2 \gg 1/H^2$. At the height where $d(\ln N_{e0})/dz = 4 \times 10^{-5}$ m^{-1}, N_e'/N_{e0} is large provided that $(\mathbf{u}\cdot\mathbf{1}_b)$ is large; $\mathbf{u}$ need not vary along the field lines to produce a significant ionospheric response. Hence we find the enhanced response to waves propagating equatorward, as shown by the dashed curve of Figure 1.

Although Figure 1 has been restricted to $I = 55°$ and downward phase propagation, it is a bit more general than it might appear, in two ways. First, had the magnetic inclination I equalled $-55°$ instead of $55°$, the same figure would have applied, at least to the extent that equation 5 is approximately valid, as long as it is understood that the equator remains at the top of the figure and the pole at the bottom. Second, had the wave phase propagation been upward instead of downward (a theoretically and observationally unlikely event [*Hines*, 1960, 1963, 1964]), the figure would still apply, but the equator and pole directions would be reversed. Similar comments apply to the remaining figures of the text.

Figures 3*a* and 3*b* show arrays of plots such as the one in Figure 1, indicating how the ionospheric response to the four different waves having the parameters shown varies as the geomagnetic inclination I varies from 0° to 90° in 5° steps. In these plots, as in Figure 1, the equator is at the top of the figure and the pole is at the bottom; solid curves show the ionospheric response for $d(\ln N_{e0})/dz = 0$, and the dashed curves show the ionospheric response for $d(\ln N_{e0})/dz = 4 \times 10^{-5}$ m^{-1}. All the waves are assumed to have the same vertical wavelength $\lambda_z = 100$ km $= -2\pi/k_z$ (satisfying $4k_z^2 \gg 1/H^2$). The horizontal wavelength λ_h, and hence the wave period τ and horizontal phase velocity v_{ph}, vary from wave to wave. For waves satisfying $4k_z^2 \gg 1/H^2$, the wave period τ uniquely determines the wave front tilts [*Hines*, 1960]; here we may refer to the waves by their periods without ambiguity.

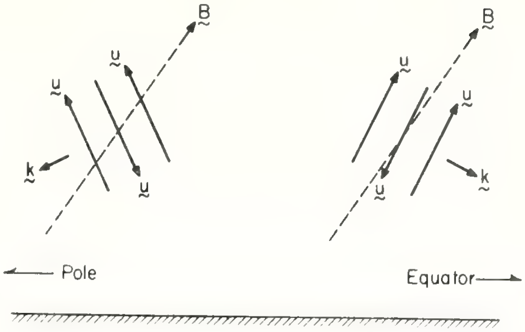

Fig. 2. Illustrating the competition between the requirements that both $\mathbf{u}\cdot\mathbf{1}_b$ and $\mathbf{k}\cdot\mathbf{1}_b$ be large if an internal gravity wave is to produce a large-amplitude ionospheric irregularity. For the wave of Figure 1, $\mathbf{u}\cdot\mathbf{1}_b$ is largest when the wave propagates equatorward, but in this event $\mathbf{k}\cdot\mathbf{1}_b$ is so small that the wave produces a relatively small ionospheric response. When the wave propagates poleward, $\mathbf{u}\cdot\mathbf{1}_b$ is small, but $\mathbf{k}\cdot\mathbf{1}_b$ is so much greater that the wave produces a significantly larger response.

Consider first the ionospheric response to the wave with 16.4-min period studied in the example of Figure 1. Figure 1 is in fact repeated as part of Figure 3*b*, and it may be used to calibrate the absolute amplitude of the other plots, all of which are drawn to the same scale. As pointed out above, this wave produces the largest response in the F_2 layer peak ionosphere at $I = 55°$ when propagating toward the pole. This general statement also appears to apply to all higher latitudes, except as I tends to 90°, where the ionospheric response is almost isotropic

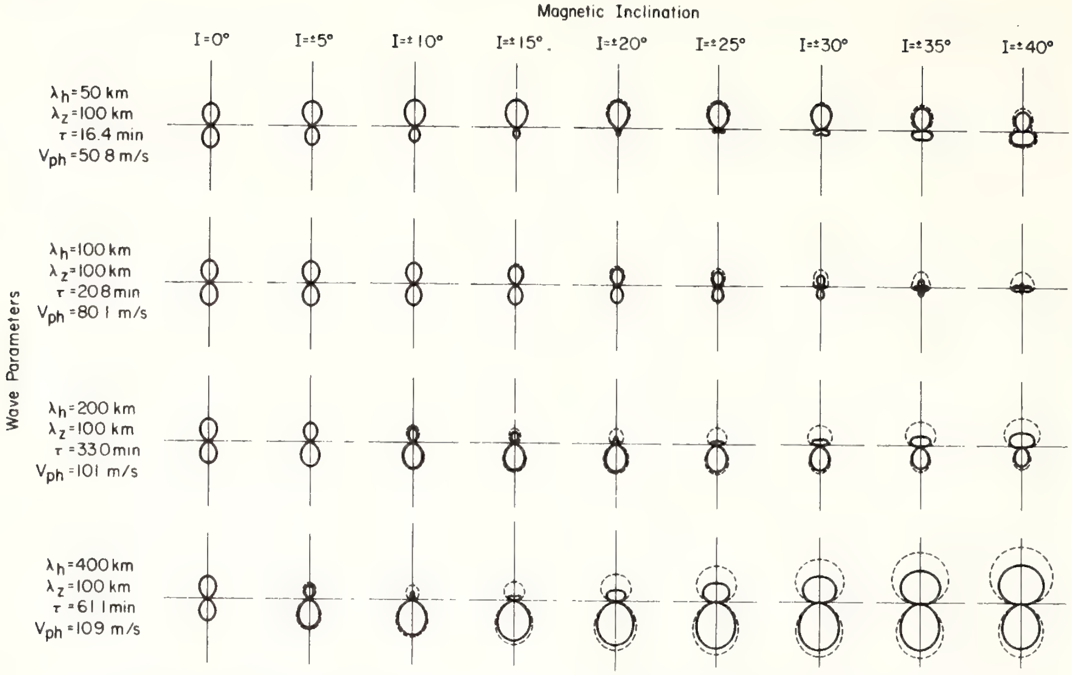

Fig. 3*a*. An array of plots like that of Figure 1, showing how the F_2 region ionospheric response to internal gravity waves varies with the wave parameters and the geomagnetic inclination ($I = 0°$ to $\pm 40°$).

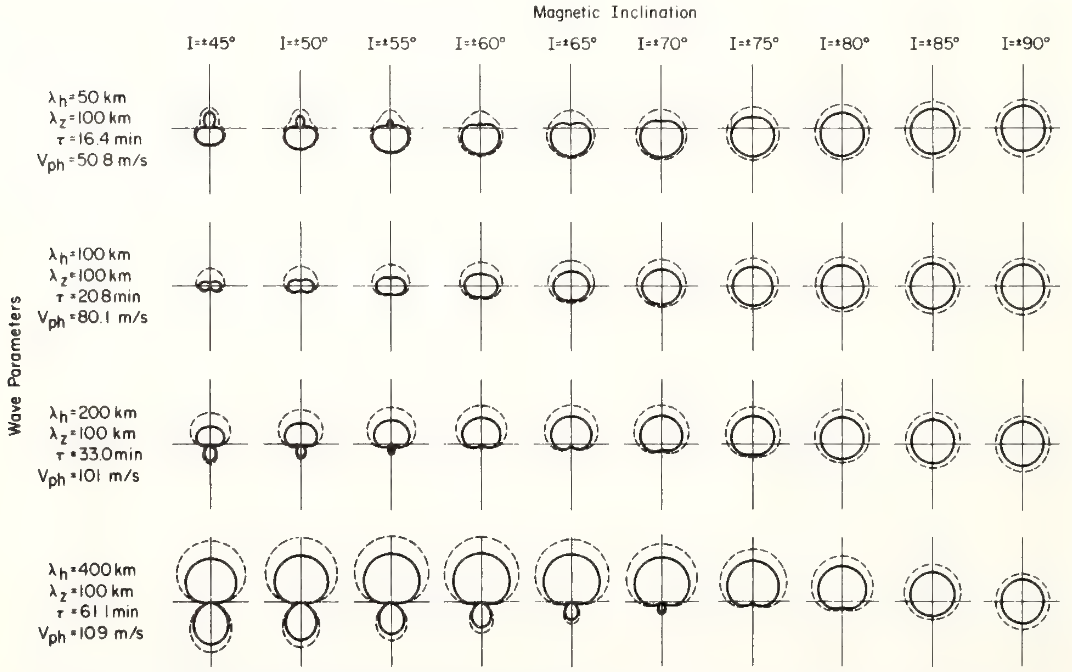

Fig. 3*b*. An array of plots like that of Figure 1. showing how the F_2 region ionospheric response to internal gravity waves varies with the wave parameters and the geomagnetic inclination ($I = \pm 45°$ to $\pm 90°$).

(as it should be, since here the orientation of **k** relative to $\mathbf{1}_b$ does not change as **k** varies in azimuth). At lower latitudes ($I \leq 40°$), however, the F_2 layer peak ionosphere responds preferentially to the wave when it is propagating equatorward. The equatorward response is a minimum at that geomagnetic inclination that satisfies $(\mathbf{k} \cdot \mathbf{1}_b) = 0$. Thus the directions of wave propagation that are preferred in terms of the ionospheric response depend on the geomagnetic inclination. Note that at all latitudes except $I = 0°$ a positive ambient ionization density gradient increases the ionospheric response to the waves propagating equatorward, the effect being most marked at the higher latitudes.

Now consider the ionospheric response to the 20.8-min wave. It differs from the response to the 16.4-min wave at all latitudes except $I = 0°$ and $I = 90°$. Thus, for example, at the dip latitude $I = 55°$, the F_2 layer peak ionosphere responds most strongly to the 20.8-min wave when it propagates east–west, but it responds most strongly to the 16.4-min wave when it propagates toward the pole. This difference may be attributed primarily to the difference in the wave front tilts of the two waves (45° from the vertical for the 20.8-min wave, and 26.5° for the 16.4-min wave), as the reader can readily convince himself by drawing figures like Figure 2 and using the reasoning accompanying that figure. One finds that at $I = 55°$, the F_2 layer peak responds only slightly to waves of 45° tilt propagating nearly meridionally, because, when $(\mathbf{k} \cdot \mathbf{1}_b)$ is large, $(\mathbf{u} \cdot \mathbf{1}_b)$ is small, and vice versa. For this particular wave the effect is still more pronounced at the dip latitude $I = 45°$, where the east–west lobes of the pattern are relatively prominent. Again, however, a steep ambient ionization density gradient enhances the ionospheric response to this wave when it propagates equatorward.

The ionosphere responds still differently to the wave having the 200-km horizontal wavelength and 33-min period. At geomagnetic dip latitudes greater than $I = \pm 45°$, this wave produces the greatest response when it propagates equatorward, and produces relatively little response when it propagates poleward, in contrast to the behavior exhibited by the shorter-period waves. At latitudes below $I = \pm 45°$, however, this wave produces the greatest ionospheric response when it propagates poleward. Again this behavior may be interpreted in terms of the geomagnetic constraints on the ion motion and the variation of the neutral atmospheric velocities **u** along the field lines by means of figures such as Figure 2.

The 61.1-min wave, with its nearly horizontal wave fronts, produces yet a different ionospheric response at each latitude, as shown. One of the striking features of the ionospheric response to this wave is its over-all magnitude, which is relatively large. This results from the inverse-ω dependence of equation 4, which implies that all else being equal, the ionospheric response to a wave will be greater the greater the wave period.

Figures 3*a* and 3*b* also show that the ionospheric response to the four different waves is identical at the latitudes $I = 0$ and $I = \pm 90°$. In fact, at any given latitude, the four different waves produce the same ionospheric response when propagating east–west. Equation 7 and various equations from *Hines* [1960] for waves satisfying the condition $4k_z^2 \gg 1/H^2$ can be manipulated to show that these results follow from a choice of a common vertical wavelength λ_z and a common energy density per unit mass E for all the waves.

The above results indicate the response of the F_2 region ionosphere to internal gravity waves satisfying the small vertical wavelength criterion $4k_z^2 \gg 1/H^2$, which are nearly transverse [*Hines*, 1960]. Although calculated from the exact formulas of the second section and *Hines* [1960] these response patterns differ by less than a line width from those that would result from formulas given in *Georges* [1968] if the waves are assumed to be strictly transverse, even though he assumes that the waves are not growing in amplitude with height. Those formulas thus provide relatively simple analytical tools for estimating F_2 region response without appreciable error, provided that $4k_z^2 \gg 1/H^2$.

Figure 4 shows the ionospheric response to internal gravity waves that do not satisfy the small vertical wavelength limit. Here the solid curves represent the ionospheric response to the waves calculated from the exact equations, and the dashed curves represent the response patterns calculated under the assumption of strict transversality of the waves. It is clear that the ellipticity of the wave motions, i.e., the departures from transversality, in this case pro-

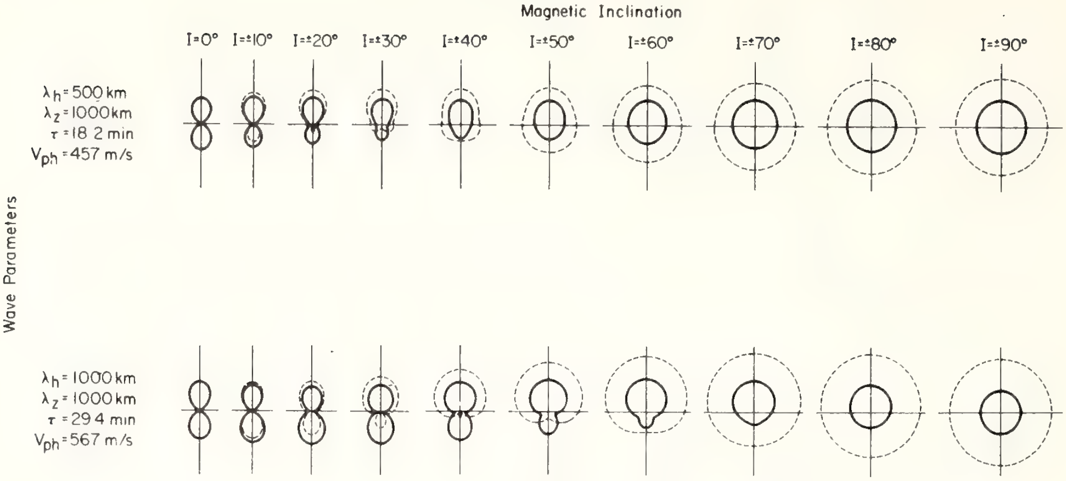

Fig. 4. Solid curves show the F_2 region ionospheric response to internal gravity waves of large vertical wavelength calculated from the full wave polarization relations of the text, whereas dashed curves show that response calculated by assuming that the waves are purely transverse. The difference between the amplitudes and shapes of the two sets of patterns shows that for these waves the non-transverse component of the associated atmospheric motions play a significant role in determining the ionospheric response. The calculations assume $d(\ln N_{e0})/dz = 4 \times 10^{-5}\ \mathrm{m}^{-1}$.

duces important effects on the ionospheric response patterns.

Concluding Remarks

The results of this paper, as presented in Figures 3 and 4, show that the F_2 region ionospheric response to internal gravity waves is indeed anisotropic. This anisotropy is sufficiently marked to suggest that in conjunction with the finite sensitivity of the TID detection apparatus, it should play some role in determining the actually observed TID statistics [*Munro*, 1950, 1958; *Price*, 1955]. It is easy to illustrate this theoretically by assuming a highly idealized internal gravity wave spectrum and various instrument sensitivities. This has in fact been done by *Hooke* [1968*b*], with the aid of the results that are presented here. One finds not only that an isotropic internal gravity wave spectrum produces anisotropic TID statistics, but also that the anisotropy in those statistics depends on instrument sensitivity.

The results presented here also imply that the F_2 region ionospheric response and its anisotropy depend on the ambient ionization density height gradient of the region under observation. Because the ambient ionospheric structure experiences considerable diurnal and seasonal variation, one would expect that fixed-frequency sounders such as those used by Munro and Price would interrogate regions experiencing such variations in their ambient gradients. This effect alone should produce some diurnal and seasonal variations in observed TID occurrence frequency and direction of travel, although wave-associated photochemical effects [*Hooke*, 1968*a*] and wind-shear filtering of the wave spectrum [*Hines and Reddy*, 1967] should also influence the results.

The calculations presented here assume that the ionization is motionless in the absence of wave perturbations. J. D. Whitehead (private communication) has shown that the ambient $\mathbf{E} \times \mathbf{B}/B^2$ drift of the F region ionization should enhance the F_2 region ionospheric response to the waves that happen to be propagating in the same direction with nearly the same speed. Thus this drift, and its diurnal and seasonal variations in direction, should also influence TID statistics.

It is asserted in the third section that the ambient logarithmic electron density height gradient above the F_2 peak has a value $-1/2H$, whose influence on the F_2 region ionospheric response to internal gravity waves is exactly canceled by the growth in wave amplitude with height. This would be true if the atmosphere were indeed inviscid, as assumed in the calculations. In fact, however, the internal gravity waves considered here would experience considerable viscous damping at heights above the height of the F_2 peak [*Hines,* 1960; *Pitteway and Hines* 1963], and the assumed growth in wave amplitude with height will not occur. Moreover, the wave-induced ion velocity would no longer be given by equation 2, since plasma diffusion effects would be important [*Hooke,* 1968*a*].

The reader should be puzzled by the fact that the F_2 region ionospheric response to internal gravity waves of 20-min period appears to be generally small, whereas there are some observational indications [*Munro,* 1950, *Titheridge,* 1968 (although see *Georges and Hooke* [1970])] that waves and irregularities of such periods predominate. The variation of the purely dynamic ionospheric response from wave to wave, as discussed here, does not account for this TID property; in fact, it would appear to make the explanation all the more difficult.

There is, however, no shortage of alternative explanations. For one thing, when we consider lower ionospheric heights and include photochemical loss effects, the perturbations N_e/N_{eo} are no longer inversely proportional to ω^{-1}, so as to favor observationally waves of longer period [see *Hooke,* 1968*a*]. For another, we have assumed that all waves have the same energy per unit mass. Since the longer-period waves should be subject to a strong viscous dissipation [*Hines,* 1960; *Pitteway and Hines,* 1963] and a severe ohmic dissipation as well [*Hines,* 1968], it may be that this assumption is inappropriate. Whitehead's mechanism, which would favor TID production at temperate latitudes by waves having smaller phase propagation velocities, may also play a role here.

Acknowledgments. I wish to thank Dr. T. M. Georges of ITS for many stimulating discussions on matters related to this paper and Mrs. Judith J. Stephenson of ITS for programming the calculations.

This work was partially supported by the National Aeronautics and Space Administration, Marshall Space Flight Center, Huntsville, Alabama.

* * *

The Editor wishes to thank M. A. MacLeod and J. E. Titheridge for their assistance in evaluating this paper.

REFERENCES

Georges, T. M., Ionospheric effects of atmospheric waves, *ESSA Tech. Rep. IER 57-ITSA 54,* U.S. Government Printing Office, Washington, D. C., 1967.

Georges, T. M., Collisional interaction of atmospheric waves in the ionospheric *F* region, in *Acoustic-Gravity Waves in the Atmosphere—Symposium Proceedings,* edited by T. M. Georges, pp. 377–380. U.S. Govt. Printing Office, Washington, D. C., 1968.

Georges, T. M., and W. H. Hooke, Wave-induced fluctuations in ionospheric total content: A model indicating some observational biases, to be published in *J. Geophys. Res.,* 1970.

Heisler, L. H., Anomalies in ionosonde records due to traveling ionospheric disturbances, *Aust. J. Phys., 11,* 79–90, 1958.

Hines, C. O., Internal atmospheric gravity waves at ionospheric heights, *Can. J. Phys., 38,* 1441–1481, 1960.

Hines, C. O., The upper atmosphere in motion, *Quart. J. Roy. Meteorol. Soc., 89,* 1–42, 1963.

Hines, C. O., Ionospheric movements and irregularities, in *Research in Geophysics,* vol. 1, pp. 299–318, MIT Press, Cambridge, Mass., 1964.

Hines, C. O., I. Paghis, T. R. Hartz, and J. A. Fejer, *Physics of the Earth's Upper Atmosphere,* Prentice-Hall, Englewood Cliffs, N. J., 1965.

Hines, C. O., and C. A. Reddy, On the propagation of atmospheric gravity waves through regions of wind shear, *J. Geophys. Res., 72,* 1015–1034, 1967.

Hines, C. O., An effect of ohmic losses in upper atmospheric gravity waves, *J. Atmos. Terr. Phys., 30,* 851–856, 1968.

Hooke, W. H., Ionospheric irregularities produced by internal atmospheric gravity waves, *J. Atmos. Terr. Phys., 30,* 795–823, 1968*a*.

Hooke, W. H., The response of the *F* region ionosphere to internal atmospheric gravity waves, in *Acoustic-Gravity Waves in the Atmosphere—Symposium Proceedings,* edited by T. M. Georges, pp. 367–372, U.S. Government Printing Office, Washington, D. C., 1968*b*.

MacLeod, M. A., Sporadic *E* theory, 1, Collision-geomagnetic equilibrium, *J. Atmos. Sci., 23,* 96–109, 1966.

Munro, G. H., Traveling disturbances in the ionosphere, *Proc. Roy. Soc. London, 202,* 208–223, 1950.

Munro, G. H., Traveling ionospheric disturbances in the *F* region, *Aust. J. Phys. 11,* 91–112, 1958.

Nelson, R. A., Response of the ionosphere to the passage of neutral atmospheric waves, *J. Atmos. Terr. Phys., 30,* 825–835, 1968.

Pitteway, M. L. V., and C. O. Hines, The viscous damping of atmospheric gravity waves, *Can. J. Phys., 41,* 1935–1948, 1963.

Price, R. E., Traveling disturbances in the ionosphere, in *The Physics of the Ionosphere,* pp.

181–190, Physical Society, London, 1955.

Thome, G. D., Incoherent scatter observations of traveling ionospheric disturbances, *J. Geophys. Res., 69,* 4047–4049, 1964.

Thome, G. D., Long-period waves generated in the polar ionosphere during the onset of magnetic storms, *J. Geophys. Res., 73,* 6319–6336, 1968.

Titheridge, J. E., Periodic disturbances in the ionosphere, *J. Geophys. Res., 73,* 243–252, 1968.

Vasseur, G., and P. Waldteufel, Thomson scatter observations of a gravity wave in the ionospheric *F* region, *J. Atmos. Terr. Phys., 31,* 885–888, 1969.

(Received May 5, 1970.)

Reprinted from Journal of Geophysical Research, Space Physics
75, No. 31, 6436-6438, 1970.

Amplification of Ionospheric Heating and Triggering of 'Spread *F*' by Natural Irregularities

T. M. Georges

ESSA Research Laboratories, Boulder, Colorado 80302

Many natural ionospheric irregularities are capable of focusing radio energy into very small volumes. In the presence of such irregularities a megawatt transmitter might be expected to produce a quasi-random distribution of small, intensely heated regions in the ionosphere, rather than the more uniform distribution of energy predicted for 'smooth' ionospheres. Rapid electron diffusion up and down the magnetic lines of force from the heated regions would cause ionization depletions, which would further enhance the radio focusing and in effect 'amplify' the original irregularities. The end result would be the growth of many small but intense field-aligned irregularities of the type known to cause at least one type of 'spread-*F*' ionosonde echo [*Bowman*, 1960]. Although the possibility of self-focusing by high-power radio waves has been widely appreciated [cf. *Bliokh and Bryukovetskiy*, 1969; *Litvak*, 1968, and references therein], little or no attention seems to have been paid to the role of natural irregularities in getting the heating started.

To examine this hypothesis, I computed ray paths through several model ionospheric irregularities, with a view toward examining the self-amplification mechanism as well as the group-delay spread of rays received by a simulated ionosonde from hypothetical amplified irregularities. The basic model represents a periodic or wave-like perturbation to a horizontally stratified Chapman layer. The electron-density perturbation varies sinusoidally in the horizontal (and sometimes the vertical) direction; in addition, the wave amplitude exhibits a Gaussian height variation, thus localizing the perturbation in height. Further details of this model can be found elsewhere [*Georges and Stephenson*, 1969]. Though the wave-like model represents a convenient idealization, the focusing effects achieved should qualitatively indicate the effects caused by less regular structures.

Appreciable ray convergence occurred just above each cycle of electron-density depletion in the several trials in which the height, vertical extent, and amplitude of the irregularities were varied. The example illustrated by the ray path plot of Figure 1*a* is typical. The wave amplitude $\Delta N_e/N_{e0}$ falls to $1/e$ 50 km above and below a maximum of 1.5% at a height of 250 km. The horizontal wavelength is 10 km. In this example the irregularities are tilted to align with the magnetic inclination at Boulder (68°) (i.e., they have a vertical wavelength of 25 km) because irregularities of this size and intensity would be expected to be field-aligned at *F*-layer heights. The ambient α-Chapman layer has a critical frequency of 7.0 MHz at a height of 300 km and a scale height of 70 km. Only upgoing rays are shown for clarity, even though all return eventually to earth. This figure also suggests that, in the presence of small field-aligned irregularities, most focusing occurs for rays more nearly aligned with the field direction. No magnetic field was included in the ray path calculations, however.

As the irregularity amplitude was lowered, the amount of focusing naturally decreased, but appreciable focusing still occurs for amplitudes less than 1%. As the height of the irregularities was lowered, focusing also decreased, but much more rapidly in my Chapman-layer model than would be expected in the real ionosphere, where an *E* layer usually exists. Even *E*-region irregularities could conceivably contribute to appreciable *F*-region focusing, though this case has not yet been simulated.

Various estimates of electron-density changes caused by heating have been in the neighborhood of a few per cent [e.g., *Meltz and LeLevier*, 1970], without irregularity focusing, such changes occurring in times varying from a

Copyright © 1970 by the American Geophysical Union.

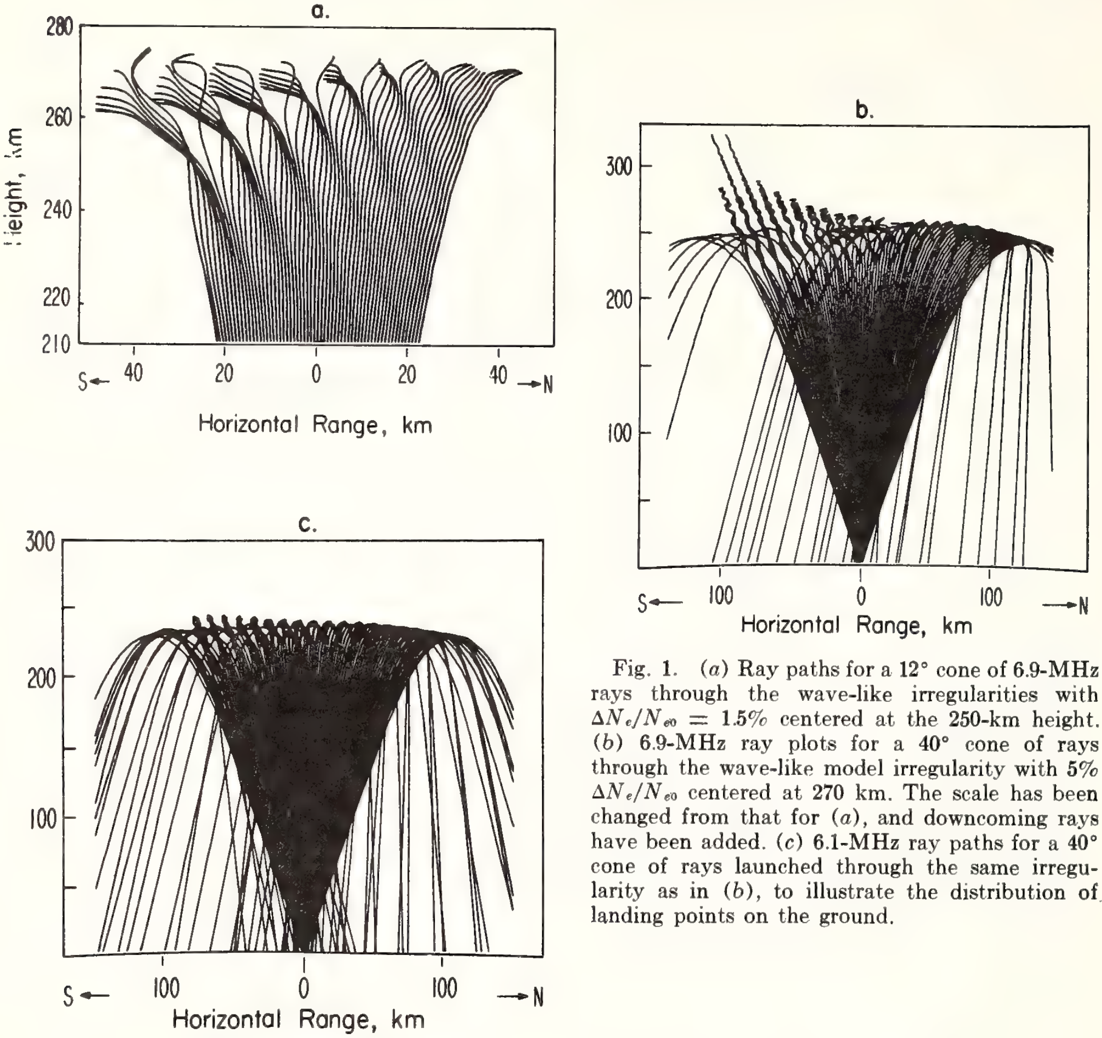

Fig. 1. (*a*) Ray paths for a 12° cone of 6.9-MHz rays through the wave-like irregularities with $\Delta N_e/N_{e0} = 1.5\%$ centered at the 250-km height. (*b*) 6.9-MHz ray plots for a 40° cone of rays through the wave-like model irregularity with 5% $\Delta N_e/N_{e0}$ centered at 270 km. The scale has been changed from that for (*a*), and downcoming rays have been added. (*c*) 6.1-MHz ray paths for a 40° cone of rays launched through the same irregularity as in (*b*), to illustrate the distribution of landing points on the ground.

few minutes to a half hour. Because ray theory breaks down in the vicinity of caustics, it is not possible to estimate from ray convergence the energy-density amplification due to focusing; however, an order-of-magnitude increase does not seem unreasonable. Therefore, we can tentatively suppose that local depletions of the order of 5% could be achieved near the foci in the relatively short time required to explain the prompt ionogram spreading actually observed by *Utlaut et al.* [1970].

Adopting this assumption, I calculated ray paths through another wave-like irregularity similar to the first, except that its amplitude is now 5% centered at 270 km. These ray paths, plotted in Figure 1*b*, show even more intense focusing and appear to support the 'self-amplification' mechanism. Determining just how far the amplification can go and how intense the irregularities can get would seem to require a careful examination of the focusing process from a full-wave point of view, as well as consideration of the effects of very high electron temperatures on diffusive and chemical processes, including perhaps the possibility of collision-induced ionization.

Some estimates of the degree of range spreading produced by the enhanced irregularities can be derived from the ray path calculations just described. Assume that the ray source is a

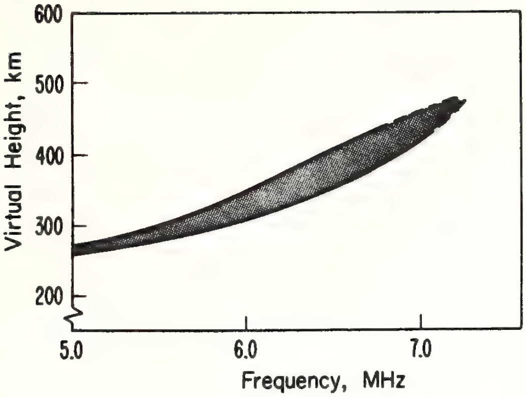

Fig. 2. The group-delay spread of rays landing within 10-km range of the ray source, for the irregularity model with $\Delta N_e/N_{e0} = 5\%$ centered at 270 km.

vertical-incidence ionosonde. Any ray that returns to the source will be recorded on the ionogram according to the group delay it suffers in transit to the ionosphere and back. Identifying by ray tracing all the rays that return precisely to the source involves a tedious iteration process; therefore I devised a crude way to estimate the number of discrete rays returning to the source as well as their group-delay spread. From the cone of rays launched every 0.2° in elevation, I tabulated the group delay of every ray landing within an arbitrary 10-km radius of the source, reasoning that each of these rays differed only slightly, in path followed and group delay suffered, from one returning precisely to the source. At least ten distinct rays were counted for each of six frequencies between 6.0 and 7.0 MHz (the ambient critical frequency); this along with their group-delay spacing suggests that the individual echoes would not be resolved by present ionosondes. Figure 1*c* shows the quasi-random distribution of rays after reflection (from the same model) as they intercept the ground. Figure 2 shows the virtual-height spread versus frequency for the irregularity model under discussion.

In the real ionosphere, one expects to find a great variety of irregularities, and thus a corresponding variety of amplification effects. Small-scale irregularities would be expected to produce many unresolved echoes, or spreading, whereas large irregularities produce discrete 'satellite' traces on ionograms resembling traveling-disturbance signatures. Experimental ionograms of heating effects would thus reflect the quasi-random nature of the ambient ionosphere, sometimes showing spreading or discrete traces alone, sometimes a mixture of both. One would also expect a corresponding variability in the promptness with which observable effects are produced, depending on the dynamic state of the ionosphere.

References

Bliokh, P. V., and A. S. Bryukovetskiy, Focusing of radio waves by an artificially created ionospheric lens, *Geomagn. Aeron., 9,* 443–447, 1969.

Bowman, G. G., Further studies of 'spread-*F*' at Brisbane, 2, Interpretation, *Planet. Space Sci., 2,* 150–156, 1960.

Georges, T. M., and J. J. Stephenson, HF radar signatures of traveling ionospheric irregularities; 3D ray-tracing simulation, *Radio Sci., 4,* 679–696, 1969.

Litvak, A. G., The possibility of self-focusing of electromagnetic waves in the ionosphere, *Izv. Vyssh. Ucheb. Zaved. Radiofiz., 11,* 1433–1435, 1968.

Meltz, G., and R. E. LeLevier, Heating the *F*-region by deviative absorption of radio waves, *J. Geophys. Res., 75,* this issue, 1970.

Utlaut, W. F., E. J. Violette, and A. K. Paul, Some ionosonde observations of ionosphere modification by very high power, high frequency ground-based transmission, *J. Geophys. Res., 75,* this issue, 1970.

(Received August 10, 1970.)
Communicated by J. R. Wait.

Reprinted from Journal of Geophysical Research, Space Physics
75, No. 31, 6295-6308, 1970.

Wave-Induced Fluctuations in Ionospheric Electron Content: A Model Indicating Some Observational Biases

T. M. Georges and W. H. Hooke

Institute for Telecommunication Sciences, ESSA Research Laboratories
Boulder, Colorado 80302

By assuming that a plane atmospheric wave acts on a plane-stratified F layer in the presence of a constant geomagnetic field, we derive an expression for the resulting perturbations in total columnar electron content as a function of wave and ionospheric-layer parameters and of the orientation of the column through the ionosphere. Although idealized, the model not only correctly predicts the order of magnitude of the observed perturbations but also makes visible much of the physics that determines the magnitude of wave-induced total-content fluctuations observed by using satellite transmissions through the ionosphere. Geomagnetic constraints on ion motion and a tendency for total-content fluctuation to be greatest when the ground-satellite path lies in a surface of constant atmospheric wave phase combine to introduce strong experimental biases that favor the observation of some waves and prevent the observation of others. The effects of these biases must be fully removed before total-content measurements can yield the statistical properties of atmospheric waves at ionospheric heights that may be useful in locating wave sources or in characterizing the dynamic state of the ionosphere.

Measuring the Faraday rotation, differential Doppler shift, or angular deviation of radio transmissions from artificial satellites has become a convenient way to monitor long-term and short-term features of ionospheric dynamics that manifest themselves as fluctuations in total columnar electron content. In particular, total-content observations often reveal wavelike irregularities in electron distribution with periods between a few minutes and a few hours [*Little and Lawrence*, 1960; *Titheridge*, 1963, 1968*a*, *b*; *Rao et al.*, 1969; *Davis and da Rosa*, 1969]. The irregularities are apparently the same phenomenon as the so-called traveling ionospheric disturbances (TID) that have been observed by ground-based radio-sounding techniques for many years [*Munro*, 1950, 1958; *Heisler*, 1958; *Chan and Villard*, 1962; *Thome*, 1964, 1968; *Georges*, 1968*a*] and have been attributed to the action of internal atmospheric gravity waves and acoustic waves on upper atmosphere ionization [*Hines*, 1960, 1963; *Georges*, 1967, and references therein].

One way to learn the temporal and geographic distribution of TID's and possibly to identify the source mechanisms ultimately responsible for their generation involves collecting the kind of extensive observational statistics that total-content measurements may well be able to provide. Unfortunately, like all radio methods for ionospheric probing, the total-content technique contains certain observational biases that must be fully understood and removed if the data are to be properly interpreted in terms of ionospheric dynamics. Because these observations indicate only the total number of electrons lying in the column oriented along the straight-line radio path from receiver to satellite, they reveal nothing about the electron distribution along that column. One might therefore expect total-content measurements through wavelike irregularities to be influenced by partial cancellation of the effects of electron density enhancements by the effects of electron density depletions. Under certain conditions, in fact, atmospheric waves may go undetected simply by altering the distribution of electrons in the column, without significantly altering its integrated content. As a result, inferences about the presence or absence of atmospheric waves along the path must be considered suspect, until a sound theory of the production of total-content fluctuations by atmospheric waves is developed and is used to assess the degree to which observational biases affect the experiment. We offer such a theory and take the first

Copyright © 1970 by the American Geophysical Union.

steps toward such an assessment here.

To calculate the fluctuations in columnar electron content caused by an atmospheric wave, we must first know the *electron density* fluctuations caused everywhere by the wave. Because that problem has already been solved for plane model atmospheric waves in a plane-stratified ionosphere [*Georges*, 1968*b*; *Hooke*, 1968*a*], here we simply perform the line integration over arbitrary straight-line ground-to-satellite paths. We find that the integration can be performed analytically for a variety of idealized electron density profiles, and that much of the physics underlying total-content fluctuations remains visible in the final formulas.

Our model, which describes the effects of both internal gravity waves and acoustic waves, correctly accounts for the observed magnitudes of total-content fluctuations. It also shows that geomagnetic constraints on electron motion and the above-mentioned 'phase-cancellation effects' combine to introduce observational biases that tend to favor the observation of some waves but prevent the observation of others. Total-content measurements are thus an imperfect sensor of atmospheric waves at ionospheric heights.

We wish to emphasize that we are not concerned with how various radio data are transformed into total-content data and the possible errors in that transformation (see, for example, *Mass* [1963] and references therein); we simply assume that whatever method is used gives an accurate measure of the integrated electron content *along a line-of-sight path to the satellite*. (The effects of ray deviation are difficult to correct for but are usually small and are thus neglected at the radio frequencies commonly used in these experiments.) Neither are we concerned with the use of total-content measurements as a tool for the study of long-term ionospheric balance problems; we simply consider their use in studies of short-period (less than a few hours) ionospheric dynamics.

REDISTRIBUTION OF IONOSPHERIC ELECTRONS BY ATMOSPHERIC WAVES

Atmospheric waves propagating at ionospheric heights perturb the distribution of ionization through both dynamical and photochemical means [*Hooke*, 1968*a*, 1969]. At all heights the wave-associated neutral-gas motions redistribute the preexisting ionization, whereas, at the lower heights (below about 250 km), where ion lifetimes are short compared with the wave periods of interest, the wave-associated neutral-gas density and temperature variations substantially alter the ionospheric photochemical balance ir a complex way that is sensitive to the details of that photochemistry. It is generally accepted, however, that the bulk of the ionospheric electron content resides primarily at heights above 250 km, and it is typically assumed that perturbations in electron density at these heights are responsible for the bulk of observed total-content fluctuations (see, for example, the references to Titheridge above). This assumption is invalid under certain conditions (discussed later) where the contribution to total-content perturbations above about 250 km vanishes, thus making any small perturbations below that height relatively important.

If we adopt this assumption, we may consider for present purposes that the atmospheric wave interacts with the ionization only through momentum transfer by collisions of neutrals with F_2 region ions and electrons, which respond by moving along the geomagnetic field direction with a speed equal to the component of the neutral-gas velocity in that direction, i.e., [*Georges*, 1967; *Hooke*, 1968*a*]:

$$\mathbf{u}_e = (\mathbf{u} \cdot \mathbf{l}_b)\mathbf{l}_b \tag{1}$$

where $\mathbf{u}_e$ is the electron velocity, $\mathbf{u}$ is the wave-associated neutral-gas velocity, and $\mathbf{l}_b$ is a unit vector in the direction of the geomagnetic induction **B**. Because the atmospheric waves of interest have wavelengths short enough that effects associated with the sphericity of the earth may be ignored, the ambient ionosphere and atmosphere can be assumed to be plane stratified. The small amplitude of the waves and the small amplitude of the resulting total-content fluctuations [*Titheridge*, 1963] suggest use of a linearized perturbation analysis in their description. Thus we take the electron density n_e at any point $\mathbf{r}$ and time t to be

$$n_e(\mathbf{r}, t) = n_{e0}(z) + n_e'(\mathbf{r}, t) \tag{2}$$

where z is the height in the plane-stratified atmosphere, and $n_e' \ll n_{e0}$ is the small departure of n_e from its unperturbed value n_{e0}. If the wave itself is planar, so that

$$\mathbf{u}(\mathbf{r}, t) = \mathbf{U} \exp i(\omega t - \mathbf{k}\cdot\mathbf{r}) \qquad (3)$$

where the amplitude $\mathbf{U}$ of the neutral-gas motions, the angular wave frequency ω, and the wave vector $\mathbf{k}$ are all constants, then the linearized equation of continuity for the free electrons becomes [*Georges*, 1968*b*; *Hooke*, 1968*a*]

$$n_e'(\mathbf{r}, t) = \frac{1}{\omega}[\mathbf{u}(\mathbf{r}, t)\cdot\mathbf{l}_b] \cdot \left[(\mathbf{k}\cdot\mathbf{l}_b) + i(\mathbf{l}_b\cdot\mathbf{l}_z)\frac{\partial}{\partial z}\right] n_{e0}(z) \qquad (4)$$

where $\mathbf{l}_z$ is a unit vector in the vertical direction. Equation 4 gives the wave-induced perturbations $n_e'(\mathbf{r}, t)$ as a function of $n_{e0}(z)$, the wave parameters, and the geomagnetic inclination.

LINE INTEGRAL THROUGH THE REDISTRIBUTED IONIZATION

Here we are concerned with the integral of $n_e'(\mathbf{r}, t)$ along an arbitrary straight-line path R between a ground based observer and a satellite. The total electron content C along the path R is defined as

$$C \equiv \int_R n_e \, dr \equiv \int_R n_{e0} \, dr + \int_R n_e' \, dr \equiv C_0 + C' \qquad (5)$$

where $C' \ll C_0$ is the wave-induced departure in C from its ambient value C_0. From equations 1–5,

$$C' = \frac{(\mathbf{U}\cdot\mathbf{l}_b)\exp(i\omega t)}{\omega}\int_R \exp(-i\mathbf{k}\cdot\mathbf{r}) \cdot \left[(\mathbf{k}\cdot\mathbf{l}_b) + i(\mathbf{l}_b\cdot\mathbf{l}_z)\frac{\partial}{\partial z}\right] n_{e0} \, dr \qquad (6)$$

Defining

$$-\eta z \equiv \left(\frac{\mathbf{k}\cdot\mathbf{l}_r}{\cos\chi}\right) z \equiv (\mathbf{k}\cdot\mathbf{l}_r) r \equiv \mathbf{k}\cdot\mathbf{r} \qquad (7)$$

where χ is the satellite zenith angle (i.e., the angle between the vertical and the vector $\mathbf{r}$ directed from the observer to the satellite), we find that

$$C' = \frac{(\mathbf{U}\cdot\mathbf{l}_b)\exp(i\omega t)}{\omega\cos\chi}\int_{z_r}^{z_s} \exp(i\eta z) \cdot \left[(\mathbf{k}\cdot\mathbf{l}_b) + i(\mathbf{l}_b\cdot\mathbf{l}_z)\frac{\partial}{\partial z}\right] n_{e0} \, dz \qquad (8)$$

where z_r and z_s are the receiver and satellite heights. Figure 1 illustrates the geometrical relationships among $\mathbf{B}$, $\mathbf{k}$, and $\mathbf{r}$.

The meaning of the parameter η can be appreciated from two physical viewpoints: for moving satellite observations of a single wave (fixed $\mathbf{k}$), variations in η reflect only changes in the direction of $\mathbf{l}_r$; for geostationary satellite observations (fixed $\mathbf{r}$), η varies as $\mathbf{k}$ varies in magnitude or direction.

The factor in equation 8 that depends on the ambient gradient of electron density can be integrated by parts to give

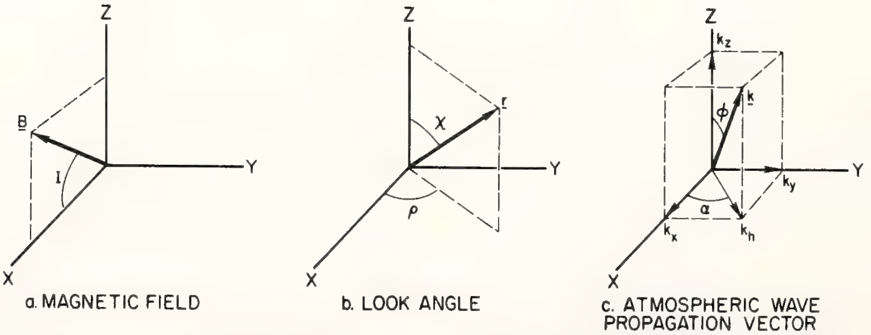

Fig. 1. Geometrical relationships among the geomagnetic field direction **B**, the vector **r** along the path from observer to satellite, and the atmospheric wavevector **k**. The positive x-direction points geomagnetic north; the positive y-direction points geomagnetic west.

$$C' = \frac{i(\mathbf{U}\cdot\mathbf{1}_b)(\mathbf{1}_b\cdot\mathbf{1}_z)}{\omega\cos\chi}\, n_{e0}\exp i(\omega t + \eta z)\Big|_{z=z_r}^{z=z_s} + \frac{(\mathbf{U}\cdot\mathbf{1}_b)\exp(i\omega t)}{\omega\cos^2\chi}[(\mathbf{1}_r\times\mathbf{1}_b)\times\mathbf{1}_z\cdot\mathbf{k}] \cdot\int_{z_r}^{z_s}\exp(i\eta z)n_{e0}\,dz \qquad (9)$$

Note that, on integration by parts, the explicit dependence of C' on the gradient of n_{e0} has disappeared. This permits us to use simple model $n_{e0}(z)$ profiles having physically unrealistic gradients and gradient discontinuities in the illustrative calculations of succeeding sections. If z_r and z_s are respectively below and above the ionosphere, $n_{e0}(z_s) = n_{e0}(z_r) = 0$, so that the first term in equation 9 vanishes, and

$$C' = \frac{(\mathbf{U}\cdot\mathbf{1}_b)\exp i(\omega t + \eta h_m)}{\omega\cos^2\chi}[(\mathbf{1}_r\times\mathbf{1}_b)\times\mathbf{1}_z\cdot\mathbf{k}] \cdot\int_{-\infty}^{\infty}\exp(i\eta z')n_{e0}(h_m + z')\,dz' \qquad (10)$$

where $z' \equiv z - h_m$. Mathematically, h_m may be chosen arbitrarily; here it is taken to be the altitude of peak ionospheric electron density.

Equations 9 and 10 are the principal mathematical results of this paper; they express the total-content fluctuations in terms of the atmospheric-wave and ionospheric parameters, the geomagnetic inclination, and the experimental geometry. Of particular concern in this paper is the degree to which the experimental geometry (represented in the equations by the influence of the unit vector $\mathbf{1}_r$) controls the perturbations C'.

Note that the above equations are valid for atmospheric waves of arbitrary type, i.e., they do not depend on particular mathematical constraints relating ω, $\mathbf{k}$, and $\mathbf{U}$. In what follows, we shall assume that 'internal gravity' waves are purely transverse, i.e., that $\mathbf{U}$ is perpendicular to $\mathbf{k}$ and lies in the vertical plane containing $\mathbf{k}$, and that the waves obey the dispersion relation given by *Hines* [1960, equation 33]. We shall assume that acoustic waves are purely longitudinal, i.e., that $\mathbf{U}$ is parallel to $\mathbf{k}$, and that the waves obey the dispersion relation $\omega^2 = C^2k^2$, where C is the speed of sound.

We assumed that the wave amplitude U is the same at all heights more for convenience than for conformity with reality; however, inclusion of a z-dependent U in the development is not difficult. A $U(z)$ would play a role completely analogous to $n_{e0}(z)$, and the integral in (10) would contain the $n_{e0}(z)$ $U(z)$ product where only $n_{e0}(z)$ now appears. We did not pursue this approach because the circumstances that cause U to vary with height (such as wave dissipation and ducting) also give rise to height variations in $\mathbf{k}$ and ω, and these effects are much more difficult to include.

It might be noted that the assumption of a plane geometry is more restrictive in this section than it was in the last. In particular, the plane geometry we assume in this section is a good approximation to the earth's spherical geometry for small satellite zenith angles but is a poor approximation when the satellite is near the observer's horizon. For example, a ray launched horizontally from the earth's surface intercepts the 300-km height level at an angle of 17° with the local horizontal. The reader should bear this in mind in considering the illustrative results of succeeding sections.

CONTRIBUTION OF WAVE PARAMETERS AND GEOMAGNETIC CONSTRAINT

Although equations 9 and 10 appear mathematically complicated, their separate terms individually contain some relatively simple physics. We examine first those terms outside the integral that do not depend on the unperturbed electron density distribution $n_{e0}(z)$.

The factor $\exp i(\omega t + \eta h_m)$ gives at least part of the phase variation in the total-content fluctuations that arises from the phase variation $\exp i(\omega t - \mathbf{k}\cdot\mathbf{r})$ of the atmospheric wave itself. (The integral in (10) contributes to the phase as well if its value is complex.) An experimenter using a geostationary satellite and therefore having a fixed geometry (i.e., a fixed η for a given $\mathbf{k}$) observes total-content fluctuations that have the same angular frequency ω as the perturbing wave. Experimenters using transmissions from low altitude satellites in motion relative to a ground based observer (i.e., η varies with time) observe temporal phase variations given by the total phase angle of C'/C_0. Where the phase contribution of the integral in (10) is negligible and where the time for satellite transit is short compared with the atmospheric wave period ($2\pi/\omega$), the temporal phase behavior due to a given wave can be attributed entirely to the factor exp $(i\eta h_m)$. If h_m can be estimated and if the satellite position (i.e., η) is known as a function of time, this temporal phase information can be translated directly into spatial phase information to determine, for example, the horizontal wavelength of the perturbing atmospheric wave. This is exactly the approach used by *Titheridge* [1963, equation 6] to estimate irregularity horizontal-scale size from total-content observations. Possible phase contributions of the integral must thus be regarded as a source of error in such procedures.

The angular wave frequency ω and the wave vector $\mathbf{k}$ not only determine the phase of the total content fluctuations C'; they also influence their magnitude: C' is proportional both to kU, a measure of the wave-associated electron convergence, and to ω^{-1}, a measure of the length of time over which that convergence acts in the same sense [*Hooke*, 1968*a*].

The wave parameters are not the sole determinants of the total-content fluctuations C', however; they share their influence with the geomagnetic-field constraint on F region electron motion (equation 1), which critically limits the ability of total-content observations to sense atmospheric wave motions. It does this in two important ways.

First, the factor $(\mathbf{U}\cdot\mathbf{l}_b)$ in all the terms of both equations 9 and 10 implies that the magnitude of total-content fluctuations depends on the degree of alignment between **U** and **B**. In particular, no electron-content fluctuations result whenever the wave-associated motions of the neutral gas are orthogonal to the geomagnetic field. This is a direct result of assumption 1, which permits no *electron density* perturbations to occur in this case. In terms of the coordinate systems of Figure 1, this condition is fulfilled whenever

$$\tan\varphi = \cot I \cos\alpha \qquad (11)$$

for internal gravity waves, and by

$$\cot\varphi = -\cot I \cos\alpha \qquad (12)$$

for acoustic waves. Electron-content fluctuations are therefore a faulty indicator of the spectrum of atmospheric waves present at ionospheric heights because the ionization itself is an imperfect tracer of the wave motions (see *Hooke* [1968*b*] for a further discussion of the ionospheric response to atmospheric waves).

Second, in cases where satellite and observer are respectively above and below the ionosphere, total-content fluctuations are proportional to the factor

$$(\mathbf{l}_r \times \mathbf{l}_b) \times \mathbf{l}_z \cdot \mathbf{k} \qquad (13)$$

Because $(\mathbf{l}_r \times \mathbf{l}_b) \times \mathbf{l}_z$ is a horizontal vector lying in the plane defined by $\mathbf{l}_r$ and $\mathbf{l}_b$, an atmospheric wave whose wave vector $\mathbf{k}$ lies anywhere in the (vertical) plane normal to this horizontal vector will produce *no* total-content fluctuations. From the point of view of geostationary satellite observations, this means that no total-content fluctuations will be produced by atmospheric waves propagating at an azimuth angle α_0, given by

$$\tan\alpha_0 = \frac{1}{\tan\chi \tan I \sin\rho} - \frac{1}{\tan\rho} \qquad (14)$$

regardless of their wave front inclination.

If instead $\mathbf{k}$ is fixed, a wide range of directions $\mathbf{l}_r$ make (13) vanish and thus yield zero content fluctuations. The direction $\mathbf{l}_r$ parallel or antiparallel to $\mathbf{l}_b$ is obviously one such case, as *Titheridge* [1969] recognized. In this special case the receiver looks toward the satellite along a geomagnetic field line, and, regardless of how the atmospheric waves redistribute the ionization along that field line, they do not change the total content along the path.

What is not so well appreciated is that (13) also vanishes for directions $\mathbf{l}_r$ lying anywhere in the plane defined by $\mathbf{l}_b$ and its projection on the vertical plane containing $\mathbf{k}$ (shown shaded in Figure 2), i.e., for values of ρ and χ that satisfy

$$\tan\chi \tan(\rho - \alpha) = \cos\alpha/\tan I \qquad (15)$$

This is a special case of the more general result that all paths lying in any given plane perpendicular to the vertical plane containing $\mathbf{k}$ intercept the same fractional total-content fluctuations. Note, however, that for satellites *immersed* in the ionosphere, total-content fluctuations can occur even if (13) vanishes because atmospheric waves can then move ionization to and fro past the satellite.

The factors of (10) that depend on the geometrical interrelationships of **r**, **B**, and **k** impose a complicated set of biases that make total-content observations sensitive to some waves and insensitive to others. Furthermore, ob-

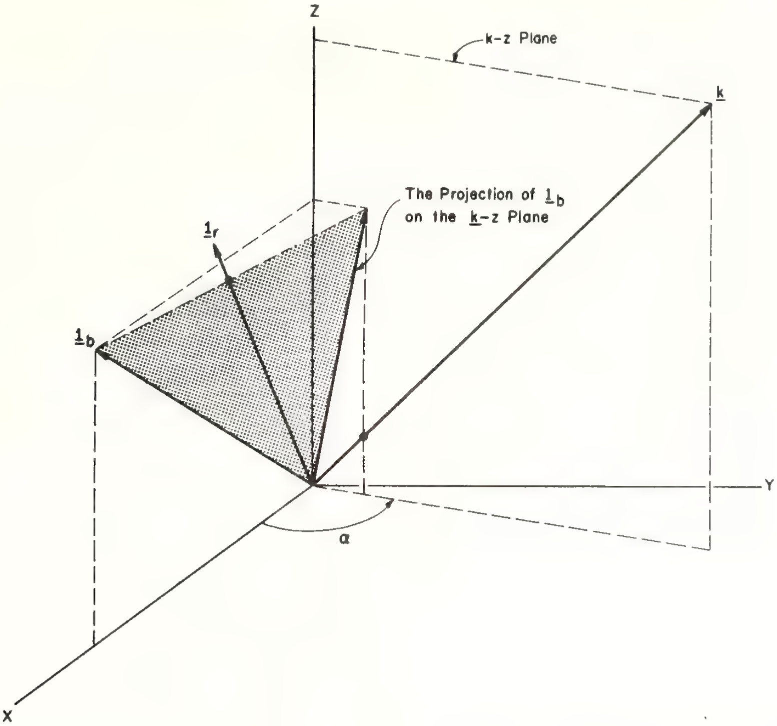
Z
k-z Plane
k
The Projection of $\underline{1}_b$ on the $\underline{k}$-z Plane
$\underline{1}_r$
$\underline{1}_b$
Y
α
X

Fig. 2. Radio paths traversing the entire ionosphere and lying in the shaded plane do not experience total content fluctuations during wave passage.

servations that satisfy conditions under which one or more of these factors vanish can falsely indicate the presence of more than one wave or of non-sinusoidal wave forms.

THE PHASE-CANCELLATION CONTRIBUTION

In the introduction we mentioned that atmospheric waves usually redistribute electrons along a radio path in such a way that regions of increased electron density compensate for regions of depleted density, and that the net result is a lessening of the changes in integrated electron content. This 'phase-cancellation effect' is expressed mathematically by the integral

$$\int_{-\infty}^{\infty} n_{e0}(h_m + z') \exp i\eta z' \, dz' \qquad (16)$$

in equation 10, which, as the Fourier transform of $n_{e0}(h_m + z')$, can be evaluated analytically for several simple model n_{e0} profiles. Evaluations of the integral for slab, parabolic, α-Chapman, and β-Chapman models are shown in Figure 3, along with the mathematical expressions for the electron density in each.

The integrals are normalized by dividing by the integral of the ambient electron content, because it is the relative fluctuations C'/C_0 rather than the absolute fluctuations C' that are of greatest interest. In each electron density model, h_m is a measure of the height of the layer (height of the center of the slab; height of the electron density peak in the other models), H is a measure of its thickness (total thickness for the slab; one-half thickness for the parabolic layer; conventional scale height for the Chapman layers), and n_{em} is the peak electron density.

The magnitudes of the integrals depend on η in the manner illustrated in Figure 3. All the curves have an absolute maximum at $\eta = 0$ and asymptotically approach zero as $|\eta|$ increases. This behavior can be interpreted physically in the following way. When the radio path lies in surfaces of constant atmospheric wave phase ($\mathbf{1}_r$ perpendicular to $\mathbf{k}$, so that $\eta = 0$), there is no cancellation along the path, and the integral then has its maximum value. As the radio path departs from this condition ($|\eta|$ increases), however, the value of the integral decreases correspondingly. In the case of the finite symmetrical (slab and parabolic) layers, several points are reached where the total-content fluctuations have zero amplitude.

The condition $\eta = 0$ is satisfied whenever

$$\cot \varphi = -\tan \chi \cos (\rho - \alpha) \qquad (17)$$

Note that the $\eta = 0$ loci do not depend on the magnetic inclination.

Of critical interest in connection with the phase-cancellation effect is not only the location of the $\eta = 0$ loci (given by equation 17) but also the width of the band of directions within which phase cancellation is not excessive. By examining the plot of the phase-cancellation integral (Figure 3) for the α-Chapman layer, we see that its value drops to $1/e$ at $|\eta H| \approx 0.85$. By using the definition of η (equation 7) and by expanding the scalar product $\mathbf{k} \cdot \mathbf{l}_r$ in the coordinate system of Figure 1, we find that the zenith angle χ where the value of the normalized cancellation integral falls to $1/e$ is given by

$$\tan \chi = \left(\pm 0.85 \frac{\lambda}{2\pi H} \csc \varphi - \cot \varphi \right) \cdot \sec (\rho - \alpha) \qquad (18)$$

By letting $\rho = \alpha$ (satellite azimuth equals wave propagation azimuth), we show in Figure 4 the width of the phase-cancellation band (to the $1/e$ points) as a function of φ (the inclination of $\mathbf{k}$) and parametric in λ/H. As expected, the width of the band increases as λ/H increases. For values of λ/H less than $(2\pi/0.85) \approx 7.4$ (where the width is 90° regardless of the value of φ), the width increases with φ, whereas the width decreases with increasing φ for greater values of λ/H. Values of λ/H of about one can be considered typical for TID's in realistic F layers. For that case, the band outside of which phase-cancellation effects are large remains less than about 20° wide.

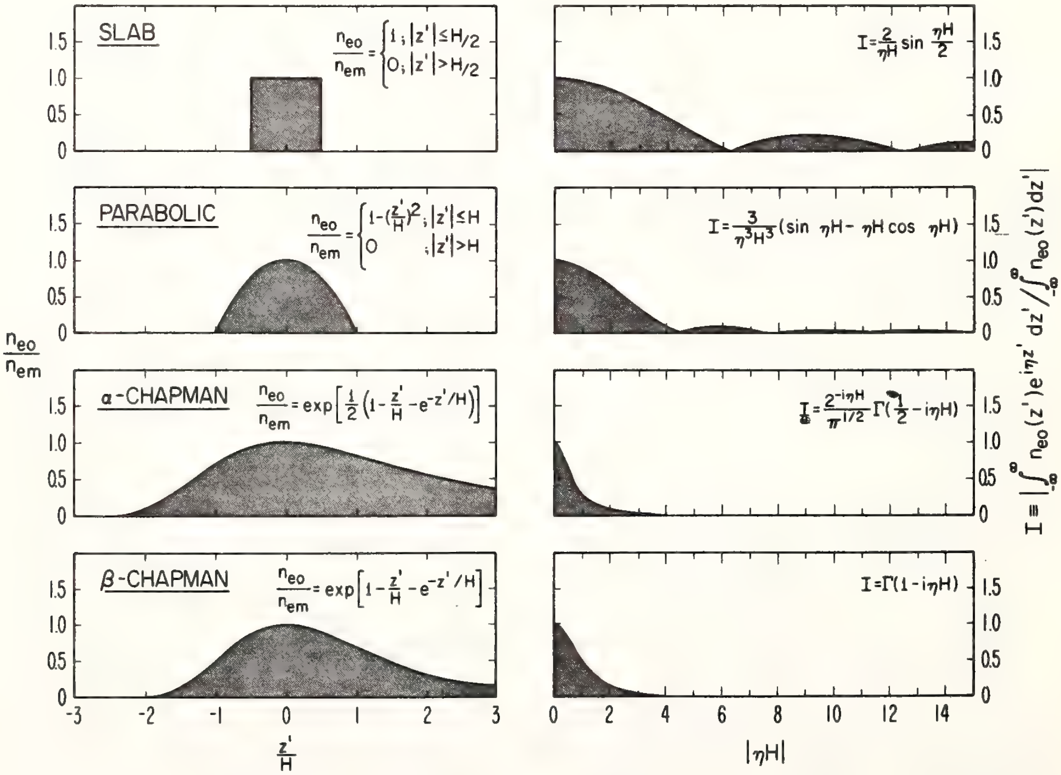

Fig. 3. Four model ionization density profiles (left) for which the integral in (10) has been evaluated, and (right) plots of the magnitude of the corresponding integrals (normalized) versus $|\eta H|$. η is a parameter relating the direction of $\mathbf{k}$ to the ground-satellite path. Here Γ indicates the gamma function of complex argument.

In the cases of the two symmetrical layers of finite extent (the slab and parabolic layers), the factor exp $i(\omega t + \eta h_m)$ completely expresses the phase behavior of C'/C_0 because the phase-cancellation integrals for these layers are purely real; in the cases of the Chapman layers, however, the integrals are complex, and thus the factor exp $i(\omega t + \eta h_m)$ represents only part of the phase contribution. For the Chapman layers the factor exp $i\ (\omega t + \eta h_m)$ can be thought of as the phase contribution from a very thin layer, whereas the phase contribution from the phase-cancellation integral can be thought of as the contribution due to finite layer thickness.

The implications of the phase-cancellation effect are that experiments using a geostationary satellite and a single receiver are biased in favor of those atmospheric waves whose phase surfaces nearly contain the ground-to-satellite path (i.e., for which $\eta \approx 0$); similarly, experiments using low altitude satellites, or those using multiple paths to geostationary satellites, can falsely indicate that wavelike perturbations in the ionosphere are not of large spatial extent on those occasions when cancellation occurs on some but not all of the radio paths.

Illustrating the Biases in the r Plane

We have given in equations 9 and 10 the mathematical expressions for the total-content fluctuations induced in a plane-stratified F layer by plane atmospheric waves and have pointed out the observational biases introduced by each factor. But an intuitive picture of the nature and extent of the biases and how they all work together is difficult to extract from the bare mathematics. We have found it practical and informative to evaluate equation 10 for many values of the problem variables by using a digital computer and by displaying the results of such computations as intensity plots that are readily produced by cathode-ray-tube output facilities [*Stephenson and Georges*, 1969]. Our displays use intensity or darkness to represent the fractional total-content fluctuations (C'/C_0) in two polar-coordinate planes: the $\mathbf{r}(\chi, \rho)$ plane and the $\mathbf{k}(\varphi, \alpha)$ plane. Plots in the $\mathbf{r}$ plane are helpful in visualizing the biases inherent in the observation of a single wave (i.e., fixed $\mathbf{k}$) as the orientation of the observer-to-satellite path varies over the sky. Plots in the $\mathbf{k}$ plane show the *spectral* biases inherent in a given observer-to-satellite path (i.e., fixed $\mathbf{r}$, as for geostationary satellites). In each display the ambient ionospheric model, the geomagnetic field inclination, the true wavelength of the atmospheric wave, and the wave amplitude are fixed. Although we have produced many displays of each type, we shall show only a few here.

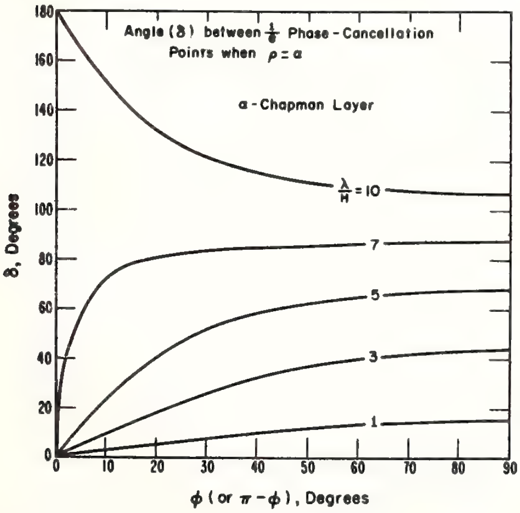

Fig. 4. Width of phase-cancellation band for an α-Chapman layer, as a function of wavefront tilt angle (φ) and the ratio of atmospheric wave length to layer scale height.

Figure 5 shows four $\mathbf{r}$-plane plots of the amplitude of content fluctuations produced by an internal gravity wave with a wave front tilt of 45° ($\varphi = 135°$) traveling toward the northwest. The wave period is 21.2 min. In each plot, satellite zenith angle χ increases linearly radially, and its azimuth angle ρ (positive westward) proceeds circumferentially with geomagnetic north at the top and geomagnetic west at the left.

The $\mathbf{r}$ plane is thus effectively a polar 'sky map' with the zenith at the center and the horizon at the perimeter. However, because the usefulness of satellite data at high zenith angles (near the horizon) is limited and because our plane geometry poorly approximates the real spherical geometry at these angles, we have let the plot perimeters represent a 75° zenith angle instead of 90°.

The four plots show that increasing the thickness of the ambient ionization density profile narrows the band of directions within which appreciable fluctuations are to be observed (because of the phase-cancellation effect). Note the limited extent of the phase-cancellation band for the Chapman layer with 100-km scale height, the one most nearly representative of realistic F layers.

The white band passing through the dark phase-cancellation band represents the effect of the factor (13) vanishing. Note that this band passes through the direction $\mathbf{r}$ corresponding to a line of sight along the geomagnetic field. (Positive I corresponds to the southern hemisphere.)

At the bottom of Figure 5 are two plots of the instantaneous fluctuations in electron content corresponding to two sections through the amplitude plots at $t = 0$. The 'amplitude envelopes' (corresponding to the intensity plots) are shown dashed. The instantaneous fluctuations 'flow through' the fixed envelope (to the left) as time progresses.

Figure 5 also shows that an atmospheric wave amplitude of 10 m/sec, which is the order of magnitude of the amplitude of gravity waves estimated in theoretical [*Hooke*, 1968*a*] and experimental [*Vasseur and Waldteufel*, 1969] studies, produces maximum total-content fluctuations of about 8%, in rough agreement with the observations of *Titheridge* [1963, 1968*a, b*].

The amplitude of total-content fluctuations that would be observed as a satellite follows a particular orbit can be determined in either of two ways. It can be determined directly from either (9) or (10) by substituting a suitable expression for the satellite position ($\mathbf{r}$) as a function of time; in our plane geometry a satellite orbit would be a straight-line horizontal path

$$\mathbf{r}(t) = \mathbf{V}t + \mathbf{r}_0 \qquad (17)$$

where $\mathbf{V}$ is the satellite velocity, and $\mathbf{r}_0$ is the position of the satellite at $t = 0$, both relative to a ground based observer. This method gives not only fluctuation amplitude, but the instantaneous fluctuations as a function of time as well.

Fluctuation amplitude can also be crudely but conveniently estimated by using $\mathbf{r}$-plane intensity plots with the aid of an overlay like the one in Figure 6. If the overlay is rotated to correspond to the azimuth of satellite travel, the solid lines indicate satellite tracks in the $\mathbf{r}$ plane for various zenith angles of closest approach. The patterns of light and dark intercepted by these tracks on the $\mathbf{r}$-plane intensity plot thus indicate the fluctuation amplitude caused by a given wave during satellite passage. The dashed lines on the overlay indicate equal horizontal (or time) intervals along the satellite track at a height of 300 km.

One kind of observational bias that may not be immediately obvious can be illustrated by considering the amplitude patterns intercepted in the $\mathbf{r}$ plane (the 50-km scale-height plot, say, in Figure 5) by two parallel satellite trajectories (at 20° zenith angles, say, but on opposite sides of the zenith) that might represent either observations using two satellites, or (more commonly) observations of a single orbiting satellite from spaced ground stations. As the overlay is rotated so that the satellite azimuth of travel coincides with that of the wave, the two tracks intercept identical amplitude patterns. But as the overlay is rotated away from this direction, the tracks begin to intercept different amplitude patterns, until, as the tracks approach perpendicularity with the wave travel direction, the amplitude patterns become quite dissimilar. Such experimental results, if not properly understood, could lead to gross errors in the estimates of wave travel direction, for example. Furthermore, data reduction processes that select 'events' for analysis on the basis of good correlation between records from spaced stations may also be selecting disturbances traveling roughly parallel to the satellite trajectory.

THE k PLANE

In the second display format we plot the amplitude of fractional content fluctuations proportional to darkness in the $\mathbf{k}$ plane. There, φ (the angle of $\mathbf{k}$ from the zenith) varies radially (from 90° to 180° for gravity waves), and α (the azimuth of $\mathbf{k}$, positive westward) varies circumferentially. Because of the unique relationship between $\mathbf{k}$ and ω defined by the gravity wave dispersion relation, the radius of the $\mathbf{k}$-plane plots also identifies the gravity wave period; short-period waves are near the center, whereas long-period waves are near the periphery of the plots.

Figure 7 shows four examples of $\mathbf{k}$-plane intensity displays for a satellite located at an azimuth of 60° and at zenith angles of 20°, 40°, 60°, and 80°, respectively. The dark bands in each plot represent the loci of $\eta \approx 0$, or near

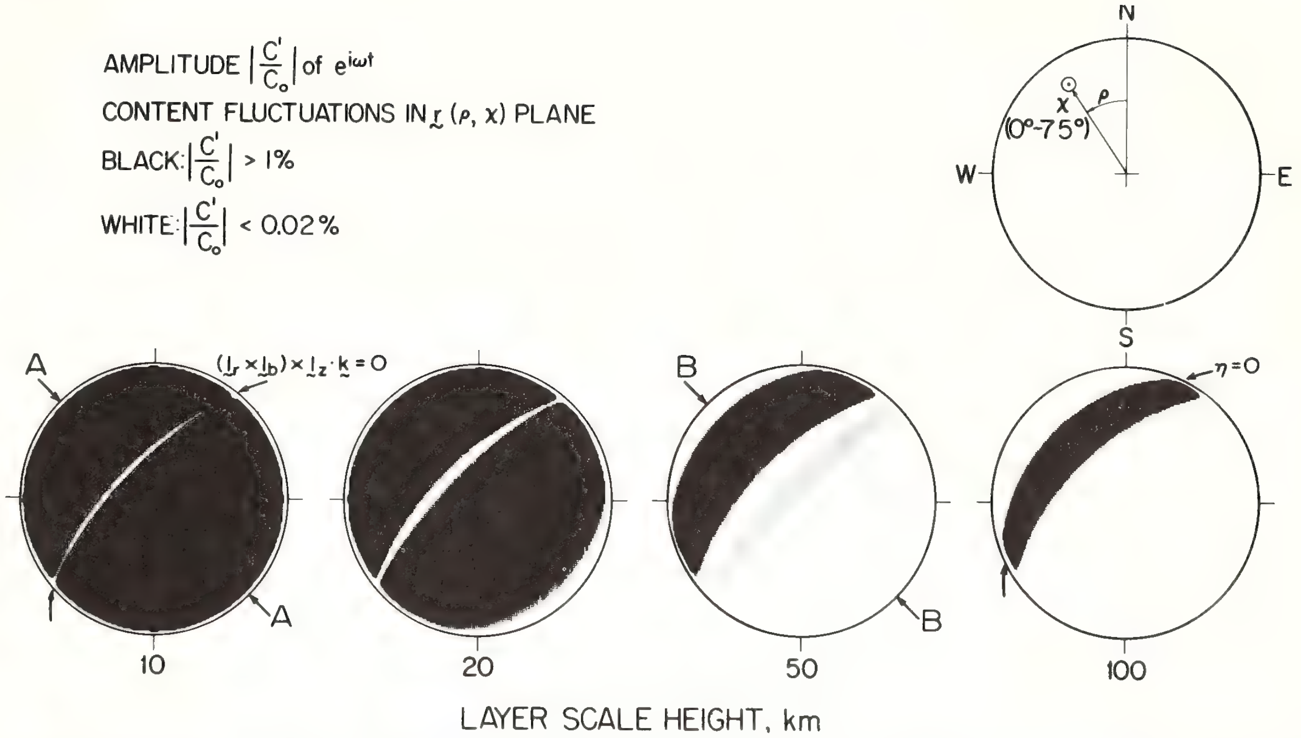

Fig. 5. Plane gravity wave in α-Chapman layers: intensity plots of the amplitude of fractional content fluctuations in the **r** plane, for four Chapman-layer scale heights. I is 60°, λ is 100 km, U is 10 m/sec, ϕ is 135°, α is 45°, and τ is 21.2 min. On the facing page are shown two plots of the instantaneous content perturbations (at $t = 0$) corresponding to the indicated sections through the intensity plots.

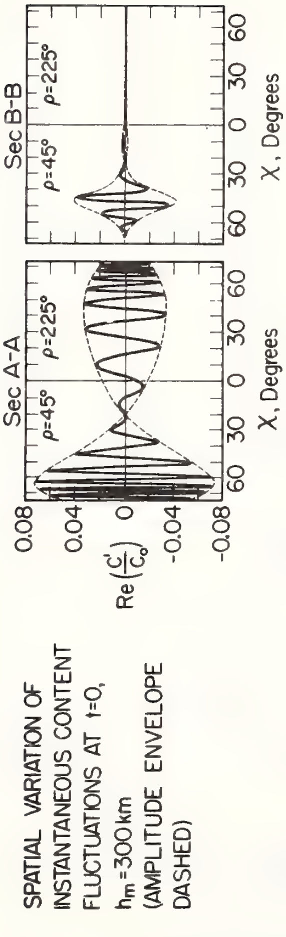

Fig. 5. Continued.

alignment of the wave phase surfaces with the line of sight to the satellite. The $\eta \approx 0$ band falls mostly near the center of the plot (steep wave front tilts and short wave periods) for small zenith angles and expands toward the edge of the plot (nearly horizontal wave fronts and long wave periods) as zenith angle increases. It also tends to fall in the quadrant centered on the azimuth of the satellite.

Two other loci are visible as white bands and show up best in the $\chi = 80°$ plot. They correspond to the waves that cause the factor (13) to vanish (the straight white lines that cut diagonally through the plots) and to the waves for which $\mathbf{U} \cdot \mathbf{1}_b = 0$ (the white arc across the lower half of each plot).

It may appear in the intensity plots that the two $C' = 0$ loci do not exert a very strong influence on the distribution of fluctuation amplitude in either the **k** or **r** planes. The intensity plots are slightly misleading in this respect, however. To optimize the appearance of the $\eta \approx 0$ bands in all the displays, it was necessary to adjust the intensity levels to a point where the other zero loci became very thin. The section A-A plot at the bottom of Figure 5 shows, however, that the influence of the factor (13) is really more marked than the corresponding intensity plot suggests. This is true of the other zero loci in the **k** plane as well.

The effects of changing the ionospheric layer thickness are similar to the effects in the **r** plane: the $\eta \approx 0$ band gets thinner for thicker layers and thicker for thinner layers, until, for very thin layers, the phase-cancellation effect is unimportant.

A single **k**-plane intensity plot gives a complete picture of which portions of the atmospheric wave spectrum are most successful in creating total-content fluctuations that are observable, given a particular fixed satellite geometry and magnetic inclination. For example, an isotropic spectrum of internal gravity waves would be seen by the $\chi = 80°$ geometry in Figure 7 as a set of long period waves propagating toward the northwest; the same spectrum of waves would be seen by the $\chi = 20°$ geometry as a set of short period waves propagating roughly northward and southward.

The examples shown here have been constructed for internal gravity waves; very similar

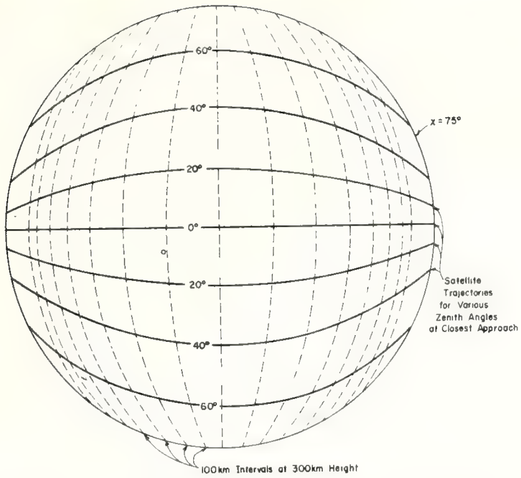
60°
40°
20°
0°
20°
40°
60°
χ = 75°
Satellite Trajectories for Various Zenith Angles at Closest Approach
100km Intervals at 300km Height

Fig. 6. An overlay for tracing satellite trajectories (solid lines) in the **r** plane. The overlay must be rotated to correspond to the azimuthal direction of satellite motion. Dashed lines indicate equal horizontal (or time) intervals along the trajectories. The trajectories do not converge at the overlay perimeter because it corresponds to a satellite zenith of 75°, not 90°.

plots result for acoustic waves, with one important difference: because no unique relation exists between wave orientation and the period of acoustic waves (as it does for internal gravity waves), unique wave periods cannot be associated with points in the **k** plane. Removal of the ω influence on the direction of **k** simply means, however, that a **k**-plane intensity plot is the same for *all* acoustic wave frequencies, with ω serving only as a constant intensity (amplitude) multiplier. The **r**-plane plots for acoustic waves tend to have a character similar to those for gravity waves.

Concluding Remarks

By constructing a very simple model of the total-content fluctuations induced in the F layer by atmospheric waves, we find that a complicated but important set of biases is built into observations of short-term content fluctuations along paths to artificial satellites. Such an assertion raises two questions: (1) can the theory be checked observationally, and (2) if substantially correct, can it help recover true atmospheric wave statistics from total-content observations?

First, we must point out several deficiencies in our model that would preclude precise checks. We have neglected the sphericity of the earth, the variations of wave amplitude and wave vector direction with height, wave-induced photochemical changes, and sporadic-E effects. Furthermore, although equation 10 would permit the use of any $n_{e0}(z)$ profile, a completely realistic model electron density distribution should allow for horizontal gradients in ambient density as well. Therefore, in its present form, the model is not likely to withstand detailed and quantitative experimental tests. Although a more comprehensive model could be devised, its utility in interpreting actual observations would be doubtful because of its complexity.

A conclusive observational check of every facet of the theory seems impossible, even if it were refined by correcting the deficiencies just mentioned. Such a check would require many simultaneous observations of waves at the same location, with both the total-content method and some other method that could yield reliable and sufficiently detailed information about the spectrum of atmospheric waves actually present, as well as a detailed determination of the three-dimensional ambient electron density distribution. No way to do this is yet known; however, a verification that at least some biases exist could be attempted by observing the same ionospheric region with both the total-content and another more reliable sounding technique. If different waves are observed, or if one technique observes waves that the other does not, then biases must be suspected. It should be emphasized, however, that the two techniques must look at precisely the same ionospheric region (within a few tens of kilometers), in view of the apparently short autocorrelation distances observed for medium-scale traveling disturbances [*Georges*, 1967].

The prospects for using our model to remove the biases in actual observations are not very bright either; this would require the same accurate knowledge of the ambient ionization distribution that we discussed in connection with the observations needed to verify the model. The very existence of instruments to provide such information would obviate the need for measuring the same thing by using total-content methods.

We would therefore conclude that, while the total-content technique is suited to studies of

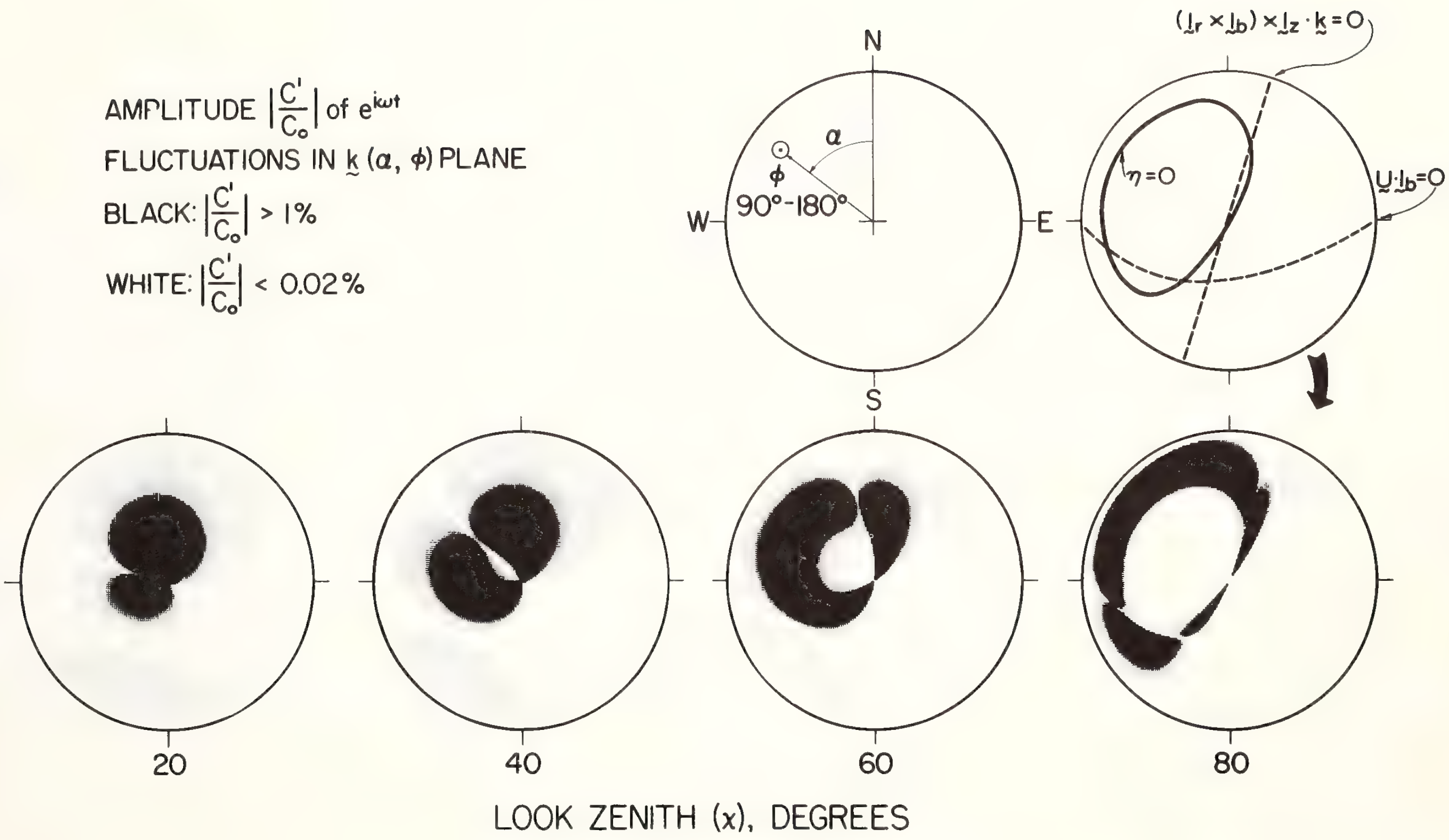

Fig. 7. Plane gravity waves in α-Chapman layer: Intensity plots of the amplitude of fractional content fluctuations in the **k** plane for four fixed satellite locations. These plots indicate the spectral biases of given satellite geometries. I is 40°, λ is 100 km, U is 10 m/sec, H is 50 km, and ρ is 60°.

gross ionospheric balance and perhaps some shorter term features of large scale, such as the polar-substorm-related TID's observed by *Davis and daRosa* [1969], it cannot provide an accurate statistical (and possibly not even instantaneous) picture of the ionosphere's dynamic state.

Acknowledgments. Mrs. Judith J. Stephenson programmed the calculations that produced the displays of this paper. We are indebted to Dr. R. H. Ott and Mr. L. A. Berry for their help in evaluating the integral in (10) for various model profiles.

This work was supported in part by the National Aeronautics and Space Administration, Marshall Space Flight Center, Huntsville, Alabama.

* * *

The Editor wishes to thank E. E. Gossard and J. E. Titheridge for their assistance in evaluating this paper.

REFERENCES

Chan, K. L., and O. G. Villard, Jr., Observation of large-scale traveling ionospheric disturbances by spaced-path high-frequency instantaneous-frequency measurements, *J. Geophys. Res., 67,* 973–988, 1962.

Davis, M. J., and A. V. daRosa, Traveling ionospheric disturbances originating in the auroral oval during polar substorms, *J. Geophys. Res., 74,* 5721–5735, 1969.

Georges, T. M., Ionospheric effects of atmospheric waves, *ESSA Tech. Rep. IER 57-ITSA 54,* 1967.

Georges, T. M., HF Doppler studies of traveling ionospheric disturbances, *J. Atmos. Terr. Phys., 30,* 735–746, 1968*a*.

Georges, T. M., Collisional interaction of atmospheric waves with the ionospheric *F* region, in *Acoustic-Gravity Waves in the Atmosphere—Symposium Proceedings,* edited by T. M. Georges, pp. 377–380, U. S. Government Printing Office, Washington, D. C., 1968*b*.

Heisler, L. H., Anomalies in ionosonde records due to traveling ionospheric disturbances, *Aust. J. Phys., 11,* 79–90, 1958.

Hines, C. O., Internal amospheric gravity waves at ionospheric heights, *Can. J. Phys., 38,* 1441–1481, 1958.

Hines, C. O., The upper atmosphere in motion, *Quart. J. Roy. Meteorol. Soc., 89,* 1–42, 1963.

Hooke, W. H., Ionospheric irregularities produced by internal atmospheric gravity waves, *J. Atmos. Terr. Phys., 30,* 795–823, 1968*a*.

Hooke, W. H., The response of the *F* region ionosphere to internal atmospheric gravity waves, in *Acoustic-Gravity Waves in the Atmosphere—Symposium Proceedings,* edited by T. M. Georges, 367–372, U. S. Government Printing Office, Washington, D. C., 1968*b*.

Hooke, W. H., *E* region ionospheric irregularities produced by internal atmospheric gravity waves, *Planet Space Sci., 17,* 749–765, 1969.

Little, C. G., and R. S. Lawrence, The use of polarization fading of satellite signals to study the electron content and irregularities in the ionosphere, *Radio Sci. 64D*(4). 335–346, 1960.

Mass, J., Survey of satellite techniques for studying propagation, in *Radio Astronomical and Satellite Studies of the Atmosphere,* edited by J. Aarons, 256–288, North-Holland, Amsterdam, 1963.

Munro, G. H., Traveling disturbances in the ionosphere, *Proc. Roy. Soc., London, 202,* 208–223, 1950.

Munro, G. H., Traveling ionospheric disturbances in the *F* region, *Aust. J. Phys., 11,* 91–112, 1958.

Rao, N. N., G. F. Lyon, and J. A. Klobuchar, Acoustic waves in the ionosphere, *J. Atmos. Terr. Phys., 31,* 539–545, 1969.

Stephenson, J. J., and T. M. Georges, Computer routines for synthesizing ground backscatter from three-dimensional raysets, *ESSA Tech. Rep. ERL 120-ITS 84,* 1969.

Thome, G. D., Incoherent scatter observations of traveling ionospheric disturbances, *J. Geophys. Res., 69,* 4047–4049, 1964.

Thome, G. D., Long-period waves generated in the polar ionosphere during the onset of magnetic storms, *J. Geophys. Res., 73,* 6319–6336, 1968.

Titheridge, J. E., Large-scale irregularities in the ionosphere, *J. Geophys. Res., 68,* 3399–3417, 1963.

Titheridge, J. E., Periodic disturbances in the ionosphere, *J. Geophys. Res., 73,* 243–252, 1968*a*.

Titheridge, J. E., The characteristics of large ionospheric irregularities, *J. Atmos. Terr. Phys., 30,* 73–84, 1968*b*.

Titheridge, J. E., A regular disturbance in the topside ionosphere, *J. Geophys. Res., 74,* 1195–1204, 1969.

Vasseur, G., and P. Waldteufel, Thomson scatter observations of a gravity wave in the ionospheric *F* region, *J. Atmos. Terr. Phys., 31,* 885–888, 1969.

(Received April 7, 1970;
revised May 15, 1970.)

Reprinted from Journal of Geophysical Research, Space Physics
75, No. 34, 7229-7238, 1970.

Ionospheric Response to Internal Gravity Waves

2. Lower *F* Region Response

WILLIAM H. HOOKE

Institute for Telecommunication Sciences,
ESSA Research Laboratories, Boulder, Colorado 80302

The response of the lower *F* region ionosphere to individual internal gravity waves is calculated as a function of the azimuth of wave propagation. This response is shown to be highly anisotropic, with the anisotropy itself depending on time of day, season, wave parameters, height, and geographic and geomagnetic location. Wave-associated changes in photoionization rate, and their dependence on the degree of alignment between the incoming solar radiation flux and surfaces of constant wave phase, play a dominant role in determining the anisotropy. Wave-associated changes in attachmentlike chemical loss are also important. The response of the lower *F* region ionosphere to internal gravity waves therefore differs fundamentally from the response at higher levels, where ion lifetimes are long and wave-associated photochemical effects can be ignored, so that geomagnetic constraints on ion motion play the primary role in determining the anisotropy.

Theory suggests [*Hooke,* 1968*a*] that internal gravity waves produce traveling ionospheric disturbances (TID) through a variety of photochemical and dynamical means, with the ionosphere responding to the waves in an anisotropic manner that varies with wave parameters, geographic latitude and geomagnetic inclination, and prevailing ionospheric conditions. The diurnal and seasonal variations in this response and its anisotropy must have some bearing on observations [*Munro,* 1950, 1958; *Price,* 1955] that reveal diurnal and seasonal variations in TID occurrence frequency and statistically preferred directions of travel. At heights above about 250 km, where ionic lifetimes are long compared with wave periods, so that wave-associated photochemical effects can be ignored, the ionospheric response and its anisotropy are particularly easy to understand and were considered in detail earlier (*Hooke* [1970], hereafter referred to as paper 1). In this case the anisotropy results solely from the geomagnetic constraints on the ion motion at these heights, while its dependence on the ambient electron density height gradient, which varies with time of day and season, produces diurnal and seasonal variations in the anisotropy.

Copyright © 1970 by the American Geophysical Union.

Because the statistical TID studies cited above pertain to 200-km heights and below [*Heisler,* 1958], however, paper 1 does not completely describe the relevant wave-ionosphere interaction. At these lower heights, internal gravity waves produce ionospheric irregularities, not only because they set the neutral atmosphere and hence the ionization into motion, but also because they produce density (and temperature) perturbations in the neutral gas that affect the rates of photochemical processes. In particular, perturbations in the photoionization rate depend in magnitude on the degree to which the incoming solar radiation is aligned with surfaces of constant wave phase [*Hooke,* 1968*a*]. Because wave-associated changes in photoionization rate obey such a solar control, the lower *F* region ionosphere should exhibit diurnal and seasonal variations in response additional to those discussed previously. This wave-associated photochemical effect is the main subject of this paper. In particular, this paper considers the questions: how important are wave-associated photochemical effects relative to wave-associated dynamic effects in TID production; and what is the degree and nature of the solar control on the ionospheric response?

Theory and Calculations

Consider an inviscid, plane-stratified isothermal atmosphere and ionosphere, stationary in the absence of internal gravity waves, and allow a plane internal gravity wave of angular frequency ω and wavevector $\mathbf{k}$ to perturb this atmosphere. This wave produces neutral atmospheric motions $\mathbf{u}$ and fractional density perturbations ρ'/ρ_0 that are proportional to

$$\exp(z/2H) \exp i(\omega t - \mathbf{k}\cdot\mathbf{r}) \qquad (1)$$

where z is the height, H is the neutral atmospheric scale height, t is the time, and $\mathbf{r}$ is a position vector. (In this paper zero subscripts will denote unperturbed values of physical quantities; primes will denote small perturbations from those unperturbed values.) The wave also produces temperature changes, whose influence will be neglected here. The horizontal and vertical components of $\mathbf{u}$ and the fractional neutral atmospheric density perturbations ρ'/ρ_0 are related in amplitude and phase by equations 24 through 26 given by *Hines* [1960]. These relations depend not only on ω, $\mathbf{k}$, and H, but also on the neutral-gas ratio of specific heats γ and the acceleration of gravity g. The magnitude of the velocity and density perturbations can be determined from the wave energy per unit mass E by equation 45 of *Hines* [1960]. The wavevector $\mathbf{k}$ is related to the angular frequency ω by the wave dispersion equation 21 of *Hines* [1960] (that equation contains a typographical error; the second k_x of that formula should be k_z).

Through collisions, the neutral atmosphere sets the ionization into motion. This ion motion is given by [*MacLeod*, 1966]

$$\mathbf{u}_i = \frac{1}{1 + R^2} \left[R^2\mathbf{u} + R(\mathbf{u} \times \mathbf{1}_b) + (\mathbf{u}\cdot\mathbf{1}_b)\mathbf{1}_b\right] \qquad (2)$$

where $R \equiv \nu_i/\omega_i$ is the ratio of the ion-neutral collision frequency ν_i to the ion gyrofrequency ω_i, and $\mathbf{1}_b$ is a constant unit vector directed parallel to the geomagnetic induction. In the calculations, it is assumed that

$$R \propto \exp(-z/H) \qquad (3)$$

The neutral atmospheric density fluctuations produce departures from the ambient photoionization rate

$$q_0 = q_m \exp\left[1 + \frac{z_m - z}{H^*} - \exp\left(\frac{z_m - z}{H^*}\right)\right] \qquad (4)$$

that are given by the real part of the expression

$$q'/q_0 = (\rho'/\rho_0) \cdot \left[1 - \frac{\cos\chi \exp[(z_m - z)/H^*]}{(1 - H^*/2H)\cos\chi + iH^*\mathbf{k}\cdot\mathbf{1}_\chi}\right] \qquad (5)$$

[*Hooke*, 1968*a*]. Here H^* is the scale height of the ionizable constituent, χ is the solar zenith angle, and $\mathbf{1}_\chi$ is a unit vector directed antiparallel to the solar ionizing radiation flux; z_m is the height of maximum photoionization rate q_m. In terms of the geographic latitude φ, the solar declination δ, and the local hour angle h of the sun,

$$\cos\chi = \sin\varphi \sin\delta + \cos\varphi \cos\delta \cos h \qquad (6)$$

In a local Cartesian coordinate system with x axis directed eastward, y axis directed northward, and z axis vertical,

$$\begin{aligned}\mathbf{k}\cdot\mathbf{1}_\chi = {} & (k_y \cos\varphi + k_z \sin\varphi) \sin\delta \\ & + (k_x \sin h - k_y \sin\varphi \cos h \\ & + k_z \cos\varphi \cos h) \cos\delta \end{aligned} \qquad (7)$$

The term $\mathbf{k}\cdot\mathbf{1}_\chi$ implies a solar control of wave-produced changes in photoionization rate, as mentioned in the introduction. Thus, at any specified time, two different waves will in general produce different changes in photoionization rate. Similarly, a single given wave will produce different changes in photoionization rate at different times of day.

Note that equation 5 contains both the neutral atmospheric scale height H and the scale height of the ionizable constituent H^*. These two scale heights need not be equal, and in the present application they are not. This inequality has implications for the theory that were not discussed earlier by *Hooke* [1968*a*] and so merits some attention here. Consider the second term on the right side of equation 5. This term gives the changes in q'/q_0 at any point caused by the wave-produced changes in the ionizing solar radiation flux at that point [*Hooke*, 1968*a*]. It is largest when $\mathbf{k}\cdot\mathbf{1}_\chi = 0$, i.e., when the solar ionizing radiation flux lies in surfaces of constant wave phase. We shall confine our attention to this case for the moment. Then, if $H = H^*$, the $\exp(z/2H)$ growth of the wave amplitude with height (implicit in the ρ'/ρ_0 factor) is more than offset by the $\exp(-z/H^*)$ decrease in the density of the ionizable constituent with height, and the second term on the right side of equation 5 is small compared with unity for $z \gg z_m$ because $(1 - H^*/2H) = 0.5$. This term becomes large only for $z \leq z_m$. On the other hand, should $2H \doteq H^*$, as is very nearly the case in the very low F region (major constituent N_2; ionizable constituent O), then the second term on the right side of equation 5 may be greater than unity even at heights z well above z_m.

Thus the earlier work [*Hooke*, 1968*a*] implicitly underestimated the importance of this flux term, which might now appear to imply enormous wave-produced fluctuations in photoionization rates at *all* heights. Such wave-associated photoionization catastrophes do not actually occur, however, for several reasons. First, and most fundamentally, H^* being greater than H implies that H must increase with height (approaching H^* as a limit). This in turn implies that above some reference level $(1 - H^*/2H)$ is no longer infinitesimal: it also implies that the derivation of equation 5, in which equations from *Hines* [1960] that assume H = constant are used, is no longer correct. Wave refraction would occur, so that $\mathbf{k}$ would be height-variable, and the condition $\mathbf{k}\cdot\mathbf{1}_\chi = 0$ would not be met at all heights. Second, equation 5 assumes that the wave amplitude increases exponentially with height, *at all heights*. Because of viscous dissipation of the wave energy, this does not occur. Third, the condition $\mathbf{k}\cdot\mathbf{1}_\chi = 0$ must be met exactly at all heights for the catastrophe to occur; this will be prevented by any wave refractive effects (including viscous dissipation [*Pitteway and Hines*, 1963; *Hines*, 1968]). Refining the theory in any of these respects should serve to reduce considerably any abnormally large changes in photoionization rate that might otherwise be expected. Note that, if q'/q_0 were large, the linearization of the equations used in deriving equation 5 would be invalid.

The preceding discussion suggests that it is somewhat inconsistent to assume both that H = constant and that $H < H^*$, as will in fact be done here. This inconsistency should be more pronounced the closer H^* is to $2H$. As we will see shortly, in the calculations presented here it is assumed that $H^* = 1.67H$. Hopefully this choice properly reflects the importance of the solar control of wave-produced changes in photoionization rate, while minimizing the influence of the inconsistency on the results, but this is only a hope. A definitive check on the errors introduced by these assumptions would require a detailed numerical analysis, which would not appear to be merited at the moment in view of the present crudeness of both theory and observation. In any event, the calculations presented suffice to show the relative importance of wave-associated photochemical and dynamical effects in TID production, as well as the degree and basic nature of the solar control of that production. (It should also be noted in passing that in the computations of an earlier paper [*Hooke*, 1968*b*], it is tacitly assumed that $H = H^*$, so that Figures 4 and 5 of that paper do not agree with the results presented here.)

The calculations themselves proceed as follows: First, equations 4 through 6 of *Hooke* [1968*a*] were used to specify the unperturbed model ionosphere. In applying those equations to the lower F region, all the diffusion terms can be ignored, and the equations reduce to

$$q_0 = \beta_0 n_0(\mathrm{O}^+) \tag{8}$$

$$\beta_0 n_0(\mathrm{O}^+) = \alpha_0 n_0(XY^+) N_{e0} \tag{9}$$

$$N_{e0} = n_0(\mathrm{O}^+) + n_0(XY^+) \tag{10}$$

Here N_e is the free electron number density, $n(\mathrm{O}^+)$ is the atomic oxygen ion number density, and $n(XY^+)$ is the molecular ion number density; α and β are reaction rate coefficients. The zero subscripts denote the unperturbed values of these quantities. Both α and β are assumed to be independent of temperature; in this case α is a constant, while β can be written

$$\beta = \beta^* n(XY) \qquad \beta_0 = \beta^* n_0(XY) \tag{11}$$

where β^* is a constant, and $n(XY)$ is the number density of the neutral molecules. Equations 4 and 8 through 11 then determine $n_0(\mathrm{O}^+)$, $n_0\ (XY^+)$, and N_{e0} at all heights algebraically, once q_{∞}, z_m, H^*, α_0, β^*, and $n_0(XY)$, and the solar zenith angle χ, have been specified. Here $n_0(XY)$ is calculated from the formula

$$n_0(XY) = n_{00}(XY)\ \exp\,(1.75[z_0 - z]/H^*) \tag{12}$$

where $n_{00}(XY)$ is the number density of neutral molecules at the height $z_0 \equiv z_m - H^* \ln(\sec \chi)$. Because all the input parameters have rather simple height variations, it is also a simple matter to derive algebraic formulas for the quantities $dn(O^+)/dz$, $dn(XY^+)/dz$, and dN_{e0}/dz that are required in the calculations. In all the calculations presented here, the values $q_0(z_0) = 3000$ cm^{-3} sec^{-1}, $z_0 = 150$ km, $H^* = 50$ km, $\alpha_0 = 10^{-7}$ cm^3 sec^{-1}, $\beta^* = 2 \times 10^{-12}$ cm^3 sec^{-1}, and $n_{00}(XY) = 3.27 \times 10^{10}$ cm^{-3} are adopted. This choice for the input parameters generates a model ionosphere of the type illustrated in Figure 1 for $\chi = 60°$.

The internal gravity wave is then taken to perturb the number densities of the various ionic species according to equations 10 through 12 of *Hooke* [1968*a*], which according to the assumptions made here reduce to

$$(\beta_0 + i\omega)n'(O^+) \\ = q' - \beta' n_0(O^+) - \nabla \cdot (n_0(O^+)\mathbf{u}_i) \qquad (13)$$

$$(\alpha_0 N_{e0} + \alpha_0 n_0(XY^+) + i\omega)(\beta_0 + i\omega)N_e' \\ = (\alpha_0 N_{e0} + \beta_0 + i\omega)q' - \alpha_0 N_{e0} q_0 \beta'/\beta_0 \\ - (\alpha_0 N_{e0} + \beta_0 + i\omega)\nabla \cdot (n_0(O^+)\mathbf{u}_i) \\ - (\beta_0 + i\omega)\nabla \cdot (n_0(XY^+)\mathbf{u}_i) \qquad (14)$$

$$N_e' = n'(O^+) + n'(XY^+) \qquad (15)$$

Here the primes denote perturbed values of these quantities. Since in the lower ionosphere diffusion processes can be ignored, the different ion species are all taken to have the same velocity $\mathbf{u}_i$. From equation 11 it follows that

$$\beta'/\beta_0 = \rho'/\rho_0 \qquad (16)$$

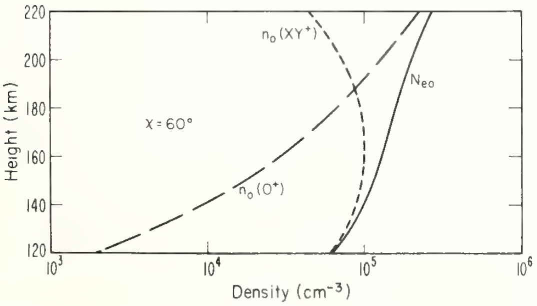

Fig. 1. The model lower *F* region ionosphere. Shown are height profiles of $n_0(O^+)$, $n_0(XY^+)$, and N_{e0} for $\chi = 60°$.

Equations 13 through 16, together with equations 5 through 7, the ambient ionospheric model, and the equations cited from *Hines* [1960], can be used to calculate the amplitude of the instantaneous electron density fluctuations N_e'/N_{e0} in terms of given values of the parameters γ, g, H, $R(z_0)$, $\mathbf{k}$, E, $\mathbf{1}_b$, $\mathbf{1}_\chi$ (or, equivalently, φ, δ, and h), and the height z of interest. In all the calculations presented here, γ is taken to be 1.4, g to be 9.35 msec^{-2}, H to be 30 km, and $R(z_0)$ to be 0.1. Because R is small in this application, it can be taken to be the same for all ion species without significantly affecting the results. The vector $\mathbf{1}_b$, specified in the figures by the geomagnetic inclination I (here taken to be positive in the southern hemisphere), the geographic latitude φ, the solar declination δ, positive during northern hemisphere winter, the hour angle h, and the height z, as well as the azimuthal orientation of $\mathbf{k}$, vary from calculation to calculation. Geomagnetic and geographic north are assumed to coincide, to simplify the formulas for $\mathbf{1}_b$ and $\mathbf{1}_\chi$. Wave phase propagation is taken to be downward, in agreement with observation [*Hines*, 1960, 1963].

To compare differences in the ionospheric response to the different waves, it is assumed in all the calculations that the wave energy per unit mass $E = 40$ m^2 sec^{-2} *at the height z of interest*, corresponding to atmospheric motions there of ~6 msec^{-1}. This value agrees in order of magnitude with observational estimates of the internal gravity wave amplitudes at these heights, although it is somewhat lower than the estimates from the very large scale, magnetic-storm-associated TID's (e.g., *Testud and Vasseur*, 1969; *Vasseur and Waldteufel*, 1969]. Note, as pointed out in paper 1, that this method of wave amplitude normalization is purely arbitrary and must certainly affect the appearance of the results as they are displayed here. More realistic normalizations can be used quite readily, however, as the data become available.

RESULTS

The results of this paper take the form of polar coordinate plots such as those shown in paper 1. Each curve shows the amplitude of the fractional perturbations in electron density (proportional to the radial distance from the curve to the plot origin) produced by a specified wave as a func-

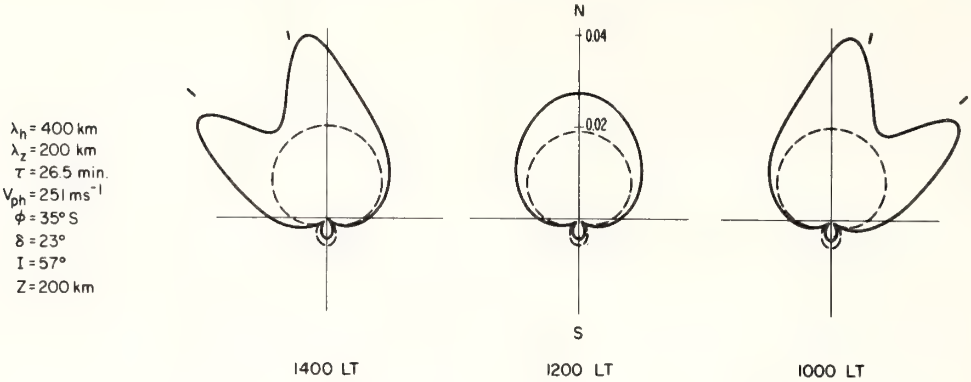

Fig. 2. Response of the lower *F* region ionosphere (very near southern hemisphere winter solstice) to an internal gravity wave (phase propagation downward) as a function of local time and the azimuth of wave propagation. In each of the three individual plots, the radial distance from points of the curves to the plot origin gives the amplitude of the fractional density perturbations N'_e/N_{e0} occurring during wave passage, for waves of energy per unit mass $E = 40$ m^2 sec^{-2} at the height of interest. The solid curves show the full ionospheric response; the dashed curves show the response calculated by assuming that wave-produced perturbations in photoionization rate and attachmentlike loss rate are zero. The tic marks indicate those azimuthal directions of wave propagation for which the solar radiation flux lies in surfaces of constant wave phase. All three plots are drawn to the same scale; the largest perturbation amplitudes on the plot equal 0.04.

tion of the azimuth of wave propagation (measured circumferentially) for given ionospheric conditions. Thus the curves in Figure 2 show the response of the lower *F* region ionosphere (height $z = 200$ km; geomagnetic inclination $I = 57°$; latitude $\varphi = 35°$ S; declination $\delta = 23°$, i.e., near southern hemisphere winter solstice) to an internal gravity wave as a function of the time of day. The geomagnetic inclination and latitude correspond to conditions at Sydney, Australia. In the model atmosphere considered here, this wave has a period $\tau = 26.5$ min and a horizontal phase velocity $v_{ph} = 251$ msec^{-1}. The tic marks indicate those azimuths of propagation for which $\mathbf{k}\cdot\mathbf{l}_\chi = 0$, i.e., for which the solar ionizing radiation flux lies in surfaces of constant wave phase. Note that the condition $\mathbf{k}\cdot\mathbf{l}_\chi = 0$ can be written in the form

$$\operatorname{ctn}\chi = \operatorname{ctn}\psi\cos\theta \qquad (17)$$

where ψ is the tilt of the surfaces of constant wave phase from the vertical, and θ is the azimuthal angle between the horizontal components of $\mathbf{k}$ and $\mathbf{l}_\chi$. This equation has either two solutions, one solution, or no solution θ, depending on whether $\psi < \chi$, $\psi = \chi$, or $\psi > \chi$, respectively. For waves with vertically downward phase propagation, ctn χ and ctn ψ are always positive, so that $|\theta|$ will always be less than 90°.

The solid curves in Figure 2 show the lower *F* region ionospheric response as calculated in the manner outlined in the previous section; the dashed curves show the ionospheric response calculated by assuming that the wave produces no changes in the rates of photochemical processes, i.e., that $q' = \beta' = 0$ in equations 13 and 14. The dashed curves are then essentially the curves that would be calculated by using the theory of paper 1, except that in paper 1 it was assumed that

$$N_e' \doteq -\frac{1}{i\omega}\nabla\cdot(N_{e0}\mathbf{u}_i) \qquad (18)$$

while here

$$N_e' \doteq \frac{-1}{\beta_0 + i\omega}\nabla\cdot(N_{e0}\mathbf{u}_i) \qquad (19)$$

at heights where atomic oxygen ions dominate (above about 150 km), and

$$N_e' \doteq \frac{-1}{2\alpha_0 N_{e0} + i\omega}\nabla\cdot(N_{e0}\mathbf{u}_i) \qquad (20)$$

at heights where molecular ions dominate (below about 150 km), since at lower *F* region heights the ion lifetimes β_0^{-1} and $(\alpha_0 N_{e0})^{-1}$ tend to be shorter than the wave periods of interest (see Figure 3 of *Hooke* [1968*a*]). In consequence, the ionospheric response at the lower heights is markedly less than the reponse that would have been calculated if the tendency for the ionosphere to remain in photochemical equilibrium despite the wave perturbation were to have been neglected. Note that, because of the imaginary unit i, there is a phase change of the N_e' variations in the vertical additional to those associated with the neutral-gas wave itself. This phase change can be interpreted physically as follows: When $\omega \gg \beta_0, \alpha_0 N_{e0}$, the ion lifetimes are long compared with a wave period, and maximum perturbations in N_e' occur a quarter of a wave cycle after the time of maximum ion convergence. When $\beta_0 \gg \omega$, or $\alpha_0 N_{e0} \gg \omega$, on the other hand, then the ion convergence is compensated for immediately (more precisely, in a time short compared with a wave period) by enhanced photochemical loss, and maxima in N_e' and the ion convergence occur simultaneously. It should perhaps be emphasized here that approximation 4 does not apply at the F_2 peak, even though $\alpha_0 N_{e0} \gg \omega$ there; this is because O^+ is the dominant ion, whereas XY^+ is only a minor constituent (see *Hooke* [1968*a*] for details).

Note, however, that the internal gravity waves do perturb the photochemical equilibrium, i.e., $q' \neq 0$, $\beta' \neq 0$, and that these perturbations are of major importance in TID production, as shown by the differences between the dashed and solid curves. Taking these wave-associated photochemical effects into account, we find that, when the wave in Figure 2 propagates in azimuthal directions such that $\mathbf{k}\cdot\mathbf{l}_x = 0$, the lower F region ionospheric response is roughly twice what would otherwise be expected. Thus at 1000 LT, the ionospheric response is enhanced for waves propagating toward the northeast. At 1200 LT, there exists no azimuthal direction of propagation satisfying $\mathbf{k}\cdot\mathbf{l}_x = 0$, and the wave-associated photochemical effects are not so marked. At 1400 LT, such directions do again exist and the ionospheric response is again enhanced; this time, however, the preferred direction of wave propagation is toward the northwest. The response pattern tends to follow the sun across the sky.

This solar control also results in seasonal variations in ionospheric response, as illustrated by Figure 3, which shows the response of the lower F region ionosphere (height $z = 200$ km; geomangetic inclination $I = 57°$; latitude $\varphi = 35°$S; 0800 LT) to the same internal gravity wave as a function of season. When $\delta = 23°$, corresponding to winter solsticial conditions, there are two azimuths of wave propagation satisfying $\mathbf{k}\cdot\mathbf{l}_x = 0$. Waves propagating in these two directions quite obviously produce the largest TID. In this case the sun is quite near the horizon, and the two preferred azimuths of wave propagation are correspondingly quite far apart. Note that, over a wide range of azimuths of propagation, the wave produces a TID of smaller amplitude than it would have if q' and β' were both equal to zero; the solid curve lies inside the dashed one. When the wave is propagating in these azimuthal directions, the wave-

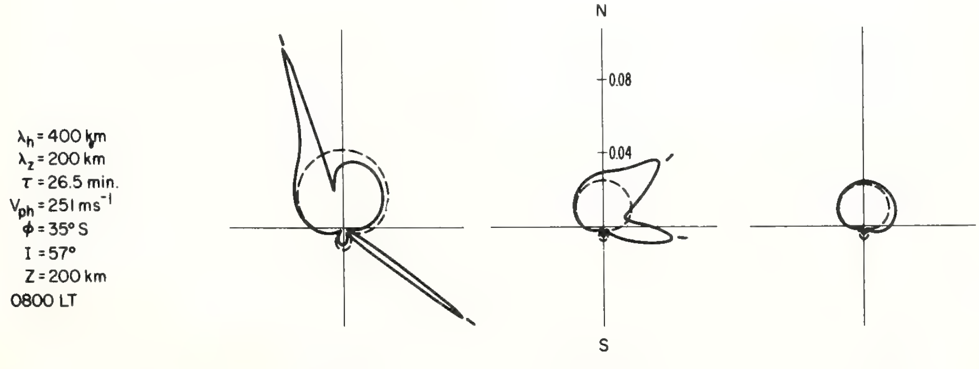

$\delta = 23°$ $\delta = 0°$ $\delta = -23°$

Fig. 3. Response of the lower F region ionosphere at temperate latitudes to an internal gravity wave as a function of season.

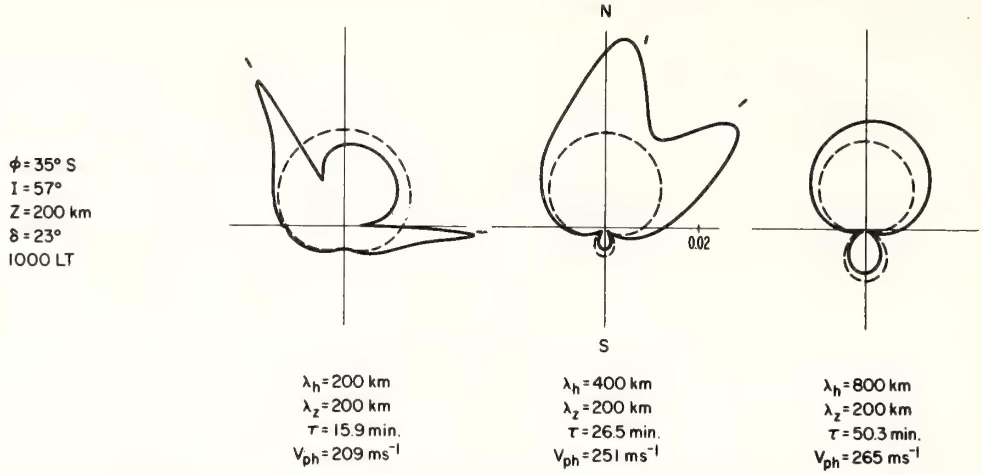

Fig. 4. Response of the lower F region ionosphere at temperate latitudes to internal gravity waves as a function of the wave parameters.

associated photochemical and dynamical effects compete with rather than complement one another, thus effectively reducing the ionospheric response. Note also that in this case the ionospheric tuning is quite sharp; the response varies extremely rapidly with changes of just a few degrees in the azimuth of wave propagation. This results from the cos χ factor in equation 5.

At the equinoxes ($\delta = 0°$), there are still two azimuthal directions of wave propagation satisfying $\mathbf{k} \cdot \mathbf{l}_x = 0$, and these are again the preferred directions of wave travel in terms of the ionospheric response evoked. The sun is somewhat higher in this case, and the two azimuthal directions are correspondingly closer together; the tuning is much coarser.

Near the summer solstice ($\delta = -23°$), the sun is relatively high at 0800 LT, and there is no azimuthal direction of wave propagation for this wave that satisfies $\mathbf{k} \cdot \mathbf{l}_x = 0$. All that remains is a slight east–west asymmetry in the ionospheric response produced by photochemical effects.

Figure 4 illustrates how the lower ionospheric F region (height $z = 200$ km; geomagnetic inclination $I = 57°$; latitude $\varphi = 35°$S; solar declination $\delta = 23°$; 1000 LT) response varies with changes in the wave parameters. Its response to the 16-min period wave is almost twice as great in these azimuthal directions of wave propagation for which $\mathbf{k} \cdot \mathbf{l}_x = 0$ as it is in other directions. Within a wide range of azimuths of wave propagation, wave-associated photochemical effects act to reduce the ionospheric response from that calculated by ignoring such effects. Its response to the 27-min period wave is also more marked in those azimuthal directions of wave propagation for which $\mathbf{k} \cdot \mathbf{l}_x = 0$; the angle between those two directions is smaller because $\mathbf{k}$ is more nearly vertical. There is also a narrower band of azimuths of wave propagation for which wave-associated photochemical effects act to reduce the ionospheric response from that calculated by ignoring such effects. The 50-min period wave has wave fronts so nearly horizontal that there exists no azimuthal direction of wave propagation for which $\mathbf{k} \cdot \mathbf{l}_x = 0$; wave-associated photochemical effects are minimal in this case. Note, as stated in paper 1, that at the lower F region heights there exists no general ω^{-1} dependence in the ionospheric response; here this has been replaced by a β_0^{-1} dependence. The wave of 50-min period produces the smallest ionospheric response in this particular case; waves of the shorter periods, since they satisfy the condition $\mathbf{k} \cdot \mathbf{l}_x = 0$, are dominant.

The ionospheric response also varies with height, as illustrated in Figure 5. At the lowest height (140 km), wave-induced photochemical effects and their dependence on the value of $\mathbf{k} \cdot \mathbf{l}_x$ are quite striking, because of the exp $[(z_m - z)/H^*]$ term in equation 5. At the greatest height (220 km), these effects are correspondingly smaller, although still important. The response is generally smallest at the intermediate heights, because the wave-associated photoionization rate

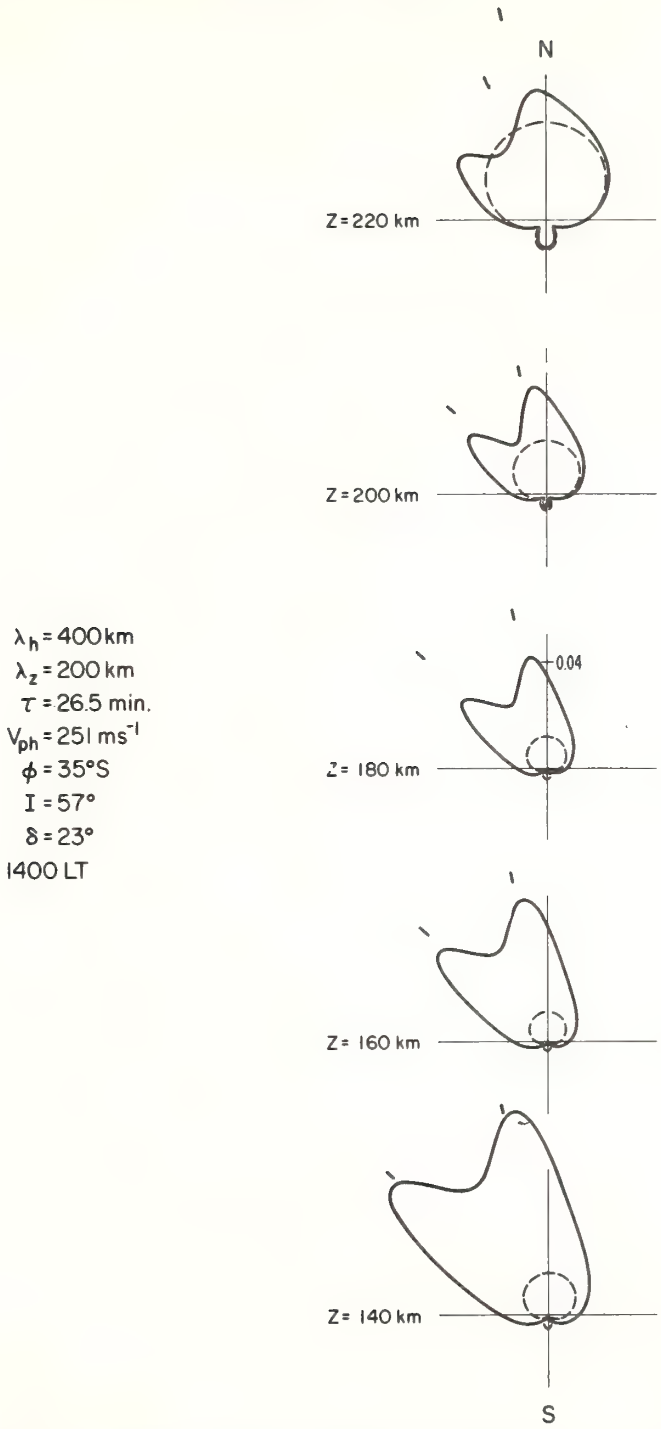

Fig. 5. Response of the lower *F* region ionosphere at temperate latitudes to an internal gravity wave as a function of height.

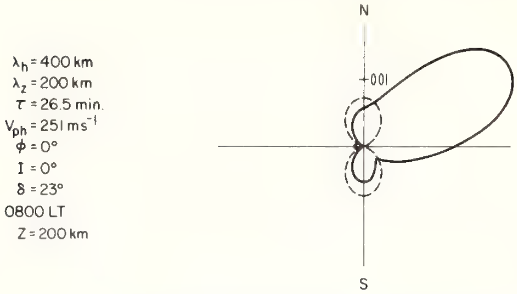

Fig. 6. Response of the lower F region ionosphere at the geomagnetic equator to an internal gravity wave.

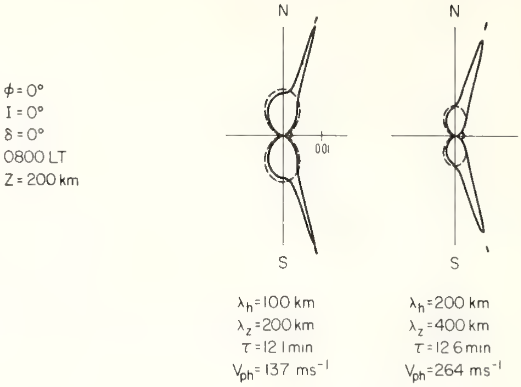

Fig. 7. Response of the lower F region ionosphere at the geomagnetic equator to internal gravity waves as a function of total wavelength.

changes are so pronounced at the lowest heights, while the decrease in β_0 with increasing height implies a decreasing ability of the ionosphere to maintain photochemical equilibrium during wave passage; i.e., the dynamic effects become more pronounced at the greatest heights. Bear in mind that in each of the five calculations presented in Figure 5, $E = 40$ m² sec⁻² at the height of interest; these curves do not reflect any increase in wave amplitude with height.

The lower F region ionospheric response also varies considerably with latitude, as does that of the F_2 region ionosphere (see paper 1). Figure 6 illustrates the response of the lower F region ionosphere at the equator (height $z = 200$ km; $I = 0°$; $\varphi = 0°$) under the conditions shown to an internal gravity wave having the parameters specified. The dynamical response shows the 'figure eight' pattern that is characteristic of the geomagnetic dip equator (see paper 1). In this case, there are then no azimuthal directions of wave propagation satisfying the condition $\mathbf{k}\cdot\mathbf{l}_x = 0$ exactly, but propagation toward the northeast very nearly satisfies this condition, and this direction is indeed preferred in terms of the ionospheric response that is evoked.

Figure 7 shows the response of the lower F region at the equator to two internal gravity waves. The two waves differ primarily in their total wavelength λ (by a factor of 2). This difference affects the wave period τ only slightly and leaves the tilt ψ of the wave fronts unchanged, so that the azimuths of wave propagation satisfying $\mathbf{k}\cdot\mathbf{l}_x = 0$ are the same in both cases. The figure illustrates two general principles. First, the wave with the shorter total wavelength produces the greater wave-associated dynamical effects, since in this case the ion convergence is greater, as discussed in paper 1. Second, this wave produces significant photochemical effects over a narrower spread of azimuthal directions, because the sharpness of the ionospheric tuning increases with increasing $\mathbf{k}$.

Quite obviously, the lower F region ionospheric response to internal gravity waves is rather variable, depending strongly on geographic location and height, as well as time of day and season. It also depends sensitively on the details of the ambient ionospheric photochemistry as well, as will be shown in another paper. As a result, it would be impossible to present a complete atlas of ionospheric response patterns here. In fact, this does not even seem desirable, since the theory demands more input variables than most experiments can now provide (although the incoherent scatter radar work comes close). Nevertheless, it is clear, even from the limited number of illustrations presented here, that wave-induced changes in photoionization and chemical loss rates (q' and β') are as important as wave-associated dynamical effects in TID production. It is also clear that there is a solar control of the lower F region ionospheric response whose main effect is that of causing the response patterns to follow the motion of the sun from east to west during the day and from east–west to equatorward from summer to winter. TID statistics exhibit a corresponding behavior [*Munro*, 1950, 1958; *Price*, 1955; see also

Hooke, 1968*a*], and it is tempting to claim the one is the cause of the other. There are, however, many other competing mechanisms that could also account for the observational statistics, as discussed earlier [*Hooke,* 1968*a*; also paper 1].

Moreover, the solar control is somewhat imperfect in the sense that for some waves and under certain conditions it favors TID production by waves propagating at nearly right angles to the direction of the sun. By using polar coordinate plots of the type presented here, it is difficult to visualize just how the ionosphere would respond to a broad spectrum of incident internal gravity waves, a situation that will be discussed in a later paper.

Acknowledgment. Mrs. Judith J. Stephenson of ITS programmed the computer calculations for this paper.

* * *

The Editor wishes to thank G. Chimonas and M. A. MacLeod for their assistance in evaluating this paper.

References

Heisler, L. H., Anomalies in ionosonde records due to travelling ionospheric disturbances, *Aust. J. Phys., 11,* 79–90, 1958.

Hines, C. O., Internal atmospheric gravity waves at ionospheric heights, *Can. J. Phys., 38,* 1441–1481, 1960.

Hines, C. O., The upper atmosphere in motion, *Quart. J. Roy. Meteorol. Soc., 89,* 1–42, 1963.

Hines, C. O., An effect of molecular dissipation in upper atmospheric gravity waves, *J. Atmos. Terr. Phys., 30,* 845–849, 1968.

Hooke, W. H., Ionospheric irregularities produced by internal atmospheric gravity waves, *J. Atmos. Terr. Phys., 30,* 795–823, 1968*a*.

Hooke, W. H., The response of the *F*-region ionosphere to internal atmospheric gravity waves, in *Acoustic-Gravity Waves in the Atmosphere-Symposium Proceedings,* edited by T. M. Georges, U. S. Govt. Printing Office, Washington, D. C., 1968*b*.

Hooke, W. H., The ionospheric response to internal gravity waves. 1, The F_2 region response, *J. Geophys. Res., 75*(28), 5535, 1970.

MacLeod, M. A., Sporadic E theory, 1, Collision-geomagnetic equilibrium, *J. Atmos. Sci., 23,* 96–109, 1966.

Munro, G. H., Travelling disturbances in the ionosphere, *Proc. Roy. Soc., 202,* 208–223, 1950.

Munro, G. H., Travelling ionospheric disturbances in the *F* region, *Aust. J. Phys., 11,* 91–112, 1958.

Pitteway, M. L. V., and C. O. Hines, The viscous damping of atmospheric gravity waves, *Can. J. Phys., 41,* 1935–1948, 1963.

Price, R. E., Travelling disturbances in the ionosphere, in *The Physics of the Ionosphere,* The Physical Society, London, 1955.

Testud, J., and G. Vasseur, Ondes de gravité dans la thermosphère, *Ann. Geophys., 25,* 525–546, 1969.

Vasseur, G., and P. Waldteufel, Thomson scatter observations of a gravity wave in the ionospheric *F*-region, *J. Atmos. Terr. Phys., 31,* 885–888, 1969.

(Received June 11, 1970.)

Reprinted from Journal of Geophysical Research, Space Physics
75, No. 34, 7239-7243, 1970.

Ionospheric Response to Internal Gravity Waves

3. Changes in the Densities of the Different Ion Species

William H. Hooke

Institute for Telecommunication Sciences
ESSA Research Laboratories, Boulder, Colorado 80302

Changes in the densities of atomic oxygen and molecular ions produced by internal gravity waves are calculated as a function of the azimuth of wave propagation. Because these two ion species play different roles in the photochemistry of the lower F region, the waves change their densities differently, thus producing changes in F region ion composition. Wave-associated changes in photoionization rate appear to be quite important in this connection, with wave-associated changes in the loss rate β (and their temperature dependence) being somewhat less significant.

In two earlier papers (*Hooke* [1970*a*], hereafter referred to as paper 1; and *Hooke* [1970*b*], hereafter referred to as paper 2), this author discussed the F region ionospheric response to internal gravity waves. It was found that this response is quite anisotropic, in a way varying with the wave parameters and with ionospheric conditions. The nature of the response changes fundamentally with height. At F_2 region heights, internal gravity waves produce ionospheric irregularities (commonly known as traveling ionospheric disturbances or TID) primarily by redistributing preexisting ionization. At lower F region heights, they produce ionospheric irregularities in large part because they affect the rates of photochemical processes.

The earlier work concentrated on the wave-produced perturbations in the electron density, since that is the end product measured in the usual radio observations. This paper focuses instead on the details of the wave-associated changes in F region photochemistry, in particular the wave-produced changes in the number densities $n(O^+)$ of atomic oxygen ions and $n(XY^+)$ of molecular ions. These changes are also anisotropic, i.e., they vary with the azimuth of wave propagation, with all other parameters remaining fixed. The two ion species play different roles in F region photochemistry, however, and the anisotropies in their response differ considerably from one another. The results provide a deeper insight into the aeronomy underlying the total ionospheric response to the waves.

Theory and Calculations

The results presented here have been calculated by the procedure outlined in paper 2, where the amplitudes of the oscillatory fractional perturbations N'_e/N_{e0} in electron density produced during wave passage were calculated from given values of the wave parameters, parameters describing the ambient or unperturbed model atmosphere and ionosphere, and parameters specifying geomagnetic dip, time of day, and season. In this paper the amplitudes of the oscillatory fractional perturbations $n'(O^+)/n_0(O^+)$ and $n'(XY^+)/n_0(XY^+)$ produced by the wave are also calculated. Here, as in what follows, the primes denote small perturbations of physical quantities from their unperturbed values, which are indicated by zero subscripts. The calculations presented here use the same values for the parameters describing the unperturbed atmosphere and ionosphere and wave energy per unit mass as those used in paper 2.

It should be obvious that, for the F region ion composition to remain unchanged during wave passage, the instantaneous perturbations in the densities of the different species must satisfy

$$\frac{n'(O^+)}{n_0(O^+)} = \frac{n'(XY^+)}{n_0(XY^+)} = \frac{N_e'}{N_{e0}} \qquad (1)$$

Copyright © 1970 by the American Geophysical Union.

at all phases of the wave cycle. A necessary but not sufficient condition for (1) to hold is that the *amplitudes* of the oscillatory fractional fluctuations in densities of the various ion species be equal. Departures from this condition therefore imply wave-associated changes in ion composition. These amplitudes are the quantities plotted in the figures of the next section.

In the calculations in paper 2, the attachmentlike loss rate coefficient β was taken to vary during wave passage according to

$$\beta'/\beta_0 = \rho'/\rho_0 \tag{2}$$

where ρ'/ρ_0 is the wave-associated fractional perturbation in neutral-gas density. Equation 2 assumes that β is independent of temperature T. Geophysical [*Hanson and Cohen*, 1968] and laboratory [*Ferguson et al.*, 1969] evidence suggests that β decreases with increasing temperature. Adopting Hanson's and Cohen's assumption that $\beta \propto T^{-1}$, one finds

$$\beta'/\beta_0 \doteq \rho'/\rho_0 - T'/T_0 \tag{3}$$

where T'/T_0 is the wave-associated fractional change in temperature, assumed to be much smaller than unity. The fluctuations T'/T_0 and ρ'/ρ_0 are related in amplitude and phase according to equation 5 given by *Hines* [1965]. In general the expressions are quite complicated, but it might be noted in passing that, for waves of small vertical wavelength ($\lambda_z^2 \ll 16\pi^2 H^2$, where H is the neutral-gas scale height) and low frequency ($\omega \ll \omega_g$, where ω_g is the *Brunt-Väisälä* frequency),

$$T'/T_0 \doteq -\rho'/\rho_0 \tag{4}$$

[*Hines*, 1960, 1965], and in these limits,

$$\beta'/\beta_0 \doteq 2\rho'/\rho_0 \tag{5}$$

The above equations assume a single temperature T, when in fact two temperatures are involved: the ion temperature T_i and the neutral gas temperature T_n. The difference between the two, however, is significant only at heights above 250 km; below this height, the unperturbed ion and neutral temperatures are equal [*Banks*, 1967]. Moreover, since the ion thermal relaxation times (the order of seconds) are much shorter than the wave periods of interest (10 min or more), the wave-associated perturbations in ion and neutral temperature are also approximately equal and in phase, i.e.

$$\frac{T_i'}{T_{i0}} \doteq \frac{T_n'}{T_{n0}} \doteq \frac{T'}{T_0} \tag{6}$$

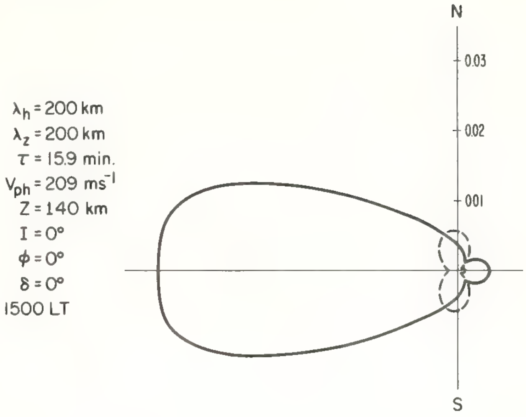

Fig. 1. The response of the lower F region ionosphere at the equator to an internal gravity wave as a function of the azimuth of wave propagation. Wave phase propagation is downward. The radial distance from the curves to the plot origin shows the amplitude of the fractional perturbations in electron density. The dashed curve shows the response calculated with wave-associated changes in photoionization rate q and attachmentlike loss rate β ignored, while the solid curve shows the response computed with these changes included (β assumed to be independent of temperature).

At the very lowest F region heights, the ion lifetimes are quite short compared with an internal gravity wave period, and internal gravity waves produce TID's primarily by affecting the rates of ionospheric photochemical processes. This point is illustrated by Figure 1, which shows the response of the lower F region ionosphere (height z = 140 km) at the equator to an internal gravity wave as a function of the azimuth of wave propagation. The dashed curve, based on a computation in which wave-associated photochemical effects were ignored, shows the north–south oriented figure-eight pattern familiar from paper 1. The ionospheric response to the wave-associated redistribution of ionization is less than 1% at this altitude, because the lower F region ionosphere tends to maintain photochemical equilibrium. The solid curve shows that the actual F region response to this wave at the 140-km level, calculated including wave-associated photochemical effects, has a strong single lobe in the west direction, because this wave, when propagating westward, produces large changes in the photoionization rate q. As explained in paper 2, the reason is that this wave, when propagating westward, contains the solar ionizing radiation flux in surfaces of constant wave phase, a condition expressed mathematically as

$$\mathbf{k} \cdot \mathbf{1}_\chi = 0 \tag{7}$$

where $\mathbf{k}$ is the wave vector and $\mathbf{1}_\chi$ is a unit vector directed toward the sun. The westward propagating wave generates a 4% TID.

Because the ionosphere at 140 km remains very nearly in photochemical equilibrium, equations 13 and 14 in paper 2 reduce approximately to

$$\beta_0 n'(\mathrm{O}^+) \doteq q' - \beta' n_0(\mathrm{O}^+) \tag{8}$$

$$(\alpha_0 N_{e0} + \alpha_0 n_0(XY^+))\beta_0 N_e'$$
$$\doteq (\alpha_0 N_{e0} + \beta_0) q' - \alpha_0 N_{e0} q_0 \beta'/\beta_0 \tag{9}$$

where α_0 is the recombinativelike loss coefficient. In the model ionosphere used here, $\beta_0 \gg \alpha_0 N_{e0}$ and $n_0(XY^+) \doteq N_{e0} \gg n_0(\mathrm{O}^+)$ at 140 km, so that with some manipulation and using equations 8 through 10 in paper 2, one finds

$$\frac{n'(\mathrm{O}^+)}{n_0(\mathrm{O}^+)} \doteq \frac{q'}{q_0} - \frac{\beta'}{\beta_0} \tag{10}$$

$$\frac{n'(XY^+)}{n_0(XY^+)} \doteq \frac{N_e'}{N_{e0}} \doteq \frac{1}{2}\frac{q'}{q_0} \tag{11}$$

The fractional perturbation in photoionization rate q can be written [*Hooke,* 1968]

$$\frac{q'}{q_0} = \frac{\rho'}{\rho_0} + \frac{S'}{S_0} \tag{12}$$

where S'/S_0 is the wave-associated perturbation in solar radiation flux. The ρ'/ρ_0 term expresses the contribution to q'/q_0 that results from local changes in the density of atomic oxygen. The S'/S_0 term expresses the contribution to q'/q_0 that results from changes in ρ'/ρ_0 that occur at higher elevations along the path of the solar radiation flux. Physically, it is obvious that changes in q at any point that result from local changes in ρ'/ρ_0 should be cancelled by the corresponding changes in β, while changes in q that result from nonlocal changes in ρ'/ρ_0 should not. This is precisely what equations 2, 10, and 12 combine to show:

$$\frac{n'(\mathrm{O}^+)}{n_0(\mathrm{O}^+)} \doteq \frac{S'}{S_0} \tag{13}$$

Using equation 3 instead of 2 gives

$$\frac{n'(\mathrm{O}^+)}{n_0(\mathrm{O}^+)} \doteq \frac{T'}{T_0} + \frac{S'}{S_0} \tag{14}$$

At the 140-km level, which is below the height of maximum photoionization rate, $S'/S_0 \gg \rho'/\rho_0$ when condition (7) is satisfied, and equation 11 becomes

$$\frac{n'(XY^+)}{n_0(XY^+)} \doteq \frac{N_e'}{N_{e0}} \doteq \frac{1}{2}\frac{S'}{S_0} \tag{15}$$

(a result independent of the temperature dependence of β).

Equations 13 through 15 have the following physical interpretation. At 140 km, where the XY^+ lifetimes are much longer than those of the O^+ parent ions, changes in $n(\mathrm{O}^+)$ are equivalent to changes in the production rate of XY^+. The fractional perturbations in $n(XY^+)$ are half those in $n(\mathrm{O}^+)$, however, because the loss rate of XY^+ ions is roughly proportional to $N_e^2 \doteq n_0^2(XY^+)$. Two of the polar diagrams in Figure 2 illustrate these features of the ionospheric response at 140 km. The wave shown produces the greatest perturbations in electron, atomic oxygen ion, and molecular ion densities at 140 km when propagating westward. The fractional perturbations in $n(\mathrm{O}^+)$ are roughly twice those of $n(XY^+)$ and N_e when the wave propagates in this direction. Because molecular ions dominate at 140 km, the wave-produced variations in $n(XY^+)$ and N_e are similar. The wave-produced variations in N_e are slightly larger in amplitude, however, because of the large variations in density of the minor constituent O^+. The temperature dependence of β affects the response at this height only slightly. Its relative importance is greatest when the wave propagates eastward, but here the ionospheric response itself is quite small.

At 220 km, $\beta_0 \ll \alpha_0 N_{e0}$, and $n_0(\mathrm{O}^+) \doteq N_{e0} \gg n_0(XY^+)$; in addition, although $\alpha_0 N_{e0} \gg \omega$, β_0 and ω are of the same order, so that wave-produced divergence in ion motion, a process that was ineffective in TID production of the lowest heights, becomes important. The geo-

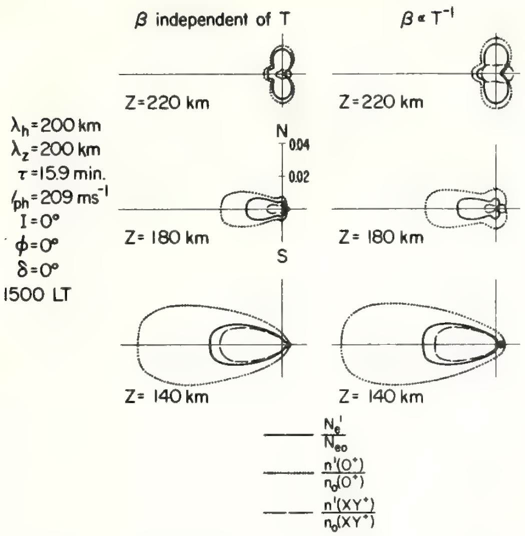

Fig. 2. The response of the lower *F* region ionosphere at the equator to an internal gravity wave as a function of the azimuth of wave propagation, ionospheric height, and temperature dependence of β. The solid curve shows the amplitude of the fractional perturbations in electron density. Here the solid curves show the amplitude of fractional perturbations in electron density, while the dotted and dashed curves show the amplitudes of fractional perturbations in $n(O^+)$ and $n(XY^+)$, respectively.

magnetic constraints on ion motion then control the response patterns for N_e and O$^+$, which have the figure-eight pattern there, as shown in Figure 2. Because the S'/S_0 fluctuations are small well above the height of peak photoionization rate [*Hooke*, 1968; paper 2], these curves show only a slight preference for TID production by those directions of wave propagation satisfying condition (7). By using equations 8 through 10 given in paper 2, one finds that at 220 km

$$\frac{N_e'}{N_{e0}} \doteq \frac{n'(O^+)}{n_0(O^+)} \doteq \frac{\beta_0}{\beta_0 + i\omega}\frac{q'}{q_0} - \frac{\beta_0}{\beta_0 + i\omega}\frac{\beta'}{\beta_0} - \frac{1}{\beta_0 + i\omega}\frac{\nabla\cdot(n_0(O^+)\mathbf{u}_i)}{n_0(O^+)} \qquad (16)$$

$$\frac{n'(XY^+)}{n_0(XY^+)} \doteq \frac{\beta'}{\beta_0} - \frac{1}{\alpha_0 N_{e0}}\frac{\nabla\cdot(n_0(XY^+)\mathbf{u}_i)}{n_0(XY^+)} \qquad (17)$$

where $\mathbf{u}_i$ is the wave-induced ion velocity. As stated above, the divergence term in equation 16 dominates at 220 km except for zonal wave propagation. Because $\alpha_0 N_{e0} \gg \beta_0$ at 220 km, the divergence term in equation 17 is relatively small; it merely serves to reduce the percentage changes in $n(XY^+)$ that occur when wave propagation is meridional. The temperature dependence of β plays a significant role in determining the wave-produced changes in $n(XY^+)$, but this is the minor ion. Similarly, the temperature dependence of β and its effect on β' is as important as the changes q' in determining $n'(O^+)/n_0(O^+)$, but both are small in comparison with wave-produced redistribution of ionization except for zonal wave propagation.

At the intermediate height, 180 km, the ionospheric response exhibits an intermediate behavior. The figure-eight pattern of the response at 220 km is considerably reduced, because of an increased ionospheric tendency toward photochemical equilibrium, but it is still visible. On the other hand, wave-associated changes in S'/S_0, while larger than at 220 km, are smaller than at 140 km; this is reflected in the moderate enhancement of the response to the wave when it propagates westward. As a result, the ionospheric response is generally smaller at this height than at greater or lower heights, regardless of the azimuthal direction of wave propagation.

Remarks similar to the above apply to Figure 3, which shows the response of the lower *F* region ionosphere at temperate latitudes to an

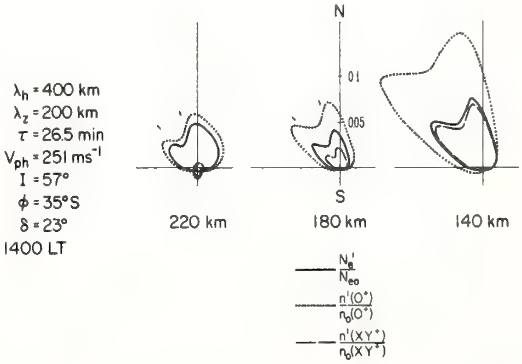

Fig. 3. The response of the lower *F* region ionosphere at temperate latitudes to an internal gravity wave as a function of the azimuth of wave propagation and ionospheric height. The attachmentlike loss coefficient β is assumed independent of temperature. Tic marks indicate azimuths of wave propagation satisfying condition (7).

internal gravity wave of horizontal wavelength 400 km, vertical wavelength 200 km, and period of 26.5 min (the solid curves of this figure correspond to those in Figure 5 in paper 2). Here the vertical component of the geomagnetic field lines permits the wave to move the ions vertically. The lower F region ionosphere tends to remain in photochemical equilibrium despite this redistribution; the fractional perturbations in $n(O^+)$ and $n(XY^+)$ occur primarily because of wave-induced changes in local photoionization rate, as one can see by studying Figure 5 in paper 2. Only at the higher levels, where the ion lifetimes are longer, does the wave-associated redistribution of ionization in the vertical come into play.

CONCLUDING REMARKS

The preceding calculations show that internal gravity waves propagating at lower F region heights perturb the ionospheric photochemical balance. Because O^+ and XY^+ ions play different roles in the F region photochemical scheme, the internal gravity waves in general perturb their densities differently, thus producing changes in ionospheric composition. Such changes might conceivably be detected by using incoherent scatter or rocket techniques.

In large part, the changes appear to be the result of wave-associated changes in the photoionization rate q. Wave-associated changes in β appear to play a lesser role. Ignored in the calculations is a similar wave-associated change in the loss rate α, which according to laboratory meaurements [*Biondi*, 1967] is inversely proportional to the electron temperature. If the wave-associated changes in electron temperature at lower F region heights are of the same order as corresponding changes in T_i and T_n, then this neglect will be no worse than the neglect of wave-associated changes in β. The problem of determining the wave-associated changes in T_e at F region heights is rather complex, however, and is not attempted here.

It should be mentioned that the relative importance of wave-associated photochemical effects and wave-associated ionization redistribution is to some extent a function of wavelength. The longer the wavelength, the smaller the relative importance of wave-associated ionization redistribution (see paper 2).

Acknowledgment. The Editor wishes to thank G. Chimonas and M. A. MacLeod for their assistance in evaluating this paper.

REFERENCES

Banks, P. M., Ion temperature in the upper atmosphere, *J. Geophys. Res., 72,* 3365–3385, 1967.

Biondi, M. A., Recombination processes (charged particles), in *DASA Reaction Rate Handbook, 11.1–11.21,* DASA Information and Analysis Center, Santa Barbara, California, 1967.

Ferguson, E. E., D. K. Bohme, F. C. Fehsenfeld, and D. B. Dunkin, Temperature dependence of slow ion-atom interchange reactions, *J. Chem. Phys., 50,* 5039–5040, 1969.

Hanson, W. B., and R. Cohen, Photoelectron heating efficiency in the ionosphere, *J. Geophys. Res., 73,* 831–840, 1968.

Hines, C. O., Internal atmospheric gravity waves at ionospheric heights, *Can. J. Phys., 38,* 1441–1481, 1960.

Hines, C. O., Dynamical heating of the upper atmosphere, *J. Geophys. Res., 70,* 177–183, 1965.

Hooke, W. H., Ionospheric irregularities produced by internal atmospheric gravity waves, *J. Atmos. Terr. Phys. 30,* 795–823, 1968.

Hooke, W. H., The ionospheric response to internal gravity waves, 1, The F_2 region response, *J. Geophys. Res., 75*(28), 5535–5544, 1970*a*.

Hooke, W. H., The ionospheric response to internal gravity waves, 2, The lower F region response, *J. Geophys. Res.,* this issue, 1970*b*.

(Received June 11, 1970.)

Reprinted from Journal of Geophysical Research 76, No. 1, 248-250, 1971.

Quasi-Stagnation Levels in the Ion Motion Induced by Internal Atmospheric Gravity Waves at Ionospheric Heights

William H. Hooke

Wave Propagation Laboratory, Environmental Research Laboratories
National Oceanic and Atmospheric Administration
Boulder, Colorado 80302

This note theoretically demonstrates the existence, under appropriate ionospheric conditions, of a height or heights at which the vertical ion motion induced by a single internal atmospheric gravity wave vanishes identically, at all phases of the wave cycle. These heights are here called quasi-stagnation levels, because the horizontal ion motions there are in general nonzero. Such quasistagnation levels can exist because of two properties of internal atmospheric gravity waves:

1. Those waves having small vertical wavelength ($4k_z^2 \gg 1/H^2$, where k_z is the vertical angular wave number, and H is the neutral-gas scale height) are very nearly transverse [*Hines*, 1960].
2. The waves all have non-zero horizontal components of phase propagation, and hence from (1), have non-zero vertical components for their associated winds.

Earlier analyses [*Axford*, 1961, 1963; *Chimonas and Axford*, 1968] of vertical ion transport by internal atmospheric gravity waves (the so-called corkscrew mechanism) assumed purely horizontal wave-associated neutral-gas motions as well as purely vertical phase propagation; as a result the existence of the quasi-stagnation levels was not discovered.

In its most general form, the analysis outlined below has been developed for waves traveling in any azimuthal direction; for the present purely illustrative purposes, however, specialization to the case of zonal (magnetic east–west) wave propagation will suffice. In this case, the vertical or z component of the ion velocity is

$$u_{iz} \doteq \frac{1}{1+\rho_i^2}\left[(\rho_i^2 + \sin^2 I)u_z + (\rho_i \cos I)u_x\right] \qquad (1)$$

[e.g., *MacLeod*, 1966]. Here u_x and u_z are the eastward-directed and vertically upward-directed components of the neutral wind, I is the magnetic inclination (here taken to be positive in the southern hemisphere), and $\rho_i \equiv \nu_i/\omega_i$ is the ratio of the ion-neutral collision frequency ν_i to the ion gyrofrequency ω_i; ρ_i decreases approximately exponentially with increasing height. Because the internal atmospheric gravity waves are very nearly transverse, we may write [*Hines*, 1960; equation 35]

$$u_z/u_x \doteq -k_x/k_z \qquad (2)$$

where k_x is the horizontal angular wave number; this gives

$$u_{iz} \doteq \frac{u_x}{1+\rho_i^2}\left[(\rho_i^2 + \sin^2 I)\cdot(-k_x/k_z) + \rho_i \cos I\right] \qquad (3)$$

Setting $u_{iz} \equiv 0$ yields

$$\rho_i = \frac{\cos I}{2(k_x/k_z)}\left\{1 \pm \left[1 - 4(k_x/k_z)^2 \tan^2 I\right]^{1/2}\right\} \qquad (4)$$

This equation implicitly determines the quasi-stagnation levels, once (k_x/k_z) and I are specified.

For such levels to exist, ρ_i must be real and positive. If we take $\cos I \geq 0$ everywhere, this requires that

$$\begin{gathered} 1 \geq 4(k_x/k_z)^2 \tan^2 I \\ (k_x/k_z) > 0 \end{gathered} \qquad (5)$$

Since the waves are usually generated below the region of observation, so that $k_z < 0$ [*Hines*, 1960], condition (5) implies that quasi-stagnation levels will usually not exist unless the zonal wave propagation is to the west ($k_x < 0$). Again, since our purposes here are merely illus-

Copyright © 1971 by the American Geophysical Union.

trative, let us assume that $(k_x/k_z)^2 \ll 1$; then, at least at temperate and low latitudes ($\tan^2 I < 1$), two solutions ρ_i exist and are given by the approximate formulas

$$\rho_i \doteq \frac{\cos I}{(k_x/k_z)} \qquad (6)$$

$$\rho_i \doteq (k_x/k_z) \sin I \tan I$$

Suppose $I = \pm 30°$; then, for $k_x/k_z = 0.1$, we find

$$\rho_i \sim 9, \sim 0.03 \qquad (7)$$

corresponding to ionospheric heights ~105 and ~180 km, respectively. Here we use values for ρ_i given by *Wright and Fedor* [1970], and equation (4.13) from *Hines et al.* [1965] (which is due to *Chapman* [1956]), together with data from the *Cira 1965* model atmosphere. It should be noted that the upper of the two stagnation levels varies significantly with solar activity. *Hines* [1960] showed that, for $k_x/k_z \ll 1$,

$$(k_x/k_z)^2 \doteq \tau_g^{\,2}/\tau^2 \qquad (8)$$

where τ_g is the atmospheric Brunt period (about 5 min at E region heights), and τ is the wave period. Thus the choice $k_x/k_z \doteq 0.1$ corresponds to a wave period about 10 times the Brunt period, or about 1 hour at E region heights.

For $I = \pm 30°$ and $(k_x/k_z) = 0.01$ (period 100 times the Brunt period, about half a day at E region heights), we find

$$\rho_i \sim 90, \sim 3 \times 10^{-3} \qquad (9)$$

corresponding to heights ~92 and ~280 km, respectively.

It is of interest to note that the quasi-stagnation levels discussed here depend only on the ratio k_x/k_z, or, equivalently, the ratio τ/τ_g, and the value of I. On the other hand, the classical theory of the corkscrew mechanism as discussed by *Axford* [1961, 1963] and *Chimonas and Axford* [1968] shows that there exists a height below which the corkscrew mechanism becomes relatively ineffective; this dumping height is determined by the ratio of the amplitude of the wave-associated neutral-gas motions to the wave phase velocity. As a result, the quasi-stagnation levels discussed here are conceptually quite different from the dumping heights considered in the earlier work. Dumping heights have been invoked to account for several of the observed features of sporadic-E layer behavior (the existence of sporadic-E layers at levels other than the nodes of the wind profile, for instance); the existence of quasi-stagnation levels may provide an alternative interpretation of the observations.

In a recent review, *Whitehead* [1970] suggested that the apparent ability of the corkscrew mechanism to sweep the E region free of metallic ions poses a problem for sporadic-E theory. Quasi-stagnation levels should hinder this sweeping process.

Several qualifying remarks are in order here. First, if the time-averaged ion flow in the vicinity of these quasi-stagnation levels should prove divergent, then the ions should not collect there; a preliminary look, however, suggests that the flow near these levels is indeed convergent in the mean. Second, a rather broad spectrum of waves is often present at ionospheric heights. Since each Fourier component of the spectrum can be expected to maintain its own stagnation levels, interferring with the existence of others in the process, such levels may exist only at times and places at which a single Fourier component of the spectrum dominates. Finally, because internal atmospheric gravity waves are not exactly transverse, but instead are elliptically polarized [*Hines*, 1960], so that equation 2 is only approximately valid, there will in fact be small fluctuations in the velocity u_{iz} at the quasi-stagnation levels. These topics and the implications of the quasi-stagnation levels for sporadic-E morphology and dynamics are currently under further investigation.

Acknowledgment. The Editor wishes to thank J. D. Whitehead for his assistance in evaluating this paper.

REFERENCES

Axford, W. I., Note on a mechanism for the vertical transport of ionization in the ionosphere, *Can. J. Phys., 39,* 1393–1396, 1961.

Axford, W. I., The formation and vertical movement of dense ionized layers in the ionosphere due to neutral wind shears, *J. Geophys. Res., 68,* 769–779, 1963.

Chapman, S., The electrical conductivity of the ionosphere; a review, *Nuovo Cimento, 4*(10), Suppl. 4, 1385–1412, 1956.

Chimonas, G., and W. I. Axford, Vertical movement of temperate-zone sporadic *E* layers, *J. Geophys. Res., 73,* 111–117, 1968.

Cira 1965 (Cospar International Reference Atmosphere 1965), North Holland, Amsterdam, 1965.

Hines, C. O., Internal atmospheric gravity waves at ionospheric heights, *Can. J. Phys., 38,* 1441–1481, 1960.

Hines, C. O., I. Paghis, T. R. Hartz, and J. A. Fejer, *Physics of the Earth's Upper Atmosphere,* Prentice-Hall, Englewood Cliffs, N. J., 1965.

MacLeod, M. A., Sporadic *E* theory, 1, Collision-geomagnetic equilibrium, *J. Atmos. Sci., 23,* 96–109, 1966.

Whitehead, J. D., Production and prediction of sporadic *E, Rev. Geophys., 8,* 65–144, 1970.

Wright, J. W., and L. S. Fedor, Errata, *J. Atmos. Terr. Phys., 32,* 451–452, 1970.

(Received September 15, 1970.)

Reprinted from Journal of Planetary and Space Science 18, 1793-1797, 1970.

IONOSPHERIC RESPONSE TO AN ISOTROPIC SPECTRUM OF INTERNAL GRAVITY WAVES

WILLIAM H. HOOKE
Institute for Telecommunication Sciences, ESSA Research Laboratories, Boulder, Colo. 80302, U.S.A.

(*Received* 30 *June* 1970)

Abstract—This paper presents computer-produced tonal-value plots in which darkness or intensity are used to display the ionospheric response to an isotropic spectrum of internal gravity waves. Each plot shows at a glance those portions of the wave spectrum, i.e. those wave periods and azimuths of propagation, producing the ionospheric irregularities of greatest magnitude. Arrays of the plots illustrate the variations of this response with time of day, season, latitude, geomagnetic dip, and height.

1. INTRODUCTION

In previous work (Hooke, 1970a, 1970b), this author has calculated the *F*-region ionospheric response to *individual* internal gravity waves as a function of the azimuthal direction of wave propagation. This response was found to be markedly anisotropic, and the anisotropy itself was shown to depend strongly upon the wave parameters, geomagnetic dip, geographic latitude, and local ionospheric conditions. The latter include the ambient ionization density height gradient, the details of the ionospheric photochemistry and composition, and the orientation of the Sun, as expressed by a unit vector $\mathbf{l}_\chi$ directed toward the Sun. These conditions, in turn, particularly the unit vector $\mathbf{l}_\chi$, vary with time of day and with season, so that the ionospheric response to internal gravity waves varies diurnally and seasonally. These findings are consistent with observed (Munro, 1950, 1958; Price, 1955) seasonal diurnal variations in occurrence frequency and statistically preferred propagation directions of travelling ionospheric disturbances (TID's), suggesting that the statistics might result from this behavior alone, quite apart from any anisotropies introduced into the wave spectrum by wind shear filtering (Hines and Reddy, 1967), ohmic dissipation (Hines, 1968), or properties of the wave sources themselves. At the very least, the anisotropy of the ionospheric response to internal gravity waves has effects on TID statistics that must be removed if such observations are to provide accurate information on the wave spectrum at these heights.

The ionospheric response and its anisotropy vary radically from wave to wave. This author (Hooke, 1970b) has shown, for example, that the lower *F*-region ionosphere responds preferentially to those waves whose wave vector $\mathbf{k}$ satisfies $\mathbf{k} \cdot \mathbf{l}_\chi = 0$. For a given $\mathbf{l}_\chi$ (hence a given solar zenith angle χ), waves having wavefront tilts ψ from the vertical comparable to χ satisfy this condition only if they propagate azimuthally toward the Sun. Waves having wavefront tilts $\psi \ll \chi$ satisfy this condition only when they propagate at nearly right angles to the azimuthal direction of the Sun.

As a result, it is rather difficult to translate the ionospheric response to *individual* waves into a coherent picture of the ionospheric response to the rather broad wave spectrum that must exist at these heights. This paper presents one approach toward overcoming this difficulty. A tonal-value computer output format developed by Stephenson and Georges (1969) is used to display more compactly calculations of the earlier type. Thus each of the polar-coordinate plots represented here contains the information of about seventy plots of the type appearing in Hooke (1970a, 1970b). Each shows how the ionospheric response to internal gravity waves varies with the wavefront tilt ψ or, equivalently, the wave period (Hines, 1960), and the azimuth of wave propagation, the total wavelength ($2\pi/k = 200$ km) and the energy per unit mass ($E = 40$ m^2 s^{-2}, which corresponds to a wind speed of about 6 m s^{-1}) being held constant. In individual plots, other problem parameters, such as local height, geomagnetic inclination, time of day, and season are held constant; arrays of the plots then illustrate the dependence of the ionospheric response on these variables. Considering an isotropic wave spectrum confines attention to a rather unlikely circumstance; however, it does isolate the role played by anisotropy in the ionospheric response to the wave spectrum in shaping TID statistics.

2. CALCULATIONS

The calculations used in constructing the plots shown in the next section are of two types. The first (Hooke, 1970a) provides the response of the *F2*-peak ionosphere and specifically ignores wave-associated photochemical effects, because the ion lifetimes at these heights far exceed the wave periods of interest. The second (Hooke, 1970b) describes the response of the lower *F*-region and takes photochemical effects into account, but it breaks down at upper *F*-region levels because the ambient ionospheric model used does not include plasma diffusion and hence fails to provide an *F2* peak. The approximations underlying the calculations have been given earlier by the author (Hooke, 1970a, 1970b). Here we consider geographic locations and geomagnetic inclinations different from those under study in the earlier papers, but the other parameters characterizing the ambient or unperturbed ionospheric model remain unchanged.

3. RESULTS

Results of the calculations are displayed in polar-coordinate tonal value plots in which intensity or darkness are used to represent a function of two variables. The displays are produced by a digital computer with a CRT display unit and a plotting routine that represents the value of the function at each location in a fine grid by a small black dot whose size is proportional to the function's value. The result is a plot resembling a halftone print showing clearly the qualitative behavior of the function in a plane (Stephenson and Georges, 1969).

In the current application, the location of any point on the plots corresponds to a particular tilt ψ of the atmospheric wavefronts from the vertical, varying radially from 0° (vertical wavefronts; horizontal wave-phase propagation) at the plot origin to 90° (horizontal wavefronts; vertically downward wave-phase propagation) at the plot perimeter, and to a particular azimuth of wave propagation, as measured circumferentially. As noted above, the wave period varies with the wavefront tilt, approaching the Brunt period at the plot origin and infinity at the plot perimeter. Thus, for example, a point located in the upper right quadrant of any of the plots halfway between the origin and the perimeter corresponds to a wave with a tilt $\psi = 45°$ and propagating toward the northeast (geomagnetic north and geographic north are assumed to coincide). This wave would have a period about 20 min for an atmospheric Brunt period of 15 min. The darkness or intensity at any point on the plots expresses the amplitude of the fractional perturbations of electron density occurring in response to the corresponding wave. Black regions indicate electron density fluctuations greater than 1 per cent, while white regions indicate perturbations of less than 0·2 per cent.

Figure 1 shows how the response of the *F2* peak ionosphere, assumed to be at a height of

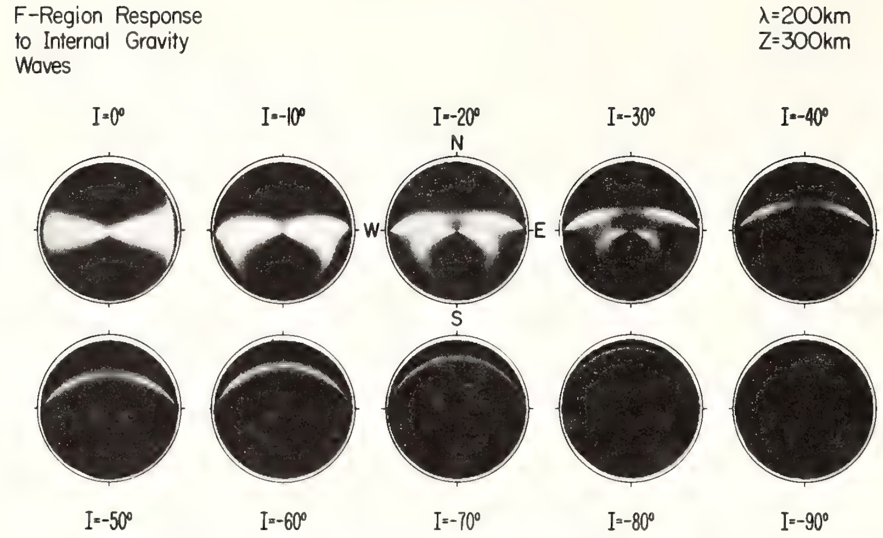

FIG. 1. RESPONSE OF THE *F2*-PEAK IONOSPHERE TO INTERNAL GRAVITY WAVES OF 200-km WAVELENGTH PRODUCING ATMOSPHERIC MOTIONS OF 6 m/s.
Black regions of the plots indicate ionization density perturbations greater than 1 per cent, while white regions indicate perturbations less than two-tenths of a per cent.

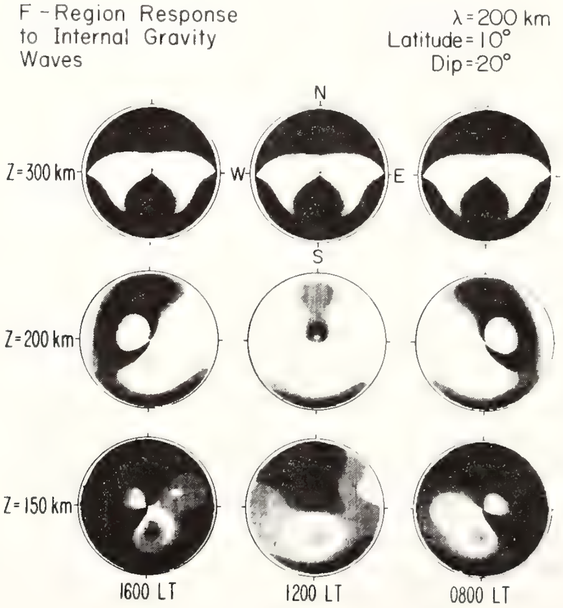

FIG. 2. RESPONSE OF THE LOW-LATITUDE *F*-REGION AT THE SUMMER SOLSTICE TO INTERNAL GRAVITY WAVES OF WAVELENGTH $\lambda = 200$ km PRODUCING ATMOSPHERIC MOTIONS OF 6 m/s.
Black regions of the plots indicate ionization density perturbations greater than 1 per cent, while white regions indicate perturbations less than two-tenths of a per cent.

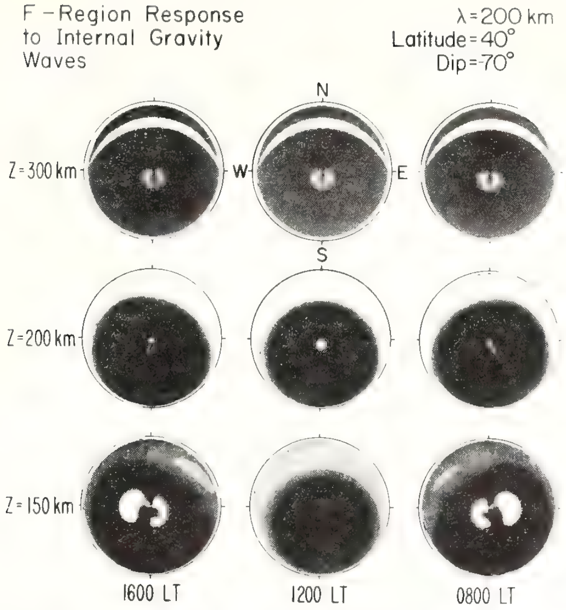

FIG. 3. RESPONSE OF THE TEMPERATE-LATITUDE F-REGION AT THE SUMMER SOLSTICE TO INTERNAL GRAVITY WAVES OF WAVELENGTH $\lambda = 200$ km PRODUCING ATMOSPHERIC MOTIONS OF 6 m/s.

Black regions of the plots indicate ionization density perturbations greater than 1 per cent, while white regions indicate perturbations less than two-tenths of a per cent.

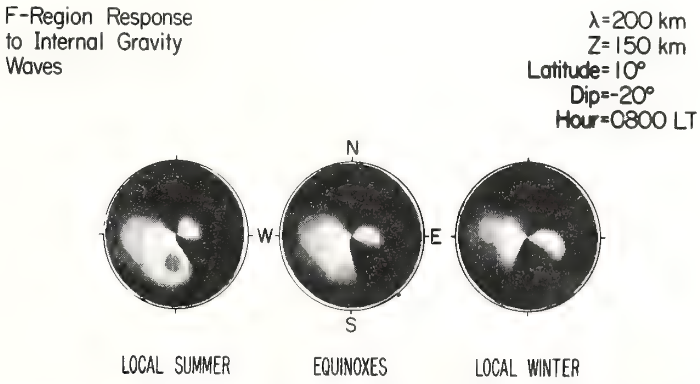

FIG. 4. RESPONSE AS A FUNCTION OF SEASON OF THE LOWER F-REGION TO INTERNAL GRAVITY WAVES OF WAVELENGTH $\lambda = 200$ km PRODUCING ATMOSPHERIC MOTIONS OF 6 m/s.

Black regions of the plots indicate ionization density perturbations greater than 1 per cent, while white regions indicate perturbations less than two-tenths of a per cent.

300 km, varies with the geomagnetic inclination I. Here the geomagnetic inclination is taken to be negative, corresponding to northern hemisphere locations.

At these heights, the mean ion lifetime greatly exceeds the wave periods of interest, so that wave-associated photochemical effects can be ignored legitimately (Hooke, 1968, 1970a). Since at the plot perimeters the wave periods tend to infinity, this assumption should be invalidated there, causing overestimates of the ionospheric perturbations produced by the longest period waves.

The waves produce ionospheric irregularities primarily because the wave-associated neutral-gas motions redistribute the preexisting ionization. The ions respond by moving with the velocity (MacLeod, 1966)

$$\mathbf{u}_i = \frac{1}{1+\rho_i^2}\,[\rho_i^2\mathbf{u} + \rho_i\mathbf{u} \times \mathbf{l}_b + (\mathbf{u}\,.\,\mathbf{l}_b)\mathbf{l}_b], \qquad (1)$$

which at $F2$-region heights reduces very nearly to the component of the neutral-gas velocity along geomagnetic field lines (i.e. Georges, 1967, 1968; Hooke, 1968)

$$\mathbf{u}_i \doteq (\mathbf{u}\,.\,\mathbf{l}_b)\mathbf{l}_b. \qquad (2)$$

The electrons move so as to maintain charge neutrality. Here $\mathbf{u}_i$ is the ion velocity, $\mathbf{u}$ is the wave-associated neutral-gas velocity, $\mathbf{l}_b$ is a unit vector in the direction of the geomagnetic induction $\mathbf{B}$, and $\rho_i \equiv \nu_i/\omega_i$ is the ratio of the ion-neutral collision frequency ν_i to the ion gyrofrequency ω_i. In general, this ion motion is divergent, producing fractional perturbations N_e'/N_{e0} in ionization density calculable at the $F2$ peak from the equation (Hooke, 1970a)

$$N_e'/N_{e0} \doteq \frac{(\mathbf{u}\,.\,\mathbf{l}_b)}{\omega}\,[(\mathbf{k}\,.\,\mathbf{l}_b) + i(\mathbf{l}_b\,.\,\mathbf{l}_z)/2H]. \qquad (3)$$

Here ω is the angular wave frequency and $\mathbf{l}_z$ is a unit vector in the vertical or z direction; H is the neutral-gas scale height. The amplitude of these perturbations is calculated by taking the absolute value of this formula (here i is the imaginary unit indicating a 90° phase difference between the two contributions to N_e'/N_{e0}).

In the plots in Fig. 1, the locus $\mathbf{u}\,.\,\mathbf{l}_b = 0$ appears as a thin light strip, indicating that waves producing neutral-gas motions nearly perpendicular to the geomagnetic field lines are relatively ineffective in producing TID's. The ionization motion is in general least divergent where $\mathbf{k}\,.\,\mathbf{l}_b = 0$, i.e. where the geomagnetic induction lies in surfaces of constant wave phase. Thus the $\mathbf{k}\,.\,\mathbf{l}_b = 0$ locus appears as a roughly circular light strip passing through the plot origin. These two loci merge at the geomagnetic dip equator ($I = 0°$). Note that the white strip in that and the other low-latitude plots does not extend to the plot perimeter. This is because the value of ρ_i, while small at these heights (here it is taken as 0·005) is finite, so that the East–West motions of the longer period waves do produce large fluctuations in electron density in this model. Note again that the theoretical model used here breaks down at the plot perimeters. The plots are valid for positive geomagnetic inclinations I, i.e. southern hemisphere locations, if the indicated North–South directions are reversed.

Figure 2 shows how the response of the ionosphere at 10°N latitude, $-20°$ geomagnetic inclination varies with time of day and height at the summer solstice. At the lower altitudes, where wave-associated photochemical effects are most important and subject to a considerable degree of solar control (Hooke, 1968, 1970b), there is generally a considerable diurnal variation in the ionospheric response. The waves producing the largest ionospheric perturbations are those whose surfaces of constant wave phase happen to contain the Sun's rays (Hooke, 1968, 1970b). Their locus in these plots is the dark roughly circular ring passing through the plot origin and following the Sun in orientation with time of day and, as shown in Fig. 4, with season. In general, the ionospheric response is greatest for the waves propagating toward the Sun. The ionospheric response at the *F2* peak (here taken to remain at 300 km throughout the day) exhibits no diurnal variation, because wave-associated photoionization effects are unimportant there. Note that the *F2* peak generally responds somewhat more sensitively than the lower levels, since, with the exception of those waves whose surfaces of constant phase contain the Sun's rays, the lower *F*-region tends to maintain photochemical equilibrium despite the wave perturbations.

Figure 3 shows how the response of the ionosphere at 40°N latitude, −70° geomagnetic inclination varies with time of day and height at the summer solstice. Here the diurnal variations in ionospheric response, though present, do not appear to be so marked. In part this is because the large ambient height gradients of electron density in the ionospheric model for these latitudes and the large geomagnetic inclination favor dynamical production of ionospheric perturbations, which then competes with the wave-associated photochemical effects. In part, however, the effect is an artificial one, introduced by the overall darkness of the plots. Note that the wave-associated redistribution of pre-existing ionization depends both upon the wave amplitude and the wave number; the wave-associated photochemical effects depend primarily upon the wave amplitude alone and are sensitive to the wave number only as that number affects the sharpness or the degree of the solar control (Hooke, 1968, 1970b). Thus, for example, if instead of a 200-km total wavelength, a 400-km wavelength had been used in these calculations, wave-associated dynamical effects would have been somewhat less evident in Figs. 2 and 3, while if a 100-km wavelength had been used, the wave-associated dynamical effects would have been more marked.

Figure 4 shows how the response of the ionosphere at 10°N latitude, −20° geomagnetic inclination, varies with season at 0800 LT and a height of 150 km. Seasonal control over the response pattern is considerable. Note that in the model used in these calculations, seasonal and diurnal variations in the ionospheric response to the waves result entirely from the change in the orientation of the Sun relative to the location in question. Diurnal and seasonal changes in the density and composition of the neutral atmosphere, such as the ones considered in the CIRA (1965) reference atmosphere, would introduce diurnal and seasonal changes in the ionospheric response additional to those considered here.

Acknowledgement—Mrs. Judith J. Stephenson of the Institute for Telecommunication Sciences wrote the computer programs for these calculations.

REFERENCES

CIRA (1965). *Cospar International Reference Atmosphere* 1965. North-Holland, Amsterdam.

Georges, T. M. (1967). Ionospheric effects of atmospheric waves. *ESSA Tech. Rep. IER 57-ITSA 54*, U.S. Government Printing Office, Washington.

Georges, T. M. (1968). Collisional interaction of atmospheric waves with the ionospheric *F*-region. *Acoustic-Gravity Waves in the Atmosphere-Symp. Proc.* (Ed. T. M. Georges), pp. 377–380. U.S. Government Printing Office, Washington.

Hines, C. O. (1960). Internal atmospheric gravity waves at ionospheric heights. *Can. J. Phys.* **38**, 1441–1481.

Hines, C. O. (1968). An effect of ohmic losses in upper atmospheric gravity waves. *J. atmos. terr. Phys.* **30**, 851–856.

Hines, C. O. and Reddy, C. A. (1967). On the propagation of atmospheric gravity waves through regions of wind shear. *J. geophys. Res.* **72**, 1015–1034.

HOOKE, W. H. (1968). Ionospheric irregularities produced by internal atmospheric gravity waves. *J. atmos. terr. Phys.* **30,** 795–823.

HOOKE, W. H. (1970a). The ionospheric response to internal gravity waves—1. The *F2*-region response. *J. geophys. Res.* **75,** No. 28.

HOOKE, W. H. (1970b). The ionospheric response to internal gravity waves—2. The lower *F*-region response. *J. geophys. Res.* **75,** No. 34.

MACLEOD, M. A. (1966). Sporadic-*E* theory—1. Collision-geomagnetic equilibrium. *J. atmos. Sci.* **23,** 96–109.

MUNRO, G. H. (1950). Travelling disturbances in the ionosphere. *Proc. R. Soc.* **202,** 208–223.

MUNRO, G. H. (1958). Travelling ionospheric disturbances in the *F*-region. *Aust. J. Phys.* **11,** 91–112.

PRICE, R. E. (1955). Travelling disturbances in the ionosphere. *The Physics of the Ionosphere,* pp. 181–190. The Physical Society, London.

STEPHENSON, J. J. and GEORGES, T. M. (1969). Computer routines for synthesizing ground backscatter from three-dimensional raysets. *ESSA Tech. Rept. ERL 120-ITS 84,* U.S. Government Printing Office, Washington.

Reprinted from Journal of Geophysical Research 76, No. 10,
2523-2525, 1971

Divergence of Ion Velocity in the *E* Region Due to Vertical Winds

J. D. WHITEHEAD[1]

Air Force Cambridge Research Laboratories
L. G. Hanscom Field, Bedford, Massachusetts 01730

W. H HOOKE

Wave Propagation Laboratory, Environmental Research Laboratories
National Oceanic and Atmospheric Administration, Boulder, Colorado 80302

The so-called magnetoshear theory of sporadic *E* shows that a shear in the neutral winds at *E* region heights produces a vertical ion motion V_{iz} that varies with height, and that the convergence $\partial V_{iz}/\partial z$ of this motion produces the increases in ion density known as sporadic *E* layers. (For a summary of the theory, see *Whitehead* [1970].) The theory shows that the vertical ion velocity V_{iz} is given in terms of the vector neutral wind velocity $\mathbf{U}$ by the formula [*MacLeod*, 1966]

$$V_{iz} = \frac{1}{1+\rho_i^2}[(\rho_i^2 + \Gamma_z^2)U_z + \rho_i\Gamma_y U_x + \Gamma_y\Gamma_z U_y] \qquad (1)$$

Here $\rho_i \equiv \nu_i/\omega_i$ is the ratio of the ion-neutral collision frequency ν_i to the ion gyrofrequency ω_i, and the x, y, and z coordinate axes are taken to coincide with geomagnetic east, geomagnetic north, and the vertical directions, respectively; Γ_y and Γ_z are the north and vertical components of a unit vector directed parallel to the local magnetic induction field. In applications of equation 1, it has typically been assumed that the neutral winds are horizontal, but recently *MacLeod* [1968] and *Wright and Fedor* [1969, 1970] have shown that, in calculating the vertical ion motion and its convergence, it is desirable to include the vertical component of the neutral winds, since vertical winds of only a few meters per second may be as effective in creating ion convergence as horizontal winds of tens of meters per second. This conclusion follows from equation 1 and the fact that $\rho_i \gg 1$ at heights below about 110 km.

However, it is important to note that, while the ion motion is often so convergent that the ion density increases several times above the ambient, hydrodynamic constraints apparently prevent the neutral air density from changing by anything like this amount. The effect of these constraints is particularly visible in the relatively simple theory that describes motions of the internal atmospheric gravity wave type. There one finds that for waves of small vertical wavelength and long period, which appear to be of fundamental importance to upper atmospheric dynamics, the neutral atmospheric motions are nearly nondivergent [*Hines*, 1960, 1963]. We show here that the existence of such constraints implies that, in cases when the $\rho_i^2 U_z$ term of equation 1 is important, the full vector velocity $\mathbf{V}_i$ and its convergence $\nabla \cdot \mathbf{V}_i$, rather than the single term $\partial V_{iz}/\partial z$, should be used to compute the ion convergence. This is because in many circumstances the contribution of the $\rho_i^2 U_z$ term is largely cancelled by other contributions to the ion convergence, particularly those resulting from horizontal variations in the horizontal neutral winds. The discussion that follows is couched in terms of internal gravity waves; thus the neutral winds are taken to be of the form [*Hines*, 1960]

$$\mathbf{U} = \mathbf{U}_0 \exp(z/2H) \exp i(\omega t - \mathbf{k}\cdot\mathbf{r}) \qquad (2)$$

where $\mathbf{U}_0$ is a constant, z is the height, H is the neutral-gas scale height, ω is the angular wave frequency, t is the time, $\mathbf{k}$ is the wave vector, and $\mathbf{r}$ is a position vector.

We begin by writing the vector form of equation 1 [*MacLeod*, 1966]:

---

[1] While on leave from the Department of Physics, University of Queensland, Australia.

Copyright © 1971 by the American Geophysical Union.

$$\mathbf{V}_i = \frac{1}{1+\rho_i^2}\left[\rho_i^2\mathbf{U} + \rho_i\mathbf{U}\times\mathbf{\Gamma} + (\mathbf{U}\cdot\mathbf{\Gamma})\mathbf{\Gamma}\right] \tag{3}$$

The ion convergence is then given by [*MacLeod*, 1966]

$$\begin{aligned}\nabla\cdot\mathbf{V}_i = {} & \frac{1}{1+\rho_i^2}\left[\rho_i^2\nabla\cdot\mathbf{U} + \rho_i\mathbf{\Gamma}\cdot\nabla\times\mathbf{U}\right.\\ & \left.+ \mathbf{\Gamma}\cdot\{(\mathbf{\Gamma}\cdot\nabla)\mathbf{U}\}\right]\\ & + \frac{1}{(1+\rho_i^2)^2}\left[2\rho_i\{\mathbf{U} - (\mathbf{U}\cdot\mathbf{\Gamma})\mathbf{\Gamma}\}\right.\\ & \left.+ (1-\rho_i^2)\mathbf{U}\times\mathbf{\Gamma}\right]\cdot\nabla\rho_i\end{aligned} \tag{4}$$

By specializing to the case $\rho_i \gg 1$ we find the approximate relation

$$\nabla\cdot\mathbf{V}_i \doteq \nabla\cdot\mathbf{U} + \frac{1}{\rho_i}\mathbf{\Gamma}\cdot\nabla\times\mathbf{U} \tag{5}$$

provided that meridional winds are not much larger than the zonal winds, and provided also that the vertical wavelength of the waves considered is not much greater than a neutral-gas scale height H (i.e., provided that $\rho_i k_z \gg 1/H$, where k_z is the vertical wave number). We note that the dominant contribution of the vertical winds U_z is contained in the $\nabla\cdot\mathbf{U}$ term; thus we suspect that, if the neutral winds are nearly nondivergent, the $\partial U_z/\partial z$ contribution to ion convergence is cancelled by $\partial U_x/\partial x + \partial U_y/\partial y$. We illustrate this for the case of internal atmospheric gravity waves. By combining equations 2 and 5, we obtain

$$\begin{aligned}\nabla\cdot\mathbf{V}_i \doteq {} & -i\mathbf{k}\cdot\mathbf{U} - \frac{i}{\rho_i}\mathbf{\Gamma}\cdot\mathbf{k}\times\mathbf{U}\\ & + \frac{U_z}{2H} + \frac{1}{\rho_i}\frac{\Gamma_y U_z}{2H}\end{aligned} \tag{6}$$

Hines [1960] gives the wave 'polarization relation'

$$\frac{U_h}{U_z} = \frac{k_h C^2[k_z - i(1-\gamma/2)g/C^2]}{\omega^2 - k_h^2C^2} \tag{7}$$

where the subscript h denotes the horizontal component of the appropriate vector, g is the acceleration of gravity, γ is the ratio of neutral-gas specific heats, and $C^2 \equiv \gamma g H$. We then find

$$\mathbf{k}\cdot\mathbf{U} = \left[\frac{\omega^2 - i(k_h^2/k_z)(1-\gamma/2)g}{\omega^2 - k_h^2C^2}\right]k_z U_z \tag{8}$$

For many waves of interest,

$$\begin{aligned} k_z^2 &\gg 1/4H^2\\ \omega &\ll g/C\end{aligned} \tag{9}$$

(At E region heights, these conditions are met by waves having vertical wavelengths less than 3 scale heights and periods greater than half an hour). For such waves,

$$\mathbf{k}\cdot\mathbf{U} \doteq \frac{i(1-\gamma/2)g}{C^2}\,U_z \ll k_z U_z \tag{10}$$

because

$$k_z^2 \gg 1/4H^2$$

and equation 6 becomes

$$\nabla\cdot\mathbf{V}_i \doteq \frac{1}{\gamma H}\,U_z - \frac{i}{\rho_i}\mathbf{\Gamma}\cdot\mathbf{k}\times\mathbf{U} + \frac{i}{\rho_i}\frac{\Gamma_y U_z}{2H} \tag{11}$$

The only other U_z term in equation 11, $i\Gamma_y k_x U_z/\rho_i$, is negligible in light of the inequalities (9), which imply $k_x \ll k_z$ [*Hines*, 1960], and the inequality $\rho_i \gg 1$. Thus the contribution of the vertical winds to the ion convergence in this case is

$$U_z/\gamma H \ll k_z U_z \doteq \partial U_z/\partial z \tag{12}$$

and it therefore appears that use of the magnitude of $\partial U_z/\partial z$ to estimate this contribution would greatly exaggerate its actual importance. It is interesting to note that in this case the ion convergence is not proportional to the vertical wind convergence $\partial U_z/\partial z$; instead, it is proportional to the magnitude of the vertical wind itself.

We therefore conclude that in calculating the ion convergence in cases where vertical neutral winds appear to be important, the full vector ion velocity $\mathbf{V}_i$ and its convergence should be calculated. To do this in experimental cases requires measurements not only of vertical variations of the three components of the neutral wind, but also of the horizontal variations of all three wind components. Such measurements would be extremely difficult and costly, since the waves producing the largest vertical winds may tend to have horizontal wavelengths comparable to or smaller than their vertical wavelengths; moreover, these waves will tend to have periods perhaps as short as 5 min [*Hines*, 1960, 1963]. In fact, we might remark that waves of the shortest periods produce predominately vertical neutral winds [*Hines*, 1960]; in such cases the effects of vertical winds are important even when $\rho_i \geq 1$, and the above analysis does not apply. The general expression (4) must then be used to compute the ion convergence; ideally, of course, (4) would be used in all comparisons between theory and observation. On the other hand, if it can be shown by some means that the particular waves observed in individual cases have small vertical wavelengths and long periods, then equation 11 may be used.

Acknowledgments. This work was started while one of us (JDW) was on leave from the University of Queensland at the Air Force Cambridge Research Laboratories. This research was continued at the University of Toronto where it was supported by the National Research Council of Canada, grant A3940, and was completed at the ESSA Research Laboratories, Boulder, Colorado. We wish to thank our many colleagues for helpful discussions.

The Editor wishes to thank M. A. MacLeod for his assistance in evaluating this letter.

REFERENCES

Hines, C. O., Internal atmospheric gravity waves at ionospheric heights, *Can. J. Phys., 38,* 1441–1481, 1960.

Hines, C. O., The upper atmosphere in motion, *Quart. J. Roy. Meteorol. Soc., 89,* 1–42, 1963.

MacLeod, M. A., Sporadic *E* theory, 1, Collision-geomagnetic equilibrium, *J. Atmos. Sci., 23,* 96–109, 1966.

MacLeod, M. A., The influence of the neutral wind field on the distribution of ionization in the *E*-region, *Meteorol. Monographs, 9,* 139–147, 1968.

Whitehead, J. D., Production and prediction of sporadic *E*, *Rev. Geophys., 8,* 65–144, 1970.

Wright, J. W., and L. S. Fedor, The interpretation of ionospheric radio drift measurements, 2, Kinesonde observations of microstructure and vertical motion in sporadic *E*, *J. Atmos. Terr. Phys., 31,* 925–942, 1969.

Wright, J. W., and L. S. Fedor, Errata, *J. Atmos. Terr. Phys., 32,* 451–452, 1970.

(Received June 15, 1970;
accepted December 22, 1970.)

Reprinted from Journal of Geophysical Research 76, No. 16, 3777-3782, 1971.

Traveling Ionospheric Disturbances Observed at the Magnetic Equator

D. L. Sterling,[1] W. H. Hooke,[2] and R. Cohen[3]

Electron concentration profiles taken every 3 min with an incoherent scatter radar at the Jicamarca Radar Observatory (near Lima, Peru) sometimes exhibit weak wavelike disturbances in the equatorial F region. The associated perturbations are typically of order ±1 to ±3%, and their phase varies with height. The periods of the observed oscillations are roughly 20 min. The disturbances are also seen on ionograms taken simultaneously. A theoretical argument is advanced to the effect that the ionospheric manifestation of a neutral wave packet differs near the magnetic equator from that at temperate latitudes.

For some years now, a class of large-scale wavelike ionospheric irregularities known as traveling ionospheric disturbances (TID) has been observed by means of a variety of radio techniques [*Munro,* 1950, 1958; *Valverde,* 1958; *Tveten,* 1961; *Chan and Villard,* 1962; *Georges,* 1967; *Davis and da Rosa,* 1969]. These disturbances have been rather successfully interpreted as the ionospheric manifestations of internal atmospheric gravity waves [*Hines,* 1960, 1963, 1968*a, b, c; Pitteway and Hines,* 1963, 1965; *Friedman,* 1966; *Hines and Reddy,* 1967]. One of the more useful tools for the study of TID's is the incoherent scatter radar, which provides nearly simultaneous information through a broad height range about a number of important ionospheric parameters (see *Evans* [1969] for a complete review). *Thome* [1964, 1968], *Testud and Vasseur* [1969], and *Vasseur and Waldteufel* [1969] have used this technique to verify certain predictions of internal gravity wave theory, some in considerable detail.

Specifically, the incoherent scatter technique complements the conventional ionosonde, since it can provide: (*a*) information about the topside ionosphere; (*b*) simultaneous measurements of electron concentrations, electron and ion temperatures, and ion motions; (*c*) a truly vertical profile (whereas ionosonde profiles may refer to off-vertical paths); and (*d*) 'true heights,' which are observed directly from the time-delay of the echoes, there being no significant retardation of the wave at the probing frequency.

The present paper reports preliminary observations made at the magnetic dip equator of what we believe to be TID's, by using the incoherent scatter radar of the Jicamarca Radar Observatory (11.95°S, 76.87°W; surface dip ~2°). In contrast to the studies at Arecibo [*Thome,* 1964, 1968] and St. Santin [*Testud and Vasseur,* 1969; *Vasseur and Waldteufel,* 1969], which employed echo power to determine electron concentration, profiles presented here were obtained by measuring the Faraday rotation of the scattered signal [*Farley,* 1969]. (*Evans* [1969] gives a brief description of the three incoherent scatter radars involved.) This technique yields absolute electron concentration profiles directly without requiring a separate normalization. The altitude range covered was 200 to 600 km, and the pulse length used was 233 μsec, thus providing a height resolution of 35 km. Integration time was 3 min, but the raw results were smoothed somewhat by taking a 3-point (9 min) running average with time for each 10-km height interval. The final results are displayed as contours of constant electron concentration [*McClure et al.,* 1970]. The interval between contours is logarithmic in ¼-db steps. (For example, the contour labeled 6.0 corresponds to a concentration of 10^6 cm^{-3}; the ad-

---

[1] Now at the University of Texas at Dallas 75230. Formerly at Jicamarca Radar Observatory, Lima, Peru.

[2] Wave Propagation Laboratory, Environmental Research Laboratories, National Oceanic and Atmospheric Administration, Boulder, Colorado 80302.

[3] Aeronomy Laboratory, Environmental Research Laboratories, National Oceanic and Atmospheric Administration, Boulder, Colorado 80302.

Copyright © 1971 by the American Geophysical Union.

jacent contours correspond to concentrations of 1.06×10^6 and 0.94×10^6 cm^{-3}, respectively, and so on.)

RESULTS

One such contour plot, made on January 10, 1967, is shown in Figure 1. The smeared points are caused by noisy data. Wavelike perturbations can be seen on the individual contours. The wave is especially recognizable at the height of the F_2 layer peak (about 350 km) and has a maximum-to-minimum amplitude of about one-half a contour interval, or ±3%. This amplitude appears to be fairly independent of altitude.

Surfaces of constant phase are indicated in Figure 1 by curves drawn through corresponding points of maximal electron concentration variations. The phase fronts are almost vertical but are progressively retarded at lower heights; phase propagation is downward. The total amount of retardation or phase lag from top to bottom is difficult to estimate, but it is about 20 min. The period of the wave is also approximately 20 min and persists without interruption through the 5-hour period shown.

Another contour plot, for March 6, 1967, is shown in Figure 2. Similar periodic perturbations, of smaller amplitude (about 1 to 2%) and 30-min period, occur in these contours.

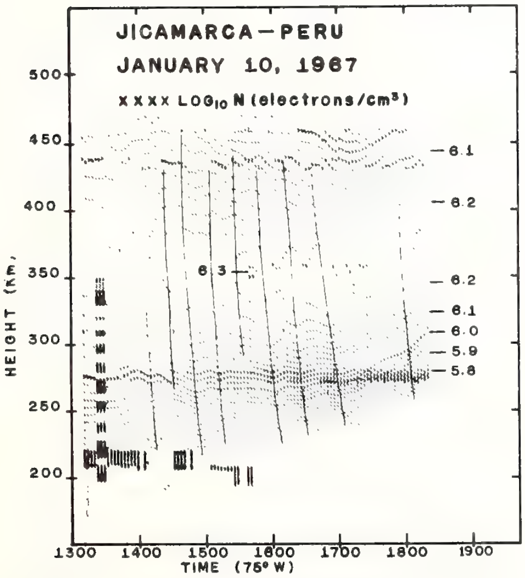

Fig. 1. Contours of electron concentration in logarithmic intervals of ¼ decibel. Surfaces of constant phase are indicated as lines through points of maximal deviation of the contours.

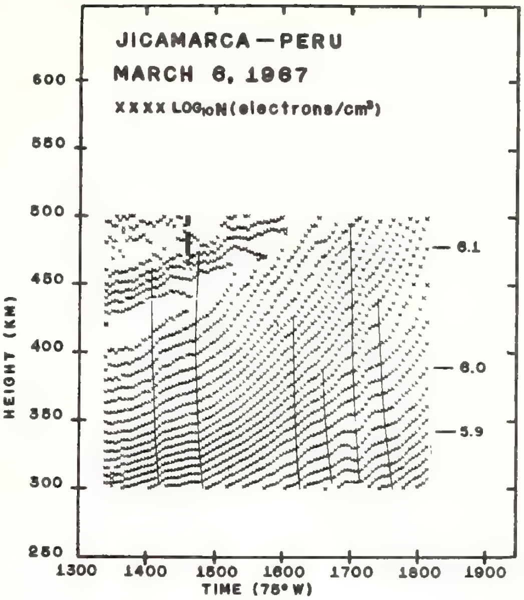

Fig. 2. Electron concentration contours and surfaces of constant phase.

Ionograms were examined to see if they revealed similar perturbations. Figure 3 shows the contour plot obtained by using radar on March 7, 1967. Figure 4 shows plots of virtual height versus time at fixed plasma frequencies, obtained from Jicamarca and Huancayo ionograms for the same day. The constant frequency contours correspond to electron concentration contours of 5.800 through 6.125. All three contour plots exhibit similar temporal variations. There is little variation on any of the plots until 1430. At this time, oscillatory perturbations of the contours begin, continuing throughout the remainder of the record.

The Huancayo and Jicamarca ionograms show similar features, simultaneous to within about 3 min. This lag is quite small compared with the wave period (~20 to 30 min). Since Huancayo is approximately 160 km due east of Jicamarca (and at the same magnetic latitude), it appears that the disturbance is traveling in an essentially north-south direction.

DISCUSSION

The incoherent scatter observations reported in the previous section are of rather limited use-

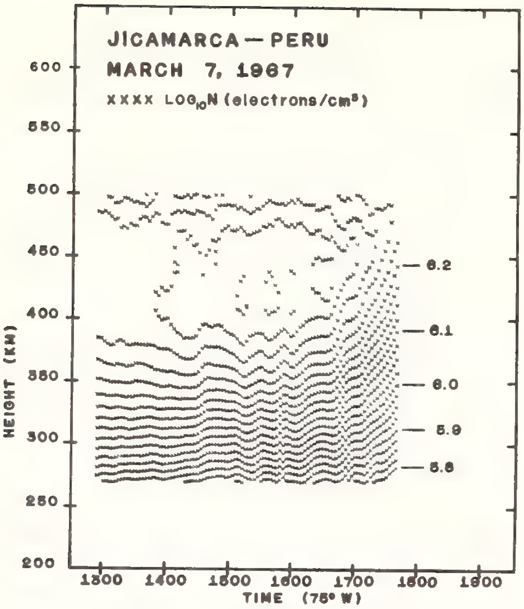

Fig. 3. Electron concentration contours for comparison with Figures 4 and 5.

fulness in the sense that they provide no definitive measurements of the direction and velocity of wave travel, such as could have been provided by the addition of complementary observations at a third (noncollinear) location. Such complete information would have enabled us to prove beyond question the wave nature of the disturbances, to check the wave dispersion equation, and to provide some insight into the probable wave sources. Instead, all we can conclude is that on March 7, 1967, the wave propagation was meridional. Nevertheless there is really no reason to doubt the wave dispersion equation, already verified by a great variety of experimental evidence, and the application of this equation to our data is instructive.

By using the phase fronts shown in Figure 1 to estimate the vertical wavelength, λ_z, of the perturbing wave of January 10, 1967, we find $\lambda_z \sim 300$ to 350 km (although the uncertainties in this estimate are enormous). From model 4 of the Cira 1965 reference atmosphere, we compute the atmospheric Brunt period τ_g at the 300-km level to be something like 16 min. *Hines* [1960, equation 4] gives the approximate dispersion relation

$$\lambda_h^2 = (\tau^2 - \tau_g^2)\lambda_z^2/\tau_g^2 \qquad (1)$$

where λ_h is the horizontal wavelength and τ is the wave period. Equation 1 is approximately valid when $16\pi^2H^2 \gg \lambda_z^2$, where H is the scale height of the neutral atmosphere. For our choice of atmospheric model, $16\pi^2H^2 \simeq 5.2 \times 10^5$ km². For $\tau \simeq 20$ min, $\tau_g \simeq 16$ min, and $\lambda_z \sim 300$ km ($\lambda_z^2 \sim 9 \times 10^4$ km²) equation 1 gives $\lambda_h \sim 225$ km, so that λ, the total wavelength, is roughly 180 km.

This wave should be strongly affected by molecular dissipation above the height z implicitly given by

$$(k^2C^2/\omega) \sim \nu(z) \qquad (2)$$

(*Hooke* [1968], equation 25, presented here in an altered form) where k $(=2\pi/\lambda)$ is the wave number, C is the speed of sound, ω is the angular wavefrequency, and $\nu(z)$ is the neutral-neutral collision frequency. The above value of τ_g implies that $C \simeq 850$ msec^{-1}; this gives $k^2C^2/\omega \simeq 0.2$. We find $\nu(z) \simeq 0.2$ at about 400 km, near the upper range of the data; presumably the wave was affected by viscosity only above this height. The uncertainties involved in estimating the wave front tilts for the events of March 6 and 7 were so large that the above calculation was not repeated in these cases.

Valverde [1958], *Georges* [1967], *Davis and da Rosa* [1969], and *Testud and Vasseur* [1969] were able to show rather convincingly that the long-period (~2 hours) waves they observed were most likely generated in the auroral zone. These waves generally had high horizontal phase velocities (>500 msec^{-1}). An auroral origin for the waves observed here therefore seems unlikely, since their periods (~30 min) and their horizontal phase velocities (calculated to be ~125 msec^{-1} on January 10, ~280 msec^{-1} on March 6) appear to have much smaller values. Moreover, the planetary *Kp* index was quite low at the time (<3 throughout all the observing periods; <2 most of the time); the authors cited above agree that *Kp* must be quite high if clearcut examples of aurorally generated TID's are to be observed.

The March 7, 1967, instance is the only one for which ionogram data are available to help determine the direction of travel, and in this case propagation does appear to be meridional, which would be consistent with a polar origin. Nevertheless, we can expect most waves observed by means of F_2 region electron concentration perturbations at the magnetic equator to be propagating meridionally, since the ionization, which is constrained to remain along field lines, responds extremely poorly to waves propagating nearly zonally at low dip latitudes [*Hooke*, 1970].

An auroral origin cannot be completely ruled out, however, for reasons discussed below. The problem is that the response of the F_2 region ionosphere to meridionally propagating internal gravity waves varies radically with the magnetic inclination I, and in very different ways depending on the wave period. At the height of the F_2 peak, the amplitude A of the fractional perturbations in electron concentration occurring during wave passage is given by [*Hooke*, 1970]

$$A = (\mathbf{k}\cdot\mathbf{l}_b)(\mathbf{u}\cdot\mathbf{l}_b)/\omega \tag{3}$$

apart from a factor, usually close to unity, that results from the growth of wave amplitude with height in the absence of energy dissipation. Here the components of the vector $\mathbf{u}$ are the amplitudes of the corresponding components of the wave-induced neutral gas velocity, and $\mathbf{l}_b$ is a unit vector directed parallel to the earth's geomagnetic field. By using equations 1 and 3 and the fact that internal gravity waves obeying equation 1 are very nearly transverse, we find that for waves propagating meridionally,

$$A = (u\tau_g/\lambda)(\tau/\tau_g) \sin [2 \sin^{-1} (\tau_g/\tau) - 2I] \tag{4}$$

We now consider 4 waves, all having the same value (u/λ) but different periods $\tau \simeq 10\tau_g$, $5\tau_g$, $2^{1/2}\tau_g$, and $1.1\tau_g$, respectively. The response of the F_2 region ionosphere to these waves varies with I in the manner shown in Figure 5. At temperate latitudes, the waves with long periods τ clearly dominate; waves with periods ~20 min ($2^{1/2}$ times the Brunt period) produce practically no ionospheric response (for a discussion of the reasons behind this result see *Hooke* [1970]). Furthermore at temperate latitudes the F_2 region ionospheric response to waves of period $\tau^2 \gg \tau_g^2$ is roughly proportional to τ (all other parameters held constant). The equatorial F_2 region ionosphere, however, exhibits a considerably reduced response to the waves of long period, while its response to waves of period $\tau \simeq 2^{1/2}\tau_g$ is a maximum. Moreover, at the magnetic equator the ionospheric response is very

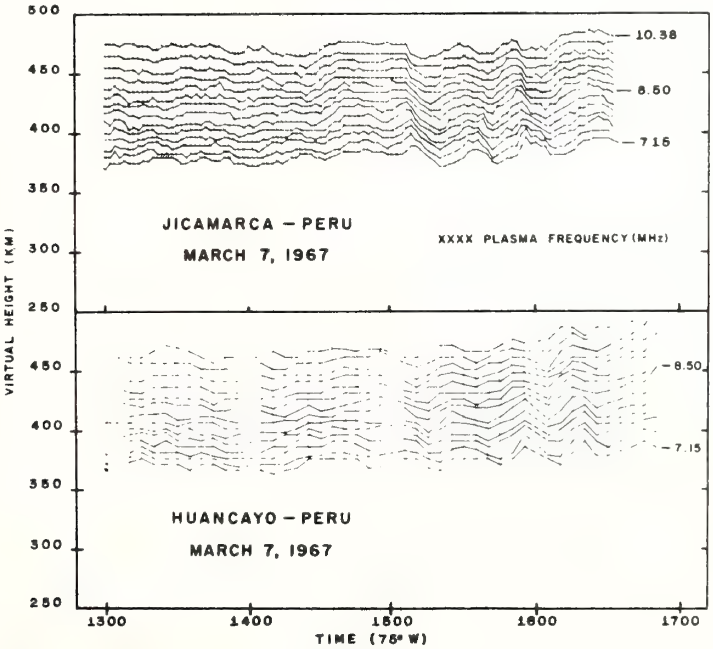

Fig. 4. Plots of virtual height versus time at fixed plasma frequencies f_n, as obtained from Jicamarca and Huancayo ionograms (30 sec frequency sweeps): $f_n = 0.009\ N^{1/2}$ MHz, where N is the electron concentration in units of cm^{-3}.

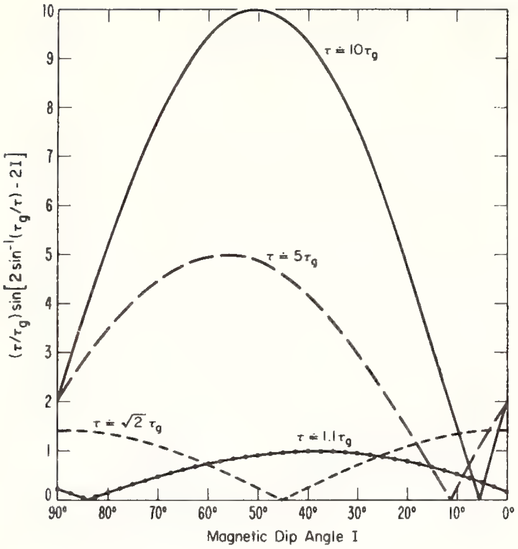

Fig. 5. Variation in the response of the F_2 region ionosphere to 4 different internal gravity waves, propagating meridionally toward the equator, as a function of the magnetic inclination I. Apart from the factor $u\tau_g/\lambda$, this is the magnitude $|A|$ of the quantity A given by equation 4. The waves all have the same ratio (u/λ), but different periods τ.

nearly independent of τ for $\tau^2 \gg \tau_g^2$. Thus a packet of long- and short-period internal gravity waves ducted at lower thermospheric heights [e.g., *Friedman*, 1966], propagating from auroral zone to equator, and continually leaking its energy upward from the duct, might be expected to manifest itself at temperate latitudes as a long-period disturbance, and at very low latitudes as a mixture of high- and low-frequency components. In other words, short-period waves that are lost in the long-period waves at temperate latitudes might in fact dominate at equatorial latitudes. It should be recognized that this deformation of the appearance of the wave packet (as manifested by ionospheric perturbations) is quite distinct from the deformation of the packet itself (resulting from dispersive effects and from the possibility that the source may radiate the energy of waves of different periods at different angles from the vertical [*Hines*, 1967]), which must also occur.

If we assume that the waves are propagating meridionally, we can use equation 4 to determine the wave amplitude $|\mathbf{u}|$ for the waves of January 10 and March 6, 1967. We find $|\mathbf{u}| \sim 5$ msec^{-1} in both cases. If these waves happened to be propagating at an azimuthal angle α relative to north-south, the above estimate should be multiplied by sec α.

Testud and Vasseur [1969] and *Vasseur and Waldteufel* [1969] have suggested that the dissipation of waves generated during magnetically disturbed times may provide an important second energy source for the atmosphere at such times. (This suggestion appears to have been made first by T. Gold, as published by *Hines* [1965, p. 180].) By performing simultaneous observations of the associated TID's at widely dispersed points (such as Arecibo and Jicamarca), it may be possible to determine the rate of wave dissipation with latitude. (It should be noted that Jicamarca may experience TID arrival from both auroral zones simultaneously.) Figure 5 and the related discussion of the text suggest that, to avoid overestimating the wave dissipation rate, it will be necessary to separate latitudinal variations in the ionospheric response to the waves from variations in the actual wave amplitudes.

Acknowledgments. This research was partially supported by NASA Fund Transfer R-06-012-008. At the time of these observations, the Jicamarca Radar Observatory was a cooperative activity of the Aeronomy Laboratory, ESSA Research Laboratories, Boulder, Colorado, and the Instituto Geofísico del Peru, Lima, Perú. Since July 1969, it has been a laboratory of the Instituto Geofísico del Perú.

* * *

The Editor wishes to thank C. O. Hines and G. Thome for their assistance in evaluating this paper.

REFERENCES

Chan, K. L., and O. G. Villard, Jr., Observation of large scale traveling ionospheric disturbances by spaced-path high-frequency instantaneous-frequency measurements, *J. Geophys. Res., 67,* 973–988, 1962.

Cira 1965 (COSPAR International Reference Atmosphere 1965), North-Holland, Amsterdam, 1965.

Davis, M. J., and A. V. da Rosa, Traveling ionospheric disturbances originating in the auroral oval during polar substorms, *J. Geophys. Res., 74,* 5721–5735, 1969.

Evans, J. V., Theory and practice of ionosphere study by Thomson scatter radar, *Proc. IEEE 57,* 496–530, 1969.

Farley, D. T., Faraday rotation measurements using incoherent scatter, *Radio Sci., 4,* 143–152, 1969.

Friedman, J. P., Propagation of internal gravity waves in a thermally stratified atmosphere, *J. Geophys. Res., 71,* 1033–1054, 1966.

Georges, T. M., Ionospheric effects of atmospheric waves, *ESSA Tech. Rep. IER 57-ITSA 54,* U.S. Govt. Printing Office, Washington, D. C., 1967.

Hines, C. O., Internal atmospheric gravity waves at ionospheric heights, *Can. J. Phys., 38,* 1441–1481, 1960.

Hines, C. O., The upper atmosphere in motion, *Quart. J. Roy. Meteorol. Soc., 89,* 1–42, 1963.

Hines, C. O., Dynamical heating of the upper atmosphere, *J. Geophys. Res., 70,* 177–183, 1965.

Hines, C. O., On the nature of traveling ionospheric disturbances launched by low-altitude nuclear explosions, *J. Geophys. Res., 72,* 1877–1882, 1967.

Hines, C. O., Some consequences of gravity-wave critical layers in the upper atmosphere, *J. Atmos. Terr. Phys., 30,* 837–843, 1968*a*.

Hines, C. O., An effect of molecular dissipation in upper atmospheric gravity waves, *J. Atmos. Terr. Phys., 30,* 845–849, 1968*b*.

Hines, C. O., An effect of ohmic losses in upper atmospheric gravity waves, *J. Atmos. Terr. Phys., 30,* 851–856, 1968*c*.

Hines, C. O., and C. A. Reddy, On the propagation of atmospheric gravity waves through regions of wind shear, *J. Geophys. Res., 72,* 1015–1034, 1967.

Hooke, W. H., Ionospheric irregularities produced by internal atmospheric gravity waves, *J. Atmos. Terr. Phys., 30,* 795–823, 1968.

Hooke, W. H., The ionospheric response to internal gravity waves, 1, The F_2 region response, *J. Geophys. Res., 75,* 5535–5544, 1970.

McClure, J. P., D. T. Farley, Jr., and Robert Cohen, Ionospheric electron concentration measurements at the magnetic equator, 1964–1966, *ESSA Tech. Rep. ERL 186-AL 4,* U.S. Govt. Printing Office, Washington, D. C., 1970.

Munro, G. H., Traveling disturbances in the ionosphere, *Proc. Roy. Soc., 202,* 208–223, 1950.

Munro, G. H., Traveling ionospheric disturbances in the *F* region, *Aust. J. Phys., 11,* 91–112, 1958.

Pitteway, M. L. V., and C. O. Hines, The viscous damping of atmospheric gravity waves, *Can. J. Phys., 41,* 1935–1948, 1963.

Pitteway, M. L. V., and C. O. Hines, The reflection and ducting of atmospheric acoustic-gravity waves, *Can. J. Phys., 43,* 2222–2243, 1965.

Testud, J., and G. Vasseur, Ondes de gravité dans la thermosphère, *Ann. Geophys., 25,* 525–546, 1969.

Thome, G. D., Incoherent scatter observations of traveling ionospheric disturbances, *J. Geophys. Res., 69,* 4047–4049, 1964.

Thome, G. D., Long-period waves generated in the polar ionosphere during the onset of magnetic storms, *J. Geophys. Res., 73,* 6319–6336, 1968.

Tveten, L. H., Ionospheric motions observed with high-frequency backscatter sounders, *J. Res. NBS, 65D,* 115–127, 1961.

Valverde, J. F., Motions of large-scale traveling disturbances determined from high-frequency backscatter and vertical incidence records, *Sci. Rep. no. 1,* Stanford Electronics Laboratories, 1958.

Vasseur, G., and P. Waldteufel, Thomson scatter observations of a gravity wave in the ionospheric *F*-region, *J. Atmos. Terr. Phys., 31,* 885–888, 1969.

(Received September 18, 1970;
accepted February 22, 1971.)

Reprinted from ESSA Technical Report, ERL 175-ITS 112, 1970.

ON THE ROLE OF VERTICAL NEUTRAL-GAS MOTIONS IN PRODUCING ION CONVERGENCE AT E-REGION HEIGHTS

William H. Hooke

Theoretical and observational results are used to suggest that vertical neutral-gas motions are generally important in applications of the magnetoshear theory of sporadic E, as has been recently demonstrated in a particular instance by M. A. MacLeod. It is argued that much of the vertical neutral-gas motion present at these heights must be of gravity-wave origin and shown that gravity-wave-associated vertical motions of the neutral gas should support (oppose) the action of wave-associated horizontal motions in producing ion convergence when the wave is propagating toward the east (toward the west). It is also argued that the full vector ion velocity, rather than only its vertical component, must be used in applications of the magnetoshear theory.

Reprinted from NOAA Technical Report, ERL 212-WPL 16, 1971. **66**

A PROGRAM FOR CALCULATING THREE-DIMENSIONAL ACOUSTIC-GRAVITY RAY PATHS IN THE ATMOSPHERE

T. M. Georges

The ITS-Jones-Haselgrove ray-tracing program is adapted to calculate acoustic-gravity ray paths in a compressible atmosphere with arbitrary three-dimensional wind and temperature variability and spherical earth. The program and its use are described, including deck listings and sample runs. Application to ocean acoustics should be possible with little modification.

Reprinted from NOAA Technical Report, ERL 187-WPL 13, 1970.

THE KINEMATIC BEHAVIOR OF SPHERICAL PARTICLES IN AN ACCELERATING ENVIRONMENT

Dean A. Wilson

The response of a spherical particle to an accelerating environment is investigated. When the Reynolds numbers associated with such accelerations are small, the particle is in Stokes' regime and the linear equations governing its motion can be solved analytically. Outside Stokes' regime, which is the general case for spheres comparable in size to precipitation particles, the equations are nonlinear and must be solved numerically.

The numerical solution indicates that particles of all sizes falling in a sheared environment are excellent tracers of the mean air motion. Even a hailstone as large as 2 cm in diameter falling at its terminal speed can be expected to follow the mean horizontal air speed within $\pm$ 0.5 m sec^{-1}, provided the vertical wind shear is less than 10^{-2} sec^{-1}. However, the time response of a spherical particle to a wind gust of constant velocity is quite sensitive to particle size. This response can be approximated by an expression of the form $1 - e^{-t/\tau}$, where τ depends on both particle size and the magnitude of the wind gust. For wind gusts of 1.0 m sec^{-1}, τ is seen to vary from less than 10^{-5} sec for particles smaller than 0.02 mm in diameter to 2.5 sec for a 2.0-cm hailstone. Also, when a particle is submitted to a substantial wind gust, a significant decrease in its terminal velocity occurs.

It is suggested that the response of a nonspherical particle to wind accelerations will be at least as fast as this study indicates for a spherical particle of the same mass.

Key Words: Acceleration, numerical solution, spherical particle, Stokes' regime, wind gust, wind shear

Reprinted from Proceedings of the Symposium on Tropical Meteorology, June 2-11, 1970, B-III-1 through B-III-6, 1970

WATER VAPOR FLUX MEASUREMENTS FROM ESSA AIRCRAFT

James D. McFadden
Charles W. Travis
ESSA Research Flight Facility, Miami, Florida

Richard O. Gilmer
Raymond E. McGavin
ESSA Wave Propagation Laboratory, Boulder, Colorado

INTRODUCTION

Efforts to measure fluxes of heat and moisture from aircraft date back over the past 15 years or so, and notable works in this area include those by Bunker, Telford and Warner, McCready, Lappe, Kaprov and Tsvang, Lenschow and Miyake. The techniques used and the success obtained by these individuals have varied, and the reader is referred to the literature for particulars. The purpose of this paper is to present a description of a system for the direct measurement of water vapor flux which was developed by ESSA personnel and employed on an ESSA Research Flight Facility DC-6 aircraft during the Barbados Oceanographic and Meteorological Experiment (BOMEX), May - July, 1969.

The basis for the direct measurement of the flux of some property of the air is that there is a correlation between the eddy velocity fluctuations of the wind and the atmospheric property in flux. In order to measure the vertical flux of water vapor directly, then, it is necessary to record simultaneously with instruments of sufficient response the vertical component of the wind and the water vapor density of the air. In general terms, this eddy flux of water vapor may be written as

$$\overline{\rho_w' w'} = \overline{\rho_w w} - \overline{\rho_w}\,\overline{w} \qquad (1)$$

where

ρ_w = absolute humity

w = vertical wind.

To obtain the eddy flux of water vapor it is necessary to evaluate the two right hand terms of this equation.

The ESSA airborne water vapor flux system, while not measuring either the vertical wind or the water vapor density of the air directly, is comprised of all the necessary components for the measurement of the quantities expressed in equation (1). Basically, an angle of attack probe and an inertial platform, which in the past have been collectively and popularly called a gust probe, is used for the vertical wind measurement, and a microwave refractometer system is used for the humidity. Each of these system will be discussed here in some detail along with a summary of the recording techniques employed, the patterns flown, data reduction procedures and the disposition of the processed data.

GUST PROBE SYSTEM

The system used for the determination of vertical wind is composed of many of the same sensors employed in the high altitude clear air turbulence (HICAT) program performed by the Lockheed-California Company for the Air Force Flight Dynamics Lab., specific details of which may be found in the reports by Crooks (1) and Crooks et al (2). The ESSA system, the components of which are listed in the Table, is made up primarily of the Lockheed angle-or-attack probe and the Litton LN-3A inertial platform. The Lockheed probe consists of vertical and lateral fixed-vane sensors arranged about a central pitot static tube as shown in Figure 1 (The lateral vane is not used for these measurements). These sensors consist of a light-weight, wedge-shaped vane (4-inch span and 2-inch chord) attached to a specially constructed strain-gage beam. The beam is of slotted construction and loads on the vane cause the beam to deflect parallel to itself. Lift is measured in terms of shear as opposed to bending moment if it were attached to a simple beam. Semi-conductor strain gages, in a wheatstone bridge configuration are bonded to the fore and aft portions of the beam. Electrical

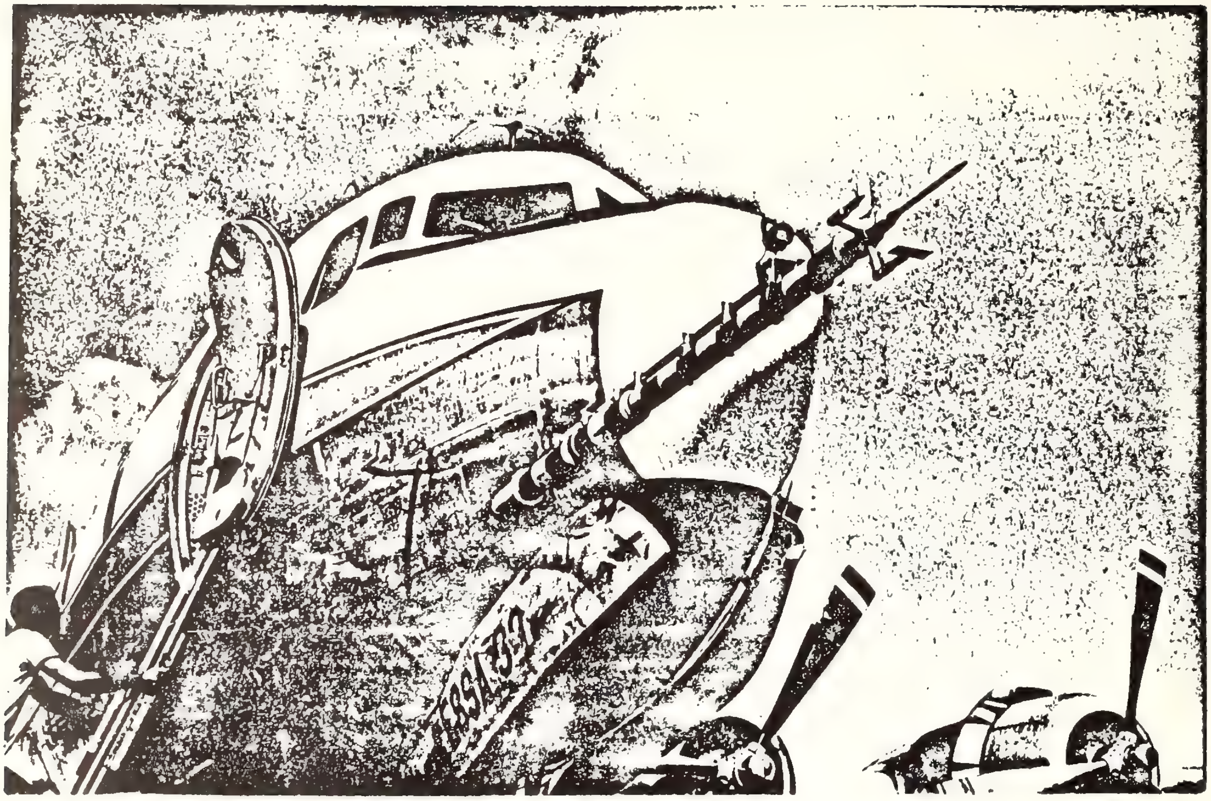

Figure 1. Nose Boom Instrumentation on ESSA/RFF, DC-6.

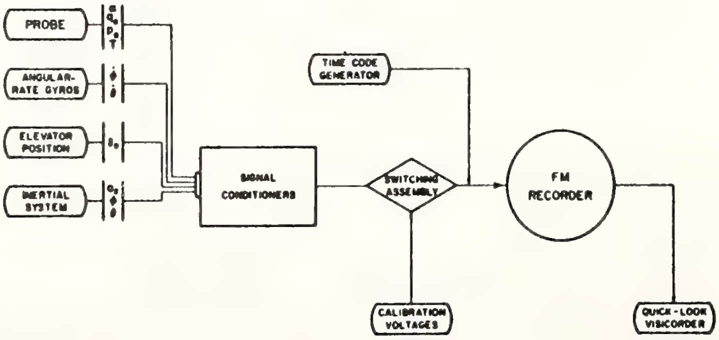

Figure 2. Block Diagram of Gust Probe System.

signals caused by deflection of the beam are amplified and conditioned to levels suitable fo imput to the recording system.

The probe housing also contains accelerometers that measure the normal and lateral accelerations of the boom. A pitot-static head and Statham strain gage transducer measure static and dynamic pressures that are used for air speed determinations.

The Litton LN-3A inertial platform is used to furnish aircraft attitude and vertical acceleration information. The system consists of a three-axis stable element mounted in a four gimbal configuration. Platform stabilization is accomplished by two, two-degree-of-freedom gyros and three accelerometers. Roll and pitch angles are obtained from the platform's follow-up servos, and its computer electronics furnishes vertical acceleration information in the form of DC voltages.

The measurement of the vertical component of the wind by an aircraft flying through the atmosphere basically requires the determination of the following quantities:

1. Motion of the air relative to the aircraft; and
2. Motion of the aircraft relative to the ground.

Utilizing the equations which mathematically describe these motions as developed by Crooks (2) and applied to the ESSA DC-6 by Lappe (4), the generalized equation for vertical wind gusts can be shown to be given by

$$W = U(\alpha-\theta) + \int_0^t a_z \, dt + \ell\dot{\theta} \qquad (2)$$

where
W = vertical wind
U = true air speed
α = angle of attack
θ = pitch angle
a_z = normal acceleration of aircraft (inertial platform)
ℓ = distance from C.G. to tip of boom
$\dot{\theta}$ = pitch rate of aircraft.

The first term represents the motion of the air relative to the aircraft while the second two represent the motion of the aircraft relative to the ground. The last term, $\ell\dot{\theta}$, represents the vertical velocity increment at the probe due to aircraft pitching velocity.

MICROWAVE REFRACTOMETER SYSTEM

The second distinct part of the ESSA water vapor flux system is the microwave refractometer - a system designed and built by the ESSA Wave Propagation Laboratory in Boulder, Colorado and used for the measurement of the refractive index of air which passe through the microwave cavity mounted on the aircraft boom (see Fig. 1). Refractive index, as used here, is defined as the ratio of the velocity of a radio wave through free space to its velocity through a particular medium, in this case ambient air.

This technique is applicable to water vapor measurements in the atmosphere because there is a strong relationship between refractive index and water vapor at radio frequencies. The development of this relationship, as given by McGavin and Vetter (5), states that the absolute humidity (water vapor density) expressed as a function of refractivity, temperature and pressure can be given as

$$\rho_w = 5.81 \times 10^{-4} NT - 4.51 \times 10^{-2} P \qquad (3)$$

where
ρ_w = absolute humidity (gm/m^3)
N = refractivity, $(n-1)10^6$ (n is refractive index)
T = temperature ($^\circ$K)
P = pressure (mb)

Temperature and pressure sensing elements on the aircraft boom provide the other two parameters necessary for the determination of ρ_w from equation (3).

In terms of refractive index the refractometer operates on the principle that a relationship exists between the resonant frequency of a microwave cavity and the refractive index or dielectric constant of the contents of the cavity. This relationship may be written as

$$\frac{\Delta f_R}{f_R} = \frac{-\Delta n}{n} \approx - \Delta n \qquad (4)$$

where f_R = original resonant frequency
n = refractive index corresponding to the resonant frequency, f.

The minus sign in (4) indicates a decrease in frequency will take place with an increase in refractive index.

The ESSA microwave refractometer has two transmission - type cavity resonators and the electronic circuitry necessary to measure and compare their resonant frequencies. One cavity - the sampling cavity located on the boom - has openings on all sides, including the end plates, that allow free passage of air through the cavity. The second cavity - the reference cavity located within the electronic console - is identical to the sampling cavity with the exception that it is completely sealed, and its frequency can be shifted by a calibrated probe inserted in the end plate.

Operationally, within the system a very accurate 3 kHz. sawtooth signal is applied to a Varian 203B reflex klystron which sweeps it linearly over a predetermined frequency range. The output of the klystron is applied to both cavities, each in turn producing a pulse as its resonating frequency is reached. The resonating frequency of the sealed referenc cavity does not change (or if it does, an error feedback signal is applied to the klystron to compensate for it). The resonant frequency of the sampling cavity is, however, largely dependent on the water vapor content of the air that passes through it, and it is the change in this resonant frequency relative to a known reference which provides us with a measure of the refractivity, N, which is used in equation (3).

TIME AND RECORDING SYSTEMS

A 14-channel, analog tape recorder, a visicorder strip chart recorder, and an Astrodata time code generator make up the recording and time components of the ESSA water vapor flux system. A Sangamo Electric Company series 3560, 14 track, 1-inch FM magnetic tape recorder was used to record the conditioned sensor signals. "IRIG" standards and compatibility were used. Twelve of the available 14 tracks were used for sensor data, and the remaining two were used for recording time and a reference frequency for servo speed control.

A Honeywell visicorder strip chart, galvonometer recorder was used for in-flight monitoring of the recorded data. The data recorded on FM tape was played back simultaneously through the reproduce electronics and passed through low-pass filters to remove the unwanted frequency components. These filters are active, 6-pole Butterworth-type with a cut off at six cycles. The primary purpose of this "quick-look" capability was to provide the operator the means to evaluate the performance of all sensors during each data run.

An Astrodata, Inc. model 5100 time code generator provided the IRIG "C" coded time for the system in the form of a DC level shift that encodes the date of the year, hour, minutes and seconds. Synchronization is with either local or Greenwich time. Figure 2 is a block diagram showing the tie-in between the components of the gust probe system and the time and recording systems.

BOMEX WATER VAPOR FLUX FLIGHT PATTERNS

During the Barbados Oceanographic and Meteorological Experiment (BOMEX) the ESSA Research Flight Facility's DC-6 (39C) aircraft outfitted with the special equipment described above flew 16 missions specifically for the purpose of gathering water vapor flux data. In addition, these flux measurements were made in support of other investigations during all of the other flights made by this aircraft during the three month BOMEX period (see Friedman, 3). During the first phase of this experiment, while FLIP was drifting within the observational array, missions were flown to collect data for comparison with flux information being gathered by this research vessel. Figure 3 depicts the pattern flown on many occasions in the vicinity of FLIP. Typically, after surveying the area the aircraft would enter the pattern approximately 10 nautical miles downwind at an altitude of 500 ft and fly a six minute, zero-drift leg past and, laterally, within 1000 ft of FLIP. A downwind leg at 150 ft and a second upwind let at 60 ft were flown subsequent to the 500 ft run as shown in the figure. At the completion of the zero-drift runs three additional runs were made at these same altitudes but normal to the wind and upwind of the ship's position. These runs are also shown in the figure. Total operational time for the completion of one pattern, including climbs and descents, was approximately one hour.

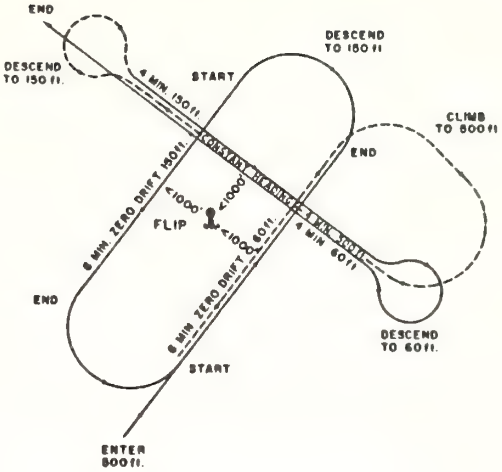

Figure 3. Water Vapor Flux Pattern

DATA PROCESSING

Processing of the water vapor flux data collected during BOMEX is being done on a contract basis by Rinaldi Data Processing Consultants, Inc. of New York. The reduction phase of this work will include the analog low-pass filtering of all FM data channels, digitizing at the rate of 20 samples per second and blocking into 15 second records, linear trend removal, computation of vertical velocity and absolute humidity, and computation of the first four statistical moments (mean, standard deviation, skewness, and kurtosis). Analysis on the resulting tapes will include numerical band pass filtering, generally between 0.05 and 4.5 Hz, computed and tabulated autocorrelation, cross-correlation, power spectral density, co-sprectum, quadrature spectrum, and coherence and phase angle for the vertical wind and absolute humidity series. A display in plot form as a function of log frequency of the normalized power spectral density, co-spectrum, coherence and phase angle of these two quantities will also be provided.

The results from the Rinaldi data processing program will be sent to ESSA's Wave Propagation Laboratory in Boulder, Colorado where they will be analyzed under the direction of Dr. Brad Bean.

ACKNOWLEDGEMENTS

The authors would like to thank all who participated in this endeavor, particularly Mr. Howard Mason and Dr. Brad Bean who were directly responsible for this project. We would also like to thank Mr. Howard Friedman for his critical comments relative to this paper.

REFERENCES

(1) Crooks, W., 1965, High Altitude Clear Air Turbulence. Tech. Rpt. No. AFFDL-TR-65-144, Air Force Flight Dynamics Laboratory, 114 p., Sept. 1965.

(2) Crooks, W. et al., 1967, Project HICAT, An Investigation of High Altitude Clear Air Turbulence. Tech. Rpt. No. AFFDL-TR-67-123, vol. 1, Air Force Flight Dynamics Laboratory, 255p., Nov. 1967.

(3) Friedman, H.A., 1970, The Use of ESSA Research Flight Facility's Instrumented Aircraft for Major Meteorological Experiments in the Tropics. Proc. Symposium on Tropical Meteorology, Honolulu, Hawaii, June 1970.

(4) Lappe, O.U., 1969, Preliminary Analysis of the RFF Turbulence System. Final Report to the RFF under ESSA Contracts Nos. E22-21-69(N) and E22-75-69(N), 122p., April 1969.

(5) McGavin, R.E. and M.J. Vetter, 1965, Radio Refractometry and Its Potential for for Humidity Studies. Humidity and Moisture, Measurement and Control in Science and Industry, A. Wexler, ed., pp. 553-560, Rheinhold, N.Y., 1965.

TABLE

ESSA GUST PROBE SYSTEM

MEASUREMENT	INSTRUMENT	LOCATION	MANUFACTURER	MODEL
Vane Force	Vane	Probe-boom	Lockheed	FT3809
Probe, Normal Acceleration	Accelerometer	Probe-boom	Statham	AJ43-2-350
Airspeed	Diff. Pressure	Probe-boom	Statham	PL283TC
Temperature	Thermistor	Probe-boom	Fenwall	KIC 26
Pressure Altitude	Press. Transducer	Boom	Rosemount	830A
Vertical Acceleration	Stable Platform	A/C C.G.	Litton	LN-3A
Roll Angle	Stable Platfrom	A/C C.G.	Litton	LN-3A
Pitch Angle	Stable Platform	A/C C.G.	Litton	LN-3A
Roll Rate	Gyro	Nose	R.C. Allen	F2880-045
Pitch Rate	Gyro	Nose	R.C. Allen	F2880-045
Elevator Position	Potentiometer	Tail		

*Reprinted from Telecommunications Research and Engineering Report
OT/TRER 23, 1971.*

LOCAL AND DIURNAL VARIATIONS IN GROUND-BASED RADIO REFRACTIVITY GRADIENTS AT TROPICAL LOCATIONS

B. A. Hart, G. D. Thayer and H. T. Dougherty

Telecommunication technology and its applications are rapidly expanding in the new or developing nations, many of which are located in tropical climates; so a knowledge of the behavior of refractivity gradients, directly related to establishing and maintaining reliable communication circuits, is especially important in this region.

The distribution and variability of ground-based radio refractivity gradients in tropical areas of the world are quite different from those found in temperate climates where the annual range of daily mean temperature is much larger than the daily temperature range. Examples of the refractivity vertical structure in locations from 30°N to 30°S, are presented to show that very large diurnal and interdiurnal fluctuations in surface gradients are the rule rather than the exception. These fluctuations, only slightly affected by seasonal cycles, are largely dependent on diurnal insolation and local features, such as terrain, prevailing winds and moisture sources.

Improved observational techniques and a careful study of local climatic effects can result in more accurate prediction methods for better telecommunication system design.

Key Words: Refractive index, tropical propagation,
ground-based refractivity gradients.

AUTHOR INDEX

Ackley, M. H. (with Clifford, Bouricius and Ochs), *Phase variations in atmospheric optical propagation,* 128-133.

Bean, B. R. *Turbulence and irregularities of the atmosphere,* 395-411.

Bean, B. R. (with R. E. McGavin), *Electromagnetic phase variability as a measure of water vapor and temperature variations over extended paths,* 230-245.

Bean, B. R. (with Dougherty and McGavin), *Remote probes for the study of atmospheric sources of fading on optical and microwave line-of-sight paths,* 252-253.

Bean, B. R. (with Thayer and Hart), *Worldwide characteristics of refractive index and climatological effects,* 412-424.

Bean, B. R. (with McGavin, Chadwick, and Warner), *Preliminary results of utilizing the high resolution FM radar as a boundary layer probe,* 254-261.

Bedard, A. J., *Seismic response of infrasonic microphones,* 19-23.

Beran, D. W., *Acoustics: A new approach for monitoring the environment near airports,* 165-167.

Beran, D. W., *Acoustic radar detection techniques,* 146-164.

Beran, D. W. (with Willmarth), *Doppler winds from a bistatic acoustic sounder,* 182-198.

Beran, D. W. (with Hall, Wescott, and Neff), *Applications of an acoustic sounder to air pollution monitoring,* 218-224.

Beran, D. W. (with Little and Willmarth), *Acoustic doppler measurements of vertical velocities,* 225-227.

Bouricius, G. M. B. (with Clifford), *An optical interferometer using polarization coding to obtain quadrature phase components,* 113-116.

Bouricius, G. M. B. (with Clifford), *Experimental study of atmospherically-induced phase fluctuations in an optical signal,* 107-112.

Bouricius, G. M. B. (with Ackley, Clifford, and Ochs), *Phase variations in atmospheric optical propagation,* 128-133.

Brown, E. H. (with Clifford) *Propagation of sound in a turbulent atmosphere*, 1-5.

Calfee, R. F., *A note on terminologies used in gaseous absorption processes (abstract)*, 137.

Chadwick, R. (with Bean, McGavin and Warner), *Preliminary results of utilizing the high resolution FM radar as a boundary layer probe*, 254-261.

Clifford, S. F., *Temporal frequency spectra for a spherical wave propagating through atmospheric turbulence*, 120-127.

Clifford, S. F. (with Bouricius) *An optical interferometer using polarization coding to obtain quadrature phase components*, 113-116.

Clifford, S. F. (with Brown), *Propagation of sound in a turbulent atmosphere*, 1-5.

Clifford, S. F. (with Strohbehn), *The theory of microwave line-of-sight propagation through turbulent atmosphere*, 68-78.

Clifford, S. F. (with Lawrence and Ochs), *Measurements of atmospheric turbulence relevant to optical propagation*, 79-83.

Clifford, S. F. (with Bouricius, Ochs, and Ackley), *Phase variations in atmospheric optical propagation*, 128-133.

Cohen, A., *The size spectrum determination of spherical aerosols by light scattering method*, 351-357.

Cohen, A. (with Sterling and Hooke), *Traveling ionospheric disturbances observed at the magnetic equator*, 480-485.

Cook, R. K., *Penetration of a sonic boom into water*, 6-12.

Cupp, R. (with Strauch and Derr), *Atmospheric temperature measurement using raman backscattering*, 358-362.

Decker, M. T. (with Dutton), *Radiometric observations of liquid water in thunderstorm cells*, 306-311.

Derr, V. E., *Research problems in the use of lidar in anti-pollution studies*, 339-350.

Derr, V. E. (with Little), *A comparison of remote sensing of the clear atmospheric by optical, radio, and acoustic radar techniques*, 363-379.

Derr, V. E. (with McNice), *Relative power losses at the two mirrors of an asymmetric, confocal laser interferometer,* 134-136.

Derr, V. E. (with Schwiesow), *A Raman-scattering method for precise measurement of atmospheric oxygen balance (Letter to the editor),* 335-338.

Derr, V. E. (with Strauch and Cupp), *Atmospheric temperature measurement using raman backscattering,* 358-362.

Derr, V. E. (with Little, Kleen, Lawrence, Lhermitte, and Thayer), *Remote sensing of wind profiles in the boundary layer* (abstract) 380.

Dougherty, H. T., *The application of stationary phase to radio propagation for finite limits of integration,* 32-37.

Dougherty, H. T., *Diffraction by irregular apertures,* 38-43.

Dougherty, H. T. (with Bean and McGavin), *Remote probes for the study of atmospheric sources of fading on optical and microwave line-of-sight paths,* 252-253.

Dougherty, H. T. (with Hart and Thayer), *Local and diurnal variations in ground-based radio refractivity gradients at tropical locations* (abstract), 495.

Dougherty, H. T. (with McGavin and Emmanuel), *Microwave space and frequency diversity performance under adverse conditions,* 44-46.

Dougherty, H. T. (with McGavin and Krinks), *An experimental study of the atmospheric conditions conducive to high radio fields* (abstract), 67.

Dutton, E. J. (with Decker), *Radiometric observations of liquid water in thunderstorm cells,* 306-311.

Emmanuel, C. B. (with McGavin and Dougherty), *Microwave space and frequency diversity performance under adverse conditions,* 44-46.

Georges, T. M., *Amplification of ionospheric heating and triggering of "Spread F" by natural irregularities,* 435-437.

Georges, T. M., *A program for calculating three-dimensional acoustic-gravity ray paths in the atmosphere* (abstract), 487.

Georges, T. M. (with Hooke), *Wave-induced fluctuations in ionospheric electron content: A model for indicating some observational biases,* 438-451.

Gilmer, R. O. (with McFadden, Travis and McGavin), *Water vapor flux measurements from ESSA aircraft,* 489-494.

Hall, F. F., *Acoustic remote sensing of temperature and velocity structure in the atmosphere,* 168-181.

Hall, F. F. (with Wescott and Simmons), *Acoustic echo sounding of atmospheric thermal wind structure,* 199-217.

Hall, F. F., (with Wescott and Simmons), *Acoustic echo sounding as related to air pollution in urban environments* (abstract), 229.

Hall, F. F. (with Beran, Wescott and Neff), *Application of an acoustic sounder to air pollution monitoring,* 218-224.

Hart, B. A. (with Thayer and Bean), *Worldwide characteristics of refractive index and climatological effects,* 412-424.

Hart, B. A. (with Thayer and Dougherty), *Local and diurnal variations in ground-based radio refractivity gradients at tropical locations* (abstract), 495.

Hooke, W. H., *The ionospheric response to internal gravity waves: 1. The* F_2 *region response,* 425-434.

Hooke, W. H., *The ionospheric response to internal gravity waves: 2. Lower F region responses,* 452-461.

Hooke, W. H., *Ionospheric response to internal gravity waves: 3. Changes in the densities of the different ion species,* 462-466.

Hooke, W. H., *Ionospheric response to an isotropic spectrum of internal gravity waves,* 470-476.

Hooke, W. H., *On the role of vertical neutral-gas motions in producing ion convergence at E-region heights* (abstract), 486.

Hooke, W. H., *Quasi-stagnation levels in the ion motion induced by internal atmospheric gravity waves at ionospheric heights,* 467-469.

Hooke, W. H. (with Georges), *Wave-induced fluctuations in ionospheric electron content: A model for indicating some observational biases,* 438-451.

Hooke, W. H. (with Whitehead), *Divergence of ion velocity in the E-region due to vertical winds,* 477-479.

Hooke, W. H. (with Sterling and Cohen), *Traveling ionospheric disturbances observed at the magnetic equator,* 480-485.

Kleen, R. H. (with Ochs), *Measurements of the wavelength dependence of scintillation in strong turbulence,* Letter to the Editor, 117-119.

Kleen, R. H. (with Little, Derr, Lawrence, Lhermitte and Thayer), *Remote sensing of wind profiles in the boundary layer* (abstract), 380.

Krinks, R. W. (with Dougherty and McGavin), *An experimental study of the atmospheric conditions conducive to high radio fields* (abstract), 67.

Lawrence, R. S. (with Strohbehn), *A survey of clear-air propagation effects relevant to optical communications,* 84-106.

Lawrence, R. S. (with Ochs and Clifford), *Measurements of atmospheric turbulence relevant to optical propagation,* 79-83.

Lawrence, R. S. (with Little, Derr, Kleen, Lhermitte, and Thayer), *Remote sensing of wind profiles in the boundary layer* (abstract), 380.

Lerfald, G. M. (with Little), *D-region electron temperature at the northern auroral zone,* 381-392.

Lhermitte, R. M., *Dual doppler radar observation of convective storm circulation,* 275-280.

Lhermitte, R. M., *Measurement of wind and wind field by microwave doppler radar techniques,* 262-274.

Lhermitte, R. M., *Probing of atmospheric motion by airborne pulse doppler radar techniques,* 287-299.

Lhermitte, R. M. (with Miller), *Doppler radar methodology for the observation of convective storms,* 300-305.

Lhermitte, R. M. (with Kleen, Little, Derr, Lawrence, and Thayer), *Remote sensing of wind profiles in the boundary layer* (abstract), 380.

Little, C. G., *Acoustic sounding of the lower atmosphere,* 138-145.

Little, C. G. (with Derr), *A comparison of remote sensing of the clear atmospheric by optical, radio, and acoustic radar techniques,* 363-379.

Little, C. G. (with Lerfald), *D-region electron temperature at the northern auroral zone,* 381-392.

Little, C. G. (with Beran and Willmarth), *Acoustic doppler measurements of vertical velocities,* 225-227.

Little, C. G. (with Wescott and Simmons), *Acoustic echo-sounding measurement of temperature and wind fluctuations* (abstract), 228.

Little, C. G. (with Derr, Kleen, Lawrence, Lhermitte, and Thayer), *Remote sensing of wind profiles in the boundary layer* (abstract), 380.

McFadden, J. D. (with Travis, Gilmer and McGavin), *Water vapor flux measurements from ESSA aircraft,* 489-494.

McGavin, R. E. (with Bean), *Electromagnetic phase variability as a measure of water vapor and temperature variations over extended paths,* 230-245.

McGavin, R. E. (with Bean and Dougherty), *Remote probes for the study of atmospheric sources of fading on optical and microwave line-of-sight paths,* 252-253.

McGavin, R. E. (with Dougherty and Emmanuel), *Microwave space and frequency diversity performance under adverse conditions,* 44-46.

McGavin, R. E. (with Dougherty and Krinks), *An experimental study of the atmospheric conditions conducive to high radio fields* (abstract), 67.

McGavin, R. E. (with Bean, Chadwick and Warner), *Preliminary results of utilizing the high resolution FM radar as a boundary layer probe,* 254-261.

McGavin, R. E. (with McFadden, Travis, and Gilmer), *Water vapor flux measurements from ESSA aircraft,* 489-494.

McNice, G. T. (with Derr), *Relative power losses at the two mirrors of an asymmetric, confocal laser interferometer,* 134-136.

Miller, L. J. (with Lhermitte), *Doppler radar methodology for the observation of convective storms,* 300-305.

Neff, W. D. (with Beran, Hall and Wescott), *Application of an acoustic sounder to air pollution monitoring,* 218-224.

Ochs, G. R. (with Kleen), *Measurements of the wavelength dependence of scintillation in strong turbulence,* Letter to the editor, 117-119.

Ochs, G. R. (with Lawrence and Clifford), *Measurements of atmospheric turbulence relevant to optical propagation,* 79-83.

Ottersten, H. *Radar observations of the turbulent structure in shear zones in the clear atmosphere,* 246-251.

Sao, K. (with Taylor), *ELF attenuation rates and phase velocities observed from slow-tail components*, 24-31.

Schwiesow, R. L. (with Derr), *A Raman-scattering method for precise measurement of atmospheric oxygen balance,* Letter, 335-338.

Simmons, W. R. (with Hall and Wescott), *Acoustic echo sounding as related to air pollution in urban environments* (abstract), 229.

Simmons, W. R. (with Hall and Wescott), *Acoustic echo sounding of atmospheric thermal wind structure,* 199-217.

Simmons, W. R. (with Little and Wescott), *Acoustic echo-sounding measurement of temperature and wind fluctuations* (abstract), 228

Snider, J. B. *Recent results in ground-based sensing of atmospheric temperature profiles,* 323-332.

Stephenson, D. A. (with Strauch), *Water vapor spectrum near 600 GHz,* 393-394.

Sterling, D. L. (with Hooke and Cohen), *Traveling ionospheric disturbances observed at the magnetic equator,* 480-485.

Strand, O. N., *Numerical study of the gain pattern of a shielded acoustic antenna,* 13-18.

Strand, O. N., *Optimization of frequencies used in indirect sensing by inversion* (abstract), 333.

Strauch, R. G. (with Stephenson), *Water vapor spectrum near 600 GHz,* 393-394.

Strauch, R. G. (with Derr and Cupp), *Atmospheric temperature measurement using raman backscattering,* 358-362.

Strohbehn, J. W. (with Clifford), *The theory of microwave line-of-sight propagation through turbulent atmosphere,* 68-78.

Strohbehn, J. W. (with Lawrence), *A survey of clear-air propagation effects relevant to optical communications,* 84-106.

Taylor, W. L., *Review of electromagnetic radiation data from severe storms in Oklahoma during April 1970* (abstract), 334.

Taylor, W. L. (with Sao), *ELF attenuation rates and phase velocities observed from slow-tail components*, 24-31.

Thayer, G. D., *Radio reflectivity of tropospheric layers*, 60-66.

Thayer, G. D., *Reflections from elevated layers in transhorizon radio propagation*, 47-59.

Thayer, G. D. (with Bean and Hart), *World-wide characteristics of refractive index and climatological effects*, 412-424.

Thayer, G. D. (with Hart and Dougherty), *Local and diurnal variations in ground-based radio refractivity gradients at tropical locations* (abstract), 495.

Thayer, G. D. (with Little, Derr, Kleen, Lawrence, and Lhermitte), *Remote sensing of wind profiles in the boundary layer* (abstract), 380.

Travis, C. W. (with McFadden, Gilmer, and McGavin), *Water vapor flux measurements from ESSA aircraft*, 489-494.

Warner, B. D. (with Bean, McGavin, and Chadwick), *Preliminary results of utilizing the high resolution FM radar as a boundary layer probe*, 254-261.

Wescott, J. W. (with Simmons and Little), *Acoustic echo-sounding measurement of temperature and wind fluctuations* (abstract), 228.

Wescott, J. W. (with Beran, Hall, and Neff), *Application of an acoustic sounder to air pollution monitoring*, 218-224.

Wescott, J. W., (with Hall and Simmons), *Acoustic echo sounding of atmospheric thermal wind structure*, 199-217.

Wescott, J. W., (with Hall and Simmons), *Acoustic echo sounding as related to air pollution in urban environments* (abstract), 229.

Westwater, E. R., *Microwave determination of low altitude temperature profiles*, 312-322.

Whitehead, J. D. (with Hooke), *Divergence of ion velocity in the E-region due to vertical winds*, 477-479.

Willmarth, B. C. (with Beran), *Doppler winds from a bistatic acoustic sounder,* 182-198.

Willmarth, B. C. (with Beran and Little), *Acoustic doppler measurements of vertical velocities,* 225-227.

Wilson, D. A., *Doppler radar studies of boundary layer wind profile and turbulence in snow conditions,* 281-286.

Wilson, D. A., *The kinematic behavior of spherical particles in an accelerating environment* (abstract), 488.

For Further Reading

Bean, B. R., Comparisons of Remote and In-situ Measurements of meteorological Parameters and Processes, *Proceedings of NATO Advanced Study Institute,* April 15-22, 1971.

Bedard, A. J., and D. M. Caldwell, Instructions for the Operation of Correlator-Analyzer N4, ESSA Technical Manual #2, March 1970.

Cook, R. K., Propagation del Sonido en le Atmosfera, Part I, *Grupo de Acusticos Latin Americanos,* Vol. I, No. 4, 5-16, 1970.

Derr, V. E., and R. G. Strauch, Application of Lidar Remote Sensing Measurements of Boundary Layer Characteristics, *Proceedings of IUGG XV General Assembly,* August 2-15, 1971.

Hines, C. O., and W. H. Hooke, Discussion of Ionization Effects on the Propagation of Acoustic-Gravity Waves in the Ionosphere, *Journal of Geophysical Research, Space Physics* 75, No. 13, 2563-2568, 1970.

Schwiesow, R. L., Spurious Scattering Attributable to Sample Cell, *Raman Newsletter,* No. 18, 18.1-18.2, 1970.

Schwiesow, R. L., and N. L. Abshire, In-Cavity Laser Raman Spectroscopy, *Raman Newsletter,* No. 27, 24, 1971.

☆U. S. Government Printing Office: 1972-781-930/29 Region 8

PENN STATE UNIVERSITY LIBRARIES
A000072832813